Yun Ouyang
Min Xu
Li Yang
Yujie Ouyang
Editors

Advanced Graphic Communications, Packaging Technology and Materials

Springer

Lecture Notes in Electrical Engineering

Volume 369

About this Series

"Lecture Notes in Electrical Engineering (LNEE)" is a book series which reports the latest research and developments in Electrical Engineering, namely:

- Communication, Networks, and Information Theory
- Computer Engineering
- Signal, Image, Speech and Information Processing
- Circuits and Systems
- Bioengineering

LNEE publishes authored monographs and contributed volumes which present cutting edge research information as well as new perspectives on classical fields, while maintaining Springer's high standards of academic excellence. Also considered for publication are lecture materials, proceedings, and other related materials of exceptionally high quality and interest. The subject matter should be original and timely, reporting the latest research and developments in all areas of electrical engineering.

The audience for the books in LNEE consists of advanced level students, researchers, and industry professionals working at the forefront of their fields. Much like Springer's other Lecture Notes series, LNEE will be distributed through Springer's print and electronic publishing channels.

More information about this series at http://www.springer.com/series/7818

Yun Ouyang · Min Xu · Li Yang
Yujie Ouyang
Editors

Advanced Graphic Communications, Packaging Technology and Materials

Editors
Yun Ouyang
China Academy of Printing Technology
Beijing
China

Li Yang
China Academy of Printing Technology
Beijing
China

Min Xu
China Academy of Printing Technology
Beijing
China

Yujie Ouyang
China Academy of Printing Technology
Beijing
China

Printed on acid-free paper

Preface

Focusing on the printing and packaging field, "China Academic Conference on Printing and Packaging" is an international academic conference initiated by China Academy of Printing Technology and Beijing Institute of Graphic Communication in 2010. Co-hosted by China Academy of Printing Technology, Beijing Institute of Graphic Communication, and Hangzhou Dianzi University, and co-organized by Beijing Key Laboratory of New Technology of Printing and Packaging, China Academy of Printing Technology, School of Printing and Packaging Engineering of Beijing Institute of Graphic Communication, and School of Media and Design of Hangzhou Dianzi University, "2015 4th China Academic Conference on Printing and Packaging (CACPP 2015)" was held on Oct 22–24, 2015, at the International Education Training Center of Hangzhou Dianzi University.

By far, "China Academic Conference on Printing and Packaging" and its series of events have been held for six sessions. Due to the influence of the sponsors, academic foresight in the keynotes, and the active participation among scholars, the conference has become the most influential academic exchange activity in printing and packing field in China.

In 2015, the Chinese economic development has entered into a new period. The printing and packaging industry in China has maintained an annual growth at the rate of 10 %. By 2014, the gross output value in printing industry has topped to RMB 1133.4 billion, increasing by 9.0 %. In the meantime, the gross output value of the packaging industry has exceeded RMB 1480 billion, raking the second worldwide. In normal development period, enhancing the capability of independent innovation in enterprises, achieving the transforming and upgrading in industries have been considered as major goals. Therefore, as an academic exchange platform for scientific research and innovation, "China Academic Conference on Printing and Packaging" made great contribution in promoting communication between Chinese scholars and their international peers, sharing the advanced international achievements in this field, as well as discussing development trend of science and technology.

In accordance with the purpose of the conference, "2015 4th China Academic Conference on Printing and Packaging" focused on new manufacturing technology, green technology, and advanced material technologies. We invited Professor Yadong Yin from University of California, Professor Dongming Lu from Zhejiang University, Dr. Jose Maria Lagaron from the Institute of Agrochemistry and Food Technology of the Spanish Council for Scientific Research, and other internal famous scholars to make keynote speeches on structural color of photonic crystal, digital protection of cultural heritage, digital publishing service, and antibiosis food packaging. All the participants shared the latest research trends and achievements on optical and color science, cultural relics and digital storage, food safety, and so on.

The conference received 238 papers this year, including 4 keynote speeches and 234 oral presentations, among which 130 were selected to be published in *Lecture Notes in Electrical Engineering* (*LNEE*) (ISSN: 1876-1100) by Springer.

Here, we greatly acknowledge all the organizations that offered great support for the conference and they are as follows: Printing Technology Association of China, Chinese Society for Imaging Science and Technology, School of Printing and Packaging of Wuhan University, College of Communication and Art Design of University of Shanghai for Science and Technology, College of Light Industry and Food Sciences of South China University of Technology, Light Industry College of Harbin University of Commerce, College of Mechanical and Energy Engineering of Ningbo Institute of Technology of Zhejiang University, School of Biological and Chemical Engineering/School of Light Industry of Zhejiang University of Science and Technology, College of Light Industry Science and Engineering of Nanjing Forestry University, College of Printing and Packaging Engineering of Qilu University of Technology, College of Materials Science and Engineering of Beijing University of Chemical Technology, Department of Graphic Communication Arts of College of Communications, National Taiwan University of Arts, Faculty of Printing, Packaging Engineering and Digital Media Technology of Xi'an University of Technology, Zhengzhou Institute of Surveying and Mapping, College of Packaging and Printing Engineering of Tianjin University of Science and Technology, School of Mechanical Engineering of Jiangnan University, School of Light Industry and Chemical Engineering of Dalian Polytechnic University, College of Engineering of Qufu Normal University, College of Light Industry and Energy of Shaanxi University of Science and Technology, School of Packaging and Material Engineering of Hunan University of Technology, School of Media and Communication of Shenzhen Polytechnic, School of Food and Chemical Engineering of Beijing Technology and Business University, College of Material Science and Engineering of Zhengzhou University, National Taiwan University of Arts, University of California, College of Computer Science and Technology of Zhejiang University, and China Academy of Printing Technology.

We would like to express our gratitude to the 46 experts from China, Germany, Britain, and Japan for reviewing and recommending papers for the conference with strict standards.

We also thank Springer Publishing Company for offering us an international platform for publishing.

We look forward to our reunion at the next China Academic Conference on Printing and Packaging.

September 2015

Edited by
China Academy of Printing Technology

Contents

Part II   Image Processing Technology

Part IV Printing Engineering Technology

Part VII   Paper and Related Technology

Part IX   Ink and Related Technology

2015 4th China Academic Conference on Printing and Packaging

Date October 22–24, 2015
Location Shujiang Hotel, Hangzhou, China

Sponsors
China Academy of Printing Technology
Beijing Institute of Graphic Communication
Hangzhou Dianzi University

Supports
China Printing Technology Association
Chinese Society for Imaging Science and Technology

Organizers
Beijing Key Laboratory of Packaging and Printing New Technology, China Academy of Printing Technology
School of Printing and Packaging Engineering, Beijing Institute of Graphic Communication
School of Media and Design, Hangzhou Dianzi University
Printing Technology Professional Committee, Chinese Society for Imaging Science and Technology

Co-Sponsors
School of Printing and Packaging, Wuhan University
College of Communication and Art Design, University of Shanghai for Science and Technology
College of Light Industry and Food Sciences, South China University of Technology
Light Industry College, Harbin University of Commerce

College of Mechanical and Energy Engineering, Ningbo Institute of Technology, Zhejiang University

School of Biological and Chemical Engineering/School of Light Industry, Zhejiang University of Science and Technology

College of Light Industry Science and Engineering, Nanjing Forestry University

College of Printing and Packaging Engineering, Qilu University of Technology

College of Materials Science and Engineering, Beijing University of Chemical Technology

Department of Graphic Communication Arts, College of Communications, National Taiwan University of Arts

Faculty of Printing, Packaging Engineering and Digital Media Technology, Xi'an University of Technology

Zhengzhou Institute of Surveying and Mapping

College of Packaging and Printing Engineering, Tianjin University of Science and Technology

School of Mechanical Engineering, Jiangnan University

School of Light Industry & Chemical Engineering, Dalian Polytechnic University

College of Engineering, Qufu Normal University

College of Light Industry and Energy, Shaanxi University of Science & Technology

School of Packaging & Material Engineering, Hunan University of Technology

School of Media and Communication, Shenzhen Polytechnic

School of Food and Chemical Engineering, Beijing Technology and Business University

College of Material Science & Engineering, Zhengzhou University

Conference Executive Committee

Chairman
Wang Yongsheng (President of Beijing Institute of Graphic Communication)
Chen Yan (President of China Academy of Printing Technology)
Xue Anke (President of Hangzhou Dianzi University)

Vice Chairman
Xu Wencai (Vice President of Beijing Institute of Graphic Communication)
Chu Tingliang (Vice President of China Academy of Printing Technology)
Wang Qiang (Dean of School of Media and Design, Hangzhou Dianzi University)

Honorary Chairman
Qu Desen (Former President of Beijing Institute of Graphic Communication)
Pu Jialing (Chairman of Chinese Society for Imaging Science and Technology)

Conference Academic Committee

Chairman

Li Deren (Academician of Chinese Academy of Sciences, Academician of China Engineering Academy, Professor of Wuhan University, Director of State Key Laboratory of Information Engineering in Surveying, Mapping and Remote)

Vice Chairman

Ni Guangnan (Academician of China Engineering Academy, Researcher of Institute of Computing Technology Chinese Academy of Sciences, Board Chairperson of Chinese Information Processing Society of China)

Chen Kefu (Academician of China Engineering Academy, Professor of South China University of Technology, Director of Academic Committee of State Key Laboratory of Pulp and Paper Engineering)

Zhuang Songlin (Academician of China Engineering Academy, Director and Professor of School of Optical-Electrical and Computer Engineering of University of Shanghai for Science and Technology, Optical Expert)

Lu Bingheng (Academician of Chinese Academy of Engineering, Professor of Xi'an Jiaotong University, Director of the National Engineering Research Center of Rapid Manufacturing)

Commissioners

Andreev Yuri (Head of Moscow State University of Printing Arts)

Bigger Stephen W. (Doctor, Professor, Vice President of Faculty of Engineering and Science of Victoria University)

Cao Congjun (Doctor, Professor of Xi'an University of Technology, Master student supervisor)

Cao Guorong (Professor of Beijing Institute of Graphic Communication, Master student supervisor)

Chen Ping (Doctor, Doctoral supervisor)

Chen Guangxue (Doctor, Professor of South China University of Technology, Doctoral supervisor)

Chen Hong (Professor of Beijing Institute of Graphic Communication)

Chen Yunzhi (Doctor, Professor of Tianjin University of Science and Technology, Doctoral supervisor)

Chu Tingliang (Professor of China Academy of Printing Technology, Master student supervisor)

Chu Fuqiang (Doctor, Professor of Qilu University of Technology, Master student supervisor)

Gao De (Professor of Ningbo Institute of Technology, Zhejiang University, Master student supervisor)

Green Phil (Professor of Colour Imaging, London College of Communication)

Hersch Roger D. [Doctor, Professor of Computer Science and Head of the Peripheral Systems Laboratory at the Ecole Polytechnique Fédérale de Lausanne (EPFL)]

Hsieh Yungcheng (Professor of Taiwan University of Arts)

Hoffmann-Walbeck Thomas (Professor of the Faculty of Print and Media Technology, Stuttgart University of Media)

Jin Guobin (Professor of Shanghai University, Vice Director of China Packaging Education Committee)

Kitamura Takashi (Doctor, Professor of Graduate School of Advanced Integration Science, Chiba University)

Kuang Shijun (Consultant Engineer of China National Pulp and Paper Research Institute, Chief Engineer)

Lagaron Jose Maria (Doctor, Professor, Leader and Founder of the Group Novel Materials and Nanotechnology for Food Related Applications at the Institute of Agrochemistry and Food Technology of the Spanish Council for Scientific Research)

Lee Benjamin (Professor, Director of Department of Technology, California State University)

Li Houbin (Doctor, Professor of Wuhan University, Doctoral supervisor)

Li Luhai (Doctor, Professor of Beijing Institute of Graphic Communication, Master student supervisor)

Li Zhijian (Doctor, Professor of Shaanxi University of Science & Technology, Doctoral supervisor)

Liu Haoxue (Doctor, Professor of Beijing Institute of Graphic Communication, Master student supervisor)

Liu Zhen (Professor of University of Shanghai for Science and Technology, Doctoral supervisor)

Lu Dongming (Doctor, Professor of Zhejiang University, Doctoral supervisor)

Luo M. Ronnier (Professor, Director of the Department of Color Science, University of Leeds)

Ma Xiufeng (Professor of Qufu Normal University, Master student supervisor)

Piergiovanni Luciano (Professor of the Department of Food, Environmental and Nutritional Sciences, Faculty of Agricultural and Food Sciences, University of Milan)

Poovarodom Ngamtip (Doctor, Associate Professor of Department of Packaging and Materials Technology of Faculty of Agro-Industry, Kasetart University)

Pu Jialing (Doctor, Professor of Beijing Institute of Graphic Communication, Doctoral supervisor)

Ren Penggang (Doctor, Associate Professor of Xi'an University of Technology, Master student supervisor)

Shi Ruizhi (Doctor, Professor of Zhengzhou Institute of Surveying and Mapping, Doctoral supervisor)

Sun Zhihui (Professor of Harbin University of Commerce, Doctoral supervisor)

Tang Shaoyan (Professor of Hunan University of Technology, Master student supervisor)

Tang Zhengning (Doctor, Professor of Jiangnan University, Master student supervisor)

Teleman Anita (Doctor, Research Manager of Printing Solutions at the Research Institute Innventia, Sweden)

Teng Yuemin (Professor of Shanghai Publishing and Printing College)

Urban Philipp (Head of Emmy-Noether Research Group, Institute of Printing Science and Technology, Technische Universität Darmstadt)

Vogl Howard E. (Visiting Professor of Rochester Institute of Technology)

Wan Xiaoxia (Doctor, Professor of Wuhan University, Doctoral supervisor)

Wang Haiqiao (Doctor, Professor of Beijing University of Chemical Technology, Doctoral supervisor)

Wang Jianqing (Professor of Tianjin University of Science and Technology, Doctoral supervisor)

Wang Lijie (Professor of Shenzhen Polytechnic)

Wang Qiang (Doctor, Professor of Hangzhou Dianzi University, Doctoral supervisor)

Wang Yiqing (Doctor, Professor of Xi'an Jiaotong University)

Wei Yuhchang (Professor of Chinese Culture University)

Wei Xianfu (Doctor, Professor of Beijing Institute of Graphic Communication, Doctoral supervisor)

Xie Punan (Professor of Beijing Institute of Graphic Communication)

Xin Xiulan (Doctor, Professor of Beijing Technology and Business University, Master student supervisor)

Xu Jinlin (Professor of Xi'an University of Technology)

Xu Wencai (Professor of Beijing Institute of Graphic Communication, Doctoral supervisor)

Yao Haigen (Professor of Shanghai Publishing and Printing College)

Yang Bin (Doctor, Researcher of Peking University)

Yin Yadong (Doctor, Professor of University of California, Riverside)

Zhou Shisheng (Doctor, Professor of Xi'an University of Technology, Doctoral supervisor)

Zhao Xiuping (Professor of Tianjin University of Science and Technology, Master student supervisor)

Zhang Haiyan (Professor of Xi'an University of Technology, Master student supervisor)

Zou Yingquan (Doctor, Professor of Beijing Normal University, Doctoral supervisor)

Reviewers

Cao Congjun (Doctor, Professor of Xi'an University of Technology)

Cao Shaozhong (Doctor, Professor of Beijing Institute of Graphic Communication)

Chen Guangxue (Doctor, Professor of South China University of Technology)

Chen Yunzhi (Doctor, Professor, Dean of College of Packaging & Printing Engineering of Tianjin University of Science and Technology)

Chu Fuqiang (Doctor, Professor of Qilu University of Technology)

Chu Tingliang (Professor, Vice President of China Academy of Printing Technology)

Fang Yi (Doctor, Teacher of Beijing Institute of Graphic Communication)

Fu Yabo (Doctor, Associate Professor of Beijing Institute of Graphic Communication)

Gao Shanshan (Doctor, Associate Professor of Qufu Normal University)

Geng Jing (Doctor, Teacher of Xi'an University of Technology)

He Minghui (Doctor of South China University of Technology)

Huang Junyan (Associate Professor of Dalian Polytechnic University)

Huang Peiqing (Associate Professor of Beijing Institute of Graphic Communication)

Huang Zhen (Doctor, Professor of Tianjin University of Commerce)

Jin Yang (Doctor, Professor of Beijing Institute of Graphic Communication)

Jiang Xiaoshan (Doctor, Engineer of China Academy of Printing Technology)

Li Dongli (Doctor, Senior Engineer of Beijing Institute of Graphic Communication)

Li Houbin (Doctor, Professor of Wuhan University)

Li Luhai (Professor of Beijing Institute of Graphic Communication)

Li Shi (Teacher of Hangzhou Dianzi University)

Li Zhijian (Doctor, Professor of Shaanxi University of Science & Technology)

Li Zhijiang (Doctor, Associate Professor of Wuhan University)

Liu Haoxue (Doctor, Professor of Beijing Institute of Graphic Communication)

Liu Zhuang (Doctor, Teacher of Harbin University of Commerce)

Lin Maohai (Associate Professor of Qilu University of Technology)

Lu Lixin (Doctor, Professor of Jiangnan University)

Luo Rubai (Doctor, Associate Professor of Xi'an University of Technology)

Luo M. Ronnier (Doctor, Professor of the Department of Color Science, University of Leeds)

Ma Yongjun (Doctor, Professor of School of Computer Science and Information Engineering (SCSIE), Tianjin University of Science and Technology)

Ouyang Yun (Vice Chief Engineer of China Academy of Printing Technology)

Qi Wenfa (Engineer of Institute of Computer Science and Technology, Peking University)

Shi Ruizhi (Doctor, Professor of Zhengzhou Institute of Surveying and Mapping)

Wang Haiqiao (Doctor, Professor of Beijing University of Chemical Technology)

Wang Hui (Teacher of Hangzhou Dianzi University)

Wang Qiang (Doctor, Professor of Hangzhou Dianzi University)

Wang Yigang (Doctor, Professor of Hangzhou Dianzi University)

Wei Xianfu (Doctor, Professor of Beijing Institute of Graphic Communication)

Xie Dehong (Doctor, Teacher of Nanjing Forestry University)

Xin Xiulan (Doctor, Professor of Beijing Technology and Business University)

Xu Hongwei (Doctor, Professor of Xi'an University of Technology)

Xu Zhuofei (Doctor, Teacher of Xi'an University of Technology)

Zhang Fazhong (Doctor, Engineer of China Academy of Printing Technology)

Zhang Hanyue (Professor of Tianjin University of Science and Technology)

Zhang Ruijing (Doctor, Teacher of Hangzhou Dianzi University)

Zheng Yuanlin (Doctor, Vice Professor of Xi'an University of Technology)

Zhu Ming (Doctor, Vice Professor of Henan Institute of Engineering)

Part I
Color Science and Technology

Chapter 1
Comparing Skin Colours Between Different Skin Groups

Yuzhao Wang, Ming Ronnier Luo, Xiaoyu Liu and Haiyan Liu

Abstract This study investigates the basic characteristic of human skin. 47 subjects from 4 groups (Chinese, Sub-Asian, Caucasian and the Dark) were recruited. All the skin colours were measured in terms of spectral reflectance using a d:8° spectrophotometer. And they included eight parts of body locations in total: forehead, right cheek, left cheek, hand back, fist back, palm, inner forearm and outer forearm. The data revealed certain pattern for human skin colour. All the data of the four skin colour groups fit a particular curve in the $L^* - C_{ab}^*$ plane, and that is very similar to the definition of 'Whiteness' and 'Blackness' as defined by NCS, and 'Depth' and 'Vividness' as defined by Berns. The result also showed that Chinese group and Caucasian group had very similar pattern: the sunburnt part of the skin had lower Lightness value and higher Chroma value, or lower Whiteness. However, for the Dark skin group, the data show reversed pattern: sunburnt area will have lower Lightness value and lower Chroma value, and all the colours were located on the 'Blackness' scale. The area where the 'Whiteness' and 'Blackness' scales cross each other is the region for Sub-Asian, where they have the highest Chroma values. The difference of different skin colour groups also appears in the shape of spectral reflectance. Dark skin colour not only means lower amplitude, but also has a flatter curve shape, while for light skin colour, the spectral reflectance has a very clear 'W' shape. 'W' shape reflects the feature of human skin spectral reflectance, and that is the result of the absorption and reflection of the haemoglobin and melanin. Future work includes the study for the reason of the particular pattern shown in $L^* - C_{ab}^*$ plane and its application in various areas.

Y. Wang · M.R. Luo (✉)
State Key Laboratory of Modern Optical Instrumentation, Zhejiang University,
Hangzhou, China
e-mail: m.r.luo@leeds.ac.uk

M.R. Luo
School of Design, University of Leeds, Leeds, UK

X. Liu
College of Science, Harbin Engineering University, Harbin, China

H. Liu
Thousand Lights Lighting (Changzhou) Limited, Changzhou, China

1.1 Introduction

Skin colour is an important subject in many research areas. In cosmetic area, different skin colour types suit different products. For one thing, different nations have different skin tones and skin conditions; for another, different nations prefer different skin tones, so different cosmetic products are necessary. For example, Asian people such as Chinese, Japanese and Korean, they prefer white skin tone, while European prefers sunburnt skin tone, which appears to be healthier. In image field, when talking about human images, the most important topic may be the skin colour. How to polish the colour of the images or how to adjust the colour of the images to meet people's preference are some important points we care about. But, first of all, it is necessary to find out the skin colour difference between different nations and reveal the basic characteristics of it. In this chapter, we try to dig out the secret of skin colour from a set of skin colour database captured from 47 subjects worldwide. The results show that skin colour has some very clear and special pattern.

1.2 Experiments

In this experiment, 47 subjects were recruited. The general information of the 47 subjects is given in Table 1.1. The 47 subjects were from many different countries, and considering their skin conditions, they are divided into 4 groups: Chinese, Caucasian, Sub-Asian and Dark, respectively. For each subject, eight locations of the body were measured: forehead, right cheek, left cheek, hand back, fist back, palm, inner forearm and outer forearm. Subjects were required to be in good skin condition before the experiment. All the chosen subjects did not have any skin disease or other problems. And also, they were not exposed to the sunburnt excessively before the experiment. During the experiment, no makeup was allowed, and subjects were asked to rinse their face and arm before measurement.

A d:8° geometry spectrophotometer was used to capture the reflectance data of all the skin. The aperture of the device was about 1 cm, which was sufficient for skin measurement. The mean colour difference of the mean (MCDM) of the device is shown in Fig. 1.1. Figure 1.1 shows the repeatability of the measurement (four repetitions for one location). The results verified that the validity of the measurement data formed a baseline for the following data analysis.

Table 1.1 The basic information of 47 subjects. The average age of all the 47 subjects is 25.4

	Number	Male	Female	Average age
Chinese	20	10	10	24.3
Caucasian	10	3	7	22.9
Sub-Asian	10	10	0	28.5
Dark	7	7	0	27.8
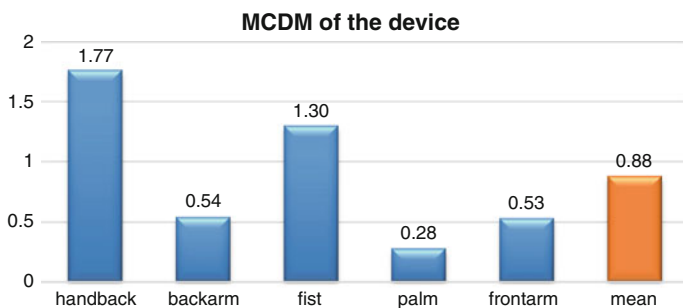
Fig. 1.1 The MCDM of the device, the average MCDM of the five locations is about 0.88. The repeatability of hand back and fist back is worst among all the measurement positions

1.3 Data Analysis and Result

All the data measured by d:8° spectrophotometer (exclude specular light) is in the form of spectral reflectance. For the convenience of analysis, the CIE XYZ and $L^*a^*b^*$ values (using D65 illuminant and 1964 colour-matching functions) were calculated from the spectral reflectance. Figure 1.2 plots measured skin colours of four groups separately on $C_{ab}^* - L^*$ charts. Four charts show very different patterns.

It can be seen that Chinese and Caucasian had similar pattern, i.e. all the dots distribute near one line. It shows a clear trend that all lower Lightness samples have higher Chroma values, and vice versa. This line is close to the 'Whiteness' defined by NCS [1] and 'Depth' defined by Berns [2] (see in Fig. 1.3). 'Whiteness' describes the degree of white content of a sample. A whiter colour does not only mean a higher Lightness value, but also a lower Chroma value, and this is truly reflected in the case of skin colour. Those whiter colours are mostly the colour of the least sunburnt areas such as inner forearm and palm.

However, for the Sub-Asian and the Dark groups, who had darker skin colour, the pattern is completely different. The Sub-Asian group data distribute near a straight line having a constant Chroma value, while the pattern of the Dark skin group is the opposite to that of Chinese and Caucasian. Apparently, for the Dark skin group, lower Lightness means lower Chroma values, vice versa. The 'line' of the Dark skin group is close the definition of 'Blackness' and 'Vividness'. If we plot all the data in one chart (see Fig. 1.3), all the data are located around one curve, which looks like a triangle. And that is exactly the shape of 'Whiteness' and
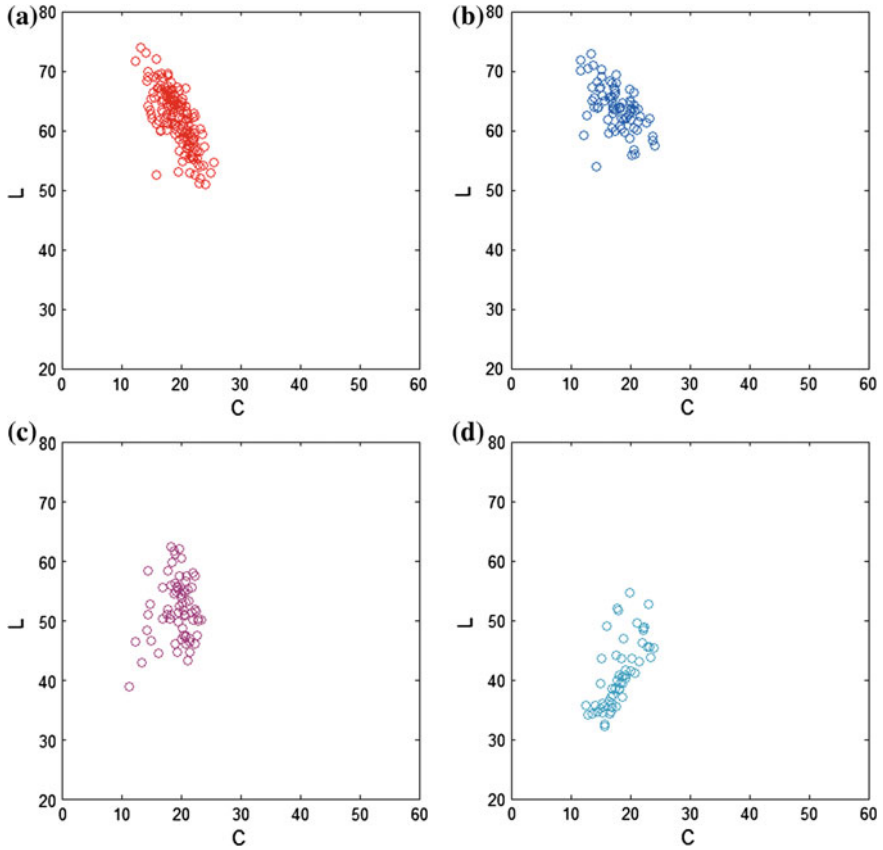
Fig. 1.2 Four skin groups data on $C–L^*$ charts **a** Chinese group data, **b** Caucasian group data, **c** Pakistani group data, and **d** Dark group data

'Blackness' or 'Depth' and 'Vividness'. Therefore, 'Whiteness' and 'Blackness' or 'Depth' and 'Vividness' are better description of human skin colour than CIELAB L^*, a^*, b^*, C^*, h values.

The colour difference of the four skin colour groups can also be found from their reflectance. Figure 1.4 plots the average reflectance of the four skin groups. The reflectance of Chinese and Caucasian was nearly overlapped. Only that Caucasian reflectance amplitude was a little higher, which means lighter or whiter the colour will be. Sub-Asian reflectance amplitude was lower than those two, and the Dark group had the lowest amplitude. That is consistent with the colour condition of the four groups. Besides the amplitude, the shape of the reflectance also differs. The reflectance of Chinese and Caucasian had a very clear 'W' shape, which was the result of melanin and haemoglobin [3]. As the skin become darker, the 'W' shape becomes less clear (see the reflectance of Sub-Asian and Dark). Darker skin means more melanin; hence, less light can penetrate the skin surface, so that
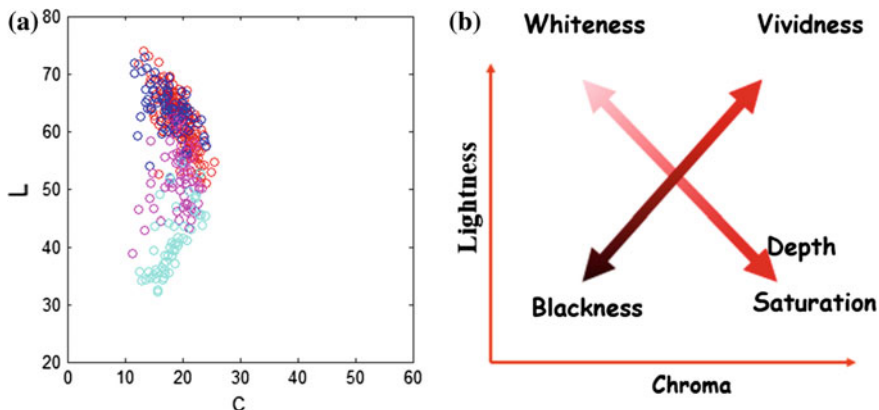
Fig. 1.3 **a** All the data of four skin colour groups on one C–L^* chart, **b** the definition of Whiteness, Blackness, Depth and Wividness found by Berns
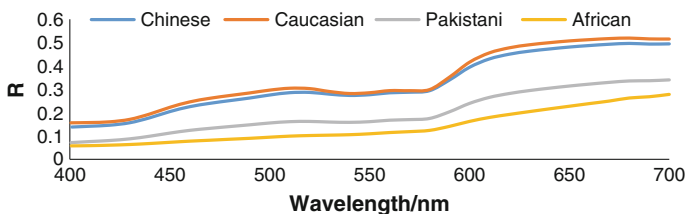
Fig. 1.4 The mean reflectance of four skin colour groups. There is a 'W' pattern in the band from 500 to 600 nm

less reflected light of the deeper skin layer reaches the measurement device. The 'W' shape of the skin contains the detail of deeper skin layer, and the variation of human skin colour is the reason of the special distribution on $C_{ab}^* - L^*$ chart. And that needs further investigation.

1.4 Conclusions

This chapter reported the difference of different skin colour groups. In total, 47 subjects participated in the experiment and each subject's eight body locations were measured. The result showed that human skin colour behaved in the correlates of 'Whiteness' and 'Blackness', or 'Depth' and 'Vividness' perceptions: Chinese and Caucasian skin colours lie in the 'Whiteness' or 'Depth' direction, while Dark skin colours lie in the 'Blackness' or 'Vividness' direction. The Sub-Asian group distributes at the cross-point of the two scales and this group has the highest Chroma

values, in other words the most saturated skin colour. This finding could be useful for developing cosmetic products or image processing.

The reflectance of the four skin colour groups is also very different. The reflectance of the lighter skin colour is more complicated and it contains more details of the skin condition.

References

1. Luo, M. R., Cui, G., & Cho, Y. J. (2013). The NCS-like colour scales based on CIECAM02. In The 21th Color and Imaging Conference (pp. 177–179).
2. Berns, R. S. (2013). Extending CIELAB: Vividness, V_{ab}^*, depth, D_{ab}^*, and clarity, T_{ab}^*. *COLOR Research and Application, 39*(4), 322–330.
3. Angelopoulu, E. (2001). Understanding the color of human skin. *Human Vision and Electronic Imaging, 4299*, 243–251.

Chapter 2
The Colour Shifting of Measuring Human Skin Colour Use Different Instruments

**Mengmeng Wang, Ming Ronnier Luo, Kaida Xiao
and Sophie Wuerger**

Abstract Human skin colour information is important for the cosmetic industries and hospitals to develop a skin product and suggest an appropriate treatment. Human skin has multi-layered structures with non-flat surface and the colour of the human skin is unevenly distributed over the body. It is difficult to get skin colour information both exhaustively and precisely. Different ethnicities exhibit significantly different skin colour. To supply the data to the CIETC 1-92 Skin Colour Database and to achieve successful colour reproduction of skin colours on multimedia, two most widely used instruments, tele-spectroradiometers (TSRs) and spectrophotometers (SPs), were employed to collect large numbers of human skin colour, including 188 subjects from four ethnic groups (Oriental Caucasian, South Asian and African). Five or ten locations from each subject were measured. At each location, three repeated measurements performed by using both instruments and their mean values were used as the measurement results. The measurement results were reported using CIELAB colour system, in terms of lightness, chroma and hue. The colour distribution between different locations of different ethnic groups was studied by plotting the data points in a^*b^* and $L^*C^*_{ab}$ planes. Systematic trends were found between different ethnicities and instruments. The result shows a significant trend of the colour shifting between different ethnicities and instruments.

Keywords Skin colour · Colour shifting · Tele-spectroradiometer · Spectrophotometer

M. Wang · M.R. Luo (✉)
School of Design, University of Leeds, Leeds LS29JT, UK
e-mail: M.R.Luo@leeds.ac.uk

K. Xiao · S. Wuerger
School of Psychological Science, University of Liverpool, Liverpool L697ZX, UK

2.1 Introduction

The colour of skin is a significant feature of human. It can reflect ethnic, health and habitat environment. It is also a critical factor for reproducing human facial image in printing and display industry. For diagnosing cutaneous disease, the skin colour is closely related to the effectiveness of the treatment. For the skin colour measurement, CIE colorimetry has been widely used for more than 30 years to provide objective measurements for human skin colour, which is of great importance for the cosmetic industry and hospitals to develop a skin product and suggest an appropriate treatment. Tele-spectroradiometers (TSRs) and spectrophotometers (SPs) are two instruments that were widely used for measuring skin colour in vivo. For example, TSRs are frequently used in cosmetic industry for developing a skin colour chart and for evaluating skincare products [1]. SPs are sometimes used for diagnosing skin disease symptom [2–6]. The measurement results are frequently reported using CIELAB colour system, in terms of lightness, chroma and hue. Different from other materials, i.e. paper, glass and textile, human skin has a multi-layer structure with non-flat and non-uniform colour surface. The pressure, measuring field size and measuring geometry can affect the measurement results. Although large amounts of work on human skin colour measurements were based on these two instruments, the research of the uncertainty of the measurement by using these two instruments to measure human skin colour was limited.

2.2 Objectives

These skin colour data were part of the Leeds Liverpool Skin colour database (LLSC) which is part of the CIE TC1-92 Skin Colour Database. A large-scale research project was set up between the University of Leeds and the University of Liverpool to measure and to collect skin colours from different ethnicities and using different instruments. The aim of this project was to investigate the uncertainty in skin colour measurements, such as ethnicity, age, gender and body location. This chapter presents a study, which aimed to investigate the uncertainty of using a SP (Konica Minolta CM700d spectrophotometer, referred as CM700d) and a TSR (Photo research inc. PR-650 Spectra Scan, referred as PR650) to measure skin colour. The colour shifting between different ethnicities and between these two instruments was evaluated.

2.3 Methodology

One hundred and eighty-eight subjects, including 86 Oriental, 79 Caucasian, 13 South Asian and 10 Africa with both genders, were measured by CM700d and PR650. For each subject, ten locations—forehead (FH), cheek, cheekbone (CB),

neck, chin, inner forearm (IF), outer forearm (OF), back of hand (BH), nose tip
(NT) and fingertip (FT)—were measured by CM700d and five locations—forehead
(FH), cheek, cheekbone (CB), neck and back of hand (BH)—were measured by
PR650. The measurement locations were selected based on the previous research
[7, 8]. Each location was measured three times using both instruments and the
average of these three repeat measurements was used as the measurement result.
A specially build imaging light booth from Verivide was used to provide illumi-
nation for the PR650. This imaging light booth is painted with natural paint inside
and proved D65 diffused illumination. The PR650 was placed behind the illumi-
nation to avoid project shadow on the subject. The measurement results, the spectral
reflectance (CM700d) and spectral power distribution (PR650), were transformed to
CIELAB values by using CIE 1931 Standard Colorimetric Observer, as both
instruments' measuring angles were set in 2^O, and the $X_0 Y_0 Z_0$ which gained form
the SPD measured inside the imaging light booth. This SPD was measured by using
the PR650 at the same position as the skin colour measurement. The equation set
list below was used to gain the $X_0 Y_0 Z_0$.

$$
\begin{aligned}
Y &= \frac{\mathrm{SPD_w}}{R_\mathrm{w}\%} \times \bar{y}(\lambda) \\
X_0 &= \sum \frac{\frac{\mathrm{SPD_w}}{R_\mathrm{w}\%} \times \bar{x}(\lambda)}{Y} \times 100 \\
Z_0 &= \sum \frac{\frac{\mathrm{SPD_w}}{R_\mathrm{w}\%} \times \bar{z}(\lambda)}{Y} \times 100 \\
Y_0 &= 100
\end{aligned}
\tag{2.1}
$$

where $\mathrm{SPD_w}$ is the spectral power distribution of a white chart measured by the
PR650. The $R_\mathrm{w}\%$ is the spectral reflectance of the same white chart that is measured by
CM700d. $\bar{x}(\lambda), \bar{y}(\lambda), \bar{z}(\lambda)$ are the CIE 1931 Standard Colorimetric Observer (D65, 2°).

The colour shifting between different ethnic groups and instruments was
investigated through the $\Delta E_{ab}^*, \Delta L^*, \Delta H_{ab}^*, \Delta C_{ab}^*$ and Δh_{ab} values and the plots of
the average CIELAB on $a^* b^*$ and $L^* C_{ab}^*$ planes. $\Delta E_{ab}^*, \Delta L^*, \Delta H_{ab}^*, \Delta C_{ab}^*$ and Δh_{ab}
were calculated, which is calculated using the formulas as listed in Eq. (2.2). The
average of each ethnic group's each location's CIELAB was used to represent the
colour of each location of each group.

$$
\begin{aligned}
\Delta E_{ab}^* &= \sqrt{\left(L_{\mathrm{PR}}^* - L_{\mathrm{CM}}^*\right)^2 + \left(a_{\mathrm{PR}}^* - a_{\mathrm{CM}}^*\right)^2 + \left(b_{\mathrm{PR}}^* - b_{\mathrm{CM}}^*\right)^2} \\
\Delta L^* &= L_{\mathrm{PR}}^* - L_{\mathrm{CM}}^* \\
\Delta C_{ab}^* &= C_{ab,\mathrm{PR}}^* - C_{ab,\mathrm{CM}}^* \\
\Delta H_{ab}^* &= \sqrt{\left(\Delta E_{ab}^*\right)^2 - \left(\Delta L^*\right)^2 - \left(\Delta C_{ab}^*\right)^2} \\
\Delta h_{ab} &= h_{ab,\mathrm{PR}} - h_{ab,\mathrm{CM}}
\end{aligned}
\tag{2.2}
$$

2.4 Result and Analysis

The colour shift was investigated through the colour difference between two instruments at each ethnic group measurement results, as listed in Table 2.1. For each group, the mean CIELAB values of five locations, including forehead, cheek, cheekbone, neck and back of hand, which measured by both instruments, were averaged and compared. $\Delta E_{ab}^*, \Delta L^*, \Delta H_{ab}^*, \Delta C_{ab}^*$ and Δh_{ab} were calculated to indicate the colour shifting of these two instruments' measurement results in lightness, chroma and hue. From the data listed in Table 2.1, the average colour difference between these two instruments is about 2.18 ΔE_{ab}^*, which is significant. The PR650 measurement results had higher chroma and lower lightness than those of the CM700d for all ethnic groups except the African, as ΔL^* and ΔC_{ab}^* of these three groups were appear as positive and negative, respectively. From Δh_{ab}, we can find that their hue angles agree well with each other. The average hue difference between these two instruments of these four ethnic groups is about 0.4. The average hue angle difference between these two instruments' measurement results is about 2°.

In Figs. 2.1a and 2.2b, the four ethnic groups' average CIELAB gained from ten locations measured by CM700d in a^*b^* and $L^*C_{ab}^*$ planes, respectively, is plotted. It can be seen that African group has the lowest lightness than the others. The Caucasian group showed the highest lightness while the African group exhibits the lowest. The other three groups had similar hue angle and chroma. The error bar plot in Fig. 2.1 is the standard deviation of ten measurement locations of each ethnic group. From the error bar, we can see the colour shifting between different measurement locations were more significant in hue for Oriental, Caucasian and South Asian Groups, as shown in Fig. 2.1a. For the African group, the colour shifting between different locations appears most significantly in lightness.

Figure 2.2 shows the PR650's measurement results of four ethnic groups, which average from four locations. Comparing the measurement results from CM700d, the distribution of four ethnic groups' measurement results is similar to the measurement results from CM700d, as shown in Fig. 2.1. However, the chroma difference between African group and other three groups is more significant in the PR650's measurement results than the results from the CM700d. The error bar in Fig. 2.2 is the standard deviation of five locations of each ethnic group. Comparing to the CM700d's plot, as shown in Fig. 2.1, the variation of the PR650's results was less than the CM700d's, as there are only five locations measured by PR650.

Table 2.1 The colour difference $(\Delta E_{ab}^*, \Delta L^*, \Delta H_{ab}^*, \Delta C_{ab}^*$ and $\Delta h_{ab})$ of four ethnic groups measured by the CM700d and PR650

	ΔE_{ab}^*	ΔL_{ab}^*	ΔH_{ab}^*	ΔC_{ab}^*	Δh_{ab}
Oriental	2.31	2.11	0.35	−0.88	−0.110
Caucasian	1.85	1.56	0.65	−0.74	−1.980
South Asian	1.50	1.35	0.38	−0.54	0.690
African	3.05	2.68	0.25	1.44	−1.530

(a)

(b)
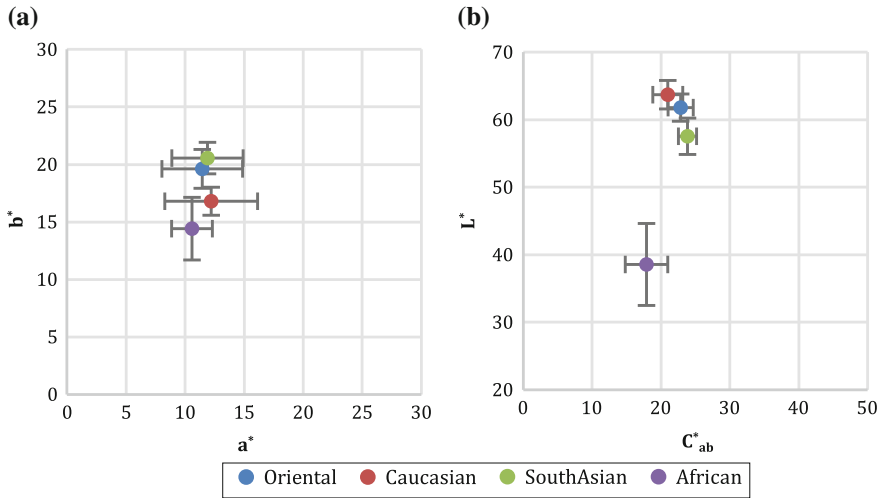
Fig. 2.1 The mean CIELAB values of ten locations of each ethnic group measured by CM700d in
a a^*b^* plane and **b** $L^*C^*_{ab}$ plane

(a)

(b)
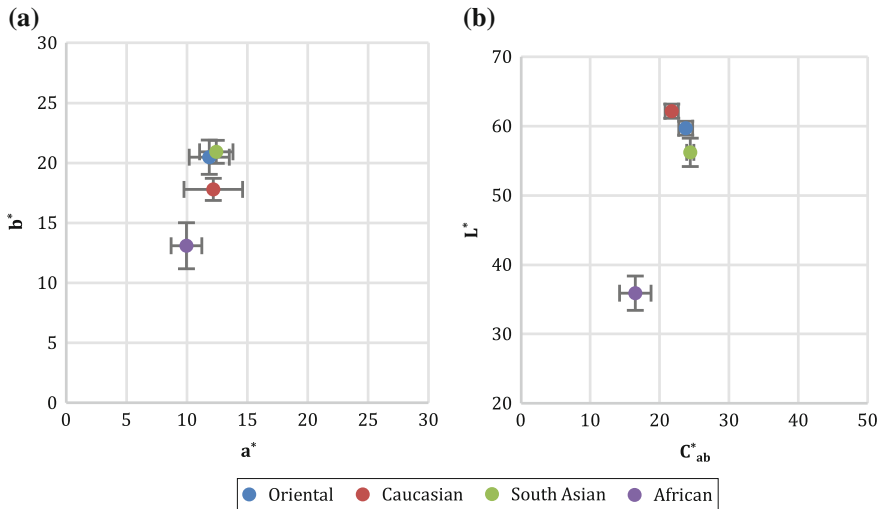
Fig. 2.2 The mean CIELAB values of five locations of each ethnic group measured by PR650 in
a a^*b^* plane and **b** $L^*C^*_{ab}$ plane

Figure 2.3 shows the measurement results of two instruments. Figure 2.3a, b
shows the 10 locations measured by the CM700d. In a^*b^* plane, we can see the
locations on face are redder than the others, except the fingertip. The measurement
results from the PR650 appear a similar trend, as shown in Fig. 2.3c, d.

(a)

(b)

(c)

(d)
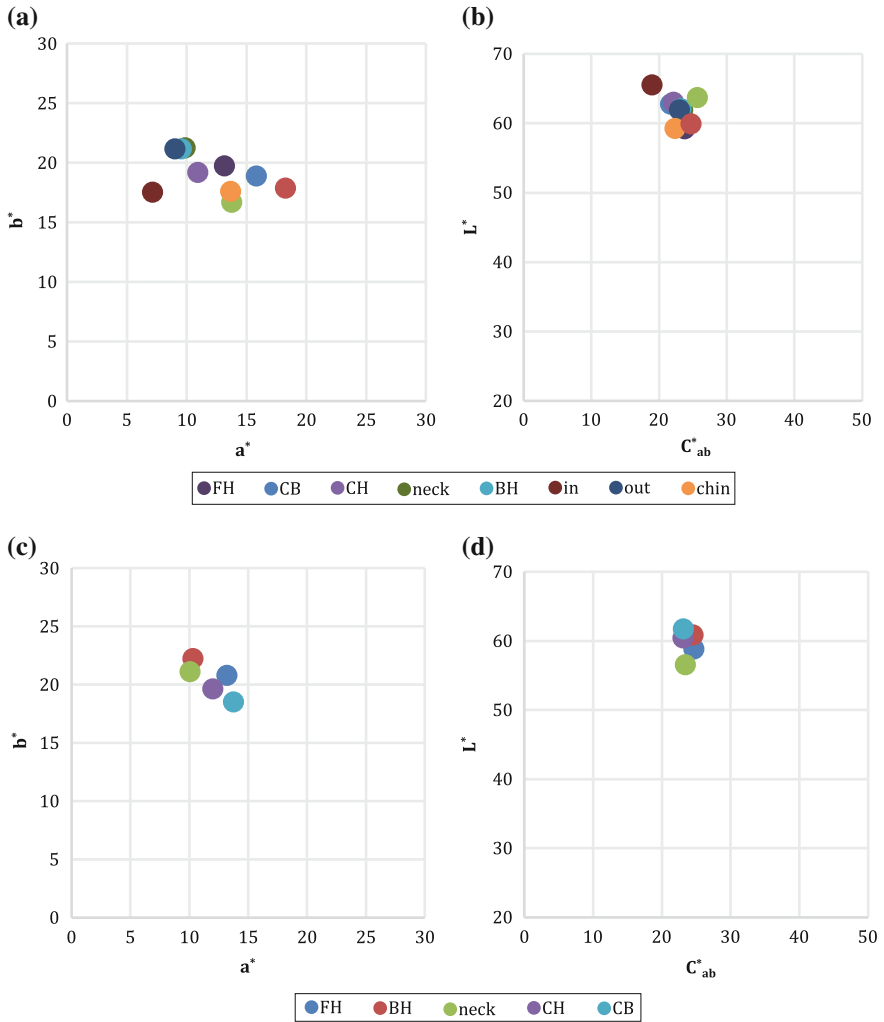
Fig. 2.3 The mean CIELAB values of ten or five locations measured by CM700d and PR650 **a** Ten locations measured by CM700d in a^*b^* plane; **b** Ten locations measured by CM700d in $L^*C^*_{ab}$ plane; **c** Five locations measured by PR650 in a^*b^* plane and **d** Five locations measured by PR650 in $L^*C^*_{ab}$ plane

The variation of the chroma and lightness between ten locations is not significant. But the data show a negative correlation in lightness and chroma. This indicates that for the Oriental group, skin with higher lightness will lower in chroma.

2.5 Conclusions

This chapter is focus on investigating the variation of four ethnic groups and two instruments. The colour appearance differences between ethnicities and instruments were determined by looking at the colour difference and plotting the results on a^*b^* and $L^*C^*_{ab}$ planes. This research provides valuable information to evaluate measurement results between TSR and SP for skin colour measurement. The results from these two instruments show that two different instruments gave different results. But they are similar in trend. The measurement results from one instrument cannot be used to replace another directly. For different ethnic groups, the Caucasian group showed the highest lightness while the African group exhibits the lowest. The other three groups had similar hue angle and chroma. The distribution of the average CIELAB of each ethnic group is similar for these two instruments. In general, the non-contact instrument's (PR650) results are darker than the contact instrument's (CM700d) results with a good agreement in hue angle. For the ten or five locations of the Oriental group measured by CM700d and PR650, the locations on the facial area appear redder than the others. For the Oriental group, the skin with higher lightness will have lower chroma.

References

1. De Rigal, J., Abella, M. L., Giron, F., Caisey, L., & Lefebvre, M. A. (2007). Development and validation of a new skin colour chart. *Skin Research and Technology, 13*, 101–109.
2. Serup, J., & Agner, T. (1990). Colourimetric quantification of erythema—A comparison of two colourimeters (Lange microcolour and Minolta chroma meter CR-200) with a clinical scoring scheme and laser-Doppler flowmetry. *Clinical and Experimental Dermatology, 15*, 267–272.
3. Clarys, P., Alewaeters, K., Lambrecht, R., & Barel, A. O. (2000). Skin colour measurements: comparison between three instruments: The Chromameter, the Derma Spectrometers and the Mexameter. *Skin Research and Technology, 6*, 230–238.
4. Barel, A. O., Clarys, P., Alewaeters, K., Duez, C., Hubinon, J.-L., & Mommaerts, M. (2001). The Visi-Chroma VC-100: A new imaging colourimeter for dermatocosmetic research. *Skin Research and Technology, 7*, 24–31.
5. Baquié, M., & Kasraee, B. (2014). Discrimination between cutaneous pigmentation and erythema: Comparison of the skin colourimeters dermacatch and mexameter. *Skin Research and Technology, 20*(2), 218–227.
6. Stamatas, G. N., Zmudzka, B., Kollias, N., & Beer, J. Z. (2008). In vivo measurement of skin erythema and pigmentation: New means of implementation of diffuse reflectance spectroscopy with a commercial instrument. *British Journal of Dermatology, 159*(3), 683–690.
7. Xiao, K., Liao, N., Zardawi, F., Liu, H., Van Noor, R., Yang, Z., et al. (2012). Investigation of Chinese skin colour and appearance for skin colour reproduction. *Chinese Optics Letters, 10*(8), 083301.
8. Tajima, J., Tsukada, M., Miyake, Y., et al. (1998). Development and standardization of a spectral characteristics database for evaluating color reproduction in image input devices. *International Society for Optics and Photonics*, pp. 42–50.

Chapter 3
Assessing Quality of Viewing Cabinets for Visual Inspection

Yang Yang and Ming Ronnier Luo

Abstract Viewing cabinets provide standard lighting conditions for visual inspection in the color-related industries such as imaging, textiles, and graphic arts. The lighting conditions are typically defined by the correlated color temperature (CCT), distance of departure from the blackbody locus (Duv), color rendering index (CRI), and metamerism index (MI). Various technologies were used to simulate the standard lighting conditions such as fluorescent, tungsten, filtered tungsten, and tunable LED lamps. This paper investigates three cabinets based on different technologies. It showed that all the three cabinets could achieve very high CRI above 95 and small Duv within the tolerance 0.005. A 14-channel LED tunable viewing cabinet performed the most accurate CCT and the best are MI_{vis} and MI_{uv} among all the cabinets tested. Furthermore, it can predict well with lighting parameters across a large range of CCTs.

Keywords LED simulator · CRI · MI · Viewing cabinet

3.1 Introduction

Viewing cabinet is generally used in the color-related industries. For example, in imaging industry, it is frequently used to characterize digital cameras. In the surface color industries such as graphic arts, textiles, coatings, and plastics, it is used for visual inspection to control the color quality. They are built to conform some international standards. For example, ISO 11664-2 [1] defined the spectral power distribution (SPD) of standard illuminants A and D65. ISO 3664 [2] has specified

---

Y. Yang · M.R. Luo (✉)
State Key Laboratory of Modern Optical Instrumentation, Zhejiang University,
Hangzhou, China
e-mail: m.r.luo@leeds.ac.uk

M.R. Luo
School of Design, University of Leeds, Leeds, UK

the standard viewing conditions for graphic arts by defining correlated color temperature (CCT), Duv, chromaticity coordinates, uniformity, color rendering index (CRI) [3], and metamerism index (MI) [4].

CRI proposed by CIE [3] has been widely used in industry. It describes the color quality of a light source. It can be simply explained as how close the color appearance of a sample viewed between a test source and a reference source, say a phase of daylight. It is first expressed in color difference unit and then transform to a scale-up to 100 (the highest quality).

MI is proposed by the CIE to test the performance of four daylight simulators, i.e. D50, D55, D65, and D75, for which D50 is specifically for graphic art industry. Taking D50 simulator as an example, there are eight specially designed sample pairs (known as metamers), for which each metamer has no color difference under standard CIE D50 illuminant. The color difference of metamer calculated under a particular D50 simulator is used to indicate its quality. The larger difference means the worse performance of this simulator. The eight metamers are divided into two groups: the former five pairs having no optical brightening agent (OBA) and the latter three pairs having OBA. Note that OBA absorbs energy in the UV region and release it in the visible region. The OBA has a large impact on the whiteness perception, which is important for the paper and textile industries. The former are used to test the quality of the visible part of SPD, and the latter are used to test the UV part of SPD. The mean color difference in CIELAB of the former five pairs is termed as MI_{vis}, and that of the latter three pairs is termed as MI_{uv}. The MI (MI_{vis} or MI_{uv}) is graded into five levels: A: <0.25, B:0.25–0.5, C:0.5–1.0, D:1.0–2.0, E: >2.0. Taking critical comparison prints as defined by the ISO 3664, the CCT should be 5000 K, the general CRI (R_a) should be above 90, and the specific CRI (R_i, i = 1:8) should be above 80. The Duv should be smaller than 0.005 in CIE1976 u'v' diagram. Furthermore, MI_{vis} should be below 1 and MI_{uv} should be below 1.5 in CIELAB color space.

Currently, there are four types of technologies for producing daylight simulators, i.e., florescent tubes, filtered tungsten, filtered Xenon, and tunable LED. Figure 3.1 illustrates the SPDs of these simulators together with the target CIE D65 SPDs. It can be seen that there are many peaks of fluorescent tubes SPD. The CIE D65 SPD is smoother than that of the simulator of fluorescent tube. Therefore, the performance of fluorescent tubes will be rather poorer due to this non-smooth SPD. Filtered tungsten could achieve a much better fit, but its lamp temperature and the voltage should be strictly controlled; otherwise, the SPD and CCT will vary. Filtered Xenon could also simulate the daylight very well while it generates large amounts of heat, which needs to be cooling down. Tunable LED could perform well by combining various narrow-band LEDs covering the whole spectrum range. Moreover, its SPD can be regulated flexibly by controlling the intensity of different LEDs. This advantage makes it attractive allowing tunable LED to simulate various SPDs.
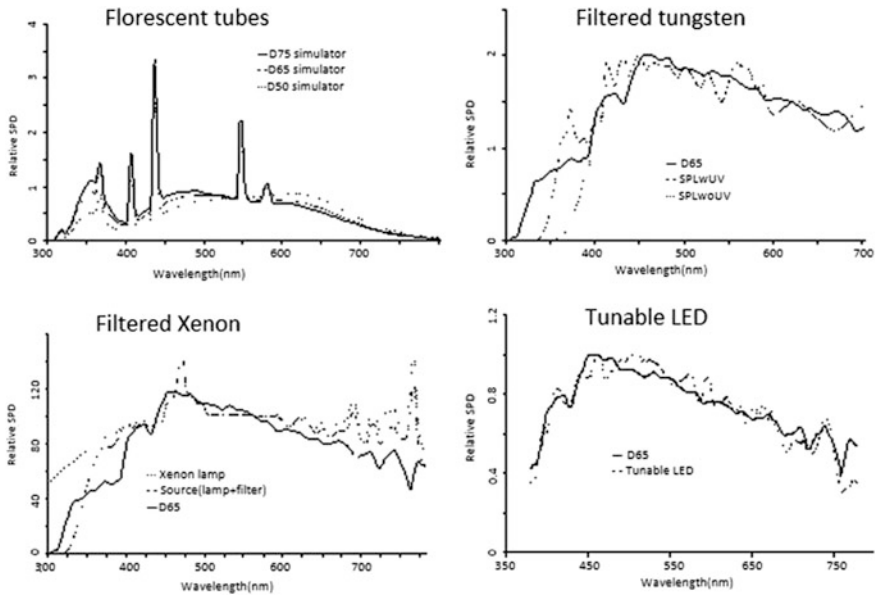
Fig. 3.1 SPDs of various simulators and standard daylight D65

The LED simulator shown in Fig. 3.1 is built by National Institute of Standards and Technology (NIST) [5]. It is an integrating sphere including 33 narrow-band LEDs to simulate target SPDs. However, all the LEDs they used were low power and were a bit weak.

If applying LEDs to viewing cabinet, its power should be high enough to reach certain luminance level. However, there is a lack of commercial high-power LED in the green–yellow range. Generally, wideband white LED is used to cover the green–yellow gap. When simulating some SPDs which have peaks in the green–yellow area, high-power LED could not match the target SPDs very well since there is only wideband white LEDs. Additionally, some types of commercial high-power LED are not as rich as low-power LEDs. Therefore, it is inconvenient to achieve perfect SPD match using high-power LEDs. However, they can achieve high color-quality parameters, e.g. CCT, CRI, and MI. For viewing cabinet manufacturers, they should balance the types of LEDs and lighting quality, the more types of LEDs means the higher cost. As mentioned earlier, some LEDs are more difficult to obtain.

In this paper, three viewing cabinets are compared: a 14-channel LED viewing cabinet, a 5-channel LED viewing cabinet, and a conventional cabinet including a tungsten and two fluorescent lamps.

Fig. 3.2 Typical measuring
setup for the evaluation of a
viewing cabinet

3.2 The Viewing Cabinets Tested

14 types of LEDs were selected to build the viewing cabinet. Their SPDs covered
the near-ultraviolet and visible range, from 360 to 660 nm. Two of them had SPD
peaks below 410 nm, two of them were white LEDs, and the others were
narrow-band LEDs in the visible range. The power of each LED was about 3 W.
Totally 120 LEDs were used. The second simulator only has five LED channels,
i.e., one white, one red, one green and two blue LEDs. The conventional viewing
cabinet included a tungsten and two fluorescent lamps to simulate CIE illuminant
A, D50, and D65, respectively.

Each viewing cabinet was first warmed up to 1 h. Each lamp was measured 8
times over a period of 8 working hours. The measurement was carried out using a
JETI 1211 tele-spectroradiometer. It measured the reflected light of 45° from a
reference white tile placed in the middle of the bottom of each cabinet. Figure 3.2
shows a typical measuring setup.

3.3 Performance

3.3.1 Comparing Performance Using Color Quality
Parameters

The performance of traditional viewing cabinet using a tungsten and a florescent
tube, as well as the other two LED cabinets including a 5-channel and a 14-channel
LED cabinets, is summarized in Table 3.1. The results are reported in terms of five
qualities CCT, Duv, CRI, $MI_{vis,}$ and MI_{uv} for the most commonly used CIE A, D50,
and D65 illuminants.

Table 3.1 Comparison between performances of different cabinets

	A	D50	D65
Traditional cabinet			
CCT	2823	4722	6227
Duv	0.004	0.001	0.005
CRI (R_a)	97.9	95.6	97.6
MI_{vis}	n/a	0.81(C)	0.41(B)
MI_{uv}	n/a	3.96(E)	5.70(E)
The 5-LED cabinet			
CCT	2954	5279	6952
Duv	0.004	0.005	0.005
CRI (R_a)	97.9	97.4	96.74
MI-vis	n/a	1.24(D)	1.42(D)
MI-uv	n/a	4.40(E)	6.03(E)
The 14-LED cabinet			
CCT	2879	5021	6475
Duv	0.004	0.001	0.002
CRI (R_a)	97.2	99.4	98.8
MI_{vis}	n/a	0.19(A)	0.24(A)
MI_{uv}	n/a	0.45(B)	0.67(C)

It is shown in Table 3.1 that the 14-channel LED cabinet outperformed the others, i.e., the highest CCT accuracy for each type of illuminant. The other two had small Duv values within the tolerance of ISO3664 (0.005). Additionally, they all achieve very high CRI above 95. In general, the 14-channel LED cabinet performed the best, then the 5-channel LED cabinet, and the traditional cabinet the worst. Finally, there are great differences among them in terms of MI. For D50, the 14-channel cabinet can achieve A and B levels for MI_{vis} and MI_{uv}, respectively, while the traditional cabinet could only reach C and E levels, and the 5-channel LED cabinets are in D and E levels. For D65, the 14-channel cabinet can achieve A and C levels, while the traditional cabinet could only reach BE level and the 5-channel LED cabinet reported DE level.

The overall results showed that the 14-channel LED simulators are performing well. The evidence is shown in Fig. 3.3 which plots the SPDs of the 14-channel LED cabinet and the CIE standard illuminants. Overall, it can be seen that the LED cabinet could simulate the SPDs of standard CIE SPDs well. Most importantly, the simulated SPDs are close to the target SPDs below 700 nm while departs from the target SPDs above 700 nm, since no LED above 700 nm was used. But it can still perform well as shown in Table 3.1.
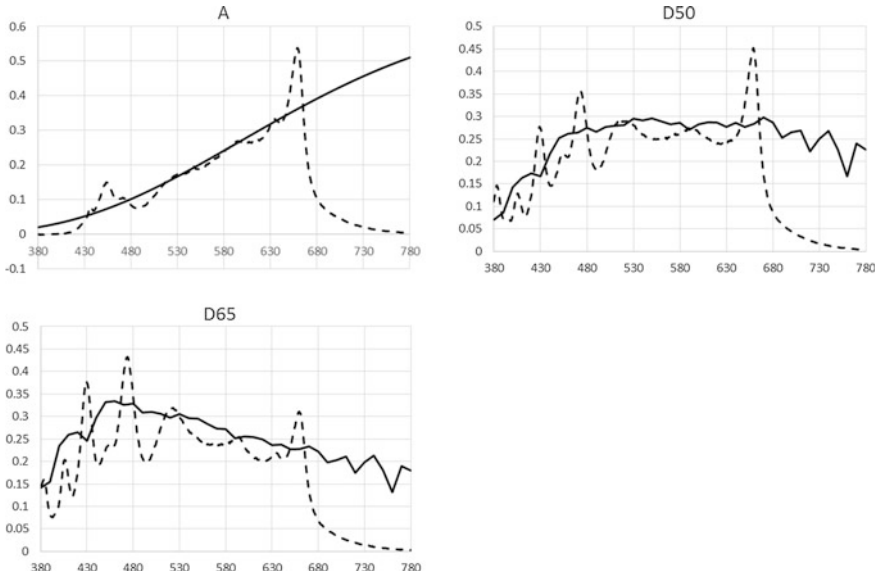
Fig. 3.3 Comparison between SPDs of 14-channel LED cabinet (*dash line*) and the target illuminant (*solid line*)

3.3.2 Reproducing SPDs Under Different CCTs

As mentioned earlier, one important feature of the 14-channel LED cabinet is to realize various target SPDs by regulating the intensity of different LED channels. Four target SPDs are used here as examples. These are: 3000 and 4000 K black body illuminants, and D55 and D75.

Table 3.2 shows the performance of the cabinet and Fig. 3.4 shows the comparison between the target SPDs and the LED-simulated SPDs. It is shown in Table 3.2 that they all could achieve relatively accurate CCT, although D75 simulator has 100 K higher CCT than true D75. Also, they can achieve small Duv within 0.005 units. They all achieve CRI above 95, and 4000 K simulator achieve the highest CRI, 99.1. D55 achieved MI in AB level and D75 in AC level.

Table 3.2 Comparison between performances of different illuminants simulators using 14-channel cabinet

	3000	4000	D55	D75
CCT	3020	4032	5426	7608
Duv	0.002	0.001	0.003	0.002
CRI (R_a)	96.6	99.1	98.9	97.6
MI$_{vis}$	n/a	n/a	0.14(A)	0.20(A)
MI$_{uv}$	n/a	n/a	0.48(B)	0.97(C)
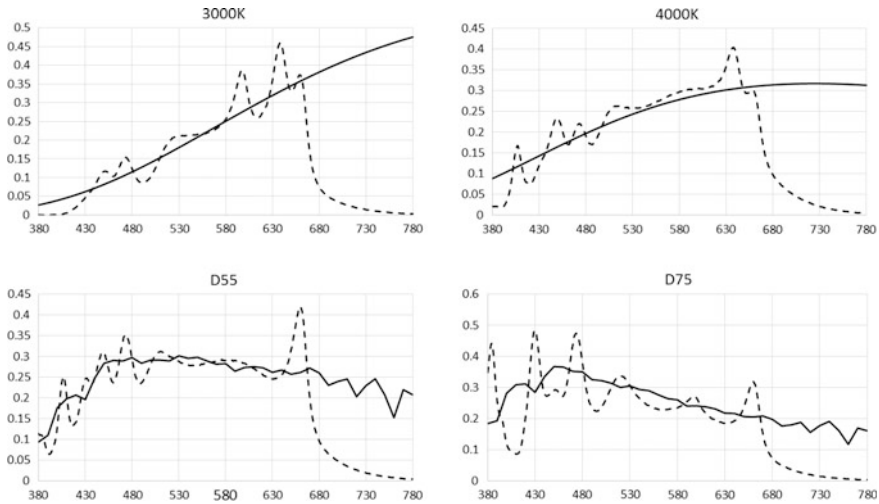
Fig. 3.4 Comparison between SPDs of 14-channel cabinet (*dash line*) and the target illuminants (*solid line*)

3.4 Conclusions

Three viewing cabinets for visual inspection were tested here. The results showed that the 14-channel LED cabinet could achieve high color quality level in terms of CCT, CRI, Duv, and MI. In particular for the latter, it performs much better than the other two, since LEDs used in this cabinet cover not only the visible but also near ultraviolet parts of wavelength range. In summary, the LED Era has arrived in the field of visual inspection. It has the way to be able to tune their intensity to match any desired SPD.

References

1. ISO 11664-2:2007(E)/CIE S 014-2/E. (2006). CIE colorimetry—Part 2: Standard illuminants for colorimetry.
2. ISO 3664: 2008 (E). (2008). Viewing conditions—Graphic technology and photography.
3. CIE Publication 13:1995. (1995). Method of measuring and specifying the color rendering properties of light sources.
4. CIE Publication 51. Standard method of assessing the spectral quality of daylight simulators for visual appraisal and measurement of colors.
5. Fryc, I., Brown, S. W., Eppeldauer, G. P., et al. (2005). LED-based spectrally tunable source for radiometric, photometric, and colorimetric applications. *Optical engineering, 44*(11), 111309.

Chapter 4
Visual Assessment of CIE Illuminant Simulators

Haiting Gu, Ming Ronnier Luo, Xiaoyu Liu, Yang Yang and Binyu Wang

Abstract This study investigated the perceived colour quality of CIE-D50 and CIE-A simulators based on multichannel LED sources and conventional fluorescent and tungsten lamps. Two psychophysical experiments were carried out to evaluate different aspects of perceived colour quality of the four simulators: colour appearance and colour difference. Ten observers with normal colour vision participated to assess thirty metameric pairs, which were consisted of colour constant and inconstant samples. The visual results were analysed to indicate the performance of the four simulators. It was found that the colour difference results clearly showed that LED-D50 simulator significantly outperformed the conventional fluorescent source.

Keywords LED simulator · Colour appearance · Colour difference · Metamerism

4.1 Introduction

The newer LED sources are taking over more and more lighting applications due to its various advantages, such as lower electricity consumption, greener energy and longer lifetime. However, their spectral power distributions (SPDs) over the visual spectrum are quite different from the conventional light sources such as tungsten

H. Gu · M.R. Luo (✉) · Y. Yang
State Key Laboratory of Modern Optical Instrumentation, Zhejiang University, Hangzhou, China
e-mail: m.r.luo@leeds.ac.uk

M.R. Luo
School of Design, University of Leeds, Leeds, UK

X. Liu
College of Science, Harbin Engineering University, Harbin, China

B. Wang
Thousand Lights Lighting (Changzhou) Limited, Changzhou, China

and fluorescent lamps, which have been used for visual inspection in the graphic and imaging industries for years. This raises questions about the feasibility of replacing the existing tungsten and fluorescent lamps by the LED light sources. Whether objects could have different colour appearance seen under LED lighting, and conventional sources are a big concern. Fryc et al. [1] built a spectrally tuneable light source using a large number of LEDs and an integrating sphere. The source was designed to be capable of producing any spectral distribution in the visible region. A series of simulations were conducted to predict the performance of the designed tuneable source when used for calibration of display colorimeters. The results indicated that the errors in colour measurements of displays can be reduced an order of magnitude comparing with those calibrated against a tungsten illuminant A simulator. The source could also simulate various CIE daylight illuminants and common lamps spectral distributions for other photometric and colorimetric applications.

ISO 3664:2008(E) [2] specified the standard viewing conditions for viewing graphic art prints, transparency and monitor by defining the luminance, correlated colour temperature (CCT), chromaticity coordinates, uniformity, colour rendering index (CRI) [3] and metamerism index (MI) [4] in the visible and UV ranges of spectrum. According to these specifications, two LED-based D50 and A simulators were constructed by a multichannel LED system.

In this paper, two psychophysical experiments were reported to verify the lighting quality of CIE-D50 and CIE-A simulators based on multichannel LED sources against conventional fluorescent and tungsten lamps. One experiment was designed for estimating colour appearance of a single sample, while the other one focused on evaluating colour difference between pairs of samples.

4.2 Experimental

4.2.1 Simulators

In total, four simulators were investigated here. As mentioned previously, two of them (called LED-D50 and LED-A hereafter) were produced by a self-built LED system to simulate CIE-D50 and CIE-A illuminants strictly following the specifications of ISO 3664 [2]. This self-built LED system included ten channels of monochromatic LEDs and one channel of white LED; therefore, the target spectrum with certain CCT, illuminance, CIE-R_a and MI values could be achieved through adjusting the intensity of each channel. The other two simulators were conventional CIE simulators, which are typically employed in the industrial inspection. One is a FL8 fluorescent lamp (called F8 hereafter) also simulating CIE illuminant D50, and the left is a tungsten bulb (named T hereafter) simulating CIE illuminant A.
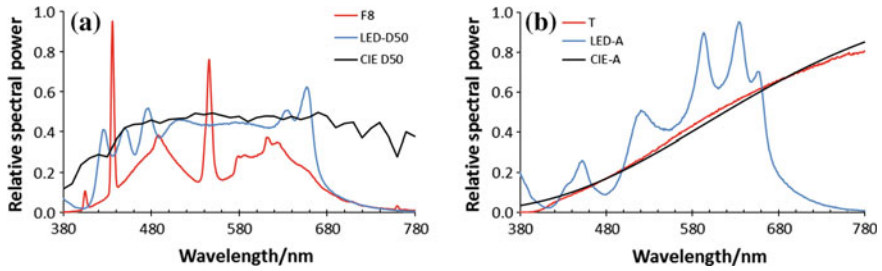
Fig. 4.1 The SPDs of the four simulators together with two CIE illuminants: **a** F8, LED-D50, CIE D50; and **b** T, LED-A, CIE-A

The SPDs of four simulators together with the standard CIE-D50 and CIE-A illuminants are shown in Fig. 4.1a, b, respectively. Comparing the spectrum, it can be seen that the SPD of T is much closer to that of CIE illuminant A than that of LED-A, while LED-D50 had less deviations from CIE-D50 illuminant than F8. Table 4.1 summarizes the colorimetric properties of these four simulators and two standard illuminants. It can be seen that F8 simulator performed poorly with a $D_{u'v'}$ value larger than the tolerance defined by ISO3664 (0.005). On the contrary, LED-D50 simulator successfully met this requirement. For the two measures recommended by the CIE to evaluate the quality of lighting, all simulators achieved high CIE-R_a values over 90, while LED-D50 simulator markedly outperformed F8 in terms of MI_{vis} values. MI_{vis} is a MI for the visible spectrum and quantifies the metamerism degree of light sources in Grades A to E. Note that LED-D50 simulator can almost achieve Grade A (CIELAB of 0.25). In addition, despite of the large difference in the SPD, LED-A simulator showed similar good performance with T in terms of all measures.

Two viewing cabinets were employed in this study with all interior painted in medium grey, which had L^*, a^* and b^* values of 49.2, 0.8 and 0.7, respectively, under D50/10 degree condition. These two cabinets provided LED and conventional simulators, respectively.

Table 4.1 The colorimetric properties of the four simulators together with two CIE illuminants

	CCT (K)	u′	v′	$D_{u'v'}$	cd/m^2	CIE-R_a	MI_{vis} (CIELAB)
CIE D50	5000	0.2102	0.4889				
LED-D50	4926	0.2104	0.4887	0.0003	154	98.5	0.27
F8	4829	0.2152	0.4842	0.0069	154	94.2	0.80
CIE-A	2850	0.2559	0.5244				
LED-A	2847	0.2553	0.5293	0.0049	156	93.4	n/a
T	2840	0.2557	0.5285	0.0041	156	97.7	n/a

Note MI_{vis} is the metamerism index for visual region rather than UV region

4.2.2   Test Samples

Thirty colour pairs prepared by Kuo and Luo [5] to study metamerism were used here, which were specially designed to have small colour difference under daylight illuminants such as D65 or D50, and large colour difference under other illuminants such as F11 or A. Note that a metameric sample pair typically included one colour constant sample and one colour inconstant sample. In other words, the former sample shows little colour difference when the illuminant changes, but the latter one has a large colour shift. Hence, under different sources, the colour appearance of the inconstant samples will change and the colour difference between the metameric pair will be different. In this study, the mean colour differences of 30 metameric pairs in CIELAB colour space are 2.44 and 7.17 under CIE-D50 and CIE-A, respectively.

4.2.3   Scaling Techniques

As mentioned earlier, two experiments focused on different aspects were conducted: colour appearance and colour difference. For scaling colour appearance, magnitude estimation method was employed to quantify the colour shift of the inconstant samples according to the earlier study by Luo et al. [5]. Observers were asked to estimate the colourfulness and hue composition of 30 samples. These samples were the inconstant sample in each metamer and were assessed under four CIE simulators, respectively. For scaling colourfulness, observers assigned a number according to a memorized colourfulness of an anchoring reference sample as 30. When it comes to hue composition, observers described the hue as one unitary colour (pure red, yellow, green and blue) or a proportion of the two. After the estimation, observers were then asked to judge colour difference of metameric pairs according to a grey scale placed beside the samples [6]. The results were reported in grade values ranged from 1 to 5 at 0.5 interval, representing large to no colour differences.

   Ten observers with normal colour vision participated in this study. Their average age was 25 with a standard deviation of about 4. Overall, 2400 colour appearance evaluations and 1200 colour difference evaluations have been accumulated, i.e. 10 observers × 2 (colourfulness and hue) or 1 (colour difference) questions × 30 pairs × 4 simulators.

4.3   Results and Discussion

The raw data given by observers were transformed to colourfulness (M) and hue composition (H), and visual colour difference (ΔV) for colour appearance and colour difference, respectively. The mean colourfulness and hue composition

calculated from ten observers were used as panel results of colour appearance for further data analysis. The ΔV results were obtained via a polynomial equation fitted between grade values and corresponding ΔE_{ab}^* colour differences. Also, the ΔV results from ten observers were averaged to represent visual results of colour difference.

4.3.1   Testing the Performance of Simulators Using Colour Appearance Results

The XYZ values for each sample under CIE 1964 standard colorimetric observer and the SPD of the two CIE illuminants were first calculated. These values then were transformed to CAM02-UCS J',a' $(a_P),b'$ (b_P) values [7] as predicted chromatic results under the two reference standard CIE illuminants. The logic behind is to consider the prediction of CAM02-UCS under the reference source (SE). As mentioned before, the mean visual data of colourfulness (M_V) and hue composition (H_V) under four different simulators will be treated as visual data. Its hue composition will afterwards be transformed to hue angle (h_V) via CIECAM02 [8]. Finally, a_V and b_V will be calculated using Eq. (4.1).

$$
\begin{aligned}
a_V &= M_V \cos(h_V) \\
b_V &= M_V \sin(h_V)
\end{aligned}
\tag{4.1}
$$

Afterwards, the final chromatic difference (ΔC) between predicted chromatic results of the CIE illuminant and visual results of corresponding simulator can be calculated via Eq. (4.2).

$$
\Delta C = \sqrt{(a_V - fa_P)^2 + (b_V - fb_P)^2}
\tag{4.2}
$$

where f is a scaling factor calculated by regression to make all the predicted chroma values to have the same scale as those of visual data. Finally, the mean ΔC for the 30 samples under each source represents the performance of each test simulator compared against reference standard CIE illuminants. For ΔC equals to zero, it means that this simulator had a perfect agreement to CIE illuminant. The results showed that LED-D50 and F8 gave the same performance having a ΔC value of 4.2. Similarly, LED-A and T performed the same having a ΔC of 4.3. It can be found that LED simulators could produce similar good perceived lighting quality as conventional CIE simulators. It is encouraging that although the SPD of LED-A simulator appears quite different from that of CIE-A, their colour appearance results were very similar.

4.3.2 Testing the Performance of Simulators Using Colour Difference Results

The colour difference of each metameric pair under each CIE illuminant was first calculated. These calculated colour differences (ΔE) in CAM02-UCS colour space and were then compared with visual colour differences (ΔV) under test simulators, using STRESS [9] as a measure of fit. STRESS can be regarded as disagreement percentage between two data sets. For example, a STRESS value of 30 means 30 % disagreement between two data sets. Thus, if the calculated STRESS value of a test simulator is larger, this simulator will have worse agreement with the CIE illuminant. The STRESS results revealed that LED-D50 simulator markedly outperformed F8 with STRESS values of 24 and 40, respectively, while LED-A simulator slightly outperformed T with STRESS values of 19 and 21, respectively.

4.4 Conclusions

Two CIE illuminant simulators based on limited numbers of LED channels and two conventional CIE simulators were evaluated. The results from measured colorimetric properties and two psychophysical experiments revealed the following major findings:

1. Comparing LED-D50 and F8 fluorescent simulators using the standard measures, LED-D50 outperformed F8 in terms of less $D_{u'v'}$, higher CIE-R_a and better MI_{vis} value. This was confirmed by the present colour difference visual results. In the colour appearance experiment, both sources gave similar performance.
2. Comparing LED-A and T (conventional tungsten lamp) using the standard measures, T has a high CIE-R_a value. The visual results from the present colour difference and colour appearance experiments both showed that although the SPD of the T simulator is much closer to CIE-A illuminant than that of the LED-A simulator, little difference was found between these two sources.
3. In conclusion, the present results showed the superiority of the LED technology, equal to and better than the most widely used conventional T and F8 sources, respectively. A fixed number of LED channels can be adjusted to any desired illuminant/source, and also, they can be constantly monitored and calibrated to the original state.

References

1. Fryc, I., Brown, S. W., Eppeldauer, G. P., et al. (2005). LED-based spectrally tunable source for radiometric, photometric, and colorimetric applications. *Optical Engineering, 44*(11), 111309.
2. ISO 3664: 2008 (E). (2008). Viewing conditions—Graphic technology and photography.
3. CIE Publication 13:1995. (1995). Method of measuring and specifying the colour rendering properties of light sources.
4. CIE Publication 51. Standard method of assessing the spectral quality of daylight simulators for visual appraisal and measurement of colours.
5. Luo, M. R., Rigg, B., & Smith, K. J. (2003). CMC 2002 colour inconstancy index; CMCCON02. *Coloration Technology, 119*(5), 280–285.
6. CIE. (2004). Publication 15: 2004, (3rd Edn.). Colorimetry.
7. Luo, M. R., Cui, G., & Li, C. (2006). Uniform colour spaces based on CIECAM02 colour appearance model. *Color Research & Application, 31*(4), 320–330.
8. CIE. (2004). Publication 159:2004. A colour appearance model for colour management systems: CIECAM02.
9. Garcia, P. A., Huertas, R., Melgosa, M., & Cui, G. (2007). Measurement of the relationship between perceived and computed color differences. *Journal of the Optical Society of America, 24*(7), 1823–1829.

Chapter 5
A Method for Reconstructing Surface Spectral Reflectance in Spectral Reproduction Workflow

Ping Yang, Sensen Huang, Wangjian Qiu, Qianyun Ma, Qiang Wang and Hong Song

Abstract In spectral color reproduction workflow, it is of key importance to reconstruct the spectral reflectance of a surface using digital cameras under given luminance and observation conditions. A new approach for solving the problem which is based on neural network and basis vectors is proposed. Compared with other traditional methods, neural network expands the space of unknown function from linear functions to more general nonlinear functions, which gives more accurate estimation of the coefficients and better reflectance reconstruction. Results show that the reflectance of standard Munsell color patch (Matte) can be reconstructed. Compared with linear approximation method, reconstruction of standard Munsell color patch (Matte) using this approach reduces the reconstruction error. Therefore, we conclude that this approach has advantages of higher accuracy, fast implementation, and adaptation, thus can be used in arts reproduction and museum art collection, etc.

Keywords Spectral color reproduction · Basis vectors · Color accuracy

5.1 Introduction

Spectral reflectance is the most complete and accurate approach for color description. It is independent of illumination and observation. Therefore, accurate color replication and object recognition can be achieved based on spectral images, which may find applications in agriculture inspection, museum art collection, medical plastic surgery, and electronic business [1, 2]. But most existing multi-spectral imaging systems are very complicated in their hardware, having conflicts in

H. Song (✉)
Ocean College, Zhejiang University, Zhejiang, China
e-mail: hongsong@zju.edu.cn

P. Yang · S. Huang · W. Qiu · Q. Ma · Q. Wang
School of Digital Media and Art Design, Hangzhou Dianzi University, Zhejiang, China

their accuracy, structure, and sampling speed. All these impose difficulty for their application in practice [3, 4]. Nowadays, color image acquisition mainly depends on broadband multi-primary color equipments, such as digital camera, scanner, and Web camera. [5, 6]. Thus, how to reconstruct the spectral images based on limited number of multi-channel images is the topic of this paper.

The contribution of our work is that a spectral reflectance reconstruction method has been proposed based on the response from a 4-channel digital color camera. By combining PCA and ANN, the accuracy is improved without introducing extra hardware complex. The paper is organized as follows. Section 5.2 introduces the reconstruction theory and the model. Section 5.3 describes the experimental setup. Section 5.4 explains the experiments and results in detail. Section 5.5 concludes the work.

5.2   Reconstruction Theory

The spectrum range studied in this paper is from 380 to 780 nm, and the reflectance is going to be a 401 dimension vector if the interval is 1 nm. If the interval is 10 nm, still the number of dimension is 41. Though the reflectance dimension is too large, it can be decomposed as a linear combination of the basis vectors by

$$r \approx \sum_{j=1}^{J} a_j \cdot u_j = U_1 \cdot \vec{a} \qquad (5.1)$$

where $a_j \in R$, $j = 1, 2 \ldots J$, which represents linear combination coefficients, $\vec{a}$ represents coefficients vector, and U_1 represents basis vector matrix [7, 8]. So the reflectance R can be written as follows:

$$R = [r_1 r_2 \ldots r_M] \approx U_1 \cdot [a_1 a_2 \ldots a_M] = U_1 \cdot A \qquad (5.2)$$

where A represents coefficients vector matrix. A commonly used decomposition method is singular value decomposition (SVD) [9, 15]. By using this method, the reflectance matrix will be decomposed into

$$R = U \cdot \Sigma \cdot V^T = [u_1 \ldots u_N] \cdot \begin{bmatrix} \sigma_1 & & & 0 \\ & \cdot & & \\ & & \cdot & \\ & & \cdot & \\ 0 & & & \sigma_N \text{ or } \sigma_M \end{bmatrix} \qquad (5.3)$$

where U and V^T are both unit orthogonal matrixes and Σ is a diagonal matrix whose diagonal elements are singular values. The diagonal elements satisfy the correlation that $\sigma_1 \geq \sigma_2 \geq \ldots \geq \sigma_J \geq \ldots \geq \sigma_N$ (or σ_M) ≥ 0. And if the first J singular values are

much larger than the subsequent, then the reflectance R matrix can be approximately written as follows:

$$R \approx R_1 = \underbrace{[u_1 \ldots u_N]}_{U_1} \cdot \underbrace{\begin{bmatrix} \sigma_1 & & 0 \\ & \cdot & \\ & \cdot & \\ & \cdot & \\ 0 & & \sigma_N \text{ or } \sigma_M \end{bmatrix} \begin{bmatrix} V_1^T \\ \cdot \\ \cdot \\ \cdot \\ V_J^T \end{bmatrix}}_{A} \tag{5.4}$$

where $J \ll N$. The contribution rate of the first J singular values can be defined as follows:

$$\eta = \frac{\|R_1\|_2^2}{\|R\|_2^2} \tag{5.5}$$

where $R_1 = U_1 \cdot A$. Then, some singular values that have the largest contribution to the model will be retained, while the others will be removed, which is the basic idea of PCA [10]. With the help of PCA, the reflectance dimension is greatly reduced. After the dimension is reduced, spectral reflectance can be estimated through either linear model or nonlinear model [10, 11].

Figure 5.1 shows the schematic representation of a two-layer feed-forward neural network consisting of Q tangent hyperbolic neurons in the first layer and M linear neurons in the second layer. The input $S \in R^P$ and output $\hat{a} \in R^M$ satisfy the following relationship:

$$\hat{a} = LW \cdot \tan h \left(IW \cdot S + b_1 \right) + b_2 \tag{5.6}$$

where $IW \in R^{Q \times P}$ and $LW \in R^{M \times Q}$ are matrices containing the input and output weights, respectively; $b_1 \in R^Q$ and $b_2 \in R^M$ are biases on the input and output neurons, respectively. IW, LW, b_1, and b_2 can be obtained during the modeling process by optimization algorithm.

From the equation above, it can be seen that a nonlinear function, tangent hyperbolic, is included in the neural network as well as offsets introduced by b_1 and b_2. Thus, the space of the unknown function $F(S)$ is expanded from linear functions
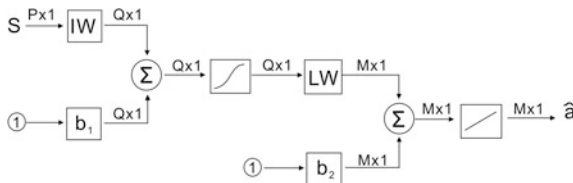
Fig. 5.1 Schematic representation of a two-layer neural network

to more general nonlinear functions. The tangent hyperbolic function has a quite linear behavior when input x is in the range $[-0.5, 0.5]$. If b_1 and b_2 are both set zero and the matrix IW is chosen such that the product of IW and S is small, then the network can be simplified to be

$$\hat{a} = \text{LW} \cdot \text{IW} \cdot S = M \cdot S \tag{5.7}$$

where matrix $M = \text{LW} \cdot \text{IW}$. Therefore, the linear input–output relationship can be considered as a specific case of this neural network. In this sense, the network should be able to approximate the unknown function $F(S)$ more accurately than any linear function, and it has been reported that a two-layer neural network is able to approximate most nonlinear functions very well [12–15].

5.3   Experimental Setup

The light is generated by a multi-light box (D65 illuminant state), and it emits at an angle of 45 degrees with the vertical direction. Then, it is reflected by the surface of Munsell color cards (Matte, new standard with 1269 cards). After that, the reflected light enters a 4-channel digital color camera and reaches the sensor through the camera's internal imaging systems and filter. Finally, the sensor converts light energy into electrical output to the computer so that the camera response is obtained. The camera response is imported into MATLAB for data processing. The spectral reflectance of the Munsell new standard color cards (matte) is acquired from the online database of University of Joensuu [16], measured by Perkin-Elmer lambda 9 UV/VIS/NIR Spectrophotometer. In 1269 color cards, let the first two in every three cards be used for modeling, and the last one in every three cards be used for testing. During the experiment, in order to ensure the constant lighting conditions and observing conditions, light source and camera are both fixed. And warm up the light box for 10 min before shooting; shooting begins from 5 min after the digital camera is turned on.

5.4   Results

Figure 5.2 shows the measured, nonlinear estimated, and linear estimated spectral reflectance of four color cards chose from 1269 color cards. As can be seen from the figure, the nonlinear estimates curves are very close to the real curves (measured), while the linear estimates curves are not similar to the real curve. Commonly, linear model can be solved by
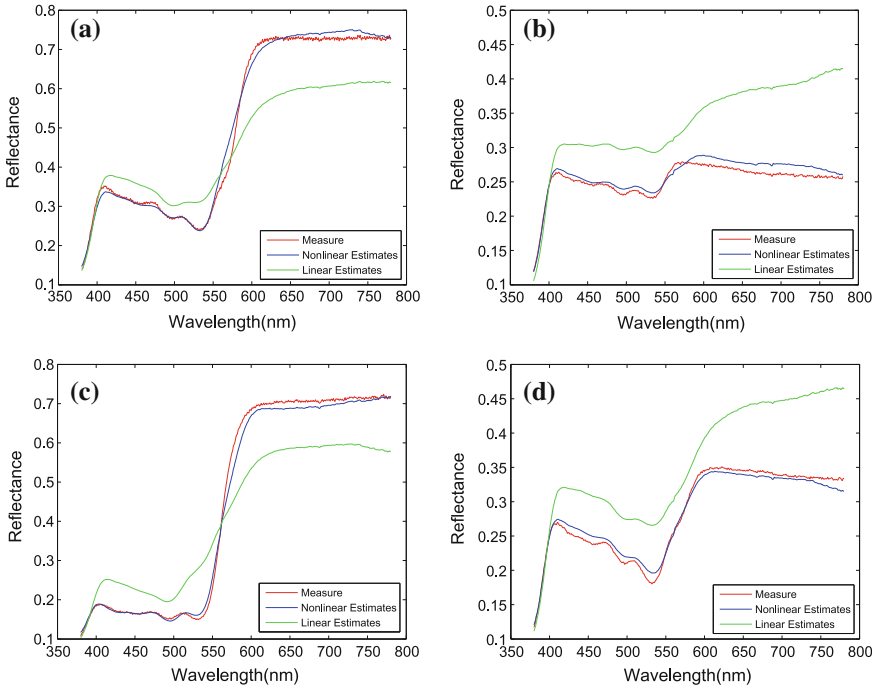
Fig. 5.2 Spectral reflectance of four color cards randomly chose from 1269 color cards **a** spectral reflectance of color card No. 14 **b** spectral reflectance of color card No. 23 **c** spectral reflectance of color card No. 90 **d** spectral reflectance of color card No. 834

$$F = U_1 \cdot A \cdot S^T \cdot (S \cdot S^T)^{-1} \tag{5.8}$$

where U_1 is basis vector matrix, A is coefficient vector matrix, and S is camera response.

And in order to evaluate the accuracy of reconstructed reflectance and to further compare the two models, another eight color cards in training set are used to obtain the $\overline{\text{RMS}}$ and $\overline{\text{STD}}$ error using both nonlinear model and linear model. And the same eight color cards in testing set are used to evaluate the reconstruction accuracy and to see whether the generalization of this kind of neural networks in nonlinear model is good. Table 5.1 shows $\overline{\text{RMS}}$ and $\overline{\text{STD}}$ error statistics of training set and testing set using both nonlinear model and linear model. It can be seen that the $\overline{\text{RMS}}$ and $\overline{\text{STD}}$ error are very close, which means this kind of neural networks used in this paper has good generalization.

Table 5.1 RMS and STD error of eight color cards randomly chose from training set and testing set

No.	Nonlinear method		Linear method	
	Training set	Testing set	Training set	Testing set
$\overline{RMS}$	0.0696	0.0698	0.0188	0.0203
$\overline{STD}$	0.0433	0.0435	0.0149	0.0159

5.5 Conclusion

In this paper, we reconstructed the spectrum reflectance based on neural network and basis vectors. Compared with other traditional methods, neural network expands the space of unknown function $F(S)$ from linear functions to more general nonlinear functions, which gives more accurate estimation of the coefficients and better reflectance reconstruction. Results show that the reflectance can be reconstructed successfully. Since the neural network can be implemented by MATLAB neural network toolbox, this method can be easily adapted in many other cases. Therefore, we conclude that this approach has advantages of higher accuracy, easy implementation, and adaptation, thus can be used in many applications.

References

1. Hunt, R. W. G. (1987). The reproduction of colour: In photography, printing and television. New York: Fountain Press.
2. Yoichi, M., Yokoyama, Y., Tsumura, T., Haneishi, H., Miyata, K., & Hayashi, J. (1998). Development of multiband color imaging systems for recordings of art paintings. In Proceedings of SPIE (Vol. 3648, pp. 218–225).
3. Imai, F. H., & Berns, R. S. (1999). Spectral estimation using trichromatic digital cameras. In *Proceedings of the International Symposium on Multispectral Imaging and Color Reproduction for Digital Archives* (Vol. 42). Hoboken: Wiley.
4. Saunders, D., & Cupitt, J. (1993). Image processing at the national gallery: The vasari project. *The National Gallery technical bulletin, 14*(1), 72–85.
5. Haneishi, H., Hasegawa, T., Hosoi, A., Yokoyama, Y., Tsumura, N., & Miyake, Y. (2000). System design for accurately estimating the spectral reflectance of art paintings. *Applied Optics, 39*(35), 6621–6632.
6. Ohya, Y., Obi, T., Yamaguchi, M., Ohyama, N., & Komiya, N. (1998). Natural color reproduction of human skin for telemedicine. In *Medical Imaging '98* (pp. 263–270). International Society for Optics and Photonics.
7. Shen, H. L., Cai, P. Q., Shao, S. J., & Xin, J. H. (2007). Reflectance reconstruction for multispectral imaging by adaptive wiener estimation. *Optics Express, 15*(23), 15545–15554.

8. Dupont, D. (2002). Study of the reconstruction of reflectance curves based on tristimulus values: Comparison of methods of optimization. *Color Research & Application, 27*(2), 88–99.
9. Wenhai, Z., Haisong, X., & Yong, W. (2007). Spectral reconstruction of images based on color scanner. *Acta Optica Sinica, 5*, 019.
10. Osorio-Gomez, C. A., Mejıa-Ospino, E., & Guerrero-Bermudez, J. E. (2009). Spectral reflectance curves for multispectral imaging, com-bining different techniques and a neural network. *Revistamexicana de f´ısica, 55*(2), 120–124.
11. Usui, Shiro, Nakauchi, Shigeki, & Nakano, Masae. (1992). Reconstruction of munsell color space by a five-layer neural network. *Journal of the Optical Society of America, 9*(4), 516–520.
12. Ribes, A., & Schmitt, F. (2003). A fully automatic method for the reconstruction of spectral reflectance curves by using mixture density networks. *Pattern Recognition Letters, 24*(11), 1691–1701.
13. Lopez-Alvarez, M. A., andez-Andres, J. H., Valero, E. M., & Romero, J. (2007). Selecting algorithms, sensors, and linear bases for optimum spectral recovery of skylight. *Journal of the Optical Society of America, 24*(4), 942–956.
14. Laamanen, H. T., Jaeaeskelaeinen, T., & Parkkinen, J. P. (2000). Comparison of PCA and ICA in color recognition. In *Intelligent Systems and Smart Manufacturing* (pp. 367–377). International Society for Optics and Photonics.
15. Hardeberg, J. Y. (2001). Acquisition and reproduction of color images: Colorimetric and multispectral approaches. Boca Raton: Universal Publishers.
16. Joensuu. Spectraldatabase. http://cs.joensuu.fi/∼spectral/databases/download/munsell_spec_matt.htm.Accessed March 10, 2015.

Chapter 6
Calibration of 3D Images in Terms of Spectral Reflectance

Muhammad Farhan Mughal, Ming Ronnier Luo, Yuzhao Wang, Lihao Xu and Muhammad Safdar

Abstract Recently, 3D image processing has become widespread in the various applications such as medical, animation, and graphics communication. There exist a number of techniques to transform 2D images into 3D. The purpose of this study was to develop a set of procedure to achieve precise color reproduction in cross-media color reproduction for 3D images and to simulate images under different illuminants. A 3dMD$^{®}$ system was used to capture images of 3D objects. A polynomial model-based camera characterization was implemented. To further enhance the scope of research, different 3D images were transformed into the spectral images via two different methods, principal component analysis (PCA) and Wiener. The spectral images were then used to transform images under different illuminants. Finally, a simulation of the appearance of 3D images on a display under different illuminants was successfully achieved.

Keywords 3dMD · PCA · Weiner · Method · 3D imaging · Spectral reflectance

6.1 Introduction

The 3D imaging has become popular in recent years. Many medical studies have been conducted for 3D imaging. Krissian et al. [3] developed a model based on the detection of tubular structure in 3D images. Markelj et al. [6] also developed a method for image-guided interventions. There have been many new studies involving in 3D imaging in the area of printing, medicine, etc.

M.F. Mughal · M.R. Luo (✉) · Y. Wang · L. Xu · M. Safdar
State Key Laboratory of Modern Optical Instrumentation, Zhejiang University,
Hangzhou, China
e-mail: m.r.luo@leeds.ac.uk

M.R. Luo
School of Design, University of Leeds, Leeds, UK

The goal of this research was to develop a method to calibrate 3D images in the form of spectral reflectance. Many models have been developed for multispectral imaging [7, 8], allowing for the estimation of the spectral reflectance from a set of colorimetric values such as XYZ tristimulus values. 3D images contain more information than 2D images by one extra dimension so that for 3D multispectral imaging, there is a need to extend the knowledge of 2D multispectral imaging by one more dimension.

A 3D system called 3dMD® was used, which captures 2D images using 6 RGB cameras and renders them to form a 3D image. So, 3dMD system can be considered as ideal system to transform knowledge of 2D images to 3D images. After the processing of the 6 captured images, 3D image can be viewed on a 2D screen by changing different viewpoints. To view high-quality 2D or 3D images on the screen, it is strongly desired to calibrate the color of the monitor to achieve accurate appearance reproduction of the image.

The main advantage to apply spectral image is to achieve non-metameric reproduction, i.e., can be acute to reproduce colored images in all illumination conditions.

6.2 Method

In the current work, Fig. 6.1 shows the workflow (see Fig. 6.1) to achieve 3D image reproduction. The 2D images were first transformed to XYZ using a camera model. The XYZ tristimulus values were then used to reconstruct spectral reflectance and finally display RGB images were achieved by using a monitor characterization model. The display RGB images were then displayed on a calibrated monitor. In total, the details of the above three stages in the workflow are described in the subsections below.

6.2.1 Camera Characterization Model

A 3dMD system first captured 2D images via 6 cameras and rendered 6 images to form a 3D image of the object. This is based on the proprietary software provided
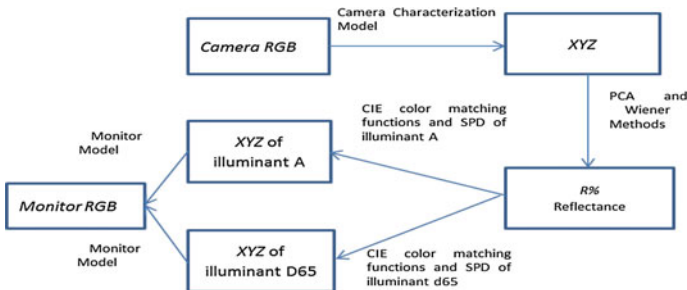
Fig. 6.1 Schematic diagram of the proposed method

by 3dMD system. To build the camera characterization model, A Macbeth Color Checker Chart (MCCC) including 24 colors was captured. Polynomial modeling-based camera characterization model was implemented to transform camera RGB values to camera independent XYZ tristimulus space [5]. The RGB to XYZ transformation equation is written as follows:

$$H = PM \qquad (6.1)$$

where P represents RGB values, H represents corresponding XYZ values, and M is the transformation matrix given by

$$M = \left(P^{\mathrm{T}}P\right)^{-1}P^{\mathrm{T}}H \qquad (6.2)$$

Equation 6.2 is solved to obtain transformation matrix M. Normally, P matrix has the dimensions of $n \times 3$ but expanding P beyond this leads to more accuracy. For example, in our case we extend P to $n \times 11$. The reason for expanding P to $n \times 11$ was optimality [5].

6.2.2 Transformation from XYZ to R%

After transformation of RGB to XYZ, the next target was to achieve multispectral image from the XYZ. Two approaches were used to achieve the target named as Principal Component Analysis (PCA) and Wiener methods [1, 10].

6.2.2.1 PCA

For the PCA method, the reflectance (r) to be reconstructed can be considered as a combination of basis vectors. Assume that B is the matrix formed by the basis vector:

$$r = B\alpha \qquad (6.3)$$

where α is an unknown. The relation between tristimulus XYZ values and reflectance (r) is given by:

$$\begin{bmatrix} X \\ Y \\ Z \end{bmatrix} = Mr \qquad (6.4)$$

Here, M is a 3 by n weighting table under D65 and CIE standard colorimetric observer functions. From Eqs. 6.3 and 6.4, Eq. 6.5 can be obtained and it is obvious that

$$\alpha = (MB)^{-1} \begin{bmatrix} X \\ Y \\ Z \end{bmatrix} \tag{6.5}$$

Substituting Eq. 6.5 in Eq. 6.3, we get the required reflectance (r).

6.2.2.2 Wiener Method

Another method to obtain spectral reflectance from tristimulus XYZ space called Wiener method was also implemented. The goal was same as PCA, i.e., to achieve the reflectance of each pixel from the XYZ values of the captured image. The reflectance in this case is given by Eq. 6.6

$$\hat{r} = W \begin{bmatrix} X \\ Y \\ Z \end{bmatrix} \tag{6.6}$$

the $n \times 3$ mapping matrix W is given by:

$$W = K_r M^{\mathrm{T}} \left(M K_r M^{\mathrm{T}} + K_n \right)^{-1} \tag{6.7}$$

where K is a covariance matrix obtained from the reflectance of weighted training data.

The spectral image can be easily converted to XYZ of different illuminants via the reflectance, SPD of the specific illuminant, and CIE color matching functions.

6.2.3 Transformation from XYZ to Monitor RGB

After obtaining XYZ from reflectance, XYZ were transformed to monitor-calibrated images. For this purpose, gain offset gamma (GOG) model was implemented [2]. All the images were transformed and displayed as the monitor-calibrated images in the 3D format.

6.3 Results and Discussions

Finally, the facial images of a person under different illuminants were calculated using the proposed method. Figure 6.2 clearly shows that there is a difference between the simulated and the original images. Comparing with the real human

Fig. 6.2 Different views of the 3D image. The *top three* images are the original images captured by 3dMD. The *second* and *third rows* show the monitor-calibrated 3D images under CIE standard illuminant D65 standard CIE illuminant A, respectively, reconstructed using method of PCA. *Fourth* and *fifth rows* show the monitor-calibrated 3D images under CIE standard illuminant D65 standard CIE illuminant A, respectively, reconstructed using Weiner method

illuminated under D65 and A simulators, the image reproduction can be considered accurate. This proves the effectiveness of the spectral reflectance to achieve color reproduction under different illuminants.

For the spectral reflectance, the images calculated from PCA and Wiener methods were compared using the 24 colors in MCCC. They were captured using 3dMD system and by using the proposed method, reflectance from the camera RGB was calculated for each color. Then, XYZ values from both the measured and the predicted reflectance were calculated. For both the PCA and the Wiener methods, the mean color difference was found to be 3.7 in CIEDE2000 units [4]. So, it can be concluded that both PCA and Wiener methods for the reconstruction of reflectance gave the same performance and the current results in terms of CIEDE2000 meet the criteria of acceptability and perceptibility with tolerance values found by Song et al. [9].

6.4   Conclusions

The workflow described here successfully worked for the 3D images. There is an obvious difference between captured image and calibrated images. Results also showed that the spectral reflectance of the 3D images can be used to simulate images on different illuminations.

References

1. Agahian, F., Amirshahi, S. A., & Amirshahi, S. H. (2008). Reconstruction of reflectance spectra using weighted principal component analysis. *Colour Research & Applications, 33*, 360–371.
2. Berns, R. S. (1996). Methods for characterizing CRT displays. *Displays, 16*(4), 173–182.
3. Krissian, K., Malandain, G., Ayache, N., Vaillant, R., & Trousset, Y. (2000). Model-based detection of tubular structures in 3D images. *Computer Vision and Image Understanding, 80*(2), 130–171.
4. Luo, M. R., Cui, G., & Rigg, B. (2001). The development of the CIE 2000 colour difference formula: CIEDE2000. *Color Research & Application, 26*, 340–350.
5. Luo, M. R., Hong, G., & Rhodes, P. A. (2001). A study of digital camera colorimetric characterization based on polynomial modeling. *Colour Research & Application, 26*(1), 76–84.
6. Markelj, P., Tomaževič, D., Likar, B., & Pernuš, F. (2012). A review of 3D/2D registration methods for image-guided interventions. *Medical Image Analysis, 16*(3), 642–661.
7. Miao, L., Qi, H., Ramanath, R., & Snyder, W. (2006). Binary tree based generic de-mosaicking algorithm for multispectral filter array. *IEEE Transaction on Image Processing, 15*(11), 3550–3558.
8. Safdar, M., Luo, M. R., Wang, Y., & Liu, X. Y. (2015). Multispectral imaging system based on tuneable LEDs. In *Proceedings of AIC/MCS2015 Tokyo, MCS1-2* (pp. 367–371).
9. Song, T., & Luo, M. R. (2000) Testing color-difference formulae on complex images using a CRT monitor. In *Proceedings of the Color and Imaging Conference, IS&T*
10. Yi-Fan, C., Cheung, V., Changjun, L., Luo, M. R., & Lee, S. L. (2012). Reflectance recovery using localised weighted method. In *Proceedings of CGIV 2012* (pp. 362–366).

Chapter 7
The Experimental Research of Color Measurements with Spectrophotometer

Yan Liu, Quanhui Tian and Xiaozhu Mou

Abstract To study the performance of the three spectrophotometers: Spectroeye, i1, and eXact, the spectral reflectance of *X*-rite ColorChecker® was measured with them. By computing the standard deviation of spectral reflectance and color difference ΔE_{ab}^*, the stability and repeatability characteristics of the three color measuring instruments were analyzed. The results showed that the standard deviations of spectral reflectance are less than 0.001. The average color difference between the measurements and reference data is less than $2\Delta E_{ab}^*$. The color difference between each two spectrophotometers is about $1\Delta E_{ab}^*$. The measurement error between the spectrophotometer is acceptable, so we could choose corresponding instrument according to the range of measurement wavelength.

Nowadays, people pay great attention to the color quality of color reproduction. The precision of the color measurement is particularly important for color reproduction. The color data mainly acquire from color measuring instruments [1]. Grasping the performance of measuring instrument and the differences between different measuring instruments for the control of printing quality is significant. This paper studies the measuring performance of Spectroeye, i1 Publish Pro2 (i1), and eXact [2]. By computing the standard deviation of spectral reflectance and color difference, we compare the stability and repeatability characteristics of the three color measuring instruments.

Y. Liu (✉) · Q. Tian · X. Mou
Department of Printing and Packaging Engineering,
Shanghai Publishing and Printing College, Shanghai, China
e-mail: sppcly@163.com

7.1   Principle of Spectrophotometer

There are two systems of print color measurement: density method and chromaticity method [3]. Density method is based on the measurement of the absorption characteristics of the ink layer. Chromaticity method is based on the measurement technology of the human perception [4].

At present, the instruments used for color measurement are densitometer, colorimeter, and spectrophotometer [5]. In these color measuring instruments, spectrophotometer has the highest measurement accuracy and is a suitable color measuring instrument for printing [6]. Spectroeye, i1, and eXact are spectrophotometers. Point location and telescopic arm are used in Spectroeye. EXact and i1 are using the measurement method of point location and hand-pressing type.

Spectrophotometer can measure the reflectivity in the visible spectrum on the color surface [7]. When a continuous spectrum light shines onto a color surface, light is reflected by the monochromator (composed of diffraction gratings or color interference filters) which is decomposed into monochromatic light with certain wavelength interval (5–10 nm, etc.) [8]. Then, measure reflectivity of the monochromatic light point by point. Using the formula given by CIE, the color tristimulus values can be calculate [9]. And the various color parameters can be further calculated.

7.2   Experimental Method

The experiment selected the *X*-rite ColorChecker® 24 color chips as the measuring sample. The color is integrated in many color series. The ColorChecker® has 24 color pieces, including the natural color, the primary color, and gray color. Most of these colors represent natural objects, such as human skin, leaves, and the blue sky. These color pieces can match the color of the natural object under any light sources. And they can also be used for any color reproduction process [10].

The measurement conditions are the D50 light source, 2° viewing angle, and under room temperature of 26 °C [11]. In order to guarantee the stability of the measurement data, the measurement started 20 min later after the spectrophotometer boot [12]. Three instrument measurement data have been got in the same period. In order to keep the consistency of the measured color piece position, we selected the center of each color piece to get the data. *X*-rite ColorChecker® was to be numbered 1–24 according to top to bottom and left to right. Three instruments all repeated the measurement 10 times on the same part. All the 24 color pieces were measured in the same way.

The data of spectral reflectance $\rho(\lambda)$ and CIE chromaticity values L^*, a^*, and b^* were directly gotten by Spectroeye, i1, and eXact [13]. X, Y, and Z were gotten by calculated. The measurement wavelength interval was 10 nm. The spectral wavelength range of i1 and Spectroeye is 380–730 nm. The spectral wavelength range of

eXact is 400–700 nm. In order to keep data consistency, the data of 400–700 nm was chosen to calculate and compare. The measuring frequency of the data was 10.

Spectroeye, i1, and eXact are all connected to the computer with a USB link. All measured data can be exported as EXCEL files by its software. The software of Spectroeye and i1 is GretagMacbeth KeyWizard V2.5. The software of eXact is DataCatcher.

7.3 Analysis of Experimental Data

7.3.1 Stability Test

In order to judge the stability of the instruments, the experiment compared the standard deviation of the spectral reflectance data of each instrument.

We denote the standard deviation by σ (see Formula 7.1).

$$\sigma = \sqrt{\frac{1}{N}\sum_{i=1}^{N}(x_i - \mu)^2} \tag{7.1}$$

In the Formula 7.1, N is the measuring frequency 10. X_i is the spectral reflectance. μ is the average of the 10 times' spectral reflectance. According to experimental design and the definition of the standard deviation, we used $N - 1$ instead of N for our calculation.

We calculated the standard deviation of the spectral reflectance of 24 color pieces and plotted the calculated results. The curves of the standard deviation closed each other. The curves of No. 11 and No. 14 color pieces' spectral reflectance standard deviation were representative as Figs. 7.1 and 7.2.
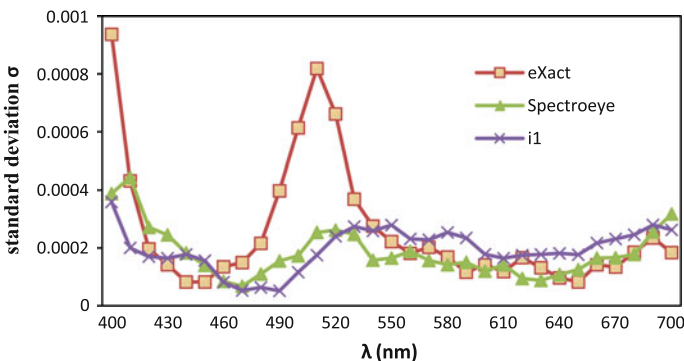
Fig. 7.1 Standard deviation curve of the spectral reflectance (No. 11 color)
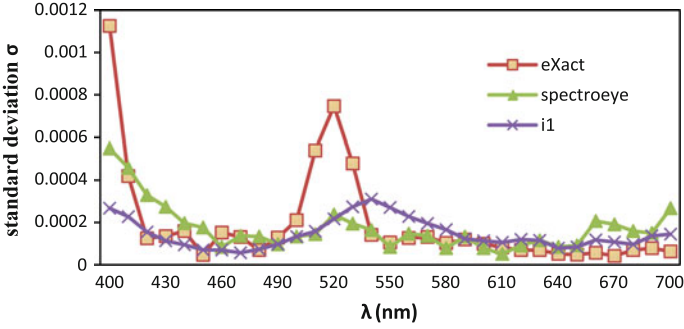
Fig. 7.2 Standard deviation curve of the spectral reflectance (No. 14 color)

From Figs. 7.1 and 7.2, the trend of the standard deviation of the spectral reflectance measured by the three instruments was basically similar. In 550–700 nm, the data of the standard deviation are small and the fluctuation is not big. In 490–550 nm, the fluctuation of the standard deviation is large. It means that the stability of these three instruments is not good in these wavelengths. The maximum standard deviation data of three instruments are all located in 400 nm, especially eXact. 400 nm is the first measured wavelength of eXact and the third of the Spectroeye and i1. The results show that the three instruments' stability in the beginning wavelength is not good enough. The results also show that the standard deviation data of Spectroeye and i1 are smaller than eXact. It means the stability of Spectroeye and i1 is better than eXact.

7.3.2 Repeatability Test

To evaluating the color reproduction quality and controlling the color reproduction, we often use the color difference to compare and control the color [14]. In the repeatability test, we calculated the color difference between the measured L^*, a^*, and b^* (average of 10 replicates) and the reference data given by GretagMacbeth (Table 7.1). Formula 7.2 is the color difference formula [15].

$$\Delta E_{ab}^* = \sqrt{\left(L_1^* - L_2^*\right)^2 + \left(a_1^* - a_2^*\right)^2 + \left(b_1^* - b_2^*\right)^2} \tag{7.2}$$

L_1^*, a_1^*, and b_1^* and L_2^*, a_2^*, and b_2^* are the CIE chromaticity values of the compared two colors.

Table 7.1 Standard reference values of *X*-rite ColorChecker®

| No. | Name | Original munsell notation | CIE 1976 *L*a*b**, D50, 2° | | |
		Hue	Value/chroma	L^*	a^*	b^*
1	Dark skin	3.05 YR	3.69/3.20	39.07	13.7	14.37
2	Light skin	2.2 YR	6.47/4.10	66.36	18.08	18.56
3	Blue sky	4.3 PB	4.95/5.55	50.66	−4.84	−21.44
4	Foliage	6.65 GY	4.19/4.15	44.03	−13.01	22.34
5	Blue flower	9.65 PB	5.47/6.70	55.87	8.88	−24.79
6	Bluish green	2.5 BG	7.0/6.0	71.47	−32.98	0.65
7	Orange	5 YR	6.0/11.0	62.37	36.05	56.58
8	Purplish blue	7.5 PB	4/10.7	40.77	9.18	−43.58
9	Moderate red	2.5 R	5.0/10.0	51.68	48.21	16.75
10	Purple	5 P	3.0/7.0	31.27	20	−20.83
11	Yellow green	5 GY	7.08/9.1	72.74	−22.6	57.15
12	Orange yellow	10 YR	7/10.5	72.35	19.57	68.76
13	Blue	7.5 PB	2.90/12.75	29.61	13.63	−49.65
14	Green	0.1 G	5.38/9.65	55.61	−37.19	31.81
15	Red	5 R	4.0/12.0	42.23	55.32	27.45
16	Yellow	5 Y	8/11.1	82.65	4.44	80.52
17	Magenta	2.5 RP	5.0/12.0	52.55	49.33	−14.42
18	Cyan	5 B	5.0/8.0	52.24	−28.24	−27.14
19	White	N	9.5/	96.37	−0.3	3.26
20	Neutral 8	N	8/	81.7	−0.56	0.25
21	Neutral 6.5	N	6.5/	66.49	−0.33	0.03
22	Neutral 5	N	5/	50.67	−1.06	−0.19
23	Neutral 3.5	N	3.5/	36.23	−0.48	−0.26
24	Black	N	2/	20.68	0.17	−0.55

7.3.2.1 Color Difference Evaluation of 24 Color Pieces

Figure 7.3 shows the color difference between the measured value and standard reference value. Table 7.1 shows the average color difference ΔE_{ab}^* between the measured value and standard value.

Judging from the color difference data in the Fig. 7.3, the ΔE_{ab}^* data are all less than 3.0. The results show that the color difference is fitted with the GB/T 7705-2008 level of high-precision products except for the No. 15 color patch. The ΔE_{ab}^* data of No. 15 are between 5.0 and 6.0, which are also fitted with the GB level of general products.

The average color differences measured by three instruments are all less than 2.0 as shown in Table 7.2. Specifically, the color difference measured by Spectroeye is the smallest, the secondary is i1, and the color difference measured by eXact is the largest.
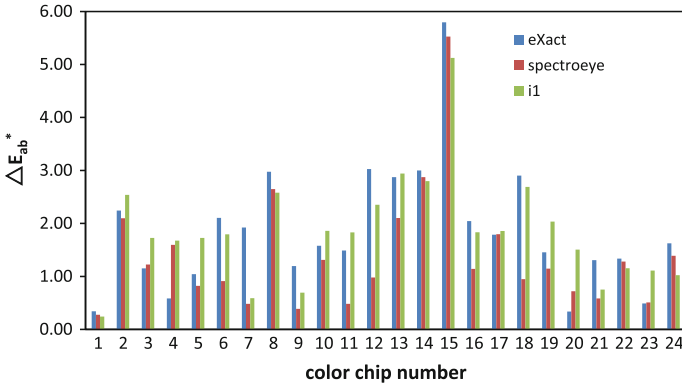
Fig. 7.3 Color difference between the measured value and standard value

Table 7.2 Average color difference of the measured value and standard value

	eXact	Spectroeye	i1
Average color difference	1.87	1.39	1.85

7.3.2.2   Measurement Evaluation of RGBCMY and Neuter Color

In order to further compare the repeatability of these spectrophotometers, we calculated the typical color-RGBCMY (Nos 13–18 color patches) and neutral color patches (Munsell hue was *N*, Nos 19–24). Table 7.3 shows the average color difference between the measured value and standard reference value of the typical colors. Table 7.4 shows the average color difference between the measured value and standard reference value of neutral color.

Judging from the Table 7.3, the average color difference of RGBCMY measured by Spectroeye is the smallest as 2.4. The secondary is i1. The average color difference of eXact is the largest.

Judging from the Table 7.4, the average color difference of neutral color measured by three instruments was closed to each other.

Table 7.3 Average color difference of the measured value and standard reference value of typical colors

	eXact	Spectroeye	i1
Average color difference	3.10	2.40	2.87

Table 7.4 Average color difference of the measured value and standard reference value of neutral colors

	eXact	Spectroeye	i1
Average color difference	1.09	0.94	1.26

Table 7.5 Color difference of the three instruments

Instrument unit	ΔE_{ab}^*		
	Minimum value	Maximum value	Average value
eXact and Spectroeye	0.24	3.1	1.17
eXact and i1	0.34	1.65	1.06
i1 and Spectroeye	0.33	2.46	1.12

7.3.3 Test of the Color Difference Between the Instruments

In order to analyze the difference among different instruments, we compared the color difference between each two instruments by Formula 7.2. The results are shown in Table 7.5.

From Table 7.4, the color difference between two instruments is very small.

7.4 Conclusions

This paper used Spectroeye, i1 Publish Pro2, and eXact to measure the *X*-rite ColorChecker®. We got the spectral reflectance and CIE chromaticity values L^*, a^*, and b^*. By computing the standard deviation of spectral reflectance and color difference ΔE_{76}, the stability and repeatability characteristics of the three color measuring instruments were analyzed. The results showed that the standard deviations were less than 0.001. The average color difference between the measurements and standard reference data was less than 2 ΔE_{ab}^*. The color difference between each two spectrophotometers was about $1\Delta E_{ab}^*$. The measurement error between the spectrophotometers is acceptable. But because of the difference of wavelength range, such as the wavelength range of eXact is 400–700 nm and the wavelength range of Spectroeye and i1 is 380–730 nm, we could choose corresponding instrument according to the range of measurement wavelength.

References

1. Draft International Standard ISO/DIS 13655.2, International Organization for Standardization, ISO/TC 130, DIN, Graphic technology—spectral measurement and colorimetric computation for graphic arts images, ICS 37.100.01, 2009.
2. 2013 A new handheld spectrophotometer—X-rite eXact. Printing Quality & Standardization, *2013*(1), 4.
3. Sun, B.-y., & Li, Y.-l. (2008). Density and chrominance measurement in printing quality control. *Packaging Engineering*, *29*(4), 48–50.
4. Yang, P. (2004). The comparison of color measuring instruments. *Printing Quality & Standardization, 10*, 11–13.

5. Ehbets, P. (2005). Spectrophotometer and its use: U.S. Patent 6,844,931.
6. Liu, L-p, & Guo, L-h. (2008). Principle of color measuring instruments and its application in printing. *Packaging Engineering, 29*(6), 101–103.
7. Mestha, L. K. (2000). 2Color printer color control system with automatic spectrophotometer calibration system: U.S. Patent 6,351,308.
8. Zhang, S-s. (2009). Research on chroma calculation methods and their influencing factors. *Packaging Engineering, 30*(11), 96–99.
9. Liu, H-x. (2008). *Printing chromatology*. Beijing: China Light Industry Press.
10. Robin Myers Imaging Home. (2009). GretagMacbeth ColorChecker®[EB/OL]. http://www.rmimaging.com/information/colorchecker.html
11. Zheng, Y-l, & Qi, Y-h. (2008). Analysis of visual field application in color measurement. *Packaging Engineering, 29*(9), 68–80.
12. Xiu, X.-j., & Tang, H.-j. (2011). A method of color calibration for different spectrophotometers. In *Communication Software and Networks (ICCSN), 2011 IEEE 3rd International Conference on IEEE.*
13. Xiu, X.-j., & Tang, H.-j. (2012). A Data Color Transferring Method for Printing & Dying Industry Using Spectrophotometer. In *Communication Systems and Network Technologies (CSNT), 2012 International Conference on IEEE.*
14. Huang, M., Liu, H.-x, & Xu, Y.-f. et al. (2006). Analysis of Uniformity of CIE94 and CIE2000 Color Difference Formulae. *Packaging Engineering*, *27*(6), 153–156.
15. Cheng, J-m, Chen, X-j, & Gu, K. (2006). *Color science*. Beijing: Science Press.

Chapter 8
The Color Characteristic Model Based on Optimized BP Neural Network

Hongtao Miao and Lizheng Zhang

Abstract Due to BP neural network's own limitations, it requires a large number of samples for complex prediction, and its generalization ability is weak. This paper puts forward an optimized BP neural network algorithm. The methods focus on data normalization in order to improve maximum speed limit, the inertia constant, and fitness function to eventually optimize BP neural network weight value and threshold value to reduce its distribution range before using BP neural network for color prediction. Reducing the possibility of BP neural network prediction model getting into local optimization has good nonlinear fitting capability and higher prediction accuracy of color space conversion. If using in the ICC profile, it will ensure the accuracy of the color conversion.

Keywords PSO · BP neural network · Color management · ICC profile

8.1 Introduction

At present, the color management system CMS uses ICC standard to manage the color space of different equipment in workflow process. The color management system is composed of Profile Connection Space (PCS), the ICC profile, and color management module (CMM). Among them, the color management module (CMM) is the core. Color space conversion requires a large amount of accurate data. These data are

H. Miao (✉)
Packaging and Printing Department, Henan University of Animal Husbandry and Economy, Zhengzhou, China
e-mail: 774609787@qq.com

L. Zhang
School of Printing and Packaging Engineering, Beijing Institute of Graphic Communication, Beijing, China
e-mail: zhanglizheng@bigc.edu.cn

collected in a lot of color space model experiments, which use common printing materials and process under different production conditions.

But at present, color-matching accuracy of main color management software cannot meet the requirements of industrial production. So in the color-matching algorithm, a new matching algorithm is needed to make up for the ICC profile. The PSO-BP neural network algorithm can combine the advantages of two algorithms so that color management can meet the practical application requirements completely (see [1, 2]).

8.2 BP Neural Network Algorithms

The neural network algorithm is inspired by the function of human brain and neural system. If color space is considered as a nonlinear control system, it can be used to simulate the system.

As show in Fig. 8.1, this is a layer network system with three inputs and three outputs. Each circle represents a neuron, a vector arrow represents a neural key, and its added value is W_{ij}, where i is the number of nerves which receive the input, and j is the number of the output nerve. So the output of a_i is as follows:

$$a_i = f\left(\sum w_{ij}a_j\right) \tag{8.1}$$

Summation range is all output of a_i. f is nonlinear function.

In order to train this network, some training data are required (x_k, y_k), which means that if the input is x_k, then output of the network should be y_k, and if the output of the network is z_k, then the error is as follows:

$$E = \sum \|y_k - z_k\|^2 \tag{8.2}$$

The sum of its summation is all training data. At this time, the error can determine the direction and intensity of the value adjustment:

$$\Delta w_{ij} = g\left(E, \Delta w_{ij}\right) \tag{8.3}$$

Fig. 8.1 Three layer networks
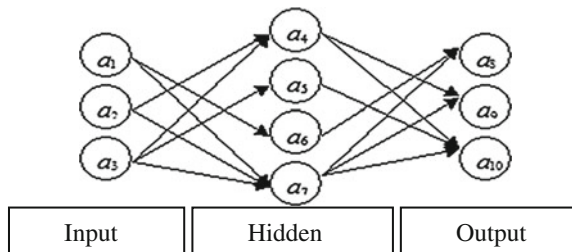
The accuracy of the neural network method depends on the structure, training method, and training data of the network. Compared with other methods, the advantages of neural network are as follow:

(1) A valuable memory space is saved, if it is used in hardware environment and the speed is not a problem.
(2) If the network structure and training method are reasonable and efficient, its precision can also meet the application requirements [3].

However, the disadvantages of applying neural network to complete color space conversion are long training time, which cannot be calculated in minutes or hours, and it will take a few days. The research found that using the PSO algorithm to optimize the neural network to complete the color space conversion can effectively improve the shortcomings of neural network algorithm. As a simple and effective random search algorithm, PSO can also be used to optimize the neural network [4]. Although the research of this aspect is still in the initial stage, the research results show that PSO has great potential in optimizing neural network.

8.3   PSO Algorithms

PSO is a very simple algorithm and can effectively optimize the various functions. To some extent, this algorithm is between genetic algorithm and evolutionary programming. The algorithm is very dependent on the random process, which is also its similarity with evolutionary programming. In this algorithm, global optimal and local optimal adjustment is very similar in crossover operator of genetic algorithm. This algorithm is also used to the concept of fitness, which is the common feature of all evolutionary computation methods [5, 6].

In the PSO algorithm, the m dimension (the dimension of each particle) is searched by a group of N particles; each particle corresponds to a potential solution to an optimization problem. The position and speed of i are expressed as $x_i = (x_{i1}, x_{i2},\ldots,x_{im})$ and $v_i = (v_{i1}, v_{i2},\ldots,v_{im})$. The target function value of x_i is called the fitness value of f_i, and the algorithm can measure the particle's quality; v_i determines the direction and distance of particle movement. Each particle is updated by tracing two optimal solutions: p_i is the historical optimal solution of particle search, and p_g is the optimal solution for the whole group. Particle velocity and position renewal formula are as follows:

$$v_{id}^{k+1} = \omega v_{id}^{k} + c_1 \xi \left(p_{id}^{k} - x_{id}^{k} \right) + c_2 \eta \left(p_{gd}^{k} - x_{id}^{k} \right) \tag{8.4}$$

$$x_{id}^{k+1} = x_{id}^{k} + v_{id}^{k+1} \tag{8.5}$$

Among them, c_1 and c_2 are the learning factors, it usually take '2'. ω is the inertia value, ξ and η are the number of random between (0, 1), and each one-dimensional speed is limited within $v_{\max}$ [7].

8.4 Improvement of PSO Algorithm

8.4.1 Dynamically Adjust the Learning Factor Strategy

In the PSO algorithm, the expression of the learning factors c_1 and c_2 is usually 2. Through the experiment, the learning factor of the time change has a great influence on the performance of the algorithm, and the expression is as follows:

$$c_1 = (c_{1f} - c_{1i}) * \text{iter}/\text{MAXITER} + c_{1i} \tag{8.6}$$

$$c_2 = (c_{2f} - c_{2i}) * \text{iter}/\text{MAXITER} + c_{2i} \tag{8.7}$$

Among them, c_{1f} and c_{1i} are the maximum and minimum values of c_1, c_{2f} and c_{2i} are the maximum and minimum values of c_2. iter is the number of iterations of the algorithm, and MAXITER is the maximum number of iterations that the algorithm allows [8].

8.4.2 Inertia Weight Factor Change

In the PSO, inertia weight factor is the most important adjustable parameter. It was found that dynamic w can obtain the stable and better results of the fixed value w.

Inertia weight expressions are as follows:

$$\omega = (\omega_1 - \omega_2) * (\text{MAXITER} - \text{iter})/\text{MAXITER} + \omega_2 \tag{8.8}$$

Among them, ω_1 and ω_2 are the maximum and the minimum of the inertia weight, iter is the number of the current iteration, and MAXITER is the maximum iteration number of the algorithm. By study, if inertia weight in the interval [0.4, 0.95], with the iteration number of linear decline, the problem has better effect [9].

8.4.3 Maximum Speed Setting

PSO algorithm has the characteristics of losing the particle diversity in the late stage of flight. It is best to maintain the particle diversity without increasing the particle number and particle dimension. Because of changing the particle diversity by increasing the number of particles or increasing the particle dimension, the number of arithmetic operations of the algorithm will increase exponentially, which will seriously affect the effectiveness of the algorithm. In order to fully and effectively maintain diversity of particle, the particle swarm can be divided into two parts. Without an increase in particle number and particle dimension, two PSO are each

used to global search and local optimization. For global search, when it is iterated, the particle velocity will be reinitialized once; with the increase of the number of iterations, it will search space and search the global optimal value, while the probability of the neighborhood value will be significantly increased. For local search, it will search the optimal value rapidly and accurately nearby the historical optimal value, which is searched by global search [10]. In this way, the different particle swarm has to do its job, and the global search and the local optimization are carried out simultaneously. In particular, the position of global search particle swarm is updated as formula (8.5), and the speed update formula is as follows:

$$v_{id}^{k+1} = \mathrm{rand}(0, v_{\max}) \tag{8.9}$$

Global search particles emphasize the particle diversity, in order to avoid the particle search space; the particle speed of the update is the random number limited between $(0, v_{\max})$. The location update is related to the last position of the particle and the current speed [11].

The formula of the position of local optimization particle swarm's single-step update is shown in formula (8.5), and the formula of the speed of local optimization particle swarm's single-step update is as follows:

$$v_{id}^{k+1} = \omega v_{id}^k + c_1 \xi (p_{id}^k - x_{id}^k) + c_2 \eta (p_{gd}^k - x_{id}^k) + c_3 \zeta (p_{sd}^k - x_{id}^k) \tag{8.10}$$

Among them, c_3 is the learning factor, ζ is the random number between (0, 1), and p_s is the global search PSO solution of the global history.

The particle swarm of global search transfers the historical optimal individual information to the particle swarm of local optimization particle swarm; the particle swarm will optimize by the formulas (8.5) and (8.10). The learning factor c_3 determines the intensity of the evolutionary information obtained from the global search PSO.

In type (8.8), the choice of ω, c_1, c_2, and c_3 has a greater impact on the performance of the algorithm. According to previous test experience, inertia weight is set in the range of [0.4, 0.95], c_1 is set in the range of [0.5, 2.5], c_2 is set in the range of [0.75, 2.5], and the optimum ranges of c_3 are in the range of [0.75, 2.5].

8.4.4 Improved Fitness Function

In order to overcome the premature phenomenon of PSO, the algorithm of PSO is improved in order to improve the search performance of the PSO. The specific transformation process is described below. Firstly, the error formula of the network is determined, "$E_k = T_k - T_{1k}$ (T_k is the measurement value of the network, T_{1k} is the predictive value of the network)." And then, the average color-difference formula of all samples is determined.

$$E_1 = \frac{1}{K} \sum_{K=1}^{N} \sqrt{E_{(1,K)}^2 + E_{(2,K)}^2 + E_{(3,K)}^2} \qquad (8.11)$$

(N is the number of samples). Finally, in the programming software determined the fitness function is 'fitness = exp (1/$E1$)'.

8.5 Particle Swarm Optimization BP Neural Network

8.5.1 Optimization Process

See Fig. 8.2

8.5.2 Data Normalization

Before training the network, the statistical distribution of the uniform sample is needed. Why use the normalized? First, you must know a concept called singular
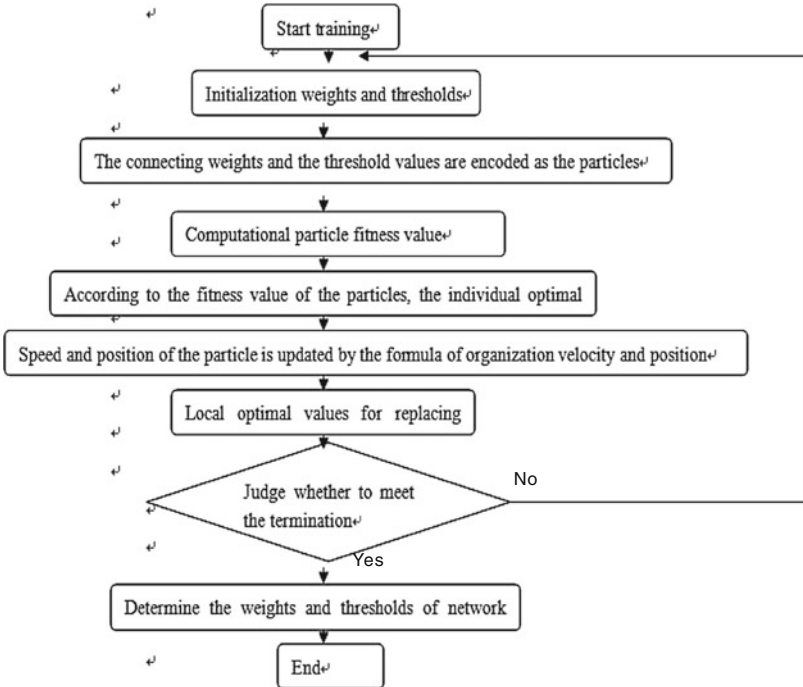
Fig. 8.2 Optimization process

sample data. The singular sample data are particularly large or small sample relative to other samples.

The following example:

$$m = \begin{bmatrix} 0.11 & 0.16 & 0.32 & 0.35 & 40; & 0.24 & 0.27 & 0.25 & 45 \end{bmatrix};$$

One of the fifth columns of data relative to the other 4 columns of data can be called singular sample data. Because of the increase of network training time caused by singular sample data, it may cause the network to be unable to converge, so the best advanced shape normalized, and if there is no singular sample data, it does not need to be normalized. [12] Premnmx function is used to normalize the input data (RGB) and output data (Lab) of the network, and the normalized data will be distributed within the range of [−1, 1].

The correlation experiment proves that the average color difference fluctuation range obtained by using data normalization is small and stable, so that the error of selection is small.

8.6   Particle Swarm Update Iterative Step Method

Through the particle dimension and neural network connection weights of the mapping relationship and the particle dimension of the search space settings, BP neural network is established, to calculate the fitness value, to update speed, and to calculate the optimal particle (i.e., optimal weights and thresholds) assigned to the neural network.

8.6.1   Simulation Experiment Principle

In order to verify the accuracy of this algorithm, the first step is to establish a standard color chart, print out the standard color chart, and measure the Lab values of every color. The Lab value of the measurement is given as the training data to optimize the BP neural network system after the PSO, so as to carry out the corresponding calculation.

Then, set up a test chart, print out the test chart, and measure the Lab values of each color, as a standard value. After the PSO, the BP neural network system is calculated, and the Lab value of the test color chart is calculated as the reference value. Then, calculate the color difference between the two.

8.6.2 Experimental Instruments

Printer: EPSON9800; color measuring instrument: X-Rite Eye-One Pro divided into light photometer; correction and characteristics of software for i1Profiler; operation platform for the Windows XP system.

8.6.3 Experiment Specific Method

Standard color chart is identified: the Lab from 0 to 100 at intervals of 20–6 level segmentation. Lab was taken from one of the values of a color. Thus, there are 216 colors. After printing, measure the color standard using the software 'Eye-One', and record 'Lab' value of the 216 colors and store it in a text file. These values as training data will impart BP neural network system, so as to train network.

The test target of identified: the lab from 0 to 100 at intervals of 10–11 level segmentation, lab were taken one of the values of a color, so a total of 1331 colors. On the one hand the color standard value will input training network where the calculated values should appear; on the other hand, after printing use 'Eye-One' measure the color standard, record test color values, and store it in a text file.

In order to facilitate comparison, in this paper program algorithm is prepared under the MATLAB environment to construct two kinds of forecasting model, BP neural network prediction model (BP model) and the particle swarm algorithm-optimized BP neural network prediction model (PSO-BP model). In the experiment, the minimum average color difference E was used as the evaluation criterion, and the color difference of the color was calculated by comparing the color difference of the color to the uniform color space of CIE1976L*a*b*:

$$\Delta E_{ab}^* = \sqrt{\Delta L^2 + \Delta a^2 + \Delta b^2} \tag{8.12}$$

Analysis in Table 8.1 shows, under the same network structure, transfer function, training function and expected color error, which are the conditions, improved PSO-BP network model accuracy (average value of 1.37) was higher than that of BP neural network (ΔE averaged 3.02), indicating that PSO-BP network model of color space conversion nonlinear quasi-ability is stronger than the BP neural network, and PSO algorithm can indeed affect optimization of initial weights of BP neural network and the threshold.

Table 8.1 Forecast effect data of BP and PSO-BP network

Model types	Maximum ΔE	Minimum ΔE	Averaged ΔE
BP	14.1	1.84	3.02
PSO-BP	3.85	1.11	1.37

8.7   Conclusions

It is important to find the network weights and threshold in BP neural network algorithm, mainly through improved maximum speed limit, setting dynamic inertia constant and fitness function to optimize the weights and thresholds of BP neural network, narrow the distribution range, and then use the BP neural network algorithm for color prediction. Experiments show that the proposed method greatly reduces the possibility of local minimum of BP neural network and improves the convergence rate of the model. And the accuracy of data prediction is improved obviously, which is of great help to color-matching in color feature file, and further guarantees the accuracy of color transfer.

References

1. Zhang, Y., Wu, Q., & Ma, Z. (2010). A survey of particle swarm optimization and its application. *Micro Computer Information, 11*(3), 72–77.
2. Zhou, J., Chen, J., & Liu, G. (2013). An overview of inertia weight in particle swarm optimization. *Guangdong Power, 32*(3), 55–56.
3. Grosan, C., & Abraham, A. (2007). Hybrid evolutionary algorithms, methodologies, architectures, and reviews. *Studies in Computational Intelligence (SCI), 75*, 1–17.
4. Garnier, S., Gautrais, J., & Theraulaz, G. (2007). The biological principles of swarm intelligence. *Swarm Intelligence, 1*, 3–31.
5. Eberhart, R., & Shi, Y. (2001). Particle swarm optimization: Developments, applications and resources. In *Proceedings of IEEE Congress Evolutionary Computation* (Vol. 1, pp. 81–86)
6. Parsopoulos, K., & Vrahatis, M. (2002). Recent approaches to global optimization problems through particle swarm optimization. *Natural Computing, 1*, 235–306.
7. Banks, A., Vincent, J., & Anyakoha, C. (2007). A review of particle swarm optimization. Part I: background and development. *Natural Computing, 6*, 467–484.
8. Poli, R., Kennedy, J., & Blackwell, T. (2007). Particle swarm optimization: An overview. *Swarm Intelligence, 1*(1), 33–57.
9. van Ast, J., Babuška, R., De Schutter, B. (2008). Particle swarms in optimization and control. In *Proceedings of the 17th World Congress The International Federation of Automatic Control* (pp. 5131–5136). Seoul, Korea, July 6–11
10. Li, R-j. (2003). Study on color space conversion model of from RGB to CIEXYZ. *Packaging Engineering, 30*(3), 79–81.
11. Hong, L., & Chu, G-l. (2013). RGB to CIEXYZ color space conversion. *Packaging Engineering, 34*(21), 85–89.
12. del Valle, Y., Venayagamoorthy, G., Mohagheghi, S., et al. (2008). Particle swarm optimization: Basic concepts, variants and applications in power systems. *IEEE Transactions on Evolutionary Computation, 12*(2), 171–195.

Chapter 9
The Model of Flexographic Spot-Color Matching Based on the Improved Kubelka–Munk Theory

Ya'nan Zhang, Maohai Lin and Xintao Gao

Abstract Because the model of flexographic spot-color matching based on Kubelka–Munk theory is proposed for the dye matching, it will produce color difference and affect color accuracy when it is applied to the ink matching. In this paper, the model of computer color matching based on double-constant Kubelka–Munk theory is improved. The model of flexographic spot-color matching in which the water-based ink is used as printing ink and corrugated paper is used as substrate is formed. In this model, first the sample data are obtained by using IGT printability tester. Then, tristimulus value matching theory is its basic, and a series of mathematical calculations are used to obtain the initial matching values. And then, a more accurate formula is obtained through multiple iterations. Finally, the improved matching model is completed. The experimental results show that the model can quickly complete the color matching, and the result is accurate and stable. Moreover, the matching model meets the requirements of environmental protection and has good prospects.

Keywords Spot-color ink · Kubelka–Munk theory · Flexographic printing

9.1 Introduction

Currently, the main matching method of spot-color ink is based on manual operation. It requires worker to have a very rich experience; moreover, it leads to the wastage of time and ink. The development of computer color matching technology

Y. Zhang · M. Lin (✉)
College of Printing and Packaging Engineering, Qi Lu University of Technology,
Jinan, China
e-mail: mhlin@spu.edu.cn

Y. Zhang
e-mail: Yanan9109@163.com

X. Gao
Shandong Hongfei Packaging Co., LTD, Dezhou, China

has solved the problem well [1]. At present, the computer color matching is mainly based on the single-constant Kubelka–Munk theory. That is to say, we just need to know the K/S value of each ink. The advantage of this method is simple calculation, but it has a poor accuracy [2, 3]. The Kubelka–Munk theory based on the double constant needs to know the unit absorption and scattering coefficients of each ink; the process of computation is complicated, so the theory needs to be improved [4].

In this paper, the new double-constant Kubelka–Munk theory is introduced and its process is derived. The new double-constant values corresponding to the each ink are obtained, and then, the exact formula is obtained; finally, the experiment is done to verify the theory.

9.2 Based on the New Double-Constant Tristimulus Value Matching Algorithm

The Kubelka–Munk formula study the relationship between object spectral reflectance and ink absorption and scattering coefficients, the function ρ is defined as

$$\rho = 1 + \frac{K}{S} - \left[\left(\frac{K}{S} \right)^2 + 2 \left(\frac{K}{S} \right) \right]^{\frac{1}{2}} \tag{9.2.1}$$

where K and S are ink absorption and scattering coefficients; ρ is the spectral reflectance.

The value of K/S in Eq. (9.2.1) can be computed as

$$\frac{K}{S} = \frac{(1 - \rho)^2}{2\rho} \tag{9.2.2}$$

When several inks are used for color matching, the absorption and scattering of the mixed ink should be the sum of each ink absorption and scattering. The mixed function of double-constant ink is defined as

$$\left(\frac{K}{S} \right)_{\text{mix}} = \frac{c_1 K_1 + c_2 K_2 + \ldots + c_n K_n + K_t}{c_1 S_1 + c_2 S_2 + \ldots + c_n S_n + S_t} \tag{9.2.3}$$

where K_i and S_i are the i kind of ink absorption and scattering coefficients, K_t and S_t are the substrate absorption and scattering coefficients, and c_i is the i kind of ink concentration.

The steps of new double-constant color model are as follows:

(1) Find out new double-constant k/S_t and s/S_t
    First, divide both numerator and denominator of Eq. (9.2.3) by S_t.

Let $K_t/S_t = (K/S)^t$, $K_i/S_t = (k/S_t)^i$, and $S_i/S_t = (s/S_t)^i$, and the function K/S can be computed as

$$\frac{K}{S} = \left(\sum c_i \left(\frac{k}{S_t} \right)^i + \left(\frac{K}{S} \right)^t \right) \Big/ \left(1 + \sum c_i \left(\frac{s}{S_t} \right)^i \right) \qquad (9.2.4)$$

When there is only one kind of ink, Eq. (9.2.4) can be computed as

$$\frac{K}{S} = \left[(K/S)^t + c \left(\frac{k}{S_t} \right) \right] \Big/ [1 + c(s/S_t)] \qquad (9.2.5)$$

where k/S_t and s/S_t are the new double constants of ink and the combination of Eqs. (9.2.1), (9.2.3), and (9.2.5) is the new double-constant Kubelka–Munk theory.

(2) Determine new double-constant value of each ink and substrate.
First, mix the C, M, and Y inks and varnish, and make their concentration be 20, 40, 60, and 80 %, respectively. Then, print color bars with IGT printability tester, measure their spectral reflectance, and finally obtain each ink and substrate's new double-constant values by using MATLAB programming.

(3) Find out the initial solution of the formulation.
The goal of the formulation is to make the tristimulus values of initial sample equal to target samples, that is,

$$t = TER^a = TER^m \qquad (9.2.6)$$

where t is the column vector of tristimulus values, R^m and R^a are the column vectors of initial sample and target sample's spectral reflectance, T is the matrix of CIE standard colorimetric observer's color matching function, and E is the matrix of CIE standard illuminant's spectral power distribution. Analogous to Allen approximate wavelength:

$$\Delta R = \frac{\partial R}{\partial \left(\frac{k}{S_t} \right)} \Delta \frac{k}{S_t} + \frac{\partial R}{\partial \left(\frac{s}{S_t} \right)} \Delta \frac{s}{S_t} \qquad (9.2.7)$$

$$R_j^a - R_j^m = \frac{\partial R_j^a}{\partial \left(\frac{k^a}{S_t} \right)_j} \left(\left(\frac{k^a}{S_t} \right)_j - \left(\frac{k^m}{S_t} \right)_j \right) + \frac{\partial R_j^a}{\partial \left(\frac{s^a}{S_t} \right)_j} \left(\left(\frac{S^a}{S_t} \right)_j - \left(\frac{S^m}{S_t} \right)_j \right) \qquad (9.2.8)$$

According to the new double-constant theory, we can know

$$\frac{k^m}{S_t} = (K/S)^t + \sum c_i (k/S_t)^i \qquad (9.2.9)$$

$$\frac{S^m}{S_t} = 1 + \sum c_i (s/S_t)^i \qquad (9.2.10)$$

According to Eqs. (9.2.8)–(9.2.10), we can know

$$
\begin{aligned}
R_j^a - R_j^m &= \frac{\partial R_j^a}{\partial \left(\frac{k^a}{S_t}\right)_j} \left(\left(\frac{k^a}{S_t}\right)_j - \left(\frac{K}{S}\right)_j^t - \sum c_i \left(\frac{k}{S_t}\right)_j^i \right) \\
&+ \frac{\partial R_j^a}{\partial \left(\frac{S^a}{S_t}\right)_j} \left(\left(\frac{S^a}{S_t}\right)_j - 1 - \sum c_i \left(\frac{s}{S_t}\right)_j^i \right)
\end{aligned}
\qquad (9.2.11)
$$

Its matrix expression is as follows:

$$R^a - R^m = D_k\left(f_K^a - f^t - \emptyset_k C\right) + D_S\left(f_S^a - n - \emptyset_s C\right) = 0 \qquad (9.2.12)$$

where n is a 16×1 identity matrix and f^t is the column matrix of $(K/S)^t$. $\emptyset_k$ and $\emptyset_k$ are matrices of the new double-constant values. C is the column matrix of each ink concentration. f_K^a and f_S^a are the column matrices of $(k^a/S_t)_i$ and $(S^a/S_t)_i$, $i = 400, 420\ldots700$ nm. $D_{K,j}$ and $D_{S,j}$ are diagonal matrices, $j = 400, 420\ldots700$ nm.

According to Eq. (9.2.7), find out the partial derivatives of k/S_t and s/S_t: $d_{k,j} = \frac{-2(R_j^a)^2}{\frac{S^a}{S_t}\left[1-(R_j^a)^2\right]}$ $d_{k,j} = \frac{R_j^a\left(1-R_j^a\right)}{\frac{S^a}{S_t}\left(1+R_j^a\right)}$, j is the wavelength, $j = 400, 420\ldots700$ nm.

After a series of matrix operations, finally the formula of ink can be obtained:

$$C = \left[TE(D_k\emptyset_k) + D_S\emptyset_S\right]^{-1} * TE * \left[D_k\left(f_K^a - f^t\right) + D_S\left(f_S^a - n\right)\right] \qquad (9.2.13)$$

Because the value of S^a/S_t is unknown, $d_{k,j}, d_{k,j}, f_K^a$ and f_S^a cannot be determined. Here, suppose $S^a/S_t = 1$, and then, find out the values of $d_{k,j}, d_{k,j}, f_K^a$ and f_S^a; finally, find out the initial formula of the ink.

(4) Determine the precise formula using iterative approximation method

During the process of iterative approximation method, first compute S^a/S_t of each wavelength; let $S^a/S_t = S^m/S_t = 1 + \sum c_i (s/S_t)^i$, then we can know $f_S^a, d_{k,j}$ and $d_{s,j}$. From Eqs. (9.2.8) and (9.2.9), we can determine K/S value, then obtain the spectral reflectance by Eq. (9.2.1), then find out tristimulus values by Eq. (9.2.6), and then determine their differences $\Delta X, \Delta Y$ and $\Delta Z, \Delta t$ is their matrix form.

Based on the principle that the tiny ΔC is proportional to the Δt, so the following approximate formula can be obtained:

$$
\begin{cases}
\Delta X = \left(\dfrac{\partial X}{\partial c_1}\right)\Delta c_1 + \left(\dfrac{\partial X}{\partial c_2}\right)\Delta c_2 + \left(\dfrac{\partial X}{\partial c_3}\right)\Delta c_3 \\[2mm]
\Delta Y = \left(\dfrac{\partial Y}{\partial c_1}\right)\Delta c_1 + \left(\dfrac{\partial Y}{\partial c_2}\right)\Delta c_2 + \left(\dfrac{\partial Y}{\partial c_3}\right)\Delta c_3 \\[2mm]
\Delta Z = \left(\dfrac{\partial Z}{\partial c_1}\right)\Delta c_1 + \left(\dfrac{\partial Z}{\partial c_2}\right)\Delta c_2 + \left(\dfrac{\partial Z}{\partial c_3}\right)\Delta c_3
\end{cases}
\tag{9.2.14}
$$

Its matrix form is as follows:

$$
\Delta t = B \times \Delta C \tag{9.2.15}
$$

Let $P = \begin{bmatrix} \frac{\partial X}{\partial \rho^m_{400}} & \frac{\partial X}{\partial \rho^m_{420}} & \cdots & \frac{\partial X}{\partial \rho^m_{700}} \\ \frac{\partial Y}{\partial \rho^m_{400}} & \frac{\partial Y}{\partial \rho^m_{420}} & \cdots & \frac{\partial Y}{\partial \rho^m_{700}} \\ \frac{\partial Z}{\partial \rho^m_{400}} & \frac{\partial Z}{\partial \rho^m_{420}} & \cdots & \frac{\partial Z}{\partial \rho^m_{700}} \end{bmatrix}$, $Q = \begin{bmatrix} \frac{\partial \rho^m_{400}}{\partial c_1} & \frac{\partial \rho^m_{400}}{\partial c_2} & \frac{\partial \rho^m_{400}}{\partial c_3} \\ \frac{\partial \rho^m_{420}}{\partial c_1} & \frac{\partial \rho^m_{420}}{\partial c_2} & \frac{\partial \rho^m_{420}}{\partial c_3} \\ \vdots & \vdots & \vdots \\ \frac{\partial \rho^m_{700}}{\partial c_1} & \frac{\partial \rho^m_{700}}{\partial c_2} & \frac{\partial \rho^m_{700}}{\partial c_3} \end{bmatrix}$, $B = PQ$.

Because $X = \bar{x}_{400}E_{400}\rho^m_{400} + \bar{x}_{420}E_{420}\rho^m_{420} + \ldots + \bar{x}_{700}E_{700}\rho^m_{700}$, solve partial derivative $\partial X/\partial \rho_{400}$, and then $P = TE$. What is more $\partial \rho^m_{400}/\partial c_1 = \frac{\partial \rho}{\partial \left(\frac{k}{s_t}\right)_{400}} \times \frac{\partial \left(\frac{k}{s_t}\right)_{400}}{\partial c_1} + \frac{\partial \rho}{\partial \left(\frac{s}{s_t}\right)_{400}} \times \frac{\partial \left(\frac{s}{s_t}\right)_{400}}{\partial c_1} = D_{K1,400}\emptyset_{K1,400} + D_{S1,400}\emptyset_{S1,400}$. So $Q = D_K\emptyset_K + D_S\emptyset_S$, then $B = TE * (D_K\emptyset_K + D_S\emptyset_S)$, and put it into the formula (9.2.15), $\Delta t = TE(D_K\emptyset_K + D_S\emptyset_S) \times \Delta C$; finally, $\Delta C = TE(D_K\emptyset_K + D_S\emptyset_S)^{-1}\Delta t$.

9.3   Experiments

9.3.1   Experimental Materials and Instruments

The instrument used for the experiment was IGT printability tester, and the experimental materials include Qingdao Tianlong water-based inks (cyan, magenta, yellow), varnish, and linerboard. The software programs we used were Color iControl and MATLAB R2009a. The printing speed was 0.3 m/s, and the pressure between printing cylinder and substrate was 200 N and that between printing cylinder and anilox roller was 300 N. The ruling number of anilox roller was 80 l/cm.

9.3.2   Experimental Procedure

First, mix the cyan, magenta, and yellow inks and varnish, and make their concentration be 20, 40, 60, and 80 %, respectively [5]. Then, print color bars with IGT printability tester, measure their spectral reflectance with iControl, and finally

Table 9.1 The new double-constant value of cyan, magenta, and yellow inks

Wavelength (nm)	$k/S_t(c)$	$s/S_t(c)$	$k/S_t(m)$	$s/S_t(m)$	$k/S_t(y)$	$s/S_t(y)$
400	1.2441	−0.4771	9.2453	0.1061	10.9757	0.0313
420	−0.5975	−0.6995	12.0983	0.382	13.9698	0.2827
440	−2.2792	−1.0091	13.7886	0.5369	15.3278	0.4156
…	…	…	…	…	…	…
700	20.967	1.4285	−0.4671	−1.2876	−0.4554	−1.2108

Table 9.2 The color difference between standard samples and target samples

Number	L1	a1	b1	L2	a2	b2	ΔE
1	69.5483	−14.1215	−10.5081	69.3639	−16.7433	−10.656	2.63
2	67.3035	0.7951	0.4553	67.6838	8.44	1.4138	7.71
3	76.3075	−23.56	−40.143	76.138	−23.1614	−39.3	0.95
4	71.80268	−18.9	−40.847	71.73	−20.2476	−38.93	2.48
5	69.44	−16.693	−11.1483	69.364	−16.744	−10.656	0.5
6	71.8027	−18.6	−40.847	71.73	−20.2476	−38.93	2.34
7	80.191	−24.864	−37.946	80.0647	−24.28	−37.52	0.73
8	89.9265	61.1124	27.32	89.359	58.954	26.277	2.46
9	85.8768	57.867	34.776	85.373	59.406	32.29	2.97
10	94.8912	7.5853	77.5711	94.7484	8.8246	77.445	1.25

obtain each ink and substrate's new double-constant values by using MATLAB programming, as shown in Table 9.1. Then, choose 10 groups of spot colors as standard samples, denoted as $A1$, $A2\ldots A10$, and then measure their spectral reflection and chromatic values. And then their concentration ratio of each ink can be known by our model. Print these color bars according to their concentration ratio as target samples. And then measure the chromatic values of target samples and finally determine their color difference, as shown in Table 9.2.

9.3.3 Experimental Results and Analysis

Table 9.1 shows the new double-constant values of cyan, magenta, and yellow inks and linerboard, k/S_t and s/S_t are the new double constants, so the calculations of k/S_t and s/S_t are very important parts in this experiment [6]. Table 9.2 shows the color differences between standard samples and target samples. From Table 9.2, we can see that all color differences are within 8, in which the maximum is 7.71, the minimum is 0.5, and the mean of them is 2.4. The result is acceptable, so we think this color matching algorithm is a practical project.

9.4 Conclusions

As we all know, the color matching algorithm based on KM theory has been the hot research of color matching theory. In this paper, we made a detailed introduction to the specific process of new double-constant KM algorithm, and an experiment is done to verify this theory. From the experimental results, we can conclude that this algorithm conforms to the printing requirement of color. There are also some shortcomings in this experiment, that is, the substrate must be the same, which affects this theory's extensive application. Next, we need to find the correction coefficient, making the color model to be applied to all the paper. Therefore, a lot of researches need to be done to make improvements.

References

1. He, G-x, & Zhou, M-x. (2009). Recipe formulation based on spectral visual response fitting. *Coloration Technology, 125*, 178–183.
2. He, G-x. (2004). The method of determining new two-constant of colorant. In *Proceedings of China Optical Society*.
3. Gomez, J. A. (2002). The new generation of color matching & correction: working smarter with today's software improvements in color formulation technology for the coating industry. *Painting & Coatings Industry, 18*(9), 88–91.
4. Zhang, L., Zhang, M., & Yang, X. (2010). Research on color difference in spot color printing. *Packaging Engineering, 31*(19), 1–2.
5. Liu, H. (2010). Practice and analysis of color matching for spot ink in offset printing. *Packing Engineering, 31*(19), 80.
6. Zhou, S., Zheng, Y., & Cao, C. (2008). *Graphic arts chromatology* (pp. 51–59). Graphic Communications Press.

Chapter 10
Parameter Optimization Experiment for Soft Proofing

Hongxia Zhou and Maohai Lin

Abstract Some experiments were designed to check the effects of monitor parameters such as color temperature, brightness, and gamma value on soft proofing. We have two illuminant levels D50 and D65, two brightness levels 100 and 120, and two gamma value levels 1.8 and 2.2 to be chosen in constructing *international color consortium* profiles (ICC profiles). Then, soft proofing simulation experiment was executed. Comparisons were made between the results of soft proofing and printer to obtain the optimum parameters. Results were evaluated by color difference analysis, individual component analysis of $\Delta L^*, \Delta a^*$, and Δb^* values, and psychophysical experiments. Experiments show that the performance of soft proofing varies a lot with different parameters. And it can get a better performance with the appropriate parameters. At last, the optimal parameter combination was obtained.

Keywords ICC profile · Soft proofing · Color difference analysis · Psychophysical experiment

10.1 Introduction

Nowadays, soft proofing technology attracted the attentions by many professional researchers. It is necessary to improve the accuracy level of soft proofing. So that we can make sure the copy color presented by other media will stay close to the original. To solve this problem, some people is improving the parameters in the display manufacturing process or selecting the reasonable modulation of the display parameters such as color temperature, brightness, and gamma values. Experiments in the paper were carried out by the Eizo display. It has some steps such as checking

H. Zhou · M. Lin (✉)

School of Printing and Packing Engineering, Qilu University of Technology, 250353 Jinan, China
e-mail: imhlin@163.com

the differences among the appearances presented by the same display using different display parameters, analyzing the gap among appearances, and finding the optimal combination of parameters for Eizo display.

Color temperature represents the white point in display. Brightness of display represents the brightness of white point. Gamma value determines the contrast of image in monitor in every brightness level [1]. Besides an accurate display profile, there are accuracy that depends on the color management module and the specified white point (color temperature) [2]. Now, no agreed method of determination of profile accuracy was available. Color difference was executed for evaluation of different profiles made based on different parameters in one monitor.

10.2   Designs of Experiments

10.2.1   Equipment Used

Eizo EV2313W liquid crystal display (LCD), Dell host, eye-one pro of X-rite company, and Konica Minolta's digital printer. Ninety-nine color patches in *i1 profiler* software were selected as test target, as some experiments show that the differences in quality of ICC profile documents produced with 99 or 4096 color are small [4].

10.2.2   Experiment

10.2.2.1   Experiment Preparation

Make sure that setting indoor lighting, cleaning the display screen, giving display a stable state by warming up for 30 min. And restore the display factory settings, turn off the screen savers [3], and connect eye-one pro to computer.

Design experiment: Let the view on the screen be close to printing image, and it required color temperature of D50 or D65. It also had brightness of 100 and 120. The gamma values have a decisive influence on lightness shadow, and 1.8 and 2.2 is chosen with Dell host. Combine three kinds of parameters into eight groups (Table 10.1).

10.2.2.2   Steps of Experiment

(1) Creation of monitor profile: compared with *Profilemaker*, *i1profiler* produced profiles with higher accuracy [5], so *i1profiler* was used. Open the Advanced Options in *i1profiler*, and select the color management. Set parameters and

Table 10.1 Eight combinations of parameters in display setting

Group	Color temperature	Brightness	Gamma value
1	D50	100	1.8
2	D50	100	2.2
3	D50	120	1.8
4	D50	120	2.2
5	D65	100	1.8
6	D65	100	2.2
7	D65	120	1.8
8	D65	120	2.2

    calibrate eye-one pro. Monitor profiles were created in *i1profiler* operation process. Twenty-four color patches coming from *Color Checker* were used to detect calibrated monitor.

(2) Creation of profile to printer: at first, keep the printer warm-up to stable point and connect the measuring instrument eye-one pro. Choose the color management button in *i1profiler* and set parameters in Advanced Options. Print IT8.7/3 target for measuring the data and use these data to create profile to printer.

(3) Implementations of soft proofing: at the beginning, keep the display on stable point in 30 min and set ICC profile to monitor. There are steps in the following text.

Step 1, Open *Photoshop*, we could find the setting option and select the Custom option in Edit option. Then, we might set the RGB color space as Adobe RGB (1998) and CMYK color space as U.S. Web Coated (SWOP) v2, and close the Color Management Policies option. Step 2, Open the color target. In View option, we might find the proof setup, select the Custom option, set the Device to Simulate option as the profile to printer, and set Rendering Intent option as Absolute Colorimetric. Step 3, Make the images full screen one by one in *Photoshop*. Comparisons were made about the views of images between printer and monitor.

(4) Experimental data: Every combination of parameters created a profile, and soft proofing was carried out in *Photoshop*. *Eye-one pro will be* used to measure the color patches presented on the Eizo monitor and will get the RGB values. Each patch should be measured 3 times and save the mean value. Taking into account the stability and effects of the sensitivity on monitor, black point should be measured eight times with 1-min interval and save the mean value.

10.2.2.3   The Analysis of Experimental Data

Every group of data measured from above experimental work by measuring instrument, was compared with the original data measured from paper subtract above experimental work. ΔE of the monitor patches and printer patches was

Table 10.2 Some analysis about ΔE in eight groups

Group	1	2	3	4	5	6	7	8
Avg	3.09	3.10	2.43	2.33	2.93	2.71	2.76	2.57
Var	1.92	1.83	1.51	1.54	1.47	1.20	1.90	1.81
Max	8.86	8.78	7.72	8.26	8.53	7.27	9.30	9.24
Min	0.48	0.66	0.53	0.44	1.05	0.68	0.48	0.76

calculated, which is recorded as $x_1, x_2, x_3 \ldots x_n$, based on the formula CIEDE2000. It is said that CIEDE2000 formula has the best result than other formula, such as CIELAB, CIE94, and CMC [6]. The calculation such as average of ΔE, variance of ΔE by Eq. 10.1, maximum of ΔE, and minimum of ΔE are shown in Table 10.2.

$$\text{Variance} = s^2 = \frac{(x_1 - M)^2 + (x_2 - M)^2 + (x_3 - M)^2 + \ldots + (x_n - M)^2}{n} \quad (10.1)$$

In Eq. 10.1, n is the number of color patches and M is the mean of ΔE.

According to the evaluation of ΔE from Table 10.1, the Group 4 has the lowest value of ΔE, and the Group 3 and Group 8 followed. The lowest variance value of ΔE is Group 6, and Group 5 and Group 4 followed. Taken together, the combination of parameters in Group 4, namely D50 on color temperature, 120 on luminance, and 2.2 on the gamma value has optimum effect in soft proofing. And Group 3, Group 6, and Group 8 followed.

Then, the analysis of each component value, namely ΔL^*, Δa^*, and Δb^*, was shown in Table 10.3. As there were more number of data in every group , we signaled the mean of original data as $\overline{\Delta L^*}$, $\overline{\Delta a^*}$, and $\overline{\Delta b^*}$ for simplification.

As shown in Table 10.3, the overall range of the variation of Δa^* values representing the D value (difference value) of the two groups with respect to red and green brightness value is higher than the range of variation of ΔL^* and Δb^* representing brightness values and yellow-blue value, respectively. The value of brightness was

Table 10.3 The average data and the variance data of $\overline{\Delta L^*}$, $\overline{\Delta a^*}$, and $\overline{\Delta b^*}$

Group	Avg			Var		
	$\overline{\Delta L^*}$	$\overline{\Delta a^*}$	$\overline{\Delta b^*}$	$\overline{\Delta L^*}$	$\overline{\Delta a^*}$	$\overline{\Delta b^*}$
1	−2.19	0.66	1.96	1.23	14.63	9.90
2	−2.28	0.89	1.92	1.12	15.66	8.51
3	1.29	−0.48	−2.05	1.01	11.97	5.25
4	1.22	−0.62	−1.67	1.01	12.63	4.75
5	2.05	−0.67	1.75	1.02	16.94	8.20
6	1.80	−0.68	1.50	0.98	17.69	7.45
7	1.24	−0.69	1.49	0.98	16.00	8.05
8	0.71	−0.73	1.52	1.07	16.31	8.55

floating small and had the good stability, the average of Δa^* values was relatively small, but was least centralized, overall had a big variance, and Δb^* values followed. From the numerical stability, we can select the optimum combination of parameter ΔL^*, the minimum variance, which explained that the difference value between the two data relatively was small changes. We can choose the minimum mean value from the eight groups of ΔL^* values as the best choice, and Group 8 had the minimum value in 8 groups data, followed by Group 4 and Group 7.

Since the variance of Δb^* values is greater than the variance of Δa^* values, the variance of Δb^* values is relatively stable on the second order; we selected the minimum value from the means of every Δb^* value as the optimum selection. The result is that the group 3 is the first and followed by the group 4 and group 5. At last, we had two methods to select the optimum parameter combination. It is received that the Group 5 combination of display parameters, namely D65 on the temperature, 100 on brightness, and 1.8 on the gamma value, is the optimum selection comprehensive of the above two methods.

At the end, ICC profiles had been loaded in the *Color Thinker pro v3.0.3* software. In that way, we can see the size of color gamut determined by the given ICC profile. According to the detection, some difference has been found that two ICC profiles made by two illuminant levels had the different sizes of color gamut. The ICC profile having D65 illuminant level had a bigger color gamut size than it having D50 illuminant level. But the profiles having different brightness levels and different gamma value levels had slight difference in color gamut size.

10.2.3   Psychophysical Experiments

Color science is developed from the development of study of psychophysical experiments and the study of human color vision characteristics. Evaluation of color reproduction is still based on the human visual effect-based assessment. Here, this paper had designed a psychophysical experiment for evaluating the result of the soft proofing color reproduction.

The design of test experiment for color reproduction is based on human visual effect: methods of observation and memory matching.

10.2.3.1   The Setting of the Environment

Keep the ambient lighting not too bright. Light box was placed on the side of display and let them kept side by side. Set the brightness of light box on the color temperature of D65. At first light box should be opened and preheated for 30 min, then put the print reproductions in the light box with its back against the light box's back wall to be observed. *Photoshop* software was started in Eizo display to carry out the soft proofing experiment, and open the image to be observed in Photoshop program.

10.2.3.2   Test Page

Choose pictures with skin colors and other colors, such as the black color representing accuracy of the neutral gray reproduction and some memory color, namely grass color, blue sky color, and so on.

10.2.3.3   Grading System

Divide the test into five grade levels. The first level has no color difference that sense is same to each color. The second level is feeling vaguely some color differences, but very weak. The third level is an acceptable color, and after careful observation, observers can see one or a few slight color difference. The fourth grade level has color differences which can be pointed out without a very careful observation.

10.2.3.4   Observation

Ten people were selected as observers; they are all accepted professional education. There were three test images such as color patch, skin color, and grasslands. Observers stood in front of the light box at a distance of 60 cm directly, forming two-degree field coverage. First observers stared light box in 1 min to suit the brightness. Then, observers looked at the prints placed in light box, then turned their eyes to Eizo monitor, and checked the images opened in the monitor. Then, evaluated the result and graded the view between the monitor and printer.

10.2.3.5   Calculation of Results

The formula for evaluation of ΔE between soft proofing and the printer toke the mean data as the result. Here, the Eq. 10.2 is given as follows:

$$A = (N_1 \times 1 + N_2 \times 2 + N_3 \times 3 + N_4 \times 4 + N_5 \times 5)/M \qquad (10.2)$$

In Eq. 10.2, A was the average value and M was the times of observations. For one test color, N_1, N_2, N_3, N_4, N_5 represent the number of scores on each level. Calculate the average scores from three images presented by each experiment with different combinations of display parameters, and save it as the final data.

10.2.3.6   Analysis of the Result

Record the evaluation scores given by viewers for each image and complete the calculation process as shown in Table 10.4.

Table 10.4 The average of evaluated scores in every group

Group	1	2	3	4	5	6	7	8
Avg	2.16	2.25	2.25	2.16	2.08	2.08	2.08	2

According to the data, colors were slightly yellowish on occasion of D50 color temperature, and view feeling of color patch was rather partial dim and had a big difference with the print. On the D65 color temperature, observers were allowed to adapt to the orient with the given color temperature. It can reduce the effect of the color temperature in the comparison. Overall, the soft proofing with a D65 color temperature is more likely to be accepted by observers.

10.3   Summaries

The comparison of ΔE, psychophysical experiments, and analysis of stability and the tendency about each variation component were carried out. The result of experiments showed that the monitor brightness has less effect on simulating color and has good stability. Overall, the hue of monitor trends to green and yellow. Results indicated that Eizo display has the parameters combination of D65 color temperature, 100 on brightness, and 1.8 on gamma value and can make the appearance of soft proofing more easily acceptable.

References

1. Tian, Q. (2004). The influence of gamma value on display. *Printing Engineering*, 43–44
2. Marin, J. (2011). Calibration and profiling for soft proofing. *Printing Industries of America*
3. Hong, L., & Jiang, X.-z. (2012). *Research of liquid crystal display color management standardization: Printing quality and standardization* (pp. 29–34, p. 6).
4. Fleming III, P. D., Sharma, A. *Color management with ICC profiles: Can't live without it so learn to live with it* (p. 19).
5. Liang, H. (2013). *Quality evaluation of LCD monitor characteristic profile: Printing quality and standardization* (pp. 38–43, p. 6).
6. Zhao, B., Zheng, Y. –l. (2012). *Evaluation on the performance of color-difference formula under various viewing conditions: China printing and packaging study* (Vol. 04 24–28, p. 5).
7. Fleming III, P. D., Chovancova, V., Starr, B., Sharma, A. *CRT and LCD Monitors for Soft Proofing* (p. 28).

Chapter 11
Research on Color Reproduction Based on Different Random Edition of IT8.7/4 Target

Chunyan Du, Peiyong Feng, Lu Chen and Zhengrong Yan

Abstract Color reproduction is always important and difficult in printing quality control. To establish standard data which are suitable for printing ink and color features is particularly important. IT8.7/4 standard is oriented to the application requirement of printing development by CGATS. There are two kinds of formats—random and visual layout; the former is more suitable for quality control of printing process. In order to control the specific device color reproduction quality effectively, customers can determine the data distribution in random edition according to specific equipment. In this paper, we set two random seeds to generate different random layouts by VC++. The correlationship between printing quality characterization and color data distribution in IT8.7/4 is discussed. That can be used in printing technology.

Keywords IT8.7/4 · Random edition · Color

11.1 Introduction

Color reproduction is always important and difficult in printing quality control, so color management is the key to reproduce the image color faithfully. Color management process is mainly divided into three steps: instrument correction, characterization, and color space conversion [1–5]. Therein, characterization is the core part of the color management technology, which is to produce characterization file of output device accurately. Color standards that defined data set of ink value combinations must be used in four-color process printing characterization.

So far, color managers in printing enterprise commonly used several input data for characterization of four-color printing, such as IT8.7/3 and ECI2002. IT8.7/3

C. Du · P. Feng (✉) · L. Chen · Z. Yan
School of Packaging and Materials Engineering, Hunan University of Technology,
Zhuzhou, China
e-mail: fpyedu@163.com

composed of 928 color pieces and gray scale was launched by ISO in 1996. This standard defines a data set of ink value combinations that may be used to characterize four-color process printing. In 2002, ECI developed a set of characterization standard data named ECI2002 that aims to meet all publishing and halftone printing. IT8.7/4 is an expanded data set by CGATS in 2005. The IT8.7/4 standard does not require that any particular arrangement can be used for printing the data set. However, it was felt by the CGATS committee that default layouts were desirable to facilitate use of the target in many applications. Accordingly, two default layouts are defined for the convenience of users. One is for "visual" use where the appearance of the target is based on the ECI visual layout, and the additional patches required by CGATS are contained in four columns across the 33 patch short dimension. This allows the row–column designators for the patches contained in the ECI visual layout to remain unchanged. In the second layout, the patches were randomized to minimize the influence of the target arrangement itself on the final results. Although CGATS support the default randomized standard, this does not mean that using IT8.7/4 is bound to achieve optimization data in printing operation [1]. In fact, in order to control the specific device color reproduction quality effectively, customers can determine the data distribution in random format according to specific equipment. In this paper, we settled two random seeds to generate different random layouts by VC++ and research the relationship of IT8.7/4 color data distribution with printing quality control, which can be used in printing technology.

11.2   Experiment

Pseudorandom number generator is an algorithm which produces a sequence of numbers approximately random. The sequence is not truly random, because it can be reproduced from a small set of initial parameters, one of them called the seed (which must be truly random). By far, the most common method for seeding a simulation is to use the time and date. While this creates what appears to be a unique number, there is very little variation in the seeds. There are two random number-related internal functions: rand() and srand(). The former provides us with access to your operating system's random number generator (which is either good or bad, depending on your operating system). The srand() function accepts a seed value that rand() will use. If we give srand() the same value each time, rand() will generate the same "random" numbers each time. In this study, we use the srand() function to generate the random seed [2–4].

We numbered the IT8.7/4 default randomized data (Fig. 11.1a) 1 to 1617 first and then rearranged the 1617 color patches by VC++. Because the original IT8.7/4 format color piece is arranged for 49 × 33, we must use the same matrix, so we can measure conveniently. Considering the data shown in VC++ should not be too much, so we assigned 11 lines in a row and 49 columns from A1 to W2. Rearranged the color patch by stochastic function, and export rearranged data and pictures of
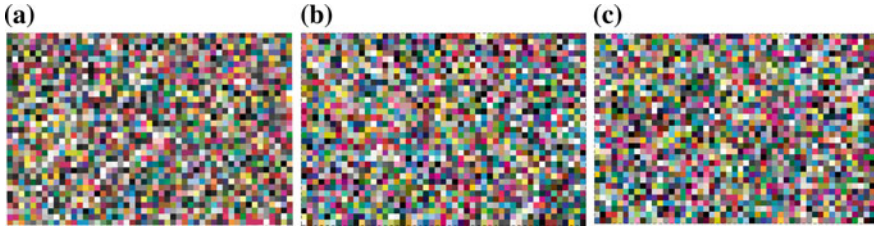
Fig. 11.1 Color target in experiment. **a** Default color target picture. **b** Rearranged randomized target 1. **c** Rearranged randomized target 2

randomize 1 (Fig. 11.1b) and randomize 2 (Fig. 11.1c). Then, we printed the three targets, measured them and done profiling.

11.3   Results and Discussion

In this section, we first investigated the color quality (L*, a*, and b*) of the three targets. And then, we do color management, because it is the key to reproduce the image color faithfully. Color management process is mainly divided into three steps: instrument correction, characterization, and color space conversion. Characterization is the core of color management technology. The gamut of device usually is noted in characteristic profile which shows the color range of device to be displayed [5–9]. Then, we compared the gamut of them later.

11.3.1   Color Quality Evaluation

As shown in Figs. 11.2, 11.3, 11.4, and 11.5, we know that the L* of two rearranged targets is larger than the L* of the default target, but a* value and b* value are diametric. It turned out that rearranged color looks brighter, and the color contains little red and yellow. When comparing the two rearranged targets, the color
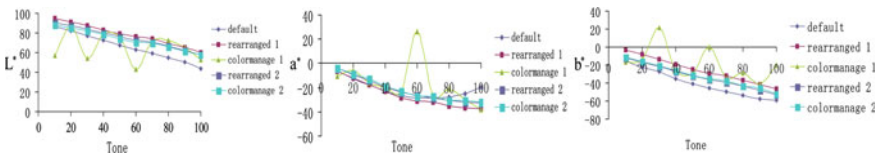
Fig. 11.2 L*, a*, and b* value of five group data of single C. The five group data are default target, rearranged target 1, color manage 1, rearranged target 2, and color manage 2. *Color manage 1* means the characteristic data of the rearranged target 1. *Color manage 2* also means the characteristic data of the rearranged target 2
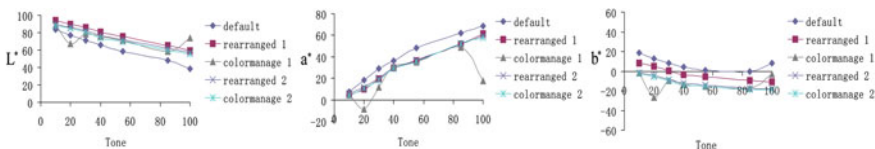
Fig. 11.3 $L*$, $a*$, and $b*$ values of five group data of overprint color of Y and M. Therein, Y is 20 %, and M changes from 0 to 100 %. The five group data are default target, rearranged target 1, color manage 1, rearranged target 2, and color manage 2. *Color manage 1* means the characteristic data of the rearranged target 1. *Color manage 2* also means the characteristic data of the rearranged target 2
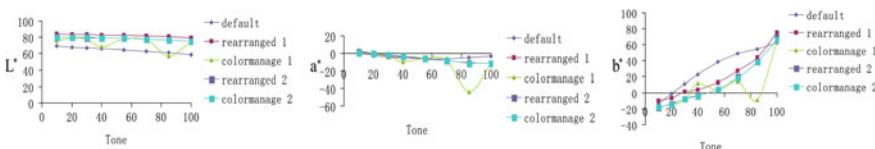
Fig. 11.4 $L*$, $a*$, and $b*$ values of five group data of overprint color of C, Y, and M. Therein, C and M are 20 %, and Y changes from 0 to 100 %. The five group data are default target, rearranged target 1, color manage 1, rearranged target 2, and color manage 2. *Color manage 1* means the characteristic data of the rearranged target 1. *Color manage 2* also means the characteristic data of the rearranged target 2
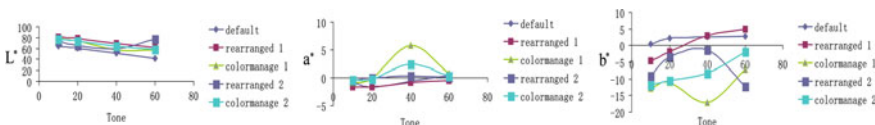
Fig. 11.5 $L*$, $a*$, and $b*$ values of five group data of overprint color of C, Y, M, and K. Therein, C, Y, and M are 20 %, and K changes from 0 to 60 %. The five group data are default target, rearranged target 1, color manage 1, rearranged target 2, and color manage 2. *Color manage 1* means the characteristic data of the rearranged target 1. *Color manage 2* also means the characteristic data of the rearranged target 2

value of random target 1 is larger than that of target 2 in single color and two tones. Nevertheless, $L*$ and $b*$ are larger, and $a*$ becomes smaller in other halftone areas.

Therefore, data configuration of targets can lead to deviation within the scope of whole tone. Printing performance is different as well.

After color management, the color value is coincident with single and double tones of randomized target 2, which means color management does not effect. For three-color and four-color areas, there are obvious differences, especially in the shadow area. For rearranged target 1, the color data are volatile in highlight, halftone, or dark area. Color management is not successful because the data are remarkably different compared with before.
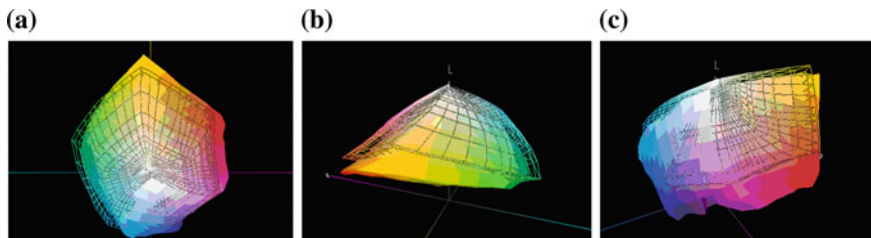
Fig. 11.6 Gamut photographs of the default target and rearranged randomize target 1 in CIELAB color space. The mesh plot is the gamut of default target. The colorized one is the gamut of rearranged randomized target 1. **a–c** are pictures from three different angles
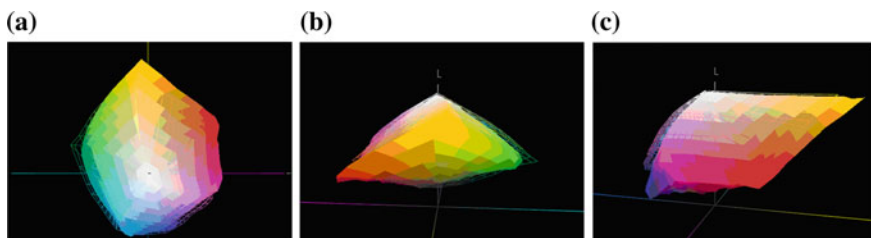
Fig. 11.7 Gamut photographs of the default target and rearranged randomize target 2 in CIELAB color space. The mesh plot is the gamut of default target. The colorized one is the gamut of rearranged randomized target 2. **a–c** are pictures from three different angles

11.3.2 Gamut Comparison

After characterization, we discussed the gamut in order to study the relationship between randomized targets of color management.

Green area of the randomized target 1 goes beyond the default standard gamut, and the yellow, magenta, and blue parts are smaller. That means random format 1 can show more green color, and the other colors are little; brightness is larger. Overall, gamut of the random format 1 is smaller than that of the default standard target (Fig. 11.6).

Randomized target 2 can show more green color and blue color. It's gamut is wide (Fig. 11.7).

11.4 Conclusions

In a nutshell, different random patterns and different arrangement of data could lead to poor printing and wrong characteristic due to the different state parameters of printing and measurement equipment. The random format layout was influenced intensively by them. In essence, the default randomized target is not completely

random. The coverage of ink is consistent per 5 rows or columns. If a color patch is 6 mm, 5 lines are equal to the inking width of modern offset press. So, the random format layout must be defined by printing and measuring equipment.

References

1. Imageable Files of IT8.7/4 Default Layouts. http://www.npes.org.html. Accessed June 19, 2015.
2. Goldreich, O., Goldwasser, S., & Micali, S. (1986). How to construct random functions. *ACM, 33*(4), 792–807.
3. Jain, R. (2006). *Random number generation*. Presentation, University of Washington. Available online at http://www.cse.wustl.edu/~jain/cse567-06/
4. Park, S. H., & Keith, W. M. (1998). Random number generators: Good ones are hard to find. *Communications of the ACM, 31*(10), 1192–1201.
5. Chai, X. L., & Luo, X. N. (2004). The analysis of mechanism and model of color management. *Computer Science, 31*(12), 1–5.
6. Morovic, J., & Luo, M. R. (2001). The fundamentals of gamut mapping: A survey. *Journal of Imaging Science and Technology, 45*(3), 283–290.
7. Wu, G. Q., Yang, X. Y., & Lei, X. (2008). Investigation of the methods of device characterization. *Packaging Engineering, 29*(9), 70–72.
8. Morovic, J. (2008). *Color gamut mapping*. England: Wiley.
9. Moroney, N. (2002). Color matching functions and blue constancy, Tokyo, Japan, pp. 419–420.

Chapter 12
Digital Camera-Based Appearance Meter (AppMeter)

Muhammad Safdar, Ming Ronnier Luo, Yuteng Zhu and Xiaoyu Liu

Abstract Currently, people use luminance or illuminance meters to measure illumination at different spots in a room to know the appearance. A more robust method is needed to measure the spatial distribution of light as the spot measurement-based methods do not correspond to visual perception. The current study was conducted to propose an instrumental method to measure the appearance. The CIE color appearance model CIECAM02 was modified and proposed as an imaging method to predict the appearance attributes from an RGB image. As brightness is a function of CCT and Duv according to the previous studies, CIECAM02 brightness formula was extended in the current study. Raw data and images from three different experiments were collected to test the model. The correlation between predictions of modified CIECAM02 and visual data was found statistically significant for three different experiments.

Keywords CIECAM02 · Brightness · Colorfulness · Hue · Uniformity

M. Safdar · M.R. Luo (✉) · Y. Zhu
State Key Laboratory of Modern Optical Instrumentation, Zhejiang University,
Hangzhou, China
e-mail: m.r.luo@leeds.ac.uk

M. Safdar
Department of Computer Science, COMSTS Institute of Information Technology,
Sahiwal, Pakistan

M.R. Luo
School of Design, University of Leeds, Leeds, UK

X. Liu
College of Science, Harbin Engineering University, Harbin, China

12.1   Introduction

Due to the advances in LED lighting, LED illuminants with a wide range of correlated color temperature (CCT) are available. The spatial brightness, appearance of objects, and perception of interiors are affected by CCT of illuminants used [1–4]. Li et al. [1] conducted an experiment to scale appearance in a real lit room. Hunt [2] investigated how does the changes in light intensity change the color saturation. Boyce et al. [3] investigated the performance of color discrimination and scaled perception of interiors under illuminations of different CCTs. Shepherd et al. [4] determined the subject's impression of a room and accessed the importance of the adaptation luminance and light distribution. The above studies show that scaling or measuring the appearance under given lighting conditions is important.

Currently, luminance or illuminance meters are used and different points in the room are measured to know the distribution of illumination. These photometric measurements do not correspond to the visual perception, and measurement errors may also occur due to a little change in measuring angle. A visual perception-based method is needed to measure appearance including brightness, hue composition, and colorfulness. The International Commission on Illumination (CIE) has formed two technical committees (TC1-80 and TC1-88) to study the methods for spatial brightness scaling and estimation [5], which shows the importance of the current study.

An instrumental method, to measure appearance that corresponds to visual perception, is needed. The ultimate objective of this study was to use an ordinary digital RGB camera as appearance measurement tool which is used to capture the interior of the room and estimate the room appearance attributes. The CIECAM02 is a well-established CIE color appearance model that was tested and modified in the current study [6].

12.2   Method

The CIECAM02 was tested as an imaging method to predict the appearance of the interior of the room. The attributes of room appearance model (RAM) include spatial brightness, colorfulness, and hue composition.

The previous studies have found that spatial brightness depends on CCT and Duv as well as luminance, e.g., a bluish (or cooler) light appears to be brighter. In the current study, brightness function of CIECAM02 was extended (see later). Note that the present brightness attribute of CIECAM02 is just a function of luminance of the adapting field, not that of CCT and Duv. The new brightness function depends on CCT and Duv as well as on luminance of adapting field, given in the equation below:

$$Q' = Q\big(-1.3 \times 10^{-8}T^2 - 30.2D^2 + 0.7 \times 10^{-4}TD$$
$$+ 0.2 \times 10^{-4}T - 6.9D + 0.4\big) \tag{12.2.1}$$

where Q, T, and D represent original CIECAM02 brightness, CCT, and Duv, respectively. The constant coefficients were determined using experimental data (see Experiment 1 later). The proposed method can calculate CCT and Duv values from the image of the scene [7]. The region of interest or uniform white area of the image is cropped and transformed to YXY space, and CCT and Duv values are calculated. The CCT concept is valid only if the distance of the test source from Planckian radiator is less than a certain limit, i.e., 0.5 in terms of Δuv. The CIECAM02 with extended brightness formula was then used to predict the appearance from RGB images of the interior of the room.

The RGB images of the scene were stored in RAW format to preserve the color information. The RAW RGB values were then transformed to device-independent color space XYZ to input to the current model. The polynomial modeling-based digital camera colorimetric characterization model was used for RGB to XYZ transformation [7]. The MCCC characterization chart was captured with the scene to use for camera characterization. The model crops uniform white area in the scene and inputs the image to the CIECAM02 after transformation to XYZ color space. The schematic diagram of the proposed model is shown in Fig. 12.1.

Fig. 12.1 Work flow of the proposed model
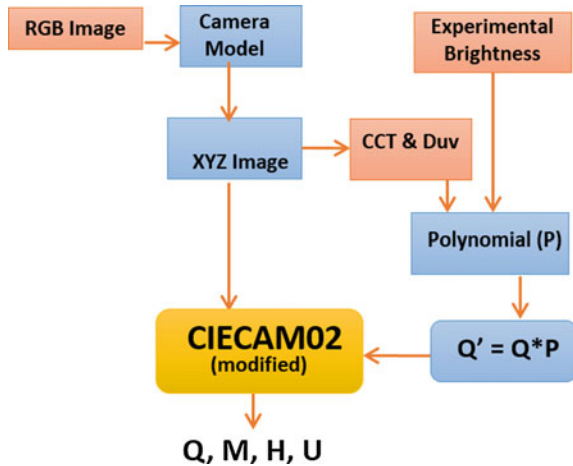
12.3   Test Results

Our research group conducted three different experiments to scale the appearance in a real living room, real shops, and office-like room, respectively. Visual data and scene images were collected from all three experiments. The first, second, and third experiments included 25, 21, and 14 different illuminations, respectively. In the first experiment, 1800 LEDs in 11 different colors were used and CCT values were varied in the range of 2850–9000 K while keeping the luminance level fixed at 85 cd/m^2 [1]. The observers were asked to scale many attributes including spatial brightness, colorfulness, hue composition, uniformity, and warmth. An RGB digital camera was used to capture the interior of the room. The MCCC chart and white wall in the scene were cropped from images for camera characterization and appearance prediction, respectively. A sample image is shown in Fig. 12.2a. The region of interest is marked with a red rectangle.

The cropped uniform white wall was transformed to XYZ for each image, and modified CIECAM02 was applied. The white patch of the MCCC was used as reference white, and average surrounding conditions were considered. The white wall was also used to calculate CCT and Duv values. As in the living room experiment, luminance was fixed at a number (85 cd/m^2) for all lighting conditions and the effect of CCT and Duv on brightness could easily be seen. The predicted results were then plotted against visual data of room appearance attributes. Plots of spatial brightness, colorfulness, and hue composition are shown in Fig. 12.3a–c, respectively, and values of correlation between visual and predicted data are given in Table 12.1.
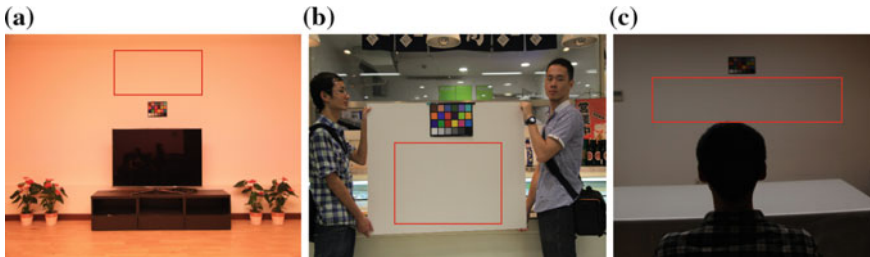
Fig. 12.2 Imported images; **a** the interior of the room used for living room experiment, **b** the interior of one of the shops used for real shops experiment, and **c** the interior of the room used for luminance contrast experiment. *Red rectangle* in each figure represents the area of interest

Table 12.1 Correlations of predicted and visual results

Attributes	Living room exp.	Real shops exp.	Luminance contrast exp.
Brightness	0.98	0.45	0.97
Colorfulness	0.69	0.65	X
Hue comp.	0.76	0.98	X

The second test data were adopted from an experiment conducted in 21 real shops [8]. Digital RGB camera, a tele-spectroradiometer (TSR), and a calibration MCCC chart and a uniform whiteboard both were used for measurements. The whiteboard was displayed along with the calibration chart in the interior of each shop, and lighting conditions were measured using a TSR, captured using digital camera, and scaled by three observers. Image of whiteboard and MCCC taken under lighting conditions in one of the shops is shown in Fig. 12.2b. The scaled data, lighting parameters, and images captured in this experiment were also adopted to the current study.

The modified CIECAM02 was applied on the XYZ images of cropped area of whiteboard, and room appearance attributes were predicted. Visual results were plotted against predicted values of spatial brightness, colorfulness, and hue com-position and are shown in Fig. 12.3a–c, respectively. All the attributes were found to be in good correlation with the visual data. The correlation coefficients were calculated for all attributes and are given in Table 12.1.
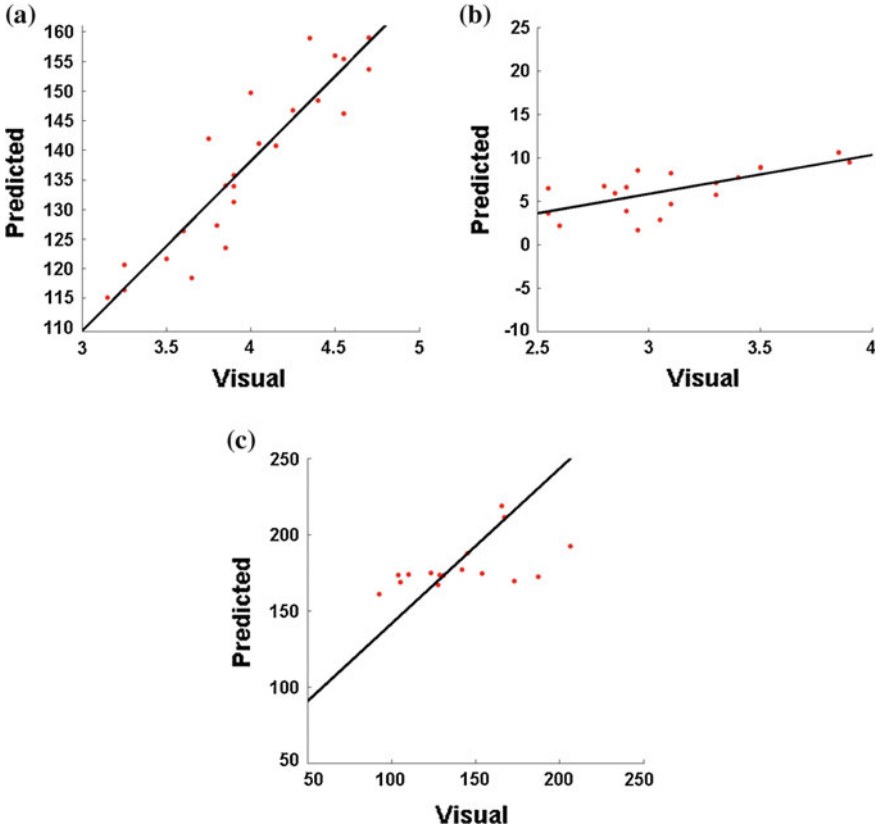
Fig. 12.3 Modified CIECAM02 predictions versus visual results of real shops experiment; a brightness, b colorfulness, and c hue composition

Another experiment was conducted to scale spatial brightness, contrast, comfort, and uniformity, at light and dark desks, and white wall of a room with LED lighting in the ceiling. Twelve LED cubes were fixed in the ceiling of the room, and each LED cube consisted of 11 different types of LEDs. Fourteen lights were designed with different luminance contrast ratios at six points on the table and white wall. All the designed lights had same CCT but different luminance levels at six different positions on the table or wall.

The visual data for brightness perception and RAW images of the white wall were adopted to test the current method for predicting spatial brightness. The experimental setup for one of the lighting conditions is shown in Fig. 12.4c with the area of interest marked with a red rectangle. The images of the white wall (cropped area of interest) were transformed to XYZ space and inputted to the current model. The modified CIECAM02 brightness function did well to predict visual brightness with statistically significant correlation. See Fig. 12.5 for the scatter plot between visual and predicted spatial brightness, and correlation value is given in Table 12.1.
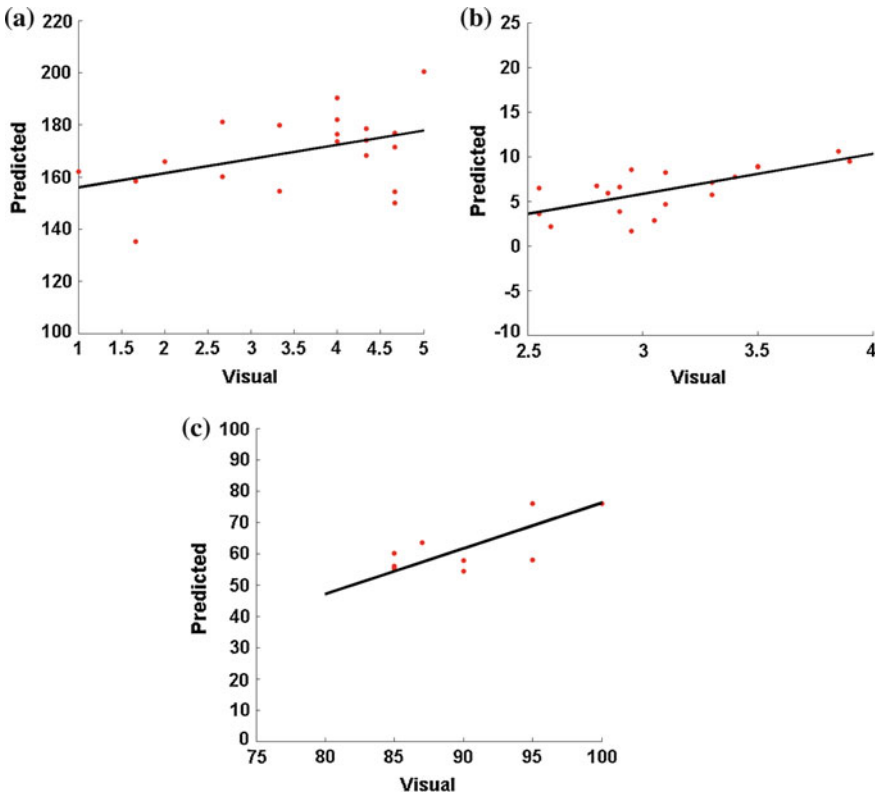
Fig. 12.4 Modified CIECAM02 predictions versus visual results of living room experiment; **a** brightness, **b** colorfulness, and **c** hue composition
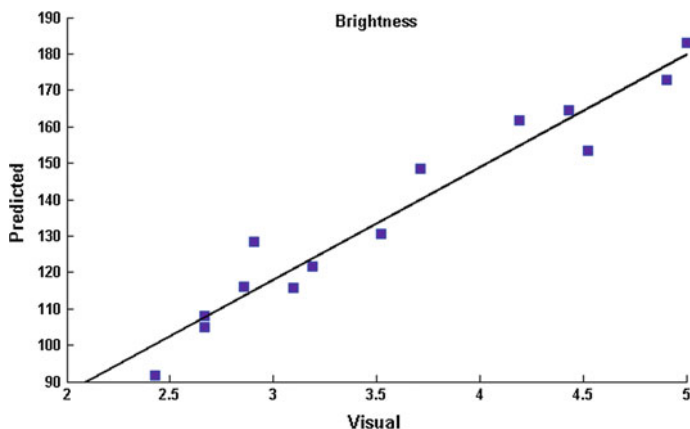
Fig. 12.5 Modified CIECAM02 predictions versus visual results of luminance contrast experiment

The correlations between visual data and predicted results of proposed model, for all three experiments, were found statistically significant as per the analysis of variance (ANOVA). The ANOVA is a statistical analysis used to find the significance of a metric (such as correlation and color difference) value for the given set of points.

12.4   Conclusions

The CIECAM02 was modified and proposed as an imaging method to predict room appearance attributes. The CIECAM02 brightness function was modified to consider the effect of CCT and Duv. As per the ANOVA analysis, predictions of proposed model were significantly correlated with the visual results. Hence, an instrumental method that can efficiently measure perceived visual appearance was proposed. It consists of an ordinary digital camera and a modified CIECAM02-based model.

References

1. Li, H., Luo, M. R., Liu, X. Y., Wang, B. Y., & Liu, H. Y. (2015). Evaluation of colour appearance in a real lit room. *Lighting Research and Technology*, 1477153515571784
2. Hunt, R. W. (1952). Light and dark adaptation and the perception of color. *Optical Society of America, 42*(3), 190–199.
3. Boyce, P. R., & Cuttle, C. (1990). Effect of correlated color temperature on the perception of interiors and color discrimination performance. *Lighting Research and Technology, 22*(1), 19–36.

4. Shepherd, A. J., Julian, W. G., & Purcell, A. T. (1992). Measuring appearance: Parameters indicated from gloom studies. *Lighting Research and Technology, 24*(4), 203–214.
5. CIE. (2014). *Guidance towards best practice in psychophysical procedures used when measuring relative spatial brightness* (CIE212:2014). Vienna: CIE.
6. CIE. (2004). *A colour appearance model for colour management systems: CIECAM02* (CIE159:2004). Vienna: CIE
7. Luo, M. R., Hong, G., & Rhodes, P. A. (2001). A study of digital camera colorimetric characterization based on polynomial modelling. *Colour Research and Application, 26*(1), 76–84.
8. Zhu, Y., Ye, M., Huang, W., Mughal, M. F., Safdar, M., & Luo, M. R. (2015). Accessing light appearance in shopping mall. In *Proceedings of AIC Midterm Meeting 2015, Tokyo, Japan* (pp. 159–164)

Chapter 13
Research on Color Reproduction Ability of Mainstream Brand Mobile Phone

Zhanjun Si, Ying Wang and Lu Zhang

Abstract Driven by consumers' higher demand, intelligent mobile phone has been updated faster and faster, which emphasizes on color rendering in mobile phone design and production. In this paper, firstly, the RGB imported to mobile phone that to be measured, and set the brightness, color temperature, and other parameters. Finally, $L*a*b*$ value in four corners of mobile phone screen and central screen is tested through X-riteI1 pro2 spectrophotometer, PC, and Measure Tool software. Through statistical analysis of these data calculate the color difference with the measurement value and the primary $L*a*b*$ value, so as to analyze the color reproduction ability of a mobile phone screen. The study of the color reproduction ability of mainstream brand intelligent mobile phone will benefit designers to design more humanized products and improve the immersion of users.

Keywords Color reproduction · Mobile phone · Color difference

13.1 Introduction

In the recent years, with the development of the mobile networks and the operating system platforms, as well as the popularization of the relevant mobile intelligent terminal, the intelligent terminals such as mobile phones are wildly used in all the aspects of people's work and life [1, 2]. As a new type of digital image display device [3], it enjoys all kinds of superiority bring about by intelligent phone terminal; meanwhile, consumers raise a claim of higher display quality day by day. At present, there are two types of evaluation methods, namely evaluation of physical data and estimate of visual perception on image quality [4, 5]. There is no comment mainly on display capability of the phone, and just via simply comparing the

Z. Si (✉) · Y. Wang · L. Zhang
College of Packaging and Printing Engineering, Tianjin University of Science and Technology, Tianjin, China
e-mail: szj@tust.edu.cn

physical parameter of the device on color gamut, brightness, and pixel density, it is not conform to the complexity of the visual system of eyes response to color images naturally, and it is not adapted to the diversified observing environment condition of the intelligent mobile terminal; what is worse is that it unable to provide quantitative evaluation result of different display screen percept image differently [6].

This paper takes use of the experiment of testing the *L*a*b** value of different place of screen and then analyzes the static data; what is more is to calculate the color difference with original color block, and finally, the reproduction ability of several main-stream brand phone based on the quantized data reached by experiment is analyzed.

13.2 Experimental Designs

13.2.1 Experimental Principle

By measuring the *L*a*b** value at the roughly similar location on the mobile phone screen of and calculating the color patch of original *L*a*b** value, we can analyze the color reproduction capability of the mobile phone screen. The color difference formula is as follows:

$$\Delta E_{ab}^* = \sqrt{\Delta L^{*2} + \Delta a^{*2} + \Delta b^{*2}}$$

$$\Delta L^* = L_{measure}^* - L_{standard}^*, \quad \Delta a^* = a_{measure}^* - a_{standard}^*, \quad \Delta b^* = b_{measure}^* - b_{standard}^*$$

13.2.2 Experimental Preparation

13.2.2.1 Making Color Patch

Setting the color profile as sRGB IEC61966-2.1 in Photoshop CS5 software and then producing 11 color blocks whose RGB value was determined, the color patch pixel size is 589 × 595 and save them as Color_patch_11.pdf, and RGB and *L*a*b** values are shown in Table 13.1.

13.2.2.2 Determine the Brands of the Testing Mobile Phone

A survey from the third quarter of 2013 to the fourth quarter of 2014 shows that the top three of the most commonly used intelligent phone brands in consumer for Samsung, iPhone, MI and ultimately were determined as the testing brands and the models are shown in Table 13.2.

Table 13.1 Color value

No.	Color	RGB	L*a*b*
1	White	(255, 255, 255)	(100, 0, 0)
2	Gray	(128, 128, 128)	(54, 0, 0)
3	Skin	(209, 157, 135)	(69, 18, 19)
4	Red (high)	(255, 0, 0)	(54, 81, 70)
5	Red (low)	(128, 0, 0)	(26, 48, 39)
6	Green (high)	(0, 255, 0)	(88, −79, 81)
7	Green (low)	(0, 128, 0)	(46, −48, 49)
8	Blue (high)	(0, 0, 255)	(30, 68, −112)
9	Blue (low)	(0, 0, 128)	(11, 41, −67)
10	yellow (high)	(255, 255, 0)	(98, −16, 93)
11	Yellow (low)	(128, 128, 0)	(52, −9, 56)

Table 13.2 Test phone brand and model parameters

Samsung	Model	I9100	I9300	I9003	
	Resolution	800 × 480	1280 × 720	480 × 800	
MI	Model	2	2s	3	
	Resolution	1280 × 720	1280 × 720	1920 × 1080	
IPhone	Model	4	4s	5	5s
	Resolution	960 × 640	960 × 640	1136 × 640	1136 × 640

13.2.3 Experimental Procedure

1. Transfer the Color_patch_11.pdf file to the testing mobile phones.
2. Adjust the brightness of the testing mobile phone. Shut off the mobile phone's auto-brightness setting slider. Put the brightness slider in the middle. Set The MI 2, MI 2S, and MI 3 mobile phones' color temperature as normal and saturation as standard. Two models of Samsung mobile phones are set as no power mode.
3. Connect the spectrophotometer of the X-rite I1 pro2 to the computer, and put it on the white board. Open the Measure Tool software, click the "Spot" in the software. The software displays it as conducting the white correction; after the correction, the software shows the interface of "measurement spot," and then selects the color space of L*a*b*.
4. Open the file named Color_patch_11.pdf in the tested mobile phone. Set the testing color block as full screen (at least more than the half of the measured screen), then use the spectrophotometer X-rite I1 pro2 to measure the L*a*b* value of 5 spot, in accordance with the point number on the screen from small to large to measure the point which located at the four corners and the central point of the screen. Because measuring the four points of the corners on the screen and the central point cannot guarantee the absolute position; so make a

Table 13.3 Position and corresponding serial number of screen point measurement

No.	1	2	3	4	5
Screen position	Upper left corner	Upper right corner	Left corner	Right corner	Central

extension to the spectrophotometer which rested on the corner of the screen as the standard of measurement and measure the relative same position of four corners and a point in the center of the screen. Specific numbers, as follows, are shown in Table 13.3.

13.3 Data Statistics and Analysis

13.3.1 *L*a*b* Measurement Statistics*

Here, we take iPhone as an example; a number of mobile phones and models are shown in Table 13.4. Before the test, hypothesis of the same phone brightness value L is considered as fixed value, and the variable is a (red and green) or b (yellow and blue) value. Here mainly $L*a*b*$ value of the testing five points is analyzed, and all the mobile phones are stuck with high permeability film. The existing data show that the color error of the screen test of high membrane permeability and membrane-free state can be neglected.

The experiment has tested the $L*a*b*$ value of 11 color blocks of 10 different types of iPhones and analyzed the data. Here take the red color block's $L*a*b*$ value (Chinese preferred) for example, Fig. 13.1.

From the above chart, we can find that the trend of average value of the orange dot is same with the screen changes in five points of measured red color patch's $L*a*b*$ value's trend (54, 81, 70), and there is no big difference. This shows that the $L*a*b*$ value's fluctuations of screen five points is small, and the red color patch is uniform. Comparing the average line of orange dots and blue standard value line, the 10 measured iPhones under the preset brightness, the red brightness values were higher than the standard red color patch brightness value. As to the ab value, In the tested 10 iPhones, iPhone4-1, iPhone4-2, iPhone4s-3, iPhone4s-4, and iPhone4s-6 mobile phones' a values are lower than the standard value of 81. That is, when the five mobile phones display red color patch, the amount of red light of the screen is less than the standard color patch. The average a value of the five points on screen of iPhone4s-5 and iPhone4s-7 is just coincident with the standard, mostly close to the composition of the standard red color patch. The average of five

Table 13.4 IPhone mobile phone test statistics

Model	iPhone4	iPhone4s	iPhone5	iPhone5s	Total
Quantity	2	4	1	2	10

		iphone4-1			iphone4-2			iPhone4s-3			iPhone4s-4			iPhone4s-5			iPhone4s-6			iPhone4s-7			iPhone5-8			iPhone5s-9			iPhone5s-10		
		L	a	b	L	a	b	L	a	b	L	a	b	L	a	b	L	a	b	L	a	b	L	a	b	L	a	b	L	a	b
◆	point1	62	75	62	70	79	68	65	74	64	62	72	58	69	80	62	68	77	66	67	80	63	62	85	70	63	86	70	63	85	71
■	point2	62	76	64	69	78	68	66	76	65	63	73	59	69	80	62	67	76	66	66	79	63	61	85	70	59	81	66	64	86	70
▲	point3	61	75	63	68	78	68	66	75	65	64	74	59	70	81	64	69	78	67	68	81	65	64	88	73	62	85	68	65	87	73
✕	point4	63	76	64	69	78	69	67	76	65	63	73	59	68	80	61	67	76	66	66	79	64	64	88	72	61	84	68	65	87	72
✳	point5	64	77	66	70	79	68	66	76	65	64	74	59	69	81	63	69	78	68	69	81	65	64	88	74	63	86	71	65	87	72
●	average	62	76	64	69	78	68	66	75	64	63	73	58	69	80	63	68	77	66	67	80	64	63	87	72	62	84	69	64	86	72
—	standard	54	81	70	54	81	70	54	81	70	54	81	70	54	81	70	54	81	70	54	81	70	54	81	70	54	81	70	54	81	70

Fig. 13.1 Line graph of $L*a*b*$ value change trend of *red block* (54, 81, 70) (iPhone)

points' a value of iPhone5-8, iPhone5s-9, iPhone5s-10 is larger than the standard value, indicating that the red color patch of the three mobile phone's display is deeper. As to the b value, the average b value of the 10 mobile phones is greater than the standard b value, showing that when the 10 mobile phones display the red color, the yellow light composition is relatively larger.

13.3.2 The Color Reproduction Capabilities Contrast of IPhone MI and Samsung

Because of the inconformity and small amount of the test phones, it is difficult to calculate the average color difference value to compare to the mobile phones. So, when comparing the three brands mobile phone's color reproduction ability, we choose the mobile phone of each brand whose central point's 11 color blocks is the minimum color difference and have the maximum frequency as representatives, and then compared the three representative brand phones' color performance.

Take the process of looking for the iPhone series machine for example. In the tested 10 iPhones, calculate the color difference value of the central point by the color difference formula. Then mark the minimum color difference in each row with the red color, and finally calculate the frequency of each mobile phone to obtain minimum color difference values. The results are shown in Table 13.5.

From Table 13.5, the minimum color difference frequency of iPhone4 is 4, so choose the first test machine of iPhone4 as the representative of iPhone series mobile phone. In the same method, the first test machine of MI 3 and Samsung i9008 are the representatives of MI and Samsung series mobile phone.

Table 13.5 IPhone series central point color table

No.	Model	White	Gray	Skin	Red	Red (low)	Green	Green (low	Blue	Blue (low)	Yellow	Yellow (low)	Min frequency
1	iPhone4	41.02	24.70	25.03	5.52	5.22	27.52	18.25	24.99	15.72	23.94	16.10	2
2	iPhone4	31.95	20.57	22.23	2.97	1.82	9.03	5.25	39.77	25.57	6.63	4.30	4
3	iPhone4s	39.64	27.33	28.14	7.71	8.52	17.27	13.57	37.92	23.38	14.55	10.84	0
4	iPhone4s	30.53	19.55	21.91	13.51	11.25	6.21	5.97	33.21	21.08	8.29	6.53	1
5	iPhone4s	30.08	26.23	19.89	6.61	5.21	17.14	11.77	46.37	28.55	13.52	9.19	0
6	iPhone4s	40.41	25.60	26.85	3.83	4.03	20.61	14.81	41.69	25.82	16.26	10.44	0
7	iPhone4s	32.09	19.82	20.76	4.72	10.21	8.51	9.56	37.54	23.64	6.61	7.75	1
8	iPhone5	27.26	16.62	15.54	8.05	4.34	25.18	11.70	43.54	23.04	19.94	11.15	1
9	iPhone5s	29.72	17.19	15.65	5.15	4.07	25.39	13.22	47.52	27.20	17.28	11.60	0
10	iPhone5s	26.58	16.93	14.46	6.45	3.89	19.81	9.62	40.54	20.37	13.99	7.53	2

To determine the mobile phone, with color difference ΔE as ordinate, choose color difference of the three mobile phone production line, as shown in Fig. 13.2.

From the graph, the blue line that represents the change of color difference value of the iPhone series mobile phone compare with the other two lines is smoother, and it displays the color of red, red (low chroma), green, green (low chroma), yellow and yellow (low chroma); the color difference is at the minimum value. The red line that represents the color line of MI mobile phone has a stable trend, and in the performance of white and gray patch, color difference is small. The color difference of the Samsung series represented by the green line has the biggest change, and only when it shows the skin color, it has the minimum color value.

	whit e(25 5,25 5,25 5)	gray(128, 128, 128)	skin(209, 157, 135	red(255, 0,0)	red(128, 0,0)	gree n(0,2 55,0)	gree n(0,1 28,0)	cyan (0,0, 255)	cyan (0,0, 128)	yello w(25 5,25 5,0)	yello w(12 8,12 8,0)
i9008	26.21	16.32	6.297	33.82	8.983	75.37	33.59	26.25	10.42	31.14	16.92
iphone4	31.95	20.57	22.23	2.973	1.825	9.027	5.25	39.77	25.57	6.629	4.295
MI3	24.67	14.47	12.48	15.04	15.5	14.64	5.63	34.61	10.68	17.53	14.58
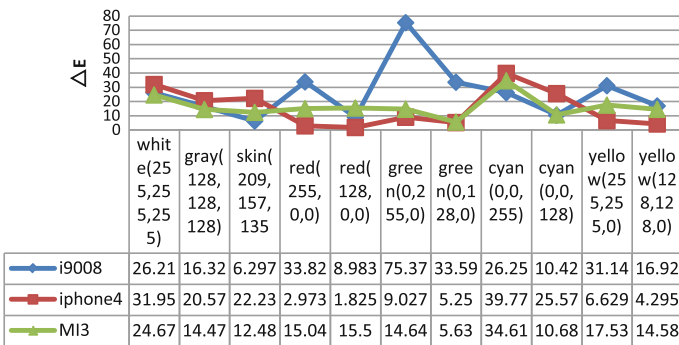
Fig. 13.2 Central point color chart

13.4   Conclusions

By testing the $L*a*b*$ value of color block of three different brands IPhone, MI, Samsung mobile phone in this experiment, and analysis and calculate the color difference with the primary $L*a*b*$ value, in order to analyze screen color reproduction ability of the mainstream brand mobile phone. In terms of displaying skin color, Samsung has the smallest color difference compared with the other two brands, which reveals that Samsung has the best skin color reproduction ability; Phone treats the color difference of the color blocks gently, and the smallest color difference appears when most colors reappear, which shows that the color reproduction ability of IPhone is better and steady; however, MI manifests the prominent color reproduction ability when displaying white and black. In all, the three mainstream brands mobile phones have the characteristics of the color reproduction ability, respectively, and can conduct the deeper research to cater for different people's different mobile phone color preferences based on the color reproduction ability. Manufacturers of mobile phone can take use of the experimental results to design more humanized products, thus improve the users' sense of immersion in the using process.

References

1. Kimmel, J. (2007). Displays enabling mobile multimedia. In *Proceedings of SPIE-IS&T Electronic Imaging* (Vol. 6507,p. 650705).
2. Parkkinen J., & Nenonen, P. (2005). Image enhancement system for mobile displays. In *Proceedings of SPIE and IS&TElectronic Imaging* (Vol. 5678,pp. 210–218).
3. Zhang, F. (2011). *New flat panel display strategic technology and industrial development*. Science Press.
4. Becker, M. E. (2005). Display-metrology for liquid-crystal-television-screens. *Displays, 26*(7), 197–207.
5. Wang, Y., Xu, H. S., & Xu, D. (2006). Comparison of the color characteristics of the display model. *Journal of Zhejiang University (Engineering)*, *40*(6), 1085–1088.
6. Gong, R. (2014). *The display performance evaluation method and application research of intelligent mobile terminal image*. Zhejiang University.

Chapter 14
Investigation of Memory Colors of Chinese Observers

Yuteng Zhu, Ming Ronnier Luo, Lihao Xu, Xiaoyu Liu, Qiyan Zhai and Guihua Cui

Abstract Long-term memory colors of familiar objects are of great significance in the applications such as imaging, lighting, and color reproduction. Previous studies of memory color were mainly conducted on the surface color samples under variable illuminations or images presented on displays. In this work, memory colors of Chinese observers with a set of 22 familiar objects have been investigated on a well-calibrated display. A specially developed psychophysical method and an operational program were applied for the observers to match the homogenous patch colors through object name descriptions with their memory colors on a self-luminous monitor in a given viewing situation. The results of inter-observer variability were analyzed in CIELAB color space by mean of color differences from the mean (MCDM) and tolerance ellipse. The two indexes were found to be consistent. Our aim is to establish a methodology both to study memory colors and to quantify the specific Chinese memory colors, which can benefit for further image enhancement.

Keywords Memory color · Long-term memory · Chinese colors · Tolerance ellipse

Y. Zhu · M.R. Luo · L. Xu · Q. Zhai
State Key Laboratory of Modern Optical Instrumentation, Zhejiang University, Hangzhou, China

M.R. Luo (✉)
School of Design, University of Leeds, Leeds, UK
e-mail: m.r.luo@leeds.ac.uk

X. Liu
College of Science, Harbin Engineering University, Harbin, China

G. Cui
School of Physics and Electronic Information Engineering, Wenzhou University, Wenzhou, China

14.1   Introduction

Memory colors have been extensively studied to achieve high-quality color reproduction [1]. The earlier studies mainly focused on three big parts: real objects, reflected color samples, and display-based images. Bartleson [2, 3] investigated the memory colors of skin, blue sky, and grass colors using Munsell color chips, which were the most important colors in color reproduction. Smet et al. [4] found saturation increased for memory colors and hue shifts toward the dominant hue compared to natural colors when investigating color appearance rating of familiar real objects. Similar results have been confirmed by many other researchers [5–8].

Tarczali et al. [9] compared the method of reproducing memory colors from a color name and from a grayscale photograph, of which the latter showed smaller variability. Moreover, they found a significant cultural difference between Hargarian and Korean. Smet et al. [10] carried out a project to investigate memory colors of eleven familiar objects across seven countries/regions by rating the similarity between the objects displayed on the calibrated monitor and that in reality. Although there was a significant difference between the regions, the effect of cultural difference was considered to be unimportant due to large inter-observer variability.

In our work, the long-term memory colors of Chinese people with a set of 22 familiar objects in different categories were studied. A homogenous color patch was manipulated by the observers to match their memory color on a calibrated display with large color gamut. This study provided quantitative data of Chinese memory colors to potentially support image reproduction and enhancement in the aspect of color.

14.2   Method

14.2.1   Selection of Objects

Twenty-two familiar objects were specially chosen for this experiment so as to cover the entire hue circle, except the green–blue quadrant, which was found to be lack of memory colors. The categories of these object colors were traditional Chinese colors, common natural colors, and vegetables and fruits colors, as given in the first column of Table 14.1. The main intention of the first category was to investigate the difference between memory colors and real historical colors in the work of museum conservation and relic restoration. Second and third categories were the most important memory colors associated with daily life for diverse applications.

Table 14.1 The memory color results of 22 familiar objects: L^*, C_{ab}^*, and h_{ab} values of color centers in CIELAB color space, detailed parameters of tolerance ellipses and chromatic MCDM

No.	Object name	L^*	C_{ab}^*	h_{ab}	Ellipse A	Ellipse A/B	Ellipse theta	Ellipse area	Chromatic MCDM
2	Caucasian face skin	73.8	13.0	33.3	6.4	2.0	43.4	64.0	6.2
2	African face skin	20.7	13.8	47.2	7.7	1.8	53.0	100.4	7.4
3	Nectarine	31.3	54.1	30.5	7.1	1.4	71.6	114.5	8.2
3	Red rose	34.6	69.1	35.9	6.8	2.5	83.6	57.6	9.4
3	Pink lotus	68.9	35.8	343.6	9.9	2.2	158.6	140.7	9.2
2	Oriental face skin	62.5	25.5	52.0	8.9	2.2	69.5	114.9	8.9
1	Dragon robe	77.4	77.3	84.7	9.0	1.5	8.3	166.2	10.2
3	Lavender	40.1	56.2	301.3	10.6	2.2	129.1	159.0	10.4
3	Aubergine	15.4	25.7	333.0	12.6	2.9	119.6	173.5	9.2
3	Banana	77.3	77.2	90.6	7.3	1.1	167.8	150.3	9.9
3	Strawberry	42.9	76.5	34.4	15.5	2.4	52.2	318.6	11.9
3	Lemon	81.6	78.6	97.3	8.9	1.2	7.4	206.5	11.0
2	Blue jean	29.6	27.0	274.3	9.3	1.8	104.9	151.8	10.0
3	Orange	64.1	75.4	64.3	10.1	2.0	12.9	164.9	11.6
1	Blue and white porcelain	34.7	46.7	283.1	10.8	2.0	123.6	186.3	10.7
1	Sausage	29.0	47.3	29.9	10.8	1.5	57.0	247.4	12.3
3	Pink lotus	62.8	71.4	125.1	12.1	1.3	0.8	348.9	12.9
4	Kiwi	68.4	68.1	115.7	11.0	1.2	120.0	321.5	13.1
3	Broccoli	41.2	49.1	141.8	12.1	1.4	5.9	341.1	14.1
3	Green apple	66.9	65.9	122.0	16.0	1.8	176.3	437.7	15.3
1	Chinese red	39.3	69.8	36.5	24.5	2.3	29.8	8066	16.4
2	Blue sky	49.1	64.3	284.9	14.6	1.7	121.0	394.0	19.3

14.2.2 Display

The color matching experiment was operated on a calibrated LED-backlighting EIZO display with correlated color temperature (CCT) of 6556 K, luminance level around 111 cd/m², and the x, y chromaticity coordinates of [0.311, 0.330]. The monitor characterization was implemented utilizing GoG model with a prediction of less than 0.6 ΔE_{ab}^* unit averaged from eighteen gray scales [11]. The observers' memory color matching results were saved as trichannel RGB values, which were device dependent. They were redisplayed on the monitor, and device-independent CIEXYZ tristimulus values were then measured by a JETI Specbos 1211 UV tele-spectroradiometer (TSR).

14.2.3 Test Procedure

Twenty-five normal color vision Chinese observers, comprising fifteen males and ten females, participated in this experiment with an average age of 24 years old. After a training of experimental instruction and related color notion, they were asked to match the colors of the objects with respect to their memory by using a MATLAB program specially developed for the experiment.

Figure 14.1 illustrates the operational interface. Taking an example of 'Imperial robe', the descriptive name of the testing object was placed at the top of the interface with a sequence number. The observers reproduced their memory color on the 2 cm by 2 cm homogenous patch in the center. The original digital RGB signal values of the color patches were obtained from internet images of a representative region of the objects and set as starting points in the matching experiment. This size
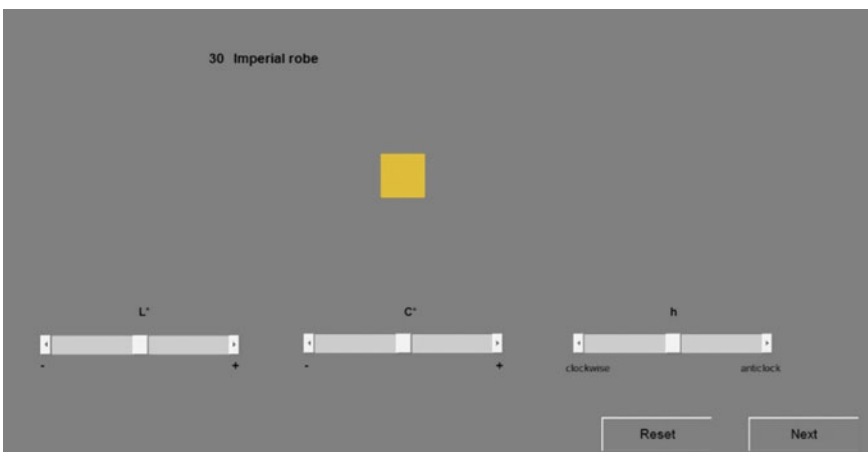
Fig. 14.1 Operational interface

resulted in a 2° of visual field from a viewing distance about 50 cm. The matching color was manipulated by continuously controlling the bars of lightness (L^*), chroma (C_{ab}^*), and hue angle (h_{ab}) in three dimensions, which were defined in the CIELAB color space. There were a 'reset' and a 'next' buttons in the bottom corner. The first button can cancel the manipulation and return to the starting point. The latter was set to continue matching after satisfactorily completing the present color patch until completing all the 22 objects.

14.3   Results and Discussions

The memory color data was first obtained from observers' matching results and stored in RGB digital values. Then they were redisplayed on the monitor and device-independent CIEXYZ values were measured by the TSR. In order to obtain the representative memory colors, the averaged results of the group were transformed from CIEXYZ into L^*, C_{ab}^*, and h_{ab} in CIELAB uniform color space (also given in Table 14.1). These data quantitatively represented the Chinese memory colors of the 22 familiar objects in the experiment.

Inter-observer variability was evaluated both by MCDM and by tolerance ellipse. It is clear that the smaller MCDM corresponds to better agreement within the observers' data. From the last column in Table 14.1, it can be seen that the largest MCDM and smallest MCDM are blue sky (19.26) and Caucasian face skin (6.23), respectively. This reveals that Chinese memory color of blue sky differs greatly from individual to individual, while Caucasian face skin stays close to each other.

The other methods employed here are tolerance ellipse [12] in the a^*b^* diagram (ellipse parameters listed in Table 14.1). The tolerance ellipse gives an elliptical boundary statistically based on the distribution of individual data with a preset confidence level. In general, a larger ellipse area indicates greater inter-observer variability. Figure 14.2 shows the 22 tolerance ellipses in the a^*b^* diagram. Their sizes and orientations vary individually. The smallest ellipse is Caucasian face skin, while the largest one is blue sky. However, it is observed that larger ellipses are located in higher chroma area. This can be ascribed to the poor uniformity of CIELAB color space. It is worth pointing out that some colors are hue direction orientated, whereas some are chroma direction orientated.

These two indexes show to be in great accordance with correlated coefficient equal to 0.92. It means a bigger MCDM value usually corresponds to a larger size of tolerance ellipse, which reveals a greater variability.

A comparison between our results and those of Liu et al. [8] and Smet et al. [10] were also provided. Both datasets were based on images on display. The MCDMs of Smet et al.'s data were presented in terms of Du'v' units. Therefore, they were transformed to CIELAB, and MCDMs were recalculated in average about 10 CIELAB units. Liu et al.'s studied sixteen color centers with an averaged MCDM value of 3. This reduction can be a consequence of a limited range of color region

Fig. 14.2 The 22 tolerance *ellipses* in a^*b^* diagram reduced by 2 times of the real size. The *red crosses* represent the color center for each object
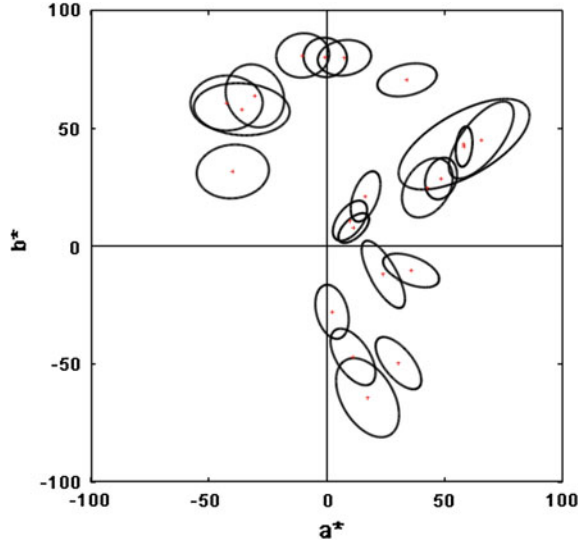
used in their experiment. The discrepancy between both datasets was about 15 units.

The overall mean MCDM of 22 memory color studied in this experiment reached 11.25 chromatic ΔE_{ab}^*. According to Bodrogi et al.'s finding, the large variance of long-term memory by observer operation was mainly due to two separable reasons [8]. One was the individual preference, and the other was the individual precision in the memory color matching. These were appropriate reasons that can explain the large variability results in the experiment.

14.4 Conclusions

Memory colors of Chinese people with a set of 22 familiar objects have been studied on a self-luminous display. The typical memory color variation of Chinese observers was about 11.25 chromatic units in terms of MCDM. The results gave larger observer variability compared with the other two datasets. It is because the observers' self-matching method employed in this work was based on descriptive objects' names, while the others were based on images that offered more explicit information. The experimental results can provide effective solutions to Chinese memory colors for further applications of image enhancement.

References

1. Fairchild, M. D. (2005). *Color appearance models* (2nd ed., p. 158). London: Wiley.
2. Bartleson, C. J. (1960). Memory colors of familiar objects. *Journal of the Optical Society of America, 50*, 73–77.
3. Bartleson, C. J. (1961). Color in memory in relation to photographic reproduction. *Photographic Science and Engineering, 5*, 327–331.
4. Smet, K. A. G., Ryckaert, W. R., Pointer, M. R., Deconinck, G., & Hanselaer, P. (2011). Color appearance rating of familiar real objects. *Color Research and Application, 36*(3), 192–200.
5. Siple, P., & Springer, R. M. (1983). Memory and preference for the colors of objects. *Perception and Psychophysics, 34*(4), 363–370.
6. Vurro, M., Ling, Y. Z., & Hurlbert, A. C. (2013). Memory color of natural familiar objects: Effects of surface texture and 3-D shape. *Journal of Vision, 13*(7), 20.
7. Yendrikhovskij, S. N., Blommaert, F. J. J., & de Ridder, H. (1999). Representation of memory prototype for an object color. *Color Research and Application, 24*(6), 393–410.
8. Liu, X. Y., Luo, M. R., Luo, D., & Bian, J. (2014). Investigating observer variability for assessing memory colors. CIEx039, pp. 200–205.
9. Tarczali, T., Park, D.-S., Bodrogi, P., & Kim, C. Y. (2006). Long-term memory colors of Korean and Hungarian observers. *Color Research and Application, 31*(3), 176–183.
10. Smet, K. A. G., Lin, Y., Nagy, B. V., Nemeth, Z., Duque-Chica, G. L., Quintero, J. M., et al. (2014). Cross-culture variation of memory colors of familiar objects. *Optics Express, 22*, 32308–32328.
11. Berns, R. S. (1996). Methods for characterizing CRT displays. *Displays, 16*, 173–182.
12. Johnson, R. A., & Wichern, D. W. (2002). *Applied multivariate statistical analysis*. Upper Saddle River, NJ: Prentice Hall.

Chapter 15
Prediction of Gray Balance Spectral Data in Digital Printing

Chenfei Zhao

Abstract Now, the calculation method of gray balance data uses the parameters of density and chroma, and there is on gray balance data based on spectral reflectance. By the reflectivity in the visible wavelength range, the gray balance data can be predicted. The BP neural network is adopted to train, in which the spectral reflectance of the black ink which is of the same dot area value is adopted as neutral gray value, and the corresponding dot area value of cyan, magenta, and yellow inks can be predicted. In digital printing, gray balance is mainly affected by the paper and ink, so it is necessary to correct the calculated gray balance data. In the correction process, the black ink's spectral data are corrected by the paper and ink's spectral data. After correction, the error of gray balance is reduced. This study plays an important role in color control by gray balance data.

Keywords Digital printing · Spectral reflectance · Gray balance · Dot area

15.1 Introduction

Neutral gray [1] color's hue and saturation cannot change, and only brightness can change. Usually, the human eye is sensitive to the color shift of the gray color, which can be found by visual. At present, the research on the gray balance data mainly focuses on the density [2] and colorimetry [3, 4]. The density parameter cannot be matched well with the human visual system. The colorimetry parameter can produce homochromatic phenomenon for different color, which is not very good to reflect the phenomenon of the same color. The reflectance in the visible light wavelength is good for the gray color's parameter, which is the color's fingerprint. In theory, when the cyan, magenta, and yellow inks overprint that is equal

C. Zhao (✉)
Light Industry and Energy Institute, Shaanxi University of Science and Technology, Shaanxi, China
e-mail: 20531919@qq.com

in quantity, a neutral gray color will be produced. But the actual is not so ideal. The black ink that is of the same dot area value is more close to the neutral gray color. So BP neural network [5] and spectral reflectance parameters are used to deduce the gray balance data in this paper.

15.2 BP Neural Network Model

15.2.1 The Spectral Reflectivity

The spectral reflectance in the wavelength of the overprint color by cyan, magenta, and yellow inks that are of the same dot area value is measured, and the spectral reflectance in the wavelength of the overprint of black ink that is of the same dot area value is measured. In the experiment X-Rite spectrophotometer and Epson 9910, large format printer is used. The experimental environment temperature is 10–35 °C, and the relative humidity is 10–85 %RH.

Tables 15.1 and 15.2 show the data that are the reflectance of the overprint color by three kinds of ink and the black ink at six wavelengths that are 430, 480, 530, 580, 630, and 680 nm.

From the reflectance whose dot area value is 0, we can find the printing paper's color that is of little blue color. From the black's reflectance whose dot area value is 100 %, we can find the black ink's color that is of little green color. From Tables 15.1 and 15.2, we can find the black ink's color that is of the same dot area value is more close to the neutral gray color, and the black ink but it is not really the neutral gray color.

Table 15.1 The reflectance of cyan, magenta, and yellow inks at six wavelengths

Wavelength (nm)	430	480	530	580	630	680
CMY = 0	80.72	82.14	79.47	79.18	80.82	83.62
CMY = 5 %	66.72	68.45	67.52	63.37	71.48	74.67
CMY = 10 %	64.91	66.23	63.34	59.47	68.93	72.67
CMY = 20 %	49.07	53.15	56.03	47.74	53.2	56.14
CMY = 30 %	33.09	35.83	39.33	31.17	46.29	49.56
CMY = 40 %	25.71	28.97	32.75	24.77	38.17	41.03
CMY = 50 %	18.85	22.26	25.6	17.64	28.43	30.97
CMY = 60 %	12.93	16.39	20.31	13.31	22.91	25.53
CMY = 70 %	11.46	14.29	16.77	11.43	17.99	20.4
CMY = 80 %	10.16	12.91	14.19	9.39	13.39	14.93
CMY = 90 %	8.36	10.73	11.39	7.78	9.62	10.94
CMY = 100 %	7.56	9.55	10.44	8.16	9.8	11.19

Table 15.2 The reflectance of black ink at six wavelengths

Wavelength (nm)	430	480	530	580	630	680
k = 0	81.28	82.59	80.08	79.53	82.77	87.43
k = 5 %	72.18	73.16	70.92	70.07	72.97	77.04
k = 10 %	70.13	71.07	68.79	67.94	70.69	74.69
k = 20 %	61.9	70.07	60.63	59.77	62.02	65.22
k = 30 %	52.46	53	51.48	50.65	52.42	55.01
k = 40 %	44.02	44.48	43.31	42.53	43.98	46.18
k = 50 %	34.97	35.3	34.52	33.91	35.01	36.77
k = 60 %	26.94	27.35	26.94	26.41	27.39	28.81
k = 70 %	19.26	19.65	19.48	19.3	20.14	21.32
k = 80 %	13.9	14.29	14.35	14.34	15.18	16.22
k = 90 %	9.45	9.9	10.18	10.41	11.42	12.23
k = 100 %	7.47	7.89	8.26	8.57	9.38	10.3

15.2.2   The BP Neural Network Model

In the MATLAB software programming, the reflectivity of overprint color in the wavelength of 430, 480, 530, 580, 630, and 680 nm is taken as inverse matrix p'. The dot area values of the inks of C, M, and Y that are 5, 10, 20, 30, 40, 50, 60, 70, 80, 90, and 100 % are taken as inverse matrix t'. The BP neural network training is followed by the code.

```
net=newff(minmax(p),[9,3],{'tansig','tansig'},'trainlm');
net.trainParam.epochs=50000;
net.trainParam.goal=0.0010;
[net,tr]=train(net,p,t);
```

The reflectivity of black color in the wavelength of 430, 480, 530, 580, 630, and 680 nm is taken as inverse matrix p_test′. When the gray balance is realized, the dot area value of the inks of C, M, Y is temp. The BP neural network test is followed by the code.

```
temp=sim(net,p_test);
```

The test data can be Table 15.3.

15.2.3   The BP Neural Network Model's Correction

In the MATLAB software programming, the reflectivity of overprint color in the wavelength of 430, 480, 530, 580, 630, and 680 nm is taken as inverse matrix p'. The dot area values of the inks of C, M, and Y that are 0, 5, 10, 20, 30, 40, 50, 60, 70, 80, and 90 % are taken as inverse matrix t'. The mean reflectivity of every black

Table 15.3 The real optimal dot percentage

Dot area value (%)	Cyan ink's dot area value (%)	Magenta ink's dot area value (%)	Yellow ink's dot area value (%)
5	19.02	19.19	13.65
10	22.78	23.08	17.17
20	41.00	41.91	34.14
30	56.50	57.73	49.20
40	62.50	63.67	55.16
50	65.63	66.28	57.59
60	71.15	67.68	63.28
70	82.62	80.00	79.49
80	89.82	92.51	90.62
90	94.14	96.74	95.08
100	95.46	97.50	95.82

Table 15.4 The real optimal dot percentage

Dot area value (%)	Cyan ink's dot area value (%)	Magenta ink's dot area value (%)	Yellow ink's dot area value (%)
5	13.33	12.27	12.56
10	18.90	16.81	17.47
20	32.38	31.53	31.43
30	45.59	41.25	47.88
40	66.36	73.07	69.06
50	62.32	59.14	60.08
60	73.79	71.54	72.53
70	77.16	73.04	75.50
80	89.44	88.96	88.98
90	97.39	94.41	96.25
100	97.73	94.23	96.49

color in the wavelength of 430, 480, 530, 580, 630, and 680 nm is calculated, and for every color, six same mean reflectivities are taken as a line data of the inverse matrix p_test′. When the gray balance is realized, the dot area value of the inks of C, M, and Y is temp. The BP neural network test is followed by the code. The test data are shown in Table 15.4.

15.3   Results and Discussion

From Table 15.3, we can see the accuracy is very good by using BP neural network for the gray balance data's prediction. From Table 15.4, we can see that the modified BP neural network for the gray balance data's prediction accuracy is further improved.

In the modified BP neural network, the reflectivity of 0% is added as the first line data of inverse matrix p', and it considers the effect of printing color of paper. In the modified BP neural network, the mean reflectivity of every black color in the wavelength of 430, 480, 530, 580, 630, and 680 nm is taken as the corresponding inverse matrix p_test′, and it considers that the black ink is not pure that is different from gray.

According to cyan, magenta, and yellow dot area values in Table 15.4, the color can be overprinted, whose $L*a*b*$ value is measured as shown in Table 15.5.

Table 15.5 The $L*a*b*$ value of overprinted color

Dot area value (%)	$L*$	$a*$	$b*$
5	8.42	−3.12	4.12
10	12.02	−2.32	3.23
20	22.87	3.23	3.13
30	35.59	4.15	4.26
40	46.20	3.15	6.32
50	61.09	5.14	6.14
60	70.29	5.38	5.11
70	76.88	4.27	5.03
80	87.55	4.26	4.27
90	91.13	3.81	3.67
100	95.42	3.61	3.24

15.4 Conclusions

In the process of the study, the reflectivity of the six wavelengths is chosen to express the color, which greatly simplifies the data. The modified BP neural network model considers the characteristics of paper and ink, which can preliminarily used to predict the gray balance data.

References

1. Tian, Q. (2011). The gray balance control of G7. *Printing Journal*, (6), 32–35.
2. Yang, S. (2009). Gray balance drip in digital printing. *Printing Quality and Standardization, 1*, 24–27.
3. Guo, Q., Sun, J., & Dong, Y. (2010). Calculation of gray balance data for printing process. *Zhongyuan University of Technology, 21*, 29–32.
4. Wang, H., Chen, G., & Cui, X. (2012). Effect of paper on color printing gray balance. *Packaging Engineering*, *33*(9), 105–109.
5. Wang, M. (2004). *Matlab and scientific computing* (pp. 225–227). Beijing: Electronic Industry Press.

Chapter 16
The Research on Gravure Spot-Color-Matching Model

Jingjing Meng, Libin Wu and Jing Qian

Abstract The demand for reproduction of printing color vastly expands, which significantly promotes the application of the spot-color ink. To improve the accuracy and practicability of color matching, the Kubelka–Munk color-matching theory and the improved spectrophotometric uniform color space weight factor color-matching method are applied to construct two matching models. The four-color (C, M, Y, W) model is established on the basis of three-color model (C, M, Y), and the derivations of the two models will be shown. In addition, a new experimental program is designed for ink toner to obtain the basic data of color matching. Prediction recipes are obtained by using MATLAB software for matrix arithmetic. And the accuracy and practicability of color-matching models are verified through the experiment. The results show that two models are feasible for better utility of the spot-color matching.

Keywords Computer color matching · Spot-color ink · Kubelka–Munk theory · Spectrophotometric color matching

16.1 Introduction

Spot-color ink attained the favors of consumer and enterprise because of its constant hue, wide color gamut, good visual effects, and unique security features. However, traditional color matching mostly relies on experienced personnel, who may be disturbed by environmental and psychological conditions [1]. This renders the matching process unreliable and the matching result unstable. To improve the

J. Meng · L. Wu · J. Qian
Department of Packaging Engineering, Jiangnan University, Jiangsu, China

J. Qian (✉)
Jiangsu Key Laboratory of Advanced Food Manufacturing Equipment and Technology, Jiangsu, China
e-mail: qj639@jiangnan.edu.cn

accuracy, ameliorate the efficiency, and reduce the cost, a computer-based color-matching model seems indispensable [2]. Scholars have proposed a series of color-matching theory, such as Kubelka–Munk theory, Neugebauer equations, and the Masking equation and the corresponded approaches such as tristimulus matching, spectrophotometric color matching, and the neural network color matching.

Single-constant Kubelka–Munk theory and the improved spectrophotometric uniform color space weight factor method are applied to the establishment of models after comprehensive evaluations of the accuracy and the practicability of various color-matching methods. After extensive efforts, two color-matching models that take the experimental conditions into account are established.

16.2   Theoretical Foundations

16.2.1   Kubelka–Munk Theory

Kubelka–Munk theory is a two luminous theory applied to the semitransparent medium and opaque medium. The simplified form is as follows [3]:

$$\frac{K}{S} = \frac{(1 - R_\infty)^2}{2R_\infty} \tag{16.1}$$

where K is absorption coefficient, S is scattering coefficient, and R_∞ is the reflectance at infinite thickness. Equation 16.1 approximately indicates the relationship between reflectance and the absorption and scattering coefficients of ink.

According to single-constant Kubelka–Munk theory, scattering coefficient can still be unchanged in some cases, although the colorant concentration changes. In other words, the single-constant theory assumes that the scattering ability of mixture does not change. Because the absorption and scattering coefficients are additive, when there are n kinds of toners in the ink layer and takes the substrate into consideration, calculation of K/S value can be simplified [3]:

$$\frac{K}{S} = \left(\frac{k}{s}\right)^t + c_1 \left(\frac{k}{s}\right)^1 + c_2 \left(\frac{k}{s}\right)^2 + \cdots + c_n \left(\frac{k}{s}\right)^n \tag{16.2}$$

where k_t and s_t are the absorption and scattering coefficients of substrate, respectively, $c_1, c_2, \ldots, c_n$ are the concentrations of various colorants, $k_1, k_2, \ldots, k_n$ are the absorption coefficients of various colorants, and $s_1, s_2, \ldots, s_n$ are the scattering coefficients of various colorants.

Equation 16.2 is the expression of the single-constant K-M theory.

16.2.2 Uniform Color Space Weight Factor Method About Spectrophotometric Color Matching

Spectrophotometric color matching minimizes the color difference between the standard and the match by fitting spectral curves directly.

Spectrophotometric color matching has a characteristic that equal changes of reflectance at different wavelengths may lead to varying degrees of color perception difference. Therefore, the wavelengths that have strong sensitivity should be emphasized in the matching process with larger weight factors. On the contrary, the wavelengths that are inert should be matched with smaller weight factors [4]. So weight factors are established in the uniform color space combining the colorimetric theory. The basic expression is as follows [4]:

$$\sum_j \left[\Delta E(\lambda_j)\right]^2 \to \min \qquad (16.3)$$

where $\Delta E(\lambda_j)$ is the color difference caused by reflectance change at the wavelength of λ_j.

Next, specific analysis is conducted about Eq. 16.3.

The color tristimulus values can be determined by Eq. 16.4 [5]:

$$\begin{cases} X = K \sum_{400}^{700} S(\lambda)R(\lambda)\bar{x}(\lambda)\Delta\lambda \\ Y = K \sum_{400}^{700} S(\lambda)R(\lambda)\bar{y}(\lambda)\Delta\lambda \\ Z = K \sum_{400}^{700} S(\lambda)R(\lambda)\bar{z}(\lambda)\Delta\lambda \end{cases} \qquad (16.4)$$

where $S(\lambda)$ is relative spectral power distribution, $R(\lambda)$ is spectral reflectance, $\bar{x}, \bar{y}, \bar{z}$ are CIE standard colorimetric observer spectral tristimulus values, and K is a constant.

Taking $\Delta\lambda = 10$ nm, the color tristimulus value differences ΔX, ΔY, and ΔZ are as follows:

$$\begin{cases} \Delta X = K \cdot S(\lambda)\bar{x}(\lambda)\Delta R(\lambda) \\ \Delta Y = K \cdot S(\lambda)\bar{y}(\lambda)\Delta R(\lambda) \\ \Delta Z = K \cdot S(\lambda)\bar{z}(\lambda)\Delta R(\lambda) \end{cases} \qquad (16.5)$$

Color difference ΔE is an ideal function to evaluate the difference between two colors in the $L*a*b*$ color space. The value of $L*$, $a*$, and $b*$ can be calculated by the tristimulus values, so that $\Delta L*$, $\Delta a*$, and $\Delta b*$ can be obtained by Eq. 16.6 [4]:

$$\Delta L^* = L'(Y)\Delta Y$$
$$\Delta a^* = A'_X(X,Y)\Delta X + A'_Y(X,Y)\Delta Y \tag{16.6}$$
$$\Delta b^* = B'_Y(Y,Z)\Delta Y + B'_Z(Y,Z)\Delta Z$$

Substituting Eq. 16.5 into Eq. 16.6 [4]:

$$\Delta L^*(\lambda) = K \cdot S(\lambda)\Delta R(\lambda)\bar{y}(\lambda)L'(Y)$$
$$\Delta a^*(\lambda) = K \cdot S(\lambda)\Delta R(\lambda)\left[\bar{y}(\lambda)A'_X(X,Y) + \bar{y}(\lambda)A'_Y(X,Y)\right] \tag{16.7}$$
$$\Delta b^*(\lambda) = K \cdot S(\lambda)\Delta R(\lambda)\left[\bar{y}(\lambda)B'_Y(Y,Z) + \bar{z}(\lambda)B'_Z(Y,Z)\right]$$

This color-matching method has been improved in this paper according to the actual situation and the difficulty level of MATLAB programming implementation.

Because of color difference formula

$$\Delta E = \sqrt{(\Delta L*)^2 + (\Delta a*)^2 + (\Delta b*)^2}$$

We found that if we want to make

$$\sum_j [\Delta E(\lambda_j)]^2 \rightarrow \min$$

It is equal to make $[\Delta L*(\lambda_j)]^2$, $[\Delta a*(\lambda_j)]^2$ and $[\Delta b*(\lambda_j)]^2$ approach minimum, respectively:

$$\sum_j [\Delta L^*(\lambda_j)]^2 \rightarrow \min$$
$$\sum_j [\Delta a^*(\lambda_j)]^2 \rightarrow \min \tag{16.8}$$
$$\sum_j [\Delta b^*(\lambda_j)]^2 \rightarrow \min$$

Consequently, new weight factors are established. These weight factors can minimize color difference caused by reflectance change at a certain wavelength.

16.2.3 Deduction of Color-Matching Models

16.2.3.1 Model Based on Three Colors (C, M, Y)

Three primary inks C, M, and Y are used as basic inks to establish a color-matching model. The wavelength range of reflectance will be measured from 400 to 700 nm at 10 nm increments.

It is known that the smaller the color difference between standard and match, the higher the precision of the model. An ideal state is assumed $\Delta E = 0$.

According to the analysis above and combining Eq. 16.7:

$$\Delta L^*(\lambda) = K \cdot S(\lambda)\Delta R(\lambda)\bar{y}(\lambda)L'(Y) = 0$$
$$\Delta a^*(\lambda) = K \cdot S(\lambda)\Delta R(\lambda)\left[\bar{x}(\lambda)A'_X(X,Y) + \bar{y}(\lambda)A'_Y(X,Y)\right] = 0 \qquad (16.9)$$
$$\Delta b^*(\lambda) = K \cdot S(\lambda)\Delta R(\lambda)\left[\bar{y}(\lambda)B'_Y(Y,Z) + \bar{z}(\lambda)B'_Z(Y,Z)\right] = 0$$

Equation 16.9 is applied to single-constant K-M theory, and the concentration recipe can be obtained after a series of derivation [6]:

$$C = (TED\Phi)^{-1} \cdot TED(f^a - f^t) \qquad (16.10)$$

Several matrices are defined and depicted to represent the parameters in Eq. 16.10:

$$
C = \begin{bmatrix} c^1 \\ c^2 \\ c^3 \end{bmatrix} \quad
T = \begin{bmatrix} L_T \\ A_T \\ B_T \end{bmatrix} \quad
\begin{aligned}
L_T &= L'(Y)\bar{y} \\
A_T &= A'_X(X,Y)\bar{x} + A'_Y(X,Y)\bar{y} \\
B_T &= B'_Y(Y,Z)\bar{y} + B'_Z(Y,Z)\bar{z}
\end{aligned}
$$

$$
E = \begin{bmatrix} S_{400} & 0 & \cdots & 0 \\ 0 & S_{410} & \cdots & 0 \\ \vdots & \vdots & \ddots & \vdots \\ 0 & 0 & \cdots & S_{700} \end{bmatrix} \quad
D = \begin{bmatrix} d_{400} & 0 & \cdots & 0 \\ 0 & d_{410} & \cdots & 0 \\ \vdots & \vdots & \ddots & \vdots \\ 0 & 0 & \cdots & d_{700} \end{bmatrix} \quad
d_j = \frac{R_j^2 - 1}{2R_j^2}
$$

$$
\Phi = \begin{bmatrix} \left(\frac{k}{s}\right)^1_{400} & \left(\frac{k}{s}\right)^2_{400} & \left(\frac{k}{s}\right)^3_{400} \\ \left(\frac{k}{s}\right)^1_{410} & \left(\frac{k}{s}\right)^2_{410} & \left(\frac{k}{s}\right)^3_{410} \\ \vdots & \vdots & \vdots \\ \left(\frac{k}{s}\right)^1_{700} & \left(\frac{k}{s}\right)^2_{700} & \left(\frac{k}{s}\right)^3_{700} \end{bmatrix} \quad
f^a = \begin{bmatrix} \left(\frac{K}{S}\right)^a_{400} \\ \left(\frac{K}{S}\right)^a_{410} \\ \vdots \\ \left(\frac{K}{S}\right)^a_{700} \end{bmatrix} \quad
f^t = \begin{bmatrix} \left(\frac{K}{S}\right)^t_{400} \\ \left(\frac{K}{S}\right)^t_{410} \\ \vdots \\ \left(\frac{K}{S}\right)^t_{700} \end{bmatrix}
$$

where C is the concentration matrix, E is relative spectral power distribution matrix, $\bar{x}, \bar{y}, \bar{z}$ are CIE standard colorimetric observer spectral tristimulus values matrices, superscript 1, 2, 3 are C, M, Y three-color inks, respectively, and superscript a and t are the reflectance matrices of standard and substrate.

16.2.3.2   Model Based on Four Colors (C, M, Y, W)

Only three primary inks to participate color matching do not meet the requirements of customer in the actual production. It is the first choice of many enterprises who use heat transfer printing on the fabric and cotton since the white ink has a strong ability to cover [1], thereby the white ink is added as the fourth basic ink, and the four-color-matching model will be derived based on the three-color-matching model.

Some parameters of Eq. 16.10 have changed after adding the white ink:

$$
\Phi = \begin{bmatrix}
\left(\frac{k}{s}\right)^1_{400} & \left(\frac{k}{s}\right)^2_{400} & \left(\frac{k}{s}\right)^3_{400} & \left(\frac{k}{s}\right)^4_{400} \\
\left(\frac{k}{s}\right)^1_{410} & \left(\frac{k}{s}\right)^2_{410} & \left(\frac{k}{s}\right)^3_{410} & \left(\frac{k}{s}\right)^4_{410} \\
\vdots & \vdots & \vdots & \vdots \\
\left(\frac{k}{s}\right)^1_{700} & \left(\frac{k}{s}\right)^2_{700} & \left(\frac{k}{s}\right)^3_{700} & \left(\frac{k}{s}\right)^4_{700}
\end{bmatrix}
\qquad
C = \begin{bmatrix} c^1 \\ c^2 \\ c^3 \\ c^4 \end{bmatrix}
$$

Equation 16.10 can be used to solve three unknowns using three linear equations; however, there are four unknowns in the concentration matrix C now, and three equations are unable to solve four unknowns according to the linear algebra theory. In Eq. 16.10, the general solution of undetermined system of equations can be obtained as the following form:

$$
\begin{bmatrix} c^1 \\ c^2 \\ c^3 \\ c^4 \end{bmatrix} = \begin{bmatrix} m^1 \\ m^2 \\ m^3 \\ 0 \end{bmatrix} + x \begin{bmatrix} n^1 \\ n^2 \\ n^3 \\ n^4 \end{bmatrix}
$$

There is only one unknown x, and one way of solving x is to add a supplementary condition. According to Eq. 16.2:

$$
\left(\frac{K}{S}\right)^m = \left(\frac{K}{S}\right)^t + c_1\left(\frac{k}{s}\right)^1 + c_2\left(\frac{k}{s}\right)^2 + c_3\left(\frac{k}{s}\right)^3 + c_4\left(\frac{k}{s}\right)^4 \tag{16.11}
$$

There are 31 sets of data between 400 and 700 nm totally. The general solution is substituted into Eq. 16.11, and the least squares techniques is applied to compute the optimal solution x, so that the concentration matrix can be solved as well.

Consequently, a mathematical model has been established to solve the concentration of the four-color recipe. This model is based on the three-color model and solves the concentration of four-color model by adding a supplementary condition.

The spectral reflectance of basic inks is stored into the computer previously, and the recipes can be obtained according to the color-matching models after inputting the reflectance and colorimetric values of the standard color.

16.3 Experimental Programs

Toner is putted into the basic recipe of ink to make four-color ink in this paper. After stirring evenly, the ink is daubed on the white paper by scratching a small amount with ink knife. Then, ink is wiped evenly using the spreader on white paper which is put on a heated glass pane. Each kind of ink requires multiple groups of

coating samples, and one of the best coating quality is selected as the sample which will be used in the experiment. In addition, the weight of toner, the date of sample making, and the other information should be recorded carefully. Last but not the least, samples should be measured after 24 h because of the dry fading phenomenon of ink.

16.3.1   Determining the Reflectance of Basic Ink

Firstly, the toner is put into the basic recipe of ink at certain weight increments, and the color difference will be measured between the sample and the former sample. When the color difference is small enough, it can be considered that the color will not change significantly even with more toner. So we add this weight into basic recipe of ink as the initial basic ink.

Secondly, regarding the initial basic ink as standard, toner is put into the basic recipe of ink according to different concentrations (5, 10, 20, 40, 80, 100 %). The reflectance data of the corresponding concentration can be obtained after measurement.

Finally, after analysis and comparison between the reflectance of each concentration of four-color inks and various types of four-color ink products, the concentrations that have better agreement are chosen as the basic inks, and then corresponding data are stored in the matching database.

16.3.2   Determining the Reflectance of Substrate

The basic recipe of ink is stirred uniformly without any toner and coated over white paper. It is regarded as the substrate. And then, its reflectance is measured and corresponding data are substituted into color-matching calculation.

16.4   Experimental Verification and Analysis

MATLAB R2009a software is used for programming [7]. Then, the relative spectral power distribution values of CIE standard light source (D65), CIE standard colorimetric observer spectral tristimulus values, and the reflectance of the basic ink are written into the program. After the commissioning test run correctly, the relevant data of standard are substituted into the program and the concentrations of basic inks can be computed. The concentrations that obtained by calculation are converted into toner weight, and experimental verification is conducted. The experimental results are shown in Table 16.1.

Table 16.1 The measurement values of standard and the computed values of color matching

No.	Toner weight (g)				Chromatic values				ΔE
	Actual values		Computed values		Standard colors		Matching colors		
1	C	0.080	C	0.075	L^*	48.658	L^*	46.755	2.84
	M	2.000	M	1.823	a^*	−2.443	a^*	−4.523	
	Y	0.600	Y	0.712	b^*	33.374	b^*	33.374	
2	C	0.080	C	0.077	L^*	50.357	L^*	51.562	3.08
	M	1.000	M	0.990	a^*	−4.643	a^*	−7.283	
	Y	0.400	Y	0.526	b^*	29.162	b^*	30.205	
3	Y	0.200	Y	0.239	L^*	68.887	L^*	67.980	5.80
	M	1.000	M	0.869	a^*	27.695	a^*	22.500	
	W	10.000	W	8.870	b^*	43.666	b^*	41.237	
4	C	1.000	C	1.048	L^*	33.643	L^*	37.794	6.37
	M	4.000	M	4.772	a^*	−13.433	a^*	−16.778	
	Y	2.000	Y	1.698	b^*	7.026	b^*	3.538	
	W	18.000	K	20.037					

According to Table 16.1, white ink is not added in Sample 1 and 2; and the matching model shows high precision, and the color difference is less than 5 which meets industry standards. Sample 3 consists of yellow, magenta, and white inks. The same three-color-matching model shows a larger color difference when the white ink is added. Sample 4 is four-color matching and shows a large color difference though still obtain a match color that is similar to the standard.

16.5 Conclusions

Experimental results show that the color-matching models established in this paper have considerable precision and practical significance to solve the spot-color-matching problem. The efficiency of the color matching has been improved to a great extent, although there is still some color difference in the four-color-matching application. There are many factors affecting the accuracy of color matching, including the limitations of Kubelka–Munk theory itself, inevitable errors during the experiment process, and precision of the experimental apparatus [8, 9]. The accuracy of color-matching models will be further enhanced if the experiment conditions and the data precision of basic inks can be improved.

Because of the limitation of experimental conditions and time, this subject remains to be further studied.

First, the precision of four-color-matching model can be further improved, and the characteristics of white ink should be studied thoroughly. The improvement of computer algorithm can also help improve the accuracy of models.

Second, there is a wide range of substrates in the actual printing, while in this paper, we only use white paper as the substrate to discuss. In future study, the color-matching models should be modified according to different substrates, so that the models can be applied more widely.

References

1. Zhao-yang, Q. I. (2001). The match of spot-color ink [J]. *Guangdong Print, 05*, 34–38.
2. Zhou, C., & Tang, Z. (2006). Theoretical study of computer color matching on spot-color ink using in packaging printing [J]. *Packaging Engineering, 27*, 121–123.
3. Kubelka, P., & Munk, F. (1931). Ein Beitrag Zur Optik Der Farbanstrische [J]. *Zeitschrift Technical Physics, 12*, 593.
4. Wang, X., Zhou, F., Yu, B., & Chen, S. (1998). Uniform color space weight factor method about spectrophotometric color matching [J]. *Optics and Precision Engineering, 6*, 1–4.
5. Liu, H. (2008). *Printing chromatics*. Beijing: China Light Industry Press.
6. Xu, C., Wang, Q. I., & Zhang, L. (2012). The research on spot-color matching model based on the tristimulus weights [J]. *Packaging Engineering, 33*, 10–14.
7. Zhou, P. (2014). *MATLAB numerical analysis and application tutorial*. Beijing: Electronic Industry Press.
8. Robinson. (1996). MATLAB Numerical Analysis and Application Tutorial [M]. *TAPPI, 10*, 152.
9. Li, Z., Zhang, Y., & Ning, Y. (2008). The application of the Kubelka-Munk color prediction model in the printing industry [J]. *Packaging Engineering, 29*, 43–45.

Chapter 17
Neighborhood Similarity-Based Color Transfer Algorithm

Yanhao Li, Zhijiang Li and Liqin Cao

Abstract Color transfer produces a new image and keeps the content of source image and the color of reference image. The technology is widely used in areas such as prepress image processing and multimedia post-production. The article proposes an adaptive local color transfer algorithm based on neighborhood similarity. Firstly, two classical algorithms—Reinhard algorithm and Welsh algorithm—are analyzed on the applicability and deficiency according to the experiments. Then, a new method is introduced to improve Welsh algorithm on incomplete point neighborhood description and the low efficiency of searching for matching points, which is calculating the neighborhood average value by adding high-frequency texture information to describe neighborhood features, and local hierarchical matching points searching strategy. The matching points searching strategy includes dividing the target image into blocks, searching for matching point based on neighborhood similarity firstly, and searching the global image to find best matching points finally. Experiments demonstrate that the improved algorithm can transfer the referential color effectively without any user intervention.

Keywords Color transfer · Welsh algorithm · Point neighborhood features

17.1 Introduction

In last decades, color transfer has drawn a lot of interests. It is a process of changing an image's color based on another image, which has been widely used in the fields of images. Color transfer involves solving such a problem: How to synthesize a new image C based on image A and image B, which is produced from the shape information of image B and the color information of image A [1].

Y. Li · Z. Li (✉) · L. Cao
School of Printing and Packaging, Wuhan University, Wuhan, China
e-mail: lizhijiang@whu.edu.cn

Recent years have witnessed the new development of color transfer algorithm. Reinhard et al. [2] presented an automatic algorithm based on l$\alpha\beta$ color space, which has small correlation between channels. According to the work of Reinhard et al., Welsh et al. [3] proposed a color transfer algorithm to transfer a source color image's color characteristics to a target gray image, based on the average value and the quadratic difference of the luminance in neighboring pixels. However, the point neighborhood features is not completely described, besides the poor efficiency.

This paper proposes a new color transfer algorithm based on the Welsh algorithm, by adding high-frequency texture information to describe the point neighborhood characteristics in the image, as well as cutting down the cost of searching matching pixels and increasing the accuracy of the matching pixels. The proposed algorithm may be beneficial to research attempting to alter image's color.

This paper is organized into the following sections. Section 17.2 highlights the theory analysis of the new algorithm of color transfer. Section 17.3 deals with the contrast and analysis of the results produced from each method. In Sect. 17.4, the conclusion is outlined.

17.2 Classical Color Transfer Algorithms

Reinhard et al. used a simple and effective approach to transfer color characteristics from the reference image to the source image based on the l$\alpha\beta$ color space [2, 4]. Equation (17.1) highlights these transformations at each axis. The algorithm has two disadvantages. First, it is a labor-intensive algorithm. Second, this algorithm is subjective. It is difficult to measure the success of the resultant image.

$$\begin{cases} l* = \left(ls - \overline{ls}\right) \times \frac{\sigma_r^l}{\sigma_s^l} + \overline{lr} \\ \alpha* = \left(\alpha s - \overline{\alpha s}\right) \times \frac{\sigma_r^\alpha}{\sigma_s^\alpha} + \overline{\alpha r} \\ \beta* = \left(\beta s - \overline{\beta s}\right) \times \frac{\sigma_r^\beta}{\sigma_s^\beta} + \overline{\beta r} \end{cases} \qquad (17.1)$$

While the procedure of the Welsh algorithm for color transfer requires a few simple steps, first each image is converted into the l$\alpha\beta$ color space. Next, go through each pixel in the grayscale image in scan-line order and select the best matching sample in the color image using neighborhood statistics. The best match is determined by using a weighted average of pixel luminance and the neighborhood statistics. The chromaticity values (α, β channels) of the best matching pixel are then transferred to the grayscale image to form the final image. Color transfer using swatches involves the same global image matching procedure but only between the source and target swatches. The colorized pixels in the target swatch regions are then used as the source pixels for the color transfer to the remaining non-colorized pixels using a texture synthesis approach [5].

The Reinhard method uses a simple statistical analysis, and it works very successfully. However, it tries to represent the overall characteristics of color used in an image via only two statistical values per color channel and then transforms all pixel colors in an image according to the same statistical information. Therefore, when the source and target images are not compatible, a user has to manually set swatches for each color region and have to match between them. Welsh method is more suitable when the source and target images are not compatible, but its efficiency is low.

17.3 Neighborhood Similarity-Based Color Transfer Algorithm

17.3.1 Neighborhood Texture Feature

To describe neighborhood texture feature, skewness and kurtosis are introduced. Skewness is used to describe the symmetry of the neighborhood of the pixel p.

$$S = \frac{\frac{1}{5 \times 5} \sum_{P \in 5 \times 5} (lp - M)^3}{\sigma^3} \tag{17.2}$$

where M is the mean and σ is the standard deviation.

Kurtosis is used to describe the extent of the image data, referring to the degree of concentration or dispersion of image data.

$$K = \frac{\frac{1}{5 \times 5} \sum_{P \in 5 \times 5} (lp - M)^4}{\sigma^4} - 3 \tag{17.3}$$

where M is the mean and σ is the standard deviation.

17.3.2 Neighborhood Search Matching Strategy

Traditional Welshs algorithm did not exploit the certain correlation between neighboring pixels. Levin et al. [6] proposed a searching method of the neighborhood correlation as shown in Fig. 17.1, where $\{A_2, B_2, C_2, D_2\}$ were calculated firstly and then became a collection of all candidate pixels of P.

Exploiting the neighborhood correlation, a new search strategy is proposed. Comparing the luminance of P and Q, where P is a pixel to be colorized and Q is the latest colorized pixel:

If P and Q have the same luminance, just transfer the color from Q to P.
If P and Q differ in luminance, and then:

Fig. 17.1 Illustration for the neighborhood correlation
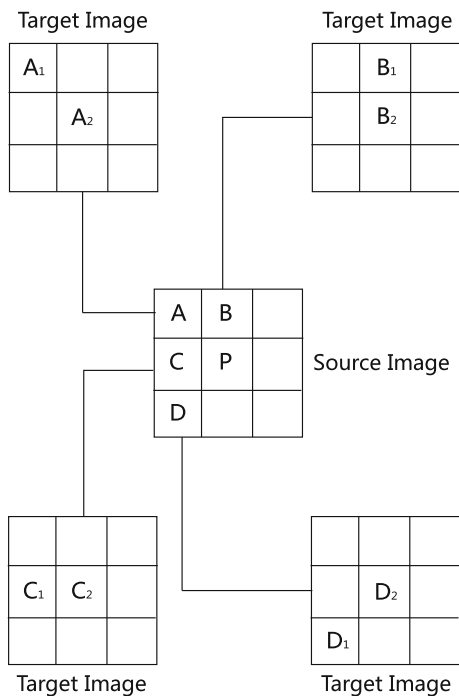
If difference is in the range of the threshold, search the neighborhood of P to look for the best matching pixel by using the neighborhood correlation;

If the difference is out the range of the threshold, search over the source color image or some of its randomly selected regions; and

In the searching strategy, the neighborhood correlation is reflected completely, and the running time of the algorithm will be cut down effectively simultaneously.

17.4 Experimental Results and Analysis

Figure 17.2a is typical testing target picture which shows a forest behind a lawn. Figure 17.2b shows a reference picture with two green tree stands on lawn and blue sky. Figure 17.2c is the result of Welsh algorithm. In that picture, we can see that the edge of the tree is colored blue; meanwhile, some green color point on the tree is not nature. Figure 17.2d is the result of proposed algorithm. There is no dyeing at the edge of the tree, and the color is much more natured than the effect of Welsh algorithm.

The experiment was done with 4G memory and Core i5 processor. The execution time in Table 17.1 is the average results sampled from many test samples.
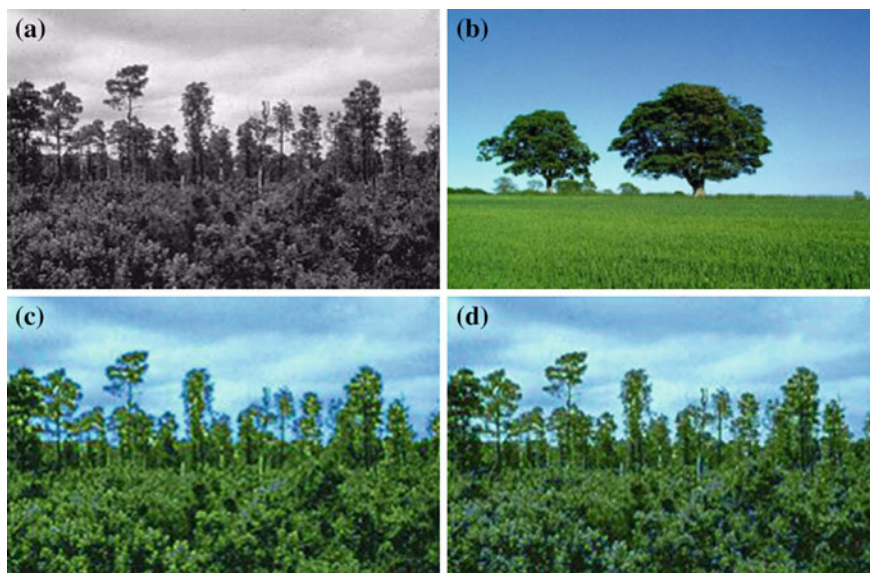
Fig. 17.2 Comparison of Welsh algorithm and our method. **a** Target picture. **b** Reference picture with two green tree stands on lawn and blue sky. **c** Result of Welsh algorithm. **d** Result of proposed algorithm

Table 17.1 The effectiveness of the experiment (seconds)

	Reinhard algorithm	Welsh algorithm	Proposed algorithm
258 * 168	0.281	7.037	3.786
615 * 640	0.936	27.431	13.674

17.5 Conclusions

This paper proposes a neighborhood similarity-based color transfer algorithm, which is implemented automatically and achieves results with continuous and uniform vision perception. The experimental results demonstrate that the proposed algorithm improves the traditional color transfer algorithm effectively. The algorithm may be used in more areas such as gray image colorization and color image artistic rendition.

References

1. Pan, J., Wang, X. S., & Cheng, Y. H. (2014). Multi-source color transfer based on active contours exploration. *Acta Automatica Sinica, 40*(4), 713–720.
2. Reinhard, E., Ashikhmin, M., Gooch, B., & Shirley, P. (2001). Color transfer between images. *Computer Graphics & Applications IEEE, 21*(5), 34–41.
3. Welsh, T., Ashikhmin, M., & Mueller, K. (2002). Transferring color to greyscale images. *Siggraph Proceedings of Annual Conference on Computer Graphics & Interactive Technique, 21*(3), 277–280.
4. Ruderman, D. L. (1998). Statistics of cone responses to natural images: Implications for visual coding. *Journal of Optical Society America, 15*(8), 2036–2045.
5. Wang, M., & Chen, Z. (2011). A color transfer algorithm based on neighborhood correlation and optimization techniques. In Computational intelligence and design, international symposium on (Vol. 2, pp. 31–34). New York: IEEE.
6. Levin, A., Lischinski, D., & Weiss, Y. (2004). Colorization using optimization. *ACM Transactions on Graphics, 23*(3), 686–691.

Chapter 18
Obtaining Absolute Scene Luminance Using HDR Imaging

Muhammad Safdar, Ming Ronnier Luo, Yuteng Zhu and Xiaoyu Liu

Abstract The absolute measure of scene luminance is needed in many applications, e.g., color image reproduction (especially outdoor), surveillance images, light appearance, and glare prediction. Currently, commercial luminance cameras are being used, which are very expensive and have limitations in dynamic range. An efficient and inexpensive method is needed to obtain absolute luminance of each of pixels in the scene. In the current study, a method was proposed to obtain absolute scene luminance (XYZ map) at each pixel using digital RGB camera and high dynamic range (HDR) imaging. The proposed model was calibrated using a tele-spectroradiometer (TSR) by means of average luminance at a small spot. A good match of results was obtained between TSR and the proposed method.

Keywords HDR · RGB · XYZ · Luminance · Radiance · Image calibration

18.1 Introduction

Measuring the absolute luminance of a scene means to measure the whole dynamic range at each pixel of a scene image in the units of cd/m^2. The measurement should cover the whole dynamic range (ratio between the densities of luminance intensity

M. Safdar · M.R. Luo (✉) · Y. Zhu
State Key Laboraory of Modern Optical Instrumentation, Zhejiang University,
Hangzhou, China
e-mail: m.r.luo@leeds.ac.uk

M. Safdar
Department of Computer Science, COMSTS Institute of Information Technology,
Sahiwal, Pakistan

M.R. Luo
School of Design, University of Leeds, Leeds, UK

X. Liu
College of Science, Harbin Engineering University, Harbin, China

of the brightest sunbeam to the darkest shadow), or maximum contrast of the scene luminance [1]. Currently, luminance cameras, e.g., LMK, Pro-Metric, and ICAM, are being used to measure absolute scene luminance. These methods are very expensive and have limitations in their dynamic range. The absolute measure of scene luminance is needed in many applications, e.g., light appearance measurement, glare prediction, and evaluation [2, 3].

An efficient and inexpensive method is needed to obtain a luminance map for all pixels in the scene. Currently available digital cameras are able to capture the images of size in megapixels with 24 bit of RGB color information which can be displayed on high-resolution screen, but its dynamic range is still 100:1. A real-world scene can produce a dynamic range as high as of the order of 10^6:1. Clearly, the dynamic range captured by a digital camera is much below the reality. The high dynamic range (HDR) imaging provides the solution for this issue.

Several methods have been developed to capture HDR image, and the most common way is to combine multiple images captured by setting different exposure times [4, 5]. Fairchild [6] did an HDR photographic survey, gave details of procedure, proposed system characterization method, and has also provided HDR images database for researchers. Debevec and Malik [4] developed a method to recover HDR radiance map from images taken from a conventional imaging device (RGB camera). In the current study, a method was developed to obtain true luminance map from radiance map recovered using HDR technology.

18.2   Method

According to the method of Debevec and Malik [4], multiple images of a scene are captured with different exposure times, and camera response functions are recovered by processing these images. Then, these images are fused together with known response functions to obtain a HDR radiance map which corresponds to the true values of radiance in the scene. To display an HDR image, the dynamic range of the radiance map needs to be compressed to a displayable range using a tone mapping operator and creates a pleasing image [7]. In the current study, a method was proposed to obtain true luminance map which uses HDR imaging to recover radiance map, and then, some further processing was done to obtain true luminance map with measurements in cd/m^2 scale.

An RGB camera was used to capture multiple images of the same scene at different camera exposure settings (vary exposure time from small to large). The Macbeth Color Checker Classic (MCCC) chart was used for calibration of the model. The colorimetric values of the 24 colors on MCCC were measured under sunlight using a tele-spectroradiometer (TSR) for calibration in a sunny day. The MCCC chart was placed under daylight at noon to obtain the bright lighting conditions. Ten different exposures (small to large) were taken by setting exposure times one stop apart. Exposure times for ten exposures in the current work were set at minimum and maximum values of 1/8000 to 1/15 s, respectively. It was ensured
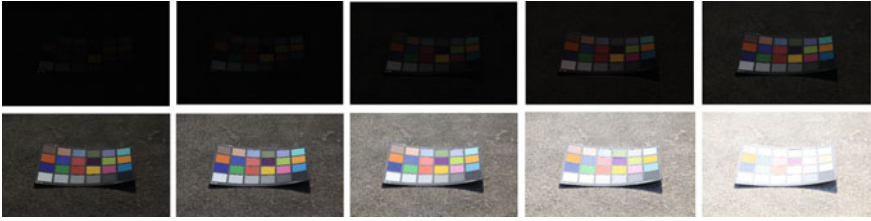
Fig. 18.1 HDR exposures for MCCC chart

that the scene should be correctly exposed at least in one of the exposures. Every next exposure was taken one stop apart from the previous. Ten exposures of MCCC taken under daylight are shown in Fig. 18.1.

Nonlinear mapping from scene radiance E_i and exposure time Δt_j to pixel brightness Z_{ij} is represented as follows:

$$Z_{ij} = f(E_i \Delta t_j) \qquad (18.2.1)$$

where i and j range over number of pixels and number of exposures, respectively, and f is a monotonic function that can be inverted. By integrating f and taking logarithm on both sides, Eq. 18.2.1 becomes:

$$\ln f^{-1}(Z_{ij}) = \ln E_i + \ln \Delta t_j \qquad (18.2.2)$$

Define a function g such that Eq. 18.2.2 takes the form:

$$g(Z_{ij}) = \ln E_i + \ln \Delta t_j \qquad (18.2.3)$$

Then, solving this system of equations for g in least-squared error sense results in camera response function f. Camera response functions may be different for different cameras. Camera response functions for the camera used in current work were computed and are shown in Fig. 18.2.

$$\ln E_i = g(Z_{ij}) - \ln \Delta t_j \qquad (18.2.4)$$

$$\ln E_i = \mathrm{sum}_{j=1}^{p}\big(w(Z_{ij})\big(g(Z_{ij}) - \ln \Delta t_j\big)\big)\Big/\mathrm{sum}_{j=1}^{p}\big(w(Z_{ij})\big) \qquad (18.2.5)$$

The Eq. 18.2.5 represents the true radiance map of the scene which has three channels R, G, and B. The defected pixels were corrected using a Gaussian smoothing filter with standard deviation and kernel size of 15 and 45 (three times of SD), respectively.

The scene radiance was then transformed to perceived luminance and chrominance channels by using RGB to *XYZ* conversion matrix as given in Eq. 18.2.6 [8].
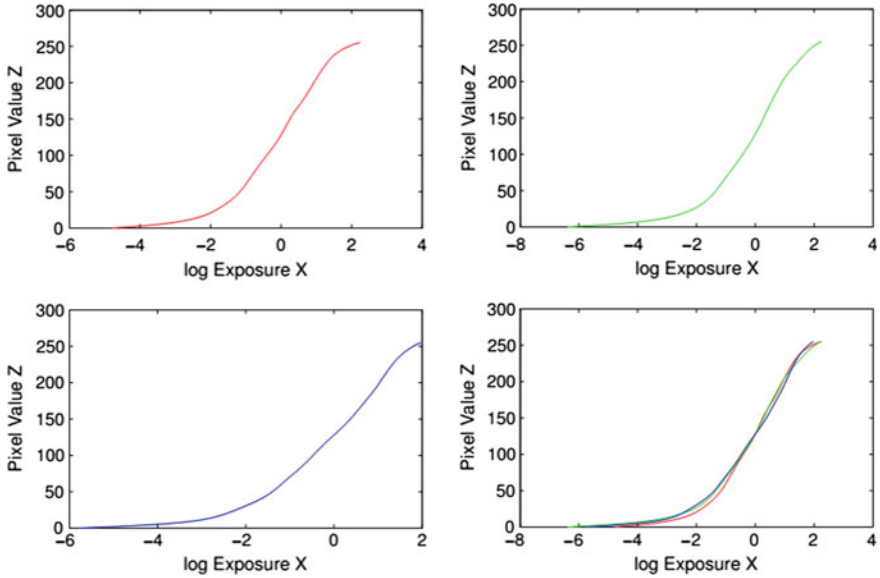
Fig. 18.2 Recovered RGB response curves

$$\begin{bmatrix} X \\ Y \\ Z \end{bmatrix} = \begin{bmatrix} 0.412453 & 0.357580 & 0.180423 \\ 0.212671 & 0.715160 & 0.072169 \\ 0.019334 & 0.119193 & 0.950227 \end{bmatrix} \begin{bmatrix} R \\ G \\ B \end{bmatrix} \tag{18.2.6}$$

The X, Y, and Z maps were then calibrated using MCCC chart color measurements by fitting a power function in least-squared sense. Three fitting equations for corrected X, Y, and Z maps, respectively, are given below.

$$X_c = K_x X^\alpha \tag{18.2.7}$$

$$Y_c = K_y Y^\beta \tag{18.2.8}$$

$$Z_c = K_z Z^\gamma \tag{18.2.9}$$

where K_x, K_y, and K_z are the scaling factors to adjust the luminance or chrominance channels [9]. And exponents $\alpha, \beta,$, and γ are the power factors to adjust the values of overexposed and underexposed pixels of the X, Y, and Z maps, respectively. Fitting values of K_x, K_y, and K_z are 23.87, 23.11, and 20.16, respectively, and that of $\alpha, \beta,$, and γ are 0.86, 0.86, and 0.85, respectively. The predicted values of 24 MCCC color patches from X, Y, and Z maps were averaged and correlated with the measured results (see Fig. 18.3).
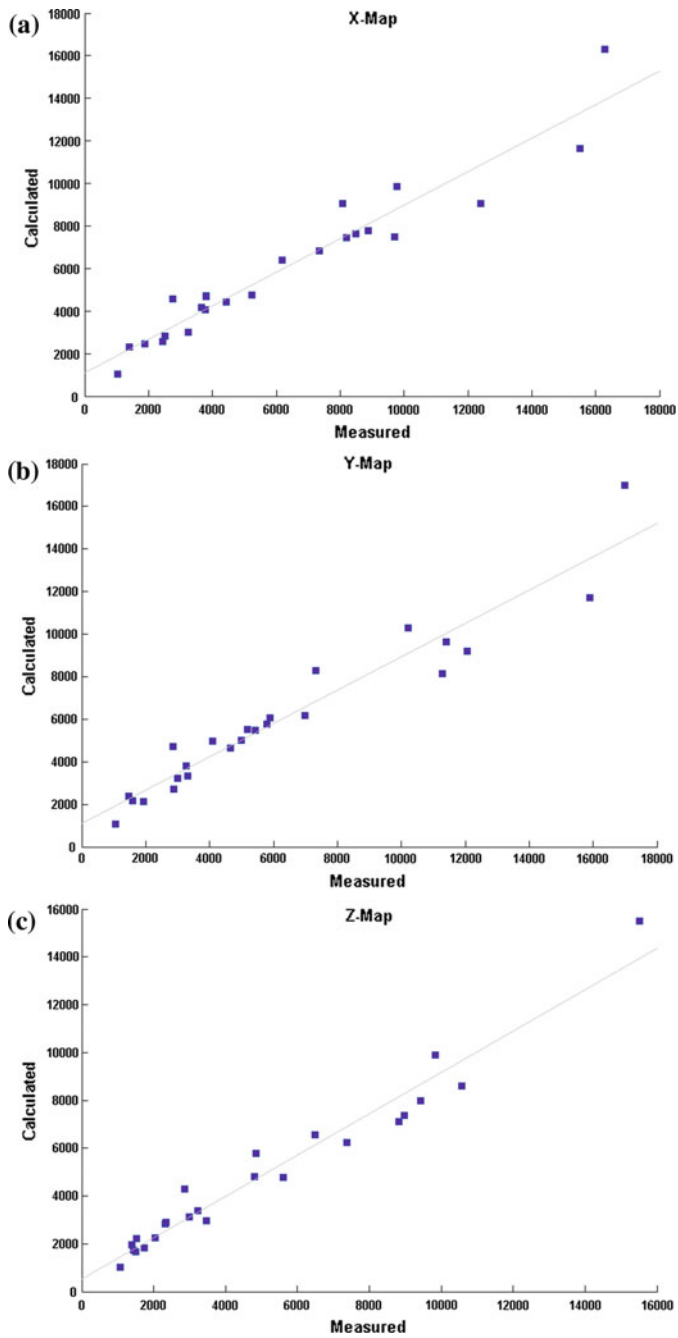
Fig. 18.3 Scatter plots of measured and predicted values. **a** *X* map, **b** *Y* map, and **c** *Z* map

The correlation coefficients calculated between measured and average values of color patches from *X*, *Y*, and *Z* maps were 0.96, 0.96, and 0.97, respectively. Hence, *X*, *Y*, and *Z* maps were recovered form HDR images with a significant correlation between measured and predicted results.

18.3   Conclusions

A digital RGB camera-based method was proposed to obtain *XYZ* image with true luminance values. The proposed method used HDR imaging to obtain true radiance of the scene and camera response functions using Debevec and Malik's method. This information was further processed to obtain device-independent *XYZ* channels that cover whole dynamic range. The MCCC calibration chart was used to calibrate the model. The results of proposed model were significantly correlated with the measured values from 24 color patches of MCCC that include 18 chromatic and 6 achromatic patches. This method can further be enhanced to obtain *XYZ* tristimulus space to predict appearance of objects.

References

1. Lukac, R. (2011). *Computational photography: Methods and applications*. Boca Raton: CRC Press, Taylor and Francis Group.
2. Yang, Y., Ma, S. N., Luo, M. R., & Liu, X. Y. (2015). Discomfort glare caused by no-uniform white LEDs. In *Proceedings of CIE Session 2015 Manchester (CIE 2015)*.
3. Safdar, M., Luo, M. R., Li, H., Zhu, Y., Mughal, M. F., & Liu, X. Y. (2015). Using digital RGB camera to measure room appearance. In *Proceedings of CIE Session 2015 Manchester (CIE 2015)*.
4. Debevec, P. E., & Malik, J. (2008). Recovering high dynamic range radiance maps from photographs. In *Proceedings of ACM SIGGRAPH (ACM 2008)*, p. 31.
5. Chaurasiya, R. K., & Ramakrishnan, K. R. (2013). High dynamic range imaging. In *Proceedings of IEEE International Conference on Communication Systems and Network Technologies, 2013*.
6. Fairchild, M. D. (2007). The HDR photographic survey. In *Proceedings of Color and Imaging Conference (IS&T 2007)*, pp. 233–238.
7. Reinhard, E., Stark, M., Shirley, P., & Ferwerda, J. (2002). Photographic tone reproduction for digital images. *ACM Transactions on Graphics (TOG), 21*(3), 267–276.
8. Reinhard, E., Ward, G., Pattanaik, S., & Debevec, P. (2007). *High dynamic range imaging (Elsevier 2007)*, p. 36.
9. Qian, T. L., Shafie, S., & Saripan, M. I. (2011). A local tone mapping operator for high dynamic range images. In *Proceedings of 4th International Conference on Modeling, Simulation and Applied Optimization (ICMSAO) (IEEE 2011)*, pp. 1–6.

Chapter 19
Evaluation of Color Perception Among Different Aged Observers Based on Color Matching Experiments

Chunjie Shi, Min Huang and Haoxue Liu

Abstract In order to study the observer variability of color perception, 53 observers aging from 20 to 79 were organized to match the 17 color stimuli on the monitor. The spectral power distribution of the target and the matched colors were measured and used to evaluate the color difference threshold at different aged group of observers. The results indicated that the mean CIEDE2000 color difference of all the tested observers was 1.07. The experimental data were calculated by CIE1964 color matching function (CMF) and CIEPO06 CMF. Comparison of the two models showed little difference in color difference thresholds for different aged observers.

Keywords Color perception · Different aged observers · CIEPO06 CMF · Color matching

19.1   Introduction

The observers have different cone fundamentals, and the colors that look similar to one will look perceptibly different to the other. With the widespread use of wide gamut displays with narrowband primaries, the phenomenon of observer metamerism becomes more evident. CIE1964 color matching functions (CMF) failed to account for the difference in color vision. In 2006, the Technical Committee TC 1-36 of CIE proposed CIE2006 physiological observer model (henceforth CIEPO06 CMF [1]). The model provides a convenient framework for calculating average cone fundamentals for any field size between 1° and 10° and for an age between 20 and 80. Subsequent research [2] has shown that the model still had some weaknesses.

C. Shi · M. Huang (✉) · H. Liu
School of Printing and Packing Engineering, Beijing Institute of Graphic Communication, Beijing, China

The authors carried out a psychophysical experiment. 53 observers with normal color vision were organized to match the 17 test stimuli on the same monitor. Color difference thresholds of different aged observers were calculated to evaluate the performance of CIE1964 CMF and CIEPO06 CMF on aging effect.

19.2 Experimental

19.2.1 Color Stimuli

Considering the color gamut of the monitor, the XYZ tristimulus values of the white point were set as 160.5, 170.1, and 162.9 (measured by PR655 spectroradiometer). The stability of the monitor was evaluated by measuring a series of colors over a period of 2 h, the color differences were below 0.5 CIELAB units 2 h later.

The samples surrounding 17 color centers recommended by the CIE [3] were randomly displayed on the LCD monitor. The color centers covered 8 hues that were uniformly selected from CIELAB color space. The experimental interface is shown in Fig. 19.1. The test and reference stimuli were divided by a black thin line, and the diameter of the circle is 7.8 cm. The distribution of the measured 17 color centers on CIELAB a^*b^* plane is shown in Fig. 19.2.

Fig. 19.1 Interface of the color matching experiment

Fig. 19.2 The distribution of 17 color centers in CIELAB a^*b^* plane
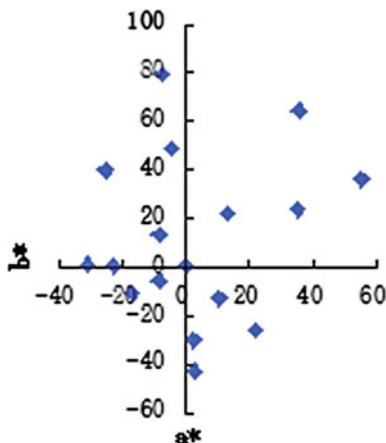
19.2.2   Observers

Table 19.1 lists the information of the observers.

19.2.3   Visual Experiment

The color matching experiments were conducted in a dark room. The reference stimulus was randomly displayed on the left or right of the monitor and all of them were presented in a random sequence. The observer matched the samples at a distance of approximately 50 cm(with the field size of 8.92°). They were asked to adjust the color on the left (or right) to match the color on the right (or left). As shown in Fig. 19.1, adjustment of opponent colors (darker–lighter, greener–redder, and bluer–yellower) was adopted in the works. The corresponding spectral data was measured by PR655 spectroradiometer. Among the 53 observers, 17 observers performed 2–6 repetitions. In total, 1649 (=97 total observations × 17 color centers) groups of data were gathered. And the experiment was carried out two months.

Table 19.1 Information of the observers

Age	Number of observers	Number of repeated observers	Total observations	Mean age
20–29	12	4	22	23.3
30–39	10	3	19	34.2
40–49	11	3	17	46
50–59	9	3	17	55.8
60+	11	4	22	66.7
Total	53	17	97	44.6

19.3 Data Analysis

19.3.1 Observer Variations

Observer variations are usually divided into intra- and inter-observer variability. For computing the intra-observer variability, first the CIEDE2000 [4] values of the differences between all match repetitions by a given observer and the mean match for that observer were obtained for each test stimulus. For each observer, the mean of these CIEDE2000 values over all matched stimuli gives the intra-observer variability. Similarly for inter-observer variability, CIEDE2000 values were computed between the mean of all observer color matched for each test stimulus, and the mean of each observer matches is computed over all repetitions.

A panel of 17 observers performed the repetitions. The observers ranging from 50 to 59 showed the largest intra-observer variability (with 1.04 CIEDE2000 units) and the observers ranging from 20 to 29 have the best stability (with 0.65 CIEDE2000 units). All intra-observer variability values were acceptable in the experiment. And all inter-observer variability values were less than 1.3, which means observers matched colors in high accuracy.

The maximum and minimum values are located in the age group of 50–59 and 30–39 respectively (see italic numbers in Table 19.2). For 50–59 age group, no observers have odd performance in color matching, and the reason for the large variant might be the lower sensitive of the chroma with the increasing age. The color difference in observers over 60 was similar to the other groups. The reasons might be in our experiment as the observers over 60 years were unfamiliar with the color matching operation; they adjusted matching colors with the experimenter's help. So there was a similar trend with the organizers' (20–29 age group) results. It can be improved by providing corresponding training for the elderly in the future.

19.3.2 Performances of Different Models

The spectral data $S(\lambda)$ of the target and matched colors were measured by the spectroradiometer and used to calculate the corresponding tristimulus values [5], and then, CIEDE2000 color difference was calculated. The spectral tristimulus values on the basis of CIEPO06 (for 20- year-old and 78-year-old observers) and CIE1964 CMF were represented (see Fig. 19.3).

Table 19.2 Observer variations

Observer variations	20–29	30–39	40–49	50–59	60+
Intra-observer variability	*0.65*	0.80	0.70	*1.04*	0.70
Inter-observer variability	0.87	*0.86*	0.89	*1.22*	0.87

Italic numbers represent the maximum and minimum values of intra-observer variability and inter-observer variability
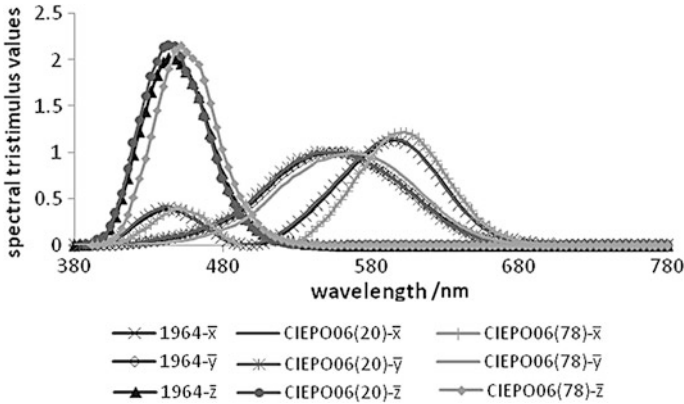
Fig. 19.3 The spectral tristimulus value distributions of CIE1964 CMF and CIEPO06 CMF

CIEPO06 CMF is the age-dependent physiological observer model, while CIE1964 CMF is used to predict the average observer data. The curves in the two models do not completely overlap. The shape of curves showed that some differences were existed in CIEPO06 and CIE1964 CMF. The peak of CIEPO06 curve has certain shift toward longer wave with the increasing of age.

19.3.3 Color Difference Thresholds

The mean CIEDE2000 of the matched color pairs was computed in CIE1964 CMF and CIEPO06 CMF (field size 8.92° and age range from 20 to 80), respectively, as shown in Table 19.3, and "H" represents high chroma.

The table was divided into two parts, on the left side is color difference for CIE1964 CMF, and the color difference of the CIEPO06 CMF is on the right. In the horizontal direction, "AVG." represents mean color difference of different aged groups. Meanwhile, "AVG." represents mean color difference of the single color stimulus in the vertical direction.

It can be seen from Table 19.3 that mean color difference of observers ranging from 20 to 39 was less than 1, which means that observers in this age range have higher color sensitivity. Mean color difference of observers ranging from 50 to 59 was the largest, which indicated that the observers have the lowest color sensitivity. And CIEDE2000 mean color difference of all the tested observers was 1.07 for CIE1964 CMF.

As for the two models, they have the similar performance. It indicated that CIEPO06 CMF had no significant improvement for the participant observers. In the two models, color difference thresholds of blue and blue with high chroma are less than 1 (see italic numbers in Table 19.3), which means that observers have the lowest tolerance for blue and blue with high chroma. Meanwhile, the observers

Table 19.3 Color difference with different CMFs

	CIE1964						CIEPO06					
	20–29	30–39	40–49	50–59	60+	AVG.	20–29	30–39	40–49	50–59	60+	AVG.
Gray	1.04	0.93	1.18	0.95	0.82	0.98	1.04	0.94	1.20	0.97	0.84	0.99
Red	1.04	0.88	0.83	1.50	1.00	1.04	1.05	0.89	0.84	1.50	1.00	1.05
Red, H	1.41	1.45	1.31	1.78	1.24	1.43	1.43	1.47	1.32	1.78	1.22	1.43
Orange	1.22	0.82	0.86	1.47	1.20	1.12	1.22	0.82	0.86	1.49	1.22	1.13
Orange, H	1.12	0.92	1.60	2.12	1.41	1.41	1.16	0.95	1.64	2.16	1.41	1.44
Yellow	0.98	0.93	1.14	1.25	0.82	1.01	0.98	0.94	1.16	1.27	0.86	1.03
Yellow, H	1.07	0.82	1.02	1.20	1.16	1.05	1.09	0.83	1.04	1.22	1.19	1.08
Yellow–green	0.87	1.17	1.12	1.24	1.15	1.10	0.87	1.17	1.14	1.26	1.18	1.11
Yellow–green, H	0.89	0.85	1.25	1.33	0.92	1.03	0.90	0.86	1.26	1.34	0.94	1.04
Green	0.96	0.91	1.17	1.48	1.01	1.09	0.96	0.92	1.19	1.50	1.02	1.10
Green, H	0.88	1.35	0.85	1.26	1.01	1.06	0.89	1.36	0.85	1.27	1.01	1.07
Blue–green	1.00	0.95	1.01	1.57	1.12	1.12	1.00	0.96	1.03	1.60	1.14	1.14
Blue–green, H	1.04	1.15	1.29	1.23	1.16	1.17	1.04	1.16	1.31	1.25	1.18	1.18
Blue	0.78	0.66	0.63	0.95	0.65	0.73	0.76	0.66	0.64	0.99	0.69	0.74
Blue, H	0.57	0.52	0.57	0.72	0.63	0.60	0.56	0.52	0.59	0.75	0.70	0.62
Purple	1.08	1.06	1.02	1.66	0.83	1.11	1.07	1.07	1.03	1.68	0.84	1.12
Purple, H	1.05	1.06	1.08	1.17	1.03	1.07	1.06	1.05	1.08	1.17	1.03	1.08
AVG.	1.00	0.97	1.05	1.35	1.01	1.07	1.00	0.98	1.07	1.36	1.03	1.09

Italic numbers represent larger (maximum) and smaller (minimum) values of color difference thresholds of color centers

have the largest tolerance for red with high chroma, orange with high chroma (see italic numbers in Table 19.3), which is accorded with the previous study using the printed samples [6].

19.4   Conclusions

In this study, 53 observers ranging from 20 to 79 were organized to match the color stimuli on the LCD monitor. In the analysis of the experimental data, it can be seen that CIEDE2000 color difference was about equal to 1.0 for most age group (except age group 50–59). It can be also seen that red with high chroma and orange with high chroma have the largest tolerance, while blue and blue with high chroma have the lowest tolerance. The mean CIEDE2000 color difference of all the tested observers was 1.07 for CIE1964 and 1.09 for CIEPO06, while CIEPO06 CMF had no significant improvement for the participant observers by considering age and visual field.

References

1. CIE. (2006). *Fundamental chromaticity diagram with physiological axes—Part I*. CIE Technical Report, pp. 170–1.
2. Sarkar, A. (2011). *Identification and assignment of colorimetric observer categories and their applications in color and vision sciences*. PhD thesis, Thomson Corporate Research, Rennes, France.
3. Witt, K. (1995). CIE guidelines for coordinated future work on industrial colour-difference evaluation. *Color Research and Application, 20*, 399–403.
4. Luo, M. R., Cui, G., & Rigg, B. (2001). The development of the CIE2000 color-difference formula: CIEDE2000. *Color Research and Application, 26*, 340–350.
5. Liu, H., et al. (2008). *Color science and technology*. Beijing: China Light Industry Press.
6. Min, H., Haoxue, L., & Ningfang, L. (2009). Study on just-noticeable color difference discrimination threshold by using printed samples: analysis of visual evaluation experimental data. *Acta Optica Sinica, 29*, 1431–1435.

Chapter 20
Evaluation of the Color-difference Formulae for Neutral Colors

Zeyang Li, Min Huang, Guihua Cui and Haoxue Liu

Abstract In printing industry, the results of quality control of neutral prints are not consistent with the visual assessments. In order to solve this problem, 50 pairs of neutral color samples were prepared, and 29 observers with normal color vision were organized to carry out the color-difference experiments with the method of gray scale. In total, 1750 judgments were gathered. The visual results were used to test the performances of different color-difference formulae in terms of the standardized residual sum of square (STRESS) factor. The results indicate that the CIEDE2000 formulae have the best performance and all the tested formulae have the best performances for the evaluation of the color pairs only with the hue differences.

Keywords Color-difference formulae · Neutral colors · Gray scale · STRESS

20.1 Introduction

It is well known that gray balance is widely used in the processing control, and the quality of printed color samples was usually evaluated by the method of color differences. But many research indicated that the results from the existing uniformity color spaces and color-difference formulae are not well agree with the visual assessments, especially for the neutral colors [1]. CIE Division 1 has investigated the visual differences between two gray color stimuli that may be different in

Z. Li · M. Huang (✉) · H. Liu
School of Printing and Packing Engineering,
Beijing Institute of Graphic Communication, Beijing, China
e-mail: huangmin@bigc.edu.cn

G. Cui
College of Physics and Electronic Information Engineering,
Wenzhou University, Wenzhou, China

chroma and hue, and in obtaining a definition of the percept of gray that is linked to a CIE color metric.

This paper organized 29 observers with normal color vision to carry out the color-difference experiments with 50 pairs of neutral color samples. All the tested formulae predicted that the hue difference near the neutral axis is better than other differences on lightness, chroma, and chroma–hue interaction. The performances of different color-difference formulae were tested, and the formulae were modified by different methods.

20.2 Experimental

20.2.1 Sample Preparation

The color samples were printed on Epson 517 semi-gloss paper by Epson 7908 inkjet printer, and the size of each sample is 4.5 cm × 4.5 cm. The color differences between the samples were ranged from 0.08 to 5.49 CIELAB units with an average color difference of 3.04 CIELAB units. The distribution of the $\Delta E^*_{ab,10}$ values is shown in Fig. 20.1.

A grayscale method as arranged in Fig. 20.2 was used to scale the color differences of sample pairs. The grayscale used in the experiment was prepared to have the same size and material as the samples being used. It was specially
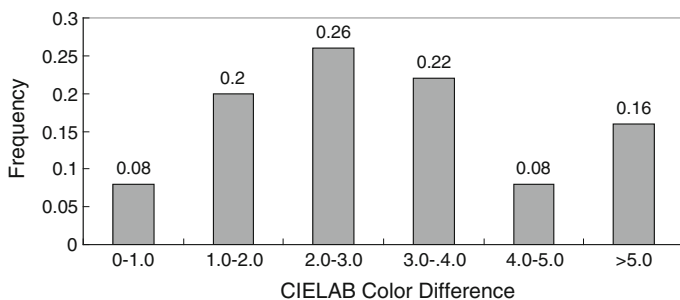
Fig. 20.1 Distribution of CIELAB $\Delta E^*_{ab,10}$ for the 50 pairs studied

Fig. 20.2 The arrangement of samples in the grayscale method

Table 20.1 Colorimetric details of the gray scale prepared under D65/10° condition

Grade	L_s^*	a_s^*	b_s^*	L_c^*	a_c^*	b_c^*	ΔE_{ab}^*	ΔL^*	$\Delta L^*/\Delta E^*$
1	60.06	0.55	−0.55	61.07	0.60	−0.59	1.00	1.00	1.00
2	60.29	0.47	−0.54	62.10	0.15	−0.12	1.88	1.81	0.96
3	59.99	0.36	−0.43	62.96	0.57	−0.61	2.98	2.97	1.00
4	60.14	0.44	−0.50	64.08	−0.26	0.00	4.04	3.95	0.98
5	60.15	0.45	−0.46	65.41	0.06	−0.25	5.27	5.25	1.00
6	59.87	−0.15	−0.21	65.68	0.49	−0.06	5.85	5.81	0.99

designed to have a range from left 1 to right 6 with an interval of approximately 1 unit of $\Delta E_{ab,10}^*$. The CIELAB $L_{ab,10}^*$ attributes for each gray sample and ΔL_{10}^* and $\Delta E_{ab,10}^*$ for each scale are shown in Table 20.1. It can be seen that ΔL_{10}^* and $\Delta E_{ab,10}^*$ values are quite close. This means the quality of grayscale is high.

20.2.2 Visual Assessments

The visual assessments of color difference were conducted in a dark room using a GretagMacbeth Judge II viewing cabinet equipped with a D65 simulator, which had a correlated color temperature of 6441 K and an illuminance value of 900 lx measured by a Photo Research PR-655 Spectroradiometer. The gray background had L_{10}^*, a_{10}^*, and b_{10}^* values of 50.3, 0.2, and 1.3, respectively. The illuminating/viewing geometry was approximately 0°/45° at a viewing distance about 25 cm. The above experimental conditions conform to the standard viewing conditions that CIE recommended [2].

During the experiment, the "sample" pair is given in the bottom of the background (Fig. 20.2), and the 6 "grayscale" pairs are presented in the top of the background. Before the real experiment, observers were trained to assess color difference using the grayscale method. Before each observing session, observers were asked to adapt to the gray background field for about 1 min. The sequence of samples being assessed followed a random order for each observer.

They were instructed to conduct visual assessment using the six grayscale pairs as references. If the color difference of a sample pair was not equal to the color difference of the closest gray scale, observers were encouraged to provide an intermediate value, e.g., 2.6 for a color difference greater than grade 2 but smaller than grade 3.

Figure 20.3 shows the line fitted between the grades of gray scale and their $\Delta E_{ab,10}^*$ values. All visual judgments in grades for each observer were transformed to visual color difference (ΔV) with the equation shown in Fig. 20.3. 29 observers were organized to make the judgments and 6 observers repeated the assessments, so 35 assessments for each sample pair were recorded. In total, 1750 judgments were gathered.

Fig. 20.3 The linear regression between CIELAB color difference and the grade of gray scale

$$y = 1.012x - 0.038$$
$$R^2 = 0.993$$
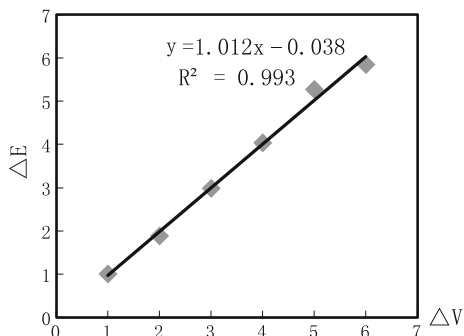
20.3 Results and Discussions

20.3.1 Observers Variation

Observer variations are divided into intra- and inter-observer variability. Observer's intra-variation is used to determine the variation of the visual assessments of a particular observer. Observer's inter-variation represents the average deviation between individuals and the mean visual results for all observers. The intra-variation and inter-variation for this study are calculated by the STRESS unit with $f = 1$. The mean value of the intra-observer variability for the six observers was 33.1 units ranging from 26.4 to 38.2, and the mean value of the inter-observer variability for all observers was 31.9 units ranging from 18.2 to 51.1.

20.3.2 Testing with Color-Difference Formulae

The performances of six color-difference formulae or uniform color spaces, CIELAB, CMC [3], CIE94 [4], CIEDE2000 [5], DIN99d [6], and CAM02-UCS [7], were tested in terms of STRESS [8] using the neutral colors, and two different optimized methods were used to improve the performances of the formulae, the lightness optimization, and the power function method [1]. The results were listed in Table 20.2.

From Table 20.2, the CIEDE2000 formulae have the best performance with the lowest STRESS value. Because CIELAB formulae are not uniform visually for small and medium color difference, in addition, CMC formulae are used for evaluating medium and large color difference in textile industry.

The color-difference formulae modified by power functions provide results in better agreement with visually perceived color differences than the lightness optimization. It is indicated that power functions are useful to improve the performance of current color-difference formulae, as desired by engineers and practitioners in

Table 20.2 Performances of different color-difference formulae in terms of STRESS

	CIELAB	CMC	CIE94	CIEDE2000	DIN99d	CAM02-UCS
Original	23.5	22.8	23.3	*18.3*	20.0	21.9
Optimized (k_L)	23.4 (0.71)	22.7 (0.64)	23.2 (0.77)	*18.1 (0.64)*	19.9 (0.6)	21.8 (0.66)
Optimized (power function)	17.7	18.3	18.4	*13.9*	16.1	18.1

Table 20.3 Classification method to paired samples

Subdata	Conditions	Pairs	Mean ΔE_{ab}^*	Max ΔE_{ab}^*
All neutral	$C_{ab}^* \leq 10$	50	3.0	5.5
$\sqrt{\Delta C^2 + \Delta H^2}$	$\sqrt{\Delta C^2 + \Delta H^2}/\Delta E \geq 90\%$	46	3.2	5.5
ΔH only	$|\Delta H/\Delta E| \geq 90\%$	32	3.3	5.5
$\Delta L + \Delta C + \Delta H$	$|\Delta L/\Delta E|$, $|\Delta C/\Delta E|$ and $|\Delta H/\Delta E|$ are $< 90\%$	16	2.9	5.5

Table 20.4 Summary of formula's performance in their original forms

Subdata	CIELAB	CMC	CIE94	CIEDE2000	DIN99d	CAM02-UCS
All neutral	23.5	22.8	23.3	18.3	20.0	21.9
Chromatic only	23.3	22.6	23.0	17.9	19.7	21.4
ΔH only	*21.3*	*21.2*	*21.1*	*17.0*	*19.0*	*20.0*
$\Delta L + \Delta C + \Delta H$	27.6	25.5	27.1	18.5	21.2	25.2

color-quality control and many other color applications, no matter the whole color space or the colors near neutral axis.

The color samples are classified by the method shown in Table 20.3, and the performances of the formulae with their original forms are summarized in Table 20.4 (those italic numbers represent the best performance for each formula).

It is shown in Table 20.4 that the best performance for each formula appeared for the samples with only hue difference in the tested subsets, which is accorded with Cui et al. [9]'s results for the test of neutral colors with $C_{ab}^* \leq 10$ from BFD dataset (see Table 20.5).

Table 20.5 Summary of formulae's performance in Cui's test

Subdata	CIELAB	CMC	CIE94	CIEDE2000	DIN99d	CAM02-UCS
All neutral	30.2	23.7	31.3	25.1	23.6	28.6
Chromatic only	24.2	22.7	23.2	21.2	21.4	24.6
ΔH only	*17.9*	*18.9*	*18.0*	*16.6*	*18.4*	*22.6*
$\Delta L + \Delta C + \Delta H$	31.6	27.7	31.4	27.8	27.5	28.2

20.4   Conclusions

50 pairs of print neutral colors were used to investigate the performance of six color-difference formulae for assessing the colors near neutral axis. The CIEDE2000 formula outperformed others, and the power function method can improve the performance of all the formulae compared with the lightness optimization. Near the neutral axis, all tested formulae performed the best in predicting mainly hue difference, but not well enough for the mixture of different tolerances, especially for mixing with lightness difference.

References

1. Huang, M., Cui, G., Melgosa, M., et al. (2015). Power functions improving the performance of color-difference formulas. *Optics Express, 23*(1), 597–610.
2. Liu, H., et al. (2008). *Color science and technology*. Beijing: China Light Industry Press.
3. Clarke, F. J. J., McDonald, R., & Rigg, B. (1984). Modification to the JPC79 colour-difference formula. *Journal of the Society of Dyers & Colourists, 100*(4), 128–132.
4. CIE (Commission Internationale de l'Éclairage). (1995). *Industrial colour-difference evaluation*. Vienna: CIE Central Bureau.
5. Luo, M. R., Cui, G., & Rigg, B. (2001). The development of the CIE 2000 colour-difference formula: CIEDE2000. *Color Research & Application, 26*(5), 340–350.
6. Cui, G., Luo, M. R., Rigg, B., Roesler, G., & Witt, K. (2002). Uniform colour spaces based on the DIN99 colour-difference formula. *Color Research & Application, 27*(4), 282–290.
7. Luo, M. R., Cui, G., & Li, C. (2006). Uniform colour spaces based on CIECAM02 colour appearance model. *Color Research & Application, 31*(4), 320–330.
8. García, P. A., Huertas, R., Melgosa, M., & Cui, G. (2007). Measurement of the relationship between perceived and computed color differences. *Journal of the Optical Society of America A, 24*(7), 1823–1829.
9. Cui, G., Luo, M. R., Huang, M. (2013). *AIC 2013-12th international congress* (pp. 1537–1540).

Chapter 21
Gender Effects on Color Discrimination

Hao Huang, Jing Liang, Buyun Yao and Guangliang Zhu

Abstract The purpose of this study was to evaluate whether the color discrimination exists effects between different genders. This paper took different 40 hue colors in NCS atlas as the experimental samples and then based on color science and visual psychophysics methods, establishing color match in relation to APP extra-double-sided coated offset paper color printing atlas. We use mathematical statistics methods, to evaluate the visual difference results of color discrimination about different gender observers under two different light sources. The experiment shows that women in the recognition of color is better than men, on the individual colors, such as orange and red, blue and green, man may not identify very well. And the light source has a great influence on the observer to identify the color difference.

Keywords Gender · NCS atlas · Color printing atlas · Psychological experiment · Color match · Color discrimination

21.1 Introduction

Colors play an important role in people's lives; the colors people interest in also vary. It is generally believed the color preference of people, owing to the different age, sex, nationality, climate, and natural environment. In daily life, almost all the

H. Huang · J. Liang
School of Light Industry and Chemical Engineering,
Dalian Polytechnic University, Liaoning, China

J. Liang (✉)
State Key Laboratory of Modern Optical Instrumentation,
Zhejiang University, Zhejiang, China
e-mail: ljlove426@163.com

B. Yao · G. Zhu
Dalian Polytechnic University, Liaoning, China

goods is related to color, such as the color display and management in electronic products included television, computer, mobile phone, and color matching application in the clothing and books [1, 2].

Domestic and foreign journalists have done a lot of research on color preferences between different people. The researchers in American CUNY Brooklyn College and Hunter College indicate that men and women have great differences on the vision: Women in the identification of colors are better than men, while the men's visual advantage is the sensitivity to the details of the distant objects as well as tracking capabilities of fast-moving object tracking [3].

21.2 Color Matching Experiments

21.2.1 Test Preparation and Explanation

The light source, which is selected for the experiment, is the F2 and D65 light source whose color temperature is 2700 and 6500 K in the standard light box which is the light environment of the experiment. Choosing color wheel diagram includes 40 color pieces whose color gamut covering most color in NCS chromatogram as the original chromatograph which is shown in Fig. 21.1, and the area of every color piece is 1.5 cm × 1.5 cm. Convenience for later processing, the 40 color pieces are labeled with the number 1–40 clockwise: −Y, −Y10R, −Y20R, −Y30R, −Y40R, −Y50R, −Y60R, −Y70R, −Y80R, −Y90R, −Y30R, −R, −R10B, −R20B, −R30B, −R40B, −R50B, −R60B, −R70B, −R80B, −R90B, −B, −B10G, −B20G, −B30G, −B40G, −B50G, −B60G, −B70G, −B80G, −B90G, −G, −G10Y, −G20Y, −G30Y, −G40Y, −G50Y, −G60Y, −G70Y, −G80Y, −G90Y. The scope of chromatograph we select in this experiment is the part of professional chromatograph printing APP super double-sided coated paper [4]. Using the chromatogram we match the 40 color patches which are labeled before the experiment.

Fig. 21.1 NCS color circle
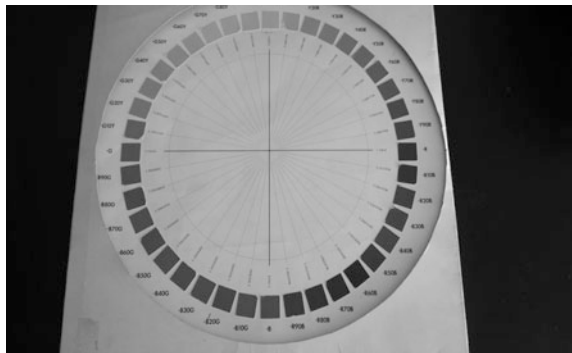
If the color gamut coverage range is larger, it can accord with the experimental conditions. Then, Select the X-Rite SP64 integrating sphere spectrophotometer to measure the color patches with matching parameter values.

21.2.2   The Experimental Process of Visual Color Matching

Choose 33 males and 12 females whose CV parameter values are below 30 % for the experiment observers. A formal visual experiment in the standard light box under the condition of a darkroom [5]. In the experiment, the observer should be 60 cm far from the standard light box. With the geometry angle 0° (lighting)/45° (observation), Each observes colors carefully and then selects the color from the APP super double-sided coated paper chromatography to compare with the 40 colors of the NCS chromatography in the vision matching. In the process of formal visual experiments, the observer is shown in Fig. 21.2. Obtain the color experiment visual matching data of the 45 color normal observers at the end of the experiment.

Requirements are in the F2 and D65, two different light sources, after the end of the experiment on visual color matching, using X-Rite SP64 integrating sphere spectrophotometer to measure the parameter values of the APP special double-sided coated printing paper chromatography color which is chosen to match the 40 colors whose color parameter values are measured and recorded.

Considering the visual data uncertainty degree, analysis of data than of the measuring instruments is more tedious and complicated. Through the analysis of the data, select 10 male observers and 10 female observers experiment data with high reliability of the group to evaluate.

Fig. 21.2 Psychophysics experiment

21.3 Data Processing and Analysis of Results

21.3.1 Random Sample Data Analysis of an Observer

Using the CIE1976LAB color formula calculate the color difference between the same color under F2 and D65, two kinds of light sources to the observers, and the color difference under the same corresponding light sources between the matching color patches and the standard experimental color sample on NCS Atlas. Obtain three groups of color differences value data at the end of calculation.

The analysis of the graphs in Figs. 21.3, 21.4, and 21.5 shows that it is very obvious that the color match values of the middle part of the NCS GATF are relatively stable to the random observer, but the front part and the rear part of the matching is not particularly satisfactory. And from the first three column chart, it can be seen that the size of the fluctuations in the latter part of the chromatic color difference will obviously too large and the ΔE shows a big jump, suggesting that the observer's color gamut color sensitivity is not very good to the rear part of the

Fig. 21.3 Color difference of color patches between the F2 and D65 light sources
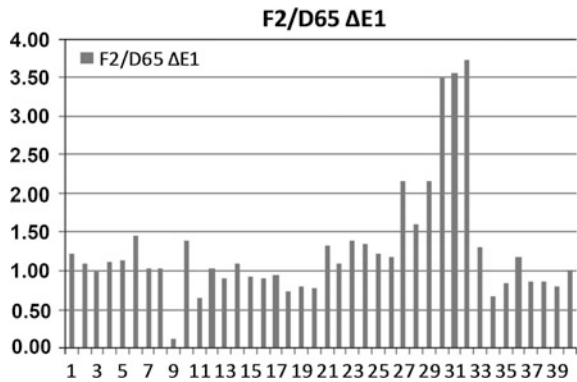
Fig. 21.4 Color difference of color patches under the F2 light source
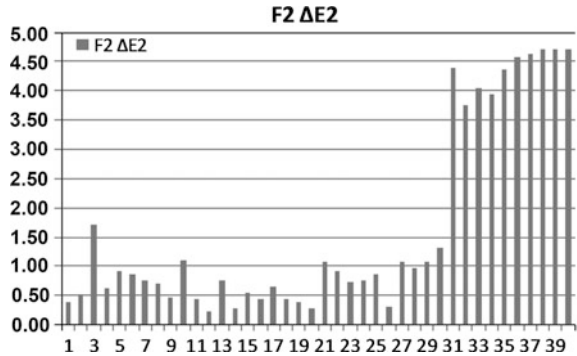
Fig. 21.5 Color difference of color patches under the D65 light source
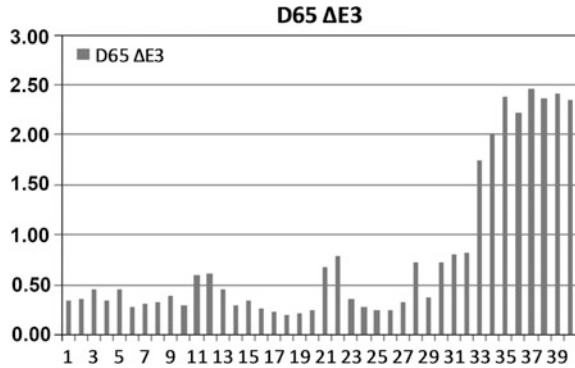
Fig. 21.6 Comparison of color difference among the 3 different types
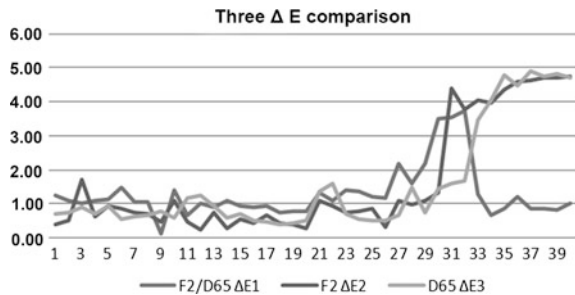
GATF in the color visual matching, resulting in obvious color difference is too large. In addition, in Fig. 21.6, from comparison of color difference among the 3 different types, in a certain color region, the F2/D65 color difference curve was floating on the top of the other two curves. This shows that in the visual color matching experiment, the different light source can affect the color matching. But in the rear part, the F2/D65 color difference curve is obviously lower than the other two kinds of curves, while the other two cases are obviously higher. To a certain extent, the observer is not very sensitive to the color of this range, resulting in a low degree of sensitivity, which affects the matching accuracy of the color.

21.3.2 Difference Comparison and Analysis of Different Gender Color Matching

According to the analysis and comparisons from the charts in Figs. 21.7, 21.8, 21.9, 21.10, 21.11, 21.12, 21.13, and 21.14, it can be seen that male observers cannot match the −Y20R piece well a common phenomenon as well as the −B and −B90G two color piece. But not evident among the female observers and the differences between colors is relatively uniform among them. Male observer data in the rear half fluctuate significantly. This illustrates the male observers who cannot match the

Fig. 21.7 Color difference of
color patches between the F2
and D65 light sources (male)
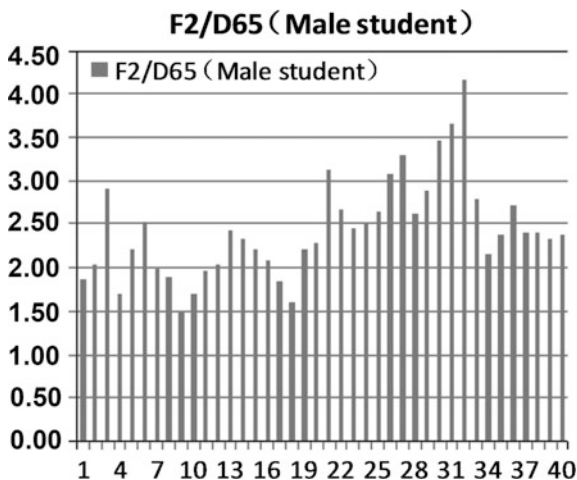
Fig. 21.8 Color difference of
color patches under the F2
light source (male)
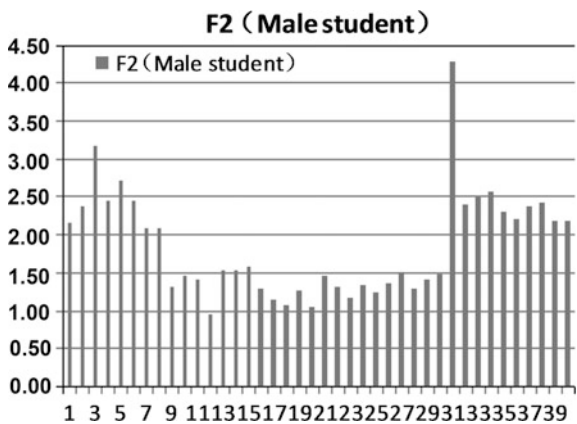
Fig. 21.9 Color difference of
color patches under the D65
light source (male)
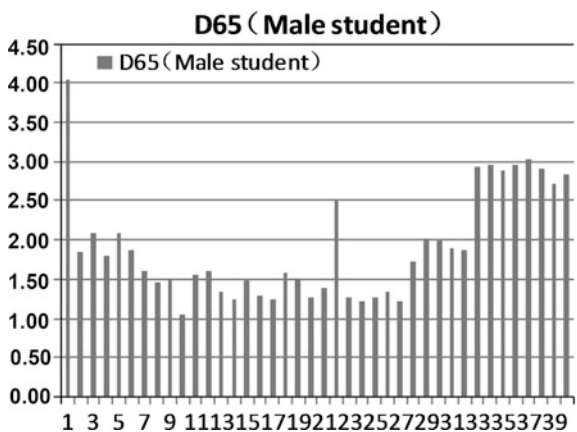
Fig. 21.10 Comparison of color difference among the 3 different types (male)
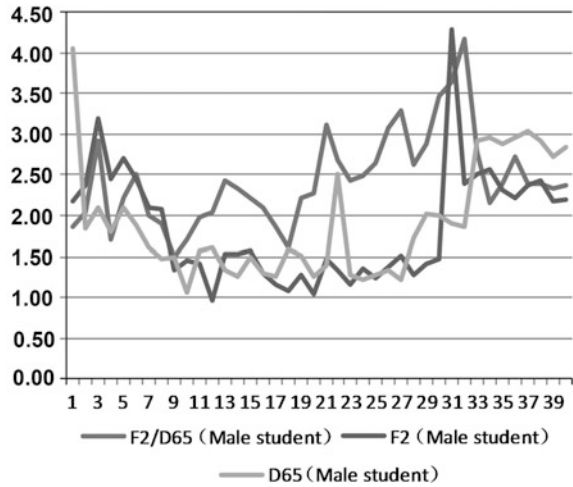
Fig. 21.11 Color difference of color patches between the F2 and D65 light sources (female)
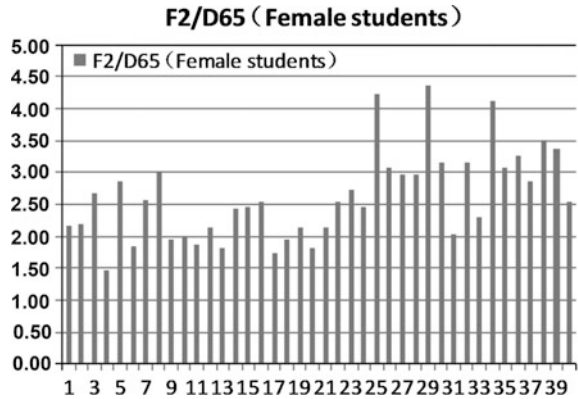
Fig. 21.12 Color difference of color patches under the F2 light source (female)
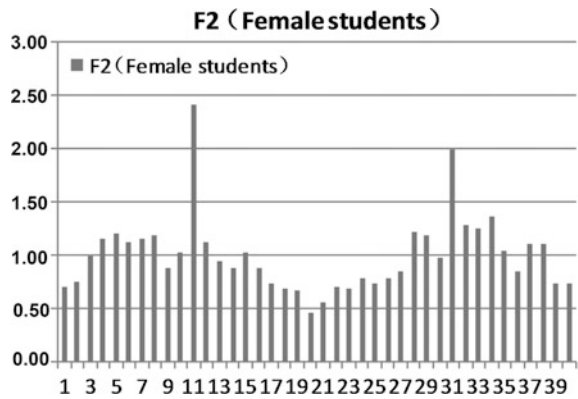
Fig. 21.13 Color difference of color patches under the D65 light source (female)
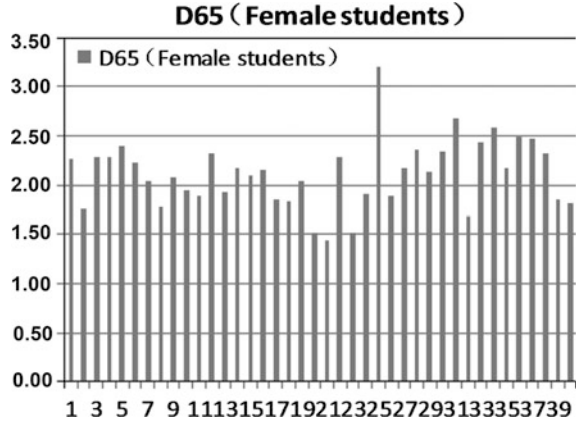
Fig. 21.14 Comparison of color difference among the 3 different types (female)
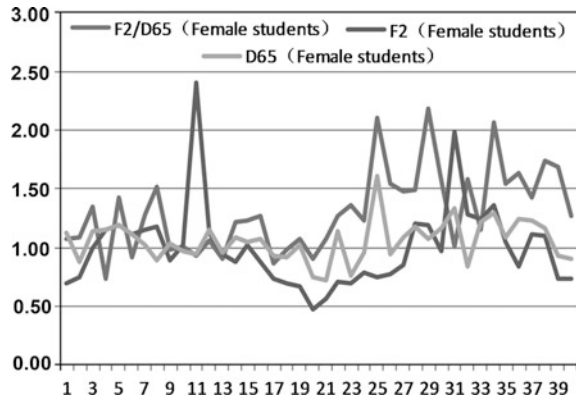
rear part of the color wheel well. In Figs. 21.10 and 21.14, the comparison shows that the color difference of color patches between the F2 and D65 light sources is significantly higher, suggesting that illumination has a great influence on the color observation.

21.4 Conclusions

Through experiments, women in the identification of colors are better than men. The male observer cannot do well in the recognition, especially the orange red and blue green. But the female observer can be sensitive to match these colors accurately through the visual color matching.

References

1. Chunhai, L. I. U. (2012). *Color and psychological emotion*. Yunnan: Psychological Science
2. Xiuyan, G. (2004). *Color psychology*. Beijing: People Education Press.
3. Hongli, C. (2002). *The colors objective study among contemporary students interested in*. Higher Education Research: Fuzhou.
4. Jing, L., Ningfang, L. (2012). The Establishment and Evaluation of Color Appearance Datasets about Low-Gloss Color Printing Atlas. *Acta Optica Sinica, 32*(5), 0533001-1–0533001-9
5. Liao, N. F., Shi, J. H., & Wu, W. M. (2009). *The Conspectus of color information management for digital images*. Beijing: Beijing Institute of Technology Press.

Chapter 22
Locate Color Tolerance for Mapping Mode Based on Human Visual and Color Difference Formula

Zhongguo Xu, Wenyan Jiang and Wenge Chen

Abstract When color digital images output on substrates, color space is converted, causing the color differences between prints and electronic manuscript. In order to locate the way to map and relatively corrected error range, the original is converted to 4 CMYK modes through the intentions of perception, saturation, relative colorimetry, and absolute colorimetry, respectively. Adobe Photoshop (Ps) software is used to draw a–b, a–L, and b–L color gamut graphs to determine the spatial domain of each color tolerance. The background is center color contrasting with the other color. Thus, the graphs can be straightly detected by human eyes easily. In complex calculation of formula, experiment successfully draws color difference ball, chroma difference cylinder, and hue difference parabolic in Lab space. It really helps figure out the tolerance range of different mappings and prints. The above numerical relationship is fed back to the process of color gamut conversion and image reproduction. Then, color measurement and calculation are further conducted to verify the accuracy of color gamut conversion.

Keywords Color tolerance · Mapping mode · Human visual · Formula calculation · Gamut conversion

22.1 Introduction

"Why doesn't the color match?" Anyone who has ever worked in color publishing has probably asked (or been asked) this question. Color management is the proper tool for users who want to match or, more realistically, get an "optimal color reproduction" [1]. Generally, the original can be converted to configuration file through the intentions of perception, saturation, relative colorimetric, and absolute

Z. Xu (✉) · W. Jiang · W. Chen
School of Biological and Chemistry Engineering/School of Light Industry, Zhejiang
University of Science and Technology, Zhejiang, China
e-mail: 978292231@qq.com

colorimetric, respectively, etc. [2]. However, mappings between color spaces are ubiquitous in image processing problems such as gamut mapping, decolorization, and image optimization for color-blind people, vehicle contour identification, and design of industrial products [3–5]. To be curious, what type of mapping and the error range of the corresponding correction are most suitable in different experiments?

Different people have different views at this question. Si Li-li gets a conclusion: It is suitable for the use of perceptual mapping to pay attention to tone and level of performance of the original type; pay attention to color rendering of the original type is suitable for the saturation mapping; and for accurate reproduction of images is suitable for the absolute colorimetric mapping [6]. Sanmartin et al. think that the appropriate parameters for converting the device-dependent RGB color space into a device-independent color space were established. The color data were then compared using the CIELAB color formula [7]. In addition, Wang Hai-wen et al. think that the color gamut mapping can be divided into one-dimensional mapping, 2-dimensional mapping, and 3-dimensional mapping in the space dimension [8, 9].

This experiment draws the color gamut mapping to search the answer. The original RGB mode is converted to four CMYK modes through four intentions. The above CMYK modes are represented in the Lab space with tolerance range calculated. Furthermore, the most suitable color gamut mapping output printing verified the accuracy of color gamut conversion.

22.2 Experimental

22.2.1 Observation of Color Tolerance

In the Lab mode of Ps, the values of the mapping colored block Lab are accurately selected as the center of the coordinates and the 3-dimensional coordinate system of Lab is well established, where a is x axis, b is y axis, and L is z axis. Unfortunately, in the limits of equipment, only Ps software is used to draw three color gamut graphs using $a–b$, $a–L$, and $b–L$ to determine the spatial domain of each color tolerance of four CMYK modes. According to the phenomenon of color contrast, however, it fills background with center color to be easily observed by human eye. For example, the Lab date of center is (52, 74, 55), red color tolerance as shown in Fig. 22.1.

In the background color, it just uses the pencil tool to circle tolerance. After the painting, the background layer is hidden, and the coordinates of the 4 points of the ellipse are recorded, for example, Fig. 22.2. It is in the laboratory standard D65 light box to observe the color range. The red color is represented as a domain of tolerance: $L = 49 \pm 1.235$, $a = 69 \pm 2.854$, and $b = 50 \pm 1.432$.

Fig. 22.1 Red *a*–*b* color tolerance
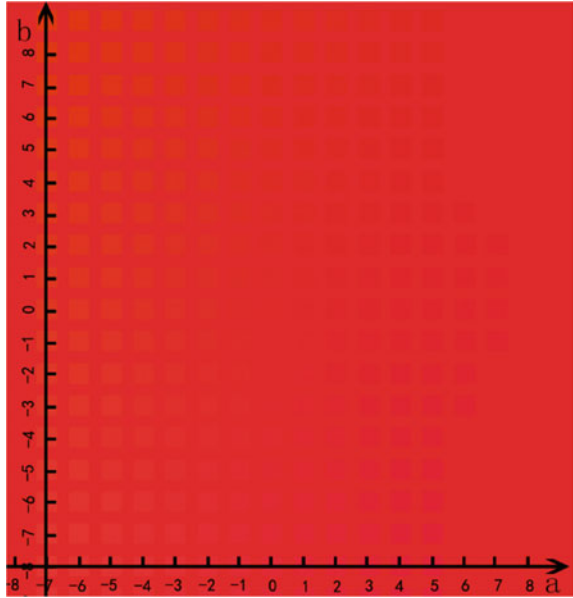
Fig. 22.2 Ellipse in red *a*–*b* color tolerance
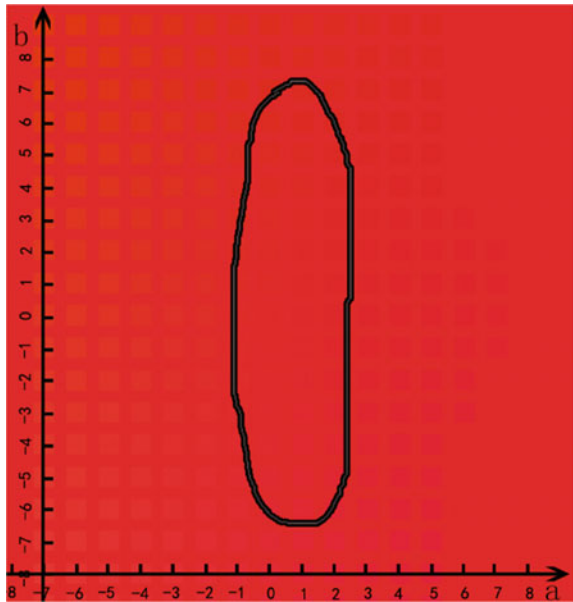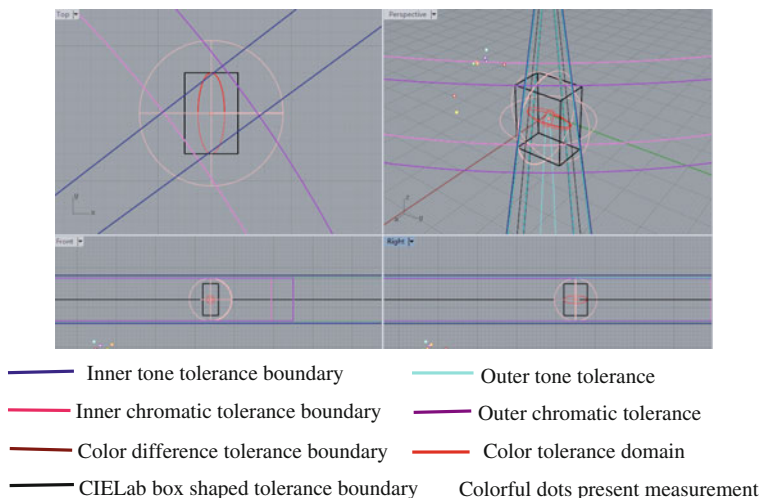
Fig. 22.3 Red color range chart

22.2.2 Calculation and Location of Color Tolerance

In Lab space, the color difference equation, the chroma difference, and hue difference equation of CIE 1931 are performed. Rhinoceros 5.0 is used to draw the above formula and observation results in the Lab color space, for example, red color range as shown in Fig. 22.3.

22.2.3 Substitute Measurement Data of Mapping Color

The intention of the document is converted into the configuration file, such as perception, saturation, relative colorimetric, absolute colorimetric. Their color difference and tolerance are located in measurement, as shown in Table 22.1 and Fig. 22.4.

From the Fig. 22.4, overall color tolerance: absolute colorimetric > saturation > relative colorimetric = perceived. So the experiment absolutely chooses absolute ratio color as an example. It is suitable for the accurate reappearance of the image in this study.

22.2.4 Print Output and Error Analysis

The experiment makes ICC color management on computer and Heidelberg printing machine, doing plate through the CTP equipment, at last using Heidelberg

Table 22.1 Color difference between RGB manuscript and four kinds of mapping

Measurement object	Color	ΔC (inner)	ΔC (outer)	ΔH (inner)	ΔH (outer)
RGB manuscript	C	3.828	3.866	1.419	1.311
	M	3.083	3.169	2.676	2.574
	Y	3.119	3.192	2.634	2.545
	R	4.037	4.041	0.608	0.582
	G	3.990	4.001	0.865	0.811
	B	3.804	3.839	1.481	1.390
Perception	C	3.823	3.866	1.432	1.313
	M	3.061	3.156	2.701	2.590
	Y	3.140	3.219	2.609	2.511
	R	4.029	4.034	0.659	0.629
	G	3.975	3.989	0.929	0.867
	B	3.787	3.826	1.524	1.425
Saturation	C	3.880	3.911	1.271	1.170
	M	3.014	3.105	2.754	2.651
	Y	3.109	3.180	2.645	2.560
	R	4.051	4.054	0.502	0.481
	G	3.979	3.991	0.914	0.860
	B	3.804	3.839	1.481	1.390
Relative colorimetric	C	3.893	3.925	1.228	1.124
	M	3.021	3.116	2.746	2.638
	Y	3.124	3.199	2.628	2.537
	R	4.026	4.031	0.676	0.646
	G	3.982	3.994	0.900	0.845
	B	3.791	3.827	1.515	1.420
Absolute colorimetric	C	3.977	3.995	0.923	0.840
	M	3.024	3.121	2.743	2.631
	Y	3.074	3.144	2.687	2.604
	R	4.019	4.025	0.715	0.682
	G	4.005	4.014	0.791	0.743
	B	3.740	3.783	1.638	1.535

Fig. 22.4 Color tolerances of 4 mapping forms
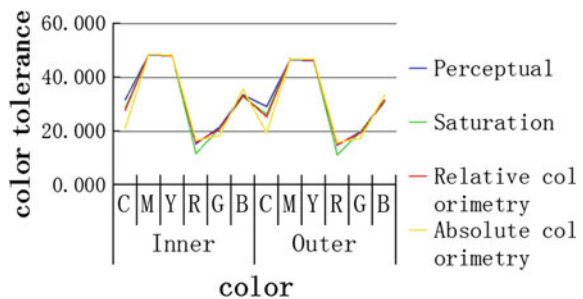
offset printing machine output proofs. In order to ensure the reliability of data, experiment selects different substrates such as powder paper, coated paper, and offset paper. The use of optical density measuring instrument gets color value of CMYK, XYZ, and Lab.

The relationship is analyzed between the measurement points and the tolerance range. Lines go through the area which is the direction of linear change and the error range is the length of point movement. The red color in digital printing 80 g copy paper is selected as an example. Its Lab value was 39.170, 45.120, and 17.310. The original red color in absolute colorimetric value of Lab is 51, 71, and 50. The error range of modified is $s = 20.204395$ ($\pm 2.1e{-}05$) square units.

22.2.5 Summary

The tolerance of different color conversion modes is calculated from two aspects of subjective and objective. In the subjective aspect, reasonable samples are selected and the ideal results are obtained; in the objective aspect, through the theoretical formula calculation of tolerance range and substituting the data, experiment draws tolerance more intuitively showed. The color gamut is intended to specify the configuration file with an absolute colorimetric based on the subjective feeling of human visual perception and color difference formula. According to the color range, L, a, and b are selected for the calculation of limit value of chromatic difference, hue difference standard.

22.3 Conclusions

This paper establishes the mathematical conversion model of Lab based on the plane theory and verifies the accuracy of the conversion model achieving the requirements of the faithful copy in printing industry. According to the different printing process, the replication scheme can be used to improve the replication accuracy between color printing and electronic manuscripts. When the color digital images output to paper, eyes cannot feel color difference between paper color and computer display, which avoids printing pale losses. The numerical relationship is fed back to the process of color gamut conversion and image reproduction, such as realization in scanning moiré. Then, color measurement and calculation are carried out again to verify the accuracy of color gamut conversion.

References

1. Changxian, C. (2009). *Contemporary language and knowledge on graphic communications*. China: Printing Industry Press.
2. Jun, L., & Quanhui, T. (2007). *Printing color management*. China: Printing Industry Press.
3. Eynard, D., Kovnatsky, A., & Bronstein, M. M. (2014). Laplacian colormaps: A framework for structure-preserving color transformations. *Computer Graphics Forum, 33*, 215–224.
4. Shuaibing, Z., & Liu Yuexiao, C. (2015). License plate location recognition based on vehicle contour. *Technology Outlook, 10*, 72.
5. Xiaohui, W. (2015). Photoshop technology in design of industrial products. *Reform in Education, 02*, 113–114.
6. Lili, S. (2011). Research on adaptability of different render intents. *Journal of Zhejiang University of Science and Technology, 23*(03), 203–206.
7. Sanmartin, P., Chorro, E., & Vazquez-Nion, D. (2014). Conversion of a digital camera into a non-contact colorimeter for use in stone cultural heritage: The application case to Spanish granites. *Measurement, 56*, 194–202.
8. Wang, H., Jiang, W., Li, J., & Wenge, C. (2008). Color gamut mapping technology on printing color management. *Journal of Zhejiang University of Science and Technology, 20*(01), 35–37 +59
9. Wang, H., Li, J., & Wan, X. (2008). Study on gamut mapping between heterogeneous types display. *Packaging Engineering, 06*, 17–20.

Chapter 23
The Effect of Different Monitors on Remote Soft Proofing

Siwen Zhu and Maohai Lin

Abstract As printing technology is developing to informatization, networking, and automation, traditional proofing methods are no longer meet the needs of the development of printing. Based on the research of the development of proofing technology at home and abroad and comprehensive analysis of the existing remote soft proofing system, we find that the high requirement to the client's display equipment in existing remote soft proofing system leads to customers' excessive costs when bringing in the remote soft proofing system. By means of color management to the display device, the paper studies the effect of different displays in the process of remote soft proofing and gets a good proofing result among the acceptable color tolerance when using normal display devices as the client and the color is also in the acceptable range for remote soft proofing. Experimental results show that in the use of professional display for remote soft proofing, the average color difference is less than 3 and proofs can achieve good results. When using conventional LCD display remote soft proofing, the average chromatic aberration is 5.71, and the maximum color difference is not more than 7. In the case of less demanding color printing, you can choose conventional LCD display.

Keywords Remote soft proofing · Color management · Display

S. Zhu · M. Lin (✉)
School of Printing and Packing Engineering, Qilu University of Technology,
Jinan 250353, China
e-mail: imhlin@163.com

23.1 Introduction

23.1.1 Brief Introduction of Remote Soft Proofing and Its Advantages and Disadvantages

23.1.1.1 The Definition of Remote Soft Proofing

The so-called soft proofing is also called screen proofing; the proofing effect is displayed on the calibrated display device to predict the color and content of the printed image of the finished product. Remote soft proofing is a combination of soft proofing, and network together with customers (publishers, magazines, and advertising companies) can see the final printing page information through the network. Through online communication for rectification and check-like, printing can get the rectification instructions through the network and quickly make changes and printing [1].

23.1.1.2 The Advantages of Remote Soft Proofing

Remote soft proofing can communication with customers online and put together proofing, finalized. Saving time is in favor of expanding large market.

Remote soft proofing not only eliminates the cost of supplies, but also saves money for transferring proofs. Contrast remote hardcopy proofing, customers no longer need the high cost of the hardware, is easy for customers to accept.

23.1.1.3 The Disadvantages of Remote Soft Proofing

Remote soft proofing is not without disadvantages. As shown in Table 23.1, remote soft proofing in color accuracy has a lot of shortage, compared with hard proofing. At this stage, remote soft proofing cannot simulate spot colors, metallic colors, fluorescent colors, and also need higher requirements on observing conditions and material consumption [2].

Table 23.1 The lack of soft proofing, contrast hard proofing

Comparison parameters	Conventional proofing	Soft proofing
Color accuracy	High (CMYK)	Relatively high (RGB)
Spot colors, metallic colors, fluorescent	Can be achieved	Difficult to achieve
Textured	Close	Strict
Observing conditions	Loose	Strict
Consumable materials	Need	Not required

23.1.2 The Purpose and Significance of the Subject

Printing has been developed toward fast track assignments and to simplify the customer check sample. Remote soft proofing technology, suitable for digital and network environment, has the characteristics of fast speed, low cost, so the remote soft proofing is bound to become mainstream proofing in the future.

But remote soft proofing is based on the additive color system (R, G, B additive color display) and printing is using the subtractive system (C, M, Y, K subtractive method printing), *so the proofs = print is a big technical problem* [3].

At the stage of the remote soft proofing, high quality, stability, and strong professional display are the preconditions of remote soft proofing technology implementation. And through the display of SWOP system, certification prices are very expensive and will seriously affect the application and popularization of remote soft proofing technology. This article wants to research the effect of professional and normal display in the process of remote soft proofing. When using a common display device for remote soft proofing, the remote soft proofing obtains good proofing effect [4].

23.1.3 The Development Status of Remote Soft Proofing

Due to the limitation of network conditions and the technical level, the application of remote soft proofing technology is also in the stage of theory. Around 2002, the digital file transfer tool gradually entered the stage of practical production [5]. Some practical online output system, the remote soft proofing tools, and color management tools entered the Chinese printing market at the same time.

In foreign countries, such as the USA and Japan, they have been widely applied the remote soft proofing. Customers can order online, according to the actual needs of customers, and then the factory finishes printing work. With the development of the relevant technology of the remote soft proofing, remote soft proofing has gradually developed to the direction of more practical, efficient, and to form a more perfect network digital workflow.

23.2 Designs of Experiments

23.2.1 Experimental Equipment and Software

As shown in Table 23.2, experimental equipment and software are as follows.

Table 23.2 Experimental equipment and software

Equipment	Software
EIZOEV231W professional display, Lenovo LCD, X-Rite eye-one pro, Konica Minolta digital color printer, D50 standard light source	Adobe Photoshop CS4, Profile Maker 5.0, Microsoft Office Excel, Measure Tool, i1Match

23.2.2 Experiment

23.2.2.1 Flow Diagram of Experiment

The work flow diagram of experiment is shown in Fig. 23.1.

23.2.2.2 The Experimental Process

The first step is calibration using display device and the generation of profile.

Display calibration. EIZOEV231W professional display and Lenovo LCD display were preheated in half an hour in closed strong ambient light. The experiment
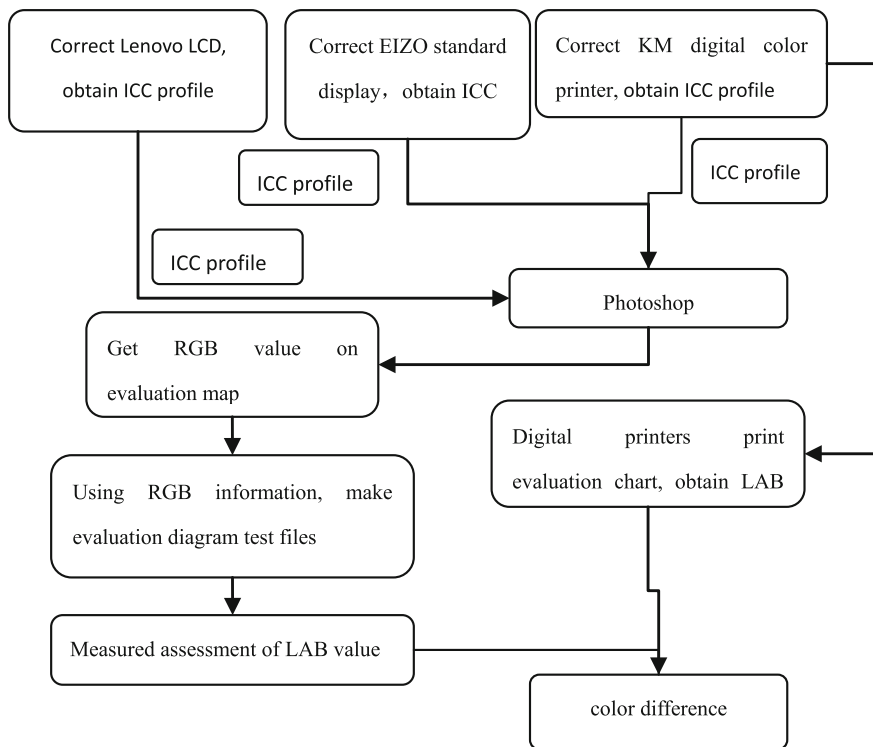
Fig. 23.1 Flow diagram of experiment

is best used with monitor hood, and after shut down of the system power management. With the screen calibration software i1Match and measuring instruments, X-Rite eye-one pro allows monitor calibration, and two ICC profiles will be generated after the completion of measurements.

Remark: White spots generally choose 5000 or 6500 k. China provides printing standard light source at 6500 k, so I chose 6500 k. For Gamma choose 1.8. For brightness choose 100 %.

The second step is calibration using Konica Minolta digital color printer. Color digital printer is a four-color CMYK, CMYK color target selection IT8.7-3 CMYK i1 (A4) .txt, using the X-Rite eye-one pro, the instrument on the base comes to standard white point, and then, a measure Tool is used to measure the last generation of ICC profiles.

Remark: In profile size option, I chose large and then generate ICC file, and the file size will be relatively large and relatively high accuracy. As for option of neutral gray treatment, I chose relative to neutral gray paper. As for option of gamut mapping, I chose Chroma Plu. In the gamut mapping options, I chose Chroma Plu [6].

The third step is color space conversion using Adobe Photoshop CS4. First import IT8.7-3 CMYK i1 (A4) .txt and evaluation map into Photoshop; at the specified configuration file, ICC properties file generated after RGB space have loaded EIZOEV231W professional display, ICC profile is generated after CMYK space have loaded Konica Minolta digital color printer. Gray choose Gray Gamma 1.8, spot color select dot gain 20 %, in the conversion options, intention choose absolute colorimetric and do not use black point compensation (T).

23.2.2.3   Results Analysis

As shown in Table 23.3, part of color piece of laboratory values.
As shown in Table 23.4,

$$\Delta E = \sqrt{L_1^2 + A_1^2 + B_1^2} - \sqrt{L_3^2 + A_3^2 + B_3^2} \tag{23.1}$$

Table 23.3 Laboratory values of color piece

	EIZO			Lenovo LCD			KM printer		
	L_1	A_1	B_1	L_2	A_2	B_2	L_3	A_3	B_3
1	49.7	73.4	59.8	50.2	75.4	62.1	48.5	71.9	58.5
2	63.2	39.7	68.3	65.5	40.7	69.3	61.5	38.2	66.8
3	88.6	−13.1	82.9	89.2	−16.1	85.5	86.2	−14.2	81.1
4	72.0	−56.4	68.7	75.2	−59.7	67.9	71.3	−54.3	68.9
5	73.3	−52.3	8.1	76.8	−51.7	9.0	72.1	−51.7	8.1
6	51.5	−3.9	−42.0	52.0	−4.1	−44.3	50.1	−2.2	−41.9
7	34.0	42.7	−40.6	37.1	44.2	-43.5	33.2	41.6	−39.9

Table 23.4 The color difference of color piece

	ΔE	$\Delta E^{'}$
1	2.31	5.21
2	2.66	5.17
3	2.84	5.40
4	1.34	4.55
5	1.32	3.84
6	1.22	1.63
7	1.51	5.74

$$\Delta E^{'} = \sqrt{L_2^2 + A_2^2 + B_2^2} - \sqrt{L_3^2 + A_3^2 + B_3^2} \tag{23.2}$$

As can been seen from Table 23.4, when using the EIZOEV231W professional display, average color difference is 2.48, which is less than 3. The experiments demonstrate the effectiveness of digitization process, so that you can accurately carry out remote soft proofing. Experimental data demonstrate the digital workflow validity, and then you can get the remote soft proofing exactly. After the Lenovo LCD display corrected, color difference is average 5.71, and the maximum color difference is not more than 7. If the requirements of color printing are not accurate, you can select the corrected Lenovo LCD display on remote soft proofing.

23.3   Conclusions

With the development of networking and electron devices, color management technology matures; China's development of digital printing will be faster. In the future, remote soft proofing technology will become the mainstream proofing way with high efficiency and low power consumption. Although remote soft proofing technology is based on professional display and color measurement instrument at this stage, the results of the use of conventional LCDs are not entirely satisfactory now. However, with the development of display technology, remote soft proofing technology will become an important part of the production of digital printing in the near future.

References

1. Hu, W., Tang, S., & Zhu, Z. (2007). *Modern color theory and application*. Beijing: Beijing Institute of Technology Press, pp. 237–245.
2. Jiu, G., & Dai, J. (2013). Screen soft proofing digital evaluation method and its implementation. *Printing Quality and Standardization, 11*, 21–25.
3. Paul, D., Fleming, I. I. I., & Sharma, A. Color management with ICC profiles: Can't live without it so learn to live with it, p. 19.
4. Fairchild, M. D. (1995). Testing color-appearance models: Guidelines for coordinated reinarch. *Color Research and Application, 20*, 251–255.
5. Yin, Y. (2001). Implementation methods and experience of color management. *Printing Technology, 11*, 8–13.
6. Liu, H., & Miao, H. *Calculation of the display color and color management*. Beijing: Beijing Institute of Graphic Communication, Vol. 11, No. 4.

Chapter 24
Color Difference Calculation of Prints for Machine Vision System

Yan Zhao, Xinyi Li, Shiqing Liu, Shiyu Zhang, Yingzhe Qiao and Haoxue Liu

Abstract Machine vision inspection system plays an increasingly important role in the printing process control, which is one of the development trends of the printing process control technology. This paper discusses the methods to inspect color of printed images online by a digital camera, by which the CIELAB color difference can be calculated directly from sampled RGB value. The algorithm is discussed in detail, and an experiment is conducted to test the method. The calculation results show that there is either linear or polynomial transformation relationship between CIEXYZ tristimulus and RGB values sampled by the camera, so the CIEXYZ tristimulus and CIELAB color difference can be expressed by the sampled RGB values. The calculation method proposed in this paper is proved by the experiment to be simple and practical, and the accuracy can meet the industry requirements.

Keywords Machine vision inspection system · Color difference calculation · Printing control

24.1 Introduction

Machine vision inspection systems are the equipment which uses CCD sensors and other hardware and software to simulate human eyes [1]. According to the sampling images, the inspection system can control and detect production quality effectively. The online detection system for printing industry uses industry camera to monitor the production procedure, and it can report the printing defects and printing situation in real time and replace human operation [2]. Because of the online detection

H. Liu (✉)
Beijing Institute of Graphic Communication, Beijing, China
e-mail: liuhaoxue@bigc.edu.cn

Y. Zhao · X. Li · S. Liu · S. Zhang · Y. Qiao
Beijing Luster LightTech Co., Ltd., Beijing, China

system, the printing quality, production rate, and operation difficulty have been improved. Such inspection systems are more and more popular in the printing industry [3].

The online inspection system for printed matter has two main functions: One is detecting and filtering out the printing defects, and the other is inspecting the situation of printing procedure and controlling the printing press status.

No matter which function is used, the system controls the printing quality with the images taken by CCD sensors [4]. In fact, it is used to compare the color values of the sampled images with the corresponding colors on the standard image. So, how to calculate and compare the color difference is a key point in the online detection system for printed matter. The main purpose of this paper is to discuss the methods of color difference calculation with sampled RGBs and discuss the calculation accuracy with real experimental data.

24.2 Color Difference Formula Derivation

Nowadays, CIE 1976 $L^*a^*b^*$ system is widely used color difference formula for controlling and evaluating printing quality, as shown in Formula 24.2.1.

$$\Delta E_{ab}^* = \sqrt{\left(L_1^* - L_2^*\right)^2 + \left(a_1^* - a_2^*\right)^2 + \left(b_1^* - b_2^*\right)^2} = \sqrt{\left(\Delta L^*\right)^2 + \left(\Delta a^*\right)^2 + \left(\Delta b^*\right)^2}$$
(24.2.1)

In this equation, L_1^*, a_1^*, b_1^* and L_2^*, a_2^*, b_2^* are CIE 1976 $L^*a^*b^*$ color values of reference and test samples, respectively, and are calculated by Formula (24.2.2).

$$\begin{cases} L^* = 116F(Y/Y_n) - 16 \\ a^* = 500[F(X/X_n) - F(Y/Y_n)] \\ b^* = 200[F(Y/Y_n) - F(Z/Z_n)] \end{cases}$$
(24.2.2)

$F(X/X_n)$, $F(Y/Y_n)$, and $F(Z/Z_n)$ in Eq. (24.2.2) are piecewise functions and expressed by Formula 24.2.3 (taking $F(X/X_n)$ for example, the other two are similar).

$$F(X/X_n) = \begin{cases} (X/X_n)^{1/3}, & (X/X_n) > 0.008856 \\ 7.787(X/X_n) + 0.1379, & (X/X_n) \leq 0.008856 \end{cases}$$
(24.2.3)

$F(Y/Y_n)$ and $F(Z/Z_n)$ have similar forms as $F(X/X_n)$. And X, Y, and Z stand for color tristimulus values; X_n, Y_n, and Z_n are tristimulus values of CIE standard illuminant.

To calculate ΔL^*, Δa^*, and Δb^*, the differentiation of Eq. (24.2.2) is made and Eq. (24.2.4) is derived.

$$\begin{cases} \Delta L^* = 116 * \Delta F(Y/Y_n) \\ \Delta a^* = 500[\Delta F(X/X_n) - \Delta F(Y/Y_n)] \\ \Delta b^* = 200[\Delta F(Y/Y_n) - \Delta F(Z/Z_n)] \end{cases} \quad (24.2.4)$$

Combining Formulas 24.2.3 and 24.2.4, Formula 24.2.5 is obtained.

$$\begin{cases} \Delta F(X/X_n) = \begin{cases} \frac{1}{3}\Delta X/(X_n X2)^{1/3}, & (X/X_n) > 0.008856 \\ 7.787(\Delta X/X_n), & (X/X_n) \le 0.008856 \end{cases} \\ \Delta F(Y/Y_n) = \begin{cases} \frac{1}{3}\Delta Y/(Y_n Y2)^{1/3}, & (Y_n Y) > 0.008856 \\ 7.787(\Delta Y/Y_n), & (Y_n Y) \le 0.008856 \end{cases} \\ \Delta F(Z/Z_n) = \begin{cases} \frac{1}{3}\Delta Z/(Z_n Z2)^{1/3}, & (Z/Z_n) > 0.008856 \\ 7.787(\Delta Z/Z_n), & (Z/Z_n) \le 0.008856 \end{cases} \end{cases} \quad (24.2.5)$$

Put Formula 24.2.5 into Formulas 24.2.4 and 24.2.1, CIE 1976 $L^* a^* b^*$ color difference formula calculated directly from CIEXYZ tristimulus is derived.

But inspection system scans RGB signals rather than CIEXYZ, so we have to find the transformation between RGB and CIEXYZ firstly.

24.3 The Conversion Between RGB and CIEXYZ

There are many methods to achieve the transformation between RGB and CIEXYZ, such as sRGB transformation [5], polynomial regression, and the lookup table (LUT) [6]. sRGB transformation is a general method used by ordinary cameras, it puts the digital RGB as sRGB with respect to a given set of equations, but it is not really accurate enough for the camera used in the system. The LUT is a common method used by scanner and camera but needs a lot of color samples to build it. In this paper, polynomial regression method is used to achieve the conversation between RGB and CIEXYZ.

24.3.1 Experimental Condition

The experimental platform is an inspection system of Luster LightTech Company. The main devices include a Dalsa Piranha 4-K color digital camera, a LED light with color temperature of 5000 K. X-rite Eye-One Pro and ProfileMaker 5.10 are used to measure the color patches of standard target. The TC9.18 standard color target, which is an RGB color target with many high saturated color samples, is used in the experiment and is printed by EPSON inkjet printer. The reference sample TC9.18 has 1100 pieces of color patches.

24.3.2 Experimental Method

Measure the CIEXYZ of TC9.18 samples by X-rite Eye-One Pro and scan the image of TC9.18 samples using the digital camera of inspection system. Both CIEXYZ and RGB values of every color patch are obtained in this way. According to these data sets, the conversation between RGB and CIEXYZ can be made using regression analysis [7].

24.3.3 Experimental Results

In accordance with the CIEXYZ and RGB values of each color patch, there is roughly a linear relation between RGB and CIEXYZ as shown in Fig. 24.1.

X-axis stands for measured CIEXYZ, y-axis stands for sampled RGB, and the linear correlation coefficient R^2 is larger than 0.95, indicating their good linearity relation. But there are some scatter points surrounding the fitted lines which were caused by non-independent relations among R, G, and B channels and the error due to real-time dynamic online sampling.

In order to eliminate the interaction between the channels, polynomial regression is used.

$$\begin{cases} X = X_0 + \sum a_{ijk} R^i G^j B^k \\ Y = Y_0 + \sum b_{ijk} R^i G^j B^k , \quad i, j, k = 0, 1, 2, \cdots \\ Z = Z_0 + \sum c_{ijk} R^i G^j B^k \end{cases} \qquad (24.3.1)$$

When i, j, and k in Formula 24.3.1 take different values, there would be different-order polynomial regression conversations, such as linear, quadratic, or triple transform conversations. Figures 24.2 and 24.3 are the results of quadratic and triple transform conversations.

Compared with Fig. 24.1, the dispersion degree of points in Figs. 24.2 and 24.3 is much less, the correlation coefficient R^2 is larger than 0.98 in both situations, and the mean color difference is less than 2.0 CIELAB unit. The performance of the different transformation methods is shown in Table 24.1.
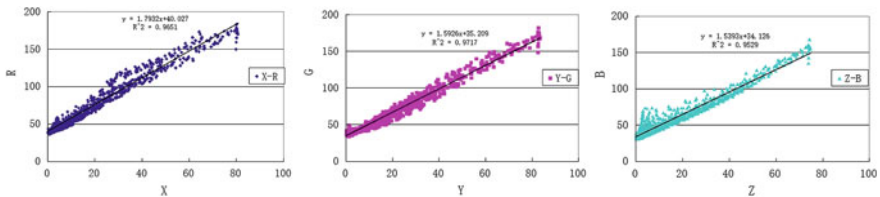
Fig. 24.1 The relation between RGB and CIEXYZ
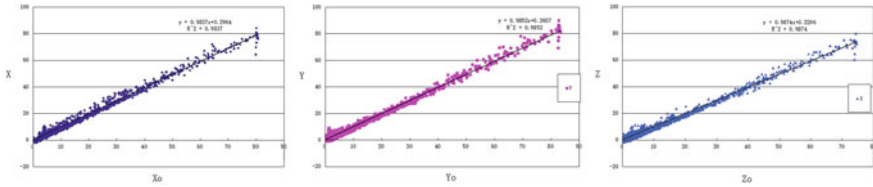
Fig. 24.2 The quadratic transformation between RGB and CIEXYZ
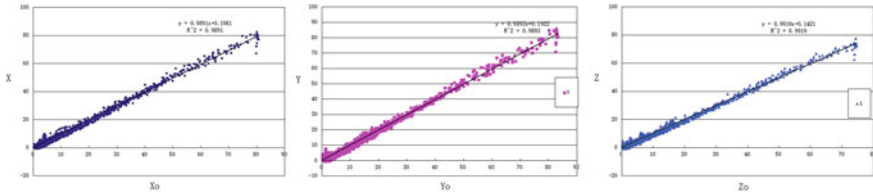
Fig. 24.3 The triple transform relation between RGB and CIEXYZ

Table 24.1 The results of several conversations

Mode	Items	Channel	R^2	Mean error	Max. error	Std. Dev.
Linear	4	X	0.984	2.05	15.40	1.44
		Y	0.985	1.71	13.24	1.69
		Z	0.987	1.55	13.59	1.26
Quadratic	7	X	0.987	1.78	14.34	1.40
		Y	0.987	1.63	13.38	1.56
		Z	0.991	1.35	12.00	1.05
Cubic	16	X	0.989	1.61	12.59	1.27
		Y	0.989	1.53	11.82	1.36
		Z	0.992	1.27	11.55	0.98

In conclusion, the CIEXYZ and RGB values of tested samples have a simple linear or polynomial conversation relation, so the difference of tristimulus ΔX, ΔY, and ΔZ can be expressed by RGB's difference.

The transformation between differentials of tristimulus and RGB values can be expressed in a matrix, as shown in Formula 24.3.2 [8].

$$\Delta XYZ = M \cdot \Delta RGB \qquad (24.3.2)$$

where ΔXYZ is a 3×1 matrix of differentials of tristimulus, ΔRGB is that of differentials of RGB values, and M is a coefficient matrix. The order of these two matrices is different according to the order of polynomial. For linear transform, ΔRGB is a 3×1 matrix and M is a 3×3 matrix. For quadratic transform, ΔRGB is a 9×1 matrix and M is a 3×9 matrix.

24.4 Conclusions

In this paper, a calculation method is discussed, by which the color difference is calculated directly from the sampled RGB values of image. The method can leave out some middle process and thus speed up computations. Especially, the method is suitable for the online printing inspection system to scan the image's color values and control the printed colors. This paper also discusses the transformation between RGB and CIEXYZ tristimulus values and tests its accuracy with data set sampled by frequently used Dalsa Piranha 4-K digital camera. The experiment results show that the method discussed in this paper is simple and has reasonably high accuracy and it can be used for online color difference inspection system and also as the characterization method for digital camera.

References

1. Lundstrom, J., Verikas, A., Tullander, E., & Larsson, B. (2013). Assessing, exploring, and monitoring quality of offset colour prints. *Measurement, 46*, 1427–1441.
2. Whisler, K., & Mauro, J. (2013). Defect detection, quality control, and efficiency through vision inspection systems. *Printing Industries of America, 5*(5), 30.
3. Verikas, A., Lundstrom, J., Bacauskiene, M., & Gelzinis, A. (2011). Advances in computational intelligence-based print quality assessment and control in offset colour printing. *Expert Systems with Applications, 38*, 13441–13447.
4. Li, M. (2011). Research on the image data system used in printing quality inspection. In Proceedings of 2011 IEEE 3rd international conference on communication software and networks (ICCSN)
5. Stokes, M., Anderson, M., & Chandrasekaret, S. (1996). A standard default color space for the internet-s RGB. http://www.w3.org/Graphics/Color/sRGB. Version 1.10
6. Yanman, M., Haoxue, L., & Xin, L. (2006). A research on the color characterization of digital camera. *Journal of Beijing Institute of Graphic Communication, 14*(6), 9–12.
7. Barnard, K., & Funt, B. (2002). Camera chararization for color research. *Color Research And Application, 27*(3), 152–163.
8. Hong, G., Luo, M. R., & Rhodes, P. A. (2001). A study of digital camera colorimetric characterization based on polynomial modelling. *Color Research and Application, 26*(2), 76–84.

Part II
Image Processing Technology

Chapter 25
Application of Digital Watermarking Technology to Artistic Screening Image

Jinghuan Ge, Jie Pan and Enyin Fang

Abstract Artistic screening is a new halftone technology for producing an illusion of continuous tones by creating artistic screens that may take any desired shape and screening effects. This screening technology is tuned to convey additional information for artistic purposes, which is desirable for digital anti-counterfeiting in today's printing industry. In order to achieve better anti-counterfeiting results, a novel data hiding algorithm is proposed by combining the artistic screening technology with digital watermarking. We present a digital watermarking algorithm in artistic screening images that divides the images into blocks and embeds a fixed number of bits in each block by changing some pixels in that block. Experiments show that watermarking-embedded artistic screening image is good at securing data hiding results and tampering of content can be detected successfully.

Keywords Digital watermarking · Artistic screening image · Binary image encryption · Halftone technology

25.1 Introduction

Digital watermarking technology is an important method to protect digital images. We can distinguish the authenticity of the image by extracting the hidden information from the image that is transmitted, compressed, or attacked maliciously in the process. Currently, the embedding or extraction for the digital watermarking technology has been developed maturely [1, 2]. However, the continuous digital image must be transformed to a binary halftone image by the screening process

J. Ge (✉) · J. Pan · E. Fang
Department of Printing and Packaging Engineering, Shanghai Publishing
and Printing College, Shanghai, China
e-mail: sytuprint@126.com

before printing, so the hidden watermarking information is greatly affected or even destroyed in this process. Therefore, the digital watermarking technology for the halftone image becomes a popular research field [3, 4]. In recent years, many researchers focus on this area, and they propose a lot of algorithms for the digital watermarking in binary images [5].

Nowadays, artistic screening technology which is also called microstructure screening is one of the latest digital screening technologies that attract more and more attention by people [6]. It uses different patterns or graphics to replace conventional dots in order to reproduce the image histogram. Specifically, it firstly describes the outline of a dot by a certain algorithm and then transforms the outlines of the dots for expanding or shrinking by nonlinear transformation algorithm; finally, we screen the image by the dots with specific outlines mentioned above. Therefore, it is an anti-counterfeit technology by defining the dot shapes arbitrary with the algorithms [7]. At present, many researchers in the areas of artistic screening technology have made much progress relatively [8, 9].

In this paper, a digital watermarking algorithm based on binary image patch which is processed by artistic screening for security protection is proposed. The new algorithm hides one bit of watermarking information in each image block. Firstly, the image is divided into the same blocks, and a fixed number of bits are embedded in each block by changing some pixels in that block according to the rules of smoothness and connectivity. We applied the watermarking technology to the artistic screening image and make sure that the watermarking is hidden well. Also, the watermarking can be embedded or extracted conveniently with the new method. Then, we can verify the authenticity of the artistic screening image. Experiments show that the proposed algorithm is effective.

25.2 The Anti-counterfeit Technology of Watermarking in Binary Digital Image

With the rapid development of information technology, digital watermarking is becoming a more and more important anti-counterfeit technology in protecting digital images. This method embeds watermarks into digital images and then extracts the hidden information from the image which may be influenced after transmission, compression, and some malicious attacks. Therefore, we can distinguish the authenticity of the image [10, 11].

Contrast to the traditional digital watermarking technology, the continuous tone images turn into the binary image via halftone process. The process will dramatically destroy the hidden watermarking information. Thus, the research on the digital watermarking of the binary image becomes very popular. Recently, bulks of researchers propose lots of digital watermarking algorithm for the binary image [9].

25.3 The Anti-counterfeit Technology of Watermarking Embedded in Artistic Screening Image

25.3.1 The Artistic Screening Image

Artistic screening technology is also known as microstructure screening technology. It uses different patterns or graphics to replace conventional dot in order to reproduce the image histogram. It firstly describes the outline of a dot by a certain algorithm and then transforms the outlines of the dots for expanding or shrinking by nonlinear transformation algorithm; finally, we screen the image by the dots with specific outlines mentioned above. Figure 25.1b shows the binary image that is screened by the dot shown in Fig. 25.1a. In the screening process, the dot size is also considered on the basis of the press precision [8].

The results of the practical application showed that the artistic screening is very appropriate for large outdoor posters. Figure 25.2b shows the halftone image that is artistically screened from Fig. 25.2a (including 512 × 512 pixels) by the special
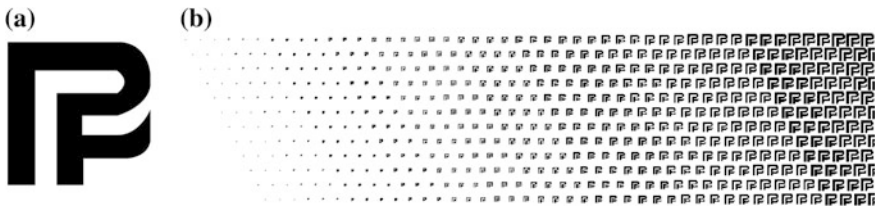
Fig. 25.1 The picture by microstructure screening with the defined *dot* shape
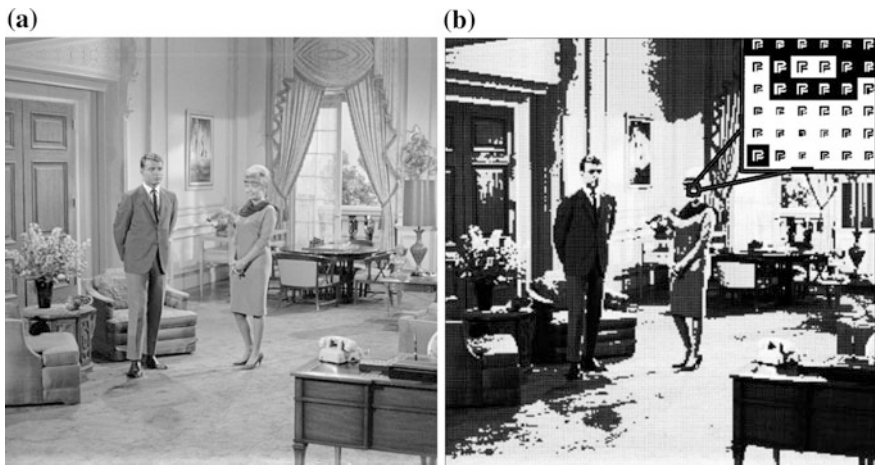
Fig. 25.2 The picture of the living room screened by the *dot* shape of picture (**a**)

dots as in Fig. 25.1a. On the upper right corner, Fig. 25.2b illustrates the detailed view of the woman's eye. Figure 25.2 shows that the specific dot shape information can be hidden in the integrity image by the artistic screening technology. In addition, the function of anti-counterfeit printing can also be realized by using the microstructure patterns or self-defined dots as unique dots in the printing process. Therefore, the information can be encrypted in the digital image by the combination of artistic screening and traditional digital screening process [8].

However, in practical applications, the artistic screening technology needs to pregenerate complicated dots which are described by the specific outlines. If this image is printed by the traditional press, precision is a problem. In order to achieve better anti-counterfeiting results, a novel data hiding algorithm is proposed by combining the artistic screening technology with digital watermarking for the purpose of double anti-counterfeiting. A detailed introduction of the method mentioned above will be discussed below.

25.3.2 Digital Watermarking Technology for Artistic Screening Image

Due to the special nature of the artistic screening image, we must select a suitable digital watermarking technology in the data hiding procedure. Specifically, most previous work on image data hiding are used for color and grayscale images, which include pixels with a wide range of values; however, the artistic screening image is a binary image which can be easily noticeable by changing the pixel values under normal viewing conditions. For images in which the pixels take value from only a few possibilities, hiding data without causing visible artifacts becomes more difficult. In particular, flipping white or black pixels that are not on the boundary is likely to introduce visible artifacts in binary images. There are few methods for hiding data in specific types of binary images which have been proposed in the literature. Most previously proposed approaches either cannot be easily extended to artistic screening images, or can only embed a small amount of data [12, 13]. According to the characteristics of the artistic screening image, we utilize the block diagram of the embedding and extraction process for artistic screening images.

Specifically, we embed multiple bits in our watermarking embedding and extraction algorithm by dividing an artistic screening image into 8×8 pixel blocks and hiding one bit in each block via the enforcement of odd–even relationship. That is to say, we divide an image into blocks and embed a fixed number of bits in each block by changing some pixels in that block (e.g., set to black if to embed a "0" and set to white if to embed a "1"). In order to embed one bit in each block, we have to select pixels in each block for modification. The key difference among the approaches to manipulate binary images is how to select pixels so as to introduce as less visual artifacts as possible. In this paper, we select pixels by means of a data embedding method proposed by Wu et al. They take the human perceptual factor

into account by studying each pixel and its immediate neighbors to establish a score of how unnoticeable a change on that pixel will cause. Similar to Wu's method, our approach is to determine the scores dynamically by observing the smoothness and connectivity. The smoothness is measured by the horizontal, vertical, and diagonal transitions in a local window (e.g., 3×3), and the connectivity is measured by the number of the black and white clusters. The score is between 0 and 1, with 0 indicating no flipping. Flipping pixels with higher scores generally introduces fewer artifacts than flipping a lower one. Therefore, the method manipulates "flippable" pixels to enforce a specific block-based relationship to embed a significant amount of data without causing noticeable artifacts. We utilize the block diagram of the embedding and extraction process for artistic screening images and present a digital watermarking algorithm for artistic screening images. For more details of how to select pixels, refer to the data hiding in binary image method in reference [9].

Watermarking extraction for the data hiding image is performed in a similar way as embedding. To extract the watermarking from an encrypted artistic screening image, the odd–even features in all non-uniform blocks of the data hiding image are extracted. This extracted watermarking is then compared with the original watermarking to give the authentication result. We use the mean-squared error (MSE) and peak signal-to-noise ratio (PSNR) to measure the performance results of our digital watermarking method. Both of them are the methods to quantify the difference between values implied by an estimator and the true values of the quantity being estimated. Specifically, MSE is a risk function, corresponding to the expected value of the squared error loss or quadratic loss, and PSNR is usually expressed in terms of the logarithmic decibel scale. Figure 25.3 shows the procedure of the proposed application of digital watermarking technology to artistic screening image. We easily find that the scanning encrypted watermarking information can be embedded into the artistic screening image, which can be kept invisible. We can also determine the authenticity and falsification of the images by detecting the extracted watermarking information from the digital image. The experiment performance of our proposed method is reported in the following section.
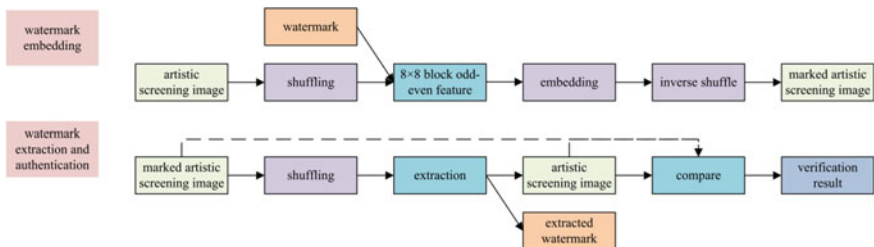
Fig. 25.3 The flowchart of the algorithm of the digital watermarking in microstructure image with divided binary image watermarking technology

25.4   Experiments

For the purpose of proving the effectiveness of the algorithm, the experimental results are obtained from the digital watermarking algorithm in microstructure image in this section. Firstly, we screen the grayscale images which have 512×512 pixels, respectively, with artistic screening technology.

25.4.1   Screening the Grayscale Image with Artistic Screening Technology

Take Fig. 25.2b for example, and the dot shapes can be hidden in the image by artistic screening. Next, the obtained artistic screening image in Fig. 25.2b will be protected by the block diagram based on binary image watermarking algorithm. We choose Fig. 25.4 (300×300 pixels, 90,000 bits) as a watermarking for the experiment. Then, the invisibility, the insertion and extraction, and the tamper inspection of the watermarking will be tested for the novel algorithm we proposed.

25.4.2   The Embedding and Certification of the Watermarking in Artistic Screening Image

Figure 25.5 shows the experimental results of the watermarking hidden in the artistic screening image. Figure 25.5a shows an original artistic screening image which contains 3000×3000 pixels, and Fig. 25.5b is obtained by embedding the watermarking image (Fig. 25.4) into the original image through flipping part of the pixels. The embedded watermarking information is difficult to be perceived because we choose the flipping pixels which make smaller influence on the vision.

Fig. 25.4 The hidden watermarking with the anti-counterfeit algorithm
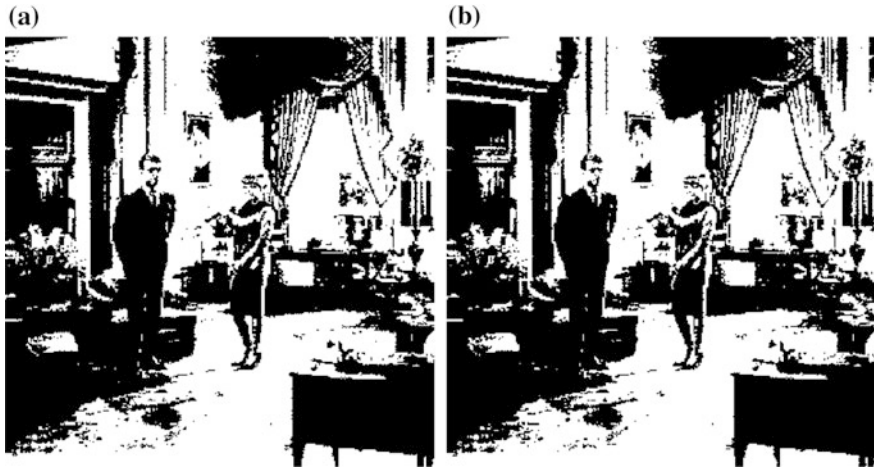
Fig. 25.5 The encoded microstructure picture by watermarking. **a** The original image. **b** The image embedded with watermarking

Figure 25.6a shows the flipped pixel location of artistic screening image that is processed by digital watermarking. The black points in the image illustrate the difference between the original and embedded images. Specifically, there are 61,777 flipped pixels in embedding the watermarking into Fig. 25.5a with the novel algorithm (MSE = 0.0069, PSNR = 21.6342). Then, we recover the embedded watermarking image using the watermarking extraction algorithm in Fig. 25.3, and then, the results are shown in Fig. 25.6b. In comparison with the original
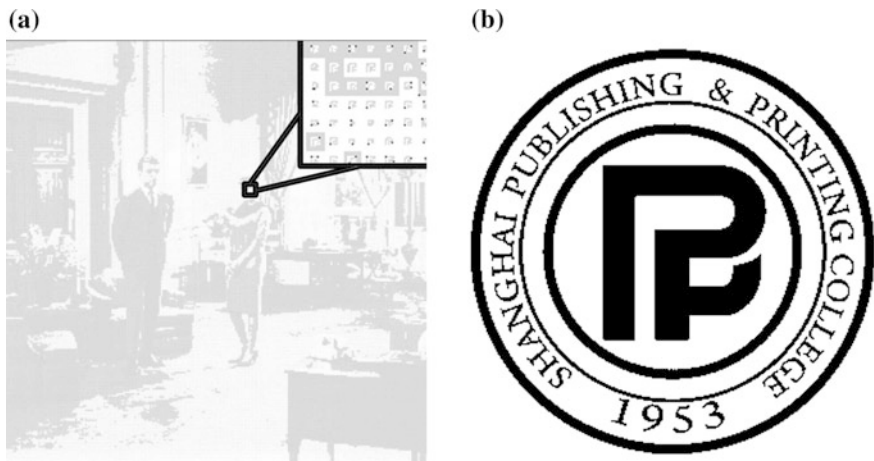
Fig. 25.6 Hide and pick up the watermarking in the microstructure picture. **a** The location of twisted pixels. **b** The watermarking extracted from the image

watermarking image (Fig. 25.4), we can find that the method we proposed is able to recover the embedded watermarking accurately. Meanwhile, we cannot obviously find the distortion in the embedded images on the vision.

25.4.3 The Tampering Detection of the Watermarking in Artistic Screening Images

Finally, the new proposed anti-counterfeit technology can be used in tampering detection of the watermarking in artistic screening images. It means that the embedded watermarking image will be easily destroyed if the image is distorted, because the encrypted watermarking information is embedded fragile in the artistic screening image. Figure 25.7 demonstrates the tampering detection of the encrypted image (Fig. 25.5b) after embedding digital watermarking image (Fig. 25.4) into the living room image. In Fig. 25.7a, after replacing the parts including person's faces in the encrypted image (Fig. 25.5b), we can find the extracted watermarking of tampering encrypted image in Fig. 25.7b. In comparison with the original watermarking image (Fig. 25.4), the original embedded watermarking cannot be recovered after tampering. Experimental results show that embedding fragile watermarking can be an effective method of certification, that is to say, by comparison between the extracted watermarking and the original, we can detect whether the artistic screening images with watermarking embedded were tampered, and find the extent of damage to the image.
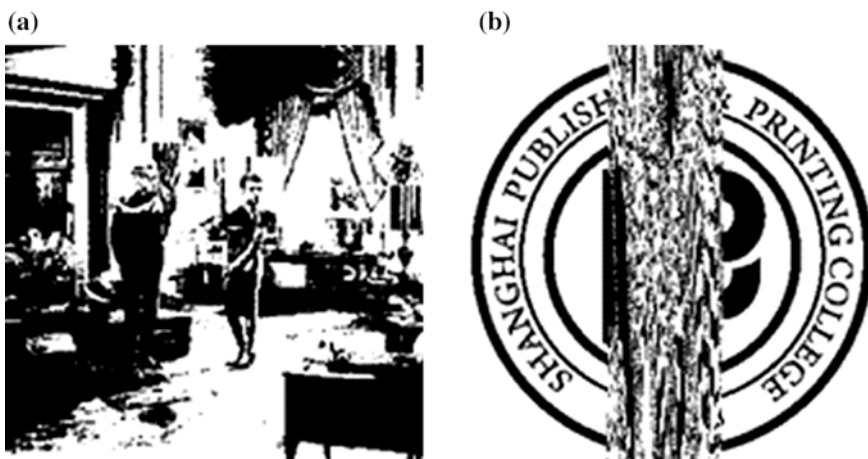
Fig. 25.7 The detection result of the microstructure picture with watermarking by distorting. **a** The distorted image containing watermarking. **b** The watermarking extracted from the image

Therefore, the experiment results show that the scanning encrypted watermarking information embedded into the artistic screening image can be kept invisible. We can also determine the authenticity and falsification of the images by detecting the extracted watermarking information from the digital image.

25.5   Conclusions

Artistic screening technology can encrypt the image with the different shapes of the dots. In order to achieve better anti-counterfeiting results, a new method is proposed by combining the artistic screening technology with the digital watermarking of binary images. By applying the digital watermarking algorithm based on image patches into the artistic screening technology, we can detect the authenticity and falsification of the content successfully by extracting the embedded watermarking information from the digital image. Experimental results effectively prove the accuracy of the above theory.

References

1. Chen, J., Zhang, L., & Sa, W. (2013). Research and realization of dynamic software watermarking technology. *Computer Applications and Software, 30*(7), 8–10.
2. He, B., Yuan, W., & Su, B. (2013). A zero watermarking algorithm resisting strong cropping and smearing attacks. *Computer Applications and Software, 30*(6), 150–153, 208.
3. Wen, S., Chen, G., Liu, Z., Xu, R., & Ren, L. (2011). Research on anti-counterfeit printing image based on the noise balance error diffusion. *Package Engineering, 32*(15), 25–28.
4. Wen, S. (2012). Anti-counterfeit technology based on digital screening. MS thesis, South China University of Technology, Guangzhou, China.
5. Wu, M., & Liu, B. (2004). Data hiding in binary image for authentication and annotation. *IEEE Transactions on Multimedia, 6*(4), 528–538.
6. Ostromoukhov, V., & Hersch, R. D. (1995). Artistic screening. In *Proceedings of the 22nd annual conference on Computer graphics and interactive technologys* (pp. 219–228).
7. Ostromoukhov, V. (2000). Artistic Halftoning: Between technology and art. In *SPIE proceedings series* (pp. 489–509).
8. Gong, Y., Zhang, Y., & Wang, K. (2008). The application of anti-counterfeit by microstructure screening. *Package Engineering, 29*(3), 62–63.
9. Gong, Y. (2008). Anti-counterfeit by microstructure screening. MS thesis, Jiangnan University, Wuxi, China.
10. Chen, H. (2013). A novel watermarking algorithm based on double hilbert scanning. *Computer Applications and Software, 30*(5), 298–300.

11. Yu, X., Li, H., & Zhang, M. (2013). A multifunctional double-watermarking algorithm of colour digital image based on lifting wavelet. *Computer Applications and Software, 30*(2), 50–53.
12. Liang, G. (2007). Steganography and steganalysis in the binary image. MS thesis, Shanghai University, Shanghai, China.
13. Wen, X. (2007). Research on binary text image watermarking. MS thesis, Shandong University, Jinan, China.

Chapter 26
Research on Description Method of Quasi-3D Appearance Data with Mathematical Surface Function

Xinggen Qian, Yang Jin and Hongguo Wang

Abstract Appearance data in quasi-three-dimensional (Quasi-3D) space are the height data, which are distributed over the grid points of a 2D plane. The quasi-3D data can be measured from a high-resolution 3D scanning device. With the help of mathematical surface function, the discrete space appearance data can be generalized; thus, some processing (e.g., interpolation, deformation) can be implemented. Based on segmentation of a 2D plane into blocks and the application of cubic surface functions (Coons, Bezier, and B-Spline), the appearance data in quasi-3D space are generalized processed, the parameters of the surface pieces are obtained, and some technical key points are determined. The quasi-3D appearance data can be used in scientific research, industry, high-fidelity 3D animation/film, image reproduction, and so on.

Keywords Quasi-3D appearance · Surface function · Generalization

26.1   Introduction

In general, a real three-dimensional object can be constructed from some key points, each of which has its coordinates (x, y, z). If the coordinates x and y are located in the same flat plane, and the coordinate z indicates "height value," the 3D coordinates can be simplified and called as "Quasi-3D" or "2.5D" coordinates.

The coordinate data z in "Quasi-3D" space are known as "appearance data" and are often obtained by high-resolution scanner, which can capture not only the color data, but also mainly the "height value" of object surface over a plane, and the pickup positions are distributed over a regular grid. Figure 26.1 shows the surface of leather (left) and its Quasi-3D appearance (scanned by Dr. Wirth GravurSysteme). Conceivably, the surface of an oil painting has the similar attribute.

X. Qian · Y. Jin (✉) · H. Wang
School of Printing and Packaging Engineering, Beijing Institute
of Graphic Communication, Beijing, China
e-mail: jinyang@bigc.edu.cn
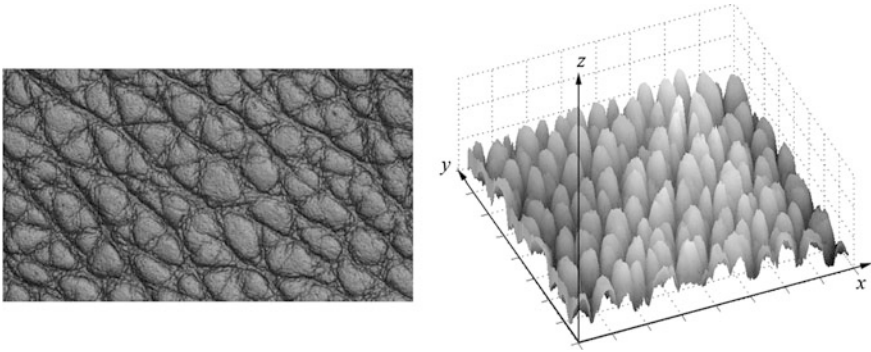
Fig. 26.1 Surface of a leather piece and its quasi-3D appearance

In order to describe and to generalize the appearance data, mathematical functions can be used [1, 2]. Since the appearance of a surface is usually quite complicated, the selection of mathematical function and the method for the generalization should be attentively investigated.

26.2 Surface Model for the Description of Quasi-3D Appearance

The natural objects possess complicate form and/or texture on their surface. In order to describe the appearance data, mathematical functions, e.g., Bezier, B-spline, and Coons, can be selected to apply. Although a higher degree of function leads to higher descriptive power, the order of complexity is also increased correspondingly. Compromised, cubic surface functions are selected. As example, Formula 26.1 is cubic surface function in the form of Bezier [3]:

$$Q_{\text{Bezier}}(x, y) = \text{U}M_{\text{Bz}}\text{P}M_{\text{Bz}}^{T}W \tag{26.1}$$

wherein

$$U = \begin{bmatrix} x^3 & x^2 & x & 1 \end{bmatrix}, M_{\text{Bz}} = \begin{bmatrix} -1 & 3 & -3 & 1 \\ 3 & -6 & 3 & 0 \\ -3 & 3 & 0 & 0 \\ 1 & 0 & 0 & 0 \end{bmatrix},$$

$$M_{\text{Bz}}^{T} = M_{\text{Bz}} = \begin{bmatrix} -1 & 3 & -3 & 1 \\ 3 & -6 & 3 & 0 \\ -3 & 3 & 0 & 0 \\ 1 & 0 & 0 & 0 \end{bmatrix}, P = \begin{bmatrix} P_{11} & P_{12} & P_{13} & P_{14} \\ P_{21} & P_{22} & P_{23} & P_{24} \\ P_{31} & P_{32} & P_{33} & P_{34} \\ P_{41} & P_{42} & P_{43} & P_{44} \end{bmatrix}, W = \begin{bmatrix} y^3 \\ y^2 \\ y \\ 1 \end{bmatrix},$$

$(x, y) \in [0, 1].$

Fig. 26.2 Bezier surface, control points, and characteristic polyhedron
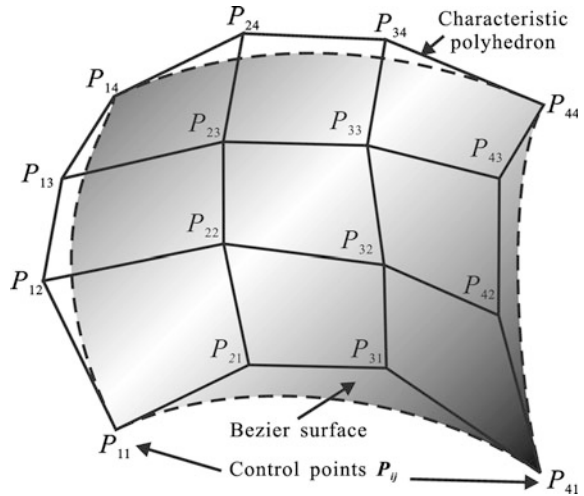
In the equation, the elements $P_{i,j}$ ($i, j \in 1, 2, 3, 4$) of matrix P are control points, which can be applied to build up "characteristic polyhedron" for the construction of surface. To construct a cubic surface function, matrix P with 4×4 control points $P_{i,j}$ must be obtained. Figure 26.2 shows the control points, characteristic polyhedron, and the Bezier surface.

It can be conceivable that in order to describe the quasi-3D appearance with mathematical function, the plane X–Y must be separated in blocks, each of which includes 4×4 height (z) data. With the 4×4 height (z) data, one piece of surface can be constructed, and the whole appearance surface consists of many pieces of subsurface. Two neighboring pieces of surface are shown in Fig. 26.3. It can be seen that the four appearance data at the common border of the subpieces are applied for the two pieces of subsurface.
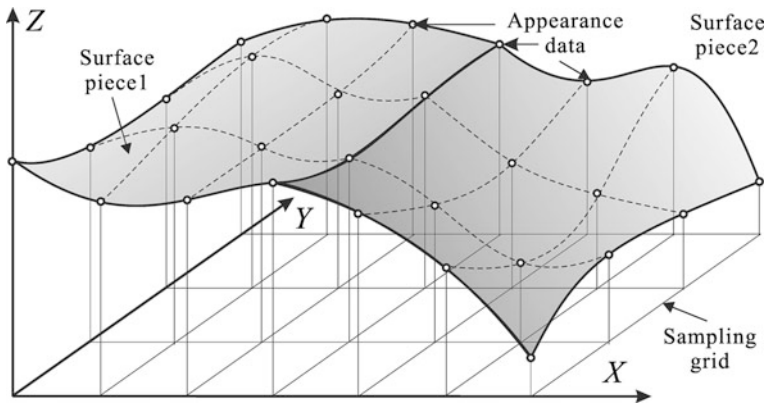
Fig. 26.3 Subsurfaces with appearance data

26.3 Basic Processing Flow and Algorithm

Essentially, the description of Quasi-3D appearance is to obtain the control parameters of the surface and/or surface pieces, which fit to the appearance data [4]. Under the condition of cubic surface function, the element data of matrix P in Formula 26.1 must be computed out. Deriving from Formula 26.1, the matrix P can be described as follows:

$$P = \left(\mathrm{U}M_{\mathrm{Bz}}M_{\mathrm{Bz}}^{T}W\right)^{-1}Q(x,y) = T^{-1}Q(x,y) \tag{26.2}$$

where $Q(x, y)$ is the appearance data at position (x, y), and M_{Bz} and M_{Bz}^{-1} are shown above. In every surface piece, the coordinates x and y are normalized to the range [0, 1]. If the sampling grid is uniformly distributed (it can also be un-uniformed arranged), the values of x and y are 0, 1/3, and 2/3, 1, respectively. Thus, the matrices U and W are also determined. The processing flow is as follows (Fig. 26.4).

It should be careful that the appearance data at the common border of surface pieces must be brought into both neighboring blocks, so that the continuity between the surface pieces is kept.

As example, a gray-level image with 511 × 430 pixels is processed. The gray level of the pixels is denoted as "appearance data," and 24310 pieces of subsurfaces are processed. Figure 26.5 shows the restored image from the surface function.

Input the appearance data	Segmentation data into 4×4 block	Solving the inverse matrix T^{-1}	Computing the matrix P of pieces
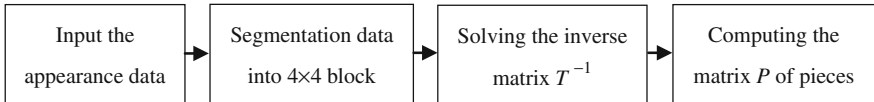
Fig. 26.4 The processing flow of computing matrix P

Fig. 26.5 Described as cubic Bezier function and from the function restored image

26.4 Discussion and Conclusions

The description and generalization of Quasi-3D data with mathematical function are implementable. Not only the "appearance data" can be from a real object body, but it can also be the data from different sources (image pixel data, frequency data, etc.). Different math functions can be applied. In the application of image processing, the surface pieces at the sides of the border can possess higher or lower degree of continuity and smoothness. The method can be used in area of object modeling, image processing, data analyzing, and fitting.

References

1. Su, D., & Willis, P. (2004). Image interpolation by pixel level data-dependent triangulation. *Computer Graphics Forum, 23*(2), 128–251.
2. Su, D., Willis, P. (2003). Demosaicing of colour images using pixel level data-dependent triangulation. *Proceedings of Theory and Practice of Computer Graphics* (pp. 16–23).
3. Tang, Z., Zhou, J., & Li, X. (2003). *Fundamental computer graphics* (2nd ed.). Beijing, China: Tsinghua University Press.
4. Yang, J. (2000). *Research on surface description of image and its processing methodology*. Dissertation. PLA Information Engineering University, Zhengzhou, China.

Chapter 27
Improved Local Adaptive Image Enhancement Algorithm Based on Lee Algorithm

Tian Song, Zhijiang Li and Liqin Cao

Abstract Experiments indicate that Lee algorithm is sensitive to noise in image enhancement, which means that the details of texture and noises will be enhanced simultaneously. Therefore, an improved adaptive local image enhancement algorithm based on Lee algorithm is proposed in the paper to reduce the negative impact of the noises. Firstly, traditional Lee algorithm is employed to improve the image brightness and enhance the image details. Then, logarithmic transformation is applied to make the image more consistent with human vision mechanism. Finally, double platform threshold based on histogram equalization is used to overcome the disadvantage that the targets and details occupying less pixels become blurred and lost due to pixel-level merging, while the background and noise are enhanced excessively by setting the threshold of the double platform. Verification experiments demonstrate that the improved algorithm can enhance image local contrast and adaptively adjust image dynamic range effectively, regardless of the impact of noises to avoid excessive enhancement.

Keywords Image enhancement · Lee algorithm · Logarithm transform · Plateau histogram equalization

27.1 Introduction

Image enhancement is a usual method for highlighting certain information in an image according to the specific need and weakening or removing some unnecessary information simultaneously to improve the image quality [1]. Literatures indicate that lots of effective algorithms in specific areas are proposed as a local algorithm for image enhancement based on models such as filtering, partial differential equation, and digital morphology [2]. Niu et al. [3] proposed a new image contrast

T. Song · Z. Li (✉) · L. Cao
School of Printing and Packaging, Wuhan University, Wuhan, China
e-mail: lizhijiang@whu.edu.cn

enhancement algorithm based on wavelet transform and un-sharp mask. Literature [4] proposed an improved image contrast enhancement algorithms based on partial differential equation (PDE). This method gives a general design method of piecewise linear stretch function to achieve better histogram equalization. Literature [5] proposed a method based on mathematical morphology with multiple structural elements, and multiscale dual-gradient edge detection. As a classic local adaptive image enhancement algorithm, Lee algorithm can reduce the complexity of calculation and enhance the image detail. However, excessive noise enhancement and large object edge oscillation is still a problem worth to be discussed further.

27.2   Lee Algorithm

The general form of Lee algorithm [6] is as follows:

$$g(i,j) = \bar{f}(i,j) + \beta \left[f(i,j) - \bar{f}(i,j) \right] \tag{27.1}$$

In the formula, the gray value of the preprocessed and postprocessed image pixels is represented by $f(i,j)$ and $g(i,j)$, respectively. $\bar{f}(i,j)$ means the arithmetic mean in the neighborhood of the preprocessed image which has taken (i,j) as the center and the size $n \times n$; β is a real number.

In order to enhance the image with ill-conditioned distribution histogram, which means to readjust the gray level of the image, the improved Lee algorithm is proposed:

$$g(i,j) = \alpha \bar{f}(i,j) + \eta + \beta \left[f(i,j) - \bar{f}(i,j) \right] \tag{27.2}$$

In the formula (27.2), $y = \alpha \bar{f}(i,j) + \eta$ is a linear gray-level stretching function, and α, β, and η are real numbers. When $\beta > 1$, the edge of the image can be sharpened. And when $\alpha > 1$, the gray value of the image can be stretched to high brightness area; otherwise, the gray value of the image can be stretched to lower intensity. Parameter η is used to adjust the dynamic range of the global image.

27.3   The Adaptive Local Image Enhancement Based on Lee

27.3.1   Logarithmic Transformation

Logarithmic transformation [7] followed by gray value normalized complement transformation is introduced into Lee algorithm, which constructs a new nonlinear transform for Lee's image enhancement. The transformation is defined as follows:

$$\bar{f} = 1 - (f/M) \tag{27.3}$$

In the formula (27.3), gray function f is defined in [0, M] interval, for 8-bit images, $M = 255$. The substituted and simplified equation can be expressed as follows:

$$\log(\bar{g}((i,j)) = \alpha \log(\bar{\alpha}(i,j)) + \beta \log[(\bar{f}(i,j))] - \log(\bar{\alpha}(i,j)) \tag{27.4}$$

In the formula (27.4), $\bar{f}(i,j)$ represents preprocessed image after normalized complement transformation, and $\bar{g}(i,j)$ represents postprocessed image after normalized complement transformation. The meaning of α and β in the formula (27.4) is the same as the formula (27.2). Among them,

$$\log(\bar{\alpha}(i,j)) = \frac{1}{n \times n} \left(\sum_{k=-\frac{n}{2}}^{\frac{n}{2}} \sum_{l=-\frac{n}{2}}^{\frac{n}{2}} \log(\bar{f}(i+k,j+l)) \right) \tag{27.5}$$

In the formula (27.5), n is the neighborhood size. In the formula (27.4), the first term $\alpha \log(\bar{\alpha}(i,j))$ is to stretch image dynamic range to expected extent, and the second term $\beta[\log(f(i,j)) - \log(\bar{\alpha}(i,j))]$ is to sharpen the image, while $g(i,j)$, which means the output image, is obtained via an inverse transformation of $\bar{g}(i,j)$, which is given in Eq. (27.4), as the following formula:

$$g(i,j) = M(1 - \bar{g}(i,j)) \tag{27.6}$$

27.3.2 Dual-Platform Histogram Equalization

In the paper, fixed dual-platform threshold is proposed. The algorithm of dual-platform histogram equalization [8] is defined as follows:

(1) Calculating the histogram of image $g(i,j)$ obtained by the formula (27.6).
(2) Transferring the histogram by dual-platform threshold as follows.

$$H(r_k) = \begin{cases} T_1 & h(r_k) \leq T_1 \\ h(r_k) & T_1 < h(r_k) < T_2 \\ T_2 & h(r_k) \geq T_2 \end{cases} \quad (k = 0, 1, 2, \ldots, L-1) \tag{27.7}$$

In the formula (27.7), T_1 is the lower threshold, T_2 is the upper threshold, L is the gray level, and $h(r_k)$ is the probability density of the grayscale image.
(3) Calculating the cumulative histogram $F(r_k)$ of images based on the modified histogram statistics in the formula (27.7).

$$F(r_k) = \sum_{j=0}^{k} H(r_k), \quad k = 0, 1, 2, \ldots, L - 1 \tag{27.8}$$

(4) Remapping the image gray levels based on the cumulative histogram $F(r_k)$ to obtain the grayscale values after equalization $D(r_k)$ as given in the following equation.

$$D(r_k) = \lfloor (L - 1)F(r_k)/F(r_{L-1}) \rfloor \tag{27.9}$$

where $\lfloor \cdot \rfloor$ means rounding operation.

27.3.3 Calculation of the Adaptive Dual-Platform Threshold

The calculation of the dual-platform threshold is referred to relative research [9]. The upper platform threshold T_2 should equal to the peak value $h(k_{\text{target}})$ of interested object in histogram. When $h(k_{\text{target}})$ is difficult to be located accurately in the histogram, the range of T_2 will be approximately calculated according to the consideration that the value of T_2 should locate between the peak value $h(k_{\text{target}})$ of the interested object and the peak value $h(k_{\text{background}})$ of the background, and it is near to $h(k_{\text{target}})$ usually. That is,

$$h(k_{\text{target}}) < T_2 < h(k_{\text{background}}) \tag{27.10}$$

and

$$T_2 - h(k_{\text{target}}) < h(k_{\text{background}}) - T_2 \tag{27.11}$$

Therefore,

$$h(k_{\text{target}}) < T_2 < \frac{h(k_{\text{target}}) + h(k_{\text{backound}})}{2} \tag{27.12}$$

In the formulas above, $h(k_{\text{target}})$ is the corresponding histogram peak value of the interested objects, and $h(k_{\text{background}})$ is the corresponding histogram peak value of the image background.

In order to avoid the combining of smaller gray levels in histogram, the rule that the intervals of adjacent gray levels in original histogram should be larger than 1 in the modified histogram should be considered in the setting of lower platform threshold. That means that

$$D = \frac{F(K) - F(K-1)}{F(L)} * L \geq 1 \tag{27.13}$$

where D is the interval of two adjacent gray levels in the valid gray level set of the modified histogram, L is the total gray levels, $F(k)$ is the modified cumulative histogram of the image, $F(L)$ is the total cumulative histogram values of the modified image, and $F(k) - F(k-1)$ is the statistical value $h(k)$ of the gray value k in modified histogram.

Let $T_1 = H_{\min}(k))$, when T_1 is used as the lower platform value, the modified image will not lose any original gray value. Then, the algorithm guarantees

$$\frac{T_1}{F(L)} * L \geq 1 \tag{27.14}$$

27.4 Experiment and Analysis

To verify the algorithm, one of the samples and experiment results is provided in Fig. 27.1, and comparison among Lee algorithm, the proposed algorithm and other algorithms is provided in Fig. 27.2. The samples are usually low-contrast images.

Figure 27.2a is an original color image with low contrast.

Figure 27.2b is the result of local Lee algorithms, which is similar to Wallis filtering. The method achieved increased global brightness and enlarged image dynamic range, but the texture in sky is enhanced improperly.

Figure 27.2c is the result of logarithmic transformation. The method also achieved increased global brightness and enlarged image dynamic range. Compared to the previous two figures, it is more coincident to human visual system, especially in global color saturation and image details. However, the sky is overenhanced.

Figure 27.2d is the result of the proposed algorithm. The details in the foreground and background images are all enhanced effectively with enlarged image dynamic range and increased global brightness. Particularly, compared with Fig. 27.2c, the proposed method avoids excessive enhancement of image
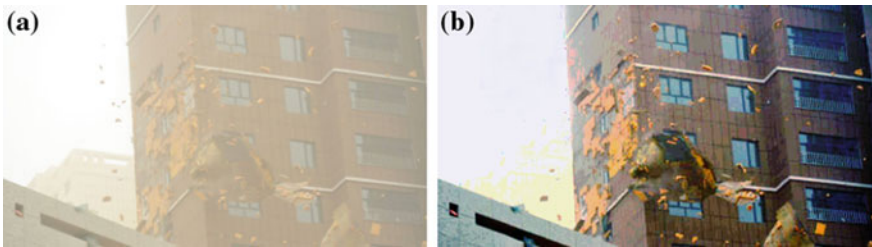
Fig. 27.1 The result of adaptive local enhancement algorithm based on Lee. **a** Original image. **b** Result

Fig. 27.2 Experiment result comparison. **a** Original image. **b** Lee method. **c** Logarithmic transformation method. **d** Proposed method

background, retains excellent color consistency, and is more coincident with human visual system. It demonstrates that the proposed algorithm shows good performance in image detail enhancement and background noise suppression. It is an effective image enhancement algorithm.

To demonstrate the result of the proposed algorithm, quantitative indicators are listed in Table 27.1. Gray mean value is used to measure the global brightness of the images. Standard deviation is used to measure the global contrast of the images. Entropy is used to measure the global quantity of information. PSNR is used to measure the feature information quantity relative to origin image.

As the indicators in Table 27.1, either the proposed method or the Lee method performs well on image brightness improvement, but the proposed method shows better performance in contrast enhancement and can effectively reduce the image noise at the same time.

Table 27.1 The quantitative comparison of the image enhancement algorithms

Algorithms Parameters	Original image	Lee algorithm	Proposed algorithm
Gray mean value	24.87	69.11	71.42
Standard deviation	18.99	18.80	23.31
Entropy	5.18	6.18	6.20
PSNR	–	33.58	38.15

Integrating subjective evaluation and objective evaluation, the proposed method has better performance than Lee and other methods, and the proposed method can enhance image details and reduce noise simultaneously, which matches the research target.

27.5   Conclusions

A novel adaptive local image enhancement algorithm is proposed in this paper, which is able to enhance images effectively and overcome the shortcomings of traditional methods. Based on Lee algorithm, logarithmic transformation, together with normalized complement transformation, was introduced, and adaptive dual-platform threshold based on histogram equalization was integrated to form a new algorithm. The algorithm proposed in this paper achieves good combination of image contrast enhancement, feature preservation and noises removing to improve image quality greatly.

References

1. Sheng, D. (2007). *Research on image enhancement algorithms*. MS Thesis, Wuhan University of Science and Technology, China.
2. Lu, L. (2002). *The research on image enhancement models and algorithms*. MS Thesis, National University of Defense Technology, China.
3. Niu, H., Chen, X. J., & Zhang, J. (2011). Image contrast enhancement based on wavelet transform and un-sharp mask. *High-tech Communications, 21*(6), 600–606.
4. Ke, J., & Hou, Y. (2009). An improved algorithm for shape preserving contrast enhancement. *Acta Photonica Sinica, 38*(1), 214–219.
5. Li, W., & Chen, P. (2009). An image contrast enhancement algorithm based on mathematical morphology. *The Modern Electronic Technology, 13*(300), 131–133.
6. Lee, J. S. (1980). Digital image enhancement and noise filtering by use of local statistics. *IEEE Transactions on Pattern Analysis and Machine Intelligence, PAMI, 2*(3), 165–168.
7. Panetta, K., Agaian, S., Zhou, Y, et al. (2011). Parameterized logarithmic framework for image enhancement. *IEEE Transactions on Systems Man & Cybernetics Part B Cybernetics. A Publication of the IEEE Systems Man & Cybernetics Society, 41*(2), 460–473.
8. Song, Y., Liu, S., & Zhou, H. (2008). Adaptive dual—Platform infrared image enhancement algorithms. *Infrared and Laser Engineering, 37*(2), 308–311.
9. Tu, Z. (2012). *A kind of infrared image enhancement algorithms by adaptive dual-platform histogram and FPGA Implementation*. MS Thesis, Huazhong University of Science and Technology, Wuhan.

Chapter 28
Application of Matrix Rotating Screening in Halftone Information Hiding Technology

Linghua Guo, Tiedou Xing, Yan Chen and Guodong Liu

Abstract Information hiding technology based on halftone screening becomes increasingly popular in anti-counterfeit printing field because of its low-cost and easy operation. But the problems of unsatisfying information hiding effect and low-safety factor remain to be solved. In this study, a new algorithm of matrix rotating screening on the basis of threshold matrix screening principle is introduced in order to create special shaped dots. The image screened with special shaped dots is then applied to hide and extract information. As expected, dot shape varying from rotating matrix is hard to copy, thus improving the security ability of image. The hiding effect of image screened with special shaped dots gets 0.9740 based on structural similarity (SSIM), while the hiding effect of image screened with traditional round dots gets 0.9655. Therefore, we demonstrate that image screened with special shaped dots created by rotating matrix achieves a better hiding effect compared with traditional method, leading to a more practical and beneficial application in halftone information hiding technology.

Keywords Information hiding · Matrix rotating screening · Special shaped dot · Safety factor

28.1 Introduction

With the development of printing industry, anti-counterfeit printing technology has been indispensable since fake and shoddy goods, diploma forgery, plagiarism is flooding the market [1]. Traditional anti-counterfeit technology has many application limitations due to its high cost and technological requirement [2]. Information hiding technology based on halftone screening [3–10] is then brought

L. Guo · T. Xing (✉) · Y. Chen · G. Liu
Light Industry and Energy Institute, Shaanxi University of Science and Technology, Shaanxi, China
e-mail: joiron@163.com

up with the advantage of low-cost and easy operation, which hides graphics information by moving its printing dots away from the original dots after an image is color separated and extract hidden information with a printed matching film on the image [11].

However, information hiding technology based on halftone screening still has two problems: one is that image screened with traditional round or square dots will appear texture when hidden information, the hiding effect needs to be improved. The other is that this technology is easy to be copied when using traditional shaped dots, and safety factor is not strong enough.

In this study, we propose a new algorithm of matrix rotating screening on the basis of threshold matrix screening principle to create special shaped dots and then hide and extract information with image screened with special shaped dots to solve the problems.

28.2 Matrix Rotating Screening

28.2.1 Threshold Matrix Design

In this study, we continue to use the research result of Dr. Xu [12, 13], who takes 12×12 recorder grid as an example and uses approximate $14.04°$ and $75.96°$ instead of $15°$ and $75°$ to achieve rational tangent screening.

Suppose θ is screening angle, $\tan \theta = \frac{mp}{mq}$, m, p, q are integer, p, q are prime, threshold matrix size is $L \times K$, then threshold maximum is $Q_{max} = L \times K$, where $L = m(p^2 + q^2)$, $K = m$. The relations between threshold matrix and 4×4 screening grid are shown in Fig. 28.1.

When screening angle $\theta = 0°/90°$, one threshold matrix fills in one screening grid, describing one dot, as is shown in Fig. 28.1a, then $p = 0$, $q = 1$. Let $m = 12$, then $K = 12$, $L = 12$, $Q_{max} = 144$.
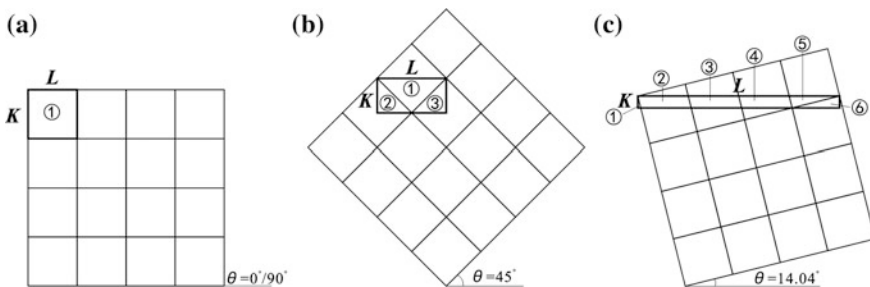
Fig. 28.1 Threshold matrix screening principle. **a** Threshold matrix screening of $\theta = 0°/90°$. **b** Threshold matrix screening of $\theta = 45°$. **c** Threshold matrix screening of $\theta = 14.04°$

When screening angle $\theta = 45°$, one threshold matrix is divided into three parts, filling in one screening grid when put together, describing one dot, as is shown in Fig. 28.1b, then $p = 1$, $q = 1$. If $m = 8$, then $K = 8$, $L = 16$, $Q_{max} = 128$, differing $144 - 128 = 16$ by Q_{max} of $\theta = 0°/90°$; if $m = 9$, then $K = 9$, $L = 18$, $Q_{max} = 162$, differing $162 - 144 = 18$ by Q_{max} of $\theta = 0°/90°$, so we adopt the former.

When screening angle $\theta = 14.04°$, one threshold matrix is divided into six parts, filling in one screening grid when put together, describing one dot, as is shown in Fig. 28.1c, then $p = 1$, $q = 4$. Let $m = 3$, then $K = 3$, $L = 51$, $Q_{max} = 153$.

Screening angle $\theta = 75.96°$ is similar to $\theta = 14.04°$, $K = 3$, $L = 51$, $Q_{max} = 153$.

After the threshold matrix size is settled, threshold figure is to be designed, which determines the dot shape. When designing a threshold matrix, one recorder grid is chosen as a center and threshold figure is written from Q_{max} to 1 in descending order until filling all the recorder grids. The dot shape changes from different threshold matrix by choosing a different recorder grid as a center so that we get several different threshold matrixes. Three different threshold matrixes with screening angle $\theta = 45°$ designed in this study are shown in Fig. 28.2 (see Fig. 28.2a, Fig. 28.2b and Fig. 28.2c).

28.2.2 Matrix Rotating Screening Algorithm

After an image is color separated, four C, M, Y, K 8-bit grayscale images will be created in general, in which the maximum value of every pixel is $2^8 - 1 = 255$, while the threshold maximum is 153, so the pixel value F of grayscale image needs to be transferred to F' to build its relationship with threshold maximum Q_{max}. The relation is given by

$$F' = \text{fix}\left(\frac{F}{255} \times Q_{max} + 0.5\right) \tag{28.1}$$

Compare F' with every corresponding threshold Q according to distribution of different threshold matrixes to decide whether the recorder grid exposure or not, if $F' < Q$, the recorder grid will exposure and vice versa. The distribution of different threshold matrixes differs from the screening angle, as is shown in Fig. 28.3. Each row of threshold matrixes moves by mq recorder grids to the left. For example, each row moves by 0 when $\theta = 0°/90°$ (see Fig. 28.3a), moves by 8 when $\theta = 45°$ (see Fig. 28.3b) and 12 when $\theta = 14.04°/75.96°$ (see Fig. 28.3c).

(a)

128	120	109	92	74	66	46	8	15	10	64	79	97	111	122	127
123	116	87	69	62	38	6	39	42	3	19	55	86	105	115	119
107	96	71	59	24	12	28	52	63	47	20	1	58	95	108	112
84	73	56	2	18	23	48	78	82	67	35	5	31	61	91	101
77	53	32	4	25	43	75	85	100	89	60	30	9	34	68	80
51	41	21	27	40	70	94	102	110	103	93	57	26	11	37	65
44	29	33	45	72	90	104	121	117	114	106	88	54	17	13	16
14	36	49	76	83	98	118	126	125	124	113	99	81	50	22	7

(b)

15	10	64	79	97	111	122	127	128	120	109	92	74	66	46	8
42	3	19	55	86	105	115	119	123	116	87	69	62	38	6	39
63	47	20	1	58	98	108	112	107	96	71	59	24	12	28	52
82	67	35	5	31	61	91	101	84	73	56	2	18	23	48	78
100	89	60	30	9	34	68	80	77	53	32	4	25	43	75	85
110	103	93	57	26	11	37	65	51	41	21	27	40	70	94	102
117	114	106	88	54	17	13	16	44	29	33	45	72	90	104	121
125	124	113	99	81	50	22	7	14	36	49	76	83	98	118	126

(c)

97	111	122	127	128	120	109	92	74	66	46	8	15	10	64	79
86	105	115	119	123	116	87	69	62	38	6	39	42	3	19	55
58	98	108	112	107	96	71	59	24	12	28	52	63	47	20	1
31	61	91	101	84	73	56	2	18	23	48	78	82	67	35	5
9	34	68	80	77	53	32	4	25	43	75	85	100	89	60	30
26	11	37	65	51	41	21	27	40	70	94	102	110	103	93	57
54	17	13	16	44	29	33	45	72	90	104	121	117	114	106	88
81	50	22	7	14	36	49	76	83	98	118	126	125	124	113	99

Fig. 28.2 Three different threshold matrixes design of $\theta = 45°$. **a** Threshold matrix A of $\theta = 45°$. **b** Threshold matrix B of $\theta = 45°$. **c** Threshold matrix C of $\theta = 45°$
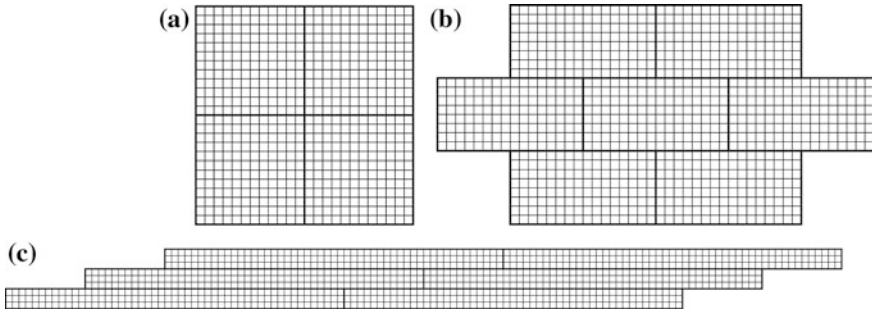
Fig. 28.3 Threshold matrixes distribution of different screening angle. **a** Threshold matrixes distribution of $\theta = 0°/90°$. **b** Threshold matrixes distribution of $\theta = 45°$. **c** Threshold matrixes distribution of $\theta = 14.04°/75.96°$

28.3   Experiment and Results

In this section, the program of matrix rotating screening algorithm is written in MATLAB to get image screened with special shaped dots, in which we hide and extract information using Photoshop CS5, and finally evaluate the hiding effect based on both human vision and structural similarity (SSIM).

28.3.1   Experimental Procedure

In this experiment, a grayscale image of 20 % at the size of 5 cm × 5 cm is chosen to create halftone image screened by the three different threshold matrixes designed in Fig. 28.2. In addition, 175l pi is chosen as screening line and 2100 dpi as output resolution in order to ensure the image quality.

First, the program of matrix rotating screening algorithm is written in MATLAB and the grayscale image of 20 % at the size of 5 cm × 5 cm is input to get a halftone image. Meanwhile, grayscale image of 50 % at the size of 5 cm × 5 cm is input to get a matching film.

Second, a new image *paper-cut* is imported into the halftone image in step 1 and a contour of the selected area in Photoshop CS5 is created, then the position of the dots in the selected area is moved away from the original dots to create hiding information.

Finally, the matching film in step 1 is imported into the halftone image with hidden information in step 2 to make *paper-cut* appear.

28.3.2 Results and Evaluation

Figure 28.4 shows the effect of halftone image screened by the three rotating threshold matrixes designed in Fig. 28.2, in which bowknot dots are created. Figure 28.5 shows the hiding and extracting effect of *paper-cut* in different halftone image, in which Fig. 28.5a, b is hiding and extracting effect of image screened with bowknot dots, while Fig. 28.5c, d is hiding and extracting effect of image screened with round dots as comparison.

By comparison, it is obvious that image screened with traditional round dots appears more texture than image screened with bowknot dots when hidden information, while both of them achieve a successful extracting effect. The prime reason is that round dot has the shortest perimeter, making it hard to contact at the edge when moving, thus forming blank area that can be noticed.

In additional, in order to prove that the newly created dots have more advantages than the traditional ones, structural similarity (SSIM) [14] is used to evaluate the image quality after hidden information, which is an image assessment measure that evaluate the similarity of original images and processed image. The calculation method is given by

$$\text{SSIM}(x, y) = \frac{(2\mu_x\mu_y + C_1)(2\sigma_x\sigma_y + C_2)}{(\mu_x^2 + \mu_y^2 + C_1)(\sigma_x^2 + \sigma_y^2 + C_2)} \tag{28.2}$$

where x is the original image, y is the processed image, μ_x, μ_y are the mean value of x, y, representing the brightness of image, σ_x, σ_y are variance of x, y, representing the contrast of image, C_1, C_2 are constants close to zero, in case of a zero denominator.

SSIM is between 0 and 1 and the result is 1 when two images are completely the same.
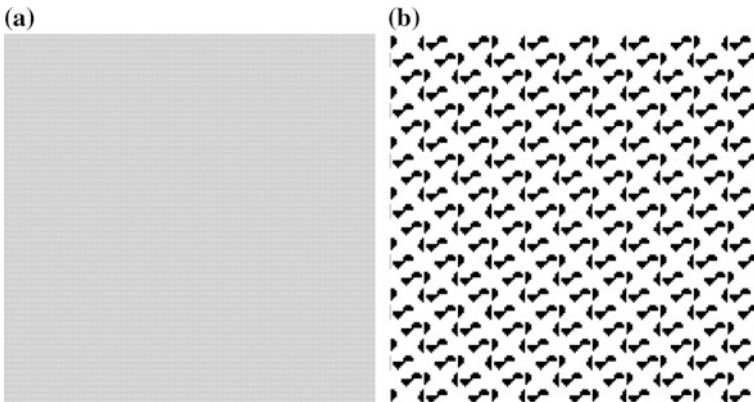
Fig. 28.4 Image screened by three rotating threshold matrixes. **a** Normal size. **b** Enlarged size
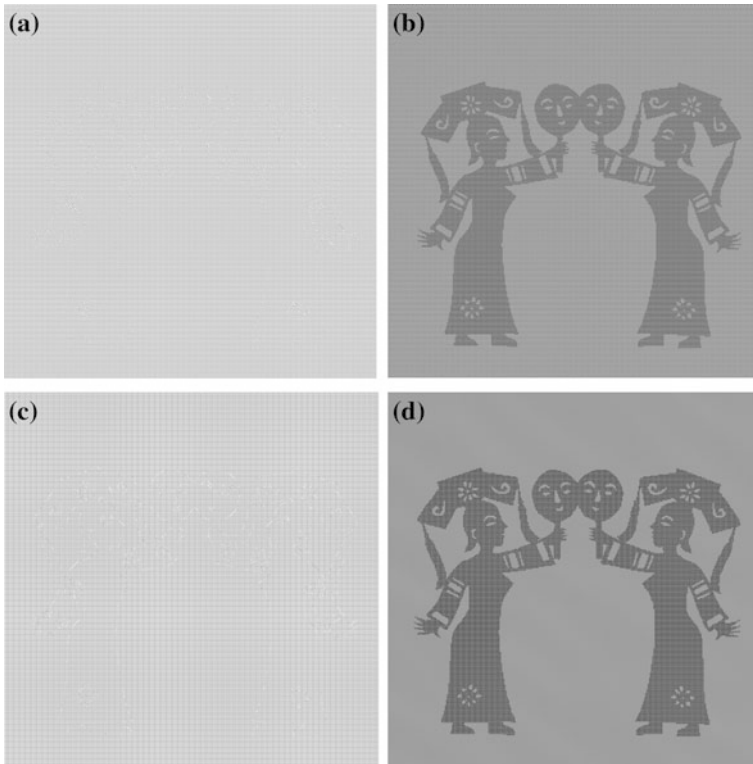
Fig. 28.5 Hiding and extracting effect of *paper-cut*. **a** Hiding effect of image screened with bowknot dots. **b** Extracting effect of image screened with bowknot dots. **c** Hiding effect of image screened with round dots. **d** Extracting effect of image screened with round dots

Table 28.1 Image assessment based on SSIM

Image type	Bowknot dots image with hidden information	Round dots image with hidden information
SSIM	0.9740	0.9655

Table 28.1 shows the image assessment result based on SSIM, the hiding effect of image screened with bowknot dots gets 0.9740 based on structural similarity (SSIM), while the hiding effect of image screened with traditional round dots gets 0.9655, demonstrating that image screened with bowknot dots created by rotating matrixes achieves a better hiding effect compared with traditional method.

28.4   Conclusions

In summary, a new algorithm of matrix rotating screening on the basis of threshold matrix screening principle is introduced, special shaped dot is created and image screened by this method is used to hide and extract information. A satisfying result is achieved through the hiding and extracting experiment in MATLAB and Photoshop CS5. The proposed method helps improve the safety factor of the image with hidden information due to special shaped dots that cannot be copied and helps reduce texture around the hidden information. The method contributes to information hiding technology based on halftone screening a lot and makes it more practical and economical for printing industry to apply anti-counterfeit technology to products.

References

1. Xu, G., & Tan, T. (2012). Survey of research on image halftone algorithm. *Computer Engineering and Science., 34*(12), 87–97.
2. Huang, L., & Duan, H. (2004). Research on progress in new digital screening technology. *Packaging Engineering, 25*(5), 24–26.
3. Bula, O., Sharma, G., & Monga, V. (2010). Orientation modulation for data hiding in clustered-dot halftone prints. *IEEE Transactions on Image Processing*, 2070–2840
4. Fu, M., & Au, O. (2012). Data hiding watermarking for halftone images. *IEEE Transaction on Image Processing, 11*(4), 477–484.
5. Rosen, J., & Javidi, B. (2001). Hiding images in halftone pictures. *Applied Optics, 40*(26), 3346–3353.
6. Liu, Z., Ren, L., & Yang, S. (2011). Application of AM screening in grating anti-counterfeit technology. *Packaging Engineering, 32*(21), 90–93.
7. Gong, Y., Zhang, Y., & Wang, K. (2008). Anti-counterfeiting of microstructure screens. *Packaging Engineering, 29*(3), 62–68.
8. Ren, L.-Y., Liu, Z., Wen, S.-S., et al. (2011). Application of random matrix pattern jitter screening in grating anti–counterfeit printing technology. *Packaging Engineering, 32*(13), 89–92.
9. Gong, Y., Zhang, Y., Liu, Z., et al. (2008). Anti-counterfeiting application of halftone screens. *Computer Engineering and Applications, 44*(22), 216–218.
10. Hao, F., & Deng, K. (2014). Halftone holographic anti-counterfeiting algorithm based on dot shape. *Packaging Engineering, 35*(9), 122–126.
11. Huang, M., & Liu, H. (2005). Selecting of the parameters of cylindrical lens sheet imaging in 3D printing. *Journal of Beijing Institute of Graphic Communication, 13*(1), 9–12.
12. Xu, J., & Chen, S. (2009). The design method of threshold matrix and principle for AM screening. *China Printing and Packaging Study, 1*(3), 38–42.

13. Xu, J., & Xu, Y. (2009). Research of screening factor in amplitude modulation screening. *China Printing and Packaging Study, 1*(6), 20–24.
14. Chu, J., Chen, Q., & Yang, X. (2014). Review on full reference image quality assessment algorithms. *Application Research of Computers, 31*(1), 13–22.

Chapter 29
An Improved SIFT Algorithm Based on Invariant Gradient

Da Li, Ruizhi Shi, Shenghui Li and Xiao Zhou

Abstract In order to make the feature descriptor stable for rotating, the SIFT (Scale Invariant Feature Transform) algorithm assigned a main direction for feature points and rotated the local image according to the main direction. This paper do some research on the rotating process of SIFT algorithm, and put forward a new algorithm based on invariant gradient. The defined pixels' gradient-invariant in the new algorithm is mainly relevant to the gray value of the nearest 8 pixels, and has nothing with the relative position of the 8 pixels around. The experimental results showed that collecting pixels' gradient-invariant statistics can effectively improve SIFT algorithm's computing speed.

Keywords Invariant gradient · Feature detection · SIFT

29.1 Introduction

As one of the hottest research field about computer vision, image recognition technology has been widely used in communications, medicine, archeology, industrial inspection, and so on. In the field of printing, the precision detection technology based on image recognition has become an essential part on the printing production line. In 1999, Professor Lowe put forward SIFT algorithm based on the invariant feature of local image (see [1, 2]), which behaved well with some image distribution such as rotation, scaling changes or illumination changes, then many scholars put forward some improved algorithm based on SIFT. Literature Two [3] introduced an improved SIFT algorithm with using LBP (local binary pattern) feature by comparing the pixels' gray level. Literature [4] simplified the process of Weighting feature descriptor and constructed RIT-SIFT descriptor through choosing concentric circular areas as described feature areas. Literature [5] posed a

D. Li (✉) · R. Shi · S. Li · X. Zhou
Zhengzhou Institute of Surveying and Mapping, Zhengzhou, China
e-mail: ldld2013@sina.com

method of reducing 128-dimensional SIFT descriptor to improve the algorithm's speed. Wan. X using the zero-crossing theory to improve the detected feature points (see [6]). Literature [7] improved SIFT algorithm by combining MSER (maximally stable extremal regions). As the main part of SIFT algorithm, the process of building SIFT feature descriptor costs the most time in SIFT algorithm, especially, the process of calculating the main direction of feature points and rotating the local image, which accounts for more than 40 % of the algorithm. This paper presents an improved SIFT algorithm based on invariant gradient (IG-SIFT). IG-SIFT algorithm can get rid of the process of calculating the feature points' main direction and rotating the local image in SIFT algorithm. Thus, it can be faster than SIFT algorithm.

29.2 Feature Point Detection

IG-SIFT algorithm has the same way as SIFT algorithm on detecting image feature points, which is based on the theory of scale space. The main steps are as follows:

Step 1 Build Gaussian image pyramid and a difference image pyramid
The process of building Gaussian image pyramid is mainly divided into Gaussian smoothing and down sampling. First, convert the source image to gray level image, then smooth the image with Gaussian method that is to say we can obtain a convolution image by multiplying the image with a Gaussian kernel. So if we use several Gaussian kernels with different scales, then we can obtain several convolution images in a group, and several group of images by down sampling the source image. That means we can get Gaussian image pyramid by down sampling and Gaussian smoothing the images alternately. Gaussian image pyramid includes several groups of images, and each group has several interval images. We can use difference of Gaussian function build DOG scale space, then obtain the difference of Gaussian images by doing subtraction between each next images in the same group of Gaussian image pyramid. Finally, using the difference of Gaussian images can build the difference image pyramid (Fig. 29.1).

Step 2 Detect the extremal points in the difference of Gaussian images, locate the points precisely with curve fitting method and remove the unstable points.

Each pixel must compare with its all neighboring pixels to see if its gray level is the highest among these pixels. The pixel should compare with the 8 pixels around in the same scale image and 18 (9×2) pixels in the next scale images to ensure the detected points are extremely big in both scale space and two- dimensional image space.

DOG operator has strong response at the edge of image, and is sensitive to noise, so after detecting the extreme points, we should use a three-dimensional quadratic

Fig. 29.1 Gaussian image pyramid
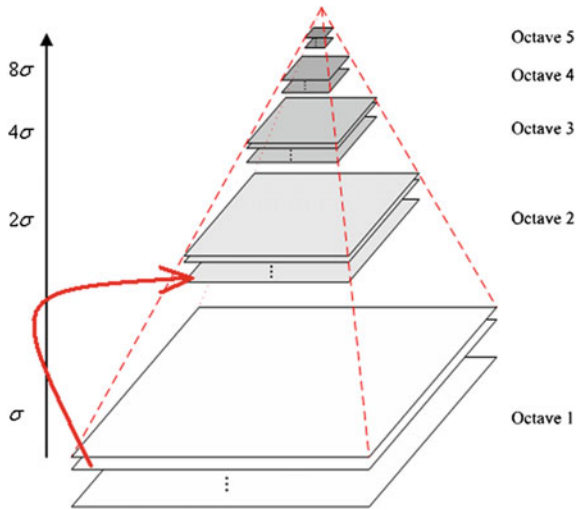
(second-order Taylor expansion) curve fitting method to locate the extremal points precisely. In the set of detected feature points, we can set a contrast threshold to eliminate those unstable feature points with low contrast. Because the feature points calculated by DOG operator which is located at the edge of image has larger principal curvature in the direction across the edge, so we can eliminate the extremal points which is uneasy to locate precisely at the edge of image by calculating Hessian matrix.

29.3   Invariant Gradient

29.3.1   Gradient

The pixel's gradient is defined as the variation of image's gray level in the direction of X axis and Y axis.

$$\text{grad } I(x, y) = \left(\frac{\partial I}{\partial x}, \frac{\partial I}{\partial y} \right) \tag{29.3.1}$$

How to calculate the direction of gradient is as follows:

$$m(x, y) = \sqrt{(L(x+1, y) - L(x-1, y))^2 + (L(x, y+1) - L(x, y-1))^2} \tag{29.3.2}$$

How to calculate the magnitude of gradient is as follows:

$$\theta(x, y) = \tan^{-1} \left[\frac{L(x, y+1) - L(x, y-1)}{L(x+1, y) - L(x-1, y)} \right] \tag{29.3.3}$$

The ordinarily defined gradient has no stability for rotation, and this paper constructed the feature descriptor by calculating invariant gradient which behaved better for rotation.

29.3.2 Invariant Gradient

29.3.2.1 Direction

How to calculate the direction of invariant gradient is as follows:

$$a_y = L(x, y+1) - L(x, y-1) \tag{29.3.4}$$

$$a_x = L(x+1, y) - L(x-1, y) \tag{29.3.5}$$

$$a_{xy} = L(x+1, y+1) - L(x-1, y-1) \quad a_x = L(x+1, y) - L(x-1, y) \tag{29.3.6}$$

$$a_{yx} = L(x-1, y+1) - L(x+1, y-1) \quad a_x = L(x+1, y) - L(x-1, y) \tag{29.3.7}$$

$L(x, y)$ is the gray level of pixel (x, y).

$$b = (b_1 + b_2)/2 \tag{29.3.8}$$

If $|a_y| > |a_x|$, $b_1 = a_x/a_y$, else $b_1 = a_y/a_x$;
If $|a_{xy}| > |a_{yx}|$, $b_2 = a_{yx}/a_{xy}$, else $b_2 = a_{xy}/a_{yx}$.
The direction of pixel's invariant gradient is defined as follow:

$$\theta = \tan^{-1}(b) + \pi/4 \tag{29.3.9}$$

Parameter θ's value ranges from 0 to $\pi/2$.

29.3.2.2 Magnitude

How to calculate the magnitude of invariant gradient is as follows:

$$c_1 = a_x^2 + a_y^2 \tag{29.3.10}$$

$$c_2 = a_{xy}^2 + a_{yx}^2 \qquad\qquad (29.3.11)$$

$$c = (c_1 + c_2)/2 \qquad\qquad (29.3.12)$$

The magnitude of pixel's invariant gradient is defined as follow:

$$m = \sqrt{c} \qquad\qquad (29.3.13)$$

29.4 IG-SIFT Feature Descriptor

29.4.1 Described Area

Divide the circular area that takes a feature point as center with a radius of 8 pixels into four concentric regions (see [8, 9]) with the interval of 2 pixels. As a whole, this concentric circular described area is largely the same with it in SIFT algorithm.

29.4.2 Weight Distribution

In fact, the pixels which are closer to the feature points have more influence to the feature points, so they should get larger weight. After calculating the direction and magnitude of invariant gradient for each pixel at the described area, multiply the magnitude with Gaussian weight.

$$\text{weight} = m \times \exp\left(-\frac{x_k^2 + y_k^2}{2\sigma}\right)/2\pi\sigma^2 \qquad\qquad (29.4.1)$$

x_k is the distance between a pixel and a feature point in the direction of X axis; y_k is the distance between a pixel and a feature point in the direction of Y axis; σ is the certain constant of Gaussian weighting function.

29.4.3 Build Descriptor

The described area selected in this article is the concentric circular areas that take a feature point as center separately with a radium of 2, 4, 6, 8 pixels. Collect statistics of the invariant gradient's direction and magnitude in the concentric circular ring area separately, and weight the magnitude with Gaussian function. Accumulate the pixels' magnitude of invariant gradient in nine directions with the interval of 10°

Fig. 29.2 Described area
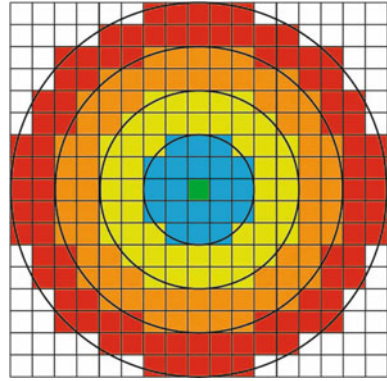
Fig. 29.3 Seed point
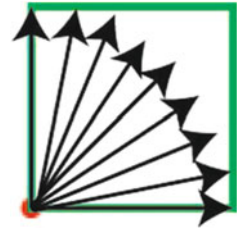
ranging from 0° to 90°. For each circular ring area, we can draw a seed point whose descriptor is constructed of the nine-dimensional feature vector.

$$D_i = (d_{i1}, d_{i2}, d_{i3}, \ldots, d_{i9}) \quad i = 1, 2, 3, 4; \tag{29.4.2}$$

As is shown in Fig. 29.2, we marked the concentric circular ring area 1, 2, 3, 4 from into outside. The final feature vector of IG-SIFT descriptor is as follows:

$$D = (D_1, D_2, D_3, D_4) \tag{29.4.3}$$

D is the 36-dimensional feature vector (Fig. 29.3).

29.4.4 Normalize the Descriptor

In order to reduce the impact of Illumination, the algorithm needs to normalize the obtained feature vector. The accumulated magnitude in each direction of histogram should be smaller than a certain threshold. This article sets it 0.2.

How to normalize the feature vector is as follows:

$$l_j = w_j / \sqrt{\sum_{i=1}^{36} w_i^2} \quad j = 1, 2, 3 \ldots 36 \tag{29.4.4}$$

$W = (w_1, w_2, w_3, \ldots, w_{36})$ is the 36-dimensional feature vector; $L = (l_1, l_2, l_3, \ldots, l_{36})$ is the normalized feature vector.

29.5 Match Image Feature

The way to recognize the objective image is through comparing the feature vectors of the reference image and objective image.

The feature points' descriptor of reference image is defined as follows:

$$R_i = (r_1, r_2, r_3, \ldots, r_{36}) \tag{29.5.1}$$

The feature points' descriptor of objective image is defined as follows:

$$S_i = (s_1, s_2, s_3, \ldots, s_{36}) \tag{29.5.2}$$

The way to measure the distance of two feature points is as follows:

$$d(R_i, S_i) = \sqrt{\sum_{j=1}^{36} (r_{ij} - s_{ij})^2} \tag{29.5.3}$$

First calculate the Euclidean distance between a feature point in objective image and each feature point in reference image. Then find the shortest distance $d_{\min}$ and the second shortest distance $d_{c\min}$, and make certain for the relative threshold T (T's value is usually ranging from 0.6 to 0.8). If $d_{\min}/d_{c\min} < T$, the algorithm deemed the two feature points match successfully.

29.6 Experiment and Conclusions

29.6.1 Matching Performance

As is shown in the following pictures, the first group of images is the experimental images for rotation. The second group is for scale change problem. The third group is aiming at the situation of illumination changes (Fig. 29.4).

We chose 10 images and distorted the images by rotating them, changing their scales or changing their illumination. Then did a experiment of detecting and

Fig. 29.4 Matching graph

SIFT algorithm　　　　　　　　IG-SIFT algorithm
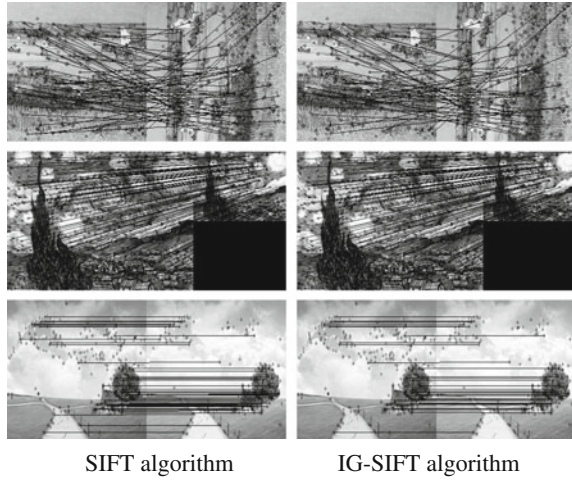
matching the feature points separately with SIFT algorithm and IG-SIFT algorithm, and contrast their matching rate and correct matching rate.

The matching rate is defined as follows:

$$MR = NS/NT \tag{29.6.1}$$

The correct matching rate is defined as follows:

$$CMR = NC/NS \tag{29.6.2}$$

Table 29.1 matching performance

Image	SIFT MR (%)	SIFT CMR (%)	IG-SIFT MR (%)	IG-SIFT CMR (%)
1	21.1	91.1	17.3	88.2
2	30.2	85.2	26.0	86.1
3	10.3	88.9	8.3	90.1
4	15.1	92.3	11.0	88.2
5	8.7	87.5	6.7	84.7
6	32.1	86.3	26.2	84.1
7	14.8	88.5	12.8	87.9
8	25.4	90.2	19.6	81.3
9	23.8	91.4	20.4	87.7
10	32.1	84.2	26.3	84.3
Average	21.4	88.6	17.5	86.3

From the results, we can see that IG-SIFT algorithm is a little poorer about MR and CMR than SIFT algorithm. The average difference of the 10 images is 3.9 % about MR and 2.3 % about CMR

Table 29.2 Computing speed

Image	NT	SIFT MN	IG-SIFT MN	SIFT time(ms)	IG-SIFT time(ms)
1	192	41	34	912	507
2	314	65	52	1516	798
3	542	116	95	2632	1316
4	723	154	126	3143	1497
5	950	190	156	3763	1710

NT: the total number of feature points in objective image
MN: the number of feature points matching successfully

MR presents the matching rate, CMR presents the correct matching rate, NC is the number of correctly matching feature points, NT is the total number of feature points in objective image, NS is the number of successfully matching feature points. We sorted out an experimental table as follows through collecting the 10 images' experimental data (Table 29.1).

29.6.2 Speed

IG-SIFT and SIFT algorithm have the same process in detecting the feature points, their difference is just about constructing the feature descriptor and matching the feature points. SIFT algorithm has an additional process of calculating the feature points' main direction and rotating the local image, however, IG-SIFT algorithm costs more time in calculating invariant gradient. In addition, SIFT descriptor has 128 dimensional feature vector, however, IG-SIFT descriptor is only 36 dimension that means IG-SIFT costs less time in matching the feature points. This article did experiment with five groups of images. The results are as follows:

Analyzing from the above data, we can see that IG-SIFT algorithm takes nearly half time of SIFT without big difference about NT and MN. So IG-SIFT algorithm is much faster than SIFT, and IG-SIFT have no big difference with SIFT about matching performance. Finally, we can draw a conclusion that IG-SIFT algorithm is more efficient than SIFT on detecting image feature points (Table 29.2).

References

1. Lowe, D. G. (2004). Distinctive image features from scale invariant keypoints. *International Journal of Computer Vision, 2*(60), 91–110.
2. Lowe, D. G. (1999). Object recognition from local scale- invariant features. In *Proceedings of the 7th IEEE International Conference on Computer Vision, Kerkyra* (pp. 1150–1157). Greece: IEEE.

3. Zheng, Y. B., Huang, X. S., & Feng, S. J. (2010). An image matching algorithm combining SIFT with LBP which is invariant for rotation. *Journal of Computer Aided Design and Graphics, 22*(2), 287–292.
4. Tang, C. W., & Xiao, J. (2012). An improved SIFT descriptor with analysis. *Journal of Wuhan University, 37*(1), 11–16.
5. Yang, K., & Sukthankar, R. (2004). PCA-SIFT: A more distinctive representation for local image descriptors. In *The IEEE Conference on Computer Visionand Pattern Recognition, Washington, DC, USA*.
6. Wan, X., Zhang, Z. X., & Ke, T. (2013). An improved SIFT algorithm based on the zero crossing theory. *Journal of Wuhan University, 38*(3), 270–273.
7. Mo, H. Y., & Wang, Z. P. (2011). A feature detection algorithm combining MSER and SIFT. *Journal of Dongbei University, 37*(5), 624–628.
8. Wang, S. (2013). *SIFT based image matching algorithm research*. MS Thesis, Xi'an Electronic technology University.
9. Feng, J. (2010). *The research and improvement of SIFT*. MS Thesis, Jilin University.

Chapter 30
Halftone Image Quality Evaluation Based on Reconstruction Index Model

Xiao Zhou, Ruizhi Shi, Da Li, Shenghui Li and Yusheng Wang

Abstract Halftone algorithm is the medium of the conversion from continuous digital image to scattered dot image, and it is the core technique of RIP prepress. Different algorithms have different characters on image nonlinear reconstruction, while corresponding halftone images have different effects. The advantages and disadvantages of halftone algorithm will determine printing images' output quality. In this paper, founded reconstruction index models are used to make objective evaluation on halftone algorithms. Quantitative study is performed on the aspect of gray level index, contrast level index, and image entropy difference. Frequency domain analysis and power spectrum analysis are also performed on respective halftone images. Through halftone image quality evaluation, advantage and disadvantage comparison of halftone algorithms based on different indexes is obtained, which provides reference for the amelioration of halftone algorithm and finally improves vision quality of printing image.

Keywords Reconstruction index · Halftone image · Image quality · Objective evaluation · Frequency domain analysis

30.1 Introduction

In image processing, digital halftoning is the technique to realize the transformation from digital image to halftoning image, which reproduces original image tone and color through binary equipment. Halftone technique depends on algorithm. Through nonlinear transformation of different algorithms, it finally obtains halftone images with different dot distribution. Therefore, algorithm is the core of halftone

X. Zhou (✉) · R. Shi · D. Li · S. Li · Y. Wang
Zhengzhou Institute of Surveying and Mapping, Zhengzhou, China
e-mail: zhou_laoge@163.com

technique. Algorithm quality will influence halftone image quality and visual effect. Since the generation of digital halftoning, various algorithms such as pattern dither, error diffusion, flat noise, blue noise, etc. are invented by people. Based on these algorithms, many ameliorated algorithms are created [1]. According to dot distribution shape, halftone technique can be divided into three groups, AM halftoning, FM halftoning, and Hybrid halftoning. They have different characters to reproduce and express image. Evaluating halftone image quality of different halftone algorithms is the method to test and compare halftone algorithms' characters, which can provide reference for algorithm development and finally improve image quality. In this paper, halftone algorithms are evaluated objectively under several basic evaluation models. Algorithms' gray level index, contrast level index, and image entropy difference are researched quantificationally. Meanwhile, frequency domain analysis and power spectrum analysis are done on the generated halftone images.

30.2 Evaluation Model Foundation of Halftone Reconstruction

Applying some objective method to evaluate halftone image can test and reflect halftone algorithm's capability objectively, which is not influenced by subjective factor. Objective evaluation's basic thought is to test and calculate the difference between halftone image and original image. In the aspect of image gray level, contrast level index, image entropy difference, frequency domain, and power spectrum, halftone algorithms and images are tested and evaluated.

30.2.1 Evaluation Model of Reconstruction Accuracy

The total level of halftone processing can be reflected on the visual quality of binary image, which should meet two conditions. First, gray level of halftone image's single part should be equal to original image's single part as much as possible. Second, halftone image should have feasible contrast level index. The two indexes are evaluated through gray level evaluation and contrast level index evaluation [2].

30.2.1.1 Gray Level Evaluation Model

Set P_m as gray level evaluation function. Original image is denoted as $g(x, y)$. Single $g(x, y)$ value stands for the gray level of the original pixel. After normalization, pixel gray level satisfies $0 \leq g(x, y) \leq 1$. Halftone image is denoted as

$b(x, y)$. Single $b(x, y)$ value stands for halftone image's pixel gray level. According to the characters of halftone image, $b(x, y)$ value should be 0 or 1, in which, 1 stands for black pixel, 0 stands for white pixel, as Formula 30.1 shows.

$$P_m = \sum_B \frac{1}{N_b^2} |g(x, y) - b_G(x, y)| \tag{30.1}$$

In Formula 30.1, B stands for the adding operation carried out in image's specific part. $b(x, y)$ is the part average gray level in the corresponding zone of the halftone image. N_b^2 is the pixel amount contained in the specific part [3]. Evaluation function P_m stands for the difference between the gray level of the original image's specific part and halftone image's corresponding part average gray level. The lower the P_m value, the closer the halftone image's gray level to the original image's gray level will be.

When the relationship between original image pixel and halftone image pixel is one-to-many, set halftone unit to contain $n \times n$ recorder grids. Original pixel gray level is A. According to gray level evaluation model (1), gray level evaluation model (2) is obtained.

$$P_m = \sum_B \frac{1}{N_b^2} \left| \frac{A}{256} - [A \cdot n^2 / 256] / n^2 \right| \tag{30.2}$$

30.2.1.2   Contrast Level Index Evaluation Model

Contrast level index evaluation function is used to evaluate visual contrast difference between original gray image and halftone image, which is denoted by P_c function, as Formula 30.3 shows. The lower the P_c value, the higher the contrast level index will be, and the greater the difference between original gray image and halftone image will be [4]. In this aspect, the higher the P_c value, the closer the halftone image to the original gray image will be.

$$P_c = \sum_B \frac{1}{N_b^2} |[g(x, y) - \bar{g}(x, y)] - b(x, y)| \tag{30.3}$$

In Formula 30.3, $\bar{g}(x, y)$ is the average value of pixel part $g(x, y)$. According to the definition of part average gray level, contrast level index model (4) under the relationship between original image pixel and halftone image pixel is obtained as one-to-many.

$$P_c = b_G(x, y) = [A \cdot n^2 / 256] / n^2 \tag{30.4}$$

30.2.2 Foundation of Reconstruction Image's Entropy Difference Model

Set the average gray value j of a certain pixel's neighborhood pixel as spatial signature value. The pixel's gray value is i, i and j constitute two tuples (i, j). Meanwhile, $f(i, j)$ is defined as the frequency of the two tuples (i, j). P_{ij} is defined as the comprehensive feature weight, in which i and j satisfy the condition $0 \leq i, j \leq 255$. P_{ij} is shown as Formula 30.5.

$$P_{ij} = f(i,j)/MN \qquad (30.5)$$

Define two-dimensional entropy through the weight P_{ij}.

$$H = \sum_{i=0}^{n} p_{ij} \log_2 p_{ij} \qquad (30.6)$$

Define image entropy difference through one-dimensional entropy which expresses the gathering feature of the gray distribution. Entropy difference is the absolute value of the difference between original image entropy and halftone image entropy, which reflects the ability of halftone algorithm to obtain image information. The closer the entropy difference to value 0, the more information the halftone image will obtain from the original image. The information amount of the two images will be closer [5]. The discrepancy between halftone image and original image will be smaller. Set the gray distribution probability of original image and halftone image as p_i and q_i, respectively. Then the image entropy difference H_c is shown as Formula 30.7.

$$H_c = \left| \sum_{i=0}^{n} p_i \log_2 p_i - \sum_{j=0}^{n} p_j \log_2 p_j \right| \qquad (30.7)$$

30.3 Experiment and Analysis

30.3.1 Experiment Content

30.3.1.1 Halftone Algorithm and Experiment Objects Confirmation

Evaluation objects are Bayer pattern dither, error diffusion, and AM halftoning. In the experiment, 8×8, 10×10, 14×14, and 16×16 are chosen as the halftone unit accuracy. The experiment chooses color patches with symmetrical gray level. Gray levels are 25, 50, 75, 100, 125, 150, 175, 200, 225, and 250. For simple statistics calculation, set each color patches' size as 8×8 pixel, as Fig. 30.1 shows. Choose
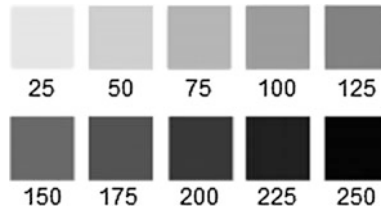
Fig. 30.1 Color patch scale

Fig. 30.2 Original image
goose and *pepper*

original images *goose* and *pepper*, as Fig. 30.2 shows. The image *goose* has abundant color and relatively big tone contrast. The image *pepper* also has abundant color, which is used to compare.

30.3.1.2   Experiment Items

Some experiments are performed as follows:

(1) Use Bayer pattern dither, error diffusion, and AM halftoning to screen color patches. Bayer pattern dither applies extended 8×8 dimension threshold matrix and uses shift algorithm to realize threshold comparison. Error diffusion applies Floyd–Steinberg filter and uses median method to choose threshold. AM halftoning applies round shape dot, screen angle is set as 0°, halftone unit accuracy is set as 8×8, 10×10, 14×14, and 16×16. Do statistics calculation on the screened experiment color patches and get the data of gray level evaluation, contrast level index, and image entropy difference.

(2) Use Bayer pattern dither, error diffusion, and AM halftoning to screen original image *goose* and *pepper* with the same method as item 1. And halftone images under the three algorithms are obtained.

(3) Do Fourier transform on the *goose* and *pepper* halftone images and get frequency domain images and power spectrum images, and their characters are analyzed. In which, AM halftoning only choose 16×16 halftone unit accuracy.

30.3.2 Evaluation Result

30.3.2.1 Statistics Analysis of Color Patch Evaluation Index

After model calculating and data statistics, gray level evaluation index P_m value, contrast level evaluation index P_c value, and image entropy difference H_c value are obtained, as Tables 30.1, 30.2, and 30.3 show, in which I, II, and III are Bayer dither, error diffusion, and AM halftoning. The four numbers under AM halftoning are halftone unit accuracy 8×8, 10×10, 14×14, and 16×16.

According to the statistics results in Tables 30.1, 30.2, and 30.3, curve images are drawn. In each curve image, abscissa is gray level, and ordinate is index value, as Fig. 30.3 shows. A, B, C1, C2, C3, and C4 represent Bayer dither, error diffusion, and AM halftoning with 8×8, 10×10, 14×14, and 16×16 halftone unit accuracy.

(1) The index values of the two dither algorithms are higher than AM halftoning, which illustrates that two dither algorithms' halftone image is less closer to original image in gray level than AM halftoning. Two dither algorithms lose image tone while the AM halftoning will lose image tone in all the halftone unit accuracy other than 16×16. The higher the halftone unit accuracy is, the less loss will occur, but the extent of the tone loss is lower than the two dither algorithms. The index value of Bayer dither is lower than error diffusion in the gray level intervals of 0–135 and 180–240 while higher in other intervals. The AM halftoning index curve waves are in different gray level intervals, thus different halftone unit accuracies in different tones have different abilities to reproduce original image gray level.

Table 30.1 Gray level evaluation index P_m value

Gray level	25	50	75	100	125
I	0.011	0.055	0.043	0.016	0.050
II	0.051	0.070	0.059	0.078	0.098
Gray level	150	175	200	225	250
I	0.148	0.121	0.031	0.027	0.023
II	0.086	0.090	0.078	0.051	0.008

Gray level	25				50			
III	0.004	0.008	0.001	0	0.007	0.005	0.001	0
Gray level	75				100			
III	0.012	0.003	0.008	0	0	0.001	0.003	0
Gray level	125				150			
III	0.004	0.008	0.003	0	0.008	0.006	0.004	0
Gray level	175				200			
III	0.012	0.004	0.005	0	0	0.001	0	0
Gray level	225				250			
III	0.004	0.005	0.003	0	0.008	0.007	0.003	0

Table 30.2 Contrast level evaluation index P_c value

Gray level	25	50		75	100		125
I	0.109	0.141		0.250	0.375		0.438
II	0.047	0.125		0.234	0.313		0.391
Gray level	150	175		200	225		250
I	0.438	0.563		0.750	0.906		1.000
II	0.5	0.594		0.703	0.844		0.984
Gray level	25				50			
III	0.094	0.090	0.097	0.098	0.188	0.190	0.194	0.195
Gray level	75				100			
III	0.281	0.290	0.291	0.293	0.391	0.390	0.388	0.391
Gray level	125				150			
III	0.484	0.480	0.485	0.488	0.578	0.580	0.582	0.586
Gray level	175				200			
III	0.672	0.680	0.679	0.684	0.781	0.780	0.781	0.781
Gray level	225				250			
III	0.875	0.870	0.878	0.879	0.969	0.970	0.974	0.977

Table 30.3 Image entropy difference H_c value

Gray level	25		50	75	100		125
I	0.349		0.398	0.500	0.531		0.522
II	0.207		0.375	0.491	0.524		0.530
Gray level	150		175	200	225		250
I	0.522		0.467	0.311	0.129		0
II	0.500		0.447	0.357	0.207		0.022
Gray level	25				50			
III	0.321	0.312	0.326	0.329	0.454	0.455	0.459	0.459
Gray level	75				100			
III	0.514	0.518	0.519	0.519	0.529	0.530	0.530	0.529
Gray level	125				150			
III	0.506	0.508	0.507	0.505	0.457	0.452	0.455	0.452
Gray level	175				200			
III	0.386	0.378	0.380	0.375	0.278	0.280	0.279	0.278
Gray level	225				250			
III	0.169	0.175	0.165	0.164	0.044	0.043	0.036	0.033

(2) Contrast level evaluation index of all algorithms are progressive increase curves. In the gray level interval of 0–255, it increases along with the gray level, thus one single algorithm has different contrast level difference in different gray tone. The higher the gray level is, the bigger the contrast level difference will be. The index values of two dither algorithms are higher than AM halftoning algorithm, thus the difference in contrast level difference
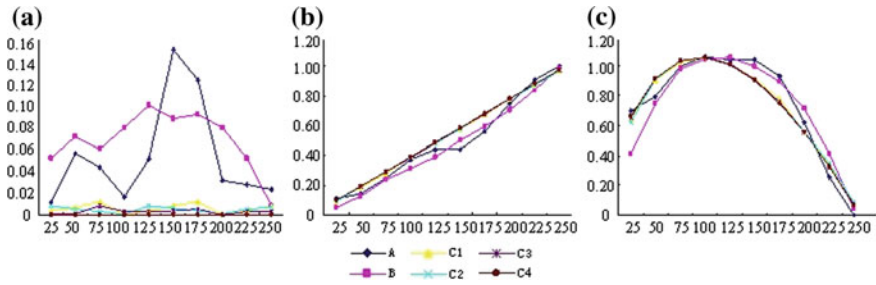
Fig. 30.3 Basic indexes evaluation curve images. **a** Gray level evaluation index. **b** Contrast level evaluation index. **c** Image entropy difference

between original image and halftone image obtained from the two dither algorithms is bigger than AM halftoning algorithm. The smaller the contrast level difference is, the smaller the visual difference between original image and halftone image will be. Therefore, the halftone image generated by AM halftoning is closer to original image in visual effect. In the gray level interval of 0–255, the index value of Bayer dither is higher than error diffusion, thus halftone image generated by error diffusion is closer to original image than Bayer dither.

(3) Image entropy difference of these algorithms increases with the increased gray level. When the value gets the maximum, it starts to decrease. The starting values are all higher than 0.4, the minimum values are all close to 0. With the increasing image entropy difference, halftone image's ability to obtain information from original image gets stronger. When the entropy difference gets to the maximum, the ability starts to get weak. In the gray level intervals of 0–110 and 130–180, image entropy difference of Bayer dither is bigger than error diffusion while smaller in other gray level intervals, which illustrates that error diffusion can get more information from original image and has stronger ability to get information than Bayer dither in gray level intervals of 0–110 and 130–180, and halftone image is closer to original image. In the gray level intervals of 0–30 and 100–210, image entropy difference of Bayer dither is bigger than AM halftoning while smaller in other gray level intervals, which illustrates that AM halftoning can get more information from original image and has stronger ability to get information than Bayer dither in gray level intervals of 0–30 and 100–210, and halftone image is closer to original image. In the gray level intervals of 105–240, image entropy difference of error diffusion is bigger than AM halftoning while smaller in other gray level intervals, and they are close in the gray level interval of 240–255, which illustrates that AM halftoning can get more information from original image and has stronger ability to get information than error diffusion in gray level intervals of 105–240, and the ability is close in the gray level interval of 240–255, and halftone image is closer to original image.

30.3.2.2   Halftone Image and Frequency Domain Analysis

Use Bayer dither, error diffusion, and AM halftoning to screen the M plate image of the experiment object in Fig. 30.2. As Fig. 30.4 shows, (a1) and (a4) are halftone images of Bayer dither, (a2) and (a5) are halftone images of error diffusion, (a3) and (a6) are halftone images of AM halftoning with halftone unit accuracy 16×16. Do Fourier transform on *goose* halftone image and then get frequency domain images and power spectrum images. As Fig. 30.4 shows, (b1) and (b4) are halftone images of Bayer dither, (b2) and (b5) are halftone images of error diffusion, (b3) and (b6) are halftone images of AM halftoning with halftone unit accuracy 16×16.

Halftone image of AM halftoning is more elaborate than two dither algorithms. Bayer dither has fixed mode added on the image. Bayer dither gets black and white dots through threshold value comparison, in which process, error is abandoned. Tone jump exists between black and white dots, which results in high frequency prominent in the frequency domain image. While the error generated from error diffusion through threshold value comparison diffuses to pixels around which one can obtain elaborate dots and relatively small tone jump. AM halftoning has more exposure dots and more data amount. Therefore, its frequency domain image has different color from the two dither algorithms. From the frequency domain images, AM halftoning is more elaborate and accurate and has better detail reproduction
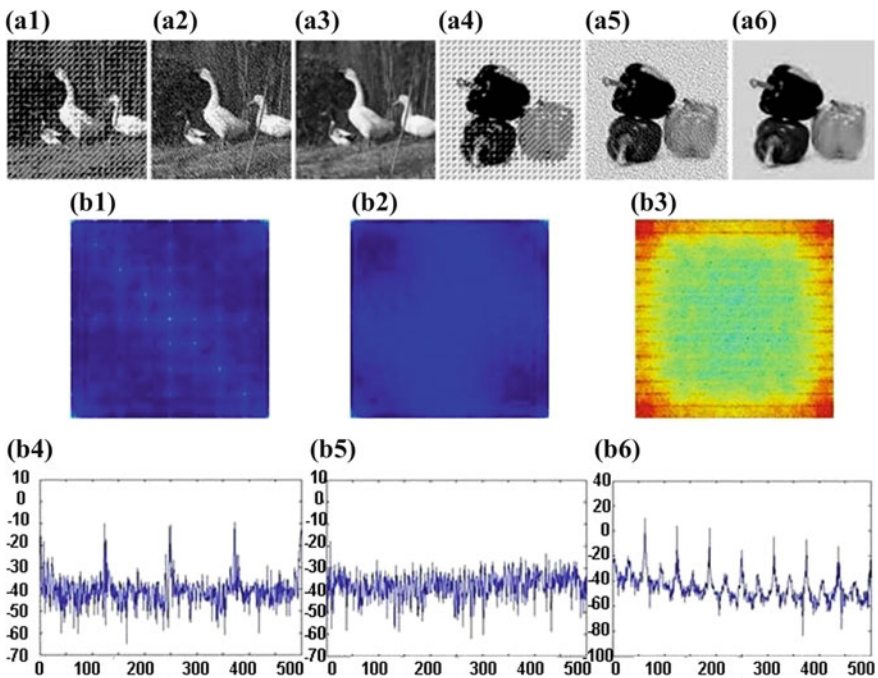

Fig. 30.4 Halftone images, frequency domain images, and power spectrum images of different algorithms

ability. In the power spectrum images obtained from periodogram method, power spectrum curve of AM halftoning is smoother than the two dither algorithms and has smaller average fluctuation.

30.4   Conclusions

Digital halftone quality evaluation is an important way to test whether halftone algorithm is good or not. On the basis of founded reconstruction index model, this paper does objective evaluation on halftone algorithms. On the aspect of gray level evaluation index, contrast level evaluation index, and image entropy difference, halftone images are researched quantificationally, meanwhile, halftone image's frequency domain character and power spectrum character are researched. Through comparison and analysis, advantage and disadvantage of each halftone algorithm are obtained, which can provide reference for the improvement of digital halftone technology.

References

1. Wan, X., Xie, D., & Jinlin, X. (2006). Quality evaluation of halftone by halftoning algorithm based on adaptive method. *Geomatics and Information Science of Wuhan University, 31*(9), 765–768.
2. Gao, S., & Song, X. (2008). Analysis of hybrid screening technology. *Digital printing, 5*, 42–43.
3. Zhou, X., Shi, R., & Sun, B. (2013). Research of reproduction characteristic based on FM screening map printing. *China Printing and Packing Study, 2*(5), 35–40.
4. Xie, S., & Cheng, G. (2009). Comparison analysis of digital screening technology. *Printing Magazine, 10*, 39–42.
5. Jones, P. R. (1994). Evolution of halftoning technology in the United States patent literature. *J Electron Imaging, 3*(3), 257–275.

Chapter 31
The Comparison of Two Image Matching Algorithms Based on Real-Time Image Acquisition

Shenghui Li and Ruizhi Shi

Abstract Compared with traditional printing, mobile phone device is easier to carry and has richer appearance of data presentation. For traditional printing, combining traditional printing with mobile phone to express more information which contained in the prints has become a new development direction. Matching the image acquired by mobile phone camera from traditional prints, if the matching is successful, the mobile phone will display animation, music, or video which associated with the print content. Hence, image matching algorithm plays a vital role in this process. Due to the constant need for real-time computation of the image, and limited capabilities of mobile devices, the matching algorithm's speed, accuracy, and efficiency should be the first priority. This paper combines the FAST feature point's detection algorithm with the FREAK feature point's description algorithm to accomplish the function of detecting feature points. Then, the two algorithms were compared in different state. Experimental results show that ORB has high matching accuracy with slower speed. The FREAK's speed is faster, and the accuracy performance can satisfy the demand of image matching.

Keywords Cellphone · Real-time · Matching algorithm · ORB · FREAK

31.1 Introduction

In recent years, mobile phone is convenient to carry and has richer data presentation, thus, it has become a necessity in people's daily life to some extent. Meanwhile, traditional paper, despite of its lower costs, can only display information limited to the content printed on the paper, which has not been able to meet

S. Li (✉) · R. Shi
Zhengzhou Institute of Surveying and Mapping, Zhengzhou, China
e-mail: lishenghui2006@126.com

R. Shi
e-mail: ruizhishi@sina.com

the diverse needs of people. Therefore, combining traditional printing with mobile phone to express more information which contained in the prints has become a new development direction.

In order to combine traditional print and mobile phones, the relationship between the mobile phone and the printing image should be established first. Mobile phones uses the camera to scan the printed image for matching, if the matching is successful, the mobile phone will display animation, music, or video associated with the print content, then the user can interact with the 3D animation using touch gestures. The image matching algorithm plays a vital role in this process. Due to the constant need for real-time computation of the image, and limited capabilities of the mobile devices, the matching algorithm's speed, accuracy, and efficiency should be emphasized. However, traditional SIFT and SURF algorithms, although the accuracy are higher, are not suitable for mobile phone equipment due to the large amount of calculation, so both of them cannot meet the needs of real-time matching.

Both of FREAK and ORB algorithms have high speed, but FREAK cannot detect the location of feature points. Therefore, making reference to the thought of the FAST feature point's detection algorithm of the ORB algorithm, this paper combines it with the FREAK feature point's description algorithm to accomplish the function of detecting feature points for FREAK algorithm. Then, the two algorithms are transplanted to mobile device for comparing the matching effect in different state (the illumination state, the rotation state, and the perspective distortion state.) Finally, detailed comparison and analysis are carried out according to the experimental results.

31.2   Algorithm Analysis

31.2.1   FAST Detector

Feature points detection of ORB (Oriented Brief) algorithm is to detect feature points by FAST (Features From Accelerated Segment Test) corner detection algorithm. The idea of FAST algorithm is to define a region, which is usually a circular area, and takes any point in the image as the center of the circle, marked as point M, then compare the gray value of point M with that of other 16 points in the neighborhood [1].

$$|m - P_i|\rangle \Delta d \quad (1 \le i \le 15) \tag{31.1}$$

In Formula 31.1, m represents the gray value of point M, P_i represents the gray value of each point in the neighborhood, and Δd represents the intensity threshold.

If the absolute value of the difference between m and P_i is more than, Δd record as a point and take the point M as corner point when the number of points like this are more than n. After experimental comparison, we use FAST-9 (n equals 9) in this algorithm, which has good performance [2].

Though Fast corner detection algorithm has high speed, the test results do not have rotation invariance. In order to solve this problem, an efficient approach for computing orientation needs to be added. Orientation by intensity centroid, a relatively simple but effective method is used by the ORB algorithm. Intensity centroid assumes that an offset existing between corner and its centroid, this offset can be used to indicate an orientation. This approach calculates the position of centroid in the neighborhood S, and then constructs a vector from the corner's center M to the centroid [3], the moment of a patch defined as Formula 31.2.

$$m_{pq} = \sum_{x,y} x^p y^q I(x, y) \tag{31.2}$$

$(x, y) \in S$, $I(x, y)$ represents the gray value. From Formula 31.2, the centroid can be found as:

$$C = \left(\frac{m_{10}}{m_{00}}, \frac{m_{01}}{m_{00}} \right) \tag{31.3}$$

We can construct a direction vector from the corner's center M to the centroid, namely $\overrightarrow{MC}$, then the orientation of the patch simply is:

$$\theta = \arctan\left(\frac{m_{01}}{m_{10}} \right) \tag{31.4}$$

31.2.2 FREAK Descriptor

FREAK (Fast Retina Key-point) descriptor and BRIEF descriptor are similar, both of which are binary descriptors. Unlike the latter, the former take the working principle of human's retina into consideration. As shown in Fig. 31.1, human's retina area can be divided into Fovea, Parafovea and Perifovea according to the distribution of the cone cells. And different areas have different characteristics, as shown in Table 31.1.

The ORB algorithm is to implement equivalent calculation for all regions in the image. The method of FREAK descriptor is used to carry out denser calculation in the fovea, but fewer calculations in the Parafovea and Perifovea respectively, as shown in Fig. 31.2. In this figure, the FREAK sampling mode is similar to the visual perception of retina, and each circle represents these corresponding regions are operated by Gaussian kernel function. With a small amount of calculations for these regions farther away from center, this method can reduce the computational complexity and improve computing speed based on the assurance of human eyes' information identification [4, 5].

Fig. 31.1 Retina areas
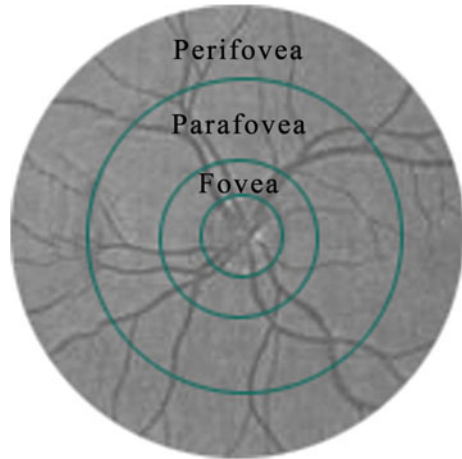
Table 31.1 Regional characteristics of retina

Areas	Characteristic
Fovea	Visual angle <1°, high resolving power, identify information directly
Parafovea	1°< Visual angle <5°, Low resolving power, eye movement required to identify information
Perifovea	Visual angle >5°, Minimum resolving power, head movement required to identify information

Fig. 31.2 FREAK sampling mode
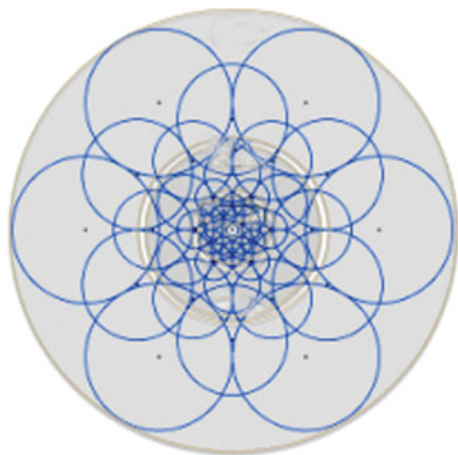
FREAK algorithm could describe the feature points but cannot detect the location of feature points, thus, making reference to the thought of the FAST feature point's detection algorithm of the ORB algorithm, this paper combines the FAST

feature point's detection algorithm with the FREAK feature point's description algorithm to accomplish the function of detecting feature points for FREAK algorithm. Based on the working principle of human's retina, the FREAK algorithm designs different sampling mode according to the different resolving power in human retina. Those regions with higher resolving power will conduct a large amount of calculations, whereas, those with lower resolving power will conduct a small amount of calculations. This method can reduce the computational complexity of information and improve computing efficiency on the basis of having enough quantity of information sampling.

31.3 Performance Evaluation

This paper experiment the FREAK algorithm and the ORB algorithm in different state, the normal state, the illumination state, the rotation state, and the perspective distortion state, as shown in Fig. 31.3. In this figure, the left image is the original image, and the right image is the captured image by cell phone camera.

The above matching results (as shown in Figs. 31.3, 31.4, 31.5 and 31.6) show that, compared with the ORB algorithm, the new algorithm, which combines the FAST algorithm with the FREAK algorithm, although has some error match, obviously, can obtain more correct matching pairs. It is known that as the number of correct matching pair's increases, the performance of the matching process is enhanced. As shown in Fig. 31.7, each matching pair from FREAK takes less matching time than ORB algorithm.

Fig. 31.3 Matching comparison of the normal state

Fig. 31.4 Matching
comparison of the
illumination state

Fig. 31.5 Matching
comparison of the rotation
state
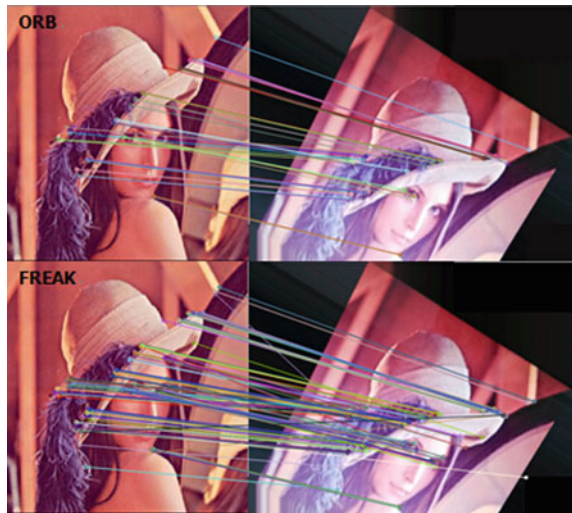
For the description of image feature points, ORB algorithm improves BRIFF while FREAK takes the working mechanism of human retina into consideration. For the amount of overall computing, FREAK algorithm conduct a small amount of calculations in the regions with lower resolving power. Meanwhile, the ORB algorithm is to implement equivalent calculation for all regions in the image.

Compared with ORB algorithm, FREAK can reduce the computational complexity of information and improve computing efficiency. This paper combines the

Fig. 31.6 Matching comparison of the perspective distortion state
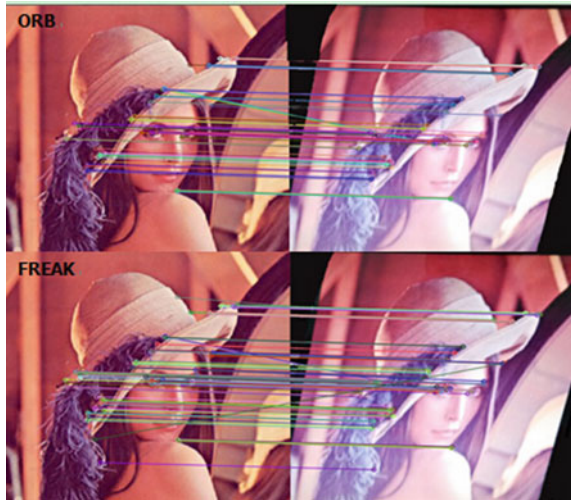
Fig. 31.7 Comparison of the average matching time (ms)
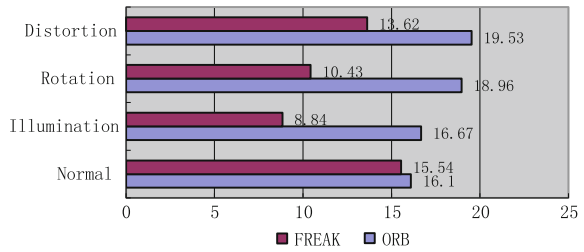
FAST feature point's detection algorithm with the FREAK feature point's description algorithm to realize image matching and compares the matching effect with ORB algorithm in different state. Experimental results show that FREAK algorithm not only can obtains more correct matching pairs, but also takes less matching time, which means FREAK has better efficiency. Hence, the proposed algorithm, combining FAST and FREAK, can reduce the computational complexity of information and improve the computing efficiency.

31.4   Conclusions

The experimental results show that the FREAK's matching speed and the number of matched pairs is better than ORB algorithm. The average time of each matched pair can even reach about half of the ORB algorithm in some state, which means FREAK has better performance.

This paper improved the calculation speed of the mobile terminal image matching by combing the FAST algorithm with the FREAK algorithm. The results

of this study can provide some reference for choosing algorithm during the process of real-time image matching in the mobile terminal. How to further enhance the FREAK algorithm of matching accuracy will be the next research target [6].

References

1. Rosin, P. L. (1999). Measuring corner properties. *Computer Vision and Image Understanding*, *73*(2), 291–307.
2. Xiaohong, L., Chengming, X., Yizhen, J., & Guofu, Z. (2013). Rapid moving object detection algorithm based on ORB features. *Journal of Electronic Measurement and Instrument, 27*(5), 455–460.
3. Rublee, E., Rabaud, V., Konolige, K., & Bradski, G. (2011). An efficient alternative to SIFT or SURF. *Computer Vision*, 2564–2571.
4. Alahi, A., Ortiz, R., & Vandergheynst, P. (2012). FREAK: Fast retina keypoint. *Computer Vision and Pattern Recognition, 6*, 510–517.
5. Ebrahimi, M., & Mayol-Cuevas, W. (2009). Susure: Speeded up surround extrema feature detector and descriptor for realtime applications.
6. Patel, A., Kasat, R. D. Jain, S., & Thakare, M. V. (2014). Performance analysis of various feature detector and descriptor for real-time video based face tracking. *International Journal of Computer Applications*, *93*(1), 37–41.

Chapter 32
Research on the Application of Image Enhancement Algorithms in Printing Defect Detection

Hongyan Zhao, Chao Li, Yujie Jiang, Yaping Ge and Peidong Hou

Abstract This article mainly aims at the application research of image enhancement algorithm in printing image defect detection process, and the purpose is to establish a better foundation for the analysis of image defects, realizing the online monitoring of the printing quality more accurate. For the actual production situation of printing, according to the characteristics of different of printing images, chose histogram equalization, contrast linear broadening, median filtering, using MATLAB to carry on the simulation experiment of image enhancement, through the experimental analysis and comparison of the enhancement effect, further verify the advantages and disadvantages of these algorithms, to provide the basis for selection of image enhancement algorithm in the practical application of printing defect detection.

Keywords Image enhancement · Image preprocessing · Printing defect detection

32.1 Introduction

In the printing production process, due to the impacts of the printing process, printing equipment and production environment and other factors, the print may rise to various defects, such as color difference, out of register, Roller mark, set off, etc. [1], thereby resulting in the generation of defective printing. So in the printing production process, the printing defects in real-time online monitoring are necessary.

H. Zhao (✉) · C. Li · Y. Jiang · Y. Ge · P. Hou
College of Packaging and Printing Engineering, Tianjin University of Science and Technology, Tianjin, China
e-mail: zhaohongyan800@tust.edu.cn

Image enhancement, typically by certain features of the image, such as edge, contour, contrast, and brightness, for emphasis or intensification [2], while weakening or removing certain unnecessary information, can make valuable information more prominent and suppress unnecessary information. So the image can be recognized easily meanwhile it can be analyzed and processed easily.

This article mainly aims at the application research of image enhancement algorithm in printing image defect detection process, using SHOTS printing simulation software and MATLAB software as experimental platform, and adopting histogram equalization, contrast linear broadening and other image enhancement algorithms, applied to different defects of printing image, enhancing the effect of defective pacts, using median filter smoothing algorithm to remove image noise, through contrasting the post-processing images with the original ones, describing the effect of image enhancement, we can draw conclusions.

32.2 Histogram Equalization Algorithm

Histogram equalization algorithm can make the source images' gray distribution more uniform using the transform function, in order to increase the dynamic range of image gray, enhance the overall image contrast, improve visual effects [3].

After the adjustment, the gray distribution denser parts are stretched and gray distribution sparse ports are compressed in the histogram, so that the image contrast is enhanced overall [4].

Selecting the printing surface scratches, printing surface appears smudges the two kinds as example s, using the MATLAB $q = histeq\ (img, n)$ function histogram equalization process, which, img is the failure of an image to be processed, n is the number of gray levels after equalization, and chosen for $n = 64$.

Figures 32.1 and 32.2, respectively, is an image with scratches and dirty spots of the results after equalization Figure.
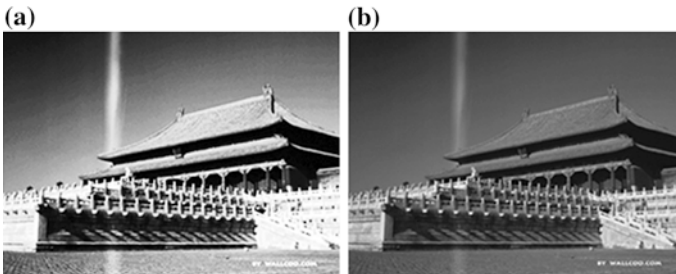

Fig. 32.1 Result of histogram equalization processing (scratch). **a** After process. **b** Print with scratch
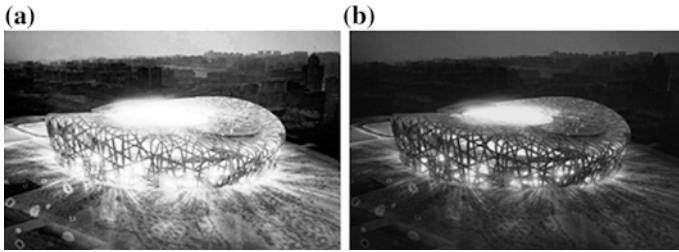
Fig. 32.2 Result of histogram equalization processing (dirty point). **a** After process. **b** Print with dirty point

32.3 Contrast Linear Broadening Algorithm

Contrast linear broadening method is the most common image enhancement techniques. It can transform an image grayscale from a range to another range, making contrast larger strengthening, so that the image can be improved due to the image processing such as subtraction after some of the negative effects caused by [5].

By contrast linear stretch dealing with pictures, you can highlight the target of interest or gray zone, this experiment were carried out on the picture contrast grayscale range broadening regional 0.1–0.3, 0.1–0.5, 0.3–0.7, using function $h = imadjust(img, [0.1, 0.3], [])$ to implement in MATLAB.

For a printed image with scratches, after applying linear contrast stretch method, the experimental results shown in Fig. 32.3.

For a printed image with dirty point, after applying linear contrast stretch method, the experimental results shown in Fig. 32.4.

Figures 32.3 and 32.4 shows the effects of the image are processed through contrast, figure can be seen, the gray value of the original image is mainly concentrated in one area, after adjustment, the image becomes clearer, more even distribution of the image pixels uniform, richer level.

For Scratches fault picture, when broadening in the range of 0.1–0.3, the gradation effect of the faulty portion of the image is the most obvious and easy to
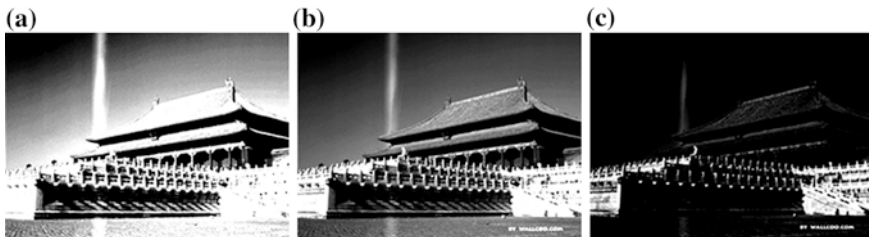

Fig. 32.3 Result of contrast linear broadening processing (scratch). **a** 0.1–0.3. **b** 0.1–0.5. **c** 0.3–0.7
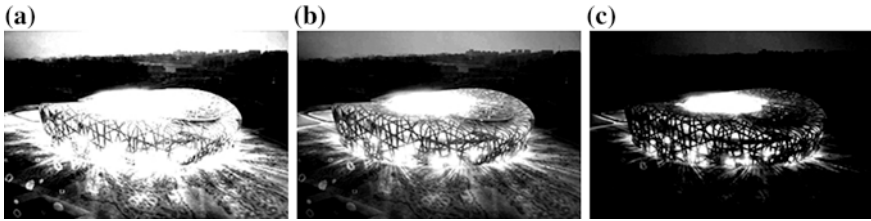
Fig. 32.4 Result of contrast linear broadening processing. (dirty point). **a** 0.1–0.3. **b** 0.1–0.5. **c** 0.3–0.7

observe; while broadening the range of 0.1–0.5, the gradation affect the faulty portion of the image to a certain degree of enhancement, clearer, and little distortion, facilitate further measurement and positioning.

Defective graph with dirty spots, also in gray as broadening the range of 0.1–0.5, the effect of the faulty portion of the image was most appropriate to strengthen, we can clearly distinguish fault conditions.

According to the different defective images, the results are different, so when using a linear contrast stretch, we should take a few more gray range, compares the process to achieve the best results. So contrast linear broadening advantages compared to the other two methods is very obvious, only the gray range of interest for processing, reducing the damage to image information.

32.4 Median Filter to Remove Image Noise Smoothing Algorithm

Median filter is a protective edge nonlinear image smoothing method has broad application in image enhancement [6].

The scratches defective is still chosen and the function $l = medfilt\ 2\ (img,\ [])$ in MATLAB was used. At first using $img = imread$ ('*picture path*') reads image, and $k = imnoise\ (img,\ 'salt\ \&\ papper')$ (by the addition of salt and pepper noise, for example) adding salt and pepper noise, then respectively the size of 3×3, 5×5, 7×7, 9×9 template for image median filtering process, the results shown in Fig. 32.5.

The experimental results show that the salt and pepper noise added is filtered out obvious, and effect is enhanced with the increase of the template. The image after median filtering is close to of the original one.

Similarly, the Gaussian noise added to the image, then using a size of 3×3, 5×5, 7×7, 9×9 median filter template, the results shows in Fig. 32.6.

The multiplicative noise added to the image, and then using 3×3, 5×5, 7×7, 9×9 size template median filtered image, the results shows in Fig. 32.7.
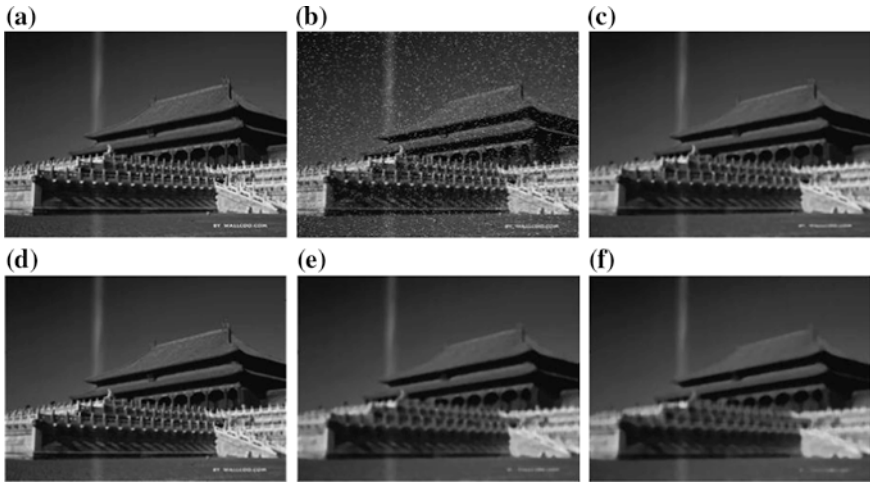
Fig. 32.5 Median filtering with salt and pepper noise. **a** Original image. **b** Salt and pepper noise. **c** 3 × 3 template. **d** 5 × 5 template. **e** 7 × 7 template. **f** 9 × 9 template
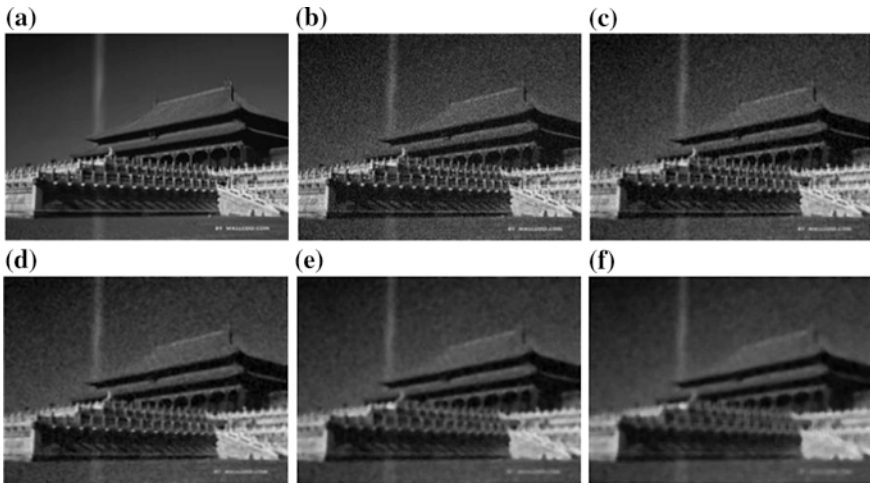
Fig. 32.6 Median filtering with gaussian noise. **a** Original image. **b** Gaussian noise. **c** 3 × 3 template. **d** 5 × 5 template. **e** 7 × 7 template. **f** 9 × 9 template

In contrast, median filtering can filter out Gaussian noise and multiplicative noise well, but compared with the original picture, there are some changes, the image is blurred to some extent, especially the image of the defective part, also will be blurred and weakened, become easy to observe.
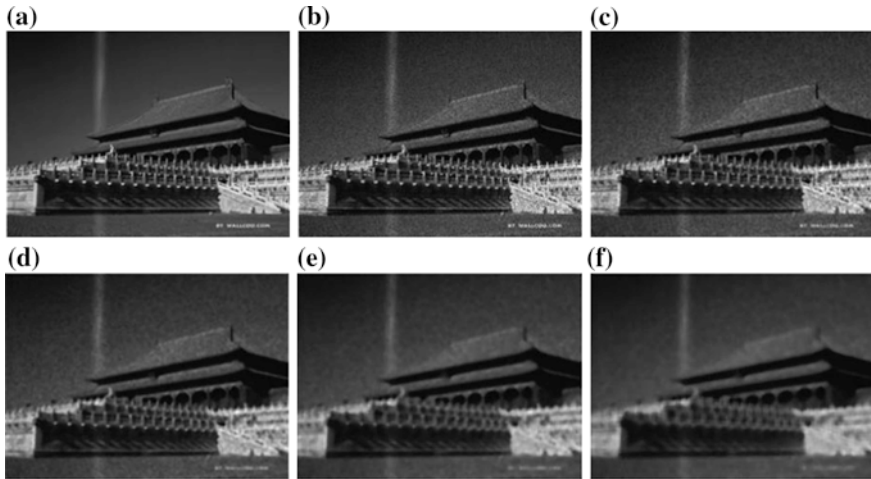
Fig. 32.7 Median filtering with multiplicative noise. **a** Original image. **b** Multiplicative noise. **c** 3 × 3 template. **d** 5 × 5 template. **e** 7 × 7 template. **f** 9 × 9 template

32.5 Conclusions

After defective picture processed by histogram equalization, the pixel gray spacing widening significantly, picture contrast enhanced, the image is clearer, defective part has been effectively enhanced, easy to observe and measure the location; using linear contrast stretch processing defective pictures, for the different defective should use different ranges of gray, defective parts is highlighted.

When there is noise in the image, you can use median filter smoothing algorithm for processing, but with filtered noise, defective parts are correspondingly weakened, especially in the case of smaller faults, for example, strong cleaning agents can make rubber blanket malfunctioned, the use of the median filter will become impossible to observe.

In summary, histogram equalization and contrast linear broadening could strengthen defective part. However, histogram equalization has a very serious drawback, it does not select processed data, after conversion the image's gray level will be reduced, disappeared some detail, this will also affect the fault enhanced; linear contrast stretch method can protruding interested gray range portion, suppress interference observed portion. For different failure pattern can used the different range of gray. Therefore, linear contrast stretch method can effectively enhance the failure pattern display, is more conducive to the next step to print defect detection and localization.

References

1. Bai, J. (2013). Image processing technology in the application of the printing defect detection. *Printing Quality & Standardization, 5*, 54–56.
2. Li, X. (2008). Image quality assessment and image enhancement technology research. MS thesis, Nanjing University of Science and Technology.
3. Shidong, C., & Fang, Y. (2012). Image enhancement based on histogram modification. *Optoelectronic Technology, 32*(3), 155–159.
4. Wu, C., & Zhu, T. (2012). Several image enhancement algorithm based on MATLAB. *Mechanical and Electrical Technology, 5*, 37–39.
5. Zhai, B. (2013). The flat crystal shape measurement system based on laser plane interferometer. MS thesis, Nanjing University of Science and Technology.
6. Wang, S. (2014). The median filtering algorithm of image enhancement based on MATLAB. *Intelligent computer and applications, 4*(6), 87–89.

Chapter 33
A Method of Color Inverse Halftoning Image Quality Assessment Based on Image Structural Property

Zhixiong Shi, Xiaodong Wang and Lujing Fu

Abstract The traditional image quality assessment method and index cannot meet with the inverse halftoning image quality assessment. We proposed a color inverse halftoning image quality assessment method based on image structural property. First, we transformed printing image into inverse halftoning image with wavelet transforming inverse halftoning algorithm. Then, taking quaternion matrix as the carrier and combining with details of image, brightness and color information, we can convert halftoning image into quaternion matrix and obtain feature vector through singular value decomposition. Finally, the inverse halftoning image quality assessment is accomplished by calculating the quaternion singular feature vector angle to indicate the similarity of the original image and the inverse halftoning image. The result of experiment shows that the assessment can excellently exhibit the reduction of the inverse halftone image quality. Meanwhile, it is also in line with subjective visual perception and provides a reference for constructing quantitative assessment index of the inverse halftone color image quality.

Keywords Inverse halftoning · Image quality assessment · Quaternion · Wavelet transform

33.1 Introduction

Halftone is a process that we use the size or density of the dot to represent the image tone in printing. It can improve reproduction quality of continuous toning printing image. If second halftoning, image compression and enhancing process are done to the halftone image directly, it will result in a serious decline in image quality. So we

Z. Shi (✉) · X. Wang · L. Fu
The People's Printing Plant of Guangzhou Co., Ltd, Guangzhou, China
e-mail: szx82@126.com

need to restore the image into a continuous tone image [1], namely halftone image reversing. Halftone inversing refers to a process of reconstructing halftone image into continuous tone image, which is mainly to meet with the processing of printing image electronization, halftone image compression, sharpening, and secondary halftone. At present, the primary methods of halftone inversing include lookup table method [2], median pyramid transforming [3], wavelet transform [4], adaptive filtering [5], super-resolution analysis [6], etc.

Evaluating the quality of inversing halftone image can provide the most basic quantitative criteria for the performance evaluation of inverse halftone algorithm and further optimize the algorithm and its related parameters settings. Yang [7] conversed the color space to S-CIE Lab space to construct quantitative indicators of evaluating the quality of the color halftone inversing images, by defining the human visual perception of color difference images and gradient images. Jiang [8] uses image structural information to describe the mass reduction degree of color halftone inversing images, realizing color halftone inversing image quality evaluation based on image quality assessment method of structural similarity. Paper [9] set up halftone inversing color quality evaluation scheme using CIE DE2000 color difference formula and NBS color perception reference on the basis of HVS characteristics. But the proposed halftone inversing image quality assessment methods at present cannot fully reflect the distortion phenomenon of the halftone inversing image, and the correlation between the evaluation results and image subjective visual effect is small.

This paper proposes a quality evaluation method of color halftone inversing image, transforming image into a quaternion matrix form. The decline in brightness, color, and HVS sensitive structure information of the color image can be all included in the quaternion matrix, which can keep the direct image evaluation structure more in line with the human visual characteristics.

33.2 Inverse Halftone Image Quality Evaluation Technology

33.2.1 Structure Similarity Inverse Halftone Image Quality Evaluation Method

Structure similarity inverse halftone image quality evaluation method is founded on structural similarity of image quality evaluation. The differences between inverse halftone image and original image are measured by image structure information in the three aspects of brightness, contrast, and structure. Finally, the evaluation is completed. The inverse halftoning evaluation process [8] is shown in Fig. 33.1.
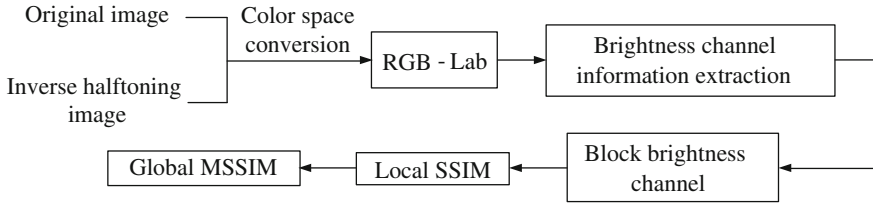
Fig. 33.1 Diagram for structure similarity inverse halftone image quality assessment

33.2.2 Quaternion Inverse Halftone Image Quality Evaluation Method

According to the basic theory of quaternion [10], assuming the quaternion real component is zero, the remaining three imaginary part can represent red, green, and blue components of color image, respectively, the color image can be represented as:

$$f(x,y) = r(x,y)i + g(x,y)j + b(x,y)k \tag{33.1}$$

$r(x, y)$, $g(x, y)$, $b(x, y)$ signify image on (x, y) color values of red green and blue. As a result, color images can be indicated by a quaternion matrix.

At the same time, quaternion matrix has singular value decomposition [11]. The color image is represented as a quaternion matrix form and obtained singular value vector through the quaternion matrix singular value decomposition. Then according to the degree of linear correlation between the two image singular value vector quaternion, we can acquire inverse halftone image quality evaluation method.

s_1, s_2 represent original image and inverse halftoning image I_1, I_2 quaternion matrix singular value vector, $s_1 = \mathrm{diag}(\lambda_1, \lambda_2, \ldots, \lambda_r)$, $s_2 = \mathrm{diag}\left(\lambda_1', \lambda_2', \ldots, \lambda_r'\right)$, QSVD evaluation index [12] can be represented as:

$$\mathrm{QSVD} = \arccos \frac{\sum\limits_{i=1}^{r} (s_1 \times s_2)}{\sqrt{\sum\limits_{i=1}^{r} (s_1 \times s_1)} \sqrt{\sum\limits_{i=1}^{r} (s_2 \times s_2)}} \tag{33.2}$$

$r = \min(\mathrm{rank}(I_{1Q}), \mathrm{rank}(I_{2Q}))$ QSVD scope for $[0, \pi/2]$ QSVD is smaller, the degree of linear correlation for image singular value vector is higher, the similarity between images is better.

The biggest advantage of using QSVD to evaluate the color inverse halftone image quality is that color inverse halftone images can be expressed with quaternion matrix and realized the parallel processing of color image color information, meanwhile the color image need not have to be decomposed into monochromatic color channel to process, which ensures the integrity of the color image processing.

33.3 Structural Characteristics of the Color Inverse Halftone Image Quality Evaluation

The method of color inverse halftoning image quality evaluation based on structure characteristics algorithm flow chart is shown in Fig. 33.2.

33.3.1 Wavelet Transform Inverse Halftone Algorithm

In inverse halftone image processing, we selects wavelet inverse halftoning algorithm for printing image processing [12], the algorithm process is shown in Fig. 33.3.

33.3.2 Quaternion Inverse Halftone Image Quality Evaluation

According to the inverse halftone image, using quaternion singular value decomposition of color inverse halftone image quality evaluation method for inverse halftone image quality evaluation, the algorithm flow chart shown in Fig. 33.4.
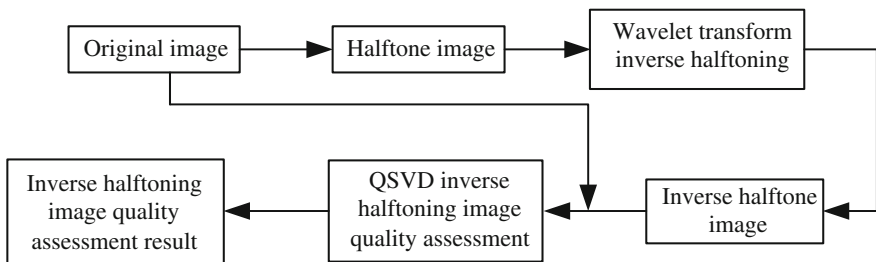

Fig. 33.2 Diagram for structural characteristics of the color inverse halftone image quality evaluation
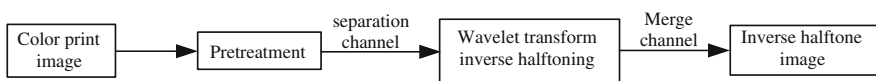
Fig. 33.3 Diagram for wavelet transform inverse halftone
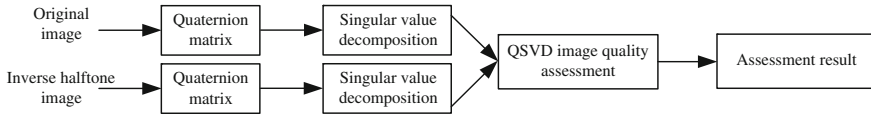
Fig. 33.4 Diagram for quaternion inverse halftone image quality evaluation

33.4 Experimental Results and Analysis

The experiment chooses TID2008 image database as the experimental images, and selects the wavelet transform algorithm for inverse halftone image processing, where the wavelet decomposition scale for two layers and the B spline wavelet as wavelet function. Meanwhile the experiment select structure similarity inverse halftone image quality evaluation method as a contrast experiments, image quality evaluation conduct to inverse halftoning for different screening modes and different dot form, respectively, the evaluation results are shown in Table 33.1.

By comparing the inverse halftone image quality evaluation results, we can see that the consistency and stability for QSVD is obviously better than SSIM for inverse halftone image quality assessment. Because compared to the original image, the image loss for inverse halftoning mainly concentrates on the image detail and the high-frequency part, and SSIM is not sensitive to the detail loss of the image, which leads to the evaluation results that inverse halftone images disagree with people's subjective feeling. At the same time, the human eye is more sensitive to the high-frequency part of image, and the quaternion matrix singular value can well describe the detail loss of the image, which can highlight the HVS sensitive information structure and improve precision of inverse halftone image quality evaluation.

Table 33.1 Inverse halftone image quality evaluation results

Screening mode	SSIM	QSVD	Screening mode	SSIM	QSVD
AM screening	0.8826	0.0455	FM screening	0.9515	0.0245
	0.7995	0.0152		0.9685	0.0132
	0.5208	0.0158		0.5108	0.0089
	0.7393	0.0234		0.7526	0.0253
	0.8616	0.0359		0.9344	0.017
	0.4271	0.0243		0.4081	0.0079
	0.9233	0.0119		0.902	0.0131
	0.4193	0.0308		0.3691	0.0204
	0.8688	0.0247		0.8674	0.0183
	0.3509	0.0476		0.3204	0.0155

33.5 Conclusions

This paper proposes color inverse halftone image quality evaluation method based on image structure characteristics, we convert color inverse halftone images into quaternion matrix and use quaternion singular value vector correlation of color inverse halftone image quality evaluation; then it improves the accuracy and stability for color inverse halftone image quality evaluation. The next step, we should conduct further research to the quaternion color image model, such as the image luminance variance as quaternion real component, highlighting the HVS sensitive image structure information of color image.

References

1. Zheng, H. H., Kong, Y. P., Zeng, P., et al. (2008). A review of inverse halftoning algorithm s for error diffusion. *Journal of Image and Graphics, 13*(1), 1–6.
2. Geng, Y., & Kong, Y. P. (2011). Mixed compression algorithm for error-diffusion halftone image based on look-up table. *Journal of Computer Application, 31*(5), 1221–1223.
3. Kong, Y. P., Zeng, P., & Wu, Zl. (2007). Color inverse halftoning algorithm based on K-L and multi-scale pyramid transform. *Acta Optica Sinica, 27*(10), 1745–1750.
4. Djebbouria, M., Djebourib, D., & Naouma, R. (2005). Wavelet-based inverse halftoning for error diffused halftones. *International Journal of Electronics and Communications, 5*, 128–133.
5. Sun, B., Li, S. T., & Sun, J. (2014). Scanned image descreening with image redundancy and adaptive filtering. *IEEE Trans Image Process, 23*(8), 3698–3710.
6. Minami, Y., Azuma, S., & Sugie, T. (2012). Inverse halftoning using super-resolution image processing. *IEEJ Transactions on Electrical and Electronic Engineering, 7*, 208–213.
7. Yang, Y. F. (2009). Space dependent quality assessment for color inverse halftoning images. *Journal of Computer Applications, 29*(6), 1699–1701.
8. Jiang, N. (2013). Color inverse halftone image quality assessment algorithm based on structure similarity. *Computer Systems and Applications, 22*(3), 125–127.
9. Kong, Y. P., Zeng, P., & Jiang, N. (2008). Image quality assessment and visualization of color difference for color inverse halftoning using HVS. *Journal of Huazhong University of Science & Technology (Natural Science Edition), 36*(8), 21–24.
10. Zhang, F. (1997). Quaternions and matrices of quaternions. *Linear Algebra Appl, 251*, 21–57.
11. Wang, Y. Q., & Zhu, M. (2013). Maximum singular value method of quaternion matrix for evaluating color image quality. *Optics and Precision Engineering, 21*(2), 469–478.
12. Wang Y., Wang Y. Q., Gu H. J., et al. (2014). Color image quality assessment method based on full quaternion structure similarity measure. *Journal of Optoelectronics Laser, 25*(10), 2033–2043

Chapter 34
An Enhancement Method of Low-Contrast Chromatic Image Based on Adaptive Threshold

Lingjun Kong, Peng Nie and Yewei Sun

Abstract The study used the image enhancement algorithm of histogram compaction equalization based on adaptive thresholds to extend the tonal range of low-contrast chromatic image. The algorithm chooses the thresholds adaptively to achieve the purpose of enhancing the image contrast, details, and sharpness of the low-contrast chromatic image according to its information characteristics of R, G, and B channel. Experimental results show that the algorithm can effectively improve the contrast and sharpness of low-contrast chromatic images, and well preserve the color appearance of the image compared to the traditional histogram equalization image enhancement method and the wavelet-based image enhancement method. The proposed method has good application value.

34.1 Introduction

In the process of digital photography, the lack of environment light makes the image dark, and loses image details and contrast. There are many kinds of image enhancement algorithms, which are mainly divided into spatial domain and frequency domain [1–6]. To solve the quality defects of low-contrast images, Zhang and Cui [7], Wu and Wang [8] used piecewise linear function to process the grayscale images. Although it can improve the image contrast in certain extent,

L. Kong (✉)
Shanghai Publishing and Printing College, Shanghai, China
e-mail: 908641376@qq.com

L. Kong · P. Nie (✉) · Y. Sun
College of Communication and Art Design, University of Shanghai for Science and Technology, Shanghai, China
e-mail: 951415464@qq.com

some adjacent gray values may be combined into the same gray value and lead to the fault phenomenon in the process of histogram segmentation. Wang et al. [9] proposed the method of histogram equalization to enhance the image contrast globally, but the effect is not obvious, and the background of the image and noises inhibits the details of the image. Huang and Jiang [10] proposed an enhancement method of low-contrast images based on wavelet transform, which might create unnecessary noise and affect the image sharpness and limit the enhancement effect of image contrast. Di et al. [11] proposed the enhancement algorithm combined with histogram compaction equalization (abbreviated as HCE), which used the threshold selection method to improve the contrast of grayscale images based on local maximum values, but the image details and sharpness were not enhanced substantially. The paper studies the image enhancement algorithm of histogram compaction equalization based on the adaptive thresholds (abbreviated as ATHCE in the following text) in the spatial domain for the low-contrast chromatic image through selecting the reasonable equalization threshold of R, G, and B channel of the image to improve the contrast and the sharpness of color images, and the performance of the algorithm is verified by a low-contrast image.

34.2   Principle of ATHCE Algorithm

Low-contrast images have the characteristic of sparse distribution in grayscale and many gray levels do not exist in the images. In order to make the sparse distribution of the grayscale histogram of R, G, and B channels of the low-contrast chromatic images compact, the histogram compaction equalization based on the adaptive thresholds (ATHCE) algorithm was proposed on basis of HCE [11] method. ATHCE algorithm removes the gray levels from the histogram of R, G, and B channels whose pixel number is zero, and chooses the threshold value between the gray value of the details and the background to inhibit the image background and noises and improve the image contrast and sharpness, and highlight the image details. The process of the algorithm is as follows.

(1) Extracting the color data from R, G, and B channel of the low-contrast chromatic image.
(2) Calculating the grayscale histogram of R, G, and B channel, $S_K(i)$, $i = 0$–255; $K = 1, 2, 3$ represent the R, G, and B channel separately.
(3) Compacting the grayscale histogram of R, G, and B channel and store the results as $S_K^*(j)$, then:

$$S_K^*(j) = S_K(i), S_K(i) \neq 0 \qquad (34.1)$$

Here i = 0–255, K = 1, 2, 3, j = 0–n, n is the gray level whose pixel number is nonzero in the grayscale histogram of each channel.
(4) Calculating the average thresholds AVE(K) of the histogram of the compacted R, G, and B channel. Find the local maxima $S_K^*(m)$ and the local minima

$S_K^*(n)$ of $S_K^*(j)$, $m = 0$–M, $n = 0$–N, M and N are the number of local maxima and local minima, and then average the mean values of all local maxima and the mean values of all local minima for each channel, see formula 34.2, the result is treated as the threshold AVE(K).

$$\text{AVE}(K) = \left(\frac{1}{M}\sum_{m=0}^{M} S_K^*(m) + \frac{1}{N}\sum_{n=0}^{N} S_K^*(n)\right)/2 \qquad (34.2)$$

(5) Compare the grayscale histogram value $S_K^*(j)$ and the average threshold AVE (K), and get the improved histogram $T_K'(i)$(see formula 34.3), $i = 0$–255; $K = 1, 2, 3$.

$$T_{K'}(i) = \begin{cases} S_K^*(i) & S_K^*(i) \leq \text{AVE}(K) \\ \text{AVE}(K) & S_K^*(i) > \text{AVE}(K) \end{cases} \qquad (34.3)$$

(6) Equalize the histogram of R, G, and B channel according to the improved histogram $T_K'(i)$ and then merge the three channels into a color image which is the new copy with enhanced contrast of the original low-contrast chromatic image.

34.3   Application and Results Analysis

(1) Experiment and the results

In order to verify the performance of ATHCE algorithm proposed in the paper, a low-contrast color image with 256 × 256 pixels (seen in Fig. 34.1a) was used and processed by ATHCE algorithm in the experiment. Meanwhile, the image was also processed by the traditional histogram equalization method and the enhancement method based on wavelet transform proposed by Huang and Jiang [10].

The enhancement effects of the three methods are shown in Fig. 34.1. Figure 34.1b–d separately represents the result of the traditional histogram equalization method, the enhancement method based on wavelet transform, and the enhancement method with ATHCE algorithm.
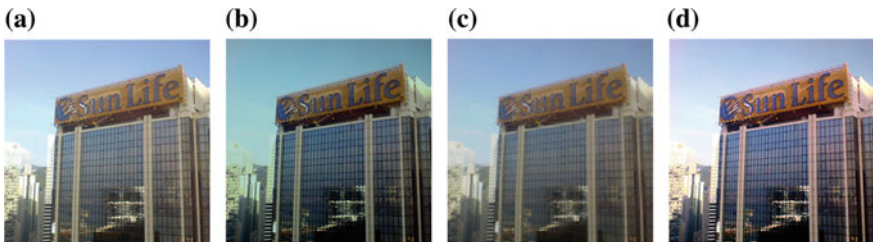

Fig. 34.1 Tested image and its enhanced effects

(2) Subjective evaluation and analysis

As shown in Fig. 34.1a, the grayscale of most pixels in the original image are concentrated in the middle tone, the image looks flat with low contrast. Figure 34.1b shows that the contrast and details of the image have a certain degree of improvement through the traditional histogram equalization method, but some of the image tonal levels are lost. Figure 34.1c shows that the tonal level of the image was well preserved after applying the enhancement method based on wavelet transform, but the image contrast was not improved obviously. While, the image details, sharpness, and brightness contrast were improved greatly with the enhanced method of ATHCE, the "Sun Life" signed on the top of the building are more prominent, seen in Fig. 34.1b. Furthermore, the image processed by ATHCE algorithm is the closest to the original image judging from the color performance.

Figure 34.2 shows the R, G, and B channel information of the images in Fig. 34.1. Compare the R, G, and B channel information in Fig. 34.2b–d, the image processed by ATHCE algorithm has better grayscale distribution than the other two images. The average thresholds of R, G, and B channel of the original color image calculated by ATHCE algorithm are 269, 267, and 247, which can keep the image details well enough and inhibit the influence of the background and noises. As shown in Fig. 34.2d, the image processed by ATHCE algorithm well preserves the proportion relationship between the R, G, and B channel and the gradation of each channel in the original image and extends the tonal distribution of the original image well, which bring about the significant contrast improvement.

(3) Objective evaluation and analysis

Here, the image quality evaluation index of root mean square error (RMSE), the sharpness index (SI), information entropy (IE) and peak signal-to-noise ratio (PSNR) are used [12]. Information entropy indicates how much information the image contains. If the number of the image grayscale is i, the probability of the grayscale of no. i is p_i, then the gray information entropy of the image is:

$$e(i) = -p_i \log p_i \tag{34.4}$$

The information entropy of the whole image is:

$$E = \sum_{i=0}^{i} e(i) = - \sum_{i=0}^{i} p_i \log p_i \tag{34.5}$$

When the probability of each gray level of the image is equal, the E value reaches the maximum, which means the image contains the maximum amount of information.
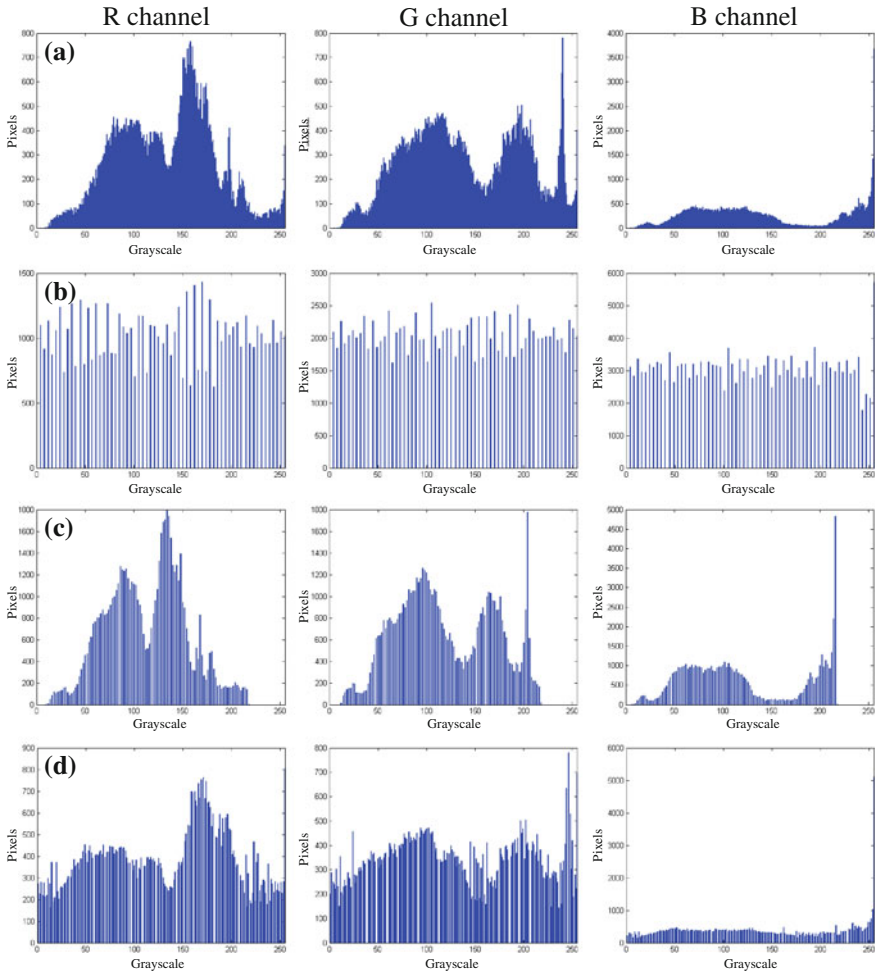
Fig. 34.2 Histograms of the tested images. **a** Histogram of image in Fig. 34.1a. **b** Histogram of image in Fig. 34.1b. **c** Histogram of image in Fig. 34.1c. **d** Histogram of image in Fig. 34.1d

Sharpness index is often used for comparing the improvement effect of image quality before and after the enhancement. To the image with $M * N$ pixels, its sharpness index is defined as:

$$L = 1 - \frac{1}{MN} \sum_{x=0}^{M-1} \sum_{y=0}^{N-1} \min[p(x, y), 1 - p(x, y)] \qquad (34.6)$$

Here, $p(x, y) = \sin[\pi/2(1 - f(x, y)/f_{\max})]$, $f_{\max}$ is the largest gray value in the image. According to the definition of formula (34.5) of the sharpness index, if the

Table 34.1 Objective quality evaluation results of the images with different enhanced methods

	RMSE	IE	PSNR	SI
Traditional method [9]	3.2725	5.2816	15.6824	0.8026
Wavelet-based method [10]	3.2565	5.7048	15.5662	0.7525
Method proposed in the paper	3.0818	6.6064	17.3130	0.8030

image has large grayscale range, the image will have good sharpness and high sharpness index, otherwise the image sharpness index will be low.

Table 34.1 contains the objective quality evaluation results of the low-contrast chromatic images processed by the traditional histogram equalization method, the enhancement method based on wavelet transform, and ATHCE algorithm proposed in the paper.

It can be seen from Table 34.1 that the color image processed by ATCHE algorithm has the smallest mean square error, the biggest information entropy, peak signal-to-noise ratio and sharpness index than the images enhanced through the other two methods.

The information entropy and sharpness index of the original image are 6.8728 and 0.7610. It can be seen from Table 34.1 that the information entropy of color image enhanced by ATCHE algorithm is the closest to the information entropy of the original image among the three methods, which means the image enhanced by this method has the least information loss. Meanwhile, the images enhanced by the traditional histogram equalization method and ATCHE algorithm have higher sharpness index than the original image, but the sharpness index of image enhanced by the enhancement method based on wavelet transform is smaller than that of the original image, which means the sharpness of the image enhanced by the enhancement method based on wavelet transform is reduced, while the sharpness of the image enhanced by the other two enhancement methods are improved. Those objective evaluation results are consistent well with the subjective evaluation results. Thus, the image enhanced by ATCHE algorithm retains more information of the original low-contrast chromatic image, and the brightness contrast, details and sharpness of the original image are well improved.

34.4   Conclusions

The traditional histogram equalization method cannot effectively enlarge the tonal range of R, G, and B channel of the low-contrast chromatic image to the largest possible extent, and may result in the loss of image information because too many grayscales are merged. Although the enhancement method based on wavelet transform remains the gradation of R, G, and B channel of the low-contrast chromatic image, the low-dimension diagonal high-frequency component of wavelet decomposition of the image is compressed which will affect the image sharpness.

The ATHCE algorithm proposed in the paper can effectively improve the contrast and sharpness of low-contrast chromatic image with the best adaptive average threshold of R, G and B channel. The experiment results show that the ATHCE algorithm can highlight the image details greatly while preserving the color appearance of the original image well.

References

1. Xu, W.-J., & Liu, G.-Z. (2009). Space domain and frequency domain combination of image enhancement technology and its realization. *China Measurement and Test, 35*(4), 52–54.
2. Zhang, W., Sun, Y. –Q., & Zhang, T. -Y. (2013). An image enhancement based on a combination of frequency domain and spatial domain. *Journal of Yangtze University*. doi:10.3969/j.issn.1673-1409
3. Wang, X.-H., & Zhang, T. (2014). Color image enhancement based on visual region of interest. *Packaging Engineering, 35*(3), 84–87.
4. Donoho, D. L. (1995). De-noising by soft-thresholding. *IEEE Transactions on Information Theory, 41*(3), 613–627.
5. Vickers, V. E. (1996). Plateau equalization algorithm for real-time display of high-quality infrared imagery. *Optical Engineering, 35*(7), 1921–1926.
6. Sakellaropoulo, S. P., Costaridou, L., & Panayiotakis, G. A. (2003). Wavelet-based spatially adaptive method for mammographic contrast enhancement. *Physics in Medicine Biology, 48* (6), 783–803.
7. Zhang, Y., & CUI, X.-M. (2010). Implementation of image enhancement based on gray level transformation. *Packaging Engineering, 31*(19), 103–106.
8. Wu, Z.-G., & Wang, Y.-J. (2010). An image enhancement algorithm based on histogram nonlinear transform. *Acta Photonica Sinica, 39*(4), 755–758.
9. Wang, Z. -Y, Huang, M. -W., Hu, P., et al. (2006). Image enhancement based on histograms and its realization with MATLAB. *Computer Engineering and Science*.
10. Huang, C. -B., & Jiang, Y. -Y. (2006). An algorithm based on wavelet transform for image contrast enhancement. *Modern Computer*. 22 Dec 2006. doi:10.3969/j.issn.1007-1423-B
11. Di, N., Tian, R., & Fu, D.-H. (2013). Image enhancement algorithm combined histogram compaction equalization. *Computer Technology and Development, 23*(12), 34–36.
12. Guo, X. -T. (2013). Research on enhancement algorithm for low-illumination image. MS thesis, South China University of Technology.

Chapter 35
Research on the WebP Image Format

Zhanjun Si and Ke Shen

Abstract WebP is a new image compression technology proposed by Google. It is derived from the VP8 video coding format; it also supports lossless and lossy compressions. Compared with the present popular image format, WebP has smaller volume than JPG and PNG in the condition of the same picture quality conditions. By coding with MATLAB, this experiment adopts the PSNR and SSIM on WebP and JPG, PNG for comparison test, then implement data compression and reduction test. Since MATLAB does not identify the WebP format, this experiment uses canvas to process WebP images, thus measuring the PSNR and WebP of SSIM. The results of experiment show that WebP has high value in the life, it will develop well in the future.

Keywords WebP · Image compression · PSNR · SSIM

35.1 Introduction

With the rapid development of the Internet, people are placing a greater demand on the quality of the picture. It is necessary to reduce the volume of pictures in the condition of ensuring the fineness. But nowadays, the optimization for JPG, PNG, and GIF has reached the extreme. It needs great courage to make something new and change the current situation, and Google has given us a new choice: WebP. WebP, which is based on VP8 coding, has higher compression ratio than JPG, and it has brought a new power for the Internet [1].

Z. Si (✉) · K. Shen
College of Packaging and Printing Engineering,
Tianjin University of Science and Technology, Tianjin, China
e-mail: szj@tust.edu.cn

35.2 Picture Format Evaluation Criterion

35.2.1 Peak Signal-to-Noise Ratio (PSNR) and SSIM

PSNR [2] is an objective standard for evaluating images, based on counting and averaging the pixel grey level. Formula is as follows:

$$PSNR = 10 \times \lg\left(\frac{255^2}{MSE}\right) \tag{35.1}$$

This measurement compares the original picture and the rebuilt picture in three aspects: brightness, contrast ratio, and structural similarity index.

$$SSIM = [l(x, y)]^{\alpha} \cdot [c(x, y)]^{\beta} \cdot [s(x, y)]^{\gamma} \tag{35.2}$$

35.3 Design of Experiments

35.3.1 Contrast of Picture Size

The experiment selects a number of PNG images, and transforms these images into WebP, JPG, and PNG whose qualities are 85 respectively. Then measure the size of these images and compare the result with the size of original image (Fig. 35.1).

Experimental environment: Windows 7 professional
Software: Photoshop CC, iSparta

Fig. 35.1 Contrast of picture size
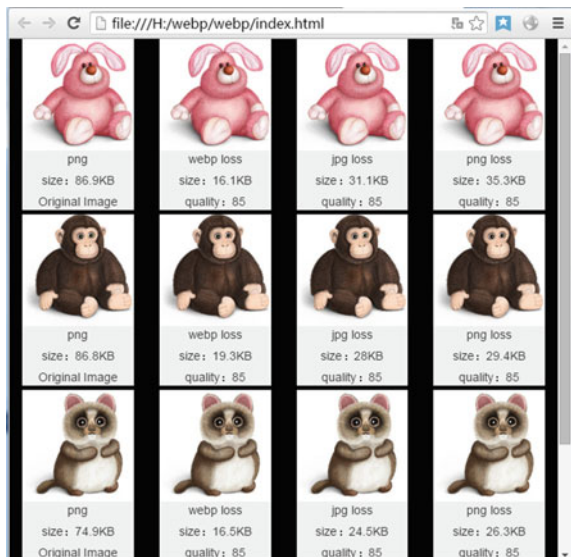
35.3.2 PSNR Test Experiment

Because MATLAB does not recognize the WebP format and we can only use Chrome to open the WebP images, so this experiment uses HTML5 canvas to process these images and write Javascript code to calculate the PSNR value.

First, paint the picture on the canvas. Then, we use 'getImageData' function to get the pixel information of images. Finally, we can calculate the PSNR.

35.3.3 WebP Performance Comparison Test

According to the data, the decoding rate of WebP is about 1.4 times slower than JPG [3], will this affect the page rendering speed of WebP? In order to test the performance of WebP in practical applications, this paper set a comparative study. There are two web pages, put a number of WebP format images on the one page, and put the JPG on another page. Then, test the rendering speed of two pages (Fig. 35.2).

Page 1 (21 images of JPG): http://www.ebo.edu.cn/test/jpg.html
Page 2 (21 images of WebP): http://www.ebo.edu.cn/test/webp.html
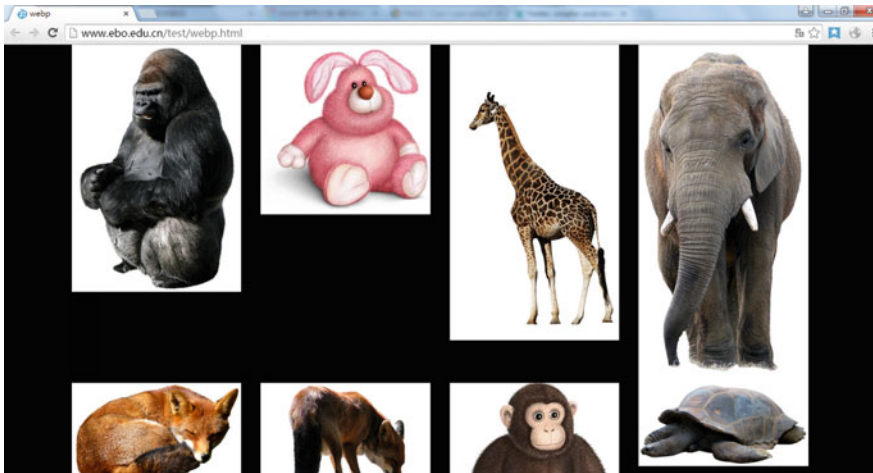
Fig. 35.2 Test page

35.4   Result and Discussion

35.4.1   Analysis of Picture Size

In the experiment, there are different sizes of the pictures; they are compressed into WebP, JPG, and PNG which has the quality of 85. Then measure the size of each picture, and make a comparison. Finally, we can make a conclusion.

As can be seen from Fig. 35.3, the size of WebP is significantly smaller than the two kinds of traditional format JPG and PNG, if they have the same quality. After calculation, the original image's size decreased by 78.15 % on average, if it converted to WebP. As well as the JPG is 66.82 % and PNG is 64.15 %. In this regard, WebP is clearly better than the other two image formats.

35.4.2   Analysis of PSNR

After using MATLAB and Javascript, we can get the value of PSNR of WebP, JPG, and PNG. The data is shown in Table 35.1 (Fig. 35.4).
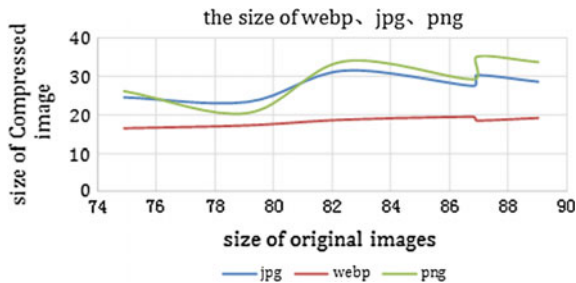
Fig. 35.3 Picture compression table

Table 35.1 Value of PSNR of different formats

Each format	WebP	JPG	PNG
1	43.7523	45.2270	46.3807
2	42.1896	45.2877	43.3205
3	44.5699	44.2936	45.9213
4	43.4572	44.4557	45.9998
5	44.3187	44.3974	46.9098
6	41.7297	43.8880	46.2013
Mean value	43.3362	44.5916	45.7889

Fig. 35.4 Test of PSNR
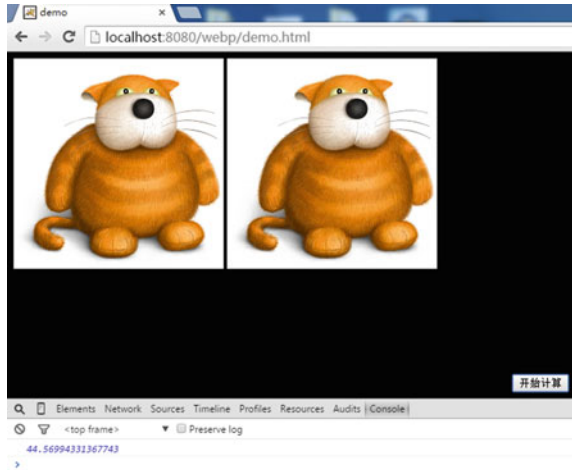
According to the data in the table, WebP's value of PSNR is about 43.3, the image quality is slightly less than JPG and PNG. But the difference cannot be resolved by the naked eye.

35.4.3 Performance Comparison Between WebP and JPG

Comparison of size: the total picture on the WebP page is 3.08M, while the volume of JPG page is 4.54M.

The comparison of overall page rendering rate is shown in the following Fig. 35.5.

It can be seen from Fig. 35.5 that WebP's rendering speed was faster than JPG's obviously. WebP spent only 12 s to load the whole page completely, while JPG but with a 14 s. Although the speed of decoding WebP is slower than JPG, It does not affect WebP's performance. The actual rendering speed is not slow.
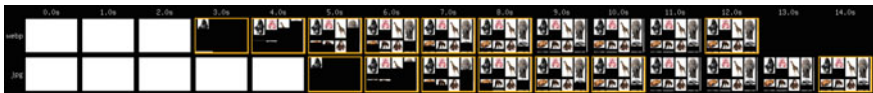
Fig. 35.5 Performance of WebP and JPG

Fig. 35.6 Support for all major browsers

Fig. 35.7 Support for mobile terminals

35.5 Conclusions and Prospects

The result of experiments indicates: WebP's compression quality is slightly inferior to JPG and PNG. But WebP has better image data compression algorithm, it can bring a smaller image size, with the lossless and lossy compression modes, alpha transparent and characteristics of animation. More important, the human eye cannot distinguish the loss of quality of WebP at all.

In addition, the compatibility of WebP is well. It can be seen from Figs. 35.6 and 35.7, Chrome, Opera, and Android browser are able to support WebP. From the perspective of equipment\operating system\browser, WebP's compatibility is up to 50 %. The browsers that do not support WebP can use WebP.js or some plug-ins to compatible WebP. Therefore, according to the analysis, we can draw the conclusions: (1) if the pictures size occupies the page size by half or more, we can use WebP; (2) if client software is embedded with webview based on chromium, we can use WebP; (3) if client software uses node-web kit development, we can use WebP. In the cases above, there are great advantages with using WebP. It can save a lot of broadband and enhance the page loading speed. Therefore, in the area of intense broadband demand, WebP will have well developed.

References

1. Google to unify the Internet image format? (2014). *China Education Network*, *08*, 80.
2. Richardson, I. E. (2004). Fast subjective video quality measurement with user feedback. *IEE Electronics Letters, 40*(13), 799–800.
3. Ilya, G. (2013). Faster, smaller and more beautiful web with WebP. http://www.tuicool.com/articles/goto?id=FFZ73y

Chapter 36
Comparing the Similarity of Image in Different Color Spaces

Jie Tang and Wenjie Yang

Abstract When the computer recognizes the original color images and the collected images without changing the color information, it is a question to choose the appropriate color space for image recognition. In order to find out the best color space for image recognition, four color spaces were chosen to compare the similarity of the image between the original images and the collected images in different color spaces. In the premise of maintaining the image recognition accuracy, it can simplify the process of the image recognition by choosing the color space as the image pretreatment process.

Keywords Color image · Image recognition · The best color space · Tolerance

36.1 Introduction

In real life, it is very useful to recognize and classify the original images and the collected images. However, the different collected location, angle, environment can affect the collected images and they will result in geometric distortion, size scaling, color inconsistency, and so on [1]. There are many mature methods to deal with the geometric changes in images such as image rotation, scaling, and translation. But in allusion to the color change of images, we do not have effective color image recognition algorithm for image recognition. As a result, the computer can be affected by the changes in the image's color easily. It will classify the original images and the collected images into different groups. The paper will not study how to

J. Tang (✉) · W. Yang
School of Printing and Packaging Engineering, Beijing Institute
of Graphic Communication, Beijing, China
e-mail: tjgoos12345@163.com

improve the image recognition algorithm, but will focus on choosing the color space for image recognition when the image color changes. Finally simplify the process of the image recognition and improve robustness by choosing the best color.

36.2 Different Color Spaces

The number of the color space classification is big. This paper involves two main classes, four color spaces totally. They are RGB, YC_bC_r, $L*a*b*$, and LCh color space respectively.

RGB color space represents red, green, and blue components. YC_bC_r color space is used in digital industry generally. The YC_bC_r values can be transferred by the relevant RGB color values through the transfer equation [2].

$L*a*b*$ and LCh color spaces belong to the uniform color space. The value of $L*a*b*$ color space is similar to the color feeling of the human eyes [3]. In this paper, the $L*a*b*$ values are translated from the RGB values by the linear matrix [4]. LCh color space corresponds to three color attributes: lightness, hue, and saturation. So the LCh color space can mimic how the human eye perceives color directly.

36.3 Image Similarity

Image similarity is used in the algorithm for intensity-based digital image matching. In this paper, image similarity was used to evaluate the correlation of two images.

The normalized cross correlation (NCC) image similarity algorithm was used in the paper. Image similarity of NCC algorithm is as follows:

$$R_i = \frac{\sum_{m=1}^{M}\sum_{n=1}^{N}[S_i(m,n) \times T_i(m,n)]}{\sqrt{\sum_{m=1}^{M}\sum_{n=1}^{N}[S_i(m,n)]^2}\sqrt{\sum_{m=1}^{M}\sum_{n=1}^{N}[T_i(m,n)]^2}} \qquad (36.1)$$

In 36.1, letter T denotes the color values of the original images, letter S denotes the color values of the collected images. The R value is larger as the relevance of the two images is higher. Through Eq. 36.1, all the R values are the normalization values. So the different dimensions of the color spaces can be compared directly [5].

In grey image, the whole decrease of the image lightness cannot affect the calculation results of NCC algorithm. This characteristic can still be applied to the RGB color image. When we decrease the image lightness, the RGB's three channels values will be multiplied by the same coefficient from 0 to 1. So the original color data is denoted as R_n, G_n, B_n, then the changed data is denoted as αR_n, αG_n, αB_n, the letter α is the coefficient. Then bring two groups of the data into the Formula 36.1. Extract the coefficient α, the value of the numerator is equal to the

denominator, the result equals 1. To sum up, NCC algorithm can eliminate the error when the image's lightness decreases in the RGB color space. Special attention is paid, when we apply the characteristic of NCC algorithm to the RGB color space, but for other color spaces we need to verify the characteristic through the experiments.

36.4   Experiments and Data Analysis

36.4.1   Experiment Process

The program is implemented in the MFC framework in VS2010. The main functions are color data transformation and image similarity calculation [6].

Process: choose one picture, make sure that other properties of the picture remains unchanged, modify the lightness, hue, saturation of the picture in fixed step length respectively to simulate different collected images in different conditions in the RGB color space. After that, calculate the R value and draw the curves according to the data.

36.4.2   Data Analysis

In actual image recognition, the computer will compare different collected images with the original image and the R values of the correlated images must be bigger than others. But in the experiments, the process of finding the matching collected image was omitted. The collected images have been matched with the original image already. So the R value change is smaller and the color space tolerance is higher.

1. As shown in Fig. 36.1, the saturation value of the pictures is changed from high to low. As analyzing the saturation changes, it includes four curves of the color space. As shown in Fig. 36.2a–d, they correspond to RGB, YC_bC_r, $L*a*b*$, LCh color space respectively.

Fig. 36.1 Saturation change schematic
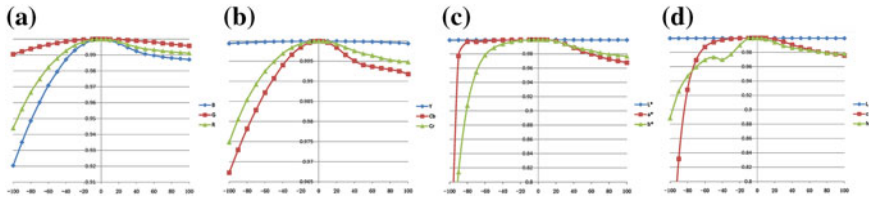
Fig. 36.2 The image similarity curves of the saturation change

Fig. 36.3 B channel change schematic
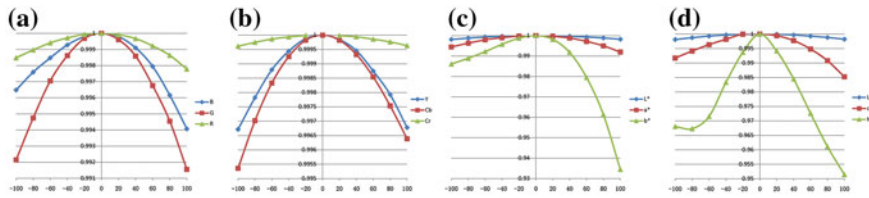
Fig. 36.4 The image similarity curves of the hue change

Through analyzing the variation range, the variation range of YC_bC_r color space is the smallest, then followed by the RGB color space. But the variation range of $L*a*b*$ and LCh color space is bigger than others. So the tolerance of YC_bC_r color space for saturation change is the biggest of all color spaces.

2. As shown in Fig. 36.3, the B channel value of the pictures is changed from high to low. Analyze the hue change, as shown in Fig. 36.4a–d, they correspond to RGB, YC_bC_r, $L*a*b*$, LCh color space respectively.

   Because the curves of the three channels of the RGB represent the similar characteristics, we choose one group of the B channel to analyze. By analyzing the variation range and the numerical magnitude of the R value, the variation range of YC_bC_r color space is the smallest and the numerical magnitude is bigger. According to the above, the tolerance of YC_bC_r color space for hue change is the biggest of all color spaces.

3. As shown in Fig. 36.5, the lightness value of the pictures is changed from high to low. Analyze the lightness change, as shown in Fig. 36.6a–d, they correspond to RGB, YC_bC_r, $L*a*b*$, LCh color space respectively.

The negative half axis part of the curve in Fig. 36.6a–d is observed. When the lightness is decreasing, the calculated R values in RGB, $L*a*b*$, LCh color space almost have no change in the wide range of brightness changes. The characteristic

Fig. 36.5 Lightness change schematic
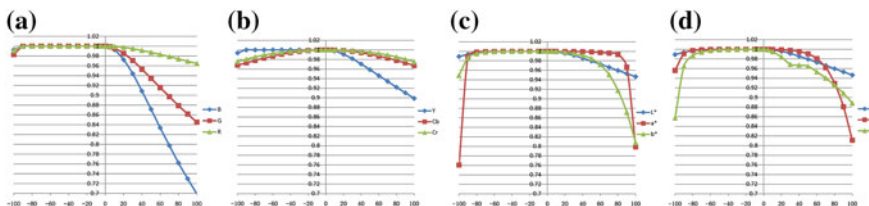
Fig. 36.6 The image similarity curves of the lightness change

of NCC algorithm is introduced before can be explained in the phenomenon, at the same time the experiments can certify that the characteristic of NCC algorithm also apply to $L*a*b*$, LCh color space. However, when the lightness changes out of the range, the R value will decrease quickly. Observing the Fig. 36.6b, because of the special characteristic of YC_bC_r color space, NCC algorithm cannot eliminate the effect of image lightness changes in the C_b and C_r channels. But the R value still remains at a high value. The tolerance of YC_bC_r color space is high.

According to the above, by analyzing from the variation range and the numerical magnitude of the R value, the R value calculated by YC_bC_r color space is the least sensitive to the color lightness change, so the tolerance of YC_bC_r color space for lightness change is the biggest of all color spaces.

36.5   Conclusions

Summing up the above, we can get the preliminary conclusion: the tolerance of YC_bC_r color space for color change is the biggest in four color spaces which are involved in the experiments. The YC_bC_r color space is the best in four color spaces. And the data of YC_bC_r color space can be transformed by the RGB color space easily, so it can be suitable for the process of fast image recognition. This conclusion can also be applied to color image matching technique and it can simplify the process of the image matching by choosing the color space as the pretreatment process.

In this paper, we only study on the situation of the single color attribute changing in four color spaces. The change of the color attribute is single and the number of color space included in the experiments is small, so we only gave a preliminary conclusion. Further work can be done by increasing the changing ways including the combination of image color attributes and the species number of color spaces. Further studies will help to make more comprehensive conclusion.

References

1. Liu, H.-B., Shen, J., & Guo, S. (2010). Chapter 9. In S.-B. Zhang (Ed.), *Digital image processing using visual C++*. China: China Machine Press.
2. Zhang, Y., Liu, X., & Li, H. (2007). The precision of RGB color space convert to YC_bC_r color space. *Journal of Southern Yangtze University (Natural Science Edition), 6*(2), 200–202.
3. Xu, Y.-F. (2011). Chapter 4. In *Color management principles and applications*. Printing Industry Press.
4. Liu, H.-X. (2008). Chapter 3. Du, Y. F. (Ed.), *Color science and technology*. China: China Light Industry Press.
5. Wang, H.-M., Zhang, K., & Li, Y.-J. (2004). *Computer Engineering and Application*, 19, 42.
6. Walter, S., & Kenrick, M. (2014). *Absolute C++* (5th ed.). China: Publishing House of Electronics.

Chapter 37
Study on Chromatic Modulation Transfer Function of Digital Camera

Wei Liu, Guangxue Chen, Yang Jin and Yuehong Song

Abstract In this paper, we reported a method to get chromatic modulation transfer function of digital camera. First, a digital camera is used to take pictures by the "edge" method as test form. The image pattern is converted into a LAB via Photoshop. The converted image is read with Lab Matlab and Fourier transform is used to transfer edge spread into modulation function. Then the different pixel value or aperture value of the same color and the different color image is observed. The changing of MTF of LCH of different Lab images can be observed as to draw the corresponding conclusions. Finally, on the test, the change of camera pixel value or camera aperture value will affect the MTF. Without other conditions changing, its MTF is better when pixel value is large. The smaller the aperture value which means the larger of aperture, MTF is smaller. Canon 7D, which is the digital camera used in this experiment, has the strongest colorful resolution ability in magenta, relatively weaker in cyan, yellow followed. The results indicated that the different digital camera pixel value and aperture value will affect the MTF, and the ability to distinguish the different colors of a camera is also different.

Keywords Digital camera · Color resolution · Modulation transfer function (MTF) · Edge method

W. Liu · G. Chen (✉)
State Key Laboratory of Pulp and Paper Engineering, South China University
of Technology, Guangzhou, China
e-mail: chengx@scut.edu.cn

W. Liu
Shenzhen Engineering Laboratory of 3D Printing Technology, Shenzhen, China

Y. Jin · Y. Song
School of Printing and Packaging Engineering, Beijing Institute of Graphic Communication,
Beijing, China

37.1   Introduction

Digital cameras are extremely important digital devices of digital printing technology, which capture the prepress graphic information and help make reproduction of the original; they combine the imaging technology with digital information technology, having an unparalleled advantage, the appearance of digital camera create a New Era reproduction of digital printing [1, 2]. With the increase requirements of image quality of digital printing systems, the relative performance of digital cameras have also been concerned, which attempt to analysis the modulation transfer function (MTF) of digit camera.

The development of modern information theory proved that in the linear space invariant systems, any imaging series can be effectively looked as a spatial frequency filter, which imaging features and image quality evaluation, can be indicated by the ratio of frequency between the images and originals [3–5]. This frequency comparison feature is called modulation transfer function. MTF is a quantitative measure of the imaging system and a method to represent the quality of image detail. In the optical modulation transfer function, MTF describes the transmission capacity for contrast ratio of the optical system. Now, it is very common and convenient to use the MTF to assess the imaging performance of the printing system and the printing image quality in printing area.

37.2   Background and Significance of the Research of Digital Cameras' MTF

Most of the former experiences are based on black and white resolution of the beta in the process of obtaining MTF [6], and in the study, in color MTF of digital cameras, the existing research are still stay R/G/B three channels. So in this article, we explore a way expanded from the traditional "black and white" beta to the color range. To test different colored blocks on the basis of color resolution testing requirements with method of moving blade [7–9], then getting the different color responses of digital camera.

In imaging system, the quality of transferred images directly related to its frequency response characteristics. Therefore, it is critical to obtain the frequency response characteristic of the imaging system to optimize the system design and use in image correction processing.

37.3 Principle of MTF

Linear system theory proves that the system frequency response function contains amplitude and phase frequency response in two parts. Set the original image is a cosine wave which frequency is f, amplitude is L_{A0}, and luminance extending transversely. Including, L_{AV0} is brightness average (Blue line in Fig. 37.1).

$$L_0(x) = L_{AV0} + L_{A0}\cos(2\pi fx) = L_{AV0} \times \left[1 + \frac{L_{A0}}{L_{AV0}}\cos(2\pi fx)\right] \qquad (37.3.1)$$

Defined modulation M as follows:

$$M = \frac{L_{Max} - L_{Min}}{L_{Max} + L_{Min}} \qquad (37.3.2)$$

Form: $L_{Max} = L_{AV0} + L_{A0}$ and $L_{Min} = L_{AV0} - L_{A0}$, then:

$$M_0 = \frac{L_{Max0} - L_{Min0}}{L_{Max0} + L_{Min0}} = \frac{L_{A0}}{L_{AV0}} \qquad (37.3.3)$$

So:

$$L_0(x) = L_{AV0} \times [1 + M_0\cos(2\pi fx)] \qquad (37.3.4)$$

Original image has captured by the imaging system, there is the line shown in Fig. 37.1, the obtained image function (Subscript is 1, red line):

$$L_1(x) = L_{AV1} \times [1 + M_1\cos(2\pi fx)] \qquad (37.3.5)$$

If there is a phase shift imaging, there is other function (Green dotted line in Fig. 37.1):

Fig. 37.1 Luminance image of cosine wave imaging
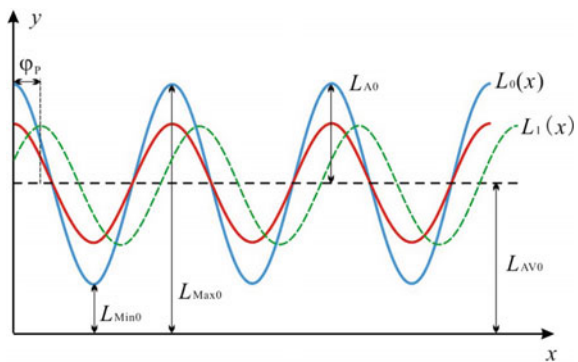
$$L_1(x) = L_{AV1} \times [1 + M_1 \cos(2\pi fx - \varphi_P)] \tag{37.3.6}$$

After imaging, modulation M_1 of image becomes:

$$M_1 = \frac{L_{A1}}{L_{AV1}} \tag{37.3.7}$$

Due to certain factors, modulation turns to go down ($M_1 \leq M_0$). In general, with the rise of the spatial frequency of the original image, modulation of image after imaging declines.

General condition, the ratio of M_1 which is the modulation after imaging and M_0 which is the modulation of original image is called "modulation transfer value", namely:

$$T = \frac{M_1}{M_0} \tag{37.3.8}$$

Relationship between spatial frequency (f) and modulation transfer value called "modulation transfer function", written as:

$$T(f) = \frac{M_1(f)}{M_0(f)} = \frac{\left(\frac{L_{A1}}{L_{AV1}}\right)}{\left(\frac{L_{A0}}{L_{AV0}}\right)} = \frac{\left(\frac{L_{Max1} - L_{Min1}}{L_{Max1} + L_{Min1}}\right)}{\left(\frac{L_{Max0} - L_{Min0}}{L_{Max0} + L_{Min0}}\right)} \tag{37.3.9}$$

37.4 Experiment Part

37.4.1 Experimental Equipment

Experimental materials: Top advanced semigloss HD170 photo paper; ruler; 35×350 mm splines used by IGTAIC2-5 type printability tester.

Experiment equipment: Profile Maker software; Photoshop CS5; digital cameras Canon 7D; IGTAIC2-5 type printability tester and supporting four-color ink: cyan, magenta, yellow, black; Color Controller transmission observation box; Matlab software.

37.4.2 Experiment Equipment Parameters

Digital Camera Canon EOS 7D is APS-C size which has 18 million effective pixels during the experiment, the aspect ratio sets to 3:2; there are L/M/S profile to choose for photo model, its color space is Adobe RGB, and file storage format is JPG.

37.4.3 Experimental Procedure

37.4.3.1 Make Beta

Use IGTAIC2-5 type printability tester with matching ink yellow, magenta, cyan, to print yellow, magenta, cyan color splines, totally 3 pieces of splines. Colored areas of each spline cut up with a sharp knife, to keep at least one side has a sharp blade edge, keep the same size of splines, then cling them to same white with double-sided adhesive glue, respectively. As shown in Fig. 37.2.

37.4.3.2 Shooting Beta

Set the camera to initial state before experiment, keep the position of camera and focal length unchanged in the experiment. Put betas in the transmission observing box and use reflected light to observe which has fixed camera angles and shooting distance, an uniform reflection light, and a fixed beta slots.

Installed the camera and adjust focus before experiment. Take one test beta and fixed it in transmission observing box, put a ruler to measure the actual shooting dimensions of the digital camera, which is 120 mm × 80 mm (Fig. 37.3).

To avoid jitter, set to time-lapse shooting of camera. Shooting three colors: yellow, magenta, and cyan, the each color shoots six groups of data. Totally 18 groups of data are got.

> a.. Pixel value(mm × mm) = L(5184 × 3456) Aperture value = 5.6
> b. Pixel value(mm × mm) = L(5184 × 3456) Aperture value = 36
> c. Pixel value(mm × mm) = M(3456 × 2304) Aperture value = 5.6
> d. Pixel value(mm × mm) = M(3456 × 2304) Aperture value = 36
> e. Pixel value(mm × mm) = S(2592 × 1728) Aperture value = 5.6
> f. Pixel value(mm × mm) = S(2592 × 1728) Aperture value = 36

Fig. 37.2 Cyan print test forme
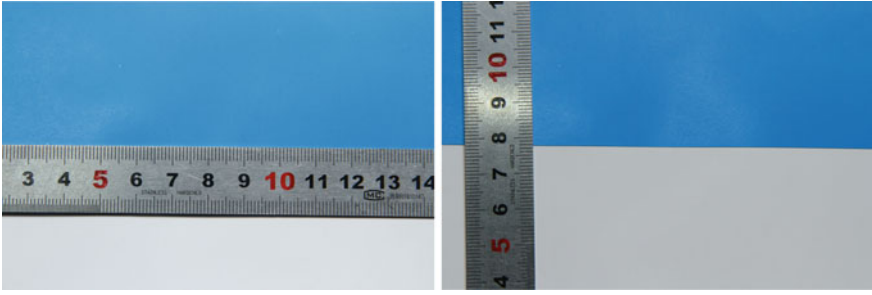
Fig. 37.3 The shot size of camera

37.4.3.3 LCH-MTF of Chromaticity Space

Since this experiment is for color images, not only black and white, so get the lightness, chroma and hue of color is very important according to color properties. It is necessary to transfer between LCH and LAB. We can obtain the frequency response characteristic of a digital camera from lightness, chroma, and hue.

The image after taken by camera should transfer into LAB mode to obtain a digital camera's MTF of LCH, and the following formulas are conversions of chroma C and hue angle H:

$$C = \sqrt{(a^2 + b^2)} \qquad (37.4.1)$$

Hue angle H should discuss the position of a^* and b^* values:

First quadrant, when $a^* > 0, b^* > 0, H = \arctan(b^*/a^*);$ (37.4.2)

The second quadrant, when $a^* < 0, b^* > 0, \quad H = 180 - \arctan(b^*/|a^*|);$

(37.4.3)

Third quadrant, when $a^* < 0, b^* < 0, \quad H = 180 + \arctan(|b^*|/|a^*|);$ (37.4.4)

Fourth quadrant, when $a^* > 0, b^* < 0, \quad H = 360 - \arctan(|b^*|/a^*);$ (37.4.5)

At the origin, when $a^* = 0$ and $b^* = 0, \quad H = 0;$ (37.4.6)

Right above the x-axis, when $a^* > 0, b^* = 0, \quad H = 0;$ (37.4.7)

Right above the y-axis, when $a^* = 0, b^* > 0, \quad H = 90;$ (37.4.8)

Right down the x-axis,   when $a^* < 0, b^* = 0,$ $H = 180;$ (37.4.9)

Right down the y-axis,   when $a^* = 0, b^* < 0,$ $H = 270.$ (37.4.10)

37.4.3.4 The Programming Calculation Process of MATLAB to MTF

After photograph all betas. Convert the image pattern into LAB mode via photoshop which stored as TIFF format, ICC color profile is Adobe RGB.

Then, Matlab software processes LAB mode image to obtain MTF curves. The following is related processes of Matlab program.

1. First, set the digital camera's in horizontal and vertical dimensions, according to the size of beta in photograph.
2. Open the image of Lab mode, turn it into double precision, and separate it into LAB three channels.
3. Clear the original data and convert into chrominance values, then operate equations to get the saturation value of the image.
4. Convert the image into LCH mode, discuss the situation the position in 1, 2, 3, 4 quadrants, at the origin, on the axis with conditional statements.
5. Find out the average value of the column of L channel, then seek differential, and take absolute value of it. Find out the maximum value and position of it by the Fourier transform and take half of the data from the maximum value. Determine the spacing between each two rows of pixels and find the frequency of each frequency data between two rows of difference [10]. Set the MTF function in the position of 5 % and take frequency coordinate values [11] of this position [12].

   It's the same process for chroma.

37.5 Results and Discussion

37.5.1 Lightness MTF Test of Canon 7D

When image lightness $L = 50$, and the camera pixel is set as L, after MATLAB programming, brightness MTF is shown in Fig. 37.4.

Frequency coordinate values in the position of 5 % of MTF as Table 37.1.

As can be seen from the data in table: when the brightness is 50, this camera's magenta ability resolution is best, cyan is followed, and yellow is poor.

Changing pixel and aperture value of the camera, photograph the same color under those different conditions, after MATLAB programming, the data is shown in Table 37.2.
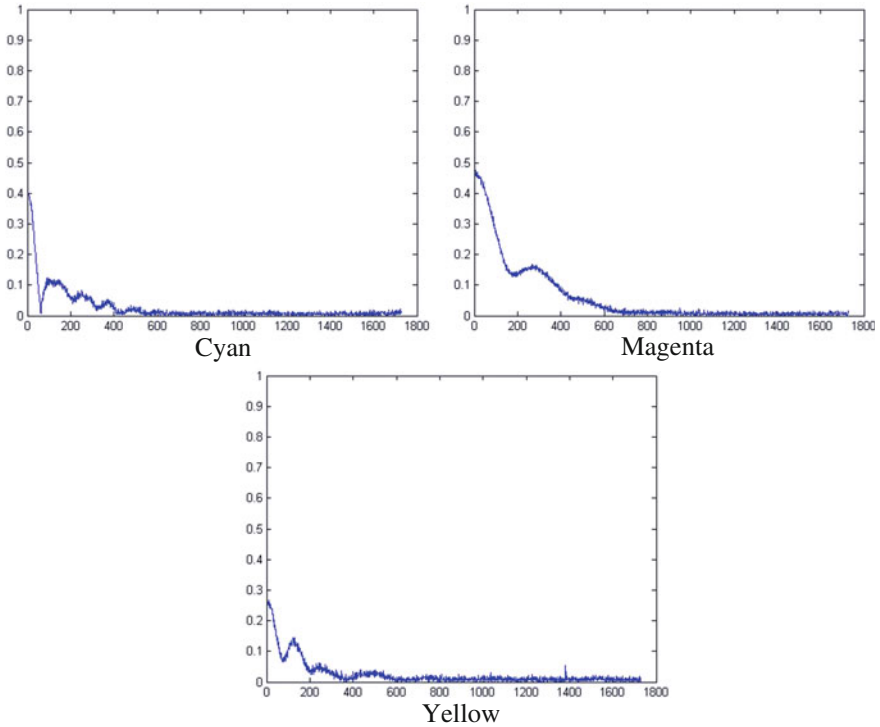
Fig. 37.4 Relationship between different color's MTF and frequency identification when $L = 50$ in experience of lightness, Cyan, Magenta, and Yellow

Table 37.1 The frequency identification value to cyan, magenta, and yellow of camera when MTF value is 5 % in test of lightness

Parameter setting	Boundary line of MTF (%)	Hue→	C	M	Y
Brightness $l = 50$ Pixel: l Aperture value $f = 5.6$	5	Frequency identification→	46.6	62.8	30.8

From the pictures and tables, in the lightness MTF test, the MTF will change with the pixel and aperture value of the camera, it means the frequency identification of this camera are different in different colors, pixels, and aperture values. Wholly the MTF is better in bigger pixel values; MTF is better in smaller aperture values. And Canon 7D's frequency identification is best in Magenta, cyan is followed, and yellow is poor.

Table 37.2 The frequency identification value to cyan, magenta, and yellow of camera when MTF value is 5 % in different situation in text of lightness

Parameter setting	Boundary line of MTF (%)	Hue→	C	M	Y
Pixel: *L* Aperture value *F* = 36	5	Frequency identification→	47.5	63.4	31.3
Pixel: *L* Aperture value *F* = 5.6	5	Frequency identification→	46.6	62.8	30.8
Pixel: *S* Aperture value *F* = 5.6	5	Frequency identification→	35.0	60.7	30.5

37.5.2 *Saturation MTF Test of Canon 7D*

In the test of saturation MTF of Canon 7D, experimental procedures are similar with the lightness MTF test.

Changing pixel and aperture value of the camera, photograph the same color under those different conditions, after MATLAB programming, the data are shown in Table 37.3.

From tables, in the saturation MTF test, we can found the MTF also will change with the pixel and aperture value of the camera; wholly the MTF is better in bigger pixel values; MTF is better in smaller aperture values. Canon 7D's frequency identification is best in magenta, cyan is followed, and yellow is poor; this is same as the test in lightness MTF test.

Table 37.3 The frequency identification value to cyan, magenta, and yellow of camera when MTF value is 5 % in different situation in test of chroma

Parameter setting	Boundary line of MTF (%)	Hue→	C	M	Y
Pixel: *L* Aperture value *F* = 36	5	Frequency identification→	28.1	40.6	26.6
Pixel: *L* Aperture value *F* = 5.6	5	Frequency identification→	22.5	39.4	29.0
Pixel: *S* Aperture value *F* = 5.6	5	Frequency identification→	21.3	43.2	28.7

37.6 Conclusions

In conclusion, the MTF will change with the pixel value and aperture value of the camera, it means the frequency identification of this camera are different in different colors, pixels, and aperture values. Wholly the MTF is better in bigger pixel values; MTF is better in smaller aperture values. And Canon 7D's frequency identification is best in magenta, cyan is followed, yellow is poor which means Canon 7D has the strongest colorful resolution ability in magenta, relatively weaker in cyan and yellow followed. The results indicated that different digital camera pixel value and aperture value will affect MTF, and the ability to distinguish different colors of a camera is also different. Of course, there are also some problems in using the knife edge method to get camera color MTF, such as in hue angle test showed a lot noise, this method does not accurately measure its frequency identification, which will be improved further. In short, it is a good guide to analysis color MTF of different colors; it has a very important significance for future digital camera color MTF.

References

1. Li, D.-c. (2007). Imaging mechanism of digital single lens reflex cameras. *Journal of Image Technology, 2*, 29–33.
2. Jiang, Y., & Zhu, W.-q. (2014). Research of image quality optimization technology for digital still camera. HuNan University of Technology.
3. Chawla, A. S., Roehrig, H., Rodriguez, J. J., & Fan, J. (2005). Determining the MTF of medical imaging displays using edge technique. *Journal of Digital Imaging, 4*, 296–310.
4. Yao, D.-j., & Liu, Z.-j. (2012). MTF measurement technology research. HeFei University of Technology.
5. Li, Y-p, & He, B. (2013). Quantitative evaluation of image quality of CCD subpixel imaging using MTF. *Infrared and Laser Engineering, 42*(2), 443–448.
6. Xu, W.-w., Zhang, L.-m., Yang, B.-o., & Chen, H.-y. (2011). On-Orbit MTF measurement of high resolution satellite optical camera using periodic targets. *Acta Optica Sinica, 31*(7), 0711001.
7. Holst, G. C. (2007). *CMOS/CCD sensors and camera systems*. USA: JCD Publishing.
8. Zhang, P., Liu, T., & Wang, H. (2009). MTF estimation based on system model for linear CCD camera and image recovery. *Optical Technology, 35*(3), 394–398.
9. Xu, H., Li, C-r, Li, X-h, & Li, Z-y. (2012). An optimized knife-edge algorithm for on-orbit MTF estimation. *Remote Sensing Information, 27*(6), 10–16.
10. Zhu, L-z. (2010). 1024 points fast Foutier Transform based on FPGA. *Journal of ShenYang LiGong University, 29*(2), 61–64.
11. Zong, J.-b., Duan, L.-y., Wang, Y., Duan, L.-x., & Li, X. (2010). Research and realization of method for making software based on MATLAB GUI. *Electronic Design Engineering, 18*(7), 54–56.
12. Thirumalai, K., Singh, A., & Ramesh, R. (2011). A MATLAB code to perform weighted linear regression with (correlated or uncorrelated) errors in bivariate data. *Journal of the Geological Society of India, 77*(4), 377–380.

Chapter 38
Extraction of Golden Area in Image Based on Region Growing

Ying Wu, Jiong Liang, Jialin Yin and Junyu Nie

Abstract The paper proposed an algorithm to extract the con-tone golden region in an image as a printing plate of metallic ink. First, the image is converted into HSV color model. H-components are selected as the original for image segmentation. Second, background interference is a problem for H-component of HSV model. Region growing method is not interfered by it. We suggest to segment H-component by region growing method. Finally, H-components of HSV model and RGB-mixed component of RGB model are combined to get a golden area image. The experimental results show that it is more suitable to determine a threshold value by Otsu algorithm than setting threshold value manually. Multipoint region growing image is more complete than single-point region growing image. Therefore we suggest using the multipoint region growing to extract the golden area of image. It brings good result, which verifies the feasibility of our suggested method.

Keywords Region growing algorithm · Golden color · RGB · HSV

38.1   Introduction

It is challenging to reproduce the texture of metal object accurately on the paper by printing process. A big difference exists between the reproduced result by CMYK inks and the appearance of real metal objects. In order to create the result of continuous tone using metallic ink, closing to the real metal appearance, it is necessary to extract the golden region from an image. Image segmentation method could be utilized to do it. There are many algorithms for the grayscale image, such as segmentation based on threshold, or edge detection, etc. The proposed method for the grayscale image can be extended to application to color image. Owing to the diversity of image contents, the choice of segmentation algorithm should match the

Y. Wu (✉) · J. Liang · J. Yin · J. Nie
Beijing Institute of Graphic Communication, Beijing, China
e-mail: jinmomo@126.com

most appropriate color space. In this paper, region growing algorithm was used to segment the image and extract the golden regions, based on RGB color space and HSV color space.

38.2 Generate Grayscale Image of Golden Information

38.2.1 RGB Color Space

An RGB color space [1] consists with R-component, G-component, and B-component. Among them, R-component represents red color property, and G-component represents green color property, as shown in Fig. 38.1.

38.2.2 Avoid White Area

To get the smaller value from R-component and G-component, the yellow and white information of the color can be obtained. The result is shown in Fig. 38.2b. Then we can determine yellow information by subtracting B-component from the component with yellow and white information, as shown in Fig. 38.3 [2].

38.3 Determine Golden Region

38.3.1 RGB to HSV Conversion

Generally, digital image that we can get is an RGB mode. Gold information shows special feature in R and G components, but only R and G components are not enough yet to determine if the pixels are owned by golden region or not. HSV color space [1] presents hue, saturation, and bright value of color, denoted by H, S, and V

Fig. 38.1 RGB color space
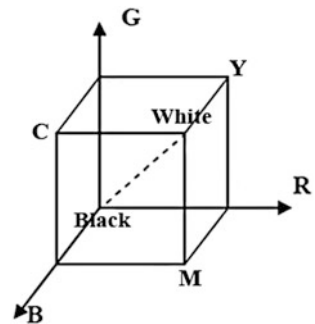
Fig. 38.2 Sample image and *yellow* and *white* information image. **a** Original. **b** *Yellow* and *white* information image

Fig. 38.3 *Yellow* information image

respectively. Generally, each uniform area in the image owns a relatively consistent color property, which means that H can be used for segmentation of the different color areas. Therefore, here chooses HSV mode as the property color space and the hue values is taken as the color feature component. The color image is converted from RGB model to HSV. RGB to HSV conversion formulas [2, 3] are as Formulas 38.1, 38.2 and 38.3.

$$
H = \begin{cases}
0° & \text{if MAX} = \text{MIN} \\
60° \times \frac{G-B}{\text{MAX}-\text{MIN}} + 0°, & \text{if MAX} = R \text{ and } G \geq B \\
60° \times \frac{G-B}{\text{MAX}-\text{MIN}} + 360°, & \text{if MAX} = R \text{ and } G < B \\
60° \times \frac{B-R}{\text{MAX}-\text{MIN}} + 120°, & \text{if MAX} = G \\
60° \times \frac{R-G}{\text{MAX}-\text{MIN}} + 240°, & \text{if MAX} = B
\end{cases}
\tag{38.1}
$$

$$
S = \begin{cases}
0, & \text{if MAX} = 0 \\
\frac{\text{MAX}-\text{MIN}}{\text{MAX}} = 1 - \frac{\text{MIN}}{\text{MAX}}, & \text{otherwise}
\end{cases}
\tag{38.2}
$$

$$
V = \text{MAX}
\tag{38.3}
$$
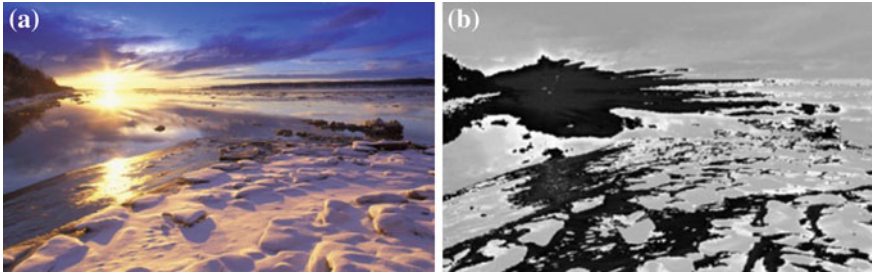
Fig. 38.4 Sample image and its H-component. **a** Original. **b** H-component image

One of the chosen sample images in the research and its converted H-components are shown in Fig. 38.4.

38.3.2 Segment H-Component Based on Hue Values

After conversation of color space from RGB to HSV, the following step in this research is to determine the H value's range of golden color. Some areas were chosen as golden region beforehand by the manual judgment. The hue values of the pixels in these golden sections are measured quantitatively and analyzed on statistical method, then we get the hue value range of golden color. The H-component image is converted to a binary image based on this value range [4, 5], where the pixels whose grayscale value are in the value range are shown in white, which means they are in golden area; non-golden area is shown in black, the grayscale value assigned to 0. The separated golden area is shown in Fig. 38.5. Background interference is a problem for H-component, therefore region growing algorithm was chosen to segment H-component image.

Fig. 38.5 Golden area after image segmentation

38.4 Region Growing Algorithm for Image Segmentation

38.4.1 Region Growing Algorithm

Region growing [6, 7] is a simple region-based image segmentation method. This approach to segmentation examines neighboring pixels of initial seed points and determines whether the pixel neighbors should be added to the region. The first step in region growing is to select a set of seed points. After determining the seed points, we have to determine the threshold. If the difference of pixels value less than threshold value, the regions will be considered as a same region.

38.4.2 Determine a Suitable Threshold Value by Otsu Algorithm

Otsu algorithm [8, 9] is one of the methods commonly used in image segmentation. Using Otsu algorithm, the image pixels are separated into two parts by a threshold value, which is determined when the variance between the separated two parts got the largest value. The threshold value will be used for the region membership criterion.

38.4.3 Experiment

In Fig. 38.6a–c is shown that the result is different from three threshold values which are manually defined. Threshold value of 0.15 is suitable for the region membership criterion. Figure 38.6d is threshold value of 0.152, which got through Otsu Algorithm. The experimental results show that it is suitable to determine a threshold value by Otsu algorithm.

38.4.4 Multipoint Region Growing Algorithm

Single-point region growing image like Fig. 38.7 is incomplete, while multipoint region growing [6] image is complete.
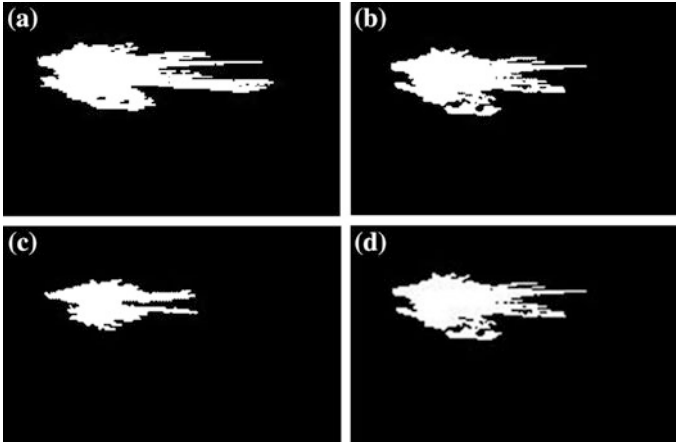
Fig. 38.6 Compare threshold value. **a** Threshold value of 0.02 (manual). **b** Threshold value of 0.15 (manual). **c** Threshold value of 0.5 (manual). **d** Threshold value of 0.152 (automatism)
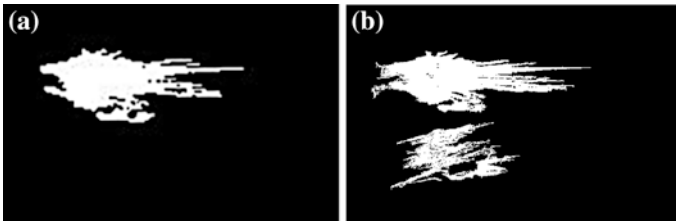
Fig. 38.7 Single-point region growing image and multipoint region growing image. **a** Single-point region growing image. **b** Multipoint region growing image

38.5 Golden Area Generation

38.5.1 Mask Yellow Component Image with Golden Area

The result of multipoint region growing image multiplying [2] the Y-component image with yellow information is shown in Fig. 38.8.

38.5.2 Image Reversing

The masked result just as in Fig. 38.8 is a negative image to the golden information, comparing with practical result that we expect. Therefore, the segmented image just as Fig. 38.8 with golden areas is required to reverse the grayscale values [2]. The reversed result is shown in Fig. 38.9.

Fig. 38.8 Golden information image
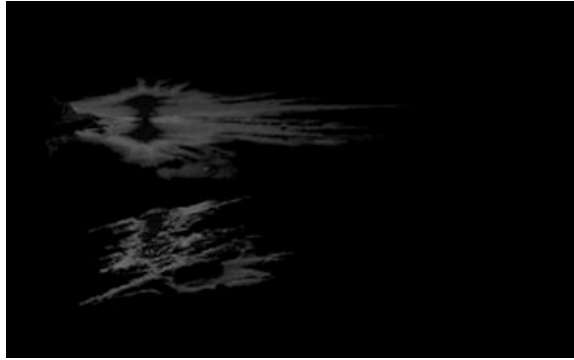
Fig. 38.9 The plate of golden ink

38.6 Conclusions

This paper researched application of region growing algorithm to printing image process. First, the image is converted into HSV color model. H-components are selected as the original for image segmentation. Second, background interference is a problem for H-component of HSV model. Region growing method not interfered by it. We suggest to segment H-component by region growing method. Finally, H-component of HSV model and RGB-mixed component of RGB model are combined to get a golden area image. The experimental results show that it is suitable to determine a threshold value by Otsu algorithm than setting threshold value manually. Multipoint region growing image is more complete than single-point region growing image. Therefore we suggest using the multipoint region growing to extract the golden area of image. It brings good result, which verifies the feasibility of our suggested method.

References

1. Liu, H. X., Wu, B., Xu, Y. F., et al. (2008). *Printing color science*. China Light Industry Press
2. Zhang, Z., Wang, Y. P, & Xue, G. X. (2010). *Digital image processing and machine vision—visual C++ and Matlab to achieve*. Beijing: Post & Telecom Press.
3. Information on http://zh.wikipedia.org
4. Zhang, M. T. (2005). *A study of spot color separating in hue centralized image*. Wuhan University
5. Bao, Q. L. (2010). Color image segmentation based on HSV space. *Software Guide, 9*(7), 171–172.
6. Cheng, F. X. (2008). Image segmentation based on region growing. *Science & Technology Information, 15*, 58–59.
7. Liu, Z. (2009). *A new color image segmentation algorithm based on region growing*. Nanjing University of Aeronautics and Astronautics
8. Yi, H., & Yi, R. (2012). Research on image segmentation based on threshold value method and regional growth method. *Electronic Test, 10*, 23–25.
9. Gonzalez, R. C., & Woods, R. E. (2005). *Digital image processing (MATLAB)*. Post &Telecom Press.

Chapter 39
A SVD-Based Color Image Watermark Algorithm in DWT Domain

Yuying Niu, Xinchun Cui, Qian Li and Jialin Ding

Abstract A color image watermarking algorithm based on SVD and DWT is proposed. First, watermark image is preprocessed by Arnold transform to improve algorithm security. Second, the low-frequency component of blue subgraph coefficients extracted from a host image decomposed by 2-DWT is analyzed by SVD. Then, the corresponding singular value of watermark image is embedded into the host image. Simulation results show that proposed method, guaranteeing algorithm high embedding capacity, has better performance in terms of invisibility and improves robustness significantly against a variety of noises, compression, shear and rotation, etc, attacks.

39.1 Introduction

Digital watermarking utilizes the ubiquitous redundant data and the randomness, making the copyright information embedded in the digital works, thus plays a role in protecting the copyright of digital works [1]. Wavelet domain watermarking has become one of the hot spots in recent years [2]. Lu and Zhu [3] exploits DWT technology selecting watermarking embedded in the low-frequency part of host image, without scrambling process. Chu et al. [4] chooses watermarking embedded in the low-frequency part. However, the correlation between extracted and original watermark is not high. SVD is an effective method of numerical analysis, and has

X. Cui (✉) · Q. Li · J. Ding
School of Information Science and Engineering, Qufu Normal University, Shandong, China
e-mail: cxcsd@126.com

Y. Niu
School of Communication, Qufu Normal University, Shandong, China

been widely used in many other fields. Liu and Tan [5] first proposed the digital watermarking method of embedding the watermark into singular values. This article proposes a watermark algorithm for color images based on the characteristic combination of DWT and SVD.

39.2 Discrete Wavelet Transform

The basic idea of wavelet transform is multi-resolution decomposition for images, which are broken into different spaces and frequency subimages, in line with the human visual system better [6]. Based on these, images can be effectively time −frequency decomposed. The first level of image can be divided into four frequency bands by DWT. Besides, low-frequency sub-band can be decomposed continuously into another four bands.

39.3 Singular Value Decomposition

Singular value decomposition is one of matrix's inherent characteristics and has some features that make it a very wide range of applications in the field of image processing. Its main features include: compressing amount of signal power to a few coefficients quickly and providing a guarantee for the watermark invisibility. The eigenvalues of digital image after conventional image processing is very stable.

39.4 Proposed Algorithm

In digital image watermarking, visual perception plays a very important role for performance evaluation. HVS has a lot of properties, in regard to the tricolor R, G, and B. The green component has the maximum luminance contribution for images, while the contribution of the blue component is relatively small. So, it is the best way of embedding watermarking into the blue component and that will get the best disguise for watermarking algorithm. Due to discrete wavelet multi-resolution, flat section of image focuses on majority of energy, corresponding to the low-frequency sub-band; so embedding watermarking into the low-frequency part has better robustness. In image scrambling technologies, Arnold transform plays an important role. This paper applies Arnold, to some extent, improving the security of watermarking algorithm.

39.4.1 Main Process of Algorithm

The process of digital watermarking for color image is shown in Fig. 39.1.

39.4.2 Embedding Process

(1) Apply separation on color image to depart three components of R, G, and B.
(2) Applying 2-DWT on B to decompose it into seven sub-bands: low-frequency approximation LL_2 and high-frequency HL_k, LH_k, and HH_k ($k = 1, 2$).
(3) Performing SVD operation on LL_2 and gray watermark image after Arnold transform, and obtain the singular values S_i, S_s as well as U_i, V_i^T, U_s, and V_s^T.
(4) Modifying S_i by adding to S_s, compute new values S and LL_2'.
(5) Applying IDWT on LL_2' and HL_2, LH_2, and HH_2 obtaining LL_1'. Then, IDWT is applied to LL_1' with HL_1, LH_1, and HH_1; and obtaining component blue B.
(6) Combining B with watermarking information with the prior components R, G together, then get the watermarked color image.

39.4.3 Extraction Process

(1) Applying separation on original and watermarked image to depart three components of R, G, and B, respectively, and extracting B′ and B″.
(2) Applying 2-DWT on B′ and B″, obtain LL_2'', LL_2''', HL_k, LH_k, and HH_k ($k = 1, 2$).
(3) Applying IDWT on LL_2'', LL_2''', obtain low-frequency matrix I″ and I‴.
(4) Performing SVD operation on matrix I″, I‴, and obtaining new singular value S′.
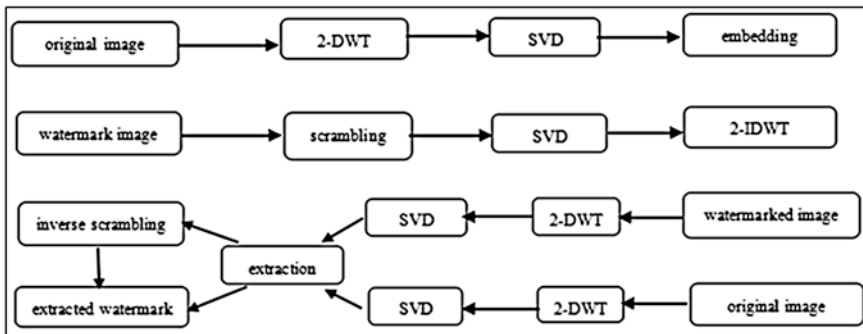
Fig. 39.1 Flow chart of watermark embedding and extraction process

(5) Performing ISVD operation on S′, obtain watermarking color image B′.
(6) Applying anti-scrambling on B′, then get the extracted watermark image.

39.5 Experimental Results and Analysis

The test images are 512 × 512 "lena" and gray scale 256 × 256 watermark (Fig. 39.2).

39.5.1 Quality of Watermark Embedding

Watermarked image and extracted watermark image are shown in Fig. 39.3.

The paper uses peak signal-to-noise ratio (PSNR) and normalized correlation (NC) to measure watermark transparency and the similarity between extracted watermark and the original [7]. Figure 39.3 shows watermarked image and extracted watermark under no attracts. Here, PSNR are 50.8166, 43.0777 and NC are 0.9926, 0.9935. PSNR is decreasing with the embedded factor α increasing. It is shown that the scheme maintains a satisfactory image quality and strong robustness.
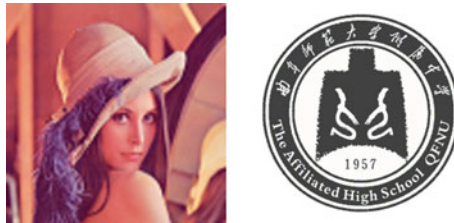
Fig. 39.2 Original image and watermark image

Fig. 39.3 Watermarked and extracted images with the different α (α = 0.1 or 0.3)

Table 39.1 The extracted watermarking images' NC values

Attack index	Distorted image	Extracted image	NC
GN			0.9896
SPN			0.9794
JPEG (40 %)			0.9945
CR(1/4)			0.9176
RT(5^0)			0.9635
MF			0.9861

39.5.2 Quality of Watermark Extraction

Watermarked image is distorted by taking various attacks including Gaussian noise (GN), salt and pepper noise (SPN), Compression (JPEG), Cropping (CR), Rotation (RT), and median filtering (MF) as follows in Table 39.1. The algorithm has high similarity between extracted watermark and original watermark.

Figure 39.4 shows the graph changes of NC values, and after six kinds of attacks, the best NC value reaches 0.9. So, the algorithm has the good robustness in terms of imperceptibility. To further illustrating the robustness of algorithm, watermarked images are attacked by different levels of salt and pepper noise and rotation, shown in Table 39.2. The results indicate that after each of salt and pepper noise of 0.05, 0.1, 0.3, and 0.5, extracted watermark image correlation coefficient
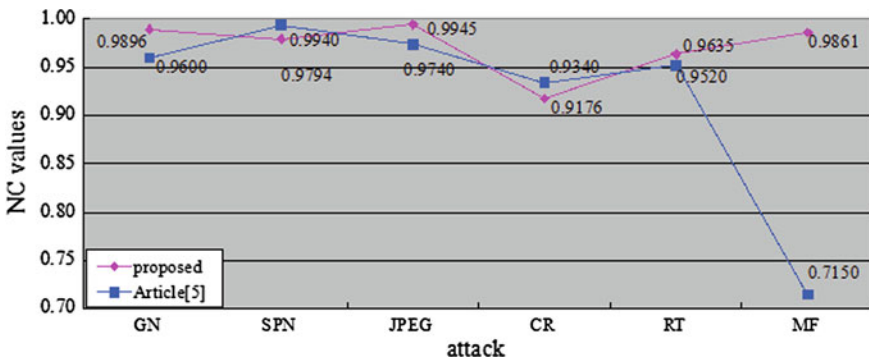
Fig. 39.4 Comparison of NC values with different algorithms

Table 39.2 The embedded image and images' NC after being extracted

SPN(α)	0.05	0.1	0.3	0.5
NC values	0.9794	0.9604	0.8630	0.7956
Extraction				
RT(α)	5^0	15^0	30^0	45^0
NC values	0.9635	0.8885	0.8120	0.7729
Extraction				

NC values are changed from 0.9794 to 0.7956. Making rotation attack about 5°, 15°, 30°, and 45° on the watermarked image, and the extracted watermark image correlation coefficient changes from 0.9635 down to 0.7729. It is shown that this algorithm has strong robustness for the pepper noise and rotation attack.

39.6 Conclusions

This study provides a new watermarking algorithm, adopting color image as the carrier, expanding application range of digital resources, making it more practical. Watermark image utilizes Arnold transform in preprocessing, increasing its security. The embedding position selects the low-frequency domain of wavelet transform and utilizes eigenvalue features, increasing algorithm robustness. Compared with other methods, under premise of good invisibility, embedding the largest watermarking information, enhancing its robustness. However, our scheme is non-blind, application of DWT, and SVD for color images adopting blind watermarking will be the focus of later research. Besides, in digital copyright protection area, how to exert watermarking technology and apply its application to audio, video, and other areas are the relevant researches in the future.

References

1. Zhao, X., & Hao, L. (2006). Overview of digital watermark[J]. *Computer Engineering and Design, 11*, 1946.
2. Li, Y. (2011). *Research on digital image scrambling algorithm* (pp. 11–12). Xi'an: School of Telecommunications Engineering, Xidian University.

3. Lu, J., & Zhu, J. (2010). A watermark algorithm for color images based on DWT SVD. *Communications Technology, 01*, 89–93.
4. Chu J., Xu A., & Zhang M. (2013). Color image watermarking based on discrete wavelet transform and singular value decomposition. *Video Engineering*, *37*(17)
5. Liu, R., & Tan, T. (2002). An SVD-Based watermarking scheme for protecting rightful ownership. *IEEE Transactions on Multimedia, 4*(1), 121–128.
6. Jin, X. (2009). *Research of digital watermarking algorithms in wavelet domain based on Arnold and SVD* (pp. 12–13). Zhejiang: College of Information Engineering of Zhejiang University of Technology.
7. Lei, L., Guo, S., & Wang, L. (2013). SVD Digital Image watermarking algorithm based on wavelet transform. *Computer Simulation, 9*, 171.

Chapter 40
Watermarking Algorithm for Color Two-Dimensional Code Based on DCT-SVD

Qian Guo, Guangxue Chen and Linlin Chen

Abstract In this paper, a new watermarking method for color QR code that has more digital watermarking capacity and robustness is presented. The QR code has a backdrop of green as the original image, watermark is the pretreated QR code information. When embedding watermark, the information is encoded into color QR code to extract its backdrop. And the watermark takes encryption algorithm based on logistic chaotic sequence to improve safety. The encoded and encrypted watermark is embedded into luminance coefficients from the sixty pixels with quantized DCT (Discrete Cosine Transform) block matrix and SVD (Singular Values Decomposition). Compared with the existing watermarking algorithm, it not only keeps fast scanning characteristics of QR codes, but also has better embedding capacity and stronger robustness against rotation, shearing, noise, and filter. It can be used as a new method of copyright protection based on color two-dimensional code.

Keywords Color QR code · Digital watermarking · Discrete cosine transform · Singular values decomposition · Printing and scanning

40.1 Introduction

In recent years, two-dimensional bar code technology with its big information capacity, strong fault tolerance, wide coding range, portable, low cost, has been widely used at home and abroad [1]. But the two-dimensional bar code trans-coding

Q. Guo · G. Chen (✉)
State Key Laboratory of Pulp and Paper Engineering,
South China University of Technology, Guangzhou, China
e-mail: chengx@scut.edu.cn

L. Chen
Shenzhen YUTO Packaging Technology Co., LTD, Shenzhen, China

Q. Guo · L. Chen
Shenzhen Engineering Laboratory of 3D Printing Technology,
Shenzhen, China

process is open, the original encryption technology simply computes bit wise exclusive-OR of its operands; it has inherent deficiencies in the security and confidentiality. For the higher security requirements or special anticounterfeit field, a two-dimensional bar code technology becomes powerless. But the digital watermarking technology is born for the security and confidentiality. Therefore, the combination of a two-dimensional bar code and digital watermarking is a chance for QR code to get rid of its own limitations [2, 3].

40.2 Color Space Transform

The pretreated color QR code is based on CIE1976Lab uniform color space. Converted from RGB color space to Lab space includes the following two processes: RGB color space converted to XYZ space and XYZ color space converted to Lab space. The tristimulus values X, Y, Z of standard colorimetric system CIE1931 is calculated based on the three basic colors of RGB, the formulation is as follows [4].

$$
\begin{cases}
X = 0.490\text{R} + 0.310\text{G} + 0.200\text{B} \\
Y = 0.177\text{R} + 0.812\text{G} + 0.011\text{B} \\
Z = \phantom{0.177\text{R} +\ } 0.010\text{G} + 0.990\text{B}
\end{cases}
\tag{40.2.1}
$$

The XYZ color space converted to the Lab color space is calculated as follows: Formula (40.2.2) is applied to $X/X_0, Y/Y_0, Z/Z_0 > 0.008856$ and (40.2.3) is applied to $X/X_0, Y/Y_0, Z/Z_0 \leq 0.008856$

$$
\begin{cases}
L = 116(Y/Y_0)^{1/3} - 16 \\
a = 500\left[(X/X_0)^{1/3} - (Y/Y_0)^{1/3}\right] \\
b = 200\left[(Y/Y_0)^{1/3} - (Z/Z_0)^{1/3}\right]
\end{cases}
\tag{40.2.2}
$$

$$
\begin{cases}
L = 903.3\frac{Y}{Y_0} \\
a = 3893.5\left(\frac{X}{X_0} - \frac{Y}{Y_0}\right) \\
b = 1557.4\left(\frac{Y}{Y_0} - \frac{Z}{Z_0}\right)
\end{cases}
\tag{40.2.3}
$$

where X, Y, Z are the tristimulus values of pixels and X_0, Y_0, Z_0 are tristimulus values of the CIE standard illumination. L is psychrometric lightness, a and b are psychological chromaticity.

40.3 Watermark Embedding and Recognition

40.3.1 Watermark Embedding

The steps of watermark embedding algorithm are as follows:

(1) The information is encoded into color QR code and watermark QR code. The color QR code has a backdrop of green as the original image.

(2) Taking distortion compensation for watermark QR code. $W'(\omega) = \partial * W(\omega) * \frac{1}{P(\omega)}$ where $W'(\omega)$ is watermark frequency response after pre-distortion, $W(\omega)$ the is original watermark frequency response, ∂ is compensation coefficient, $P(\omega)$, and is impulse response of printing and scanning model [4].

(3) Scrambling watermark sequence by chaos transform to get new sequence, $W'' = W'_1, W'_2, \ldots, W'_{m \times n}$.

(4) Converting color space from RGB to Lab for backdrop, then extracting the luminance component L.

(5) Segmenting L into nonoverlapping $K \times K$ blocks BLKK, making N be the account of blocks, K ranges from 1 to N. Decomposing each block BLKK by Discrete Cosine Transform (DCT) to obtain coefficient matrix. Then, optimizing them based on the quantized matrix.

(6) Decomposing optimized coefficient matrix by SVD to obtain singular values S_I. The watermark is embedded into singular values S_I from the 60 values by $S_{I-W} = S_I + \alpha W_W$. α is embedding strength and W_W is a matrix which contains watermark information in the 300 pixel positions [5].

(7) Decomposing singular values S_{I-W} by SVD to get the watermarked diagonal matrix and left singular matrix U and right singular matrix V. Performing singular value reconstruction and IDCT to obtain the luminance component L'.

(8) Converting color space from Lab to RGB for L to get the watermarked color backdrop. Combining backdrop and QR code in the Photoshop. Printing out watermarked color QR code in 600dpi by digital printing.

40.3.2 Extracting Watermark

The steps of watermark extracting algorithm are as follows:

(1) Scan the printed color QR code in 600DPI resolution and eight level Gray. Take the image processing operations such as edge detection, and adjust its size.

(2) Convert color space from RGB to Lab for color QR code, then extract the luminance component L_w.

(3) Decompose L_w matrix by DCT and SVD to obtain singular values S_2, perform singular value reconstruction to get S_3.
(4) Get information bits $W = (S_3 - S_I)/\alpha$.
(5) Watermark information obtained by chaotic system transforming, decode the standard QR code image to get the original information.

40.4 Experimental Results and Discussion

In this study, we used color scale QR code as our host image of size 1120×1120, and the gray QR code for watermark image of size 140×140. In our experiments, we used the scaling factor $\alpha = 0.3$. Figure 40.1 shows cover image, original QR code and watermark. Figure 40.2 shows watermarked image, combined image and the extracted watermark.

To investigate the robustness of the algorithm, the watermarked image was attacked by applying rotation, cropping, JPEG compression, median filtering, low-pass filtering, Gaussian noise, salt and pepper noise, speckle noise, and printing and scanning. The results of these attacks are shown in Fig. 40.3.

(a)   **(b)**   **(c)**

Fig. 40.1 Cover images and watermark. **a** Background. **b** QR code. **c** Watermark

(a)   **(b)**   **(c)**
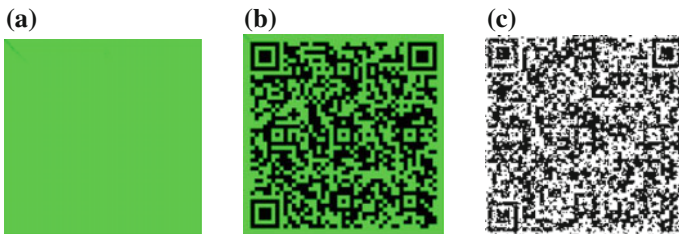
Fig. 40.2 Watermarked images and extracted watermark. **a** Watermarked image. **b** Combined image. **c** Recovered watermark

(a)

Rotate50°	Cropping	JPEG compression 50%
Median filter [3x3]	Low-pass filtering[3x3]	Gaussian noise(var=0.001)
Salt & pepper (noise density 0.005)	Speckle noise (var0.04)	Printing and scanning

(b)

Rotate50°	Cropping	JPEG Compression50%	Median filter [3x3]	Low-pass filtering [3x3]
Gaussian noise	Salt & pepper	Speckle noise	Printing and scanning	
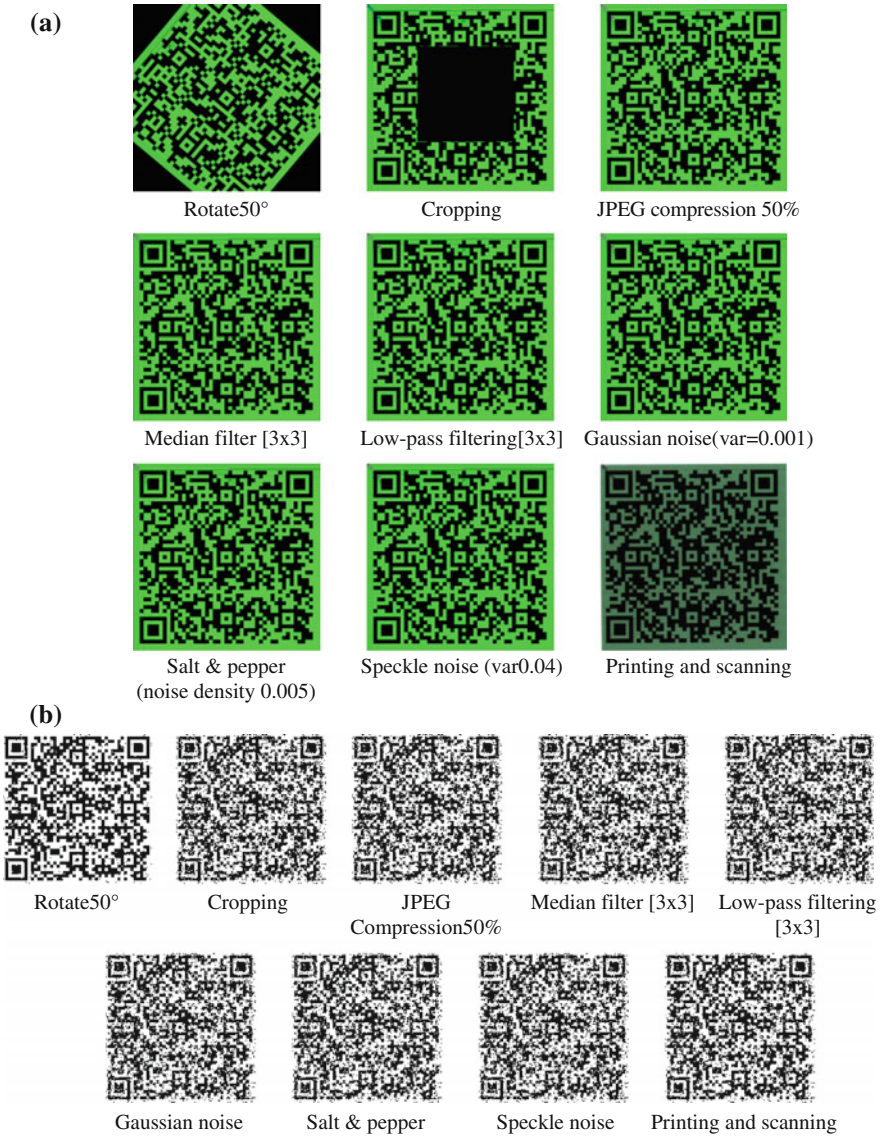
Fig. 40.3 Watermarked images under different attacks (**a**) and extracted watermarks under different attacks (**b**)

According to the experimental results, it proves that this algorithm can resist all kinds of attracts, such as rotate, cropping, JPEG compress, median filtering, Gaussian noise, printing and scanning, and so on. Additionally, QR code not only has the capability to soundly recover the saved data by correcting the errors even if

the parts of the images are damaged, but also can hide more information in the original images, compared with the existing method. This capability enables to overcome the restricted storage limits.

40.5 Conclusions

This paper presents a robust watermarking algorithm based on color two-dimensional code. Combining the encoded techniques of color two-dimensional code, watermark pre-distortion processing techniques, chaotic system encryption technique, color space conversion techniques, singular value decomposition techniques, and DCT with quantized matrix techniques. The encoded watermark information is embedded into backdrop of color QR code, it not only affects the fast reading of two-dimensional code but also improves digital watermark embedding capacity and robustness.

References

1. Liu, L-l. (2012). *Design and implementation of watermarking algorithm for color code image* (pp. 1–63). Suzhou: Soochow University.
2. Xie, R-s, Zhao, H-x, & Wu, K-s. (2013). QR 2D bar-code anti-counterfeiting technique based on discrete wavelet transform. *Computer Engineering, 39*(12), 126–129.
3. Wang, R-l. (2010). *A study on the technology of digital watermarking in two-dimension bar-code* (pp. 1–65). Hangzhou: Hangzhou Dianzi University.
4. Kikuchi, M., Fujiyoshi, M., & Kiya, H. (2013). A new color QR code forward compatible with the standard QR code decoder. In *2013 International Symposium on Intelligent Signal Processing and Communications Systems* (pp. 26–31)
5. Gao G. (2010). A blind gray scale watermark algorithm based on chaos and mixed transform domain. In *2nd International Conference on Computer and Automation Engineering*

Chapter 41
Research on Evaluating Method for Print Mottle Based on Digital Image Processing

Ying Huang, Guangxue Chen, Linlin Chen and Qifeng Chen

Abstract Mottling is one of the most important printing defects in modern offset printing. It can be defined as undesired unevenness in perceived print density. In our research, the print mottle image on paper surface was acquired through a scanner, and then through software analysis. It was studied from the perspective of digital image processing. Then, the method was proposed to apply in newsprint paper, inkjet paper, offset paper, and coated paper. We compared the proposed method with the traditional method. The results showed that the print mottle index in descending order is: offset paper, newspaper, coated paper, and inkjet paper. The new method can be easily used to analyze print mottle. Meanwhile, it is simpler and more objective using the modified coefficient of variation to characterize print mottle. The evaluating method for print mottle based on digital image processing technology has some practical value for analyzing and solving various paper print mottle problems.

Keywords Print mottle · Evaluation models · Digital image

41.1 Introduction

The print mottle is a long-term technical problem in paper and printing industry. Print mottle can be as reflectance disturbances in the print that leads to deterioration in the perceived quality of the print. The lack of inhomogeneities can thus be

Y. Huang · G. Chen (✉) · Q. Chen
State Key Laboratory of Pulp and Paper Engineering, South China University
of Technology, Guangzhou, China
e-mail: chengx@scut.edu.cn

L. Chen
Shenzhen YUTO Packaging Technology Co., LTD, Shenzhen, China

L. Chen
Shenzhen Engineering Laboratory of 3D Printing Technology, Shenzhen, China

assumed to correspond to a high print quality [1]. In the ISO/IEC 13660 standard, a more technical definition is given [2]: "aperiodic fluctuations of density at a spatial frequency less than 0.4 cycles per millimeter in all directions." There exist three types of mottle: back-trap mottle, water-interface mottle, and ink-trap mottle [3]. In most situations, mottling is a stochastic phenomenon, but noise in print related to mottling can include some form of regularity. The causes are various; it may arise from uneven ink transfer or penetration. The presence of binder on a surface may also cause mottle [4].

In recent years, the print mottle is mainly based on the theory of digital image and the fast data processing algorithm to build mode. Albert [5], who took into account the characteristics of the human visual system, proposed three methods to evaluate the print mottle. Dubé [6] proposed the method using wavelet denoising and gray level gradient analysis of the print image.

The subjective test method is time-consuming and susceptible. It is not realistic in many cases. Some equipment testing methods are accurate, but expensive. A convenient and effective method is necessary. In this paper, we provided a new method based on the scanner and STFI-Mottling Expert testing software to detect and use the modified coefficient of variation to characterize the print mottle of papers, and compared with the traditional method.

41.2 Methods

41.2.1 Traditional Methods to Detect Print Mottle

The mathematical model of the conventional method to detect print mottle is based on the definition of print mottle. As for a digital image $f(x, y)$ containing print mottle, the CoV (gray value coefficient of variation) may reflect the unevenness of print mottle. The greater the variation of coefficient value, the more obvious the unevenness. Specific steps are as follows:

The image containing print mottle was collected. After sampling, calculate the average, standard deviation, and CoV of the image on the basis of knowledge of mathematical statistics. For ease of calculation, an original image $f(x, y)$ is dispersed into a matrix of size $N \times N$, using Formulas (41.1)–(41.3) to calculate the CoV of this image [7].

$$\bar{f} = \frac{1}{N^2} \sum_{x=0}^{N-1} \sum_{y=0}^{N-1} f(x, y) \tag{41.1}$$

$$\sigma_f = \sqrt{\frac{1}{N^2} \sum_{x=0}^{N-1} \sum_{y=0}^{N-1} [f(x, y) - \bar{f}]^2} \tag{41.2}$$

$$\mathrm{CoV} = \frac{\sigma_f}{\bar{f}} \qquad (41.3)$$

where, *x, y* are the horizontal and vertical coordinates of the print mottle discrete image matrix, $f(x, y)$ is the image gray value print mottle discrete matrix, *N* is the size of the discrete matrix, $\bar{f}, \sigma_f$, respectively, are the mean and standard gray value, CoV is the print mottle image variation coefficient matrix of discrete gray values.

41.2.2 The Proposed Method

The STFI-Mottling Expert software tool is used to quantify printing mottle. Epson Perfection V700 flatbed scanner with a reflectance standard calibration sheet scans the sample. It can convert the scanned gray scale levels into reflectance. The software changes the image from the time domain to the frequency domain using fast Fourier transform, based on a series of band-pass filters, and calculates CoV of the image as a gray value print mottle index.

As for the parameter CoV above, it has a lot of shortcomings. It considers only the frequency spectrum of printing. The modified coefficient of variation Mod CoV is a modification of CoV. It is the standard deviation divided by the square root of the average reflectance. Using a contrast sensitivity that the human eye can perceive wavelength range, which is 0.25–16 mm. It divides the standard deviation of prints with the square root of the average reflectance values.

$$\mathrm{Mod\ CoV} = \frac{\sigma_f}{\sqrt{\mathrm{Refl.}}} \qquad (41.4)$$

where, σ_f is the standard gray value of the discrete image matrix. The Refl. is the average reflectance of printed products.

Considering the effect of contrast sensitivity on the evaluation of print mottle, it is an improved method to characterize the print mottle using Mod CoV. Particularly, in cases where there are differences in mean reflectance level between the samples. Instead of using the variation in range 1–8 mm, a weight function is used to compensate for how the human vision system works. Variation in the range 2–4 mm is given a higher weight, and the variation in the shorter and longer wavelengths are given lower weights.

41.3 Experiments

We present the results for the 30 C400 (400 % cyan, printing four times) samples. The original samples are approximately 5 cm × 5 cm in size. The papers used for printing are newspaper, offset paper, inkjet paper, and coated paper. The performance of

Table 41.1 The characterizations of four papers

Papers	Basis weight (G/M^2)	Roughness (Mm)	Opacity (%)	Gloss (60°)	Whiteness (%Iso)	Uniformity
Newspaper	47	3.68	94.53	4.08	58.43	103.11
Offset paper	98	4.79	98.56	3.83	97.95	85.68
Inkjet paper	190	1.94	91.39	20.38	110.79	23.58
Coated paper	128	0.85	97.54	33.20	89.85	26.7

papers is shown in Table 41.1. The samples were printed using IGT printability tester, where printing pressure is 500 N (default), the printing speed of 0.2 m/s (default), time between printing and set off's of 10 s, inking time of 5 s, and the ink film thickness of 8 μm (0.35 cm^3). The samples were originally scanned with 150 dpi and 16 gray image type using flatbed scanner. We inspected mottle sizes ranging from 0.5 to 16 mm while viewing the sample from a distance of 30 cm (spatial frequency range 0.03–1 cycles/mm). Also the inspected contrast of print density was limited to ±10 % of the median gray-value of an image.

41.3.1 New Method to Detect the Print Mottle of Papers

The traditional model and the improved print mottle model used in this study were applied to newspaper, offset paper, inkjet paper, and coated paper. The results are shown in Table 41.2.

In Table 41.2, the results of different print mottle parameters are presented. Within 1–8 mm wavelength range, the CoV values of four papers in descending order are: offset paper, newspaper, coated paper, and ink jet paper. The smaller the CoV, which is the value of print mottle index, the less visual perception to the print mottle. The Mod CoV values in descending order are: offset paper, newspaper, coated paper, and ink jet paper. The results obtained by the two methods are very consistent. There are differences in mean reflectance level between the samples. A weight function is used to compensate for how the human vision system works. The amount of change in the range of 2–4 mm accounts a large weight, so we focus

Table 41.2 The print mottle values of four papers

Print mottle parameter papers	1–8 mm (CoV)	1–8 mm (Mod CoV)	2–4 mm (CS)
Newspaper	4.578	12.715	0.95
Offset paper	5.642	17.228	1.31
Inkjet paper	1.898	4.852	0.39
Coated paper	2.718	8.712	0.57

on the print mottle contrast sensitivity in wavelength the range of 2–4 mm. The *CS* values of four papers in descending order are: offset paper, newspaper, coated paper, and ink jet paper. Print mottle is more severe, the more visual perception to the mottle, the higher sensitivity of the human eye to this.

41.3.2   Print Mottle of Different Wavelengths

As for different wavelength bands (Band 1: wavelength range 0.5–1 mm; Band 2: wavelength range 1–2 mm; Band 3: wavelength range 2–4 mm; Band 4: wavelength range 4–8 mm; Band 5: wavelength range 8–16 mm; Band 6: wavelength range of 16–32 mm), the print mottle test results are shown in Figs. 41.1 and 41.2.

The results can be seen in Figs. 41.1 and 41.2. It showed that the print mottle of four papers was concerned with the wavelength range with the weight function of contrast sensitivity. As for the four papers, within the wavelength range of 0.5–1 mm, 1–2 mm, 2–4 mm, 8–16 mm, and 16–32 mm, the print mottle index values in descending order are: offset paper, newspaper, coated paper, and ink jet paper. And with the increase of the wavelength, the coefficient of variation CoV and modified coefficient of variation Mod CoV show a downward trend, and finally basically stable. This is because the print mottle has a slight difference with contrast sensitivity in different wavelength bands within normal arm length visual distance. The human eyes have different sensitivities with the scale characteristic of different wavelength ranges. We cannot perceive anything beyond a certain range. In addition, as for the same kind of paper, the Mod CoV in different wavelength ranges was different with the CoV. It is better to reflect this rule.

Fig. 41.1 The print mottle of newspaper and offset paper within different wavelength
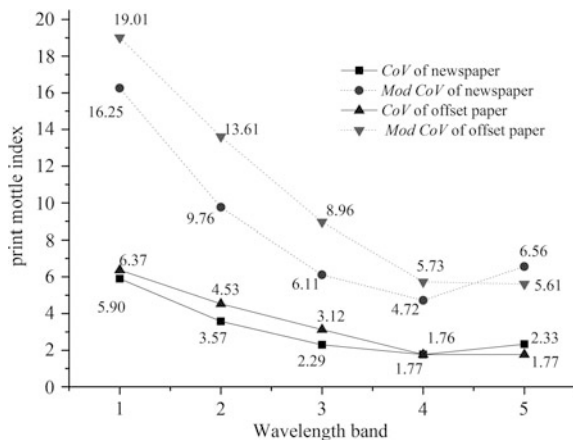
Fig. 41.2 The print mottle of inkjet paper and coated paper within different wavelength
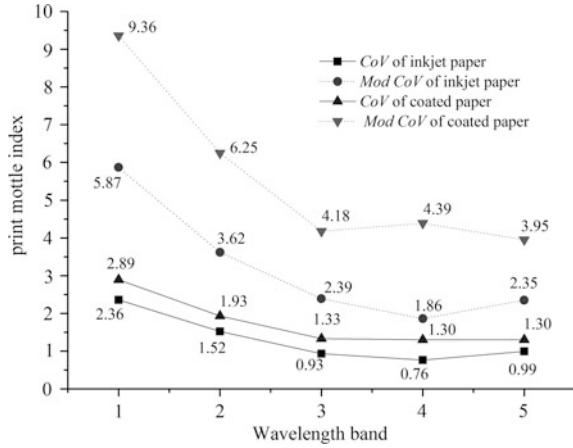
41.3.3 Contrast Sensitivity

The ability of the human eyes that can distinguish differences in brightness are called contrast sensitivity. The contrast sensitivity of the human eye can perceive the wavelength range of 0.25–16 mm. To compare the results of the implemented methods to human perception, the contrast sensitivity values obtained by two methods were listed in Table 41.3. As we can see, the contrast sensitivity values obtained by two methods are almost the same. At the same time, the reflectance of four samples is also almost the same. So, the effect of contrast sensitivity on the evaluation of print mottle must be considered, in other words, the reflectance is the determinant factor.

Table 41.3 The contrast sensitivity obtained by two methods

Wavelength band, Mm	Cs obtained By the CoV				Cs obtained By the Mod CoV			
	Newspaper	Offset paper	Inkjet paper	Coated paper	Newspaper	Offset paper	Inkjet paper	Coated paper
0.5–1.0	0.25	0.28	0.1	0.12	0.25	0.28	0.09	0.12
1–2	0.62	0.82	0.27	0.35	0.62	0.82	0.24	0.35
2–4	0.95	1.31	0.39	0.57	0.93	1.25	0.38	0.55
4–8	0.98	0.98	0.42	0.72	0.95	1.07	0.38	0.76
8–16	1.12	0.87	0.48	0.64	1.15	0.93	0.42	0.6
Reflectance (%)	7.60	8.80	7.20	10.40	7.60	8.90	7.20	10.40

41.4 Conclusions

In the presented work, we presented a new method based on digital image processing technology. Then the method was proposed to apply in different papers. We performed an initial comparison between the traditional method using CoV to characterize the print mottle and the presented method using Mod CoV. The results showed that the print mottle index in descending order is: offset paper, newspaper, coated paper, and ink jet paper. The new method can be easily used to analyze print mottle. Meanwhile, it is simpler and more objective using Mod CoV. As for the four papers, within the wavelength of 0.5–1 mm, 1–2 mm, 2–4 mm, 8–16 mm, and 16–32 mm, the print mottle index in descending order is: offset paper, newspaper, coated paper, and ink jet paper. And with the increase of the wavelength, the print mottle index shown a downward trend, and finally basically stable. The contrast sensitivity on the evaluation of print mottle must be considered, and the reflectance is the determinant factor. The method based on digital image processing technology has shown potential for improvement and is definitely a candidate for an industrial level software vision application.

References

1. Fahlcrantz, C. M., & Johansson, P.-A. (2005). *On the evaluation of print mottle*. Stockholm: Kungliga Tekniska Hogskolan.
2. ISO: ISO/IEC 13660: 2001(e) standard. Information technology—office equipment measurement of image quality attributes for hardcopy output—binary mono chrome text and graphic images. ISO/IEC
3. Sandreuter, P. N. (1994). Predicting print mottle a method of differentiating between three types of mottle. *Tappi Journal, 77*(7), 173–187.
4. Dubé, M., Mairesse, F., Boisvert, J.-P et al. (2005). Wavelet analysis of print mottle. *IEEE Transactions on Image Process*, 1–8
5. Sadovnikov, A., Salmela, P., & Lensu, L. (2005). Mottling assessment of solid printed areas and its correlation to perceived uniformity. *Lecture Notes in Computer Science, 3440*(14), 409–418.
6. Dubé, M., Mairesse, F., Boisvert, J. P et al. (2007). Wavelet analysis of print mottle. http://www.uqtr.ca/~dubma/double.pdf
7. Xu, L-p. (2009). *Digital image processing study guide*. Beijing: Science Press.

Chapter 42
Optimization of Multilevel Error Diffusion Based on Pixel Distribution

Yukun Li, Yigang Wang and Shi Li

Abstract To improve the visual effect of multilevel halftone image, a multilevel quantization interval division method based on pixel distribution and a dynamic error limits method are presented. First, the impact of quantization intervals on the mean square error (MSE) of the image is analyzed. According to that, quantization intervals optimization is presented to make the number of pixels in each interval equal based on the pixel distribution of original image. That optimization leads to uneven quantization intervals. Then, a dynamic error limit of error diffusion method is utilized to minimize the statistical error between the resulted image and the original one. The results show that the peak signal-to-noise ratio (PSNR) of proposed method is increased about 2 dB compared with the Floyd–Steinberg algorithm. And the efficiency of our quantization is nearly twice of Octree quantization algorithm. The resulted images receive acceptable visual effect.

Keywords Multilevel halftone · Error diffusion · Multilevel quantization · Dynamic error

42.1 Introduction

The gray scales of E-ink screen have increased from two-level gray to 16-level gray now. How to make continuous tone images, be better presented in a multilevel E-ink screen is a challenging issue for traditional halftone technology.

Multilevel digital halftone technology has three classic algorithms, such as point processes [1, 2], iterative algorithms [3, 4], and neighborhood processes [5–9]. Neighborhood process is most popular for: they have advantage in quality and speed. Error diffusion quantization threshold is discussed by neighborhood process

Y. Li · Y. Wang · S. Li (✉)
School of Media and Design, Hangzhou DianZi University, Hangzhou, China
e-mail: brightlishi@yeah.net

algorithms, but multilevel quantization intervals generation method has not been concerned about by those algorithms.

To improve visual effects of halftone image, a multilevel quantization interval division method and dynamic error limits algorithm are proposed in this work.

42.2 Analysis of Quantization Error

PSNR is often utilized to objectively evaluate images' quality. This section analyzes the effect of multilevel quantization intervals division on MSE.

42.2.1 Individual Quantization Error

According to the multilevel error diffusion model [9], the square of error $D(m, n)$ at (m, n) point can be written as

$$
\begin{aligned}
D(m, n) &= [O(m, n) - I(m, n)]^2 \\
&= \left[Q \left[I(m, n) + \sum_{k,l} W(k, l) * e(m - k - l) \right] - I(m, n) \right]^2
\end{aligned} \tag{42.1}
$$

By the expression of quantization error $e(m, n) = O(m, n) - I^*(m, n)$, Formula 42.1 can be rewritten as

$$
D(m, n) = \left[e(m, n) + \sum_{k,l} W(k, l) * e(m - k, n - l) \right]^2 = [\Delta E_1(m, n) + \Delta E_2(m, n)]^2 \tag{42.2}
$$

where

$$
\Delta E_1(m, n) = e(m, n) = O(m, n) - I^*(m, n) \tag{42.3}
$$

$$
\Delta E_2(m, n) = \sum_{k,l} W(k, l) * e(m - k, n - l) \tag{42.4}
$$

$\Delta E_1(m, n)$ is the quantization error of (m, n) point, $\Delta E_2(m, n)$ represents the diffusion error which come from the neighborhood points of (m, n). From Formula 42.3, Formula 42.4 can be seen that ΔE_2 is affected by ΔE_1. When ΔE_1 is getting smaller, the square of error $D(m, n)$ is smaller. It can be seen that different multilevel quantization interval division methods will lead to the different $D(m, n)$.

42.2.2 Image MSE

The function $f(x)$ denoting the statistics number of grayscale x in image, ϕ_i is quantization interval. And set $\overline{f(\phi_i)}$ to be the average value of $f(x)$ in range ϕ_i.

The MSE of range ϕ_i can be described as follow:

$$
\begin{aligned}
D_{\phi_i} &= \frac{1}{k_i \cdot \overline{f(\phi_i)}} \sum_{j=1}^{k_i} \Delta x_j^2 \cdot \overline{f(\phi_i)} = \frac{1}{k_i}\left(\Delta x_1^2 + \cdots + \Delta x_{k_i}^2\right) \\
&= \frac{1}{k_i}\left[\left(x_1 - x_{\frac{k_i}{2}}\right)^2 + \cdots + \left(x_{\frac{k_i}{2}} - x_{\frac{k_i}{2}}\right)^2 + \cdots + \left(x_{k_i} - x_{\frac{k_i}{2}}\right)^2\right] \\
&\approx \frac{2}{k_i}\left[1^2 + 2^2 + \cdots + \left(\frac{k_i}{2}\right)^2\right] = \frac{1}{12k_i}k_i(k_i+1)(k_i+2) \\
&= \frac{1}{12}(k_i+1)(k_i+2)
\end{aligned}
\tag{42.5}
$$

where k_i is the number of grayscales in range ϕ_i, Δx_j is the quantization error of the jth grayscale in range ϕ_i.

According to formula 42.5, the overall MSE D of image can be obtained as follow:

$$
D = \sum_{i=1}^{n} D_{\phi_i} = \frac{1}{12}\sum_{i=1}^{n}(k_i+1)(k_i+2)
\tag{42.6}
$$

Formula 42.6 shows that the MSE of quantized image is affected by the number of grayscales in each quantization interval. Different division methods of quantization interval will result in different number of grayscales in each quantization interval that will lead to different overall MSE of quantized image.

42.3 Multilevel Error Diffusion Algorithm Optimization

42.3.1 Multilevel Quantization Intervals Optimization Based on Pixel Distribution

Traditional multilevel quantization interval method divides gray scale range of image equally based on the gray levels of output device. If the distribution of the image pixels is uneven, traditional method's quantization errors and the MSE of image will be increased. In order to reduce the quantization errors, quantization intervals are optimized as the following is presented to make the number of pixels in each interval equally based on pixel distribution of original image.
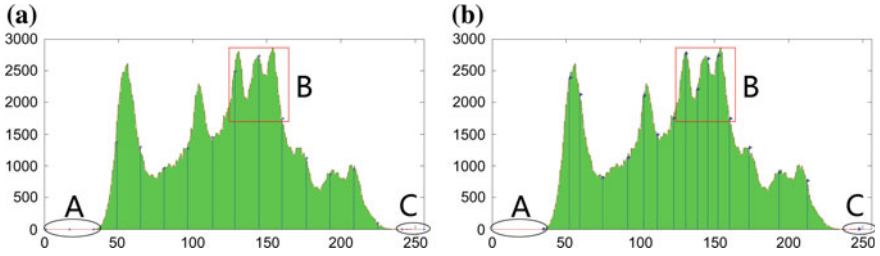
Fig. 42.1 Relationship between quantization intervals and pixel distribution of Lena. **a** Traditional method. **b** Our method

1. With the pixels number n_j at each grayscale of image, the nearly average of overall pixels number A under quantization levels n can be obtained.

$$A = \frac{1}{n} \sum_{j=0}^{255} n_j \tag{42.7}$$

2. Quantization interval ϕ_i where the number of pixels is nearly A, can be generated as the following equation:

$$\sum_{j \in \phi_i} n_j = A \quad 1 \le i < n \tag{42.8}$$

The 16 level quantization interval results of Lena generated by the traditional method and proposed method are shown in Fig. 42.1. Figure 42.1a illustrates that there is no pixel in region A and C, the traditional method still generates three empty quantization intervals. The number of pixels in the region B in Fig. 42.1a is more than other intervals, but there are only two quantization intervals. Quantization intervals generated by proposed method in Fig. 42.1b show that the empty region A and C are combined by their nearby region, the pixel number in each 16 intervals is nearly equal. And in the high density region B, there are five quantization intervals. It can be seen in Fig. 42.1b that the proposed method generates quantization intervals according to the pixel number in the interval region dynamically, which take full advantage of the all 16 quantization intervals.

42.3.2 Dynamic Error Limits Algorithm

The proposed quantization method usually generates uneven quantization intervals which is show in Fig. 42.1b. Traditional error diffusion method applied on that uneven quantization intervals often make the gray value of some pixels jump more than one gray level, which will result some noise pixels as shown in Fig. 42.2a.

(a) **(b)**
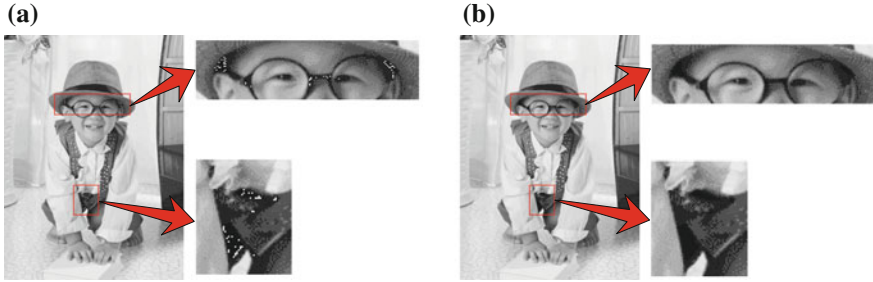
Fig. 42.2 Result images. **a** Traditional error diffusion method. **b** Our method

To constrain the jump range of pixels' gray value based on the length of quantization interval, the dynamic error limits method is designed as follows:

1. Find the middle length l_{mid} of the interval;
2. Generate thresholds M_i of error diffusion for each interval:

$$M_i = \begin{cases} 0 & l_i \leq l_{\mathrm{mid}} \\ (l_i - l_{\mathrm{mid}})/2 & l_i > l_{\mathrm{mid}} \end{cases} \quad 1 \leq i < n \qquad (42.9)$$

where l_i is the length of ith interval;
3. According to M_i, generate specific error diffusion coefficient filter $W(k, l)$ of each quantization interval

$$W(k, l) = \begin{cases} 0 & e(m, n) \leq M_i \\ \frac{1}{16} \begin{bmatrix} 0 & 0 & 0 \\ 0 & 0 & 7 \\ 3 & 5 & 1 \end{bmatrix} & e(m, n) > M_i \end{cases} \qquad (42.10)$$

The resulted image, which utilized proposed method to limit the error diffusion by its own interval length, is shown in Fig. 42.2b.

42.4 Experiment Results

The histograms of resulted images by traditional multilevel quantizer [10], Octree's multilevel quantizer, and our method are shown in Fig. 42.3. It can be seen that our method gets an equalization histogram which has good contrast after error diffusion. Figure 42.4 illusion that the red patch has a better visual effect utilized our method than Octree algorithm. Experiment results reveal that the proposed method keeps the details of image better than traditional method and Octree method.
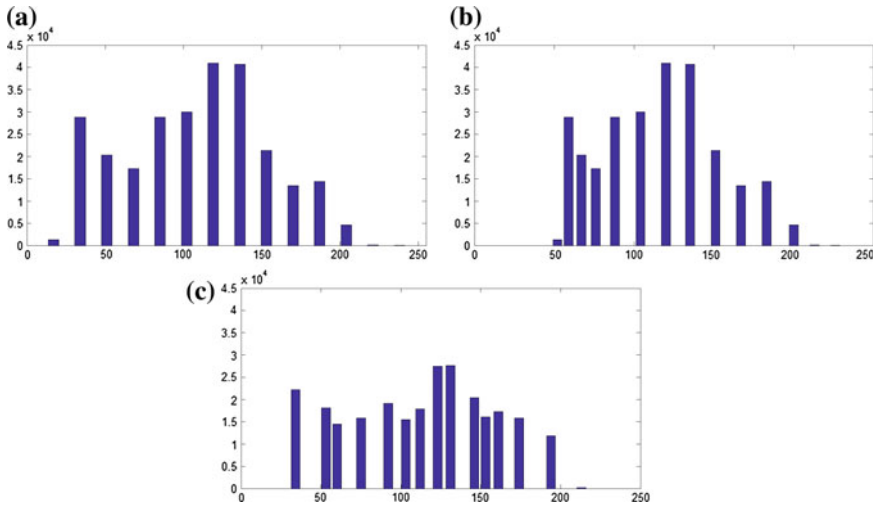
Fig. 42.3 The histograms of resulted images. **a** Traditional multilevel quantizer. **b** Octree's multilevel quantizer. **c** Our method

Fig. 42.4 Visual effect of resulted image. **a** Octree algorithm. **b** Our method

The PSNR of the images in the experiment is shown in Table 42.1. It can be seen that the PSNR which obtained by Octree algorithm and our method is higher than the traditional method. But Octree algorithm efficiency is lower. Table 42.2 shows the computation comparison between Octree algorithm and our method. It can be seen that our method is nearly twice than Octree algorithm in time and cost of generation and the multilevel quantization intervals.

Table 42.1 PSNR comparison

	Floyd-Steinberg algorithm	Octree algorithm	Our method
Lena	33.01	34.28	34.97
Boat	32.51	34.14	34.07
Cameraman	39.87	32.34	31.94
Scenery	32.78	33.12	32.89
Child	32.80	33.73	33.26

Table 42.2 Computational efficiency comparison

	Number of pixels	Octree (ms)	Our method (ms)
Lena	262144	36	23
Boat	262144	39	24
Cameraman	262144	35	22
Scenery	552960	79	54
Child	246654	35	21

42.5   Conclusions

This paper analyzes the error diffusion contribution, and focus on the quantization error limit. A multilevel quantization interval optimization based on pixel distribution is proposed to reduce the quantization error, and a dynamic error limited algorithm is presented to solve the noise introduced by uneven quantization intervals. The experimental results revel that the proposed method can effectively restrain the quantization error, and improve computational efficiency.

References

1. Lin, G. Y., & Allebach, J. P. (2002). Multilevel screen design using direct binary search. *JOSAA,*. doi:10.1364/JOSAA.19.001969.
2. Park, T. Y., Jang, I. S., & Ha, Y. H. (2009). Banding artifact reduction with interweaving dot dispersion based on probability model and human visual system weighted root mean squared error in blue noise multilevel dithering. *Journal of Imaging Science and Technology, 53*(6), 1–60504.
3. Chandu, K., Stanich, M., Wu, C. W., & Trager, B. (2012). Direct multi-bit search (DMS) screen algorithm. In *Proceedings of 19th IEEE International Conference on Image Processing (ICIP)* (pp. 817–820). doi:10.1109/ICIP.2012.6466985

4. Umemura, T., Aguirre, H., & Tanaka, K. (2002). Multi-level image halftoning technique with genetic algorithms. *IEICE Transactions on Fundamentals of Electronics, Communications and Computer Sciences, 85*(8), 1892–1897.
5. Zeng, P. (1999). The model and algorithm for tone self-compensation halftone printing. *Journal of Computer Aided Design and Computer Graphics, 11*, 352–355.
6. Kang, H. R. (1999). Digital color halftoning. SPIE press
7. Eschbach, R., & Knox, K. T. (1991). Error-diffusion algorithm with edge enhancement. *JOSAA*. doi:10.1364/JOSAA.8.001844
8. Yan, Y., & Xiaodan, L. (2008). On study of multitoning to remove false contouring in output. *China Science and Technology Information, 9*, 51–52.
9. Jianhua, H., Yunkuan, W., Shenhang, W., Xinbo, W., & Shaohong, W. (2014). An adaptive noise modulation multilevel error diffusion algorithm. *Journal of Computer-Aided Design and Computer Graphics,*. doi:10.3969/j.issn.1003-9775.2014.11.008.
10. Floyd, R. W. (1975). An adaptive algorithm for spatial gray-scale. *Proceedings of International Symposium Digest of Technical, Society for Information Displays, 17*, 75–77.

Chapter 43
Visualization of Large-Size Model Based on Paper-Based 3D Printing

Jiangping Yuan, Guangxue Chen, Junhao Liao and Zhaohui Yu

Abstract In order to solve printing size limitation issue in the paper-based 3D printing industrialization in the culture creative field, using printing time index, a fast visualization based on cutting angle and composition was proposed for large-size 3D model color printing. Using four categories of simplified 3D models, given the centroid as the symmetrical center, the quantitative relationship between printing time and variable parameters including cutting angle, scale value, and cutting parts composition were analyzed and compared clearly. According to our results, for four models with the different structures in each type, the printing time is mostly increasing linear along with scale value. Whether the composition of cutting face is same or opposite in vertical plane, the printing time of white model with 0.3 scale size is also increasing with linear trend, however, it is not obvious in horizontal plane.

Keywords 3D printing · Large-size 3D model · 3D model visualization · Paper-based printing · 3D industrialization

43.1 Introduction

Recently, 3D printing was hailed as one of the most promising technology, and applied widely in the customized manufacturing and culture creative fields [1]. Based on different forming principle, industrialized issues with special features are obvious for the 3D printer, especially for printing size. Given inherent advantages including unique color reproduction and environmental protection, Since 2012, the

J. Yuan · G. Chen (✉) · J. Liao · Z. Yu
State Key Laboratory of Pulp and Paper Engineering, South China University
of Technology, Guangzhou, China
e-mail: chengx@scut.edu.cn

Z. Yu
Shenzhen Engineering Laboratory of 3D Printing Technology, Shenzhen, China

first paper-based 3D color printer was distributed in Germany [2], which was developed by the Mcor technology company, 3D full color printing with papers was really appeared into public view.

Based on the principle of layer manufacturing, paper-based 3D color printing should belong to a rapid prototyping (RP) technique [3]. For paper-based 3D printer, it includes two main processes: colorization and cutting model. The colorization is a process that both side of A4 office paper are printed by the Epson inkjet printer, and delivered to forming base to cut contour and bond layer by layer. However, this 3D printer is just limited to A4 size in horizontal level and extended in the height level. In culture creative field, the large-size application models occupy a big market proportion, but they cannot be directly printed by existing paper-based 3D printer. For the paper-based 3D color models, splitting and cutting is an effective low-cost method for manufacturers.

Currently, researches about color 3D printing focused on slicing precision and color reproduction features based on power-based substrates, few about printing size and speed. For example, Liao and Chiu [4] developed a new slicing rule for uniform thickness to ensure that the entire work piece has either a positive or negative tolerance. Yuan and Chen [5] put forward a speedup method for paper-based 3D color printing which used STL file. Stanic et al. [6] discussed clearly the colorimetric probability and stability of 3D prints produced by the Z510 3D printer. Vaezi et al. [7] mainly presented the effects of layer thickness and blinder saturation level parameters on 3D printing process. Comparing to power-based 3D color printing, printing size issue was more urgent than that in its industrialization. In this paper, based on the designed four categories of regular models, the quantitative relationship between scale value, cutting angle, cutting parts composition, and printing time were discussed and contrasted. These results can provide basic database and optimization frame to its industrialization in culture creative field.

43.2   Experiments and Methodology

In creative culture field, large-size color models are mostly consisted of whole big model or local structures beyond the printing area. Therefore, based on the existed 3D printer, the visualization of 3D model should be feasible for the indirect method. That is to say, the whole model is divided into two parts before slicing, and the cutting parts were recomposing to print at the same time. The quality indices for cutting methods can be found easily such as detail feature, slicing precision, and printing time. However, printing time is a popular factor for evaluating 3D model visualization.

In this paper, three experiments were conducted including substrate colorization quantitative test, quantitative trials between printing time and scale size, and cutting angle with fixed scale value. Four categories of regular large-size models are sampled as cuboid, cylinder, sphere, and whole with four different local structures. All the 3D models used in this paper were designed by open-source Blender software and printed by Mcor Matrix 300+ 3D printer with 256 × 169 × 150 mm build size.

Substrate colorization quantitative test is that printing one to five sheets from random page with three different color ink, and calculated printing time to build its general linear equation. The color is white (not printing any ink), cyan and cyan + magenta, respectively. Quantitative trials between printing time and scale size is that the scale size of white model is printing from 0.1 to 0.9 with 0.1 interval (the designed original model cannot be printed directly but less than 0.9 times can archive). Quantitative trials between printing time and cutting angle with 0.3 times is that cutting angle choose from 0° to 75° with 15° interval, and cutting parts were composing into same and opposite direction in vertical plane and opposite direction in horizontal plane. To control variables and simplify trials, all models would be just divided into two parts and other factors seen as constants.

43.3   Results and Analysis

43.3.1   Substrate Colorization Quantitative Test

Substrate colorization was made up of paper suction, paper inkjet and paper delivery, and the paper inkjet time is an ink-dependant variable. From Fig. 43.1, it can be found that one or two color ink mixture printing had little effect on the colonization time. However, the paper-based colorization time was positively correlated with the numbers of sheets and behaved an obvious linear relationship. From the linear fitting formulas and R-square value which marked by different color in Fig. 43.1, the substrate colorization time can be expressed as a
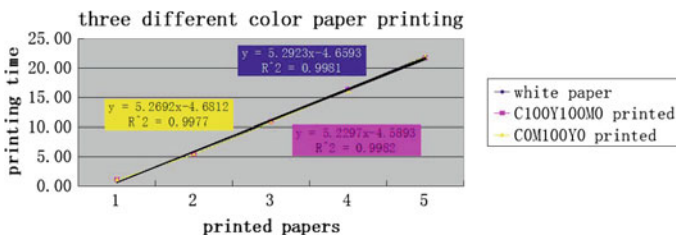
Fig. 43.1 Quantitative relationship between printed color sheets and printing time
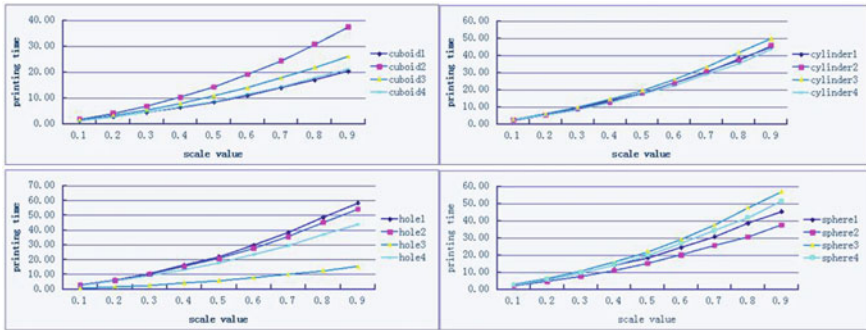
Fig. 43.2 Printing time and scale value in four categories

general linear fitting equation, which is calculated by the mean of the abovementioned coefficients and relative intercepts, shown in Eq. 43.1, y is printing time, x is the printed sheets bigger than zero.

$$y = 5.2637x - 4.5433 \tag{43.1}$$

43.3.2 Quantitative Trials Between Printing Time and Scale Size

This experiment was to investigate the printing time at a different scale based on Matrix 300+ 3D printer, and predict printing time of the nonregular scale size models. In Fig. 43.2, it is indicated that each printing time at nine kinds of scale size, and the quantitative relationship was increasing exponentially to some degree. For cylinder model category, the dependence on local structure is extremely weak, but strong in other three categories. This dependence becomes more obvious when scale value is increasing.

43.3.3 Quantitative Trials Between Printing Time and Cutting Angle with 0.3 Times

The different cutting angle result in various cross-section, and produced changeable printing time. From Figs. 43.3, 43.4, 43.5, and 43.6, it can be found that in each category, model cutting faces composing in vertical plane took less time than that in horizontal plane, and the same or opposite direction had few effects on printing time. The gap between two composing styles in vertical and horizontal plane was shown more obvious in sphere category because of its high symmetry. When
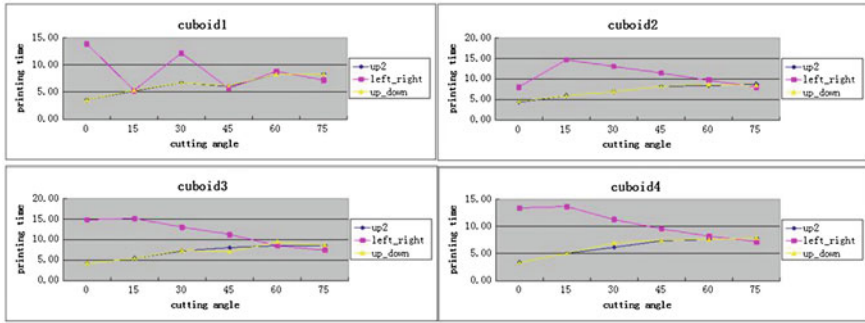
Fig. 43.3 Printing time and cutting angle in cuboid category
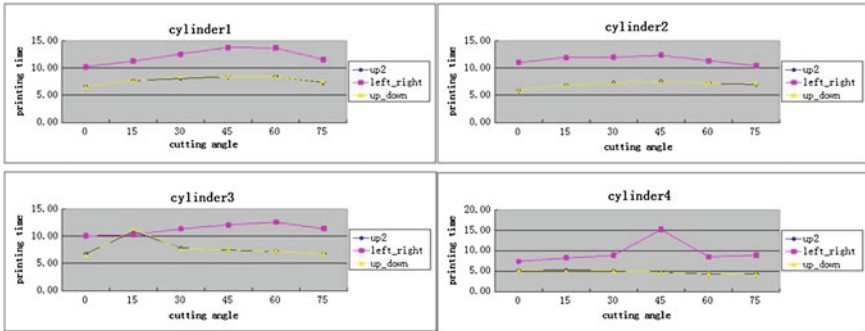
Fig. 43.4 Printing time and cutting angle in cylinder category
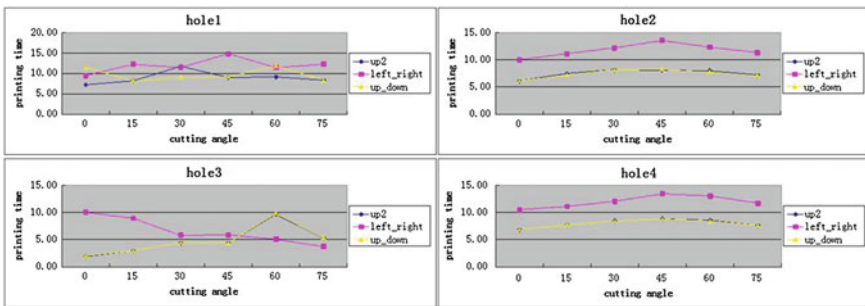
Fig. 43.5 Printing time and cutting angle in hole category

composing in vertical plane, the printing time increased slowly along with the increasing cutting angle, but in horizontal plane, this trend become more complicated.
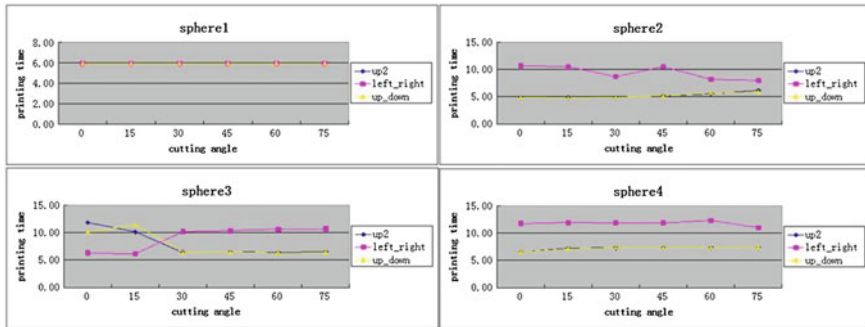
Fig. 43.6 Printing time and cutting angle in sphere category

43.4 Conclusions

Based on the maximum printing size of current Mcor Matrix 300+ 3D printer, changing the combination between cutting angle and composing style, it provided useful prediction and measurement for optimizing the printing time of large-size model. In this paper, substrate colorization time is linearly correlated with printed sheets, and the given fitted formula can provide a base to predict more complicated color models. In quantitative trials between printing time and scale size, exponential model can be expressed as this quantitative relationship well. The general formula can be calculated by more detailed database. When large-size model is used in printing, the 45° cutting angle and composing in vertical plane can be an optimized visualization method for different paper-based color models.

References

1. Wang, H. M., & Chen, G. X. (2014). 3D printing of topographic map based on UV inks. *Packaging Journal, 6*, 48–52.
2. Information on http:// www. mcortechnology.com
3. Ippolito, R., Iuliano, L., & Gatto, A. (1995). Benchmarking of rapid prototyping techniques in terms of dimensional accuracy and surface finish. *CIRP Annals-Manufacturing Technology, 44* (1), 157–160.
4. Liao, Y. S., & Chiu, Y. Y. (2001). A new slicing procedure for rapid prototyping systems. *The International Journal of Advanced Manufacturing Technology, 18*(8), 579–585.
5. Yuan, J. P., & Chen, G. X. (2015). Speedup method for paper-based 3d color printing based on STL file. *Applied Mechanics and Materials, 731*, 269–272.
6. Stanic, M., Lozo, B., & Gregor, Svetec D. (2012). Colorimetric properties and stability of 3D prints. *Rapid Prototyping Journal, 18*(2), 120–128.
7. Vaezi, M., Seitz, H., & Yang, S. (2013). A review on 3D micro-additive manufacturing technologies. *The International Journal of Advanced Manufacturing Technology, 67*(5–8), 1721–1754.

Chapter 44
Physical Modeling of Topographic Maps by Paper-Based 3D Printer Using NSDTF-DEM Data

Liuxi He, Zhaohui Yu and Guangxue Chen

Abstract The purpose of the present work is to develop a simple procedure for making physical models of three-dimensional (3D) digital topographic maps by rapid prototyping (RP) using digital elevation model (DEM) data. It is also intended to reduce data loss by choosing the right tools and minimizing intermediate data translations. As a typical digital map, NSDTF-DEM can be translated into ArcInfo ASCII Grid format, so that it can be manipulated by ARCGIS to restore the elevation, and in this way any data loss associated with intermediate file transfer will be eliminated. By AccuTrans3D software DEM files can further be converted into Stereo lithography (STL) surface with intricate geometries. The STL surface is then manipulated in Materialise Magics software to obtain a solid STL part, which can be used as input files for RP to obtain a physical model. All the openly available software that used in this method runs under Microsoft Windows 7 operating systems. The RP machine applied in this procedure is paper-based 3D printer, which takes less time and costs less but produces environmental friendly models with high accuracy.

Keywords DEM · STL · Conversion · Paper-based 3D printer · Physical model

44.1 Introduction

Map is one of the old and effective ways to record the face of the earth in the process of understanding the planet. Along with the development of computer science and graphics, a variety of digital topographic maps appears and develops

L. He · Z. Yu · G. Chen (✉)
State Key Laboratory of Pulp and Paper Engineering, South China University
of Technology, Guangzhou, China
e-mail: chengx@scut.edu.cn

Z. Yu
Shenzhen YUTO Packaging Technology Co., LTD, Shenzhen, China

L. He
Shenzhen Engineering Laboratory of 3D Printing Technology, Shenzhen, China

rapidly. As just one example, DEM plays a very important role in mapping, meteorology, hydrology, engineering construction, communication, and military, etc. Compared with traditional map, digital map is in favor of the preservation and update of data. However, digital map cannot convey the actual and accurate 3D information to people in the practical application, although it can display 3D information on the specific system. What is worse, traditional mold manufacturing is difficult and the process is time-consuming and costly. Thereby, an ability to easily build physical models of digital map is clearly important and needed.

The main disconnect between the digital topographic structure of DEM and the 3D printing software lies in the mutual incompatibility of file formats. The file format most commonly used in 3D printing is triangular mesh model, like STL, so the triangular mesh molding approach can be applied to achieve the conversion from DEM to 3D-printed physical model. As a typical format of DEM, NSDTF-DEM is the object of our study. Since NSDTF-DEM cannot be recognized and dealt with by most of the 3D software, it turns to be difficult to restore the magnification of elevation and do the surface molding. Referring to the research results of some Chinese experts [1–3], we rewrite the file header according to the data structure of NSDTF-DEM and resort to using open programs, which together offer greater flexibility in manipulating both the DEM structure and the 3D model.

Step-by-step instructions are proposed on how to convert a NSDTF-DEM file into a 3D-printed physical model. The procedure is neither the only nor the first method for achieving the conversion of digital topographic maps into 3D-printed models. S. Agrawal and J.P. Antunes have proposed a method to convert DEM ASCII XYZ data into physical model [4], Teng-Hao Chen and Semin Lee have provided a procedure to convert crystallographic information files into physical model [5]. This method has its special advantages: (1) the ability to produce models of NSDTF-DEM; (2) the conversion process with high accuracy from NSDTF-DEM to STL is rapid and stable; (3) the use of open and highly intuitive software packages with ample helpful documentation available online; (4) its reliance on a commercial paper-based 3D printing service-Matrix 300A-provided by MCOR technologies, whose process combines 'additive manufacturing' and 'subtraction manufacturing' together, this printer can ensure layer thickness uniform and less printing time, and does not need other supporting materials; and (e) the mainly consumables in this research are A4 or Letter paper and aqueous adhesives, which is environmental friendly.

44.2   NSDTF-DEM Format

DEM is a typical format of digital map. In fact, DEM is a special case of digital terrain model (DTM), which is an order numerical array describing the spatial distribution of various forms of information, proposed by Miller and La Flamme in 1958 [6]. As the most basic part of DTM, DEM is the discrete expression of the

elevation information on the earth's surface, as shown in Formula 44.1, where X_i and Y_i are the plane coordinates, and Z_i is the elevation value corresponding to (X_i, Y_i).

$$V_i = (X_i, Y_i, Z_i); \quad i = 1, 2, \ldots, n \tag{44.1}$$

NSDTF-DEM is the interchange format standard of spatial data in China, for data sharing and system integration. The file contains the file header and the data body. And the file header is composed of two parts, one is the basic and necessary data, and the other is the expansion and additional information which can be omitted. The file header contains several basic items, and every item occupies a single line [7], and there are some items which can be left out, such as coordinate, projection, spheroid, and parameters. The data body is ordered from north to south and from west to east, storing in ASCII code.

44.3 Procedures and Results

44.3.1 Conversion Instructions

Three separate pieces of software are required for this conversion: ARCGIS 10.2, AccuTrans3D, and Materialise Magics 15.0. Under the Microsoft Windows 7 operating system, the instructions are as follows:

(1) Right click on the NSDTF-DEM file (Example0.dem) and open it in notepad. Rewrite the file header into ArcInfo ASCII Grid format (the data is still stored in ASCII format). ArcInfo ASCII Grid refers to a specific interchange format developed for ARC/INFO raster in ASCII format. The format consists of a header that specifies the geographic domain and resolution, followed by the actual grid cell values. What needs to be noted is: yllcorner$_{(txt)}$ = yllcorner$_{(dem)}$ − nrows × cellsize, this operation is to make two adjacent files stitch together well after the conversion, because of the small difference in the records of grid cell data. The suffix of the file name should be rewritten into *.txt.

(2) Open ARCGIS 10.2, click on ArcToolbox > Conversion Tools > To Raster > ASCII to Raster, choose the *.txt file and convert it to a raster data (ASCIITo_txt). Then, click on ArcToolbox > 3D Analyst Tools > Raster Math > Divide, choose the ASCIITo_txt file and fill the magnification in the blank of the dialog box, so as to restore the elevation value amplified in raster data, and store the data after restoration as raster (Divide_ASCIITo_txt). Afterwards, click on ArcToolbox > Conversion Tools > From Raster > Raster to ASCII, choose the Divide_ASCIITo_txt file and convert it to a *.txt file. Finally, the suffix of the file name should be rewritten into *.asc (Example0.asc).

(3) Open AccuTrans3D and click on File > Open DEM As > ArcInfo ASCII Grid (*.asc). Then choose the Example0.asc file and click on Dem > Convert to 3D (less water), to display 3D surface of DEM data. The resulting data should be saved as a STL file (Example0.stl) which can be used in 3D printing by clicking on File > Save As. There are ASCII and binary two kinds of STL format, which can be selected according to actual needs.

(4) A non-closed 3D surface can't directly be used in 3D printing. Materialise Magics 15.0 was used to achieve the process from a STL surface to a 3D solid model. Materialise Magics provide an ideal, perfect solution for the users using STL files, and have an advanced and highly automatic function of STL operating. Load the Example0.stl file in Materialise Magics 15.0, the first step is to translate the 3D surface 1 mm along the elevation direction with the tool of 'OFFSET PART,' so that the 3D surface can get a small thickness. The second step is to mark the bottom of the 3D surface and stretch it to construct a solid model (the stretched length parameter is set to 500 mm) with the tool of 'EXTRUDE' (Fig. 44.1a). The last step is to cut the bottom of the solid model with the tool of 'CUT/PUNCH', the goal is to ensure a smooth bottom, which can support the 3D surface (Fig. 44.1b). The final model we get should also be saved as a STL file, and the top of the final model is the 3D surface of DEM data, the front, back, left, and bottom are all smooth faces playing the roles of supporting the 3D surface. For the final 3D viewing, we put the elevation of the model eight times magnification, as is shown in Fig. 44.2.

44.3.2 3D Printing

Matrix 300A is provided by MCOR technologies. Its main consumables are A4 or letter paper and aqueous adhesives. The paper does not need any processing or preprocessing and the adhesives have no volatilization of harmful gas after coated between two pieces of paper. The printer contains two parts, one is a standard Epson 310 N printer supplied with the color system, the other is 3D printer responsible for the 3D building.
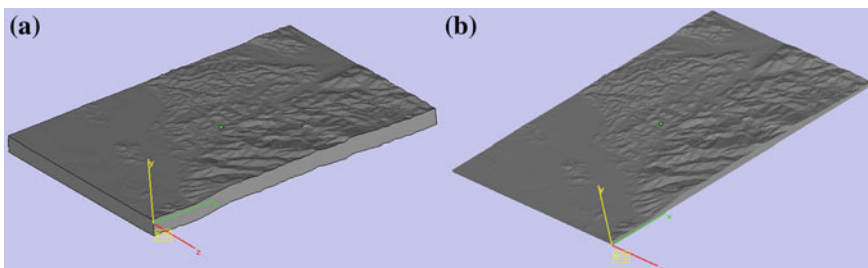
Fig. 44.1 3D solid models. **a** Model after stretching. **b** Model after cutting
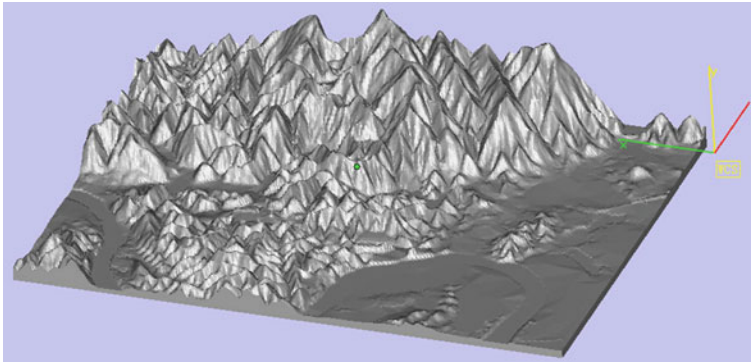
Fig. 44.2 The final solid model with eight times magnification of elevation

Printing process began with a 3D digital model. This model was sliced into 2D cross sections by the Slice IT software, as was shown in Fig. 44.3. These slices would be printed on two-sides of paper to produce colorful layers in Epson 310N. These colorful layers were in order sent into Matrix 300A to build the 3D object. Before the 3D building, there should be a piece of white paper sticking on the Build Plate, and Clue Spreader would uniformly deposit aqueous adhesive on the paper. Then, the colorful layers would be laid on the Paper Tray and the top layer would be pulled onto the Built Plate by Paper-feed Roller and Cripper. As shown in Fig. 44.3-Step3, Build Plate rose to press the Heat Plate at the top of build space, the top layer would be smooth in this way and be adhered firmly to the white paper at high temperature. When Build Plate down, Knife cut the top layer into the contour of corresponding 2D cross section, and Clue Spreader uniformly deposited aqueous adhesive on the top layer. Afterwards, next colorful layer would be sent in, and the process would be repeated until all the necessary layers had been sent into complete the 3D object. Took out the 3D object from Matrix 300A, we could get a cube of paper. Removed the excess portions, we got the physical model. In terms of colorful models, the printer only colored the surface of object, the excess portions, and interior portions were all white, which contributed to low-cost and high efficiency.
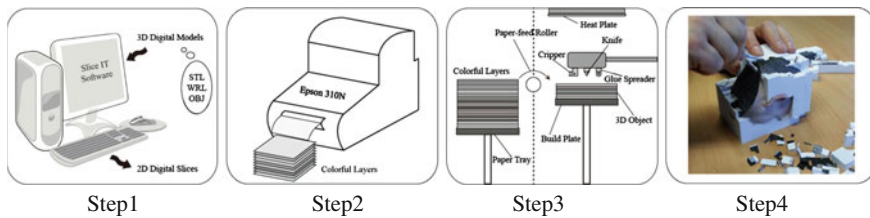
Fig. 44.3 Flowchart of steps followed in the printing process of the Matrix 300A printer

Fig. 44.4 Photograph of the physical model of NSDTF-DEM printed by Matrix 300A

In our study, we just printed a monochromatic physical model of NSDTF-DEM data as example, as was shown in Fig. 44.4. In the process, there were not colorful layers printed by Epson 310N and A4 paper was directly sent into Matrix 300A after slicing procedure of Slice IT software.

44.4 Conclusions

In conclusion, we presented here a method on how to convert any digital topographic maps in NSDTF-DEM format into a 3D printed model. Owing to the fact that DEMs are free-form surfaces, traditional manual modeling techniques are inaccurate and tedious, as it is difficult to visualize and convert DEM data. Our set of instructions uses openly available software and requires no programming knowledge and no knowledge of 3D printing techniques. Paper-based 3D printing could easily and accurately produce intricate geometries in less time and lower cost and without much human intervention. As with many rapidly development technologies, this method applies rapid layer-by-layer fabrication and environmental concept to solve the problem on how to produce 3D topographic map. Such topographic models can be used in catchment modeling, city planning, landscaping for architecture, etc. Moreover, the value of these models could be an effective tool for watershed and geological education.

References

1. Zhang, H. (2008). The conversion method from NSDTF-DEM to USGS-DEM. *Fortune World, 9*, 113.
2. Tan, W. J., & Luan, C. J. (2008). The data format exchange between self-defined DEM and USGS DEM. *Computer Knowledge and Technology, 7*, 1352–1354.

3. Li, S., & Peng, M. (2008). Preliminary discussion on automatic transferring among three common formats of DEM. *Geomatics & Spatial Information Technology, 31*, 6–11.
4. Agrawal, S., Antunes, J. P., Theron, E., et al. (2006). Physical modeling of catchment area by rapid prototyping using GIS data. *Rapid Prototyping Journal, 12*, 78–85.
5. Chen, T. H., Lee, S., Flood, A. H., et al. (2014). How to print a crystal structure model in 3D. *CrystEngComm, 16*, 5488–5493.
6. Makarovic, B. (1973). Progressive sampling for DTMs. *ITC Journal, 4*, 397–416.
7. Li, Z. L., & Zhu, Q. (2003). *Digital Elevation Model* (2nd ed.). Wuchang: Wuhan University Press.

Chapter 45
The Dynamic Display of Fractal Graphics on Computer

Wenjie Yang and Yuanyuan Zhu

Abstract It is the realization process about a software which shows the fractal graphics by a game. First, it introduces camera acquisition image, captured image process, and image basic point calculation. Second, it represents the basic elements and computer-generated methods of a few fractal samples and gives their programs. At last, it describes that the software uses VC++ programming language to achieve the moving fractal graphics with the camera captured images dynamically. It mixes the knowledge and interest to one, so that people have a deeper understanding of fractal graphics like playing a game.

Keywords Fractal graphics · Dynamic display · Image acquisition · VC++

45.1 Introduction

Image acquisition processing system includes image acquisition and image processing. Image acquisition is the processing procedure by sampling, quantizing, converting to a digital image, and storing [1]. Here a image acquisition system is designed. Fractal contains the beauty of science, but its principle is very abstract. Therefore, a game software is programmed to display fractal exquisite design and attractive color to people. In order to better show the fractal, the game software is as the following process: one thing like person's hand is projected onto the image carrier (ground or platform) by the projector, using image acquisition technology to collect the shadow image, calculating the basic point of the image by the computer, generating a fractal and displaying it on the computer. When the hand moves, the shadow moves, then the fractal moves. When the hand stops, the fractal changes its color or brightness continuously. So persons can learn more about this irregular graphics by the fun game.

W. Yang (✉) · Y. Zhu
Beijing Institute of Graphic Communication, Beijing, China
e-mail: ywj@bigc.edu.cn

45.2   Composing Dynamic Display System

The image acquisition system is by programmed by the VC++ language [2]. It is not only to control the quality of collected images by parameters' setting, but also to display the collected images by camera on the computer. Figure 45.1 is the diagram of dynamic display system, which includes computer, projector, camera, and an image bearing material such as curtain.

45.2.1   Image Acquisition System Device

In terms of the camera to capture images, it achieves dynamic image acquisition and synchronous process. Meanwhile, it is also set the timer to control the image processing response time by the program.

As shown in Fig. 45.1, the hand is projected by the projector to display the hand shadow on an image bearing material. And then through image acquisition, the shadow was collected and entered into a computer to calculate the area of the shadow. Then a fixed point like finger tip is calculated by programming. When the fixed point of the shadow changing, the fractal basic position also changes dynamically. So the software interestingly shows the moving fractal in different locations with the shadow.

45.2.2   Image Processing Flow

First, the software can adjust the camera's focus, brightness, direction, searchlights, and other sources, etc., and then start collecting command. The collected image is
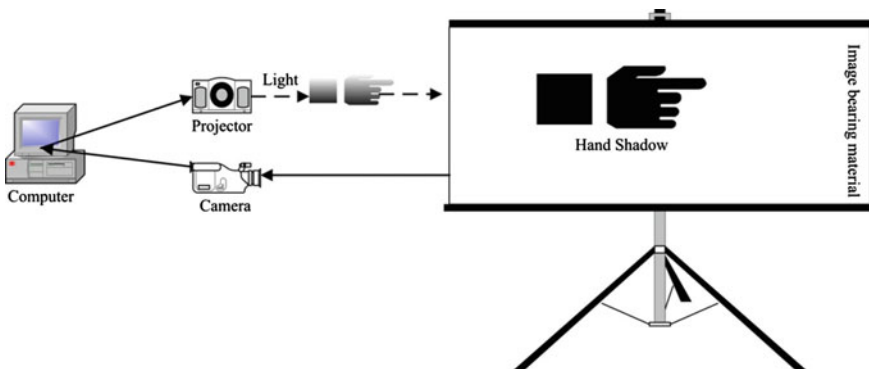
Fig. 45.1 Diagram of dynamic display system

displayed on the computer screen, processed to get the fixed point. Lastly, it achieves to generate dynamically fractal based on the shadow fixed point.

45.3   The Fractal Computer Realization

There are many ways to realize fractal graphics. The following mainly discusses the two classic generation method, which are complex iteration and IFS.

45.3.1   Implement Julia Set Complex Iteration

Nonlinear scientists study the complex mapping on $F(Z) = Z^2 + C$ [3]. The trajectory point Z form is determined by determining the parameter C. At design time, it collects coloration according to a point where the number of iterations. Julia set is to take a fixed value of C and then observes the iteration of performance at the complex plane's each point (x, y). Finally, it records the results. Figure 45.2 is Julia set by changing the value C.

45.3.2   Implement Fractal IFS

IFS' charm is that it is generated fractal iteration "Inverse Problems" [4], person just need to adjust the parameters, which can generate a variety of different biological forms. The iteration is affine transformation rule. It is a linear transformation including graphics for rotation around the source point, zoom by proportion, mirror, and other changes.

For a complex graphics, you can use the affine transformation family $\{\omega n\}$, which transformations can be set according to the probability P. The probability gets greater; the corresponding affine transform coefficients probability of being selected will be greater. Therefore, affine transform coefficients (a, b, c, d, e, f) and probability P are used compose an IFS code. Different IFS codes can generate different graphics [5]. Figure 45.3 shows a fractal tree by IFS.

C=0.2-0. 7i   C=0.31+0.04i   C=-0.12+1.24i   C=1.25
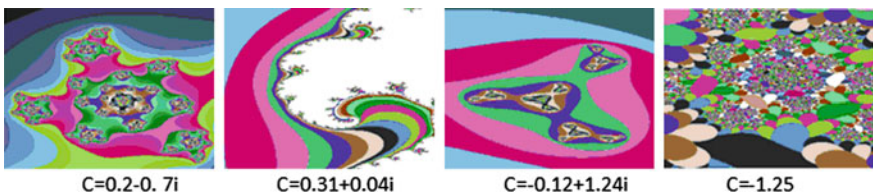
Fig. 45.2 Julia set graph with different values C changing

Fig. 45.3 Fractal tree's changing process

45.4 Realization Image Dynamic

The main interface diagram of the software is shown in Fig. 45.4.

By using image acquisition technology the software collects the shadow image and processes it. The hand is projected onto the image carrier (ground or platform) by the projector. Then, the computer processes the collecting shadow image by camera to identify the location of the shadow area as the fixed point. It will generate the dynamic fractal image based on the fixed point in the shadow, which is showed in the curtain (such as the ground or platform). The fractal graphic can move with the shadow moving.
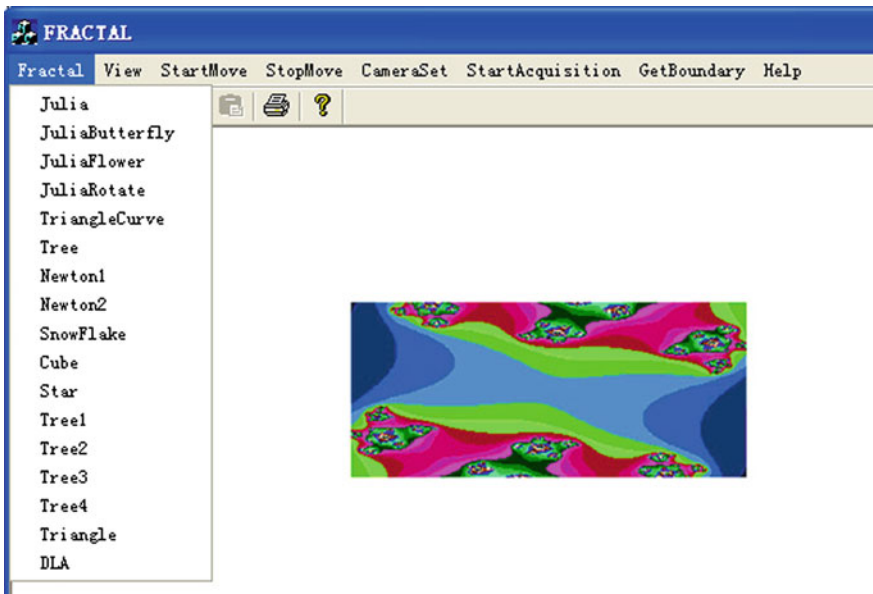
Fig. 45.4 The main interface of the software

45.4.1   Determining the Boundaries of Shadow

It needs to determine the boundaries of shadow, which has two main reasons: first, the imaging area and the projection area are inconsistent; second, the resolution of computer and projector is inconsistent. Before drawing fractal, the screen is white and the other area is deeper. So you can determine fractal displaying area by the appropriate pixels of the collecting image. Assuming the pixel color value of the collected image center is "0", and its position is (i, j). Its eight-neighborhood distance formula is:

$$d_s[(i,j),(h,k)] = \mathrm{Max}\{|i-h|,|j-k|\} \qquad (45.1)$$

Traversing each pixel, it does not stop scanning pixel until the distance condition is satisfied by a square equidistant lines form scanning pixels to the computing pixel.

45.4.2   Calculating the Image Basic Point

The basic point is from the shadow image with the calculated boundary, such as the center, the rightmost endpoint, or the leftmost end point. The (x, y) coordinate is recorded. Here the rightmost endpoint is used as Fig. 45.5.

45.4.3   Dynamic Displaying

The software screen shot is as Fig. 45.5. It is different effects fractal diagrams from the left to right respectively in Fig. 45.5a–d. Here is a fractal tree which moves with the position change of the hand tip to produce. When the hand shadow stops, the fractal tree changes itself from unclear to completely clear. It shows graphic's physical appearance. And it also shows the dynamic process that graphics moves with the finger tip's position moves. So it achieves the effect of the image tracking.

(a)   (b)   (c)   (d)
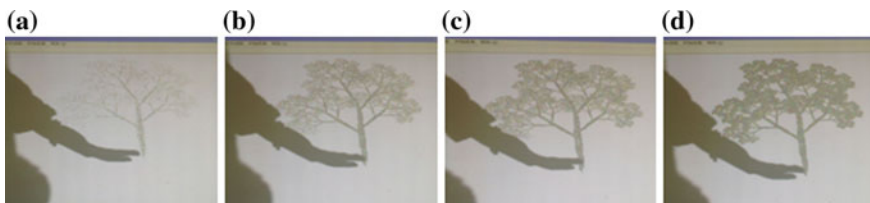
Fig. 45.5 Dynamic displaying

45.5   Conclusions

Fractal is abstract and beautiful, person can understand it easily by a game way. Here, we program a software by Visual C++ to get the above effect, which includes image acquisition and processing system, the fractal show by the two classical methods, and dynamic fractal moving with the moving hand. Here determining the boundary and calculating the basic point are more difficult. With the development of the software, it makes persons have a deeper understanding about fractal principles by a simple way. Also it can better demonstrate and explain fractals to students in classroom, or be used in technology museum exhibition so as to achieve popular science effect.

References

1. He, B., et al. (2001). Digital image processing using visual C++. Beijing: Post & Telecom Press
2. Liu, C., et al. (2005). Visual C++ development collection case. Electronic Industry Press
3. Tian-xiang, Chang. (2013). The application of fractal geometry in computer graphics. *Computer CD Software and Applications, 17*, 314–315.
4. Yun-Di, C. (2001). Fractal theory: The geometry of nature. *Computer Education*
5. Dong-Xu, Q. (2001). The fractal and its computer generation. *Computer Education*

Part III
Digital Media Technology

Chapter 46
"Creative Commons" Public Licensing for the Competitive Markets of the Publishing, Printing, and Packaging Industries

Yaojen Liu

Abstract Intellectual property rights protection is one of the major strategies of publishing, printing, and packaging companies. It strengthens competitive advantages in a highly competitive environment, particularly, in the digital age. New packaging structure, and packaging content and visual design are valuable targets to be protected under IPR mechanisms. Under IPR mechanisms, not only IPR costs are high for R&D but also the high risk being charged with IPR infringement. For small and mid-size design service companies, it is too complicate to treat IPR issues and difficult to reduce IPR costs. Is there any IPR mechanism that small and mid-size design companies could follow to reduce intellectual property costs and the cost of being charged with IPR infringement? "Technology and knowledge sharing" has developed since the last decade of the 20th century. The open-source movement philosophy has developed to several mechanisms, such as, Open Design, Science Commons, and Creative Commons. This paper is focused on "Creative Commons and IP sharing", to discuss the value of IP sharing for design fields. "Increasing marginal utility" is a major economic theory in this paper used to describe what benefits Open Design And Creative Commons could contribute to the design, publishing, printing, and packaging industries. Expert interviews and case studies are major research methods of this article.

Keywords Technology and knowledge sharing · Creative commons · Digital intellectual property management · Licensing management · Open design

Y. Liu (✉)
Department of Graphic Communications and Digital Publishing, Shih Hsin University, Taipei, China
e-mail: yjliu@cc.shu.edu.tw

46.1   Introduction

Creative and cultural industries, such as publishing, graphic design, photography, and packaging design, are a wide diversified and fast growing field. Most major countries are investing to develop their creative and cultural industries. Printing, publishing, package designs are depend highly on creativity and highly creation oriented to accumulate competitive advantages for twenty first century.

In the design field and the fully digitized design environment, there are several critical issues that will influence the costs and legal risks of the publishing, printing, and packaging printing industries. These critical issues are two: copyrights and patents protection, and licensing process cost. Patent licensing fees are another expense to creating new package construction. For art work of design, being charged in copyright or patent infringement by a competitor is a large risk.

The major goal of this paper is to discuss the question: "Is there any solution or mechanism that design, publishing, printing and packaging printing industries can follow in order to reduce design and development costs and to reduce infringement risk in intellectual property rights?" Open Design philosophy and Creative Commons mechanism is the approach discussed in this paper to figure out a different way for design and printing industries. Open Design encourages creators to share design information and knowledge to the design society. Creative Commons has developed a legal code system that any creator who wants release their contents to the public can choose the appropriate license code to describe his/her license agreement. Sharing of information and knowledge of design is a different philosophy compared to protecting design secrets. Creative Commons' allowance of partial rights is a possible solution that the design, printing, publishing, and packaging printing companies can follow to avoid legal risk and gain strong competitive advantages.

This paper will discuss how Creative Commons be developed and how it can help the design and printing industries to accumulate its own competitive advantages.

46.2   Definition and Development of Creative Commons

Creative Commons (CC) is a global nonprofit organization devoted to expanding the range of creative works and contents available for others to build upon legally and to share [1]. The organization was founded in 2001 by Lawrence Lessig, Hal Abelson, and Eric Eldred with the support of the Center for the Public Domain. The first version of CC was released in December 2002 [2]. From 2002 to 2003, there were an estimated 1 million licenses in use. In 2009, there were an estimated 350 million CC licensed works being licensed to the public. This is a 350 times

growth over 6 years. As of November 2014 there were an estimated 882 million works licensed under the various Creative Commons licenses. This number reached 1 billion in 2015 [3]. As of May 2015, Flickr alone hosts over 342 million Creative Commons licensed photos [4].

These licensing mechanisms allow creators, such as photographers, graphic designers, packaging designers, and painting creators, to communicate which rights they reserve, and which rights they waive for the benefit of recipients or other creators. An easy-to-understand licensing agreement set with associated visual symbols, explains the specifics of each Creative Commons license.

The Creative Commons licensing mechanism does not replace conventional copyright law, but is based upon it. CC replaces individual negotiations for specific rights between copyright owner (licensor) and licensee, which are necessary under an "all rights reserved" copyright management, with a "some rights reserved" management employing standardized licenses for reuse cases where no commercial compensation is sought by the copyright owner. The result is an agile, low-overhead and low-cost copyright-management regime, profiting both copyright owners and licensees. Wikipedia uses one of these licensesb [2].

46.2.1   Creative Commons Licenses Statement

CC has developed a set of tools to give everyone, from individual creators to large companies and institutions, a simple and standardized way to grant copyright permissions to their creative work [5]. Here are six license code of CC licensing mechanism [5]:

Attribution, CC BY

This license lets anyone distribute, remix, tweak, and rework, even with commercial purpose. The only thing the user must do is note the name of the original work. This is the most accommodating of the licenses offered and is recommended for maximum dissemination and use of licensed materials.

Attribution-ShareAlike, CC BY-SA
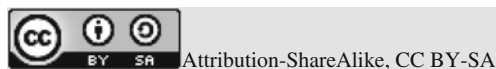
This license lets others remix, tweak, and rework for new works even for commercial purposes, as long as they credit the original artist and license their new

creations under identical terms. All new works based on original work will carry the same license, so any derivatives will also allow commercial use.

Attribution-NoDerivs, CC BY-ND
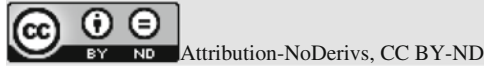
This license allows for redistribution, commercial, and noncommercial, as long as it is passed along unchanged and in whole, with credit to original creator.

Attribution-noncommercial, CC BY-NC
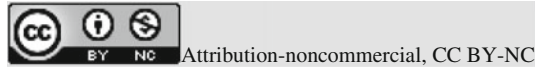
This license lets the user remix, tweak, and builds new works only for non-commercial purposes, and although the new works must also acknowledge original creator and be noncommercial, the user does not have to license their derivative works on the same terms.

Attribution-NonCommercial-ShareAlike, CCBY-NC-SA

This license lets the user remix, tweak, and builds new works for noncommercial purposes. The user must credit the original creator and license their new creations under the identical terms.

Attribution-NonCommercial-NoDerivs, CCBY-NC-ND

This license is the most restrictive of the six main licenses. It only allows others to download works and share them with others as long as they credit the original creator. The user cannot change the work in any way or use it commercially.

46.2.2 Benefits of Creative Commons: Case

No matter graphic designer, publisher, or photographer or package designer, cite from creation database that has well-developed contents is a successful way to finish her/his art work. CC licensing mechanism offers an opportunity to generate appropriate design work at low cost and reduce negotiation time and cost for the

licensing process. In some cases, the original creator can present his work in CC, and allow these works to be used under a CC licensing agreement.

Case 1 Katrina Nieh, A-Cube package design, CC BY-ND, Flicker.
        Nieh [6] is a young designer in Taiwan who represents design ideas and energy of the new generation of packaging design of Taiwan; she presented her design work to the world by CC, designers know her and her design capabilities through CC, and the world knows the commercial culture of Taiwan through her work in CC. For her and for designers all over the world, CC is good bridge to connect over. She benefitted from CC and in a short time, was able to be acknowledged, as a successful designer and gain the attention of many potential clients through the web.

Case 2 Designer-WG, how-the-packaging-works, CC BY-NC, Flicker.
        Dssigner-WG [7] is a German designer from Munich. He represents a design idea: "The Package presents the Bottle like a butler!" This work is licensed to the world in CC BY-NC, for nonprofit purpose of nonprofit organization and or individuals to use t for noncommercial purposes in low-cost design, such as gift packaging to those who donate to organizations. He released his design work to the public and earned a reputation in the fields of industrial design and packaging design, which has quickly grown the size of his client list.

Case 3 ABC pool, online media platform, Australia, CC BY-NC-ND.
        ABC pool is a collaborative online media platform under development by the Australian Broadcasting Corporation [8]. This project is a contribution to build up an online collaborative media publishing platform where contributors share and connect with people to grow ideas. Since 2011, this project has been gaining popularity with contributors and increasing usage as an audience engagement platform for ABC broad casting. The ABC broadcasting department uses this platform frequently to share and reuse media contents. External users outside of the ABC broadcasting department also connect to this platform frequently and contribute and use the content.

46.2.3 Open Design Mechanism and Creative Commons

Open Design is based on "Sharing Information" to development products from concept to idea to final product. Sharing of manufacturing information is not a new idea; it can be traced back to the eighteenthth and nineteenth centuries [9, 10]. The basic concept is using knowledge shared openly by other designers to design and development merchandise, such as products, software, and package designs.

Principles of Open Design have been related to the open source movements of the late 90s [11], the engineering industry has potential benefits of Open Design in machine design applications in late 1998 [12]. Moreover, developing countries could reduce developing cost to new invention development in technologies and

products [13]. Until late June, 2015, there was 2057 open-source web design templates "Download For Free" [14]. Design service workshop can save cost through Open Design resources.

Ronen Kadushin, an industrial designer who sharing his designs through Open Design, said: "An Open Design value is increased with wider modification possibilities and transformation potentials into other products. Designs that typically live only a few years in the marketplace can live on and develop into new shapes and uses" [15].

Creative Commons and Open Design are two approaches to guide designers to share their work with society and have different intellectual property rights protection agreements. These two are different mechanisms with the same philosophy: to encourage creator use and share ideas, knowledge, and experiences to improve design environment and make life better.

46.3 Increasing Marginal Utility of Content Sharing

According to Economic theory, the marginal utility, or marginal revenue, of a good or service is the gain from an increase, or loss from a decrease, in the consumption of that good or service. Positive marginal utility is when the consumption of an additional item increases the total utility. For creation product such as a photo, when this photo had been used on two individual designs for two separate clients, total utility created by this photo is higher than single use. Articles by Cole et al. [16] and Latzko [17] are typical research papers to describe increasing marginal utility.

The present is a knowledge and creativity-driven economic world where the input of more units of knowledge and creativity translates to higher competitive advantages. Utility increased and accumulated in a company transforms to intangible assets for that company. This creation energy input not only diffuses from team-to-team within the company, but also to the design society outside the company. Theoretically, through Open Design or CC, total utility contributed by creation sharing can be very high within a company and can be accumulated in the entire society. Total utility can be increased by the "share to public" decision.

46.4 Research Design and Methodology

Expert interview was the major research method used in this paper. There were five creation experts in Taiwan interviewed from late April through mid-June, 2015. These experts include the Director of editing department of travel magazine, Freelancing photographer, Director of design department of Food Company, Art director of Design Company, and technical director of Packaging Printing Company. Each expert was sent a copy and interviewed separated to avoid research

bias: opinions influenced by the other people in same time, same place. Research questionnaire and summarize of expert opinion list below:

(1) What is major impact factor that will influence your company to compete in industry?
Impact factors include: designer training, high competition for new contract, high risk of copyright infringement, and cost down pressure.
Each of the five experts mentioned "copyright infringement risk and legal issues" and concern over high content licensing expenses pushing companies into the "creation cost is getting high but contract price is getting low" dilemma. "Well-trained designer with copyright protection sense are very difficult to hire" is another impact factor.

(2) What are major issues related with Intellectual property rights that will influence your company?
Patent and copyright are two field experts mentioned the most often. The technical director from the packaging company paid higher attention in package engineering and package patent licensing for new product than the other experts. Engineer wish to have an easy way to explore information and experiences from other technicians.
Copyright is another topic every expert mentioned. Copyright infringement risks and license fees are the most concerning factors. Copyright contracts require highly specialized legal knowledge and experience but designer do not have.

(3) Do you have any IPR management system in your company? Or human resources training in IPR issue?
In Taiwan, most of design workshops are too small to have legal capability in company. Creation companies outsource to law firm to solve legal issues. Contract consultants, infringement defense, and legal knowledge training are service categories offered by law firms. This is a high cost but useful solution for creation companies. Finding a balance point between legal expenses and IPR protection is critical and very urgent for design companies.

(4) Have you had any experience with IPR issues? Were they positive or negative experiences?
Every expert answered this question aggressively. Eachexpert has had many encounters with IPR issues. There were some good experiences, such as receiving licensing fee income. Most experiences were bad experiences, including paying more license fees than fair license rate, spending too much time in contract negotiations, and having a hard time to find third party opinions to support legal decision. The worst experience was facing a judge in court.

(5) If there were an approach or solution that might be help you to solve IPR issues, reduce IPR licensing costs, and help you to reduce IPR infringement risk, would you want to know more about this approach? Would you consider putting this approach into your strategical development plan in your department for the upcoming year?

All five experts had reacted with same attitude in this question: "If there is a mechanism that I can follow to protect my IPR and help me to use contents from publicly available databases more easily, I am highly interested to study this system and will apply this mechanism into my company. I would like to know what will happen in industry. I am eager for an efficient solution that can help me manage the IPR of my company. I will apply this concept into my strategic development plan when I have more information about this mechanism."

46.5 Discussions and Conclusions

According to literature review and research interview results, I bring forth the following discussion points:

(1) Open Design philosophy is an open-minded philosophy that encourages designers and engineers who want make more contributions to society to share their creation with the world. This will contribute towards the advancement of society. Encouraging designers to gain experience and use the content for the Open Design Archive will help new designers and design school students to quickly pick up knowledge and experience from talented designers [18].

(2) Creative Commons is a good alternative compared to conventional copyright management. The Creative Commons pre-licensed to public means anyone who is planning to use this content only has to follow the license code attached with content without face-to-face contract signature. This mechanism will eliminate huge costs, not only for design companies, but also for society as a whole.

(3) Design companies must choose a balance point between "how much content to release to public" and "how much to keep in all rights reserved" before applying CC into the company. There still exist many gray areas in the CC mechanism that require a clearer definition [19]. Different interpretations and different development approaches in different countries make CC remain in a complex and unclear situation [20]. CC can be well developed and applied into society, like folk song music industry [21].

(4) Open Design and CC are very useful and valuable for nonprofit purposes. Nonprofit organizations do not have the budget to fix copyright valuation in a commercial world. Academic institutions invest resources to educate students on how to build capabilities for a highly competitive world. The budget is quite low to purchase contents in the commercial market. If talented designers could release contents in CC for students, it would make a huge impact on the industry [22]. Not only does this boost the reputation of designers, but it also sets an example for students to have an open mind for sharing their ideas. It is a good way to educate designers for both industry and society [23].

Is Open Design or CC the future answer to improving design service efficiencies, reducing copyright infringement risks, and making competitive advantages for design and printing companies? There are still great strides that need to be made to increase involvement, definition, and design society's understanding of CC. Fully implementing these open innovation mechanisms require attention to four key elements: developing networks to facilitate the flow of knowledge, strengthening knowledge exchange, creating intellectual property (IP) protection structures that accommodate open exchanges, and creating a business model to support openness [24, 25].

Every visual design service workshop, photographer, publishing company, and printing company needs to develop their own approach in applying Creative Commons. There is no shortcut to help them in this world.

References

1. CC. (2015). Frequently asked questions: what is creative commons and what do you do? https://wiki.creativecommons.org/FAQ#What_is_Creative_Commons_and_what_do_you_do. 3F. Cited May 15, 2015.
2. CC. (2015). Creative commons: History. https://creativecommons.org/about/history. Cited May 15, 2015.
3. CC. (2015). State of the commons. https://stateof.creativecommons.org/report/. Cited May 15, 2015
4. Flicker. (2015). Explore creative commons. https://www.flickr.com/creativecommons. Cited May 25, 2015
5. CC. (2015). About the licenses. http://creativecommons.org/licenses/?lang=en. Cited May 25, 2015
6. Nieh, K. (2009). A-Cube package design. https://www.flickr.com/photos/dlgarden/3787256775/in/photolist-6LEFuB-5XeFY5-E4x5H-5qhV2y-5qhUp7-4Y59dC-5qhVwW-9sC9Ae-AEpQF-oabnZ-5Xa9Mp-4Y597y-4Y58Rb-4VomK2-8MfWHb-5qdBn6-bXCS5Y-rxR7p2-27Bfcb-2x6tGj-5CbrwM-7wyiYk-7wC8jq-9dT2SC-9dT2Mo-ea7xyc-eXE6iS-7RBq7C-9rsNsV-7Tq5A6-6f1trm-6f1v2G-6eWkzn-6f1udd-6eWiQH-6f1uum-6f1tX1-6eWisi-4GDeeU-57WwYV-a1HJNU-a1ESrK-biaEk-9unSJG-c3Lz7u-a9J2pU-qNjzcU-6LJQ71-cbHDz-7wyiLB. Cited June 2, 2015
7. Designer-WG. (2006). Show-the-packaging-works. https://www.flickr.com/photos/spliffx/261374735/in/photolist-p6BAX-9rFsf-spiYUX-7wyiXx-Dqfin-9Hk35c-a58XeU-5tYxQW-eaQtW4-p5zhb-7qvSVc-eaW6LA-6F1EAj-eaW6SJ-eDNvNT-7QsfN-7wt7Hw-5abg2Y-afDQaC-56DYQT-9GgH7D-9HnUfJ-5QST-nuCp4-9gY6fG-5YiGdK-D4rpR-fWhZfY-MUzya-eG5c42-eGb7Uw-eG5aNZ-eGbd9A-eGbjfC-eG544p-eGb68q-eG57hp-eG53fp-eGb3Ky-eG53Fa-eGb7uU-eGb9os-eG4Wcg-eGbhK9-eG4X1t-eGbi5S-eGb3hj-eG4Ykv-eGbe2C-eGbet3. Cited June 2, 2015
8. CC. (2012). Case study/ABC pool. https://wiki.creativecommons.org/wiki/Case_Studies/ABC_Pool. Cited June 2, 2015
9. Nuvolari, A. (2004). Collective invention during the British industrial revolution: The case of the cornish pumping engine. Cambridge Journal of Economics, 28(3), 347–363.
10. Allen, R. C. (1983). Collective invention. Journal of Economic Behavior & Organization, 4(1), 1–24.
11. Vallance, R., Kiani, S., & Nayfeh, S. (2001). Open design of manufacturing equipment. In CIRP 1st International Conference on Agile, 2001.

12. Vallance, R. (2000). Bazaar design of nano and micro manufacturing equipment. Paper presented at Nanotechnology Workshop, July 14, University of Kentucky
13. Thakur, D. (2010). Open access nanotechnology for developing countries: lessons from open source software. *Nanotechnology and the Challenges of Equity, Equality and Development Yearbook of Nanotechnology in Society, 2*, 331–347.
14. Open Designs. (2015). 2057 open source web design templates, Open Designs. http://www.opendesigns.org/. Cited June 20, 2015
15. Kadushin, R. (2010), Open design manifesto. http://www.ronen-kadushin.com/files/4613/4530/1263/Open_Design_Manifesto-Ronen_Kadushin_pdf. Cited June 20, 2015
16. Cole, V. J., Michael O. M., & Jeffrey B. J. (2014). Assumption: Diminishing marginal utility from consumption, Pennsylvania State University. https://www.e-education.psu.edu/eme444/node/216. Cited March 3, 2015
17. Latzko, D. A. (2015). Lecture 15: Marginal utility, lecture material of introductory microeconomic, Business and Economics Division, Pennsylvania State University. http://www2.yk.psu.edu/~dxl31/econ2/2lecture15.html. Cited March 3, 2015
18. Christiansen, J. K., Gasparin, M., Claus. J., & Varnes, C. J. (2013). Improving design with open innovation: A flexible management technology. Research-Technology Management, March/April, pp. 36–44.
19. Simmonds, T. (2010). Common knowledge? The rise of creative commons licensing. *Legal Information Management, 10*(2010), 162–165.
20. Bloemsaat, B., & Kleve, P. (2009). Creative commons: A business model for products nobody wants to buy. *International Review of Law, Computers & Technology, 23*(3), 237–249.
21. Jones, R., & Cameron, E. (2005). Full fat, semi-skimmed or no milk today—creative commons licences and English folk music. *International Review of Law Computers & Technology, 19*(3), 259–275.
22. Liu, C. C., Tao, S. Y., Chen, W. H., Chen, S. Y., & Liu, B. J. (2013). The effects of a creative commons approach on collaborative learning. *Behaviour & Information Technology, 32*(1), 37–51.
23. Liu, C. C., Lin, C. C., Chang, C. Y., & Chao, P. Y. (2014). Knowledge sharing among university students facilitated with a creative commons licensing mechanism: A case study in a programming course. *Educational Technology & Society, 17*(3), 154–167.
24. Ches brough, H. W. (2003). *Open innovation: The new imperative for creating and profiting from technology*. Cambridge, MA: Harvard Business Press.
25. Ches brough, H. W. (2004). Managing open innovation: Chess and poker. *Research-Technology Management, 47*(1), 23–26.

Chapter 47
Design and Implementation of Location-Based Services on Campus Navigation System

Zhanjun Si and Chen Wang

Abstract Using panorama technology and location services to research and design campus navigation system that provide basic mobile navigation service for users. The real map of Hexi campus of Tianjin University of Science and Technology is taken as the research object. It takes the camera to collect pictures and uses PTGui software to make 720° panorama. Transform panorama images by Pano2VR software into dynamic display files for webpage. At last, the corresponding hot spot information and navigation function in webpage are achieved by using the Html5 technology. The final campus navigation system will provide real view display, navigation, and other function. Design and development of campus navigation system of panorama technology and location services, can not only provide the service for the students and teachers in campus to learn about the facilities position, to understand the campus layout and access location of resources information, and to offer better option and more helpful information to other users out of campus to understand the campus.

Keywords Panorama · Campus navigation · Location services

47.1 Introduction

In recent years, the information technology develops rapidly. The mobile terminal devices are also increasingly high and advanced, such as tablet PCs, high-end mobile phones. With these devices more and more popular, universal, thus providing information resources services to users through mobile terminal devices receives major operators increasingly favor and attention. Location service is one of the trends of information service. Campus tour guide location service system has

Z. Si (✉) · C. Wang
College of Packaging and Printing Engineering, Tianjin University of Science& Technology, Tianjin, China
e-mail: szj@tust.edu.cn

become an important part of the development of the construction of digital campus, information technology.

47.2 Location-Based Services

LBS is in the condition of communication network, an information content service through the mobile terminal access user location information to provide users with positioning technology [1]. As the fourth generation mobile communication system (4G) development, information transmission accuracy, and popularity has been improved. In support of system software and hardware performance increasingly powerful, the position of mobile terminal application can show the simulation interface clearer map, more real and more realistic 3D effect. At the same time, the integration of mobile location services and Web2.0 services to enhance the mobile location service value [2]. Figure 47.1 is the LBS system structure.

47.3 Spherical Panorama Technology

Panorama is a new interactive media technology. Through the computer technology to generate 360° horizontal, vertical direction of 180° is in a three-dimensional environment. It enables the user to have more realistic specific experience. In order to get the best effect of mosaic, images need to be in the same coordinate system [3]. The panoramic models commonly used including planar, cylindrical, and spherical, etc. Figure 47.2 is schematic diagram of the spherical model.

Spherical panoramic image mosaicing can not only realize 720° around at the scene, but also is in accord with the habits of the observation; achieve real
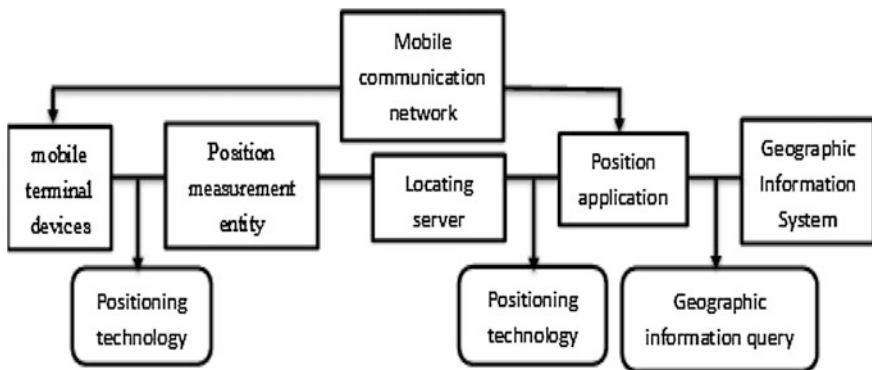
Fig. 47.1 LBS system structure
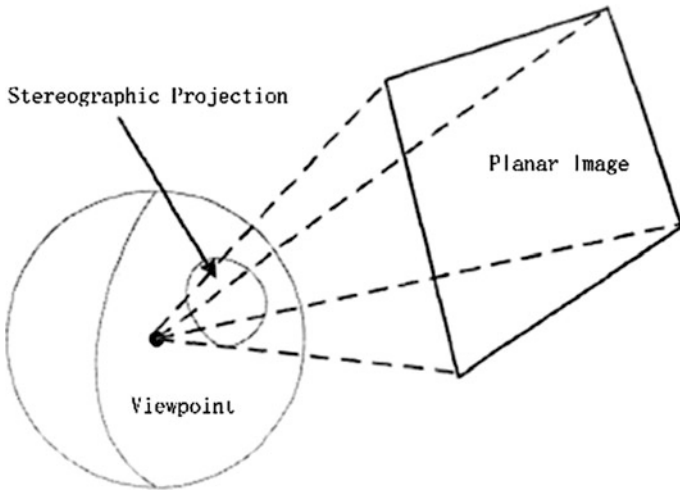
Fig. 47.2 Schematic diagram of the spherical model

panoramic view [4]. Because the sphere is not a developable surface, in order to make the image storage into spherical panorama, we need to adopt parametric spherical projection model. The first mapping on the surface of the visible part to the viewing plane, then display the image plane. As the plane coordinates (x, y, z) to the spherical panorama coordinates (U, V) of the projection formula:

$$\begin{cases} u = r \arctan(x/z) \\ v = r \arctan(y/\sqrt{x^2 + y^2}) \end{cases} \tag{47.1}$$

R is the radius of sphere [5].

47.4   System Framework

Campus navigation system is built by PTGUI software, Pano2VR, Dreamweaver, and related design software. The system can realize the real panorama preview on the mobile terminal. Figure 47.3 is flow chart of system development.

First, select the collection points, use the camera to take pictures, and each collection point to collect as many photos as possible. Second, using PTGUI software synthetic panorama, and using Pano2vr software to create panoramic roaming. Finally, build navigation website.
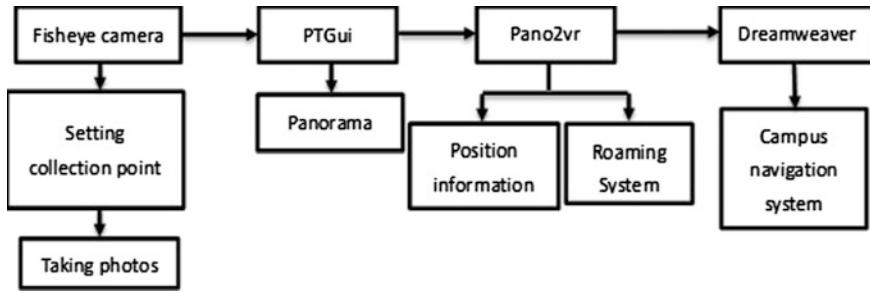
Fig. 47.3 Flow chart of system development

47.5 Design and Implementation of the Panorama Application

47.5.1 Collection and Mosaic of the Panorama

The sample collection of the campus panorama is the basis of making the campus panorama. The fisheye camera takes school 54 key points of the sample pictures. In order to ensure the effect of the panorama, the amount of exposure, contrast, focus distance, and white balance must be consistent when shooting pictures [6]. Standard setting: The fixed focus lens; the exposure metering accurately in the metering of a proper area, using manual exposure; the parameters of aperture and shutter speed; exposure should consider the extremes of light and dark exposure, avoiding overexposure and underexposure; the manual focus mode [7].

The operation of PTGUI software, in a clockwise direction into the picture, and then set the picture of the actual parameters by adjusting the control points to get the most accurate of Panorama. Figure 47.4 is adjusting the control point. Finally, the panoramic images are modified by using Photoshop software. Figure 47.5 is mosaic panorama.

47.5.2 System of Panoramic Roaming

Html5 has successfully replaced the Flash technology based on Webpage. Since the mobile device has little support for the Flash plug-in, the Html5 has good inter-activity and vision. Html5 is more suitable for mobile devices browsing in the IOS and Android systems, bringing more excellent immersive roaming experience. Panorama common production tools are Pano2vr, Krpano, and panorama Maker, etc. In these tools, Pano2VR is undoubtedly one of the best software. The Pano2vr interface is simple, quick, complete function, and can import a variety of panoramic picture format.
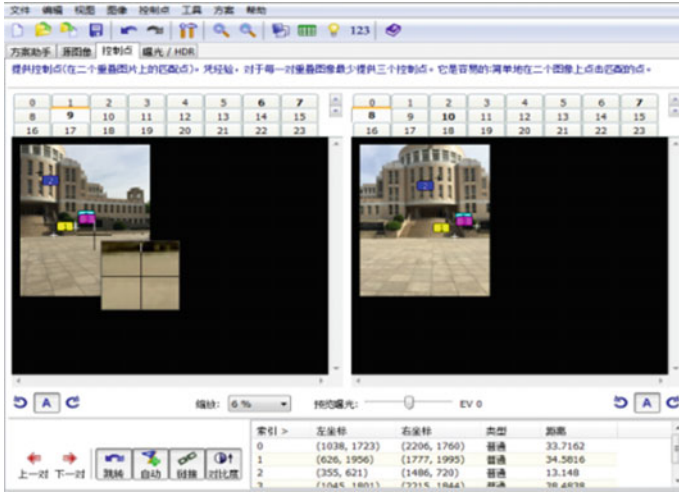
Fig. 47.4 Adjust the control point

Fig. 47.5 Mosaic panorama

The Pano2vr has the function of realizing interactive hotspot, and it can generate two files of Flash and Html5 directly, and can run directly in the Web browser [8].

To make a panoramic picture imported into Pano2VR for setting angle and parameters. By adding the hot spot in the interactive panorama to achieve different scenes of coherent conversion, get the panoramic navigation. Figure 47.6 is campus panorama roaming.

Fig. 47.6 Campus panorama
roaming

47.5.3 Release and Test Website

As we launch platform for mobile terminal equipment, thus making the website to take into account the mobile terminal and the parameter information of Webpage code changes into adaptive screen effect. The basic framework of Dreamweaver software design website, determines the homepage interface of basic tone, and then edit the corresponding subpage. In the navigation interface content, add hot link into campus with the coordinates of the plane map to the Dreamweaver software. Using the "Polygon hotspot" tool in the plane map with the coordinates of the points out of the corresponding hot polygon and select it. Figure 47.7 is the interaction hotspot. In the properties panel settings need to link to the destination address of the campus panorama point, and then release the website to the server. Finally, tested by mobile terminal.
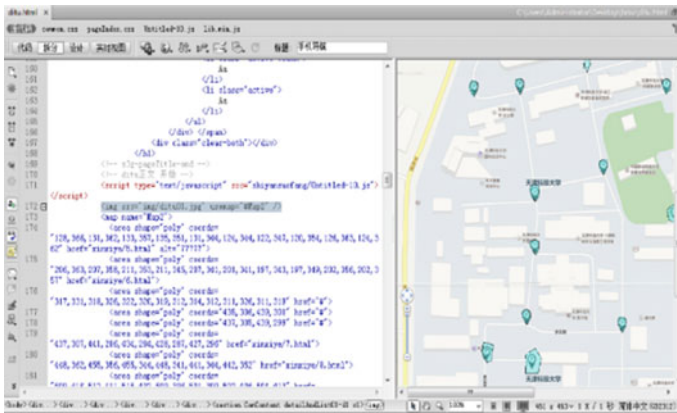
Fig. 47.7 Interaction hotspot

47.6   Conclusions

Based on the technology of location-based services, the first is to obtain the user location information. When the user responds to the location of the information service, it will send location information service to the user through the communication network. The location information service can not only support the position of the body in the panorama, but also be able to look around the terminal at 720°. The navigation service can get around the user related buildings, and other facilities, and provide timely information services for the users. Campus navigation location service system can not only provide service for college teachers and students to learn the position coordinates based on the understanding of the campus, timely access to campus resources and real information, and can understand the campus information for other users need to provide more direct pathways and more precise information.

At present, the development of science and technology make a spurt of progress and meet the needs of individual users more important. The application of the technology based on location services is becoming wider and wider. Based on the development of campus navigation location services in this direction will be more and more attention and construction in Colleges and Universities. It is conducive to the university campus into digital and network era, and greatly enriches the content of campus construction.

References

1. Zhu, H. J. (2008). *The GIS-based mobile terminal LBS system construction and implementation*. Master Thesis, East China Normal University, Shanghai.
2. Wang, P. (2011). Research on mobile learning based on position service. *China Educational Technology, 299*, 114–119.
3. Yang, C. R. (2013). *Research and implementation of fisheye image mosaic technology based on spherical model*. Master thesis, North China Electric Power University, China.
4. Li, S., Zhang, Q. Q., Lv, Z., & Yang, J. H. (2012). Fast spherical panorama generation algorithm based on feature points. *Journal of Changchun University of Science and Technology, 35*(3), 75–78.
5. Zhao, Y. L. (2011). Spherical panorama Navigation algorithm research. *Computer Knowledge and Technology, l7*(13), 3112–3113.
6. Zhuang, H. (2010). Mosaic scene panorama with PTGui software. *Police Technology, 6*, 71–72.
7. Hao, X. H., Peng, H. J., & Liu, Y. (2008). Application of PTGui software in the field of Criminal Photography. *Guangdong Public Security Science and Technology, 4*, 23–27.
8. Huang, G. Z. (2015). Research on interactive campus roaming system based on Pano2VR. *Software Engineer, 18*(1), 17–18.

Chapter 48
Establishment of Color Matching Database Based on MySQL

Yan Zhang, Shisheng Zhou and Congjun Cao

Abstract Color matching system is a specialized software solution geared towards spot color matching. It contains spectral reflectance import, data calculation, and formula export. In virtue of a generic open data base connectivity (ODBC) interface, data analysis is performed by statistics and analysis software connecting to a database. The color matching database (CMD) application is developed in ink formulation studies, and is established including four modules: primary ink information database, substrate information database, spot color database (target color), and ink formula database. This paper describes the design and establishing of CMD. The database is built on MySQL. Formula ink can be selected by searching target color number. The results show that the adoption of MySQL program application is feasible, flexible, low-cost and user-friendly way of managing research data in color matching system.

Keywords Database design · Spot color matching · MySQL · Ink formulation management

48.1 Introduction

With the development of computer technology and the requirement of "green printing," there is a digital and intelligent trend in the printing industry, whether color management in prepress, online detection or printing quality control in press.

Y. Zhang
Faculty of Mechanical and Precision Instrument Engineering,
Xi'an University of Technology, Shaanxi, China

S. Zhou · C. Cao
Faculty of Printing, Packaging Engineering and Digital Media Technology,
Xi'an University of Technology, Shaanxi, China

Y. Zhang · S. Zhou (✉) · C. Cao
Shaanxi Provincial Key Laboratory of Printing & Packaging Engineering, Shaanxi, China
e-mail: zhoushisheng@xaut.edu.cn
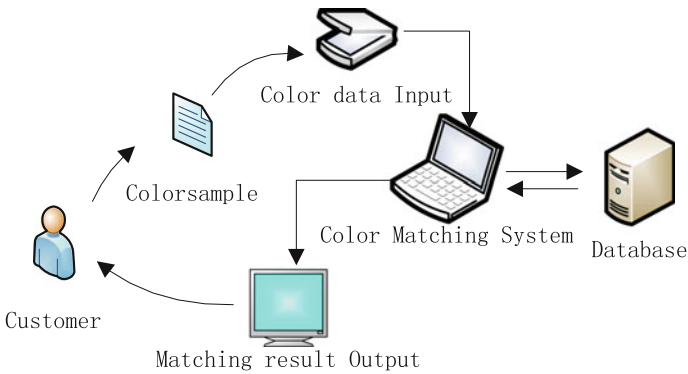
Fig. 48.1 Workflow of color matching system

Spot colors are widely used in gravure printing. At present, most manufacturers in China still use a hand-mixed color matching that submitted by the designer who designs the basic color mixing formula according to Pantone color reference and then fine adjusts it comparing with the original color [1]. The hand-mixed method has shortcomings of wasting of time and materials and highly depends on experience of the handler. For these reasons, there are a few color matching systems developed, including Ink Formulation by X-Rite [2], Colibri® [3] and EasyMatch® Coatings [4]. But the development of color matching system is still relatively backward in China. SRICI developed by Shenyang Chemical Institute and GretagMacbeth is also color matching software but the core algorithm belongs to GretagMacbeth Company. Color matching system is studied in this paper, and the formula of target spot color is calculated according to the input primary color ink and paper (Fig. 48.1).

In color matching system, all of the information needs to be saved in database. Whether for color matching or ink management, database establishing is important and pivotal. This paper describes the design process of building a color matching database (CMD).

At present, there are some frequently used database software, by contrast, MySQL has program served its purpose well in developing a well-structured format database for the systematic compilation, storage, and retrieval of extremely large amounts of historic data in an open domain [5, 6]. It can be written with C++, which is the basic programming language of the system. For the management of MySQL database, Command Line Client, and Navicat for MySQL were used in the study [7].

48.2   Function and Structure of the Database

Database is the core of the color matching system. Logical design will not only reduces the difficulty of programming, but improve the operation performance.

48.2.1   Database Design

According to the standardization of design and development process, the database is divided into six stages: requirement analysis, conception structure design, logical structure design, physical structure design, database implementation, operation, and maintenance of the database [8].

48.2.2   Structure of Color Matching Database

In order to save, use and manage color data, the CMD is established including the following four modules: ink information databank, substrate information databank, spot color (target color) databank and ink formula databank. Administrator can enter the management system with password to import, modify and export the information of primary inks, substrates, spot color samples, and color formula (Fig. 48.2).

As the core objects the E-R diagram are designed as follows (Fig. 48.3).
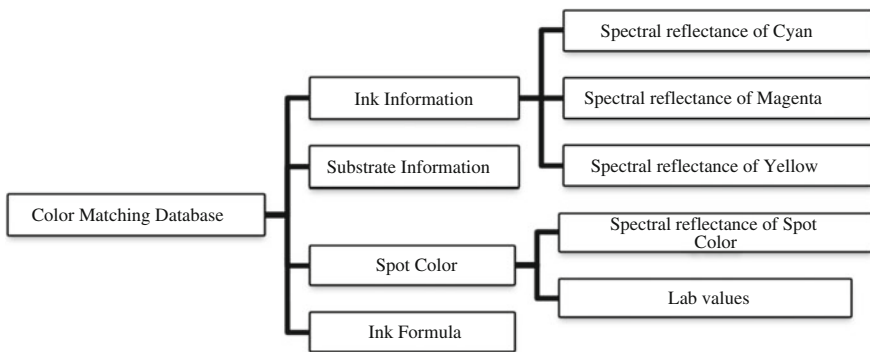
Fig. 48.2 Structure of color matching database

(a)

(b)

(c)
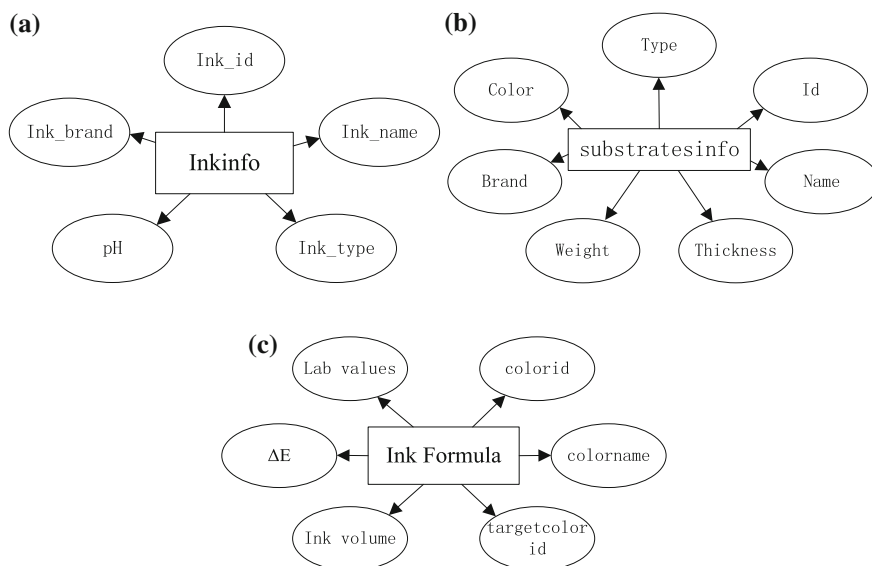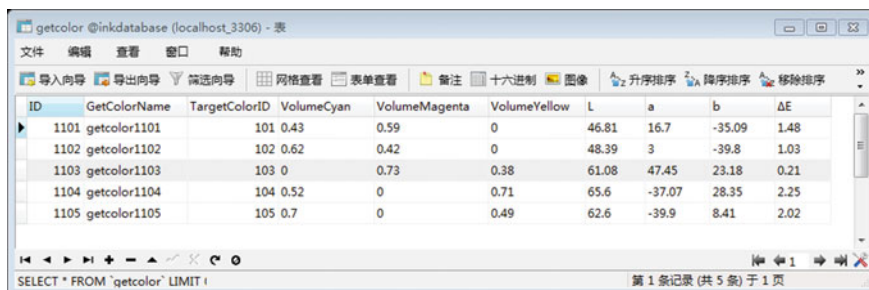
Fig. 48.3 E-R Diagram of **a** ink information databank, **b** substrate information databank and **c** ink formula databank

48.2.3 Establishing of Color Matching Database

First of all, database was established, which was named Color Matching Database. In the database, ink information databank (inkinfo) was created, in which ink id, ink name, ink type, brand, and pH of primary inks were saved. For each primary color, for example, cyan, magenta, and yellow, a databank was created to store color spectral reflectance from 400 to 700 nm. The range of spectral reflectance depends on the measuring equipment. In this databank, it contains color id and color name, which are the same as ink id and ink name in the ink information databank. Substrate information databank (substratesinfo) was established, which included the id of substrates, name, type, thickness, weight, brand, and color. Spot Colors databank was established, which contained color spectral reflectance and color Lab values. Color id and name were common information for each spot color. Finally, the ink formula databank (getcolor table) was created to save the calculated ratio of primary inks and Color Lab values, in which id and name were added at the same time for ink formula. It also contained ΔE value between the formula color and target color. Each formula should be related to the number of target color, which existed in the Spot Color databank.

Fig. 48.4 Screenshot for ink formula table

48.3 Application and Discussion

In the experiments primary ink information and paper information were imported into database. Five spot color samples were used as target colors. For example, the proportions of CMY inks were 2:3:0, 3:2:0, 0:3:2, 2:0:3, 3:0:2, while their spectral reflectance was measured with spectrophotometer. Ink quantity proportions of primary inks were calculated according to color matching module. Primary ink and paper can be chosen from ink databank and substrate databank. Finally, the matching results were saved into ink formula databank. Meanwhile color differences between samples and formula colors were shown in the databank. As a result, ink formula databank is shown as follows (Fig. 48.4).

Common primary colors, such as cyan, magenta, and yellow are already saved in the database as preset information. Formula ink can be selected by searching target color number (id of Spot Color). New formula can be also calculated and saved in the ink formula table, while in spot color table for new spot color originals. Calculation process will be no longer described in this paper. The calculated results are very close to design samples. Maximum color difference ΔE is 2.25, minimum color difference ΔE 0.21, and average 1.40. Meanwhile the calculated proportions of primary inks are almost consistent with the designed target colors. That is to say, the color matching module is accurate, and establishing of CMD is available.

48.4 Conclusions

This study has demonstrated the structure and application of a CMD. CMD has been developed in a user-friendly environment and each established table can be saved as txt format or in an excel sheet. The database is useful as a preliminary design tool for color matching system and can be used not only in gravure, but in other printing processes. In addition, it can be a source of essential data and spot color information for engineers. The database can be extended with the amount of collated test modules and their applications.

References

1. Luo, R. B., Zhou, S. S., Jiang, N., & Yang, Q. J. (2011). Mathematical model and implementation of the density-based gravure spot-color matching. *Advanced Materials Research, 174*, 56–59.
2. Ink Formulation 6.2-overview of Enhancements. (2014). http://www.xrite.com/documents/literature/en/InkFormulation62_Enhancements_en.pdf
3. Colibri color management suite. http://sensing.konicaminolta.us/products/colibri/
4. EasyMatch QC-Color measurement software. http://www.hunterlab.com
5. Lin, S. S., Marcos, M. C. M., Chang, H. W., & Chen, Y. J. (2012). Design and implementation of a drilled shaft load test database. *Computers and Geotechnics, 41*, 106–113.
6. Lan, X. H., Xiong, J. J., & Deng, G. (2004). Development of application program based on MySQL. *Computer Engineering and Design, 25*(3), 442–468.
7. Yuan, Y., & Zeng, W. H. (2002). Realization and application of MySQL database interfaces based o visual C++. *Journal of East China Shipbuilding Institute., 16*(5), 41–45.
8. Rob, P., & Coronel, C. (2004). *Database system: design, implementation and management* (6th ed.). UK: Thompson course technology.

Chapter 49
Research and Implementation of Campus Tour System Based on Mobile Terminal

Zhanjun Si, Lu Zhang and Ying Wang

Abstract With the advent of the information society, the construction of digital campus is the inevitable trend of the development of colleges and universities. With Tianjin TEDA campus of the University of science and technology as the main object of study, application based on the Apple Mac OS X system with Xcode software swift programming language written code works, the development of campus tour guide system based on mobile terminal is made in order to make user conveniently to understand the layout of the campus information and campus introduction. This application has many functions, such as zooming map, searching the location, introducing campus. For strangers, it also supports a convenient and quick visualization service to them, so that they are familiar with the school quickly and fully anytime anywhere.

Keywords iOS · Mobile application · Position search · Campus tour guide system

49.1 Introduction

With the rapid development of mobile Internet technology, the mobile Internet technology has been playing more and more important role in the digital campus constructing [1]. The campus tour systems for mobile not only satisfy the user with most information of campus, but also provide the user different kinds of tour lines in the university. This software contents many kinds of requirements with foreign exchange and tourism. Also, it is the important part of the digital campus construction. Nowadays, this sort of software is still very few [2], but, with the development of digital campus building in Chinese universities, it will have a good future [3].

Z. Si (✉) · L. Zhang · Y. Wang
College of Packaging and Printing Engineering, Tianjin University of Science
and Technology, Tianjin, China
e-mail: szj@tust.edu.cn

49.2 Preparation

49.2.1 Design Arrangement

In order to meet the needs of users in the campus, the application should have a map display, query, and other functions. According to the research content set design ideas. As shown in Fig. 49.1.

49.2.2 Data Collection and Processing

First of all, the paper collected the information about campus information, such as history, land scape pictures, school bus timetable, and so on. According to the construction plan of Tianjin University of Science and Technology TEDA campus, the map was made of Photoshop software. Furthermore, the overall planning of the campus structure was carried out. The coordinates of each building in the campus plan are marked as their own mark points. Finally, best sightseeing route was set according the actual situation.
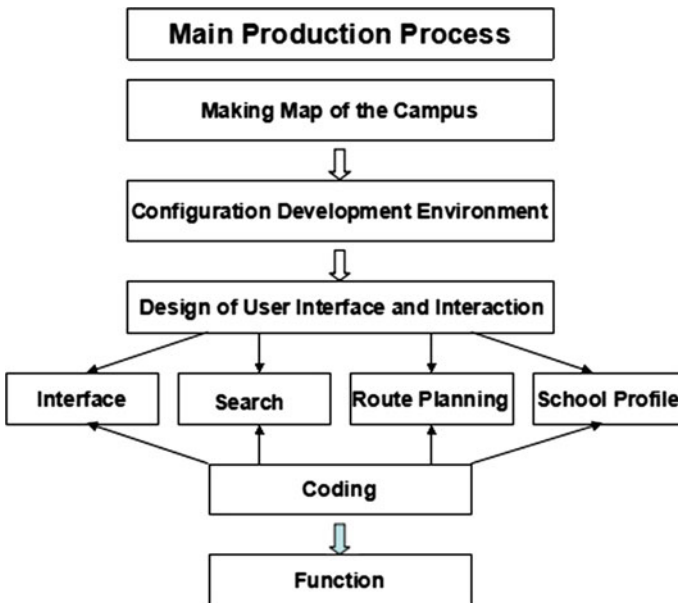
Fig. 49.1 Main production process

49.2.3   Configuration Development Environment

Design and development based on the apple iOS system the client of the mobile system is based on the apple iOS7 system, the development environment is the OS X Yosemite Mac system. The software is required to install the Xcode software. It needs an Apple Developer certification, Apple Developer Certificate, and apple developer team development account [4]. Apple's development software Xcode provides developers with many tools to help developers. In Xcode software can be added directly to the view controller interface, and then it can add other in the above, for example, search, list boxes, input boxes, and other controls to help developers of software development. At the same time, Xcode software also provides the two different testing environments of virtual machines and testing environment. The test environment of the client is the smart phone of the iOS 8.3 system [5].

49.3   Design of User Interface and Interaction

The most significant part of the mobile application designing is the user interface. It should be designed to cater the needs and preferences of user, for a good design can improve experience. This app is designed in such way that is based on the situation service, and make sure that users can get their position easily. It faces user groups include teachers and new students. Its interactive is convenient and smooth. This design application interface is mainly divided into four parts.

49.3.1   Main Interface

The main interface design of application considers location-based services. The map of TEDA area of TUST of planning and designing is main part of interface; it can be imported into the mobile application through code. There are three buttons, the query button, the route button, and more buttons. As shown in Fig. 49.2.

49.3.2   Search Interface

On the Query Interface, the cable box has a hint of text "query." Searching location range includes Eastern Region, Central Region, and Western Region. If Clicking on the search box, text input keyboard will appear. What is more, when users search

Fig. 49.2 Design of main
interface
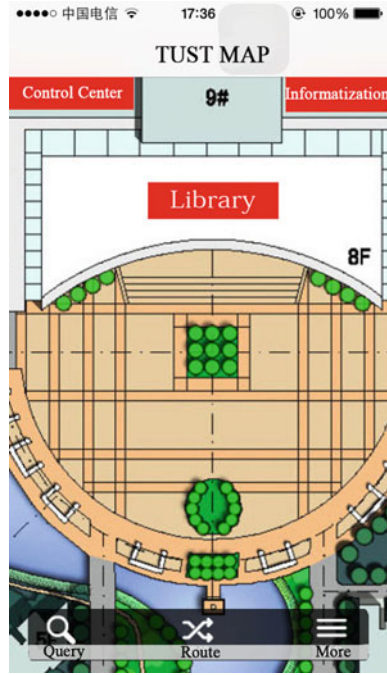
location; it is not only real-time filtering searches keyword but also fuzzy search. In
the lower part of the search box is divided into three parts, respectively for the
campus, West Campus and East campus. Under the specific campus is presented is
each campus in place, the user can read in view, when users click on any one
location corresponding to the location can be present in the main interface. The
advantage of this design is allowing users for each campus locations can be quickly
retrieved. Each campus in different locations can have a clear understanding of the
campus. As shown in Fig. 49.3.

49.3.3 Route Planning Interface

The function is set up for the first visit. The function set several optimal tour guide
line, the user can choose the appropriate line in order to click on the image line to
load the selected information into the software, and the map will appear blue lines
to express which line the user needs to go. Users can also be combined with query
function to determine the location. It is designed that first visit users can quickly
and easily to understand the layout of the school.

Fig. 49.3 Query search
interface

49.3.4   More Features of the Interface

The More features interface support a detailed presentation about TUST, which introduce the history and culture of the university with vivid pictures and language.

49.4   Code Written

At first, opening the Xcode software and creating a new Project engineering document. This APP is written in the swift language,The platform is set to iPhone. After founding the new subject, it will be written in the Xcode environment. The steps of the development are that: design and development of software interfaces first, and then writing the codes of related functions to impel interactive features. For making the developers developing application software easily, the Xcode integrates the entire code hints feature. The code can be hinted by some related code which developers inputting. That design improves the ease of development and makes the developer develop the software more comfortably. In addition, you need to create a new class file, used to write functions in different interfaces.

During using this TUST MAP, user can move the 2D TEDA campus picture and operate zoom in-out orders according to their different needs. The functions of moving, zoom in-out by double-kicks and zoom by gestures can make the users check the TEDA campus pictures conveniently in anytime [6].

The function of location searching is to find and highlights the destination on the School campus construction plans according to their needs. When compiling location list, the program founds a new file whose name is "college. List." The file can save the data of names and locations, so that take an advantage in the APP calling for data.

The 2D TEDA campus picture determines the data of local situations. Every point of the situation reflects a pixel that has determined data of the X-axis and the Y-axis on the picture. After achieving the list of local situations, the searching location function will be taken into the list. After adding a search box, writing the corresponding code to achieve the search box search function. For using conveniently, the program is added in the data filtering code when writing this code, so that the program can filter the data which the user used to search and keyword search when the user type in. The list also changes according to the users typing the searching keywords.

49.5 Software Function Testing and Release

Xcode application development software can be used in the development of the procedures for rapid detection. The application provides two software-testing methods, which are in Apple's Mac OS X Yosemite system using the simulator application running and testing can be carried out, or operation and test the application using the iPhone prototype. Use iPhone prototype of application of detection of advantage is can be true on the phone simulated user usage and detect problems at any time. Detecting the application on a real machine operation interface is consistent with the design of the interface. Ensure that the program is debugged to the best operating results and the use of results.

After the application of the software test is correct, the final package is packaged, and then the application software will be uploaded to Apple's Store APP. users can download the software according to the needs. The design takes into account only for learning and is not released in Store APP. After the package output to the iPhone mobile phone, it should be the application testing work, and finally complete the design and development of the application.

49.6   Conclusions

This paper is based on the iOS system to achieve the school's campus guide system development. The search box and the location list with the realization of the interface can filter real-time search information, fuzzy query, finally realizes the function of campus planning map browsing, and search function. For the first visit of the user can be in accordance with the established tour guideline to visit through the introduction of a more profound understanding of the school campus culture. The design meets the needs of the college's foreign exchange and tourists and is also an important part of the construction of digital campus.

References

1. Peng, Y. (2013). *Research and implementation of campus location service system based on android*. Dalian: DaLian University of Technology.
2. Zhang, X., & Dongk, B. (2013). Campus geography information management system based on mobile terminal. *Geomatics World, 3*, 98–102.
3. Craig, A. (2012). The academy goes mobile: an overview of mobile applications in higher education. *Social Media for Academics*, 123–138.
4. Wang, C. (2013). *Embedded development based on telemedicine mobile terminal platform*. Harbin: Harbin Institute of Technology.
5. Li, N. (2015). *Research on the key technology of smart phone guide system*. Kaifeng: Henan University.
6. He, G. (2012). *Development and application of land information management system based on the second of Engine Arcgis*. Jinan: Shandong Normal University.

Chapter 50
Optimization of Chinese Reproduction on Mobile Terminal Based on Reading Experience

Wangjian Qiu, Qiang Wang and Yan Shi

Abstract This paper uses Chinese reproduction on mobile terminal to analyze frequently used Chinese reproduction combinations in digital publishing by questionnaires and AHP, and gets Chinese reproduction parameters which impact weighting sequences and optimizing reading experience in mobile reading. The results prove that the weighting sequences of Chinese reproduction in mobile terminal are font recognition, font legibility, and layout rationality in turn. Users reading experience can be better by improving the weighting ratio, and be optimized.

Keywords Mobile terminal · Reading experience · AHP · Optimization

50.1 Introduction

Mobile internet era promotes development of digital media rapidly, which causes increasing demand of smart mobile terminal [1]. With great tendency of the-whole-people digital reading, improving users' digital reading experience has become one of major study fields in digital publishing industry. And optimization of Chinese reproduction is the key to improve digital reading experience.

Chinese reading effect is impacted by hardware, format, font style, font size, line spacing, and paragraph spacing in mobile reading. Huang et al. [2] analyzed effects of font size, screen resolution, and task type on Chinese character in mobile terminal; Ling and van Schaik [3] studied influences of English font style and line space on reading experience; Lin [4] explored Chinese font design applied to screen display; Zhao and Bu [5] discussed determinant factor on Chinese font reading in mobile terminal. While studies above considered no more than single font effect on reading experience, but not comprehensive font impaction on reading experience.

This paper takes Chinese word in digital publishing as case to study effects of Chinese character on users' reading experience on mobile terminal from three

W. Qiu (✉) · Q. Wang · Y. Shi
School of Media and Design, Hangzhou Dianzi University, Hangzhou, China
e-mail: 141220003@hdu.edu.cn

dimensions, encompassing font recognition, font legibility, and layout rationality. Then the repeated siftings have brought optimized Chinese word combination from existing combinations to improve users' reading experience by AHP.

50.2   Reading Experience

As is known to all, user state, display performance and external environments are several key factors affecting the user's reading experience. In the process of reading, the human eye movements for text are not continuous downward, but dance around lines with pauses. Eyes stop to recognize words and move for following text. Text material from visual center is received by brain and then through language center processing is identified and analyzed to deepen cognitive ability of character. Therefore, character cognition and understanding is promoted by font recognition, font legibility, and layout rationality.

Font with high recognition stimulates reader's optic nerve, which consequently is identified by brain in a higher degree. At present, there are two kinds of font styles on mobile terminal, including serif and san-serif [6]. SimSun and Microsoft YaHei are two most frequently used fonts. Distinguished shape of stroke of font SimSun in the beginning and end causes relatively much difference of font weight and font width. Thus reading with font SimSun in a long period leads to excessive tension of optic nerve that brings visual fatigue. And this causes negative reading effect. On the contrary, with right angle in the beginning, end and turning of strokes, equally font weight and font width of Microsoft YaHei shapes eye-catching and strong volume [7]. Meanwhile, thicker font contour line increases word visualization and recognition.

Relevant studies have shown that an eye pause is around 1/3 s. Font legibility has effect on eye pause on text. Based on screen pixilation and character render, font in size 30px to 38px is displayed clearly on mobile screen that brings less visual pressure, therefore eye pause on the text is shorter. While font in size 12px to 20px on the mobile screen causes uneven weight stroke and structure adhesion as well as serrated font contour line because of pixel restriction to font, displaying no more clearly, which make eye pause longer and go against users' reading effect. Obviously, bigger font size make font legible, help readers concentrate on text, keep positive visual and mind state, and accelerate understanding on text.

Paragraph spacing and line spacing need to comfort to readers' visual and psychical feelings in format design. With too much wider paragraph spacing and line spacing, scope of eyesight is increased, making line skipping. A little narrow paragraph spacing and line spacing break reading fluency, increase sense of reading tension and increment eyes' pressure. Suitable paragraph spacing and line spacing form lexicon chunks according with reading psychology, hierarchical and flexible, which assists reader control reading rhythm and left then thinking space [8]. If format is suitable, readers can not only control text within eyesight, quicken reading speed, but also concentrate on what they are reading as well.

50.3 Experiment Design

50.3.1 Experiment Principle

Analytic Hierarchy Process (AHP) used in this paper, disintegrates factors related decision into several hierarchies, including motivation, criterion, and project. Based on that, a comprehensive analysis encompassing quantitative analysis and qualitative analysis was made [9].

This paper divided reading experience in Chinese into four factors: font size, font style, paragraph spacing, and line spacing to achieve optimization of Chinese reproduction on mobile terminal. According to their interrelationships and relevant influences, four factors was formed a multi-hierarchical structure model by different hierarchical combinations to test four-factors weight sequences and relative important weight values of the best reading experience. In sequence calculation, scale from 1 to 9 was brought to construct judgment matrix and to calculate eigenvalue of maximum of judgment matrix and its corresponding eigenvector. And relative important weight value at every hierarchy compared to a certain factor at prior hierarchy was also calculated [10, 11]. Finally, total weight value rank in Chinese reproduction project was worked out through the sum of the weight values.

50.3.2 Construction of Hierarchical Structure Model

This experiment divided Chinese reproduction into font size, font style, paragraph spacing, and line spacing according to font recognition, font legibility and layout rationality on mobile terminal for the best reader mobile reading experience. Based on that, a hierarchical model was constructed shown as Fig. 50.1.

A was motivation hierarchy, representing optimized display combinations of Chinese character; B_1, B_2, B_3, B_4 was criterion hierarchy, respectively referring to
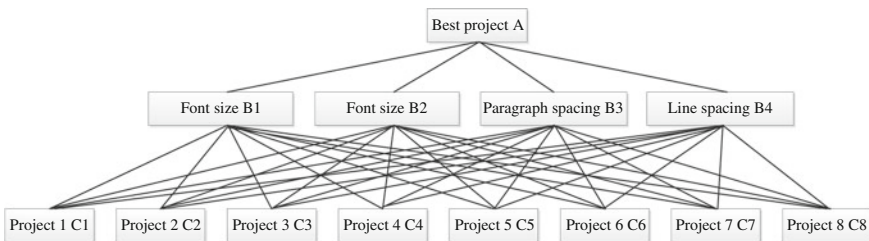
Fig. 50.1 The hierarchical model on the best Chinese reproduction projects

Table 50.1 The best display scheme of Chinese characters

	Font	Size	Paragraph spacing	Line spacing
Project 1 C_1	Microsoft YaHei	32px	0.36 times	1.16 times
Project 2 C_2	SimSun	32px	0.36 times	1.16 times
Project 3 C_3	Microsoft YaHei	26px	0.39 times	1.25 times
Project 4 C_4	SimSun	26px	0.39 times	1.25 times
Project 5 C_5	Microsoft YaHei	22px	0.41 times	1.3 times
Project 6 C_6	SimSun	22px	0.41 times	1.3 times
Project 7 C_7	SimSun	20px	0.42 times	1.37 times
Project 8 C_8	Microsoft YaHei	20px	0.42 times	1.37 times

font size, font style, paragraph spacing, and line spacing; C_1–C_8 indicates project hierarchy, showing currently mainstream Chinese character combinations on the screen based on reading experience through literatures and field investigation. Compared with applied scopes, users' approval and firsthand for these projects, a specific project was word out, shown as Table 50.1.

50.3.3 Construction of Paired Comparison Matrix

In investigation, respondents are 30 students with normal vision (physical normal vision and corrected vision to normal). Half of all respondents are men and half are women. 30 respondents read 10 pages digital content on iphone5 according to individual reading habits in a comfortable reading environment and filled in questionnaires based on their reading experience. Then factors as basis of questionnaire were compared in pairs in scale 1–9. a_{ij} refers to result that factor i compared with factor j. Compared scale was as Table 50.2.

Scale 2, 4, 6, 8 represented that influence factor i on factor j was in two adjacent scale,

$$A = \left(a_{ij}\right)_{n\times n} = \begin{pmatrix} a_{11} & a_{12} & \cdots & a_{1n} \\ a_{21} & a_{22} & \cdots & a_{2n} \\ \cdots & \cdots & \cdots & \cdots \\ a_{n1} & a_{n2} & \cdots & a_{nn} \end{pmatrix} \tag{50.1}$$

Table 50.2 Compare scale (The meaning of scale 1–9)

Scale	Factor i compared with factor j
1	The same strong
3	A little stronger
5	Stronger
7	Much strong
9	Absolutely stronger

Therefore, A became paired comparison matrix. Bn was paired comparison matrix of all projects relative to some certain factor. In 30 valid questionnaires, the results showed the paired comparison matrix as follow:

$$
A = \begin{bmatrix}
1 & 1/3 & 7 & 7 \\
3 & 1 & 7 & 7 \\
1/7 & 1/7 & 1 & 1 \\
1/7 & 1/7 & 1 & 1
\end{bmatrix},
$$

$$
B_1 = \begin{bmatrix}
1 & 1 & 5 & 7 & 1 & 3 & 5 & 7 \\
1 & 1 & 3 & 4 & 1/3 & 1 & 3 & 4 \\
1/5 & 1/3 & 1 & 3 & 1/5 & 1/3 & 1 & 3 \\
1/7 & 1/4 & 1/3 & 1 & 1/7 & 1/4 & 1/3 & 1 \\
1 & 3 & 5 & 7 & 1 & 3 & 5 & 7 \\
1/3 & 1 & 3 & 4 & 1/3 & 1 & 3 & 4 \\
1/5 & 1/3 & 1 & 3 & 1/5 & 1/3 & 1 & 3 \\
1/7 & 1/4 & 1/3 & 1 & 1/7 & 1/4 & 1/3 & 1
\end{bmatrix},
$$

$$
B_2 = \begin{bmatrix}
1 & 1 & 1 & 1 & 5 & 5 & 5 & 5 \\
1 & 1 & 1 & 1 & 5 & 5 & 5 & 5 \\
1 & 1 & 1 & 1 & 5 & 5 & 5 & 5 \\
1 & 1 & 1 & 1 & 5 & 5 & 5 & 5 \\
1/5 & 1/5 & 1/5 & 1/5 & 1 & 1 & 1 & 1 \\
1/5 & 1/5 & 1/5 & 1/5 & 1 & 1 & 1 & 1 \\
1/5 & 1/5 & 1/5 & 1/5 & 1 & 1 & 1 & 1 \\
1/5 & 1/5 & 1/5 & 1/5 & 1 & 1 & 1 & 1
\end{bmatrix},
$$

$$
B_3 = \begin{bmatrix}
1 & 2 & 1/3 & 1 & 1/2 & 1/3 & 1/7 & 2 \\
1/2 & 1 & 1/5 & 3 & 1/2 & 1/3 & 1/6 & 3 \\
3 & 5 & 1 & 4 & 4 & 2 & 1/3 & 4 \\
1 & 1/3 & 1/4 & 1 & 1/2 & 1/4 & 1/5 & 1 \\
2 & 2 & 1/4 & 2 & 1 & 1/5 & 1/4 & 2 \\
3 & 3 & 1/2 & 4 & 5 & 1 & 1/3 & 4 \\
7 & 6 & 3 & 5 & 4 & 3 & 1 & 7 \\
1/2 & 1/3 & 1/4 & 1 & 1/2 & 1/4 & 1/7 & 1
\end{bmatrix},
$$

$$
B_4 = \begin{bmatrix}
1 & 1 & 1/3 & 1/2 & 2 & 1/2 & 1/3 & 1/3 \\
1 & 1 & 1/2 & 2 & 1 & 2 & 1/2 & 1/2 \\
3 & 2 & 1 & 3 & 2 & 1/3 & 1 & 2 \\
2 & 1/2 & 1/3 & 1 & 1/2 & 1/4 & 1/3 & 1/2 \\
1/2 & 1 & 1/2 & 2 & 1 & 1/2 & 1/2 & 1/4 \\
2 & 1/2 & 3 & 4 & 2 & 1 & 2 & 3 \\
3 & 2 & 1 & 3 & 2 & 1/2 & 1 & 1 \\
3 & 2 & 1/2 & 2 & 4 & 1/3 & 1 & 1
\end{bmatrix}
$$

50.3.4 Single Ranking Weight Vector and Test of Chinese Reproduction Project

Consistency test was made to check maximum eigenvalue of every paired comparison matrix and their eigenvectors according to consistency index, random consistency index, and consistency ratio. Once test past, eigenvector (after normalization) became weigh vector; once failed, paired comparison matrix had to be reconstructed.

By calculation, maximum eigenvalue of paired comparison matrix A was $\lambda\text{max} = 4.1547$. And its normalized eigenvector were: $\omega = \{0.3286, 0.5482, 0.616, 0.616\}$, CI $= 0.0516$, CR $=$ CI/RI $= 0.0579 < 0.1$, so A pass the consistency test.

By calculation, maximum eigenvalue of paired comparison matrix A was $\lambda_{max} = 4.1547$. And its normalized eigenvector were: $\omega = \{0.3286, 0.5482, 0.616, 0.616\}$, CI $= 0.0516$, CR $=$ CI/RI $= 0.0579 < 0.1$, so A pass the consistency test.

In the similar way, rest of eigenvectors and characteristic roots were calculated and shown as Table 50.3.

Through calculations, B_1, B_2, B_3, B_4 pass the consistency test.

50.3.5 Total Ranking Weight Vector and Test of Chinese Reproduction Project

Consistency ratio of total rank:

$$\text{CR} = \frac{a_1\text{CI}_1 + a_2\text{CI}_2 + \cdots + a_m\text{CI}_m}{a_1\text{RI}_1 + a_2\text{RI}_2 + \cdots + a_m\text{RI}_m}, \text{CR} < 0.1 \qquad (50.2)$$

Weight vector of total rank for the best reading experience in Chinese reproduction was tested. If the test was past, a decision would be done based on the

Table 50.3 The eigenvectors and eigenvalues of comparison matrixes and consistency ratio

k	1	2	3	4
ω_{k1}	0.2520	0.2083	0.0597	0.0698
ω_{k2}	0.1481	0.2083	0.0653	0.1150
ω_{k3}	0.0624	0.2083	0.2003	0.1609
ω_{k4}	0.0303	0.2083	0.0435	0.0589
ω_{k5}	0.2869	0.0417	0.0777	0.0727
ω_{k6}	0.1274	0.0417	0.1676	0.2248
ω_{k7}	0.0624	0.0417	0.3486	0.1502
ω_{k8}	0.0303	0.0417	0.0373	0.1477
$\lambda_{\max}$	8.2750	8.0000	8.5659	8.9509
CR	0.0279	0.0000	0.0573	0.0963

Table 50.4 The total ranking table of Chinese reproduction

Hierarchy	B_1	B_2	B_3	B_4	Total ranking weight
	0.3286	0.5482	0.0616	0.0616	
C_1	0.2520	0.02083	0.0597	0.0698	0.2050
C_2	0.1481	0.02083	0.0653	0.1150	0.1740
C_3	0.0624	0.02083	0.2003	0.1609	0.1570
C_4	0.0303	0.02083	0.0435	0.0589	0.1305
C_5	0.2869	0.0417	0.0777	0.0727	0.1264
C_6	0.1274	0.0417	0.1676	0.2248	0.0889
C_7	0.0624	0.0417	0.3486	0.1502	0.0741
C_8	0.0303	0.0417	0.0373	0.1477	0.0442

$CR = 0.0579 < 0.1$, thus total rank pass the consistency test

results of total rank of weight vectors, or would reconstructed paired comparison matrix that were with relatively higher CR consistency ratio. The results were displayed in Table 50.4.

50.3.6 Discussion and Analysis

According to experiment data, the result of reading experience weight sequence was font style, do not size, paragraph spacing, and line spacing in a diminishing turn. Font style took the largest weight because readers recognize character first. In addition, compared with big font size and small font size, which was comparison between project 1, project 2, and project 7, project 8, the result showed that big font size with san-serif got better feedback in mobile reading experience. What's more, font in small size with serif was superior to san-serif and small size font.

Duration of eye pause by 30 respondents reading in experiment in the same page in eight different projects was timing, shown as Table 50.5.

Table 50.5 showed that distinguishable Chinese character combination made readers different reading feelings, causing diverse users' reading experiences. With the same reading content, Chinese character reading in project 1 cost shortest time. It indicated that Chinese character display in project 1 could promote users' reading experience. Through face-to-face interview after experiment, 30 respondents, from perspective of reading experience, consistently held the view that project 1 (font style in Microsoft YaHei, font size in 32px, paragraph spacing in 0.36 times and

Table 50.5 Standing time in pages

	Project 1	Project 2	Project 3	Project 4	Project 5	Project 6	Project 7	Project 8
Time (s)	273	279	283	290	297	299	312	320

line spacing in 1.16 times) achieved optimized character readability, which was provided with highest font legibility, decreased readers' visual pressure and made users pay more attention on text and content understanding.

However, there are some limitations in the paper. First, the experiment in this paper sifted the optimized Chinese character combination project in existing combination projects, but not supplied with a new Chinese character combination project. Second, age of sample in the investigation was in a single scope. It needed more scholars to complete and perfect.

50.4 Conclusions

This paper compares relative effects of font size, font style, paragraph spacing and line spacing by studying of influencing factors of reading experience on mobile terminal and filtrate comparative optimized weighting sequence and font combination in Chinese font combination study cases. Applied in practice, the experimental result is proved that it brings users' better reading experience on mobile terminal, that supplies designers with choice of Chinese font combinations and that promotes users' digital reading experience on mobile terminal.

References

1. NetEase. (2015). *2015 Global digital report*. Guangzhou: Easy Reader.
2. Huang, D. L., Patrick Rau, P. L., & Liu, Y. (2009). Effect of font size, display resolution and type on reading Chinese fonts from mobile devices. *International Journal of Industrial Ergonomics, 39*, 81–89.
3. Ling, J., & van Schaik, P. (2006). The influence of font type and line length on visual search and information retrieval in web pages. *Human-Computer Studies, 64*, 395–404.
4. Lin, X. (2014). The discussion of the Chinese font design for screen display. *Art & Design, 214*, 127–128.
5. Zhao, J. L., & Bu, L. F. (2014). Study on the reading experience determinants of Chinese fonts in the mobile terminal. *Design Research, 3*, 65–69.
6. Li, B. (2004). *Study on Chinese character*. Beijing: The Commercial Press.
7. Chiyoda, Ida. (2011). *Principle of character design*. Beijing: China Citic Press.
8. DA, L. (2013). Fon, Font Size and Line spacing. http://www.woshipm.com/pd/24677.html
9. Saaty, T. L. (1980). *The analytic hierarchy process*. Mc.Graw: Hill International Book Company.
10. Armstrong, M., & Baron, A. (1998). *Performance management*. London: The Cromwell Press.
11. Moers, F. (2005). Discretion and bias in performance evaluation: the impact of diversity and subjectivity. *Accounting Information Systems, 30*(1), 67–80.

Chapter 51
Research and Development on e-book Apps Based on iOS Development Platform

Ying Hu

Abstract E-books are made available in both Android and iOS platforms as increasingly, technology savvy readers choose to read digital e-books. E-book apps have transformed reading habits. The exponentially rising popularity of iOS and Android platforms is attributed to the incessant innovation of functions and appealing apps that are introduced every day. E-book apps are central to publishers worldwide to present prevailing content in an altogether interesting environment. In particular, many e-book application developers have chosen Apple's iOS mobile devices such as iPad, or iPhone as the target device to provide more creative and richer user experience, as evidenced by the rapidly increasing number of publication apps in Apple's App Store. In this paper, three major types of e-book apps from the App Store were examined from a developer's perspective to provide a focused overview of the status and trends of iOS e-book apps and an analysis of related technology, architecture, and user interface design issues. Three representative e-book apps were analyzed according to their purposes, functions, and user satisfaction, so that a user interface design guideline is established for developer implementation. It was clear that e-book apps still had plenty of room to grow to take full advantage of unique mobile platform features and truly fulfill their potential. In particular, introduction of two- or three-dimensional visualization and context awareness for the behavior component could further enhance e-book app's usability and utility. This paper aims to serve as a reference point and guide for developers and practitioners interested in using iOS as a platform for e-book applications, particularly from the technical perspective.

Keywords e-book · User interface · Component · Mobile development

Y. Hu (✉)
Hangzhou Dianzi University, Hangzhou, China
e-mail: hdhy@hdu.edu.cn

51.1 Introduction

An electronic book (variously: e-book, eBook, e-Book, ebook, digital book, or even e-edition) is a book-length publication in digital form, consisting of text, images, or both, readable on computers or other electronic devices [1]. Although sometimes defined as "an electronic version of a printed book" [2]. Many e-books exist without any printed equivalent. Commercially produced and sold e-books are usually intended to be read on dedicated e-readers. However, almost any sophisticated electronic device that features a controllable viewing screen, including computers, tablets, and smartphones can also be used to read e-books.

There are many options available now for writers looking to self-publish their e-books. Both new and established authors are increasingly self-publishing their books due to the hassles and difficulties associated with the traditional publishing route. To cater to these authors, many self-publishing platforms have sprung up offering a range of services. Amazon is the most popular self-publishing platform at this time. E-books self-published with the Amazon's kindle direct publishing (KDP) program only appear in Amazon bookstores. However, as Amazon is by far the leading global bookseller in both print and digital formats, authors are assured of reaching a large audience who trust Amazon. KDP also offers a 'Select' program which requires exclusivity in exchange for higher royalties, and the chance to have your book in Amazon's popular e-book lending library. This is a great way to get your books into as many readers' hands as possible. Both the KDP and Select programs are free for authors to self-publish with, and require no upfront costs. Regarding the nitty-gritty, Amazon pays authors 70 % royalty of e-books priced in the $2.99–9.99 range, and participating in the Select program. E-books outside this price range receive only 35 % royalty in some cases.

Nook Press, a self-publishing platform from Barnes and Nobles is the new, rebranded version of PubIt, and the e-books are sold through the Nook bookstore. There is a lower reach for books through this platform, and the royalty rates are also somewhat lower. The authors receive 65 % royalty of e-books priced $2.99–9.99, and 40 % royalty for e-books outside of this price range.

iBook Authors platform is for book sales through Apple's iBookstore only, so again the circulation is a bit lower. However, this platform is especially good for image-rich books which are difficult to upload using Amazon's KDP. Photography, recipe, and children's books are easy to create with the user friendly book design process and many templates available. The royalty rate is 70 % throughout.

Book apps are primarily designed for touchscreen devices such as mobile tablets and smartphones. Apple has considerable control over the app content. In order for any "app to be distributed anywhere on the App Store, it must first be examined and approved by Apple's App Review Board." The review board commonly rejects book apps that have limited interactivity and that lack media features. Apple states that if an app has "insufficient functionality" or is just a digitized version of a printed book then it will not be approved for App Store sales. Apple has been

instrumental in providing not only hardware and software, but also sales categories, terminology, and standards relating to app design.

51.2 The iOS Mobile Platform

iOS (originally iPhone OS) is a mobile operating system created and developed by Apple Inc. and distributed exclusively for the Apple hardware. It is the operating system that at present powers many of the company's mobile devices, including the iPhone, iPad, and iPod touch. During Apple's quarterly earnings call in January 27, 2015, Apple announced that they have now sold one billion iOS devices since the original iPhone in 2007.

iOS was derived from Mac OS X. It shares the Darwin foundation, and is based on a Unix-like operating system. There are four layers in the iOS technology architecture. Core OS is the bottom layer and core services is the second layer from the bottom. They both provide basic support for e-book applications including database and networking support. Media layer contains a set of fundamental technologies that can be used to support 2D/3D visualization, and audio or video playback. Cocoa Touch is the top layer [3]. Although iOS was derived from Mac OS X, there was no Cocoa Touch layer in Mac OS X architecture. Cocoa Touch was derived from the Cocoa in Mac OS X, and was uniquely designed for touch-based interfaces. Code libraries at this layer provide fundamental infrastructure for developers [4, 5]. Apple refers to these code libraries as frameworks.

In this paper, the term "framework" refers to the application architecture, the term "library" is used instead to avoid confusion. All iOS applications, including e-book applications, start from the Cocoa Touch layer. In particular, UIKit and Foundation libraries are used by all apps [4]. The classes in the UIKit library are to construct and manage an application's user interface. The most frequently used interface elements of the UIKit class hierarchy include UIViewController, UIView, UITableview, UIButton, UIAlertView, UIWebview, UINib, etc. The Foundation library provides a set of classes that work as a base layer for Objective-C classes. Objective-C is the preferred programming language for all iOS applications. The Foundation library includes a small set of basic utility classes. For example, one of the classes provides memory management services such as memory allocation and deallocation. Classes in the Foundation library define data types such as NSString, NSArray, or NSDictionary, provide operating system services such as NSError, NSBundle, NSStream, NSurl, and provide Objective-C Language services such as NSAutorelease-Pool, NSException. When developing e-book applications, developers usually start with frameworks in higher level layers. Lower level libraries are only used when more precise control or more powerful capabilities are needed.

51.3 Enabling JQuery Technologies for e-book Applications

Certain technologies available on smart mobile devices are well suited to improve the usability, utility, and appeal of ebook applications. This section describes major service components for designing the user interface of e-book app based on top ten featured and top ten paid book apps. Furthermore, in order to collect book types in various domains, we randomly selected five more applications with higher customer rating (four or more out of five). These applications include GE Annual Report from business category, The Daily from newsstand category, bella from lifestyle category, Aries the Sheep from entertainment category, and Zite Personalized Magazine from news category. Owing to the content language, bella apps may be restricted to download from some area. All of these 25 apps were selected for further analysis that factors every page layout within each application.

Take the fantastic flying books of Mr. Morris Lessmore application for example. The left side of Fig. 51.1, is composed of the image and text components; right is composed of text, video, and menu components. Different components can be combined together to display the content or to interact the contents with readers. Hence, we summarize a component guideline on the grounds of 25 chosen apps.

The component guideline is first divided into two groups by the function. One is the display function for solely exhibiting the material data, and the other is the interactive function such as touch-enabled 360° rotations, inline audio and video, step-by-step instruction, quizzes and surveys, interactive slideshows, and more. In regard to display the component group, there are seven components extracted from
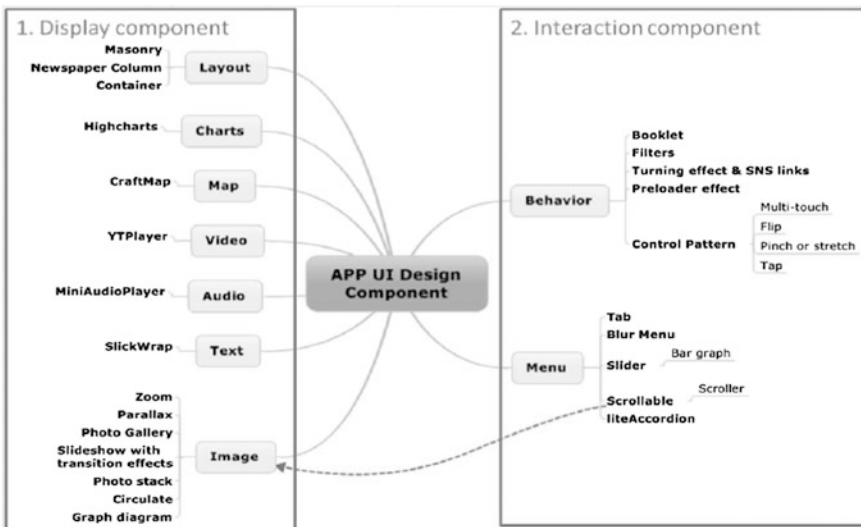
Fig. 51.1 JQuery mobile components for e-book applications [6]

present e-book apps including layout, charts, map, video, audio, text, and image. Each component can set the material data to various effects. In regard to interaction component group, there are two components including behavior and menu. Behavior component refers to how users operate the elements within the page. It is a two-way communication between the users and the application to provide dynamic, updated, and personalized reading experience. This behavior component is usually triggered by context awareness. In other words, the context input is derived from multi-touch or devices sensor such as accelerometer, gsensor, and microphones which contribute to ground breaking interface. *Al Gore-Our Choice: A Plan to Solve the Climate Crisis* is an example app to utilize device sensor for immersive reading. Besides, the menu component refers to extending the operation for users. The operation may be the preference setting or application description or other external website connections. Hence, each component of both the groups has a subcomponent in order to provide a detailed practice that helps the developers to implement user interface design via Java library technology.

51.4 Conclusions

E-book apps are commonly hybrid. Although making a hybrid, native plus web, app is hardly an ideal solution adding complexity, many companies have begun to develop cross-platform tools that integrate web standards like HTML5 with native interactions on specific tablet platforms that function as a framework to build multiple types of content. Hence, developers need to be familiar with certain open source such as PhoneGap or Appcelerator framework in order to fill the gap by exposing native features as web services. When developers build a hybrid app like this, they are also able to hook into those platform features like widgets, notifications, and intents. The media layer in iOS provides the 2D/3D visualization support for applications. Developers can use Open GL ES or native rendering such as Quartz, Core Animation, and UIKit to implement data visualization. Yet, the analysis data such as downloads or customer rating is still limited in Apple's App Store. This presents potential opportunities to app developers because this is an area of great needs from both the end users and the publishers. Moreover, there are more and more e-book apps like fashion magazine which start to embed the accessory image with electronic commerce function. Therefore, it is essential to gain insight into the sales process by tracking every swipe, tap, and session length or even the GPS location to help publishers better understand what their sales force is selling, how they are selling, and where they could be selling more. Besides, this analytic information can be used as significant indicators to advertisers.

It was clear that e-book apps have great potentials in improving business, education, and leisure for the public. There was still plenty of space to grow for e-book apps to take full advantage of unique mobile platform features. In particular, introduction of two- or three-dimensional visualization and deeper integration of context awareness could further enhance e-book app's usability and utility.

References

1. Gardiner, E., & Musto, R. G. (2010). The electronic book. In M. F. Suarez, & H. R. Woudhuysen (eds.), *The Oxford companion to the book* (p. 164). Oxford: Oxford University Press.
2. e-book. (2010). *Oxford dictionaries*. Oxford: Oxford University Press.
3. Buck, E. M., & Yacktman, D. A. (2009). *Cocoa design patterns* (1st ed.). Boston: Addison-Wesley Professional.
4. iTunes preview, *GE Annual Report 2010 By General Electric Company*: http://itunes.apple.com/us/app/ge-annual-repor-2010/id425705238?mt=8t. Last verified in April 2012.
5. Boudreaux, T. (2009). *Programming the iphone user experience: Developing and designing cocoa touch applications* (1st edn.). California: O'Reilly Media Inc
6. Zdziarski, J. A. (2008). *iphone Open Application Development* (1st edn.). California: O'Reilly

Chapter 52
Design of Automated Typesetting System for Digital Content

Tingyun Fang and Jingcheng Li

Abstract An automated typesetting system containing two automatic algorithms for use in cross-media digital content applications are proposed in this paper. These algorithms are designed to repair defects in streaming text, page size, and image conversion. By combining these two algorithms, the automatic typesetting system significantly improves the quality of digital content using JavaScript language. The simulation results show that this system enhances the degree of automation of typesetting in publications. Specifically, users of the system will find that the layouts of publications are more fixed, the cycle of typesetting is shortened, and the efficiency and accuracy of the typesetting process are improved. Furthermore, the system enhances the overall aesthetic appeal and the specifications of the layout.

Keywords Digital content · Automated typesetting system · Specification showing

52.1 Introduction

With the development of network technology, scope of reading mode has been extended from traditional paper reading to terminal reading, encompassing reading modes through desktop computers, notebook computer, tablet computer, phone, e-book reader, which is more convenient for readers to choose.

Currently, more than half of the digital content is mainly for single main terminal. If it released another terminal, the digital content is needed to remake according to the resolution, the screen size, and other characteristics of the terminal. However, it does not fit the tendency of "once produced in multi-terminal publication" and is difficult to maximize the content value and the added value of that [1]. In addition, nonstandard typesetting errors could not be controlled effectively in

T. Fang (✉) · J. Li
School of Media and Design, Hangzhou Dianzi University, Hangzhou, China
e-mail: onlyclouds@126.com

digital publications by programming, including bottom line title, solitary word, single line, punctuation Kinsoku, and so on, which obviously influence much of readability and aesthetics. Thus, it is a key and difficult point in the study of digital publication on how publishing content can be adapted to multiterminal, multi-standard, multi-window, flexibly, normally, and beautifully.

In this paper, insufficiency of technology in the standardization terms of content presentation and reasons of that are summarized, and an automatic algorithm on the streaming text and an image automatically converted algorithm according to the page size are proposed. By combining these two algorithms, the automatic type-setting system can be realized through JavaScript language. Accordingly, it saves time and energy and effectively improves the quality of the digital content.

52.2 The Principle of Automated Typesetting for Digital Content

52.2.1 The Principle of Automatic Algorithm on the Streaming Text

Well-balanced and regular text layout is a visual form and quality driven in media culture. The design practice and typesetting specifications of Chinese text play a prominent role in cross-media publishing [2]. In order to the readability and aesthetic of the page text, the algorithm automatically compensates for text parameters (font size, etc.) based on reading terminal parameters (resolution, page size). The mobile terminal recommends fonts shown in Table 52.1 [3].

First, the leading, space before and space after of text are determined by font size. The text and title font size are secured, which are named zw.pointSize and BT.pointSize. Therefore, a calculation of the leading, space before and space after of text are as follows:

The leading: zw.leading = zw.pointSize*1.5.

The space of primary title: BT1.spaceBefore = zw.leading * n, BT1. spaceAfter = zw.leading * m; the space of two-level heading: BT2. spaceBefore = zw. leading * n/2, BT2.spaceAfter = zw.leading * m/2; The space of three-level heading: BT3.spaceBefore = zw.leading * n/3, BT3.spaceAfter = zw.leading * m/3, and so on.

Table 52.1 Mobile terminal classification and font recommended

Terminal device screen size	Physical dimensions	Screen resolution	Recommended font size (px)
Small screen	<2.6		12
Middle screen	2.6–3.0	240 * 320	14
Big screen	3.0–7.0	1280 * 720	16
Large screen	>7.0	1024 * 768	18

In the next place, for typesetting standardization, an automatic algorithm on the streaming text based on the Japanese publishing standards-JISX 4051 (it is called Kinsoku Shori) [4] is used in this paper to design an automatic inquiry system and automatic control system with regard to the problem of bottom line title, solitary word, single line, punctuation Kinsoku. Such algorithm uses automatic control system to solve problems found by query system.

52.2.2 The Principle of Images Automatically Converted Algorithm with the Page Size

This article designs a model that automatically converted image with the page size, the model is studied to calculate the requirements for image format, image postilion, and image size according to the different media environments. The algorithm can be achieved the image format conversion through judging terminal format support and resolution. Besides, the size of the image domain can be determined according to the terminal size.

The size of image domain bases on the size of the remaining pages to determine the exact location and the size of domain. The algorithm used the cursor readout method to calculate the height of the remaining space, depending on the size ratio of the image and the remaining space to determine whether the image is scaled in this page. If image cannot be placed in this page, the algorithm is drawn the next page, and depended on the size ratio of the image to the version heart, finally decided to the scale size of the domain.

52.3 Design of Automated Typesetting Algorithm for Digital Content

52.3.1 Design of Automatic Algorithm on the Streaming Text

To improve the layout specification, in this paper, an automatic algorithm on the streaming text is proposed as shown in Fig. 52.1. At first, the system can be got a text label, set template, and placed text. Second, the system can be searched titles, judged whether there is a bottom line title from the location of title and content after title of convergence. If the title was shown on the end of pages, the title should be placed on the next page or the next module by increasing the before space of title. Third, line breaking rules (punctuation Kinsoku) for Chinese language have been described in the reference of office open XML, ECMA standard [5]. There are rules about certain characters that are not allowed to start or end a line, such as shown in Fig. 52.2. If the unsuitable punctuation has happened, the system can be controlled by adjusting
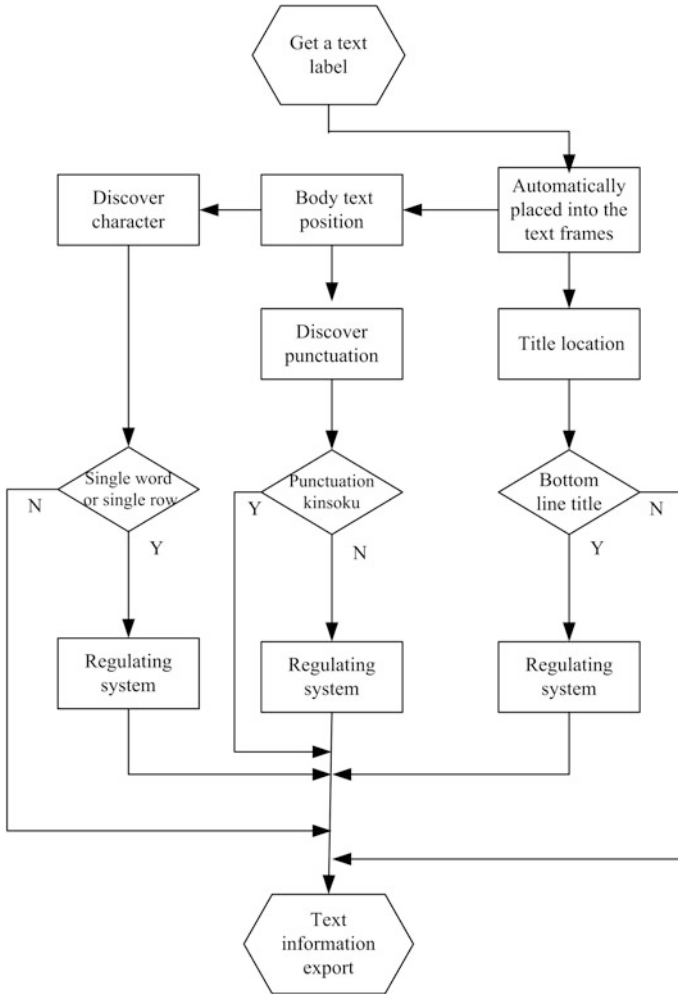
Fig. 52.1 Process of an automatic algorithm on the streaming text
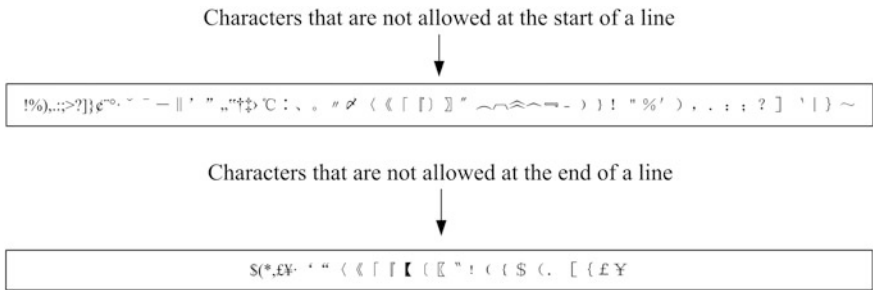
Fig. 52.2 Line breaking rules in Chinese text

system. There are two adjusted methods: on the one hand, the character of previous row is moved to the line by increasing the word spacing of the previous line. On the other hand, the character of the line can be moved to the previous line by squeezing punctuation or reducing the word spacing of the previous line.

Finally, the system is searched text characters, analyzed whether there is no more than a word (a character or isolated words) in a row. If the problem exists, the system can be controlled by adjusting the system. In other words, the system determined the value of word character. If the number is greater than four characters, isolated character of the previous line is moved to the line by means of increasing the word space of the previous line. On the contrary, isolated character of the line is moved to the previous line by means of reducing the word space of the previous line. At the same time, it is analyzed whether there is a row in a page in the system. If the problem exists, the system still can be controlled by adjusting the system. Specific operations are as follows: it can be located in the previous paragraph, and adjusted the space of paragraph. It is noted that it must gradually adjust (less than 1 Pounds) until the content reduced to the previous period. If the line space is outside this range, it still needs to up the location, and adjust the space of paragraph. Furthermore, the space ought to gradually adjust (less than 1 Pounds) until the content reduced to the previous period. In a word, the single-line content is reduced to the previous period, then resolve the problem by repeating the above operation [6]. In conclusion, typesetting standard text message can be exported by the above method.

52.3.2 Design of Images Automatically Converted Algorithm with the Page Size

The images render on different terminal have different size, format, and color mode. It effectively implemented intelligent image rendering depend on the automatically images converted algorithm with the page size. As shown in Fig. 52.3, first, the system can get image size, format, and other parameters. Second, it adjusted the image format depending on the performance of the current reading devices in the system. Third, the system can obtain terminal equipment space and reading image size, then set scaling to change the position of image domain according to the remaining space parameters. Finally, the size of image domain is calculated, and then the image is filled into the domain according to the position of image domain.

52.4 Simulation of Automated Typesetting System

52.4.1 Experimental Design

With "group version technology" textbook content, for example, the content of Chap. 2 has been implemented by automatic typesetting system. If user selected the
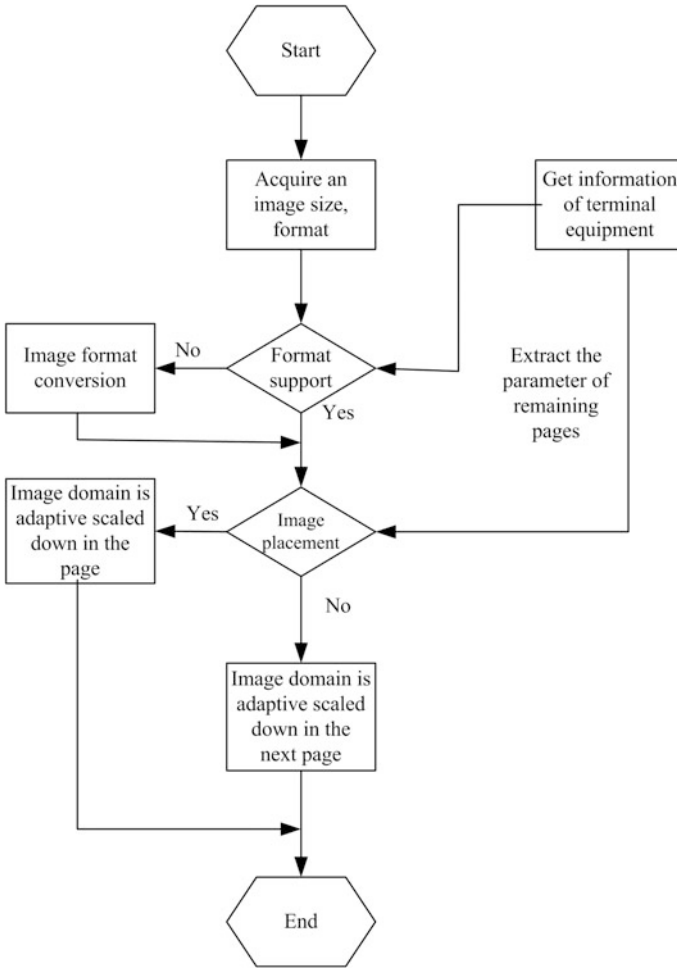
Fig. 52.3 Process of an automatically converted image algorithm with the page size

name of appropriate equipment (iPad, iPhone, A4 paper), the system can automatically obtain a series of parameters from the information databases of terminal equipment. At the same time, it can gain the text data from the text information databases, and get the image data from the image information databases. The information in this series is available for the use of automatic typesetting.

52.4.1.1 Standardized Presentation of Flow Text

First, the font of body text, the title font, and the size of domain are decided by the size of terminal interface. Besides, the leading, space before and space after of text,

alignment is determined by the font size. This article has realized the pseudocode fragment according to Javascript programming [7]. The pseudocode fragment is as follows:

```
  var stlBT1 = doc.paragraphStyles.add();              // Create a paragraph style
  stlBT1.name = "BT1";                                 // Named BT1
  try{stlBT1.appliedFont = "heiti";}catch(e){}
  stlBT1.fontStyle = "Regular";
                                                       //Creating composite fonts
 …………
  stlBT1.pointSize = n pt;
  stlBT1.leading = n*1.5 pt;
  stlBT1.justification = Justification.centerAlign;
  stlBT1.spaceBefore = n*m pt;
  stlBT1.spaceAfter = n*k pt;
  //Determine the font, paragraph before, percentage margin, alignment, etc.
 …………
```

Second, the size of text frames is determined, text content is placed into the text frames, and automatically solve problems of nonstandard typesetting. The pseudocode fragment is as follows:

```
  var txf = doc.pages.item(0). textFrames. Add
  ({ geometricBounds:[x1,y1,z1,m1] } );
                                    // The size of text frames is determined
     …………
  txf.paragraphs.item(-1).applyParagraphStyle(stlBT1, true);
                                    //Apply the appropriate paragraph styles
     …………
  if(a!=0){
  z.leading = n*1.5 pt*k1;
 …………
                        //Automatically solve problems of non-standard typesetting
```

52.4.1.2 Intelligent Zoom of Image

First, the system is analyzed whether the acquired image format is supported by the terminal according to the parameters of terminal equipment. And the size (position) of image domain is judged by the remaining space parameters. The pseudocode fragment is as follows:

```
var Y= txf.insertionPoints[-1].endBaseline;
R=Y1-Y-m1-e;
                              // Get the position of remaining space parameters
…………
var hangsu=Math.floor(correctImageHeight/hangju);
var h2=hangsu*hangju;
…………
var w2=correctImageWidth*k3;
                              //Calculate the width and height of image domain
var myFrame=pg_next .rectangles.add({geometricBounds:[x1,y1,z1,h1]});
myFrame.place (myimages[0], false);
…………
                //Determine the domain location, and placed the image to be ranked
```

52.4.2   Simulation Discussions

In this paper, automatic typesetting system exclusive image size effect is shown in Fig. 52.4.

As is shown in Fig. 52.4, the sharpness of scaled image and the enlarged image is as same as the manuscript image. Moreover, the images are completely presented in the right size on the different devices.

In addition, image rendered position in the layout has changed (see Fig. 52.5).

The location of image domain is determined by the device's screen size. As shown in Fig. 52.5, automatically typesetting system ensures that the image of the visibility of the basic, the aesthetics of the whole layout. Besides, by rendering text analysis, different title, body text, caption have different font, alignment, before space, and so on. Moreover, the size of fonts still has changed on different devices, and effectively solve the problem about nonstandardized typesetting.
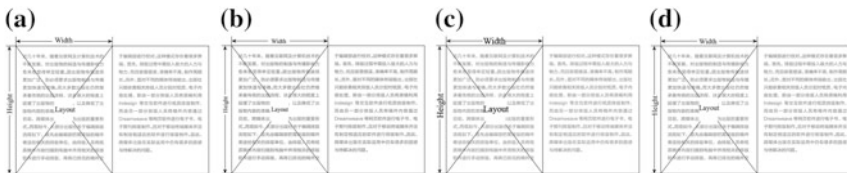
Fig. 52.4 Presenting image of different terminal devices (thumbnails). **a** Manuscript. **b**. A4 paper. **c**. iPhone. **d**. iPad
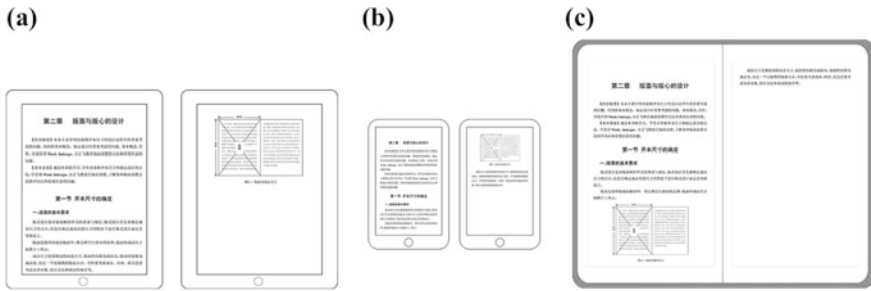
Fig. 52.5 Digital content (interception) shows the results in the different terminal equipment (thumbnails). **a**. iPad. **b**. iPhone. **c**. A4 paper

Users of the system will find that the layouts of publications are more fixed, the cycle of typesetting is shortened, and the efficiency and accuracy of the typesetting process are improved. Furthermore, the system enhances the overall aesthetic appeal and the specifications of the layout.

52.5 Conclusions

An automated typesetting system containing two automatic algorithms for use in cross-media digital content applications is proposed in this paper. By combining these two algorithms, the automatic typesetting system can be realized through JavaScript language, thus, the quality of the digital content is effectively improved. Simulation results show that the proposed system can automatically compensate for text parameters (font size, etc.) based on reading terminal parameters (resolution, page size), and automatically design the size, position of image. The system can effectively avoid mistakes such as repeated proofreading error and manual type-setting error. In conclusion, the proposed system is a good solution in typesetting of digital content.

References

1. Zeng, G. C., Xiang, Z. Y., & Qing, F. (2013). The trend of the multiple terminal adaptive release of digital content. *Journal of Information Resource Management, 02*, 79–85.
2. Lei, C. (2013). *Key techniques of digital content across the terminal publishing*. Hefei: Hefei University of Technology.
3. Qin, D. (2014). *A study in modern Chinese text image and typographic norms*. Beijing: Central Academy of Fine Arts.

4. JIS X 4051. (2004). *Formatting rules for Japanese documents*. Japanese Standards Association.
5. MS office open xml part 4—markup language reference. (2010). *Ecma International,* 85–87.
6. Xu, W., Hu, W., Wu, J., & Su, R. (2011). A method and system for automated typesetting of books. CN102147791A.
7. Gamble, G. (2011). *InDesign CS5 automation using XML and JavaScript*. Training Company.

Chapter 53
The Study on the Competence Criteria on Digital Content Designs for Digital Publishing Editors

Chiupai Ho and Mingju Hsu

Abstract The aim of the study is to understand the competence of digital content design for digital publishing editors. The study used document analysis first and then followed by in-depth interviews and evaluations with experts secondly, to explore the required competence of digital content designs for digital publishing editors. The study collected and analyzed various literatures and documents in competences required in digital content designs and publishing. Digital publishing experts who were top executives of their respective companies in Taiwan were invited and participated in this study 11 and 8 were attended meeting respectively as to provide their opinions and assessments on competence considered essential for digital publishing editors in digital content designs. The study resulted in six key functional elements such as design contents and platforms based on user-interface principles, processing final productions based on different publishing formats and specifications, etc. Further, a total of 40 performance criteria were also derived from this study, to name a few: designing suitable reading interfaces; planning layouts depending on the interfaces; capable of using editing software; using of digitized features; producing sound and images and editing of multiple materials, etc. The studied results could provide a set of standards or a merit basis for the relevant industries to recruit employees, the universities to teach students, and the government to select talents, etc.

Keywords Digital publishing · Competence · Editors · Digital content · Layout design

C. Ho (✉)
Department of Graphic Communication Arts, Taiwan University of Arts,
New Taipei, China
e-mail: cpho@ntua.edu.tw

M. Hsu
Department of Communication, Fo Guang University, Yi-land, China
e-mail: mjhsu@mail.fgu.edu.tw

53.1 Introduction

In the digital era, publishing in electronic form went beyond the traditional print-driven paradigm. Numerous digital devices with Internet and Wi-Fi capabilities such as smart phones, laptop, tablets, etc., which equipped with Apple, Microsoft or Android operation systems all made it easier and more convenient in searching, retrieving, and using of information than ever before. Digital carriers not only enriched the contents and forms of publications, but also changed people's lifestyle and consumption concepts and behaviors [1, 2]. Besides breaking traditional forms and patterns of content deliveries, digital publishing also redefined various scopes and methods of publishing. More specifically, publishing was no longer limited to a finite, physical container; but the organic publishing combined the texts, images, audios, and videos, and became an interactive publishing with dynamic, digitized, and humanized layouts in its overall scheme [3–7]. Digital publishing attracted many readers to stay hooked and lingered longer with its multiple sensory and human touches, bringing a rich audio-visual experience to what was once a pure reading routine. The interactive multimedia design has become a hot trend in the new era of digital publication [8–10].

53.2 Competence of Digital Content Designs for Editors

53.2.1 Layout Design Is a Critically Important Competence for Editors

The role editors played became more important in the digital publishing era, tasks such as editing and layout design of digital contents, or coordinating design and production, were all vital skills required for today's digital publishing editors [11]. The conventional method of reading was dictated by the traditional publishing process, i.e., readers had to passively accept the established, singular methods of reading without alternative choices. On the other hand, digital publishing mode provided a more vivid, dynamic, and enjoyable reading experience. For example, depending on the reader's preference, he can change the font, size, background color, and light intensities of an ebook; or he can download any number of books, songs, and movies into his mobile device and access them wherever, whenever he wants to at a later time. It creates a profound, everlasting change in way of how people read books, watch videos, and listen to the music. Moreover, in recent years, the emergence of new media, technologies, and vehicles of publications brings in dramatic changes in the digital content industry. For example, the development of digital hypertext and hypermedia technologies enabled the upload, download, and streaming of various information in any digital formats such as text, still image, video, and audio. Each word or picture in digital publications could also be searched by the "keyword" or by its hyperlinks, so that it could be extended to

animation, audio-visual, and other related digital information. Thus, ebooks enabled users cross over from a linear reading pattern into new horizons of interactions with the contents in various digital forms [7, 12, 13]. With the rapid development in digital publishing, the demand in the publishing major also increased inevitably in response to the dynamic, fast changing environment. According to the 2011, 2012, and 2013 annual surveys of personnel job function demands in the field of digital publishing in Taiwan, the supplies of experienced multimedia designers were extremely short and inadequate. These survey reports also indicated that demands for layout design talents and specialists for designing of digital contents were, understandably, extremely strong [14–16]. Therefore, the objective of the study is to investigate the essential competence in designing of the digital content for digital publishing editors. The results of this study could provide valuable references for colleges and universities in selecting and training of students and cultivating talents for the Digital Publishing industry; it also can be used by the digital publishing industry as standards and merits in recruitment, training, and evaluations of its layout design staff and personnel.

53.2.2   The Required Competences for Editors in Digital Content Designs

The required competences for editors in digital content designs included but not limited to the followings: designing contents and platforms based on user-interface principles; processing final productions based on different publishing formats and specifications; using diversified editing software to design layouts; using animation software to create special effect images; showing abilities to use storyboard techniques to narrate images and stories and capable of conducting film editing and organizing mixed media materials, etc.

(1) Designing contents and platforms based on user-interface principles.
Interactive Designs should be "user friendly and user-based", the designs should focus on users' convenience, efficiency, and even pleasure experienced during the usage of the program [17]. Layout designs should create conditions taken into account of various types of readers' using abilities, methods, habits, and convenience [18]. Increasing readability of the page content, raising the readers' participation interest, and empowering readers to choose pages or contents in accordance with their preferences or desire were all important skills to be a successful digital editor [3]. Under the Internet environment, common interactive behaviors of "Human Machine Interface" such as mouse clicks, drag and drop, move, input text via keyboard or hand writing; menu-controlled items and Window software including methods in communicating with users such as tips, confirmation, etc. should all be considered and applied [19]. Meanwhile, the nonlinear features of multimedia technologies would change people's traditionally sequential reading behavior, instead of the

more conventional page-section-chapter frame of reading, the hypertext link method would provide a more flexible, varying, and vivid method in absorbing of all kinds knowledge [20].

(2) Processing final productions based on different publishing formats and specifications.

In the development of digital technology, the segmentation of media was no longer of traditional style; rather, through the integration of multimedia links, resources sharing, and information reusage became possible. The files would need to be tested on various ereaders to ensure compatibilities. Editors might need to carry out the validation, testing, and quality assurance themselves. Even if they did not, they would have to communicate with code-writers and programmers, who are the new entrants and essential participants in the ebook publishing value chain nowadays. An epub file was basically a zip archive containing XHTML metadata describing the book, and a navigation map describing the structure of the book. Therefore, digital publishing editors would be required to understand the format of ePub, the fundamental knowledge of HTML, XHTML, CSS, and various web standards, respectively [5]. Furthermore, when both readers and authors were trying to understand how to read and write in the digital age, editors also needed to reconsider the whole approach to the process of making books such as wide arrays of digital formats, associated creations, consumptions, and everything that happened around and in connection. For example, "formless content" could be diverted from layout and reflowed into different formats without losing any of its intrinsic meaning. Most novels and works of nonfictions have formless content [21]. Also to be aware of was that different formats, carriers, and screens might result in the displacement or misplacement in the layouts of contents. The widespread use of PDF files or the ebook format standard ePUB were internationally accepted because of their typographical characteristics in controlling or minimizing the layout problems. Therefore, digital editors should thoroughly understand the characteristics of different editing software, get familiar with their respective operation strengths and weaknesses, make good use of its advantages and optimize the multimedia's interactive hyperlinks of the characteristics as to preserve or even enhance the content's original forum and diversity, when presented under different vectors and platforms [22].

(3) Using various editing software to design layouts.

Digital editors must be able to tag in layout and digital content in accordance with the XML language, the tagged contents then could be disassembled. When the data were required in reuse on different platforms or carriers, they could be automatically traced and found at their exact locations, then dynamically flew them into positions per interactive or re-combination demands. Thus optimizing placement and rearranging their structures into new forms of layout across the platform from printed-to-digital media [22]. Digital editors should be capable of performing layout designs in expressing unique characteristic such as qualities of sequential order, balance, beauty, harmony,

attraction, intrigue of page layout, etc. [23]. Editors also must be able to apply a variety of editing tools, not only grasping the text, images, audio, and video features, but also capable of using them in integral and skillful applications. Editors should also understand E-readers related knowledge in order to fully realize online interactive, citation, automatic link etc. [1].

(4) Using animation software to create special effect images.
Digital Publications were capable of carrying new elements such as audio, video, motion pictures, animations etc., of which stimulations for readers' sensory were more intense or exciting than that of traditional printed media. The primary purpose of various illustrations was through the rich manifestation of images to convey the connotation of the context; for example, to shape characters more vividly; portray characters' inner minds and thinking ways; narrate a specific time in history; depict scenes of space and environment uniquely fitting the storyline; transfer lessons and information, etc. Dynamic illustrations could create superior artistic expressions and far influencing effects than those of traditional illustrations, they were also more interactive and diversified; the animation used in the ebook increased the vitality of the page, presented a strong visual impact and better reflected the narrative functions. These visual effects could become greater interactive, more fun, and everlasting experience for readers [24]. Digital editors should be able to assess when and where the content interactive was required and be able to apply the interactive design features and hyperlinked them to specific pages; or hyperlink them to the web and the URL destinations in satisfying the human-machine interaction demands from the readers. Digital editors should also make full use of the characteristics of the layout design software, expanding the benefits of media consolidation and bridging over the gap between the printed and digital media in achieving the cross-media integration target for digital publishing [22].

(5) Showing abilities to use storyboard techniques to narrate images and stories.
Pictures or images properly positioned can affect the layout of page composition positively, it could raise the subject focus, reveal inner layers of subject story, and provide a strong visual impact [25]. Images and pictures resorted to human's visual thinking and reaction, which were more readily and effectively translated and registered in human mind than the words and sentences which resorted to the abstract thinking of human mind [26]. Editors should be able to extract design thinking and utilize visual effects such as images, pictures, video, etc. expertly through the storyboard technique and video narration, to present a superior design layout in achieving a satisfactory digital editing assignment.

(6) Capable of conducting film editing and organizing of mixed media materials.
Digital content focused more on visual effects and strengthened the expressive intensity of images; using flash, audio, and video technologies to send audiovisual contents that could register strong emotions and grab the eyes and ears of the viewers [23]. Configuring animation, sound, video, and other

multimedia effects for images and pictures increased the realism and three-dimensional effect and elevated the reading and viewing experience to a higher, more attractive, and entertaining level than that of reading of traditional printed media [27]. Digital editors should be able to edit various audio, videos mediums in creating various audio-video background effects to enhance the reading and viewing experiences [28].

53.3 Research Methods

53.3.1 Document Analysis

This study has collected and reviewed various documents and works related with job functions and competence factors in designing of digital contents for digital publishing editors; including but not limited to the following institutions and organizations: Council of Australian Societies of Editors [29], Cultural Human Resources Council of Canada [30], Creative Skillset of UK [31], Editors' Association of Canada [32], Printing and Publishing Industry Training Advisory Committee of Hong Kong [33], Ministry of Education of Taiwan [34], O*net OnLine of U.S.A. [35], South African Qualifications Authority [36], etc. Related literatures from academic research discussions were also collected and incorporated as additional references to formulate the framework for the study.

The literature review and document analysis resulted in the summary of six key Functional Elements as described in Sect. 2.2 "The Required Competences for Editors in Digital Content Designs". These functional elements were then served as the basic framework in establishing the draft of competence criteria for digital publishing editors in digital content designs specifically in Taiwan area.

53.3.2 Experts Meeting

An open-ended, discovery-oriented method was applied to explore the expert panelists' experiences, perspective views, and opinions in various digital competence criteria considered important to digital publishing editors. Experts Meeting, first round meeting, were carried out on February 6, 2015 to review the drafted Competence Standard. The expert panel was composed of 11 digital publishing experts (Expert A–Expert K) who were top executives of their respective companies.

In addition, a total of eight digital publishing experts (Expert 1–Expert 8) who possessed in-depth knowledge and experiences in digital publishing industries in Taiwan were invited to participate in the Experts Meeting, second round on May 1, 2015, to review and assess the criticalities of various competence criteria considered important to editors in digital content designs.

53.4 Results and Discussions

53.4.1 Experts' Opinions

The experts' opinions from the assessment results from the Experts Advisory Meeting were grouped into functional elements and performance criteria in establishing the competence guideline for digital publishing editors. Table 53.1 showed a

Table 53.1 The key functional elements and performance criteria on digital content designs for digital publishing editors

Key functional elements	Code	Performance criteria
Designing contents and platforms based on user-interface principles	A01	Design suitable reading interfaces
	A02	Design layouts in accordance with readers' preferences
	A03	Consider the interactive features
	A04	Design in accordance with the characteristics
	A05	Present user-intuitive navigations
	A06	Guide path by users' objectives
	A07	Guide users to access the contents
	A08	Guide the readers into the situations
	A09	Capable of communicating with users
	A10	Apply interactive user-interfaces
	A11	Design digital contents by analyzing users' experiences
	A12	Meet audience's expectations
	A13	Focus on user-centered designs
	A14	Design superior layouts of digital contents
	A15	Design superior digital contents for multiple channels
	A16	Create continual reading demands
	A17	Design interfaces based on usage behaviors
	A18	Design user interfaces in nonlinear reading experiences
	A19	Produce based on readers' needs and requirements

(continued)

Table 53.1 (continued)

Key functional elements	Code	Performance criteria
Processing final productions based on different publishing formats and specifications	B01	Plan layouts depending on the interfaces
	B02	Design according to different specifications
	B03	Edit based on the carrier's regulations
	B04	Typeset by carrier's needs
	B05	Produce based on the sizes of interfaces
	B06	Design in response to the carrier's specifications
	B07	Design layouts based on carrier's features
	B08	Design layouts considering the screen formats
Using various editing software to design layouts	C01	Capable of using editing software
	C02	Use software to auto-edit
	C03	Apply software to maximize benefits
	C04	Apply software to layout designs
Using animation software to create special effect images	D01	Use digitized features
	D02	Use animation software to enrich multiple contents
	D03	Conduct interactive designs
	D04	Produce special effects for digital contents
	D05	Apply interactive software
Showing abilities to use storyboard techniques to narrate images and stories	E01	Produce sound and images
	E02	Edit digital contents
Capable of conducting film editing and organizing mixed media materials	F01	Edit multiple materials
	F02	Edit audio and video

total of 40 performance criteria grouped under the 6 Functional Elements into A01–A19 (19 criteria); B01–B08 (8); C01–C04(4); D01–D05(5); E01–E02(2); and F01–F02 (2), respectively.

53.4.2 Competence Criteria on Digital Content Designs for Digital Publishing Editors

The competences considered important for digital publishing editors in designing digital contents were constructed by a detailed document and literature analysis combined with the expert's advisory assessment meeting. In short, the competence criteria were consisted of 40 Performance Criteria (A01–A19, B01–B08, C01–04, D01–D05, E01–E02, F01–F02) under 6 Functional Units (A–F), respectively, as shown in Table 53.1.

53.5 Conclusions

Various literatures and documents related to competences of digital publishing editors were reviewed thoroughly to identify the competence criteria in designing of digital contents for digital publishing editors. The competences could be categorized into 6 key functional elements and 40 performance criteria. The 6 key functional elements were: (1) designing contents and platforms based on user-interface principles; (2) processing final productions based on different publishing formats and specifications; (3) using diversified editing software to design layouts; (4) using animation software to create special effect images; (5) showing abilities to use storyboard techniques to narrate images and stories, and (6) Capable of conducting film editing and organizing mixed media materials, respectively. A total of 40 performance criteria were also derived from the study, such as Designing suitable reading interfaces, Planning layouts depending on the interfaces, Capable of using editing software, Using Digitized features, Producing sound and images, and Editing multiple materials, etc. (see Table 53.1). This study provides valuable references for colleges and universities in adequately selecting and training of students and cultivating talents for the digital publishing industry; it also could be used by the digital publishing industry as standards in recruitment, training, and evaluations of editing staff and personnel.

References

1. Cao, L. (2011). The era of digital publishing editorial staff literacy discussion. *Management Engineer, 2011*(4), 15–17.
2. PricewaterhouseCoopers (PwC). (2006). *The rise of lifestyle media: Achieving success in the digital convergence era*. Technology Center, PricewaterhouseCoopers International Limited.

3. Ding, H. (2009). Study on interactive design of multimedia interactive magazine. *Press Circles, 6*, 18–20.

4. Kelly, K. (2011, April 15). *What books will become.* Retrieved from http://kk.org/thetechnium/archives/2011/04/what_books_will.php

5. Mrva-Montoya, A. (2013). *Editing skills in the era of digital [r]evolution.* Paper presented at the 6th IPEd National Editors Conference, Perth, Western Australia.

6. Procter, A. R. (2001). Electronic paper and the e-books: A real or imagined threat to paper? *Pulp & Paper of Canada, 102*(6), 8.

7. Roberts, J., Slattery, O., & Kardos, D. (2000). Rotating-wheel Braille display for continuous refreshable. *SID Symposium Digest of Technical Papers, 31*(1), 1130–1133. doi:10.1889/1.1832864.

8. Davenport, T. H., & Prusak, L. (1998). *Working knowledge: How organizations manage what they know.* Boston, MA: Harvard Business School Press.

9. Sun, D. L. (2008). Analysis the Interactive design of the network. *Art and Design (Theoretical), 4*, 69–71.

10. Wu, X. H. (2013). On the layout design of modern network design. *Business, 16*, 384.

11. Hsu, M. J. (2014). The study of critically essential competences for digital publishing editors. *Publishing Research Quarterly, 30*(1), 11–22. doi:10.1007/s12109-013-9340-5.

12. Rech, D. A. (2012). Instituting an XML-first workflow. *Publishing Research Quarterly, 28*(3), 192–196. doi:10.1007/s12109-012-9278-z.

13. Lai, H. L. (2011). Compilation and publication of the Yearbook in the digital age. *Guangxi Chronicles, 2*, 36–39.

14. MOEA (Ministry of Economic Affairs). (2011). *The report on professional supply and demand for digital content industry 2011–2013.* Taiwan: Ministry of Economic Affairs. Retrieved from http://itriexpress.blogspot.tw/2012/07/20122014_3817.html

15. MOEA. (2012). *The report on professional supply and demand for digital content industry 2012–2014.* Taiwan: Ministry of Economic Affairs. Retrieved from http://itriexpress.blogspot.tw/2012/07/20122014_4914.html

16. MOEA. (2013). *The report on professional supply and demand for digital content industry 2014–2016.* Taiwan: Ministry of Economic Affairs. Retrieved from http://itriexpress.blogspot.tw/2014/01/2014-2016_190.html

17. Li, Y. (2008). The main features of good interaction design. *Package Engineering, 29*(1), 162–164.

18. Li, S. D. (1998). Layout awareness of technical editors. *China Publishing Journal, 09*, 63.

19. Liu, W. P. (2011). Four propositions based on internet environment for interactive design. *History of Art and Design,* 76–77.

20. Chen, J., & Su, X. (2010). Multimedia man-machine interface and interaction design of courseware. *Information Development & Economy, 20*(23), 128–130.

21. Mod, C. (2012). Designing books in the digital age. In H. McGuire & B. O. Leary (Eds.), *A futurist's manifesto—Essays from the bleeding edge of publishing.* Boston, MA: O'Reilly Media.

22. Tang, C., Hu, B., & Yang, L. (2011). InDesign application practice of cross-media publishing in journals. *Chinese Journal of Scientific and Technical Periodicals, 22*(2), 245–247.

23. Ma, Y. L. (2008). Discussion on the functionality and artistry of electronic journal. *Art Research: Harbin Normal University Art, 3*, 86–87.

24. Zhou, L. (2013). Advantages of dynamic illustrations of ebooks. *Modern Decoration, 5*, 141.

25. Zhang, J. (2007). Applications of visual elements in the layout design. *Modern Business, 31*, 96.

26. Wang, Y. (2008). The study on periodical pictures layout design. *Charming China, 19*, 139.

27. Li, Z. R. (2013). *The development policy for printed media in the iPAD Era, The audio-video world, July, 2013.* Retrieved from http://www.cnki.com.cn/Article/CJFDTotal-GGRZ201307095.htm

28. Zhou, W. H. (2012). The status quo and prospect on graphic design of electronic books. *Arts Education, 12*, 164–165.

29. Council of Australian Societies of Editors. (2001). *Australian standards for editing practice*. Australian: Author
30. Cultural Human Resources Council of Canada. (2006). *Chart of competencies for book publishers*. Ottawa, Canada: Author.
31. Creative Skillset. (2012). *Book and journal publishing national occupational standards*. London, UK: Creative Skillsets. Retrieved from http://standards.creativeskillset.org/assets/0000/0572/Book_and_Journal_Publishing_2012_FINAL.pdf
32. Editors' Association of Canada. (2009). *Professional editorial standards.* Toronto: Canada Author.
33. Printing and Publishing Industry Training Advisory Committee. (2006). *Specification of competency standards for the publishing of Hong Kong.* Wan Chai, Hong Kong: Author.
34. MOE (Ministry of Education). (2010). *University career and competency assessment network (UCAN).* Taiwan: Ministry of Education. Retrieved from https://ucan.moe.edu.tw/
35. O*NET. (2010). *Summary report for: 27-3041.00—Editors*. U. S. Department of Labor: O*NET OnLine. Retrieved from http://www.onetonline.org/link/summary/27-3041.00
36. South African Qualifications Authority. (2009). *National certificate: Publishing*. South African: Author.

Chapter 54
The Design of Network Printing Function Model

Nana Liu and Congjun Cao

Abstract With the rapid development of science technology, the application of computer and internet technology has been increasing widely. The combination of digital printing technology and the internet has created a new printing model, network printing. A growing numbers of printing enterprises focus on network, and begin to build network platform for printing. Domestic network printing is in the beginning stage and faces many problems to be solved, for instance, the application scope is not enough, the market development is still low, the existing network printing platform can not meet the actual needs of customers, and so on. To solve these problems mentioned above, this thesis establishes the basic functional module of network printing platform by comparing and analyzing the four existing typical representative network printing platforms, such as EastnetPrint and Xie88.com, and discusses future trends and outlook of printing technology.

Keywords Network printing · E-commerce of printing · Printing platform

54.1 Introduction

Network printing is not exactly a way for printing industry, but a solution to printing production management, which utilizes network server to general personal documents and it provides customers with professional printing services by digitizing printing business processes [1]. Network printing has an advantage of digital printing, such as personalization, process standardization, which also avoids the disadvantages of digital printing, such as the high cost of digital printing products.

N. Liu (✉) · C. Cao (✉)
Faculty of Printing, Packaging Engineering and Digital Media Technology,
Xi' an University of Technology, Xi'an, China
e-mail: 805071563@qq.com

C. Cao
e-mail: caocongjun@xaut.edu.cn

Meanwhile, by using the application of network technology, it helps customers achieve efficient marketing management, information feedback and analysis, convenient financial management, and expand more different types of products and value-added services, etc. [1, 2].

Network printing is bounded to be the new trend in the printing business. Yet, it is in the beginning stages and faces so many problems to be solved.

54.2   Development Situation of Network Printing

Field of network printing application focuses on short-run business printing. With the development of computer technology and popularization of Internet e-commerce, the marketing share of network printing is increasing at a rate of 200 % [3].

Abroad, there are many web-based products of printing workflow management information system, which are also called network printing solutions. Products such as Agfa's Delano, EFI's Digital StoreFront are characterized by using web to transfer working requirements and file structure to the whole production process etc., supporting the management throughout the whole course of printing processes.

Products like Cendix's PrintShop Portal, InterlinkOne's ilinkOne and so on, focus on enhancing the communications with customers, by utilizing the automated email, automatic bill tracking system, and other functions to increase the automation degree of customer communications. Whereas, FORIX's and Ink2's W2P focus on online editing, meeting customer's individual needs, and the improvement of the data flow management system, etc. [4].

Currently, network printing in the domestic market, mainly small sites, is prior to making personalized printing products. As domestic network printing just started up, domestic users' understanding of the network printing is still very low with printing suppliers and network printing systems, only about 10 % of these enterprises consider network printing as the best sales opportunity [5].

Overall, the development of domestic network printing is much less than in foreign countries. In recent years, a variety of similar news printing websites are springing up in the domestic market. The network printing market is developing rapidly.

54.3   Analysis of Network Printing Cases at Home and Abroad

Through research on existing network printing sites, this study briefly introduces and analyzes the four existing typical representative network printing platforms at home and abroad, namely EastnetPrint, Xie88.com, Konica Minolta, and OnPrintshop.

54.3.1   Brief Introduction of the Four Websites

EastnetPrint is a state-owned holding national digital printing franchise, established in 2002. EastnetPrint started to accept franchisee in 2013. The number of franchisees increases greatly and has covered areas including Shanghai, Zhejiang, Guangdong, Beijing, and other places [6].

Xie88.com is website for a network printing overall solution of printing, advertising, and design industry. It includes various products, such as business cards, greeting cards, color leaflets, catalogs, bags, stickers, etc.

Konica Minolta was founded in Japan in December, 1936. In 2011, Konica Minolta Office System (China) Limited company launched a new version of their digital printing system website. It provides innovative products, professional services and solutions.

OnPrintshop is one of Radixweb's flagship products. Radixweb Company mainly provides a one-stop solution to all the IT fields and design requirements. OnPrintShop provides the network solutions for the printing industry.

The home pages of four websites are shown in the figure (Fig. 54.1).

54.3.2   The Contrast and Analysis of the Four Websites

(1) EastnetPrint: It has enormous influence in domestic printing industry, related media, and other manufacturers, but the platform is not comprehensive. It mainly regards the platform as a marketing method. The website does not

Fig. 54.1 Website diagrams of four main network printing platforms

provide enough choice of services for customers. It does not contain network printing specific modules, such as online design and online order. It cannot conduct online transactions directly.

(2) Xie88 network printing: It covers self-help quotation, online order, and order management, online business card design, upload files online, online communication, member management, invoice management, and other important parts in printing. It is based on the self-help quotation, guided with online design, has complete order process and customer management, and contains strong core competitive advantages of network printing [7]. Still the site only gives priority to small, personalized products.

(3) Konica Minolta: Print groove POD Ready and Printgroove POD Queue correspond to prepress processing and equipment management functions. The prepress solutions cover from the variable data, on-demand printing, work flow, to the color management, network printing, etc. [8]. The website not only contains personalized, small printed products, but also involves printing teaching materials and books. While it only provides download templates, it does not provide an independent design module. Network printing solutions is just a small part of its business domain.

(4) OnPrintshop: It is dedicated to the research and development of high-end function solutions. The website mainly provides all kinds of network printing solutions and function module design involved in all aspects of a printing company, including online photo album software, printing middlemen, variable data printing, web designers studio integration and online shopping connector, workflow automation/printing service supplier integration, and ordering module solution [9]. The website provides service for both individuals and network printing vendors and it provides a variety of software and customized solutions to merchants. It has complete functions and a wide application. Still it is a foreign website, uses English language, and is seldom applied in the domestic market.

By analysis and comparison of these websites function, the function demand of network printing services platform should at least have the following aspects.

Step 1: An online system should allow customers to perform transactions over the Internet. Platforms should provide users with a variety of template products, and allow users to personally edit on the template they select, such as uploading and editing photographs and entering personalized words and content.

Step 2: The edited work should upload to network printing service providers, and then complete the orders.

Step 3: They should have necessary auxiliary functions, like online payment, order tracking and so on.

In addition, the platform interacts with customers, suppliers, and employees. So the information communication among them must be convenient, quick and accurate [10, 11].

54.4   The Planning and Design of Network Printing Services Platform Function Model

By analysis of the existing website function modules and market research on the printing company, this thesis mainly designs from the following aspects.

54.4.1   Functional Analysis

(1) Homepage. The most basic part of a network platform is to have a perfect home page. It is convenient for customers to know about the website. It plays an important role in directivity.
(2) Web-to-print. It is the main functional module in website, including the important parts, such as editing, choosing, purchasing, and posting of products.
(3) Dynamic demonstration. This module can provide operation processes and related videos of network printing. It can help customers learn how to effectively use the modules.
(4) Products showcase. This module will show the featured products to customers for reference.
(5) Service and guidance. This module will provide service and operational guidance for everyone who visits the website.
(6) Members area. The area gives discounts and gifts to members of company.
(7) Contact us. This module makes easier to communicate with the staff and better for the development of the website.

54.4.2   System Design

(1) Homepage
Homepage module is used to facilitate the customers to understand the content of the website. It can be divided into the following five submodules.

- Company information. This module introduces history, background, business, and development prospects of the company to which the website belongs.
- Product introduction. This module details all company products for customers to understand and from which to choose.
- Successful cases. This module introduces the success story of the website or other online printing platform associated with the website.

- News. This module introduces important news about the printing industry as well as the important events of the website.
- The storefront to be chosen. This module details all storefronts of the website from which customers can choose.

(2) Web-to-print

It is the core module in the website. It can be divided into six submodules.

- Product type. This module describes the kinds of products the website could produce.
- Online design. This module provides customers with product design and the operation of the choice. It mainly includes self-help design and online designer design through two operation modules. The self-help design includes an online template and a customer design area.
- Online proofing. This module can predict the output effect of printing and it relies on the development of soft proofing technology.
- Order system. This module records the order flow of customers, including the online order, order records, statistical order, and order tracking.
- Product quotation. This module provides customers with reasonable prices of products. Customer can make a choice from a series of prices. It includes independent quotation, online inquiry, customer inquiry area, and historical quotation.
- Payment management. This module ensures the safety and reliability of the process of payment, including online payment, payment order, and payment records.
- Shipping method. This module includes two options of self pickup and express delivery.

(3) Service and guidance

Service and guide module provides service and guidance for customers. It can be divided into five modules.

- Freshman guidance. This module provides operation instructions for customers who make their first contact with network printing, including member registration, account management, common problems, and other operating functions.
- Service guidance. This module provides instructions for the design of product, including product design, image processing, graphics, and text layout.
- Shopping guidance. This module provides instructions for the whole shopping process, including ordering process, mode of payment, delivery time.

- After-sale service. This module provides a reference basis for the customer who needs after-sale service, including return and exchange norms, service flow, complaints, and suggestions.
- Help. This module provides help for customers, including retrieval of passwords, about us, and contacts us.

(4) Contact Us

Contact Us module is an essential function module of the website. It is easy to understand the hearts of customers and construction sites better. It can be divided into two submodules.

- Email messages. This module realizes management and maintenance of the websites' email information.
- Online customer service consulting. This module can timely solve the problems for customers, including online consultation and free online telephone counseling.

Dynamic demonstration, products showcase, and member area modules do not contain any child module. The frame diagram of the network printing function model is shown in the figure (Fig. 54.2).

In order to offer a user-friendly environment for foreign customers, the platform should take bilingual user interface into account. The platform should also provide copyright management and online legal advice service [12].

Besides, network printing has special marketing method in website, such as advertising, book tours, revenue sharing with famous websites, like Amazon, etc. [13].

54.5   Conclusions

Network printing will develop into the main form of printing in the future. The key problem now is, how to create a enterprise and user-friendly platform of the network printing need to be researched and discussed at the present stage. To solve that problem, this study compares and analyzes the four existing typical representative network printing platforms, such as EastnetPrint and Xie88.com; it comes to a conclusion that the functional module needed of network printing platform is to be assured.

In recent years, cloud computing as a new Internet technology has gradually risen; almost all Internet companies have started to research and develop cloud technology to improve efficiency of their platforms. Therefore, the combination of cloud computing and web printing will become mainstream in the future.
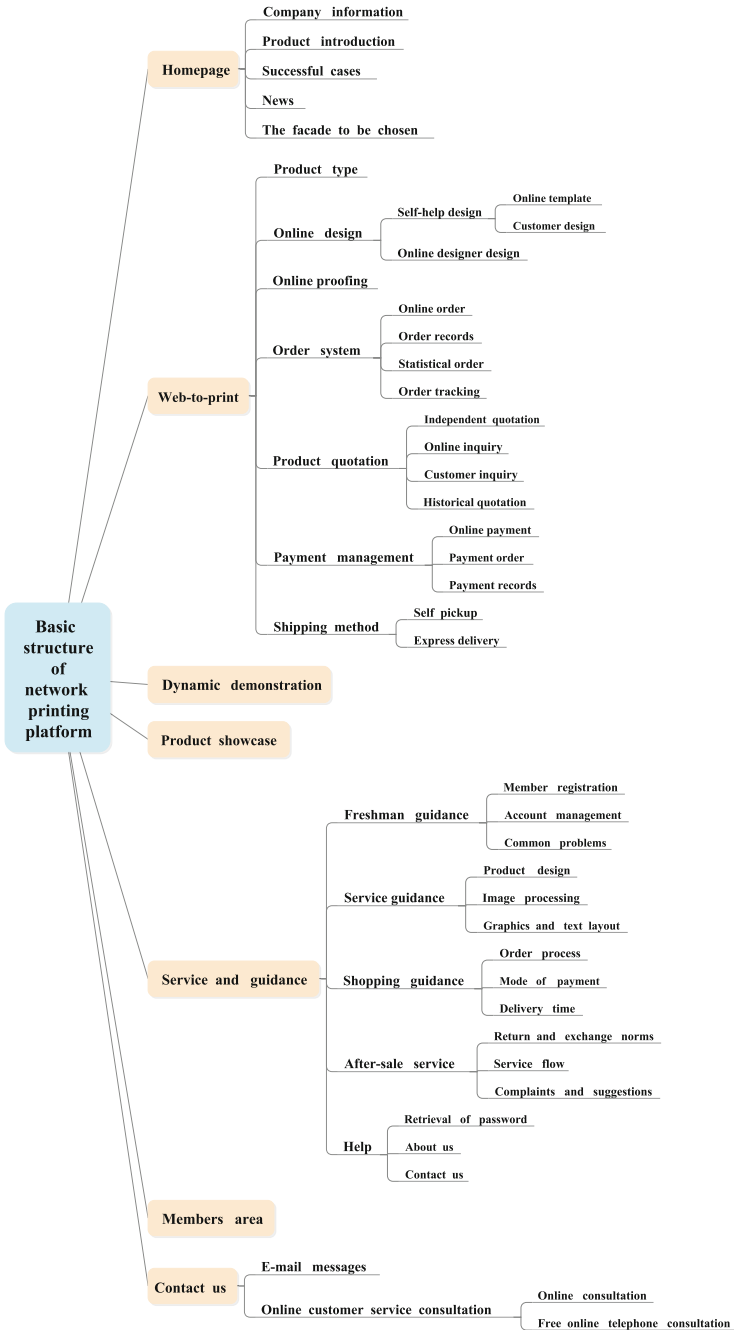
Fig. 54.2 Basic structure of network printing platform

References

1. Zheng, A. L. (2010). The development investigation of domestic network printing. *Printing Technology, 19*, 13–17.
2. Liu, F. Y. (2013). Network printing: The stepping stone of high profitable mode. *Printing Field, 8*, 19–22.
3. Besenet. (2013). *Network printing: Both capital investment and profit model are necessary.* http://www.bisenet.com/article/201312/133131.htm. Accessed August 21, 2015.
4. Xiao, F. F. (2013). *Research of network printing services platform system modeling.* Master thesis, Nanjing Forestry University.
5. Zhang, D. S. (2013). *Network printing services platform based on cloud computing function model.* Master thesis, Beijing Printing Institute.
6. EastnetPrint Website. (2015). http://www.eastnetprint.com/. Accessed August 21, 2015.
7. Xie88 Website. (2015). http://www.xie88.com/. Accessed August 21, 2015.
8. Konica Minolta Website. (2015). http://www.konicaminolta.com.cn/business/products/hi_speed_copiers/solution_case/solution/05/details.html. Accessed August 21, 2015.
9. Onprintshop Website. (2015). http://www.onprintshop.com/. Accessed August 21, 2015.
10. Wang, J. P., Liu, Z., & Lu, L. (2011). Network printing system design based on smart phone. *Packaging Engineering, 32*, 13–16.
11. Adam D. (2008). *Web-enabled print architectures.* Master thesis, A Research Monograph of the Printing Industry Center at RIT.
12. Hsieh, Y., Lin, C., & Hung, S. (2011). A study of the functionalities and workflow for web-to-print platform. *Advanced Materials Research, 174*, 151–154.
13. Prakash, R., Benedict, R., Shariff, D., & Anil, D. V. (2013). Building a print on demand web service. *Proceedings of SPIE-IS&T Electronic Imaging, 7879*, 0–7.

Part IV
Printing Engineering Technology

Chapter 55
Study on the Relationship Between Ink Drop Size and Dot Cover Area of Inkjet Plate Making

Junlong Xu, Huanhuan Jia and Yulei Zhao

Abstract Ink drop size is an important indicator of the quality of inkjet stencil, which directly affects the accuracy of the printing dot cover area and the stability of the inkjet stencil. According to the nozzle print control principle, this paper has designed the test file, realized the measurement of microcosmic ink droplet shape by using edge detection, contour extraction, and other image processing technology and studied the relationship between the microdroplet size and the printing dot cover area. Through the methods, this paper realizes the rapid detection of ink drop size.

Keywords Inkjet plate making · Ink drop size · Dot cover area

55.1 Introduction

Inkjet printing technology has become the focus of the global printing industry. The nano inkjet plate making technology is a new technology to achieve green printing. It divides the hydrophilic region and oil region, by printing the ink containing nanoparticles directly on the plate, and then realizes the division of the image area and the nongraphic area after curing [1–5]. Inkjet plate making has advantages of simple process, environmental protection, low cost, etc. The detection of the shape and size of the ink is the key to guarantee the quality of the plate making, but the method of micro measurement has the disadvantages such as high equipment requirement and long detection time. In this paper, the relationship between ink drop size and dot cover area is studied based on the principle of inkjet technology, and the drop size prediction method based on measurement of dot area is realized.

J. Xu (✉) · Y. Zhao
Beijing Zhongke Nano-Think Print Technology Co., Ltd., Beijing, China
e-mail: a943747151@gmail.com

H. Jia
Tianjin University of Science and Technology, Tianjin, China

55.2 Inkjet Technology

55.2.1 Physical Resolution of the Print Head

Inkjet technology according to the principle can be divided into continuous inkjet and on-demand inkjet, and nozzle arrays are used to realize high production capacity and high physical resolution of the imaging system, which is restricted by manufacturing factors, electronic circuit and other relevant factors. The physical resolution of a single line nozzle is too low for a print head, so multi slightly inclined lines of nozzles is usually used and the nozzle columns toward the direction of the substrate transport to achieve higher physical resolution [6, 7], as in Eq. 55.1.

$$\text{Resolution of nozzle array:} A = A_x \times n$$
$$\text{Inclination angle:} \tan \alpha = (n - 1) \times a_y \times A_x \tag{55.1}$$

In the formula, A is resolution of the array resolution, A_x is resolution of each line of nozzles, n is the line number of the nozzle array, a_y is the nozzle row spacing, α is the tilt angle.

55.2.2 Output Resolution of Device

At present, the physical resolution of the nozzle cannot meet the requirements of the output resolution and interpolation methods are usually used, which can be divided into two kinds, one is the method of using multiple print heads, and the second way is multiple interpolation by using the high-precision motion control technology. In addition, the consistency of droplet size and raster pixel size is also the key to guarantee the accuracy of the image. If the droplet diameter is just the outer circle of a single pixel, then the relationship between output resolution and the drop size is shown in Fig. 55.1 and formula 55.2. In the formula, D is the single pixel length (μm), A is the output resolution, R is the drop radius (μm).

$$D = \frac{25.4 \times 1000}{A}$$
$$R = \frac{\sqrt{2}}{2} D \tag{55.2}$$
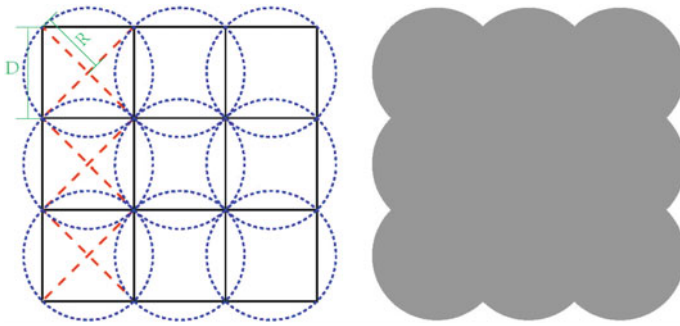
Fig. 55.1 Ink drop filling diagram

55.2.3 The Gray Levels of Digital AM Screening

Digital screening technology can be divided into AM screening, FM screening, and hybrid screening. FM screening has some shortcomings, such as the difficulty of quality control in printing process, the problem of image granularity, and so on, so AM screening is still the mainstream in the domestic and the requirement of the output of AM screening is needed. For AM screening, the relation of image resolution, image gray level, and the screen lines is shown in formula 55.3, which L is the screen lines, A is the image resolution, G is the gray level.

$$G = \left(\frac{A}{L}\right)^2 + 1 \qquad (55.3)$$

55.3 Relationship of Drop Size and Dot Cover Area

The ink characteristic and the voltage waveform of print head directly affect the shape size of the ink drop and it must be strictly controlled and detected depend on the accuracy requirement of the inkjet plate making. Based on the relationship between the size of ink drop and the dot area, this paper presents a method to predict the droplet size. When the image resolution outputted and the screen ruling is determined, the change of the size of the ink drop directly affects the dot cover area of AM screening, which can cause the problem of reproduction accuracy of the image color. In order to unify the printing quality control and the micro ink drop size forecast, this test has selected 50 % of AM screen as the feature point. If the output image resolution is 1800 dpi and the screen ruling is 120 lpi using digital circle screen, the raster diagram of the 50 % circular screen is shown in Fig. 55.2.

Figure 55.2a is a raster diagram of 50 % dot cover area and the length of each pixel is 14 μm. Figure 55.2b is a theoretical ink drop coverage of 20 μm for 50 %

(a)   **(b)**   **(c)**
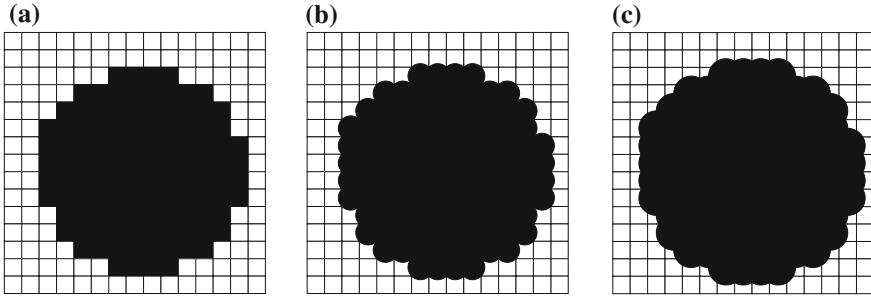
Fig. 55.2 50 % dots of digital circle screen

dot cover area, when the droplet diameter is the outer circle of single pixel. When the drop diameter is increased to 28 μm, the ink drop coverage is shown in Fig. 55.2c. The calculation can be obtained that the two kinds of ink cover area with different diameter were increased by 4 and 10 %, respectively. It indicates that the average fluctuation of one percent of the dot cover area can corresponds to the variation of about one micron of drop diameter, which can be used to predict the ink drop size quickly.

55.4   Experiments Design

55.4.1   *Experimental Conditions*

Experimental equipment: Think-NT220-116C NANO inkjet direct plate making machine, Digital microscopic imaging system, a printing plate measuring instrument, Matlab, and universal electric meter.

Experimental environment: laboratory with constant temperature and humidity.

55.4.2   *Test File*

The test file should contain the following test units, (1) a bitmap of ink drop array is designed depend on the type of print head and the printing principle [8–10]; (2) a printing gradient ladder containing 50 % flat screen is also designed. The test bitmap is shown in Fig. 55.3.
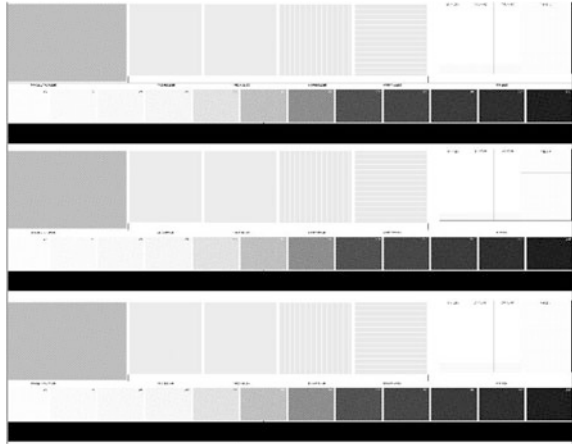
55.4.3 Test Method

(1) Adjust the temperature of the laboratory with constant temperature and humidity to change the ink droplet size, according to the properties of that ink viscosity is affected by temperature, and the selected temperature was 10, 15, 20, 25, 30, and 35 °C.

(2) Output the test file using the ink-jet plate making system without loading any compensation curve, under different temperature conditions and measure the resistance values of print head's thermistor by using universal electric meter, then repeat the test five times.

(3) Measure the temperature of the print head, the size of the ink drop, and the dot area of the printing plate, then calculate and analysis the measurement data.

55.5 Data Measurement and Analysis

First, set up different temperatures and print the test file on the printing plate by using the Think-NT220-116C NANO inkjet direct plate making. Second, randomly select 100 groups of ink droplets in the microdetection region on the plate using the digital microscope, and then edge extraction technique is used to measure the parameters [11, 12] of ink drop, such as area, diameter, etc. For dot cover area, average measurement values are used to ensure the reliability of measurement and each test color block should be measured three times at least. The measurement results are shown in Figs. 55.4 and 55.5.

Ink drop size and dot cover area are related to the temperature of the print head and the logarithmic function, according to Figs. 55.4 and 55.5, which can indicate that the higher the temperature is, the more obvious the drop deformation is and the

Fig. 55.4 The relationship
between the temperature of
the print head and the area of
the ink drop
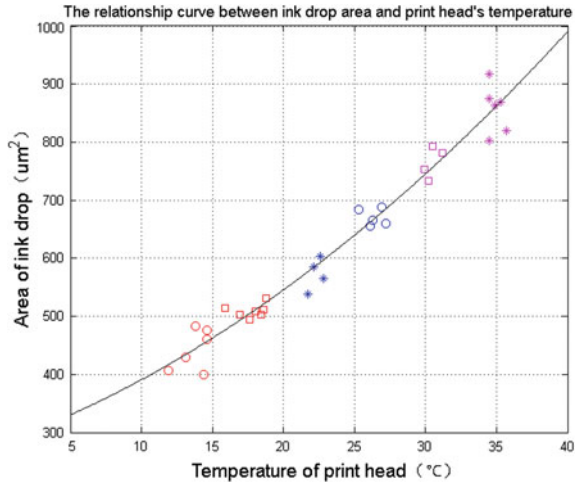
Fig. 55.5 The relationship
between the temperature of
the print head and the dot
cover area
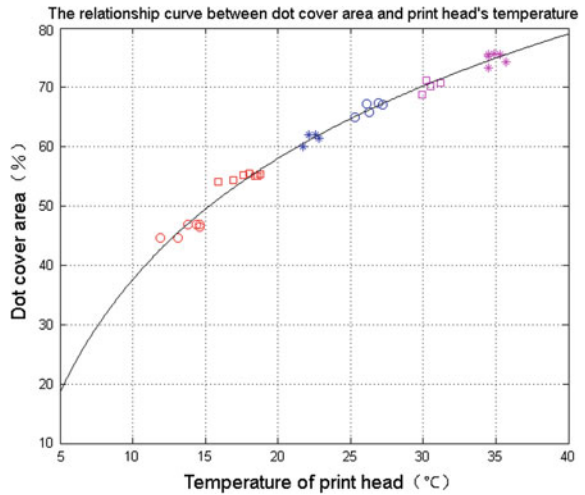
change of dot cover area tends to be linear. In addition, the roundness of the ink
drop gradually decreased with the increase of temperature, after analyzing the
change trend of the ink drop shape. What is more is the length of the ink drop of
nozzle moving direction changes obviously while the other direction is basically
unchanged.

A further analysis of the relationship between the length of long axis of the ink
drop and the dot cover area is carried out, according to the results of the above
analysis. The sample data corresponding to 10, 15, 25, and 35 °C is selected to get
the nonlinear least squares fitting function and the function curve between the
length of long axis of the ink drop and the dot cover area is shown in Fig. 55.6.

Fig. 55.6 Function relation of the long axis of the ink drop and the dot cover area

The relationship curve between dot cover area and print head's temperature
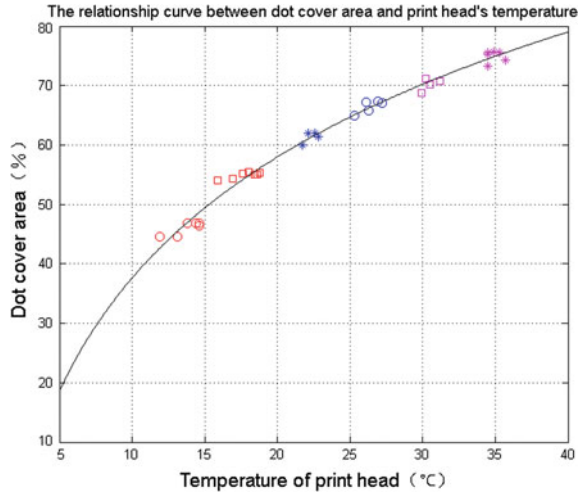
Table 55.1 Prediction error of the length of ink drop

	Ave	Med	Max
ΔE (μm)	1.76	1.72	2.64

According to the test sample data and fitting function, the diameters of ink drops are predicted, and the result of comparison between predictions and actual measurements is shown in Table 55.1.

The average deviation and the maximum deviation shown in table are 1.76 and 2.64 μm. Because of the measurement error and uniformity of a printing plate surface, the prediction results can meet the needs of the preliminary testing, which can be used to quickly detect the ink drop state of the device. On the other hand, the drop in the number of plate spreading affected the uniformity of the layout, there are also some fluctuations. As a result, the drop diameter prediction accuracy meets the needs of the actual use, and can be used as a method for measuring the ink drop size anomaly.

55.6 Conclusions

A function relationship between the dot reproduction on printing plate and the ink drop axis length has been established in this paper, according to the experimental design and data analysis. Then a prediction method based on the 50 % order is proposed, which can effectively solve the difficulty of micromeasurement of ink droplets in the equipment routine testing process and simplify the work of equipment inspection.

References

1. Chinese Academy of Sciences, Institute of Chemistry. (2005). *Nano pigment ink for ink-jet CTP printmaking technique*. China ZL200510132249.9, 12.27.
2. Chinese Academy of Sciences, Institute of Chemistry. (2006). *Process for preparing highly hydrophilic alumina film material*. China ZL200610011259.1, 1.23.
3. Zhang, L., & Xin, X. (2010). Research status and development of water based inkjet ink. *Packaging Engineering, 11*, 128–131.
4. Chinese Academy of Sciences, Institute of Chemistry. (2005). *Computer direct printmaking plate and preparation method there of*. China ZL200510132247.X, 12.27.
5. Zhang, Y. (2013). *Study on the key technology of the new inkjet plating-making equipment*. Beijing: Beijing Institute of Graphic Communication.
6. Kipphan, H. (2001). *Handbook of print media: technologies and production methods*. Berlin: Springer.
7. Wang, C. (2008). Analysis and research of the ink-jet printing quality. *Packaging Engineering, 2*, 62–64.
8. Chinese Academy of Sciences, Institute of Chemistry. (2009). *CTP plate making method and apparatus by using ink jet imaging principle*. China ZL200510132248.4. 11.25.
9. Beijing Nano Think New Printing Technology Co., Ltd. (2010). *Automated inkjet printing plate-making equipment and continuous transport mechanism thereof*. China ZL201020581058.7.2.1.
10. Zhiguo, M., & Zhu, Y. (2015). CNC system design of array dual-mode jet printing platform. *Packaging Engineering, 05*, 95–99.
11. Song, B., & Tang, Z. (2011). Parameter analysis of droplet ejection of piezoelectric ink-jet printing. *Packaging Engineering, 19*, 101–104.
12. Song, B., & Tang, Z. (2014). Effect of fluid viscoelasticity on the droplet parameters of inkjet printing. *Packaging Engineering, 15*, 118–123.

Chapter 56
Application of the New Hybrid Screen Dot in Inkjet Plate-Making Technology

Huanhuan Jia, Yunzhi Chen and Xin Wang

Abstract According to the characteristics of inkjet plate-making technology, the development and application of new hybrid screen dot is aimed to improve the quality of the inkjet plate and the reliability of inkjet plate-making technology. First, theoretically we prove the mechanism why the new hybrid screen dot can eliminate the inherent limitations of the inkjet technology, then compared to analysis the plate image effects between the hybrid screen dot and Amplitude Modulated (AM) screen dot which is outputted in the same print mode. The experimental results show that the hybrid screen dot significantly improves the image quality in the plate. The application of new hybrid screen dot not only reduces the human visual sensitivity when droplet deviations occur, but also breaks the frequency of each horizontal line in some degree, thus effectively improves the quality of the inkjet plate.

Keywords Inkjet plate-making technology · Hybrid screen dot · Screening

56.1 Introduction

Inkjet plate-making technology is a new Computer to Plate (CTP) technology. This kind of CTP output the information after separation, Raster Image Processor (RIP) and imposition to the plate by inkjet printing method without developing, fixing, washing, and other cumbersome process and this plate can be used for

H. Jia (✉) · Y. Chen (✉)
Tianjin University of Science and Technology, Tianjin, China
e-mail: jiahuanhuan_tust@126.com

Y. Chen
e-mail: yzchen@tust.edu.cn

X. Wang
Beijing Zhongke Nano-Think Print Technology Co., Ltd, Beijing, China

printing just by direct heating curing. This new plate-making technology not only reduces the cost of supplies, but also is environment-friendly without any pollution, so, it is called a green plate-making technology in the true sense [1, 2]. But for inkjet plate-making technology, it is an emerging technology system which is very different from the photographic imaging system. So, the inkjet technology inherent difficulty of inkjet ink dot positioning is a huge challenge for the quality control of the inkjet plate image. The actual landing position of ink droplets may have some part of the deviation, which will lead to some dark and light stripes extending along the X-axis direction and directly using the conventional screen dot on the market mainly for laser CTP cannot effectively solve the quality problem.

Therefore, according to the characteristics of inkjet plate-making technology, this article presents the development and application of new hybrid screen dot improvement ideas that in the conventional AM screen dot edge to join around a certain amount of Frequency Modulated (FM) random scatter dot, to improve or eliminate the nonuniform stripes and interference streaks in the process of making a plate, by reducing the human visual sensitivity of droplet deviations and breaking the output frequency of each horizontal line of PASS to a certain extent. The development and application of new hybrid screen dot to improve the inkjet plate quality is not only an eager need to overcome the difficulties, but also a research topic and the key to enhance the reliability of the inkjet plate-making technology [3].

56.2 Control Principle of Inkjet Plate-Making Technology

56.2.1 Analysis of Multi-PASS Inkjet Printing Mode

Inkjet plate-making technology finishes image output through controlling two-dimensional motion. During the process of two-dimensional motion, the carriage unit lateral direction of movement is called X-axis direction, while the direction of the plate longitudinal movement is called Y-axis direction. A complete inkjet plate-making movement of the printhead along X-axis direction is called 1PASS, and the image formed in this process is called 1PASS-image. The multi-PASS printing mode refers to that the printhead must pass through multiple inkjet printing to get a complete one-bit image [4, 5].

Due to the limitation of the physical arrangement of the nozzles, getting a complete high-resolution image needs to get through multi-PASS print. The first or previous PASS print does not achieve the required resolution, so, in order to achieve different print resolution, it needs to get through the horizontal and vertical embedded multi-PASS print. It also means that multi-PASS printing mode is designed to meet the requirements of different print resolution [6]. Take, for example, the 1200 dpi solid that is printed by a resolution of 600 dpi printhead. The
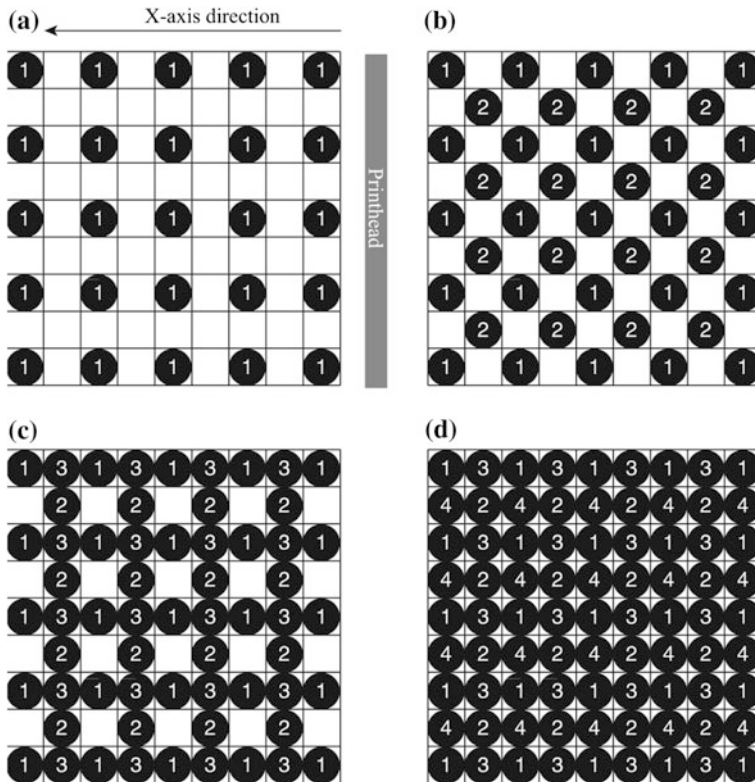
Fig. 56.1 Printing process of 1200 dpi solid in multi-PASS mode. **a** After the first PASS. **b** After the 1+2 PASS. **c** After the 1+2+3 PASS. **d** Completed solid after a period 4 PASS

basic principle of multi-PASS printing process is shown as Fig. 56.1 in which the black dots indicate print and is filled with 1 data while the blank indicates non-print and is filled with 0 data.

Seen from the inkjet printing process in multi-PASS mode, each row of pixels in each PASS are jetted by the same nozzle, while each column of pixels by different nozzles. When 4PASS is completed, an effective period of 1200 dpi image will be printed out. As it happens, the entire printhead also has moved one period, so constantly repeated until the entire image has been completed. Correct step distance can ensure that the ink dot overlap or separation phenomenon will not happen in inkjet printing process [7].

Fig. 56.2 Problems caused by the deviation of ink droplets landing position
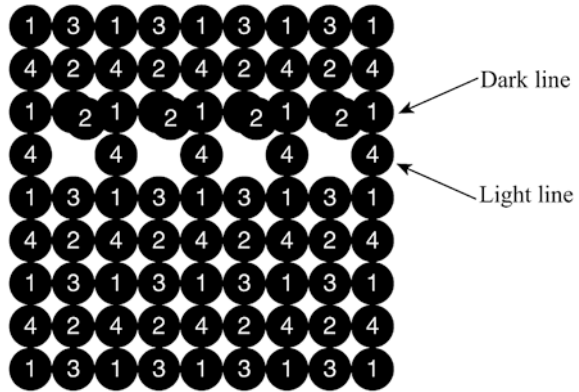
56.2.2 Shortage of the Multi-PASS Inkjet Printing Mode and Application of the New Hybrid Screen Dot

Analysis of multi-PASS inkjet printing mode shows, in X-axis direction every single pixel line of 1200 dpi solid formed by the two nozzles through 2PASS embedded print. While in reality, after the inkjet ink dots jetted, the actual landing position of ink droplets may have some part of the deviation, which will lead to some dark and light stripes extending along the X-axis direction [8, 9], as shown in Fig. 56.2.

Furthermore, since the same frequency for each horizontal line in every PASS and the deviation of the actual ink dots placement, it will inevitably produce interference fringes phenomena [10, 11], and with the increase in the number of PASS, the probability of the emergence of streaks also increased significantly, leading to the inkjet plate quality deterioration.

In order to solve this bottleneck restricting problem of the inkjet plate quality, this paper presents the development and application of new hybrid screen dot improvement ideas, that in the conventional AM screen dot edge to join around a certain amount of FM random scatter dot, to improve or eliminate the nonuniform stripes and interference streaks in the process of making a plate. Take 1800 dpi, 150L, 75° RIP screen output as the example, the microscopic effect contrast between AM screen dot and the hybrid screen dot is shown in Fig. 56.3.

Using Photoshop software to simulate the deviation of the actual ink dots placement in the process of making a plate, the microscopic effect contrast of above is shown as Fig. 56.4.

Apparently seen from the above simulation results comparison, when the ink droplets placement deviations occur in the process of making a plate, along the X-axis direction, the deviation ink droplets will appear regularly in the blank space among the AM dots. This will be shown as dark and light stripes at the macro level. However, the hybrid screen dot since the edge there are random scatter dots, not only reduces the human visual sensitivity when droplet deviations occur, which will

(a)   (b)
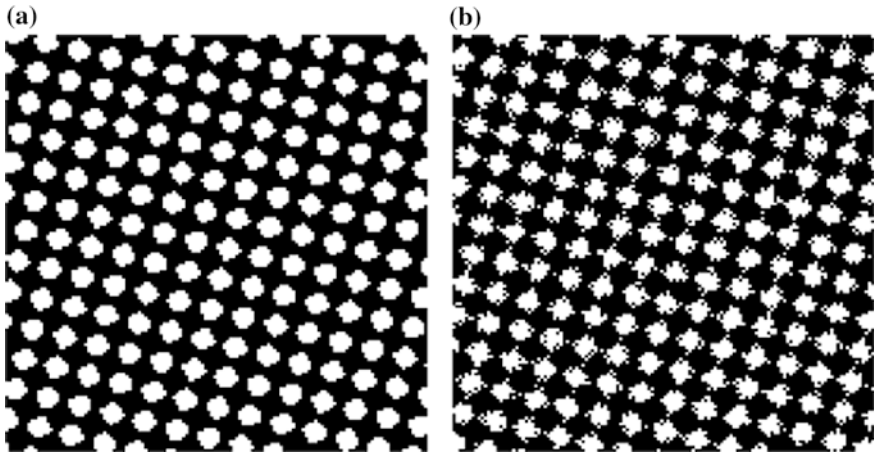
Fig. 56.3 Microscopic effect contrast between *AM* screen dot and the hybrid screen dot. **a** 60 % *AM* screen dot. **b** 60 % Hybrid screen dot

(a)   (b)
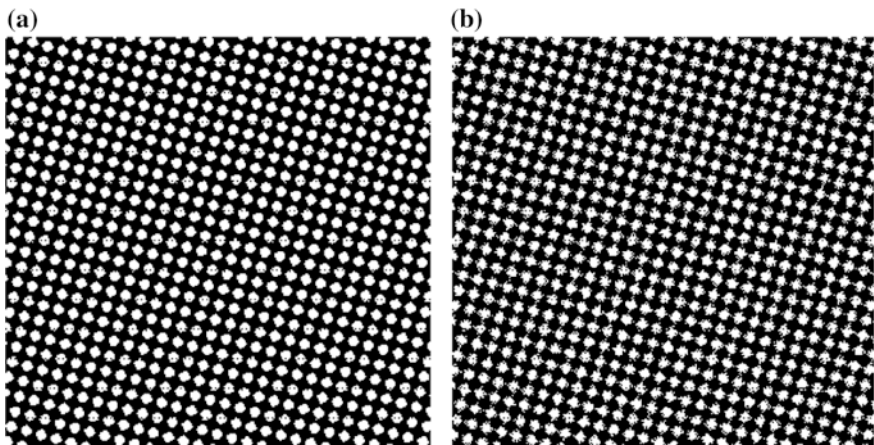
Fig. 56.4 Microscopic effect contrast between *AM* dot and hybrid dot when the ink dot landing deviations occur. **a** 60 % *AM* screen dot. **b** 60 % Hybrid screen dot

greatly reduce the chances of stripes at the macro level, but also breaks to a certain extent the frequency of each horizontal line in every PASS, which will eliminate the interference streaks, thus improving the image quality on the plate. It should be noted that no matter what kind of screen dot output, the screen grids of solid color are all completely filled, so the two output effect is the same. Therefore, for the solid color, adjusting the single droplet size can make sure that the leakage white still does not appear even when the ink dot placement deviations occur.

56.3   Experimental Design

56.3.1   Conditions and Environments

Zhongke Nano-Think NT220-116C inkjet plate-making system, HandPic ReView PRO, Photoshop CS5, Illustrator CS5, temperature 21–25 °C, relative humidity 50–60 %.

56.3.2   Test File

Test file is composed by 10–100 % gray gradation separated by 10 %, as shown in Fig. 56.5.

56.3.3   Test Method

Get the one-bit tiff file of round AM screen dot and hybrid screen dot, respectively, using the NT220–116C inkjet plate-making system at the parameter of 1800 dpi, 75°, then put the two files together with Photoshop CS5 software, as shown in Fig. 56.6.

Make plate with the combined one-bit tiff file in 1800 dpi, 3PASS printing mode, then compared to analyze the plate image effects between the two kind of screen dot.

56.3.4   Results and Discussion

Compare and observe the plate image effects between AM and hybrid screen dot, and the statistical data of stripes at each tone of the gray gradation is shown in Table 56.1

Take the 60 % tone for example, at the same position where AM screen dot has stripes at the macro level, while hybrid screen dot does not, both microscopic screenshots (50X) are shown in Fig. 56.7, and the red box outlines the position where the stripe appears.
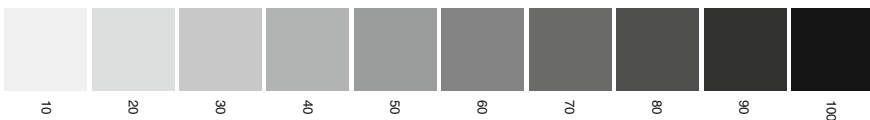
Fig. 56.5 10–100 % *gray* gradation test file
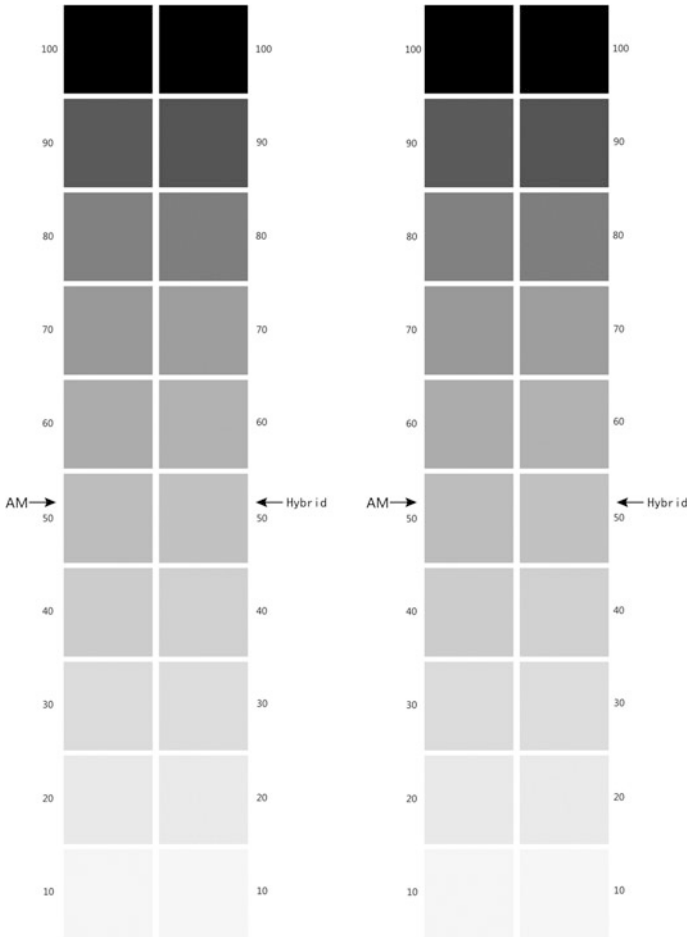
Fig. 56.6 Schematic drawing of the combined one bit-tiff file

Table 56.1 Statistical data of stripes at each tone of the gray gradation

Tone of gray gradation (%)	10	20	30	40	50	60	70	80	90	100
Amount of AM screen dot	0	2	5	10	12	15	17	17	19	0
Amount of hybrid screen dot	0	0	0	0	0	0	0	0	0	0

As is apparent, in AM screening parameters, at the gray gradation there are a lot of stripes throughout the image along the X-axis direction, while in hybrid screening parameters, visually there is not stripe at the macro level.

So it shows that hybrid screen dot than traditional AM screening significantly reduces the probability of stripes appeared at the gray gradation, thus obviously
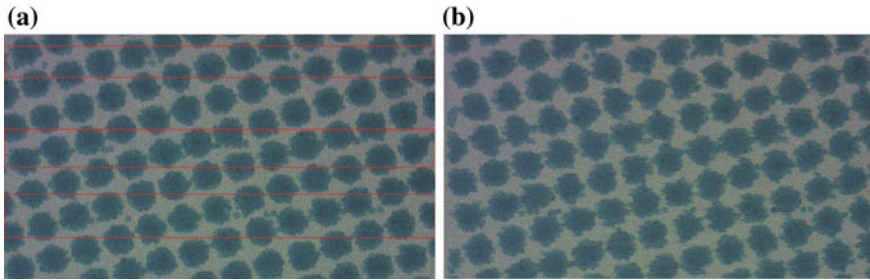
Fig. 56.7 Microscopic screenshots of the position where *AM* has stripes at the macro level, while hybrid screen dot does not, **a** 60 % AM screen dot, **b** 60 % hybrid screen dot

improves the image quality of inkjet plate. In addition, compared and observed visually the plate image effects between AM and hybrid screen dot, there are a lot of interference streaks at AM screening parameter, while the hybrid screen dot at the entire tone has eliminated these problems.

56.4 Conclusions

Based on the principle analysis of inkjet plate-making technology in multi-PASS printing mode, this paper discovered the mechanism producing stripes along the X-axis direction and the reason why the image interference streaks occur, thus it proposes the development and application of a new hybrid screen dot to improve and optimize the phenomena. Experimental comparison of two screening methods and results of the analysis show that the hybrid screening can successfully solve this bottleneck restricting problem of the graphic quality on inkjet plate. Besides, to achieve high-quality inkjet plate-making, it provides new ideas, new methods and new technology, and has laid a solid foundation for industrial applications of the inkjet plate-making system.

References

1. Song, Y. (2011). Green plate-making technology based on nanomaterials. *Bulletin of the Chinese Academy of Sciences, 1*, 52–53.
2. Offset Printing CTP, Commonly Used Lasers in CTP Systems.
3. Wang, C. (2007). Analysis and Research of the inkjet printing quality[J]. *Packaging Engineering, 02*, 55–57.
4. Kipphan, H., & Xiepunan, W. (2004). Handbook of print media. *The world book publishing in guangdong, 11*.
5. Liu, T. (2005). Overview of inkjet printing technology. *Image Technology, 3*, 26–29.

6. Luo, J. (2010). Design of control system of the wide-format digital inkjet printer. Chongqing: Chongqing University.
7. Mcllroy, C., Harlen, O. G., Morrison, N. F. (2013). Modelling the jetting of dilute polymer solutions in drop-on-demand inkjet printing. *Journal of Non-Newtonian Fluid Mechannics*, *201*, 17–28.
8. Wang, Y., & Zhang, X. (2009). *Freeform fabrication with micro-droplet jetting* (p. 10). Wuhan: Huanzhong Universtity of Science and Technolog Press.
9. Lee, E. R. (2003). Microdrop generation. Boca Raton: CRC Press LLC.
10. Yao, H. (2000). Digital screening technology. Printing Industry Press, 7.
11. Yao, H. (2005). Printing image processing. *Shanghai Science and Technology Press, 3*, 209–307.

Chapter 57
Effect of Paper Optical Characteristics on Tonal Gradation Reproduction in Inkjet Printing

Yumei Li, Xiaomeng Cui, Shengming Zhang, Qianqian Sun and Chuanjie Liu

Abstract Paper characteristics are important determinants to print quality, especially the optical characteristics of paper to color reproduction. In order to analyze the correlation between characteristic details and results, a simulation experiment was conducted. Five kinds of paper in three major categories were selected and three major optical characteristics, including whiteness, opacity, and chromaticity, were detected. Then a standard digital test format was printed with digital inkjet printer to optimize the output color quality. The tone reproduction and color gamut accuracy were analyzed by comparing the tonal gradation of primary color, secondary color and tertiary color. And the color gamut was created by Verify module in EFI software and was compared by pairwise comparison analysis. Finally, the primary relationships between paper optical characteristics and tone reproduction were summarized tentatively. The experimental results show that paper whiteness and chromaticity have a significant effect on tone reproduction, yet the effect of opacity is not obvious. This study provides good foundation to further mechanism study in the future work.

Keywords Optical characteristics of paper · Printing quality · Color reproduction · Color tonal gradation

57.1 Introduction

Paper is the most popular printing material used in printing products. The effect of paper optical characteristics on tonal gradation reproduction is one of the hot research focuses for domestic and overseas researchers to promote the development of new theory and technology study in printing quality optimization continuously [1]. The paper optical characteristic will determine the color reproduction in inkjet

Y. Li · X. Cui (✉) · S. Zhang · Q. Sun · C. Liu
Engineering College, QuFu Normal University, Shandong Province, China
e-mail: Cuixiaomeng.serena@qq.com

Table 57.1 The paper type and number

The paper number	Paper type	Grammage
1#	High glossy photo paper	240
2#	Semiglossy paper	190
3#	Semiglossy paper	180
4#	Matte inkjet paper	130
5#	Matte inkjet paper	130

printing [2]. In this research, the effect of optical characteristics was emphasized by analyzing tonal gradation reproduction in color printing which could be of some help to technologists in choosing appreciate paper in craftsmanship design. And a simulation experiment was carried out to discuss the primary relationships between paper optical characteristics and tonal gradation.

57.2 Experiments

In this experiment, whiteness, opacity, and chromaticity of paper were tested. Then a simulated printing with standard digital inkjet printer was conducted by using color management technology, and the chromaticity reproduction accuracy was measured.

Samples

In the experiment, five kinds of three categories of paper selected are shown in Table 57.1.

Detecting equipments

YT—48 Digital whiteness meter
X—rite I1 Pro2 Spectrophotometer3
GretagMacbeth Profile maker 5.0.8 software
Target A 600dpi CMYK 071025color standard digital format

Inkjet printing equipments

Epson stylus Pro 7880C
Epson eight-color ultra Chrome K3 ink
EFI Colorproof XF software driver

57.3 Results and Discussion

57.3.1 Paper Optical Characteristics Analysis

In this study, five kinds of three categories of paper were detected. On each sheet, 10 different positions were selected randomly to measure the paper optical

Table 57.2 Optical characteristic parameters of five kinds of paper

Sample	Opacity (%)	Whiteness (%)	Lab		
			L	a^*	b^*
1# 240 g/m^2 High glossy photo paper	98.07	87.27	94.94	−0.49	−2.20
2# 190 g/m^2 Semiglossy paper	94.93	88.39	94.76	−0.09	−3.12
3# 180 g/m^2 Semiglossy paper	92.69	87.66	94.51	0.25	−4.24
4# 130 g/m^2 Matte inkjet paper	97.33	91.90	96.05	0.84	−4.67
5# 130 g/m^2 Matte inkjet paper	99.41	92.93	90.91	2.83	−12.56
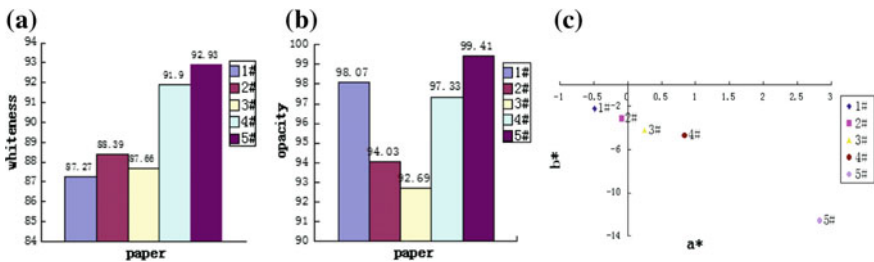
Fig. 57.1 The figures of optical characteristics of five kinds of paper **a** Whiteness of samples. **b** Opacity of samples. **c** Relative position of chromaticity

characteristics including whiteness, opacity, and chromaticity. Then the average values were calculated and were accurate to 0.01. The experimental results are listed in Table 57.2.

The charts of different optical characteristics are shown in Fig. 57.1.

Figure 57.1 describes paper whiteness. The whiteness of paper 1#, 2#, and 3# are close. The whiteness of 4# is close to 5#, both of which are higher than the other three. Correspondingly, the opacity of 4# and 5# are also higher. That is because white paint leads to the increase of opacity which is coated on paper surface [3].

In Fig. 57.1, the opacity of 1#, 5#, and 4# is higher, 3# is the lowest and 2# is in the middle. This shows that the paper opacity is associated with grammage and paper surface coating method [4].

Relative position of each paper chromaticity is plotted in CIEL$^*a^*b^*$ color space as is shown in Fig. 57.1. 5# paper looks blue-violet. 4# and 3# paper looks slightly blue. Only 1# and 2# paper are close to visual whiteness. From Table 57.2, compared with the value of a^*, b^*, 5# is obviously different and the visual effect is blue.

57.3.2 *Paper Chromaticity Reproduction Analysis*

The chromaticity value of the self-made standard board was measured. Then the tonal gradation accuracy was analyzed and the color gamut figure was compared, forming the space figure as follows.

57.3.2.1 Analysis of the Tonal Gradation

Primary color tonal gradation

From Fig. 57.2, except for two apparent measuring errors in K and C tone curves, the coincidence of C tone curve is high. The curves of K and M are relatively centralized. In Y tone curves, the reproduction ability of 5# is obviously inferior to others. The coincidence of 1# and 2# is high.

Secondary color tonal gradation

From Fig. 57.3, the coincidence of secondary color tone is higher than primary color. Except for 5#, other curves are quite similar. The value in shaft b^* of 5# is obviously different from others, which means that the dynamic range of tone is apparently lower than others.

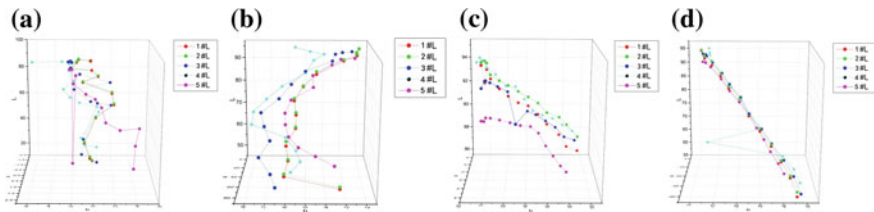**Fig. 57.2** The tone–chroma relationship curves of primary color **a** K tone curve, **b** M tone curve, **c** Y tone curve, **d** C tone curve
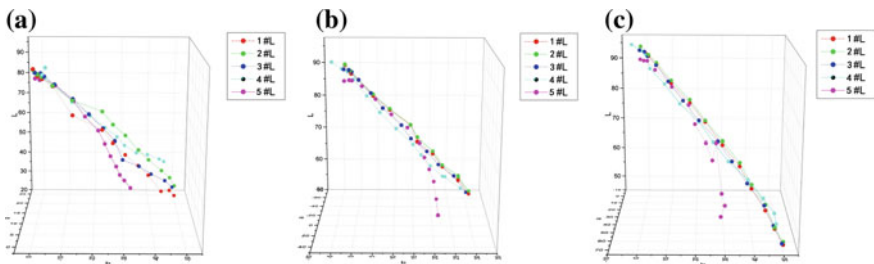
Fig. 57.3 The tone–chroma relationship curves of secondary color **a** B tone curve, **b** G tone curve, **c** R tone curve
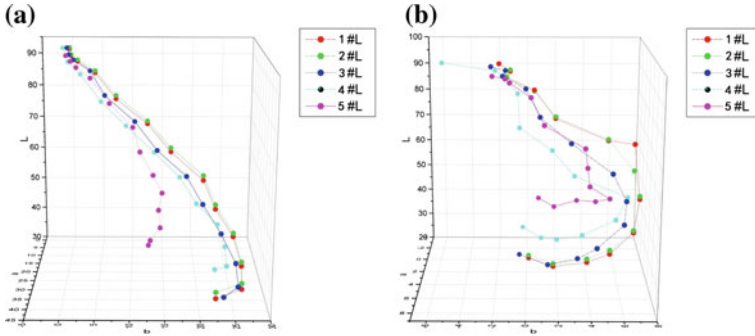
Fig. 57.4 The tone–chroma relationship curves of tertiary color **a** Skin Tone curve, **b** C + M + Y tone curve

Tertiary color tonal gradation

In Fig. 57.4, in skin color reproduction, 5# deviates seriously and shows low dynamic range. The coincidence is higher in other curves. In gray color reproduction, the coincidence of 1#, 2# is higher, while others are more dispersed. These indicate that gray color is more sensitive to optical properties [5], as is shown in highlight and in shadow, the coincidence is high, yet in mid-tone it is scattered.

From above, the comparison of primary color, secondary color, and tertiary color shows that the tone reproduction of 1# and 2# is very close, 4# and 3# is scattered; however, 5# deviates seriously from all the others and the tone compression is serious.

57.3.2.2   Analysis of the Color Gamut

The color gamut of pair combination was compared. Three kinds of representative combinations were revealed in the following figures. The color of 5# is partial blue, while 2# is visual whiteness; therefore, they are combined to analyze the effect of paper chromaticity on tonal gradation. Except for 5#, the opacity of 1# is the highest, and 3# is the lowest. The whiteness of 4# is the highest and 1# is the lowest.

In Fig. 57.5, blue-violet part is the color gamut of 1#, which is larger than 3#, blue part is the overlap of 1# and 3#, cyan-blue part of 3# is more than 1#. The majority of the stereogram is blue, indicating the color space of 1# and 3# is close. While there is more color reproduction in 3#. In the lightness, the reproduction of 1# is better than 3# paper.

In Fig. 57.6, blue-violet part is the part of 1#, which is beyond 4#, the emerald green part is the overlap of 1# and 4#, and the blue part of 4# is beyond 1#. Differences are in light tone, and the color reproduction of 4# is better than 1#. In shadows, the reproduction of 1# is better than 4#.
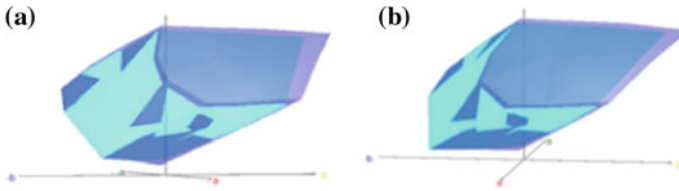
Fig. 57.5 Color gamut comparison of 1# and 3#
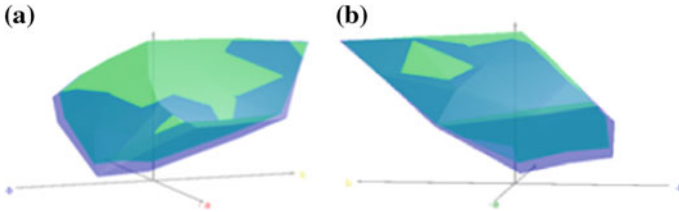
Fig. 57.6 Color gamut comparison of 1# and 4#
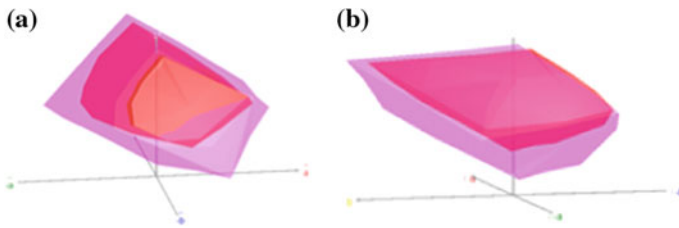
Fig. 57.7 Color gamut comparison of 2# and 5#

In Fig. 57.7, the pink part of 2# is beyond 5#; the rose red is the overlap of 2# and 5#. The color space of 5# is smaller. In the shadow, the ability of color saturation reproduction in blue space of 5# is stronger.

57.3.3 Analysis of Effect

In the simulation experiment, the effect of optical properties on tonal gradation was analyzed.

Concerning whiteness characteristic, the whiteness of 5# is the highest, but the tone copy and color gamut is poor, which was mainly affected by the partial color [6]. The whiteness of 4# is higher and its color is not partial. In light tone and mid-tone, the color gamut of 4# is very rich. So if the whiteness is higher, the printing color in light tone and mid-tone is better.

Concerning opacity characteristic, except for 5#, the opacity of 1# is the highest. The tone copy of 1# is good, which is close to 2#, but the opacity of 2# is far lower than 1#. The opacity of 3# is the lowest, but its color gamut and tone copy are also good. So in a certain range, there is no obvious effect of the opacity on the color of printed image.

Concerning $L^*a^*b^*$ value characteristic, the color of 5# is serious blue-violet. Although the whiteness and opacity of 5# is higher, the tonal gradation copy is poor, and only the blue reproduction is better than that of others. The color of 1# and 2# is close to visual whiteness. Their tonal gradation copies are all good. It is obvious that the color of paper has an effect on tonal gradation reproduction.

57.4   Conclusions

In this study, three paper optical properties, including whiteness, opacity, and chromaticity, were focused. A simulation experiment was carried out to analyze the effect of optical properties on different tone range gradation. Through the experimental data and the above analysis, conclusions can be drawn as follows.

The whiteness of paper has an obvious effect on tonal gradation. The higher the whiteness of paper is, the better the printing color in light tone and mid-tone would be. In a certain range, both the highest opacity in 1# and the lowest in 3# are all good at color image reproduction, so there is no obvious effect of the opacity on tonal gradation. The color shift of paper has an obvious impact on the copy of tonal gradation. When the color of paper is visual whiteness, the tonal gradation reproduction is good. The color shift causes the tonal gradation reproduction inaccurate. In this case, special attention should be paid to the color shift phenomenon when doing technological design.

References

1. Kibirkštis, E., & Kabelkaitė, A. (2013). Microscopic analysis of recycled paper effect on print quality parameters. doi:10.1002/jemt.22243
2. Zhao, C. (2014). The effect of paper characteristics on control of printing color. *Shanxi University of Technology, 07*, 26–28.
3. Lundström, J., & Verikas, A. (2013). Assessing print quality by machine in offset colour printing. *Knowledge-Based Systems, 37*, 70–79.
4. Wang, H., & Cui, X. (2012). Effect of paper color on color printing gray balance. *Packaging Engineering, 17*:105–108 + 121.
5. Yuan, W., & Jiang, Q. (2012). A brief analysis of the effect of the paper on the quality of printing reproduction. *Guangdong Print, 01*, 58–60.
6. Jiang, L., & Zhao, L. (2008). Effect of paper whiteness on the quality of printed matter. *Packaging engineering, 03*, 66–68.

Chapter 58
Research on the Technique of Ink Presetting for Domestic Small and Medium-Sized Packaging Printing Enterprises

Xiaoli Liu, Bingzhong Qiu, Longlong Bian, Hongxiu Pang and Fan Zhang

Abstract In most small-size packaging printing enterprises, waste of paper and ink and low production efficiency still exist. The reason is that ink supply amount is estimated according to the operator's experience and ink key is adjusted by hand in the process of ink presetting. This article discusses the digitalization of ink supply in printing equipments with interface of CIP3/CIP4. The experiment result shows that the effect of ink presetting is good, the preparation time is decreased, the production efficiency is improved, the waste of paper and ink are reduced, and the cost is lowered.

58.1 Introduction

With the rapid development of printing industry, the production capacity of packaging printing enterprise has been greatly improved. Many new materials, new techniques, and new equipments appear. This article researches the digitalization of ink supply in printing presses. The design idea is shown in Fig. 58.1. First of all, the images need to be divided into several zones of equal width according to the width of the ink zone. Then find out the dot percentage of each zone on the image and store them to prepare for calculating the ink key open degree. The corresponding relationship between ink key open degree and dot percentage is written into a lookup table. The information of ink is read according to the lookup table when a program is running. The corresponding relationship between ink key open degree

X. Liu (✉) · B. Qiu · L. Bian · H. Pang · F. Zhang
Department of Printing Technology, Shi Jiazhuang Information Engineering Vocational College, Shi Jiazhuang, China
e-mail: 343625567@qq.com

Fig. 58.1 Design ideas
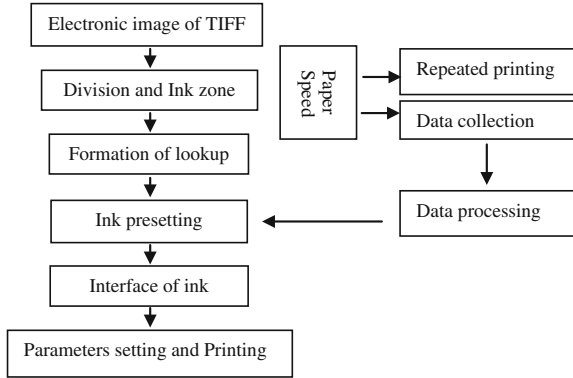
and dot percentage depends on the structure of printing press, paper, printing speed, temperature, and humidity, the balance of ink and water, and so on. At last, workers can open image in the interface of ink presetting software and set parameters in the file menu.

58.2 Ink Coverage Calculation

When a color image is printed, we need to make many pieces of plates. In most cases, there are great differences between plates. In order to get accurate color, we need to adjust the volume of ink in each ink zone of printing. The volume of ink is determined by ink coverage percentage of each ink zone on plate. Consequently, we first need to divide TIFF file into multiple zones and calculate dot percentage of each ink zone on plate [1]. The TIFF file processing is shown in Fig. 58.2.

58.2.1 Number of Ink Zone Calculation

Considering the work habits of factory masters, the TIFF file needs to be divided multiple zones from the middle of the image. Suppose image height is a, image width is b, image resolution is r, the total number of ink zone for printing press is s, the number of ink zone occupied by the image is n, p represents the number of pixel on the width of one ink zone, q is the number of pixel on the length of one ink zone, the width of ink zone is v, the maximum width in the length direction of plate is w.

Consequently, the width of ink zone: $v = w/s$; The number of pixel on the width of one ink zone: $p = w * r/s$; The number of ink zone is described as Eq. (58.2.1).

$$n = \begin{cases} as/w, & as/2w \text{ is an integer,} \\ as/w + 1, & as/2w \text{ is not an integer.} \end{cases} \quad (58.2.1)$$

Fig. 58.2 TIFF processing
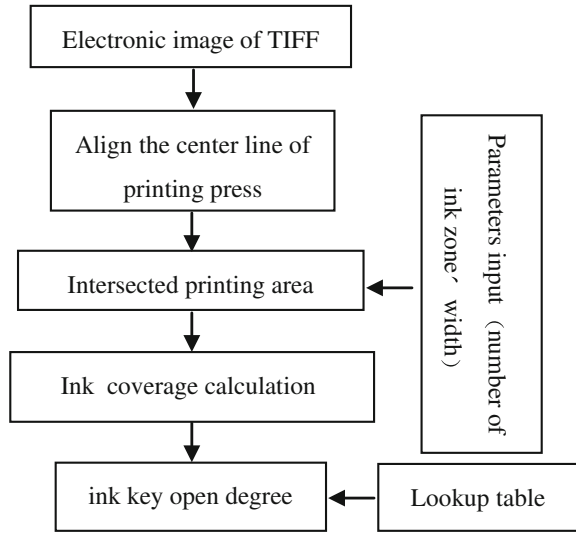
when $(a*s)/2w$ is an integer, $(a*s)/w+1$ represents the number of ink zone in the print. When $(a*s)/2w$ is not an integer, $(a*s)/w+1$ represents the number of ink zone in the print [2]. The image location is shown in Fig. 58.3.

58.2.2 Ink Coverage Calculation

According to the above partition, the number of pixel in one ink zone is p in the horizontal direction, $p = w*r/s$; The number of pixel on one ink zone is q in the vertical direction, $q = b*r$; The number of ink zone occupied by the image is n; $S_y x$
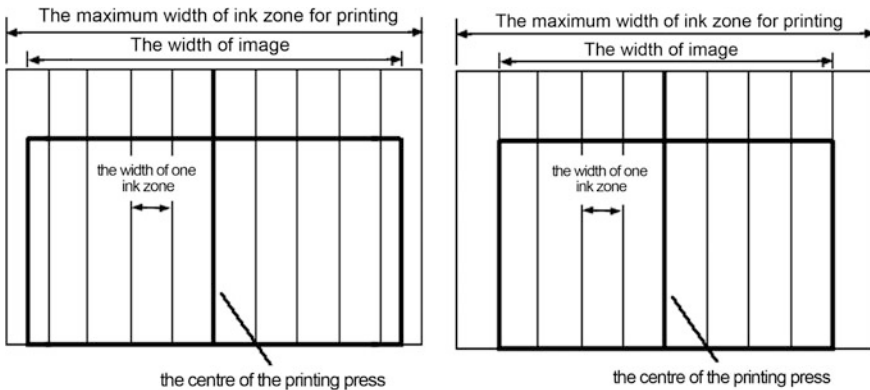
Fig. 58.3 Image location

(i, j), $S_m x(i, j)$, $S_c x(i, j)$ and $S_k x(i, j)$ represent Y, M, C, K ink coverage of pixel (i, j) in x ink zone; $i = (x - 1)p, \ldots xp$; $j = 1, 2 \ldots q$; $x = 1, 2, \ldots n$ [2, 3].

Taking cyan as an example, $S_c(i, j)$ is C ink coverage of pixel (i, j) in x ink zone, $S_c[x]$ is C ink coverage of total pixel in x ink zone.

$$S_c[x] = \sum_{j=1}^{q} \sum_{i=(x-1)p}^{xp} S_c x(i, j), \quad (i = (x - 1)p, \ldots xp; \ j = 1, 2, \ldots q). \quad (58.2.2)$$

Therefore, we can find the average ink coverage by dividing C ink coverage of total pixel by total pixels. The average ink coverage is described as Eq. (58.2.3).

$$C[x] = S_c[x]/(p * q), \quad (x = 1, 2, \ldots n). \quad (58.2.3)$$

Similarly, Eq. (58.2.4), Eq. (58.2.5), and Eq. (58.2.6) can be used to calculate the Y, M, and K ink coverage for every ink zone [4].

$$M[x] = S_m[x]/(p * q), \quad (x = 1, 2, \ldots n). \quad (58.2.4)$$

$$Y[x] = S_y[x]/(p * q), \quad (x = 1, 2, \ldots n). \quad (58.2.5)$$

$$K[x] = S_k[x]/(p * q), \quad (x = 1, 2, \ldots n). \quad (58.2.6)$$

58.3 Formation of Lookup Table for Ink Presetting

If we want to find the relationship between ink coverage and ink key open degree, we need to record the relationship between ink coverage and ink key opening for various printed images and set up the lookup table of ink presetting.

58.3.1 Experimental Environment and Condition

Equipment: MITSUBISHI DIAMOND3000LX,
Material: Tianjin Toyo TK THK offset printing ink, 150 g copperplate paper, 350 g whiteboard paper, 80 g offset paper.

58.3.2 Experiment Procedure

(1) We design two pieces of test plate with photoshop software. On the first test plate, there are cyan, magenta, yellow and black color scales. Ink coverages are 0, 5, 10, 15, 20, 25, 30, 35, 40, 45, 50, 55, 60, 65, 70, 80, 90, 100 % for

each color. On the second test plate, there are cyan, magenta, yellow, and black color scales. Ink coverages are 100, 90, 80, 70, 60, 50, 40, 30, 20, 10, 0, 10, 20, 30, 40, 50, 60, 70, 80, 90, 100 %.

(2) The test begins on MITSUBISHI DIAMOND3000LX at speeds of 8000 sheets per hour and 5000 sheets per hour. At the same time, we recorded the data which represents the relationship between ink coverage and ink key open degree.

(3) At last, we summarize a lookup table of ink presetting which consists of ink coverage and ink key values by printing a series of impressions in different printing conditions. If we cannot find ink coverages form the lookup table, we can calculate ink key open degree by the following formula. The calculation of ink key open degree is described as Eq. (58.3.1). X_r is on X_a's right, X_l is on X_a's left, Y_l is ink key open degree for X_l [4, 5].

$$\text{ink key open degree} = \begin{cases} (X_r - X_l)/5 * (X_a - Y_l) + X_l, & X_r - X_l = 5\%. \\ (X_r - X_l)/10 * (X_a - X_l) + X_l, & X_r - X_l = 10\%. \end{cases}$$
(58.3.1)

58.4 Rotation Angle of Ink Roller

The adjustment of ink supply is accomplished by ink key open degree and rotation angle of ink roller. The ink key open degree is discussed above. The rotation angle of ink roller can be obtained by experience. The calculation of rotation angle is described as Eq. (58.4.1). Rotation angle is θ, ink key open degree is H_m, the number of ink zone occupied by the image is m [3].

$$\theta = \begin{cases} 12 + \max\{H_1 \ldots H_m\}/6 * (25 - 12), & \max\{H_1 \ldots H_m\} \leq 6; \\ 25 + \max\{H_1 \ldots H_m\}/12 * (35 - 25), & \max\{H_1 \ldots H_m\} \leq 12; \\ 35 + \max\{H_1 \ldots K_m\}/16 * (50 - 35), & \max\{H_1 \ldots H_m\} \leq 16; \\ 50, & \max\{H_1 \ldots H_m\} \succ 16; \end{cases}$$
(58.4.1)

58.5 Software Design

The ink presetting software was written with Visual C++ platform. The system interface includes three parts: toolbar, menu bar, and display area. Open an image in the file menu and input the type of ink, the type of paper, and ink zone width. The software automatically calculates the ink coverage and display ink distribution by column [6].

58.6   Application Example

58.6.1   Production Conditions

Printing equipment: MITSUBISHI DIAMOND3000LX, the maximum printable width is 102 cm, the number of ink zone is 30.

Printing machine: 150 g coated paper, Tianjin Toyo TK THK offset printing ink.

Environmental temperature and humidity: temperature is 25 °C, relative humidity is 60 %.

Preferences: speed is 8000 sph.

Testing tool: colorimeter, magnifier.

58.6.2   Printing Process

(1) Workers open image in the file menu of ink presetting software, as shown in Fig. 58.4.
(2) Set the number and types of parameters, as shown in Fig. 58.5.
(3) Click on the display button, get the ink key values, as shown in Fig. 58.6.
(4) At last, workers preset ink key values on press. We can get qualified printing by fine tuning. The qualified printing is shown in the Fig. 58.7.
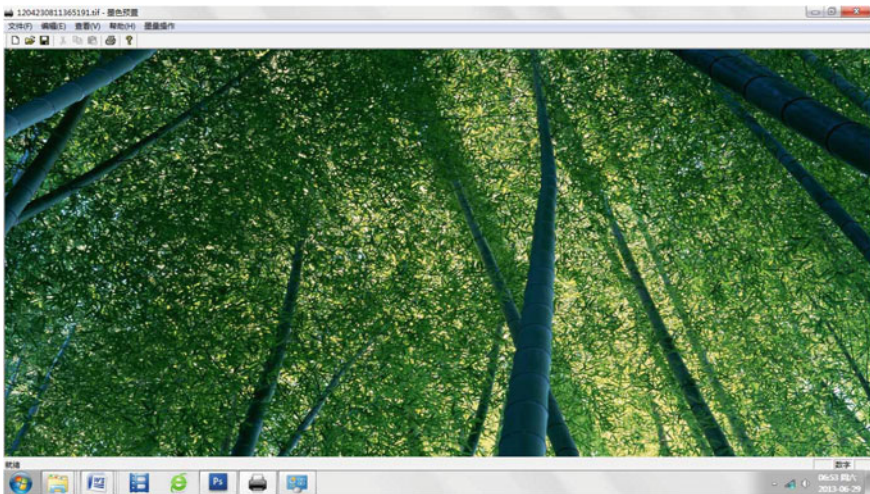
Fig. 58.4 Electronic manuscript of TIFF
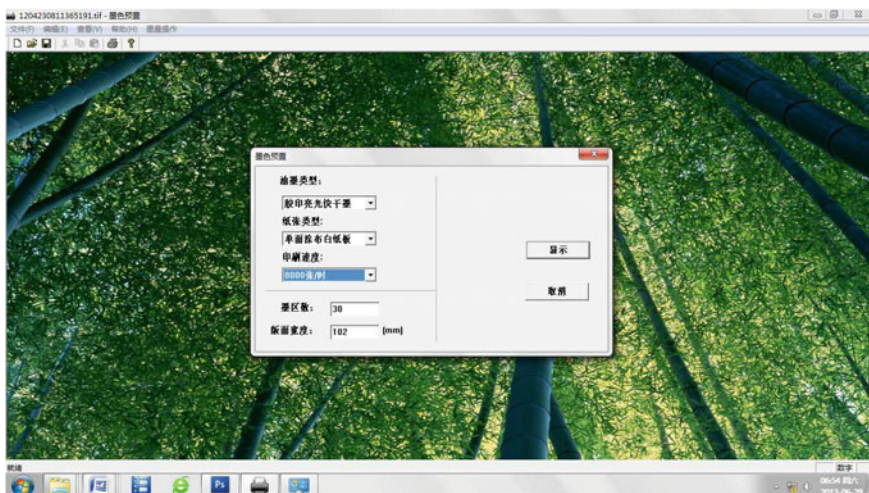
Fig. 58.5 Interface of printing information setting
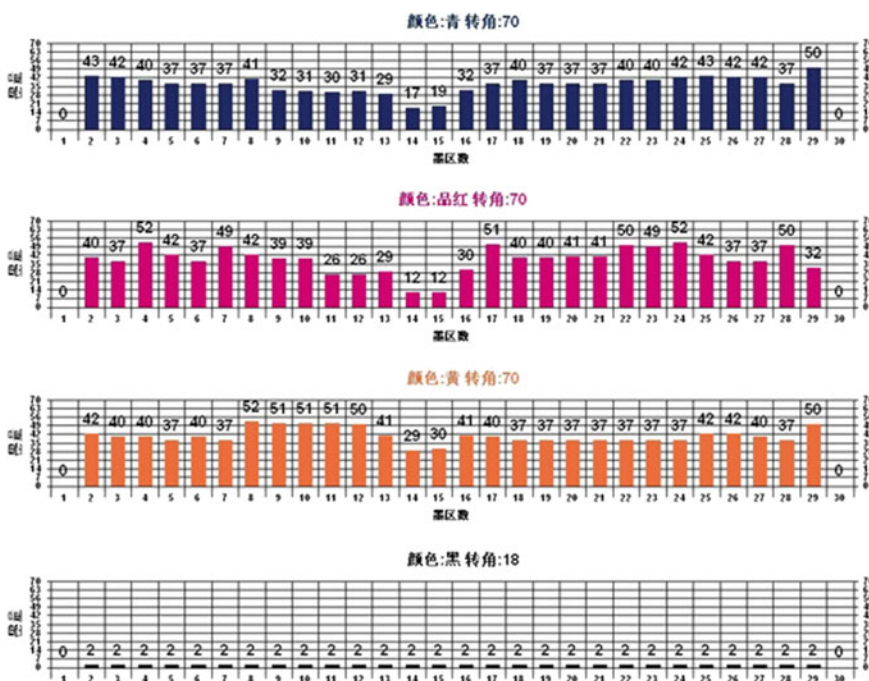
Fig. 58.6 Interface of ink presetting

Fig. 58.7 Printed matter

58.6.3 Analysis of Printed Matter Quality

Solid density for Y, C, M, and K are 1.10, 1.55, 1.25, and 1.10. We can get 4 % dot in the bright region. Printings are aligned with the national standard.

58.7 Conclusions

The experiment results show that the effect of ink presetting is good, the preparation time is shortened, the quality of products and production efficiency are improved, the waste of paper and ink is reduced, and the cost is lowered. Small medium-sized packaging printing enterprises can benefit in the quality of printing production and efficiency.

References

1. Qiu, B.-z., Liu, X.-l., Wei, W., & Zhou, H.-e. (2013). Realization of digital printing workflow for domestic small and medium-sized printing enterprises. *Applied Mechanics and Materials*, *262*, 235.
2. Qiu, B.-z., Liu, X.-l., & Wei, W. (2012). Research on techique of ink presetting and system development based on TIFF file. *Package Engineering*, *33*, 120.
3. Zhang, Y.-m., Zhang, Y.-m., & Zhang, N.-l. (2010). Research on technique of realizing ink key presetting by utilizing PPF file. *Package Engineering*, *31*, 77.
4. Fang, E.-y., & Ge, Z.-h. (2011). Press ink variable feedback technology overview. *Package Engineering*, *15*, 46.
5. Fan, M., Li, H., & Yang, J. (2006). The technology and application of manual—ink presetting. *Printing Field*, *34*, 67.
6. Dong, Z.-b. (2005). The analysis of digital workflow in printing. *Guangdong printing*, *26*, 72.
7. http://www.bisenet.com/article/201002/61612_1.htm.

Chapter 59
Research on Prediction Model of Cyan Ink Dot Area Rate Based on Ink Spectrum

Lizheng Zhang, Guorong Cao, Yue Zhuo and Hongtao Miao

Abstract At particular wavelength point, establish a polynomial model for cyan ink spectrum reflectivity and dot area rate, based on three basic color ink spectrum reflectivity research. Using spectrophotometer to measure sample colors that printed by different proportion two or three basic inks. Through prediction model to get cyan dot area rate, prediction area rates are compared with real printed area rates. Then analyze the model accuracy and establish the compensation curve. The deviation influence of magenta is bigger than yellow, and the deviation is connected with magenta or yellow proportion. Experimental results indicate that the average error range is less than three percents, and using quadratic polynomial model to predict the cyan ink dot area rate is feasible. This study method also can be used in color spectrum separation and replication research.

Keywords Ink spectrum · Ink dot area rate · Polynomial

59.1 Introduction

Precise printing color reproduction is important to printing quality control. There are three color management methods, density control [1], chromaticity control [2], and spectrum control [3]. ZHAO Chenfei analysis the prediction model based on normalization method [4]. The algorithm based on higher derivative is also useful for extracting ink spectrum peak value, but higher derivative requires a large amount of calculations [5]. Li Fang presents a method to build the CYNSN model

L. Zhang (✉) · G. Cao · Y. Zhuo
School of Printing and Packaging Engineering, Beijing Institute of Graphic Communication, Beijing, China
e-mail: zhanglizheng@bigc.edu.cn

H. Miao
Packaging and Printing Department, Henan University of Animal Husbandry and Economy, Zhengzhou, Henan, China

by nonuniform sampling with the standard of error distribution. Yang Huifang divided the color space into five or six partitions that are subdivided into several cells, then establish polynomial color separation model for each cell [6].

In this study, based on analysis of the characteristics of the spectral reflectance curves of primary color ink, establish a polynomial model for cyan ink spectrum reflectivity at 670 nm and dot area rate. Spectrum independent region and cyan spectral curve first-derivative are the methods to identify the 670 nm. The deviation of the polynomial model is also to be discussed, and the average deviation is around two percentage dot values.

59.2 Materials and Methods

59.2.1 Materials

The printing paper is a glossy coated paper from Korea Molin. Printing ink is new caps-g series from DIC. Printing press is Heidelberg SM 102 sheet paper printing machine. Dot value of cyan ink is from 0 to 100 %, every 5 %. Each level cyan is mixed with magenta or yellow. Dot value of mixed magenta or yellow is also from 0 to 100 %, every 5 %. So the number of two inks mixed is 400.

59.2.2 Treatments

Ten printed papers chose randomly were measured, after 15 days. X-rite i1io was used to get the spectrum reflectivity in the range of 380–730 nm, every 10 nm wavelength.

59.2.3 Methods

59.2.3.1 Drawing Spectrum Reflectivity Image

The measured data was be averaged fist, Then matlab software was used to draw the spectrum reflectivity image in the range of 380–700 nm. Every curve corresponded with different ink value and different wave range. The number of each kind ink spectrum reflectivity curve was 20. Three different ink spectrum reflectivity images were put together through image deviation analysis [7]. Independent areas were not marked gray. Intersection areas were marked different level grays. The deepest gray area included three ink spectrum reflectivity values.

59.2.3.2   Spectrum Data Fitting

All cyan spectrum reflectivity curves first-order derivative were got in the matlab software. The relationship between spectrum derivative and wavelength was established. In cyan independent area, and the spectrum derivative similar point, established cyan dot value and reflectivity relationship curves.

59.2.3.3   Reliability Compliance Test

Different proportion of magenta or yellow is used to mix with cyan. The sample spectrum data is used to test the polynomial model precision. The deviation of different mixing proportion is compared.

59.3   Results and Discussion

59.3.1   Ink Spectrum Reflectivity Image Deviation

Three color reflectivity spectrum images are shown in one map, Fig. 59.1. Three light areas represent independent spectrum regions, two darker areas represent two color ink spectrum intersection regions, and the darkest area represent three color ink spectrum intersection region.

   Cyan ink independent spectrum region is the biggest in three colors. It is easy to identify the value of cyan dot percent. Combined with cyan spectrum derivative, Fig. 59.2. The relationship between spectrum reflectivity and dot percent can be made up through using data at 670 nm.

Fig. 59.1 Three ink reflectivity versus wavelength
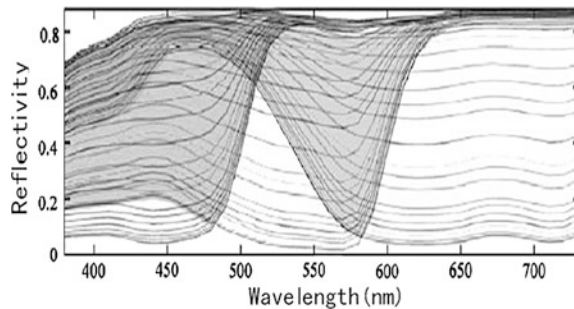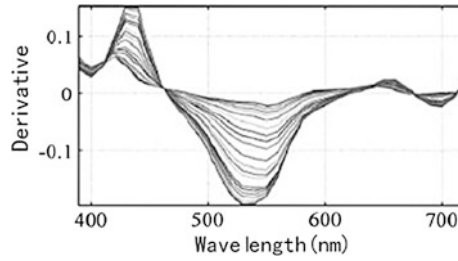
Fig. 59.2 Cyan derivative versus wavelength
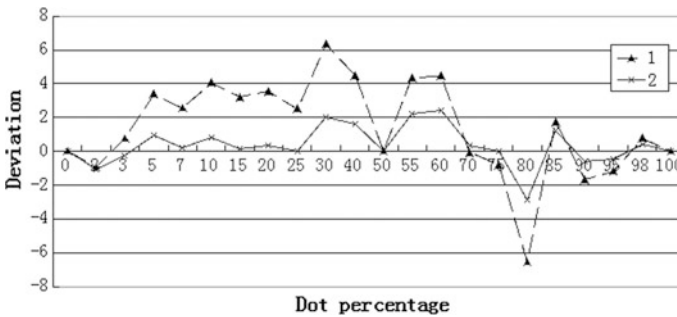
Fig. 59.3 Dot percentage versus Deviation

59.3.2 Spectrum Data Fitting

In order to decrease the data testing, the degree of three point spectrum fitting is compared with the degree of five point spectrum fitting at 670 nm. Use cyan dot value at 0, 50, and 100 % to create predicate polynomial. Use cyan dot value at 0, 25, 50, 75, and 100 % to create other predicate polynomial. The deviation of different percentage for two predicate is compared at Fig. 59.3. Line 1 is deviation from three points fitting, and line 2 is deviation from five point fitting. To insure the predication accuracy, 20 points are used to fitting, and quadratic polynomial is used to predicate cyan dot percentage.

59.3.3 Deviation Changing with Cyan Proportion

Test the spectrum data at 670 nm, when different dot percentage of cyan is mixed with different proportion magenta or yellow. Then the cyan dot percentage is predicated and showed at Tables 59.1 and 59.2. Comparing the predication data and

Table 59.1 Predicate cyan dot percentage when cyan is mixed with magenta

Magenta dot	Cyan dot						
	$M = 10$	$M = 20$	$M = 30$	$M = 40$	$M = 55$	$M = 70$	$M = 85$
$C = 10$	11.32	9.48	9.94	10.76	11.32	11.63	12.22
$C = 20$	19.81	19.32	20.66	21.33	20.85	21.81	22.33
$C = 30$	28.32	29.87	29.35	30.8	31.1	31.21	31.14
$C = 40$	39.98	40.26	40.85	41.05	42.29	41.88	42.95
$C = 55$	55.95	56.37	55.21	58.33	57.11	58.19	58.1
$C = 70$	72.12	71.15	72.27	72.25	71.93	72.49	73.1
$C = 85$	87.42	88.83	86.22	85.97	85.62	87.26	88.9

Table 59.2 Predicate cyan dot percentage when cyan is mixed with yellow

Yellow dot	Cyan dot						
	$Y = 10$	$Y = 20$	$Y = 30$	$Y = 40$	$Y = 55$	$Y = 70$	$Y = 85$
$C = 10$	9.06	9.95	10.24	10.13	9.77	9.76	11.02
$C = 20$	20.78	19.47	19.52	19.68	20.22	19.7	20.76
$C = 30$	31.23	29.54	29.96	30.67	29.97	31.6	31.43
$C = 40$	38.34	38.84	39.89	41.82	40.81	42.78	42.31
$C = 55$	57.34	55.53	55.53	56.1	56.18	55.67	57.96
$C = 70$	72.19	70.96	70.33	72.84	72.09	72.82	72.97
$C = 85$	87.1	85.99	85.78	87.03	86.86	87.55	85.11
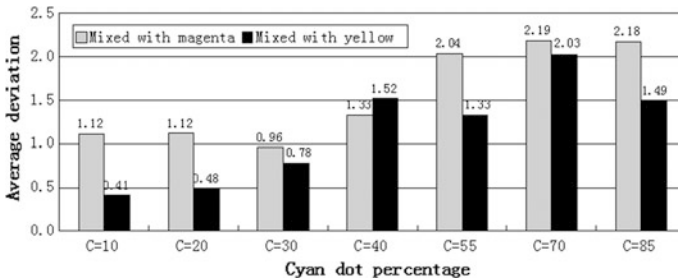
Fig. 59.4 Cyan dot percentage versus average deviation. The number of *gray strip* is cyan average deviation when cyan is mixed with magenta at different percentage. The number of *dark strip* is cyan average deviation when cyan is mixed with yellow at different percentage

real mixing percentage to get the deviations. From Fig. 59.4, deviations of cyan predication value are changing large when the cyan proportion is increased. The largest deviation is controlled below 2.5.
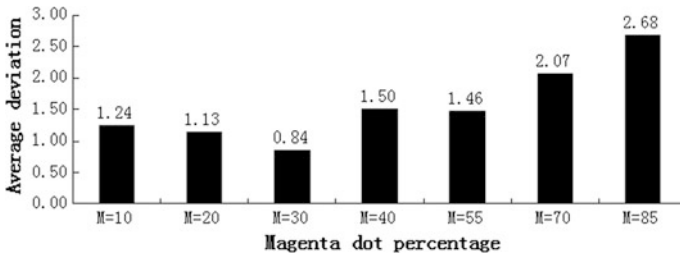
Fig. 59.5 Magenta dot percentage versus average deviation
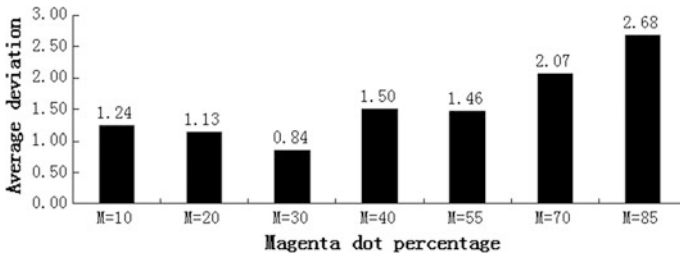
Fig. 59.6 Cyan dot area rate versus reflectivity

59.3.4 Deviation Changing with Magenta and Yellow Proportion

When magenta or yellow proportion changed, the average cyan predication deviation is shown in Figs. 59.5 and 59.6. Increasing other ink proportion, the cyan predication deviation is changing large, but data is under 2.7. The influence of Magenta is bigger than yellow. For increasing the predication precise, the deviation compensating is connected with magenta or yellow proportion judging. The method is similar but magenta and yellow spectrum region are more complex.

59.4 Conclusions

The analysis in independent spectrum region, choose the spectrum reflectivity value at 670 nm for cyan ink to establish the relationship with ink dot value. The deviation becomes large at high proportion mixing situation. Using a polynomial model and spectrum data fitting to predicate cyan dot rate in three basic color printing region is a feasible method. This method also could be used to predicate magenta dot rate, when the magenta dot rate is higher 50 % in three basic color printing

region. When the basic ink has independent area, the dot rate predication can use a polynomial model which is established in particular wavelength. This method also could be used to spot color predication.

References

1. Yuan, W., Zhao, X-p, & Jiang, Q-y. (2011). Study of offset printing parameter control method based on densimetry. *Packaging Engineering, 32*(9), 81–84.
2. Zhang, Z-x, Wang, L-j, & Zhu, Y-h. (2005). The application of chromaticity detection in packaging printing. *Packaging Engineering, 26*(1), 65–69.
3. Wang, H., & Li, J. (2014). Reaserch development of multispectral color reproduction technology. *Journal of Zhe Jiang University of Science and Technology, 26*(1), 46–51.
4. Zhao, C-f, Han, Q., & Zou, C. (2013). Research on correction factor of Yule-Nielsen Spectral Neugebauer Model [J]. *Packaging Engineering, 34*(3), 113–115.
5. Yang, S., Liu, Z., & Wu, M. (2015). Color separation mehod based on characteristic spectrum matching for multi-color reproduction. *Geomatics and Informatin Science of Wuhan University, 40*(4), 563–568.
6. Yang, H., Yi, Y., Liu, J., & Wang, X. (2015). Research on multi-color separation model based on polynomial regression. *Applied Mechanics and Materials, 731*, 27–31.
7. Zhang, L., & Li, J. (2015). Ink spectrum data feature extraction research. *Applied Mechanics and Materials, 731*, 87–91.

Chapter 60
Research on the Performance of Screen Printing Line in Water Conductive Ink

Zhencai Qu, Shiwei Liu, Qingbao Wei and Yan Zhang

Abstract Water-based conductive inks are environmentally friendly and energy efficient, when applied to the screen printing; they not only reduce the production costs, but also improve the working environment. The performance of conductive ink will be affected by the screen's printing pressure, substrate types, line shapes, and other factors. Single factor experiments were chosen, the resistance value of the printed circuit under different factors were tested by changing the screen printing squeegee pressure, the substrate type, and the shape of printed electronic circuits. The results show that the thickness of the ink layer can be improved by greater squeegee pressure, thereby improving the conductivity; substrates with large surface tension can easily contribute to good conductivity; the conductivity on PET film was higher than that on the PE film; with different shapes on the printed electronic circuits, the conductive properties were not the same, the order of the conductivity was rectangular wave > broken line > annulus > linear. The performance of screen printing line has a certain influence on the conductivity of the conductive ink which should be strictly controlled in production to obtain production optimization.

Keywords Screen printing · Unit resistance · Water conductive ink

60.1 Introduction

The electronic circuit for membrane switches, FRID tags, flexible displays, and other new electronic products not only requires to have good conductivity, but also some availability and strength properties [1]. As all know, conductive ink was printed on the insulating substrate material, which can form a conductive circuit to

Z. Qu (✉) · S. Liu · Q. Wei · Y. Zhang
Department of Packaging and Printing, Henan University
of Animal Husbandry & Economy, Zhengzhou, Henan, China
e-mail: quzhencai@126.com

make the electronic devices. Therefore, the conductivity of the ink was directly affected by the printing process, width, and shape. As the substrate requirements on screen printing were very low, it had been printed on substrates with different shapes; therefore, screen printing on electronic products was relatively wide and screen printing on the printed circuit board has been used for decades; it was the most mature technology on electronic manufacture [2]. In this study, single factor experiments were selected to obtain optimum resistance value on the printing process conditions. Through 200-mesh screen version, the aqueous conductive ink was printed on the PET and the PE films, squeegee pressure, substrate type, and the shape of printed electronic circuits were changed, and the resistance value under different factors was tested.

60.2 Experiment

60.2.1 Experimental Apparatus

Materials: Homemade water-based conductive ink (fineness: 5–10 um; viscosity: 70–100 s (Tu-4 cup, 25 °C); pH value: 8–9; Adhesion: 100 % (tape peeling test)), PET film, PE film, Zhuhai Le Tong Chemical Co., Ltd.

Equipment: SYP6 flat screen printing machine, Shanghai Shuo Zhi Machinery Co., Ltd.; Heated oven blast, Shanghai Shen Xian heng temperature equipment factory; "Quick" swing machine, Changzhou Aohua Instrument Co., Ltd; Scraper fineness tester, Shanghai Pushen Chemical Machinery Co., Ltd.; Adhesive tape pressure roller machine, Disc peeling machine, Labthink Instruments Co., Ltd.; Multimeter (2001C), Shenzhen Huayi Instrument Co., Ltd.

60.2.2 Ink Preparation

Aqueous conductive ink formulations on carbon black were designed as shown in Table 60.1. First, A amount of ethanol was filled in 200 ml cans, and 1/2 of the total

Table 60.1 Water-borne conductive ink formulations in experiments

Raw material	Mass fraction(%)
Water-borne polyurethane	21
Aqueous solution acrylate resin	14
Superconductive carbon black	20
Deionized water	10–15
Wetting-dispersing agents	4–8
Ammonia water (28 %)	2–5
Alcohol	15
Water-based defoamer	0.5–2

water-borne polyurethane and water-based acrylic urethane resin solution, ethanol, deionized water were taken in cans according to the formula, carbon black, wetting agents and defoamers were also contained in the mixed pulp, 100 g glass sand was added in it, manual swing several times to obtain a pre-dispersed paste. Next, the predispersed paste was dispersed for 90 min on the "Quick" swing machine, the fineness of ink was controlled less than 10 um, and ammonia was added to control the pH value at 8–9. Subsequently, the rest of the urethane resin solution, ethanol, ethyl acetate, and deionized water were added to the preparative paste, sealed, and continued to disperse for 10 min; while the viscosity and fineness of the ink were tested to achieve the desired quality requirements, mechanical impurities were removed by 200-mesh sieve, then the ink was made [3].

60.2.3 Performance Testing

Before printing, the surface of PET and PE film would need to be cleaned with cotton dipped in a small amount of alcohol, and then the two kinds of films were treated until PET's surface tension was more than 52 dyne and PE's surface tension was more than 38 dyne. The self-made conductive ink was stirred uniformly, and then printed on the PET and PE films with a 200-mesh screen version. Performances were measured after the ink was naturally dried for 48 h; the resistance of the printed electronic circuits were tested by a multimeter and the influence of different squeegee pressure, substrate type, and the shape of the electronic circuits on conductive properties were discussed in the experiments [4].

60.3 Results and Discussion

60.3.1 Formulation on Water-Borne Conductive Ink

Specific formulations were as shown in Table 60.1.

60.3.2 Effect of Squeegee Pressure on the Conductivity

The thickness of the ink layer was changed by changing the squeegee pressure, thereby the resistance value of the electronic circuit will also be changed, and the results were shown as in Fig. 60.1.

As shown in Fig. 60.1, the average resistance of the electronic circuit was decreased with the increase of the printing squeegee pressure, because the thickness of the ink film will increase with the increasing squeegee pressure, which will result
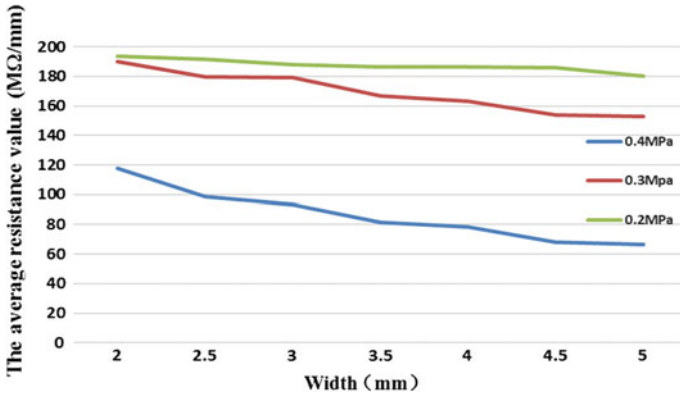
Fig. 60.1 The average resistance under different pressures

in an increase of conductivity. Meanwhile, with the increase of the line width of ink, the resistance value of the electronic circuit would gradually decrease, which was conformed to the formula to calculate the resistance value [5]. According to the experiments, with an appropriate increase in the squeegee pressure, the conductivity of electronic circuits can be improved.

60.3.3 *Effect of Substrate Type on the Conductivity*

Water-based conductive inks were printed on a transparent PET film and PE film by a 200-mesh screen, the resistance was tested by a multimeter, as shown in Fig. 60.2.

As shown in Fig. 60.2, when the printing squeegee pressure was 0.3 MPa, the average resistance value on the PET film was smaller than the average resistance value on PE film. In the experiment, the adsorption of PET film was stronger than that on a PE film and as more conductive fillers were contained in the conductive line, the conductivity on PET film was better than that on PE film.

Fig. 60.2 Average resistance under different substrate types
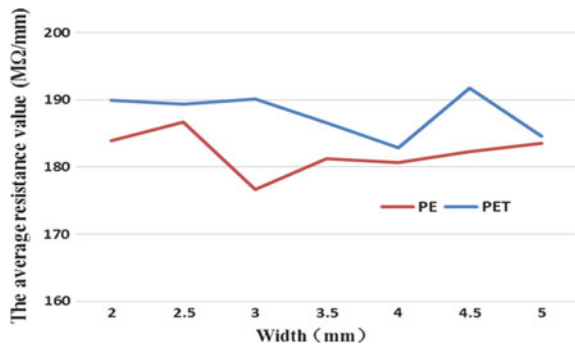
Fig. 60.3 Electronic circuit with different shapes

Fig. 60.4 The average resistance under different shapes
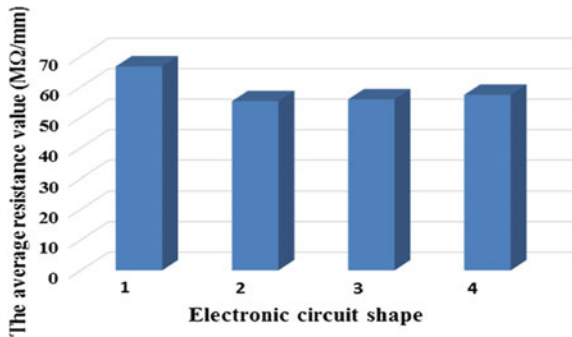
60.3.4 Effect of Electronic Circuits on the Conductivity

The shape of the electronic circuit will have an impact on the conductivity of the conductive ink. Different shapes of circuit's pattern were printed on the PET transparent film; the results were shown in Fig. 60.3.

Unit resistance in different shapes was tested by a new digital multimeter UT39B; the resistance values on linear, rectangular waveform, broken line, and annulus were, respectively, marked as '1, 2, 3, 4' and the results were as shown in Fig. 60.4.

From the Fig. 60.4, the conductivity of the printing ink was changed with the different shapes. The connection of the conductive path was affected by the shape of the conductive line; only in the case of the connected conductive path, the conductivity will be good. Through the experiment, the order of the conductivity was rectangular wave > broken line > annulus > linear.

60.4   Conclusions

In the screen printing process, the content of the conductive filler in the ink was affected by the thickness of the ink layer. When the ink layer was thicker, the conductive filler was much contained; if the resistance value is reduced, then the

conductivity will be improved. An appropriate increase in squeegee pressure will help to improve the conductivity of the electronic circuits. Substrates relied on their surface adsorption to impact the conductivity of the ink, the adsorption properties of the PET film was better than that for PE film. Better printing effect can be easily obtained for those substrates with large surface tension, which was conducive to the formation of a closed loop circuit. The connection of the electronic circuit will be affected by the shape of circuit; electronics with rectangular waveform were easy to form a closed-loop circuit which had a higher conductivity.

References

1. Chen, H. S., Qu, Z. C., Guan, Y. Y., & Tang, B. L. (2013). Preparation of nano-silver dispersions for water-based conductive ink. *Packaging Engineering, 34*(13), 102–104.
2. Ran, J., Mo, L. X., & Li, W. B. (2013). A nano-silver inkjet conductive ink with excellent adhesion. *Applied Mechanics and Materials, 262*, 501–504.
3. Kosmala, A., Wright, R., & Zhang, Q. (2011). Synthesis of silver nanoparticles and fabrication of aqueous Ag inks for inkjet printing. *Materials Chemistry and Physics, 129*, 1075–1080.
4. Shlomo, M., Michael, G., & Berezin, O. (2010). Triggering the sintering of silver nanoparticles at room temperature. *ACS Nano, 4*, 1943–1948.
5. Cherrington, M., & Tim, C. (2011). Ultrafast near-infrared sintering of a slot-die coated nano-silver conducting ink. *Journal of Materials Chemistry, 21*, 7562–7564.

Chapter 61
Research on Carving Effect's Reproduction of Art Deco Painting Based on UV Inkjet Technology

Chong Gu and Yongkai Wang

Abstract This paper aims at opening a new way to convert the reproduction of traditional drawings' "visual stereo effect" into "reality relief stereoscopic effect." Through analysis of some decorative paintings, we found that it could be reproduced through multiple-layered printing by UV inkjet printer to change the part of the specific positions' UV ink layer thickness. After the completion of the split from three dimensions to multiple two-dimensional planes of this work, we should make sure the best number of plies to print it off. Finally, it is proved that this method is feasible and effective.

Keywords UV ink · Relief effect · 3D printing

61.1 Introduction

Decorative painting is a kind of art, which does not emphasize high artistic quality, but it is very particular about the coordination and the beautification of the environment. It originated in the decorative patterns of painted pottery's body in the Neolithic Age, such as animal patterns, human patterns, geometric patterns, are exaggerated deformation, highly refined graphics [1]. Because of its exquisite patterns and extremely strong relief in the three-dimensional sense, it can be converted from "visual three-dimensional effect" to "relief three-dimensional effect" to highlight its features and enhance the decorative effect.

The traditional printing method can only get two-dimensional print, but the use of 3D printing technology can be a good solution to solve this problem. In 3D printing, additive processes are used in which successive layers of material are laid down under computer control [2, 3]. A large number of additive processes are now

C. Gu · Y. Wang (✉)
College of Packaging and Printing Engineering, Tianjin University of Science and Technology, Tianjin, China
e-mail: wangyk91@126.com

available. The main differences between the processes are in the way layers are deposited to create the parts and in the materials that are used. Some methods melt or soften material to produce the layers, e.g., selective laser melting (SLM) or direct metal laser sintering (DMLS), selective laser sintering (SLS), fused deposition modeling (FDM), or fused filament fabrication (FFF), while others cure liquid materials using different sophisticated technologies, e.g., stereo lithography (SLA). With laminated object manufacturing (LOM), thin layers are cut to shape and join together (e.g., paper, polymer, and metal) [4].

For decorative painting, the use of LOM, method can better reproduce the three-dimensional relief effect. So, in this work, we use the UJF-3042HG UV inkjet printer, with LOM, to achieve 3D printing process.

61.2 Experimental Method

61.2.1 Manuscript

The used decorative painting's manuscript size is 120 mm × 65 mm, as shown in Fig. 61.1. In order to show that the original elements as three-dimensional, we selected the moon, clouds, tree, red plums, and birds as the stereo part to highlight in the production process and present a better three-dimensional relief effect.

61.2.2 Method

First, we draw the vector of original decorative painting in Adobe Illustrator and slice it into some layers as shown in Fig. 61.2. In this way, we can easily obtain several two-dimensional files to the print out. Moreover, with the increase in print times, the UV inks' thickness also increases correspondingly.

In order to determine the two elements' best difference between the two printed layers, we made a square sized 10 mm by 10 mm and printed it from 1 to 12 layers. According to the actual touch of the thickness of UV ink layers, it is found that when the difference between the numbers of layers is five, the stereo effect could be felt obviously.

Fig. 61.1 Decorative painting manuscript
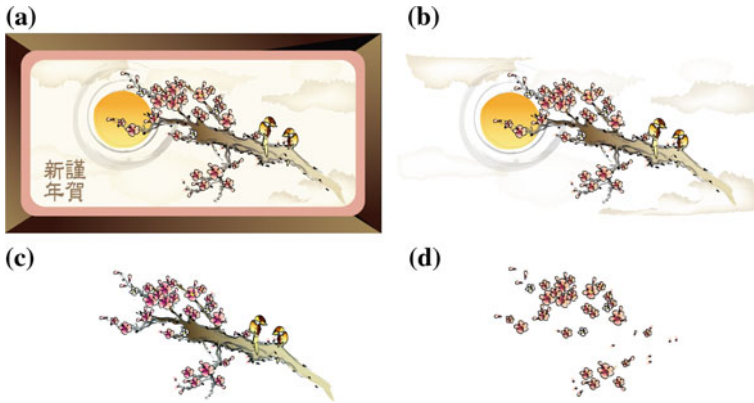
Fig. 61.2 Partial delamination effect

Table 61.1 Main elements' print layer

Elements	Layers
Moon	5
Clouds	10
Tree	15
Birds	20
Red Plums	25

Then, two experiments were compared, where both of them could achieve the stereo effects. In both the experiments, main elements were printed by different layers, which are shown in Table 61.1.

The layers are decided according to the distance of the elements: the further, the fewer; the closer, the more.

Before printing the final decorative painting, we first explore the color gamut, print head distance, and the print accuracy of the printer. Meanwhile, we find that the use of UJF-3042HG UV inkjet printer's color gamut and print accuracy can reach the requirements of recreating a stereo effect of the relief. What's more, we can also achieve the best reality relief stereoscopic effect when the print head distance is set from 1.5 to 3 mm.

After that we used the UV printer to print. The effects of experiment A, shown in Fig. 61.3, displays that the more layers we print directly, the darker color we will get.

In order to avoid this phenomenon of experiment A, we have to change the way we print. In the next experiment, which we called experiment B, we improved it such that we use at least two layers' white ink to cover the bottom color before we print the last layer. Finally, we got a better three-dimensional carving effect as shown in Fig. 61.4.

Fig. 61.3 Experiment A's final effect

Fig. 61.4 Experiment B's final effect
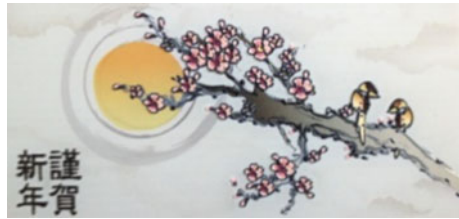
61.3 Results and Discussion

61.3.1 Ink Adhesion

In order to investigate the ink adhesion of the line and the plane of C, M, Y, K, and W, five kinds of UV inks and two kinds of test versions are designed. The first one is under the same width while with different thickness. The second one is under the same thickness while with different width. The test versions are designed for 1–12 pounds wide lines and 10 mm × 10 mm of planes, and then printed it from 1 to 25 layers in order. According to the standard of GBT 5210-1985 adhesion test, the adhesion of UV inks is measured with the 3 M-610 ink adhesion test tape. The results show that it can meet the criterion when the print layer is 25.

When we finished the complete print processes, we also use this method to test the final decorative painting reproduction. Furthermore, the final results show that the adhesion of UV ink can also completely meet the requirements of the three-dimensional printing.

61.3.2 Thickness

After finishing the print process completely, we measured the thickness of the main elements by using the Labthink CHY-C2 thickness gauge. The results were shown in Table 61.2.

Table 61.2 Main elements' final thickness

Elements	Layers	Thickness (μm)
Moon	5	81.5
Clouds	10	110.8
Tree	15	159.2
Birds	20	207.1
Red plums	25	295.6

Table 61.3 Every single layer thickness of the UV inks

Color	Thickness(μm)
C	11
M	13.2
Y	7.9
K	9
W	13.6

In addition to the overall thickness of the ink layer's thickness measurement, each single layer thickness of the C, M, Y, K, and W five kinds of colors' of the UV ink were also measured. After calculation, we can easily get the average thickness of the UV inks, which is shown in Table 61.3.

61.4   Conclusion

The purpose of this study is to use a new method, which is different from the traditional "visual three-dimensional effect" to reproduce decorative paintings into the "relief effect." The experimental results show that the integration of 3D printing method is a very effective method in the representation of some kinds of decorative paintings that have strong sense of three dimensions. In this paper, we used the 3D printing technology to make up the deficiency of traditional print method and provided a new idea for the relief effect of decorative painting's reproduction. Combined with the characteristics of UV light curing, on this basis, this paper also had opened up a new direction for the application of environment-friendly UV inks.

References

1. Information on http://baike.baidu.com/view/748167.htm
2. Excell, J. The rise of additive manufacturing. *The engineer*. Retrieved October 30, 2013.
3. Wang, H. (2014). *Study on mathematical model and quality control of the 3D printing using UV inks*. China: South China University of Technology.
4. Information on https://en.wikipedia.org/wiki/3D_printing

Chapter 62
Design of Digital Printing Process Based on G7

Yiwei Li, Guangxue Chen and Liyu Liao

Abstract According to the core idea of the G7 technology process, we can use Curve2 software combined with ICC profile and utilize the gray balance control, calculation of dot gain, rip compensation curve, NPDC curve drawing, subjective evaluation of test image, and the analysis of the frequency matrix of the image to achieve the control of image quality. The effect of the image after color management and G7 correction is better than both the original image and the image only with the color management. In the printing process, the use of G7 process can be more convenient and effective for printing quality control.

Keywords G7 technology process · Curve2 software · ICC profile

62.1 Introduction

G7 is a new calibration method based on GRACOL7 standard. It can use a new NPDC (neutral density gray curve) curve to match the visual effect of the image [1]. G represents gray value calibration, while the 7 represents the 7 basic colors defined in ISO12647-2 printing standards [2]. Compared with the traditional method, the main advantages of G7 is the introduction of new parameters [3].

Y. Li · G. Chen (✉)
State Key Laboratory of Pulp and Paper Engineering, South China University
of Technology, Guangzhou, China
e-mail: chengx@scut.edu.cn

Y. Li
e-mail: 86312391@qq.com

L. Liao
Shenzhen YUTO Packaging Technology Co., LTD, Shenzhen, China

Y. Li · L. Liao
Shenzhen Engineering Laboratory of 3D Printing Technology, Shenzhen, China

62.2 Experiment

62.2.1 Experimental Materials and Equipment and Professional Software

Liner Calibration Chart for i1, Spectrolino, Printer, measurement slider, computer, P2P test target, ECI2003CMYK.

Centro color measuring instrument, Profile Maker5.0, i1 Pro, PS and G7 curve.

62.2.2 Experiment Process

(1) Printer Linearization: Connect measuring instrument. Print Linear color table. Measure Linear color table and keep the linear file.
(2) The G7 Calibration: Calibration printing comes first. Print and measure the P2P test target. We must use the same version of TXT definition files when measuring [4]. Load the measurement file into the Curve2. Draw RIP calibration curve. Assign a new control point for RIP. Manually input the new RIP values to color centro. Adjust and retain the curve.
(3) The Production of the Characteristic File: Print ECI2003CMYK. Connect measuring instruments and open Profile Maker5.0 software. Measure linear color table. Save measurement data. Make characteristics file.
(4) G7 Verify: Create a new validation print Run. Load a new RIP curve to generate one or more P2P measurement file [5]. All the diagrams and results shown in the Run, and this can check the coincidence degree between the equipment NPDC curve and the target curve.
(5) Subjective Evaluation: This experiment used the ranking method of psychophysical experiments. Selected 10 college students for the experiment and these observations are all through the Ishihara color blindness test. We use the kodim03 test image shown in Fig. 62.1.

Fig. 62.1 Kodim03 test image

In this experiment, there are three images: print images not processed, G7 corrected print images, and images processed by G7 and ICC. Then observers made an evaluation. In the evaluation of the three sets of images, the 1 represents the best, 2 on behalf of the general, the worst is 3.

(6) Test the frequency matrix, the percentage matrix and the Z-score matrix of the image Ski.

62.3 Results and Discussion

62.3.1 G7 Calibration Process of the RIP Curve and RIP New Correction Value and the Adjusted Chart

In general, we added enough points on NPDC at the most obvious bending place (compared with the ideal NPDC curve), to make the curve smoother. We should set more points at the mediate of brighter places because human eyes are most sensitive to light. The control points are shown in Table 62.1.

62.3.2 G7 Verify Curve

G7 verify curve allows a slight deviation of 50 %. From Fig. 62.2, the new curve was almost entirely coincident with the target curve, and it can achieve the expected results after calibration.

Table 62.1 New control points in RIP

Entry	C	M	Y	K
0.0	0.00	0.00	0.00	0.00
10.0	8.65	12.51	7.79	12.04
20.0	17.36	26.18	16.01	19.74
30.0	25.24	36.82	23.23	27.24
40.0	36.97	44.31	28.47	36.22
50.0	46.92	52.16	36.31	43.04
60.0	56.41	58.68	46.28	49.75
70.0	65.19	65.66	55.27	59.44
80.0	73.64	75.29	66.48	69.10
90.0	85.09	84.94	77.55	83.26
100.0	100.0	100.0	100.0	100.0
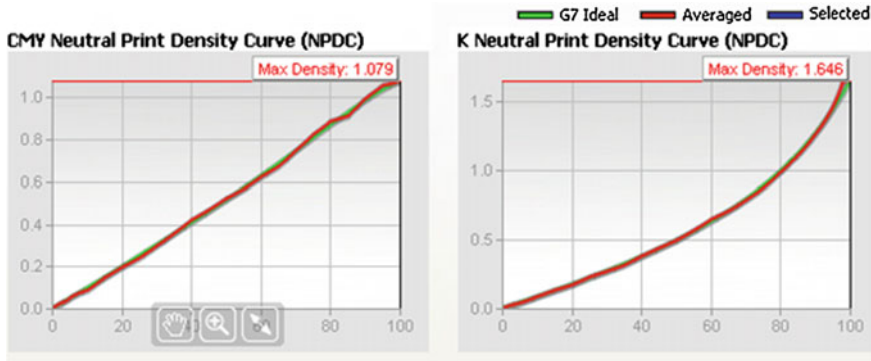
Fig. 62.2 G7 verify curve

62.3.3 Results Discussion of Subjective Evaluation

For the test image kodim03, the evaluation results are shown in Table 62.2. From left to right represent the 10 observers, each column corresponding to the choices made by each observer. The frequency matrix of the test image Ski is shown in Table 62.3. The percentage of the test image Ski is shown in Table 62.4. The Z-score matrix of the image Ski is shown in Table 62.5. We can calculate Z-score matrix from the percentage of matrix. This Z-score represents the area of the standard normal distribution $(-\infty, z]$.

The average Z-score of each color gamut mapping algorithm can be calculated from the Z-score matrix and the confidence interval of 95 % can be calculated, which represents the accuracy of Z-score. The average Z-score of the test image Ski was (The original image, The G7 corrected picture, the image corrected after G7 and ICC): $(-1.495, 0.375, 1.805)$.

The average z-score diagram of test images kodim03i is shown in Fig. 62.3. We can see the Z-score of the original image was minimum, indicating that HPMI image effect was the worst. The Z-score of the image corrected by G7 and ICC was

Table 62.2 Kodim03 raw data

	1	2	3	4	5	6	7	8	9	10
Default setting	3	3	3	2	3	3	3	3	3	3
G7	2	2	1	3	1	2	2	1	2	2
G7+ICC	1	1	2	1	2	1	1	2	1	1

Table 62.3 The frequency matrix of kodim03

	Default setting	G7	G7+ICC
Default setting		9	10
G7	1		7
G7+ICC	0	3	

Table 62.4 The percentage matrix of kodim03

	Default setting	G7	G7+ICC
Default setting		0.9	1
G7	0.1		0.7
G7+ICC	0	0.3	

Table 62.5 The Z-score matrix of kodim03

	Default setting	G7	G7+ICC
Default setting		1.28	3.09
G7	0.1		0.52
G7+ICC	−3.09	−0.53	

Fig. 62.3 The average Z-score diagram of kodim03
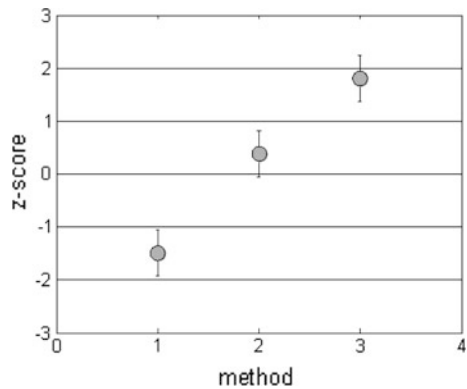
maximum, which means the effect of the image is the best. And the second was the printed image only with G7 correction. This shows that after the G7 and ICC processing of the printed image and after the G7 correction of the printed image is better than the print image processing.

62.4   Conclusions

Compared to the traditional printing dot and the density control, the G7 process needs less measured data. G7 process parameters can guarantee the consistency of the measurement results of printing density. It is beneficial for the development of printing with the quality control of G7 process.

References

1. Liu, X. T. (2001). Basic principle and application method of G7 process. *Guangdong Printing, 5*, 21–23.
2. Mou, X. Z., & Liu, Y. (2013). Describe the correction flow of G7 process detail. *Printing Quality and Standardization, 10*, 23–26.
3. Xu, H. P. (2001). The main parameters of the GRACoL7 correction method. *Printing Quality and Standardization, 12*, 42–44.
4. Hutcheson, D. (2009). G7 how—to. *Graphic Arts Monthly*(S), 5.
5. Zan, G. F., Zeng, S. L., & Dai, J. P. (2013). Application of curve 2 in G7 correction flow. *Guangdong Printing, 1*, 10–12.

Chapter 63
Research on Halftoning Algorithm of Fabric Inkjet Printing Based on Printer Model

Qianyun Ma, Qiang Wang and Ping Yang

Abstract Hardcopies such as those produced by inkjet printers do not display isolated pixels; the printed binary patterns produced by frequency modulation (FM) halftoning are significantly darker than originals due to dot gain. This research establishes a halftoning algorithm based on the Floyd–Steinberg error diffusion method for fabric inkjet printing using a circular dot simulation of fabric inkjet printers which accurately represents the image tone of fabric inkjet printing. The proposed halftoning approach is easily adapted to a wide variety of silk substrates based on the way the specific printer model and the proposed measurement-based algorithm together estimate the print-dot radius. Experimental results show that the proposed algorithm significantly improves tone matching, improves the tone-appropriate quality, and enhances control over the process and forecast level of production.

Keywords Fabric inkjet printing · Halftoning algorithm · Dot simulation · Dot gain

63.1 Introduction

During the process of fabric inkjet printing, the key problem to restrict quality of production is instability and distortion of tone reproduction [1], which mainly solved by linearization or dot compensation currently. However, in most cases, the effect on tone reproduction by physical forms and coloration mechanism of ink droplet on fabric is neglected. Consequently, the printing accuracy unable to comply the requirement of product quality.

Q. Ma (✉) · Q. Wang · P. Yang
School of Digital Media and Art Design, Hangzhou Dianzi University, Zhejiang, China
e-mail: 141220006@hdu.edu.cn

Domestic and foreign scholars have researched the tone reproduction of image in the fabric inkjet printing industry since 2000. Lai et al. [2] proposed printer model and least-squares halftoning using genetic algorithms, and Xie [3] and Wang [4] proposed adaptive halftone algorithm based on visual and printer model, respectively. However, the main digital halftone technology they used is based on the characteristics of paper in inkjet printing. Therefore, the visual effects are not ideal and the tone cannot be represented perfectly. In this paper, we propose a new inkjet printer model algorithm which applies to the fabric digital printing with Floyd–Steinerr or diffusion for gray-level distortion. Through the prediction of the reproduction quality of the original gray level, we able to simulate the circular dot on the fabric and control the dot gain of inkjet printer to realize the accurate reproduction of the tone value. The method proposed in this paper can improve the capability of predicting and controlling the product quality of fabric digital printing and reduce visual effect and compression of tone range limitation.

63.2 The Mechanism of Tone Reproduction of Fabric Digital Printing

Fabric inkjet printing is a new technology that printing reactive dyes on fabric with inkjet printing technique and getting continuous-tone images after dyeing and finishing, which is a key and difficult technology in high-end fabric manufacturer.

63.2.1 The Process of Fabric Digital Printing

No pressure inkjet printing technique is used in fabric digital printing, inkjet media is reactive dyes, the substrate is fabric, and its process is more complex than inkjet printing [5]. Especially, it has complexly sizing pretreatment and steaming dye fixing process which is shown in Fig. 63.1.

63.2.2 The Mechanism of Tone Reproduction

Fabric dyeing by inkjet printing technique creates all the illusion of continuous-tone images from the judicious arrangement of binary picture elements [6]. In halftone printing, we always assume that printed dot is square; however, most printers

Fig. 63.1 Fabric digital printing process flow chart

Fig. 63.2 The physical dot gain
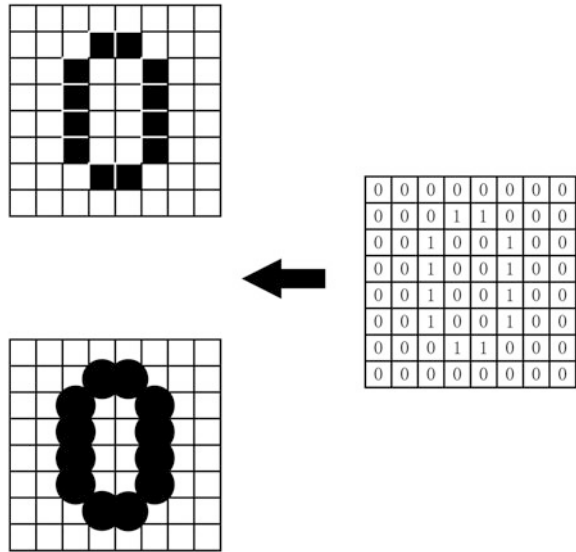
Fig. 63.3 Dot-overlap
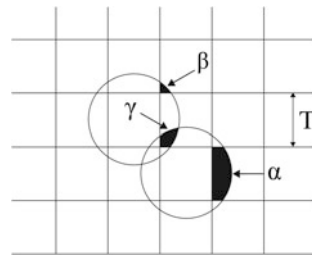
produce circular size because of ink spread, ink absorption into fabric and the way to printing. The increase in dot size was termed as the physical dot gain as shown in Fig. 63.2. Because of the impact of dot gain, the actual dot will be larger than the size of the grid square equipment, we call it dot-overlap (Fig. 63.3), and the halftone model bases on dot-overlap is named printer model [7].

According to the characteristics of the lap record of the circular points shown in Fig. 63.2, the model can be used to describe the record points:

$$
\begin{aligned}
p(i,j) &= p[w(i,j)] \\
&= \begin{cases} 1, & b(i,j) = 1 \\ f_1\alpha + f_2\beta - f_3\gamma, & b(i,j) = 0 \end{cases}
\end{aligned} \tag{63.1}
$$

$$
w(i,j) = \begin{bmatrix} b_{nw} & b_n & b_{ne} \\ b_w & b_{ij} & b_e \\ b_{sw} & b_s & b_{se} \end{bmatrix}
$$

where $w(i, j)$ denotes a window consisting of halftone image $b(i, j)$ and its eight neighbors, f_1 is the number of horizontal and vertical neighboring black dots, f_2 is the number of diagonal neighboring black dots not adjacent to any horizontal or vertical neighboring black dots, and f_3 is the number of pairs of neighboring black dots in which one is a horizontal neighbor and the other is a vertical neighbor [7]. ρ donates the ratio of the actual dot radius to the ideal dot radius $T/\sqrt{2}$, where T is the spacing of the Cartesian grid. The amount of dot gain area at each pixel is expressed in terms of parameters α, β and γ as shown in Fig. 63.3

$$\alpha = \frac{1}{4}\sqrt{2\rho^2 - 1} + \frac{\rho^2}{2}\sin^{-1}\left(\frac{1}{\rho\sqrt{2}}\right) - \frac{1}{2} \tag{63.2}$$

$$\beta = \frac{\pi\rho^2}{8} - \frac{\rho^2}{2}\sin^{-1}\left(\frac{1}{\rho\sqrt{2}}\right) - \frac{1}{4}\sqrt{2\rho^2 - 1} + \frac{1}{4} \tag{63.3}$$

$$\gamma = \frac{\rho^2}{2}\sin^{-1}\left(\sqrt{\frac{\rho^2 - 1}{\rho^2}}\right) - \frac{1}{2}\sqrt{\rho^2 - 1} - \beta \tag{63.4}$$

63.3 Experiments

63.3.1 Experimental Conditions

Silk Heavy Crepe Satin as the substrate is used in this experiment. It belongs to a kind of silk fabric products which has bright color and smooth feel [5]. Experimental silk heavy crepe satin is 14,656, (20D + 22D)/(20D + 22D),1289 line/10 cm × 530 line/10 cm, 71 g/m^2. The physical structure satin structure is shown in Fig. 63.4.

Reactive dye is an important coloration media in dye fixing process. Active groups and the fabric fibers occur nucleophilic substitution reaction to form a dye—fiber covalent bonds, so as to achieve the role of fixing. The microcosmic form dot structure is shown in Fig. 63.5 (fiber structure of 500 times under a magnifying glass).

63.3.2 Experimental Design

By the last section of fabric dot morphological analysis, we are unable to apply the rules to describe the shape of dot. Therefore, before the establishment of digital printing printer model, we must first build up virtual dot in fabric digital printing. In this experiment, we use Adobe Illustrator software to design a monochrome black color target, the scope of the theoretical dot area varies from of 10–30 % dot area

Fig. 63.4 The physical structure of silk heavy crepe satin
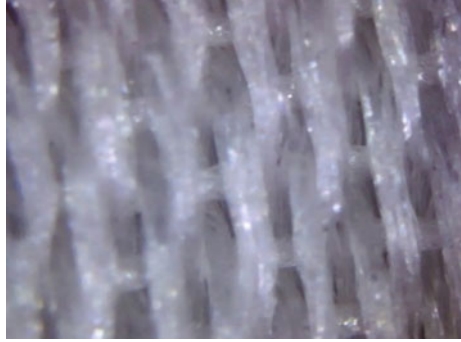
Fig. 63.5 30 % dot pattern
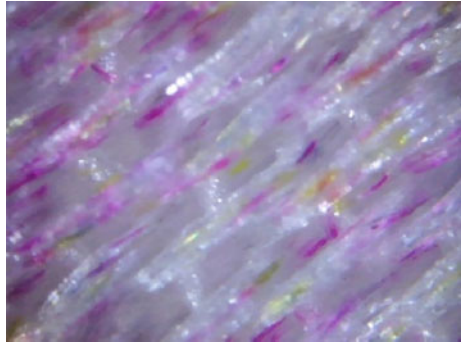
rate of change in steps of 2 %, a total of 11 tone, then print it to the silk heavy crepe satin; after fixing, washing and other process, we use X-rite 939 high-precision reflection densitometer measures the density, then the Murray-Davies equation [8, 9] is utilized to describe the relationship among the effective dot area, A; virtual dot radius of fabric, r; the density of a solid dot, D_s; the resultant density of the dot area pattern, D_t; the unit pixel area, S; physical resolution of digital printing machine, N; and image resolution, P;

$$A = \frac{1 - 10^{-D_t}}{1 - 10^{-D_s}} \times 100 \ \% \tag{63.5}$$

$$r = \frac{P}{N} \sqrt{\frac{AS}{\pi}} \tag{63.6}$$

By the Eqs. (63.5), (63.6) and the data in Table 63.1, we can first obtain the average measured virtual circular dot radius Evaluation: $r = 10.2 \ \mu m$ ($T > r > T/\sqrt{2}$); secondly, we can get other variable $\rho, \alpha, \beta, \gamma$ by Eqs. (63.2), (63.3), (63.4): $\rho = 1.081, \alpha = 0.206, \beta = 0.003, \gamma = 0.019$.

Table 63.1 Virtual dot radius

Dot area (%)	10	12	14	16	18	20	22	24	26	28	30
Density	0.20	0.21	0.24	0.27	0.31	0.35	0.39	0.42	0.50	0.52	0.59
Virtual dot radius (μm)	11.71	10.87	10.60	10.36	10.19	10.11	9.95	9.74	9.82	9.55	9.45
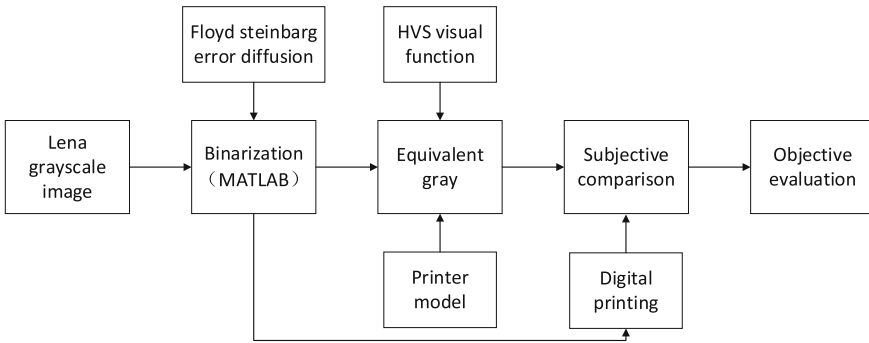
Fig. 63.6 Experimental operation flowchart

63.3.3 Experiment Process

The size of 292 × 292, 73 dpi Lena grayscale image is used as the test sample in this experiment. High-speed digital printing machine EPSON S70680 is used as laboratory equipment and the ink is EPSON special reactive dye. Software we used in experiment is: Ink Master7.0 and MATLAB 2009b. Experimental operation flowchart is shown in Fig. 63.6.

(1) Assume the original grayscale image is represented by $g(i,j)$, then transform it to halftone image $b(i, j)$ by Floyd–Stein error diffusion, the conversion resolution is physical resolution.

(2) $p(i, j)$ is a printer parameter of the modified dot-overlap printer model utilized instead of the original halftone image $b(i, j)$ for compensating the gray-level distortion, then we translate it to equivalent grayscale image $g'(i,j)$, the Eq. (63.7) is described in the Printer Model section. Next, we use a 2-D Gaussian filter $h(i,j)$ with impulse response which sigma is 1.6 to simulate the eye model to evaluate the gray-level difference between original image and its objective image, * indicates a convolution operator.

$$p(i,j) = p[w(i,j)] \tag{63.7}$$

$$g'(i,j) = p(i,j) * 255 \tag{63.8}$$

$$s(i,j) = g'(i,j) * h(i,j) \qquad (63.9)$$

(3) Output the halftone image $b(i, j)$ to silk heavy crepe satin directly, after going through the process of fixing and washing, we get the objective image.

(4) Compare objective image with simulate image of Lena $s(i, j)$ in screen subjectively, and objective evaluate both of them.

63.3.4 Results and Evaluation

63.3.4.1 Subjective Evaluation

Experiment uses the classical Lena grayscale image and 21 grades grayscale image (e) to evaluate the image subjectively and objectively [10]. We use the grayscale image which is reformed in the Gray Gamma 2.2 work space as original image (a); we use Photoshop to transform (a) to workspace of 20 % dot gain to acquire the preview image (b); we use image which based on printer model and visual-perception model as the simulate image (c); finally, we use the spray printing image (d) to compare with other groups. Subjective evaluation shown in Fig. 63.7 is that our experiment's simulate image is closer to the visual perception of the objective image.
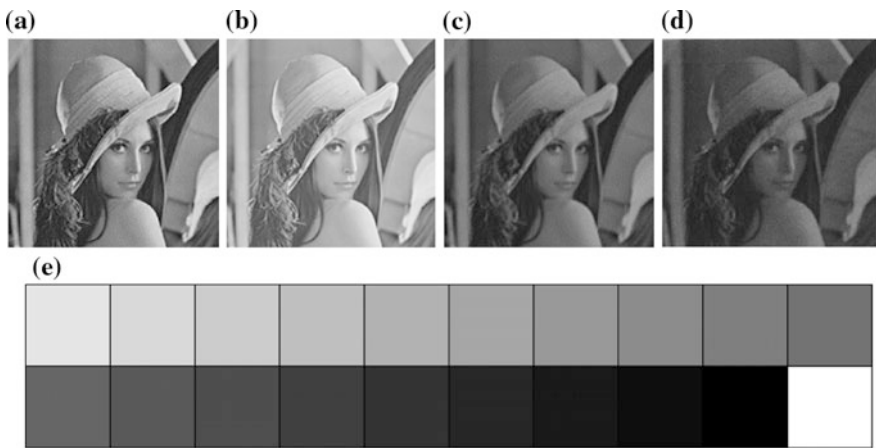
Fig. 63.7 Contrast experiment **a** original, **b** dot gain 10 %, **c** print model + HVS, **d** object, **e** 21 grade gray scale

63.3.4.2 Objective Evaluation

21 grade grayscale image (e) are used to evaluate step wedge objectively and spectrophotometer (i1 pro) is used to get L value in variety grade type. ΔL is calculated to reflect the degree of tone reproduction between the original and objective images. The distribution of ΔL is shown in Fig. 63.8. The abscissa from 0 to 100 indicates the input dot acreage and the ordinate indicates the ΔL in different model (Table 63.2).

The purpose of this study is to present a halftone digital image with a minimum gray-level distortion on the screen. Soft proofing is a useful application to simulate how an image will appear on a printer, by simply using a monitor [10]; however, as figure shows, the tone-response curves of original digital image and transformed image deviates from the axis with varying degrees at different input dot acreage, and the one using printer model and visual-perception model [11] is more faithful to the print version and has the least error. We conclude that the proposed halftoning approach produces less distortion than other commonly used soft proofing techniques.
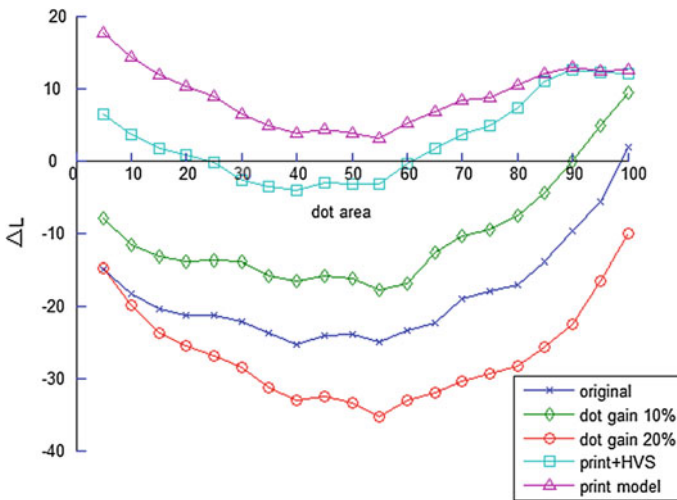
Fig. 63.8 Objective evaluation chart

Table 63.2 Error evaluation sheet

Mode	Average error	Max (absolute)
Original	−18.41	25.34
Dot gain 10 %	−10.22	17.81
Dot gain 20 %	−26.68	35.41
Print model	8.91	14.27
Print model + HVS	2.85	12.60

63.4   Conclusions

Based on the status analysis of image tone reproduction in fabric digital printing and the theoretical research of dot-overlap printer model, we solve the problem of tone compression and improve the visual effects significantly. It surmounts the bottleneck of simulation technology for printing tone reproduction and obtains a more accurate tonal change. Due to the experimental conditions and equipment accuracy limitations, this article has following problems: (1) the cumulative effect of density during dot superimposing is ignored; (2) there is an optical dot gain error in density measurement affects the accuracy of measurement date.

References

1. Yao, H. (2013). *Digital halftoning technique* (1st ed., p. 266). Printing industry press.
2. Lai, C.-C., Tseng, D.-C., et al. (1998). Printer model and least-squares halftoning using genetic algorithms. *Journal of Imaging Science and Technology, 42*, 241–249.
3. Xie, D. (2005). *Printer models and HVS models based halftoning with blue-green noise dither matrix*. Wu Han University.
4. Wang,Y. (2011). *Adaptive halftone algorithm based on visual and printer model*. Xi Dian University.
5. Shang, R.-L. (2013). Digital printing of crepe satin. *Dyeing and Finishing, 39*(19), 28–30.
6. Zhang, J. (2008). *The research of halftoning technology*. Xi Dian University.
7. Qi, W. (2003). Research on image information printing based on dot structure. *Decoration, 02*, 92–93.
8. Zhao, X. (2003). Research on quality evaluation of digital image. *Decoration, 02*, 92–93.
9. Xu, G., & Tan, Q. (2010). Research on the method of quality evaluation of half tone image based on non ideal printer model. *Computer Science*, 228–232.
10. Xie, S. (2010). *Research on the error analysis of the network based on the idea simulation*. Xi'an University of Technology.
11. Zhang, L. (2013). *FPGA design of date process and printing control system for high-speed digital inkjet printer*. Zhe Jiang University.

Chapter 64
Hologram Paper Printing Quality Detection and Research

Yu Liu, Zehui Liu and Hongmei Chen

Abstract In order to study color control and quality test of hologram paper printing, make a test form. Under the same printing conditions, print a test form on different substrates including different hologram papers and coated paper. Measure chromatic value and a series of dot area density using SP64, which is an integrating sphere color measurement instrument test, and then integrate and analyze the data. Under the same dot area, make a color reproduction comparison between hologram paper and coated paper. Scan the print proofs which are within different horizontal and vertical pound lines and fonts, and then make a reproduction comparison between hologram paper and coated paper in different fonts and different color aspect. Ascertain the differences between coated and hologram paper.

Keywords Hologram paper · Spectrophotometer · Chromatic value measurement · Density measurement

64.1 Introduction

In recent years, with increasing substrate material types and continuous process of technologies, many new materials and technologies appear in the packaging and printing industry; the most dazzling material is hologram paper, which is used for wine and toothpaste boxes and other packaging. The colorful "rainbow" effect may bring not only unexpected benefits for the enterprise, but also problems in color control and printing quality inspection [1].

ISO13660 is the first international objective image quality evaluation criteria. Constitutors clearly indicate that ISO13660 is for digital printing. ISO13660 defines

Y. Liu (✉) · Z. Liu · H. Chen
Beijing Institute of Graphic Communication, Beijing, China
e-mail: liuyu@bigc.edu.cn

the character/line quality attributes including blurriness, Raggedness, line width, character darkness and contrast, filling, and extraneous marks of background haze of character field [2–4].

In this experiment, test form was printed on different hologram papers and coated paper. Use different measurement to test the proofs and make an analysis and comparison about reproduction and character/line on different papers.

64.2 Experiment

Hologram paper with a special microstructure has a great impact on color reproduction, so it is necessary to ensure that the hologram paper is eligible for products used in this experiment and layout is reasonable. This experiment can be divided into four parts: First, identification hologram paper quality; second, design layout; third, color analysis; fourth, analysis each print character/line properties. The flow diagram describes the experiment (Fig. 64.1).

64.2.1 Experiment Instruments and Materials

Experiment instruments: Spectrophotometer SP64 (Parameters setting: large area view (LAV), specular component included (SCI), D65 light source, CIE1964 observer [5, 6], Cézanne scanner (2400 dpi), Canon plane scanner (600 dpi), Print quality measurement and control software.

Experiment material: Four kinds of hologram paper: wiredrawing beam hologram paper, beam hologram paper 400 dpi (H_b 400 dpi), beam hologram paper 100 dpi (H_b 100 dpi), hydrogen sulfide beam hologram paper plating 400 dpi (H_{H_2S} 400 dpi), and the 500X-microstructure of hologram papers (Table 64.1).
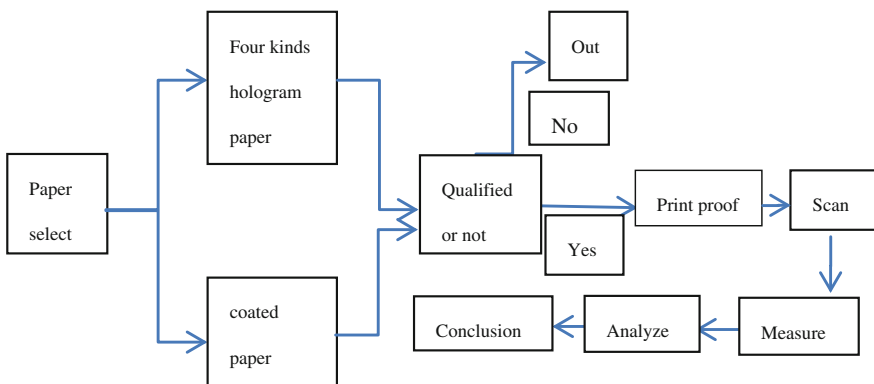
Fig. 64.1 Experiment flow

Table 64.1 Four kinds of hologram paper
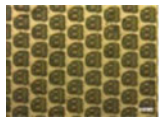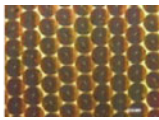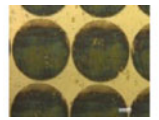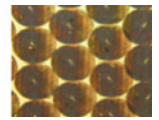
Type	H_W	$H_{b(400dpi)}$	$H_{b(100dpi)}$	$H_{H2S(400dpi)}$

Fig. 64.2 Layout

64.2.2 Design Printing Sample

According to the early experiments, it can be known that for color difference within 1.0 at the same period of paper base of hologram paper (i.e., the same position microstructure), color difference is within 4.0 at any position of beam hologram paper [7]. Therefore, the period of beam hologram paper tested by scanner is 5 cm. So design a form as follows: sample consists of patches of different color dot area, CMYRGB with white ink background, different width of horizontal and vertical lines, and different font size of the characters and inverse characters (Fig. 64.2).

64.3 The Data Processing and Analysis

64.3.1 Make a Comparison and Analysis About Printed Color Between Hologram Paper and Coated Paper

It can be seen from the Fig. 64.3, in the blue-green color region, spectral reflectance curves of hologram paper are significantly higher than the coated paper; in red and yellow region, spectral reflectance of H_{H_2S} is maximum, followed by coated paper. This is because printing color is affected by substrate colors, aluminum hologram paper is bluish and coated paper is yellowish, spectral reflectance of paper based of H_{H_2S} is highest in red and yellow region.
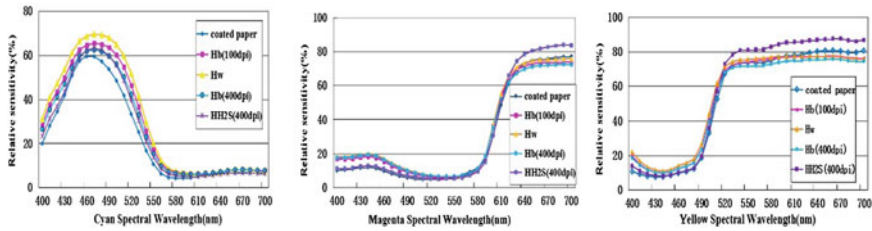
Fig. 64.3 Spectral reflectance curve of CMY ink of five kinds of paper

64.3.2 Uniformity of Hologram Paper with Printing White Ink

Take into account the difficulty of hologram paper color control. When printers test image and color quality on hologram paper, the control strip was printed on white color ink, print color value can be controlled because white ink has a good covering power. In order to examine the effect of white ink covering power, there are some of solid colors without white ink base and some of solid color with white ink base. Measure five different points of each solid color including white ink base and non-white ink base. Average the five values of each color and compare with each other. The maximum color difference value is shown in Table 64.2. As we can see from Table 64.2, the maximum color difference with white ink base is less than non-white base. This indicates that white ink has a good covering power, so printers can use this method to determine the hologram paper print quality.

Table 64.2 The max color difference between printed white ink and non-printed

	H_W (PW)	H_W (NPW)	H_b (400 dpi) (PW)	H_b (400 dpi) (NPW)	H_{H_2S} (400 dpi) (PW)	H_{H_2S} (400 dpi) (NPW)	H_b (100 dpi) (PW)	H_b (100 dpi) (NPW)
C	0.97	3.14	1.52	3.58	0.50	0.69	1.22	2.69
Y	0.83	1.84	1.42	1.87	0.92	1.10	1.12	2.34
M	1.28	1.61	1.47	1.55	0.67	1.07	1.11	2.85
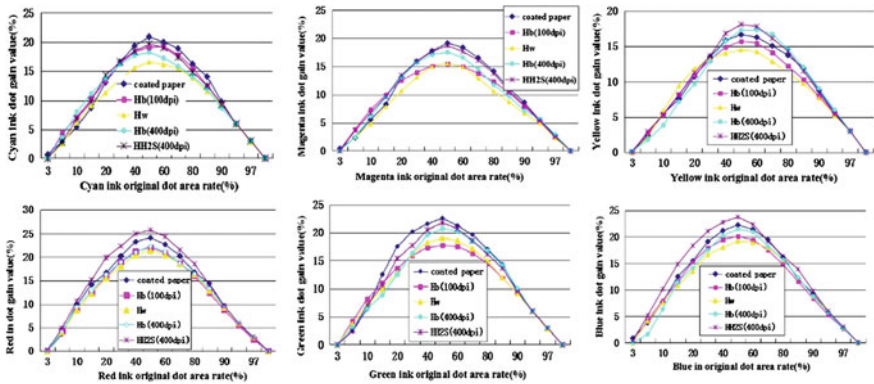
Fig. 64.4 CMYRGB dot gain value of five papers

64.3.3 Hologram Paper and Coated Paper Printed Dot Gain Analysis

From Fig. 64.4, it can be seen that the dot gain of coated paper is closest to hydrogen sulfide hologram paper and is the most serious; the dot gain of wiredrawing beam hologram paper is relatively small. Coated paper's dot gain is the largest for CMG; 400 dpi hydrogen sulfide hologram paper's dot gain is most serious for yellow and blue color. Max dot gain field and min dot gain field of five kinds paper is basically similar. The max of dot gain appears at 50–60 %. For the six color ink, the dot gain from small to large is YMCGBR.

64.3.4 Line Comparative Analysis

Line width:

Figure 64.5 is an example using wiredrawing beam hologram paper to analyze line width and contrast variation with the original line width increasing. It can be seen that contrast increases in proofs because the original width increases; vertical lines width and contrast is greater than the horizontal one; at the same size, the maximum width increase is green ink, the minimum line width increase is magenta ink, the contrast of yellow and magenta is basically unchanged with the increasing original line width, but the contrast of cyan ink increases significantly. Line width is under 0.75 pounds, contrast ordering is magenta > yellow > cyan; Line width is more than 1 pound, contrast ordering is cyan > magenta > yellow; for CMY ink, contrast of 400 dpi hydrogen sulfide coated hologram paper is similar to coated paper, followed by 400 dpi beam hologram paper, and 100 dpi beam hologram paper is minimized.
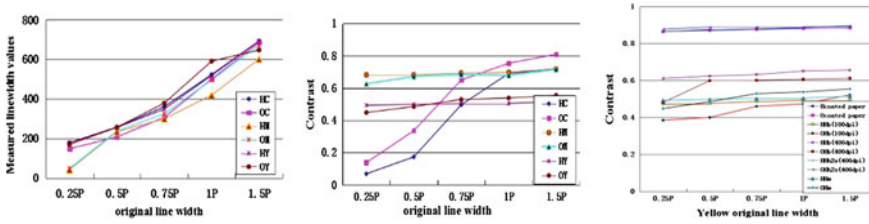
Fig. 64.5 Line width/height and contrast
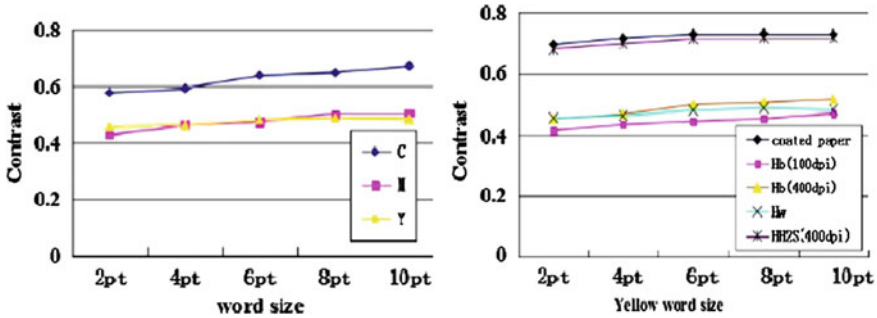
Fig. 64.6 Contrast of character with changing type size

64.3.5 Character Comparative Analysis

It can be seen from Fig. 64.5 that the following 10 pound font, color character contrast is slowly increasing with the increasing size of the character under the 10 pound font. At the same size, blue character has the maximum contrast; magenta contrast is similar to yellow. Different paper used the same ink; in hydrogen sulfide hologram paper the contrast is similar to coated and larger than the other three hologram papers. The other three hologram papers contrast present the law as following: 400 dpi beam hologram paper > wiredrawing beam Hologram paper > 100 dpi beam Hologram paper (Fig. 64.6).

64.4 Conclusions

Through the above analysis, the following four conclusions can be summarized in this paper:

1. Color difference of four kinds of hologram paper print and coated paper print meets the following rules: 400 dpi hydrogen sulfide hologram paper and coated paper are most similar in color reproduction aspect, followed by 400 dpi beam hologram paper, third is wiredrawing beam paper hologram, and finally is 100 dpi beam hologram paper.

2. White ink has a relatively good covering power; color control strip, which is printed on white ink can be used as a method to test the hologram paper print quality, especially in wiredrawing beam paper hologram.
3. Contrast of color character meets the following rules: cyan > magenta > yellow; four kinds of hologram paper contrast law: 400 dpi hydrogen sulfide hologram paper > 400 dpi beam hologram paper > wiredrawing beam hologram paper > 100 dpi beam hologram paper.
4. Vertical and horizontal lines width, and contrast relationship meets the following rules: the vertical line is greater than the horizontal lines; contrast relationship of four kinds of hologram paper is: 400 dpi hydrogen sulfide hologram paper > 400 dpi beam hologram paper > wiredrawing beam hologram paper > 100 dpi beam hologram paper.

References

1. Guan, D. (2010). Printability of hologram paper analysis. *Print magazine 10*.
2. Jiang, G., Jin, Y., & Xu, Y. (2011). *Character clarity perceive quality of digital print evaluation method research* (Vol. 4). Qufu Normal University.
3. Jiang, G., Xu, Y., & Guo, G. (2010). Evaluation method research of digital print lines clarity. *China Printing and Packaging Study*, *10*.
4. Xiaomeng, C. & Guangxue, C. (2013). Micro detection and analysis of digital color printing line quality. *China Printing and Packaging Study*, *06*.
5. Huang, X., Wan, X., & Liu, Z. (2011). *Optimization of the method for color measurement of printing on holographic paper*. Wuhan University.
6. Wan, X., Huang, X., & Liu, Z. (2011). *Color measurement for holographic photopaper*. Wuhan University.
7. Huang, M., Wang, L., & Liu, Y. (2014). Spectroscopy and chromaticity of beam Hologram paper measurement analysis. *Journal of Optics*, *06*.

Part V
Packaging Engineering Technology

Chapter 65
An Application Study of Electronic Shelf Label on Cultural Creative Merchandise

Mingchw Wei and Yungcheng Hsieh

Abstract The application of network technology develops rapidly. Cultural and creative merchandise are always adapting their various marketing modes to match consistently changing trends. This phenomenon illustrates that in order for company managers to receive maximum benefits they must replace traditional marketing methods and utilize the most up-to-date modes of application. Electronic shelf label (ESL) is one the most recently updated applications within this field. The purpose of this study was to analyze the correspondence between subject's intentions and behavior when using various cultural and creative merchandise. This study explores the topic via aspects of usability and usefulness which is cited from the theory of technology acceptance model (TAM). Subjects within this study consist of employees from different backgrounds in the cultural and creative industry. They were interviewed through a questionnaire in which all questions were given randomly and collected for analysis through the SPSS software. The main findings of the study are described in the following. The differences in subjects' backgrounds did not have enough evidence to be statistically significant in influencing the usability of ESL, usefulness of ESL, intention of use, and use behavior. However, the usability and usefulness of ESL were revealed to have a heavy influence on subjects' intention behavior of when using cultural and creative merchandise, but no significant influence on use behavior. Furthermore, this study found that use behavior is significantly influenced by the intention of use. With the results of this study, it is revealed that the ESL application to cultural and creative merchandise is feasible. However, one of the major drawbacks is that the object (ESL panel) is limited by its small scale and color. Therefore, it is recommended to use ESL with a large-scale and colored panel, because it is much a suitable choice for practical application in cultural and creative merchandise.

M. Wei (✉)
Graduate School of Creative Industry Design, National Taiwan University of Arts, Taiwan, China
e-mail: winnie.wei@msa.hinet.net

Y. Hsieh (✉)
College of Communications, National Taiwan University of Arts, Taiwan, China
e-mail: ych@ntua.edu.tw

65.1 Introduction

In recent years, there has been a global rise and upsurge of creativity stemming from cultural tradition and beliefs. This cultural creativity phenomenon has become the focus of development projects in many countries, but most of these projects belong to entrepreneurs of micro-enterprises. These enterprises are often only able to focus on the creation aspect, due to low manpower and lack of capital to be used for marketing promotion. If entrepreneurs were given a tool to enhance the awareness of developed goods and marketing, this new wave of culturally creative industry would help sustain a balanced growth in the marketplace.

Electronic shelf labels (ELS) (Fig. 65.1) are an electronic paper display that utilizes business applications in an efficient manner. These advantages consist of wide angle, low power consumption, reusable, easy operation, and reduction of high labor cost. This product has been widely incorporated into markets with premium labor cost–Europe, America, and Japan. In this study, ESL is the focal point that meets the needs of producers and consumers. It enables the producers of cultural goods to have their own proprietary QR Code while capitalizing on existing consumer behavior of carrying mobile device(s).

When a QR Cord is scanned by a mobile device, users are directed to sites that give information about the creator and merchandise, followed by a questionnaire. The questionnaire was given to collect data for analysis on whether the industry would adopt this marketing application. The essence and motive is to determine the

Fig. 65.1 Electronic shelf labels (ESL). *Source* Proprietary

effectiveness of ESL marketing tool in helping micro-entrepreneurs to promote their business. This study aims to investigate the use of ESL through the TAM as the theoretical framework when observing perceived usefulness and ease of use.

65.2   Discussion

In 2010, Taiwan government promulgated the "Cultural and Creative Industry Development Act" (referred to cultural and creative method), with the industry defined as: "Stems from creative or cultural accumulation, through the formation and use of intellectual property, has potential to create wealth and employment opportunity and the promotion of universal esthetic qualities and promoting overall improvement of life." The current development of Taiwan's cultural and creative industries is experiencing centralization and increasingly more competition in the market. There are three indispensable key components of industrial innovation: culture, creativity, and industry—no matter which comes first, the focus is how to "differentiate" [1, 2].

ELS is a commercial application of an electronic paper display. It uses a dot-matrix screen to display any pattern or bar code. This enabled a variety of specifications including a customized panel, size, appearance, logo design, etc. In terms of efficiency, it has an error rate of less than one ten-millionth, low power consumption, zero power static work, reusability, and the use of electronic paper that enables content to be instantly updated by a computer. Essentially, all the components not only are environmentally friendly, but also reduce the chance of errors occurring and help companies optimize the performance of commodity information [3–8].

Davis first proposed in 1989, the TAM. This model was based on perceived usefulness (PU) and perceived ease of use (PEU) as potential variables in theoretical verification of technology and use behavior. In order to understand the impact of external factors on the user's internal beliefs, attitudes, and intentions, as well as how these internal factors impacted the use of new information technology [9–11].

65.3   Subjects

Cultural and creative industry practitioners—National Taiwan University of Arts, Cultural and Creative Industry Park—total of 49 industry companies. Survey period from 2013 June 10 to July 30, total of 170 questionnaires issued (158 recovered/92 % recovery rate).

65.4   Research Method and Approach

Questionnaire Design:

1. Part 1 focus on the use of ELS, including "easiness," "usefulness," "willingness to use." Part 2 captured "basic respondents data" and Likert measurement seven-point scale from "fully agree" to "completely disagree".
2. Experimental Environmental Design: Hot springs in Yilan County Park (Jiao Si Hot Springs Park, Yilan County) build hardware device on site and entered the information on the ESL, transmitted via Zig Bee to for users to scan the QR to read the cultural and creative merchandise related information.
3. Surveying process: Questionnaire provided to subject when experience was complete.

65.5   Data Analysis

65.5.1   Demographic Information

Total of 170 questionnaires issued, 158 valid questionnaires returned, the use of frequency allocation calculated respondents "basic personal information" (including gender, age, education, job title, company size, company age, smart phone, and QR Code usage count and percentage) (Table 65.1).

65.5.2   Basic Differences in the Variables of Each Study (Aggregated)—Table 65.2

Respondents over the age of 41 ranked highest in both usefulness and willingness to use. We can conclude that older respondents are not necessarily discouraged by the use of new technology, this infers that the older respondents are willing to try new things and accept new challenges, potentially knowing that if they do not adapt, they can potentially be eliminated. Level of usage, willingness to use, and usage behavior were the three things asked to the department heads and executives, who responded with high favorability. They are responsible for driving results and obtaining good talent, therefore, they would like to capitalize on any tool that helps executives work more efficiently and effectively.

Table 65.1 Personal information

Data	Pop.	%	Data	Pop.	%
Gender			Number of employees		
Male	70	44.9	Under 5	44	29.1
Female	86	55.1	6–15	25	16.6
N/A	2		16–30	6	4.0
Age			30–50	12	7.9
20–30	36	22.8	51+	64	42.4
31–40	44	27.8	N/A	7	
41–50	52	32.9	Company Established		
51–60	21	13.3	Less than 1 year	8	5.4
61+	5	3.2	1–3 years	18	12.1
Education			3–5 years	19	12.8
Middle school	1	0.6	5–10 years	23	15.4
High school	4	2.5	10+ years	81	54.4
Technical school	13	8.3	N/A	9	
College	14	8.9	Do you use a smart phone?		
University	75	47.8	Yes	135	86.0
Master/PhD	50	31.8	No	22	14.0
N/A	1		N/A	1	
Job title/Function			Have you scanned a QR Code before?		
Employee	71	47.0	Yes	117	75.0
Designer	22	14.6	No	39	25.0
Head of design	6	4.0	N/A	2	
Head of mang't	28	18.5			
Head of sales	9	6.0			
C-level	15	9.9			
N/A	7				

Note N = 158

65.5.3 Electronic Shelf Label Usage Intent

Used multiple regression analysis to investigate the respondents' ELS "ease of use" and "usefulness" of the "intention to use" influence. The regression equation is: Use willingness = B0 + B1 × usability + B2 × usefulness (shown in Table 65.3). Ease of use and usefulness have a significant joint impact and influence on willingness to use. Questionnaire revealed that the easier it is to use and the utility it provides will increase willingness to use.

Table 65.2 Basic differences in the variables of each study (aggregated)

Basic Information	Usage			
	Ease	Effectiveness	Willingness	Behavior
Gender				
Age		41+ > 20–40	41+ > 20–40	
Education				
Job		Supervisor > Chairman	Supervisor > Chairman	Supervisor > Chairman
Company size				
Company age	Less than 3 > 5–10 years			Less than 3 years, over 10 > 5–10 years
Smartphone usage				
QR code usage				

Table 65.3 Electronic shelf labels regression coefficient summary table

Independent variable	No standardized regression on coefficients (B)	Standard error (S.E.)	Standardization regression on coefficients(β)	T value	P value
Constant term	0.73	0.23		3.16*	.002
ESL ease of use	0.25	0.06	0.25	4.46*	<.001
ESL usefulness	0.60	0.05	0.67	11.90*	<.001
R^2	0.74				
F	215.06*				
p	<0.001				

*$p < 0.05$

65.6 Conclusion

In this study, the theoretical framework of the TAM attempts to observe the cultural and creative industries workers with ESL and their potential application of the device. Regardless of the respondent's background, the majority agrees that the ELS not only is a handy tool but also can provide a positive function to cultural and creative merchandise. Most respondents also believe that the ease of use combined with usefulness impacts their willingness to adopt. This further validates the theoretical basis of this study, "TAM."

From the statistical analysis of the survey, respondents' willingness to use ESL is an average of 4.99, 4.66 average usage behavior, showing that the majority of respondents hold a positive acceptance rate. The results of this study can be used as a reference for related industries.

65.7   Discovery

During the investigation visit, it was found that creative industry professionals are often alone focusing on their product with low interaction with the outside world. They regard their work as art and deem that it can only be shared with enthusiasts and are reluctant to sell based solely on money. This mentality hinders many talented entrepreneurs in the market and as a result, explains why a lot of cultural and creative merchandise were often not recognized as the best on the market.

65.8   Recommendation

The widespread use of the Internet in the past decade has revolutionized communication between mankind along with the rapid rise of mobile networks in the pasts few years. People are easily accepting and quickly adapting to new technology. As wireless technology matures, convenience and immediate results are now a benchmark requirement. All marketers are striving for the next best thing in terms of how to get information directly to the consumer in the quickest and most efficient way possible.

Taiwan has a famous electronics industry, but whether the industry can apply insights from research and development is essentially important to its growth and survival. Despite the government's strong support for this key industry, Taiwanese entrepreneurs are still part of small and medium micro-enterprises who often do not have sufficient financial and human resources to fully succeed. Their potential is hindered by lack of marketing efforts and as a result, a large amount of creative entrepreneurs are left unknown from the market.

The end goal of this study is to show that ESL is an easy to use marketing tool for entrepreneurs. The government should assist and support this wave by connecting electronic paper companies with micro-enterprises. This enables the two parties to share resources to increase development and the growth of Taiwan's economy.

Currently, QR Code design for the ESL panel is only black and white, but development of new color panel is expected to begin production in third quarter 2015. Furthermore, the respondents have expressed their opinion/concern that the ESL specifications are too small and may not attract the consumer's attention and reduce total usage by consumers. Firms who wish to use ESL should consider the

overall user experience with the technology and strike a balance between consumer view and business/technological limitations against marketing objectives.

From the research findings, cultural and creative practitioners need to change their mindset and be open to marketing their work and selling their merchandise. This can potentially be a good subject for a follow-up research.

References

1. Wu, H.-J. (2011). *Taiwan's cultural and creative enterprises need competitiveness— competitiveness needed to build cultural and creative management thinking and policy recommendations* (pp. 208–214). Taipei: Taiwan's cultural and creative industries Report.
2. Orgeron, C. P., & Goodman, D. (2011), Assessing citizen adoption of e-Government initiatives in Gambia: A validation of the technology acceptance model in information systems success. *MANDELEY*, 271–279.
3. Wang, J.-S., Xyu, S.-F., Lin, Y.-C., & Zeng, Z.-M. (2008). *Implementation of the electronic shelf label-to construct systems using zig bee* (pp. P58–P63). Taipei: Electro pioneer.
4. Wang, J. (2009), Electronic paper chambers construction and properties, graduate school of physical and chemical research institute. *Chinese Academy of doctoral thesis*, Beijing China, pp. 8–13.
5. HO, Meng-Ying. (2008). *Electronic paper application market and future development* (pp. 11–22). Taipei: Through the global LCD Display All.
6. Zhang, Fan, & Hai-Peng, Zhang. (2010). *An electronic shelf label system (ESLS) design* (pp. 95–100). Hangzhou, China: Electronic Technology.
7. Liu, R. –Q. (2010), Electronic paper and development. *China Pulp & Paper Industry*, 78–82.
8. Ciou, M.-H., Wei, S.-Y., & Wu, S.-J. (2012). *Electronic shelf label design based on radio frequency technology*. Beijing China: Railway Computer Application. P33.
9. Hu, K.-J., Zhong, W.-J., & Ciao, J.-W. (2010). *Technology Acceptance Model to explore the impact of fiber optic broadband network user behavior intention of factors* (pp. P161–P186). Taipei: Marketing Comments.
10. Davis, F.D.(1989), Perceived usefulness, perceived ease of use, and user acceptance of information technology. *MIS Quarterly*, 319–340.
11. Venkatesh, V., & Davis, D. (2000). A theoretical extension of the technology acceptance model: Four longitudinal field studies. *Management Science, 46*(2), 186–204.

Chapter 66
Preservation Effect of Thymol Active MAP Packaging on Fresh-Cut Lotus Root

Yabo Fu, Hui Liu, Lu Fu, Wencai Xu and Dongli Li

Abstract In order to extend the preservation period of fresh-cut lotus, three kinds of packaging films were applied to investigate the modified atmosphere effect on fresh-cut lotus. In the experiments, LDPE packaging was used as control while laboratory, self-made SBS/LDPE packaging with and without thymol natural extract active MAP packaging were comparatively studied. The quality properties of samples were measured during 8 days at 4 ± 1 °C and 60 ± 2 % relative humidity. The gas concentration in the package atmosphere and the physiological parameters including browning index, weight loss, hardness, and appearance were measured periodically. The experimental results show that thymol active packaging can slow down the fresh-cut lotus respiration and thus extend the preservation period of fresh vegetables.

Keywords Active MAP · Thymol · Preservation · Fresh-cut · Lotus

66.1 Introduction

Fresh-cut vegetable, also known as light-processing vegetable, was originated from 1950s in the United States. After the fresh vegetable grading, cleaning, peeling and trimming, segmentation, packaging, and other processing, they become immediately edible foods for consumers [1]. Fresh-cut vegetables could be regulated to needs of people from different and avoid the economic loss caused by short-term

Y. Fu (✉) · W. Xu
College of Packaging and Printing Engineering, Tianjin University of Science and Technology, Tianjin, China
e-mail: fuyabo@126.com

Y. Fu · H. Liu · L. Fu · W. Xu · D. Li
Beijing Key Lab. of Printing & Packaging Materials and Technology,
Beijing Institute of Graphic Communication, Beijing, China

excessive supply. But there were many unavoidable problems in the storage of fresh-cut vegetables, for example the oxides and peroxides impacted the nutrient substances of vegetables, so that it resulted in fresh-cut browning. After physical treatment, such as cutting, the vitamin C in fruits and vegetables were easily running off with water loss, the sugar–acid ratio and the flavor of the original fruits and vegetables had changed. At the same time, cutting and peeling increased the contact area of vegetables with oxygen and caused pollution or rot by various microorganisms. Pectin and cellulose separated in the influence of enzyme catalysis, pectin became pectic acid which made cells lost their adhesion force, then the fruits became soft and decayed. Preservation technology is an urgent problem to be solved [2–6].

Active packaging was a good method to solve the above problems on fresh-cut foods. Active packaging systems interacted dynamically between the product it contained and the surrounding environment it existed, which resulted in the activation of some mechanisms to extend the shelf life or quality of the product. Use the plastic films with different air permeability and moisture permeability to make different seal packaging and achieve the spontaneous adjustment of the proportion of gas in the packaging. It could slow down the respiration rate of fruits and vegetables, could slow down physiological aging, and could achieve the purpose of preservation [7]. Italy is the country with the highest postharvest fruit storage ability, where more than 95 % of fresh fruit used MAP to reduce losses.

In this study, we used laboratory self-made SBS/LDPE film with thymol natural extract as active MAP packaging for fresh-cut lotus root preservation experiments, through the performance of physical and physiological measurements of lotus roots to verify the preservation effects of SBS/LDPE films and thymol active packaging on fresh-cut lotus root.

66.2 Experiments

66.2.1 Experimental Materials

Lotus roots were purchased from a nearby produce market. The experimental packaging films were from laboratory and self-made, including LDPE film, SBS (styrene-butadiene rubber) modified LDPE film [8] containing 3 % thymol and SBS modified LDPE film containing 5 % thymol.

66.2.2 Laboratory Apparatus

The main experimental apparatus: PAC CHECK 450 headspace analyzer (Mocon company, USA), GY-2 fruit hardness (Hangzhou Top Instrument Co., Ltd.),

PR-101 digital sugar meter (Atago Co., Ltd., Tokyo, Japan), DT-200B electronic counting scales (Changshu City, Kim Yang Yang weight balance Instrument Co., Ltd.), and WSC-S colorimeter.

66.2.3   Experimental Method

The white, fresh lotus roots with strong organization and without injury were chosen. After purchasing from the market, lotus were transported immediately to laboratory and stored in freezer at 4 °C to pre-cold for 12 h initially. Then the pre-cold lotus roots were treated by washing, peeling, cutting them into 0.5 cm thickness slices and placed in PP trays. After that, fresh-cut lotus roots with PP trays were put into three kinds of films heat sealing packaging bag, each group had six bags as a parallel experiment group, at 4 °C freezer storage. The group A used LDPE film, group B used SBS-LDPE with 3 % thymol film (S-L-3 % thymol), and group C used SBS-LDPE with 5 % thymol film (S-L-5 % thymol). Samples were made the determinations of the relevant indicators every 2 days. Every indicator of the test was repeated three times to achieve the average value.

66.2.4   Fresh-Cut Lotus Test Index and Method

According to the physiological features changes of lotus roots, the following parameters were tested to assess the quality of fresh-cut lotus roots during storage.

1. Browning. Use WSC-S color-meter to determine the color change of lotus root section. L* value was the brightness index, the larger L* value meant the surface of samples tending to be white, otherwise tending to be black, which indicated the browning degree of samples [9, 10].
2. Weight loss rate. To measure the weight change of each group originally and after storage.
3. Hardness. Use the hardness tester to test. Vertical pressure cylinder with a diameter of 5 mm probe broken lotus root section and the maximum pressure could describe the hardness of sample.
4. Headspace gas composition analysis. The concentration of O_2 and CO_2 in the packaging bag were detected with headspace gas analyzer.
5. Appearance evaluation. The main observation of the sample-included surface color, odor, surface morphology, and so on.

66.3   Experimental Results and Analysis

66.3.1   Browning Test

If the appearance of fruits and vegetables with mechanical damage, cell compartments were broken, polyphenol oxidase catalyzed polyphenols to the lower level of aggregation and then caused tissue browning and affected the quality of fruits and vegetables. The segmentation process of fresh-cut fruits and vegetables would accelerate the enzymatic browning [4–6]. From Fig. 66.1, in the first 4 days of the experiment, the samples in different packaging materials appeared with some browning, the reason was that the adequate oxygen supply at first. After 4 to 8 days, the rate of decrease of luminance values became significantly larger. The browning of lotus roots significantly affected sales and consumption. The reason may be the reduced oxygen concentration inside the package. The preservation effects of group C was best, its decrease degree of brightness was the minimum.

66.3.2   Weight Loss Rate

Fresh-cut fruits and vegetables in the storage process were easy to dry. The weight loss rate of the bare sample group was very obvious in the storage period of 8 days, even reached 35 % or so. The fresh-cut lotus roots had lost the value of consumption. The water loss rate of fruits and vegetables in modified atmosphere packaging had a good inhibitory effect. As shown in Fig. 66.2, the weight loss rate of group B throughout the experimental period remained below 0.6 %, showed the best inhibitory effect on water loss. So the moisture permeability of film in group B was conducive to keep moisture of fruits and vegetables.

Fig. 66.1 Samples' brightness variation with storage time
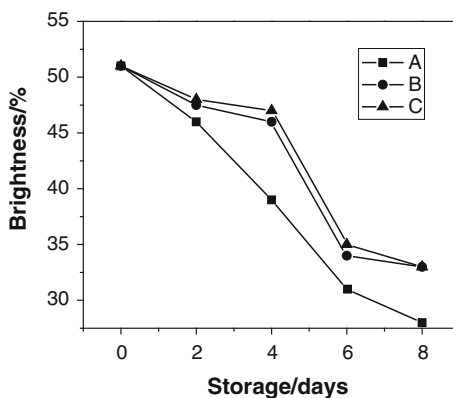
Fig. 66.2 Weight loss rate changes with storage time
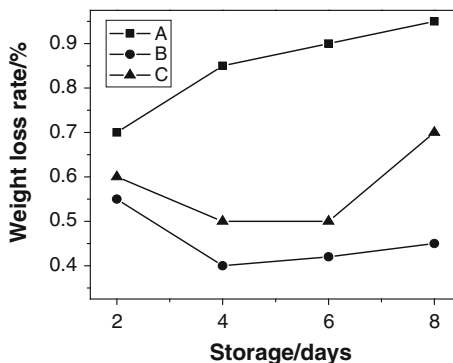
Fig. 66.3 Changes in hardness with storage time
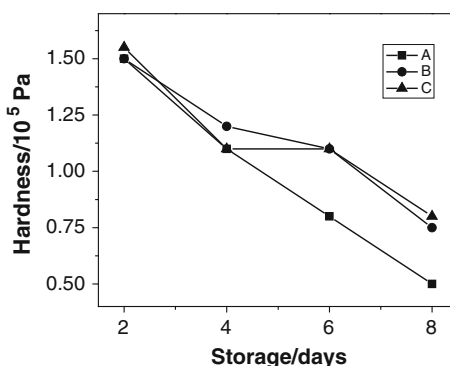
66.3.3 Hardness Analysis

Hardness was one of the main indicators of the quality of fresh-cut fruits and vegetables. It is closely related to the maturation and senescence of fruits and vegetables. As fruits and vegetables progressed in maturity, the decline degree of hardness of the fruits and vegetables became larger. The decreased hardness of fresh-cut lotus roots during storage was shown in Fig. 66.3. At the end of the experiment, the hardness value of group C was the largest among all the experiment groups. The atmosphere was most suitable for the preservation of the environment, had the best preservation effect on fresh-cut lotus roots in the group C.

66.3.4 Headspace Gas Composition Analysis

In the experiment, different kinds of films sealed into bags and the interior included air at first. Fresh-cut lotus roots in the packaging bags breathed was ongoing, and the samples consumed the oxygen of bags and produced carbon dioxide. As the

Fig. 66.4 Variation of
oxygen volume fraction with
storage time
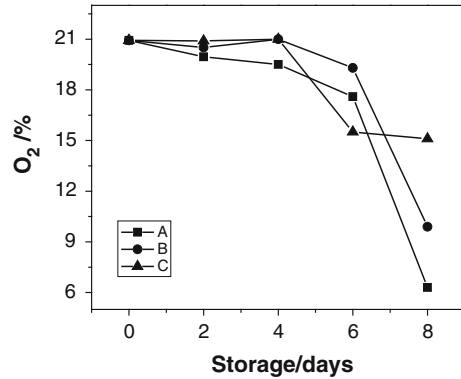
Fig. 66.5 Variation of carbon
dioxide volume fraction with
storage time
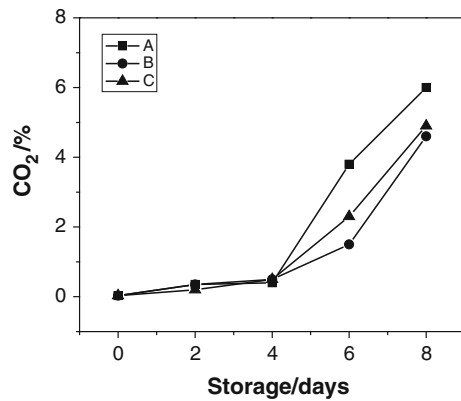
data in Figs. 66.4 and 66.5 were shown, there were little differences between the gas
composition in the package bags and the air in the second day, and there were small
changes in the fourth day. With the increase of storage time and the change of
respiration rate, the content of oxygen in the packages was decreasing and the
content of carbon dioxide was increasing continuously. The headspace gas of group
C had little change. It indicated that the gas permeability and the bactericidal action
of thymol of the films inhibited the respiration of samples. Provide the most suitable
atmosphere for the preservation of fresh-cut lotus roots, so that it was the ideal
material for preservation. In addition, the oxygen content in the group B was also
higher, which showed that the respiration rate of the samples was controlled. Other
dates showed that the preservation effects were general.

66.3.5   Appearance Evaluation

During the test time, the quality of fresh-cut lotus roots changed gradually.
According to the changes in appearance and flavor with the test data, the observation

Table 66.1 Fresh-cut lotus root morphology record

Time	Group A	Group B	Group C
Day 2	No change	No change	No change
Day 4	Become red slightly	Gloss surface, white	Gloss surface, white
Day 6	Become red and black	Become red slightly	Become red slightly
Day 8	Become black	Become red partially	Become red partially
	Severely	Black area <20 %	Black area <10 %

Table 66.2 Appearance evaluation of fresh-cut lotus roots during storage

Time	Group A	Group B	Group C
Day 2	9.5	10	10
Day 4	7.5	9.0	9.5
Day 6	6.5	7.5	8.0
Day 8	5.0	6.0	6.5

records were gave in Table 66.1. We provided 10 points for excellent character of samples and 5 points or below for non-edible. The subjective evaluation data of fresh-cut lotus roots were shown in Table 66.2, the fresh-keeping effects from the looks of group B and group C were good, thus thymol modified LDPE film for the preservation of fresh-cut lotus roots had good effects.

66.4 Conclusions

This work used LDPE film packaging as a control group, the preservation effect of SBS/LDPE with thymol active packaging films on fresh-cut lotus were verified during 8-day-experiment. The experimental results showed that the laboratory, self-made SBS/LDPE with thymol natural active film demonstrated good preservation effects on extending the shelf life of fresh-cut lotus. The film could provide relatively suitable gas atmosphere for the respiration rate of fresh-cut lotus and retard the growth of fungus on the samples. The experimental results also proved that the SBS/LDPE packaging film might provide suitable gas permeability for the fresh-cut lotus roots [8]. The film combined with thymol natural fungicide was a feasible way to keep low-rate respiration and prohibit fungus growth of fresh-cut ones, and thus extended the shelf life of the fresh-cut lotus roots effectively.

References

1. Meng, X., Gao, Z., & Jiang, N. (2008). Recent progress on processing and preservation techniques of fresh-cut fruit. *Preservation and Processing*, *05*, 4–7. (In Chinese).
2. Atda, E., Abe, K., & Yamauchi, N. (1990). Physiological activities of partially processed fruits and vegetables. *Food Technol, 44*(116), 120–122.
3. Gil, M. I., Aguayo, E., & Kader, A. (2006). Quality changes and nutrientretention in fresh-cut versus whole fruits during storage. *Journal of Agriculture and Food Chemistry, 54*, 4284–4429.
4. Zhen, Z. (2009). Fresh-cut fruit browning mechanism and effective way to control. *Preservation and processing, 04*, 5–7. (In Chinese).
5. Liu, J. (2008). Study on fresh-cut fruits and vegetables in question and control. *Chinese fruits and vegetables, 03*, 49. (In Chinese).
6. Song, X. X., Hu, W., Bi, Y., & Jiang, A. (2013). Progress key enzyme enzymatic browning of fruits and vegetables fresh-cut. *Food Industry, 15*, 390–392. (In Chinese).
7. Xu, W., Li, D., & Fu, D. (2013). Preparation and measurement of controlled release SO_2 fungicide active packaging at room temperature. *Packaging Technology and Science*, *26*(S1), 51–58. (In Chinese).
8. Yanru, J. I., Fu, Y., Li, D., & Xu, W. (2014). Effects of Molecular Sieve or 1-methylcyclopropene combined with SBS/LDPE packaging on the shelf-life of cherry tomatoes. *Applied Mechanics and Materials, 469*, 180–184. (In Chinese).
9. Zhenze, W. U. (2001). Modified atmosphere packaging of fresh fruits and vegetables. *Packaging world, 03*, 84–86. (In Chinese).
10. Tao, Y., & Lu, L. (2004). Fruits and vegetables modified atmosphere packaging modified atmosphere packaging mechanism. *Electrical and mechanical information, 05*, 37–41. (In Chinese).
11. Zhang, C. (2004). Study respiration models in modified atmosphere packaging of fruits and vegetables for development. *Agricultural engineering Newspaper, 20*, 281–285. (In Chinese).
12. Glesias, I., Echeverria, G., & Soria, Y. (2008). Differences in fruit colour development. Anthocyanin content, fruit quality and consumer acceptability of eight 'Gala' apple strains. *Scientia Horticulturae*, *119*(1), 32–40.

Chapter 67
Laptop Cushion Packaging Structure Design Based on Green Theory

Yunfei Zhong, Ruirui Chen, Die Hu and Yinghui Zhong

Abstract Laptop, a high-precision electronic product which cannot be avoidable, is subject to various external forces in transportation and sales process. Currently the cushion packaging of the laptop mainly uses plastic foam whose production process often cannot meet the standard, which does not conform to the concept of environmental protection in the twenty-first century. Lenovo laptops of E40 series, for example, were designed cushion packaging structure based on the concept of environmental protection. Three kinds of green materials were selected, such as molded pulp, cardboard, and corrugated board. Three buffer structure packaging solutions were designed based on three different materials. Three schemes were compared according to three different perspectives. In the light of three kinds of schemes' protection performance, price performance, and other aspects, the best scheme was achieved. In this article the best scheme's size calculation, strength checking analysis, and other research aspects were put forward too. The corrugated board solution can be used in both the transport and the sales process for fixing and protecting laptop and in the process of using laptop as a support plate. The design process uses green design processes and methods, which can provide a reference for the later green packaging design.

Keywords Green design · Cushion packaging · Corrugated board · Laptop

Y. Zhong (✉) · D. Hu · Y. Zhong
School of Packaging and Materials Engineering, Hunan University of Technology, Hunan, China
e-mail: maczone@163.com

R. Chen
Zhejiang Dongjing Holdings Ltd, Wenzhou, Zhejiang, China

67.1   Introduction

At present, problems of environment-friendly packaging are gradually going global, becoming the common direction of the joint efforts of the world packaging organization. International environmental groups made clear requirements of that, such as new environmentally friendly packing ISO14000 standards and regulations [1, 2].In contrast, the study and effort of China in that are far below the world leading level. In recent years, the economy of China has entered a period of rapid development; the computer market, especially the laptop market, has been growing at an unprecedentedly speed. However, electronics like laptop is easily to be affected by external forces, such as shack and impact. That is to say, laptop needs more effective production than promotional methods. Scientific and reasonable cushion packaging designs are crucial to achieve this goal. Nowadays, laptop cushion packaging mainly includes the following materials: Foam materials, represented by EPS and EPE which are hazardous to environment, are hard to be recycled, also, such material occupy a lot of space and cost more money on transportation; molded pulp materials, which need to be replaced.

Composite materials, such as paper–plastic composite material, are costly because composite molding process is complicate and this kind of material is hard to be recycled [3–5]. In conclusion, most cushion structures of laptop packaging do not have any features except function of protection. And they will be discarded as trash after used; this way betrays the ideals of low carbon economy and be environment-friendly.

Green packaging is the development direction of the packaging discipline and the road to of the sustainable development of China's packaging industry [6–9]. There are five characteristics principles and standards of green packaging design [10, 11]; (a) Optimality, i.e., optimizing packaging structure and reducing the material cost; (b) Conservation, i.e., using environmental protection material and avoiding waste; (c) Simplicity, i.e., simplifying packaging modeling and guiding green consumption; (d) Easiness, i.e., extending packaging function and making recycle easy; (e) Less streamlining of the plane design.

This article comes up with three kinds of cushion packaging design of Lenovo laptop based on the principle of environment protection, and the best one is explained through comparison.

67.2   Structure Design of Laptop E40 Series

67.2.1   Analysis of Object

The vulnerable position of product is located in the vertical direction of center position of the surface. In order to prevent the products from being damaged when affected by external force, the cushion packaging and the outside shipment packing

Table 67.1 The basic information of Lenovo laptop E40 series

	Lenovo laptop E40 series			
Product information	Length (mm)	344	Sensitivity factor	Dropping
	Width (mm)	233		Shock
	Thickness (mm)	33		Shake
	Weight (kg)	2.25		Humidity
	Fragility (g)	70		Temperature
	Gravity	center		Pressure

should be separated by proper space. In this article, $[G] = 70$ g is adopted after comparison. Another important parameter of packaging design is the product's natural frequency, which is generally measured by actual production test. When vibration frequency is close to the natural frequency, great damage occurs. So, cushion packaging should keep natural frequency of product far from natural frequency of the packaging (Table 67.1).

67.2.2 Physical Distribution Environment

Products are stored in warehouse generally; stack height of seven layers is 1.5 m. Handling operation of normal product's drop height is 90 cm, mainly including manual handling and mechanical loading and unloading two kinds. Products are mainly sent by car or train from Guangzhou to all over the country. Normally, random vibration power spectral density has a larger peak at around 2 and 10 Hz, and there is a maximum peak for the whole frequency band when the frequency arrives at 2 Hz. The natural frequencies of the cushion packaging design should not be close to above two frequencies. Railway transportation has two kinds of impact: vertical impact and horizontal impact. Vertical impact is usually produced when wheels roll on rail, maximum acceleration is 1 g and horizontal acceleration can be up to 2–4 N/s^2. Products transport across the country, temperature, and air humidity change a lot during the process. Since laptop is an electronic product, packaging the product by plastic film and putting desiccant into the package avoids condensation.

67.2.3 Original Analysis of Lenovo Laptop E40

Polyvinyl chloride (PVC) was originally used for packaging cushion of Lenovo laptop of E40 series. Figure 67.1a–c show the cushion packaging, the structure schematic, and cushioning schematic.

The defects of the packaging are as follows: (a) Weather resistance of this cushioning material is poor and the material will slowly decompose harmful hydrogen chloride gas about 50 °C; (b) PVC will produce large amounts of

Fig. 67.1 Original packaging of Lenovo laptop E40. **a** The cushion packaging. **b** The structure schematic. **c** The cushioning schematic

hazardous substances in the process of manufacture, using and disposal of, such as dioxins, halogen acid, which will harm human health. Those substances can cause contamination of soil and water after burned or buried; (c) Such material is thin and prone to distortion, and as the result the product protection ability is weak.

67.3 Design Schemes Based on Green Packaging Material

67.3.1 Scheme of Honeycomb Paperboard

This scheme mainly included honeycomb paperboard cushioning packaging and shipment packaging. The former plays a role in cushion in packaging, which can fix the laptop and accessories. Shipment packing plays the role of logistics transportation and protection. The honeycomb paperboard cushion structure diagram, cushion systems schematic, and package diagram are shown in Fig. 67.2.

67.3.2 Scheme of Pulp Molding

The scheme of pulp molding mainly included pulp molding lining (including the upper cushion pieces and the lower buffers) and shipment packing. The lower buffers fix laptop and its accessories, whereas upper cushioning protects laptop. Shipment packing as an external packing box plays the role in logistics transportation and protection.
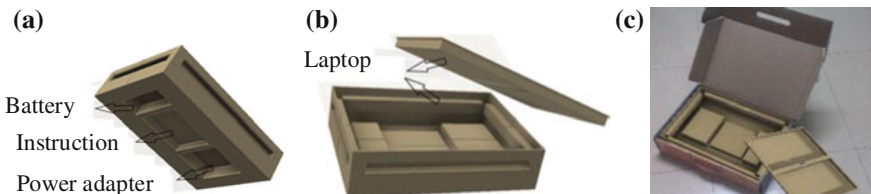
Fig. 67.2 Packaging of Lenovo laptop E40 series based on the honeycomb paperboard. **a** Cushion structure diagram. **b** Cushion systems schematic. **c** Packaging diagram
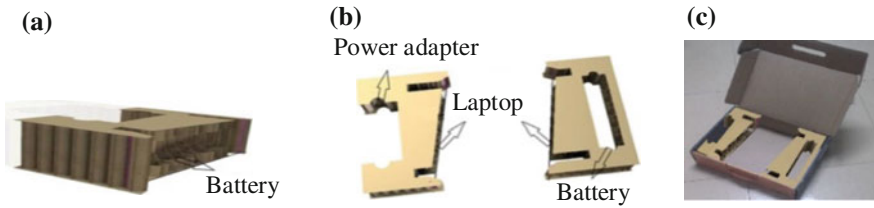
Fig. 67.3 Packaging of Lenovo laptop E40 series based on the pulp molding. **a** Lower cushion schematic. **b** Liner schematic. **c** Whole packaging diagram

Figure 67.3a–c shows the lower cushion schematic, the liner schematic and the whole packaging diagram.

67.3.3   Scheme of Corrugated Board

This design mainly contained the corrugated board cushioning packaging and transportation packaging. The bottom of the cushion protects the product by folding. Functional cushioning cushion consists of two parts, one has the effect of fixed and the other has the effect of protect. Once taking out the product and changing the liners into support bases, the packaging cannot only fix a laptop, but also increase the contact area between the bottom of laptop and air that accelerates the cooling speed. Functional transportation packaging box as an external packing plays the role in logistics transportation and protection. Figure 67.4a–d shows the bottom cushion, combination schematic, cushion packaging diagram, and the whole packaging.
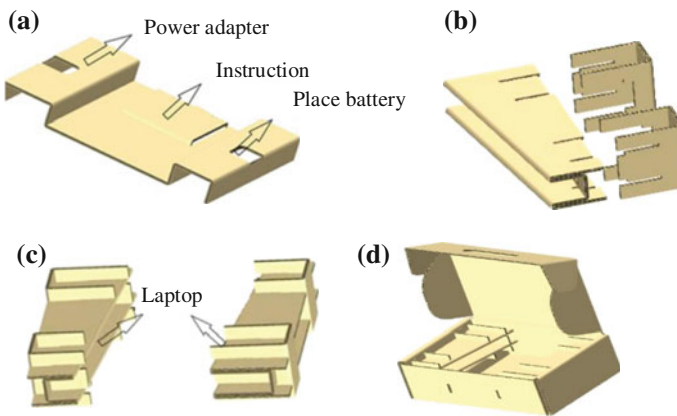
Fig. 67.4 Packaging of Lenovo laptop E40 series based on the corrugated board. **a** The bottom cushion. **b** The combination schematic. **c** The cushion packaging. **d** The whole packaging
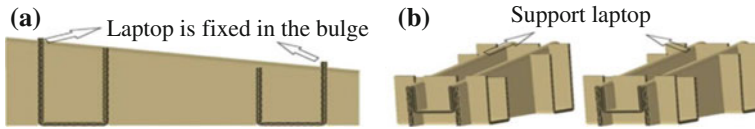
Fig. 67.5 Transition of liner diagram. **a** Liner section diagram. **b** Supporting liner function display diagram

Function liner is designed to realize the transition of the two functions. The liner section diagram and supporting liner function display diagram are shown in Figure 67.5a, b.

67.3.4 Scheme Comparison

According to Table 67.2, all three schemes use green material, the lightest is the paper pulp molding, but it is close to the other two schemes. The paper pulp molding and the honeycomb paperboard cannot be folded, and need more space increasing the cost. While another material is different, the board can be folded into a table to transport, decrease the cost and it is easy to shape by socketing in downstream processes. After comparing with three schemes, the best choice is third scheme.

Table 67.2 Comparison of three kinds of cushion packaging scheme

Scheme	1	2	3
Material	Paper pulp molding	Honeycomb paperboard	Corrugated board
Weight (Kg)	2.9	3.2	3.5
Price (Yuan)	6.8	6.5	5
Packing assembly	No assembly, biggest conveyance space	No assembly, bigger conveyance space	Easy assembly, can be transported as a table
Convenience	Convenient	Most convenient	More convenient
Recycling	Once	Once	Twice

67.4 Strength Checking

67.4.1 The Compressive Strength of Corrugated Case

Laptop is exported in containers. Imaging the rate of decrease caused by dumping time is 30 %, caused by temperature and humidity is 52 %, caused by dumping way is 20 %, caused by handling process is 20 %, and caused by single color printing is 6 %. $P = 1499$ N is pressure on the side of shipping carton box, $C \approx 213$ cm.

Table 67.3 The quantify and ring crush index of corrugated board

Quantify (g/m²)	Ring crush index (N m/g)	Ring crush value (kg)
150	7.6	14.5
105	3.5	4.69
127	6	9.7

The compressive strength of carton box is $B = 5.874 \times E \times T \times C = 0.06E$

To ensure the safety of circulation, $B \geq P$ is necessary. It means that $0.06E \geq 1499$ N, $E \geq 24{,}983$ N/m $= 2.5$ N/cm (Table 67.3)

Laptop is between mid- and high-end goods. The orders of BE, which adopted by the type of corrugated board, from the outside to the inside is $150 + 105 + 105 + 105 + 127$ g/m². The ring crush index and ring crush value of the above cover paper, corrugating medium, and inner paper are as follows.

By using the methods of table lookups, contractibility rate of corrugated board B is 1.36, contractibility rate of corrugated board E is 1.25. So: $P_X = 2.709$ N/cm

$P_X = 2.709 > 2.5$ N/cm,so corrugated board designed above is strong enough to bear such ring crush strength.

67.4.2 Intensity Check of Corrugated Case

Anti-compressing of the packaging is checked by experiments, the instrument adopted is compression equipment, whose model is DC-KT50 KB. In Figure 67.6 b is the contrast of samples before and after the experiments (Table 67.4).

Three experiments average pressure is $P_C = 2827$ N

With calculation methods of anti-compressing and stacking strengths, the results are as follows: (Table 67.5)

According the table above, the practical values are greater than theoretically required value, so the conclusion is: the corrugated case is safe and steady.
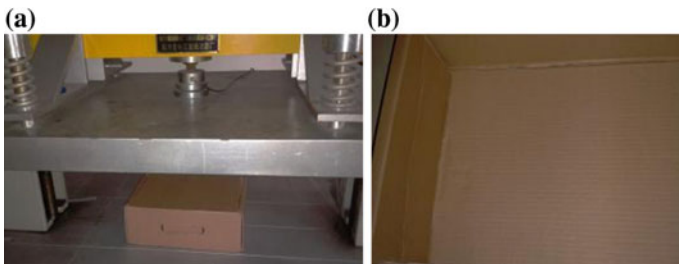
Fig. 67.6 The contrast of samples before and after the test. **a** Sample before the test. **b** Sample after the test

Table 67.4 The experimental data statistics

Times of experiments	1	2	3
Deformation (mm)	11.7	12.6	12.7
Pressure (N)	2820	2830	2830

Table 67.5 Intensity check

	Theoretically required value	Practical value
Anti-compressing strength	1499 N	2827 N
Side strength	7.04 N/cm	13.3 N/cm
Stacking strength	1015.4 N	2827 N

67.5 Conclusions

The principle, flow, and method of green design were used in cushion packaging design of Lenovo laptop E40 series. Three schemes of cushion packaging based on the pulp molding, the honeycomb paperboard, and the corrugated board were compared in many ways, such as price, the ability to protect, and the cost of transportation. The best scheme is the last one–the scheme based on the corrugated board. It can fix and protect the laptop in the process of transportation, storage, and sales; it can also support the computer and be a benefit to the dissipating heat after opened.

References

1. Haijun, J., Han, Z., & Shu, Z. (2007). Packing design for laptops shipping package. *Food and Packaging Machinery, 6*(25), 48–52.
2. Tao, S., & Zhong, Y. (2012). Research and development of green packaging structure design. *Advanced Science Letters, 10*(1), 225–228.
3. Hu, H., Liu, J., & Lu, H. (2010). Research on the application of materials used in green packaging design. *Journal of Shandong Agricultural University (Natural Science)*, *41*(3), 451–454.
4. Qu, C., & Li, Y. (2011). Assembly packaging design of blue and white porcelain tableware. *Packaging Journal, 3*(4), 83–87.
5. Wang, H., & Dong, J. (2013). Drop simulation analysis of plant fiber cushion packaging based on ANSYS. *Packing Engineering, 34*(1), 47–49.
6. Pereira, L., Mafalda, R., & Marconcini, J. M. (2015). The use of sugarcane bagasse-based green materials for sustainable packaging design. *Smart Innovation Systems & Technologies, 35*, 113–123.

7. Zhang, Q., Jiang, X., & He, W. (2011). A research into the tendency of green package design. *Communications in Computer & Information Science, 234*, 219–223.
8. Sun, H., & Wu, Y. (2010). Products optimization based on green design—restructuring and integration of package and packaged article. In *2010 IEEE 11th International Conference on Computer-Aided Industrial Design & Conceptual Design (CAIDCD)*, Vol. 2, pp. 919–921.
9. Liu, Z., Tan, X. D, Wang, H. (2012). Compact thermal modeling for package design with practical power maps. In *2012 International Green Computing Conference (IGCC)*. IEEE, pp. 1–5.
10. Jongmin, K., Sungduk, K., & Jinho, K. (2012). Green design for green business. *Design for Innovative Value towards A Sustainable Society.*
11. Jie, M. (2012). Probing Concepts of Sustainable Package Design. *Lecture Notes in Electrical Engineering, 122*, 109–114.

Chapter 68
Influences of Cleaning and Coating Conditions on the Quality of Eggs

Xiujuan Zhi, Yinghao Xing, Dongxiao Huang, Qigen Tong, Bin Du and Jun Wu

Abstract China maintains a leading position in egg production in the world, but the rate of the mass and the industrialized cleaning for eggs remain low. In this study, different preservation conditions and cleaning processes were applied on fresh eggs, a day after it has been laid. Some conditions were compared, including the coating process (single-layer coating and double–layer coating)—2 % polyvinyl alcohol (PVA) solution and 2‰ dehydrogenation sodium acetate solution, temperature of the solution, hot air drying, and white mineral oil coating. An analysis was conducted on the results, including the weight loss rate, Haugh value, pH value, height of albumen, and the color of yolk. The results are as follows: the color of yolk had no significant difference; set 7 had the highest Haugh value; sets 5, 6, 8 had the lowest weight loss rate; set 1 owned the highest pH value while set 8 the lowest. Heat treatment is useful for reducing the weight loss rate. Coating is good for reducing weight loss rate and delaying the decline of Haugh value.

Keywords Egg cleaning · Coating · Conditions · Freshness

X. Zhi · Q. Tong (✉) · B. Du (✉) · J. Wu
Beijing Laboratory of Food Quality and Safety,
Beijing Engineering Research Center of Egg Production and Processing,
Beijing University of Agriculture, Beijing, China
e-mail: tongqigen@163.com

B. Du
e-mail: bindu80@bua.edu.cn

Y. Xing
Beijing Haoyi Livestock Farming Limited Company, Beijing, China

D. Huang
Heibei Jiaotong Vocational & Technical College, Hebei, China

68.1   Introduction

In recent years, the worldwide occurrence of epidemic like bird flu had triggered high attention for cleaning and sterilization of eggs, impacting China's conventional consumption habits on dirty eggs. The egg coating preservation technology is a top guarantee for the safety and the quality of clean eggs. Moreover, with the improvements in livelihood, people have put forward higher demands to the quality and the safety of poultry eggs [1]. The egg shells without any treatment could be adhered with a big number of microorganisms, resulting in hidden risks to food safety [2]. Existing methods of egg cleaning often involve washing with warm water, sterilization with hot water, ultraviolet sterilization, coating film, and so on [3]. When eggs are washed with water to remove the attached dirt, the wax protective film on the surface of the shell is also destroyed, resulting in easier invasion of pathogenic microorganism [4].

In this study, an egg cleaner was used to perform egg cleaning adopting different treatment combinations. A comparison was made on the influences on eggs, involving factors such as polyvinyl alcohol (PVA) coating film, sodium dehydroacetate solution and its temperature, drying temperature of hot air, white mineral oil membrane. At last, we figured out cost-effective process conditions to inspire the proper egg cleaning methods and processes.

68.2   Experiment and Method

68.2.1   Material and Instrument

Materials and reagents: eggs, Beijing Haoyi Livestock Farming Limited Company; polyvinyl alcohol 088-05 (alcoholysis degree (mole fraction) 86.0–90.0 %, the purity ≥ 91.5 %), Shanxi Sanwei Group Co., Ltd; 10 # white mineral oil, Dongguan Luofu Lubricating Oil Co., Ltd.

Instruments: ZYX–JS1 egg cleaner, Shenzhen Zhenye Intelligent Egg Machinery Co., Ltd.; egg analyzer, ORKA Food Technology Ltd.; electronic balance, Germany Sartorius Co., Ltd; XPT-D high-speed disperser, The HI-2225 pH meter, egg candler, compasses, homogenizer, pH acidity meter.

68.2.2   Method

Fresh eggs, 24 h after being laid, went through water cleaning, water bathing (2 % PVA solution, 2 ‰ dehydrogenation sodium acetate, and water temperature control), the controlled air drying, and white mineral oil film. The storage conditions

Table 68.1 Condition numbers and treatment methods

No.	2 % PVA solution	2 ‰ dehydrogenation sodium acetate	85 °C water temperature	100 °C air drying	White mineral oil membrane
0 (blank)	Void	Void	Void	Void	Void
1	Void	Being	Being	Being	Void
2	Being	Being	Being	Being	Void
3	Being	Being	Being	Being	Being
4	Being	Void	Being	Being	Being
5	Void	Void	Being	Being	Being
6	Void	Void	Void	Being	Being
7	Being	Being	Void	Being	Void
8	Being	Being	Void	Being	Being
9	Void	Void	Being	Being	Void
10	Being	Being	Being	Being	Being

are as follows: a temperature of 32 ± 5 °C, normal temperature of Beijing between July and September, and humidity of 60 ± 5 %. The experiment was repeated five times on each combination. According to the actual production conditions, 11 sets of conditions were compared (Table 68.1).

68.2.3 Measurement Indicators

Weight loss: egg weight loss rate after the storage period.

$$w = (m_1 - m_2) \times 100\,\%/m_1 \qquad (68.2.1)$$

w: weight loss rate; m_1: pre-storage weight; m_2: post-storage weight.

Haugh units: an indicator of egg quality, it is calculated with an egg analyzer by measuring the swan's egg weight and thick albumen height [5].

$$\mathrm{Hu} = 100 \times \lg\left(H - 1.7m^{0.37} + 7.57\right) \qquad (68.2.2)$$

Hu: Haugh Unit; H: thick albumen height (mm); m: weight of swan egg(s).

Yolk color: measured by egg analyzer.

pH value(whole egg): eggs were homogenized by homogenizer and then measured with pH acidity meter.

68.2.4 Data Processing

Five parallel data were analyzed through Duncan's multiple comparison. MS Excel 2007 was used to perform SPSS 19.0 and 90 % confidence level (CL) evaluation on the data [6]. The drawings were completed with, Origin 8.0.

68.3 Results and Discussion

68.3.1 Weight Loss Rate

As shown in Fig. 68.1, the weight loss rate rose gradually in the whole storage. Sets 0, 1, 2, 7, and 9, which had no white oil films, had a higher weight loss than the sets of non-white mineral oil membranes, indicating that the membranes had a remarkable effect. Moreover, slight denaturation of eggshell membrane protein resulted from temporary temperature increase, along with PVA membranes, also had certain influence. Set 10, which got through high temperature, PVA, and white mineral oil membranes treatment, had a low weight loss rate from door to door, but there was no significant statistical difference between set 10 and sets 3, 4, 5, 6, and 8 in these white mineral oil sets. PVA could prompt the solution to have a relatively high viscosity, influencing the rotation of the conveyors and the sediment of PVA at the bottom, which was not easy to remove, resulting in increase of labor and material cost. In the perspective of the weight loss rate, temporary temperature increase and white mineral oil film worked well.

Fig. 68.1 Weight loss rate in each set

Fig. 68.2 pH value in each set
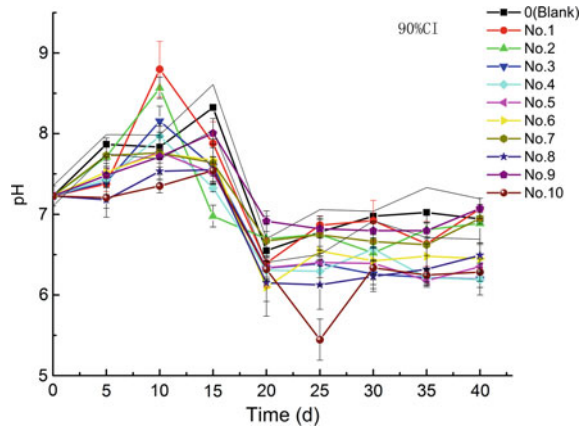
68.3.2 pH Value (Whole Egg)

The results of pH value are shown in Fig. 68.2. On the whole, the pH value rose first, then fell and was flat at last. The uptrend was caused by less CO_2 out flow from eggs; and a drop of pH value was due to the fact that remaining CO_2 was higher than CO_2 emitted from biochemical reaction in the shell chamber or egg protein; at last, the balanced trend was resulted from a dynamic balance between the emitted and outflowed CO_2. Temporary heating could make the above process go forward. The CO_2 permeability of eggshell protein membrane was likely to be lower due to slight denaturation. For this point, temporary heating is beneficial to the relatively bigger change of pH value and increased stress resistance performance of the processed eggs.

68.3.3 Haugh Values

Haugh value is an important indicator of the freshness of eggs. The higher Haugh value is, the fresher the egg is. As shown in Fig. 68.3, the Haugh values gradually decreased in the storage periods. There were significant variations on the fifth, tenth, and fifteenth day; on the twentieth day, set 9, which had non-white oil membrane or non-PVA film and sets 5 and 8, which had white oil membranes, had significant variations; on the twenty-fifth day, the variation is higher between these sets, and sets 8 and 5 had the highest value; at last, the variation tended to be low. From the point of Haugh values, white oil sets had obvious advantages, especially from the twentieth to twenty-fifth days. PVA film, dehydrogenation sodium acetate, and temporary heating process were only better than blank. Possibly, white oil film polyvinyl alcohol membrane and slight denaturation caused by heating could partly seal the eggshell microporous to some extent, and then restrain inner physiological

Fig. 68.3 Haugh value in each set

and biochemical reaction [7]. White oil membranes worked best in all of the three. Temporary heating treatment and white mineral oil membranes are more cost-effective.

68.3.4 Yolk Color

As shown in Fig. 68.4, yolk color was slightly higher in storage and had no significant variation in sets. A few outliers may be caused by the error. The yolk color somewhat changed while selecting processing conditions. Yolk color was not an important indicator in these sets.

Fig. 68.4 Yolk color in each set

68.4   Conclusion

The protective eggshell, inner film, and lysozyme in albumen can help eggs to prevent invasion of microbes. Cleaning with water alone can damage the egg's self-protection mechanism. As indicated from the results of weight loss rate and Haugh value, temporary heating and white mineral oil membranes are more cost-effective, easy to operate. The yolk color did not have a significant variation in each condition. All in all, the conditions of set 5, including washing with water of 36 °C, heating with water of 85 °C, drying with 100 °C hot air to dry, and spraying of white mineral oil, are of low-cost and convenience. With a lower cost of maintenance, they can effectively extend the shelf life of eggs and ensure the quality.

References

1. Yang, S.-f. (2008). The studies on the formulations of cleaning disinfectant of the Egg and the technology for washing Egg. *Hunan Agricultural University*, 2–5.
2. Yang, S.-f., Ma, M.-h., & Zhong, K.-m. (2007). The importance of key techniques of clean egg production and consumption in our country. *Modern Food Science and Technology*, *23*(3), 53–56.
3. Lin, W.-t. (2008). The study of egg cleaning. *The Light and Textile Industries of Fujian*, *1*, 12–15.
4. Hu, X.-b., Ren, Y.-l., & Chen, H. (2007). Effect of different dry conditions on freshness of eggs. *Food and Machinery*, *3*(5), 112–115.
5. I, J.-y., & Tong, Q.-g. (2014). Investigation and analysis of sale time and freshness of eggs in supermarket. *Academic Periodical of Farm Products Processing*, *4*(2), 66–68 + 70.
6. Wang, L., & Wang, G. (2002). *Basis of analytical chemistry* (2nd ed.). Beijing, China: Chemical Industry Press.
7. Liu, H.-z. (2005). Study on the preservation techniques of eggs with film. *China Agricultural University*, 15–23.

Chapter 69
The Research on Modified Atmosphere Packaging Preservation of Fresh-Cut Iceberg Lettuce

Yanxin Xu, Xiangning Chen, Li Xu and Bin Du

Abstract Modified atmosphere packaging has broad prospects for development. This experiment in order to study the effect of modified atmosphere packaging on the preservation effect of fresh-cut lettuce, lettuce after cleaning, disinfection, dehydration, cutting a series of machining process, with different packaging materials and the proportion of different gases to modified atmosphere packaging, refrigerated at 4 °C, the respiration, intensity microorganism, weightlessness rate, vitamin C, chlorophyll, and conductivity of the lettuce were determined in the bag every two day, screened the best material and the best ratio of gas for lettuce; the results showed that the suitable packaging materials and gas ratio of O_2 and CO_2 were beneficial to extend the shelf life of fresh-cut lettuce, maintained the appropriate respiration intensity, effectively inhibited the growth of microorganisms and reduced VC, chlorophyll, and other nutrient loss. Lettuce in the storage process is to maintain the quality of test results. Test obtained the best packaging materials and the best gas proportion of fresh-cut lettuce, namely best packaging materials for PE composite nylon, inflatable proportion for 3 % O_2 + 10 % CO_2, this combination can keep the quality good of fresh-cut lettuce in the process of storage, the preservation period of lettuce extended from 4–5 days to 14 days.

Keywords Modified atmosphere packaging (MAP) · Preservation · Fresh cut · Iceberg lettuce · Quality

Y. Xu · X. Chen (✉) · L. Xu · B. Du
Department of Food Science and Engineering,
Beijing University of Agricultural, Beijing, China
e-mail: chenxiangning@bua.edu.cn

69.1   Introduction

Lettuce has wide planting area and large output in our country, is rich in carbo-hydrates, protein, vitamins, inorganic salt, and fat, and has become an important source of nutrition Lettuce. With the improvement of people's consumption level, fresh-cut lettuce consumption demand is more and more large, and the proportion of food composition for an increasingly higher and higher, but this kind of veg-etable because of its large leaf area, crisp texture and high moisture content etc., so the water of harvest lettuce evaporates quickly, be susceptible to mechanical injury, and have high respiratory intensity and thermal breathing [1], so it often happens wilting, yellowing and rotting, and difficult to fresh-keeping, resulting in complete loss of commodity value.

Modified atmosphere packaging preservation is an effective means to solve the problem of fresh vegetables. The traditional method of keeping lettuce fresh has low-temperature preservation, and antistaling agent, etc. Practice shows that these methods for the preservation of lettuce have played a positive and effective role, but also defects in different degrees, such as high-energy consumption of the low-temperature storage, chemical pollution of antistaling agent lead to health hazards and other issues. Therefore, the vegetable industry is in urgent need of a low-energy consumption, safe and effective method of keeping fresh [2]. Controlled atmosphere (CA) is a preservation method of cold storage which uses low tem-perature to control the gas concentration of O_2, CO_2 and maintains minimum breathing of vegetables, it can effectively inhibit ethylene synthesis speed of fruit vegetable and root vegetables, so as to achieve better preservation effect [3, 4]. Modified atmosphere packaging (MAP) is a new type of fresh-keeping means which has developed in recent years on the basis of CA, it can be used to adjust the gas composition ratio of packaging materials, by regulating the concentration of O_2, CO_2 concentration and humidity in storage microenvironment to achieve the pur-pose of preservation.

The study found that the packaged lettuce can be effectively avoided of water loss and wilting phenomenon during storage, the key of modified atmosphere packaging materials development is to keep the transmittance of O_2, CO_2, and water vapor permeability rate of packaging materials to match the leafy vegetables res-piratory rate. This research agrees with Nandane [5] and Rahman's [6] results, namely modified atmosphere packaging preservation by regulating and controlling gas composition and proportion of packaging container, to make vegetables to maintain lower respiratory rate and not produce anaerobic respiration, thus delaying the maturity of fresh vegetables. But at present, aiming at the lack of modified atmosphere packaging materials of for lettuce shortage, the development of appropriate MAP materials is the key step to improve the effect of controlled atmosphere packaging of fresh lettuce and speed up the commercial application and promotion [7–9]. Therefore, developing a highly targeted and good preservation effect material will undoubtedly is necessary to solve the problem of rapid commercialization.

69.2   Materials and Methods

69.2.1   Materials

The supply of lettuce were produced in Hebei province Qinhuangdao lettuce planting base, transporting to Beijing University of Agricultural by the Beijing Yunong High-quality Farm Product Planting Company under the condition of cold chain, then precooling to 4 °C. Choosing fresh, medium maturity, free from infestation and damage, the same size of lettuce, after cutting, cleaning, first time disinfection (concentration of sodium hypochlorite 40–50 ppm), secondary sterilization (concentration of sodium hypochlorite 70–80 ppm), dehydration, and a series of processing for modified atmosphere packaging test. Four kinds of packaging materials used in the test are, respectively, A: PE composite nylon, B: PD961, C: PE (poly ethylene), and D: PVC (polyvinyl chloride) (Specifications are length * width = 225 mm * 225 mm)

69.2.2   Sample Preparation and Treatment

After treatment, fresh-cut lettuce was put into the above four kinds of bags, each bag about 150 g, modified atmosphere packaging machine vacuum pumping first and one-time charge into CO_2 and O_2, N_2 balance, air packaging as control group, the proportion of gas filling was shown in the following Table 69.1, and after sealed, storage in the (4 + 1) °C refrigerator, take one sample every other one day, for the best sensory evaluation as an index, screening out the best fresh packaging materials and the best proportion of gas range.

Under the condition of the best packaging materials, selecting the best our types of gas ratio within the scope, modified after atmosphere packaging sealing, storage in the (4 + 1) °C refrigerator, take one sample every other one day, respectively, measuring the indexes, each test was repeated three times, charged into the air, as the control group, so as to screen out the optimum gas ratio.

Table 69.1 Proportion of gas inside the packaging bag

Serial number	The proportion of gas volume fraction		
	O_2 (%)	CO_2 (%)	N_2 (%)
1	3	10	87
2	10	17	73
3	20	30	50
CK	21	0.03	78

69.2.3 Measurements

69.2.3.1 Weight Loss

Weighing method: the raw data of lettuce was measured by 0 day, and the quality of each sample was measured every other day, and the three times of each group were measured. Weight loss was calculated as loss of weight from the initial weight of the same packages.

69.2.3.2 Atmosphere Composition

The O_2 and CO_2 concentrations inside the bags were monitored using an accurate gas analyzer (Checkpoint, PBI Dansensor, Ringsted, Denmark). O_2 and CO_2 values are expressed as partial pressures. In this case O_2, CO_2 and N_2 concentration were determined. N_2 concentrations in the bags were calculated using $[N_2] = 100 - [O_2] - [CO_2]$, where the concentration values are expressed as a percentage (%) [10].

69.2.3.3 Chlorophyll Content

In 0.5 g frozen crushed leaves, plus 9 ml of *n*-hexane and 15 ml of ethanol:acetone (1:2) mixture was placed in the dark for 5 h at 5 °C, vibration once every 15 min. After reaction, 25 ml of 1 mol/L NaCl solution was added, with oscillation, in 4 °C 10,000 r/min, the centrifugal 30 min. The absorbance of 1 ml supernatant under 644 and 662 nm was measured by spectrophotometer.

69.2.3.4 Vitamin C Determination

According to the determination of GB 6195-1986, the measurement for content of vitamin C of fruits and vegetables (2,6- two chlorine indophenols titration method).

69.2.3.5 Relative Conductivity

Take five leaves (fresh weight 150–200 mg, excluding the main vein) in 20 ml of demonized water after cleaning; record the electrical conductivity of water, for P0. After the vibration of 3H, the electrical conductivity of the measurement was recorded as P1. Then a boiling water bath for 5 min, measuring its largest electrical conductivity after cooling, remember to P2.

69.2.3.6 Total Number of Colonies

Refer to GB 4789.2-2010, national food safety standards for food microbiology inspection of the total number of colonies.

69.2.3.7 Sensory Evaluation

The sensory characteristics of fresh lettuce were evaluated by 5 trained judges. In the taste chamber, the sensory characteristics including the taste, smell, and brittleness of the sensory characteristics were evaluated. Each person has a separate booth to avoid the interaction of sensory evaluation. The visual features include color, general freshness, general appearance are scored [11].

69.3 Results and Discussion

69.3.1 Screening Results of Optimal Packing Material and the Optimum Gas Proportion

With different packing materials of fresh-cut lettuce for modified atmosphere packaging, proportional gas filling carried out in accordance with Table 69.1, in 2–5 °C storage to 14 days, every two days of sensory evaluation. As can be seen from Table 69.2: the preservation effect on fresh air control group of different packaging materials was relatively poor, effect of packaging materials A on the preservation was best, materials B, C, and D between the 6–10 days in turn lose commercial value, effect on preservation was poor, A1 also has commercial value after 14 days, lettuce leaves without browning decay happened, so PE composite

Table 69.2 Sensory score of lettuce for different packaging materials and air conditioning packages

Storage days	Different packaging materials and different gas proportion combination															
	A	A	A	A	B	B	B	B	C	C	C	C	D	D	D	D
	1	2	3	CK	1	2	3	CK	1	2	3	CK	1	2	3	CK
0	9	9	9	9	9	9	9	9	9	9	9	9	9	9	9	9
2	9	9	9	9	9	9	9	7	9	9	9	7	7	9	9	7
4	9	9	9	7	7	7	9	7	7	9	7	5	7	7	7	5
6	9	9	9	7	7	5	7	5	7	7	5	3	5	7	7	5
8	9	9	9	5	5	5	5	5	5	5	3	5	5	7	5	3
10	9	9	7	3	5	3	5	3	5	3	1	1	3	5	5	1
12	9	7	7	1	3	1	1	1	3	1	1	1	1	3	3	1
14	9	7	5	1	1	1	1	1	1	1	1	1	1	1	1	1

nylon materials had the longest storage days. The next step is to select the optimum proportion of gas in the range of 3 % O_2 + 10 % CO_2 with PE nylon composite material. Selecting four proportions of A: 3 % O_2 + 10 % CO_2, B: 2 % O_2 + 7 % CO_2, C: 3 % O_2 + 8 CO_2 %, D: 4 % O_2 + 9 % CO_2 and CK: air control group, and carried out all the indexes.

69.3.2 Screening of the Gas Proportion Under the Condition of Modified Atmosphere Packaging

69.3.2.1 Weight Loss

As shown in Fig. 69.1, the weight loss rate changes of fresh-cut lettuce is not big during the whole period of storage, but modified atmosphere packaging can reduce the water loss of fresh-cut lettuce, which the processing effect in group A and group D is best, from the 4th day, weightlessness rate is lower than the other groups, weightlessness rate of groups CK is the highest.

69.3.2.2 Atmosphere Composition

The proportion of O_2 in 14 days became very small, so the CO_2 was used to describe the change of gas composition. As shown in Fig. 69.2, the proportion of CO_2 gradually increases with the storage time, the CO_2 associated with the air permeability of the bags, from the 10th days, the ratio of CO_2 gradually close to the dynamic balance, CO_2 of CK group increase from 0.03 to 15 %.

Fig. 69.1 Effect of modified atmosphere packaging treatment at low temperature on weight loss in fresh-cut iceberg lettuce
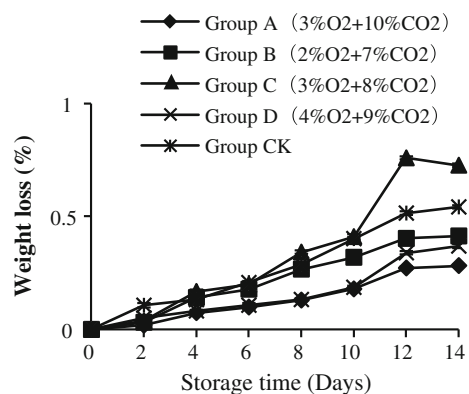
Fig. 69.2 Effect of modified atmosphere packaging treatment at low temperature on CO_2 proportion in fresh-cut iceberg lettuce
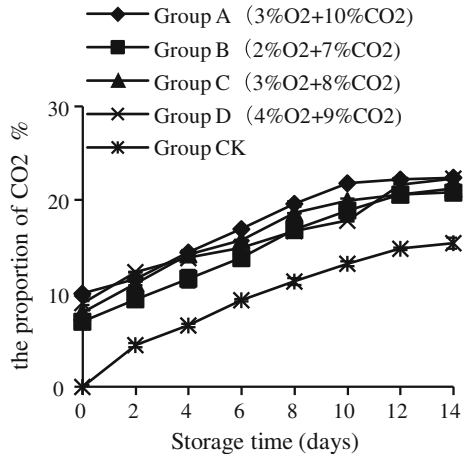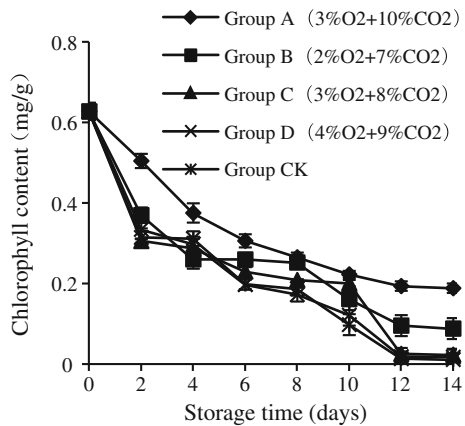

Fig. 69.3 Effect of modified atmosphere packaging treatment at low temperature on chlorophyll content in fresh-cut iceberg lettuce

69.3.2.3   Chlorophyll Content

Figure 69.3 shows that in the whole process of storage and chlorophyll content in each group was decreased, the CK group decreased most quickly, the content of chlorophyll in group A was significantly higher than that of other groups, to the end of the storage, the content of chlorophyll in group A is 10 times that of CK, the content of O_2 in CK group was high, the tissue respiration inhibition degree was not strong, chlorophyll and environmental oxygen has full contact, as well as was be oxidized and decomposed.

Fig. 69.4 Effect of modified atmosphere packaging treatment at low temperature on vitamin C content in fresh-cut iceberg lettuce
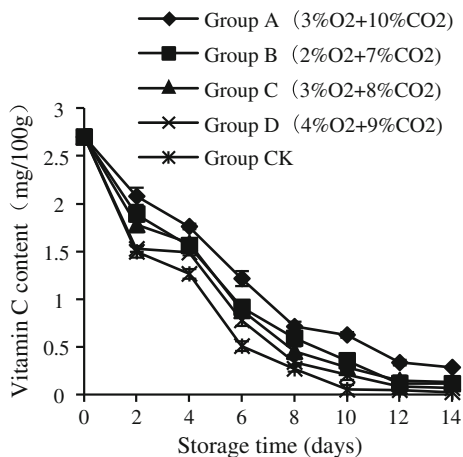
69.3.2.4   Vitamin C Determination

As shown in Fig. 69.4, in the whole process of storage, vitamin C content in each group showed different amplitude decreased, the amplitude of the group A decreased minimum, the biggest drop was CK group, at the end of storage, the VC content in CK group was only 0.023 mg/100 g, the differences in the effects of different gas proportion on VC content in vegetable tissues was large, so regulating appropriate gas proportion is very important for the protective effect of VC, CK group has relatively high oxygen content, respiration, so VC content declined rapidly.

69.3.2.5   Relative Conductivity

Figure 69.5 shows that the relative electric conductivity of fresh-cut iceberg lettuce in the treatment group and control group increased gradually in the storage process, reflecting the permeability of cell membrane and the aging degree increased. At the end of storage, the relative electrical conductivity of A, B, C, D four groups were significantly lower than that of the CK group. Among them, the reduction range of group A was the smallest.

69.3.2.6   Total Number of Colonies

From Fig. 69.6 shows, different ratio of gas treatment were able to inhibited microbial growth of fresh-cut lettuce in the process of storage, which A group inhibited microbial effect best. After 14 days of storage, the mean log of bacteria is still lower than 6 CFU/g, while the control group, stored to 6 day, the mean logarithm of bacteria is higher than 6 CFU/g.

Fig. 69.5 Effect of modified atmosphere packaging treatment at low temperature on relative conductivity in fresh-cut iceberg lettuce
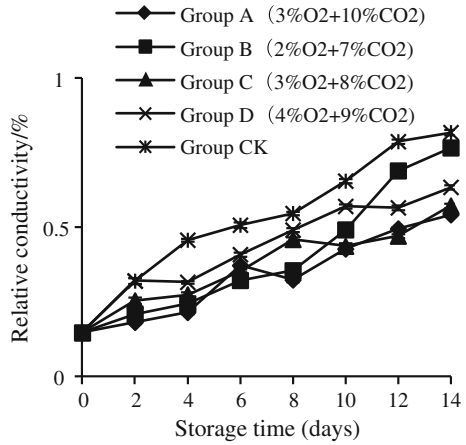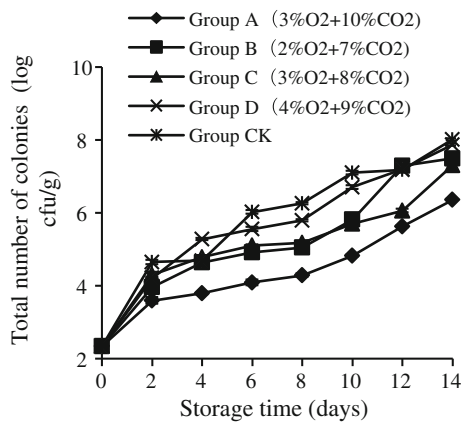

Fig. 69.6 Effect of modified atmosphere packaging treatment at low temperature on total number of colonies in fresh-cut iceberg lettuce

69.3.2.7   Sensory Evaluation

Table 69.3 shows that storage for up to 14 days, the sensory quality of group A fresh-cut lettuce was best, control group was the worst, storage to the 4 day reached commodity boundaries and with the extension of storage time, decay degree is more and more serious, group C and group D were stored to 8 days and 6 days when browning and rotting were appeared, decaying to commercial boundaries. B group to the 14th day appeared rotten phenomenon at the leaf cut, but during the whole storage browning lighter, so low O_2 proportion and a high proportion of CO_2 treatment for fresh-cut lettuce could be in a certain extent to suppress the decay deterioration and browning occurred.

Table 69.3 Effect of modified atmosphere packaging treatment at low temperature on sensory evaluation in fresh-cut iceberg lettuce

Storage days	Group				
	A	B	C	D	CK
0	9	9	9	9	9
2	9	9	9	9	7
4	9	9	7	7	5
6	9	7	7	7	5
8	9	7	7	5	3
10	7	7	5	3	3
12	7	5	5	3	1
14	7	5	5	3	1

69.4 Conclusions

The results showed that suitable packaging materials and gas proportion of O_2 and CO_2 can extend the shelf life of fresh-cut lettuce, under the condition of 4 °C, using the gas proportion of 3 % O_2 + 10 % CO_2 and PE composite nylon [Oxygen transmittance of 102.545GTR/(cc/m^2 day); carbon dioxide transmittance of 150.765GTR/(cc/m^2 day)] packaging materials for modified atmosphere packaging, can maintain appropriate respiratory intensity of fresh-cut lettuce, effectively inhibited the growth of microorganisms, and reduce the loss of VC, chlorophyll and other nutrients, the preservation period of lettuce was extended from 4–5 days to 14 days. The principle of preservation of PE composite nylon needs to continue to study. This has a strong application value in actual production and circulation.

References

1. Bhat, S. (2013). Minimal processing and preservation of fruits and vegetables by active packaging. *International Journal of Herbal Medicine, 1*(2), 131–138.
2. Koraddi, V. V., & Devendrappa, S. (2012). Analysis of physiological loss of weight of vegetables under refrigerated conditions. *International Journal of Farm Sciences, 1*(1), 61–68.
3. Fonseca, S. C., Oliveira, F. A., & Brecht, J. K. (2002). Modelling respiration rate of fresh fruits and vegetables for modified atmosphere packages: A review. *Journal of Food Engineering, 52* (2), 99–119.
4. Dash, S. K., Kar, A., & Gorrepati, K. (2013). Modified atmosphere packaging of minimally processed fruits and vegetables. *Trends in Post Harvest Technology*, *1*(1), 1–19.
5. Nandane, A. S., & Jain, R. K. (2011). Value addition of fruits and vegetables by edible packaging: Scope and constraints. *A Journal of Food Science & Technology*, *1*(1), 1–11.

6. Rahman, M. M., Miaruddin, M., Chowdhury, M. G. F., Khan, M. H. H., & Matin, M. A. (2013). Effect of different packaging systems and chlorination on the quality and shelf life of green chilli. *Bangladesh Journal of Agricultural Research, 37*(4), 729–736.
7. Varoquaux, P., Mazollier, J., & Albagnac, G. (1996). The influence of raw material characteristics on the storage life of fresh cut butter head lettuce. *Postharvest Biology and Technology*, *9*(2), 127–139.
8. Berger, H., Galletti, L., Escalona, V., Saenz, C., & Gorny, J. R. (1997). *Fresh Cut Fruits and Vegetables and MAP, Davis, California, USA*, July 13–18, *Postharvest Horticulture Series,* Vol. 19. Department of Pomology, University of California, pp. 16–22.
9. Barriga, M. I., Trachy, G., Willemot, C., et al. (1991). Microbial changes in shredded iceberg lettuce stored under controlled atmospheres. *Journal of Food Science*, *56*(6), 1586–1588.
10. Aday, M. S., Caner, C., & Rahvalı, F. (2011). Effect of oxygen and carbon dioxide absorbers on strawberry quality. *Postharvest Biology and Technology, 62*, 179–187.
11. Agüero, M. V., & Ponce, A. G. (2011). Lettuce quality loss under conditions that favor the wilting phenomenon. *Postharvest Biology and Technology, 59*, 124–131.

Chapter 70
Research of 9 Storage Factors' Impacts on Swan Egg Quality by Using Plackett–Burman Design

Xiujuan Zhi, Yinghao Xing, Qigen Tong, Bin Du and Jun Wu

Abstract Thanks to the species characteristics and loose breeding for swans and swan eggs feature high nutritional and commercial values. So it is of great significance to take technical means to prolong the storage period of swan eggs. Adopting the PB experiment, the study makes an analysis on the impacts of some factors on the storage effect, including outer shell film of swan eggs, polyvinyl alcohol (PVA) membrane, coating temperature of PVA membrane, temperature of wind drying, storage temperature, white mineral oil membrane, bran storage, piled storage, and placement (horizontal or vertical). Analytical models show that: as for weight loss, the storage temperature for 5 °C and white mineral oil membrane are key factors; for haugh unit, the storage temperature for 5 °C, temperature of hot air drying for 70 °C, and white mineral oil membrane are the remarkable influencing factors; coating oil membrane, storage temperature, and placement influence the diameter of air chamber. The conclusion of the study provides a certain theoretical bases for properly selecting and effectively using the methods to improve the freshness of eggs in a manufacturing process.

Keywords Swan egg · Coating · Storage · Plackett–Burman design

X. Zhi · Q. Tong · B. Du (✉) · J. Wu (✉)
Beijing Laboratory of Food Quality and Safety, Beijing Engineering Research
Center of Egg Production and Processing, Beijing University of Agriculture, Beijing, China
e-mail: bindu80@bua.edu.cn

J. Wu
e-mail: wujun9173@163.com

Y. Xing
Beijing Haoyi Livestock Farming Limited Company, Beijing, China

70.1 Introduction

China has been the world's top poultry egg manufacturer for 20 consecutive years [1]. Poultry eggs boast high moisture and nutrition. Swan eggs have been rated by the World Health Organization (WHO) as one of the top green food. Improper storages may cause a change of freshness indicators of swan eggs. Therefore swan eggs are in urgent need of preservation. There are a variety of technical methods in this regard, such as low temperature [2], clean and sterilization [3], coating [4–6], and upright placement. We will discuss how to reasonably select and effectively use a variety of methods or factors to keep eggs' freshness and lay a theoretical foundation for the future of industrial production.

Plackett–Burman design is put forward by Plackett and Burman (PB), which was based on incomplete balance principle of plate, using N experiments to study $(N − 1)$ variable (N generally a multiple of 4) [7]. The PB design, based on the equilibrium principle and the least amount of experiments, effectively estimates the main effect and most important factors from numerous investigation factors for further study [8].

70.2 Experiment and Method

70.2.1 Material and Instrument

Materials and Reagents: swan eggs, Haoyi Livestock Farming Limited Company; Polyvinyl alcohol 088-05 [alcoholysis degree (mole fraction) 86.0–90.0 %, the purity ≥ 91.5 %], Shanxi Sanwei Group Co., Ltd; 10 # white mineral oil, Dongguan Luofu Lubricating Oil Co., Ltd.

Instruments: ZYX-JS1 egg cleaner, Shenzhen Zhenye Intelligent Egg Machinery Co., Ltd.; Egg analyzer, ORKA Food Technology Ltd.; 514 tpd035480 Sartorius electronic balance, Germany Sartorius Co., Ltd; Design-Expert software, Stat-Ease, Inc.; egg candler, compasses.

70.2.2 Method

70.2.2.1 Processing of Swan Eggs

Take fresh swan eggs within 48 h after being laid. The process is as follows:

Polish the outer shell film with steel wire ball $\rightarrow$ egg cleaning(warm water $\rightarrow$ manual removal of cracked eggs $\rightarrow$ coating by PVA membrane at a certain temperature $\rightarrow$ drying by hot air at a certain temperature $\rightarrow$ white mineral oil film like spraying $\rightarrow$ Bran storage $\rightarrow$ piled storage $\rightarrow$ placement(horizontal or vertical) $\rightarrow$ storeroom. Take them out after 45 days to measure the indicators.

70.2.2.2   Indicators

Weight loss: weight loss rate of eggs after a certain storage period. The weight of swan eggs is measured by an electric balance.

$$w = (m_1 - m_2) \times 100\,\%/m_1 \qquad (70.2.1)$$

w: weight loss rate; m_1: prestorage weight; m_2: post-storage weight.

Haugh unit: an indicator of egg quality, it is calculated with an egg analyzer by measuring swan egg weight and thick albumen height [9].

$$\mathrm{Hu} = 100 \times \lg\left(H - 1.7m^{0.37} + 7.57\right) \qquad (70.2.2)$$

Hu: Haugh Unit; H: thick albumen height (mm); m: weight of swan egg(s).

Increase rate of air chamber diameter: the increase rate of chamber diameter after a certain storage period. Use an egg candler to identify the air chamber and draw the chamber area with a pencil. Then the air chamber diameter is measured by compasses in every 120°. Compared with the measurement of chamber height, this method is easier to operate; compared with the sole measurement of air chamber diameter, this method can eliminate differentiation resulted from egg sizes.

$$v = (l_1 - l_2) \times 100\,\%/l_2 \qquad (70.2.3)$$

v: increase rate; l_1: post-air chamber diameter; l_2: pre-air chamber diameter.

70.2.2.3   Experimental Design

In Plackett–Burman design, each variable factor has two levels, being marked with − and +, respectively. And several virtual variables are for error analysis. This type of Plackett–Burman is referred to an almost saturated 2-level trial [10]. There are 9 factors including outer shell film of swan eggs, polyvinyl alcohol (PVA) membrane, coating temperature of PVA membrane, temperature of wind drying, storage temperature, white mineral oil membrane, bran storage, piled storage, and placement and 2 virtual factors including dummy 1 and dummy 2. The responses were weight loss, haugh unit, and increase rate of air chamber diameter. Linear function and noninteraction were used for the selection of factors [11]. The design is shown in Table 70.1.

Table 70.1 Plackett–Burman design elements and levels

Variation	Condition	Type	Low (−)	High (+)
X1	Outer shell film of swan eggs	Categorical	Void	Being
X2	PVA membrane (1.5 % w/V)	Categorical	Void	Being
X3	Coating temperature of PVA membrane	Numeric	25 °C	85 °C
X4	Temperature of wind drying	Numeric	70 °C	110 °C
X5	Storage temperature,	Numeric	5 °C	25 °C
X6	White mineral oil membrane	Categorical	Void	Being
X7	Bran storage	Categorical	Void	Being
X8	Piled storage	Categorical	Single	Stack
X9	Placement	Categorical	Horizontal	Vertical
X10	Dummy 1	Categorical	Level 1	Level 2
X11	Dummy 2	Categorical	Level 1	Level 2

70.2.3　Data Processing

The data were analyzed with MS Excel 2007 and 90 % confidence level evaluation was performed [12]. The Plackett–Burman design function of Design Expert software was used for principal factor analysis.

70.3　Results and Discussion

The response values and their 90 % confidence coefficients are shown in Table 70.2. The Design Expert software was used to perform analysis of variance on the weight loss rate, haugh unit and increase rate of air chamber diameter of Table 70.2, so as to obtain the results of variance analysis for the influence factors and their significances. The results are shown in Tables 70.3, 70.4 and 70.5.

This variance model was the results produced by forward and backward regression on the factors. As shown in the variance model, p-value (Prob > F value) was 0.0015, which meant a significant regression equation for weight loss rate, namely, the model was fitted well at the entire researched regression area. Multiple correlation coefficient R^2 = 76.56 % and adjusted determination coefficient AdjR^2 = 71.35 %, meaning that 71.35 % experimental data of the variability could be explained by this regression model. Generally speaking, the lower the coefficient of variation (CV) is, the higher the credibility and accuracy of the experiment is. The CV value equaled 48.6 %, showing that this experiment had certain reliability and accuracy. Precision is the ratio between effective signal and noise. A precision value greater than 4.0 is deemed reasonable. The precision of weight loss rate was 8.852, meaning that the analysis was reasonable. For this model, the storage

Table 70.2 Plackett–Burman response values and 90 % confidence levels

No.	X1	X2	X3	X4	X5	X6	X7	X8	X9	X10	X11	Weight loss (%)	Haugh unit	Increase rate of air chamber diameter (%)
1	{1}	{1}	−1	1	1	{1}	{−1}	{−1}	{−1}	{1}	{−1}	0.9 ± 0.2	63.0 ± 2.4	24.9 ± 3.3
2	{−1}	{1}	1	−1	1	{1}	{1}	{−1}	{−1}	{−1}	{1}	1.8 ± 0.5	58.0 ± 4.7	30.7 ± 10.5
3	{1}	{−1}	1	1	−1	{1}	{1}	{1}	{−1}	{−1}	{−1}	0.5 ± 0.1	69.6 ± 5.4	26.4 ± 4.5
4	{−1}	{1}	−1	1	1	{−1}	{1}	{1}	{1}	{−1}	{−1}	4.9 ± 0.5	41.1 ± 15.8	37.0 ± 2.0
5	{−1}	{−1}	1	−1	1	{1}	{−1}	{1}	{1}	{1}	{−1}	0.8 ± 0.1	65.6 ± 5.1	17.9 ± 6.2
6	{−1}	{−1}	−1	1	−1	{1}	{1}	{−1}	{1}	{1}	{1}	0.6 ± 0.1	66.6 ± 9.8	22.2 ± 4.7
7	{1}	{−1}	−1	−1	1	{−1}	{1}	{1}	{−1}	{1}	{1}	4.9 ± 0.5	55.5 ± 11.1	51.8 ± 2.8
8	{1}	{1}	−1	−1	−1	{1}	{−1}	{1}	{1}	{1}	{1}	0.8 ± 0.6	67.3 ± 3.5	16.1 ± 0.4
9	{1}	{1}	1	−1	−1	{−1}	{1}	{−1}	{1}	{1}	{−1}	1.7 ± 0.2	75.4 ± 3.4	32.4 ± 6.4
10	{−1}	{1}	1	1	−1	{−1}	{−1}	{1}	{−1}	{1}	{1}	0.9 ± 0.2	62.7 ± 5.6	20.6 ± 5.7
11	{1}	{−1}	1	1	1	{−1}	{−1}	{−1}	{1}	{−1}	{1}	4.9 ± 0.9	45.4 ± 3.8	20.8 ± 7.0
12	{−1}	{−1}	−1	−1	−1	{−1}	{−1}	{−1}	{−1}	{−1}	{−1}	1.1 ± 0.1	69.6 ± 15.8	24.6 ± 1.3

The figures following '±' are the 90 % confidence level

Table 70.3 Variance analysis of weight loss rate

Source	Sum of squares	df	Mean square	F value	p-value Prob > F	Significance
Model	27.31333	2	13.65667	14.69629	0.0015	**
X5	13.23	1	13.23	14.23715	0.0044	**
X6	14.08333	1	14.08333	15.15544	0.0037	**
Residual	8.363333	9	0.929259			
Total variation	35.67667	11				

Note: $P \le 0.01$, notable significant, **; $P \le 0.05$, significant, *; $P > 0.05$, not significant

Table 70.4 Variance analysis of haugh unit

Source	Sum of squares	df	Mean square	F Value	p-value Prob > F	Significance
Model	1046.85	5	209.37	15.49359	0.0022	**
X4	154.0833	1	154.0833	11.40232	0.0149	*
X5	568.5633	1	568.5633	42.07425	0.0006	**
X6	136.0133	1	136.0133	10.06512	0.0193	*
X10	119.07	1	119.07	8.811297	0.0250	
X11	69.12	1	69.12	5.114948	0.0644	
Residual	81.08	6	13.51333			
Total variation	1127.93	11				

Note: $P \le 0.01$, notable significant,**; $P \le 0.05$, significant, *; $P > 0.05$, not significant

Table 70.5 Variance analysis of increase rate of air chamber diameter

Source	Sum of squares	df	Mean square	F Value	p-value Prob > F	significance
Model	903.6467	4	225.9117	9.375595	0.0061	**
X5	138.72	1	138.72	5.75704	0.0475	*
X6	200.0833	1	200.0833	8.30369	0.0236	*
X7	476.28	1	476.28	19.76617	0.0030	**
X9	88.56333	1	88.56333	3.675481	0.0967	
Residual	168.67	7	24.09571			
Total variation	1072.317	11				

Note: $P \le 0.01$, notable significant,**; $P \le 0.05$, significant, *; $P > 0.05$, not significant

temperature (X5) and white mineral oil membrane (X6) were highly significant factors. Low storage temperature could reduce evaporation, thus reducing the weight loss rate. White mineral oil membranes could partly seal the surface pores of egg shell, thereby inhibiting water evaporation and reducing weight loss rate. The model did not include other factors affecting the weight loss rate.

This variance model was the results produced by forward and backward regression on the factors. In this model, *p*-value was 0.0022, which showed that regression model of haugh units was extremely significant, fitting very well throughout the regression area. Multiple correlation coefficient R^2 = 92.81 % and adjusted determination coefficient AdjR^2 = 86.82 %, meaning that 86.82 % experimental data of the variability could be explained by this model; CV value of this model equaled 5.96 %, showing that this experiment had highly reliability and accuracy; the precision was 12.324, showing that the analysis was reliable. The storage temperature (X5) was a notable significant factor, with air drying temperature (X4) and white mineral oil membrane (X6) as significant factors. A low storage temperature could decrease the whole physiological and biochemical reaction of the swan eggs, and suppress the internal and external microorganism, reducing the rate of haugh unit loss; a high-drying temperature (110 °C) of hot air could make the inner protein membrane slightly degenerated, decreasing the permeability; white mineral oil membrane partly sealed the surface pores of egg shell, reducing the permeability of swan eggs. Relatively higher drying temperature and white mineral oil membrane actually inhibit the swan eggs' physiological and biochemical reactions, increasing the haugh unit instead. Virtual factors(X10, X11) were chosen as the model parameters. Other factors which were less notable than virtual factors should not be considered.

The increase rate of air chamber diameter variance model was the results of forward regression. *P*-value was 0.0061, showing that the regression model had reached notable significance, fitting well in the regression area. Multiple correlation coefficient R^2 = 84.27 % and adjusted determination coefficient AdjR^2 = 75.28 %, meaning that 75.28 % experimental data of the variability could be reliable; CV value was 18.10 %, meaning that this experiment had good reliability and accuracy. The precision was reliable as 10.415. Bran storage (X7) was an outstanding significant factor; storage temperature (X5) and white mineral oil membrane (X6) were significant factors. Placement (X9) is selected, but not a significant factor. Bran storage may produce equilibrium temperature, humidity, and air permeability for swan eggs and make the environment stabler than non-bran storage; a low storage temperature, which had reduced the physiological and biochemical reaction, and white mineral oil membrane, which partly sealed the surface pores of egg shell, may decrease the increase rate of air chamber diameter.

70.4   Conclusions

A low storage temperature (X5) can reduce water evaporation and inhibit the growth of microbial activity, repress the protease activity, suppress all the physical and chemical reaction, delaying the change of content in the eggs, which had a significant influence on weight loss rate, haugh unit and increase rate of air chamber diameter. White mineral oil film (X6) can party seal the surface pores of egg shell, prevent the microbial decomposition, suppress the evaporation and CO_2 exchange,

inhibiting physiological and biochemical reaction. The factor also made a significant influence on these three indicators. Drying process of hot air(X4) can sterilize. The inner membrane of the eggs consists of different length and diameter reticular structure of keratin protein fiber. These fibers are thick, with rough mesh structure rough and large fiber space. Some microorganism can directly get through the membrane into the eggs. Short-time heating may cause the swan egg micro degeneration of inner membrane and reduce their permeability, inhibiting evaporation, air exchange, and microbial invasion. It can have significant influence on haugh unit. Bran storage (X7) can make the storage environment stable, thus slowing down the decrease of egg quality; Placement (bigger-side up, X9) can make the egg yolk in the middle position and air chamber at the top, which is helpful of reducing external microbial invasion and preventing the swan eggs from turning black. For the black swan eggs in this experiment, the spoil species should be identified and classified, providing theoretical basis of choosing coating materials. Central Composite Design (CCD) of Design Expert software should be used to optimize experiment under significant factors.

References

1. Wei, R. C., Wang, R., Zhen, Q., Liu, T. Z., & Sun, Z. (2007). Microbes and quality study of storage time. *China Animal Husbandry and Veterinary Medicine, 11*, 129–131. (in Chinese with English abstract).
2. Liu, M., Lian, H., & Ren, F. (2011). Effects of storage temperature and modified atmosphere packaging on egg preservation. *Transactions of the CSAE, 27*, 378–382.
3. Jiang, Y.-h., Ma, M.-h., Mei, J.-h., & Wang, S.-c. (2010). Influence of clean egg treatment on egg fresh degree. *Journal of Huazhong Agricultural University*, *05*, 654–657 (in Chinese with English abstract).
4. Alleoni, A. C. C., & Antunes, A. J. (2004). Internal quality of eggs coated with whey protein concentrate. *Science and Agriculture, 61*, 276–280.
5. Caner, C. (2005). The effect of edible eggshell coating on egg quality and consumer perception. *Journal of the Science of Food and Agriculture, 85*, 1897–1902.
6. Bhale, S., No, H. K., Prinyawiwatkul, W., et al. (2003). Chitosan coating improves shelf of eggs. *Journal of Food Science, 68*, 2378–2383.
7. Plackett, R. L., & Burman, J. P. (1946). Thedesign of optimum multifactorial experiments. *Biometrika, 33*, 305–325.
8. Wang, B., & Che, Z. (2011). Optimization of Rhizopus fermentation medium for glucoamylase production by Plackett-Burman and Box-Benhnken Design. *Food Science and Technology, 05*, 41–45. (in Chinese with English abstract).
9. Li, J.-y., Tong, Q.-g. (2014). Investigation and analysis of sale time and freshness of eggs in supermarket. *Academic Periodical of Farm Products Processing*, *04*, 66–68 + 70 (in Chinese with English abstract).

10. Han, J., Liu, Z-h, Qi, W., & HE, Z-m. (2007). Optimization of the flocculation conditions of β-mannanase broth using statistical screening and response surface method. *Chinese Journal of Bioprocess Engineering, 02*, 29–35. (in Chinese with English abstract).
11. Plackett, R. L., & Burman, J. P. (1946). The design of optimum multifactorial experiments. *Biometrika, 33*, 305–325.
12. Wang, L., & Wang, G. (2002). *Basis of analytical chemistry* (2nd ed.). Beijing, China: Chemical Industry Press (in Chinese with English abstract).

Chapter 71
Experimental Study on the Cold Meat by High Pressure Preservation Technology

Xue Gong and Jiang Chang

Abstract It was studied the effects of ultra high pressure fresh-keeping packaging technology on quality of cold fresh meat in the storage period. Applying different pressure on cold meat and keep a certain time, every 3 days on the sample by one measurement were used to detect the cold fresh meat TVB-N value, color, pH value, and the total number of colonies, to test the UHP fresh-keeping packaging on chilled pork preservation effect. After 15 days of storage, samples of ultra high pressure to maintain 5 min 300 MPa, its TVB-N value is 15.3 mg/100 g, the pH value is 6.6, chromatic values ($a*$) of 14.1, the total number of colonies is 4.8×10^4 cfu/g, reached the first class standard of national standard of fresh meat, it can be good fresh preservation effect.

Keywords Cold meat · Ultra high pressure · Preservation · Quality

71.1 Introduction

The shorter form of ultra high pressure processing was UHPP, it was also called high hydro static pressure technology. In the processing, the raw food was sealed to super high pressure vessel after packed, kept the object under ultra high pressure in the right time, by disrupted the microbial survival environment to kill the main microbial spoilage of food in circulation, so then inhibited the growth and reproduction, destroyed the new supersedes the old to achieve the purpose of retain freshness [1].

Cold meat was slaughtered carcass in 24 h of rapid cooling to 0–4 °C and kept the temperature of the fresh meat in the circulation during the subsequent [2]. With the improvement of people's living standard, more and more attention of

X. Gong (✉) · J. Chang
Light Industry College, Harbin University of Commerce, Hei Longjiang, China
e-mail: kahnannie@163.com

571

people were on the nutritional value and edible quality of food, while compared with the traditional meat traditional cry preservation method, the cold fresh meat followed the basic rules of biochemistry, at the proper temperature, muscle protein degraded normally, acid discharged soften [3], tenderness enhanced obviously, it good for human body digestion and absorption [4], at the same time. Because of its without freezing, without thawing before eating, no loss of nutrients. Therefore, the cold fresh meat would become the main way of meat storage [5].

Due to the presence of microorganisms and enzymes during storage of the cold fresh meat, the flesh was decayed in a short period of time, caused the body to sticky, brought odor, my globulin oxidation discoloration would effect the outer color of meat [6]. Therefore, through the packaging technology to extend the shelf life of chilled meat is the key problem in the process of production of cold fresh meat. Currently, air conditioning fresh preservation technology was widely used of chilled meat circulation in the supply chain, by changing the gas inside the packaging components to achieve bactericidal anticorrosion purpose [7]. But the research and application was relatively less of ultra high pressure technology on cold fresh meat, with the development of ultra high pressure technology, used the fresh-keeping packaging method of ultra high pressure technology to extend the shelf life of chilled meat will be widely used.

71.2 Experimental Research and Analysis of Super High Pressure Preservation of Chilled Meat

71.2.1 Experimental Preparation

Experimental materials: commercially available fresh cold meat, composite packaging bag, the experimental method: split charged the cold meat, each 50 g into a sample, applied ultra high pressure as 100, 200, 300, 400, 500 MPa by ultra high pressure experiment equipment for sample, then kept 5 min, storage at normal temperature, tested the indexes such as TVB-N, pH value, chromatic values ($a*$) and the total number of colonies every 3 days.

71.2.2 Experimental Result and Analysis

71.2.2.1 Initial Value of Sample

Determined the quality indexes of commercially available cold meat, gained the initial value of every index, showed as Table 71.1. According to the national standards, when the pH value was between 5.8 and 6.2, TVB-N value not more than 15 mg/100 g, the total number of colonies was less than 5.0×10^4 cfu/g [8] of meat

Table 71.1 The initial value of cold meat quality indicts

The samples	pH value	TVB-N (mg/100 g)	The total number of colonies ($\times 10^4$ cfu/g)	chroma values (a^*)
Cold pork meat	6.0	9.8	2.3	16

was the best cold meat. According to the initial measurement results, the sample was the one-level fresh meat, it can be used as the detection object super high pressure packing technique of keeping fresh preservation effect.

71.2.2.2 Effect of Pressure on TVB-N Value of Cold Meat

Total volatile basic nitrogen was mean the corruption changes under the action of microorganisms and enzymes of animal food, in the processing of decay, protein decomposition of ammonia and amines basic nitrogen-containing substances. This kind of material can be produced from the decomposition of organic acids and corruption in the combination of basic nitrogen compounds and accumulate in the meat varieties [9]. TVB-N value was often used as an important indicator to measure water food quality of freshness indicators. In recent years was used as an important index of feed products from animal sources, mainly reflects the animal food freshness [10]. Figure 71.1 was shown the effect of different pressure on TVB-N value.

We can saw from Fig. 71.1, the TVB-N value of the cold meat exerted different pressure increased with storage time, according to the experimental data, the TVB-N value of the cold meat applied 300 MPa pressure increases more slowly, at the 12th days. TVB-N value was 13.4 mg/100 g, at the 15th days was

Fig. 71.1 Effect on the value of TVB-N of pressure
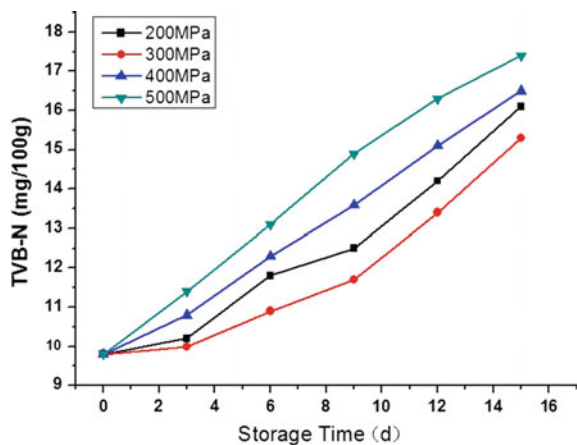
Fig. 71.2 Effect on the value of pH of pressure
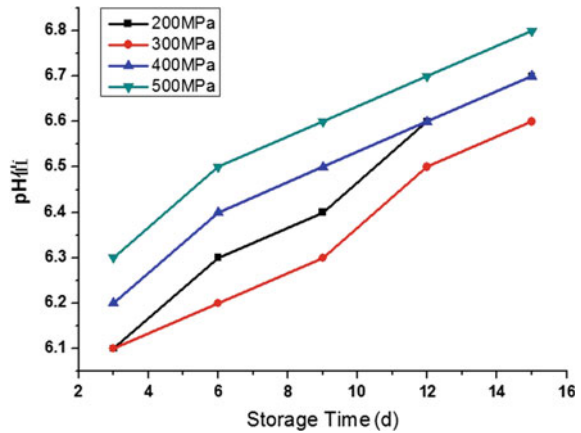
15.3 mg/100 g, it was only higher 0.3 mg/100 g, than the national standard of one-level fresh meat. The result explained that high pressure as 300 MPa on cold meat can extend the shelf life to 15 days.

71.2.2.3 Effect of Pressure on pH Value of Cold Meat

Because of the cold meat carcass was in the anaerobic state after slaughter, the animal starch produced acetylformic acid and other acid under the action of glycolysis in body, in order to change the body pH [11]. Therefore, The pH values can be used as evaluation index of fresh meat and metamorphic meat and could be used to be the auxiliary and reference as comprehensive evaluation of fresh degree for cold fresh meat. By dealing with different pressure and some days storage, the variation rule of pH value as shown in Fig. 71.2.

From Fig. 71.2 we can knew, the cold fresh meat of ultra high pressure processing of pH values increased with the storage time prolonging, the experimental data showed that at the 15th days the pH value of the cold meat which processed with 300 MPa was 6.6, according to the national standard, it was still at the one-level of fresh meat category, so it had a better preservation effect.

71.2.2.4 Effect of Pressure on the Cold Meat Red Value (a*)

The red value (a*) referred to the red and green colored substances bias, the bigger a* value the more deviation to red. For the cold meat, Whether maintained its special bright red in the storage period is a more important indicator of freshness, consequently, tested the red value (a*) of cold meat has an important significance [12]. Through cutting the thick slices of cold fresh meat in different pressure processing into 0.2 cm, blot up the surface moisture, put the samples on the light

Fig. 71.3 Effect on the color values (a^*) of pressure
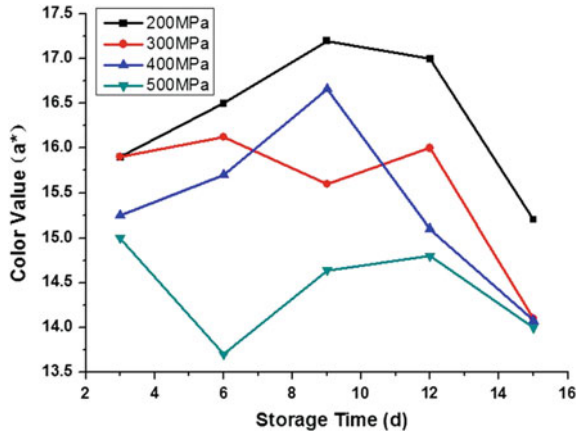
source directly, corrected the whiteboard, then read the numerical value of the color difference meter, wrote down the values of X, Y, Z and calculated the a^* [13], the changing rules with the storage period is shown in Fig. 71.3.

Figure 71.3 showed the a^* value decreased obviously after 6 days of the cold fresh meat applied 500 Mpa, while the group of 200 and 300 Mpa increased slowly, it illustrated the meat is still keep fresh color, after 9 days, each group showed a downward trend, the reason is the meat of myoglobin reacts with oxygen to temporarily generate unstable bright red oxymyoglobin, after 12 days, the a^* value decreased significantly, the color of meat was get old. But after all the experimental groups of a^* ultra high pressure processing value is higher than the normal control group.

71.2.2.5 Effect of Pressure on the Total Number of Colonies of Cold Fresh Meat

The total number of colonies was referred to the total number of bacterial colonies in certain conditions per gram of sample grown, under the action of the bacteria, the meat would spoilage [14]. The total number of colonies are usually used as a marked degree to judge whether the food was polluted [15]. After the specimens with different pressure treatment, the change of the total number of colonies is shown in Fig. 71.4.

We could see from Fig. 71.4, the total number of colonies of chilled meat was increased with the extend of the storage time, growth rate is inversely proportional to the applied pressure, under the pressure of 200 MPa, after 15 days of storage, the total number of colonies was 6.3×10^4 cfu/g, and the sample treated with 500 MPa pressure was 4.2×10^4 cfu/g, the total number of colonies of all the samples were all within the scope of fresh cold meat of provisions of national standards expect the samples treated by 200 MPa.

Fig. 71.4 Effect on the total number of colonies of pressure
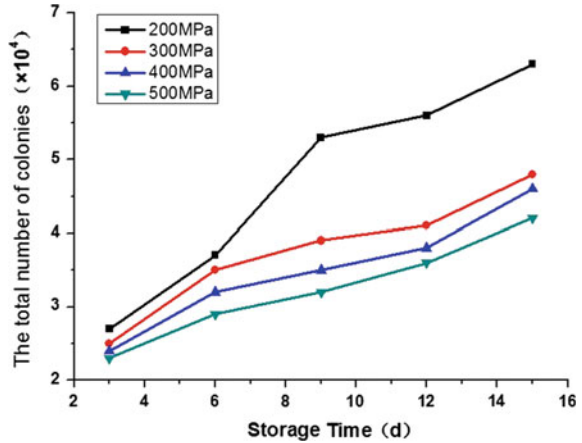
71.3 Conclusions

Based on treating the samples with ultra high pressure, after 15 days, the TVB-N values, pH values, color values (a^*), and the total number of colonies all changed largely of the samples, comprehensive all of the experimental data, it showed that kept the ultra high pressure of 300 MPa for 5 min, each index of cold fresh meat was within one-level fresh range in national standards, the effect of fresh preservation was better. Through the experimental verification of the super high pressure packing technique of keeping fresh in cold fresh meat packing in the feasibility and effect of preservation, provide theory foundation and technology support for some hope that the development of ultra high pressure preservation technology of chilled meat.

References

1. Gong, X., Chang, J., & Li, D-t. (2013). Research progress of super high pressure packing technique of keeping fresh. *Packaging Engineering, 35*(3), 97–101.
2. Zhao, Y.-z. (2012). The cold fresh meat preservative research. Hunan Agricultural University, Chang Sha.
3. Li, X.-g., & Wang, F.-f. (2010). Research progress on chilled meat and fresh keeping technology. *The Processing of Agricultural Products* (New Edition), (2), 49–51.
4. Chen, G.-h. (2003). How to promote the production and consumption of cooling meat in China. *The Meat Industry*, (1), 45–46.
5. Song, Z.-j., & Huang, S.-z. (2009). Research progress of microbial control and preservation technology of chilled meat. *Meat Research*, (6), 31–36.
6. Zhao, Y.-z., Liu, C.-g., & Zhou, X. (2011). Study progress of modified atmosphere packaging technology in the cold fresh meat. *Meat Research*, (1), 72–77.
7. Cheng, X-x, Wang, Y-h, & Gan, Q. (2009). The common problems of fresh meat of modified atmosphere packaging industrial production. *The Meat Industry, 6*, 7–10.

8. Wang, C., Ma, W., & Jiang, Y. (2007). Detection of pork freshness and synthetic evaluation of meat quality. *The Processing of Agricultural Products, 10*, 75–77.
9. Lin, J. (2013). Research on preservation technology of gas storage of fresh pork. Jiang Xi Agricultural University, Nan Chang.
10. Wang, T.-y., Wang, Y.-j., & Qin, W. (2007). Study on the differences and sensory index value of pork volatile basic nitrogen. *Food Industry Science and Technology*, *28*(12), 124–126.
11. Yuan, X-q, He, Z-f, Li, H-j, et al. (2012). The quality change of different storage temperature pallet packaging cold fresh pork. *Food Science, 33*(06), 264–268.
12. Zhou, G.-h., Li, C.-b., & Xu, X.-l. (2007). Research progress of meat quality evaluation method. *China Science Paper Online*, *2*(2), 75–82.
13. Wang, X.-y. (2012). Cooling pork quality assessment method of standard. Nan Jing Agricultural University, Nan Jing.
14. Tsigarida, E., & Nychas, G.-J. E. (2001). Eco physiological attributes of a Lactobacillus sp. and a Pseudomonas sp. on sterile beef fillets in relation to storage temperature and film permeability. *Journal of Applied Microbiology, 90*, 696–705.
15. Nychas, G.-J. E., Skandamis, P. N., Tassou, C. C., et al. (2008). Meat spoilage during distribution. *Meat Science, 78*, 77–89.

Chapter 72
Study on Logistics Information Packaging Technology of Fresh Food in Cold Chain

Xiaomin Li and Lijiang Huo

Abstract The paper describes the type and operational principle of packaging for fresh food in cold chain logistics. It gives an overview on the mechanism, features, applications, and present development of the trace-ability technology (Bar Code, RFID), data acquisition technology (temperature sensors and humidity sensors), and positioning technology (GPS, GIS). The paper also analyzes problems that currently exist in technique progress, standard construction and application system, also points out the way to solve the problems in aspects of technical intelligence, improvement of quality standards, integrity of the cold chain system and logistics green in China.

Keywords Packaging for fresh food · Logistics information · Cold chain

72.1 Introduction

In the process of from producer to final consumer, the fresh food is in the shipping transportation link more than 80 % of the time, so tracing information timely and accurate have a vital role on logistics activities. The related researches and application include trace-ability (bar code technology, RFID) technology, data acquisition technology (temperature and humidity), and positioning technology (GPS, GIS) [1–7]. However, some problems still remain.

X. Li · L. Huo (✉)
Dalian Polytechnic University, Liaoning, China
e-mail: lijianghuo@163.com

72.2   Mechanism and Application of Logistics Information Packaging Technology of Fresh Food in Cold Chain

72.2.1   Traceable Technology

72.2.1.1   Bar Code Technology

Bar code reading system is the basic part for adopting bar code technology which is composed of scanning part, signal plastic part, and decoding part. The mechanism is converting light signal into electrical signal through the circuit system for signal amplification and plastic, after reading a set of rules to arrange article and empty and the corresponding characters of tag using the photoelectric scanning devices. Then decoder will analyze and process the acquiring binary pulse signal. When the bar code information is obtained, the information display will store it in the computer system. The focus of current research application of Bar code is present more information in the limited space geometry. A feasible way is using a one-dimensional bar codes upward in vertical direction and extend to the two-dimensional direction. It is also practical that design the new dimensional bar codes using the image recognition principle. The Symbol company has launched stack of PDF417 two-dimensional bar code is already very mature using the current technology [1, 7]. The development trend of current international logistics is to build modern logistics which is based on the application automation system of bar code technology, and this trend also can made bar code technology be integrated with other automatic identification technologies.

72.2.1.2   Radio-Frequency Identification Technology

The basic components of radio-frequency identification technology (RFID) are electronic labels, readers, and antennas. The mechanism is electromagnetic theory, which means the electronic label attached to the identified object and record the information of the object. The tags receive RF signal from reader after come into the magnetic field, and update the product information data of the chips with the energy gained by the induced current. Data to be sent to the central information system after decoding, and generate data changing chart, so as to complete the process of cold chain logistics monitoring of temperature change [1–3]. Currently, its focus is combining the RFID technology with the application in all walks of life and developing Multiple frequencies RFID technology. The development of hardware design and manufacture of RFID will go to the direction of multifunction and multi-interface. RFID also pay much attention to the developing function to be more module, miniature, and embedded. In addition these designing developments, the function of RFID tags can be extended, such as the function of monitoring temperature, pressure, and humidity of the recognition of biometrics. The

combination of RFID tag packaging technology with other necessary factors including printing, packaging, and logistics. The mass production with low cost of RFID tag production by conductive ink printing label packaging technology.

72.2.2 Data Acquisition Technology

Data acquisition technology is mainly divided into temperature sampling and humidity, the temperature and humidity sensor is the main tool. According to its type, temperature sensor can be divided into thermonuclear, heat resistance, digital temperature sensor, and infrared sensor. Two main types of humidity sensor includes resistance and capacitance. The mechanism is converting the actual physical quantities such as temperature and humidity to electrical signals for storage and computing, and then parsing temperature and humidity information in the electrical signal through the microcontroller. Temperature and humidity sensor is mainly used in the process of cold chain storage and transportation. In the current data acquisition technology, such factors become the focus as intelligent, integrated, and networked. There are also some other crucial factors including the miniaturization sensor and temperature and humidity sensor integration [1].

72.2.3 Positioning Technology

Positioning technology includes global positioning system (GPS) and geographic information system (GIS).

GPS consists of three subsystems, including space systems, satellite ground receiving system monitoring system, and users. The mechanism of GPS is achieving space satellite observation data for ground stations. After the preliminary processing, the data will be transmitted to the master station, which collects trace data and calculates the satellite orbit and clock parameters, then send the results to the injection station. After acceptance system, the user will calculate the user's three-dimensional position, three-dimensional direction, according to the locating and calculating method. The research focus is to develop GPS software products and promote and deepen the all kinds of applications of GPS.

GIS is composed of five main elements: hardware, software, data, personnel, and method. The mechanism of it is supporting computer software and hardware, making the information of various resources and the environment parameters distributed according to the spatial or geographic coordinates. Then parameters and the information will be classified and coded, input, processed, and stored in a certain format. Then the needed information will be output conveniently and quickly in various forms, such as picture, video, figure, which through the operation and comprehensive analysis on the multiparameter data. GIS technology is mainly used in logistics analysis, and the focus of research is to develop the decision support

system and key technology application services which based on GIS. At present, some foreign companies have developed and provided tools software that is analyzed for logistics using GIS. Some foreign GIS that have more perfect function system software such as ARC/INFO, GENAMAP, and MGE. In our country, MAP/GIS, Geostar, etc. are famous [8]. Using GIS can efficiently handle the advantage of spatial and attribute data to build a logistics distribution system of Map Objects, which will be the development trend of the future.

72.2.4 Application Progress of Logistics Information Packaging for Fresh Food in Cold Chain

Nowadays, the European and American developed countries have formed a complete cold chain logistics system of agricultural products. In the process of transportation, they all have adopted the refrigerator or freezer and matched with the advanced management of information technology. They also have built frozen, cold chain of fresh food, including the production, processing, storage, and transportation, sales and so on. According to the survey, Europe, United States, Japan, and other developed countries that more than 90 % agricultural products in cold chain circulation, which the fruit cold chain circulation rate is above 95 %. Taking the cold chain logistics in the United States as an example, CR England equipped GPS tracking equipment, network tracing, and network billing function for each vehicle, which can send the food according to the designated and accurately time of the guests. CR also has advanced auxiliary equipment, such as trucks satellite positioning system, on-board computer and remote control platform, project management software, and a lot of self developed software. CR England also has a TENFOLD programming language. So CR England can complete software with full intellectual property rights through their own programming [9].

72.3 Problems and Solutions to Logistics Information Packaging Technology of Fresh Food in Cold Chain in China

72.3.1 Backward Information Technology of Cold Chain Logistics and Low Level of Information

The information technology of cold chain logistics is backward and it has not formed a sound information network in China. And the temperature-control technology of our country is not advanced, we could only provide uniform temperature. The ability of automatic temperature control and recording is not sufficient, and the application of satellite monitoring is limited make it impossible to transport goods

that need different temperature requirements. Therefore, we should probe more deeply into the key technology of cold chain logistics and invent equipments which is multifunctional and portable, form the products that owns independent intellectual property, and improve the acquisition technology of dynamic logistics information and the technology of logistics safety, and promote the construction of public information platform of logistics.

72.3.2 Defective Technological Standard and Unsound Legislation

We could know that related technology standard of cold chain logistics is not sound in China. For example, in terms of the standard of RFID, our country only currently issued some industrial standard related to electronic tag technique, the products of different factories have different information format, volume and so on, so they could not compatible with each other, which make the enterprises could not conduct data exchange and cooperate. Therefore, the government and relevant department should proceed to improve the standard of packaging technology, environment temperature, and the quality supervision of refrigeration, then they should establish the evaluation system of technology and quality of cold chain logistics [2, 3, 10].

72.3.3 A Sound System Has not Formed and the Traditional Mode Is not Reasonable

At present, China mainly depends on normal temperature logistics and natural logistics. We have not yet formed coherent technology system of cold chain logistics. Under the marketing environment that the commercialization of the vegetables and fruits has been over 60 %, the vegetables and fruits which have been in the process of cold chain system only occupy 20 %, which quite far from that of 95 % of developed countries. However, our traditional mode of distribution of cold chain logistics mainly reflects in some enterprises that manufacture perishable food accomplish distribution tasks by their own, low mercerization, few intervention of third party, all these lead to the high cost of distribution [9–11]. So we should establish green cold chain logistics strategy, we should make jointly transportation and distribution and multimodal transport, reduce the environmental pollution, advocate green operation strategy and management [12].

72.4 Conclusions

With the development of theory research and technology, every aspects of pack-aging technology of cold chain logistics of fresh food will be improved. The government should take effective measures, formulate more comprehensive legis-lations to proceed the standardization and industrialization of packaging for cold chain logistics of fresh food, create more economic benefits for society, and provide guarantee for the will-being of the people.

References

1. Shen, J.(2014). Introduction to logistics technology at low temperature, 151–160.
2. Zhang, H., Xu, S., et al. (2014). Application of RFID technology in the vegetable cold chain logistics management research. *Logistics technology*, (4), 348–353.
3. Guo, Y. (2013). *Packaging logistics technology*. Printing Industry Press.
4. Murphy, P. R., Jr., & Wood, D.F. (2009). *Contemporary logistics*.
5. Wu, H., Zhou, J., et al. (2013). The development of RFID and its application review. *Computer Applications and Software, 30*(12), 203–206.
6. He, L., & Zhang, C. (2013). RFID development to explore the present situation and development trend at home and abroad. *Electronic Test*, (8), 217–218.
7. Zhou, Q. (2007). *Modern logistics technology and equipment*. Bei Jing: Supplies of China Publishing.
8. Rodriguez Lado, L., Polya, D. A., & Hegan, A. (2008). A logistic regression method for mapping the as hazard risk in shallow. *Mineralogical Magazine, 72*(1), 437–440.
9. Excellent examples of cold-chain logistics mode in aboard. (2014). http://www.56lem.com/news/show-922.html
10. Xiao, H. (2014). Problems and countermeasures in the development of cold chain logistics in China. *Logistics Engineering and Management, 36*(11), 6–7.
11. Miu, X., Zhou, X., et al. (2009). Fresh food cold chain logistics is reviewed. *Logistics Technology, 2*, 24–27.
12. Chen, H., & Li, J. (2013). How to build a fresh food cold chain logistics service quality evaluation index system. *Logistics Technology*, (7), 20–22.

Chapter 73
Analyze Thickness Precision of Irregular Metal Aerosol Can Based on ANSYS

Lingjiang Chen, Zhongguo Xu and Feng Guo

Abstract Irregular metal aerosol can should not only satisfy consumer's individual demand, but also reduce thickness as much as possible with long-term pressure resistance. In this study, three difference can structures are designed with ergonomics considerations. SolidWorks software is adopted for modeling and ANSYS for simulation and analysis. The relevance between can thickness as well as long-time pressure resistance is discussed. The thickness of the shell is set to 0.45, 0.50, 0.55, 0.60, and 0.65 mm, respectively. The models from SolidWorks are then imported into ANSYS and 1.2 MPa pressure is imposed from inside wall. Based on the resulted curves of thickness stress, an optimum thickness is obtained for each can. Combined with aesthetics and ergonomic factors, the third model is considered to be the best design, with a maximum stress value of 707.8 Mpa in 0.51 mm thickness. It is less than the standard 720.0 Mpa and verified on remodeling of the third model. Summarily, this discussion aims to improve the design accuracy and provide a profit basis.

Keywords Irregular metal aerosol · Structure optimization analysis · Reduction design

73.1 Introduction

The technology of irregular metal aerosol can has been widely developed and used in food, cosmetics, and other industries [1]. In the next few years, this unique design will be more attractive to the eyes of consumers. So how to build a charming product image will become an important strategic tool for enterprise development. However, the existing aerosol cans are mostly designed in straight canister shape.

L. Chen · Z. Xu (✉) · F. Guo
School of Biological and Chemistry Engineering/School of Light Industry,
Zhejiang University of Science and Technology, Hangzhou, Zhejiang Provence, China
e-mail: 978292231@qq.com

Generally, most of the aerosol models are used in metal materials and easy to shape. As a result, production process is relatively simple [2].

Metal aerosol container, as a pressure vessel, often due to unreasonable structure design causes some explosive incidents. According to incomplete statistics, there are thousands of pressure vessel explosions in China in recent years [3]. In January 5, 2004, a bad case occurring in Yangpu District, Shanghai, a series of explosive accidents was caused by the abandoned spray can and made many injuries. Hence, the reasonable structure design requires that the structure of the container should be easy to manufacture, cut down the local stress concentration and additional stress, reduce even avoid the manufacturing defect.

Therefore, the most important aerosol can be designed a reasonable and reliable structure. Designed with the references of domestic and international metal aerosol can, they are imported into ANSYS to solve the thickness precision. General speaking, the experimental data can help make improvement of design accuracy and advantage in materials.

73.2 Design Principles

Aerosol can, also called spray can, is a metal container used in the disposable containers of aerosol products. Aerosol can mainly show five kinds of qualities respectively in pressure resistance, sealing, corrosion resistance, safety, and surface. The national standard "packaging container—aerosol model" in the provisions of the deformation pressure is not less than 1.2 MPa and bursting pressure is not less than 1.4 MPa [4]. At present the domestic market the most aerosol cans under the pre-requisite to meet the safety requirements are produced in accordance with national standards of qualified tinplate [5]. The use of tinplate is thicker than ordinary metal for pressure resistance and model cover is over body 50 % in thickness.

Besides, aerosol can structure design must ensure the pressure resistance. Supporting the entire container, the bottom of the model body is usually designed into circular arch [6–9]. From the mechanical properties of the pressure vessel to consider the structural strength, the general aerosol can often use two piece can, a pot body and a pot bottom into one. The problem of molding, the complex structure and the equipment requirements should be also considered. In addition, ergonomic design is the most cutting-edge trend and reflection of human spirit [10–12].

73.3   Experiments

73.3.1   Model Design

The model of the aerosol can be built through drawing line, circle, pouring fillet, and shell by SolidWorks. Thickness of model one is uniform without sharp corners. The model is simple in structure and low in machining process requirements. Moreover, it is favorable for saving the time of the machining process. The middle segment of model two is an arc shape with ergonomics and conducive to consumer hand. It is consistent with the meaning of cool in simple and refreshing shape. Model three is generally straight cylinder, but compared with model two, the shape is more beautiful, upper and lower part with four long straight radian. The groove

Fig. 73.1 Model one
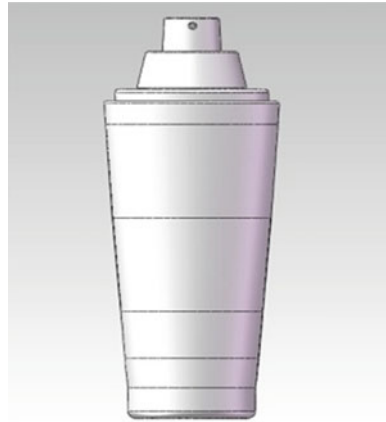
Fig. 73.2 Model two
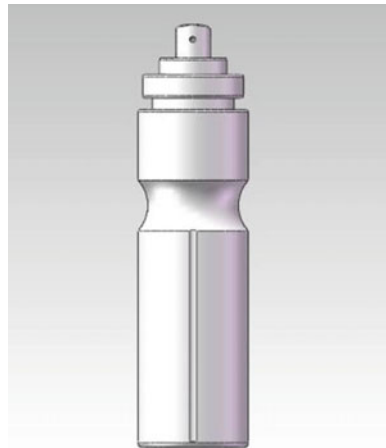
Fig. 73.3 Model three
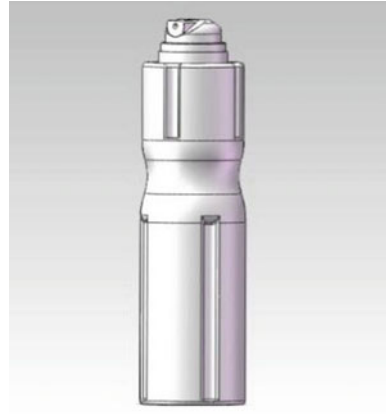
Table 73.1 Model parameters

Model	Main body diameter (mm)	Total length (mm)
Model one	52	150
Model two	52	200
Model three	52	200

design can play a buffer role and the bottle body can withstand greater pressure. Model types are showed in Figs. 73.1, 73.2, and 73.3 while parameters are showed in Table 73.1.

73.3.2 Optimization Analysis

First of all, the three cans are imported by Workbench ANSYS 14.0 to analyze thickness. The material is tin plate, the property density is 7.8 kg/m^3, Young's modulus is 202 Gpa and Poisson's ratio is 0.3. In selection of the fine mode of the partial dense grid division, shown as Figs. 73.4 and 73.5, the outer surface of the

Fig. 73.4 The type of mesh choice

Fig. 73.5 Model one grid graph
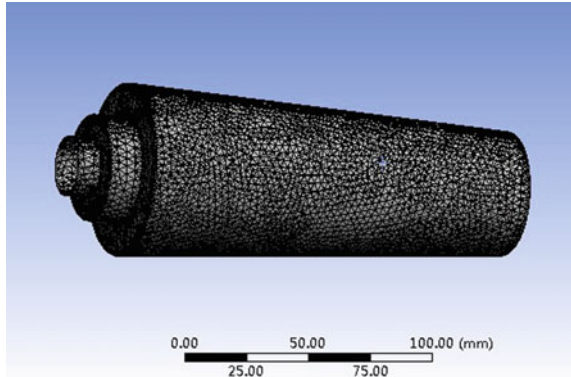
Fig. 73.6 Stress of 0.60 mm model one
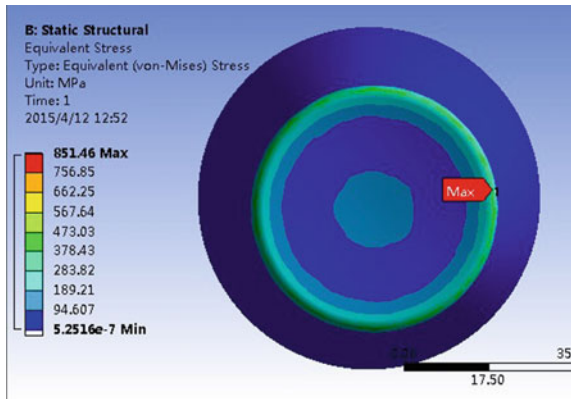
bottle body is applied to fixed constraint. It is solved that the inner surface of bottle pressure is applied uniformly $P = 1.2$ MPa perpendicular to the wall. After the solution, the stress of the bottle body is not exceeding the yield limit of the material. The stress data is calculated from the results of the solution. The stress is graphically displayed and the stress analysis chart is obtained. For example, Fig. 73.6 shows stress of 0.6 mm model one.

73.3.3   Regression Model Analysis and Results

In Excel, three kinds of stress thickness of model type are established, and the stresses of them are obtained, as shown in Fig. 73.7.

The curves of stress thickness show that there may be an inverse linear relationship between the stress and the thickness. In the Excel, the reciprocal of the
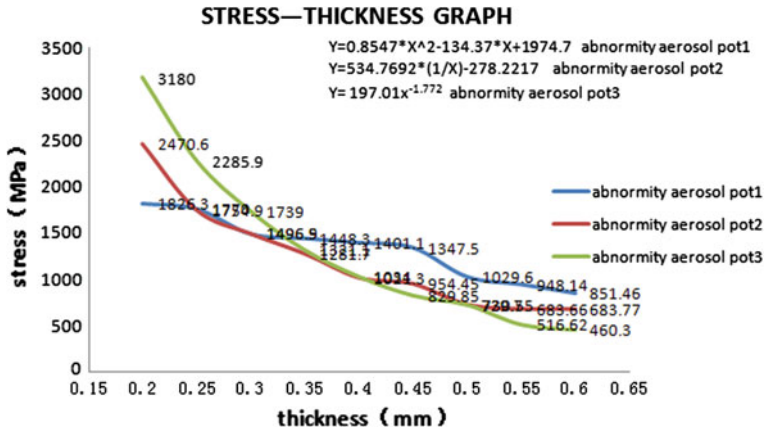
Fig. 73.7 Stress-thickness chart of model

force and the thickness of the scatter plot are fitted, and the coefficient is obtained. The correlation test of the equation obtained by MATLAB is carried out.

By mathematical analysis, the optimum thickness of model one is 0.71 mm, the optimum thickness of model two is 0.54 mm, and the thickness of model three is 0.51 mm. The results of three structural optimization analyses are: aerosol can three is less than other two structures, and the groove is more, which is advantageous to strengthen the rigidity of bottle, easy to display, and transportation. The thickness of the model is thicker than that of the pot, and it is not suitable for the production. Therefore, the design of the model three is the most reasonable one of the three structures.

73.3.4 Regression Verification

For the more reasonable model three, the stress analysis should be carried out, and the maximum stress of the model is ensured in the standard range. The third model is remodeled with shell wall thickness of 0.51 mm, repeatedly imported into ANSYS which gets the maximum stress value indeed 707.8 Mpa. It is less than the standard 720.0 Mpa with national standard and suitable for investment in the production.

73.4   Conclusions

The three metal aerosol cans are designed to meet the long-term pressure and reduce the material thickness. According to the development and performance characteristics of metal aerosol cans, the research is on the combination of domestic and international metal aerosol cans. The structure model of three metal aerosol cans was designed by SolidWorks software. And through the finite element analysis of the three kinds of metal aerosol tank model, the structure is optimized. The three different structures are given with an inner pressure in different thicknesses. According to the stress diagram, the maximum stress point of each model is figured out. At the same time, it is intuitive to see same structure belongs to aerosol cans in different thickness by stress, so as to select the reasonable thickness of structure.

References

1. Zhang, Y., & Shi, C. (2009). Analysis of metal spray cans packaging. *Based on the Optimization Design of Mechanical and Electronic, 08*, 57–60.
2. Li, X., & Lu, J. P. (2008). Study on spray model container. *Chemical Engineering and Equipment Spray Models*, (12), 72–74.
3. Zheng, C., Guo, J., & Xie, Y. B. (2006). *The Chinese version of SolidWorks 2006 senior mechanical design application examples*. China: Mechanical Industry Press.
4. Gao, Yu. (2004). Hot international aerosol can perspective. *China Packaging, 5*, 22–23.
5. Cao, Y. (2004). The finite element analysis software ANSYS and its use. *Popular Science and Technology, 2*, 55–56.
6. Zhang, Z. (2012). Unlimited innovation of tangible packaging. *Metal Packaging, 3*, 53–56.
7. Da, Y. (2014). Research on thin lightweight technology reduced tinplate EOE. *Food and Machinery, 30*, 126–128.
8. Fu, G. (2010). Design of modern cosmetic packaging. *Printing Technology, 4*, 22–24.
9. Luo, W., Tao, Z. t., & Zou, Y. (2010). Analysis of the high speed automatic packaging equipment for the valve industry. *Mechanical Design and Manufacturing*, (11), 22–23.
10. Hisashi, H., & Takeo, N. (1994). Recent trends in sheet metals and their formability in manufacturing automotive panels. *Journal of Materials Processing Technology, 46*, 455–487.
11. Kisioglu, Y. (2001). Determination of burst pressure and locations of the DOT-39 refrgerant cylinders. *Transactions of the ASME Journal of Pressure Vessel Technology, 123*, 240–247.
12. Cui, S. (2010). The influence of two kinds of material on the shape of the shape of the shape of aerosol. *Plastic Engineering Journal, 17*, 78–81.

Chapter 74
Application of Laminated Steel in Stone Coating Packaging

Chong Gu

Abstract At present, bagging treatment has to be done in stone coating's canning and transportation, because it is usually packaged by tinplate three-piece can, which could be corroded and scratched inside. Focusing on solving the corrosion and scratch problem of natural stone coating, this paper discussed the performance improvement by using laminated steel packaging. On the basis of studying the composition, physical, and chemical properties of stone coating, the following three comparison experiments were accomplished: (a) increasing thickness of inner coating; (b) double coating instead of single; and (c) using laminated steel on can body. The experiment results indicate that the package can in experiment C has the best corrosion resistance and scratch resistance. Moreover, production cost and material cost were also reduced in laminated steel method. It is thus clear that applying laminated steel not only enhances the performance of the tinplate can, but also cuts the cost, which means laminated steel packaging can be used in natural stone coating and is suitable for mass production.

Keywords Stone coating · Tinplate · Laminated steel · Corrosion resistance

74.1 Introduction

Stone coating, made of colorful natural stone powders, has been favored for its excellent performances, such as high hardness, water resistance, and aging resistance in the construction industry. At present, bagging treatment has to be done in stone coating's canning and transportation, because it is usually packaged by tinplate three-piece can, which could be corroded and scratched inside.

C. Gu (✉)
College of Packaging and Printing Engineering, Tianjin University of Science and Technology, Tianjin, China
e-mail: guchong217@126.com

Table 74.1 Ingredients of stone coating

Ingredients	Percentage (%)
Pure acrylic acid	30
Natural stone sand	65
Additives	5

The ingredients of stone coating are shown in Table 74.1. Natural stone sand, the main ingredient of stone coating, is composed of different size stones chosen by manufacturers to improve the performance of stone coating. Movements of sand and gravel may scratch the inside of the tinplate can, and the results will be more serious in the process of transportation and distribution. More than that stone coating presents weak alkalinity (pH value = 7–9) and will damage the interior wall as well.

After discussing the characteristics of natural stone coating, this article aims at how to solve the corrosion and scratch injury in the tinplate can and not to use inner packaged anymore. Laminated steel is considered as a good solution to this problem.

Laminated steel is made of polymer resin film and steel substrate, and the plastic film is compounded on metallic substrate by melt or bonding process [1]. Different from the tinplate, which needs inner coating before can making, laminated steel uses polymer resin film instead [2].

In this paper, tinplate and laminated steel were both used in the packaging of stone coating. Experimental results show that the corrosion resistance and the scratch resistance are excellent in laminated steel can compared to the two kinds of coated tinplate, and the production cost is also greatly reduced.

74.2 Materials and Methods

74.2.1 Methods

Can type in this study is drum shape, and the capacity is 18 L. Three different tests were taken in this experiment as follows:

(A) Increase coating thickness: Inner single coating amounts up to 8–10 g/m^2 from 5–7 g/m^2.
(B) Double inner coating times: the first coating amount was 4–6 g/m^2; the second was 5–7 g/m^2.
(C) Using laminated steel instead of tinplate.

74.2.2   Experiment Materials

74.2.2.1   Inner Coating

The same inner coating was used in method A and method B, and its properties are shown in Table 74.2.

74.2.2.2   Laminated Steel

Method C adopted tinplate as the substrate of laminated steel; its properties are shown in Table 74.3.

PET film was covered as the inner side of the can; its properties are shown in Table 74.4.

74.2.3   Testing

74.2.3.1   Practical Testing

Canning the products of methods A, B, and C with stone coatings; all three were transported about 4000 km in 5 days. After that, cans were put under constant temperature 55 °C for 30 days, then collected the damage of the inner.

Table 74.2 Properties of inner coating

Main component	Solid content (%)	Stoving temperature (°C)	Viscosity (Sec. FORD 4 at 25 °C)
Epoxy-Amino	34.5–38.5	200–205	80–120

Table 74.3 Mechanical properties of substrate

Name	Thickness (mm)	Hardness (HR-30Tm)	Yield strength (MPa)	Tensile strength (MPa)	Elongation (%)
Tinplate	0.35	55/57	415–450	350/370	8–17

Table 74.4 Parameter of PET covered

Type	Thickness (μm)	Tg (°C)	Tm (°C)	Tc (°C)	Laminating temperature (°C)
PET	15–20	67–81	248–275	190–230	240–260

74.2.3.2 Laboratory Testing

Three methods' products were injected with 90 % (volume) saline alkali water, which have the pH value 12, and preserved for 7 days in hermetic, homeothermic environment.

74.3 Results and Discussion

74.3.1 Practical Results

The result from method A is similar to that of method B: There are obvious stretches and corrosion points on the interior walls of the cans, while no visible damage is seen in the can from method C.

74.3.2 Laboratory Results

In this part, result from method C is the optimal solution, no stretches, corrosion and any damage, and interior wall keeps smooth, as shown in Fig. 74.1; result from method B takes the second place, and there are 3 light frictions inside, as shown in Fig. 74.2; the worst result comes from method A: Interior wall suffers a lot of corrosion points, abrasion marks, much more apparent, shown in Fig. 74.3.

Fig. 74.1 Result of method A
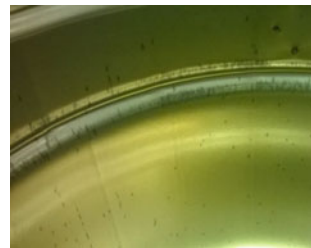
Fig. 74.2 Result of method B
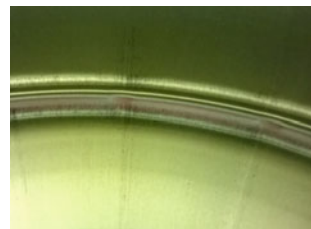
Fig. 74.3 Result of method C
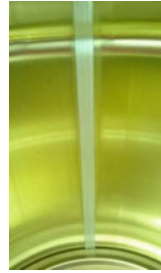
74.3.3 Discussion

74.3.3.1 Performances

The comparisons above show that the laminated steel has better corrosion resistance and scratch resistance against tinplate-coating system, the reasons are as follows:

(1) Because the covered material of laminated steel is a multilayer polyester film (PET), whose barrier penetration is close to "complete repression," the resistance from damage is incomparable by coating. The traditional can making materials cannot solve the contradictions between corrosion resistance and adhesion, but for laminated steel it is easy to be conquered [3].

(2) Generally, film thickness of the coating is 1.1 times as laminated steel film, so it will be better than the current coating on the wear resistance and scratch resistance.

For the reasons above, laminated steel can is superior to the tinplate-coating system on stretch and corrosion resistance.

74.3.3.2 Cost

The size of the tinplate pieces tested is 0.35 mm × 860 mm × 730 mm. Using coating amount 9 g/m^2 as an example, coating is 27.59 Yuan/Kg, tax including; 1 pass coating (single coating) include gas, and labor expense is about 0.285 Yuan, so method A cost is computed as Table 74.5.

The laminated steel in method C is tinplate covered by PET film. According to the current market price, 0.35-mm laminating steel is 382.2 Yuan/Ton; 0.38-mm laminating steel is 352 Yuan/Ton, so the cost of laminating steel is shown in Table 74.6.

One piece steel can be divided into 2 can bodies or 6 can tops (bottoms). Thus, if method C is used, the cost could be saved about 642.28 Yuan per 10 thousand cans, shown in Table 74.7. In other words, if a factory produces 10,000,000 cans per year, it could save 642,280 Yuan.

Table 74.5 Cost of coating (computed as 10 thousands tinplate)

Component	Specifications (mm)	Coating cost (kg)	Other cost (Yuan)	Total coat (Yuan)
Can body	0.35 * 860 * 730	163.4	4508.2	2850
Can top	0.35 * 970 * 710	179.25	4945.51	2850
Can bottom	0.38 * 874 * 640	145.59	4016.83	2850

Table 74.6 Cost of Laminating (computed as 10 thousands tinplate)

Component	Specifications (mm)	Laminating price (Yuan/Ton)	Tons needed	Total coat (Yuan)
Can body	0.35 * 860 * 730	382.2	17.249	6592.57
Can top	0.35 * 970 * 710	382.2	18.922	7231.99
Can bottom	0.38 * 874 * 640	352	16.686	5873.47

Table 74.7 Cost comparisons between laminating and coating systems

Component	Method A cost (Yuan)	Method C cost (Yuan)	Piece number per sheet	Saving cost (Yuan)
Can body	7358.2	6592.57	2	382.8
Can top	7795.51	7231.99	6	93.92
Can bottom	6866.83	5873.47	6	165.56
Total	–	–	–	642.28

Tinplate was used as the substrate of laminated steel in this paper. However, cold-reduced sheet could also do the same thing; in this way the cost advantage is more obvious.

The coating in methods A and B is based on epoxy resin, adding curing agent, plasticizer, toner, and other ingredients dissolved in solution agent and diluent, and environmental issues need to be resolved; in method C, the laminated steel surface is thermal plastic resin film; no solvent gas is discharged during production process, and this is helpful to environmental protection [4].

74.4 Conclusions

Laminated steel method, which is less energy consumption, low cost, and suitable to green packaging idea, has better performance, safety, and environmental protection compared of tinplate method. So, it is a kind of ideal green canning material. In the near future, laminated steel will be more and more popular in the field of metal packaging.

References

1. Han, M. H, Jegal, J. P, Park, K. W., et al. (2007). Surface modification for adhesion enhancement of PET-laminated steel using atmospheric pressure plasma. *Surface & Coatings Technology*, *201*, 4948–4952.
2. Chen, Y., Huang, J, Li, J., et al. (2010). Properties of laminated steel product and its development situation Steel Rolling. *27*, 45–62.
3. Zumelzu, E., Rull, F., & Boettcher, A. A. (2006). Characterization and micro-and ultra-structural analysis of PET-based Co-rolled composite electrolytic chromium coated steel (ECCS). *Journal of Materials Processing Technology, 173*, 34–39.
4. Zumelzu, E., Cabezas, C., & Delgado, F. (2004). Performance and degradation analyses of traditional and ECCS canning tinplates in citric-citrate medium. *Journal of Materials Processing Technology*, *152*, 384–388.

Chapter 75
Influence of Process Parameters on the Thickness Distribution of Beverage Bottles in Injection-Stretch-Blow Process

Weisheng Song and Yan Zhang

Abstract PET bottle for beverage is mostly made by the process of injection-stretch-blow. The process parameters influence the thickness distribution obviously. To research the influencing laws of process parameters on thickness distribution, first, we simulate the process of injection-stretch-blow under three different stretching velocities of 0.65, 0.7, and 0.81 m/s, second, we simulate the process under three different delaying times for blowing, such as 0.2, 0.25, 0.3 s. Because the parison needs to be blew when it is stretched in some time of the manufacturing process. Therefore, contact release must be enabled, and which can be enabled only for 3D and shell models. We choose the shell model in the simulation because it has absolutely advantage in calculating speed. The results show that the material of the bottle's bottom and the thickness on the middle of the bottle increased, and the thickness on the neck of the bottle decrease with the increasing of stretching velocity. And the same thing happened when the delaying time for blowing increase. The increasing of stretching velocity or delaying time is beneficial to the uniformity of bottle's thickness distribution and helps to improving compressive strength of the bottle. But we must ensure that the parison is not pulled off when the stretching velocity increases, and the impact on the parison's temperature distribution should be minimized when increasing delaying time. In addition, numerical simulations can provide more help in estimating the thickness distribution of bottle.

Keywords PET bottle · Thickness distribution · Finite element analysis · Stretching velocity · Delaying time for blowing

PET bottle for beverage is mostly made by the process of injection-stretch-blow. The settings of various process parameter mostly rely on the operating people's experience in the real manufacturing [1]. Therefore, the method of FEA is used to

W. Song (✉) · Y. Zhang
College of Packaging and Printing Engineering, Henan University of Animal Husbandry and Economy, Zhengzhou, Henan, China
e-mail: songweisheng2012@sohu.com

Y. Zhang
e-mail: yanzhang05@yahoo.com.cn

601

research various laws in the process of injection-stretch-blow recently, through which we can get rid of the reliance on experience [2].

C.W. Tan simulated the process of injection-stretch-blow using the commercial finite element package ABAQUS/standard. In the simulating process, the blowing air to inflate the PET parison was modeled via two different approaches; a direct pressure input (as measured in the blowing machine) and a constant mass flow rate input (based on a pressure-volume-time relationship). The results clearly show that simulation with a constant mass flow rate as input gave an excellent prediction of volume [3]. F. Daver optimized the cooling time of injection blowing process of PET bottle using finite element method [4]. Ye Zhou predicted the size distribution of the wall thickness of PET bottle molded by its parison with different sizes through the simulation analysis of stretch-blow molding process of multiple performing. The effect of parison sizes on the thickness distribution was analyzed as well. The results show that the size of stretch-blow molding parison of PET bottles have a greater impact on the wall thickness uniformity of products [5]. Hong Zheng researched the influence of the injection-stretch-blow molding process of bottles on features of the product using numerical simulations. Results showed that profiles of the thickness were greatly influenced by stretching speed; both high speed and low speed influenced the thickness adversely. It was found that the thickness of bottles were well predicted by computer simulation [6].

However, the analysis of the above researches are mostly based on 2D solid modeling or 3D solid modeling [7], which have some defects in the efficiency and accuracy. In this paper, the 3D shell model is built in workbench, the forming process of 550 ml mineral water bottle is simulated using Flow Fluid (Polyflow) module. Finally, the influence of the stretching velocity and the delaying time for blowing on bottle's thickness distribution is analyzed.

75.1 Geometry Model and Material Model

75.1.1 Geometry Model

The geometric model is built in workbench using Design Modeler, which can be seen in Fig. 75.1. The geometric model consists of three parts: stretching rod, parison, and mold [8]. This paper assumes that the shape of the bottle is axisymmetric. In order to improve the efficiency of the analysis, 3D axis symmetry model is used to model and analyze. In the simulation, the temperature of the material and the quality of the parison are kept constant. In the process of analysis, the function of Y coordinate multi-ramp function is used to set the parison's thickness as the continuous change along the Y axis. The thickness values of the corresponding key points are shown in Fig. 75.2.

Fig. 75.1 Geometry model

Stretching rod

Parison

Mold
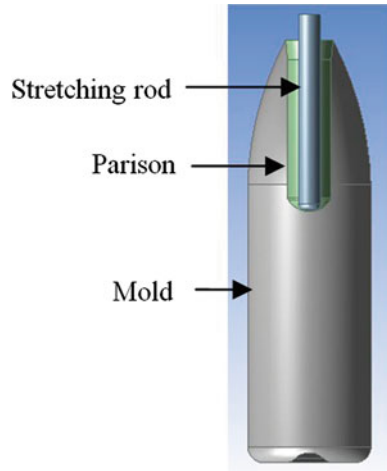
Fig. 75.2 Thickness of parison's key points

0.9mm

1.28mm

1.28mm

1.2mm
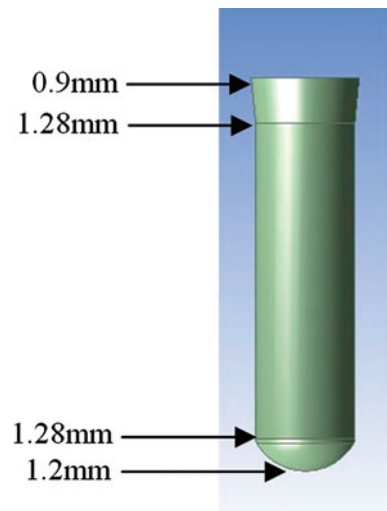
75.1.2 Material Model

A large number of datum display that the KBKZ model with Wagner and Papanastasiou—Scriven—Macosko damping equation which belongs to integral viscoelastic material model can capture and predict the material's viscoelastic property in the molding process, and reduce the deviation relative to the actual process [9]. In this paper, the KBKZ model is adopted as the material constitutive equation. And the main parameters of the model is discrete relaxation time spectrum. The discrete relaxation time spectrum data used in this article is: $\lambda_i = \{0.01, 0.1, 1\}$, $\eta_i = \{10^5, 3 \times 10^5, 10^6\}$ [10]. And the unit of λ_i is S, the unit of η_i is Pa $\cdot$ S.

75.2 Test Design and Contact Settings

75.2.1 Test Design

NO. 1: In order to analyze the influence of stretching velocity on the distribution of the thickness, this paper adopts three different stretching velocities for the simulated analysis which are, respectively, 0.81, 0.75, 0.65 m/s. The multi-ramp function curve of ratio of stretching velocity relative to time is shown in Fig. 75.3. In the process of the three analysis, low blowing pressure, high blowing pressure, and blowing time distribution are the same, respectively, as shown in Fig. 75.4.

NO. 2: In order to analyze the influence of delaying time for blowing on the distribution of the thickness, this paper adopts three different stretching velocities for the simulated analysis which are, respectively, 0.2, 0.25, 0.3 s. The concrete blowing pressure and its time distribution as shown in Fig. 75.5. Stretching speeds are 0.65 m/s all.
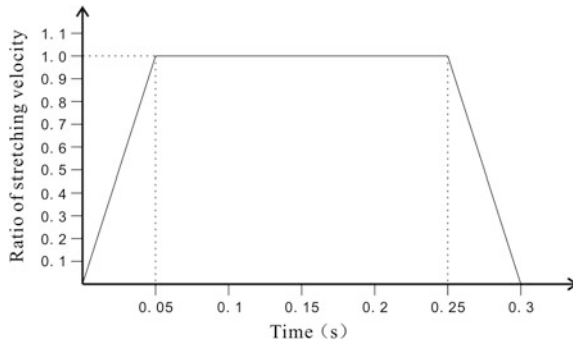
Fig. 75.3 Multi-ramp function curve of stretching velocity ratio relative to time
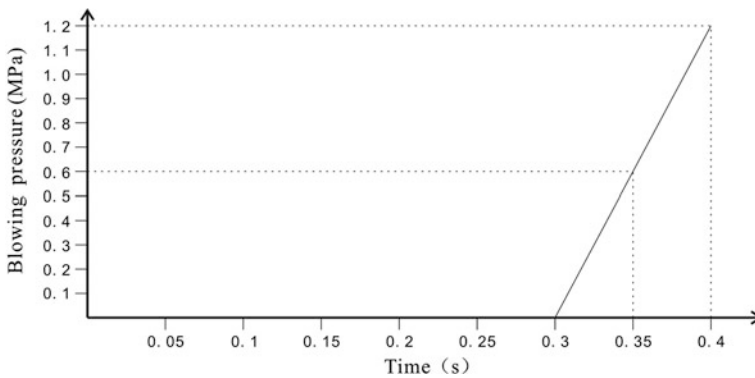
Fig. 75.4 Blowing pressure values and time distribution

75.2.2 Contact Settings

It needs to set up the contact relationship of parison with stretching rod and mold, respectively in the process of simulation. It is also worthy to note that contact release between parison and stretching rod should be activated. Otherwise, the parison and the stretching rod will stick together when they contact, and the parison cannot fall off from the stretching rod in the moment of later blowing process [11].

75.3 Results Analysis

75.3.1 Process of Stretching and Blowing

After the analysis, results are extracted using CFD-Post software in the workbench platform. The process of stretch-blow from the time of beginning to stretch to the time of finishing blowing is shown in Fig. 75.5.

In this process, the finishing time of stretching and the beginning time of blowing are 0.3 s all. And the wall thickness of parison is uniform in the process of stretching, which can be seen in cloud chart of 0.3 s. The radial inflation by blowing begins from bottle neck first, and then expand to the below, finally forms the bottom of the bottle.

The thickness distribution curve after stretching and blowing is showed in Fig. 75.6. From which we can see that the side wall's thickness distribution is uniform basically. The part near the bottom is a bit thin, and the thickness of the part near the bottleneck increases gradually, which is same to the actual measured value. There is a maximal value of thickness on the part of 5 mm from the bottom which is the center of the bottle bottom, it is the thickest part of the bottle which is also same to the actual measured value.
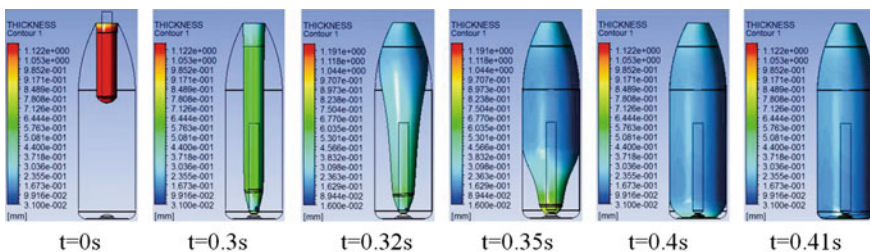
Fig. 75.5 Process of stretching and blowing

Fig. 75.6 Thickness
distribution of the bottle
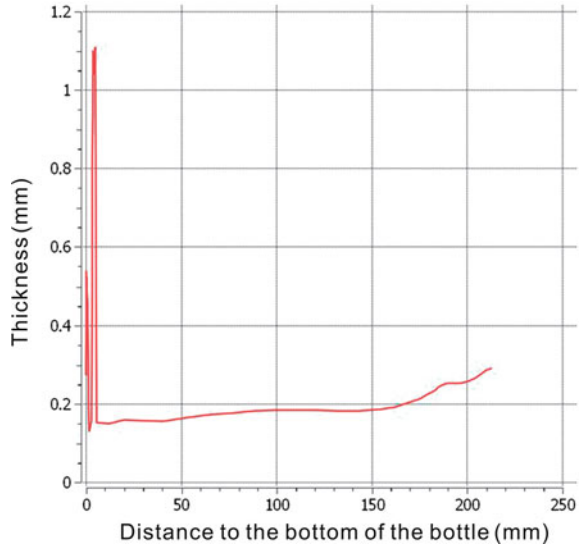
75.3.2 Influence of Stretching Velocity on Thickness Distribution

The data of thickness distribution can be exported in the form of a CSV file in the software of CFD-Post after finishing simulation. In order to analyze the thickness distribution in all parts of the bottles in detail. The datum of longitudinal thickness distribution of the side wall and radial thickness distribution at the bottom are extracted respectively from the CSV file using the excel software. The longitudinal thickness distribution curves of the side wall on different stretching velocity are showed in Fig. 75.7, the radial thickness distribution curves at the bottom on different stretching velocity are showed in Fig. 75.8.

Fig. 75.7 Thickness
distribution of the side wall
on different stretching
velocity
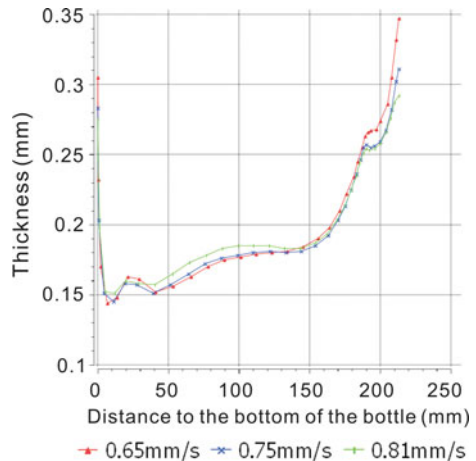
Fig. 75.8 Thickness
distribution of the bottom on
different stretching velocity
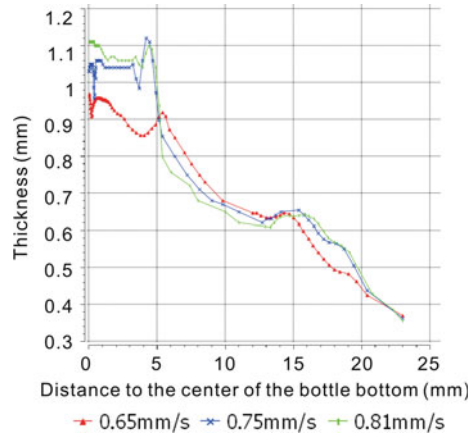
The thickness of the part higher than 150 mm decreases with the increasing of stretching velocity, and increases at the part lower than 150 mm, which can be seen in Fig. 75.7. The thickness of the part within a radius of 5 mm and 15–23 mm at the bottom center increases with the stretching velocity, decreases within a radius of 5–15 mm which can be seen in Fig. 75.8.

From Fig. 75.6, we can see that the thickness decreases from the top to the bottom of the bottle. Therefore, the increasing of stretching velocity can help to the uniform of the thickness distribution. Because the lower portion of the bottle body is easy to be deformed when it is pressed, the increasing of stretching velocity also can help to improve compressive strength of the bottle.

Otherwise, higher stretching velocity also helps to the molecular orientation and the improvement of the mechanics performance of the material in the actual process of Injection-Stretch-Blow. But, the parison will be pulled off when the stretching velocity is too high.

75.3.3 Influence of Delaying Time for Blowing on Thickness Distribution

The datum of longitudinal thickness distribution of the side wall and radial thickness distribution at the bottom are also extracted, respectively from the CSV file using the excel software. The longitudinal thickness distribution curves of the side wall on different delaying time for blowing are showed in Fig. 75.9, and the radial thickness distribution curves at the bottom on different delaying time for blowing are showed in Fig. 75.10. The thickness of the part higher than 100 mm decreases with the increasing of delaying time for blowing, and increases at the part lower than 100 mm, which can be seen in Fig. 75.9. The thickness of the bottom center increases with the delaying time for blowing, which can be seen in Fig. 75.10.

Fig. 75.9 Thickness
distribution of the side wall
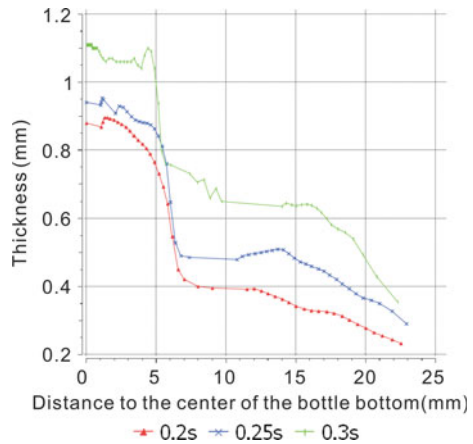on different delaying time for
blowing
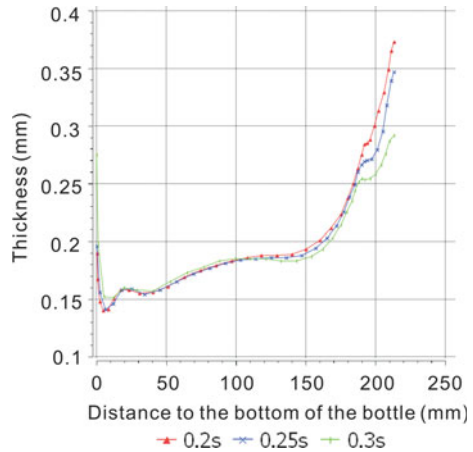
Fig. 75.10 Thickness
distribution of the bottom on
different delaying time for
blowing

The above-mentioned changing trend is almost same to that of increasing stretching velocity, the increasing of delaying time is also beneficial to the uniform of the thickness distribution. However, the increasing of delaying time will lead to changes in temperature distribution and the processing time of the bottle. The longer processing time will reduce production efficiency, and the changes of temperature distribution will result in a more complex effect on the thickness distribution of the bottle.

75.4 Conclusion

Through the above simulation analysis, we can see that the stretching velocity and the delaying time for blowing influence the thickness distribution significantly in the process of Injection-Stretch-Blow. Overall, the increasing of stretching velocity or delaying time is beneficial to the uniformity of bottle's thickness distribution and helps to improving compressive strength of the bottle. But we must ensure that the parison is not pulled off when the stretching velocity increases, and the impact on the parison's temperature distribution should be minimized when increasing delaying time.

Moreover, the method of processing the datum of the wall thickness and the bottom thickness separately helps to researching the influence of different factors on the thickness distribution of the bottle's different position more carefully, which has a certain significance to both research and actual production.

References

1. Hui, Y., Li, X., & Wang, C-h. (2007). Parametric design of packaging container structure based on solid works. *Packaging, Engineering, 28*(12), 119–120.
2. Qin, S-x, Ding, K., & Ren, L-x. (2011). Computer simulation of isothermal blow molding for plastic containers. *Packaging, Engineering, 32*(19), 78–81.
3. Tan, C. W., Menary, G. H., & Salomeia, Y. (2008). Modeling of the injection stretch blow molding of PET containers via a pressure-volume-time (PV-t) thermodynamic relationship. *International Journal of Material Forming*, *1*(1), 799–802.
4. Daver, F., & Demirel, B. (2012). A simulation study of the effect of perform cooling time in injection stretch blow molding. *Journal of Materials Processing Technology, 212*(11), 2400–2405.
5. Zhou, Y., & Xin, Y. (2014). Effects of preform size on the thickness distribution of stretch-blow PET molded bottle. *Engineering Plastics Application, 42*(4), 56–61.
6. Zheng, H., Zhou, C., & Yu, W. (2004). Numerical simulation of injection- stretch-blow molding process. *China Plastics, 18*(2), 48–51.
7. Su, L-y, Li, X-s, & Yin, X-f. (2011). Research about the bottle structure process design based on the finite element analysis. *China Plastics Industry, 2*, 53–55.
8. Yin, Z.-s., Huang, H.-x., & Liu J.-h. (2006). Study of thickness distribution of injection-stretch-blow PET molded part. *China Plastics Industry*, 7, 22–25.
9. Wang, H-j, Liu, H-j, & Geng, Z-d. (2008). Thermoforming container and its applications in packaging. *Packaging, Engineering, 29*(9), 221–224.
10. Yang, Z. J., Jones, E. H., & Menary, G. H. (2004). A non-isothermal finite element model for injection stretch blow molding of PET bottles with parametric studies. *Polymer Engineering & Science, 44*(7), 1379–1390.
11. Chung, K. (1989). Finite element simulation of pet stretch/blow molding process. *Journal of Materials Shaping Technology*, 7, 229–239.

Chapter 76
Application of ZigBee Networking Technology in Oil Field

Hanyue Zhang, Xuehong Wang and Jiao Wen

Abstract The Internet of things is a network that connects the goods and the network. It can exchange and communicate information through several of information sensor equipment in order to achieve intelligent monitoring and management. The wells information is collected by installing sensors on the wells; information include temperature, liquid, and oil-water ratio. Then design an appropriate scheme of wireless communication to solve the problem of how achieve information transport in oil field based on ZigBee terminal transport distance. The maximum stable distance of the ZigBee terminal node is obtained by testing. At the same time, the maximum stable transmission distance arranges the stratification of the wells reasonably. Well as ZigBee terminal node, the information is transmitted via the approach of hop-by-hop relaying to the data management center for achieving the application of ZigBee wireless transmission technology in the oil field and managing and monitoring oil field information easily.

Keywords Internet of things · ZigBee · Wireless networking · Hop by hop relaying

76.1 Introduction

The oil well is the smallest unit in oil field. It is important for oil field safety and efficient production. Therefore, understanding the operation situation of oil filed must grasp all kinds' information of oil well timely. According to the actual investigation, the distance between the oil wells is far, and the use of artificial statistics will cause the delay of information transmission. So, a quantity of data transmission terminal is installed on the oil well to collect information instead of the

H. Zhang · X. Wang (✉) · J. Wen
College of Packaging and Printing Engineering, Tianjin University of Science and Technology, Tianjin, China
e-mail: wwangxuehong@163.com

artificial way. However, the structure of oil field kowtow machine is tight relatively if the wired transmit information not only causes the wiring trouble, but will also have an impact on the normal operation kowtow machine. So, wireless transmission is becoming the major trends.

Because the wireless transmission of information is greatly influenced by the distance, when the distance between the two wells is greater than that of wireless transmission, we need form a wireless network to expand the transmission distance. ZigBee wireless sensor network in the oil filed management system uses a large number of sensors to transmit information and give up the traditional single oil well monitoring methods including wired, digital radio. The method not only reduces the cost of investment and operation, but also improves the stability of the system and achieves oil filed wireless management.

76.2 Select the Radio Communication Method

Free 2.4 GHz band wireless communication technologies include ZigBee, Bluetooth, and Wi-Fi; they are compared in Table 76.1. Bluetooth and Wi-Fi can accommodate a small number of nodes and limit the large-scale application of wireless sensor network, so the paper chooses ZigBee technology.

Oil field area is huge, the layout is uneven, and the number of wells is very many. So, information collected needs to take wireless data transmission and requires large coverage. Since coverage of a single ZigBee node is determinate, the distance between two nodes is greater than the ZigBee node transmission distance, and the wells can transfer information along other sensor hop-by-hop relay to form transmission network. In this way, communication distance to achieve ZigBee wireless network can increase. A ZigBee network can support up to 65,000 nodes and meet the requirement of large-scale data transmission.

Table 76.1 Comparison of ZigBee with several other wireless communication technologies

Item	ZigBee	Bluetooth	Wi-Fi
Single-point distance (m)	400	10	50
Extensibility	Automatic extension	None	None
Power consumption (MW)	1–3	1–100	100
Complexity	Simple	Complex	Very complex
Transmission rate	250 Kb/s	1 Mb/s	1–11 Mb/s
Network nodes	65,000	8	50
Transport time	30 ms	10 s	3 s
Ease of installation	Very simple	General	Difficult

76.3 Overall Design of ZigBee Wireless Network in Oil Field

Distribution of wells is wider and they are generally distributed in groups [1, 2]; the situation that a single oil well farther apart other wells is very rare. Oil field will be divided into a plurality of small regions to collect information of each oil well [3]. Each small region sets up independent ZigBee wireless sensor network, when transmitting information to the remote data management center need to combine with GPRS. The network structure diagram of oil field data transmission is shown in Fig. 76.1.

76.3.1 Confirm Transmission Distance of ZigBee Terminal Node through Test

The maximum output power of the ZigBee module is 22 dBm (5 dBi antenna), and the operating frequency is 2.38–2.50 GHz in remote data testing. In this way, it can avoid the interference of Wi-Fi and Bluetooth effectively.
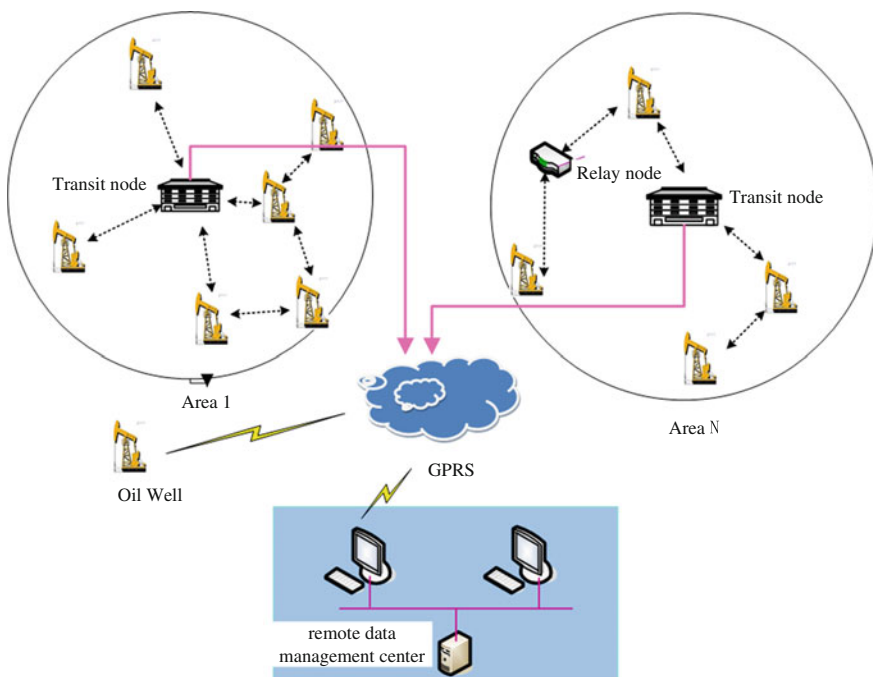
Fig. 76.1 Network structure of oil field data transmission
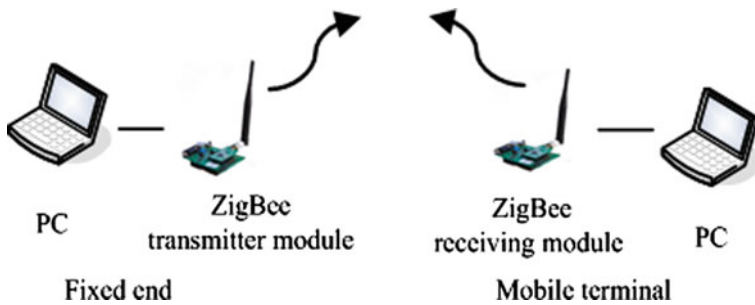
Fig. 76.2 Data transmission test chart

Table 76.2 Test distance relationship and packet loss rate

Test distance (m)	Send byte data	Receive byte data	Packet loss rate (%)
200	2368	2368	0
400	2368	2341	1
600	2368	2307	2.5
800	2368	2281	3.6
1500	2368	1102	53.5

September 2013, Hekou District, Dongying City, Shandong Province, we took a communication distance test for ZigBee module of data transmission.

Test acceptance criteria: When the test evaluation board sends data, the send light flashes; when data are received, the receiving light flashes. The test program sends a packet of 64 bytes every 1.6 s. In a minute, we analyze the communication distance according to the returning actual packet loss rate. Test data transfer process is shown in Fig. 76.2.

In practical test, the information is received by meters. The test result is shown in Table 76.2.

Analyzing the test results, when the test distance reached 400 m, the evaluation board found packet loss, the packet loss long 27 bytes; when the test distance is 1.5 km, it still can receive data packet, but the acceptance rate is less than 50 %. There was a serious situation that a large of data packet loss made the communication quality worse. According to the test analysis, it is reliable communication when the packet loss rate is less than 1 %. The maximum stable communication distance of ZigBee network node can reach up to 400 m; in the following chapters, oil-well-specific program overview and stratification based on this test is introduced.

76.3.2 Overview of the Program

76.3.2.1 Option One: For Farther Single Well

Because this kind of oil well is far from well group, it is difficult to set up ZigBee wireless transmission network. When the data are transmitted, we can adopt the manner that the temperature, liquid production, and oil–water ratio sensor groups are connected to their respective ZigBee module as terminal node of ZigBee network. Then, a small coordinator that is equipped with GPRS data module loads the power control box of oil well. In this way, the terminal node and coordinator of the oil well can form a small ZigBee network. After the well's data acquisition is completed, data are transmitted to the coordinator node. Finally, the coordinator node transmits the data to the remote data management center through its GPRS data module.

76.3.2.2 Option Two: For a Wide Range of Wells Throughout the Field

A large area of oil field is divided into different small regions. The oil wells in different regions construct different ZigBee network but they cannot communicate with each other. Nodes in the same area can communicate with each other and exchange data. In this paper, the ZigBee network uses hop-by-hop relay technology to form mesh network which is composed of a coordinator node and a number of sensor nodes in a network. The sensor node that is installed in each well is responsible for collecting information of wells, and at the same time each sensor node is the routing node; it can transmit information along the routing nodes and sent to the coordinator node at the end.

   Through field measurements, the distance of two oil wells is different from a few meters to several hundred meters. When the ZigBee wireless network transmits data, the transmission effect is becoming worse and worse as the distance between the oil wells is farther and farther. So, we take the hop-by-hop technology to form network of oil well in every region. However, even if the oil well is in a certain area, it is possible that the distance between the oil wells is greater than the stable transmission distance. Therefore, two different network schemes are set up for different distances in each region. Firstly, when the distance between oil wells is within 400 m, the oil–water ratio, liquid volume, and temperature sensor group are installed in the oil well as the terminal node directly. The node can not only receive information from other oil well nodes but also forward data. The oil well information is gathered to the coordinator node at the relay station (namely the gateway) in each region, and then data are transmitted to the remote data management center via GPRS network. Secondly, when the distance between the two wells is greater than 400 m, we can install relay node between two wells, and the node is only responsible for forwarding data.

76.3.3 Determination of Oil Well Layered

According to the maximum stable distance of ZigBee terminal node, the transfer station (where the coordinator position) is center in region, and then wells are stratified with a radius of 400 m. Close to the transfer station of the first circle is the first layer and the first jump; after that, each additional jump outwardly the layer will increase; by analogy, it will form a ring in which center is the transfer station. So, all of oil well information, where in the outer layer must transport information, reaches the data center by oil wells in the first layer (distance relay terminal equipment). But the number of layers is large; the first layer terminal nodes will appear in the phenomenon of data congestion bottleneck, and when data-forwarding needs are more than the maximum transmission capacity of the terminal node, the network will be paralyzed or outer wells subject to greater throughput decreases.

Above all, this paper uses a way that each layer's width is unequal [4] (the specific layer width algorithm see the Ref. [5]), and it can decide stratification of oil well through inside to outside gradually reduce. In this way, the number of inner oil wells will be correspondingly increased, and the number of layers of outer layer is reduced, which can be more close to the actual situation of the lower complexity of the oil well terminal; finally, it can eliminate the bottleneck of network transmission.

76.4 Information Transmissions

The communication range of nodes is limited, but when it attempts to communicate with the nodes they are outside of communication range which require an intermediate node to forward. However, unlike general hop relay routing, ZigBee wireless self-organization network is a hop relay routing through oil well nodes collaborative rather than special router device. The design takes the 3.2 program to achieve transmission of information between wells.

The basic idea is that according to the layered scheme of oil wells, they will be connected through the imaginary "routing" line; wells online can communicate without other well forward. Information transmission routing line between wells is shown in Fig. 76.3, and the red dot indicates the well [5].

It is very simple that the outermost oil wells transport information via the inner oil wells hop relay to information center as long as judge direction of transfer station. However, a variety of routing choice, which the hop is too much will cause the effect of information received not ideal. In Fig. 76.3, for example, 1st well send information to transfer station via 2nd–6th wells. In fact, 1st, 3rd, and 4th wells are within coverage of the communication node, and they can transmit information directly without intermediate wells forwarding. Seen above, it is possible to find transmission shortcut and reduce routing hops according to the maximum distance of nodes transmission.

Fig. 76.3 Transmission routing
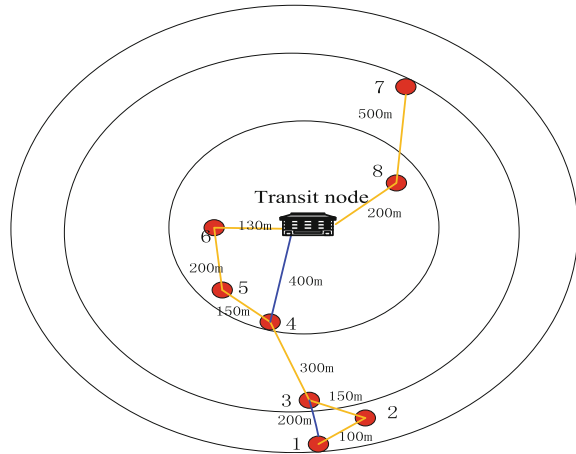
This design takes a quick way to find the nearest neighbor node via hop-by-hop routing. The neighbor node which is within the coverage of node can communicate with other nodes directly. When a terminal node in the ZigBee network needs to transfer data, it must start neighbor discovery that is the node sends a signal to the neighbor nodes. After the neighbor node receives and stores it in their list to look for shortcuts. Finally, information will be transmitted to the coordinator node. However, this approach has a disadvantage that multiple neighbors will cause data duplication and even cause cycle mode, resulting in information that cannot reach the transit station.

Considering the aforementioned communication schemes to design route between 1st well and 6th well, since 3rd well is in range of 1st oil well, information can be passed to 3rd well directly. Then, judging whether 3rd well be in two hops coordinator, if so 3rd can communicate with 4th. In this case, 1st oil well can transfer information by two nodes forwarding to arrive coordinator, and the intermediate nodes from five down to two. Above all, it is effective to find the best shortcut and reduce routing hops though using the maximum stable communication distance of node.

However, there is also a case such 7th and 8th well, their distance is more than maximum distance of ZigBee terminal node. Transmitting data will result in a small part of the data loss, so using second way for large area network scheme in Sect. 76.3.2. A ZigBee node is installed between the two oil wells, which is responsible for forwarding the data to the oil well which can communicate with the relay station via hop-by-hop technology.

76.5 Conclusions

The design has implemented application of the Internet of things and transmission of information in oil field. ZigBee low price can reduce investment of thousands of oil wells. When transmitting information uses simple and practical routing process to achieve high-performance and low-cost ZigBee wireless network. However, ZigBee wireless network is disturbed evenly affected stability of data transmission by weather, terrain, and other external factors. So, it still needs to be improved.

References

1. Anhu, R., Honghai, B. (2014). Urban road safety monitoring system based on ZigBee. In *The technology for network of things* (Vol. 11, pp. 81–83).
2. Yang, P. (2012). *Oil monitoring system based on ZigBee wireless networking technology*. Xi'an: Xi'an Petroleum University.
3. Sun, B., Wang, W., & Lei, G. (2014). Paddy information in real time monitoring system based on wireless sensor networks. *Agricultural Machinery, 45*(9), 241–246.
4. Sun, J. (2008). *The research of next generation wireless communication in multi hops cellular key technology*. Beijing: Beijing University of Posts and Telecommunications.
5. Li, Z. (2012). The solution of smart home wireless networking based on nRF24L01P. In Based electronics and software engineering (pp. 76–78).

Chapter 77
RFID Technology Application on the Supervision of Cold-Chain Logistics Warehousing

Li Yang, Hanyue Zhang and Suzhou Tang

Abstract At present, a gap exists in the supervision of cold-chain logistics (CCL). Applying contactless and automatic radio frequency identification (RFID) technology on cold-chain storage to achieve the traceability of CCL is proposed in this study. First, the status of CCL is described. Then, the principles of RFID technology, its advantages, and its disadvantages are elaborated. Finally, applying RFID technology on cold-chain storage is proposed so that a full process automation warehousing, inventory management, visualization, and traceability can be implemented. In this process, we can extract supervision index of the CCL warehousing environment. A cold-chain traceability system stored procedure based on RFID technology is established. Compared with the traditional cold chain logistics warehouse management technology, the real-time monitoring function of cold chain storage is added to improve the automation and information level of storage, and improve the quality of cold chain logistics storage.

Keywords Cold-chain logistics · Warehouse · Supervision

77.1 Introduction

With the development of the economy, quality of life gradually improved, and food quality and food safety issues became increasingly important. Hence, the rapid development of cold-chain logistics (CCL) became a top priority. CCL is a systematic project to ensure quality and reduce loss for refrigerated, frozen, and perishable commodities by maintaining a low temperature in each link in circulation. Warehouse

L. Yang (✉)
Beijing Institute of Technology, Beijing, China
e-mail: yangli414319@tust.edu.cn

L. Yang · H. Zhang · S. Tang
College of Packaging and Printing Engineering,
Tianjin University Science and Technology, Tianjin, China

storage is a part of the logistics, including the conversion of the procurement, production, sales, and transport. For CCL, the accurate and efficient monitoring of the warehouse can effectively ensure the quality and spoilage of goods.

77.2   Radio Frequency Identification

Radio frequency identification (RFID) technology is an automatic identification and no-contact technology [1]. The RFID system mainly consists of three parts: the reader, the RFID tag, and the computer system. The working process of RFID is as follows: The reader sends out radio waves of a specific frequency to the electronic tags, and the electronic tag receives the radio waves. If the tag is passive, the induced current obtained with the energy stored in the chip information is sent to the reader. If the tag is active, the active information in the chip of a particular frequency of the signal is sent to the reader. The reader receives the feedback signal sent to the information system for processing [2].

Compared with other identification technologies, the RFID system has more advantages, such as high degree of automation, durability, reliability, recognition speed, and ability to adapt to the working environment [3]. RFID will be the most versatile automatic identification technology in the twenty-first century. RFID technology is also widely used in supply chain management.

77.3   CCL and Business Process

The CCL system is a temperature-controlled logistics supply chain system. This process includes receiving products from production, storage, transportation, sales, and other links, wherein each link is kept at a low temperature. The logistics of cold-chain products have higher temperature, humidity, light intensity, and timeliness requirements. The logistics management of cold-chain products is mainly based on refrigeration technology and environment control and emphasizes the seamlessness of each link to ensure the integrity of the CCL and the product quality [4].

The CCL center is an important node in the CCL process, which is the transit point for the production and sale of goods. To maximize the quality of cold-chain products, cold storage and frozen goods generally need to be in a cool or cold storage conditions during reception and delivery. Usually, the CCL center operation consists of inspection, warehousing, storage, sorting, distribution, inspection, and packaging.

1. Inspection. The logistics center receives instructions. After checking the quantity, quality, and items of goods, the accepted goods are stored in the storage buffer.
2. Storage. The accepted goods shipped to the storage area are placed in accordance with other qualified goods. The goods are stored and maintained

according to the required storage temperature, humidity, light, and other conditions. The storage space indicates the quantity, quantity, and storage time.

3. Sorting. The goods are sorted in the low-temperature environment according to the type.
4. Distribution. Based on the demand for commodities by downstream sales enterprises, order forms are generated and printed. The warehouse is responsible for distribution and delivery.
5. Review. After cold-chain distribution, the warehousing department reviews the goods according to the order to avoid mistakes that can increase CCL cost.
6. Packing. For some cold-chain products, heat preservation and packaging are required to maintain the flow of goods in the process of temperature.

77.4 Cold-Chain Logistics Warehouse Management System Based on RFID Technology

77.4.1 Basic Functional Analysis

According to the special requirements of the CCL system, determining the CCL warehouse management system mainly includes five modules: system management, basic data management, inventory management, RFID dynamic management, and data management, as shown in Table 77.1 and Fig. 77.1.

Table 77.1 Basic function operation table

Basic module	Specific function	Operation can be implemented
System management	Order management	Query, add, modify, bar management
	Role management	Authority management
	Warning management	Temperature, humidity, illumination
Basic data	Employee management	Add, modify, disable, start, password change
	Goods management	Add, modify, bar management
	Storage management	Add, modify, disable, start, related information management
	Tray management	Add, modify, disable, start, related information management, bar management
Inventory management	Warehouse operation	Storage, out of library, check, special case, return goods
RFID dynamic management	RFID management	Information collection, information instruction
Data management	Data backup	Data backup, data recovery
	Operation log	Operation log
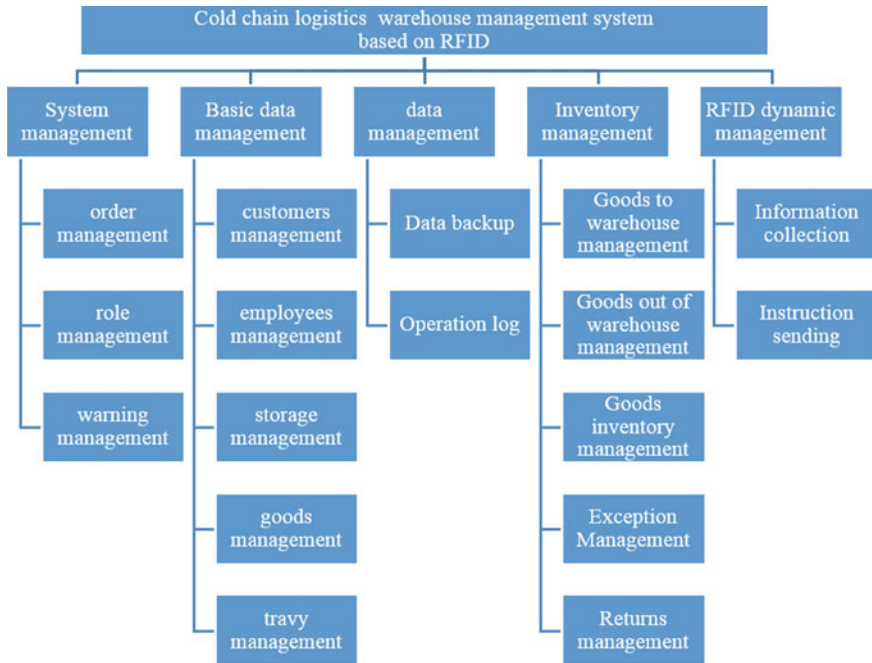
Fig. 77.1 CCL warehouse management system based on RFID technology

77.4.2 Cold-Chain Storage Operation Based on RFID Technology

When cold-chain goods are stored, the system first automatically generates inbound orders according to the purchasing department orders. Then, the free space available is determined. When the products arrive, pre-storage orders and commodity details on the storage of goods are used for reception. Specific operating procedures are shown as follows in Fig. 77.2.

(1) Goods receipt. When cold-chain goods arrive, the RFID reader first automatically identifies and reads the information on the RFID tag on the packaging, including good name, quantity, specifications, producers, and other related information. The information is then fed back to the management of the background network host. The item is automatically assigned storage shelves based on item information. Information is stored through the RFID reader in cold-chain commodity packaging on electronic tags. The system simultaneously generates cold-chain temperature records of goods receiving and arrival. The RFID reader tags the storage location information on the packaging to produce the cold-chain goods receipt.
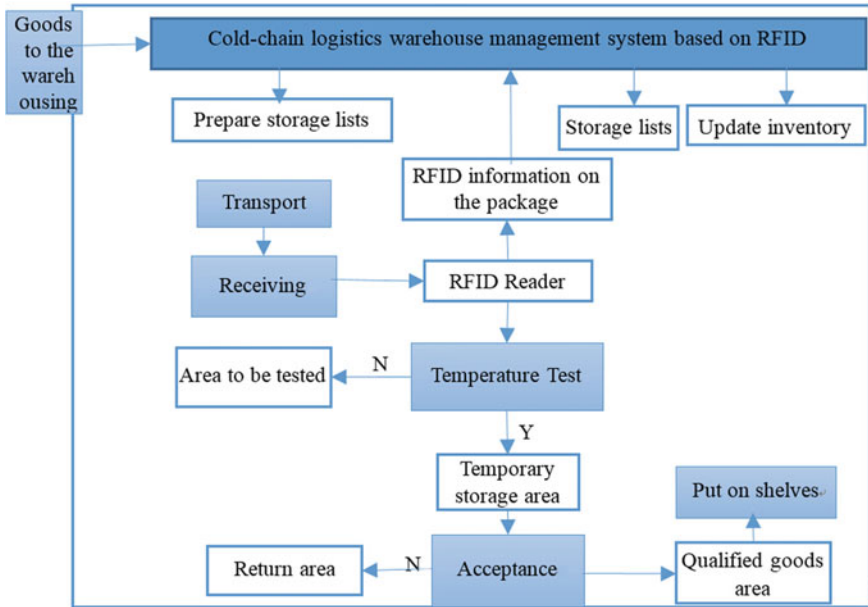
Fig. 77.2 RFID-based goods storage operation flow chart

(2) Commodity inspection. Personnel accept and record data through handheld terminals and temperature recorders. When the product qualifies for reception, the cold-chain product is transported to the qualified product area; otherwise, the cold-chain products will be transferred to the temporary storage area. Acceptance records of commodity inspection and acceptance include supplier, quantity, delivery date, commodity name, quality, and temperature during transportation.

(3) Storage. The cold-chain goods are stored after commodity inspection. Based on the storage notice, cold storage workers will receive the temporary storage of goods individually. The management host is responsible for sending storage information for shelving. At the same time, the warehouse operator uses a handheld terminal to send a storage confirmation message to the management host.

77.4.3   Cold-Chain Warehouse Operation Process Based on RFID Technology

When the goods are out of the library, first of all, the picking orders should be generated according to customer order information, then the picking workers start to sort, pick, and confirm the goods according to the picking orders. The system simultaneously and automatically updates the stock information. The specific operating procedures are shown in Fig. 77.3.
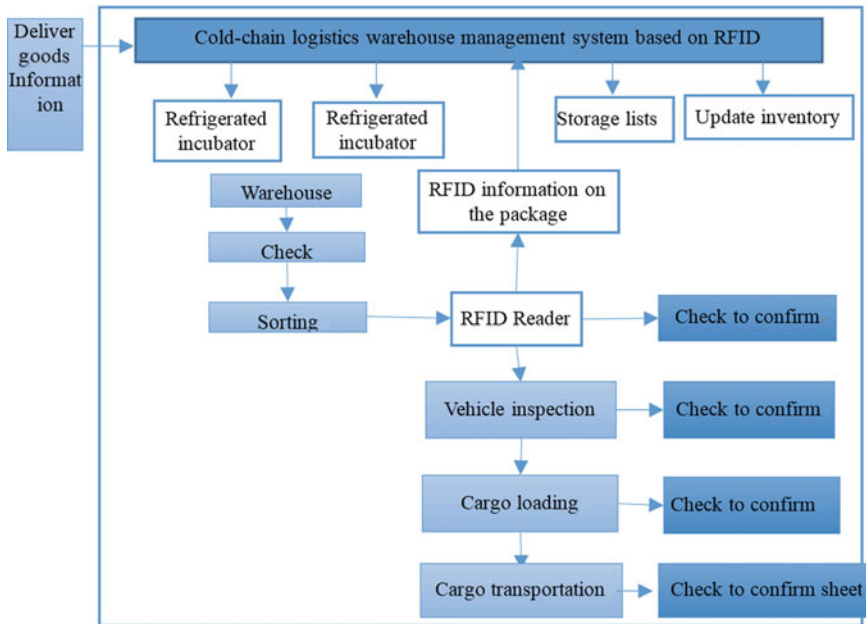
Fig. 77.3 RFID-based goods delivery process flow chart

1. Outbound instruction. When receiving procurement of goods information from downstream distributors, the background network management host automatically matches the storage of goods with library information and generates picking orders. The order is simultaneously sent to workers picking orders from cold storage.
2. Sorting. Workers following picking order instructions determine the storage requirements of outbound commodity goods, chosen in accordance with the name, quantity, and specifications. The delivery of goods is simultaneously shifted to the warehouse area.
3. Packing. Commodity packaging is a key link in the process of cold-chain transportation. The management of the host following factors such as storage requirements, quantity, weather conditions, and transportation time automatically matches the size and capacity of the refrigeration room.
4. Check. After commodity packaging, the RFID system can be used to conduct the automatic verification of goods from the library. RFID reader in the library automatically reads the RFID tag on the product packaging. The tag includes information such as library storage, commodity name, quantity, manufacturers, shelf life information, and return information. This information is sent to network, testing the current delivery of goods by the management host. The library is subsequently included in the RFID reader. The host automatically prints the loading instructions after the RFID calibration.

5. Loading. Loading is conducted according to the required storage conditions of the commodity once the refrigerated truck reaches the specified temperature. Delivery drivers sign the loading form on the warehouse floor after loading.
6. Out to confirm. After the loading of goods from the warehouse, the warehouse personnel use a handheld terminal to confirm the information with the database and to complete the delivery of the goods.

77.5   Temperature Control Based on RFID Technology

RFID transmits the temperature sensor measurements of the warehouse to the temperature control center. When the temperature is higher than the set temperature, a signal is transmitted to the refrigeration equipment system, which starts the refrigeration. Then, the temperature decreases. If the warehouse interior temperature is lower than the set temperature, then the signal stops. The temperature sensor makes precise measurements of the warehouse temperature, so that the temperature is maintained in a certain temperature range to ensure the quality of goods within the warehouse. The specific operating procedures are shown in Fig. 77.4.
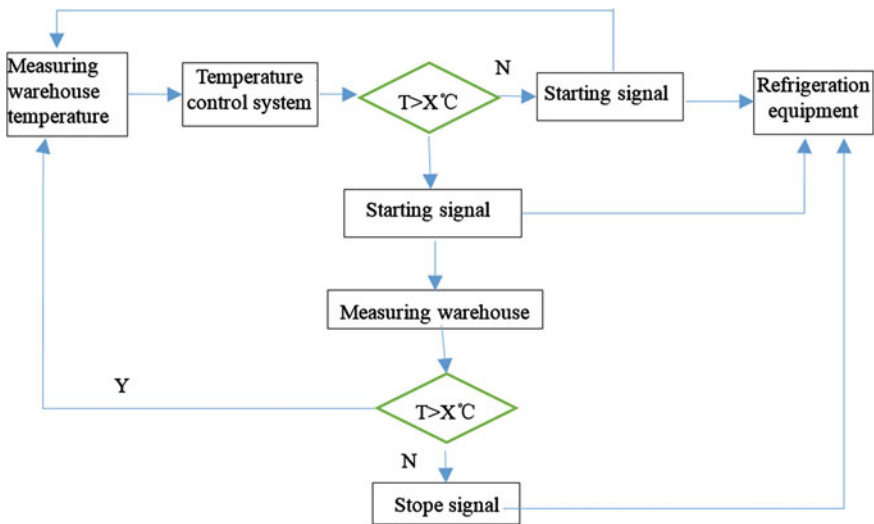
Fig. 77.4 RFID temperature monitoring system

77.6 Conclusions

Advanced information technology and efficient information management can not only ensure the real-time symmetry of logistics and information flow, make enterprise inventory management transparent, and enhance the ability of an enterprise to quickly react to customer needs, but also help reduce the inventory of the enterprise risk and improve the rate of inventory turnover of enterprises.

References

1. Runxian, Y., Ainai, G., & Yongsheng, D. (2005). The RFID system against collision processing queuing modeling and analysis. *Journal of Computer Simulation, 22*(8), 286–288.
2. He, M. (2006). The introduction of RFID development. In *EB/OL*. http://tech.rfidworld.com.cn/200682212332760.htm. Accessed August 22, 2006.
3. Shunqing, L. (2015). Design of pharmaceutical cold chain logistics and storage management system based on RFID. *Logistics Technology, 2015*(1), 130–133.
4. Shufang, X., Jinhai, W., & Yulong, G. (2013). Research and design of monitoring network cold-chain transport based on RFID. *Measurement Control Technology and Instruments, 2013* (7), 70–73.

Chapter 78
Design of Oil Well Monitoring Information Management System Based on IOT Technology

Hanyue Zhang, Fei Cheng and Chen Hu

Abstract Information management methods of oil production plant of the traditional way are backward. All the departments are in the stand-alone mode, lacking a unified information network platform, generating large amounts of information islands. This backward working model has seriously hindered the development of oil production plant. This paper uses LC-40DR-A-type multiphase flow monitor as remote data acquisition terminal, focusing on three aspects of data acquisition, data management, and data application, to establish the remote data acquisition and control system improvement. The realization of the five major functions—real-time monitoring, automatic alarm, the user management, report management, and equipment management—can not only improve the measurement accuracy, but also provide strong support for the daily production management in oil production plant.

Keywords Oil well data acquisition · Visual monitoring · Information management

78.1 Introduction

Petroleum is an important resource, involving economic, military, and industrial fields. With the modernization of production management requirements improving continuously, the requirement of digital oil field is more and more important. The accurate measurement of the produced fluid is an important factor in the development and production of oil wells. The single function and most traditional way is measured by the metering separator. Metering workers adjust valves to lead the single well test separator liquid into the separator gas and liquid separation, and then the liquid is introduced into a graduated container. Workers record the filled container's time, and speculate the well's liquid production per day [1]. Then, the

H. Zhang · F. Cheng (✉) · C. Hu
Tianjin University of Science and Technology, Tianjin, China
e-mail: chengfei5102@163.com

dedicated staff take liquid samples for testing to detect moisture. The staff will collect data and report them to the higher authorities once every 2 h through the telephone. After that, the higher authorities get Excel form filled to record data manually. There is a lack of information communication and interconnection between the various departments of oil production plant. What is worse, no unified information management system exists, either. The efficiency of traditional information management, information accuracy, and security are low. Besides, the data are easy to lose, and timeliness cannot be guaranteed.

The oil production plant has the characteristics of large quantity and wide distribution. Manual data collection is time-consuming and laborious, and the pumping unit is 7 * 24 h of work mode, so we think manual collection has severe limitations. It cannot get the complete data, and the total flow of oil pumping machine can only be estimated. The basic data of oil wells are directly related to the stability and quality of crude oil; thus, the oil information is particularly important.

In summary, we should use sensors, instead of manual testing and measurement method, to establish and improve the supervisory control and data acquisition (SCADA) systems. The purpose is to integrate the information islands of widely distributed oil fields, monitor oil fields real time, improve the measurement accuracy of the well fluid production, reduce labor intensity, and improve production efficiency of oil extraction plant.

78.2 System Components

78.2.1 Structure

This design of Oil Production Plant Visualization Information Management System includes four structures: the acquisition layer, transport layer, service layer, and management. Oil Production Plant Visualization Information Management System structure diagram is shown in Fig. 78.1.

78.2.2 Acquisition Layer

Data acquisition layer is the basis of the Internet of things. The important technical support of data acquisition and monitoring system is the automatic acquisition equipment, but the immaturity of oil–water ratio sensor technology (the metering accuracy is not up to the requirements of oil field automation) is the biggest bottleneck of information management. This design uses the LC-40DR-A-type multiphase flow monitor, which is a kind of special oil–water flow measuring instrument. The principle of the design is a fixed relationship with the dielectric constant and the oil–water ratio and medium. It consists of flow sensors, water
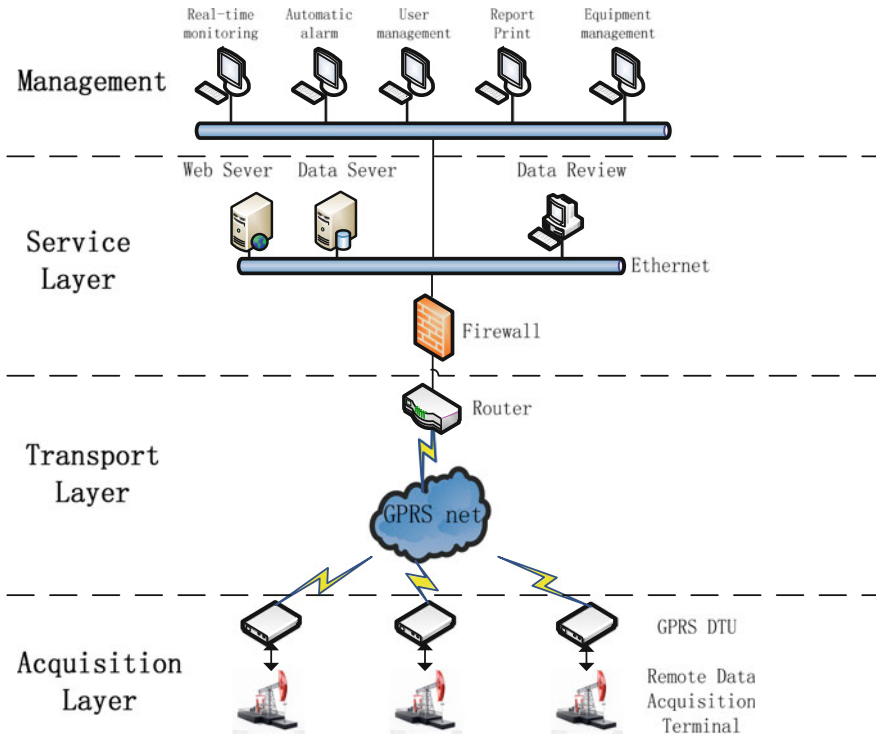
Fig. 78.1 Oil Production Plant Visualization Information Management System structure diagram

temperature sensors, and oil–water ratio sensors as three parts, so it can simultaneously detect four kinds of data, which are fluid production, oil production, water ratio, and temperature. It is a collection of four data detection functions with high precision and good stability and easy installation features. Because of it, the real-time collection of data is accessible, and MCU processes the data and uploads it every 1 h. This provides the feasibility of measurement automation. LC-40DR-A-type multiphase flow monitor is installed in the pumping of the oil export pipeline, as is shown in Fig. 78.2.

78.2.3   Transport Layer

The oil production plant has the characteristics of wide distribution as well as scattered distribution. Wireless digital radio, wireless bridge, satellite communication, and ZigBee data transmission mode could be easily influenced by the environment, so the high error rate makes its application limited. GPRS, as the world's current mobile communication system, has comprehensive coverage of the GPRS signal in the domestic oil field [2]. This system adopts advanced GPRS-DTU

Fig. 78.2 LC-40DR-A
multiphase flow monitor
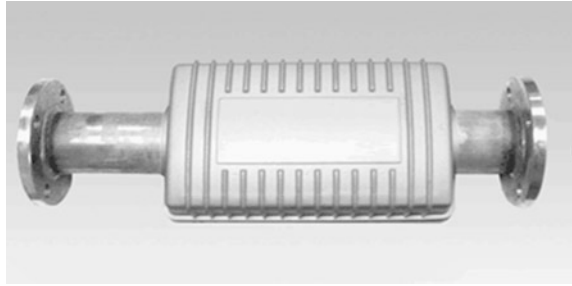
module for remote data transmission module, relying on stable and reliable GPRS network of China Mobile. Under the premise of ensuring timely and accurate data transmission, data monitoring system's operation cost is also reduced to minimum. The flow monitor MCU processes the data in each period of time and transforms the analog signal to digital signal and then sends data to go out by GPRS-DTU module integrated in the flow monitor. Data are finally uploaded to the oil production plant server via GPRS network.

78.2.4 Service Layer

The service layer is an important part of the large amount of data processing and provides the background service to the management software. The service layer of the system includes three parts: Web server, database server, and data review. LC-40DR-A-type multiphase flow monitor collects four types of data: liquid production, oil production, water ratio, and temperature. Data are uploaded to the service layer system through the GPRS network. The system checks the data through a firewall, which will go into the database if approved.

78.2.5 Management

For the purpose of achieving the production plant SCADA, department managers use client query and management database, which were collected by the remote terminal data. The system can achieve the five features, namely real-time monitoring, automatic alarm, user management, report management, and equipment management.

78.3 System Development and Application

78.3.1 Software Environment

The type of system network architecture of this design needs to be selected according to the characteristics of oil field. Browser/Server (B/S) network architecture has the characteristics of the "fat Server, thin client," based on the client Browser [3]. It can exchange data through Web and Server database. When the system needs to change, it will only need to change the server on the line, but the client does not need to make any changes. Thus, when there are a large number of clients, the network architecture of B/S will have a great advantage over C/S network architecture, so the system adopts the B/S architecture based on the network.

At the same time, it makes use of the .net framework with the strong flexibility and extensibility of ASP.NET development technology and the language development by adopting C#, which is a safe, stable, and simple computer language. This system uses SQL Server 2008, which, with strong network function, can be the perfect backup for the B/S architecture to support the release of Web page as the backstage database management.

78.3.2 Operation Environment

Database: SQL Server 2008 as the backstage database management.
Development tools: Visual Studio 2008 for developing Web code and business logic code, and FrontPage 2003 for Web production.
Server: CPU Core i3, RAM 4G, ROM 1 TB.
Client: CPU Core 2 or above, RAM 1G, ROM 40 GB or more.
Network configuration: hubs and related network adapters, network lines, etc.

78.3.3 Software Functions

Oil Production Plant Visualization Information Management System has five main functions.

78.3.3.1 Real-Time Monitoring Function

Real-time monitoring function is the real-time display of pumping oil machine operation status and production data (including liquid production, oil production, water ratio, and temperature). Remote data acquisition terminal collects data and

uploads the total fluid production, the total amount of oil, the average water content ratio, the average temperature, oil well ID, and current time to the monitoring center database server once an hour. Web server starts up middleware ASP, and then, middleware gets access to the database. The results are returned by the Web server and then shown on the user's client browser. They are presented in the form of a digital display, line charts, and histograms.

78.3.3.2 Automatic Alarm Function

Set safety threshold of operating parameters for each oil pumping machine in advance; when the sensor data collected are not in the safety threshold range, the system automatically alarms in the form of popping, thus making sound and sending a fault message. The staff will take appropriate measures according to the reason for failure, such as the liquid temperature below the safety threshold. If the temperature is too low, oil will become viscous liquid. There is a risk of clogging pipes. If the monitoring staff receive an alert, they will arrange for repair personnel to rush to the fault spot in time. After troubleshooting, the alarm will be cleared. Automatic alarm function allows the staff to find the problem in no time and correct the fault as early as possible, reducing the damage to minimum. The system records the failure time, pumping ID, and abnormal parameters. When the fault is removed, the staff will input failure lifting time and the reason. The system records abnormal conditions and stores it in the database to facilitate the analysis in the future.

78.3.3.3 User Management Function

The user possesses addition, deletion, and managing user permission and other functions. Oil field area is vast, and pumping units' distribution gets scattered. Oil plants set the transfer station and combination station in order to facilitate the production. They are local monitoring centers of the pumping unit, but scattered as well. Each user has a login account. When an oil production plant has personnel changes, separation, new recruits, promotion, or other situations, the administrator will login to the accounts to do corresponding operations.

78.3.3.4 Report Management Function

Report management is the statistics and management of historical data. Oil production plant has large quantities of pumping, and a large amount of data get generated everyday. Users can query historical data for a time node by accessing the database, and one can also check the data for a period of time (such as a day, a month, or a year). The system will automatically analyze the statistical data

(calculate the total value or average) for a period of time. Users can conveniently query a pumping unit production of a month or a year through this function, and statistics can also be convenient for users to calculate the units of some dozens of pumping unit production hub in a month or a year. This function is convenient for the managers to do the production management in the transfer station and combination station. This avoids the phenomenon of forging production data in order to achieve the production targets. The clients can be directly connected to the printer, making statements convenient and practical.

78.3.3.5   Equipment Management Function

Oil production plants are in a large number but differ in pumping models, for example, Daqing oil field has 70,000 pumping units, so the management is very difficult. Using the system, the staff can enter the pumping information into the database. The information includes the model of the pumping, production time, installation location, department, and fault records, and the staff also need to input the end time when the well is abandoned. The well distribution has the trend of intensity, while the equipment management also has the function of adding a new pumping unit.

78.3.4   Software Interface

Good human–machine interface can improve the work efficiency [4]. Traditional supervisory control, data acquisition, and data presented in the digital form are not intuitive. This system shows the results in the form of the combination of data and graphics. The user can choose a line chart, histogram, or pie chart types according to their own habits. The interface is shown in Fig. 78.3.

Graphics make the data display more intuitive, so it can help users to find the abnormal data more convenient and efficient. They also enable the staff to understand the operational status of the pumping unit quickly.

Software is the main form of the title as "Oil Pumping Machine Visualization Information Management System." On the left side of the interface is the navigation menu, including real-time monitoring, automatic alarm, user management, report management, and equipment management, which are five functions of navigation. The top right of the interface is a graphical display and data display tab.

There are several pull-down options at the bottom of the interface, including graph type, data type, equipment department, pumping wells number, and time. The user can select the appropriate item on demand.
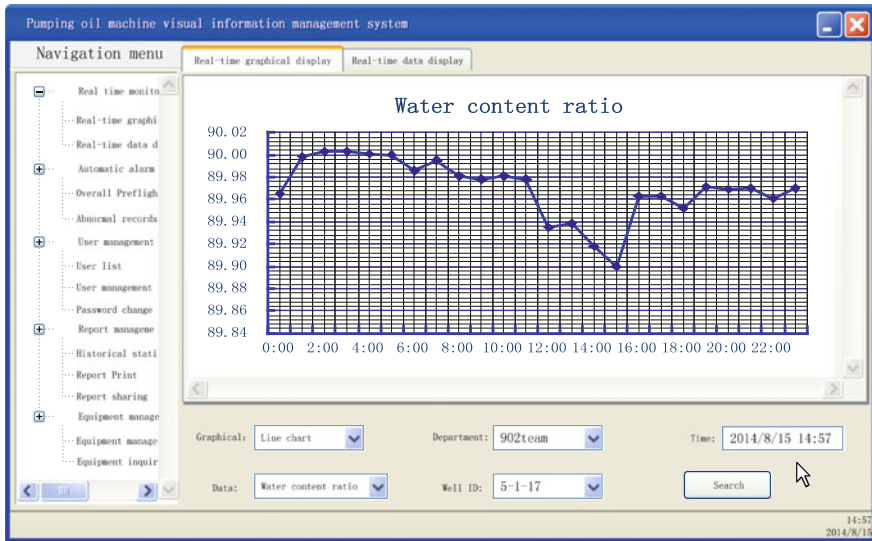
Fig. 78.3 Pumping visual information management system interface

78.4 Conclusions

We build the perfect system of Internet of things by adopting LC-40DR-A type multiphase flow monitor instead of manual production data, utilize GPRS network as the data transmission way, and the visualization of information management software. It can provide great support for the oil production plant through enhanced oil measurement accuracy so as to improve the equipment management, user management, and other sides. The system realizes the production plant digitization, improves work efficiency, and reduces downtime and equipment failure. It also decreases the labor intensity of the staff as well as provides objective economic benefits for the production plant.

References

1. Wang, X. (2013). The application and development of measurement technology in Linpan oil production plant. *Inner Mongolia Petrochemical, 19*, 127–128.
2. Geng, S., Wang, N., Jiang, S., & Liu, Q. (2015). Pumping unit remote real-time monitoring system based on GPRS. *Manufacturing Automation, 1*, 140–144.

3. Zou, J. (2012). *Design and implementation of oil production plant dynamic monitoring information management system*. Jilin: Jilin University.
4. Zuo, W., Jing, X., & Li, H. (2008). The design of a data acquisition system human-computer interaction interface. *Micro Computer Information, 26*, 103–104.

Part VI
Mechanical Engineering and Numerical Control Technology

Chapter 79
Application of Machine Vision for Geometric Dimensions Measurement

Yong Wang, Xiandou Zhang and Mei Chen

Abstract A machine vision system with high precision and easy operation was designed to measure the position, height, and verticality of an automobile part which were very difficult by traditional inspection methods. It consisted of two cameras, two lights, and one embedded image processing unit DMV1000. After being carefully calibrated, the system performed well with the maximum distance absolute error of about 0.02 mm and angle absolute error of 0.26°. Combined with server motor system and pneumatic system, all measuring procedures automatically worked after one start button push. In this paper, the hardware and software designs of this system were introduced in detail and the verification test data were discussed which proved the high stability and precision of this equipment.

Keywords Machine vision · Geometric dimension · DMV1000 · Measurement

79.1 Introduction

Machine vision system has been widely used in industry [1], agriculture [2], printing [3], and so on. The digital camera equipped with light and lens was the "eyes" of the machine, and the programmable control units, for example programmable logical controller (PLC) and industrial personal computer (IPC), were the "brain."

It was very important to improve the automation of assembly in automobile industry. In this application, the positions of two pins of the coil were strictly restricted as shown in Fig. 79.1. The pins were so thin that their positions were instable with contact measurement. Three-dimensional projection measurement was untouched and precise, so it was applicable to measure the positions of the pins. However, the measurement was inefficient and not satisfied for online

Y. Wang (✉) · X. Zhang · M. Chen
School of Digital Media and Art Design, Hangzhou Dianzi University, Hangzhou, China
e-mail: wangyong_zju@163.com
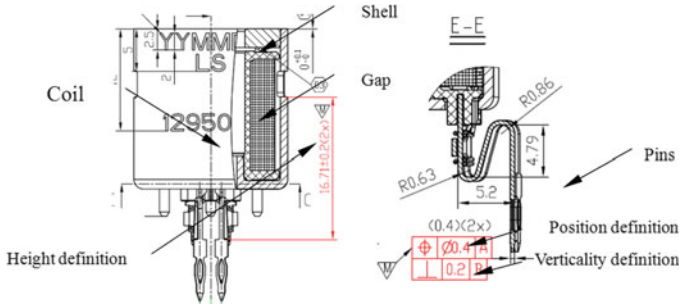
Fig. 79.1 Geometrical dimensions of the pins

measurement. Therefore, the machine vision system was the best choice to realize the efficient, precise, and untouched measurement for the geometric dimensions of the pins.

79.2 Hardware Design

The machine vision system included two cameras, two lights, and one embedded image processing unit DMV1000 specially designed for machine vision measurement as shown in Fig. 79.2. The top camera and the top ring LED light were designed for the inspection of the position Φ0.4 according to the reference line marked as A, which was the center line of the shell. The side camera and the back LED light were used for verticality and height measurement. The workpiece was clamped by a cylinder from bottom and the position of circumference was limited by a little pneumatic slider from the backside. Hence, the position of the measured piece was unique after being clamped. The whole clamp was set on a rotatable axis driven by a servo motor in order to measure the verticality from two orthogonal planes.

Both the top camera and the side camera were 80,000 pixels gray scale with 1394 high-speed port for communication with the image processing unit. The focal length of the lens for million pixels camera was 35 mm. A red ring light with 70 mm diameter was chosen as the top LED light and a red back light with 60 mm × 60 mm square shape as side illuminant. The image processing unit known as DMV-1000 was the core of this machine vision system. The images captured and processed were shown on the vision display. The touch screen was used for system debugging and parameter setting.
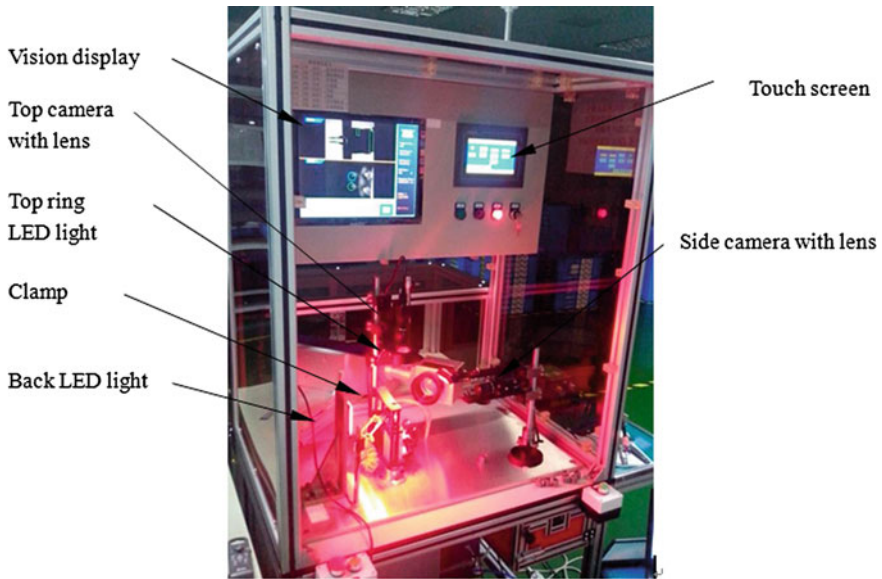
Fig. 79.2 Hardware of the vision system

79.3 Software Design

The software could be divided into two parts. The one was PLC program to control the movement of servo motor, cylinder, and so on, and the other was the image processing program. The former was ordinary and not be discussed, and the latter would be introduced in detail in this paper.

The program procedure was carried out by simple four steps as shown in Fig. 79.3. The first step was image capture. It could be stimulated by either outer switch signal or internal programmable pulse. In this application, the capture stimulus was generated by PLC. In the second step, the image was processed using inspection tools embedded in the development platform, including tens of image process methods, such as image smoothing, image sharpening, speckle detection, and edge searching. In the next step, the feature values obtained could be calculated for result judgment. At last, the result output could be programmed to input–output (IO) ports, display, and secure digital (SD) card or ethernet.

Fig. 79.3 Program procedure
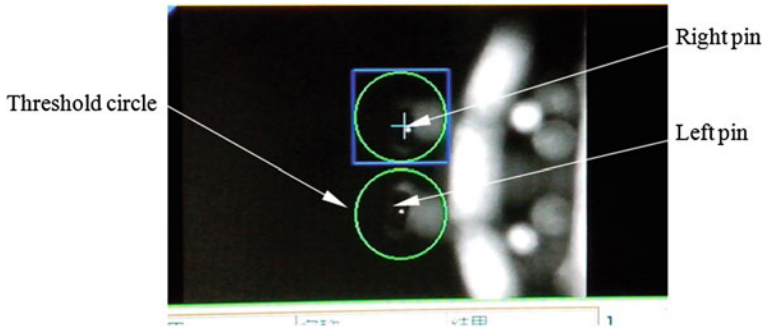
Fig. 79.4 The inspection of the top camera
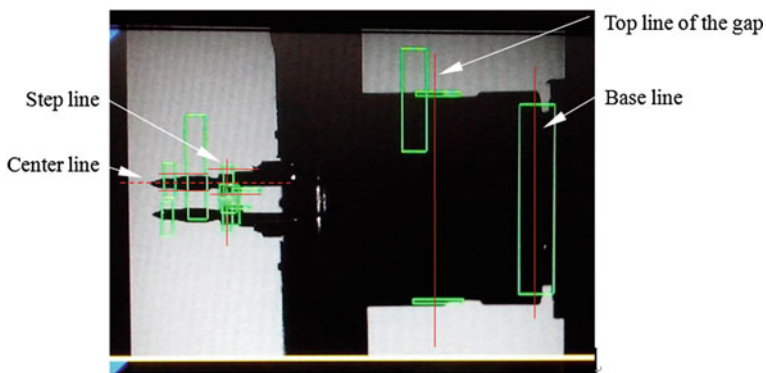
Fig. 79.5 The inspection of the side camera

There are two channels in the DMV-1000 unit for independent processing of two cameras. Therefore, the position inspection of the top camera and the height, and one plane verticality inspection of the side camera were executed simultaneously. The other plane verticality inspection was implemented after the measured piece rotated 90° around the axis of the shell driven by the servo motor.

The position inspection of the pins ends applied speckle detection tool as shown in Fig. 79.4. If the speckle of the pins located out of the threshold circle, the result of the position inspection was Not Good (NG).

The inspection of the 16.71 mm height was carried out by the side camera. The dimension measurement also was implemented separately for two pins using edge detection tools as shown in Fig. 79.5. After the edge detection of the step line and the top line of the gap, the height was calculated.
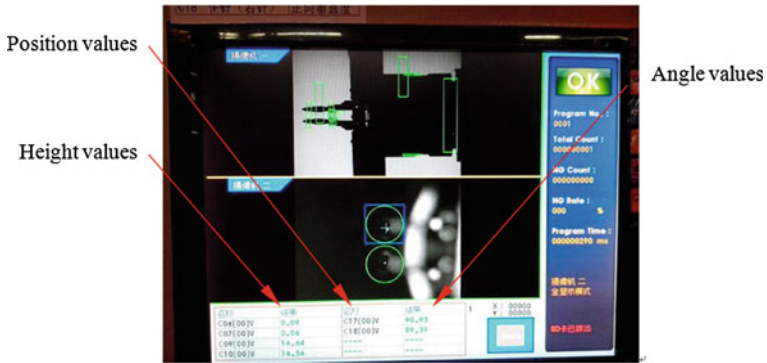
Fig. 79.6 Inspection result

The verticality measurement was complicated because the center line of the pin was difficult to be found directly. The problem was solved by searching the two sides of the pin firstly, and then the center line could be calculated. The judgment of the verticality was transformed to calculating the angle between the center line and the base line. A single plane image was not sufficient for measuring verticality. The other plane image after 90° rotation was captured and processed in the next procedure.

The result is displayed in Fig. 79.6. The position values were 0.09 mm and 0.06 mm, the height values were 16.64 and 16.56 mm, and the angle values were 90.93° and 89.39°, respectively, for two pins. Therefore, the judgment result of this workpiece was OK.

These procedures introduced above were saved as a test project in the DMV1000 unit. For the inspection of other parts, the project was loaded and stimulated by a simple start button push.

79.4 Data Analysis

In order to investigate the precision of the machine vision system, five workpieces were selected in random and each of them was measured for ten times. The statistical results are shown in Table 79.1.

For the height measurement, the maximum variance of ten times was 0.006 mm, so the estimate absolute error was three times of the maximum variance as 0.018 mm. Similarly, the estimate absolute error of the position and angle was 0.021 mm and 0.261°. The machine vision system was proved to be high precise and satisfies the quality inspection on the assembly line.

Table 79.1 Statistical results of five workpieces

No.		Height		Position		Verticality (side plane)		Verticality (front plane)	
		Left pin	Right pin	Left pin	Right pin	Left pin	Right pin	Left pin	Right pin
1	Mean	16.30	16.25	0.24	0.43	90.15	90.49	92.10	88.65
	Variance	0.004	0.000	0.006	0.000	0.010	0.010	0.031	0.047
2	Mean	16.58	16.56	0.07	0.03	89.16	89.68	91.49	88.44
	Variance	0.005	0.000	0.007	0.005	0.017	0.017	0.044	0.087
3	Mean	16.24	16.35	0.17	0.24	88.64	88.82	91.78	91.82
	Variance	0.005	0.003	0.003	0.005	0.020	0.020	0.027	0.025
4	Mean	16.55	16.58	0.10	0.24	87.85	88.42	92.26	88.99
	Variance	0.004	0.000	0.005	0.005	0.018	0.020	0.015	0.019
5	Mean	16.32	16.39	0.21	0.01	92.31	90.05	92.40	88.02
	Variance	0.006	0.005	0.006	0.005	0.018	0.019	0.012	0.055
Max. variance		0.006	0.005	0.007	0.005	0.020	0.020	0.044	0.087

79.5 Conclusions

In this paper, the hardware and software designs of a machine vision system were introduced in detail and the verification test data were discussed which proved the high stability and precision of this equipment.

References

1. Hong, T. (2010). The research of computer vision measurement technology based on LabView. In *2010 International Conference on Future Information Technology and Management Engineering,* pp. 284–287.
2. Wan, P., & Long, C. J. (2010). A machine vision determination method of rice milling degree based on gray gradient co-occurrence matri. *Grain Storage, 39*(4), 48–51.
3. You, F. C., Zhang, L. F., & Zhang, Y. B. (2009). The research of printing's image defect inspection based on machine vision. In *Proceedings of the 2009 IEEE International Conference on Mechatronics and Automation*, pp. 2404–2408.

Chapter 80
The Research of Auto Quantitative Extracting Equipment for Offset Ink

Guorong Cao, Lizheng Zhang, Bo Gao and Lianfang Li

Abstract In spot color ink blending filed, accurate quantitative extracting equipment makes work easy. The auto quantitative extracting equipment is designed for offset ink and is assembled from ink delivery unit, double different diameter values which are controlled by electromagnetism, measurement unit, and control software. The system degree of accuracy and stability declines, but the system efficiency for extracting ink is improved, when pumping pressure in ink delivery unit is increased. The optimal work parameters are determined by accuracy, stability, and efficiency. The pumping pressure scale of ink delivery unit, the relationship of double valves, and the control software of system are discussed. The fluid characteristics of ink also are considered. It is showed that the auto quantitative measuring equipment meets the requirements of spot color blending requirement, and the waste is avoided.

Keywords Quantitative extracting · Offset ink · Double valves

80.1 Introduction

A large number of spot colors are commonly used in packaging and printing. Spot color inks are generally obtained through blending several basic inks or directly purchase. Generally, the color matching depends on technician experiences of the type and the proportion of each primary color, and so a large amount of basic ink is wasted. Many works have been done to improve the spot color matching. There are a lot of works on matching spot color software. Bai Weiguo adopts the method of three stimulate values matching to establish the spot color-matching model based on Kubelka–Munk law [1]. Wei yuchang examines the performance of color

G. Cao (✉) · L. Zhang (✉) · B. Gao · L. Li
School of Printing and Packaging Engineering, Beijing Institute of Graphic Communication, Beijing, China
e-mail: caoguorong@bigc.edu.cn
e-mail:

rending based on the computerized spectrum color-matching method [2]. Luo Guanglin presents color-matching algorithm for spot color ink used in gravure printing plastic film and sets up a database of absorbing coefficient and dispersing coefficient [3]. In the research of ink performance, Yuan Ye use a high precision force sensor to detect tack force and analyzes the rheological characteristics of ink and dynamic process of tack-measurement system [4]. Based on the analysis of jetting method, Sun hui develops a non-contact jetting device aimed at dispensing adhesive with high viscosity [5]. For ink cleaning, Li Xiaoyu proposes a printing ink cleaner containing d-limonene [6, 7]. The matching color theory and software are researched, but in printing factory, ink is always wasted too much because there is no machine to extract ink precisely. In this paper, the quantitative extracting equipment is developed especially for high viscosity offset ink, and the precision and efficiency of the equipment are tested.

80.2 Design of Auto Quantitative Measuring Device

Auto quantitative measuring device is mainly composed of mute air compressor, pressure relief value, high pressure pipeline, displacement pump, and double different diameter values which are controlled by electromagnetism, measurement unit, and control software. Offset ink viscosity is very high, so the pressure control, sealing property, security, and precision of the equipment are important subjects. Different diameter values are shown in Fig. 80.1.

The large and small valve stems are designed to accurately control the flow of liquid. Relying on the valve structures, the fast and the slow methods of acquiring liquid can be achieved. When the ink is taken, it is sent to the valve body through ink inlet by the displacement pump. At the beginning of work, it is not necessary to accurately control the amount of ink. Ink is extracted from first ink nozzle under the first valve stem. When the critical value is approached, the first ink nozzle is closed
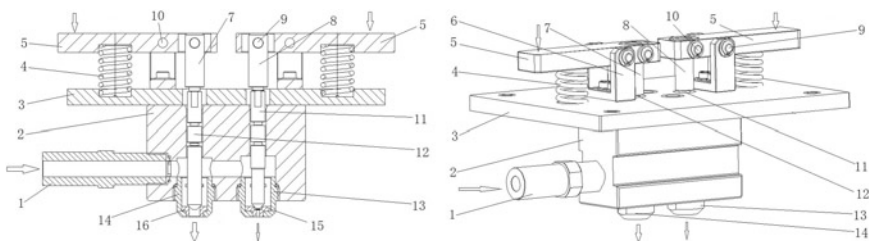
Fig. 80.1 Structure of two different diameter values. *1* ink inlet, *2* value body, *3* support plate, *4* compression spring, *5* press plate, *6* pedestal, *7* first compensation lever, *8* second compensation lever, *9* first pin shaft, *10* second pin shaft, *11* second valve stem, *12* first valve stem, *13* second ink nozzle, *14* first ink nozzle, *15* second sealing ring, *16* first sealing ring

and the second ink nozzle under the second value stem is opened which keeps the ink flows slowly. The critical values of two ink nozzles can be set in advance. The first ink nozzle is closed and the second ink nozzle is opened, when threshold value is tested. For example, take 100 g of ink and set the critical value at 90 g. The electromagnetism valve is controlled to push down the press plate for switching between the two nozzles by software. Measurement unit is arranged below two ink nozzles and can send datum to computer.

80.3   Pressure Test Experimental Analysis

Accurate weighting, speed and uniformity of ink flowing, avoiding ink splashing are several factors to ensure the suitable pressure. When the pumping pressure is too large, there will be a splash phenomenon, and weighting sensor will be dirty. The result is inaccurate. If the pressure is too small, the accuracy may be improved, but the efficiency is greatly reduced, and the time used for weighting is increased. Another factor is the height between ink nozzle and measurement unit. When the pressure is set at pressure of 0.6, 0.8, 1.0, 1.2 Mpa, respectively, the correction values for different weight are tested. Also correction levels are considered at different height. The testing data are shown in Figs. 80.2, 80.3, and 80.4.

The accuracy of equipment is not affected by the testing weight. With the increase of pressure, the average value of correction is also increasing. The ink flow speed is changed with pressure. The impact force will affect the measurement sensor. The height is selected at 170–190 mm, pressure is set at 0.6–0.8 Mpa, and correction value is set at 0.6–0.8 g.
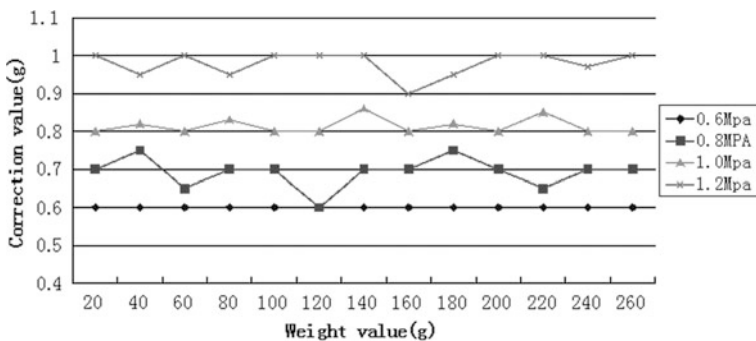
Fig. 80.2   130 mm testing height
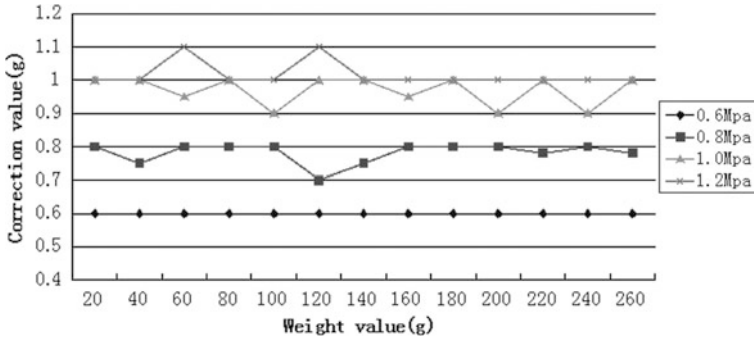
Fig. 80.3 170 mm testing height
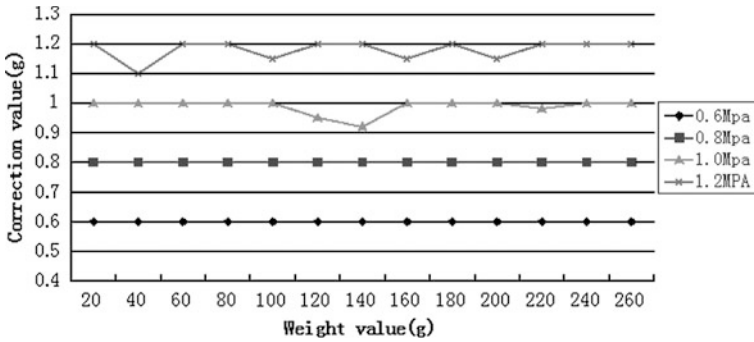
Fig. 80.4 210 mm testing height

80.4 Critical Value Experiment Analyses

With the increase of the control proportion of small ink nozzle, more time is need for test. When critical values are set at 5, 10, 15 g, testing times are collected as in Table 80.1. The time graph is not too much at different test. But more ink residual is left in the large ink nozzle in the experiment. When ink residual at small ink nozzle sheds, ink residual at large ink nozzle still not drips. According to the accuracy and efficiency of the equipment, critical value is set at 10 g.

Table 80.1 Testing time of different critical value

Testing Time (s) / Critical Value (g) Set Value (g)	5	10	15
50	37	40	42
100	57	61	60
150	84	86	87
200	104	106	110
250	137	138	141
300	149	150	152
350	171	177	184
400	205	208	215

80.5   Conclusions

According to the characteristics of fluid ink, the correction value experiments and the critical value experiments are carried out. The impact of the pressure and the height of the ink drop are overcome. Ink weighting experiment is affected by many parameters. These factors are mutually affecting each other. The pressure has a great influence on the accuracy. As the pressure increases, the accuracy of equipment is decreased, and the stability is also decreased. With the increase of height, the accuracy of equipment has a slight decrease, and the stability of the measurement will also be changed to a certain extent but the scope of the change is very small. This equipment is suit to extract offset ink or other kind of ink for mixing spot color.

References

1. Bai, W., Hu, X., & Yan, Y. (2010). Research on the spot color matching system based on ink volume. *China Printing and Packaging Study, 2*(4), 84–88.
2. Wei, Y., Chou, W., & Chen, Z. (2010). Performance of computerized spectrum color matching based on Kubelka-Munk Theory and its color rendering on offset ink sets. *China Printing and Packaging Study, 2*(4), 94–97.

3. Luo, G., Gao, H., & Wang, H. (2006). Method of ink color matching used in gravure printing based on Kubelka-Munk Theory and two constants. *Packaging Engineering, 27*(6), 12–14.
4. Yuan, Y., Ding, F., & Fan, Y. (2008). Theoretical analysis and measurement of printing ink tack. *Chinese Journal of Sensors and Actuators, 21*(10), 1812–1816.
5. Sun, H. (2011). Research on topology optimization and integrated closed-loop control of micro-displacement positioning stage. Harbin: Harbin Institute of Technology, pp. 49–51.
6. Li, X., & Chen, J. (2010). Preparation of a printing ink cleaner containing d-limonene. *China Surfactant Detergent Cosmetics, 40*(3), 178–180.
7. Yang, M., & Li, X. (2008). Study and development progress in printing ink cleaner. *Guang Dong Chemistry, 35*(6), 61–63.

Chapter 81
Preparation and Performance Investigation of the Flexible Pressure Sensor

Qingbin Zhai, Lixin Mo, Wei Yang, Dongyan Zhu, Xincan Chen, Lu Geng and Luhai Li

Abstract Recently, the flexible pressure sensor has attracted significant attentions as its high performance and wide applications, including wearable electronics, environmental monitoring device, and human-machine interfaces device and robotics. In this paper, silver nanowires (AgNWs) as the electrode materials were synthesized by polyol process, and the laboratory-made silver nanoparticles (AgNPs) as well as commercial carbon nanotubes (CNTs) were also chosen as the electrode materials in comparison. The flexible plastic, PI, PET, and PE films were chosen as the dielectric layer. The flexible pressure sensor was prepared with a simple, low-cost, and low energy-consuming method as sandwiching the dielectric layer between two opposing electrodes. The effects of the different electrode materials and the dielectric layer on the properties of the flexible pressure sensor were investigated. Results showed that the sensor with larger dielectric constant PI film and easy deformation AgNW/PDMS electrode had a greater sensitivity (1. 284 kPa^{-1}), fast response time, and high stability. The applied testing showed that the prepared flexible pressure sensor could detect tiny pressure signals and has the potential to be used in the electronic skins filed.

Keywords Silver nanowire · Flexible pressure sensor · Electronic skin

Q. Zhai · L. Mo (✉) · W. Yang · D. Zhu · X. Chen · L. Geng · L. Li (✉)
Beijing Engineering Research Center of Printed Electronics, Beijing Institute
of Graphic Communication, Beijing 102600, China
e-mail: molixin@bigc.edu.cn

L. Li
e-mail: liluhai@bigc.edu.cn

81.1 Introduction

Flexible pressure sensors have attracted great interests as soft and rubbery components for various applications, such as hand-held consumer electronics, displays, ultra-thin health monitoring device, and electronic skin (e-skin). [1–3]. Various kinds of flexible pressure sensors such as capacitive [4], piezoresistive [5], piezoelectric [6], and optical [7] have been developed to achieve the high performance. Among above kinds of sensors, the capacitive flexible pressure sensor has attracted tremendous attentions because of its high sensitive and tiny pressure detection, which is suitable for the wearable electronics and e-skin. As the important components of the capacitive sensor, the electrodes and dielectrics have the significant influences on the properties of the sensor [8]. Recently, various conductive materials were used as the electrodes, such as AgNPs, AgNWs, CNTs, and graphene. However, the effects of the different materials on the properties of the capacitive flexible sensor lack the systematic study. On the other hand, the dielectric layer was also ignored in some extent by academia.

In this paper, AgNWs as the electrode materials were synthesized by polyol process and the laboratory-made AgNPs as well as commercial CNTs were also chosen as the electrode materials in comparison. The flexible plastic, PI, PET, and PE films were chosen as the dielectric layer. Sandwiching the dielectric layer between two opposing electrodes, the flexible pressure sensor was prepared. The effects of the different electrode materials and the dielectrics on the properties of the flexible pressure sensor were investigated. Finally, the Morse code was tested by our sensor showed fast response time and high stability.

81.2 Experiments

81.2.1 Synthesis of Silver Nanowires

AgNWs with a diameter of about 100 nm and a length of about 3–30 μm were synthesized by polyol process [9]. 3 g PVP (MW = 10000–70000, AR, Sinopharm Chemical Reagent Company) was dissolved in 240 ml EG (AR, Sinopharm Chemical Reagent Company) with moderate stirring and heated to 433 K until the temperature was stable. Then, 480 ml of 0.2 M NaCl (AR, Tianjing Guang Fu Technology Company) was added into the flask. After 1 min, 10 ml EG solution containing 3.1 g of $AgNO_3$ (AR, Beijing Chemical Works) was added to the flask by pipette. Once the reaction solution turned hoar white with glittering, the reaction was stopped immediately. The obtained AgNWs were washed three times with acetone (AR, Beijing Chemical Works) and deionized water to remove the PVP residue. AgNWs were collected and dispersed into an ethyl alcohol (AR, Beijing

Chemical Works). Silver nanowires were characterized by SEM (Hitachi New Generation Cold Field Emission SEM SU8020) and ultraviolet and visible spectrophotometer (UV-2501PC).

81.2.2 Pressure Sensors Fabrication and Measurements

AgNWs (AgNPs or CNTs) ink with 15 wt% were coated on the photographic paper using automatic coating machine (ZAA 2300) with number 7 Mayer rod at 50 mm/s. When the AgNW (AgNPs or CNTs) film was dry at room temperature, the PDMS prepared using Sylgard184 (Dow coning) by mixing the "base" and the "curing agent" with a ratio of 10:1 was coated onto target substrate, afterward, the film with mixed PDMS was cured at 343 K for 2 h. At last, the cured AgNW (AgNPs or CNTs)/PDMS film was peeled off the substrate. This film was cut into 1×2 cm^2 as electrodes of pressure sensor. Electrodes were superposed face to face, and a dielectric layer (PI or PET or PE) was packaged between two electrodes. The structural representation of pressure sensor was shown in Fig. 81.1. In addition, force gauge (Handpi Digital force gauge, HP-5) was used to apply the external pressure. Two Cu wires of the sensor were connected to the digital capacitance multimeter (TH2617) to measure capacitance. Effects of different electrode materials and dielectrics on the properties of flexible pressure sensor were respectively studied.

81.3 Results and Discussion

81.3.1 Characterization of the AgNWs

The AgNWs have two characteristic absorption peaks at ~ 376 and ~ 350 nm by UV light, as shown in Fig. 81.2a, attributing to the transverse plasmon resonance and longitudinal surface plasmon, respectively. The synthesized AgNWs were 80 nm in diameter and 3–50 μm in length as shown in the SEM images from Fig. 81.2b.
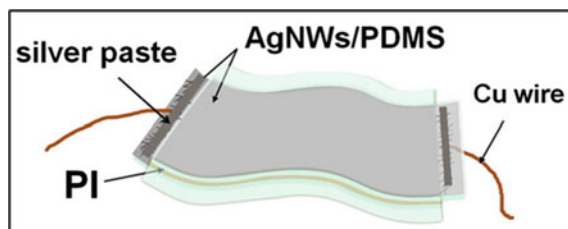
Fig. 81.1 The structural representation of pressure sensor
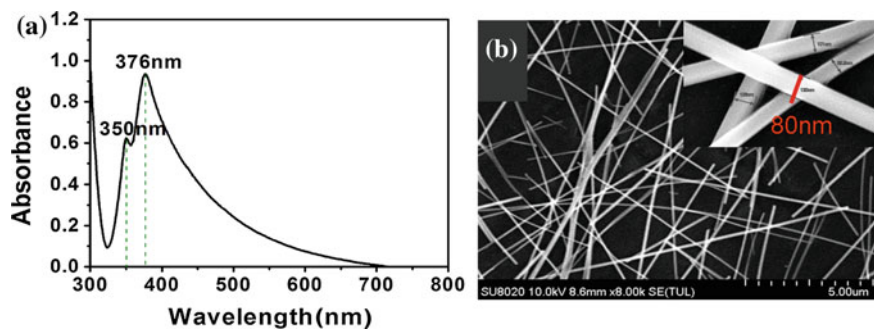
Fig. 81.2 **a** UV–Vis absorption spectrum of silver AgNWs. **b** SEM image of the AgNWs

81.3.2 Effects of Electrode Materials on the Properties of Flexible Pressure Sensor

The capacitive change of the flexible pressure sensors with different electrode materials under various pressures was shown in Fig. 81.3. The three curves have the similar trend, which could be divided into two sections with different slopes. In the
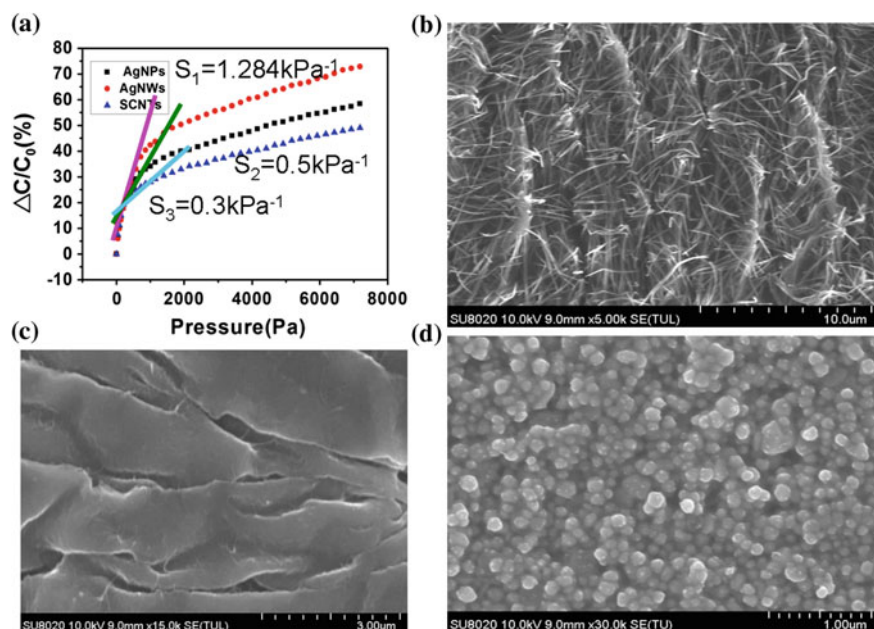

Fig. 81.3 **a** The capacitive change of the flexible pressure sensors with different electrode materials under various pressures. The morphology of the electrodes with different materials. **b** Loosened AgNW/PDMS electrode surface. **c** Flat SCNTs/PDMS electrode surface. **d** Tight AgNPs/PDMS electrode surface

field of sensor, the slope of the capacitive change/pressure line is usually used to represent the sensitivity. Thus, it could be seen that the sensitivity of AgNW/PDMS sensor was about 1.284 kPa^{-1} under 1000 Pa pressure, AgNPs/PDMS sensors was 0.5 kPa^{-1}, while SCNTs/PDMS sensor was 0.3 kPa^{-1}.

The reason was that the structures of three kinds of electrode materials were different as shown in Fig. 81.3b–d. The loosened AgNW/PDMS electrode surface can store a mass of air, the air was discharged, which has a lower dielectric constant ($\varepsilon = 1$) than PI ($\varepsilon = 3.4$). The increase in capacitance of loosened electrode arises from the reduction in the distance between the two electrode plates when pressure is applied and is enhanced further by the increase in effective dielectric constant. Therefore, the sensitivity of sensor with loosened electrode surface is higher than that with flat electrode.

81.3.3 Effects of Different Dielectric Layers on the Properties of Flexible Pressure Sensor

To study the effects of different dielectric layers on the properties of flexible pressure sensor, PE, PI, PET were, respectively, used as dielectric layers. In this filed, the permittivity of PI is the largest about 3.4, while PE is about 2.3 and the permittivity of PET is 3. The result was shown in Fig. 81.4, the higher the dielectric constant, the greater the sensitivity of the sensor. Owing to the larger dielectric constant film can retain high electric charges, the sensor has a bigger capacitive change at a given level of pressure. Therefore, the sensitivity of sensor with PI film is higher.

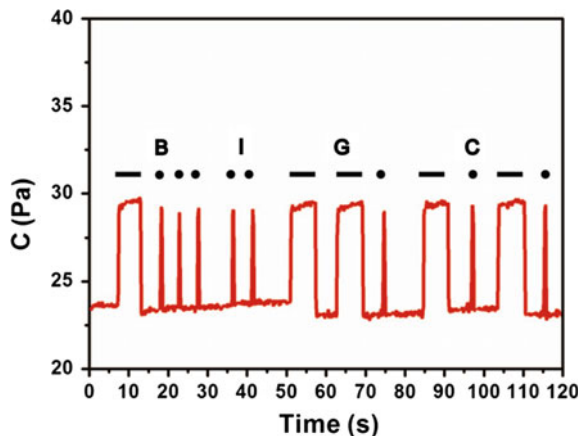

Fig. 81.4 Influence of different dielectric on sensors
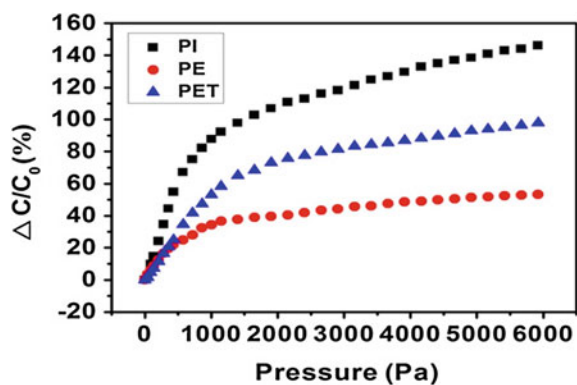
Fig. 81.5 The Morse code was tested by applying temporal touch and static touch to the sensor

81.3.4 The Application of Sensors

Finally, the Morse code was tested with this flexible pressure sensor to demonstrate the potential usefulness of this device. By applying temporal touch and static touch to the sensor, standardized sequences of short and long signals in Morse code, namely "dots" and "dashes," can be transmitted from human to the sensor. Lastly, we got that the BIGC was shown in Fig. 81.5. So, this sensor can be used to transmit signals due to its ultra-fast response and high stability.

81.4 Conclusions

In conclusion, the AgNWs were synthesized by polyol process and the size of it was 80 nm in diameter and 3–50 μm in length. Sandwiching two opposing AgNW electrodes and a dielectric layer, we obtained the flexible capacitive pressure sensor. Furthermore, we have analyzed the factors that influence the properties of the sensor. This device can detect tiny pressure may open and widen its application to wearable electronic skins.

References

1. Tiwana, M., Redmond, I. J. S., Lovell, N. H., et al. (2012). A review of tactile sensing technologies with applications in biomedical engineering. *Sensors and Actuators, A: Physical, 179*, 17–31.
2. Rogers, J., & Huang, (2009). A Influence of the cellulose substrate on the electrochemical properties of paper-based polypyrrole electrode materials. *Proceedings of National Academy of Sciences, 106*, 10875–10876.
3. Pang, C., Lee, C., Suh, K. Y., et al. (2013). Recent advances in flexible sensors for wearable and implantable devices. *Applied Polymer Science, 130*, 1429–1441.
4. Meyer, J., & Arnrich, B. (2010). Design and modeling of a textile pressure sensor for sitting posture classification. *IEEE Sensors Journal, 10*, 1391–1396.
5. Wang, X., Gu, Y., Zhang, T., et al. (2014). Hydrothermal transformation of dried grass into graphitic carbon-based high performance electrocatalyst for oxygen reduction reaction. *Advanced Materials, 26*, 1336–1340.
6. Wang, Y. R., Zhang, P., Xu, H. C., et al. (2011). Highly luminescent organosilane-functionalized carbon dots. *Smart Materials and Structures, 20*, 45–51.
7. Rothmaier, M., Luong, M. P., Clemens, F., et al. (2008). Textile pressure sensor made of flexible plastic optical fibers. *Sensors, 8*, 4318–4326.
8. Pang, C., Lee, G., Suh, Y., et al. (2012). A flexible and highly sensitive strain-gauge sensor using reversible interlocking of nanofibres. *Nature Materials, 11*, 795–801.
9. Takei, K., Takahashi, T., Javey, A., et al. (2010). Nanowire active-matrix circuitry for low-voltage macroscale artificial skin. *Nature Materials, 9*, 821–826.

Chapter 82
Fault Diagnosis Method of Feeding Mechanism in Printing Machine Based on Multivariate Statistical Process Control

Zhuofei Xu, Haiyan Zhang, Heping Hou, Linghui Ren, Yankun Sun and Qianqian Xu

Abstract Device feeding is considered as the primary condition for printing production industry, which also determines the accuracy and quality of printing production. Having observed the difficulty of detecting the feeding fault in printing machine, the present study intends to propose an effective method on the basis of multivariate statistical process control. Firstly, the printing deviations in both circumferential and axial directions are calculated. Then, a principle model in normal working condition is build. Secondly, the working state of feeding unit is evaluated according to PSE control limits and data changing. Finally, the fault diagnosis and explanation are undertaken through the analysis of principle loading and the calculation of scoring. This study aims to establish a theory of fault diagnosis for press feeding system, which will offer a new theoretical instruction for the research in same field.

Keywords Feed mechanism in printing machine · Principal component analysis · Multivariate statistical process control · Fault diagnosis

82.1 Introduction

It is hard to diagnose the fault in feeding mechanism of printing machine because there is a strong concealment. Because there is not an effective method to find fault in paper feeding, the adjusting and maintaining time occupy a lot of man-hours and

Z. Xu · H. Zhang (✉) · H. Hou · Y. Sun · Q. Xu
School of Printing Packaging and Digital Media, Xi'an University of Technology, Shanxi, China
e-mail: hyzhang@xaut.edu.cn

Z. Xu
e-mail: xzf_34216606@163.com

L. Ren
Xi'an Aerospace-Huayang Mechanical and Electrical equipment CO., LTD, Shanxi, China

make high maintenance costs; meanwhile, a lot of printing supplies are wasted which lead to pollution [1, 2]. Many researches for fault diagnosis has been made on feeding mechanism: Liu Peng make an analyze on the basic properties of bias data in feeding paper and find that continuous printing deviations are in a normal distribution [3]. Xu Qianqian makes a study on feeding fault in printing machine with principal component analysis (PCA) and support vector machines. Many different fault modes are successfully classified, but this method cannot explain the fault principle clearly [4]. LUCHS automatic precision detection device is made by SID Company in order to adjust the feeding of a printing machine. It can judge whether the feeding paper is qualified or not based on continuous printing deviations [5]. It can be concluded that the data from continuous printing deviations has a good effect in study and analysis of feeding paper faults.

82.2 The Fault Analysis Based on MSPC

The feeding fault in printing press has a characteristic of multi-parameters, so it is suitable for analysis with multivariate statistical process control (MSPC) method. Main elements with different variables or latent variables result in different MSPC methods. Because it has a good ability in remove correlation and calculation, principle component analysis is one of the most common methods in MSPC [6, 7].

It can realize the fault diagnosis with continuous deviation calculation, but these kinds of methods are always based on the artificial experience and cannot accurately explain the specific reasons for the failure. The PCA method achieves the interpretation of original spatial data on the base of constructing low-dimensional space containing key information by linear transformation. The introduction of deviations of feeding paper method based on PCA MSPC can not only find faults in machine, but make a system analysis on failure reason as well. It can also extract the fault feature set and realize the automatic faults diagnosis in press feeding. PCA establishes the main element model of printer paper feed unit in steady state with the correlation relationship among process variables. It achieves a detection of anomalies and fault model by the degree of deviation between the new bias values and the steady-state model. The fault diagnosis method based on PCA mainly includes the establishment of the steady-state model, principal component analysis, fault detection, and analysis. A specific process is shown in Fig. 82.1.

82.3 The Fault Diagnosis of Feeding Mechanism

Characteristic variables are included in observation data X which is standardized to eliminate the singularity by Eq. 82.1.

Fig. 82.1 Flow chart of fault diagnosis with PCA
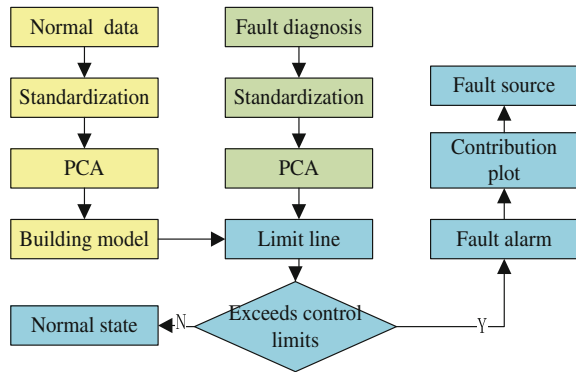
$$\bar{X} = (X - u)/\mathrm{std}(X) \tag{82.1}$$

u is average matrix of characteristic variables and std(X) denoted the standard deviation of X. The standardized matrix $\bar{X}$ is decomposed by Eq. 82.2.

$$\bar{X} = t_1 p_1^T + t_1 p_1^T + \cdots + t_m p_m^T = \sum_{i=1}^{m} t_i p_i^T = TP^T \tag{82.2}$$

t_i is principal component score vector and p_i. Rewrite Eq. 82.2 as Eq. 82.3 and definite Eq. 82.4.

$$\bar{X} = t_1 p_1^T + t_1 p_1^T + \cdots + t_l p_l^T + t_{l+1} p_{l+1}^T + \cdots + t_m p_m^T \tag{82.3}$$

$$\hat{X} = \sum_{i=1}^{l} t_i p_i^T = \hat{T}\hat{P}^T, \quad E = \sum_{i=l+m}^{m} t_i p_i^T = \tilde{T}\tilde{P}^T \tag{82.4}$$

$\hat{T}$ is PCA scoring matrix and $\hat{P}$ is PCA loading matrix. L is the selected number according to cumulative contribution rate. $\hat{X}$ is PCA model values. E indicates the residual matrix. $\tilde{T}$ is residual scoring matrix, and $\tilde{P}$ is residual loading matrix.

After the PCA model has been built, it can be determined whether the fault occurred with the corresponding control statistics. We can usually establish squared prediction error statistics for statistical test in residual space as Eq. 82.5 to diagnose the statistical abnormal state. An industrial process detection of multiple variables can be realized by SPE value. It exhibits a certain moment measurements relative to deviations in steady state. When a fault occurs, SPE value will be significantly increased.

When *SPE* is not more than δ^2, we consider that the system is normal and vice versa. δ^2 is the confidence limits of SPE as Eq. 82.5.

$$\delta^2 = \theta_1 \left[\frac{c_\alpha \sqrt{2\theta_2 h_0^2}}{\theta_1} + 1 + \frac{\theta_2 h_0 (h_0 - 1)}{\theta_1^2} \right]^{\frac{1}{h_0}}, h_0 = 1 - \frac{2\theta_1 \theta_3}{3\theta_2}, \theta_i = \sum_{j=1+l}^{m} \lambda_j^i \quad (82.5)$$

λj is the jth eigenvalue in the covariance matrix of $\bar{X}$. c_α is a threshold with test level α in normal distribution. It can determine that whether a fault occurred according to the control limits, but cannot determine which parameters are abnormal. With score plot and load diagrams, we can effectively know what kind of fault happens and explains the reason [8, 9].

82.4 Experiments

The device of experiment is 4-color offset press made by Wei Fang Huaguang precision equipment Co., Ltd. Printing color order is KCMY. Two common fault samples of press feeding unit are collected. The specific fault types are recorded in Table 82.1. Catch the axial and circumferential deviation. One sample contains successive 100 pieces of sheet. The sample data are standardized. Threshold of accumulative contribution rate is 85 % that based on the empirical value. Principal component model of data A is built for normal state. The 1st–3rd principal component is selected to create PCA model.

Calculate the corresponding SPE limit line according to Eq. 82.5. When the significant level is 0.01, the SPE limit line is 2.096. Calculate the SPE value and then draw the SPE limit line and the SPE diagram. SPE control chart of steady data of A shown in Fig. 82.2a reveals that every point of steady data is under the SPE limit line. Figure 82.2b, c is corresponding to fault data A and B. The two groups of fault data have several SPE values above the control line with the range of 10–200 %, so the fault is happened.

The results mentioned above reveal that the MSPC method based on PCA can work on fault diagnosis of feeding mechanism, but the score figure of principal component has to be analyzed if the most sensitive diagnosing variable should be found and judge the fault source. By analyzing the score figure of principal component on each fault, the most sensitive fault variable on the four original diagnosis variable can be found and then judged the fault model.

Figure 82.3 shows each coefficient matrix of main elements. Variable number 1–4 represents circumferential feeding deviation of two areas and axial feeding deviation of two areas. The principal component can be analyzed. The principal

Table 82.1 Fault sample in feeding paper unit

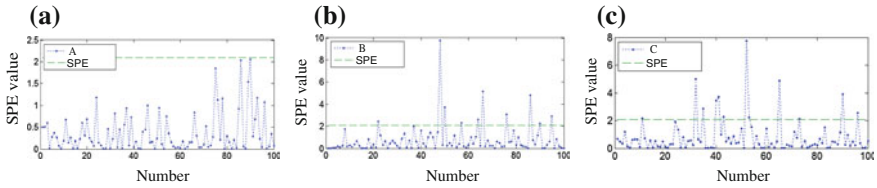| Number	Cause of feeding fault
A	Normal state
B	Improperly adjusting of tension in side regulation
C	Loose screws in the side regulation

Fig. 82.2 SPE control chart of feeding paper data. **a** SPE control chart of steady data. **b** SPE control chart of B. **c** SPE control chart of C
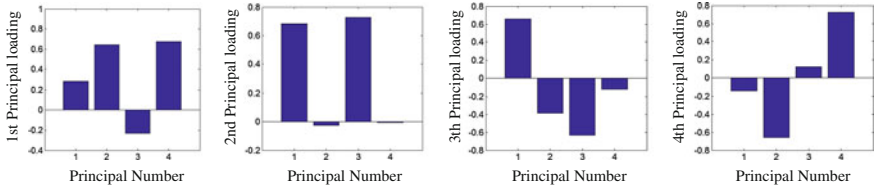

Fig. 82.3 PCA loading plot of principal component

components 1 and 4 mainly show the characteristic of axial deviation. The principal component 1 comprises the syntonic axial deviation data, and the principal component 4 comprises the reversed axial deviation data. The principal components 2 and 3 mainly show the characteristic of circumferential deviation. The principal component 2 comprises the syntonic circumferential deviation data, and the principal component 3 comprises the reversed circumferential deviation data.

The three states in Table 82.1 are analyzed specifically as follows. Through the principal component vector of different fault, the most sensitive principal component of fault can be found. And then, the fault diagnosis can be realized on the base of principal components in different states.

A. Normal state: Three points of sample A are selected and analyzed randomly. Score plots of them are shown in Fig. 82.4. It can be seen that the score of different principal is uniform and none of them is outstanding. This means that each of the original variables is detected in a relatively stable state.
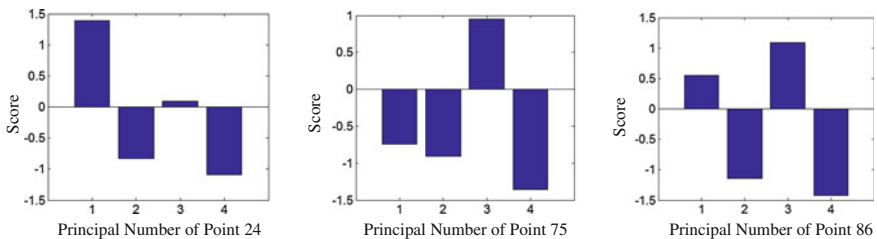

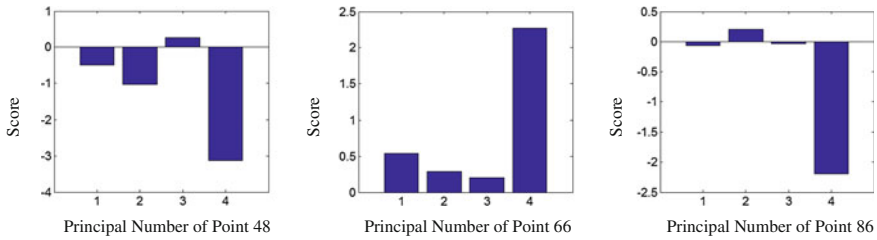**Fig. 82.4** Score chart of fault point in sample A

Fig. 82.5 Score chart of fault point in sample B

B. Improperly adjusting of tension in side regulation: Side regulation is the key part in feeding mechanism. Once the adjustment of tension is not suitable, the paper will shake when the regulation is lifting up. Paper will swing in the axial direction.

Figure 82.2b is the SPE control plot of sample B. There are five faulting points, and we get three of them to analyze. The numbers are 48, 66, and 86. The score plot is shown in Fig. 82.5. The faulting points have a similar distribution and the 4th principal is dominated. From Fig. 82.3, we can know that 4th principal component represent a reverse bias, while 1st is normal; thus, we know that it has been made by paper tilt and there is not an obvious axial bias.

C. Loose screws in the side regulation: Loose screws will change the cycle of side regulation and make it hard to accurately fit former regulation. Then, the paper will be transferred incorrectly and cause early or late arrival of paper, double sheets, and will be jammed. Figure 82.2c is the SPE control plot of sample C, and there is six fault points. We get four of them to analyze and the number is 32, 52, 65, and 90. The score plot is shown in Fig. 82.6.

From Fig. 82.6, we can see that the first principal component increases substantially and is to be negative. This means that there is a more stable bias in axial direction on the full sheet. From the score, we know that loose screws lead to the abnormal work cycle and a periodic vibration. There is a substantial displacement in axial of paper under inertial force. The loose screw can also make the fitting between side and former regulations to be incorrect such as point 52.
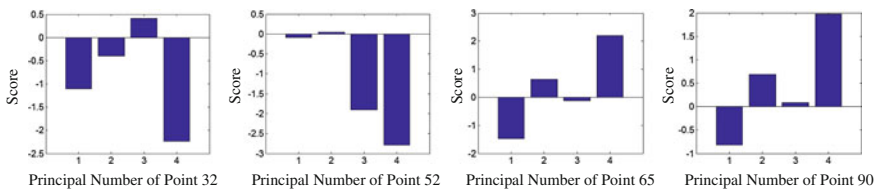

Fig. 82.6 Score chart of fault point in sample C

82.5   Conclusions

A fault diagnosis method for feeding mechanism in printing machine is given in this paper, and the main contents are as follows: (1) PCA model has a good effect on the classification of fault mode in feeding paper unit. The fault samples are detected correctly with SPE control limits. (2) As to feeding paper fault, we can get the key principal component which has a better reflection on fault and find the source of fault through loading plot. Through theoretical analysis and experimental verification, it has been found that the conclusion keep consistent with explanations and features of fault.

References

1. Amon-Tran, I., Anayath, R., Pai, A., et al. (2012). An approach to minimize carbon footprint for an environmental friendly printing by optimizing an offset machine in a printing facility. *Procedia-Social and Behavioral Sciences, 37*, 514–527.
2. Wang, W., Golnaraghi, F., & Ismail, F. (2005). Condition monitoring of multistage printing presses. *Journal of Sound and Vibration, 27*(4), 755–766.
3. Liu, P., Xu, Z., & Wang, D. (2013). A method for the fault prediction of printing press based on statistical process control of registration accuracy. *Journal of Information and Computational Science, 10*(17), 5579–5587.
4. Xu, Q., Zhang, H., Hou, H., et al. (2014). A fault diagnosis method of offset printer feeding mechanism based on kernel principal component analysis and K-means clustering. *Applied Mechanics and Materials, 731*, 395–400.
5. Jackson, J. E., & Mudholkar, G. (1979). Control procedures for residuals associated with principal component analysis. *Technimetrics, 21*(3), 341–349.
6. Qin, S. J. (2003). Statistical process monitoring: Based and beyond. *Journal of Chemo-Metrics, 17*(8), 480–502.
7. Kourti, T. (2005). Application of latent variable methods to process control and multivariate statistical process control in industry. *International Journal of Adaptive Control and Signal Processing, 19*(4), 213–246.
8. Tsung, F. (2000). Statistical monitoring and diagnosis of automatic controlled process using dynamic PCA. *International Journal of Production Research, 38*(3), 625–637.
9. MacGregor, J. F., & Kourti, T. (1995). Statistical process control of multivariate process. *Control Engineering Practice, 3*(3), 403–414.

Chapter 83
Study on Contact Stress of Cylinder Gear and Tooth Profile Modification of Offset Press

Qiumin Wu, Min Feng and Jimei Wu

Abstract The cylinder gear is an important part of offset press. It has great significance to ensure the speed of the cylinder gear constant and stable. In this paper, the finite element analysis software ANSYS is used to analyze the gear tooth deformation on influence of gear meshing transmission performance, and it comes to the conclusion that the gear before modification exists interference and stress concentration phenomenon. Adopting a method of cylinder gear–tooth profile modification for gear tooth, it shows that the gear tooth interference and the stress concentration phenomenon disappear after the modification, the gear-bearing capacity is greatly improved, and the gear runs more smoothly.

Keywords Contact stress · Profile modification · Finite element

In offset printing, the cylinder is derived by the cylinder gear. The printing image is transferred by rolling of plate cylinder and blanket cylinder, and blanket cylinder and impression cylinder. Therefore, the primary conditions to get the high printing quality, with the uniform ink layer and clear images and dot, is to ensure gear transmission uniform, stable, and synchronization, and the cylinder gear must be in high-precision engagement state in the process of movement. However, there is gear tooth deformation under load in the practical work. In gear teeth meshing, the actual position and shape deviate from the theoretical position and shape because of the deformation, which destroy the correct meshing condition theory, and make the engaging position deviate from theoretic meshing line. It causes instantaneous transmission ratio fluctuation of gear, forces the gear non-uniform speed, and causes vibration, shock, and noise of gear transmission system, and that will aggravate the fluctuation amplitude of gear tooth dynamic meshing force. Then, the

Q. Wu (✉) · M. Feng · J. Wu
Institute of Printing and Packing Engineering, Xi'an University of Technology, Xi'an, China
e-mail: wuqiumin@xaut.edu.cn

M. Feng
e-mail: 365325069@qq.com

J. Wu
e-mail: wujimei@xaut.edu.cn

transmission accuracy of gear transmission system reduces, even the whole machine cannot work normally. In this paper, the contact analysis module of ANSYS software is used to analyze the gear tooth deformation effect on gear meshing transmission performance and then select a gear modification program to optimize the drum gear to reduce the tooth deformation effect on gear transmission performance.

83.1 Finite Element Contact Analysis of the Cylinder Gear Meshing Model

83.1.1 The Establishment of the Cylinder Gear Solid Model

In this paper, the J2108-type offset press blanket cylinder gear and impression cylinder gear are selected as the sample. Main parameters are as follows: normal module $m_n = 3.25$ mm, number of gears teeth $z = 88$, pressure angle $\alpha = 15°$, helix angle $\beta = 17° \, 34' \, 23''$, addendum coefficient ha* = 1, and tip clearance coefficient $c* = 0.25$. The impression cylinder gear is the left-hand gear, blanket cylinder gear is the right-hand gear.

According to the above parameters, Pro/ENGINEER three-dimensional modeling software is used to establish the meshing model of the J2108 offset press blanket cylinder gear and impression cylinder gear as shown in Fig. 83.1. The upper is the blanket cylinder gear, and the bottom is the impression roller gear. The impression cylinder gear is regarded as the main pulley, rotating counterclockwise.
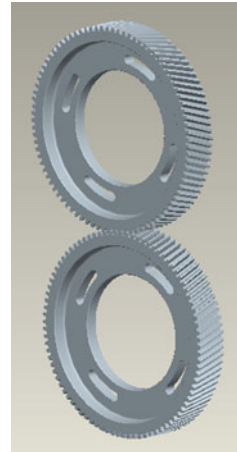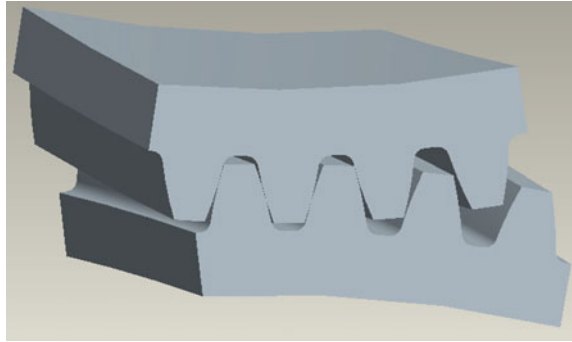
Fig. 83.1 Drum gear mesh model

Fig. 83.2 Gear mesh model

Blanket cylinder gear is the driven wheel and rotates clockwise. As is shown in Fig. 83.1, the meshing time is the same as the moment for the far right tooth of the impression cylinder gear has just entered into a state of meshing.

In the literature [1], the stress and strain results from the whole gear meshing model were compared with that from the three tooth meshing model. It showed that the whole model analysis results are in accordance with the facts. But the difference of the two kinds of model is within 2 %. Thus, in the range of allowable error, using local model instead of the whole model can meet the requirements. Considering the limitation of computer resources, the model of cylinder gear mesh was simplified accordingly. Only the four pairs of tooth which participate in gear meshing was chosen to finite element analyze, and the gear mesh model intercepted is shown in Fig. 83.2.

83.1.2   The Grid Division of Cylinder Gear Meshing Model

The gear meshing model intercepted is imported into ANSYS finite element software for grid division [2–4]. Grid division is an important part of finite element analysis. It will directly affect the accuracy of the calculation results, so the high-precision surface units Plane 82 and Solid 95 are selected in paper. The end surface model is divided first (including mesh refinement in tooth profile contact side) and then divide the model along the direction of a helical line by scanning command. The cylinder gear meshing finite element model after the grid division is shown in Fig. 83.3.
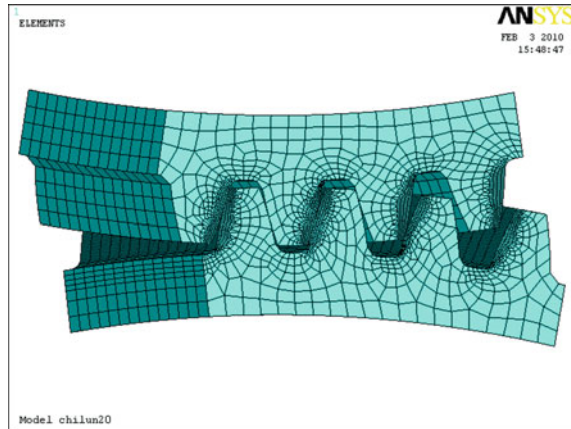
83.1.3 The Definition of Contact

Before to establish contact relation, the contact type and the contact way of the gear model must be determined first. In this paper, the two gears are considered as elastomer in the analysis [5], so the contact type is soft body versus soft body. The way of surface–surface contact, which has relatively less amount of calculation, is suitable for complex surface, large deformation, and friction contact problem solving. So the surface–surface contact way is chosen based on the characteristics of cylinder gear mesh in this paper.

The simulation of the state of contact surface in the ANSYS contact analysis is realized by contact relation [6]. The finite element model identifies the possible contact pair by the specified contact element, which is covered in the contact surface of analysis model. A contact pair includes two units: the target unit and contact unit. In this paper, Targe170 is used to simulate the target surface, and Conta174 is used to simulate the contact surface. The program identifies the contact pair through a shared constant, in order to establish a contact which is for the target element and contact element specify the same real constants. In this paper, four meshing tooth profiles are selected to establish four contact pairs, as shown in Fig. 83.4.

83.1.4 The Definition of the Boundary Conditions and Load

At any instant, the gear meshing transmission is taken as a quasi-static process [7, 8]. The driven wheel away from tooth has no effect which comes from the driving wheel, and it is fixed. The displacement can be regarded as zero, so the circular arc surface of the blanket cylinder gear is all constraints. Because of the limit of bearing, the driving gear can only rotate around the gear axis, so the nodes on the arc surface of the impression cylinder gear to cylindrical coordinates. Constraint the
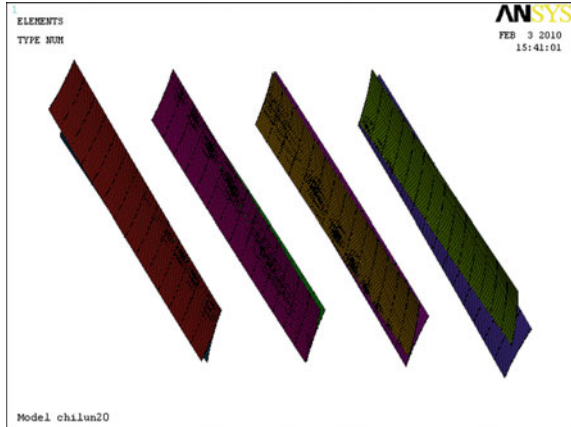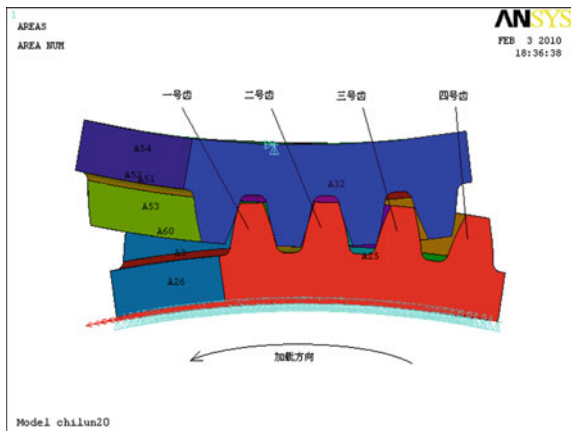
Fig. 83.4 Four contact pairs

Fig. 83.5 Model of gear constraint and loading

degree of freedom of nodes along the X, Z, only retaining the rotational degree of freedom along the circumferential direction (Y direction), and it rotates anticlockwise.

For the convenience of applied torque, the torque is converted to an equivalent force of the driving gear surface arc-node. The total torque of the driving gear input is 1312.46 Nm, the circular arc surface radius of the driving gear is 138.885 mm, and then the circumferential force of lower arc surface nodes is as follows:

$$F = \frac{T}{R} = \frac{1312.46}{0.1389} = 9448.96\,\text{N}$$

The cylinder gear constraint and the loading method are shown in Fig. 83.5. In order to facilitate the description below, the impression cylinder gear model intercepted is defined as follows: the first tooth on the left for No. 1 tooth, followed by No. 2 tooth, and so on.

83.1.5   The Calculation Result Display and Analysis
of the Gear Meshing Transmission

After meshing, defining contact, and applying constraints and loads, the finite element model is evaluated. The contact stress distribution in the four gear contact surface of the impression cylinder gear is obtained, while the No. 4 tooth is meshing, as shown in Fig. 83.6.

The No. 4 tooth is just meshed, and the ideal contact stress is zero. But because of the gear elastic deformation, No. 4 tooth have produced larger contact stress and the meshing interference. It causes greater pressure than normal stress between gears, and the oil film between gears may also be damaged.

The maximum contact stress of No. 3 tooth occurs in the root part. This is because of the stress concentration caused by the contact of driven wheel gear tooth edge and driving wheel gear tooth root. The maximum contact stress of No. 1 tooth occurs in the tooth edge, and it is a maximum of four tooth contact stress, 596.778 MPa, higher than the maximum contact stress of No. 2 tooth 309.335 MPa and higher than the maximum contact stress of No. 3 tooth 278.743 MPa. It greatly affects the gear-bearing capacity. The reason why tooth No. 1 has such large contact stress, on the one hand, is that the tooth edge parts tend to stress concentration, and on the other hand, the No. 1 tooth meshing position is close to meshing away position, and thus the displacement of tooth is large.

It is showed that there is interference and stress concentration of the cylinder gear. It is necessary to carry out gear modification to improve the meshing transmission performance of the cylinder gear.
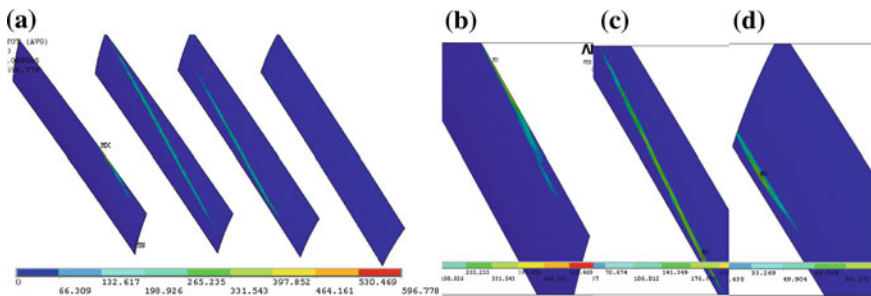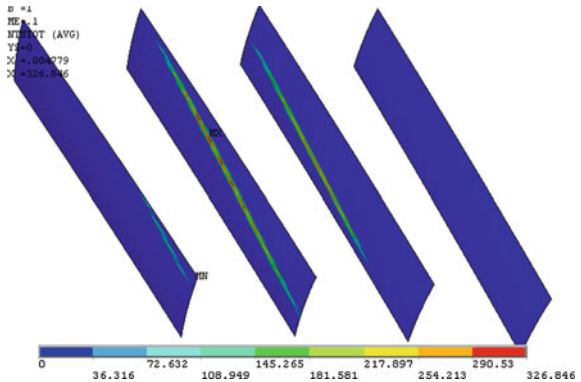

Fig. 83.6 Tooth contact stress distribution after modification. **a** Tooth contact stress distribution. **b** No. 1. **c** No. 3. **d** No. 4

Fig. 83.7 Tooth contact stress distribution after tooth profile

83.2 The Gear Contact Finite Element Analysis After Tooth Profile Modification

In this paper, the addendum modification approach is selected to the modification of the cylinder gear. The three elements of the modification are defined as follows: Addendum modification amount is 0.02 mm, modification of height is 0.5 m_n, and modification curve is a circular arc curve. The cylinder gear finite element contact analysis is carried out again after the gear profile modification and obtains the contact stress distribution on the contact surface of the impression cylinder gear after modification, as shown in Fig. 83.7.

As shown in Fig. 83.7, No. 1 tooth stress concentration phenomenon disappears. The maximum contact stress of single tooth reduce from 596.77 MPa before modification to 157.082 MPa, effectively reducing the tooth crest wear of No. 1 tooth due to the small top tooth meshing stiffness. No. 3 tooth stress concentration phenomenon disappears. No. 4 tooth eliminates the interference phenomenon at the moment of meshing, and the bear load is zero. Maximum contact stress of the impression cylinder gear is transferred from No. 1 tooth before modification to the No. 2 tooth after the modification, and the maximum value is reduced from 596.778 to 326.046 MPa. It is showed that after modification, the tooth interference and the stress concentration have been significantly improved, the tooth-bearing capacity has a substantial increase, and the gear runs more smoothly.

83.3 Conclusions

In this paper, the finite element analysis software ANSYS is used to analyze the gear tooth deformation on influence of gear meshing transmission performance. It shows that the interference and stress concentration phenomenon exists on the cylinder gear before modification. Select the tooth profile modification way to

modify the gear, and new finite element contact analysis is carried out on the cylinder gear. The results show that the gear interference and the stress concentration phenomenon disappear after modification, and the bearing capacity of gear tooth improves. It shows that the modification is feasible.

References

1. Ohno, K., & Tanak, N. (2001). A contact stress analysis for helical gear with 3-dimensional finite element method, pp. l–7.
2. Chen, Y. C., & Tsay, C. B. (2002). Stress analysis of a helical gear set with localized bearing contact. *Finite Elements in Analysis and Design, 38*, 707–723.
3. Wang, J., & Howard, I. (2004). The torsional stifness of involute spur gears. *Mechanical Engineering Science, 218*, 1–12.
4. Howard, I., Jia, S., & Wang, J. (2001). The dynamic modeling of a spur in mesh including friction and a crack. *Mechanical Systems and Signal Processing, 15*(5), 831–853.
5. Alvaro, S. P., & Recardo, G. (2001). Amplitude deformation and Phase shift in amplitude modulation atomic force microscopy. *Surface Science, 471*, 71–79.
6. Tang, Z., Xu, Y., Li, G., & Aluru, N. (2005). Physical models for coupled electromechanical analysis of silicon nanoelectromechanical systems. *Applied Phsics, 11*(97).
7. Zhao, Y. P., Wang, L. S., & Yu, T. X. (2003). Mechanics of adhesion in MEMS-a review. *Journal of Adhesion Science and Technology, 17*(4), 519–546.
8. Dedkov, G. V., & Dyshekov, M. B. (2000). Deformation of the contact region and adhesive friction between nanoprobe and surface. *Surface Science, 463*, 125–134.

Chapter 84
Study on Interpolation Algorithm of Printing Screen Transferred Manipulator

Zhao Nie, Hongwei Xu, Guowei Yao and Laixiang Wu

Abstract Screen printing is very common technology in printing and dye factory, now. Silk screen which was used be clean is a born work. In this paper, robot which used in silk screen cleaning is discussed. For silk screen cleaning machine, the robot is used to transfer the silk screen which is ready to be washed. According to the structures of robot and machine, the algorithms of arc interpolation are proposed. In this algorithm, the path of robot end actuator is divided into a series of discrete points. The location and gesture of robot end actuator are computed and the motion parameters of every joint are computed by one dimension scanning optimization algorithm. The algorithm is composed and used in manipulator of robot which is used to transfer the silk screen into washing machine. The experiment results prove that the algorithm is valid and helpful.

Keywords Silk screen · Robot · Interpolation algorithm

84.1 Introduction

Now, screen printing is very important technology in printing and dyeing factory. Screen printing can be used to printing on the surface of package, textile and paper.

Screen printing is widely used owing to its high machine reliability, low cost of screen mask, and simple fabrication process [1]. For screen printing, the silk screen can be used repeat. Before the silk screen is used in next time, the silk screen have to washed to avoid the ink is dry on the silk screen. In the past time, the silk screen is washed manually which is difficult to collect and treat the water.

Z. Nie · H. Xu (✉)
Xi'an University of Technology, Xi'an, China
e-mail: xuhongwei@xaut.edu.cn

Z. Nie · G. Yao · L. Wu
Shaoxing Ruiqun Textile Machinery Technology Co. LTD, Shaoxing, China

Now, the labor cost becomes higher and higher. Therefore, the machine which can replace people for the human's working is widely welcomed. In this situation, the silk screen washing machine is made. In order to make it more automatic, a robot of 4R serial mechanisms is designed to transfer silk screen into the wash machine. For the 4R serial robot, the motion of each joint is the key point which can ensure the right position and gesture of end actuators.

Recently, many control methods were proposed to manipulate the end actuators [1]. For the various robot structures, the motion controlling algorithm is difference. Mirkhani et al. [2] proposed a novel algorithm which is based on harmony search algorithm for robot localization through scan matching. For most motion robot controlling, the iterative closest point algorithm is a popular method. The main challenge for robot automation is the development of a simple and robust motion algorithm that can be applied to an industrial robot. Chang et al. [3] proposed a new seam-tracking algorithm through characteristic-point detection for a portable welding robot.

During industrial robot working, there will be some obstacles on the way of the end actuator of robot. Therefore, the trajectory tracking of end actuator of robot is one of the main problems in robot control [4]. Miao and Tian [5] use enhanced simulated annealing approach to plan dynamic robot path. Aly and Abbas [6] use genetic algorithm to simulate the obstacles' effect on industrial robots' working space. In some ways, some advanced algorithms are used to optimization robot structure and control system [7]. In this paper, the arc interpolation algorithms are studied according to the working of robot which is used to transfer silk screen into the silk screen washing machine.

84.2   Arc Interpolation Algorithms for Screen Transferring Robot

For the robot which is used to transfer silk screen into washing machine, the bottom of washing machine is an obstacle which limit the work space of screen transfer robot. In order to avoid this obstacle, the path of robot's end actuator is planed to be an arc. And in the meantime, the gesture of actuator of robot has to keep straight down to keep the silk screen gesture during screen transferring. All the position and gesture of actuator is assured by the motions of all joins of robot. The begin location of actuator is as shown as in Fig. 84.1.

The motion of end actuator in WCS of 0A-XA-YA is decided by the motion of shoulder joint, elbow joint, and wrist joint. Therefore, the motion track of end actuator must be divided into the motion of shoulder joint, elbow joint, and wrist joint. First, the wrist joint's motion is computed as follows.

As shown in Fig. 84.1, a LCS of wrist Joint is set as 0B-XB-YB. The coordinates of wrist joint are set as (x_w, y_w), Then,

Fig. 84.1 Screen transferring diagram
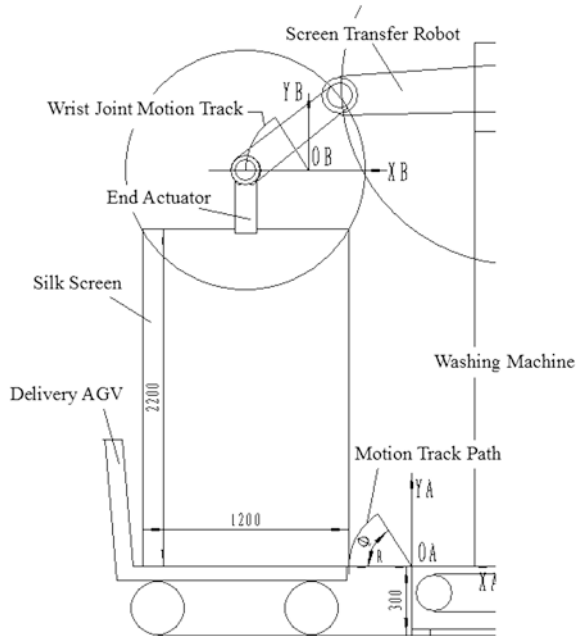
$$x_w^2 + y_w^2 = R^2 \tag{84.1}$$

where, R is the radius of arc track. Therefore, the begin point coordinates of track are $(x_{w0}, y_{w0}) = (-R, 0)$, then the end point coordinates of track can be computed as $x_{wt} = -R\cos\phi$, and $y_{wt} = R\sin\phi$. Where, ϕ is the corresponding arc angle.

Here, the track of wrist joint will be divided into 10 points, and the interval step between two points of x axis is:

$$\Delta = \frac{x_{wt} - x_{w0}}{9} = \frac{R}{9}(1 - \cos\phi) \tag{84.2}$$

Then, the coordinates of n point (x_{wn}, y_{wn}) is:

$$x_{wn} = x_{w0} + n\Delta = n\Delta - R \tag{84.3}$$

$$y_{wn} = \sqrt{R^2 - x_{wn}^2} = \sqrt{R^2 - (n\Delta - R)^2} \tag{84.4}$$

Elbow joint track path can be computed by set another LCS of 0C-XC-YC (shown in Fig. 84.2).

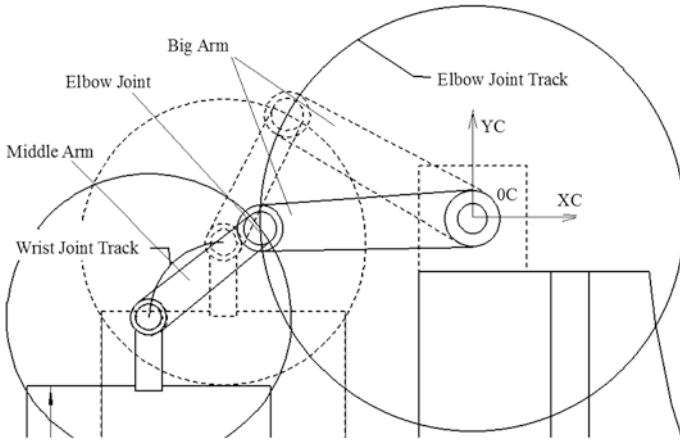Here, the coordinates of elbow joint are set as (x_C, y_C). Then,

Fig. 84.2 Elbow joint track diagram

$$x_C^2 + y_C^2 = R_b^2 \tag{84.5}$$

where, R_b is the length of the big arm of the robot. In this machine, the length of big arm of the robot is 500 mm, then, Eq. (84.5) can be change as:

$$x_C^2 + y_C^2 = 250{,}000 \tag{84.6}$$

In another way, the elbow joint connects with middle arm. Then the elbow track can be expressed as:

$$(x_c - x_w)^2 + (y_c - y_x)^2 = R_M^2 \tag{84.7}$$

Because the length of middle arm is 500 mm, then Eq. (84.7) can be change as:

$$(x_c - x_w)^2 + (y_c - y_x)^2 = 250{,}000 \tag{84.8}$$

According to the Eqs. (84.1)–(84.8), the coordinates of the discrete points can be computed. Then, the motion of every joint will be gotten through the computing results of above computing. Through the coordinates of computed, the coordinate transformation matrix of 0A-XA-YA and 0B-XB-YB is:

$$_B^A T = \begin{bmatrix} _B^A R & _B^A p \\ 0 \ \ 0 \ \ 0 & 1 \end{bmatrix} = \begin{bmatrix} 1 & 0 & 0 & -600 \\ 0 & 1 & 0 & 2200 \\ 0 & 0 & 1 & 0 \\ 0 & 0 & 0 & 1 \end{bmatrix} \tag{84.9}$$

Then, the coordinates of discrete points of wrist joint in coordinate system of 0A-XA-YA is:

$$
\begin{bmatrix} X_{wn} \\ Y_{wn} \\ 0 \\ 1 \end{bmatrix} = \begin{bmatrix} 1 & 0 & 0 & -600 \\ 0 & 1 & 0 & 2200 \\ 0 & 0 & 1 & 0 \\ 0 & 0 & 0 & 1 \end{bmatrix} \begin{bmatrix} x_{wn} \\ y_{wn} \\ 0 \\ 1 \end{bmatrix}
\tag{84.10}
$$

Then, according to the structure parameters, the coordinate transformation matrix of 0A-XA-YA and 0C-XC-YC is:

$$
{}^A_B T = \begin{bmatrix} {}^A_C R & {}^A_C P \\ 0 \quad 0 \quad 0 & 1 \end{bmatrix} = \begin{bmatrix} 1 & 0 & 0 & 100 \\ 0 & 1 & 0 & 3000 \\ 0 & 0 & 1 & 0 \\ 0 & 0 & 0 & 1 \end{bmatrix}
\tag{84.11}
$$

Then, the coordinates of discrete points of elbow joint in coordinate system of 0A-XA-YA is:

$$
\begin{bmatrix} X_{cn} \\ Y_{cn} \\ 0 \\ 1 \end{bmatrix} = \begin{bmatrix} 1 & 0 & 0 & 100 \\ 0 & 1 & 0 & 3000 \\ 0 & 0 & 1 & 0 \\ 0 & 0 & 0 & 1 \end{bmatrix} \begin{bmatrix} x_{cn} \\ y_{cn} \\ 0 \\ 1 \end{bmatrix}
\tag{84.12}
$$

Therefore,

$$
(X_{cn} - 100)^2 + (Y_{cn} - 3000)^2 = 250{,}000
\tag{84.13}
$$

Then, a equation can be obtained according to Eqs. (84.8) and (84.13),

$$
(100 - \sqrt{250{,}000 - (Y_{cn} - 3000)^2} - X_{wn})^2 + (Y_{cn} - Y_{wn})^2 = 250{,}000
\tag{84.14}
$$

Solve the Eq. (84.14) directly is difficult, then the one dimension scanning optimization algorithm can be used to get the answer. Then, the object function is written as:

$$
F = \left| (100 - \sqrt{250{,}000 - (Y_{cn} - 3000)^2} - X_{wn})^2 + (Y_{cn} - Y_{wn})^2 - 250{,}000 \right|
\tag{84.15}
$$

The computing step length is set, and the computing will be gotten. After the coordinates of all discrete points of elbow joint and wrist joint are gotten, the corresponding motion parameters of every joint can be computed as follows;

Big arm location angle computing equation is:

$$\theta_n = \tan^{-1}\left(\frac{X_{cn} - 100}{Y_{cn} - 3000}\right) \tag{84.16}$$

Middle arm location angle computing equation is:

$$\varphi_n = \tan^{-1}\left(\frac{X_{cn} - X_{wn}}{Y_{cn} - Y_{wn}}\right) \tag{84.17}$$

Then, the rotation angle equation of shoulder joint is:

$$\alpha_n = \theta_n - \theta_{n-1} \tag{84.18}$$

The rotation angle equation of elbow joint is:

$$\beta_n = \varphi_n - \varphi_{n-1} - \alpha_n \tag{84.19}$$

The rotation angle equation of wrist joint is:

$$\gamma_n = \varphi_{n-1} - \varphi_n \tag{84.20}$$

Therefore, the computing results will be used to compose the controlling program which is used in control the robot to transfer the silk screen.

Fig. 84.3 Screen transfer experiment

84.3   Experimental Practices

According the method of computing, the rotation angles of shoulder joint, elbow joint, and wrist joint are gotten. And the controlling program is composed and used in the screen transferring robot (Shown in Fig. 84.3).

The experiment result shows that the arc interpolation algorithm works well which can make the robot transfer the silk screen as wish.

84.4   Conclusions

This paper investigates the arc interpolation algorithm which is used to control the screen transferring robot work. The corresponding rotation angle computation equations are derived through a series of equation computing and one dimension scanning optimization algorithm. The computation results are used to compose the controlling program and used to practical experiments. The experiment result shows that the arc interpolation algorithm is valid and helpful.

References

1. Khoa, L. D., Truong, D. Q., & Ahn, K. K. (2013). Synchronization controller for a 3-R planar parallel pneumatic artificial muscle (PAM) robot using modified ANFIS algorithm. *Mechatronics, 23*, 462–479.
2. Mirkhani, M., Forsati, R., Shahri, A. M., et al. (2013). A novel efficient algorithm for mobile robot localization. *Robotics and Autonomous Systems, 61*, 920–931.
3. Chang, D., Son, D., Lee, J., et al. (2012). A new seam-tracking algorithm through characteristic-point detection for a portable welding robot. *Robotics and Computer- integrated Manufacturing, 28*, 1–13.
4. Scaglia, G., Rosales, A., Quintero, L., et al. (2012). A linear-interpolation-based controller design for trajectory tracking of mobile robots. *Control Engineering Practice, 18*, 318–329.
5. Miao, H., & Tian, Y.-C. (2013). Dynamic robot path planning using an enhanced simulated annealing approach. *Applied Mathematics and Computation, 222*, 420–437.
6. Aly, M. F., & Abbas, A. T. (2013). Simulation of obstacles' effect on industrial robots' working space using genetic algorithm. *Journal of King Saud University—Engineering Sciences*. doi:10.1016/j.jksues.2012.12.005
7. Sato, M., & Ishii, K. (2010). Simultaneous optimization of robot structure and control system using evolutionary algorithm. *Journal of Bionic Engineering 7*(Suppl.), S185–S190.

Chapter 85
System Design for Temperature Control and Distribution Detection Based on 485 Communications

Bo Gao, Xiaogui Zhang and Wuqi Wang

Abstract This paper introduces the temperature control and detection system under the monitoring of computer, which was applied SRS14A temperature controller and the K8511 thermal resistance acquisition module, based on the 485 communication for the exploration of trial-manufacture dry sintering of the heating chamber. The authors make a brief introduction about the communication of SRS14A temperature controller and the K8511 thermal resistance collection module, give the principle of the double timer timing cycle data acquisition, provide for the control program flow chart and related program code. Through the VB6.0 programming, the serial communication between the computer and the modules is realized. The temperature is collected and controlled. The centralized control is realized, and the operation and data processing is easy. Based on the idea of programming, this method can be used for the expansion of the similar principle module control.

Keywords Temperature detection module · VB6.0 · Serial communication · 485 interface

85.1 Introduction

This new technology of printed electronics has been applied in many fields [1–3]. In producing printed electronic products, dry sintering is an important process in machining process [4, 5]. In the process of manufacture dry sintering device, in

B. Gao (✉)
Department of Printing Engineering, Beijing Institute of Graphic Communication, Beijing, China
e-mail: gaobozx@163.com

X. Zhang · W. Wang
Department of Mechanical Engineering, Beijing Institute of Graphic Communication, Beijing, China

order to discuss the manufacture of the temperature field distribution of dry sintering device, we designed the system of a temperature control and distribution testing of temperature field.

Under the computer control, the system is connected to the field temperature controller and measuring temperature module through 485. The temperature controller is a general-purpose digital temperature controller SRS14A which is produced by the SHIMADEN Company [6], with the advantages of high speed, high performance, simple setup, strong visibility, and so on, suitable for all kinds of industries. The temperature acquisition module chosen is a production of the K8511 thermal resistance acquisition module by the KERUIXINGYE Company [7]. Each module in a thermal resistance signal collected six roads, translating into the corresponding temperature value, without PC program for nonlinear transformation.

85.2 The Communication Theory

The SRS14A temperature controller and the K8511 thermal resistance acquisition module itself possess 485 communication interfaces. At present, the RS-232 serial interface is widely used in the conventional computer, in order to realize the communication of the RS-485 interface and the computer, the RS-232/RS-485 communication interface converter is needed. The RS-232 communication interfaces on the computer is converted into the RS-485 communication interfaces, and then connected to serial port equipment.

85.2.1 The Computer Communication Protocol of the SRS14A Temperature Controller and the K8511 Thermal Resistance Acquisition Module

The SRS14A temperature controller and the K8511 thermal resistance acquisition module may communicate by way of two kinds of communication protocol, the custom protocol, or Modbus protocol. The custom protocol of the SRS14A temperature controller for Shimaden communication protocols is a unified frame format, whose communication instruction format more complicated than the standard Modbus protocol. The Modbus protocol uses two kinds of mode: ASCII mode and RTU mode, these two different kinds of mode of data formats and error checking method. The K8511 thermal resistance acquisition module also has a custom protocol and the standard Modbus-RTU.

The Modbus-RTU is a kind of communication protocol, which is developed by the Modicon Company. It uses the master-slave response works. The specification has been published on the Internet, is a truly open standard network communication

protocol and widely used in industrial field [8]. In this paper, the communication adopts the Modbus-RUT protocol between the computer and the SRS14A temperature controller and the K8511 thermal resistance acquisition module, using the ordered subset of the Modbus-RTU protocol. Under the mode of RUT, the message frame starts after a pause of at least 3.5 characters of time interval, and is finished after a pause within the range of at least 3.5 characters time [9]. Its message frame format is shown in the below Table 85.1.

85.2.2 The Program Frame of the SRS14A Temperature Controller

Although the SRS14A temperature controller and the K8511 thermal resistance acquisition module can be controlled through the communication, the functions of the SRS14A temperature controller are various, complex operation. Here just list associated with the temperature setting and measuring program frame. The K8511 thermal resistance acquisition module has a single function, only has the read instruction of measured values, and must be working under computer control.

85.2.2.1 Read the Current Temperature Value of the Temperature Controller (PV)

The Modbus RTU communication protocol—command frame of reading the current temperature value of the temperature controller is shown in below Table 85.2.

A computer address 01 indicates the communication unit number of the temperature controller in the network of the Modbus-RUT, to identify the temperature controller. Function code 03 shows reading variables. Data address 0100H shows reading type-current temperature measurements. The data item number 0001H shows reading a data item of the address. The CRC check result 85F6 is obtained by the command string between the machine address and the number of data items.

Table 85.1 Modbus RTU message frame

Pause interval	Address	Function code	Data	CRC-16	Pause interval
>3.5 characters Pause interval	A byte	A byte	N bytes	2 bytes	>3.5 characters pause interval

Table 85.2 Read the PV value command frame

Address	Function code	Data address	Number of data items	CRC check code
(01H)	(03H)	(0100H)	(0001H)	(85F6H)

When the temperature controller receives a command frame shown in Table 85.2, returning to the normal response frame format shown in below Table 85.3.

The computer address 01 used the machine address of the command frame. The function code 03 like function code of a command frames, shows the normal end of the function. The response data item number 02H shows the bytes number of reading data. The reading the data 0064H shows the current temperature value (10 °C). The CRC check result (0B9AFH) is obtained by the command string between the machine address and the number of data items.

85.2.2.2   Written to the Temperature Controller Set Value (SV)

The Modbus RTU communication protocol-command frame of written temperature controller set point is shown in below Table 85.4. The normal returned response frame format is shown in below Table 85.5. The function code 06H shows written variables. The data address 0101H shows written types-set temperature. 0064H indicates the written temperature setting.

85.2.3   The Program Frame of the K8511 Thermal Resistance Acquisition Module

The Modbus-RTU communication protocol command frame of the current temperature value of the thermal resistance acquisition module is shown in Table 85.6. The function code 04H shows variable read code. The channel address represents the starting channel number of the measurement, starting from the 0000H. The number of channels indicates the number of reading channels, and the total value of

Table 85.3 Read the PV value command frame

Address	Function code	Response data item number	Data	CRC check code
(01H)	(03H)	(02H)	(0064H)	(B9AFH)

Table 85.4 Written command frame of the SV values

Address	Function code	Data address	Data	CRC check code
(01H)	(06H)	(0101H)	(0064H)	(8865H)

Table 85.5 Write response frame of SV

Address	Function code	Data address	Data	CRC check code
(01H)	(06H)	(0101H)	(0064H)	(8865H)

Table 85.6 Read command frame of PV

Address	Function code	Channel address	Channel number	CRC check code
(02H)	(04H)	(0000H)	(0006H)	(703BH)

Table 85.7 Read response frame of PV

Address	Function code	Data length	Data	CRC check code
(02H)	(04H)	(0CH)	xxxxxxxxx	(xxxxxH)

the 6 channel temperature is read. Through the combination of channel address and channel number, it can acquire any channel data.

Returning the normal response frame format as shown in Table 85.7, the data length indicates the number of data returned, and the number of channels associated with Table 85.6. The data indicates the different temperature values of selected channels.

85.3 The Temperature Control and the Theory of Multichannel Inspection

Using MSComm (Microsoft Communication Control) serial communication control in VB6.0 to realize the communication between the SRS14A temperature controller and the K8511 heat resistance acquisition module, and realize temperature control and multi-inspection.

85.3.1 The Temperature Control and the Constitution of the Multi-inspection System

The temperature control and multichannel inspection system is composed of a computer, a SRS14A temperature controller and two K8511 thermal resistance acquisition modules. Temperature control through the SRS14A temperature controller, its relevant settings can be carried out on the computer, no site operation, more convenient. Each K8511 thermal resistance acquisition module has six channels of temperature acquisition, and two temperature acquisition modules have 12 channels, mainly used for collecting temperature. Figure 85.1 is temperature control and multi inspection system chart.

SRS1   K8511-1   K8511-2
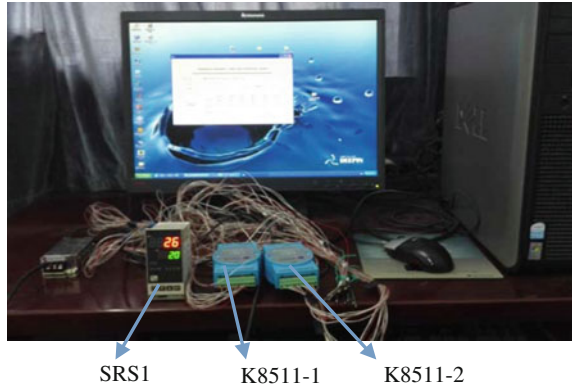
85.3.2 The Theory of Timing Acquisition Data

When the data is collected, the information of each module is collected in order in time, and the two timers are set up, and the working theory is shown in the following diagram. Timer T1 defined the cycle of acquisition data, in a cycle of acquisition data, circularly collecting temperature controller SRS14A (B to C), the K8511 thermal resistance acquisition module1 (D to E) and the K8511 heat resistance acquisition module 2 (F to G). Timer T1 defined the cycle of acquisition data, in a cycle of acquisition data, circularly collecting temperature controller SRS14A (B to C), the K8511 thermal resistance acquisition module1 (D to E) and the K8511 heat resistance acquisition module 2 (F to G). Timer T1 starting the timer T2 in A position, timer T2 has ended in the B position, closing the timer T2, sending the acquisition command to the SRS14A temperature controller. The part of BC is the data processing time, after receiving the processing response in the C position, restarting the timer T2. Timer T2 has ended in the D position, closing the timer T2, sending the acquisition command to the K8511 thermal resistance acquisition module1. Similarly, send the acquisition command to the K8511 thermal resistance acquisition module 2. Finally, after receiving the processing response in the C position, the timer T2 is closed until the next acquisition cycle started, and then the timer T1 is started.

Under the condition of the computer dominant frequency 3.0 GHz, the setting time of the timer T2 is 5 ms. By measurement, the required time of completing data at a time (from A to G) is about 150 ms. Therefore, the cycle time of the data acquisition, that is the timing settings of the timer T1, is greater than 150 ms. This can guarantee that each data acquisition in data area is completed, and there will not leak the collection and interference situation (Fig. 85.2)
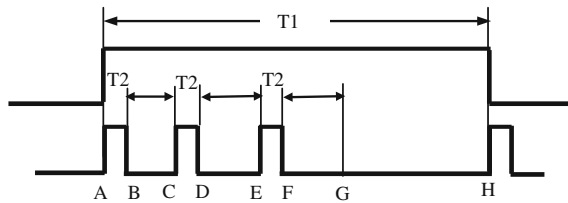
Fig. 85.2 Timer working schematic diagram

85.3.3 *The Process Design of Control Procedure*

VB6.0 programming using event control mode [10], in the design of the design, there are two main events: one is the set value writing of the SRS14A temperature controller; the other is the data reading of all modules. In the design, the SRS14A temperature controller sets the value, after the end of the timing cycle of the timer T1, or after a cycle all acquisition data completed. The value is written, a series

Fig. 85.3 The work process diagram for setting values to write
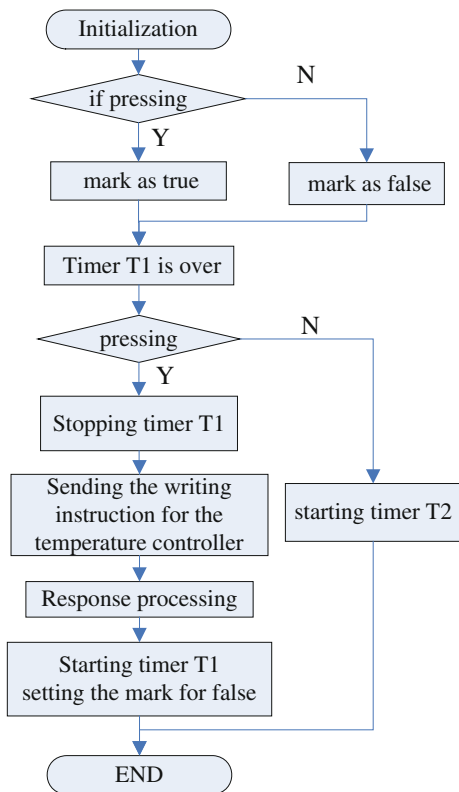
process of program operation as shown in Fig. 85.3. Timer T1 starts the processing, and the code is as follows.

```
Private Sub Timer1_Timer()        'Inspection cycle
 If Setup = True Then    'If the temperature controller writes signal
        Dim tarr(0 To 7) As Byte  'Temperature controller reads the command
        Dim CRC() As Byte
        Timer1.Enabled = False     'Close inspectional time
        Timer2.Enabled = False     'Close sequential acquisition
         tarr(0) = 1
         tarr(1) = 6
         tarr(2) = 3
         tarr(3) = 0
         tarr(4) = Hex(Val(i_sub(0)))   'Set data
         tarr(5) = Hex(Val(i_sub(1)))   'Set data
         Call CRC16(tarr, 5)        'Call the function CRC16
         tarr(6) = LoCRC            'CRC low order
         tarr(7) = HiCRC            'CRC high order
         MSComm1.RThreshold = 8
         MSComm1.InBufferCount = 0
         MSComm1.OutBufferCount = 0
         MSComm1.Output = tarr
      Else
        Timer2.Enabled = True    'Startup sequential acquisition
        i = 0          'The first address of the signal acquisition
      End If
 End Sub
```

85.4   The System Testing

The final operating interface of the automatic temperature control and multi-inspection system is shown in Fig. 85.4. The measurement values for the SRS14A temperature controller, the input for setting the values and setting the parts are shown in the left. The temperature inspection operation and display interface on the rightside, the time of the timing acquisition is set up in this position, pressing the starting button for the temperature measurement, and the value is displayed in the display box under the respective channel. The system is tested and the results are shown on the graph. From the picture, it can be seen that the effect of the temperature control setting and the detection.
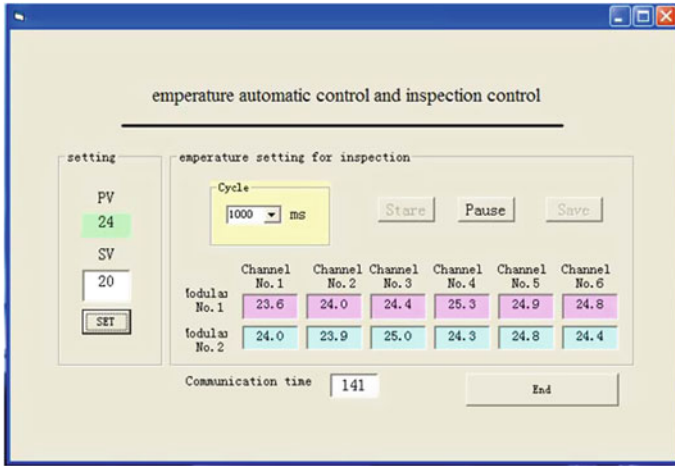
Fig. 85.4 Temperature control and the real-time display interface of acquisition information

85.5 Conclusions

In this paper, the temperature control of the SRS14A temperature controller and the K8511 thermal resistance collection module and multi—Inspection System are introduced. By using of VB6.0 and its MSComm serial communications controls, and with the help of the Modbus-RTU protocol command frame, achieves the time control of temperature and multi-roads inspection acquisition tasks in the Windows. Because the connecting of 485 communications is simple, and the distance of the communication is long. So the system is easy to expand, and it is convenient for long-distance control and measurement. In the software, the programming of this paper is good for the development of similar procedures in the future.

References

1. Park, S. K., Kim, Y. H., & Han, J. I. (2009). High-resolution patterned nano particulate ag electrodes toward all printed organic thin film transistors. *Organic Electronics, 10*(6), 1102–1108.
2. Mahajan, A., Frisbie, C. D., & Francis, L. F. (2013). Optimization of aerosol jet printing for high-resolution, high-aspect ratio silver lines. *ACS Applied Materials & Interfaces, 5*(11), 4856–4864.

3. Kelley, T. W., Baude, P. F., Gerlach, C., et al. (2004). Recent progressin organic electronics: materials, devices, and processes. *Chemistry of Materials, 16*(23), 4413–4422.
4. Luhai, L. I., Lixin, M. O., Jun, R. A. N., et al. (2014). Conductive ink and its application technology progress. *Imaging Science and Photochemistry, 4*(32), 393–401.
5. cuizheng, qiusong, chenzheng, et al. (2012). *Printed electronics: Materials, technologies and applications*. Beijing: Higher Education Press.
6. Shimaden. Communications (Interface)(RS-485)Instruction Manual. http://www.shimaden.co.jp. Accessed 20 June 2015.
7. KERUIXINGYE. K-8511(RS-485) Heat resistance acquisition module. http://www.krxgk.com/product_detail2.asp?id=119. Accessed 20 June 2015.
8. Wang, X., Zhang, M., & ying, D. U. (2008). Application of modbus RTU protocol in the communication between IPC and intelligent instrument. *Low Voltage Apparatus, 2*, 8–11.
9. Jiating, R. (2009). Serial communication programming OFRS232 based on VB6.0 for the eurotherm 3504 tmperature controller. *Sichuan Metallurgy, 31*(4), 54–57.
10. lili, C., Liu, X., Zhaocun, et al. (2014). *Communications programming using visual basic*. Beijing: China Petrochemical Press.

Chapter 86
Research of Printing Machinery Parts Classification and Coding System

Qian Li, Hongqiang Wan and Gang Gao

Abstract The printing machinery parts have no uniform coding system, which caused many problems in the process of design and manufacture. Its classification and coding can not only improve management efficiency but also enable to accelerate product development. Now, this article is based on the study of existing parts classification system, the combination of chain structure, tree structure and hybrid structure, designing a decimal and ten code printing machinery parts classification, and coding system by using group technology. It is composed of Arabic numerals and letters, and it used T-slot bolts modeling process in order to illustrate classification and coding system for using of each code attributes and specific. The coding system has many advantages, such as simple structure, appropriate classification number links, and easy to remember. It is convenient for the unified management of printing machinery parts. Besides, it has a great role in the establishment of standardized parts library.

Keywords Pro/Engineer · Family table · Group technology · Classification and coding

86.1 Introduction

There are many kinds of printing machinery, including prepress equipment, printing equipment, and printed equipment. Most important, each printing equipment has different models and structures, which has caused unnecessary problems in the process of design and manufacture. Through classification and coding for printing machinery parts can make the design and manufacturing work simple and fast [1].

Q. Li (✉) · H. Wan · G. Gao
Mechanical and Electrical Engineering Institute, Xi'an Technological University, Shaanxi, China
e-mail: 642313501@qq.com

693

Currently, the basis of parts classification using has the following three. First, according to the characteristics of the product structure, second according to functional applications of the product, and finally, according to group technology classification method. There are many classification systems used in the implementation of group technology. As VUOSO parts classification coding system, OPITZ parts classification and coding system, KK-3 parts classification coding system, JLBM-1 parts classification and coding system, etc. [2, 3]. It not only can be described in detail structure of the part and contribute to the organization of similar parts, but also can provide CAD library management and input of the CAPP to provide basic information by using group technology to classify parts resources [4]. According to the form of the classification structure, there are following basic form. On the basis of the link number have less link classification system and a multi-link classification system. Based on the lateral relationship of classification system, it was divided into independent links, related links, and hybrid links classification system, which are both independent links and related links. Therefore, hybrid links classification system belongs to the mixed structure with chain structure and tree structure. In fact, there is a large number of parts' classification and coding system belongs to this.

According to the characteristics of the existing encoding system, the paper used the mixed classification system. Design a decimal and ten code printing machinery parts classification and coding system. It is composed of Arabic numerals and letters of the alphabet.

86.2 Printing Machinery Parts Classification and Coding System

86.2.1 Printing Machinery Parts Classification

There are many kinds of printing machinery parts. According to the principle of group technology, these parts can be divided into different similar types according to the similarity degree, which make the parts of the same type have similar shape or function [5, 6]. According to the Standardization degree, the printing machinery parts can be divided into standard parts, common parts, and special parts.

The Standard parts including seven categories, such as Bolt, Nut, Screws, Pin, Washers, Collar, Rivet, each category is divided into many subcategories.

The common parts are including about 23 categories. For example, Gear, Cam, Bearing, Spring, Roller, Cots, Blade, etc.

The special parts including about 14 categories, for instance, tablet, block teeth, teeth, dental pad, tooth plate, etc.

86.2.2 *Printing Machinery Parts Coding System*

The printing machinery parts' encode is based on the classification of printing machinery parts. The encoding system is a decimal and 10 bit code system, which using tree and chain hybrid structure. Its basic structure is shown in Fig. 86.1.

The encoding system is composed of the main code and the auxiliary code. The main code is in the top 6, which is mainly used to distinguish the basic information of the parts and descript the parts. The auxiliary code is used to describe the parts in detail, so that the code of each part is uniquely determined.

The first part of the classification and encoding system is named by the English letter. It is the capital of the first letter of the standard parts, common parts, and special parts, and they are namely B, T, and Z.

The second and the third place is the rough classification code of parts category. In other words it is encoded in the light of the classification order, such as bolt stud is 01.

The fourth bit is a detailed classification code of the parts, which is the refinement classification of the parts classification, such as the special bolts for 5.

The fifth and the sixth bit is code bit for the specific parts, it encoded by the frequency order after subdivision of component category, for example, T-slot bolts which belong to the special bolts, its code is 01.

The eighth and the seventh is the characteristic parameters of the parts that is to say the main specifications of the parameters, such as bolts, is its nominal diameter size.

The ninth and the tenth bit is sequence encoding for the same type parts so as to statistics the number of same type of parts and convenient to management.

1	2	3	4	5	6	7	8	9	10
standard parts code (B)	Part name coarse code		Part name sub division code	Specific parts of code		Feature parameters		Part sequence number of the same type	
Common parts code(T)									
special parts code(Z)									

Fig. 86.1 Basic structure of printing machinery parts classification and coding system

The coding system has the advantages of simple structure. Horizontal classification number is moderate, easy to remember, and classification. Taking into account, the coding system is mainly used for the design. The main parameters of parts are in the seventh and eighth bits. When deciding to choose which parts, through the size of the bits can be a clear understanding of the basic dimensions of parts and choose the suitable parts. For example, the code of M20 T-slot bolt is B015012000. The following is T-slot bolts in Pro/E modeling process to illustrate the use of classification coding.

86.3 Application Examples

86.3.1 Create a Common Model

According to the standard size provided by "mechanical design manual," after the analysis of T type slot size with bolt, the paper use a two class table family for data classification management [7].

First, using B01501 as the name, a model of T-slot bolt is established by using a set of parameters and the name of the dimension symbol is modified by using the function of "modifying dimension attribute" so as to correspond to dimension specification of the T type slot. It can make a good readability of the family table which later established and easy to modify. The two-dimensional diagram of T type groove bolt is shown in Fig. 86.2 and three-dimensional model which modified the name of the dimension symbol is shown in Fig. 86.3.

86.3.2 Set up the First Family Table

According to the data characteristics, the D, D1, S, K is put in the first family table. The instance named is B01501 plus nominal diameter of the bolt. As shown in Fig. 86.4.
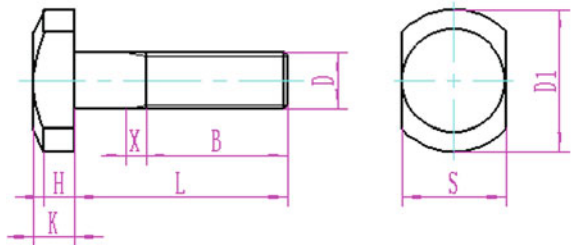
Fig. 86.2 Two-dimensional graph
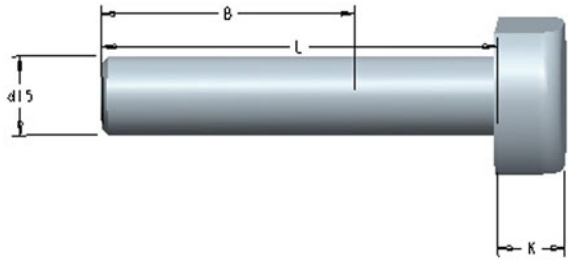
Fig. 86.3 Three-dimensional model

Fig. 86.4 The first family table

86.3.3 Set Up the Second Family Table

In the family table editor, select an instance of the family table. Clicking "Insert/instance level table" can open a new family table editor. Then adding L, B size to the family table can create secondary family table of this instance. The instance name is B01501 plus nominal diameter of the T-slot bolts and the sequence number. As shown in Fig. 86.5. In the same way, you can create other instances' second family table.

Enter all of the instance parameters. Checking instance is whether can be successfully regenerated. If an instance validation is failure, opening the instance, finding out the problems to modify and rechecking again. Until all instances verification is successful, turn it off and save in the pro/E.

Fig. 86.5 The second family table

86.4   Conclusions

After printing machinery parts classification and coding, using it to named parts and folders. So the high efficiency of technical personnel's work is in the side of search, access, and management. At the same time, using Pro/E to establish a similar multilevel family table parts can eliminate tedious repetitive work, improve the design efficiency and avoid some errors of the repetitive structure.

References

1. Peng, W. (2002). Enterprise standard parts' classification and coding. *Machinery Industry Standardization & Quality, 08*, 26–29.
2. Zheng, J. (2009), *The research of parts' coding & management based on the theory group technology (GT)*. Shanghai Jiao Tong University.
3. Song, M., & Wu, Q. (2003). The establishment of injection mold parts' classification coding system. *Group Technology & Production Modernization, 20*(3), 5–49.
4. Li, R., & Zhang, H. (2009). The Parts' classification and naming for PDM system. *Machinery, 47*(543), 76–78.
5. Wang, X., Zhu, H., & Zhang, S. (2012). Research on component coding system for friction welding machine based on group technology. *Electric Welding Machine, 42*(2), 44–46.
6. Yang, Y. (2014). Parts' classification and coding based on group technology. *Precise Manufacturing & Automation, 1*, 4–5.
7. Zhang, X. (2007). Application of pro/engineer multilayered family table in the parts library. *Die and Mould Technology, 2*, 8–16.

Chapter 87
Characteristic Research of Static Mixer Used in Solventless Laminator

Hongwei Xu, Hang Zhang and Donghong Liu

Abstract Solventless lamination is a new technique which is widely used in package printing industry now. For solventless lamination, the mixing result of A/B materials has an important impact on the performances of solventless lamination adhesives. Furthermore, the parameters of the mixing process and the structure of static mixer have a strong effect on the mixing efficiency. In this paper, the structure of static mixer which is used in solventless lamination machine is modeled with Pro/E software. The model is transferred into Fluent software, and the computing regime is determined and meshed. The mixing result is simulated with Fluent software and the result shows that the mixture results under the different diameters of mixer and different of inlet flow speeds of A and B materials are very different. Through this simulation and analysis, the optimized parameters of mixing process and diameter of mixer are obtained to improve the mixing efficiency. This research will supply a good help for the design of solventless laminating machine and give the guide for the setting of solventless laminating technology parameters.

Keywords Solventless laminator · Static mixer · Fluent · Mixing

87.1 Introduction

Now, solventless lamination is widely used in package printing industry. Today, solventless lamination technique can meet the requirements of 70–80 % of flexible packaging products [1]. Solventless lamination is the technique that uses mixture of two materials as the laminating adhesive. One is adhesive material, the other is curing agent. The lamination materials don't need drying and not volatile a harmful

H. Xu (✉) · H. Zhang
Xi'an University of Technology, Xi'an, China
e-mail: xuhongwei@xaut.edu.cn

D. Liu
Weinan Outai Printing Machinery Technology Co. LTD, Weinan, China

gas which pollute the environment. Therefore, solventless lamination has the advantages of energy saving and environment protection. Solventless lamination machine include two main devices. One is solventless lamination adhesive mixing machine which is used to mix the lamination adhesive, the other is lamination machine which is used to make two kinds of material into one lamination material.

For lamination adhesive mixing, the mixer is very importing part which has an effect to the quality of lamination adhesive mixture. In most of lamination machine, static mixer is widely used because of its advantages of energy saving and structure simple. The static mixer includes two parts. One is composed with inserts and the other is a tube. The inserts are put inside the tube to cut, fold twist and recombine fluid elements to make the fluid elements mixing enough [2]. Static mixer is applied in variety of industries, ranging from polymer processing, and biotechnology to water treatment. There are various types of static mixers in different industry. However, despite widespread use of static mixer, the scarcity of information about flow and mixing in static mixers is partially available due to static mixer's complex construction [3].

For many use of static mixer, the structure has an important impact on the mixture results. But it is impractical to analytical solute the mixture result due to the complex geometry of static mixers. Now, advanced simulation software can be used to study the mixing performance of static mixer. Lehwald et al. [4] number study the macro- and micro-mixing in a static mixer and this mixing efficiency is measured by calculating the segregation index. Jovanovic et al. [5] use the discrete element method (DEM) for modeling of granular flow in various multiple Komax and Ross mixing applications, and use computational fluid dynamic (CFD) method for modeling of fluid flow through the Eulerian multiphase model. Experimental analysis is often used to investigate the influence of physical parameters on liquid-liquid dispersion at in static mixer [6]. In this paper, the effects of the diameter of static mixer and the inlet flow speed of A/B on the mixing result are investigated through simulation.

87.2 Mathematical Model Descriptions

The mathematical model is solved by CFD. For CFD, the fluid flow problems of continuity equation, momentum equation and energy equation can all be expressed by the follow general variable equation.

$$\frac{\partial(\rho u \phi)}{\partial t} + \mathrm{div}(\rho u \phi) = \mathrm{div}(\Gamma \mathrm{grad} \phi) \ + \ \mathrm{S} \tag{87.1}$$

where ρ is the density of fluid (kg/m^3), u is velocity of fluid (m/s), ϕ is general various parameters, Γ is the generalized diffusion coefficient, t is time (s), div is the divergence function of vector function, grad is the gradient function of vector function, S is the generalized source item.

In this paper, the mixture model is applied. Mixture model is a simple multiphase model which is used to simulate the fluid flow under different speed of double phase or multiphase. Solve the continuity equation, and energy equation of mixture phase, volume fraction of second phase.

Mixture continuity equation is

$$\frac{\partial \rho_m}{\partial t} + \nabla \bullet (\rho_m \bar{v}_m) = 0 \tag{87.2}$$

And,

$$\bar{v}_m = \frac{\sum_{k=1}^{n} \phi_k \rho_k \bar{v}_k}{\rho_m}, \rho_m = \sum_{k=1}^{n} \phi_k \rho_k$$

where, ρ_k is the density of phase k, $\bar{v}_k$ is the average speed of phase k, and ϕ_k is the volume fraction of phase k.

The momentum equation of mixture model can be obtained by computing the summation of all the momentum equation of each phase, and can be express as,

$$\frac{\partial}{\partial t} (\rho_m \bar{v}_m) + \nabla \bullet (\rho_m \bar{v}_m \bar{v}_m) = -\nabla p + \nabla \bullet \left[\mu_m \left(\nabla \bar{v}_m + \nabla \bar{v}_m^T \right) \right] + \rho mg + F \tag{87.3}$$

where, n is number of phase, F is the force of volume, g is the acceleration of gravity, μ_m is mix viscosity, and can be gotten as,

$$\mu_m = \sum_{k=1}^{n} \phi_k \mu_k$$

The volume fraction equation of phase p is,

$$\frac{\partial}{\partial t} (\phi_p \bar{v}_p) + \nabla \bullet (\phi_p \bar{v}_p \bar{v}_m) = -\nabla \bullet (\phi_p \bar{v}_p \bar{v}_{dr,p}) \tag{87.4}$$

87.3 Simulation Model and Computing

It is very difficult to compute the mixing result by analytical solution to the complex geometry of static mixers. The standard mixing element of a static mixer is usually composed of a number of helical blades mounted in a cylindrical pipe. The blades are all twisted which plates which are twisted [7]. The structure of the static mixer can make A/B materials mixing enough. The problems related to the analysis of the mixing result can be overcome by using number simulation by computer. The Pro/E software can be used to model the static mixer as shown as Fig. 87.1.
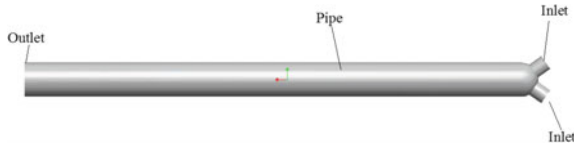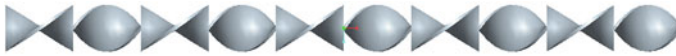
Fig. 87.1 Structure of the static mixer

Fig. 87.2 Structure of the insert

Figure 87.1 shows that there are two inlets for the material of A and B, and one outlet for the mixture lamination adhesive. The main part is the insert which is mounted inside of the pipe. The structure of insert is shown as Fig. 87.2

The 3D model is founded and meshed using Gambit. The meshed model can be transmissed into Fluent software which is used to simulation the fluid flow. The computing regime is determined.

In this simulation, mixture model with standard k-ε turbulence model equation is chosen. The wall function is chosen as enhanced wall treatment. The two inlets are set as flow velocity inlets. The outlet is set as pressure outlet. The pipe wall is all set as wall. The fluid is set as self-determine fluid. The density and viscosity of material A are set as 1.12 kg/m^3 and 1.1 kg/ms, and the density and viscosity of material B are set as 0.98 kg/m^3 and 0.7 kg/ms. Governing equation is solved by the finite volume method. The couple item of pressure and velocity is chosen as Simple algorithm. The volume fraction equation is chosen as Quick type, and the rest is chosen as second order upwind. All the setting is done, and the simulation is started.

87.4 Simulation Results and Discussions

Numerical simulations are performed for static mixers with different diameters and different inlet velocities of the mixing process. The mixing results are obtained via CFD calculations. Figure 87.3 is a mixing process simulation of fluid mixing trajectories.

The length of static mixer is 330 mm. there is ten elements blades inside of pipe. The diameters of pipe are, respectively, set as 15–20 mm. The simulation results are shown in Fig. 87.4.

Figure 87.4 shows that the mixing results reduced with the increasing of the diameter of pipe. When the diameter of pipe is 15 mm, the mixing result of A/B is 50–55, near best (50 means mixing enough).
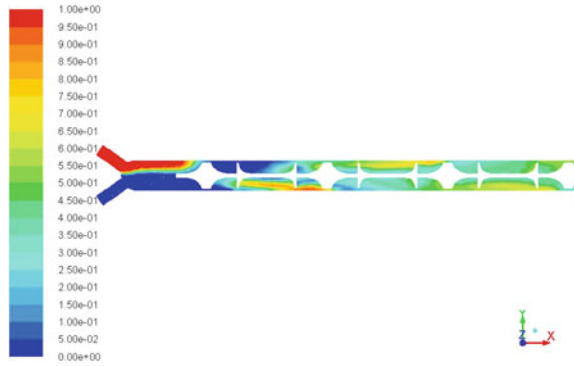
Fig. 87.3 Fluid mixing trajectories of *A/B* inside of pipe

Diameter is 15mm   Diameter is 16mm   Diameter is 17mm

Diameter is 18mm   Diameter is 19mm   Diameter is 20mm
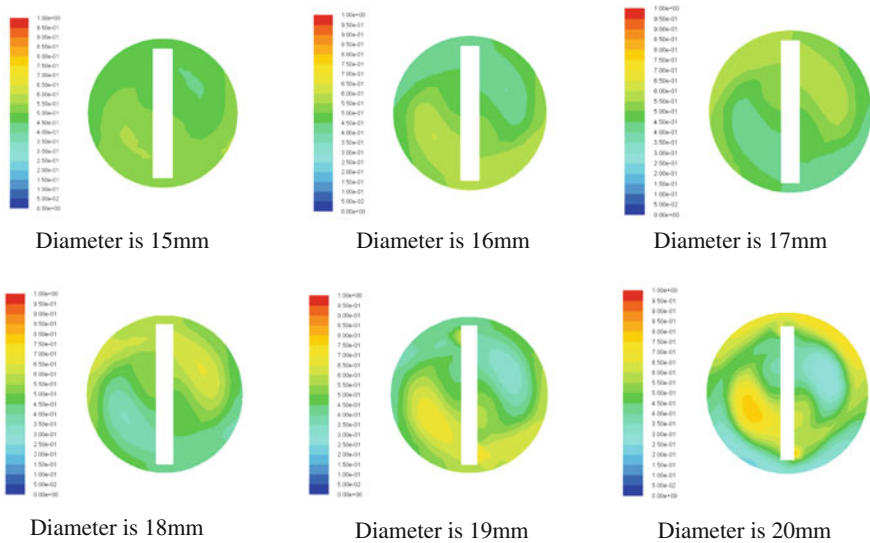
Fig. 87.4 Simulation results under different diameters

The inlet velocities of *A/B* influence the mixing result too. Therefore, the inlet velocities are, respectively, set as 0.00001, 0.0001, 0.001, 0.01, 0.02, 0.04 m/s., and the diameter of pipe is set as 15 mm. The simulation results are shown in Fig. 87.5.

Figure 87.5 shows that when the inlet velocities of *A/B* are 0.0001 and 0.00001 m/s, the mixing result is not very good. When the inlet velocities of *A/B* are quicker than 0.001 m/s, the mixing results are good, and with the further increasing of the inlet velocities of *A/B*, the mixing results not change much.
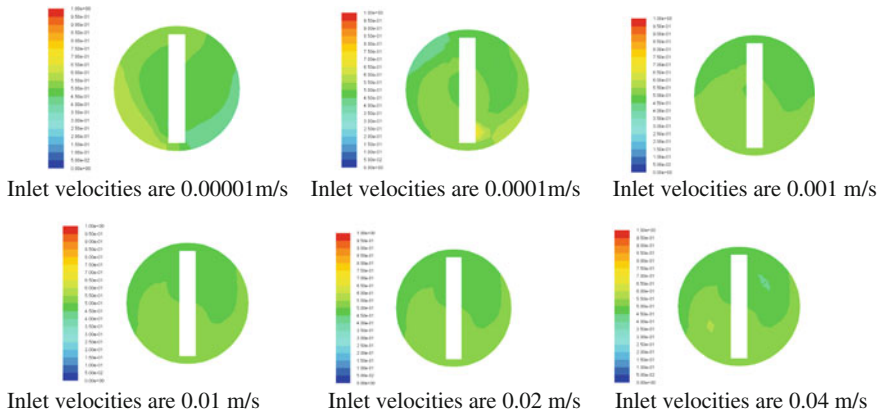
Inlet velocities are 0.00001m/s

Inlet velocities are 0.0001m/s

Inlet velocities are 0.001 m/s

Inlet velocities are 0.01 m/s

Inlet velocities are 0.02 m/s

Inlet velocities are 0.04 m/s

Fig. 87.5 Simulation results under different inlet velocities

87.5 Conclusions

Finite volume method is applied to solve an engineering problem in solventless laminating, in another word, mixing result. Pro/E software is used to found the static mixer model. The Fluent software is used to simulate the mixer results under different diameters of pipe and different inlet velocities of A/B. The simulation results are analyzed and compared. When the length of static mixer is 330 mm, and the diameter of pipe is less than 15 mm will obtain an enough mixing. And, it is better for the mixing that the inlet velocities of A/B are quicker than 0.001 m/s. The research will benefit the design of static mixer of solventless laminating machine, and give the guide for the technology of solventless laminating.

References

1. Lv. L., Xu, W., & Zuo, G. (2010). Characteristics research about coating system of solventless laminator. In *Proceedings of the 17th IAPRI World Conference on Packaging*, pp. 63–68.
2. Saatdjian, E., Rodrigo, A. J. S., & Mota, J. P. B. (2012). On chaotic advection in a static mixer. *Chemical Engineering Journal, 187*, 289–298.
3. Kumar, V., Shirke, V., & Nigam, K. D. P. (2008). Performance of Kenics static mixer over a wide range of Reynolds number. *Chemical Engineering Journal*, *139*, 284–295.
4. Lehwald, A., Janiga, G., Thevenin, D., et al. (2012). Simultaneous investigation of macro- and micro-mixing in a static mixer. *Chemical Engineering Science, 79*, 8–18.
5. Jovanovic, A., Pezo, M., Pezo, L., et al. (2014). DEM/CFD analysis of granular flow in static mixers. *Powder Technology, 266*, 240–248.

6. Hammoudi, M., Si-Ahmed, E. K., & Legrand, J. (2012). Dispersed two-phase flow analysis by pulsed ultrasonic velocimetry in SMX static mixer. *Chemical Engineering Journal, 191*, 463–474.
7. Paglianti, A., & Montante, G. (2013). A mechanistic model for pressure drops in corrygated plates static mixers. *Chemical Engineering Science, 97*, 376–384.

Chapter 88
Structure Design of Die Cutting Unit in Corrugated Carton Production Line

Rongyu Ge, Yimin Wu and Haitao Wang

Abstract The corrugated carton as a common packaging tool is usually produced in production line including feeding unit of corrugated boards, printing unit, slotting unit, die cutting unit, and gluing unit. Among them, the die cutting unit is a very important device in this line, which has a large influence on the accuracy of cutting position. So it is crucial to design the structure of die cutting unit. First, both main structure and motion of rotary die cutting unit are analyzed. It is explained that die cutting unit is mainly composed of two rollers, rubber roller and die roller. Both the rollers rotate synchronously. In order to promote the cutting quality, adjustments of rubber roller and die roller are necessary, such as roller position, rotating speed, so adjusting structure in detail and its principle of die cutting unit are illustrated in this paper.

Keywords Corrugated carton · Die cutting · Rubber roller · Die roller

88.1 Introduction

Corrugated carton has good mechanical properties, such as light weight, compressive and tensile resistance, and easy processing. In addition, it has many advantages including non-pollution, low cost, and recycling, so corrugated carton has become the most widely used packaging container in modern packaging [1].

With the rapid development of packaging industry, corrugated carton is produced in production line, which is made up of corrugated paper feeding unit, printing unit, slotting unit, die cutting unit and gluing unit. Die-cutter is an important post-printing process in production line. While die cutting, a cutting die is first made with blades

R. Ge (✉)
School of Mechanical Engineering, University of Jinan, Jinan, Shandong, China
e-mail: me_gery@ujn.edu.cn

Y. Wu · H. Wang
Shandong Binzhou Bohai Piston Co., Ltd, Binzhou, Shandong, China

bent into desired shape and mounted on a plywood according to the carton design drawing, and then corrugated board, pressed onto the cutting die, will be sheared and marked [2]. Die cutting can be done on either flatbed or rotary presses. The primary difference between rotary die cutting and flatbed die cutting is that the rotary is faster but the die is not cheap. Most insiders in packaging industry insist that rotary die cutting represents the development direction of die cutting machine. In this paper the structure of rotary die cutting unit is designed in detail.

88.2 Analysis of Main Motion

Rotary die cutting unit, shown in Fig. 88.1, contains two barrels. One is rubber roller with covered rubber cushion, and the other is die roller with cutting die mounted on. A series of drive gears will force the die roller to rotate at the same speed as other units, ensuring that any cuts the die makes line up with the printing on the corrugated board. And the rubber roller can also generate synchronous rotary motion following the rotary motion of die roller. In this way, when a long sheet of corrugated board is fed in the gap between the two rollers, the board will be cut out shapes by the cutting die mounted on the die roller surface [3]. It is a work cycle when the two rollers revolve in a circle.

88.3 Adjustment of Die Roller

The cutting die with blades is fixed by threaded connection on the surface of die roller, so the cutter position on the corrugated board is constant. But it maybe is inaccurate. Therefore, the die roller must be adjusted along its axial or circumferential direction [4].

The adjustment structure of the die roller in axial direction is shown in Fig. 88.2. There is a fixed adjusting pedestal that has a threaded hole in the middle. An adjusting shaft is joined with die roller at the shaft end and is machined to external thread at the middle segment. The die roller, like the rubber roller, is supported by special RNU324 bearing and assembled with a sleeve. When the handle joined with
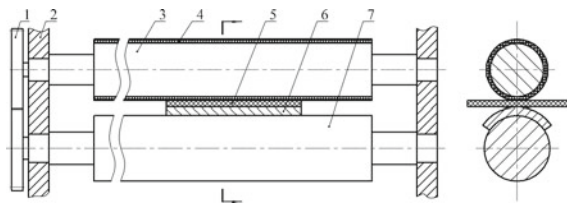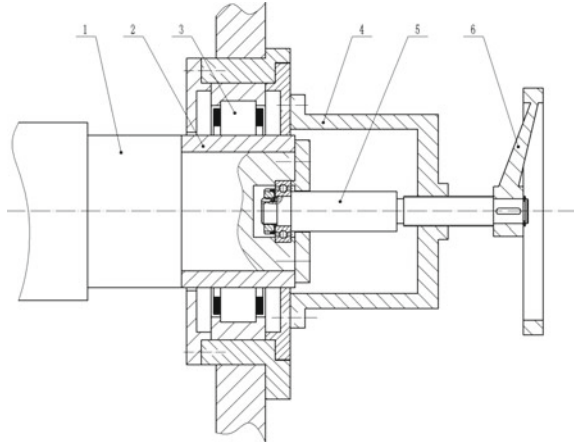

Fig. 88.1 General structure diagram of die cutting unit. *1* Main drive gear, *2* wall board, *3* rubber roller, *4* rubber cushion, *5* corrugated board, *6* cutting die, and *7* die roller

adjusting shaft is operated, the adjusting shaft as well as the die roller will be rotated. And under the action of thread driving, the adjusting shaft and the die roller can be also moved right to left.

88.4   Adjustment of Rubber Roller

### 88.4.1   Adjustment Along Axial Direction

The cushion covered on the rubber roller can protect the die blades and the rubber roller from being destroyed. But when both the die roller and the rubber roller make relative rotation, the cushion will be plunged by blades at the same position in any cycle. This means some area of cushion would be damaged repeatedly leaving others unused. In order to increase the life of cushion, axial adjustment of rubber roller is necessary.

Axial adjustment structure, shown in Fig. 88.3, adopts a special kind of cylindrical roller bearing RNU324 that has no inner ring. There is a sleeve assembled on a shaft segment of rubber roller. As a result, the rubber roller can slide along the bearing. The axial adjustment can be made by electrical or manual control. An eccentric wheel is continuously driven by motor or manual operation by way of a reducer, so rubber roller pushed by eccentric wheel can be moved right to left.

88.4.2   Gap Adjustment

Because corrugated board varies in thickness in the range 1–10 mm, the gap between die roller and rubber roller should adapt to the board thickness. It can be

Fig. 88.3 Axial adjusting
diagram of rubber roller.
1 Rubber roller, *2* sleeve,
3 RNU324, and *4* eccentric
wheel
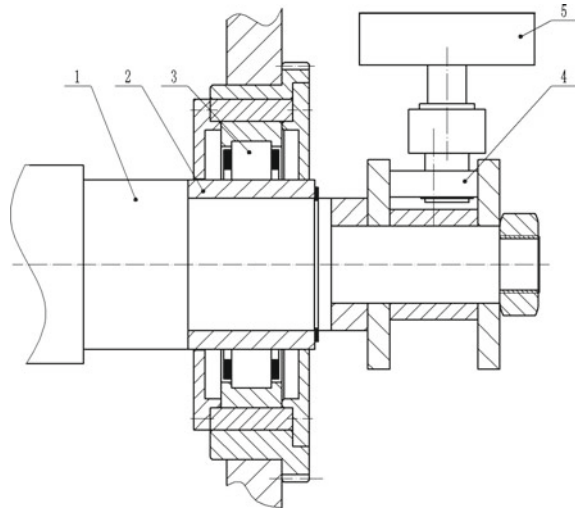
realized by moving either rubber roller or die roller. In this paper, the rubber roller
through an eccentric gear shown in Fig. 88.4 will be moved. An eccentric gear
means that there is a hole that is not concentric with gear axis in the gear solid.
When the eccentric gear is meshed and driven by the upper small gear, the rubber
roller would be forced to move up and down. So the gap between die roller and
rubber roller can be adjusted to appropriate position. Since it is based on the
RNU325 bearing, the rotation of eccentric gear has no effect on the one of rubber
rollers.

Fig. 88.4 Diagram on the
gap adjustment and speed
compensation. *1* Overrunning
clutch *2* cross-shaped
coupling, *3* drive gear, *4* small
gear, *5* RNU324, and *6* rubber
roller
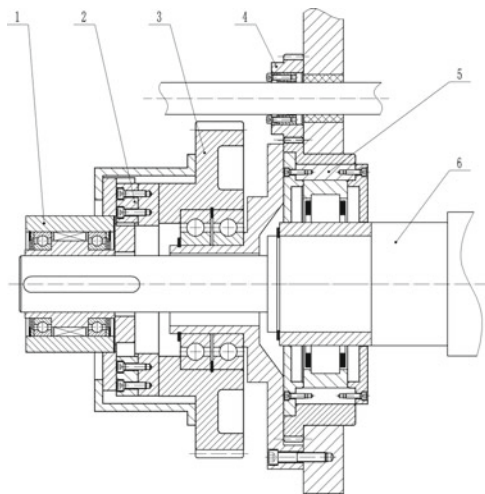
88.4.3   Speed Compensation

The rubber roller has theoretically the same linear speed as the die roller. Otherwise the corrugated board will be torn. However, after a long time wear, the diameter of rubber cushion becomes smaller, which leads to a lower linear speed. For this reason, an apparatus to compensate the speed difference must be equipped.

The apparatus, shown in Fig. 88.4, is made of driven gear, cross-shaped coupling, and overrunning clutch. The cross-shaped coupling links the driven gear and overrunning clutch together and the overrunning clutch works with the rubber roller by a key. So it is innovative that the rubber roller is controlled by driven gear not directly but indirectly. Under normal conditions, the rubber roller will rotate as long as the driven gear does. But if the linear speed of rubber roller cannot agree with one of die roller, the clutch will allow the rubber roller shaft to turn free. In this case, the rubber roller would be only driven by the moving corrugated board, not by driven gear. In this way, the linear speeds between the two rollers can keep accordance. With the compensating device, no matter how much the cushion diameter changes, the speed of the cushion can be compensated automatically without manual adjustment.

88.5   Conclusions

In recent years, with the rapid development of packaging industry, the request for die cutting technology and the performance of die cutting machine is much higher, and it has been paid much attention by industry. For the die cutting unit in the production line of corrugated carton, all the adjustment mechanisms mentioned above are absolutely necessary, and hence it is proved that they can meet the production requirement.

References

1. Geng, W. S., & Qi, Y. S. (2011). The design-manufacturing technology and the trends of the development of full automatic plane die-cutting machine. In *Proceedings of International Symposium on Advanced the Technology of Design and Manufacture* (pp. 125–130).
2. Zhang, X. S. (2007). *Process and equipment of post press* (pp. 251–260). China: Printing industrial Press.
3. Wu, Y. F. (2004). Working principle of common used die cutting machine. *Print World, 30*(9), 30312–30320.
4. Pang, C. H. (2007). Principle and application of die cutting technology. *China packaging News, 25*(3), 4–5.

Part VII
Paper and Related Technology

Chapter 89
Study on the Flexural and Water Absorption Properties of Mixed Office Wastepaper/Recycled-PP Composites

Xiaolin Zhang and Xiangfeng Bo

Abstract How to use the waste printing and packaging materials such as wastepaper, and waste plastic effectively has received considerable attention from the printing and packaging industry in recent years. In this paper, mixed office wastepaper (MOW) and recycled polypropylene (rPP) were used as the main raw materials to product composite materials by hot press molding process. The composition and morphology of MOW fiber, flexural properties, water absorption, and interfacial properties of composites were analyzed. The results found that MOW fiber mainly included cellulose, hemicelluloses, inks, and a certain amount of $CaCO_3$ filler, which can be used as reinforcement for wood-plastic composites (WPC). The maximum flexural strength (FS) of the composite with 30 wt% fibers increased by 65 % compared to rPP. The flexural modulus (FM) increased with the increasing of the fiber loading. With the increasing of the fiber content and the immersion time, the water absorption of the composites increased gradually. The water absorption rate tended to stability after soaking 150 h. The FS of the composites filled by 35 wt% MOW fibers decreased 14 % approximately after soaking two weeks. Scanning electron microscopy (SEM) found that when the MOW fiber content was 30 %, the composites had good interfacial performance.

Keywords Mixed office wastepaper · Waste plastic · Wood-plastic composites · Recycle utilization technology

X. Zhang (✉)
Faculty of Printing, Packaging Engineering and Digital Media Technology, Xi'an University of Technology, Xi'an, Shaanxi, China
e-mail: zxlbmm@sina.com

X. Bo
School of Mechanical and Electrical Engineering, Xi'an University of Architecture and Technology, Xi'an 710055, Shaanxi, China

89.1 Introduction

In recent years, along with the improvement of printing technology and office automation, the amount of the mixed office wastepaper (MOW) is increasing rapidly. The main ingredient of the MOW includes waste laser-printing paper and copy paper, which are mainly composed of pure wood pulp and known as the high-quality wastepaper in the paper making industry [1]. However, MOW is not the preferred secondary fiber in the paper making factory for its hard-deinking feature, which results in the restriction for the utilization of this kind of wastepaper. Exploring and developing of new technologies for the utilization of MOW resources has important practical significance in the field of using wastepaper sources effectively, improving the recycle rate of MOW and protecting environment.

In the field of wastepaper recycling industry, there are several main kinds of wastepaper, such as old newspaper (ONP), old magazine paper (OMG), and MOW. Several studies have reported the mechanical properties of the wastepaper reinforced composites [2–8]. Ashori and Nourbakhsh [5, 6] studied mechanical properties and water absorption behavior of fiber-reinforced polypropylene composites made by old Corrugated Container (OCC) and ONP. The authors suggested that OCC and ONP fibers could be considered as a good alternative source for WPC. Faisal and Salmah [7] researched the effect of maleic anhydride-polyethylene compatibilizing agent on mechanical and thermal properties of waste white paper-filled low-density polyethylene composites and found that the addition of compatibilizing agent can enhance dispersion of filler in matrix and improve the mechanical properties. All of these studies have proved that wastepaper can almost meet all the requirements in order to replace natural wood fibers in thermoplastic composites.

As a main kind of wastepaper, work done on MOW fiber-reinforced rPP composites is still limited. Therefore, the aim of this study was to investigate the potential of using the MOW and recycled plastic (polypropylene) as materials for making WPC. The fiber morphology, the mechanical properties such as flexural properties, water absorption properties and micrographs of MOW fiber-reinforced rPP composites were evaluated. The effect of water absorption on the flexural strength (FS) of the composites was also investigated.

89.2 Experimental

Materials. The MOW was collected in the office. The main components of the wastepaper included the waste laser-printing paper and the waste copy paper. The wastepaper was pretreated to dispersive fibers by multifunctional beater. Then the mixed office wastepaper fibers (MOWF) were dried at a 70 °C for 24 h in order to avoid moisture content. The recycled polypropylene (rPP) was obtained from a local recycled plastic factory in Xi'an city. Maleated polypropylene (MAPP) was supplied by Hefei Ampang Chemical Co., Ltd.

Experimental Method. The MOWF, rPP, and MAPP were blended in a SK-160B double-roller blender with different mixing temperature and mixing time. The composites were then collected and stored in zipper bags. The samples were produced by compression–molding using in a hot press at 180 °C under a pressure of 12 MPa for 15 min followed by cooling to room temperature under pressure.

Mechanical Properties. Flexural properties, such as FS and FM, were measured using a digital universal testing equipment (Model CMT6303) according to the GB/T 1449-2005.

Water Absorption Properties. The water absorption of the samples was measured according to GB/T 1034-2008 in which the samples were immersed in water for 24, 48, 72, 96, 120, 144,168, and 336 h. After excess water had been drained off, the weights were measured. The following equations are applied: $WA(\%) = 100 (M1 - M0)/M0$ (1), where WA is the water absorption percentage, and M0 and M1 are the sample weights weighed in a high-precision balance before and after immersion (g).

FTIR Analysis. FTIR-8400S Fourier infrared spectrometer was used to analyze MOWF specimens IR spectra. Date were collected from 4500 to 500 cm^{-1} wave length with 30 scans for each sample.

Scanning Electron Microscopy (SEM). Morphological studies were conducted using a scanning electron microscope (model JSM-6700F). In order to ensure the observing effect, specimens were sputter coated with gold for 2 h.

89.3 Results and Discussion

89.3.1 *Morphology Characteristics and Chemical Composition of the MOWF*

The morphological properties of the MOWF were tested by fiber morphology analyzer and the results were as follows: fiber length 0.722 mm, aspect ratio 35.6, fines content 24.6 %, and the kink index 2.24. The fiber length distribution is shown in Fig. 89.1. As can be seen, most of the fiber length of waste paper is distributed in the area of 0.5–1.0 mm, the second is the 0.2–0.5 mm range, and the fiber length distribution frequency turns lower and lower when the fiber length is more than 1.5 mm.

FTIR spectrum of the MOWF is presented in Fig. 89.2. It can be seen that the peak of absorbance at 3330 cm^{-1} corresponded to –OH functional group of MOWF. There are almost no bands at 1510 and 1605 cm^{-1} which belong to characteristic absorption peak of aromatic ring of lignin [8]. That means that a little quantity of lignin was contained in the MOWF [9]. The bands at 1450 and 874 cm^{-1} illustrate that there are a high content of ink and $CaCO_3$ filler in the sample.

Fig. 89.1 Wastepaper fiber
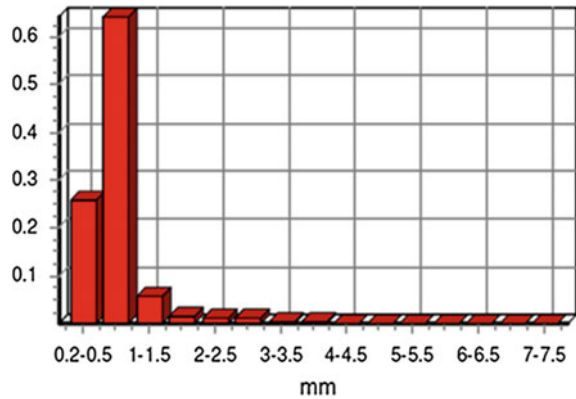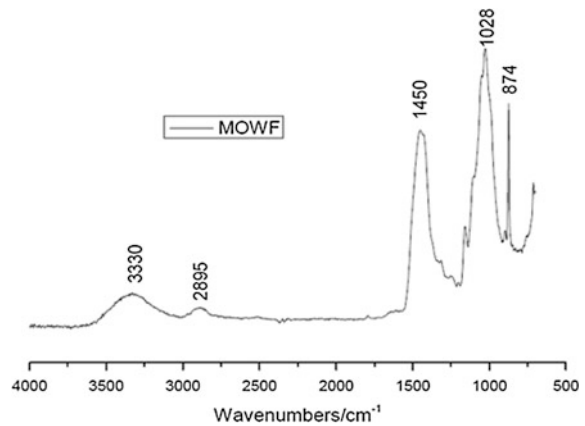length distribution


Fig. 89.2 FTIR of the
MOWF

89.3.2 Flexural Properties of the Composites

Figure 89.3 shows the effect of fiber loading on the flexural properties of
MOWF/rPP composites. It can be seen that the increase of MOW fiber loading does
significantly increase the FS and FM of the composites. The FS of rPP-based
composites is increased by 23 % when reinforced with 15 wt% of MOW fiber as
compared to neat rPP. As fiber loading increases FS increase up to a fiber load of
30 wt%. Further increase in the fiber loading results in a decrease in FS. The
improvement in FS achieved may be attributed to high strength of wastepaper
fibers, to the uniform dispersion of fibers in the matrix and to good interfacial
adhesion between the matrix and fiber by MAPP [10, 11].

From the curve of Fig. 89.3, it is obvious that FM of the composite exhibits a
gradual increasing trend with increasing fiber loading in the MOWF/rPP compos-
ites. The FM of rPP-based composites having 35 wt% of fiber content exhibits a
notable increase of 56 % when compare with rPP. This can be explained that, on the

**Fig. 89.3** Effect of MOWF loading on the flexural properties
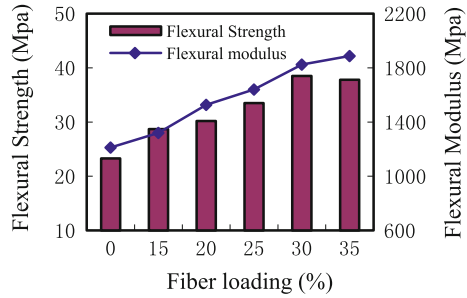
one side, the wastepaper fibers are stiffer than neat polymers [11], and on the other side, there are a high content of $CaCO_3$ and fines content in the fibers, which can improve the interfacial properties between fibers and the matrix as filler.

89.3.3   Water Absorption of the Composites

The effect of fiber loading and immersion time on water uptake of the composites is significant, as shown in Fig. 89.4. The water absorption increases with increasing MOW fiber loading in the composites. The PP is a kind of hydrophobic material which almost does not absorb any moisture. As we know from the FTIR spectrum of the MOWF, there are a lot of –OH hydrophilic groups in the fiber structure. Therefore, the moisture is mainly absorbed by the lignocellulosic fibers in the MOWF/rPP composites. When the MOW fiber content in the composite is low, the interfacial properties of the composites are good, i.e., that there is a good adhesion between fibers and matrix, less hydrophilic hydroxyl groups expose which results in the low-bibulous rate of the composites. As the fiber content increases, the exposed fiber ends in the composites and water residence sites increase, which results in

Fig. 89.4 Effect of immersion time on water absorption of the composites
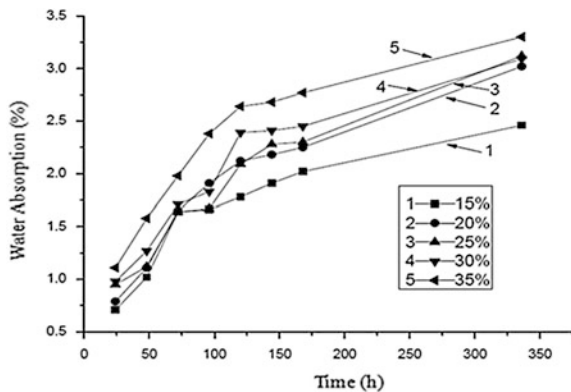
increasing water absorption [12]. That's why the water absorption of the composites with 35 wt% MOW fiber is much higher than that of other samples.

With the increase of immersion time, water absorption rate of the composites shows an upward trend. As the immersion time increases from 24 to 150 h, the water absorption rate of the composites increases rapidly, while that is gradually reduced when the water absorption time is over 150 h, as shown in Fig. 89.4. That is to say that the water absorption of the MOWF/rPP composites tends to increase up to 150 h of immersion. Because most of the fibers in the composites are coated with thin hydrophobic polymer film, and the moisture is mostly absorbed by the exposed fiber surface and some voids between the fibers and the matrix, the MOWF/rPP composites cannot reach saturation at short immersion times. The water absorption of the composites may be slowed down with the increasing of immersion time and trended to stable after about two weeks of immersion. A similar trend was observed by Bouafif et al. [12] who reported that WPC water uptake may actually be slowed down rather than delayed.

89.3.4 Effect of the Water Absorption on the Flexural Strength of the Composites

Water sensitivity is an important criterion for mechanical properties of plant fiber-reinforced composites. It can be seen from Fig. 89.5 that the FS of all of the samples decreases after two weeks of water absorption. The FS of the composites with 15 wt% fiber content is decreased by 9 %, while FS of the composites with 35 wt% fiber content decreases by 14 %, from 37.8 to 32.5 MPa when the composites are soaked in water for two weeks.

The low fall rate of the FS of the composites with less fiber content can be attributed to the good interfacial adhesion between the fibers and the matrix. With the increasing of the fiber loading, the quantity of the –OH hydrophilic groups are increased, and the water absorbing capacity in the composites is increased greatly

Fig. 89.5 Effect of the immersion time on the flexural properties (different fiber loading)
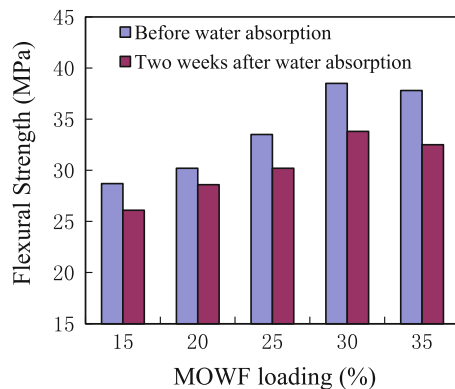
which lead to the bad interfacial properties. At the same time, the interface gap between fibers and matrix will turn wider and wider which results in the great decrease of the FS of the composites. Therefore, the interfacial adhesion of the composites with high-fiber loading should be further improved if we want to get high mechanical properties for this kind of composites.

89.3.5   SEM Microscopy

Figure 89.6 shows the photomicrographs of the MOW fibers and the MOWF/rPP composites with 30 wt% of MOWF. It can be seen from Fig. 89.6a that the surface of the MOW fiber is even and almost intact. Some fines are located on the surface of the long fibers or at the end of the fibers. We can also find that some fines and some

Fig. 89.6 SEM of **a** MOWF and **b** composites
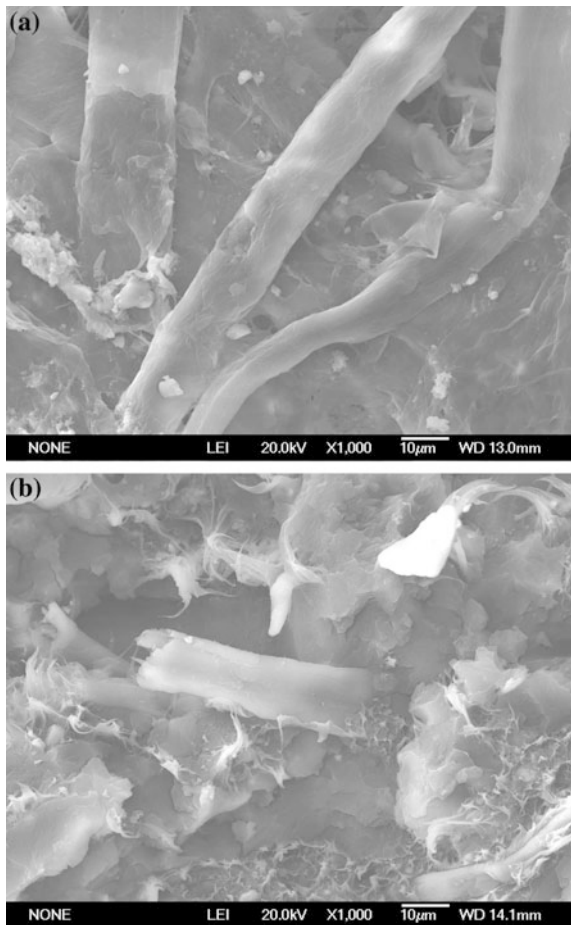
filler particles disperse between the fibers, which in good agreement with the results of the fiber morphology analyzer (89.3.1). Figure 89.6b shows the SEM micrography of the rPP-based composites filled with 30 wt% MOW fibers. From Fig. 89.6b, it is evident that the MOW fibers are well dispersed in the rPP matrix and the fibers are covered with a thin layer of matrix linking the fiber surface to the rPP. The interfacial adhesion between MOW fibers and rPP is so good which results in the better stress transfer for the composites. At the same time, there are too many fines and small particles ($CaCO_3$) which fill in the interstice between fibers and the matrix. These fillers can improve the interfacial properties and have a positive effect of the FM of the composites.

89.4 Conclusions

The MOW mainly included cellulose, hemicelluloses, inks, and a certain amount of $CaCO_3$ filler, which can be considered as a potential resource of low cost, environmental fibers for composites. It has been proved that the fiber loading can affect the FS and modulus of the rPP-based composites significantly. According to the results of this investigation, the highest FS of the MOW fibers reinforced rPP composites can be reached when the fiber loading is 30 wt%. The FM increased with the increasing of the fiber loading.

Both the MOW fiber content and the immersion time have the greatest effect on the water uptake of the composites. The water uptake increases substantially with increasing MOW fiber loading in the composites. The water absorption of the MOW fibers reinforced rPP composites may be slowed down with the increasing of immersion time and trended to stable after about two weeks of immersion. The water absorption behaviors can affect the FS of the composites obviously. The FS of the composites filled by 35 wt% MOW fibers decreased 14 % approximately after soaking two weeks. SEM photomicrographs found that when the MOW fiber content was 30 %, the composites had good interfacial compatibility.

References

1. Zhang, X., & Wang, R. (2012). Effect of deinking process on wastepaper fiber properties. *Transactions of China Pulp and Paper, 27*(1), 45–50.
2. Baroulaki, I., Karakasi, O., & Pappa, G, et al. (2006). Preparation and study of plastic compounds containing polyolefins and post used newspaper fibers.*Composites Part A, 37*(10), 1613–1625.

3. López, J. P., Boufi, S., El Mansouri, N. E., Mutjé, P., & Vilaseca, F. (2012). PP composites based on mechanical pulp, deinked newspaper and jute strands: A comparative study. *Composites Part B*, *43*, 3453–3461.

4. Huda, M. S., Drzal, L. T., & Mohanty, A. K. (2007). The effect of silane treated-and untreated-talc on the mechanical and physico-mechanical properties of poly(lactic acid)/newspaper fibers/talc hybrid composites. *Composites Part B*, *38*(3), 367–379.

5. Ashori, A., & Nourbakhsh, A. (2008). A comparative study on mechanical properties and water absorption behavior of fiber-reinforced polypropylene composites prepared by OCC fiber and aspen fiber. *Polymer Composites, 29*(5), 574–578.

6. Ashori, A., & Nourbakhsh, A. (2009). Characteristics of wood–fiber plastic composites made of recycled materials. *Waste Management, 29*, 1291–1295.

7. Faisal, A., & Salmah, H. (2012). Mechanical and thermal properties of compatibilized waste office white paper-filled low-density polyethylene composites. *Journal of Thermoplastic Composite Materials, 25*, 193–206.

8. Xu, Q. H., Wang, Y. P., Qin, M. H., et al. (2006). Fiber surface characterization of old newsprint pulp deinked by combining hemicellulase with laccase-mediator system. *Bioresource technology, 102*, 6536–6540.

9. Zhang, X., & Bo, X. (2013). Study on mechanical properties and water absorption behavior of wastepaper fiber-recycled polypropylene composites. *Polymers and Polymer Composites, 21*(6), 395–401.

10. García, M., Hidalgo, J., & Garmendia, I., & García-Jaca, J. (2009). Wood-plastics composites with better fire retardancy and durability performance. Composites *Part A*, *40*, 1772–1776.

11. Laurent, S. (2007). New application: PLA-wood fiber composites. *JEC Composites Magazine, 37*, 42–43.

12. Bouafif, H., Koubaa, A., & Perré, P., et al. (2009). Effects of fiber characteristics on the physical and mechanical properties of wood plastic composites. *Composites Part A*, *40* (12), 1975–1981.

Chapter 90
Studies on the Compound Conditions of Nano-SiO$_2$ Based ACQ Preservative

Xinyan Liu, Lili Yu, Xiaojun Ma and Lizhi Zhu

Abstract The stability of nano-SiO$_2$ based amine copper quat (ACQ) solution with different compound conditions was investigated using orthogonal and single factor tests in this paper. The results show that the degree of influence of various factors on the solution subsidence, in sequence, is: ultrasonication time > SiO$_2$:Sodium hexametaphosphate ratio > ACQ concentration > SiO$_2$ amount. The stability of the SiO$_2$ particles in the ACQ preservative solution first increases and then decreases as the ACQ concentration increases. The sedimentation rate of the SiO$_2$ particles in ACQ solution exhibits a linear increase when the amount increases. Thus, it is critical to select the reasonable compound conditions of ACQ preservative including the proportion of SiO$_2$/sodium hexametaphosphate and ultrasonication time to improve the whole stability of nano-SiO$_2$ within ACQ.

Keywords Amine copper quat (ACQ) · Nano-SiO$_2$ · Weatherability · Sedimentation rate · Dispersibility

90.1 Introduction

Given its light weight, good process ability, excellent resistance ability for biological hazard prevention, natural wood texture, pleasing esthetics, and many other advantages, preservative-treated wood has become a preferred material for wooden outdoor applications. However, the preservative wood treated has poor natural aging resistance in outdoor use because of the severe environmental conditions, such as the sun, rain, snow, dew, and sand [1, 2]. Some studies have shown that using a preservative solution containing chromium elements to treat the wood can improve its resistance to photolysis [3, 4]. However, it only can delay the process of

X. Liu · L. Yu (✉) · X. Ma · L. Zhu
College of Packing and Printing, Tianjin University of Science and Technology,
Tianjin, China
e-mail: yulilucky@tust.edu.cn

UV degradation and does not improve the anti-photochemical degradation of preservative-treated wood essentially [4]. Besides, the preservatives containing chromium are being prohibited or restricted to use in many countries [5]. The aging problem of the preservative-treated wood will not only reduce its service life but also increase its maintenance cost.

Nano-based technology has been introduced into wood research and presents new opportunities to enhance wood attributes more effectively [3]. Many new researches have been reported in wood modification, for example, the nanoparticle powder such as TiO_2, SiO_2, and ZnO, can improve the resistance abilities of wood decay fungi, insects and molds [6]. To increase the hydrophobicity of the inorganic silica particle, the surface is modified by different silane compounds [7]. It was reported that nano-SiO_2 was beneficial to improve the bonding strength of UF adhesive and subside its free formaldehyde emission [8].

Among of them inorganic nano-SiO_2 has strong ultraviolet absorption and infrared reflection features. The UV–VIS spectrum test of SiO_2 shows that the absorptivity of the ultraviolet light can be up to 70 % at the wavelengths within 400 nm, and the reflectivity of the infrared light also can be up to 70 % at wavelengths outside 800 nm. In addition, inorganic nano-SiO_2 has strong sterilization and insect resistance, and it is non-toxic, tasteless, environmental-friendly, and non-metallic [6]. When used in modified preservative solutions, it has a great development potential for improving the degradation ability of antiseptic processing material and promoting environmental protection. This research aims to investigate the ideal compound conditions of a nano-SiO_2 based preservative solution to enhance the outdoor weather resistance of amine copper quat (ACQ) treated wood.

90.2 Materials and Methods

90.2.1 Materials

Nano-SiO_2 (hydrophilic type, analytically pure) was produced by Zhejiang Hongsheng Material Technology Co., Ltd.; the average particle size was 20 nm and its purity was 99.5 %. Sodium hexametaphosphate was produced by Tianjin Kemi Chemical Reagent Co., Ltd. (analytically pure), 65.0–70.0 % content (calculated by P_2O_5). The active component in ACQ preservative is 15 %.

90.2.2 Treatments

0.01 g/0.05 g/0.1 g of nano-SiO_2 powder was obtained and placed in a beaker containing different concentrations of 45 mL ACQ solutions. The samples were then mixed with different amount of sodium hexametaphosphate. The ratios of

Table 90.1 The test conditions in the orthogonal test

Experiment no.	Concentration of ACQ (%)	Amount of SiO$_2$ (g)	SiO$_2$: Sodium metaphosphate	Ultrasonic time (min)
1	0.4	0.01	1:1	15
2	0.4	0.05	1:8	30
3	0.4	0.1	1:15	60
4	0.8	0.01	1:08	60
5	0.8	0.05	1:15	15
6	0.8	0.1	1:01	30
7	1	0.01	1:15	30
8	1	0.05	1:01	60
9	1	0.1	1:08	15

Table 90.2 The test conditions in the single-factor test

Experiment no.	Concentration of ACQ (%)	Amount of SiO$_2$ (g)	SiO$_2$: Sodium metaphosphate	Ultrasonic time (min)
1	0.8, 1, 1.4, 2	0.01	1:15	30
2	1	0.005, 0.01, 0.03, 0.05	1:15	30
3	1	0.01	1:1, 1:8, 1:15, 1:20	30
4	1	0.01	1:15	5, 15, 30, 60

sodium hexametaphosphate to nano-SiO$_2$ were 1:1, 8:1, and 15:1. The samples were stirred using a magnetic stirrer for 1 h and then subjected to ultrasonic processing for 15, 30, and 60 min to speed up the dispersion of the powder in the ACQ solution. To investigate the effects of different factors on the stability of the compound preservative solutions, an orthogonal test was used as shown in Table 90.1 L-9 (four factors and three levels).

According to the results of the orthogonal test, the effects of the ACQ concentration and SiO$_2$ content on the stability of the compound solutions were investigated using the single-factor analysis method. The proportion of sodium hexametaphosphate to SiO$_2$, the effect of ultrasonication time on the solution sedimentation rate, and the test conditions are shown in Table 90.2.

90.2.3 Measurement and Calculation

Sedimentation experiments were used to evaluate the stability of the compound preservative solution. The nano-SiO$_2$ based ACQ preservative prepared under different compound conditions was transferred to a 50 mL measuring cylinder and left to stand. After stabilization of the solution system, the volume of the

supernatant fluid was recorded and the sedimentation rate of the compound solutions was calculated according to Eq. 90.1,

$$W = \frac{V_1 - V_2}{V_1} \times 100\,\%$$ (90.1)

where
V_1 total volume of the compound solution (ml),
V_2 volume of supernatant fluid (ml),
W sedimentation rate (%).

90.2.4   Results and Discussions

90.2.4.1   Orthogonal Test Analysis

Given its small particle size and very large specific surface area, nano-SiO_2 is affected by Van der Waals forces in liquid media. As Wang et al. [9] pointed that nano-powder could be easily gathered together, and formed agglomerates, which would seriously obstruct the application of nanoparticles and subsequent preparation of the nano materials. In addition, given the complexity of components in the ACQ solution, it is essential to select the appropriate dispersant to make nano-SiO_2 disperse into ACQ sole union easily.

According to the results of the orthogonal test (Table 90.1), among the following factors, the optimal conditions of the sedimentation rate were: ACQ concentration is 1.0 %, SiO_2 amount is 0.01 g, SiO_2:Sodium hexametaphosphate ratio is 1:8, and ultrasonication time is 60 min. The degree of these factors on the sedimentation rate in sequence was: ultrasonication time > SiO_2: Sodium hexametaphosphate > ACQ concentration > SiO_2 quality.

The results are consistent with Sandberg [10] that ultrasonication can accelerate the dispersion of SiO_2 particles in the ACQ solution. An ultrasonication time of 60 min can completely dissolve the SiO_2 particles. The ratio of SiO_2 to sodium hexametaphosphate is another important factor for dispersion of SiO_2 particles in the compound solution. A previous study pointed out that sodium hexametaphosphate in aqueous solution can be ionized into $NaAB = Na^+ + AB^-$ [10]. Surface adsorption of SiO_2 in the solution was with negative charge, but the outer layer adsorption Na + positive charge formed the double electrode layer, and the diffusion layer was mainly made up of Na^+ and AB^-. Given the presence of a double electrode layer, the charged corpuscle would result in the repulsive interaction when Brownian motion, which ensures the stable existence of the double electrode layer, and prevents dissolving the SiO_2 particle in the solution.
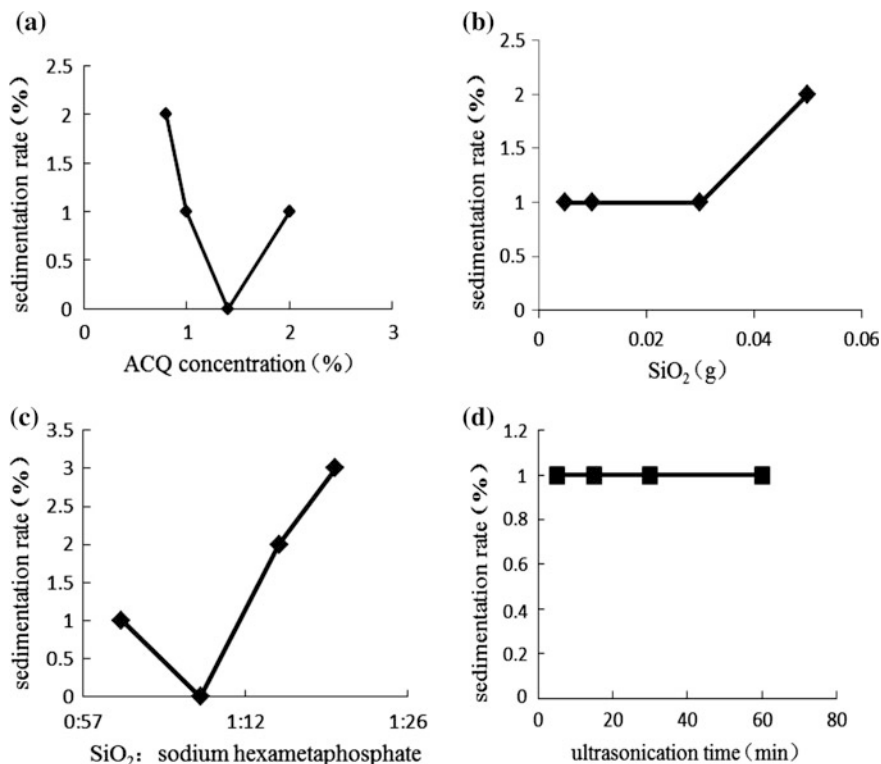
Fig. 90.1 The effects of different factors on the SiO$_2$ particle sedimentation rate in the ACQ preservative solution

90.2.4.2 Single-Factor Analysis

The effects of different factors on the SiO$_2$ particle sedimentation rate in the ACQ preservative solution are shown in Fig. 90.1. Figure 90.1a shows that ACQ concentration is a very important factor affecting the stability of the SiO$_2$ particles in the compound solutions, which will gradually increase with increasing ACQ concentration from 0.8 to 1.5 %. When the ACQ concentration was 1.5 %, 0.01 g of SiO$_2$ particles could be completely dissolved in the solution. However, when the ACQ concentration increased to 2 %, the opposite result could be observed. The reasonable reason is that a higher concentration of the ACQ solution contains large amounts of didecyl dimethyl ammonium chloride (DDAC), which is beneficial to SiO$_2$ particles dissolving in the compound solutions. The result conforms to the previous research [11], in which DDAC has been modified the compound solutions with montmorillonite particles, and it also has the similar tendency of the dispersion stability that the organic montmorillonite suspension liquids first increase and then decrease with increasing DDAC concentration. The results indicate that although

DDAC can increase the dispersion stability of SiO_2 particles in ACQ preservative solution, it can also inhibit the full dispersion of SiO_2 particles in excess amounts.

Figure 90.1b shows that the sedimentation rate of SiO_2 particles in solution exhibits a linear increasing trend with increase of ACQ concentration. At a certain concentration of ACQ solution, the amount of the allowed dispersed SiO_2 particle was fixed, and the excess SiO_2 particles cannot be dispersed into ACQ solution, which would cause the higher sedimentation rate. Figure 90.1c, d show that the proportion of SiO_2 and sodium hexametaphosphate and the ultrasonication time of the solution are also two important factors affecting the sedimentation rate of SiO_2 particles. Thus, for a certain concentration of ACQ solution, the reasonable proportion of SiO_2 and sodium hexametaphosphate and the reasonable ultrasonic time are critical to the stability of the compound solution.

90.3   Conclusions

The dispersion of SiO_2 particles in the ACQ preservative solution involves a series of complex chemical reactions obtained from the combined action of various factors. In this experiment, the optimal compound conditions of SiO_2-based ACQ preservative solution were ACQ concentration of 1.0 %, SiO_2 amount of 0.01 g, SiO_2:Sodium hexametaphosphate ratio of 1:8, and ultrasonication time of 60 min. The mechanism of the weathering resistance of SiO_2-based ACQ preservative-treated wood will be further studied to provide a theoretical direction for preservative-treated wood production in the faculty.

References

1. Yu, L., Cao, J., Gao, W., & Su, H. (2011). Evaluation of ACQ-D treated Chinese fir and Mongolian Scotspine with different post-treatments after 20 months of exposure. *International Biodeterioration and Biodegradation, 65*(4), 585–590.
2. Pali, J., & Tan, J. (2013). A photochemical method for improvement of color stability at polymer-wood biointerfaces. *Colloids and Surfaces B: Biointerfaces, 108*, 152–157.
3. Giorgi, R., Chelazzi, D., & Baglioni, P. (2005). Nanoparticles of calcium hydroxide for wood conservation. The deacidification of the vasa warship. *Langmuir, 21*, 10743–10748.
4. Panov, D., & Terziev, N. (2009). Study on some alkoxysilanes used for hydrophobation and protection of wood against decay. *International Biodeterioration & Biodegradation, 63*(4), 456–461.
5. Evans, P. (2003). Emerging technologies in wood protection. *Forest Products Journal, 53*(1), 14–22.

6. Yang, Y., Bao, B., & Shen, Z. H. (2012). Outdoor mold-resistance and flame retardance of Pinus massoniana treated with nano-ZnO. *Journal of Zhejiang A & F University, 29*(2), 197–202.

7. Hu, Y. H., Chen, C. Y., & Wang, C. C. (2004). Viscoelastic properties and thermal degradation kinetics of silica/PMMA nanocomposites. *Polymer Degradation and Stability, 84*, 545–553.

8. Lin, Q. J., Yang, G. D., & Liu, J. H. (2005). Application and mechanism principium research on nano-SiO2/ureaformaldehyde resin. *Journal of Fujian College of Forestry, 25*(2), 97–102.

9. Wang, M., Wu, Y. Q., Hu, Y., et al. (2012). Dispersion and interface characteristics of nano-TiO$_2$ based wood preservatives. *Journal of Central South University of Forestry & Technology, 32*(1), 51–55.

10. Sandberg, D. (2006). Crack formation due to weathering of radial and tangential sections of pine and spruce. *Wood Material Science and Engineering, 1*(1), 12–20.

11. Jiang, Y. H. (2011). *Preparation of micronized montmorillonite suspension and the properties and characterization of treated wood*. Beijing: (PhD thesis of Beijing Forestry University), 1–144.

Chapter 91
Research on Secondary Fiber Elastic Repair for High-Strength Packaging Materials

Xiaojuan Shi, Chao Li, Wensheng Wang, Junyan Huang, Huanxiu Liu and Qi Xu

Abstract To research the method of improving the secondary fiber strength for high-strength packaging paper products, on the basis of analyzing the secondary fiber species and performance, we emphatically analyzed the principle and repair effect of mechanical method and enzymatic method. Probing the effect of repair technology of secondary fiber combined with the two methods has environmental characteristics. The results demonstrate that mechanical treatment and enzyme treatment method can make the secondary fiber main packaging performance increased by more than 20 % including ring crush strength and breaking length. Combining the two methods will be more to restore the strength of the secondary fiber performance.

Keywords Secondary fiber · Elastic restoration · Paper products · Mechanical method · Enzymatic method

91.1 Introduction

Secondary fiber, as an important source of fiber, not only can ease the papermaking raw material shortage and energy shortage of contradictions, but also can reduce the increasingly serious problem of environmental pollution and have an important role to maintain the ecological balance of the region [1]. If the plant fiber can be repeatedly used, its social significance and economic benefits will be considerable. The world waste paper pulp production has exceeded the world's total output of 1/3, which is only after chemical pulping. The rapid increase of waste paper utilization is becoming the important development trend of the world paper industry [2–4].

X. Shi (✉) · C. Li · W. Wang · J. Huang · H. Liu · Q. Xu
Dalian Polytechnic University, Dalian, Liaoning, China
e-mail: shixj@dlpu.edu.cn

Facing the greatly increase trend of the use of secondary fiber, how to improve the quality of secondary fiber, researching the recovery mode and processing technology, and the application of direction are significant problems to be urgently resolved. The annual wrapping paper amount is more than 60 % of paper and paperboard consumption. On the one hand, the packaging waste generated a lot of secondary fiber source; on the other hand, the repeatedly used paper is hard to meet the high performance requirements of packaging paper. It is significant to research on the repair technology of the secondary fibers, the maximum degree of resilience, and the strength of the fiber. From this point of view, this paper studies the appropriate secondary fiber repair methods and technology.

91.2 Secondary Fiber Processing Method

91.2.1 Mechanical Pulping and Grinding Processing

Traditional low concentration beating of secondary fiber has certain effect, but it will cut off the fibers seriously, and add to the damage of secondary fiber. In addition, the surface of secondary fiber fine fibrosis is low and uneven; it is arduous to meet the requirements of packaging and printing required for high-strength products. The medium concentration beating can meet the above requirements. Firstly, when beating at higher concentration (more than 6 %), the main force for fiber is "internal friction." Under the action of the force, the horny layer of secondary fiber has been peeled, and more hydroxyl groups were free. Hydrogen bond of the fiber was regenerated. Secondly, due to the generation of fiber "spillover effect" and special structure of medium concentration beating plate [5, 6], the secondary fiber surface crust phenomenon and cell-cavity-closed phenomenon were partially activated. As a result, absorbing the moisture and swelling can enhance the deflection of secondary fiber. Fiber length has been retained after beating, fiber strength has less loss, and fiber surface fine fibrosis was improved. This is conducive to the production of high-quality packaging board.

91.2.2 Enzymatic Method

The recovery of the properties of the secondary fibers by biological enzymes is a new research method for the production of international paper products in recent years. Different processing methods have varying degrees of impact on secondary fiber protective ability of water, surface activity, and paper physical properties [7]. Enzymatic treatment saves energy, and environmental load is small and has higher research and application value.

Foreign researchers have studied the secondary fibers of the enzyme to improve their performance. The results of Sarkar and Jackson manifest that cellulose and compound cellulose can effectively improve the filtering performance of the secondary fiber. Thus, the fiber strength property has the minor loss [8, 9]. Stork et al. treated secondary fibers of different properties and compositions by cellulose, compared with waste pulp containing more chemical pulp and mechanical pulp. They found the latter was better [10]. After the biological enzymatic treatment, the physical properties of the paper made with these secondary fibers can be improved, including the tightness of the paper, tensile strength, and smoothness of the paper. There are also a few studies published in China, but it is not many researches with the purpose to produce high-strength packaging paper products regardless of domestic and foreign.

91.3 Experiment and Research Methods

91.3.1 Studies on the Modification of Pulp Concentration Change

Choose domestic scrap carton, beat in the low (3.5 %) and medium (6.5 %) concentration to the beating degree we needed, and then make paper. Test items are as follows: (1) beating degree; (2) wet weight (WW, g); (3) ring crush index (RCI, N m/g); and (4) tensile strength to express with transverse breaking length (BL, Km).

91.3.2 Modified Experiment of Enzymatic Treatment

Use domestic scrap corrugated paper, treat them with cellulose and hemicellulose at a certain concentration after low concentration beating of 3.5 % in the beating degree we desired, and then make papers. Treated conditions are as follows: Pulp concentration was 6 %; the dosage of cellulose and hemicellulose were 0.2 and 0.1 U/g, respectively; temperature was 50 °C; pH was 4.5; and treated time of cellulose and hemicellulose were 20 and 30 min, respectively. The beating degree was 31° SR. These conditions are obtained from the experimental exploration [4].

Test items are as follows: (1) beating degree; (2) water retention (WR, %); (3) breaking length (BL, Km); (4) ring crush index (RCI, N m/g); and (5) pore rate (PR, %).

91.3.3 Modification of Mechanical Treatment and Enzymatic Treatment

Improving the beating concentration and enzymatic treatment method can both recover the properties of secondary fibers to some extent. But there are some limitations. In order to explore the method of restoring the fiber properties greatly, the paper carried out the exploration of the combination of the two methods. Pretreat the secondary fibers before beat and detect the effect of performance improvement.

Used domestic scrap corrugated paper, treated with enzymatic first, and then beat under medium concentration, finally made papers. Test items are as follows: (1) beating degree; (2) wet weight; (3) ring crush index; and (4) tensile strength to express with transverse breaking length.

91.4 Results and Analysis

91.4.1 Studies on the Modification of Pulp Concentration Change

Figure 91.1 shows the comparison of the secondary fiber with medium concentration (M) and traditional low concentration (L) refining effect with the beating degree 31° SR. Test results indicated that in the same beating degree, the medium concentration beating wet weight was about 26 % higher than the low concentration beating, breaking length was about 20 % higher, and ring crush strength increased much more. This manifested that medium concentration beating made the fiber length retain and water retention capacity better [3]. As a result, the breaking length and the ring crush strength were greatly improved. It can meet the requirements of high-strength corrugated paper.

Fig. 91.1 Effect comparison of low and medium concentration in waste pulp beating
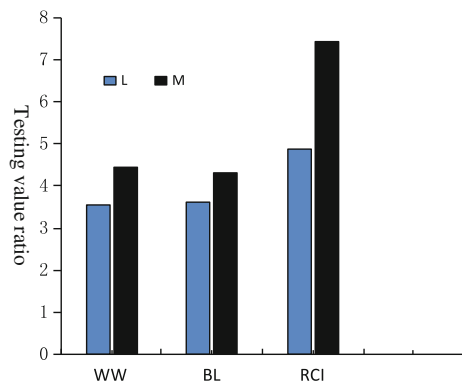
The secondary fiber after the medium concentration beating suffered more friction, extrusion, and rubbing from fiber interior and between the fibers. It could promote the rigid secondary fiber resilience. On the other hand, it has played a role of fully rubbing fiber surface, stripping surface crust, and re-refining the secondary fibers. At the same time, the high concentration of beating loosed internal structure of the secondary fibers, exposed free hydroxyl, and increased the water retention. Therefore, in the same beating degree, the secondary fiber pulp after the medium concentration beating had higher wet weight, and higher physical strength, conformed to the high strength of packaging corrugated paper.

91.4.2 Modified Experiment of Enzymatic Treatment

Figure 91.2 shows the comparison of properties results of the corrugated core paper by enzymatic treatment. By modified with enzymatic treatment, the water retention of secondary fibers improved about 20 %, closed to the primary fiber. This shows that under the action of the enzyme, a large amount of hydroxyl was free from the enzyme destroyed crystallization region, increased the capacity of secondary fiber swelling. The porosity of the paper was greatly reduced after papered. It also confirmed that the increase of the free hydroxyl group made more hydrogen bond when the fibers were woven. Swelling made the fibers became soft and more closely interwoven; as a result, the breaking length and ring crush index were improved substantially.

An important property of the carton is moisture resistance. In order to detect the moisture resistance of secondary fiber products by enzymatic treatment, place the paper samples of secondary fibers treated with enzyme in environment of humidity 80 %. Detecting the ring crush strength, we found that the drop of the ring crush was lower than that of the untreated samples. The enzymatic treatment made the secondary fiber packaging board has certain moisture resistance and could still

Fig. 91.2 Performance comparison of different secondary fibers
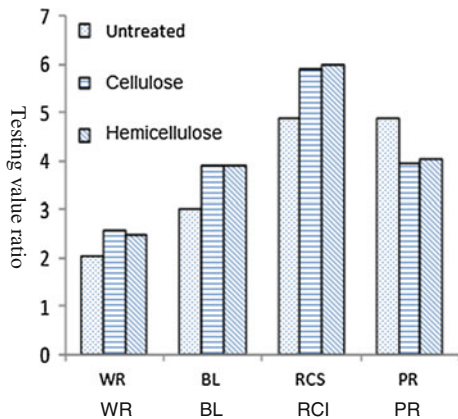
maintain better strength in wet environment. It is an essential performance for the use of high-strength corrugated paper packaging boxes.

91.4.3 Modification of Mechanical Treatment and Enzymatic Treatment

The results manifested that the beating degree was 31° SR, the wet weight was 5.3 g, the ring crush index was 8.3 N m/g, and the transverse breaking length was 4.8 km. The performances have greatly improved than ones of medium concentration only. Pretreatment before beating of the pulp with cellulose, hydroxyl groups in the fiber can be released in limited, the fiber surface has been a certain degree of activation and relaxation, promote fiber swelling and fine fibrosis degree, and beating performance is improved. It could also play a role in reducing the energy consumption of refining. For this reason, the combination of the two secondary fiber processing method was the value further experimental research and extension.

91.5 Conclusions

(1) The waste carton secondary fiber beating concentration increased from 3.5 to 6 %, the breaking length could be raised from 3.62 to 4.33 km, and the ring crush index was raised from 4.88 to 7.42 N m/g. Enzymatic treatment before beating could increase the ring crush index to 8.3 N m/g and increase the breaking length to 4.8 km.
(2) The corrugated paper secondary fiber of enzymatic treatment could increase the breaking length from 3.03 to 3.93 km and increase the ring crush index from 4.9 to 6.3 N m/g. The effects of cellulose and hemicellulose were similar.
(3) Combination of mechanical treatment and enzymatic treatment method could greatly improve the secondary fibers elastic degree of repair. They could be directly used as high-strength packaging board.

References

1. Zhan, H. (1999). One of the lectures about waste classification and the change of the nature of the regeneration process of waste paper recycling technology. *Guangdong Paper Making, 1*, 48–52.
2. Fillat, U., de Eugenio, L. I., & Martínez, M. J. (2015). Assessing enzymatic deinking for secondary fibers paper recycling in the presence of flexographic inks. *Chemical Engineering Journal, 260*(15), 486–491.

3. Kanking, S., Niltui, P., & Wimolmala, E. (2012). Use of bagasse fiber ash as secondary filler in silica or carbon black filled natural rubber compound. *Materials and Design, 41*(12), 74–82.
4. Bhardwaj, N. K., Kumar, S., & Bajpai, P. K. (2014). Effect of zeta potential on retention and drainage of secondary fibres. *Colloids and Surfaces A: Physicochemical and Engineering Aspects, 260*(7), 245–250.
5. Liu, S. I., Cao, G. P., Li, S. Y., et al. (2004). Strong beating to high strength in the packaging paper production practice. *Journal of Shanxi University of Science and Technology, 22*, 13–17.
6. Liu, S. I., Li, S. Y., Chen, Z. H., et al. (2000). ZDPM Hydraulic disc mill in beating production application. *China Papermaking, 4*, 14–18.
7. Cui, X-l. (2007). The application of enzymes in papermaking industry. *Hubei Paper Making, 2*, 31–34.
8. Sarkar, J. M., Cosper, D. R., & Hartig, E. J. (1995). Applying enzymes and polymers to enhance the freeness of recycled fiber. *Tappi Journal, 78*(2), 89–95.
9. Jackson, L. S., Heitmann, J. A., & Joyce, T. W. (1993). Enzymatic modifi2 cations of secondary fiber. *Tappi Journal, 76*(3), 147–154.
10. Stork, G., Pereira, H., Wood, T., Dusterhoft, E., Toft, A., & Puls, J. (1995). Upgrading recycled pulps using enzymatic treatment. *Tappi Journal, 78*(2), 79–88.

Chapter 92
The Amount of Modified Acrylate Effects on Paper Performance for Printing Electronics

Bei Liu, Congjun Cao and Zhen Jia

Abstract In the digital age, while people enjoy the convenience of electronic products, we also have to face the problems of the electronic waste disposition. The most promising way to solve this problem is to use paper instead of non-biodegradable polymer, but paper has the strong capability to absorb conductive ink, which diffuses readily, and the roughness of paper surface has impact on the conductivity of the line, so that it limits paper's application area. This paper mainly discussed how the concentrations of modified acrylic resin in the coating liquid affected coated paper's surface structure and ability and how the paper's ability finally affects the printed circuit quality. Then, we analyze the appearance quality and electrical conductivity of the conductive lines printed on the coated paper by screen printing. The conductive ink can form the compact line on the coating paper, which improves the circuit's conductivity. The method used in this experiment can make the coated paper suitable for printing.

Keywords Paper · Acrylate · Surface modification · Printed electronics

92.1 Introduction

A huge amount of E-waste is formed with the development of information technology and the replacement rate of electronic products in recent years [1]. According to United Nations Environment Program estimated, it is about 20 million to 500 million discarded electronic products, with the growth rate of 3–5 % per year [2]. E-waste becomes a new kind of environmental pollution after chemical industry, metallurgy, pulp and paper making, and dyeing waste after the industrial era [3]. Researchers use R2R or inkjet to print on paper for low-cost "electronic paper" [4]. Paper and conductive metal can be recycled by puller and flotation cell,

B. Liu (✉) · C. Cao · Z. Jia
Xi'an University of Technology, Xi'an, Shanxi, China
e-mail: 08liuxiaobei@163.com

so it is a kind of potential "green" electronic materials. The typical requirement of very smooth and non-absorbing substrates for printed electronic components is an important issue while using paper. The surface can be laminated with polyethylene (PE), polypropylene (PP), PET, wax, or aluminum. In the literature, polymer-covered paper substrates have been used to demonstrate electrochemical displays [5]. While these paper coatings compromise the low cost and recyclability, this might still be acceptable for relatively high-value electronic applications that required relatively expensive materials, many processing steps, and encapsulation [6]. The main effect of modified acrylic resin article can smooth the paper surface and enhance oil resistance and waterproof. In this research, it mainly discussed the relationship between paper surface properties and the printed conductive circuit quality.

92.2 Materials and Methods

92.2.1 Paper Samples and Conductive Ink

Several types of paper samples were compared in order to evaluate the relationship between the paper property parameters and printed circuit qualities by different coating materials. Properties of base paper are listed in Table 92.1.

A precoated wood-free base paper (multipurpose, Chenming Paper Holdings Limited) was coated with a barrier layer. The barrier layer consisted of kaolin (Kemiou Chemical reagent Ltd.), PCC (Kemiou Chemical reagent Ltd.), and silica (Kemiou Chemical Reagent Ltd.) with fluoroacrylate polyacrylate (FP) (Laboratory synthesis) as binder [7]. Carboxymethyl cellulose (Kemiou Chemical Reagent Ltd.) was used as thickeners. Besocoll (Ciba Specialty Chemicals Ltd.) was used as sizing agent. They were mixed together in the water, and then coated on the paper for a grammage of 10 g/m^2. It is used as the barrier layer. The coating formulation is shown in Table 92.2.

The mixture was mixed by the high cuts of the dispersible mulser (AD 300SH, Xi'an Dafu Experiment Instrument Ltd.). The coating liquid was required to ensure free runnability on the curtain coating roller (XB rod coating apparatus, Wanjiang Guangmei Precision Instrument Ltd.). 80 g/m^2 copypaper was used as coating substrate. After coating, the paper was calendared with a laboratory three-roll soft calender (DP, DT-Science Ltd.).

Table 92.1 Quality of paper

Thickness/mm	Smoothness/s	Tensile strength N/mm^2		Glossiness/GU
		Transverse	Vertical	
0.09	34.4	33.77	14.13	3.8

Table 92.2 The coated substrates of barrier-coating formulation

Substrate	1	2	3	4	5	6	7	8
Kaolin (%)	15	15	15	15	15	15	15	0
PCC (%)	10	10	10	10	10	10	10	0
Thickeners (%)	1	1	1	1	1	1	1	0
Sizing agent	0.1	0.1	0.1	0.1	0.1	0.1	0.1	0.1
FP (%)	8	12	16	20	24	28	32	100
Water	65.9	61.9	57.9	53.9	49.9	45.9	41.9	0

92.2.2 Sample Property Analysis

The surface roughness was measured with Bekk smoothness tester (PN-BST, Jingtong boke Automation Technology Ltd.) according to ISO 5627, and the glossiness was characterized with a vancometer (BYK4446, Shanghai Jingtian Instrument Ltd.) according to ISO 8254-1:2009. The sizing degree was tested according to GBT 5405-2002. Contact angle measurements were performed according to test method Tappi T558 om-07. Drop absorption tester (JC2000A) was used to test with 4 μL distilled water. Measurements were made for getting the water contact angle on the test paper.

92.2.3 Functional Ink

Laboratory preparation graphite conductive inks (Table 92.3) were used for printing [8]. Carbon black dissolved in a solvent mixture of water-based polyurethane (Huachi Chemical Co. Ltd.), water-based acrylic resin (Huachi Chemical Co. Ltd., Guangzhou), absolute alcohol (Sanpu Chemical Co. Ltd.), and glycerol (The Second Tianjin Chemical Plant) in deionized water, according to the formula. The solvent mixture should be adjusted for pH to 8.3–9 by ammonia water (25–28 %)

Table 92.3 The formula for conductive ink

Substrate	Wt/%
Water-based polyurethane	1.8
Water-based acrylic resin	1.8
Carbon black	3.6
Water	89.39
Ammonia water (25–28 %)	0.36
Absolute alcohol	1.80
Glycerol	0.61
Antifoaming agent	0.16
Dispersant	0.48

(Jinchao Co. Ltd.). After mixture by blender (JY-40B, Changzhou Guangqi Chemical Instrument Ltd.), the conductive ink was finely powdered by three-roll grinder (SG65, Jingben Machinery Co. Ltd.).

92.2.4 Printing Methods

Conductive ink was filtered through 80 mushes net three times to ensure good printing. Screen printing was carried out with 80 mesh counts screen to form conductive lines with different widths (2, 4, 6, 8, 10 mm). After screen printing, the substrates were first dried in an oven at 50 °C for 20 min to remove solvents. The samples were then subjected to be analyzed by scanning electron microscopy (JSM-6700, JEOL Co. Ltd.) for high-resolution imaging of paper topography and cross sections.

The resistance of printed line was measured by multimeter (TES-2732, TASI Electronic Company). Wire width and length were measured with ruler, and the resistivity was calculated by formula (92.1)

$$\rho = R \frac{S}{L} \tag{92.1}$$

In the formula, S is the cross-sectional area, L is the length of conduct line, R is the resistance, and the layer thickness calculated is 3 μm ($S = s \times L$).

92.3 Results and Discussion

92.3.1 Analysis of Products

FTIR showed that the strongest absorption peak of O–H in the polyvinyl alcohol appears at 3338 cm^{-1}, the characteristic absorption peak of C–H in the benzene ring appears at 3027 cm^{-1}, the absorption peak of C–H in the –CH$_3$ appears at 2924 cm^{-1}, the absorption peak of C=H appears at 1725 cm^{-1}, the absorption peak of C=H in the benzene ring appears at 1451 cm^{-1}, the absorption peak of C–O–C in the ester group appears at 1155 cm^{-1}, the absorption peak of symmetric and asymmetric C–F appears at 1098 and 1237 cm^{-1}, the absorption peak of O–H in the carboxyl appears at 1155 cm^{-1}, the absorption peak of quaternary ammonium salt appears at 950 cm^{-1}, and the absorption peak of C–H on the benzene ring appears at 752 cm^{-1}. This polymer map confirms that each monomer exists in the copolymer by means of Fourier transform infrared spectrometer (Fig. 92.1). Fluoropolymers have characteristics of waterproof and oil proofing. It can endow the paper with unique performance [9].

Fig. 92.1 FTIR spectra of the polymer
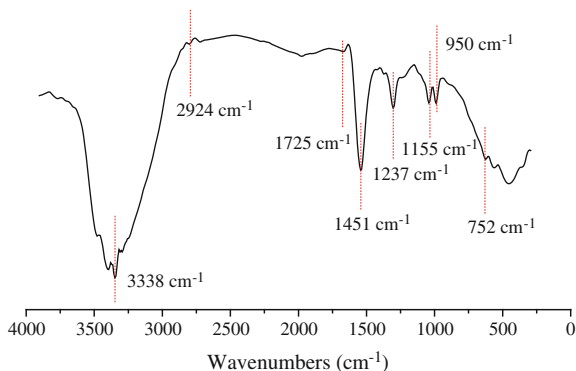
92.3.2   Paper Properties

Papers were coated by different amount of fluoroacrylate polyacrylate emulsion. After coating, they were dried and calendered, then the testing samples were obtained, and their performance tests' results are shown in Fig. 92.2. The characteristic of coating formula was concentration of fluoroacrylate polyacrylate (FP) change, according to Table 92.2. The most probable reason for this is the fluoroacrylate polyacrylate can increase the water resistance property of paper, which significantly improves the water contact angles and sizing degree. In addition, kaolin has hexagonal flake structure and fluoroacrylate polyacrylate latex has good film-forming properties [10]. When they are mixed together, fluoroacrylate polyacrylate latex can change pigment particle dispersion and arrangement and porosity size and distribution [11]. With increasing the amounts of fluoroacrylate polyacrylate latex, coating porosity is declining. Coating porosity controls penetration by liquids, thus paper performance is improved. Because paper surface was finished by calendaring, the smoothness and the glossiness were increased. With increasing amount of fluoroacrylate polyacrylate, kaolin was well dispersed and coating layer got better surface qualities after calendaring.

92.3.3   Print Quality and Conductivity

The conductive graphite particles form had irregular borders and its size is about 10 μm as shown in Fig. 92.3a. The conductive line image was clear-cut by screen-printing in Fig. 92.3b. We printed four sizes square, four width lines, and two length lines to analyze screen printing accuracy. The finest line width of 2 mm can be accurately printed, so we can use this kind of printing method to print RFID tag, film transistor, and so on. In this research, fluoroacrylate polyacrylate latex was used for getting high sizing degree. We chose four kinds of coated paper with different formulations to print, in order to study coating and how to influence
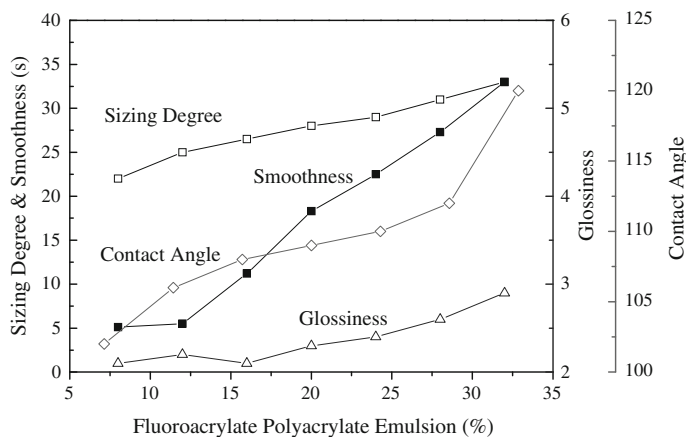
Fig. 92.2 The relationship between fluorinated acrylate emulsion amount and paper quality

printed circuit. They are sample 1, sample 2, sample 3, and sample 4. We studied the printed line surface situation and the cross section of each samples, and the results are shown in Fig. 92.3c–f and i–l. It obviously affects the surface conjunctiva of the printed line by the fluoroacrylate polyacrylate latex amount. There exists an obvious law that the ink film had less effect on "coffee ring" and was smoothened in the surface, and the ink connected with paper was more compact in the paper's Z-direction with increasing amount of fluoroacrylate polyacrylate latex.

The coffee stain effect is a common phenomenon in ink-jet printing, and it also occurs in this test, especially the ink contained a lot of water. It is caused by faster evaporation at the edges of the deposited low viscosity ink and the larger air interface while ink occurs in the compensating capillary flow at this place. Another problem is it effects on conductivity and it is detrimental. The visible conductive line breaks can explain that the non-conducting and electrical measurements support this result.

The printed layers often contain pinholes in the Z-direction. There is no report above defect-free layers. This kind of water-based graphite conductive ink dries through solvent evaporation [12]. Recent studies [13, 14] show that ink spreading and the final printed shape strongly depend on the viscosity, which in turn is a function of the molar mass of the polymer. As paper sizing degree increases, the ink drying characteristic has more effect on its own characteristics. The surface tension gradient creates an opposing Marangoni flow, which results in recirculation of the solvent in the printed line [15]. The resistance of printed line is different after drying. The cross section of printed line with changing paper surface characteristics reveals a formation change from a "hill-like" to a "ring" formation [16].

Moreover, the structure of printed circuit is studied, and the result is shown in Fig. 92.3h. Some graphite particles flocculate into a unit. Some units link together, while some units have some distance. Hence the printed lines have a different
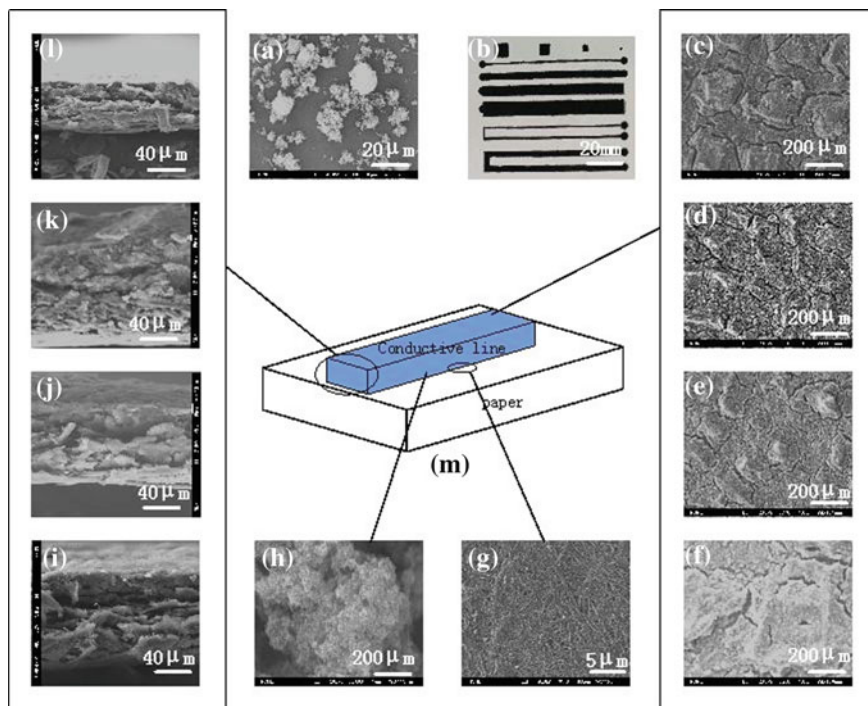
Fig. 92.3 Printed conductive line. **a** SEM image of graphite powder. **b** Optical image of the printed conductive graphite line on the paper. **c** SEM of the surface of printed line on the sample 1. **d** SEM of the surface of printed line on the sample 2. **e** SEM of the surface of printed line on the sample 3. **f** SEM of the surface of printed line on the sample 4. **g** SEM of the printed line edge on the sample 4. **h** SEM of the conductive graphite in the conductive line. **i** Cross-sectional SEM image of the printed line on the sample 4. **j** Cross-sectional SEM image of the printed line on the sample 3. **k** Cross-sectional SEM image of the printed line on the sample 2. **l** Cross-sectional SEM image of the printed line on the sample 1. **m** Printed circuit schematic diagram

conductivity, even by the same conductive ink. If the conductive material can contact closer, the conductivity should be increased.

This study also analyzed the line edge. The result shows in Fig. 92.3g, the graphite conductive ink is diffused at the printed circuit edge and it cannot be seen by eye. That is mainly due to the high water content in the conductive ink. During volatile drying process, a part of the water could not be dried in time and this makes the graphite to get out of the boundary. Therefore, the printing accuracy can be improved by increasing the volatility of ink.

Line raggedness was discussed by SEM and could be found to have relationship with resistance. Then, we studied the printed line resistance on different paper samples, and the results are shown in Table 92.4. Even the resistance of each line is big, the resistivity decreased with the enhanced performance of the paper.

Table 92.4 Electrical conductivity test results

Sample	1	2	3	4
Resistivity ($\Omega \cdot m$)	0.746	0.700	0.550	0.268

92.4 Conclusions

Coating is suitable method for regulating paper surface structure in pilot or full industrial scale. It can improve electronics printability through increasing quality of smoothness and water resistance. The functional coating allowed using curtain chemistry to get the closed and sealed coated layer. This kind of layer is suited for printing functional devices, such as transistor, RFID, cells, and so on, which need no-absorbing surface to form the functional conductive line. We still do not get the most suitable lay, so that there is a lot of work to do for selecting the best performing materials for electronic printing.

References

1. Grant, R., & Oteng-Ababio, M. (2012). Mapping the invisible and real "African" economy: Urban e-waste circuitry. *Urban Geography, 33*(1), 1–21.
2. Sthiannopkao, S., & Wong, M. H. (2013). Handling e-waste in developed and developing countries: Initiatives, practices, and consequences. *Science of the Total Environment, 463*, 1147–1153.
3. Nnorom, I. C., & Osibanjo, O. (2008). Overview of electronic waste (e-waste) management practices and legislations, and their poor applications in the developing countries. *Resources, Conservation and Recycling, 52*(6), 843–858.
4. Kiddee, P., Naidu, R., & Wong, M. H. (2013). Electronic waste management approaches: An overview. *Waste Management, 33*(5), 1237–1250.
5. Andersson, P., Nilsson, D., Svensson, P.-O., Chen, M., Malmström, A., Remonen, T., et al. (2002). Active matrix displays based on all-organic electrochemical smart pixels printed on paper. *Advanced Materials, 14*(20), 1460–1464.
6. Sheats, J. R., Biesty, D., Noel, J., & Taylor, G. N. (2010). Printing technology for ubiquitous electronics. *Circuit World, 36*(2), 40–47.
7. Li, X-r, Xu, X., & Li, P-z. (2008). Synthesis and surface propertes of latex film of a cationic fluoride-bearing polyacrylate emulsion. *Polymer Materials Science and Engineering, 24*(11), 58–61.
8. Kossyrev, P. (2012). Carbon black supercapacitors employing thin electrodes. *Journal of Power Sources, 201*, 347–352.
9. Anton, D. (1998). Surface-fluorinated coatings. *Advanced Materials, 10*(15), 1197–1205.
10. Murray, H. H. (2000). Traditional and new applications for kaolin, smectite, and palygorskite: a general overview. *Applied Clay Science, 17*(5), 207–221.
11. Dandenault, F., Daidj, D. B. & Berube, S. (2013). *Fast film formation water based barrier coating*. Google Patents.
12. Layani, M., Gruchko, M., Milo, O., Balberg, I., Azulay, D., & Magdassi, S. (2009). Transparent conductive coatings by printing coffee ring arrays obtained at room temperature. *ACS Nano, 3*(11), 3537–3542.
13. Soltman, D., & Subramanian, V. (2008). Inkjet-printed line morphologies and temperature control of the coffee ring effect. *Langmuir, 24*(5), 2224–2231.

14. Hu, H., & Larson, R. G. (2006). Marangoni effect reverses coffee-ring depositions. *The Journal of Physical Chemistry B, 110*(14), 7090–7094.
15. Perelaer, J., Smith, P. J., van den Bosch, E., van Grootel, S. S., Ketelaars, P. H., & Schubert, U. S. (2009). The spreading of inkjet-printed droplets with varying polymer molar mass on a dry solid substrate. *Macromolecular Chemistry and Physics, 210*(6), 495–502.
16. Majumder, M., Rendall, C. S., Eukel, J. A., Wang, J. Y., Behabtu, N., Pint, C. L., et al. (2012). Overcoming the "coffee-stain" effect by compositional Marangoni-flow-assisted drop-drying. *The Journal of Physical Chemistry B, 116*(22), 6536–6542.

Chapter 93
Study on the Enzymatic Deinking Technology of Waste Newsprint Paper

Jiang Chang and Xue Gong

Abstract The deinking experiments of waste newsprint with biological enzymes had been done to evaluate the effect of enzyme deinking and to improve the quality of regeneration of waste paper. A newsprint enzyme deinking process had been established, and the deinking samples had been prepared. The quality of deinking process was evaluated by whiteness and residual ink area percentage. The deinking effect had been compared with one-component enzyme preparation and two-component complex enzyme preparation. The results show that the best one of one-component enzyme preparation deinking is lipase, with the whiteness of 55.33 % and the residual ink area percentage of 2.11 %; two-component complex results show that the cellulase and lipase enzyme works best with the whiteness of 55.69 % and the residual ink area percentage of 1.85 %. Three enzymes all can remove ink from waste newsprint and the deinking effect could be enhanced when mixed.

Keywords Deinking · Waste newsprint · Enzyme

93.1 Introduction

In recent years, the application of waste paper recycling products is growing rapidly and the requirements of the quality of the recycled paper are also increasingly high. The traditional methods of chemical deinking have many shortcomings, such as the great number of chemical reagents, heavy pollution, and the decreasing of fiber

J. Chang (✉)
Key Laboratory of Bio-Based Material Science and Technology of Ministry of Education, Northeast Forestry University, Harbin, China
e-mail: kahn82@163.com

J. Chang · X. Gong
Light Industry College, Harbin University of Commerce, Harbin, Hei Longjiang, China

properties, which becomes increasingly obvious. Enzymatic deinking becomes the new method to solve this problem [1].

Active biological enzyme is used as deinking agent by enzymatic deinking which is a kind of green deinking technology [2]. Deinking technology can to a large degree remove the printing ink, filler, impurity, etc. of waste paper, increase the brightness of deinked pulp, reduce the loss of fiber, and improve the pulp yield, while the strength of pulp does not decrease. Enzymatic deinking process greatly reduces the number of chemicals which is used to deink and the treatment of wastewater and it can effectively reduce the discharge of harmful substances of wastewater of papermaking [3].

In the 1980s, Japan first appeared the patent of the enzymatic deinking [4]. After that the study of enzymatic deinking mainly concentrated on the process of enzymatic deinking and the mechanism of enzymatic deinking. Ji [5] introduced feasibility of enzymatic deinking. Zollner [6], Viesturs [7], You [8], Li [9], Wang [10] did the experiment of deinking of waste paper with different enzyme reagents and evaluated the results, which demonstrated the feasibility of enzymatic deinking on the aspect of technology. On the other hand, Heikki [11] reasoned the mechanism of enzymatic deinking and divided it into two aspects: enzyme reacted with fiber, enzyme reacted with printing ink. Pratima [12] thought in the deinking process, cellulase plays an important role in the hydrolysis of cellulose pulp part. Zeyer [13] thought that the mechanical action is an important prerequisite for deinking effect of enzymes.

93.2 Experiment

93.2.1 Experimental Materials and Instrumentation

The waste paper of this experiment is Guangming Daily Newspaper. The experiments involve enzyme reagent parameters which are shown in Table 93.1.

93.2.2 Experimental Procedure

Enzymatic deinking process is shown in Fig. 93.1

Take a certain amount of waste newsprint, cut it into 2.5 cm × 2.5 cm block, and then put it into a beaker immersion with distilled water. The paper fibers swell after a complete absorption. Add it to the pulper, pulp for 1 min, and ensure that newspaper can be fully broken and standing. Take a certain amount of enzyme reagent, add a small amount of warm water to fully dissolve, and after that, add it to the pulp and mix it evenly. Determine the mixed liquid enzyme and the pH of the pulp; if it is not the most suitable for the enzyme activity range, it requires to be

Table 93.1 Enzyme reagent in experiments

Enzyme reagent	Activity	Suitable temperature (°C)	Suitable (pH)	Company of the production
Lipase	20,000 U/g	30–50	3.6–6.5	Ruiyang Biotechnology Co. Ltd
		The optimum 40	The optimum 6.0	
Cellulase	50,000 U/g	30–60	4.0–5.5	Ruiyang Biotechnology Co. Ltd
		The optimum 50	The optimum 4.8	
Hemicellulase	500,000 U/g	20–60	4.0–5.5	Ruiyang Biotechnology Co. Ltd
		The optimum 50	The optimum 5.0	
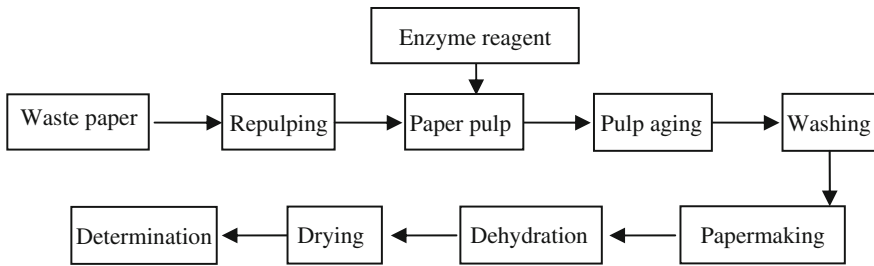
Fig. 93.1 Deinking experiment process of waste newsprint paper

adjusted to the optimum pH range. The beaker is placed with a mixed liquid enzyme and pulp in a constant temperature bath with the optimum temperature of the enzyme, and glass rod is used to stir the mixture interruptedly during the period. After the reaction is finished, pour the mixture into the flotation mechanism to float and wash. Dehydrate and dry the washed pulp in papermaking copper net. Use whiteness and color meter to determine the whiteness for the preparation of sample. Use Micro Capture to sample fixed area on the specimen surface. Use the MATLAB program to calculate the percentage of sampling area of black ink to know the ink residual area percentage. The above test for each sample was conducted 5 times to calculate the average data.

93.3 Analyses and Discussion

93.3.1 Deinking Effect of One-Component Enzyme

Deinking technological conditions are as follows: weight of the waste newspaper is 18 g, pulp density is 1.7 %; the repulping time is 10 min, the repulping temperature is 40 °C, the reaction time is 25 min, and the drying temperature is 80 °C. Use enzyme reagent of 5 levels (10, 20, 50, 70, and 100 mg), respectively, for newsprint deinking treatment in accordance with the above process parameters. Whiteness (Fig. 93.2) and ink residual area percentage (Fig. 93.3) detection results are shown as follows.

From the graph, we can see directly the deinking effect of different enzymes in different dosage, the three enzymes in the selected, lipase deinking sample is the highest, it was followed by cellulase, and hemicellulase deinking whiteness was the minimum. The three highest degrees of whiteness deinking samples were 55.33, 48.72, and 41.11 %, which were higher than in the same process without any enzyme (the degree of whiteness 39.08 %) pulp papermaking.

From the graph, we find that the ink residual area of the samples processed by three kinds of enzymes have different effects. The lipase has the best effect, followed by cellulose and hemicellulase. The residual ink area percentage of three kinds of enzyme-treated samples was from 1.82 to 2.86 %, which were less than in the same process without any enzyme (the percentage of the residual ink is 4.88 %) pulp papermaking.

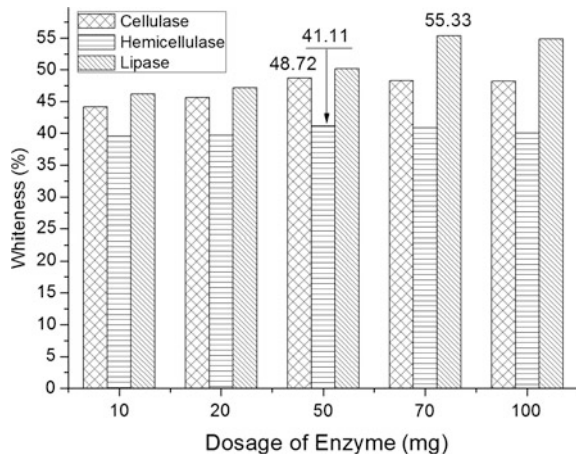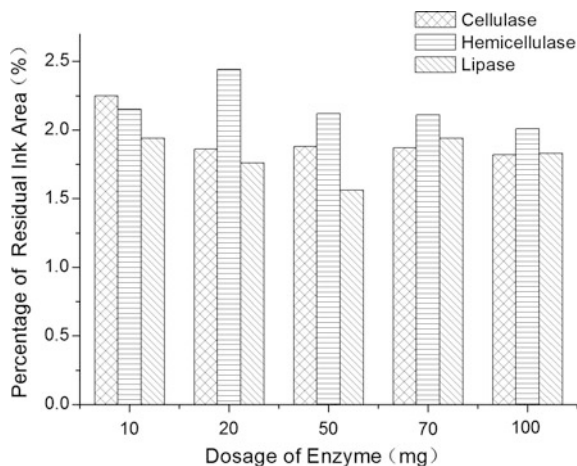**Fig. 93.2** Whiteness comparison on one-component experiments

Fig. 93.3 Residual ink area percentage comparison on one-component experiments

The main reason is the lipase can decompose the ink binders, so that the ink has no adhesion and the pigment of ink will disperse in deinked pulp which can be removed by washing or flotation [15–16]. And because of the specificity of enzyme, lipase cannot hydrolyze fiber, preserving the integrity of the paper fibers, which is good for the latter papermaking. Therefore, the quality of whiteness of the deinking sample was the best.

93.3.2 Effect of Compound Enzyme Deinking

Select cellulase and lipase to do the experiment of compound enzyme. Take 50 mg as the total mass of complex enzyme, 2 mg is a horizontal interval. In the complex enzyme under the condition of the same total quality, change the ratio of two enzymes, to do the experiment of compound enzyme as shown in Table 93.2.

It can be seen from the table, while the dosage of cellulase was 28 mg and lipase was 22 mg, the degree of the whiteness was the highest, reaching 55.69 %, the ink residual area percentage is relatively small, about 1.85 %. Test results showed that the mixed cellulase and lipase can play better deinking role, which is close to the optimal value of one component of deinking.

Table 93.2 Test data tables of two-component complex enzyme preparation

Experimental no.	The dosage of lipase (mg)	The dosage of cellulase (mg)	Whiteness (%)	The percentage of residual ink area (%)
1	2	48	44.93	2.94
2	4	46	45.83	4.03
3	6	44	47.64	2.02
4	8	42	45.33	2.01
5	10	40	50.05	1.96
6	12	38	46.05	2.16
7	14	36	47.42	2.87
8	16	34	46.54	2.15
9	18	32	49.41	2.16
10	20	30	48.61	2.51
11	22	28	49.59	1.96
12	24	26	51.23	2.39
13	26	24	53.79	2.70
14	28	22	55.69	1.85
15	30	20	53.58	2.22
16	32	18	52.64	2.13
17	34	16	51.61	1.99
18	36	14	50.01	1.82
19	38	12	48.49	2.39
20	40	10	47.17	2.47
21	42	8	43.95	2.86
22	44	6	51.48	2.45
23	46	4	46.41	2.57
24	48	2	41.30	2.19

93.4 Conclusions

Under the same condition, cellulase, hemicellulase, and lipase were able to deink; the best effect of deinking was lipase, it was followed by cellulase, and hemicellulase was the worst. The degree of whiteness of deinking sample was 55.33 %, the treated ink residual area percentage is less than the untreated specimen about 3 %.

Cellulase and lipase can play a role in the synergistic deinking of mixed deinking process, but the specific effects and mode of action remain to be further study.

References

1. Wang, S., Diao, L-l, & Hao, H-l. (2013). Preliminary study on the mechanism of enzymatic deinking. *Chinese Journal of Environmental Science, 32*(4), 83–86.
2. Stork, G. (1995). Upgrading recycled pulps using enzymatic treatment. *Tappi Journal, 78*(2), 79.
3. Welt, T., & Dinus, R. J. (1998). Enzymatic deinking: Effectiveness and mechanisms. *Paper Science and Technology, 126*(9), 396–407.
4. Urushibata, H. Deinking agent for regenerating used paper: JP, 59223391-3(A) [P].1984-12-15.
5. Ji, Y-c, Yang, Y-r, Wang, Z-l, et al. (2010). Application and pilot test on enzyme deinking agent in old newspaper deinking line. *Paper Chemicals, 22*(3), 28.
6. Zollner, H. K., Schroeder, L. R. (1998). Enzymatic deinking of non-impact printed white office paper with α-amylase. *Tappi Journal, 81*(3), 166.
7. Viesturs, U., Leite, M., Eisimonte, M., et al. (1999). Biological deinking technology for the recycling of office waste papers. *Bioresource Technology, 67*(3), 255.
8. You, J.-x., Ye, H.-l., Zhao, Y.-r. (2010). Study on the mixed office waste paper deinking of laccase/amylase. *China Paper*, *22*(3), 28.
9. Li, H-j, Wang, H-y, & Deng, F-w. (2010). Application of enzymatic deinking agent in waste paper pulp and the flotation process. *Paper and Paper Making, 29*(6), 56.
10. Wang, Y.-p. (2009). *Study on synergistic deinking and mechanism of old newspapers with laccase/mediatorand cellulose*. Jinan: Shandong Light Industries College.
11. Heikki, P. (2002). *Recycled fiber and papermaking*. Finland: Fapet Oy.
12. Pratima, B. (1997). Enzymatic deinking. *Advances in Applied Microbiology, 45*(3), 241–269.
13. Zeyer, C., Heitamann, J. A., Jooyce, T. W., et al. (1993). Factors influencing enzyme deinking of recycled fiber. *Tappi Journal, 3*(1), 36–44.

Chapter 94
Discussing Processing Technology and Method of Honeycomb Cardboard

Shangjie Jiang, Junyan Huang, Linlin Yu and Huanxiu Liu

Abstract **Purpose** The purpose of the study was offering technical reference for production and products of honeycomb cardboard and its application in modern packaging industry. **Method** The forming principal, process technology, and production process of honeycomb cardboard were introduced. The factors such as raw material, forming process, and other factors on the properties of honeycomb cardboard were analyzed. **Result** As a new green packaging material, the honeycomb cardboard and packing products have the characteristics of light weight, high strength, low cost, good cushioning performance, and so on; they have great potential to develop and application prospect. **Conclusion** The honeycomb cardboard and packing products are a new type of environmental protection material which is consistent with the circular economy, low carbon, green packaging, and sustainable development requirements. They will play more and more important roles in the modern packaging field.

Keywords Honeycomb cardboard · Forming process · Production process · Influence factors

94.1 Introduction

In recent years, honeycomb cardboard and packaging products have been transformed into an environmental protection packaging material and have a promising potential to be developed further [1]. It has plenty of irreplaceable advantages that could compare with corrugated board, wood, and plastic. The pallet made of honeycomb board has better features of light weight, high strength, low cost, perfect cushioning performance, and so on [2].

S. Jiang · J. Huang (✉) · L. Yu · H. Liu
School of Light Industry & Chemical Engineering,
Dalian Polytechnic University, Dalian, Liaoning, China
e-mail: hjunyan@126.com

Fig. 94.1 Schematic diagram of honeycomb cardboard
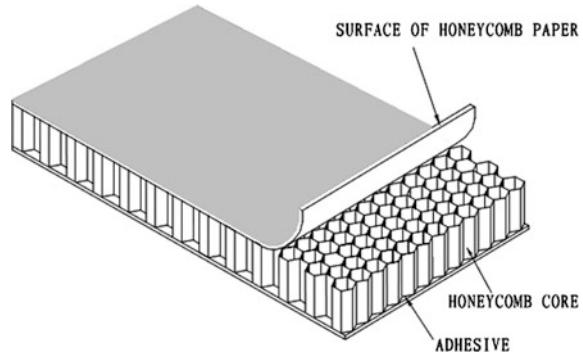
It is a new type of environmental protection material which is consistent with the circular economy, low carbon, green packaging, and sustainable development requirements.

The honeycomb cardboard is making use of the principle of bionics, applying honeycomb structure theory to the production of packaging materials. Thus, the solid honeycomb structure can be built with the least amount of material consumption, as shown in Fig. 94.1. The honeycomb paperboard production line is composed of honeycomb core manufacturing equipment, honeycomb cardboard manufacturing equipment, paper cutting equipment, and so on. The honeycomb cardboard production process generally divided into two processes: making a hexagonal structure of honeycomb paper core and compositing honeycomb core upper and lower to make of honeycomb cardboard.

94.2 Honeycomb Core Molding Technologies

94.2.1 Raw Materials for Production of Honeycomb Core

94.2.1.1 Base Paper

The honeycomb cardboard base paper is divided into honeycomb face paper and honeycomb core paper. Now, there is no special standard of base paper used in honeycomb paperboard in China. Therefore, the main technical performance of honeycomb face paper conforms to the requirements for case board paper standard (GB/T13024-2003) and the honeycomb core paper conforms to the requirements for corrugated base paper standard (GB/T13023-2008). The effect of base paper on honeycomb board performance is mainly manifested in the following aspects:

(1) In general, the higher grammage of paper, the higher the strength of the board, but it is more difficult to pull the honeycomb core in the production process. In the actual production, the grammage of honeycomb core paper is between

120 and 180 g/m^2 and the grammage of honeycomb face paper is between 200 and 500 g/m^2. The more grammage of paper, the better anti-wear, anti-pressure, and moisture resistance, but the cost will be higher [3].

(2) The paper has a certain direction. Most of the fiber is arranged longitudinally. In the honeycomb cardboard production process, when the honeycomb core fiber direction is perpendicular to the honeycomb face paper, the honeycomb cardboard compressive strength is the highest.

(3) The moisture content of paper has obviously effect on the flexibility, elasticity, and strength of paper. Generally, honeycomb cardboard base paper moisture is controlled between 8 and 12 %; otherwise, it will influence the paperboard compressive strength and buffer performance [4].

(4) The ring crush strength of paper is the most influence on the pressure resistance of honeycomb cardboard. The higher the crush compressive strength, the higher the flat compressive strength of the honeycomb board and the bearing capacity is higher. Usually, the ring crush strength of the honeycomb core paper is between 4.4 and 5.5 N m/g, and the ring crush strength of the surface of honeycomb paper is about 6.5 N m/g [5].

94.2.1.2 Adhesive

Adhesive plays a very important role in the production of honeycomb paperboard, its adhesion property. Drying speed and film hardness all affect the quality of honeycomb cardboard. So when choosing adhesive, first the adhesion is considered; secondly the drying speed and the film hardness are considered; and the final consideration is the use of convenience, price factors, etc. At present, the adhesive used by honeycomb products production can be divided into four types.

(1) **Corn starch adhesive** It is under the alkaline condition, obtained the oxidized starch containing the negative charge after oxidation processing and other process of starch raw materials. This kind of powder and ordinary carton glue has no essential difference, just solid content increased slightly, generally applicable to non-bearing force of the honeycomb cardboard product manufacturing.

(2) **White latex** It is mainly composed of polyvinyl acetate, and it is a pollution-free and non-toxic green product. White latex can bond a variety of materials, its main features are quick drying, good strength, high solid content, long life and suitable for large areas of work, etc. However, the waterproof and moisture resistance of this adhesive is poor, and the heat resistance is not good.

(3) **Cyclodextrin** The preparation of cyclodextrin is under acidic conditions, and the starch was degraded by heating, thus increasing the solubility of starch in water; therefore, the cyclodextrin is also a kind of starch-modified products. This kind of adhesive has the following characteristics: higher solid content, good initial adhesion, higher adhesion strength, good using time, good

rigidity, lower price, and fast drying speed. But the water resistance of these adhesives is poorer, so its application is limited to some extent.

(4) **Graft copolymer of starch resin adhesive** The characteristics of this kind of adhesives is fast drying speed, its bond strength is much better than ordinary corn starch adhesive and cyclodextrin, and it is an ideal adhesive for honeycomb paperboard products, especially suitable for composite honeycomb paperboard.

94.2.2 Honeycomb Core Molding Technology

94.2.2.1 Honeycomb Core Forming Mechanism

The honeycomb cardboard is composed of surface paper, adhesive, and paper core; paper core presents honeycomb shape and bonded into a certain law by a number of core paper, mainly for shear stress. The surface paper is combined with the same thickness and isotropic paper with paper core to make honeycomb cardboard, mainly for stress, bending moment, and torque [6].

The forming of honeycomb paper core is mainly through the dislocation glue of core paper. Dislocation glue between each layer of paper core according to certain regularity forms an alternate bonding compound layer structure as shown in Fig. 94.2. The pitch is 4 L and the width of the gluing is λ L. Draw the alternate bonding compound layer structure along the perpendicular direction of the paper, and then, the cellular structure is formed.

94.2.2.2 Honeycomb Core Molding Process

The main forming process of honeycomb paper core is used to manufacture honeycomb core. There are two kinds of manufacturing core technology: cascading and winding.

(1) **The cascading type** Cutting the reel-shaped paper core into the certain size of single paper, stacking the dislocation paper which is glued after bonding, and
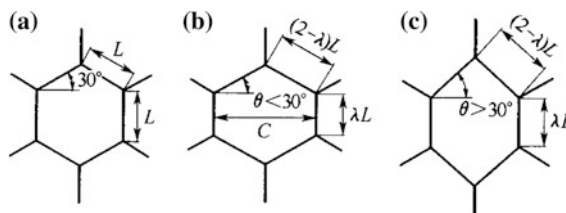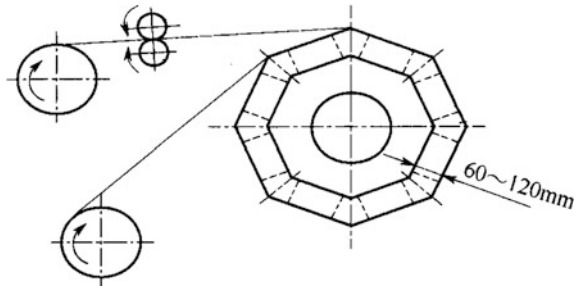

Fig. 94.2 Three constitutional unit of honeycomb

Fig. 94.3 Voluble core
making technique

then putting it on press machine in a certain time to keep it bonded firmly,
forming paper core blocks and cutting into core strip by cutting machine, and
finally joining together the core strips to make continuous paper core.

(2) **The winding type** The process principle of winding type of manufacturing
core is shown in Fig. 94.3 [7]. Two-volume core papers are used; one roll of
the paper dislocation is glued on both sides, winding through the octagonal
drum, volume the thickness of 60–120 mm and then cut after drying, paper
core block is completed, cutting into core strip after drying, finally, joining
together the core strip to make continuous paper.

94.3 Honeycomb Paperboard Production Technologies

94.3.1 Honeycomb Paperboard Production Technology Form

Manufacturing line of honeycomb paper board generally consists of 7 sets stan-
dalone: base paper rack, honeycomb core tensile dryer, honeycomb paper core
gluing machine, honeycomb paperboard composite machine, longitudinal cutting
machine, transverse cutting machine, and electric control cabinet. The working
principle is shown in Fig. 94.4. There are 2 sets of paper racks, supply honeycomb
core and surface paper, respectively. After the honeycomb core and surface paper
are released, they enter the stretch dryer. The honeycomb core paper was stretched
into hexagonal grid and shaped by using the setting device. After drying and
shaping, paper was sent to gluing machine. And then together with the upper and
lower cardboard send into the honeycomb board composite machine, at this time,
the upper and lower boards are heated and dried, and fitted closely to honeycomb
core paper in the composite device. In the process of heating and pressing, the
honeycomb board is composite. The honeycomb cardboard is sent into vertical
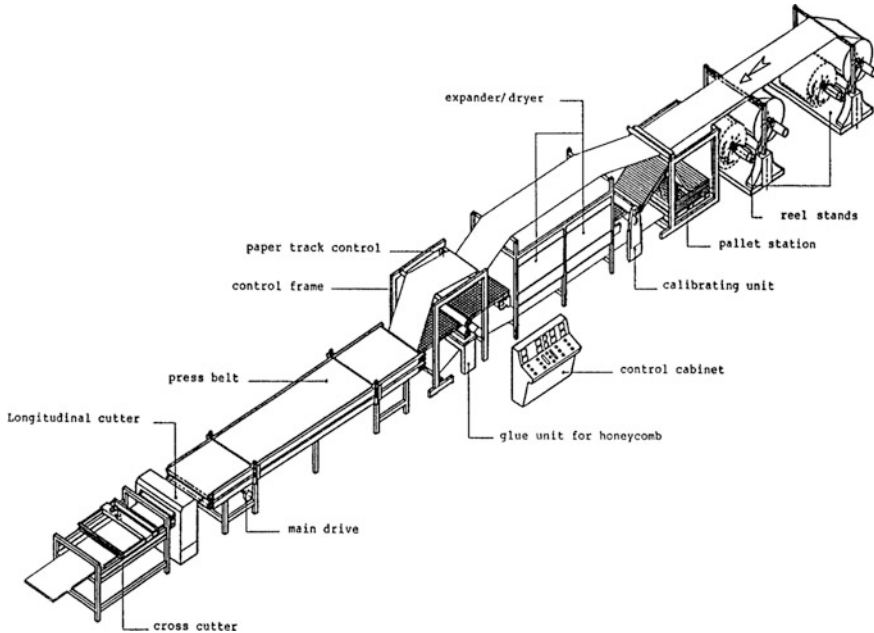cutting machine and horizontal cutting machine and cut into required size.

Fig. 94.4 The principle of honeycomb cardboard production line

94.3.2 *Honeycomb Paperboard Production Process*

(1) **Paper Core Stretching** Honeycomb paper core stretching comes in many forms. (1) limited wide stretch type: take use of the width limit and pull the core open; (2) different speed tensile type: take use of different speed and pull the core open; (3) the combination of differential speed and limited wide type is applied to core required docking production line; and (4) transverse tensile type: pull the paper core along the horizontal, which is characterized by the changing speed of the strip in the process of drawing.

(2) **Composite Surface Honeycomb Paper** There are two main ways to composite surface honeycomb paper: surface honeycomb paper glue composite and honeycomb core glue composite on end face. In fact, the adhesive will be wasted more than three-quarters by using the process of surface paper glued. Honeycomb paper core adopts the method of end face adhesive and the dosage of adhesive liquid is less than 1/4 adhesive liquid of surface honeycomb paper. The roll strength of the honeycomb core product which is a glued composite on the end face with low water content is far greater than the product of surface honeycomb paper, which is glued composite.

(3) **Compaction** There are methods of press compaction, squeeze compaction, and roller compaction. (1) Press compaction is mainly used for the core board. (2) Squeeze compaction is mainly used for core docking and paper docking

compaction. (3) Roller compaction is divided into continuous roller compaction and transfer belt combined with pressure roller compaction.

(4) **Heat Drying** In the production of honeycomb paperboard, there are three heating modes: electric heating, steam heating, and heat conduction oil heating. In the production of honeycomb cardboard, glue liquid adhesive, water exclusion, and paper core shape all need to heat and drying.

(5) **Vertical and Horizontal Cut** It refers to the longitudinal cutting and horizontal disconnection of the honeycomb board. Longitudinal cutting generally adopts circular knife cutting at a high speed, horizontal disconnection generally adopts no tooth circular knife.

94.4 Conclusions

As a new green packaging material, honeycomb cardboard and packing products have features of natural degradation, recycled, export without epidemic prevention and quarantine, cause no pollution to the environment [8]. Therefore, the research on the forming mechanism, process technology, and production process of honeycomb board and its packaging products, analyzing the influence of raw material, molding process, and other factors on the properties of honeycomb cardboard is benefit to improve production technology and quality of honeycomb board and its products, and also conducive to further promote the honeycomb cardboard and its products generalization and application, and has an important economic significance and environmental protection significance.

References

1. Ye, B-z. (2010). The development of low carbon economy prompted the paper honeycomb material "running out". *Shanghai packaging, 3*, 27–29.
2. Liu, X-h, & Wang, W-m. (2005). The technical condition and production technology of honeycomb panel tray. *Wood Industry, 11*, 21–24.
3. Hao, X-h, Lin, Y-p, & Hu, X-f. (2002). The quality analysis of honeycomb paperboard and the way of improving the quality of honeycomb paperboard. *Packaging Industry in China, 9*, 21–23.
4. Modzelewska, I. (2006). Climatic condition VS hygrostability and strength properties of corrugated board. *Institute of Chemical Word Technology, 4*, 33–45.
5. Ye, B-z, & Tang, X-j. (2004). Application and common quality analysis of honeycomb paperboard in air conditioning packaging. *Packaging Engineering, 1*, 131–133.
6. Li, Y.-m., Luo, G.-l. Development direction of corrugated board and honeycomb paperboard, 28–30. www.cnki.net
7. Dai, H.-m. (2004). *New type of green packaging material* (pp. 42–50). Beijing: Chemical Industry Press.
8. Snu, S.-j. (2004). Honeycomb paperboard-new type of industrial packaging material. *Hunan packaging, 5*, 32.

Part VIII
Film and Related Material Technology

Chapter 95
Synthesis and Characterization of Nano-Porous Oxidized Silica Film with Low Dielectric Constant

Can Wang, Gaimei Zhang, Xiaoli Song, Qiang Chen and Jingting Zhang

Abstract A route to prepare nano-porous oxidized silica film using plasma-enhanced chemical vapor deposition (PECVD) is reported in this paper. Taking hexamethyldisiloxane (HMDSO) as the monomer, doping with O_2, while adding a small amount of ether, the oxidized silica film is synthesized on the glass substrate using glow discharge. At last, the film is heated to produce more pores to reduce its dielectric constant. Fourier transform infrared spectroscopy (FTIR), scanning electron microscope (SEM), and atomic force microscopy (AFM) are used to characterize the film; the refractive index is measured by the ellipsometer; and then, the dielectric constant of the films is calculated. The results show that the films with dielectric constant smaller than 2.0 can be acquired by adjusting the proportion of HMDSO and O2, discharge time, and discharge power.

Keywords PECVD · Dielectric constant · Porous oxidized silica · Films

95.1 Introduction

With the decrease of characteristic dimension of integrated circuits and increase of wiring density, adopting low dielectric constant material between metal wire and interlayer dielectric instead of traditional silicon dioxide material is needed to reduce the interconnect delay, crosstalk, and energy consumption. Therefore, the preparation of low dielectric constant materials becomes a hot spot in research of electronic packaging materials [1], and the porous silica film has been widely used as a special kind of dielectric and insulation in microelectronics, optoelectronics, and optical integration device [2]. The preparation of low dielectric constant non-porous silica films in this article is to improve the porosity of the membrane and

---

C. Wang · G. Zhang (✉) · X. Song · Q. Chen · J. Zhang
School of Printing &Packaging Engineering, Beijing Institute
of Graphic Communication, Beijing, China
e-mail: zhang_gaimei@163.com

reduce the dielectric constant of thin film. It is because the air has a low dielectric constant [3], so using nano-porous in the membrane material to reduce the dielectric constant of thin films is a very effective method. In this paper, the films with dielectric constant smaller than 2.0 has been acquired by adjusting the permittivity of the films [4].

95.2 Material Preparation Method

95.2.1 Experimental Method

The material is prepared by plasma-enhanced chemical vapor deposition (PECVD). In the experiment, the 13.56 MHz radio frequency power and parallel-plate aggregation device are used [5]. The experimental materials include hexamethyl-disiloxane (HMDSO), oxygen, and a small amount of organic matter. The oxidized silica films are deposited on glass substrate through glow discharge. Then, the films are heated in the high temperature of 450 °C with vacuum conditions [6]. The –CH3 is broken down to remove organic constituents in the film with annealing, a gap is produced, and the permittivity of the film has been decreased.

95.2.2 Experimental Parameters

Different oxidized silica films with different experimental parameters in the experiment are obtained by adjusting the proportion of HMDSO and O2, discharge time, and discharge power [7], and then, the thin films have been characterized by the step profiler, fourier transform infrared spectroscopy (FTIR), scanning electron microscope (SEM), and atomic force microscopy (AFM) [8]. The refractivity of the films is measured using spectroscopic ellipsometer, and the dielectric constants of the films are calculated at last.

95.3 Experimental Characterization

95.3.1 Deposition Rate

The thickness of the films with different experimental parameters is measured by step profiler (Dektak150, Veeco, US), and then, the deposition rate of the films is calculated. Table 95.1 shows that the deposition rate of silicon oxide film decreases with the increase of discharge time; the proportion of HMDSO and O2 is 1:4; and the discharge power is 50 W. Table 95.2 shows that the deposition rate of silicon oxide film increases with the increase of discharge power; the proportion of

Table 95.1 The thickness of silicon oxide film with different discharge time

| Time (min)	Thickness without annealing (nm)	Deposition rate (nm/min)	Thickness after annealing (nm)
5	90	18	63
10	113	11.3	82
15	162	10.8	136
20	210	10.5	196

Table 95.2 The thickness of silicon oxide film with different discharge power

Power (W)	Thickness without annealing (nm)	Deposition rate (nm/min)	Thickness after annealing (nm)
50	117	11.7	75
100	134	13.4	105
150	168	16.8	143

HMDSO and O2 is 1:8; and the discharge time is 10 min. The thickness of the films with annealing is also measured and shown in the tables; Tables 95.1 and 95.2 present the same trend that the thickness of the films has changed with annealing, and it also means that the internal structure of the silicon oxide film has changed.

95.3.2 FTIR

The FTIR spectra of silicon oxide film are shown in Fig. 95.1. It can be seen that there are four strong adsorption peaks appeared at 2962, 1260, 1030, and 798 cm^{-1}, respectively. There is a strong adsorption peak appeared at 2962 cm^{-1} for C–H

Fig. 95.1 FTIR spectra of silicon oxide film
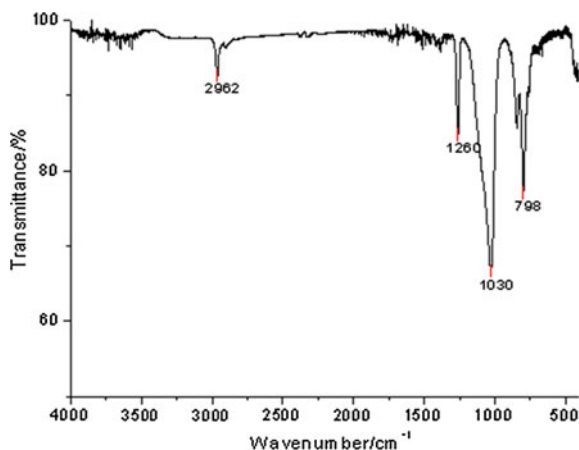
stretching vibration. The characteristic absorption peak of C–O stretching vibration appeared at 1260 cm^{-1}. Signals at 1030 and 798 cm^{-1}, respectively, are assigned to Si–O–Si stretching and wagging vibrations. FTIR spectrum shows that HMDSO and O2 both took part in the reaction and silicon oxide film were prepared.

95.3.3 AFM

The AFM photographs of silicon oxide films are shown in Fig. 95.2. Figure 95.2 shows the surface of the silicon oxide film under different experimental conditions. We can see from the figure that the surface of the films is relatively flat; however, we can still see the difference between the films when they are deposited under different experimental conditions, and it also means the films with different experimental parameters have different structural features.

95.3.4 SEM

The SEM photographs of silicon oxide films are shown in Fig. 95.3. The experimental conditions are as follows: the ratio of monomer to oxygen is 1:4, the discharge power is 100 W, and the discharge time is 5 min. The figures show that surface particles of silicon oxide films spread evenly, and there are gaps between the particles.
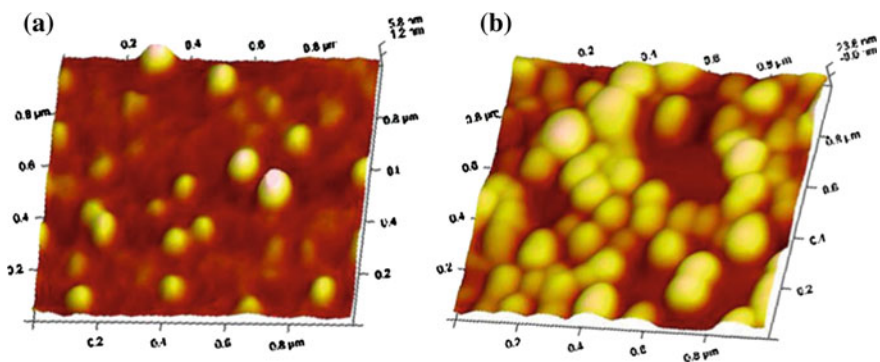
Fig. 95.2 AFM photograph of silicon oxide film

Fig. 95.3 SEM photograph of silicon oxide film
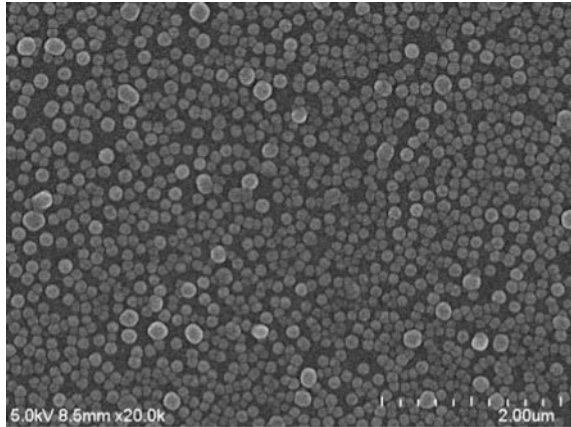
95.4 Result and Discussion

95.4.1 Refractivity

When the porous silicon oxide film is used as structural layers and insulation materials, the porosity of the silicon oxide film is important. It not only affects the mechanical properties, but also affects the thermal insulation performance. In the experiment, the refractivity of the films is measured using spectroscopic ellipsometer and then, the porosity of the films is calculated by Lorentz-Lorenz formula:

$$\frac{n_0^2 - 1}{n_0^2 + 2}(1 - p) = \frac{n^2 - 1}{n^2 + 1} \tag{95.1}$$

In the formula, n_0 is the refractivity of the substrate and n is the refractivity of the measured film.

The dielectric constant of the films is calculated by Maxwell-Garnett formula:

$$K = n^2 \tag{95.2}$$

In the formula, K is the permittivity of the film and n is the refractivity of the film.

95.4.2 Result and Discussion

Figure 95.4 shows the permittivity of the silicon oxide film. The experimental conditions are as follows: The discharge power is 100 W, the discharge time is 10 min, and the ratio of monomer to oxygen is changing from 1:3 to 1:11. In the figure, a represents the permittivity of the silicon oxide film without annealing, and
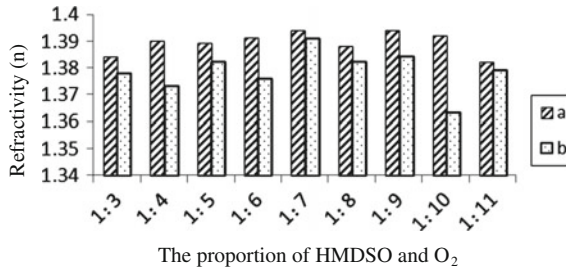
Fig. 95.4 The permittivity of the silicon oxide film under the condition of different proportions

b represents the permittivity of the silicon oxide film with annealing. From the figure, the results can be obtained that the permittivity of the silicon oxide film has decreased with annealing. This is due to the –CH3 is broken down to remove organic constituents in the film with annealing, a gap is produced, and the permittivity of the film has been decreased. The figure shows that the films with permittivity smaller than two are prepared successfully.

95.5 Conclusions

From the numerical analysis and experimental investigation, the following conclusions are obtained:

(1) The experiment results show that annealing affects the dielectric constant of the films with organic matter.
(2) Nano-porous oxidized silica film with dielectric constant smaller than 2.0 is prepared using PECVD, by adjusting the proportion of HMDSO and O2, discharge time, and discharge power.

But the refractivity of the film cannot be tuned with the change of experimental conditions. This will be studied the future work.

References

1. Zou, Y. K., Zhan, Y. Q., Zhao, R., et al. (2013). *Journal of Materials Science: Materials in Electronics, 24*(4), 1238–1242.
2. Yang, C.-M., Cho, A.-T., Pan, F.-M., et al. (2001). Spin-on mesoporous silica films with ultralow dielectric constants, ordered pore structures, and hydrophobic surface. *Advanced Materials, 13*(14), 1099–1102.

3. Timothy, M. L., & Timothy, M. S. (2013). *Journal of the American Chemical Society, 125*(46), 14113–14119.
4. Lee, W. W., & Ho, P. S. (1997). Low-dielectric–constant materials for ULSI interlayer-dielectric applications. *MRS Bulletin, 22*(10), 19–23.
5. Endo, Kazuhiko. (1997). Toru Tatsumi (1997). Plasma fluorination of polyimide thin films. *Journal of Vacuum Science & Technology, 15*(6), 3134–3137.
6. Wu, G., et al. (2001). Effect of experimental conditions on the structures and properties of Nano-porous silica films. *Acta Physica Sinica, 1*(50), 175–181.
7. Wu, Z-f, et al. (2005). Preparation and study of low dielectric constant mesoporous silica films. *Journal of Materials Science & Engineering, 23*(3), 408–411.
8. Hao, Y., et al. (2007). Synthesis of mesoporous thin silica films with ultra low dielectric constant. *Chinese Journal of Inorganic Chemistry, 9*(23), 1587–1592.

Chapter 96
Research on the Preservation Effect of Paper Plastic Compound Bags on the Lychee

Qing Liu, Dongli Li, Ruijuan Liao and Jiazi Shi

Abstract The influence of a paper plastic compound bag and commercially available storage bags on the storage quality of the lychee at low temperature (5 °C) was investigated. The packed lychee qualities during storage were determined by the browning index, decay rate, soluble solids content, titrate acidity, and Vitamin C concentration. The lychee with ordinary commercial packaging bags could be kept 6 days and the shelf life of lychee with a paper plastic compound bag was 11 days. The obvious browning and water loss rate of lychee were obtained with ordinary commercial packaging bags. The paper plastic compound bag could delay effectively the appearance of the white mold.

96.1 Introduction

Lychee is a tropical fruit native to South China, which is in bright color and rich in nutrition, for South of the Five Ridges fruit in the top grade. But of special structure and metabolism of them, and mature in summer, it will be soon after harvested. According to the statistics, 20 % of the total production of lychee was lost every year due to the decay rate [1–3].

Technology of storage and fresh-keeping of lychee is the concern of researchers. Main purpose of lychee's fresh-keeping is inhibiting browning of pericarp and mildewing of fruit. As early as 1987, Ji Tang Cha and his team have studied the storage temperature on hiya and kiwi lychee, found lychee has the lower respiration rate and browning under 5 °C [4]. Studied the influence of different temperature on

Q. Liu · D. Li (✉) · R. Liao · J. Shi
School of Printing and Packaging Engineering, Beijing Institute of Graphic Communication, Beijing, China
e-mail: lidongli@bigc.edu.cn

storage effect of Huai Lai Chi Kok and glutinous rice, found lychee has the lower decay rates at 1 (±1) and 5 (±1) degree after a storage of 20 days, so identify the most appropriate storage temperature for lychee 1–5 °C [5].

We tested the storage effect of lychee with homemade paper plastic compound bags compared with that of sale preservation film at 5 °C. The packed lychee qualities during storage were determined by the browning index, decay rate, soluble solids content, titrate acidity, and Vitamin C concentration.

96.2 Materials and Methods

96.2.1 Sample Preparation

We buy the fresh lychee, and they were maintained in the supermarket box and most of them have green leaves and branches. The freshest lychees were chased to experiment, and they have the same size and sharp. Finally, we chose 180 lychees and randomly put them into paper plastic compound bags and the sale preservation bags; each bag contains 10 lychees. Each bag as a test set, the packed lychee qualities were determined by the browning index, decay rate, soluble solids content, titrate acidity, and Vitamin C concentration.

96.2.2 Browning Index

Open the bags and observe the browning degree of the lychee during storage period; if 100 % of pericarp turn withered and brown, the browning index is 10, or if 90 % of pericarp turn withered and brown, the browning index is 9, and similarly, if 10 % of pericarp turn withered and brown, the browning index is 1, and the browning index of fresh grape is 0.

96.2.3 Weight Loss

Firstly, test the water loss rate of lychee. Each experimental group was weighted and recorded them (M_0). And then both bags were weighted and recorded them (M_t) at different days. The percentage weight loss was determined according to the following expression:

$$ML(t) \% = \frac{M_0 - M_t}{M_0} \times 100 \% \qquad (96.2.1)$$

96.2.4   Decay Rate

Weight the dropped berry and decay fruit, and calculate the weight percent of dropped berry and decay fruit. Berry drop and decay rate can be, respectively, calculated according to the following expression:

$$D(t)\,\% = \frac{M_d}{M_0} \times 100\,\% \qquad (96.2.2)$$

M_0 is the initial sample mass M_d is, respectively, the decay lychee at time t. The sample weight was determined by means of the same digital precision balance.

96.2.5   TSS

Total soluble solid (TSS) content of grape juice during storage was measured by ATAGO portable digital refractometer. The basic principle is that total soluble solid content of juice is proportional to the refractive index of juice. Each sample should be tested for 3 times and take the average value [6].

96.2.6   TA

Titrate acidity (TA) of lychee juice was determined by sodium hydroxide according to Artés-Hernández et al. (2004), and TA value is repressed by %. Each sample should be tested for 3 times and take the average value [7].

96.2.7   VC

The Vitamin C content of grape juice during storage was determined according to Chinese standard GB/T 6195-1986 [8], and 2 % (w/v) oxalic acid solution was used as blank titration. Juice sample was diluted 10 times with 2 % (w/v) oxalic acid solution, and prepared samples were titrated with 2,6-dichlorophenolindophenol. Each sample should be tested for 3 times and take the average value.

96.3 Results and Discussion

96.3.1 Lychee Appearance

The just-harvested lychee is red, and most of them are linked with green leaves. If it is placed at the room temperature without package, the water loss rate of lychee will rise sharply, the same to the browning index. The trend of browning with paper plastic compound bags package is significantly lower than that of the sale preservation film package at 5 °C (Fig. 96.1). After 6 days, the browning index, as shown in Fig. 96.1, is above score 2, and the water loss rate of fruits decreased by 0.3 % as shown in Fig. 96.2. In this condition, commercial value of the lychee still retained. On the 7th day, the lychee with sale preservation film package occurred white mold as shown in Fig. 96.4 and they lost their commercial value. So, if the browning index achieved score 4, we deemed that the shelf life is ended.

On the 11th day, browning index of lychee with paper plastic compound bags has reached score 2 as shown in Fig. 96.1, and the water loss rate of the fruits decreased by 0.3 % as shown in Fig. 96.2. In other words, lychee with paper plastic

Fig. 96.1 Browning index of lychee in different package during storage time
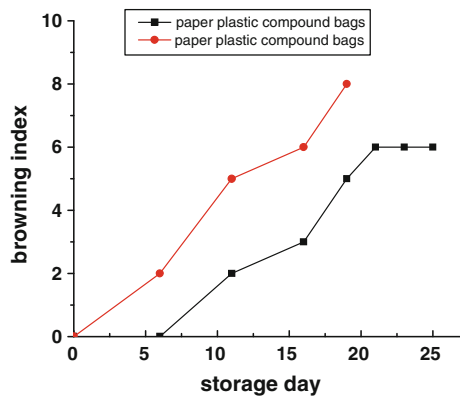
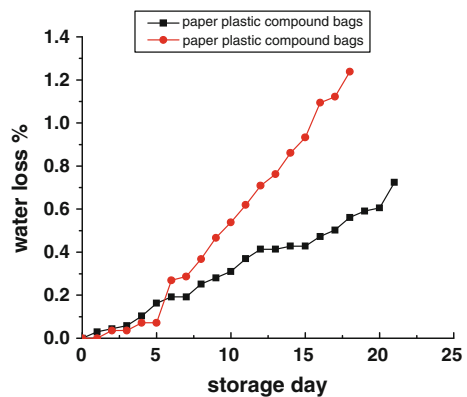**Fig. 96.2** Effect of storage bags on water loss of lychee

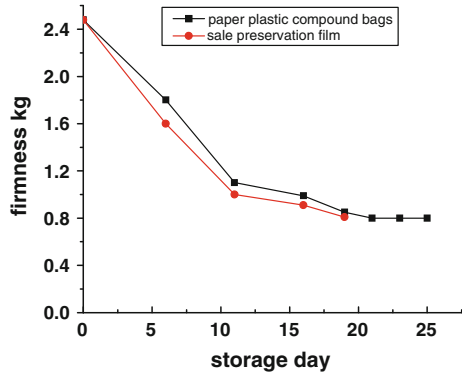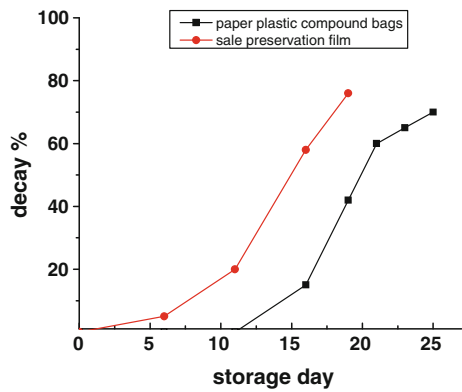**Fig. 96.3** Effect of storage
bags on firmness of lychee

Fig. 96.4 Effect of storage
bags on fruit decay

compound bags can contain their commercial value for 11 days. The paper plastic
compound bags can also prevent the water loss rate, slowing the hardness reduction
of fruit effectively.

96.3.2 Water Loss and Firmness of Lychee

Water loss is one of the reasons why lychee turns brown, and the water loss rate of
the lychee with paper plastic compound bags is lower than that of the sale
preservation film. The water loss rate of the lychee with sale preservation film has
reached 0.27 % on the 6th day, and the browning index has reached 2; the firmness
decreased by 27.4 %, as shown in picture 2 and picture 3. The water loss rate of the
lychee with sale preservation film has reached 0.36 % on the 7th day; in this
condition, lychee has turned brown and the firmness decreased obviously, and be
with white mold (Fig. 96.3).

The water loss rates of the lychee with paper plastic compound bags and sale
preservation film are all under 1 % within 15 days. The water loss rate of the lychee

with paper plastic compound bags has reached 0.37 % in the 11th day, and the browning index is 2; the firmness decreased by 27 % and there is no decay fruit as shown in picture 3 and picture 4. In this condition, lychee still kept the commercial value. On 13th day, the water loss rate has reached 0.42 %, and there has been white mold. So, our paper plastic compound bags could contain lychee's commercial value for 11 days.

96.3.3 Decay Rate of Lychee

Water vapor transmission rate is an important factor for fresh-keeping of fruit, because it is very easy for the high humidity environment to breed and spread bacteria. Compared with the sale preservation film, paper plastic compound bags have the higher water vapor transmission rate, so there is lower humidity environment in the paper plastic compound bags. Lychee with the sale preservation film appeared on the second day, but its growth rate is very slow. The decay rate has reached 5 % on the 6th day. Lychee with paper plastic compound bags did not appear as decay fruit until the 12th day. The growth speed of decay is higher, and the decay rate has reached 10 % on the 15th day as shown in picture 4. The paper plastic compound bags could effectively postpone the time of decay.

96.3.4 Lychee's Quality

Sugar content is one of the important indexes of lychee's quality. The sugar content of fresh lychee is low, and it will increase along with the growth of lychee. During the storage process, the sugar would be oxidized gradually and be composited with carbon dioxide and water, so it is totally kept in a steady state. The lower respiratory intensity of lychee with paper plastic compound bags and the higher sugar content, in contrast the sugar content of lychee with paper plastic compound bags, are lower than those of the sale preservation film. The reason has yet to be further studied (Figs. 96.5 and 96.6).

Acidity is an important index of lychee quality, and lychee is rich in amino acid and some organic acid. Fruits can also produce these organic acids during the respiration, and acids are the intermediate product during the oxidation process of sugar, and they can be oxidized into carbon dioxide and water further. During the storage after the lychee was picked, increase first and then decrease the acidity, keep a steady value. The most likely cause is that the interval is long while testing within 15 days, leading to the accurate line not being shown.

Although the overall trend does not show well, the acidity of lychee with the sale preservation film is lower than that of the paper plastic compound bags as shown in Fig. 96.4. This is because respiratory intensity of lychee with paper plastic compound bags is less, and the remaining acidity of lychee is more than the control group after respiration.

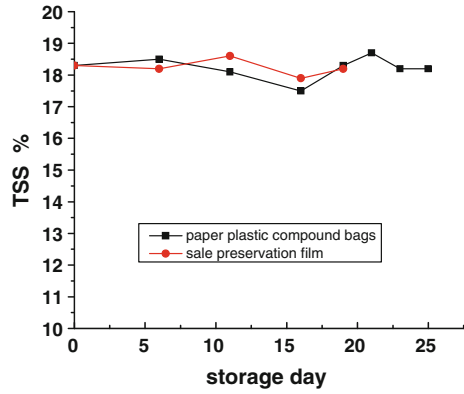**Fig. 96.5** Effect of storage bags on lychee sugar content

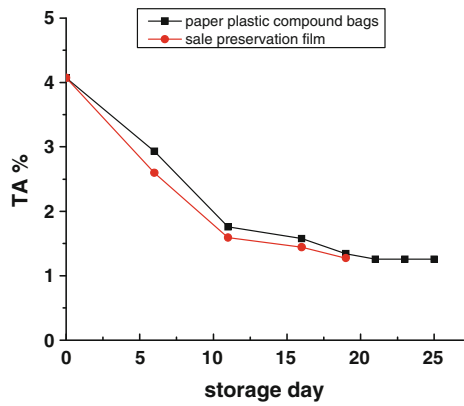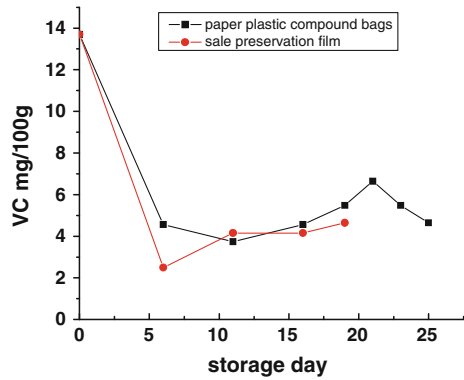**Fig. 96.6** Effect of storage bags on lychee

Fig. 96.7 Effect of storage bags on *VC* in lychee

The Vitamin C content decreased rapidly first as shown in Fig. 96.7. The Vitamin C content of lychee with the paper plastic compound bags and the control group were decreased by 70.36 and 82.21 %, respectively. And then increased slowly and the Vitamin C content keeps a steady value.

96.4　Conclusions

The paper plastic compound bags can prolong the shelf life of lychee to 11 day; it is doubled the shelf life of lychee with the sale preservation film. The obviously browning and water loss rate of lychee was obtained with ordinary commercial packaging bags. The paper plastic compound bags also could delay effectively the appearance of the white mold.

References

1. Guangquan, S., Jianliang, L., & Lianquan, G. (1999). *Journal of Zhongshan: University Journal, 4*, 35–43.
2. Fan, Z. J. (1990). *Guangzhou science and technology of food industry*, (2), 8–11.
3. Fuchs, Y. (1993). The physiological basis of lychee fruit pericarp colorrelenlion[J]. *Tropic science., 2*, 29–33.
4. Liu, K. (2006). Relying on technological progress to promote the upgrading of cassava industry. In *Cassava Industry Development Forum Material*, pp. 19–29.
5. Fang, C. (1992). *Study on the appropriate temperature of lychee fruit storage*, (1), 11–19.
6. Valverde, J. M., Valero, D., & Martiänez-Romero, D. (2005). Novel edible coating based on aloe vera gel to maintain table grape quality and safety. *Journal of Agriculture and Food Chemistry, 53*, 7807–7813.
7. Chena, S., Zhanga, M., & Wang, S. (2011). Effect of initial hermetic sealing on quality of 'Kyoho' lychee during storage[J]. *Postharvest Biology and Technology, 59*, 194–199.
8. GB/T6195-1986. *Determination of vitamin C in vegetables and fruits (2,6-Indophenol Titration Method)*. Beijing: Standard Press of China, 1986.

Chapter 97
Preparation and Characterization of PLLA/OMMT–MAH Nanocomposite by Esterification Method

Ruixia Duan, Kai Guo, Yingning He, Jinzhou Chen and Mingjun Niu

Abstract In this study, in order to avoid the serious degradation of poly (L-lactic acid) (PLLA) caused by maleic anhydride (MAH) while taking advantages of its interfacial compatibility, an esterification between OMMT and MAH was designed to form OMMT–MAH composite. The experiments showed that the esterification rate of OMMT (100 °C, without oxygen and using cyclohexanone as a solvent) is 6.5 %. Compared with pure PLA, PLA/OMMT–MAH (OMMT–MAH 1 wt%) obtained an optimum performance except impacting strength. And the crystallinity increased from 6.36 to 9.49 %. Compared with composites without initiator, the mechanical properties of composites with initiator improved slightly except bending modulus, which indicated that double bond on OMMT–MAH was opened under the effect of dicumyl peroxide (DCP) and connected with PLLA main chain by bonding. In this study, a novel method to modify MMT was found, and it was an effective way to improve the performance of PLLA.

Keywords Poly (L-lactic acid) · Modified montmorillonite · Esterification

97.1 Introduction

Poly (lactic acid) (PLA) is a kind of biodegradable and biocompatible thermoplastic polyester. It can be used in various fields, such as industrial packaging and biomedical applications [1]. However, some disadvantages of PLA greatly limit its application, such as lower crystalline and thermal stability. Many researchers have proved that PLA/organically modified montmorillonite (PLA/OMMT) nanocomposite can greatly improve the mechanical properties and many other properties [2–4].

In this study, PLLA/OMMT nanocomposite is prepared to improve some properties. The key to prepare nanocomposites is to scatter MMT into PLA matrix

R. Duan · K. Guo · Y. He · J. Chen (✉) · M. Niu
School of Material Science and Engineering, Zhengzhou University, Zhengzhou, China
e-mail: cjz@zzu.edu.cn

and enhance the compatibility of their interface. Maleic anhydride (MAH) has strong activity. It can melt grafting with PLA easily and can be esterified with MMT. So the two methods (grafting and esterification) to improve the compatibility of PLA and MMT were usually adopted [5–11].

When using grafting method, the grafting process can induce great degradation of PLA [12]. So the esterification method was adopted in this study to improve the compatibility of PLLA and OMMT without degradation of PLLA.

Hu et al. [13] had studied the esterification of MAH and octadecanol and found that they could react and the reaction rate is related with the concentration of the catalyst. Zhang et al. [14] modified vermiculite and analyzed the effect of different solvents, such as deionized water, ethyl acid, and acetone. They found that vermiculite was peeled off in the water and could be peeled more off with the increase of milling time, but cannot be peeled off in the other kind of organic solvent.

97.2 Experiments

97.2.1 Materials

The PLLA (4032D) used in this study is a commercial product of Nature Works. The OMMT (DK2 series) is also commercial products of Zhejiang Fenghong New material Co. Ltd. The MAH (analytical quality) is purchased from Kameo Chemistry Reagent Co. Ltd. in Tianjin. The cyclohexanone (analytical quality) and the ethanol (analytical quality) are provided by Fengchuan Chemistry Reagent Co. Ltd. in Tianjin. The dicumyl peroxide (DCP, chemical quality) was purchased from National Medicine Group Chemistry Reagent Co. Ltd.

97.2.2 Sample Preparation

At first, the raw materials were ready: The cyclohexanone was dried in oil bath pan in atmosphere at 100 °C for 4 h by magnetic blender, and OMMT was dried in vacuum at 60 °C for 4 h. Then, OMMT–MAH was prepared: fetching OMMT and MAH by the blend ratio for completely reaction, dissolving the blend in about 300 ml acetone solution, making them react in oil bath pan at 100 °C for 5 h by the protection of nitrogen, cooling the product and washing it twice by pure ethanol, and then drying and ball milling OMMT–MAH to powder. At last, PLLA/OMMT–MAH nanocomposite was prepared: measuring 1 g DCP, OMMT–MAH 0, 1, 3, 5 wt% separately, adding PLLA granule and mixing them with silicon oil, and then feeding the mixture to twin-screw extruder machine (TE-34, graduate school of extruding machine, Institute of chemical machine) to obtain PLLA/OMMT–MAH nanocomposite.

97.2.3   Characterization

In order to conclude the reaction extent of OMMT and MAH, the acid number was determined by chemical titration method. After mixing the OMMT–MAH and KBr (potassium bromide) powder and pressing the mixture to flake, it was characterized by Fourier transform infrared (FT-IR) spectrophotometer. Then, the melt flow rate and mechanical properties of the nanocomposite were measured. Finally, the heat properties were characterized by differential scanning calorimeter (DSC) and thermogravimetry (TG).

97.3   Results and Discussion

97.3.1   Calculation of Acid Number

The content of OMMT participating in esterification reaction is 6.5 % through the titration and the sequent calculation.

97.3.2   FT-IR Spectroscopy Analysis

Figure 97.1 shows the FT-IR graphs of OMMT and OMMT–MAH. The two curves were basically accord with each other. Compared with the curve of OMMT, the strong absorption peaks appeared in 1734 cm^{-1} on the OMMT–MAH curve, which was the characteristic absorption of C=O group in ester bonds. And the peak in 1734 cm^{-1} was the characteristic absorption of C–O group in ester bonds. The

Fig. 97.1 Infrared spectrum graph of OMMT and OMMT–MAH
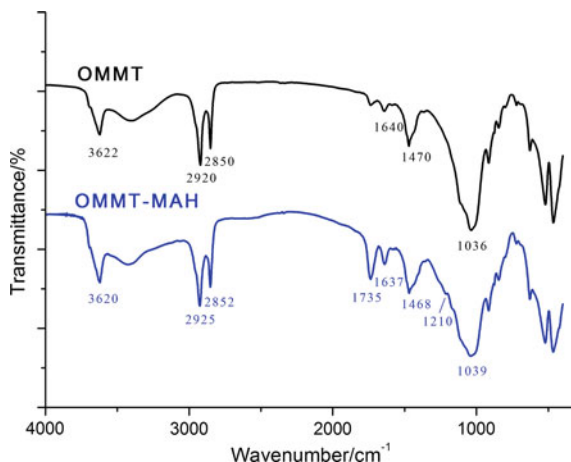
absorption peaks around 1637 cm^{-1} were strengthened, which was caused by the overlap of –C=C– double bond in maleic acid ester obtained and OH group. According to the information above, it can be deemed that MAH and OMMT had reacted with each other and the product was OMMT–MAH.

97.3.3 Melt Flow Rate (MFR) of the Nanocomposite

Table 97.1 shows the MFR of PLLA/OMMT–MAH nanocomposites with different OMMT–MAH contents. Along with the increase of OMMT–MAH content, MFR of nanocomposites became higher gradually, and viscosity of nanocomposites decreased, so that processing properties of PLLA were improved.

97.3.4 Mechanical Properties

Table 97.2 shows the data of mechanical properties of nanocomposites with different OMMT–MAH content and DCP content, and Fig. 97.2 shows the corresponding graphs. When the OMMT–MAH content was 1 wt%, the strength and modulus properties of the composites were the best in all of the samples. When the content of OMMT–MAH was 3 wt%, the elongation at break was the highest in all samples, which means the toughness was the best in this condition. But the impacting strength decrease gradually along with the increase of OMMT–MAH content, which may be caused by uneven dispersion of OMMT. The condition without DCP was also listed in the table. It is revealed that DCP enhances the

Table 97.1 MFR of nanocomposites with different OMMT–MAH content

OMMT–MAH content (wt%)	0	1	3	5
MFR (g/10 min)	3.343	3.642	3.906	4.304

Note The testing temperature was 15 °C, and the load was 10.34 kg

Table 97.2 Mechanical properties of PLLA/OMMT–MAH nanocomposites

OMMT–MAH content (%)	Tensile strength (MPa)	Elongation at break (%)	Tensile modulus (MPa)	Bending modulus (MPa)	Bending strength (MPa)	Impacting strength (kJ m^{-2})
1	67.2	3.29	3830	3800	105.4	25.9
1*	65.0	3.57	3730	4390	103.5	14.5
3	65.3	6.85	4200	4080	104.8	17.9
3*	64.1	5.10	4230	4670	104.3	13.6

The temperature was 20 °C; the relative humidity was 30 %; and the extending rate was 25 mm/min. "1" shows that no initiator DCP was added in the same condition as "1"
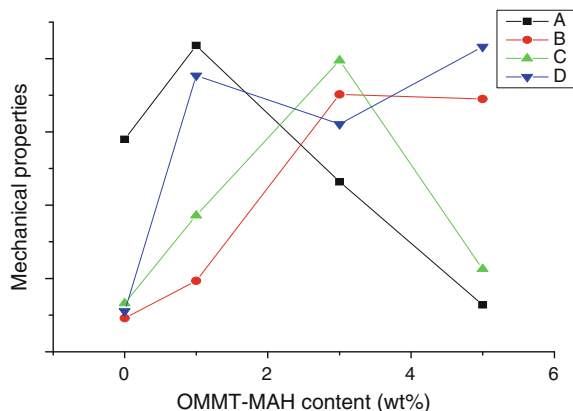
Fig. 97.2 Mechanical properties of PLLA/OMMT–MAH composite (*A*) tensile strength; (*B*) elongation at break; (*C*) tensile elastic modulus; (*D*) bending strength

mechanical properties slightly, which was limited by the process of blending DCP and OMMT–MAH. They were just physically blended so that the collision probability was too little and coupling action was too weak.

97.3.5 Differential Scanning Calorimeter (DSC) Analysis

The DSC curves of all samples are shown in Fig. 97.3. The data of the DSC curves are listed in Table 97.3. The glass temperature (T_g), crystalline temperature (T_c), and melting temperature (T_m) of nanocomposite (OMMT–MAH, 1 wt%) were slight higher than the pure PLLA. The crystallinity increases from 6.36 to 9.49 %. That was because OMMT–MAH played a part of reactive compatibilizer which
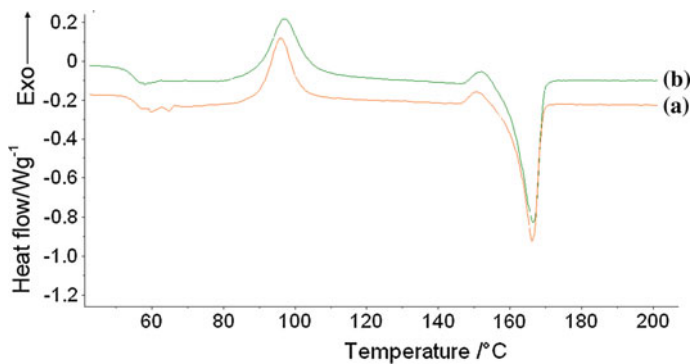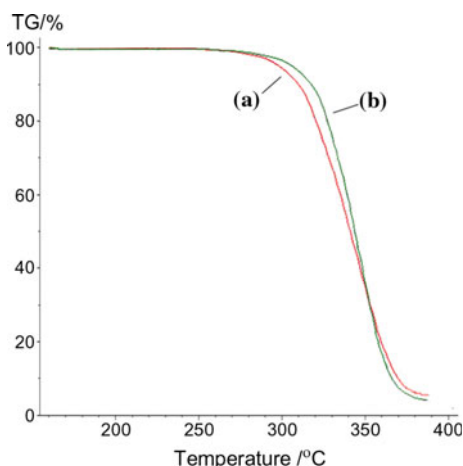

Fig. 97.3 DSC *curves* of pure PLLA and nanocomposite (*a*) pure PLLA (*b*) PLLA/OMMT–MAH (OMMT–MAH, 1 wt%)

Table 97.3 DSC parameters and crystallinity

Sample	T_g (°C)	T_c (°C)	T_m (°C)	ΔH_f (J g^{-1})	X_c (%)
Pure PLLA	55.4	97.8	166.3	5.96	6.36
PLLA/OMMT–MAH(99:1)	54.9	97.6	166.8	8.89	9.49

Fig. 97.4 TG *curves* of pure PLLA and nanocomposite (*a*) pure PLLA (*b*) PLLA/OMMT–MAH nanocomposite (OMMT–MAH, 1 wt%)

Table 97.4 TG parameters of pure PLLA and nanocomposites

Sample	T_o (°C)	T_f (°C)
Pure PLLA	332.0	364.7
PLLA/OMMT–MAH (99:1)	334.8	363.6

improved the compatibility of PLLA and OMMT and increased the thermal stability of the nanocomposite. At the same time, OMMT–MAH acted as a heterogeneous nucleation and advances the crystallinity consequently.

97.3.6 Thermogravimetry (TG) Analysis

Figure 97.4 shows TG curves of pure PLLA and PLLA/OMMT–MAH nanocomposite (OMMT–MAH, 1 wt%), and Table 97.4 shows the relevant parameters. The original TG temperature (T_o) increased by 2.8°C, and the final TG temperature (T_f) decreased by 1.1 °C. So the thermal stability of nanocomposite was a little higher than the pure PLLA.

97.4 Conclusions

An esterification between OMMT and MAH happened to prepare OMMT–MAH, and 6.5 % OMMT was esterified (100 °C, without oxygen and cyclohexanone as a solvent). Compared with pure PLLA, PLLA/OMMT–MAH (OMMT–MAH, 1 wt %) obtained a optimum performance in mechanical properties except impact strength. The crystallinity increased from 6.36 to 9.49 %. Compared with nanocomposites without initiator, the mechanical property improved slightly except bending modulus, which indicated that double bond on OMMT–MAH was opened under the effect of DCP and connect with PLLA main chain. The crystallinity of nanocomposite increased to 9.49 %, and the thermal stability was a little higher compared with the pure PLLA. However, OMMT–MAH played very limited function in improving properties of PLLA by this study, and the possible reason was that in the process of blending DCP and OMMT–MAH, they were just physically blended so that the coupling action was too weak.

References

1. Chen, G. X., Kim, H. S., Park, B. H., et al. (2005). Controlled functionalization of multiwalled carbon nanotubes with various molecular-weight poly(L-lactic acid). *Journal of Physical Chemistry B, 109*(47), 22237–22243.
2. Xu, X., Chen, X., Liu, A., et al. (2007). Eletrospun poly(L-lactide)-grafted hydroxyapatite/poly (L-lactide) nanocomposite fibers. *European Polymer Journal, 43*(8), 3187–3196.
3. Hong, Z. K., Zhang, P. B., He, C. L., et al. (2005). Nanocomposite of poly(L-lactide) and surface grafted hydroxyapatite: Mechanical Properties And Biocompatibility. *Biomaterials, 26* (32), 6296–6304.
4. Yan, Shifeng, Yin, Jingbo, Yang, Jiaying, & Chen, Xuesi. (2007). Stuctural characteristics and thermal properties of plasticized poly(L-lactide)-silica nanocomposites synthesized by solgel method: Materials letters. *Elsevier., 61*, 2683–2686.
5. Yan, S. F., Yin, J. B., & Yang, Y. (2007). Surface-grafted silica linked with L-lactic acid oligomer: a novel nanofiller to improve the performance of biodegradable poly(L-lactide). *Polymer, 48*(6), 1688–1694.
6. McLauchlin, Andrew, Bao, Xujin, & Zhao, Feng. (2011). Organoclay polybutylene terephthalate nanocomposites using dualsurfactant modified montmorillonite prepared by the masterbatch method. *Applied Clay Science, 53*(4), 749–753.
7. Shah, R. K., & Paul, D. R. (2004). Nylon6 nanocomposites prepared by a melt mixing masterbatch process. *Polymer, 45*(9), 2991–3000.
8. Pluta, M., & Galeski, A. (2002). Crystalline and supermolecular structure of polylactide in relation to the crystallization method. *Supermolecular Structure of Polylactide, 86*, 1386–1395.
9. Okamoto, M. (2006). Recent advances in polymer/layered silicate nanocomposites: an overview from science to technology. *Materials Science and Technology, 22*(24), 756–779.
10. Gopakumar, T. G., & Pagé, D. J. Y. S. (2004). Polypropylene/graphite nanocomposites by thermo-kinetic mixing. *Polymer Engineering & Science, 44*(6), 1162–1169.
11. Zhang, X., Guo, F., Chen, J., Wang, G., & Liu, H. (2005). Investigation of interfacial retardant ethylene vinyl acetate copolymer/alumina trihydrate nanocomposites. *Polymer Degradation and Stability, 47*, 411–418.

12. Fowlks, A. C., & Narayan, R. (2010). The effect of maleated polylactic acid (PLA) as an interfacial modifier in PLA-talc composites. *Journal of Applied Polymer Science, 118*(5), 2810–2820.
13. Hu, H. G., Qi, G. R., & Li, X. H. (1999). Research on esterification of maleic anhydride and eighteen alcohol. *Journal of collegechemical engine, 13*(5), 466–469.
14. Zhang, Y., Han, W., Li, Q. Y., & Wu, C. F. (2008). Characterization of vermiculite modified by maleic anhydride. *Journal of the Chinese Ceramic society, 36*(6), 850–853.

Chapter 98
Effect of Film-Forming Conditions on the Properties of Fluorinated Acrylate Film

Mengke Feng, Guorong Cao and Jiazi Shi

Abstract The fluorinated acrylate composite emulsion was synthesized by seeded emulsion polymerization. With the resultant emulsion, a number of hydrophobic films were prepared. The contact angles of water on the films were measured using Kruss DSA100 automatic video contact angle measuring instrument. The influences of film-forming conditions, such as heating temperature, heating time, and film thickness, on the film properties were discussed. The film with a thickness of 50 μm after 4-h-long heat treatment at 80 °C can obtain best properties. The results indicate that the formation conditions have greatly affected film properties.

Keywords Fluorinated acrylate · Film-forming conditions · Film properties

98.1 Introduction

Acrylate emulsion is easy to synthesize and has excellent properties of flexibility, adhesion, film forming, making it an important environmentally friendly coating. However, defects of hardness, heat resistance, and solvent resistance restricted its application [1, 2]. Fluorine-modified acrylate can retain excellent properties of acrylate latex while obtaining good performance of fluoropolymer to some extent,

M. Feng · G. Cao (✉) · J. Shi
School of Printing and Packaging Engineering, Beijing Institute
of Graphic Communication, Beijing, China
e-mail: caoguorong@bigc.edu.cn

M. Feng
e-mail: 476853760@qq.com

J. Shi
e-mail: shijiazi@bigc.edu.cn

M. Feng · G. Cao · J. Shi
Key Laboratory of Packaging Materials, Beijing Key Laboratory of Printing
and Packaging Materials and Technology, Beijing, China

such as hydrophobic, oleophobic, and antifouling properties. Fluorine-containing acrylate has very promising prospects in optical coating, optical element protection coating, packaging coating, automobile coating, architectural coating, textile finishing agent, and other fields [3–5]. The properties of fluorinated acrylate film were influenced by the polymerization conditions, film-forming conditions, and film preparation methods. Based on stable fluorine-containing emulsion, film-forming factors which will affect the performance of fluorinated polymer film are investigated in this paper.

98.2 Experimental Section

98.2.1 Materials

Methyl methacrylate (MMA, A.R), butyl acrylate (BA, A.R), acrylic acid (AA, A. R), ammonium persulfate (APS, A.R), polyoxyethylene octyl phenyl ether (OP-10, A.R), and sodium dodecyl sulfate (SDS, A.R) were supplied by Guangfu chemical industry institute (Tianjin). Sodium bicarbonate ($NaHCO_3$, A.R), aqua ammonia ($NH_3 \cdot H_2O$, A.R) were provided by Beijing chemical works (Beijing). Hexafluorobutyl methacrylate (HFMA, > 95 %) were purchased form J&K chemical Co. Ltd (Beijing). APS, OP-10, SDS, and $NaHCO_3$ were dissolved in deionized water with the ratio of 1:50. Other reagents were used as received.

98.2.2 Preparation of Fluorinated Acrylate Copolymer Emulsion

Firstly, the nuclear monomer pre-emulsion was prepared. The nuclear monomer (4.67 g MMA, 2.8 g BA, 0.1 g AA), 1/4 of emulsifier mixture (7.67 g OP-10, 3.83 g SDS), and 9.67 g deionized water were added into a beaker and underwent ultrasonic emulsification at room temperature for 10 min.

Secondly, seed emulsion was prepared following the next procedures. A 250-mL four-necked round-bottom flask was equipped with a thermometer, a reflux condenser, a dropping funnel, and an inlet. To this flask was charged 1/2 of nuclear monomer pre-emulsion mixtures, 1/2 of emulsifier mixture (15.3 g OP-10, 7.67 g SDS), 1/3 of aqueous initiator solution (3.06 g APS), and buffering solution (1.53 g $NaHCO_3$) mechanical stirring at 75 °C for 20 min under nitrogen atmosphere. When the mixture appears blue, 1/3 of initiator (3.06 g APS) and the remaining nuclear monomer pre-emulsion were dropped into the flask via syringe in 2 h. Subsequently, the temperature was adjusted to 80 °C and the reaction continued for 40 min.

Thirdly, the shell monomer pre-emulsion was prepared following the next procedures. The shell monomer (9.33 g MMA, 5.6 g BA, 0.2 g AA), 1/4 of emulsifier mixture (7.67 g OP-10, 3.83 g SDS), and 4.83 g deionized water were added into a beaker. Then, hexafluorobutyl methacrylate was dropped into the beaker slowly and underwent ultrasonic emulsification at room temperature for 10 min.

At last, the shell monomer pre-emulsion and the remaining initiator were added into the reactor filled with seed emulsion for 2 h. Then, ammonia was dropped into the synthesized emulsion to control the pH value of emulsion in the range of 6–7.

98.2.3   Film Preparation

Latex film was obtained by directly coating the freshly prepared latex solution onto a slide glass, which was pre-cleaned by ultrasonic treatment in isopropyl alcohol, acetone, ethanol, and deionized water, respectively, for 10 min at room temperature. The film was heated at different temperature in the oven for different time. In addition, the film thickness is changed with different coated rod.

98.2.4   Measurements

98.2.4.1   FTIR

FTIR (Fourier transform infrared) spectra were recorded by a Shimadzu FTIR-8400 spectrometer with KBr pellets and films.

98.2.4.2   Water Contact Angle (WCA)

Water contact angle was measured by Kruss DSA100 automatic video contact angle measuring instrument. The values quoted are the average of five measurements made at different positions of the film surface.

98.2.4.3   Water Absorption Rate

Prepare the film according to the method mentioned in 2.3. Remove films from the slide glasses and then take weight of the films. Get rid of moisture on the surface of the films which have been soaked in deionized water for 24 h with filter paper and then weigh the films. Each film takes three test samples and then calculate the average value. The water absorption rate was determined from Eq. (98.1):

$$\text{Water Absorption Rate} \, (\%) = \frac{m_2 - m_1}{m_1} \times 100 \,\% \qquad (98.1)$$

where m_1 is the weight of the sample to be soaked, and m_2 is the weight of the sample after being soaked.

98.2.4.4   Hardness

The film hardness is measured according to paints and varnishes–determination of film hardness by pencil test GB/T 6739-2006. The result is expressed by pencil hardness.

98.2.4.5   Coating Adhesion

Coating adhesion is measured according to paints and varnishes–crosscut test for films GB/T 9286-1998. The best is level 0, and the worst is level 5.

98.3   Results and Discussion

98.3.1   FTIR Spectrum of Latex Film

The FTIR spectra of fluorinated acrylate film are shown in Fig. 98.1. It can be seen that a strong adsorption peak appeared at 2957 cm^{-1} for –CH3. The characteristic absorption peak of C = O stretching vibration appeared at 1733 cm^{-1}. The peak at about 1250–1150 cm^{-1} in the FTIR spectra is the characteristic absorption of

Fig. 98.1 FTIR spectra of fluorinated acrylate film
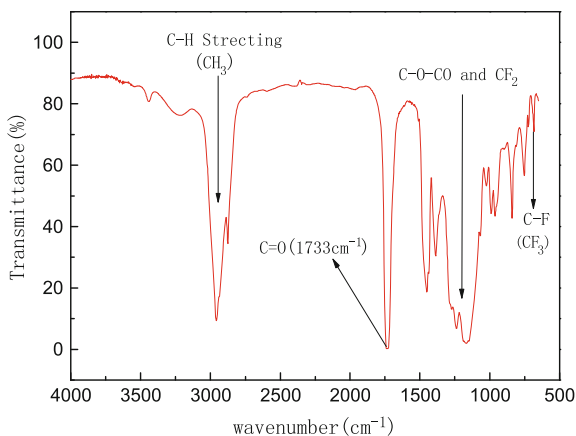
C–O–C groups and –CF2. Signals at 1250 and 679 cm^{-1} are assigned to C-F stretching and wagging vibrations [6]. FTIR spectrum shows that MMA, BA, AA, and HFMA all took part in the copolymerization reaction and fluorinated acrylate was prepared.

98.3.2   AFM Image of Latex Film

The composite latex film was heated at 80 °C for 4 h. Figure 98.2 shows the 3D AFM image of fluorinated acrylate composite coating. In Fig. 98.2, it could be seen that the film surface was flat. The small bumps and waves appeared on the surface might be caused by the phase separation and migration of fluorinated chains [7].

98.3.3   Influence of Temperature

The influence of temperature was studied on the films which had been heat-treated for 4 h with the thickness of 50 μm. The heating temperatures were 60, 80, and 120° C. The result was shown in Fig. 98.3.

With the increase in temperature, water contact angle increases first and then decreases. This also works for water absorption rate as temperature increases, and the random molecular motions are more vigorous than at a low temperature, which promote C-F group to migrate to the film surface faster. When the temperature is above 80 °C, the cross-link network of the film surface has been formed, while there still has some C-F groups that have no enough time to migrate to the film surface, causing water contact angle to reduce.

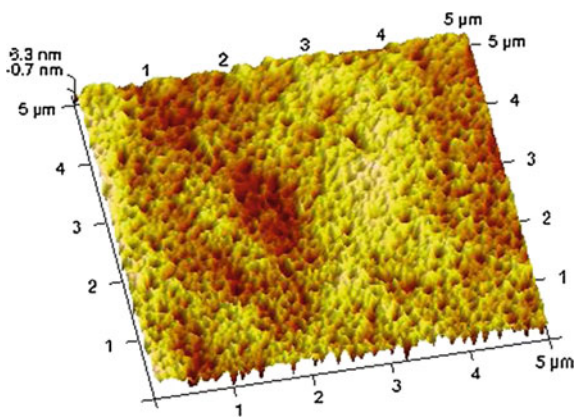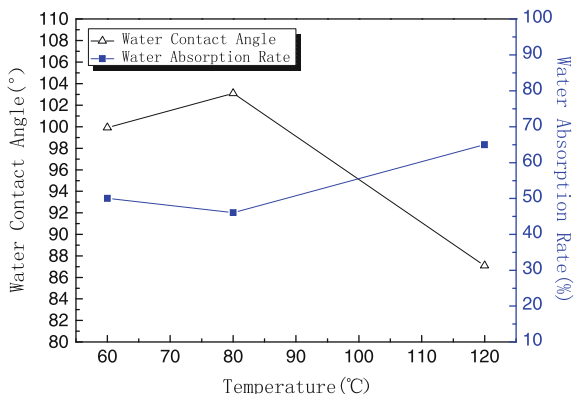**Fig. 98.2** AFM image (5 μm * 5 μm) of fluorinated acrylate film

Fig. 98.3 Influence of temperature on hydrophobicity of latex films

98.3.4 Influence of Film Heating Time

Films with the thickness of 50 μm were prepared at 80 °C. By changing heating time, film properties varied from each other. The change of hydrophobicity was recorded in Fig. 98.4. Heat treatment accelerates molecular motion, which makes C-F groups move to the surface faster, while the prolonging of heating time makes C-F groups to have adequate time for migration.

98.3.5 Influence of Film Thickness

The influence of film thickness is similar to temperature. Figure 98.5 shows water contact angles and water absorption rate of films which had been heated at 80 °C for 4 h. Water contact angle rises up first and then declines. This phenomenon can be explained as following reasons: (1) The thicker the film is, the shorter the distance

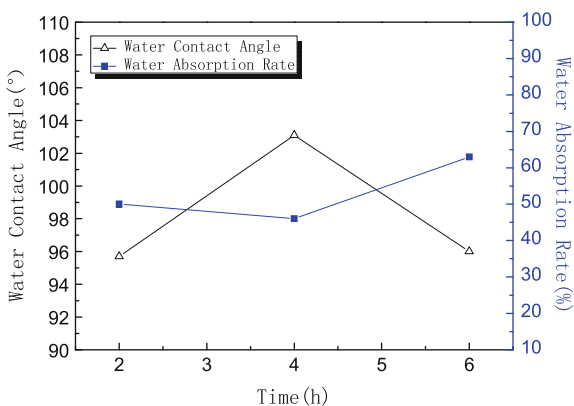**Fig. 98.4** Influence of heating time on hydrophobicity of latex films

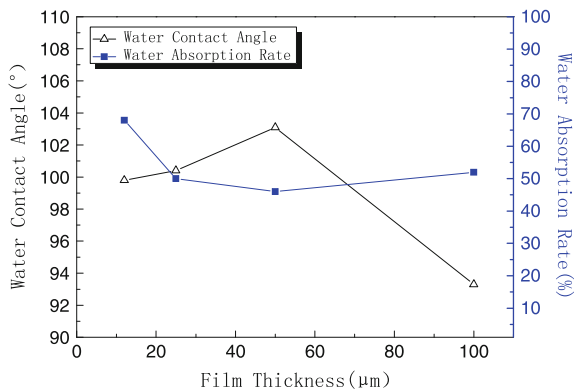**Fig. 98.5** Influence of film thickness on hydrophobicity of latex films

Table 98.1 Properties of latex film

Appearance	Water contact angle	Water absorption rate	Hardness	Coating adhesion
Transparent	103.1°	46 %	2H	Level 2

C-F groups go through to the film surface. (2) C-F groups are distributed at different depths. Thus, the amount of C-F groups distributed at the surface of film decreased, which leads to the decline of water contact angle.

98.3.6   Film Property

The composite latex film was obtained by 4-h-long heat treatment at 80 °C. The property of fluorinated acrylate film is listed in Table 98.1.

As shown in Table 98.1, the fluorinated acrylate film has excellent hydrophobicity. The water contact angle reached at 103.1°. Improved polymerization process and film-forming conditions can affect film properties greatly.

98.4   Conclusions

The properties of the fluorinated latex film were not only influenced by the polymerization process but also influenced by film-forming conditions [8] such as heating temperature, heating time, and film thickness. The film with a thickness of 50 μm after 4-h-long heat treatment at 80 °C can obtain best properties, the contact angle is 103.1°, hardness is 2H, and coating adhesion level is 2.

References

1. Liao, W. B., Qu, J. Q., Li, Z., et al. (2010). Preparation of organic/inorganic hybrid polymer emulsions with high silicon content and sol-gel derived thin films. *Chinese Journal of Chemical Engineering, 18*(1), 156–163.
2. Zhou, X. D., Gu, G. H., Li, W. H., et al. (2004). Preparation and properties of fluoroacrylate copolymer. *Fine Chemicals, 21*(z1), 136–139.
3. Mazzola, M., Frediani, P., Bracci, S., et al. (2003). New strategies for the synthesis of partially fluorinated acrylic polymers as possible materials for the protection of stone monuments. *European Polymer Journal, 39*, 1995–2003.
4. Cheng, S. Y., & Chen, Y. J. (2003). Development of systhesis and surface characters of fluorinated acrylate polymers used in coating field. *Material Science and Engineering, 19*(3), 49–53.
5. Thomas, R. R., Graham, W. F., Darmon, M. J., et al. (1997). Preparation and surface properties of acrylic of polymers containing fluorinated monomers. *Macromolecules, 30*(10), 2883.
6. Chen, L. J., Shi, H. X., Wu, H. K., et al. (2010). Preparation and characterization of a novel fluorinated acrylate resin. *Journal of Fluorine Chemistry, 131*, 731–737.
7. Xu, W., An, Q. F., Hao, L. F., et al. (2013). Synthesis and characterization of self-crosslinking fluorinated polyacrylate soap-free latices with core–shell structures. *Applied Surface Science, 268*, 373–380.
8. Qin, Z. G., Tu, W. P., Xia, Z. B., et al. (2004). Research on Blend of Expoxy Latex and Fluorinated Latex. *Modern Chemical Industry, 24*(5), 34–37.

Chapter 99
Preparation and Properties Research on Electrostatic Spinning Acetate/Chitosan Composite Fiber

Yating Wu, Liqiang Huang, Jing Wang and Na Wei

Abstract In this paper, composite fiber membranes of cellulose acetate/chistosan (CA/CS) were prepared by electrospinning using two different injection methods involving co-injection and two-step injection. The antibacterial and micro-morphology properties of the CA/CS composite fiber membranes were also investigated. The results show that the optimum conditions of co-injection method were as follows: voltage 13 kV, flow rate 1.0 ml/h, and receiving distance 10 cm. For the two-step injection method, the voltage of 15 kV, flow rate of 1.0 ml/h, and receiving distance of 10 cm were adopted to prepare cellulose acetate membrane at first, and then, the chitosan liquid was injected into the cellulose acetate membrane under the condition of 13 kV voltage and 0.5 ml/h flow rate. The CA/CS composite fiber membrane prepared by the co-injection method had a better fibrous structure arrangement, smooth fiber surface, and uniform thickness, but the poor antibacterial effect was also indicated. However, the two-step injection method has excellent antibacterial effects. When the CS/PEO ratio is 9:1, composite fiber membrane has the best antibacterial property, but the fiber surface is not smooth enough.

Keywords Nanofibers · Electrospinning · Composite fibers · Cellulose acetate · Chitosan · Antibacterial

99.1 Introduction

Electrospinning technology, which is perceived as one of the simplest and most effective methods to prepare nanofibers [1], has been widely applied in the fabrication of nanofibers in recent years. Compared to traditional spinning method, fiber

Y. Wu · L. Huang (✉) · J. Wang
Tianjin University of Science and Technology, Tianjin, China
e-mail: hlq@tust.edu.cn

N. Wei
Tianjin Vocational College, Tianjin, China

prepared by electrospinning has lower diameter and can achieve the minimum diameter of one nanometer [2]. Moreover, the nanofibers prepared by electrospinning have the advantages of large surface area, high porosity, large length to diameter ratio, and good mechanical properties [3, 4].

Cellulose acetate (CA) is a kind of white solid material with good stability, easy to manufacture, and nonflammable properties and commonly used as the raw materials of electrospinning process to replace natural cellulose [5]. Due to its biodegradability, cellulose acetate membrane is widely used in the packaging field to reduce white pollution. Considering the weak antibacterial property of cellulose acetate membrane, the chitosan with high antibacterial property was used to prepare cellulose acetate/chistosan (CA/CS) composite fiber membrane. Polyethylene oxide (PEO) is a kind of water soluble polymer, which has the characteristics of low toxicity and easy processing. Because chitosan is not easy to be spun, PEO was used as the agent for electrospinning of chitosan.

99.2 Materials and Methods

99.2.1 Experimental Materials

Cellulose acetate was purchased from Aladdin Industrial Corporation. Acetic acid, acetone, NaoH, powdered agar, NaCl, beef extract, and peptone were purchased from Tianjin FengChuan Chemical Reagent Co., Ltd. PEO was purchased from Guangzhou SPX Trading Co., Ltd.

99.2.2 Experimental Methods

99.2.2.1 Spinning Solution Preparation

The cellulose acetate spinning solution of different mass percent (3, 4 and 6 %) was prepared by a constant temperature magnetic stirrer under the condition of 48 °C for 1 h using the acetone and DMAc (N-N dimethylacetamide) with the volume ratio of 4:1 as solvent. In order to avoid the volatilizing of solvent, the beaker was wrapped with preservative film.

The chitosan/PEO (9:1, 3:1) spinning solution with the mass 2 % was formulated using acetate 90 % (w/w) as solvent and stirred for 24 h at room temperature by using magnetic stirrer. In order to avoid the volatilizing of solvent, the beaker was wrapped with preservative film.

99.2.2.2   Cellulose/Chitosan Composite Fiber Membrane Preparation

The spinning solution was put into a 50-ml syringe containing a needle with inner diameter of 0.8 mm. The voltage increased from 13 to 20 kV. The flow rate of the injection pump was adjusted to 0.5 and 1.0 ml/h, respectively. The aluminum foil was the receiver with a receiving distance of 10 cm.

Two-step injection methods were utilized to prepare cellulose acetate/chitosan composite fiber membranes. The first method was co-injected by which the cellulose acetate solution and chitosan solution were injected by double needle at the same time. The second method is two-step injection, which is to inject the cellulose acetate first and then inject the chitosan solution on it.

99.2.2.3   Antibacterial Experiment

Antibacterial activity of cellulose acetate/chitosan composite fiber membrane was examined against Escherichia coli and Staphylococcus aureus by using chip culture method. Antibacterial activity of the CA/CS composite fiber membrane was directly characterized by monitoring the growth of microorganisms around the sample.

99.2.2.4   Microscopic Morphology Analysis

The microscopic morphology of CA/CS composite fiber membrane samples was observed using a scanning electron microscope (SEM, Model: JSM-6380LV, FEI Co., Ltd. USA), which has 5 kV accelerating voltage. The beam current (measured between the condenser lens and objective lens) is approximately 3×10–3×11 A. Prior to the examination, a thin coating (~ 10 nm) of gold was deposited on the sample, to enhance the conductivity and secondary electron emission characteristics.

99.3   Results and Discussion

99.3.1   Effect of Chitosan Concentration to Composite Fiber Membrane

Comparing the Sample A1 and Sample A of Fig. 99.1, the presence of inhibition zone could not be observed and there were many microorganisms around the Sample A1 and Sample A. This revealed that the chitosan content in the Sample A1 and Sample A was low and with limited dissolution, which could not be unable to reach a concentration that created effective antimicrobial activity. Therefore, it can be concluded that the antimicrobial activity of the Sample A1 and Sample A were not obvious (Tables 99.1 and 99.2).
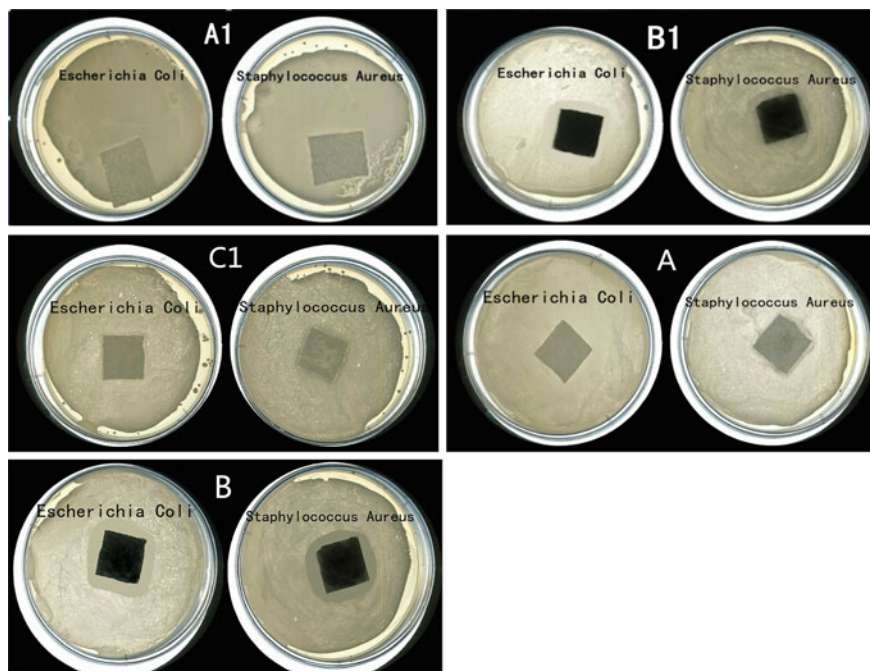
Fig. 99.1 Antibacterial effects of Samples *A1*, *B1*, *A*, *B*, and *C1* against Escherichia coli and Staphylococcus aureus

Comparing Sample A1 and Sample C1, when the chitosan concentration was constant, changing the concentration of cellulose acetate did not appear an obvious effect for antimicrobial activity of composite fiber membrane against Escherichia coli and Staphylococcus aureus. It can be concluded that the concentration of cellulose acetate has no significant influence on the antimicrobial effect of composite fiber membrane.

Comparing Sample A1 and Sample B1, and Sample A and Sample B, the bacteriostatic effects of composite fiber membrane against Escherichia coli and Staphylococcus aureus were improved with the increase in mass ratio of chitosan

Table 99.1 Processing parameters of co-injection method

	Cellulose acetate solution		Chitosan solution		
	Ratio of acetone/DMAc	Solution concentration (wt %)	Ratio of CS/PEO	Concentration of acetic acid (%)	Solution concentration (wt %)
A1	4:1	4	3:1	90	2
B1	4:1	4	9:1	90	2
C1	4:1	6	3:1	90	2

Table 99.2 Processing parameters of two-step injection method

	Cellulose acetate solution		Chitosan solution		
	The ratio of acetone/DMAc	Solution concentration (wt %)	The ratio of acetone/DMAc	Solution concentration (%)	Solution concentration (wt %)
A	4:1	4	3:1	90	2
B	4:1	4	9:1	90	2

and PEO. Sample B1 and Sample B revealed apparent antimicrobial activity. There were no microorganisms grown around the samples, and an apparent inhibition zone was observed. It is presented that the chitosan dissolution of the Sample B1 and Sample B had reached to a level ensuring the content of the adjacent area to satisfy the requirement of antimicrobial activity.

Comparing Samples B1 and B, the bacteriostatic effect of the two-step injection method is apparently better than the co-injection method. It means that the composite fiber membranes with different preparation processes have significant differences of bacteriostatic effects. The antimicrobial effect of the composite fiber membrane produced by two-step injection method was better than the composite fiber membrane manufactured by co-injection method.

In general, when the CS/PEO ratio was 9:1, composite fiber membrane had an effective antibacterial property. But the antibacterial effect of chitosan was slow and could not kill the bacteria instantly. It took a long time to reach to a level of antibacterial activity. In other words, the antibacterial activity could maintain in a certain period of time.

99.3.2 *Effect of Injection Method to Composite Fiber Membrane*

99.3.2.1 Co-injection of Double Needle

The experimental parameters of co-injection method were as follows: flow rate 1.0 ml/h and receiving distance 10 cm. When the voltage of Sample A in Fig. 99.2 is 20 kV, the spun fibers had uneven thickness, and fibers were intricate cross-hybrids due to the high voltage. As shown in Fig. 99.2, the bonding phenomenon of fibers was improved with the reduction of the voltage in the range of 13–20 kV, and the fiber clarity and thickness of the fibers were also improved greatly. When the voltage of Sample C was 13 kv, the obtained fiber was better than Samples A and B (the voltage of Sample B was 15 kv). When the voltage of Sample D was 10 kV lower than 13 kV, the obtained fiber structure was disordered and of uneven thickness.
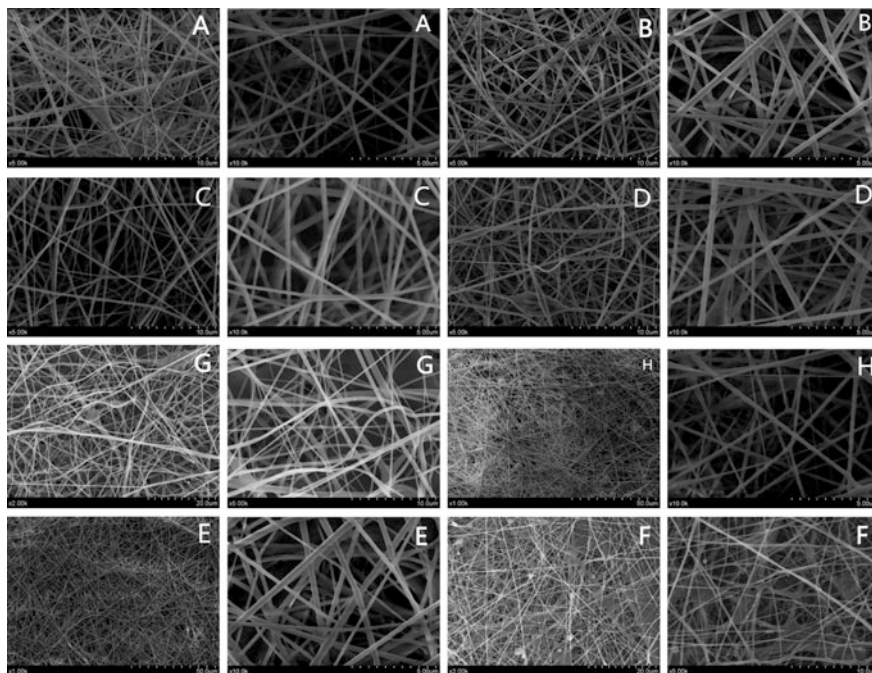
Fig. 99.2 SEM of the sample prepared by co-injection method and two-step injection method

Comparing previous data, it shows that the optimum voltage of co-injection method was 13 kV. The composite fiber membrane produced under this voltage has a better fibrous structure arrangement. The fiber surface was smooth and had substantially uniform thickness. By using this parameter and continuously injecting for 10 h, good uniformity of composite fiber membranes could be obtained (Fig. 99.2-E).

99.3.2.2 Two-Step Injection

In order to obtain the perfect composite fiber membrane, each process of two-step injection method could be done under the optimum condition, respectively.

The parameters used for preparing cellulose acetate membrane were voltage of 15 kV, flow rate of 1.0 ml/h, and receiving distance of 10 cm.

The parameters used for preparing chitosan membrane in Fig. 99.2-F were as follows:

Voltage of 13 kV, flow rate of 1.0 ml/h, and receiving distance of 10 cm. Due to the large viscosity and the difficulty of spinning of chitosan solution, the formed fiber had a large number of rollerballs induced uneven fiber thickness and rough surface, when the flow rate was 1.0 ml/h.

The parameters used for preparing chitosan membrane in Fig. 99.2-G were as follows: voltage of 13 kV, flow rate of 0.5 ml/h, and receiving distance of 10 cm. It is shown in Fig. 99.2-G that reducing the injection rate appropriately could help evaporate the solvent and facilitate the formation of the fibers, decrease the rollerballs in the fiber greatly, and improve the fibers uniformity and length. Under this condition, the manufacturing of composite fiber membrane takes a long time. First of all, the cellulose acetate was needed to be injected at a rate of 1.0 ml/h for 10 h. Then, chitosan was needed to be injected at a rate of 0.5 ml/h for 20 h in order to obtain a composite fiber membrane (Fig. 99.2-H).

As shown in Figs. 99.2-E and 99.2-H, the fiber surface of the composite fiber membrane prepared by two-step injection was not smooth enough compared to co-injection method prepared sample.

99.4 Conclusions

The properties of the CA/CS composite fiber membrane produced by using electrospinning technology can be affected by many parameters during the composition manufacturing process. The results show that the optimum parameters of co-injection method were as follows: voltage 13 kV, flow rate 1.0 ml/h, and receiving distance 10 cm. Under this conditions, the CA/CS composite fiber membrane had a better fibrous structure arrangement, smooth fiber surface, and uniform thickness, but with poor antibacterial effect.

As for the two-step injection method, the parameters for preparing cellulose acetate membrane in the first step were as follows: voltage 15 kV, flow rate 1.0 ml/h, and receiving distance 10 cm, and the parameters for preparing chitosan fiber membrane in the second step were as follows: voltage 13 kV and flow rate 0.5 ml/h. Compared to co-injection method, the two-step injection method needed longer time to produce the electrospinned CA/CS composite fiber membrane, and its fiber surface was not smooth enough, but it appeared excellent antibacterial effect.

References

1. Li, Y., Qiu, T., Zhou, Z., & Xu, X. (2011). Progress in the application of electrospinning nanofibers[J]. *Materials review A: summary, 25*(9), 84–88.
2. Shi, Q., Yu, J., Gu, K., et al. (2005). Electrospinning technique and its application. *Chemical world, 5*, 313–316.
3. Schiffman, J. D., et al. (2007). One-step electrospinning of crosslinked chitosan fibers. *Biomacromolecules, 8*(9), 2665.

4. Bhardwaja, N., et al. (2010). Electrospinning: A fascinating fiber fabrication technique. *Biotechnology Advances, 28*(3), 325.
5. Hou, J., Zhang, W. X., et al. (2012). Application of electrospinning method in the preparation of modified cellulose acetate. *Chemical progress, 12*, 2359–2366.

Chapter 100
Preparation of POSS Modified PLLA Film and Research of Its Part Properties

Xiaohui Zhang and Yanfen Zhang

Abstract Star-shaped POSS-g-PLLA is prepared by using L-lactic acid (L-LA) and octa (γ-chloroammoniumpropyl) octasilsesquioxane (POSS-NH$_3$Cl). Then, a series of modified PLLA films are prepared by using POSS-g-PLLA, and their part properties are investigated. The conclusions are as follows: (1) Water absorption of modified PLLA films increases with the increase of POSS-NH$_3$Cl, and the maximum is up to 11.35 %. (2) Oil resistance of the modified PLLA films is decreased, but it is not affected by the dosage of POSS-NH$_3$Cl. (3) Air permeability of the modified PLLA films is excellently increased, and the maximum is 11.3 g/(m^2 · 24 h). (4) Water vapor permeability of the modified PLLA films is obviously decreased, and the minimum is 38.5 g/(m^2 · 24 h) which is obviously lower than that of PLLA films (112.7 g/(m^2 · 24 h)).

Keywords PLLA · POSS-NH$_3$Cl · Modified PLLA films · Air permeability · Water vapor permeability

100.1 Introduction

Polylactic acid (PLLA) is one of the simplest and fully biodegradable new synthetic polyesters and has been produced from renewable resources [1–4]. PLLA has many good properties including innocuity, non-pollution, biodegradability, biocompatibility, and bioabsorbability. [5–7]. However, the application of PLLA is strictly restricted because of its defects, for example, hydrophobicity, high brittleness, difficult control degradation period, and high cost. In recent years, many methods such as copolymer synthesis polymer blending and reinforced composite have been

X. Zhang (✉)
School of Media and Design, Hangzhou Dianzi University, Zhejiang, China
e-mail: zhang_xiao_hui2014@126.com

Y. Zhang
Media Communication System, Dongguan Polytechnic, Guangdong, China

used to overcome these disadvantages. The modified reagents include not only organic polymers or inorganic substances [7] but also nanocomposites [8, 9]. Compared with other inorganic nanofillers, POSS can greatly improve comprehensive properties of PLLA composites [10–13]. Up to now, although the method of blending PLLA with POSS has been studied [11, 12], only a few studies on POSS grafting with PLLA have been researched [13]. In the article [13], POSS-PLA (polylactide tethered with POSS) is synthesized via the ring-opening polymerization of L-lactide with 3-hydroxylhep-taisobytyl (POSS), and then, the properties of PLLA blended with POSS-PLA are studied.

The paper is studied based on the previous research [14]. Firstly, star-shaped polylactic acid with polyhedral oligomeric silsesquioxane (POSS-g-PLLA) is synthesized. Secondly, the modified PLLA films are prepared. Thirdly, the water absorption, oil resistance, air permeability, and water vapor permeability of the modified PLLA films are characterized and studied theoretically.

100.2 Experimental Procedure

100.2.1 Materials

L-LA (optical purity ≥97 %, concentration = 88 wt%) is purchased from Shenzhen Brightchina Industry Co., Ltd., and it is used after distilling to eliminate the water with the conditions of vacuum 7 h and the temperature of 70 °C. $Sn(Oct)_2$ (A.R), ethanol (A.R), and xylene(A.R) are obtained from Chemical Reagent Co., Ltd. Chloroform (A.R) is purchased from Shanghai Experiment Reagent Co., Ltd. Octa(γ-chloroammoniumpropyl) octasilsesquioxane (POSS-NH_3Cl) is prepared according to the method described in the reference [15]. Deionized water is prepared in the laboratories.

100.2.2 Preparations of PLLA, POSS-G-PLLA, and Composite Films with and Without POSS-G-PLLA

PLLA and POSS-g-PLLA are prepared according to the method described in the reference [14].The preparation procedure of film is as follows: An amount of PLLA (or POSS-g-PLLA) and chloroform are charged into a flask which is equipped with a magnetic stirrer. After the mixture is fully dissolved, a certain percentage of TDI [14] and dibutyltin are added into the mixture which is stirred at 80 °C for 5 h by magnetic stirrer. Then, a certain percentage of PEG, TDI, and dibutyltin are charged into the reaction mixture. The mixture is stirred at 80 °C for 5 h by magnetic stirrer. After being cooled to room temperature, the mixture is poured into a Teflon mold

subsequently and cured for about 24 h at room temperature to give about 0.5-mm-thick sheet of films with smooth surface.

100.2.3   Characterizations

Water absorption of films is studied according to GB1034-86. Firstly, the films are dried at vacuum and 40 °C to constant weight which is W_0. Secondly, the films are placed in a glass filled with deionized water and soaked for 24 h (30.0 ± 0.5 °C). Thirdly, the films are removed and wiped with a paper, and the weight is Wm; the water absorption is as 1.1:

$$\text{Water absorption (WAR)}: WAR = \frac{W_m - W_0}{W_0} \times 100 \ \% \qquad (100.1)$$

Oil resistance of films is studied according to the article [16]. The weight of film is W_0. Then, the films are placed in a glass filled with xylene and soaked for 24 h. Finally, the films are removed and wiped with a paper, the weight is Wn, and the oil resistance is as 1.2 [16]:

$$\text{Oil resistance (OAR)}: OAR = \frac{W_n - W_0}{W_0} \times 100 \ \% \qquad (100.2)$$

Air Permeability of the films is studied by oxygen permeability tester (8001, IIinois Instruments, Inc, America), which is calibrated regularly with PET film. The films are maintained to equilibrium under the experimental conditions (23 ± 2 °C, 0 % RH) for 24 h. Then, air permeability of the films is tested for 24 h.

Water vapor permeability of the films is studied by water vapor transmission rate tester (7000, IIinois Instruments, Inc, America), which is calibrated regularly with PET film. The films are maintained to equilibrium under the conditions (23 ± 2 °C, 50 % ± 10 % RH) for 24 h. And then, air permeability of the films is tested under the experimental conditions (38 °C, 100 % RH) for 24 h.

100.3   Results and Discussion

100.3.1   Water Absorption of Films

The water absorption of films is shown in Fig. 100.1. The water absorption of modified PLLA films is enhanced with the increase of POSS-NH$_3$Cl. It achieved the maximum (11.35 %) ($W_{\text{POSS-NH3Cl}}$: $W_{\text{L-LA}}$ = 0.84/20). While after more than a certain amount ($W_{\text{POSS-NH3Cl}}$: $W_{\text{L-LA}}$ = 0.84/20), the water absorption of modified PLLA films is reduced with the increase of POSS-NH$_3$Cl. But the water absorption

**Fig. 100.1** Water absorption of films
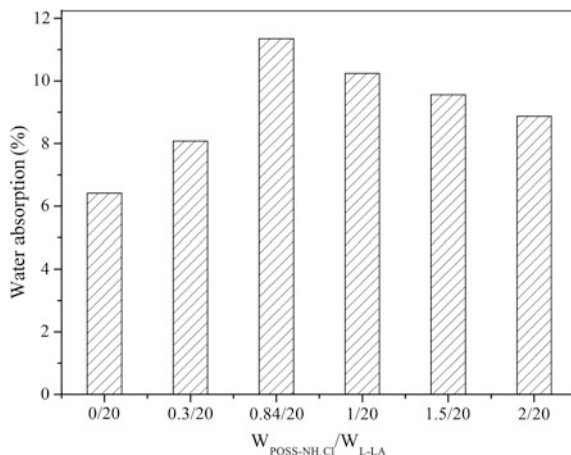
of modified PLLA films is higher than that of PLLA film. On the one hand, the POSS-g-PLLA possesses cage-type structure which can hold water. On the other hand, the polarity of POSS-g-PLLA is lower than that of PLLA because of the amide bond of POSS-g-PLLA. The water absorption of films is reacted by the cage structure mainly when the films are modified by a lower content of POSS-NH$_3$Cl. However, the polarity of the films is larger declined with the increase of POSS-NH$_3$Cl. And the polarity of the films can affect the water absorption of modified films gradually. So the water absorption of modified PLLA films is firstly enhanced and then reduced with the increase of POSS-NH$_3$Cl.

100.3.2 Oil Resistance of Films

The oil resistance of films is displayed in Fig. 100.2. The oil absorption of PLLA film is 7.93 %, and the oil absorption of modified PLLA films is 13.26 % (± 0.01 %). It may be explained that the cage-type structure of POSS-g-PLLA can hold xylene and the amide bond [14] of POSS-g-PLLA makes the polarity of POSS-g-PLLA lower than that of PLLA. And the polarity of xylene is lower, so the oil resistance of modified PLLA films is lower than that of PLLA film according to the principle of "like dissolves like." Besides, the branch of POSS-g-PLLA becomes shorter with the increase of POSS-NH$_3$Cl which can improve the crystalline of POSS-g-PLLA. So it is very difficult for xylene to penetrate the films which can reduce the oil resistance of films. Therefore, the oil resistance of modified films almost does not change because of the effect of crystalline and polarity with the increase of POSS-NH$_3$Cl.

Fig. 100.2 Oil resistance of films
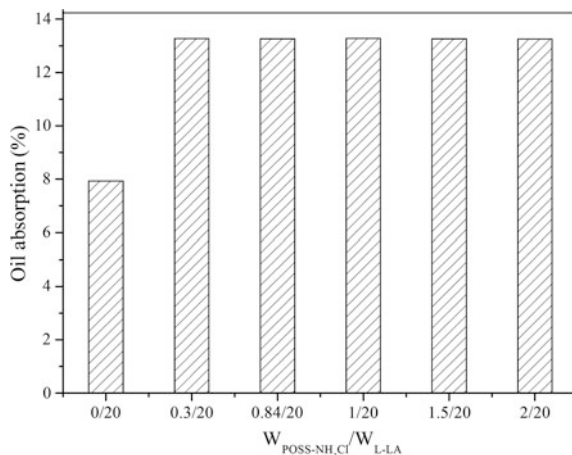
100.3.3 Air Permeability of Films

Air permeability of the films is displayed in Fig. 100.3. The air permeability of modified PLLA films is increased with the increase of POSS-NH$_3$Cl. It achieved the maximum which is 11.3 g/(m^2 · 24 h)(W$_{POSS-NH3Cl}$: W$_{L-LA}$ = 1/20). While after more than a certain amount, the air permeability of modified PLLA films is declined slowly with the increase of POSS-NH$_3$Cl. But the air permeability of modified PLLA films is higher than that of PLLA film (8.8 g/(m^2 · 24 h)). The cage-type structure of POSS-g-PLLA has good gas permeability. And the polarity of POSS-g-PLLA is lower than that of PLLA because of amide bond of POSS-g-PLLA. So it is easy for air permeability to penetrate the modified PLLA films according to the principle of "like dissolves like." Therefore, the air

Fig. 100.3 Air permeability of films
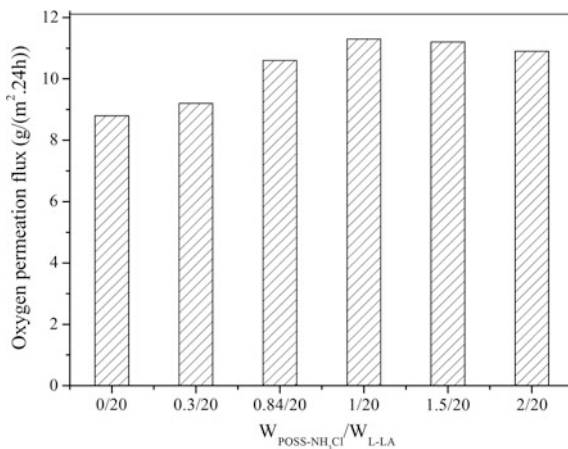
permeability of modified PLLA films is higher than that of PLLA film, which is consistent with the literature [17]. The air permeability of modified PLLA films is increased with the increase of POSS-NH$_3$Cl, which could be explain why amide bond [14] makes polarity of POSS-g-PLLA lower than that of PLLA. So it is easy for air permeability to penetrate the modified PLLA films according to principle of "like dissolves like." However, after more than a certain amount of POSS-NH$_3$Cl, the branch of POSS-g-PLLA becomes shorter with the increase of POSS-NH$_3$Cl which can improve the crystalline of POSS-g-PLLA. So it is very difficult for air to penetrate the films. But polarity of POSS-g-PLLA becomes much lower with the increase of POSS-NH$_3$Cl, which can increase the air permeability of modified PLLA. Therefore, the air permeability of modified films has a little decline with the increase of POSS-NH$_3$Cl.

100.3.4 Water Vapor Permeability of Films

Water vapor permeability of the films is displayed in Fig. 100.4. Firstly, water vapor permeability of modified PLLA films is less than that of PLLA film. Secondly, the water vapor permeability of modified PLLA films is descended with the increase of POSS-NH$_3$Cl. Thirdly, water vapor permeability of modified PLLA films reached the minimum which is 38.5 g/(m^2 · 24 h) (w$_{POSS-NH_3Cl}$: w$_{L-LA}$ = 1/20). Then, the water vapor permeability of modified PLLA films is increased very slowly with the increase of POSS-NH$_3$Cl. The water vapor permeability of modified PLLA films descends even 60 %. Although the cage-type structure of POSS-g-PLLA can make it easy to permeate the films for water vapor, the amide bond of POSS-g-PLLA makes the polarity of POSS-g-PLLA lower than that of PLLA, so it is difficult for water vapor to permeate the films. For another thing, after more than a certain amount of POSS-NH$_3$Cl, the branch of

Fig. 100.4 Water vapor permeability of films
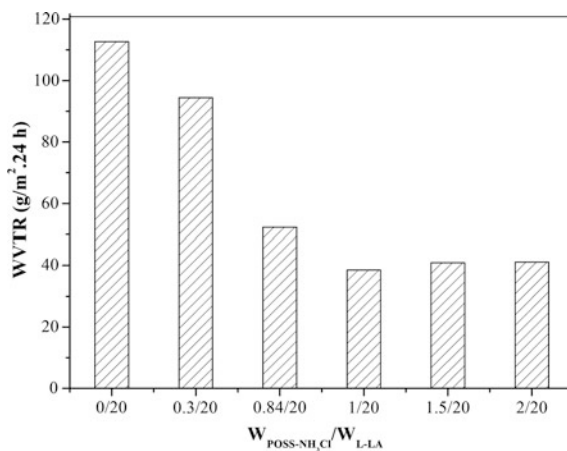
POSS-g-PLLA becomes shorter with the increase of POSS-NH$_3$Cl, so the crystalline of POSS-g-PLLA can be improved. So it is very difficult for air to penetrate the films. However, the lower polarity of POSS-g-PLLA can increase the water vapor permeability of modified PLLA films. Therefore, the water vapor permeability of modified films has a little increase with the increase of POSS-NH$_3$Cl.

100.4 Conclusions

In this research, modified PLLA films are prepared. Meanwhile, the water absorption, oil resistance, air permeability, and water vapor permeability of the films are characterized and studied. It is found that the water absorption and air permeability of the films are increased, while the oil resistance and water vapor permeability of the films are decreased. And these phenomena are explained theoretically.

References

1. Cinelli, P., & Chiellini, E. (2006). Foamed articles based on potato starch, corn fibers and poly (vinyl alcohol). *Polymer Degradation and Stability, 91*, 1147–1155.
2. Holland, S. J., & Tighe B. J. (1992). Biodegradable polymers. *Advance Pharmaceutica Science*, 101–165.
3. Gewin, V. (2003). Genetically modified corn-environmental benefits and risks. *PLoS Biology, 1*, 15–19.
4. Sawyer, D. J. (2003). Bioprocessing—no longer a field of dreams. *Macromolecular Symposium, 201*, 271–281.
5. Deplaine, H., Lebourg, M., & Ripalda, P. (2013). Biomimetic hydroxyapatite coating on pore walls improves osteointegration of poly(L-lactic acid) scaffolds. *Journal of Biomedical Materials Research, Part B: Applied Biomaterials, 101*, 173–186.
6. Jonnalagadda, S., & Robinson, D. H. (2004). Effect of the Inclusion of PEG on the solid-state properties and drug release from polylactic acid films and microcapsules. *Journal of Applied Polymer Science, 93*, 2025–2030.
7. Kondratowicz, F. Q., & Ukielski, R. (2009). Synthesis and hydrolytic degradation of poly (ethylene succinate) and poly(ethylene terephthalate) copolymers. *Polymer Degradation and Stability, 94*, 375–382.
8. Chiang, M. F., & Wu, T. M. (2010). Synthesis and characterization of biodegradable poly(L-lactide)/layered double hydroxide nanocomposites'. *Composites Science and Technology, 70*, 110–115.
9. Chen, H. M., Chen, J., & Shao, L. N. (2013). Comparative Study of poly(L-lactide) nanocomposites with organic montmorillonite and carbon nanotubes. *Jornal of Polymer Science Part B: Polymer Physics, 51*, 183–196.
10. Kim, H. S., Choi, Y. S., & Kwon, H. (2009). Thermal degradation behaviour of multi-walled carbon nanotube-reinforced poly(L-lavtide) nanocomposite. *Polymer International, 58*, 826–831.

11. Qiu, Z. B., & Pan, H. (2010). Preparation, crystallization and hydrolytic degradation of biodegradable poly(L-lactide)/polyhedral oligomeric silsesquioxanes nanocomposite'. *Composites Science and Technology, 70*, 1089–1094.
12. Pan, H., & Qiu, Z. B. (2010). Biodegradable poly(L-lactide)/polyhedral oligomeric silsesquioxanes nanocomposites: enhanced crystallization, mechanical properties, and hydrolytic degradation. *Macromolecules, 43*, 1499–1506.
13. Lee, J. H., & Jeong, Y. G. (2010). Preparation and characterization of nanocomposites based on polylactides tethered with polyhedral oligomeric silsesquioxane. *Journal of Applied Polymer Science, 115*, 1039–1046.
14. Zhang, X. H., Gu, W. J., & Li, H. B. (2012). Synthesis and Characterization of Star-shaped polylactic acid with polyhedral oligomeric silsesquioxanes. *AMM, 200*, 397–400.
15. Gravel, M. C., & Zhang, C. (1999). Octa(3-chloroammoniumpropyl) octasilsesquioxane. *Applied Organometallic Chemistry, 13*, 329–336.
16. Singh, G., Bhunia, H., & Rajor, A. (2010). Mechanical properties and morphology of polylactide, linear low density polyethylene and their blends. *Journal of Applied Polymer Science, 118*, 496–502.
17. Li, G., & Wang, L. (2001). Polyhedral Oligomeric Silsesquioxane (POSS) polymers and copolymers: A review. *Journal of Inorganic and Organometallic Polymers, 11*, 123–154.

Chapter 101
Application of a Multi-functional Integrated Bag in the Preservation of Pitaya

Huan Chang, Dongli Li, Qing Liu and Hui Liu

Abstract To extend the shelf life of pitaya at room temperature (25 ± 1 °C), study the preservation of fresh pitaya packed by a multi-functional integrated bag, the AP bag, which is prepared by the intelligent hydrogel antiseptic film and the high permeability silicon window film. Compared with the experimental group, a set of parameters of the naked put in the control group have been measured, such as top air of bags, body composition, hardness of pitaya, total soluble solid content, total acid, and vitamin C content. At room temperature, the shelf life of pitaya naked put was just 6 days, and pitaya's shelf life could be extended by 4 days with the AP bags, and it could keep the overall appearance of pitaya better. Since the gas permeation rate of the AP Bags is high, it can prevent pitaya from browning effectively and slow down the firmness reduction, and the micro-atmosphere effect inhibits the respiration of the fruit effectively. AP could effectively reduce the decrease of hardness and the water loss, and at the same time, the total soluble solid content and the total acid of AP were higher than the control group.

Keywords Hydrogel · Intelligent hydrogel antiseptic film · Permeability silicon window film · Multi-functional integrated bags

101.1 Introduction

Pitaya, a kind of typical tropical plant, is one of the most popular fruits [1]. It is nutrition rich, the content of dietary fiber and protein is much higher than the drupe fruit, and the mineral elements such as potassium, calcium, magnesium, and phosphorus are also rich [2]. Because of the above advantages and its higher economic value, the cultivation of the pitaya has become a new, unique, excellent,

H. Chang · D. Li (✉) · Q. Liu · H. Liu
Beijing Key Laboratory of Printing and Packing Materials and Technology,
Beijing Institute of Graphic Communication, Beijing, China
e-mail: lidongli@bigc.edu.cn

and high development project of agriculture. Its development has been increasingly promising [3].

The disadvantage of pitaya is its intolerance storage. The scales will appear the phenomenon of yellowing and wilting when it has been stored for 3 days at room temperature [4]. Some researches on pitaya have been done by the scholars of domestic and foreign countries; however, the majority of them concentrate on health care effectiveness, beverage processing, drying process, and nutrient analysis but less for its preservation [5]. Lu [6], and many people believe that the best harvest time of pitaya is 25–28 days after the withering of flowers. In recent years, pitaya main storage method is cold storage. Recently, there are also researches on the effect of preservation of pitaya which are measured by other conditions, such as low temperature, radiation, and 1-MCP. The shelf life of pitaya can up to 20–25 days in the condition of 4–8 °C and relative humidity of 85–95 %. Pitaya's freshness and quality will not decline in 28–30 days when received radiation treatment at 5 °C.

The pitaya will be better preserved when measured by the combination of low temperature and radiation treatment or 1-MCP, respectively. However, the pitaya is mostly sold under normal temperature conditions, the environment is much complex, and packaging is also not very perfect at room temperature. Therefore, for the present situation of pitaya package on the shelf life, an integrated multi-function AP plastic bag (early experiments were conducted pitaya preservation with AA, PP, and AP and founded that the best effect of pitaya preservation is AP) for pitaya atmosphere packaging is studied to extend the shelf life of pitaya by slowing down moisture loss and inhibiting breathing of pitaya.

101.2 Experiments

101.2.1 AP Storage Bag Preparation

Smart sterilization material film of 200 mm × 250 mm (oxygen transmission rate of 9.87×10^{-2} mL/m^2 days Pa, water vapor transmission rate of 9.87×10^{-5} mL/m^2 days Pa) and high permeability silicon window film of 200 mm × 250 mm (oxygen transmission rate of 0.987 mL/m^2 days Pa, the water vapor transmission rate of 1.97×10^{-3} mL/m^2 days Pa) were heat-sealed into multi-functional integrated AP plastic bags.

101.2.2 The Processing of Pitaya

Several pitayas with similar appearance, pink, about 400 g, similar hardness, and diameter controlled at 10–12 cm are selected at the Beijing new market and then divided into two groups, and each group have 24 pitayas. One group was the

experimental group of which the 24 pitayas are placed into 24 functional storage bags; the other was the control group with pitayas naked on the air at room temperature. Take out 4 sample group (4 pitayas as a sample group) from the experimental and bare group, respectively, every 2 days from the day. Then firmness, soluble solids content, total acid content, vitamin C content of the pitaya of each sample group, and the composition of CO_2 and O_2 of each bag are measured then averaged.

101.2.3   The Measurement of Performance

101.2.3.1   Browning Index Determination

In the above experiment, the degree of browning during the storage of pitaya can be directly observed. If all the peel and fronds are not dried or browning, the browning index will be 0, while 10 % are browning, and the index is 1, et cetera.

101.2.3.2   Headspace Gas Composition

Oxygen and carbon dioxide headspace concentration of packaged pitaya were measured using an O_2 and CO_2 meter (Pac Check® Model 650 Mocon America). To avoid modifying the gas composition in the headspace, due to gas sampling, each package was used only for a single determination of the headspace gas composition.

101.2.3.3   Pitaya Weightlessness Rate Determination

Physical weightlessness of pitaya was measured. The initial mass of each sample was recorded before bagging, and then, the final quality in the subsequent observation period (after bagging of 2, 4, 6, 8, 10 days) was weighed and recorded. The weightlessness rate was the ratio of the reduced quality and the beginning quality.

101.2.3.4   Pitaya Hardness Determination

The hardness of the pitaya was measured by FHM-5 fruit hardness analyzer (Japanese TAKEMURA Electric Engineering Co., Ltd.) with a conical probe (tip diameter 12 mm, height 10 mm). 1 cm^2 of each fruit was peeled, and the pressure with a diameter of 2-mm penetration probe measurements was recorded. Then wore 10 mm with the rate of 20 mm/min, and the results were the average value of the hardness of the fruit in each test group [7].

101.2.3.5 Pitaya Soluble Solids Content (TSS), Titratable Acidity (TA), and VC Determination

Four pitayas were squeezed with gauze. The juice was measured for SSC using a portable sugar refract meter. Then, put the juice of pitaya and moderated tap water into the pulp refiner, and we got the mixed liquor. TA was determined on a composite sample of the same berries using 0.1 mol/L NaOH up to a pH of 8.2, and phenolphthalein as indicator [8]. The VC was determined by means of the titration of 2, 6-two chlorophenol indophenols sodium solution [9].

101.3 Results and Discussion

101.3.1 The Influence of AP Plastic Bags to the Appearance of Pitaya

Due to the effect of the water loss and germs, pitaya grow browning. At the beginning of the storage, the thallus browning is mainly caused by water loss. In the later period of the storage, the water loss of thallus is so serious that part of the thallus and epidermis of the pitaya is separated (Fig. 101.1), and the breeding of germs speeds up the browning and decay of the fruit. After 6 days' storage, the browning index of thallus arrives three (Fig. 101.2), and the hardness is reduced by 42 % (Fig. 101.3), which has lost its commercial value. Therefore, in the condition of naked putting, the shelf life of pitaya is 6 days. During the period of storage, the

Fig. 101.1 Contrast of pitaya after 2, 6, 8 days storage

**Fig. 101.2** The change of fruit browning with storage time
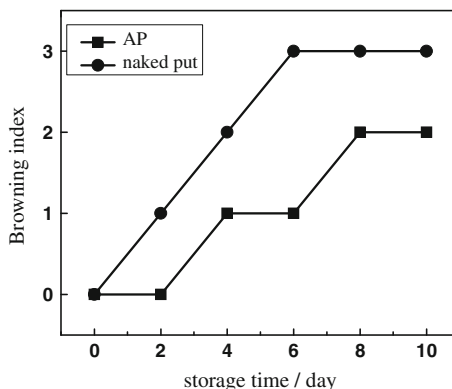
appearance of the pitaya in experimental group with lower bare stem and browning index is obviously better than the naked group. Within 10 days, the browning index of pitaya in AP bag has been controlled within two, the browning due to the water loss of pitaya has reduced, and the wrinkle phenomenon are also not more serious because of the high fresh-keeping effect of the AP. Therefore, it is concluded that AP bags can keep pitaya fresh for 10 days and prolong the shelf life for 4 days (Fig. 101.2).

101.3.2   The Influence of AP Plastic Bags to the Weight Loss Rate and Hardness of Pitaya

The main reason of mass loss during storage of fruits and vegetables is substrate consumption caused by dehydration and respiration [10]. The moisture loss of pitaya is serious when there is no pack, reaching 8.23 % in the 4 days and 10.51 % in the 6 days. The water vapor transmittance of the A and K film made of the AP plastic bag is 9.87×10^{-5} and 1.97×10^{-3} mL/m^2 days Pa. It reduces the moisture loss and has a small change in mass.

Hardness is the strength of the pulp resistance to pressure, to some extent; it means the maturity and water loss of the fruit. Generally, the fruit firmness will increase with the degree of maturity and decline after picking, and this is due to the decline in the quality of fruit cell wall, and the cell turgor pressure decreases caused by water loss. Pitaya hardness values in the experimental group are consistently higher than the group with no pack. Figure 101.3, which turns out AP bag, has good effect on the maintenance of hardness of the pitaya.

Fig. 101.3 Firmness of
pitaya with storage time
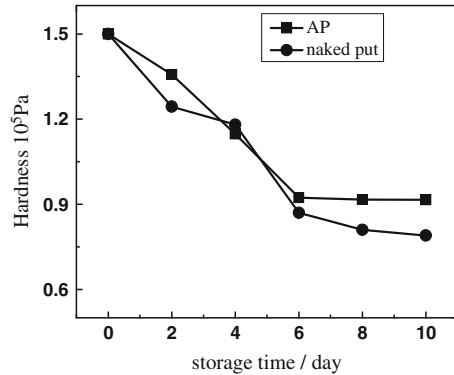
101.3.3   Influence of AP Plastic Bags to the Quality of Pitaya

In the storage process of pitaya, the soluble solids content is oxidized and
decomposed into carbon dioxide and water, and this lead to the decrease of the
soluble solids content in the experimental and the control group. The respiratory
function and weight loss rate of the group with no pack are higher than the
experimental group (Fig. 101.4), so the soluble solids content of pitaya of AP bag is
higher than the control group (Table 101.1).

Pitaya is rich in malic acid, citric acid, and other organic acids. The respiration of
pitaya needs to consume the nutrients of the storage (sugar, organic acid) as res-
piratory substrates [11]. Organic acids preferentially as respiratory substrate are
consumed, and its content falls. The respiration of pitaya of the group with no pack
is stronger than the experimental group, and the titratable acidity value of the group
with no pack is lower than the experimental group (Table 101.1).

Fig. 101.4 Weight loss of
pitaya with storage time
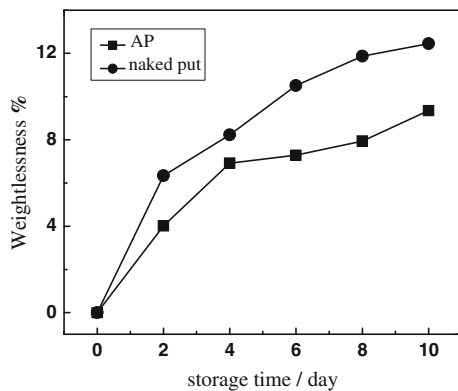
Table 101.1 Effect of different packaging conditions on the TSS, TA content, and VC

Index	Experimental group and control group	Storage time/days					
		0	2	4	6	8	10
TSS/(%)	AP	10.9 ± 0.1	10.5 ± 0.2	11.5 ± 0.2	10.4 ± 0.2	10.5 ± 0.1	10.5 ± 0.2
	Naked put	10.9 ± 0.1	10.6 ± 0.2	6.7 ± 0.2	9.1 ± 0.2	12.9 ± 0.2	12.9 ± 0.2
TA/(%)	AP	0.53 ± 0.01	0.44 ± 0.01	0.18 ± 0.006	0.18 ± 0.005	0.22 ± 0.006	0.22 ± 0.006
	Naked put	0.53 ± 0.02	0.35 ± 0.015	0.26 ± 0.001	0.26 ± 0.009	0.09 ± 0.003	0.09 ± 0.003
VC/ (mg/100 g)	AP	8.5 ± 0.3	8.9 ± 0.2	4.9 ± 0.1	6.0 ± 0.3	9.8 ± 0.1	9.7 ± 0.1
	Naked put	8.5 ± 0.2	8.3 ± 0.2	7.0 ± 0.1	8.0 ± 0.1	11.9 ± 0.2	11.9 ± 0.1
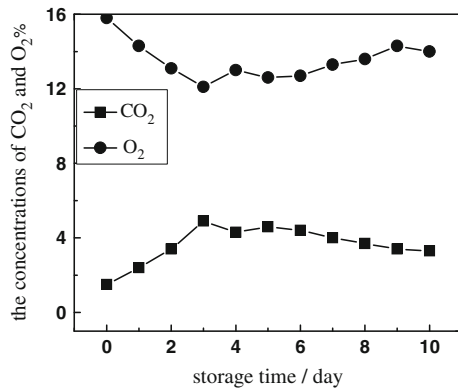
The content of vitamin C gradually increases with the mature of the fruit. With the extension of storage time, the content of VC of pitaya in the experimental group and the control group firstly decreases and then increases. In the 4 days, the content of VC reaches the lowest value (Table 101.1), then the content of VC increases due to the incomplete maturation of fruit in time of picking, and the ripening process leads to the increase of the content of VC. In the 8 days, the content of VC tends to stabilize and the content of VC in the experimental group is lower than the control group. In conclusion, AP bags can effectively reduce the respiration intensity of pitaya and slow the aging process.

101.3.4 The Influence of the Composition of Atmosphere of AP Plastic Bags to Preservation Effect

Pitaya has strong respiration. CO_2 content in the bag increases to a maximum value (4.9 %) in the 3 days. Similarly, O_2 content reduces to the lowest value (12.1 %). Later, the content of CO_2 and O_2 values decreases and increases, respectively, and finally achieves a relatively stable value (Fig. 101.5). The process of reaching a stable value is mainly due to two reasons: With the maturity increases, respiration relatively becomes weak; the micro-atmosphere effect of AP bag is reflected in that AP has a high gas permeability, and a part of the gas transferred to the outside of the bag, so CO_2 and O_2 content reaches a relatively stable value quickly. Meanwhile, the micro-atmosphere effect of AP bags makes the CO_2 content more than naked one, and it can suppress respiration to some extent and slow down ripening and senescence of fruit.

101.4 Conclusions

In the experiment, no pack pitaya is made as a control group at normal temperature to study the preservation effect of the AP bag for pitaya. Studies have shown that AP bag can extend the shelf life of pitaya to the 10 days, which is 4 days longer than the bare pitaya. Since the gas permeation rate of the AP bags is high, it can prevent pitaya from browning effectively and slow down the firmness reduction, and the effect of micro-atmosphere can inhibit the respiration of the fruit effectively.

References

1. Yang, H.-Y., & Huang, K.-S. (2009). Study on the extraction technology and properties of the red pigment of pitaya. *Anhui Agricultural Science Bulletin, 15*(3), 151–152.
2. Cai, Y.-Q., Xiang, Q.-Y., & Chen, J.-L. (2008). Analysis of nutritional components in pitaya fruit. *Nonwood Forest Research, 26*(4), 253–256.
3. Deng, R.-J., Fan, J.-X., & Cai, Y.-Q. (2011). Present research status and industrial development of pitaya at home and abroad. *Guizhou Agricultural Sciences, 39*(6), 188–192.
4. Li, R.-T., Zhang, Y.-N., Li, Y.-Z., et al. (2007). Introduction and cultivation of pitaya. *The Fruit of Chinese Southern, 36*(3), 35–36.
5. Zhang, Na, Li, J.-Z., Guan, W.-Q., et al. (2010). Research process on biology and storage preservation technology of pitaya. *Northern Horticulture, 1*, 229–231.
6. Lu, K. (2006). Storage and transport technology of pitaya after harvest. *The World Information of Tropical Agriculture, 7*, 24–25.
7. Valverde, J. M., Valero, D., & Martianez-Romero, D. (2005). Novel edible coating based on aloe vera gel to maintain table grape quality and safety. *Journal of Agricultural and Food Chemistry, 53*, 7807–7813.
8. Chen, S.-J., Zhang, M., & Wang, S. (2011). Effect of initial hermetic sealing on quality of 'Kyoho' grapes during storage. *Postharvest Biology and Technology, 59*(2011), 194–199.
9. GB/T6195-1986. (1986). *Determination of vitamin C in vegetables and fruits (2, 6-Indophenol Titration Method)*. Beijing: Standard Press of China.
10. Zhang, J.-Y. (2013). Effect of SO_2 controlled release packaging on preservation performance of cherry. *Packaging Engineering, 8*, 49–52.
11. Li, C., Liu, Y., Weng, Z., et al. (2013). The impact of transportation environment on grape quality. *Modern Food Science and Technology, 29*(2), 230–235.

Chapter 102
Preparation and Characterization of Natural Cellulose Packaging Film

Xiaojuan Shi, Chao Li, Junyan Huang, Wensheng Wang, Huanxiu Liu and Qi Xu

Abstract The aim of this paper was to research the production conditions and the properties of the natural cellulose food packaging film. We used cotton pulp, bleached wood pulp, and bleached reed pulp as raw materials. We adopt environment-friendly cellulose solvent N-methylmorpholine-N-oxide (NMMO) method, after degassing, scraping, and bathing made of thin films. The single-factor experiment investigated cellulose types, cellulose concentration, coagulation bath concentration and temperature, and plasticizer concentration. Natural cellulose film-forming optimum conditions were explored by the orthogonal. Single-factor experiment got the greater impact factors such as cellulose types, cellulose concentration, and plasticizer concentration. The optimum conditions are the cotton pulp of concentration is 6 %, the plasticizers glycerol of concentration is 4 %, and the coagulation bath temperature is 20 °C. The performance of films is tested under the following conditions: TS is 4.764 MPa, E is 47.0 %, WVP is 2.58×10^{-7}g (m s Pa)$^{-1}$, H is 27.5 %, OTR is 4.98 (cm^3 mm) (m^2 d 0.1 MPa)$^{-1}$, Po is 6.52 (g mm) (m^2 d)$^{-1}$, and T is 85.3 %. The films can be used for packaging low-moisture greasy food.

Keywords Packaging film · Cellulose membrane · NMMO · Barrier property · Environment friendly

102.1 Introduction

The packaging film produced with natural cellulose can be degraded to CO_2 and H_2O after abandoned, comparing with the plastic packaging film, exhibits greater environmental friendly [1–3]. But its market share is still small because of its low-moisture-proof performance, complex production process, and contaminated

X. Shi (✉) · C. Li · J. Huang · W. Wang · H. Liu · Q. Xu
Dalian Polytechnic University, Dalian, Liaoning, China
e-mail: shixj@dlpu.edu.cn

production process [4]. In recent years, the strong solubility for cellulose of N-methylmorpholine-N-oxide (NMMO) has been found, the solvent is non-toxic and non-corrosive, also can be recycled, and is an environment-friendly solvent. Dissolving cellulose method belongs to the physical process and has no pollution [5–10].

Ordinary food packaging film has higher requirements for the barrier, health, mechanical strength, and printing properties. Taking into account the cost of packaging, we adopt cotton pulp, bleached wood pulp, and bleached reed pulp instead of pure cellulose [11]. Their film-forming performance with NMMO dissolution method was studied under the condition of laboratory, and the properties especially moisture barrier property was tested.

102.2   Experiments

102.2.1   Materials and Equipment

Absorbent cotton pulp: polymerization degree 1327 and 98.6 % alpha-cellulose content; wood pulp board: polymerization degree 914 and 76.7 % alpha-cellulose content; reed pulp board: polymerization degree 752 and 62.5 % alpha-cellulose content; NMMO; propyl gallate; glycerol; electronic balance; thermostat water bath; thermostat magnetic stirrer; circulating water vacuum pump; rotary evaporator; scattering device; computer control tensile test machine; 725 N UV-visible spectrophotometer.

102.2.2   Methods

102.2.2.1   Preparation of Cellulose Membranes

Taken a certain quality 50 % (w/w), NMMO solution mixed with a suitable amount of antioxidant, into a rotary evaporator. it was vacuumed at a certain temperature and then mixed uniformly with the pulp until the pulp was completely dissolved. The obtained cellulose/NMMO/H_2O solution was degassed 2 h under −0.1 Mpa, scraped into a film, then quickly immersed it into the coagulation bath, and finally washed with deionized water. It was dipped into an aqueous solution of a certain concentration of glycerol plasticized processing 48 h and placed into a desiccator until drying to be tested.

102.2.2.2   Determination of Water Vapor Permeability and Hygroscopicity

Water vapor permeability (WVP) was tested according to GB/T l037-88. Hygroscopicity (H) was tested by the following method: The membrane was dried sufficiently, and taken the dry membrane of weight M_0 into distilled water for soaking 24 h. Surface moisture was dried quickly with filter paper and then, its wet weight M_1 was measured. Absorption rate is calculated as follows: $H = \{(M_1 - M_0)/M_0\} \times 100\,\%$ [12].

102.2.2.3   Determination of Other Properties

Tensile strength (TS) and elongation at break (E) were tested according to GB/T 1039-92. Oxygen permeability (OTR) was tested according to GB/T 1038-70. Penetration oily (Po) was tested by this method: 5 ml soybean oil was added into the test tube and sealed it with a cellulose membrane tested. Upside down it on a filter paper and placed it in a desiccator for 72 h. Then, weighed the quality change, the area, and the thickness of the filter paper calculated the Po. Transmittance (T): The test samples were trimmed to small pieces of 70×15 (mm) and then attached them to the surface of the cuvette. The transmittance at the wavelength of 540 nm was measured, and at the same time, an empty cuvette was used for comparison.

102.3   Results and Discussion

102.3.1   Cellulose-Type Influence on WVP and H

Taken a certain quality NMMO solution, weighed cotton pulp, wood pulp and reed pulp of NMMO mass fraction 5 %, obtained there kinds of cellulose solution. Made them to membranes under same conditions, we can see the cellulose-type influence on WVP and H in Fig. 102.1.

Fig. 102.1 Cellulose-type influence on WVP and H
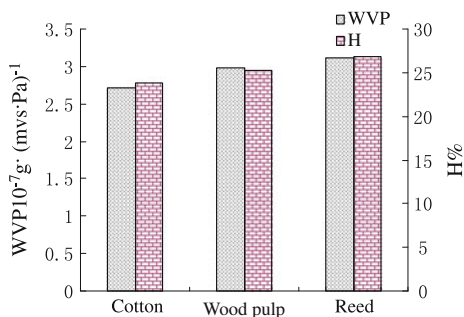
Cotton fiber has the highest degree of polymerization and long molecular link. As a result, the film's structure is compact. Wood pulp and reed pulp have a lower degree of polymerization and more exposed hydroxyl that can easily form hydrogen hood. In addition, wood pulp and reed pulp contain hemicelluloses, resulting in more micropores then cotton fiber membrane, accordingly wood pulp membrane and reed pulp membrane are relatively easy to imbibe.

102.3.2 Cellulose Concentration Influence on WVP and H

Taken a certain quality NMMO solution, weighed wood pulp of NMMO mass fraction 3, 4, 5, 6, and 7 %, and made them into membranes. We can see the cellulose concentration influence on WVP and H in Fig. 102.2.

Cellulose concentration has great influence on moisture absorption performance and permeability of cellulose membrane. The higher concentration and larger number of hydroxyl groups, which is more hydrophilic toward water molecules, leading to higher WVP and H. Possibly, with the increase of cellulose concentration, the twining of molecular link became closer. Result in that crystalline of the membrane was increasing, so the blocking performance improvement.

102.3.3 Coagulation Bath Concentration Influence on WVP and H

Weighed wood pulp of NMMO mass fraction 5 %, made into cellulose solutions. The coagulation bath concentration was 0, 4, 8, 12, 16, and 20 %, the temperature was 20 °C, and plasticizing liquid concentration was 3 %. We can see the WVP and H detection results of obtained membranes in Fig. 102.3.

According to Fig. 102.3, we got that coagulation bath concentration has great influence on permeability of the cellulose membrane, following the increase in

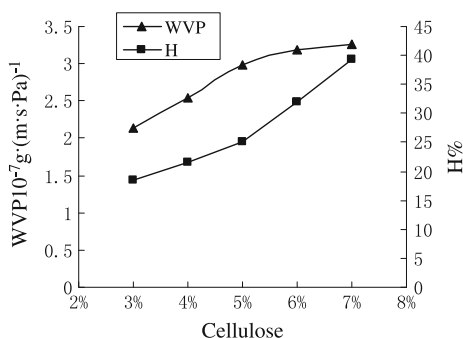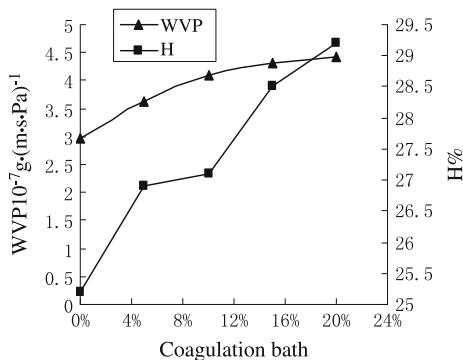**Fig. 102.2** Cellulose concentration influence on WVP and H

Fig. 102.3 Coagulation bath concentration influence on WVP and *H*


coagulation bath concentration; the permeability of cellulose was increasing gradually. It may be because the increase in NMMO concentration can lead to enlarge of membrane surface bore. However, we want to get barrier property membrane, so we need low coagulation bath concentration as 0 %.

102.3.4 Coagulation Bath Temperature Influence on WVP and H

Weighed wood pulp of NMMO mass fraction 5 %, made into cellulose solutions. The coagulation bath temperature was 10, 15, 20, 25, and 30 °C, the concentration was 0 %, and plasticizing liquid concentration was 3 %. We can see the WVP and *H* results of obtained membranes in Fig. 102.4.

According to Fig. 102.4, we got that the *H* of membranes will increase accompanying with coagulation bath temperature increment. Improving the coagulation bath temperature can quicken diffusion rate of solvent and coagulator and

Fig. 102.4 Coagulation bath temperature influence on WVP and *H*
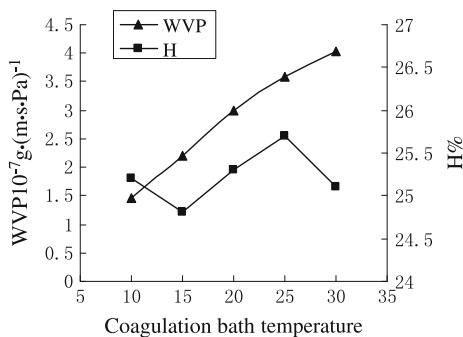
then quicken the casting film solution phase separation rate of solidification and the curing rate of high polymer. Consequently, there was no enough time for high polymer macromolecule to shrink and rearrangement, ultimately obtained membranes with bigger bores [13]. We can see that lower coagulation bath temperature and concentration are good for improving barrier property and saving energy.

102.3.5 Plasticizer Concentration Influence on WVP and H

Glycerol is one of the most used plasticizers, by virtue of its well stability and consistency. More significantly, it is effective, low cost, and available. We selected glycerol as plasticizer [14]. Weighed wood pulp of NMMO mass fraction 5 %, made into cellulose solutions, under the coagulation bath concentration 0 %, temperature was 20 °C. Dipped the films, respectively, in mass fraction 1, 2, 3, 4, and 5 % glycerol–water solution for plasticizing. We can see the WVP and H results of membranes in Fig. 102.5.

Accompanying with the increasing of glycerol concentration, the WVP and H were also increasing. Hydroxyls in the glycerol and cellulose member generated dipole attraction formed hydrogen bonding, so that the number of hydrogen bonding between cellulose macromolecule was reduced, and the cellulose

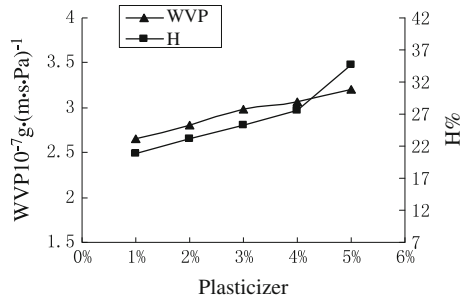**Fig. 102.5** Plasticizer concentration influence on WVP and H

Table 102.1 Factors and levels of orthogonal experiment

Factors	Levels		
	1	2	3
Cellulose types	Cotton	Wood	Reed
Cellulose concentration (%)	4	5	6
Glycerol concentration (%)	2	3	4

macromolecule closed with difficulty. As a result, water can permeate easily. In addition, glycerol has hydrophily, so increasing its mass fraction can improve the H of the membrane [15] (Table 102.1).

102.3.6   The Best Preparation Conditions of Membrane

The previous discussion shows that the major factors influencing barrier property are cellulose types, cellulose concentration, and glycerol concentration. In order to get the best preparation conditions, we will use orthogonal experiment; furthermore, others test items are added. Factors and levels of the orthogonal experiment are in lab 1, and lab 2 is the result of the orthogonal experiment.

According to the result of the orthogonal experiment, arranging influence factors on the membrane performance from high to low: cellulose types, cellulose concentration, and glycerol concentration. Suppose we want to package greasy food, we can choose the preparation conditions: cotton pulp of 6 %, glycerol concentration of 4 %, the coagulation bath concentration 0 %, and temperature 20 °C. Under this condition, TS is 4.764 MPa, E is 47.0 %, WVP is 2.58×10^{-7} g (m s Pa)$^{-1}$, H is 27.5 %, OTR is 4.98(cm^3 mm) (m^2 d 0.1 MPa)$^{-1}$, Po is 6.52 (g mm) (m^2 d)$^{-1}$, and T is 85.3 % (Table 102.2).

102.4   Conclusions

We confirmed the major factors of membrane preparation conditions by single-factor experiment. In addition, we explored the best preparation conditions by orthogonal experiment. You can choose your best preparation conditions according to your packaging requirement. We choose the conditions: cotton pulp of 6 %, glycerol concentration of 4 %, the coagulation bath concentration 0 %, and temperature 20 °C. The packaging film under the conditions can be used for packaging low-moisture greasy food. On the whole, compared with the plastic film, moisture resistance of the natural cellulose packaging film is still poor, and we need further research to improve it.

Table 102.2 Result of orthogonal experiment

No.	Factors			TS (MPa)	E (%)	WVP 10^{-7} g $(m\ s\ Pa)^{-1}$	H (%)	OTR $(cm^3\ mm)$ $(m^2\ day\ 0.1\ MPa)^{-1}$	Po g mm $(m^2\ day)^{-1}$	T (%)
	A	B	C							
	Cellulose types	Cellulose concentration	Glycerol concentration							
1	1	1	1	4.090	41.2	2.68	25.1	5.21	7.66	77.7
2	1	2	2	4.434	45.7	2.71	26.8	5.03	7.01	79.2
3	1	3	3	4.764	47.0	2.58	27.5	4.98	6.52	85.3
4	2	1	2	3.363	36.3	3.01	26.8	5.98	7.84	61.7
5	2	2	3	3.708	37.1	3.07	27.9	5.63	7.91	65.8
6	2	3	1	4.362	42.8	2.72	27.6	5.17	7.89	68.6
7	3	1	3	2.868	28.9	3.21	28.6	6.61	8.24	61.7
8	3	2	1	3.652	35.5	3.19	29.3	6.85	8.48	60.3
9	3	3	2	3.807	39.9	2.76	29.6	6.02	8.06	64

References

1. Li, L. L., & Wang, D. (2012). Preparation and performance of cellulose acetate forward osmosis membrane. *Journal of Functional Materials, 43*(5), 595–598.
2. Zhang, C.-J., Wang, L., Wang, Z.-K., et al. (2011). Structure and properties of three kinds of bacterial cellulose films. *Journal of Functional Materials, 42*(IV), 617–620.
3. Bian, X., & Cao, L.-K. (2010). Study of preparation technology of edible packaging film with potato dregs. *Packaging Engineering, 31*(1), 48–50.
4. Li, D.-N., & Ma, X.-J. (2013). Study on the enhancement effect of additives on properties of natural cellulose membrane. *Chinese Packaging Industry, 4*, 10–11.
5. Biganska, O., & Savard, P. (2005). Kinetics of precipitation of cellulose from cellulose-NMMO-water solutions. *Biomacromolecules, 6*(4), 1948–1953.
6. Adelwöhrer, C., Yoneda, Y., Takano, T. (2009). Synthesis of the perdeuterated cellulose solvents N-methylmorpholine N-oxide (NMMO-d_{11} and NMMO-^{15}N-d_{11}), N, N-dimethylacetamide (DMAc-d_9 and DMAc-^{15}N-d_9), 1-ethyl-3-methylimidazolium acetate (EMIM-OAc-d_{14}) and 1-butyl-3-methylimidazolium acetate (BMIM-OAc-d_{18}). *Cellulose, 16*(1), 139–150.
7. Eckert, J., Eich, T., RÖder, T., et al. (2009). Phase diagram of the ternary system NMMO/water/cellulose. *Cellulose, 16*(3), 373–379.
8. Wendler, F., Persian, Z., Stana-Kleinschek, K., et al. (2011). Morphology of polysaccharide blend fibers shaped from NaOH, N-methylmorpholine-N-oxide and 1-ethyl-3-methylimidazolium aacetate. *Cellulose, 18*(5), 1165–1178.
9. Khodaverdi, M., Jeihanipour, A., Karimi, K., et al. (2012). Kinetic modeling of rapid enzymatic hydrolysis of crystalline cellulose after pretreatment by NMMO. *Journal of Industrial Microbiology and Biotechnology, 39*(3), 429–438.
10. Kabir, M., Castillo, M., del Pilar, T., Mohammad, J., et al. (2013). Effect of the N-Methylmorpholine-N-Oxide (NMMO) pretreatment on anaerobic digestion of forest residues. *Bio Resources, 8*(4), 5409–5423.
11. Gao, S.-S., Wang, J.-Q., Jin, Z.-W., et al. (2011). Influence of type and polymerization degree of pulp on structure and properties of cellulose packaging film. *Packaging Engineering, 32*(13), 8–10.
12. Wang, F.-X., Yang, F.-X., & Liu, X.-M. (2012). Study on moisture absorption of polyvinyl alcohol-methyl cellulose film optimized by uniform design method. *Packaging Engineering, 33*(19), 32–34.
13. Yang, L.-L., HU, L.-X., & Yu, Y.-T. (2013). Effect of coagulation bath temperature on performance of cellulose antibacterial film by NMMO process. *Packaging Engineering, 34*(5), 1–5.
14. Bin, Z., Dong-Feng, W., Shang-Qui, D., et al. (2012). Preparation and anti-aspergillus flavus activity of chitosan-trypsin inhibitor blend edible film. *Transactions of the CSAE, 28*(4), 287–291.
15. Xu-Yun, W., Xue-Hai, Y., & Qing-Jie, G. (2011). Effect of glycerol additive on the morphology and crystallization of prepared PVDF membranes. *Polymer Materials Science and Engineering, 27*(8), 137–140.

Chapter 103
Influence of Glycerol on Potato Starch-Based Biodegradable Packaging Films

Xinlin Zhang, Shiyong Luo, Wenyu Zhang and Wencai XU

Abstract Low price of potato starch as a wide range of sources of biodegradable packaging film substrate, glycerol as a plasticizer, polyvinyl alcohol as a film-forming agent, potato starch-based biodegradable packaging films were prepared by solution casting. Tests were run on potato starch-based biodegradable packaging films to determine mechanical properties, transparency, and color evaluation. It was observed that the increase of the glycerol content in the films increased the macromolecular mobility, and the potato starch films became less stiff and more flexible. Meanwhile, the transparency was decreased obviously.

Keywords Biodegradable packaging films · Potato starch · Glycerol · Polyvinyl alcohol

103.1 Introduction

Edible films and coatings have been particularly considered in food preservation, because of their capability in improving global food quality as green packaging materials [1]. Film production by natural and abundant biodegradable polymeric materials, such as cellulose, gums, starches, or proteins, is also convenient due to the lower environmental consequences compared with common synthetic plastic materials [2].

Flores et al. found that the gelatinization technique and drying method used to obtain edible films affected network characteristics determining changes in physical properties [3]. Glycerol is one of the most popular plasticizers used in film-making techniques, due to stability and compatibility with hydrophilic biopolymeric packaging chain.

X. Zhang (✉) · S. Luo · W. Zhang · W. XU
The Laboratory of Printing and Packaging Material and Technology,
Beijing Institute of Graphic Communication, Beijing, China
e-mail: zhangxinlin@bigc.edu.cn

The property of potato starch-based biodegradable packaging films in relation to different concentrations of glycerol is a subject of great importance as it provides the knowledge of the advantages and disadvantages of its possible applications in the future. The objective of this study was to determine the influence of glycerol on the properties of potato starch-based packaging films, using an experimental design.

103.2 Materials and Methods

103.2.1 Materials

Potato starch (CAS Number: 9005-25-8) and polyvinyl alcohol (CAS Number: 9002-89-5) were obtained from Sinopharm Chemical Reagent Co., Ltd. (Shanghai, China). Samples were stored in darkness at room temperature. Glycerol was obtained from Beijing Chemical Works (Beijing, China).

103.2.2 Potato Starch, Polyvinyl Alcohol, and Glycerol Blend for Film Formation

Potato starch, polyvinyl alcohol, and glycerol were mixed (25 °C) with distilled water (100 ml) as shown in Table 103.1. The resultant solutions were kept hot in a water bath (80 °C) with mechanical stirring (450 rpm) for 50 min. After that, they were degassed by means of a vacuum pump to eliminate non-condensable gases. Film-forming solutions were poured over Plexiglas plates placed on the leveled surfaces. The solutions were dried in a climatic chamber (EXCAL, France) under controlled conditions (50° and 35 % RH) for approx. 240 min. Finally, films were separated from the Plexiglas plates for their evaluation.

Table 103.1 Mass of potato starch, polyvinyl alcohol, and glycerol blends per 100 ml of distilled water

Blends	Composition		
	Potato starch [g]	Polyvinyl alcohol [g]	Glycerol [g]
1	4.50	0.60	0.50
2	4.50	0.60	1.00
3	4.50	0.60	1.25
4	4.50	0.60	1.50
5	4.50	0.60	2.00

103.2.3   Mechanical Properties

Environmental Electronic Tensile Testing Machine (Instron, USA) was used to measure the tensile properties of the films according to ASTM D882-00 [4].

103.2.4   Transparency Measurement

Transparency of potato starch-based edible films was measured by UV spectrophotometer (UV-2501PC, Shimadzu, Japan) at 400–800 nm in the empty cuvette as a corrective.

103.2.5   Color Evaluation

Film disks of appropriate diameter were rested on a standard white background [5]. Measurements were performed by colorimeter (DTP22, X-Rite, USA). The Hunter parameters: L, a, and b, were measured according to a standard test method [6]. Color parameters range from $L = 0$ (black) to $L = 100$ (white), $-a$ (greenness) to $+a$ (redness), and b (blueness) to $+b$ (yellowness). Standard values considered were those of the white background. Measurements were made for C illuminant and 2° observers.

103.3   Results and Discussion

103.3.1   Mechanical Properties

As expected, the increase in glycerol content of the potato starch-based films that were less stiff and rigid, and more extendible. It caused a reduction on tensile strength from 50.00 to 7.37 MPa and an increase of the elongation at break of films from 18.9 to 171.0 % , respectively (Fig. 103.1). These trends were probably due to the reduction in interactions between the biopolymers chains. The resulting trends of the mechanical properties of the films could be explained in a general manner, by the effect of glycerol on the state properties of the films. The plasticizer was intended to decrease the intermolecular forces along the polymer chains, imparting increased film flexibility. The results suggested that glycerol was mainly responsible for the above behavior.

Fig. 103.1 Effect of glycerol content on mechanical properties of potato starch-based films
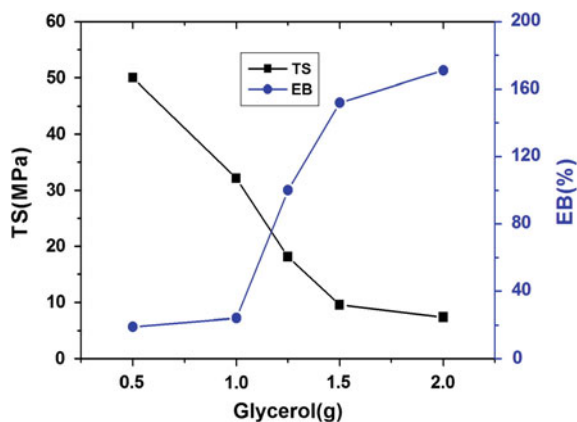
Fig. 103.2 Effect of glycerol content on transparency of potato starch-based films
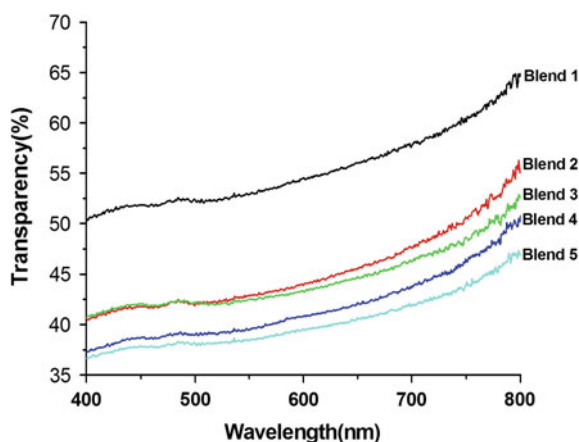
103.3.2 Transparency

As can be seen from Fig. 103.2, the transparency of potato starch-based films shows gradually decreasing trend, while the glycerol content increased. It may be due to the fact that the transparency of the films was closely related to the crystallinity of the material. The higher the crystallinity was, the higher the transparency became. Glycerol was added to weaken hydrogen bonding and destructed the crystalline structure of the potato starch molecules. So the crystallinity decreased, while the transparency decreased.

Table 103.2 Color parameters of the film samples

Blends	L	a	b
1	98.57	3.76	−13.16
2	98.36	3.77	−13.12
3	98.07	3.86	−13.02
4	97.60	3.67	−12.85
5	97.22	3.57	−12.49

103.3.3 Color Evaluation

Color attributes were of prime importance because they directly influenced consumer acceptability. Potato starch films, containing different amounts of glycerol, resulted homogeneous and transparent materials. The color attributes obtained for each film sample were summarized in Table 103.2. The results showed that L parameter decreased and b parameter of Hunter scale increased with glycerol content. These results suggested that the presence of investigated biopolymer gave origin to a darker film. It was also observed that the increase of the glycerol content produced an increase in yellow index generally.

103.4 Conclusions

The properties of potato starch-based films were influenced by glycerol content. In particular, tensile strength and transparency were negatively influenced. The glycerol content had a positive influence on elongation at break. And *L* parameter decreased and *b* parameter of Hunter scale increased with glycerol content. The results of the statistical analysis leading to the optimal composition of potato starch-based edible films were 4.50 g potato starch/100 ml distilled water and contained values of polyvinyl alcohol and glycerol content equal to 0.60 and 1.25 g, respectively.

References

1. Franssen, L. R., Rumsey, T. R., Krochta, J. M. (2002). *Modeling of natamycin and potassium sorbate diffusion in whey protein isolate films for application to cheddar cheese*. Anaheim, California: Poster 28-5, Institute of Food Technologists Annual Meeting.
2. Cutter, C. N. (2006). Opportunities for bio-based packaging technologies to improve the quality and safety of fresh and further processed muscle foods. *Meat Science, 74*, 131–142.

3. Flores, S., Famá, L., Rojas, A. M., Goyanes, S., & Gerschenson, L. (2007). Physical properties of tapioca-starch edible films: influence of filmmaking and potassium sorbate. *Food Research International, 40*, 257–265.
4. ASTM (2000). Standard test method for tensile properties of thin plastic sheeting, designation: D882-00. In ASTM (Ed.), *Annual Book of ASTM standard* (pp. 160–168). Philadelphia: American Society for Testing and Materials.
5. Trezza, T. A., & Krochta, J. M. (2000). Color stability of edible coatings during prolonged storage. *Journal of Food Science, 65*(1), 1166–1169.
6. ASTM D1925. (1995). Standard test method for yellowness index of plastics. Philadelphia: American Society for Testing and Materials.

Chapter 104
Study on the Biodegradation Performance of P(3HB-co-4HB) in Phosphate Buffer

Jing Zhang, Bin Liang, Rui Zang and Fazhong Zhang

Abstract As a kind of fully biodegradable, biocompatible, and environment-friendly thermoplastic polymer materials, more and more scholars began to study the P(3HB-co-4HB). In this paper, five kinds of 4HB molar fraction of P(3HB-co-4HB) biodegradability in phosphate buffer containing lipase were studied in the analysis of the degradation mechanism and degradation factors. Characterization of biodegradable performance was characterized by weight loss, molecular weight change, and membrane surface morphology. The results showed that 4HB molar fraction has little effect on the enzymatic degradation. During the five kinds of P(3HB-co-4HB) degradation process, the weight loss rate and molecular weight decreased rate have little difference. P(3HB-co-15 %4HB) has a lower degree of crystallinity and good surface roughness, so the degradation rate is the best of all. SEM image indicated that lipase for P(3HB-co-4HB) has a faster degradation, and its enzymatic degradation process is a surface corrosion process.

Keywords P(3HB-co-4HB) · Biodegradation performance · Enzymatic degradation · Phosphate buffer

J. Zhang (✉)
Beijing Key Laboratory of Packaging and Printing New Technology,
China Academy of Printing Technology, Beijing, China
e-mail: zhangjing@keyin.cn

B. Liang
Beijing Xinghang Electro-Mechanical Equipment Co., Ltd., Beijing, China

R. Zang
College of Food Science and Technology, Agricultural University of Hebei, Baoding, China

J. Zhang · F. Zhang
Key Laboratory of Printing Environmental Protection Technology,
China Academy of Printing Technology, Beijing, China

104.1 Introduction

In spite of the population growth and economic development, white trash has become a global environmental problem. Therefore, more and more people pay attention to the research and development of biodegradable material performance. P(3HB-co-4HB), is a kind of fully biodegradable, biocompatible, and environment friendly thermoplastic polymer material [1]; because of the 4HB monomer involvement and adjustable resistance, it has excellent mechanical properties and biodegrade ability. Loocy and Sudeshk [2] and other scholars found that, with the change of 4HB content, the physical properties of P(3HB-co-4HB) had a great change. When 4HB molar fraction increased from 0 to 16 %, the tensile strength decreased from 43 to 26 MPa, elongation increased from 5 to 444 %, and crystallinity decreased from 60 to 45 %. This indicates that the flexibility and toughness of P(3HB-co-4HB) have greatly improved than those of PHB. Thus, it can be widely used in packaging film, sheet, injection-molded parts, elastomer, and other fields.

At present, the research on the P(3HB-co-4HB) focused on the biosynthesis and modification field [3] and little systematic research on its biodegradability. The enzymatic degradation experiment was adopted in this study [4], for five different 4HB molar fractions of P(3HB-co-4HB). Biological degradation in phosphate buffer containing lipase were studied, and provide theoretical data for the study of biodegradable plastics biodegradability.

104.2 Materials and Methods

104.2.1 Materials

Phosphate buffer, Chloroform, P(3HB-co-4HB), 4HB molar fraction of 0, 5, 10, 15, 20, 30 % were showed by P(3HB-co-5 %4HB), P(3HB-co-10 %4HB), P(3HB-co-15 %4HB), P(3HB-co-20 %4HB), P(3HB-co-30 %4HB) in this paper.

104.2.2 Methods

104.2.2.1 Sample Preparation

Different 4HB molar fractions of P(3HB-co-4HB) samples were dissolved in a certain amount of chloroform solvent, electromagnetic stirring is for 2–3 h, until polymer is completely dissolved, poured into a petri dish, and placing 1–2 d, solvent evaporation as film.

104.2.2.2 Weight Loss Rate Test

P(3HB-co-4HB) enzymatic degradation experiments were processed in 1 mol/L lipase (pH = 7.4) with phosphate buffer solution. The sample film (1 cm × 1 cm, the initial weight 20–30 mg) is placed in bottles which contain 15 ml phosphate buffer solution, with temperature at 37 °C for degradation in oven. Replace twice enzyme solution every week to keep the activity of enzyme. Regular sampling, with three specimens each time, and observe the film surface degradation situation, three times with distilled water washing, measuring weight loss rate after vacuum drying.

104.2.2.3 Dilution Method Measuring Molecular Weight Change Rate

The solvent of this experiment is chloroform, matched into 0.018 g/25ml dilute solution and the control temperature is over 30 °C. To simplify the process, the flow time of solvent greater than 100 s is made in order to make sure the liquid flow in the capillary produces energy loss effects that are negligible. By formula (104.2.1) the measured molecular weight change rate as follows:

$$M = \frac{M_{\eta 0} - M_{\eta}}{M_{\eta 0}} \times 100\% \qquad (104.2.1)$$

where $M_{\eta 0}$ is the molecular weight of the sample before degradation and M_{η} is the molecular weight of the sample after degradation.

104.2.2.4 Scanning Electron Microscopy (SEM)

SEM images were placed on a JEOL-JSM-6380 instrument, the film samples with different degradation time were sputtered with gold and observed with scanning electron microscopy, magnification×2000 times, to observe the surface morphology of samples before and after degradation.

104.3 Results and Discussion

104.3.1 Weight Loss in the Process of Enzymatic Degradation

The weight loss curve is shown in Fig. 104.1. As can be seen, the enzymatic rate of five kinds of P(3HB-co-4HB) were slow at the beginning, then the degradation speeded up, the degradation rate increased with time, 7 weeks later, the fastest rate of degradation is P(3HB-co-15 %4HB), the weight loss is more than 30 %. Moreover, during definite degradation time, with the content of 4HB increased

Fig. 104.1 Weight loss of P (3HB-co-4HB) films biodegraded by lipase
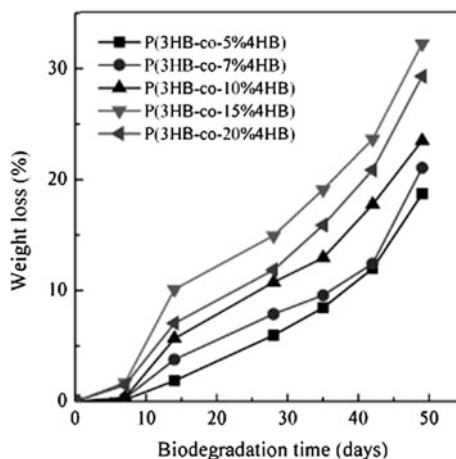
Fig. 104.2 Molecular weight change of P(3HB-co-4HB) biodegraded by lipase
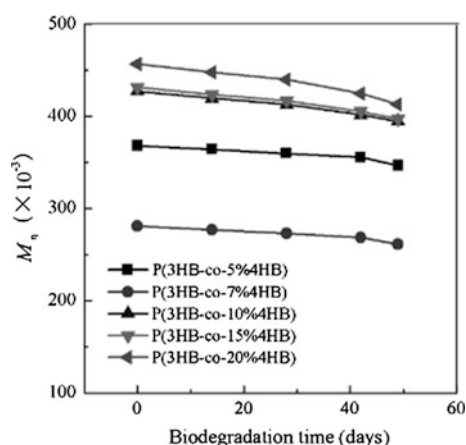
gradually, both the weight loss rate of P(3HB-co-4HB) and the degradation rate increased.

As the figure shows, lipase has a faster degradation ability for P(3HB-co-4HB); in the degradation process, flocculent substance appeared on the surface of the film, and gradually shedding dissolved in water, the weight of the film decreases, thinner, showed that the enzymatic degradation process is a surface corrosion process of P(3HB-co-4HB).

104.3.2 Molecular Weight Changes in the Process of Enzymatic Degradation

The molecular weight change of P(3HB-co-4HB) is shown in Fig. 104.2. With the degradation time becoming longer, five kinds of P(3HB-co-4HB) molecular weight
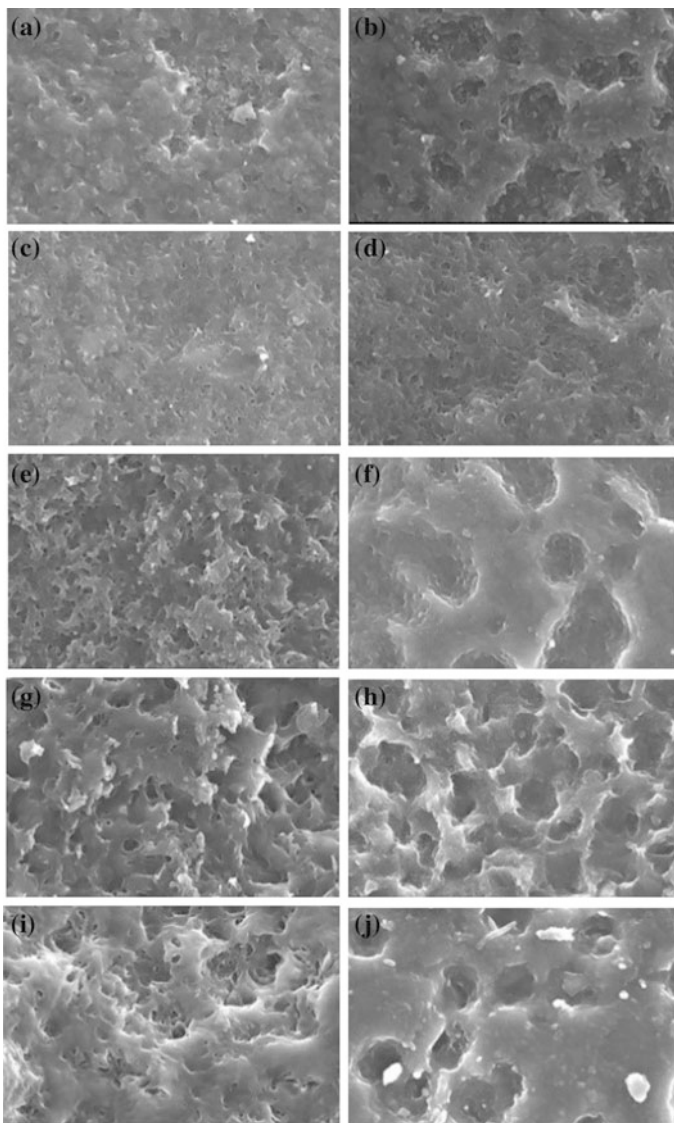
Fig. 104.3 SEM photographs of P(3HB-co-4HB) films biodegraded by lipase after 14 and 42 days, respectively

are reduced. This is mainly due to the fact that the water molecules in phosphate buffer have undergone hydrolysis reaction with P(3HB-co-4HB) and the ester bond of molecular chain is cut off, resulting in the molecular reduction. In addition, with the increase in 4HB molar fraction, the crystallinity of P(3HB-co-4HB) becomes reduced [5]. Reducing the degree of dense membranes, the water molecules can more readily penetrate into the interior of the film and undergo hydrolysis reaction with P(3HB-co-4HB) molecules.

104.3.3 SEM Analysis of Membrane Surface in the Process of Enzymatic Degradation

Figure 104.3 is an SEM photograph at different times about the film surface during enzymatic degradation. The film surface became rough and small holes appeared after 14-day-enzyme degradation; the holes became larger after 42 days, indicating the increase in the degree of film surface corrosion.

After 14 days, the sample films of P(3HB-co-10 %4HB), P(3HB-co-15 %4HB), and P(3HB-co-20 %4HB) generated a large number of holes, thus making the surface flaky. After 42 days, a large area of surface corrosion appeared, holes further increased, and the edge of the material becomes blurred. Mainly because of the different crystallinity of P(3HB-co-4HB), P(3HB-co-5 %4HB) and P(3HB-co-7 %4HB) have a higher crystallinity, strong anti-enzymatic ability and it will maintain crystal structure even after 42-day-degradation . By contrast, P(3HB-co-10 %4HB), P(3HB-co-15 % 4HB), and P(3HB-co-20 %4HB) have a lower crystallinity and higher degradation rate.

104.4 Conclusions

In this study, the biodegradability of different 4HB molar fraction of P (3HB-co-4HB) in phosphate buffer containing lipase were studied, and researched the P(3HB-co-4HB) which is as a biodegradable plastic degradation possibility under the action of lipase, the results are as follows:

(1) In the research of the five kinds of P(3HB-co-4HB), P(3HB-co-15 %4HB) has a lower crystallinity and better surface roughness and thus has the fastest rate of degradation.
(2) Different 4HB molar fractions of P(3HB-co-4HB) have little effect on the degradation process and the weight loss rate, and the extent of molecular weight changes.
(3) Lipase has the ability of faster degradation of P(3HB-co-4HB). The enzymatic degradation of P(3HBco-4HB) is a corrosion process on the surface.

References

1. Zhang, J., & Chu, T. (2012). Property analysis of biodegradable material P(3HB-co-4HB)[J]. *China Printing and Packaging Study, 4*(3), 52–56.
2. Loo, C. Y., & Sudesh, K. (2007). Polyhydroxyalkanoates: Bio-based microbial plastics and their properties. *Malaysian Polymer Journal, 2*(2), 31–57.
3. Hou, H., Chen, F., Cheng, X., et al. (2009). Research progress on the biodegradability of the biodegradable materials. *Plastics Science and Technology, 37*(3), 89–93.

4. Fu-ian, X. U. E. (2003). Bio-degradability and the text of the plastics. *Shanghai Plastics, 31*(1), 19–20.
5. Lu, X., Wen, X., & Yang, D. (2011). Crystal structure and isothermal crystallization kinetics of biodegradable Poly(3-hydroxybutyrate-co-4-hydroxybutyrate). *Journal of Materials Science, 46*(5), 1281–1288.

Part IX
Ink and Related Technology

Chapter 105
The Influence of Temperature Control Microcapsule Drying Agent Applies to Water-Based Gravure Ink on the Printability

Yingjie Xu, Tengfei Zhou, Xianfu Wei and Beiqing Huang

Abstract In order to solve the low drying velocity problem of the water-based gravure ink, the temperature control microcapsule drying agent is prepared. The influence of the temperature control microcapsule drying agent on the drying characteristics of the ink is described in this chapter. The dispersibility of the temperature control microcapsule drying agent is tested in this chapter. The printing proofs which are made by the ink that contain temperature control microcapsule drying agent are tested, and the glossiness is also tested. Experimental results show that the temperature control microcapsule drying agent is able to enhance the drying velocity of the water-based gravure printing ink. The dispersibility of the temperature control microcapsule drying agent and the glossiness of the printing can meet the quality requirements.

Keywords Water-based gravure ink · Temperature control microcapsule drying agent · Printability

105.1   Introduction

Gravure ink mainly includes solvent-based ink and water-based ink. Solvent-based ink contains volatile organic compounds (VOC), which can cause environmental pollution, harm to health of the printer, and pollute the commodity in package [see 1]. Water-based ink has no VOC, can improve the working environment, eliminates the pollution of the packaging commodity by ink, which is an environment-friendly ink, but it has the problem of low drying velocity [2–5].

The past research on the water-based gravure ink drying property is R&D new rapid film forming resin and adding organic solvents (e.g., alcohol). These methods

Y. Xu (✉) · T. Zhou · X. Wei · B. Huang
Beijing Institute of Graphic Communication, Beijing, China
e-mail: xuyingjie@bigc.edu.cn

cannot completely solve the problem of low drying velocity. The temperature control microcapsule drying agent prepared in the experiment can release the calcium oxide which can react with water and release heat to promote the drying velocity [6–10].

105.2 Experiments

105.2.1 Experimental Materials

Pigment: Phthalocyanine blue; resin: Acrylic resin 91-5; water repellent compound; calcium oxide; surfactant.

105.2.2 Equipments

Basket mill: SBM-T, China; electric blender: D2004W, China; printability tester: IGT F1, Netherlands; rheometer: AR2000, USA; and grossmeters: NOVO-GLOSS, England.

105.2.3 Sample Preparation

First, calcium oxide, water repellent compound, and alcohol are added into the beaker in a certain percentage, stirred for 30 min, and then left the mixture undisturbed for 60 min. Secondly, the surfactant is added into the mixture and stirred for 60 min. Thirdly, the mixture is placed in a drying oven in 60 °C for about 4 h.

105.2.4 Ink Performance Test

Viscosity test method: use the AR2000 rheometer to test the viscosity of ink. Select the 60-mm aluminum parallel plate as the tongs and the shear rate range is 0.1–100 (1/s);

Printability test method: add the temperature control microcapsule drying agent into the ink, using the printability tester to prepare the printing specimen and using the grossmeters to test the glossiness of the printing specimen.

105.3   Results and Analysis

105.3.1   The Study on the Drying Effect of the Temperature Control Microcapsule Drying Agent

The setting test temperature of rheometer is 30, 40, 50, and 60 °C, the viscosity of the ink contain 1 wt% drying agent is measured. The measurement time is 5 min. The results are demonstrated in Fig. 105.1

According to the above data analysis, the viscosity of the ink contains drying agent increased at 60 °C, due to which the organics fall off from the surface of calcium oxide powder at 60 °C, and the calcium oxide react with water. The viscosity of the ink did not change at 30, 40, and 50 °C, and it is because of that the temperature control microcapsule drying agent is stable under these temperatures. So the excitation temperature of the temperature control microcapsule drying agent is at 60 °C.

In order to test the drying effect of the temperature control microcapsule drying agent to the water-based gravure ink, the original ink and the ink added the 3 wt% temperature control microcapsule drying agent are used to print on the BOPP plastic film. The temperature of the drying box of gravure printing machine is kept at 80 °C, the drying effect of the ink at the print speed of 20,40, 60, 80, 100, 120 m/min is recorded, classifying the drying agent in four grades: excellent is 5, good is 4, acceptable is 3, and poor is 2. The results are demonstrated in Fig. 105.2.

According to the above data analysis, the drying effect of the original ink is good under 40 °C and is poor above 60 °C. The drying effect of the ink added the
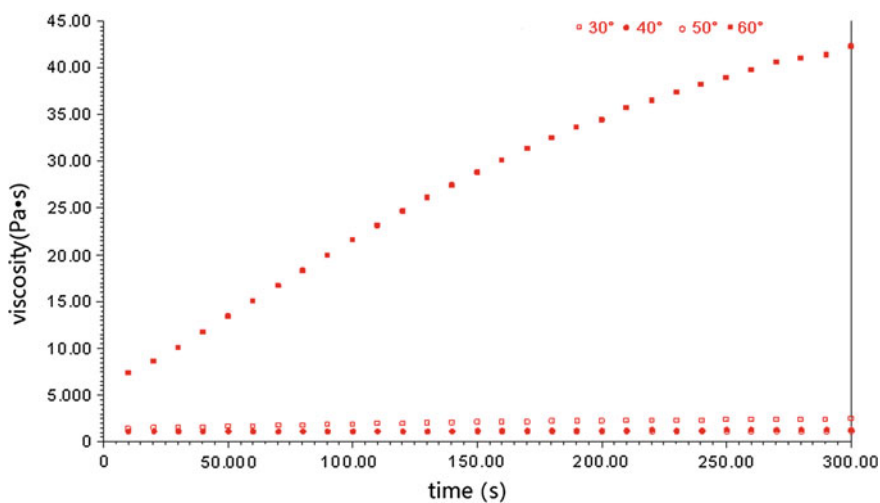
Fig. 105.1 Characterization of the temperature control microcapsule drying agent drying effect by rheometer
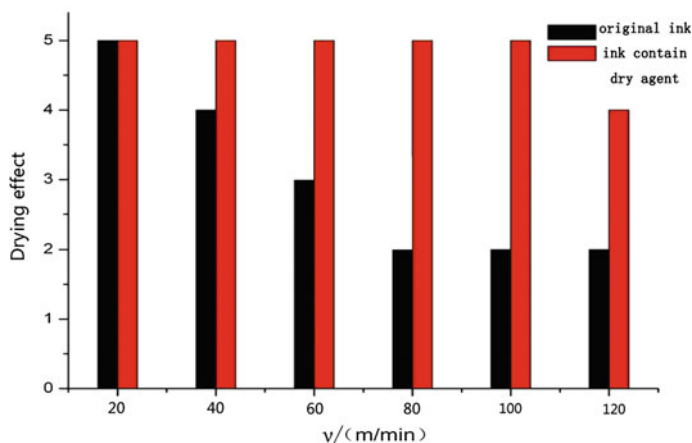
Fig. 105.2 Drying effect of the temperature control microcapsule drying agent on the water-based gravure ink

3 wt% temperature control microcapsule drying agent is good at 120 °C when the temperature of the drying box of gravure printing machine is at 80 °C. It is because of that above 60 °C, the temperature control microcapsule drying agent in the ink is trigged.

In order to test the influence of the temperature control microcapsule drying agent content on the water-based gravure ink drying effect, the original ink and the inks added the 1, 2, 3 wt% temperature control microcapsule drying agent are used to print on the BOPP plastic film, the temperature of the drying box of gravure printing machine is kept at 80 °C, and the highest print speed of the each ink own good drying effect is recorded. The results are demonstrated in Fig. 105.3.
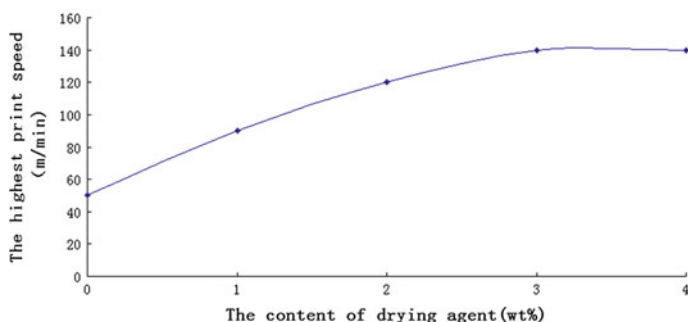
Fig. 105.3 Influence of the temperature control microcapsule drying agent content on the water-based gravure ink drying effect

According to the above data analysis, the highest print speed of the original ink is 50 m/min, the highest print speed of the ink added the temperature control microcapsule drying agent increases gradually with the increasing content of the drying agent, and there is no effect when the content of the drying agent increases above 3 wt% on the highest print speed of the ink.

105.3.2 The Study on the Dispersibility of the Temperature Control Microcapsule Drying Agent

The temperature control microcapsule drying agent is dispersed in acrylic emulsion by electric blender about 30 min and then grinded by basket mill at the rotational speed of 1000 r/min. The sample is extracted every 15 min to test the particle size by using laser particle size instrument. The results are demonstrated in Fig. 105.4

According to the above data analysis, the particle size of the temperature control microcapsule drying agent is gradually reduced, and the particle size distribution narrows down. Above 45 min, the particle size of the temperature control microcapsule drying agent increases, it is because of that the organics were destroyed when grinded time is too long.
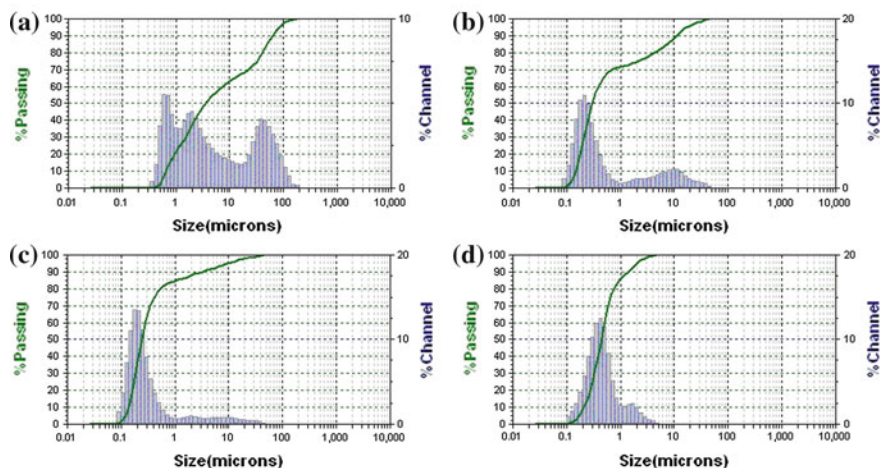
Fig. 105.4 Dispersibility of the temperature control microcapsule drying agent at different milling time. **a** 15 min **b** 30 min **c** 45 min and **d** 60 min
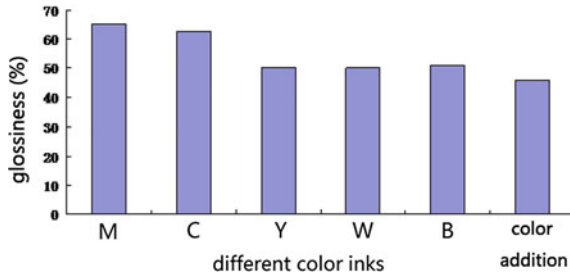
Fig. 105.5 The influence of the temperature control microcapsule drying agent on the water-based gravure ink glossiness

105.3.3 The Study on the Glossiness of the Temperature Control Microcapsule Drying Agent

In order to test the influence of the drying agent content on the glossiness of the water-based gravure ink, the ink containing 3 wt% drying agent is used to print on the BOPP plastic film. The glossiness of the printing specimen with grossmeters is tested. The results are demonstrated in Fig. 105.5

According to the above data analysis, Magenta ink and cyan ink have higher glossiness, the glossiness of each ink and the color addition can satisfy the application requirement of the gravure print.

105.4 Conclusions

Based on the above study, it can be concluded as the following:

1) The excitation temperature of the temperature control microcapsule drying agent is at 60 °C.
2) The temperature control microcapsule drying agent is able to enhance the drying velocity of the water-based gravure printing ink.
3) The ink added 3 wt% temperature control microcapsule drying agent has the highest print speed.
4) The dispersibility of the temperature control microcapsule drying agent and the glossiness of each ink and the color addition can satisfy the application requirement of the gravure print.

References

1. Xu, Y., Wei, X., & Huang, B. (2014). Study on temperature control microcapsule drying agent applies to water-based gravure ink. *Applied Mechanics and Materials, 469*(2014), 46–50.
2. Frederiksen, L., Anton, K., Hoogevest, P., et al. (1997). Preparation of liposomes encapsulating water-soluble compounds using supercritical carbon dioxide. *J Pharm Sci, 86*(8), 921–928.
3. Xue, Y. L., Wang, Z. F., Zhong, D. G., et al. (2000). Xenotransplantation of microencapsulated bovine chromaffin cells into hemiparkinsonian monkeys. *Artif Cells Blood Substit Immobil Biotechol, 28*(4), 337–345.
4. Johnson, O. L., Jaworowicz, W., Cleland, J. L., et al. (1997). The stabillzation and encapsulation of human growth hormone into biodegradable microspheres. *Pharm Res*, 1997, 14(6): 730–735.
5. Liu X D, Yu W Y, Zhang Y, et a1.(2002). Characterization of structure and diffusion behaviour of Ca-alginate beads prepared with external or internal calcium sources. *J Microencapsul*, *19*(6), 775–782.
6. Liu, X. D., Bao, D. C., Xue W. M., et al. (2003). Preparation of uniform calcium alginate gel beads by membrane emulsification coupled with internal gelation. *Journal of Applied Polymer Science*, *87*(5), 848–852.
7. Xue, Y. L., Wang, Z. F., Zhong D. G., et al. (2000). Xenotransplantation of microencapsulated bovine chromaffin cells into Hemiparkinsonian monkeys. *Art Cells Blood Subs, and Immob Biotech*, *28*(4), 337–345.
8. Sook, J. S., Kim, J. S., Kwak, H. S. (2003). Microencapsulation of watersoluble isoflavone and physico-chemical property in milk. *Archives of Pharmacal Research*, *26*(5), 426–431.
9. Esquisabel, A., Hernandez, R. M., Igartua, M., et a1. (2002). Preparation and stability of agarose microcapsules containing BCG. *Journal of Microencapsulation*, *19*(2), 237–244.
10. Gibbs, B. F., Kermasha, S., Alli, I., et al. (1999). Encapsulation in the food industry: A review. *International Journal of Food Science and Nutrition*, *50*(3), 213–224.

Chapter 106
Synthesis and Characterization of Alumina Sol-Modified Polyacrylate Emulsion

Xiaoyan Yu, Xiulan Xin, Baocai Xu, Tao Wu and Peng Wang

Abstract Alumina sol-modified polyacrylate emulsion was prepared by semi-continuous seeded emulsion polymerization using methyl methacrylate (MMA), butyl acrylate (BA), and acrylic acid (AA) as monomers, alumina sol as modifier. The chemical structure, particle size, and zeta potential of composite emulsion were characterized by Fourier transform infrared (FTIR) spectroscopy and dynamic light scattering (DLS). The influences of different contents of alumina sol on the surface tension and drying rate of composite emulsion were also investigated. The results showed that alumina sol existed in polyacrylate emulsion. The average particle size of composite emulsion was bigger than that of pure polyacrylate emulsion, and the zeta potential changed from negative value to positive value with the increase of alumina sol content. The introduction of alumina sol lowered the surface tension and accelerated the drying rate of pure polyacrylate emulsion. When the composite emulsion contained 3 wt‰ alumina sol, the surface tension reached the minimum with 31.79 mN/m and composite emulsion exhibited the fastest drying rate.

Keyword Alumina sol · Modifier · Polyacrylate emulsion · Semi-continuous seeded emulsion polymerization · Surface tension · Drying rate

106.1 Introduction

Reducing volatile organic compounds (VOCs) in paints, inks, and coatings is of particular importance due to their adverse effects on the environment. As the water-based binder, polyacrylate emulsion is considered environmental-friendly which possesses many outstanding performances such as excellent film forming,

X. Yu · X. Xin (✉) · B. Xu · T. Wu · P. Wang
School of Food and Chemical Engineering, Beijing Technology and Business University, Beijing, China
e-mail: xinxl2007@126.com

high transparency, good flexibility, strong adhesion, color and gloss retention, and coating fullness. [1, 2]. However, polymerlate emulsion being used as the binder of water-based ink has some shortcomings. For instance, drying rate is a major factor to be considered during the printing process [3]. Hamid and Raza [1] reported that drying rate was related to the free volume and surface tension of the material. Therefore, the interest to synthesize polyacrylate emulsion with smaller particle size, lower surface tension, and fast drying rate has increased considerably. Organic–inorganic nanocomposite particles have high function and high performance because of the small size effect, high surface effect, and quantum size effect of nanoparticles. Thus, incorporation of metal oxide nanoparticles into polymer has made a broad attention, such as SiO_2 [4], TiO_2 [5], CeO_2 [6], and ZnO [7]. However, there have been few studies on the alumina sol-modified polyacrylate emulsion. Alumina sol is positively charged colloidal solution of alumina fine particles dispersed in water.

In this present study, we prepared the alumina sol-modified polyacrylate emulsion with different contents of alumina sol (0, 1, 2, 3, 4, and 5 wt‰) by semi-continuous seeded emulsion polymerization. The chemical structure of composite emulsion was mainly characterized by FTIR. And we focused on the influence of different contents of alumina sol on the surface tension and drying rate of composite emulsion.

106.2 Experimental

106.2.1 Materials

Methyl methacrylate (MMA) and butyl acrylate (BA) were washed with 5–10 % sodium hydroxide solution to remove inhibitors and then washed with deionized water to neutralize. Acrylic acid (AA) was used without further purification. Sodium dodecyl sulfate (SDS) and alkylphenol polyoxyethylene (OP-10) were used as the anionic emulsifier and nonionic emulsifier, respectively. Ammonium persulfate (APS) and sodium bicarbonate ($NaHCO_3$) were used as the initiator and buffer agent, respectively. All the chemicals were all purchased in chemical pure from Sinopharm Chemical Reagent Co., Ltd. Alumina sol (solid content with 3.55 wt‰) was directly prepared in the laboratory.

106.2.2 Synthesis of Alumina Sol-Modified Polyacrylate Emulsion

Alumina sol-modified polyacrylate composite emulsion was synthesized by semi-continuous seeded emulsion polymerization. A certain amount of composite emulsifier and $NaHCO_3$ were dissolved in the requisite amount of deionized water

in a 250-mL four-necked round-bottom flask equipped with a reflux condenser, a thermometer, a mechanical stirrer, and dropping funnels to form uniform solution. Then, proportional monomers were dropped in the mixed solution with the stirring speed of 200 rpm. When the monomers were completely added, the mixture was pre-emulsified under stirring for 30 min. Then, 1/3 of pre-emulsified mixture, 1/3 of APS aqueous solution, appropriate alumina sol, and deionized water were fed in the flask. The rest pre-emulsified mixture and APS aqueous solution were added in different dropping funnels. When the temperature was ramped to 85 °C during which the mixture appeared blue fluorescence, the rest pre-emulsified mixture and APS aqueous solution were dropped into the reactor over a period of 2–3 h. When the mixture and APS aqueous solution were completely added, the mixture was allowed to react continuously for another 2 h at 90 °C. Then, the composite emulsion was cooled to 50 °C, and the pH was adjusted to 8–9 with thick ammonia. Finally, the composite emulsion was filtered through a filter of 100-mesh sieve. Scheme 106.1 shows the process for the synthesis of alumina sol-modified polyacrylate emulsion.

106.2.3 Characterization

Fourier transform infrared (FTIR) spectroscopy measurement was used to identify the structure of composite emulsion. The infrared spectra were obtained using a Nicolet Avatar 370 FTIR spectrometer in the wave number frequency range of 400 cm–4000 cm^{-1} with potassium bromide pellet technique. The average particle size and zeta potential of composite emulsion were measured by dynamic light scattering (DLS) using a Zetasizer Nano Series. The emulsion samples were
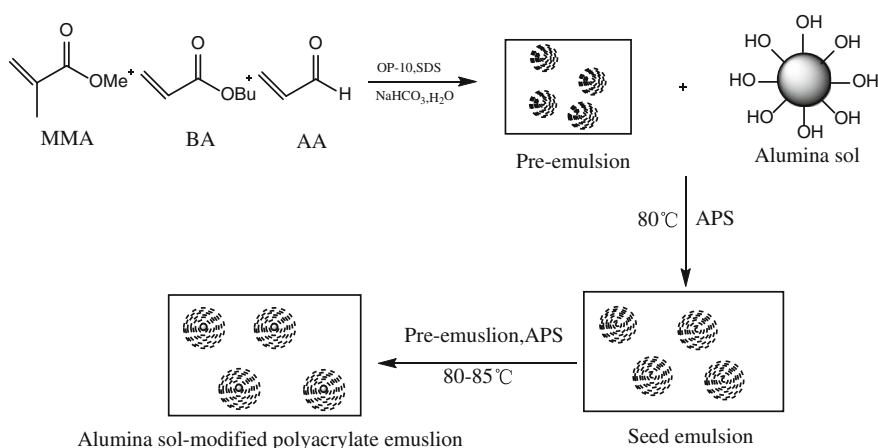
Scheme 106.1 Process of the alumina sol-modified polyacrylate emulsion

determined the zeta potential directly without dilution, while the samples were diluted with deionized water to 1 wt‰ before testing the particle size. Surface tension was performed by a DCAT11 surface/interface tension meter. The drying speed of polyacrylate emulsion was obtained by weighing the emulsion before and after dried at 50 °C every for 10 min, and the concrete formulations were as follows:

$$T = \frac{W_2 - W_1}{W_0} \times 100 \% \tag{106.1}$$

$$\text{Dehydration rate } (\%) = \frac{W_3}{W_0 \times (1 - T)} \times 100 \% \tag{106.2}$$

where T is solid content, W_0 is the weight of the emulsion, W_1 is the weight of the vessel, W_2 is the weight of the dried emulsion and the vessel, and W_3 is the weight of the lost water.

106.3 Results and Discussion

106.3.1 Chemical Structure Analysis of Alumina Sol-Modified Polyacrylate Emulsion

Figure 106.1 illustrates the FTIR spectra of alumina sol (a), pure polyacrylate emulsion (b), and alumina sol-modified polyacrylate emulsion (c). In the FTIR spectrum of alumina sol (curve a), the broad band centered near 3390 cm^{-1} is attributed to the -OH stretching vibrations of water. The -OH stretching vibrations of

Fig. 106.1 FTIR spectra of alumina sol (**a**), pure polyacrylate emulsion (**b**), alumina sol-modified polyacrylate emulsion (**c**)
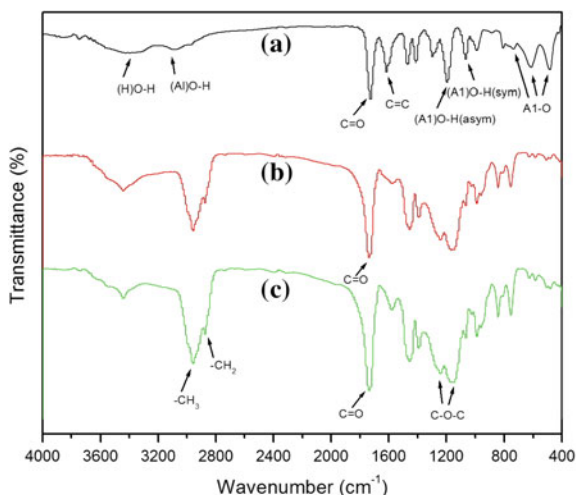
alumina sol is at 3080 cm^{-1} and its bending vibrations are at 1190 cm^{-1} and 1070 cm^{-1}. The characteristic absorption peak at 1165 cm^{-1} corresponds to the C=C bending vibrations. The results demonstrate that alumina sol has many hydroxyl groups and carbon-carbon double bonds. Compared with the FTIR spectrum of alumina sol, there are no characteristic absorption peaks of –OH in the FTIR spectra of alumina sol-modified polyacrylate emulsion (curve c), which can indicate that alumina sol was involved in the polymerization. The characteristic absorption peaks at 735, 615, and 483 cm^{-1} are due to Al–O stretching and bending vibrations in curve a.

For the FTIR of polyacrylate emulsion (curve b and c), the characteristic stretching absorption peaks of –CH$_3$, –CH$_2$, and –C = O occur at 2958, 2875, and 1730 cm^{-1}, respectively, and stretching vibration of C–O–C occurs at 1240 and 1166 cm^{-1}. Compared with the FTIR spectrum of pure polyacrylate emulsion (curve b), the absorption peak near at 482 cm^{-1} in curve c is stronger and broader than that in curve b owing to the some strong interactions in the alumina sol-modified polyacrylate emulsion, which is likely to be connected with the bending vibrations of Al–O.

106.3.2   Particle Size and Zeta Potential of Alumina Sol-Modified Polyacrylate Emulsion

The average particle size and zeta potential of composite emulsion are shown in Fig. 106.2. Obviously, the average particle size of modified polyacrylate emulsion is bigger than that of alumina-free emulsion. And the average particle size increases along with the increase of alumina sol content. The results demonstrate that the alumina sol is formed inside of latex particles.

The zeta potential reflects an upward trend as well, which increases from −33.33 to 8.89 mV when the alumina sol content increases from 0 to 5 wt‰. Owing to the positive charges of alumina sol, the zeta potential changes from negative value to positive value.

106.3.3   Surface Tension of Alumina Sol-Modified Polyacrylate Emulsion

Surface tension of emulsion is directly related to the wettability to printing substrate. The lower the surface tension is, the better the wettability is. Surface tension of composite emulsion is shown in Fig. 106.3. Clearly, surface tension decreases with the increase of the alumina sol content, and it reaches the minimum with 31.79 mN/m at the content of 3 wt‰. According to the results, it can be concluded that alumina sol can be used as cationic emulsifier and lead to the lower surface tension of composite emulsion further.
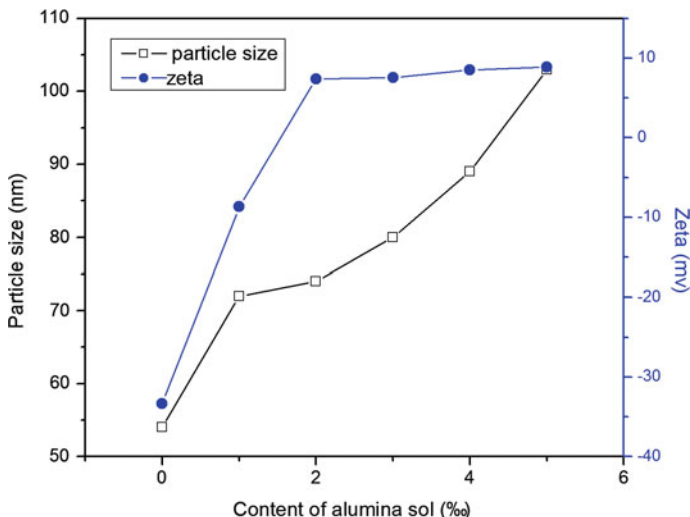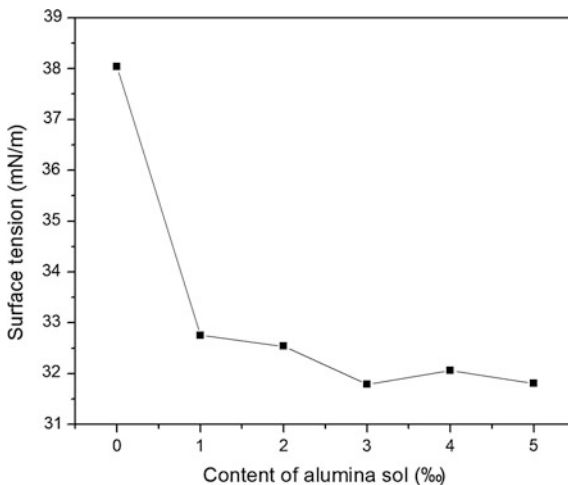
**Fig. 106.2** Effect of alumina sol content on the average particle size and zeta potential for emulsions

Fig. 106.3 Effect of alumina sol content on the surface tension for emulsions

106.3.4 Drying Rate of Alumina Sol-Modified Polyacrylate Emulsion

Figure 106.4 reveals that the drying rate of alumina-containing polyacrylate emulsions is faster than that of the alumina-free polyacrylate emulsion. And the composite emulsion containing 3 wt‰ alumina sol is the fastest one. Water volatilization is related to the free volume and the surface tension of the material

Fig. 106.4 Effect of alumina sol content on the drying rate for emulsions
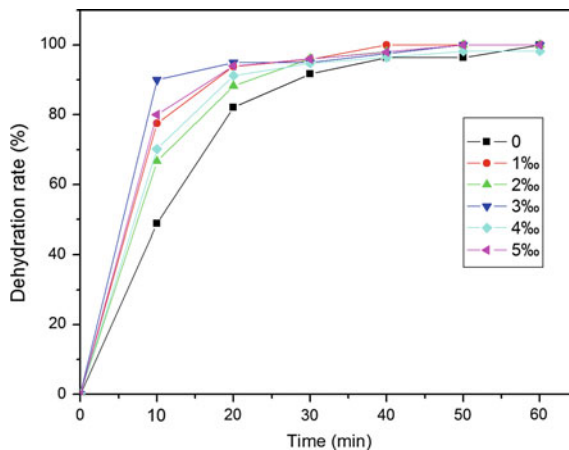
when the solid content is constant [3]. And there is a negative correlation between free volume and particle size. Bigger free volume and lower surface tension can lead to quicker volatilization. The composite emulsion containing 3 wt‰ alumina sol has the fastest drying rate, which is probably due to its lowest surface tension and relatively smaller average particle size.

106.4   Conclusions

Alumina sol-modified polyacrylate emulsion was successfully prepared by semi-continuous seeded emulsion polymerization. Alumina sol existed in the composite emulsion, and the average particle size of modified emulsion was bigger than that of pure polyacrylate emulsion, and the zeta potential changed from negative value to positive value along with the increase of alumina sol content. The introduction of alumina sol lowered the surface tension further and accelerated the drying rate of pure polyacrylate emulsion. When the composite emulsion contained 3 wt‰ alumina sol, the surface tension reached the minimum with 31.79 mN/m and composite emulsion exhibited fastest drying rate.

References

1. Hamid, J. N., & Reza, M. (2011). Synthesis and characterization of new polysiloxane bearing vinylic function and its application for the preparation of poly (silicone-co-acrylate)/montmorillonite nanocomposite emulsion. *Progress in Organic Coatings, 70*, 32–38.
2. Bao, Y., Shi, C. H., Ma, J. Z., Wang, B., & Zhang, Y. H. (2015). Double in-situ synthesis of polyacrylate/nano-TiO$_2$ composite latex. *Progress in Organic Coatings, 85*, 101–108.
3. Iraj, H., Ali, R. M., & Hamid, S. M. (2014). Particle size and shell composition as effective parameters on MFFT for acrylic core–shell particles prepared via seeded emulsion polymerization. *Progress in Organic Coatings, 77*, 1874–1882.
4. Wu, Y., Hu, D., Su, Y. H., Hsiao, Y. L., You, B., & Wu, L. M. (2014). Synthesis and film performances of SiO$_2$/P(MMA-BA) core–shell structural latex. *Progress in Organic Coatings, 77*, 1015–1022.
5. Lewis, O. D., Critchlow, G. W., Wilcox, G. D., Zeeuw, A., & Sander, J. (2012). A study of the corrosion resistance of a waterborne acrylic coating modified with nano-sized titanium dioxide. *Progress in Organic Coatings, 73*, 88–94.
6. Miren, A., Maria, P., & Jose, R. L. (2014). Particle nucleation and growth in seeded semibatch miniemulsion polymerization of hybrid CeO$_2$/acrylic latexes. *Polymer, 55*, 752–761.
7. Petchthanasombat, C., Tiensing, T., & Sunintaboon, P. (2012). Synthesis of zinc oxide-encapsulated poly (methyl thacrylate)-chitosan core-shell hybrid particles and their electrochemical property. *Journal of Colloid Interface Science, 369*, 52–57.

Chapter 107
The Effect of the Protective Colloid on the Property of Acrylic Emulsion

Luolin Han, Feng Qin, Xiaoyu Li and Haiqiao Wang

Abstract How to improve the stability of the acrylic emulsion to meet the needs of the practical application has always been an important research topic in this field. In this contribution, an alkali-soluble resin is used as protective colloids to improve the stability of the acrylic emulsion. The effects of protective colloids on the performance of acrylic emulsion were studied in detail. The results demonstrated that the alkali-soluble resins used as protective colloids can improve the stability of the emulsions against added calcium ion and ethanol. In addition, some other properties of the emulsions, such as viscosity, surface tension, adhesion, and water resistance, are also affected to some extent.

Keywords Protective colloid · Acrylic emulsion · Stability · Performance

107.1 Introduction

With the increasingly stringent environmental requirements, most of the researchers attach importance to the water-based ink. The performance of water-based ink is determined by the ink binder, and polyacrylate emulsion has been major binder for inks [1, 2], due to the superior properties in accordance with chemical resistance, film-forming ability, affinity to the pigment, and so on [3]. However, polyacrylate

H. Wang (✉)
Beijing Engineering Research Center for the Synthesis and Applications of Waterborne Polymers, Key Laboratory of Carbon Fiber and Functional Polymers, Ministry of Education, Beijing University of Chemical Technology, Beijing, China
e-mail: wanghaiqiao@mail.buct.edu.cn

L. Han · F. Qin · X. Li (✉)
Beijing University of Chemical Technology, Beijing, China
e-mail: lixy@mail.buct.edu.cn

L. Han
e-mail: hanluolin1990@163.com

emulsions show poor calcium ion stability and ethanol resistance. So improving the stability of the acrylic emulsions has been a challenging topic.

So far, most literatures have proved that the use of protective colloids is the most effective method. For example, Nakamae [4] employed the modified poly(vinyl alcohol) (PVA) as protective colloid to prepare the poly(vinyl acetate) emulsion and found that the PVA as protective colloid can endow the emulsion with good stability and viscosity stability at low temperature. Berber [5] compared the effects of oligomeric NMA with PVA used as protective colloid on poly(VAc-co-BA) latexes and their films, and they observed that the stabilization, monodisperse property, and film-forming ability of latexes made by oligomeric NMA are much better. Okaya [6] prepared a stable emulsion using PVA as protective colloid. Nowadays, the most widely used protective colloids are PVA, hydroxyethyl cellulose, and polyethylene glycol. However, these protective colloids did not perform well on polyacrylate emulsions.

Herein, in this paper, we chose a commercially available alkali-soluble acrylic resin as protective colloid and prepared different polyacrylate emulsions based on two-formulation systems. For the convenience of study, the polyacrylate emulsions without protective colloid were simultaneously prepared to investigate the effect of alkali-soluble acrylic resin on the properties of polyacrylate emulsions.

107.2 Experimental

107.2.1 Materials

Methacrylate (MMA), butyl acrylate (BA), 2-ethylhexyl acrylate (EHA), and isobornyl acrylate (IBOA) were of technical grade. Acrylic acid was provided by Tianjin Fuchen Chemical Reagents Factory. Dodecyl mercaptan was provided by Sinopharm Chemical Reagent Co., Ltd. Formulation 1 consists of the monomers MMA, BA, EHA, and AA. Formulation 2 consists of the monomers MMA, BA, IBOA, AA, and dodecyl mercaptan.

107.2.2 Emulsion Preparation

The polymerization was in a 2-L four-necked round flask equipped with a stirrer, a reflux condenser, a nitrogen (N_2) inlet, and a thermometer. A certain amount of protective colloid, emulsifier, buffer agent, distilled water, and a part of mixed monomers were added into the flask and then heated to 80 °C for 15 min under N_2. At the same time, the remaining monomers and emulsifier were premixed evenly. One-third of the initiator was added into the flask. After the reaction mixture turned into light blue, let the reaction run further for half an hour at 80 °C. Then, the rest of monomers and emulsifier were added to the flask in 2 h, and polymerization was

carried out for 3 h and finally cooled to room temperature and filtered through a 200-mesh filter cloth and neutralized to pH 9.0–9.3.

107.2.3 Characteristic

1. Particle size: The particle size was determined by dynamic light scattering using a Zetasizer Nano-ZS. The reported results are the average of 3 runs.
2. Gel ratio: Aluminum foil (weight m_1) containing gel was dried in an oven at 50 °C until constant weight, and the total weight was weighted as m_2.

$$\text{gel ratio} = \frac{m_2 - m_1}{\text{the total weight of monomers}} \times 100\,\% \tag{107.1}$$

$$\text{water absorption} = \frac{m_2 - m_1}{m_1} \times 100\,\% \tag{107.2}$$

3. Water absorption: A certain amount of latex was cast into a container with an area of $6 \times 8 \text{ cm}^2$ and was dried under 45 °C for 24 h to obtain films. Take a part of the film (weight m_1), put it into deionized water for 24 h, then take out from water, absorb the water from the surface, and assign the weight as m_2.
4. Surface tension: The surface tension of each emulsion was measured three times by contact angle meter, and then, the average was calculated.
5. Calcium ion stability: Calcium chloride solution with concentration (1, 2, 3, 4, or 5 %) was added into the emulsion until mass fraction of 20 % to the emulsion weight. If the emulsion did not appear demulsification or thickening, the calcium ion stability was evaluated as pass.
6. Ethanol resistance: 40 g emulsion and 15 g grinding resin were placed into a beaker and mixed using high mixing machine at the speed of 2000 rpm for 0.5 h. Next, 15 g ethanol was added and stirred for another 15 min. Finally, 20 g as-prepared sample was put into the oven of 50 °C and recorded the time when the emulsion begin to thicken.

107.3 Results and Discussion

107.3.1 Effect of the Protective Colloid on the Properties of Emulsion

We prepared two emulsions based on two formulations and studied the effects of protective colloid on the emulsion performance. Table 107.1 demonstrates that the protective colloid can improve the polymerization stability, calcium ion stability, and ethanol resistance of the relative emulsions. The best calcium ion stability and ethanol resistance reached 5 % and 7 days for formulation 1 and 5 % and 2 weeks

Table 107.1 Impact of dosage of the protective colloid (based on formulation 2)

Protective colloid (mass fraction to the total monomers)	Outward appearance	Gel ratio (%)	Particle size (nm)	Surface tension (mN/m)	Calcium ion stability (%)	Ethanol resistance
Formulation 1						
0	Pale blue	0.08	112.9	56.25	2	<2 h
0.25	Pale blue	1.18	112.53	54.09	2	<3 h
0.5	Pale blue	0.08	111.4	54.59	4	≈2 h
1.0	Pale blue	1.16	116.93	53.93	5	>7 days
1.5	Plenty of gel, failed					
Formulation 2						
0	Pale blue	1.93	113.63	54.35	2	<12 h
0.25	Pale blue	0	101.37	51.47	2	<12 h
0.5	Pale blue	2.03	121.87	49.93	5	>10 days
1.0	Pale blue	0.96	106.90	51.21	5	>2 weeks
1.5	Plenty of gel, failed					

for formulation 2. Besides, the other properties of the latexes with protective colloid are not much different from that with no protective colloid.

As a waterborne binder for water-based ink, it is vital for latex to possess good stability against ion and ethanol. The latex particles are encapsulated by the emulsifiers, and charges around the latex particle are in an equilibrium state. Therefore, the charges of electrolytes or additives will react with opposite charges on the surface of the latex particles, which can destroy the electrical double layer outside the latex particles and cause imbalance between positive and negative charges. As a result, the emulsion becomes instable. On the other hand, ethanol is a demulsifier of polyacrylate emulsions because it can dissolve emulsifiers, which would lead to the loss of protective effect of the emulsifiers for the emulsions and cause the emulsion demulsification.

When the protective colloid is introduced into the emulsions, the protective colloid can cover the surface of the latex particles and thicken the hydration layer, as shown in Fig. 107.1. Once electrolytes or ethanol are added into the emulsion, they cannot act directly with the charges and emulsions on the surface of the latex particles due to the blocking function of protective colloid located on the periphery of the latex particles. Thus, protective colloid can effectively improve the stability of the emulsions against added electrolytes and ethanol.

Fig. 107.1 Particle with protective colloid

hydration layer of protective colloid
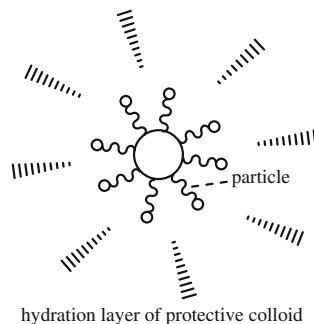
## 107.3.2   Impact of Dosage of the Protective Colloid on the Properties of the Emulsions

We also investigated the impact of dosage of the protective colloid on the performance of the emulsions. Table 107.1 summarized the basic properties of the emulsions prepared based on different dosage of the protective colloid. It is obviously excessive protective colloid, which resulted in plenty of gel or demulsification. The optimal dosages of protective colloid for the two systems are both 1 %. The emulsions prepared with the optimal conditions possess the smallest particle size, as well as the best polymerization stability and stability against added electrolytes and ethanol.

107.3.3   Impact of the Protective Colloid on the Water Absorption Ratio of the Latex Films

Figure 107.2 shows the relationship between the dosage of protective colloid and water absorption. We can see that the water absorption ratio rises with the increase of protective colloid. Because alkali-soluble resin possesses plentiful hydrophilic groups, introduction of the protective colloid endows the polymer with stronger hydrophilicity, which increases the water absorption of latex films. Thus, protective colloid has negative effect on the water resistance of the films.

Considering calcium ion stability, ethanol resistance, and water resistance, the optimal dosage of the protective colloid is 1.0 % for the formulation 1 and 0.5 % for the formulation 2, indicating that the dosage of the protective colloid must be carefully optimized based on different emulsions.

Fig. 107.2 Connection between protective colloid and water absorption
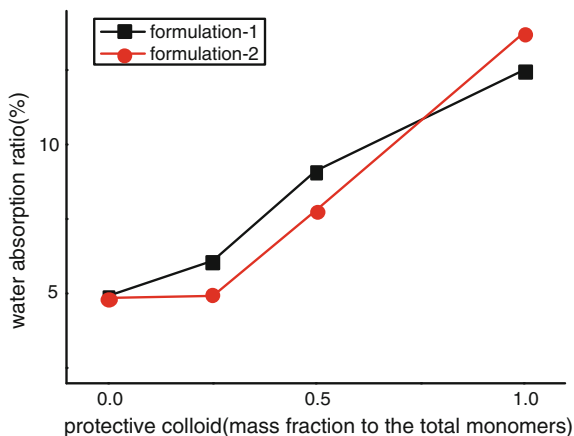
107.4 Conclusions

The protective colloid of an alkali-soluble resin has significant effect on emulsion. The introduction of small amount of the protective colloid can greatly improve the stability of the emulsions, but increase the water absorption and reduce the water resistance of the relative latex films. This phenomenon indicates that employing alkali-soluble resins as protective colloid is an effective strategy to improve the stability of polyacrylate emulsions.

References

1. Chai, S. L., & Jin, M. M. (2009). Morphology and particle size of nanograde polyurethane/polyacrylate hybrid emulsions. *Journal of Applied Polymer Science, 114*(4), 2030–2035.
2. Hirose, M., Kadowaki, F., & Zhou, J. (1997). The structure and properties of core-shell type acrylic-polyurethane hybrid aqueous emulsions. *Progress in Organic Coatings, 31*(1–2), 156–169.
3. Zhang, J., Li, X., Shi, X., et al. (2012). Synthesis of core-shell acrylic-polyurethane hybrid latex as binder of aqueous pigment inks for digital inkjet printing. *Chinese Material Research Society, 22*(1), 71–78.
4. Nakamae, M., Yuki, K., Sato, T., et al. (1999). Preparation of polymer emulsions using a poly (vinyl alcohol) as protective colloid. *Colloids and Surfaces A: Physicochemical and Engineering Aspects, 153*(1–3), 367–372.
5. Berber, H., Sarac, A., & Yıldırım, H. (2011). A comparative study on water-based coatings prepared in the presence of oligomeric and conventional protective colloids. *Progress in Organic Coatings, 71*(3), 225–233.
6. Okaya, T., Suzuki, A., & Kikuchi, K.(1999). Importance of grafting in the emulsion polymerization of MMA using PVA as a protective colloid. *Effect of Initiators. Colloids & Surfaces A Physicochemical & Engineering Aspects, 153*(1–3), 123–125.

Chapter 108
Effects of Polymerization Variables on the Electrical Conductivity of Polypyrrole–Anionic Spherical Polyelectrolyte Brush (PPy/ASPB) Composite

Na Su, Heng Xu and Zhengmin Cao

Abstract A series of polypyrrole (PPy) doped with anionic spherical polyelectrolyte brushes (ASPB) (PPy/ASPB composite) at different polymerization variables (the amount of ASPB, molecular weight of grafted chains, polymerization time, and polymerization temperature) were synthesized by means of chemical oxidative polymerization, characterized with FTIR and analyzed by electrical conductivity measurements. Results verified that long grafted chains and low temperature helped to increase the electrical conductivity. ASPB acted both as dopant and as template in the polymerization process as a result of offering favorable space factors for the growth of pyrrole.

Keywords Spherical polyelectrolyte brushes · Conducting polymers · Doping · Template · Electrical conductivity

108.1 Introduction

With the development of printed electronics, three development directions of electronic ink have emerged [1–3]. First, the use of organic ink will make it possible to print electronic devices with complex graphics and photovoltaic cells. Second, the use of nanomaterials in the ink can provide an efficient method of manufacturing ink. Last, the realization of printed silicon will import large amounts of

N. Su (✉) · H. Xu
Department of Printing and Packaging Engineering, Shanghai Publishing and Printing College, Shanghai, China
e-mail: suna@whu.edu.cn

Z. Cao
Shanghai Electric Power Generation Equipment Co., Ltd., Shanghai, China

silicon processing knowledge and technology in printed electronics. Additionally, as the fastest growing printing technology in recent years, inkjet printing is one of the easiest technologies to achieve miniaturization, and its versatility is unmatched by other printing technologies [4]. The digital information in computer can be directly sprayed onto the materials of any shape. In the actual production process, printing ink needs to have good liquidity to prevent the nozzle from clogging [5].

In view of this, polypyrrole (PPy) doped with anionic spherical polyelectrolyte brushes (ASPB) (PPy/ASPB composite) may be conducting composite with excellent properties. On the one hand, the electrical conductivity of PPy with light molecular weight, low price, and ease of synthesis can reach 10^3 S/cm by doping [6, 7]. On the other hand, the micro-nanoparticles are obtained by loading high symmetry or quasi-spherical symmetry particles. These particles have good liquidity [8], which can meet the requirements of inkjet printing for conducting material. Furthermore, as one of the three development directions of electronic ink, nanosilica is selected as the cores of ASPB. Recent research reports have proved that conducting ink has good film-forming properties, which are mainly because SPB serve as the carrier of conducting polymer [9].

On the basis of the previous work [10], we focus to object in this study for the effects of polymerization variables (the amount of ASPB, molecular weight of grafted chains, polymerization time and polymerization temperature) on the electrical conductivity of PPy/ASPB composite. As Fourier transform infrared spectroscopy (FTIR) and electrical conductivity are convenient techniques to monitor changes in the structure and conductive property of conducting polymer, the resulting composite was characterized with FTIR and analyzed by electrical conductivity measurements.

108.2 Experimental Part

108.2.1 Materials

Pyrrole (Sinopharm Chemical Reagent Co., Ltd, Shanghai, China) was distilled under reduced pressure before use. Iron (III) chloride hexahydrate ($FeCl_3 \cdot 6H_2O$) and ethanol were purchased from Sinopharm Chemical Reagent Co., Ltd, Shanghai, China. They were analytical reagents and were used without further purification. ASPB ($D_z \approx 100$ nm, $M_w = 500, 1000, 2000$ g/mol, $M_w/M_n = 1.6$) consisting of modified SiO_2 cores and poly(sodium-p-styrenesulfonate) (PSS) brushes were prepared by surface-initiated polymerization.
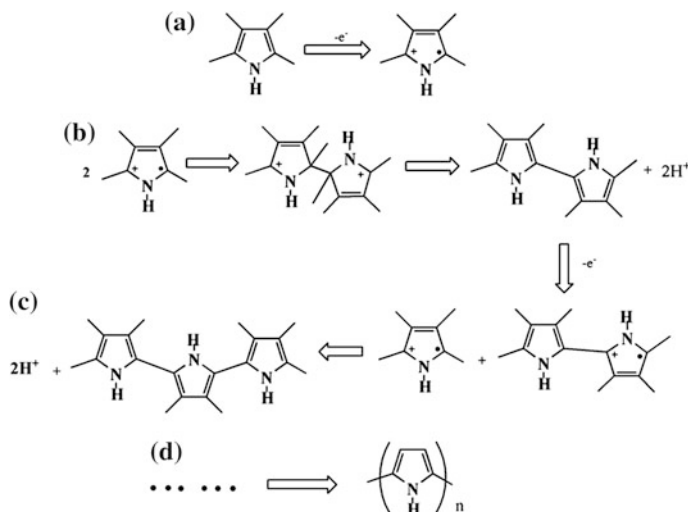
Fig. 108.1 Polymerization mechanism of pyrrole by in situ chemical oxidation polymerization

108.2.2   Synthesis of PPy

The procedure for the synthesis of polypyrrole (PPy) by means of in situ chemical oxidative polymerization is presented in Fig. 108.1. A neutral pyrrole was oxidized into cation radical firstly. Then, two cation radicals are combined together to form a double polypyrrole cation, which generated neutral dicationic polypyrrole through disproportionation. The tripolymer was generated by the oxidation of dicationic polypyrrole after repeating the above procedure. This cycle continued until the linear polymer was generated with a polymerization degree of n.

108.2.3   Synthesis of PPy/ASPB Composite

The amount of 5, 10, 15, 20, and 25 wt% of ASPB was firstly added to 45 ml mixture of water and ethanol (v/v, 2/1) with ultrasonic dispersion for 30 min, and 1.34 g of distilled pyrrole (0.2 mol) was then added. The mixture was degassed under N_2 flow for 30 min and cooled to 5 °C followed by the addition of 2.7 g (0.1 mol) of $FeCl_3 \cdot 6H_2O$ in 15 ml aqueous solution. Polymerization was allowed to proceed for 8 h. The samples were collected via filtration for every two hours, washed with ethanol and distilled water for three times, and were dried in vacuum at 60 °C for 12 h.

108.2.4   Characterization of PPy/ASPB Composite

FTIR was obtained using a Nicolet AVATAR 360FT spectrometer (USA). The electrical conductivity of samples was measured in a four-point probe (RTS-4, China) apparatus at room temperature. The resistivity ρ of the material was shown according to the following equation:

$$\rho = \frac{V}{I} C \qquad (108.1)$$

where C is the probe factor and is determined by the geometric position of the probe. When the resistivity of the sample is uniformly distributed, and the size of the sample is semi-infinite, C is calculated according to formula (2.2):

$$C = \frac{2\pi}{\frac{1}{S1} + \frac{1}{S2} - \frac{1}{S1+S2} - \frac{1}{S2+S3}} \qquad (2.2)$$

The experimental procedure refers to the literature [11], and the electrical conductivity of the samples can be calculated according to formula (2.3):

$$I = F(W/S) \times F(D/S) \times W \times 0.1 \qquad (2.3)$$

where S is the distance of the adjacent probe ($S_1 = S_2 = S_3 = 1$ mm), $F(W/S)$ is the width correction coefficient, $F(D/S)$ is the diameter correction coefficient, and W is the thickness of each sample.

108.3   Results and Discussion

108.3.1   Effect of Polymerization Temperature on Electrical Conductivity

To examine the effect of polymerization temperature on electrical conductivity, the FTIR spectra of products were analyzed under 5 and 30 °C, respectively (see Fig. 108.2a).

According to the aforementioned method, electrical conductivity has a qualitative description by the area ratio of asymmetric stretching vibration absorption and symmetric stretching vibration absorption peaks of pyrrole ring [12]. As shown in Fig. 108.2a, the ratio of integrated absorption areas of the 1451 and 1546 cm^{-1} (A_{1451}/A_{1546}) bands for the PPy/ASPB composite is 0.38 at 5 °C, which is higher than that of ($A_{1463}/A_{1531} = 0.21$) at 30 °C, indicating that the conjugation length increases. The increase in conjugation length means excellent electrical conductivity at low temperatures. As the semiconductor theory shows, the electrical conductivity is described as equation ($\sigma = ne\mu$), where e is the charge number, n is
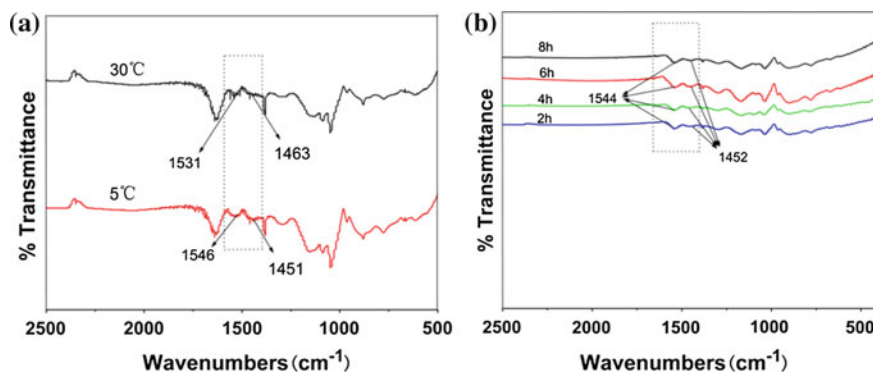
Fig. 108.2 Effects of polymerization: **a** temperature and **b** time on electrical conductivity

the density of the charge carrier, and μ is the carrier mobility. As n is not changed essentially in a certain temperature range, the effect of temperature on electrical conductivity mainly comes from the carrier mobility. Polymerization process is slow at low temperatures, so the content of defect structure in the molecular structure of composite decreases, which helps to improve the electrical conductivity. While the reaction temperature is high, the formation of increased defects in the composite makes the surface rough. The electrical conductivity is affected.

108.3.2 Effect of Polymerization Time on Electrical Conductivity

When polymerization temperature is at 5 °C, the amount of ASPB is fixed at 15 wt%, and the effect of polymerization time on the electrical conductivity is shown in Fig. 108.2b. Similarly, the electrical conductivity is reflected by the area ratio of asymmetric stretching vibration absorption and symmetric stretching vibration absorption peaks (A_{1452}/A_{1544}) of pyrrole ring. Result shows that when the polymerization time is 2, 4, 6, and 8 h, the ratio of integrated absorption areas of A_{1452}/A_{1544} is 0.17, 0.29, 0.38, and 0.32, respectively. At the same time, the electrical conductivity of each product measured by four-point probe method is 8.3, 12, 20, and 19.5 S/cm. The results are consistent with FTIR analysis. That is to say, few polymers are formed at the beginning of polymerization, resulting in a low electrical conductivity. The interaction chance between PPy and ASPB increases gradually with the extension of polymerization time, leading to long polymer, good regularity, and excellent electrical conductivity. The highest electrical conductivity is appeared when polymerization time is at 6 h. However, too long time may cause the local peroxidation of pyrrole ring accompanied by some side effects, resulting in a decreased electrical conductivity of composite [13].

Fig. 108.3 Effect of the amount of ASPB and molecular weight of grafted chains on the electrical conductivity
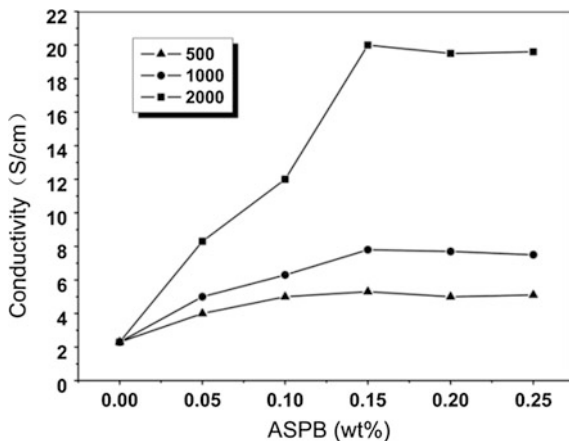
108.3.3 Effects of the Amount of ASPB and Molecular Weight of Grafted Chains on the Electrical Conductivity

As shown in Fig. 108.3, the electrical conductivity of composite increases with the increased amount of ASPB. When the amount of ASPB is at 15 wt%, the electrical conductivity can reach 20 S/cm. This may be because that an increase of doping level can promote the electrostatic interaction and between ASPB and PPy. That is to say that the delocalization of charge increases [14]. This strong interaction may make the electrical conductivity of PPy increase by adding ASPB. However, excess ASPB result in a decreased electrical conductivity. It may be due to the insulating properties of silica in the composite. In addition, when other conditions remain the same, ASPB with different molecular weights of grafted brushes (500, 1000, 2000 g/mol) are selected for doping experiments, and the results are also shown in Fig. 108.3. It can be seen that with the increasing of the molecular weight of grafted polyelectrolyte brushes, the electrical conductivities of PPy/ASPB composites increase. It may be because that the long polyelectrolyte chains help the growth of pyrrole monomers in the ASPB system. The cross-linking degree of conducting polymer chains reduces, leading to more extended polymer chains with extended conjugation length.

108.3.4 Doping Mechanism of ASPB

The doping process is abided by the charge transfer mechanism. As shown in Fig. 108.4, polymerization of pyrrole happens in the PSS chains. R denotes the distance between the two PPy chains. We can see that the amount of positive charge
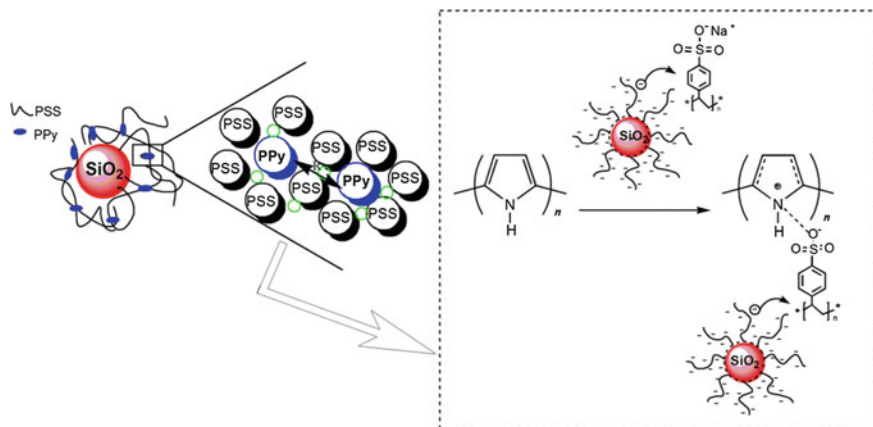
Fig. 108.4 Doping mechanism of ASPB

per unit length in PPy chains is much less than the amount of negative charge per unit length in PSS chains, so part of SO_3^- is balanced by Na^+. As the effects of density gradient are formed by densely grafted PSS chains, polymerization occurs preferentially in high-concentration pyrrole monomers. A polymeric cation is formed by the polymerization of pyrrole monomers. These polymeric cations rise the function of multivalent counterions in brush layers. Therefore, the complexation between PPy and PSS is irreversible. Consequently, the polymerization of pyrrole monomers is fixed in the brush layers, and ASPB serve as a template in the synthesis of PPy/ASPB composite.

108.4 Conclusions

The effects of polymerization variables (the amount of ASPB, molecular weight of grafted chains, polymerization time, and polymerization temperature) on the electrical conductivity of PPy/ASPB composite were discussed in this paper. Results showed that the electrical conductivity of PPy/ASPB composite was 20 S/cm when the polymerization variables of polymerization time, polymerization temperature, the amount of ASPB, and molecular weight of grafted chains are 6 h, 5 °C, 15 wt%, 178 (Mw = 2000 g/mol), respectively. Improvement of electrical conductivity was mainly attributed to the role of dopant and template (ASPB) in the synthesis of PPy/ASPB composite. As a template, ASPB offered favorable space factors for the growth of PPy. Therefore, PSS brushes densely grafted on the surface of SiO_2 cores could reduce the cross-linking of PPy.

References

1. Hara, K., Kurashige, M., Ito, S., Shinpo, A., Suga, S., Sayama, K., et al. (2003). Novel polyene dyes for highly efficient dye-sensitized solar cells. *Chemical Communications*, 252–253.
2. Saurin, M., & Armes, S. P. (1995). Study of the chemical polymerization of pyrrole onto printed circuit boards for electroplating applications. *Journal of Applied Polymer Science, 56* (1), 41–50.
3. Liu, C. F., Wang, Z. Y., Du, Y. B., et al. (2008). Analysis and improvement of conductive performance of ink in RFID antenna. *IEEE, 11*, 264–267.
4. Cho, J., Shin, K. H., & Jang, J. (2010). Micropatterning of conducting polymer tracks on plasma treated flexible substrate using vapor phase polymerization-mediated inkjet printing. *Synthetic Metals, 160*, 1119–1125.
5. Hubbe, M. A., Heitmann, J. A., Cole, C. A. (2008). Water release from fractionated stock suspensions part 2: Effects of consistency, flocculants, shear, and order of mixing. *Tappi Journal, 7,* 14–19.
6. Shirakawa, H., Louis, E. L., & MacDiarmid, A. G. (1977). Synthesis of electrically conducting organic polymers: Halogen derivatives of polyacetylene. *Chemical Communications, 16*, 578.
7. Hatchett, D. W., & Josowicz, M. (2008). Composites of intrinsically conducting polymers as sensing nanomaterials. *Chemical Reviews, 108*, 746–769.
8. Hariharan, R., Biver, C., Mays, J., & Russel, W. B. (1998). Ionic strength and curvature effects in flat and highly curved polyelectrolyte brushes. *Macromolecules, 31*, 7506–7513.
9. Caimsti, D. B., & Armes, S. P. (1999). Synthesis and characterization of submicrometer-sized polypyrrole-polystyrene composite particles. *Langmuir, 15*, 8052–8058.
10. Su, N., Li, H. B., Yuan, S. J., Yi, S. P., & Yin, E. Q. (2012). Synthesis and characterization of polypyrrole doped with anionic spherical polyelectrolyte brushes. *Exp Polym Lett, 6*(9), 697–705.
11. Su, N., Gu, P., & Zhao, J. (2015). Preparation and properties of polyaniline-anionic spherical polyelectrolyte brushes (PANI/ASPB) nanocomposite. *Micro & Nano Letters, 10*(3), 175–178.
12. Menon, V. P., Lei, J., & Martin, C. R. (1996). Investigation of molecular and supermolecular structure in template-synthesized polypyrrole tubules and fibrils. *Chemistry of Materials, 8*, 2382–3290.
13. Castillo-Grtega, M. M., Inoue, M. B., & Inoue, M. J. (1989). Chemical synthesis of highly conducting polyrrole by the use of copper perchlorate as an oxidant. *Synthetic Metals, 28*, 65–70.
14. Gosh, M., Barman, A., Meikap, A. K., et al. (1999). Hopping transport in HCl doped conducting polyaniline. *Physics Letters A, 260*, 138–148.

Chapter 109
Preparation and Properties of Infrared Heat-Sensitive Polymer Nanoparticles

Jinjuan Teng, Zhongxiao Li and Jialing Pu

Abstract Polymer nanoparticles containing near-infrared absorbing dye (maximum absorption at about 830 nm) were prepared by a two-staged emulsion copolymerization of styrene (ST), acrylonitrile (AN), and benzoic acid in the presence of sodium dodecyl sulfate. After the two-staged polymerization process, the conversion rate can be increased to 96 % or higher. The emulsion was stable, and little precipitation was observed. The prepared polymer nanoparticle was characterized with TEM, UV-Vis spectroscopy, DSC, and TGA. Thin coatings were prepared with the IR830-containing emulsion and a small amount of other additives. The polymer nanoparticles in the coating would keep the original spherical structure and clear outline could be observed, provided that the coating was dried at a proper temperature, such as at 100 °C or at a lower temperature. However, the infrared dye-containing polymer nanoparticles would be readily fused under image-wise IR laser exposure (exposure dose: 200 mJ/cm2). As a result, the laser-exposed areas of the coating firmly adhered to the substrate and showed enough resistance to water flushing, whereas the non-exposed areas were easy to develop.

Keywords Dye-containing polymer particle · Two-staged emulsion polymerization · Imaging performance

J. Teng (✉) · Z. Li (✉)
Lab of Printing & Packaging Material and Technology,
Beijing Institute of Graphic Communication, Beijing, China
e-mail: 1039564989@qq.com

Z. Li
e-mail: lizhongxiao@bigc.edu.cn

J. Pu
Beijing Institute of Graphic Communication, Beijing, China
e-mail: pujialing@bigc.edu.cn

109.1 Introduction

Latex solutions consist of polymer particles dispersed in an aqueous medium. Water has many advantages over organic solvent, including non-volatile organic compounds, odor, inflammability, and non-toxicity. Polymer latexes are frequently coated onto solid substrates to make functional thin films for applications, such as water-developable information materials [1], which have attracted much attention because they should be environment-friendly, easy to operate, and economic. Gries et al. reported water-developable radiation-sensitive recording materials for producing offset printing plates [2]. Sakaguchi et al. developed a water-developable flexographic printing plate [3]. Agfa has developed a chemistry-free plate system based on thermostable microparticles, and the image formation is a physical process [4]. Recently, we have done some work dealt with an infrared heat-sensitive polymer matrix and studied their imaging performance [5].

In this paper, polymer nanoparticles containing near-infrared absorbing dye (maximum absorption at about 830 nm which is denoted as IR830) were synthesized by means of a two-step method through emulsion polymerization. By the two-step method, the conversion rate can be increased above 96 %. Preliminary works were also done to prepare a thermo-sensitive water-developable emulsion coating and investigate the imaging performance.

109.2 Experimental

109.2.1 Materials and Methods

Styrene, acrylonitrile, benzoic acid, IR-830, sodium dodecyl sulfate, lactic acid (LC), N-vinyl-2-pyrrolidone, diacetone acrylamide, tert-butylhydroperoxide, and 2,2′- azobis-(2,4-dimethylvaleronitrile) (AVBN) were commercial products from Beijing Chemicals Co. Styrene, acrylonitrile, and N-vinyl-2-pyrrolidone were purified by vacuum distillation before use.

FTIR spectra were obtained with a Shimadzu FTIR-8400 infrared spectrophotometer. The average particle size of the latex was measured by transmission electron microscopy (TEM) with a H-7000 apparatus (Hitachi, Japan). Differential scanning calorimetry (DSC) was recorded on a Netzsch DSC200PC analysis apparatus. Thermogravimetric analysis (TGA) was made with a Netzsch TG209C instrument. The thickness of the latex films was measured with a FTS-S3c ultra-surface analysis instrument (Taylor Hobson Ltd., England). Laser exposure was carried out on a TP-46XX thermal plate-setter (the laser wavelength is 830 nm, and its pulse width is 10 ns, Hangzhou CRON Machinery and Electronics Co., Ltd).

109.2.2   Preparation of the Infrared Heat-Sensitive Polymer Nanoparticles

IR-830 (0.9 g) and AVBN (0.23 g) were dissolved in a mixture of styrene (15 g), acrylonitrile (7.5 g), and benzoic acid (0.28 g) under magnetic stirring for 2 h. The mixture was subsequently dispersed in dilute SDS aqueous solution (0.78 g SDS/85 g water) through a high-pressure homogenizer for about 2 min to obtain a pre-emulsion. Then, lactic acid (0.34 g) was added and dissolved in the pre-emulsion at ambient temperature under constant stirring. Subsequently, the pre-emulsion was placed in a 500-ml four-necked flask equipped with a mechanical stirrer and a reflux condenser, which was stirred for about 1 h. Then, tert-butylhydroperoxide aqueous solution (0.27 g TBHP/15 g water) was added drop-wise (at a speed of 1.8 ml/min) to initiate the emulsion polymerization. At the first-stage polymerization initiated by a redox system, IR-830 and AVBN were encapsulated in the polymer particle and near 90 % conversion rate of the monomers was obtained. The emulsion temperature was heated to 70 °C for another 5 h to allow further polymerization of the residual monomers which was in situ initiated by AVBN encapsulated in the polymer particles. By the so-called second-stage high-temperature polymerization, the conversion rate can be increased to 96 % or higher. The emulsion was stable, and little precipitation was observed. The latex was allowed to cool to room temperature with constant stirring. Finally, the emulsion was filtered with a sintered filter funnel, and the filtrate was collected and kept for later use.

109.2.3   Preparation of the Thin Coating Derived from the IR830-containing Emulsion and Evaluation of Infrared Laser-Induced Imaging Performance

20 g aqueous solution of the water-soluble polymer (10 wt%, synthesized by N-vinyl-2-pyrrolidone and diacetone acrylamide in our laboratory), 17.62 g of dye dispersion aqueous solution (2.27 wt%), 13.88 g of water, and 0.01 g of additives (FC-4430) were successively added to the prepared polymer emulsion (40 g, 20 wt %) under magnetic stirring. The mixture was filtered with a sintered filter funnel, the filtrate was spin-coated on a clean anodized aluminum plate (aluminum plate for offset printing with a specially prepared surface), and this was followed by drying at 90 °C for 5 min. Then, the sample CTP plate was mounted on the exposure device for laser scanning. Finally, the exposed plate was developed with water at 25 °C, and the surface topography was recorded with optical microscope and TEM.

109.3 Results and Discussion

109.3.1 Properties of Styrene–Acrylonitrile Copolymer Emulsion

The polymer emulsion was prepared through co-polymerization of styrene and acrylonitrile in the presence of SDS which acts as the surfactant. IR-830, AVBN, and benzoic acid were dissolved in the mixture of the monomers and encapsulated in the polymer particles with the progress of the emulsion polymerization. AVBN is a radical initiator, which initiates further conversation of the unreacted monomers at the second-stage polymerization under higher temperature (70 °C). Benzoic acid was employed to improve the solubility of the IR dye and facilitate the stability of the emulsion. The emulsion was characterized by TEM (Fig. 109.1) and UV-Vis spectroscopy (Fig. 109.2). The average diameter of the polymer particles was around 30 nm, and the emulsion has a maximum absorption peak at approximately 830 nm.

Fig. 109.1 TEM of the polymer particles
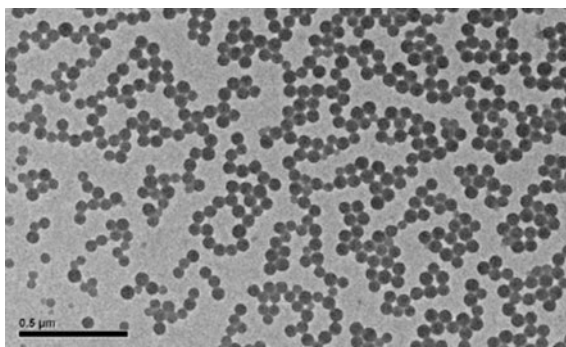
Fig. 109.2 UV-Vis spectroscopy of the emulsion
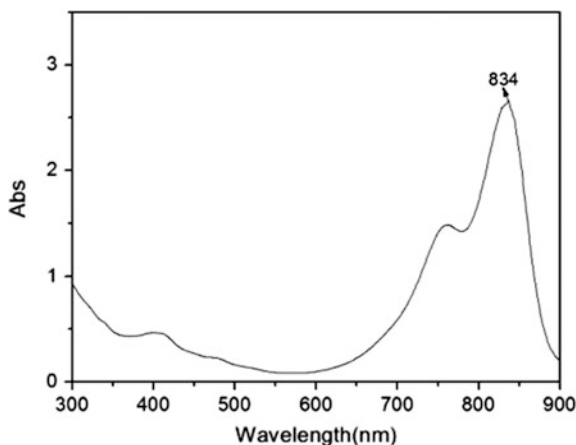
Fig. 109.3 DSC analysis of the polymer particles
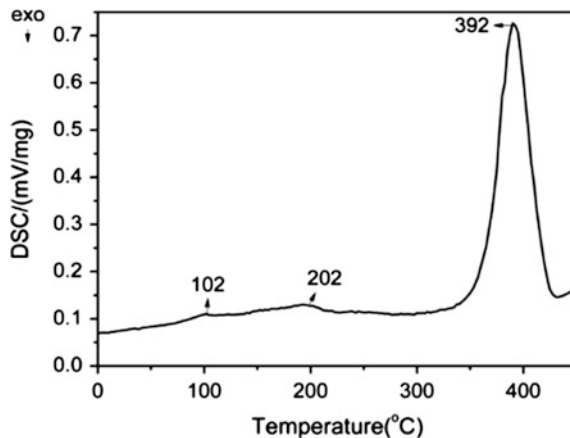
Thermal properties of the latex particle were measured by DSC and TG. The DSC curve (Fig. 109.3) shows a small endothermal peak around 102 °C, which is the glass transition temperature of poly(styrene-co-acrylonitrile). Therefore, the particles should withstand heat condition (90 °C) in the drying process of the preparation of the thin emulsion coating. In other words, the shape and structure of the polymer nanoparticles will remain unchanged during the coating preparation. This is verified by the fact that the dried emulsion coating could be easily washed off by water from the substrate. According to the DSC and TG curves (Fig. 109.4), the top endothermic peak at about 390 °C is due to the fast decomposition of the polymer and the small peak at 202 °C is assigned to the decomposition and of the small molecules including benzoic acid and the initiator components.

Fig. 109.4 TG analysis of the polymer particles
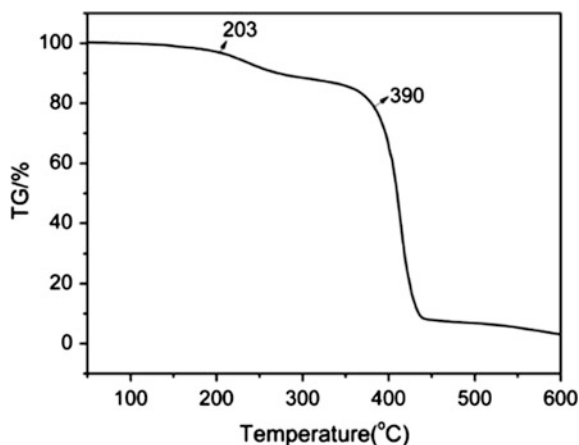
109.3.2 Laser Imaging of the Coating Derived from the Polymer Nanoparticles

In this study, we investigated the possibility of a water-developable laser imaging material based on polymer emulsion, which can be used to develop environmentally friendly CTP plate. As mentioned, the laser imaging coating consists of the following main components: the polymer emulsion, dye dispersion aqueous solution, and water-soluble resin polymer (10 wt%, synthesized by N-vinyl-2-pyrrolidone and diacetone acrylamide) acting as the binder resin.

Once the sample CTP plate was exposed to IR laser beam, the temperature of the exposed area increased sharply (typically above 300 °C). By the action of heat, the latex particles would melt and their original geometry would be broken to combine into a unified whole (Fig. 109.5). Considering that the hydrophobic core comprised the majority (about 90 %) of the latex particles and IR-830 (4 % weight parts of monomer) in the particles largely improved the sensitivity of the coating, the exposed area could not be removed from the substrate any longer. However, the unexposed area of the latex film could be easily washed away by water because the core–shell particles remain intact and still possessed a hydrophilic shell and the water-soluble resin also played an important role. This argument was supported by the fact that the contact angle of the latex film with water would undergo great change after heat treatment at elevated temperature. The core–shell latex film was hydrophilic before heat treatment, and the contact angle with water was around 15° (Fig. 109.7). However, once the coating was heated at a higher temperature (above 300 °C) for short period of time, the contact angle with water of the coating became larger than 60° (Fig. 109.8). So the contrast between the exposed area and the unexposed area of the latex coating made it possible to obtain a negative image after water development (Fig. 109.6).

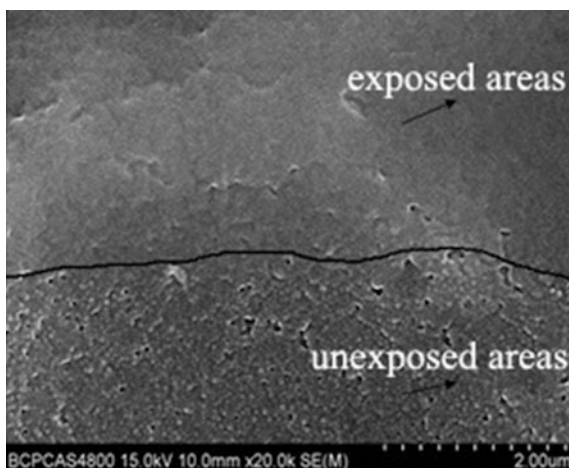**Fig. 109.5** SEM of exposed area and unexposed area

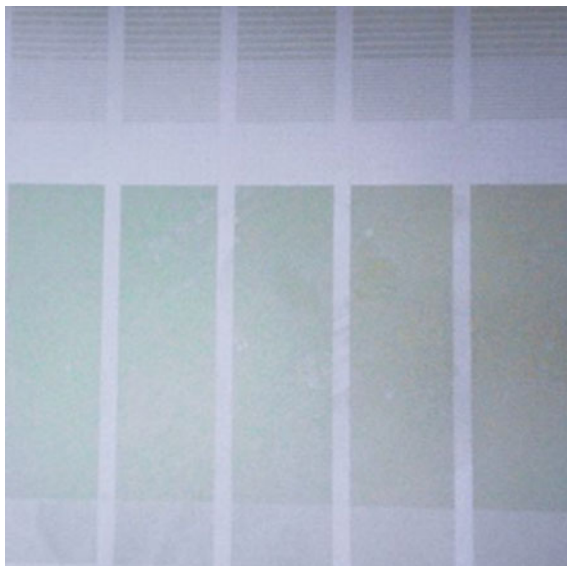**Fig. 109.6** Micrograph of the IR laser-exposed coating after water cleaning (25 °C)

Fig. 109.7 Contact angle image of the unexposed area of the coating
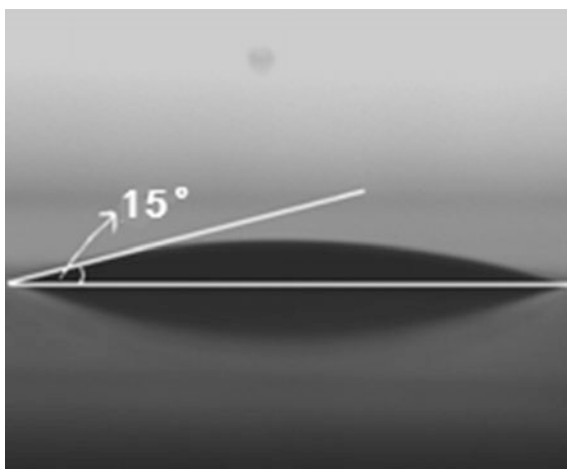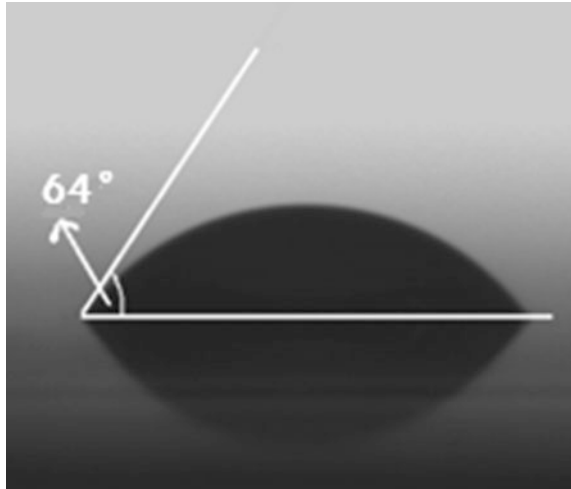
Fig. 109.8 Contact angle
image of the exposed area of
the coating

109.4   Conclusions

A stable and uniform particle size contained IR-830 polymer emulsion was pre-
pared through a simple two-step method polymerization in the presence of SDS.
A negative working and water-developable laser thermal-imaging material was
built through the combination of the prepared heat-sensitive polymer nanoparticles,
a binder polymer, and an IR-830 absorbing dye. This kind of material could give
clean images, indicating that it might be used in process-free thermal CTP plate.

References

1. Khosravi, A., King, J. A., Jamieson, H. L., & Lind, M. L. (2014). Latex barrier thin film
   formation on porous substrates. *Langmuir*, *30*(46), 13994–14003. doi:10.1021/la502812d
2. Mora-Huertas, C. E., Fessi, H., & Elaissari, A. (2010). Polymer-based nanocapsules for drug
   delivery. *International Journal of Pharmaceutics, 385*(1–2), 113–142. doi:10.1016/j.ijpharm.
   2009.10.018.
3. Sakaguchi, Y., Kawahara, K., Yamada, T., Okazaki, Y., & Imah-ashi, S. (2004). Diffusion of
   unreacted monomers detected by ATR FTIR spectroscopy in a photosensitive printing plate
   after the photoreaction. *Journal of Applied Polymer Science, 92*(5), 2903–2907.
4. Shi, W. (2007). Environment friendly chemistry-free CTP plates. *Print Field, 8*, 20–24.
5. Li, Z., Feng, Y., Li, L., Pu, J., & Yang, H. (2008). Preparation and properties of a
   thermo-sensitive latex film. *European polymer, 44*, 1899–1906. doi:10.1016/j.eurpolymj.2007.
   12.008.

Chapter 110
Study on Performance of Yellow Water-Based Ink for Flexographic Printing

Yang Liu, Peiqing Huang, Xianfu Wei and Weidong Liu

Abstract Flexo water-based ink was currently approved as green ink by the US Food and Drug Association. However, the quality of domestic water-based flexographic ink on a non-absorbent material such as PP plastic film had obvious deficiencies. The influence of dispersion was discussed by changing the kinds of pigments, grinding resin, and pigment/resin ratio to determine the optimal dispersion of based ink. The influence of color density, gloss, surface tension, and leveling property of ink was discussed by changing the kinds of film-forming resin to adjust formula better on the based ink formula. Finally, the experiment design formula was used to optimize the experiment and then best performance of ink could be obtained. The results showed that best printing performance of yellow ink could be obtained by choosing benzidine yellow as the pigment, grinding resin 96 as the ultimate grinding resin, electing ratio of pigment to resin as 2 to 1 and choosing S2916 as the film-forming resin.

Y. Liu (✉) · P. Huang · X. Wei · W. Liu
Beijing Institute of Graphic Communication, Beijing, China
e-mail: 13011849882@163.com

P. Huang
e-mail: huangpeiqing@bigc.edu.cn

X. Wei
e-mail: weixianfu@bigc.edu.cn

W. Liu
e-mail: 281060119@qq.com

110.1   Introduction

Water-based ink emerges as a new type of ink when people pay more attention to low-carbon and environment-friendly. The most important feature of the ink is that water is used as the only solvent and hence the kind of ink is safe and has no pollution for the environment. Water-based ink is mainly used in flexographic and gravure printing and especially in water-based flexographic ink has got rapid development in recent years. In some developed countries, 90 % flexographic printing ink is water-based ink. In China, water-based ink is gradually replacing the traditional solvent-based inks, and water-based flexographic ink is a kind of promising environment-friendly printing ink which is gradually accepted by people [1–3].

Although water-based flexographic ink has obvious advantages, domestic water-based flexographic ink still has some problems printed on nonabsorbent materials such as PP plastic film and nowadays the material used in packaging industry is generally plastic. So it is particularly important to improve the quality of water-based flexographic ink printing on non-absorbent material and develop on water-based flexographic ink that is suitable for non-absorbent materials has very important significance for the industrialization applications.

110.2   Experiments

110.2.1   Materials

Permanent yellow Y1, Hansa yellow Y2, benzidine yellow Y3 (Shan dong yu hong Co., Ltd.); grinding resin: HPD96 (Germany BASF), AZR acrylic resin (Tian jin company); Film-forming resin: Joncryl ® 74-A, Joncryl ® 617-A, Joncryl ® S2916, Joncryl ® 624, Joncryl ® 90(BASF); Dispersant: 750, 760 (Degussa Corporation); defoamers: 810 (Deutsche Degussa); deionized water.

110.2.2   Equipments

JG-2S high-speed stirring disperser (Shanghai Division Music Instrument Co., Ltd.), D2004 W electric mixer (Shanghai Division Music Instrument Co., Ltd.), Microtrac S3500 series laser particle size analyzer (Microtrac US company), KRUSS surface tension meter K100 (Germany company), X-528 spectroscopic densitometer (X-Rite), IGT-F1-type printability tester (the Netherlands), and AR2000 rheometer (TA US company).

110.2.3   Preparation Method of Water-Based Ink

Pigment, grind resin, dispersant, defoamer, and deionized water are added to the beaker with stirring with a glass rod, and then dispersed for 30 min in a pre-D2004W electric mixer. Finally, the mixture is speed-ground for 2 h with zirconia beads in a JG-2S digital high-speed mixer.

The base ink, and the film-forming resin are added in HJ-6 A-type digital thermostat long magnetic stirrer for 30 min, and water-based flexographic ink is obtained.

110.3   Test Methods

110.3.1   Proofing Method

Use flexographic proofing device. Wherein, the printing pressure is 85 N, printing speed is 0.5 m/s, and the anilox line screen number is 200 dpi.

110.3.2   Dispersion Performance Test

Test the ink's dispersion by the laser particle size analyzer to obtain aluminum pigment particle size distribution, and the particle size at 95 % works as the final particle size of ink.

110.3.3   Color Density Test

Taking into account the characteristics of the plastic substrate, the test was performed by using a reflection densitometer. Specific test method: Put a piece of coated paper below the spline, the first part of the plastic film is measuring no ink color density values for calibration, then measuring the colored portion of the ink density, this measurement value is the color density of the ink.

110.3.4   Surface Tension Test

At room temperature 25 °C conditions, surface tension measurement was performed by using KRUSS Process Tensimeter K100 Tensiometer.

110.3.5 The Apparent Performance Test

Apparent property is measured by the method of eye-measurement. The apparent properties of the ink are directly related to leveling. If the leveling of the ink on a non-absorbent material is higher, then the apparent property is better. The apparent performance is good. The apparent performance is divided into five levels as follows (Table 110.1).

110.4 Dispersion of Water-Based Flexographic Ink
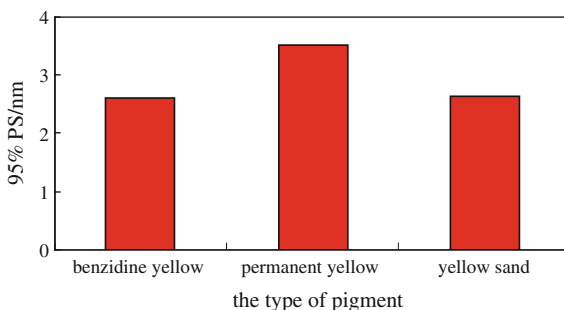
110.4.1 Impact on the Dispersion of Different Pigment

Considering this experiment, aqueous binder resin is an acrylic resin, and depending on the performance of different pigments, the selected yellow pigments have a good printability and are a representative of the three pigments [1]: benzidine yellow, permanent yellow, and yellow sand. The particle size distribution is shown below in Figs. 110.1 and 110.2.

As shown in Figs. 110.1 and 110.2, the effect of the different pigments is different. Benzidine yellow of three yellow pigments has the smallest particle size and the best dispersion. Due to the interaction with the resin, the affinity of the benzidine yellow surface modifier with the resin is preferably easier to wetting; hence, the ink with benzidine yellow has a better dispersion [4].

Table 110.1 Apparent property grading standards

Performance	Chaotic	Irregular	General	Smooth	Flow completely
Level	1	2	3	4	5

Fig. 110.1 Effect of different pigment on the dispersion property
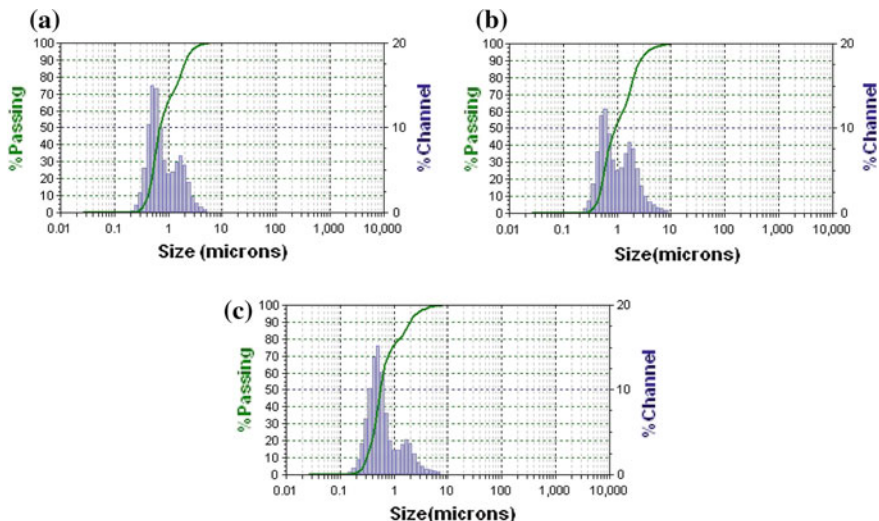
(a)

(b)

(c)

Fig. 110.2 Particle size distribution of different pigments. **a** Benzidine yellow. **b** Permanent yellow. **c** Yellow sand

110.4.2   Impact on the Dispersion of Different Grinding Resin

Due to different grinding resins, the covering effect of the pigment particle and the state of aggregation are different. Different grinding resins are used to compound ink formulation. The particle size distribution is shown below in Figs. 110.3 and 110.4.

As shown in Figs. 110.3 and 110.4, after the interaction with the pigment, grinding resin 96 has smaller particle size and better dispersion. Different grinding resins have different chemical structures, so the affinity with pigment surface modifier is different. Grinding resin 96 has ammonia-soluble, strong affinity with the pigment surface modifier and is easier to pigment wetting, so its dispersing is better [4].
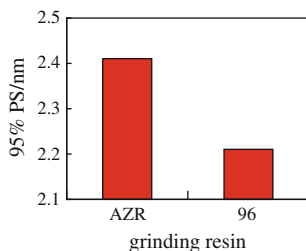
Fig. 110.3 Effect of different grinding resin on the dispersion property

Fig. 110.4 Particle size distribution of different grinding resin. **a** AZR. **b** 96
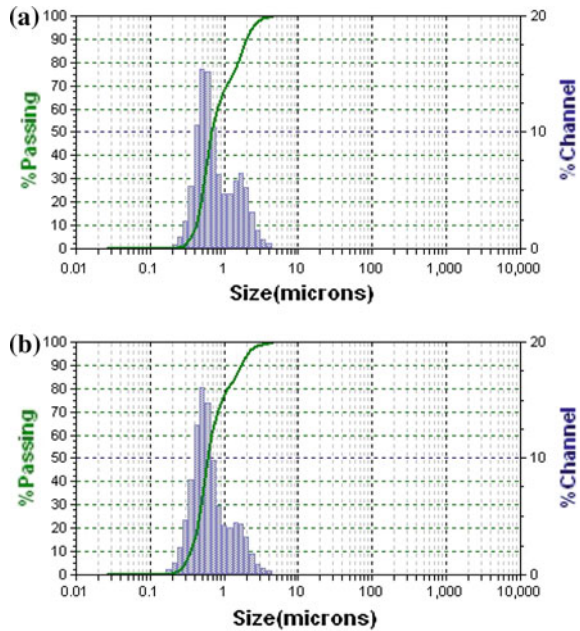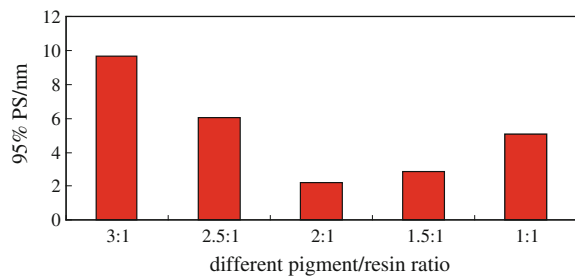

110.4.3 Impact on the Dispersion of Different Pigment/Resin Ratio

Pigment/binder ratio has also an important impact on the dispersion of water-based flexographic ink. The different pigment/binder ratio leads to the different effect of dispersion. Benzidine yellow was chosen as pigment; 96 was chosen as grinding resin. Under different conditions of pigment/resin ratio of the ink dispersion test, particle size distribution is shown below in Figs. 110.5 and 110.6.

As shown in Figs. 110.5 and 110.6, the different pigment/resin ratio leads to the different effect of dispersion. When the pigment/resin ratio is 2:1, the ink has the smallest particle size and narrow particle size distribution, and its dispersion is best. Because the dispersion process is actually the flow process, only reaching the

Fig. 110.5 Effect of different pigment/resin ratio on the dispersion property
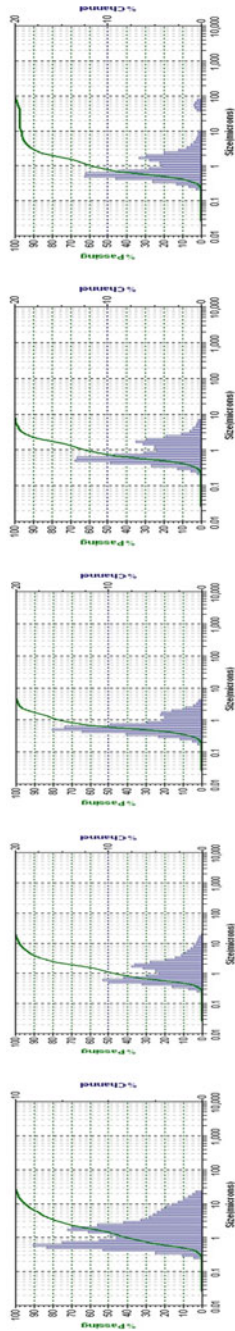
Fig. 110.6 Particle size distribution of different pigment/resin ratio

optimum flow point achieves grinding the best result and has the best dispersed state. Therefore, before obtaining the best state of ink dispersion, the optimal pigment to resin ratio should be decided.

### 110.4.4 The Impact on the Dispersion of Different Dispersant

The ink with no dispersant and the ink with different kinds of dispersant were prepared. Compared with the dispersibility of these inks, the content is the same when adding dispersant. The particle size of the ink is shown in Fig. 110.7.

As shown in Fig. 110.7, the dispersion of ink with a dispersant is significantly better than that without a dispersant. Mainly, because the dispersant is a surfactant the function of which is to reduce the surface tension of the material in the form of positive or negative ions is adsorbed on the pigment surface, a corresponding charge is diffused into the binders medium, due to which charge repulsion occurs; thus, according to the principle of charge repulsion, the ink with the dispersant has a better dispersion and stability [2]. The effects of the two dispersants are not very clear; dispersant 750 dispersed good relatively. Since different chemical composition of two dispersants, dispersant 750 shows stronger affinity with yellow pigment, and the effect of reducing the surface tension of the pigment is more obvious with better wetting and better dispersion [4].

110.5 Research on Printing Quality and Performance of Ink

Properties such as color ink density, gloss, leveling, and surface tension had a direct impact on the quality of the ink. The better the printability of ink is, the fine the print quality of ink is. Film-forming resin is the main factor of the ink. Based on the best formulation, the different film-forming resins and formulation experiments are taken, and then the water-based flexographic ink printing performance on nonabsorbent materials -PP films such as color density, gloss, leveling properties are

Fig. 110.7 Effect of different dispersant on the dispersion property
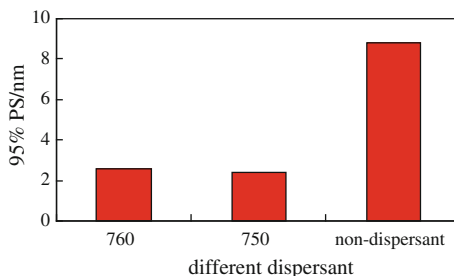
tested. Viscosity of different inks must be controlled to optimum values to ensure that the ink could be transferred better.

110.5.1 Quality and Properties of the Film-Forming Resin for Printing Ink

Different film-forming resins have a different molecular structure; cohesion of different ink molecules will be produced in the ink system, which affects the color density, gloss, and adhesion properties of the ink. Performance test results in the following Table 110.2 and Figs. 110.7, 110.8, and 110.9.

As shown in Fig. 110.8, color density values of different film-forming resins are in the range of 1.2–1.3; especially, color density values of S2916 and 90 after interacted with based ink are relatively higher, i.e., the ink transfer property of S2916 and 90 is better. Because the prints of ink with S2916 or 90 are steady, thick, and uniform, after ink are transferred onto a PP film.therefore,ink with S2916 or 90 has a higher value of color density and better transferability.

As shown in Fig. 110.9, gloss value of the film-forming resins S2916, 74-A, and 90 is significantly higher than other types of film-forming resin. Because the con-junctival performance of 617-A and 624 is inferior to S2916, 74-A, and 90, it affects the gloss.

Table 110.2 Research on printing quality and performance of ink

Film-forming resin	S2916	617-A	74-A	90	624
Color density	1.32	1.24	1.27	1.32	1.26
Gloss	24	19.8	23.7	24.3	18.9
Surface tension	37.19	36.72	36.25	37.25	34.09
Leveling	4	4	5	4	3

Fig. 110.8 Effect of different film-forming resin on the color density
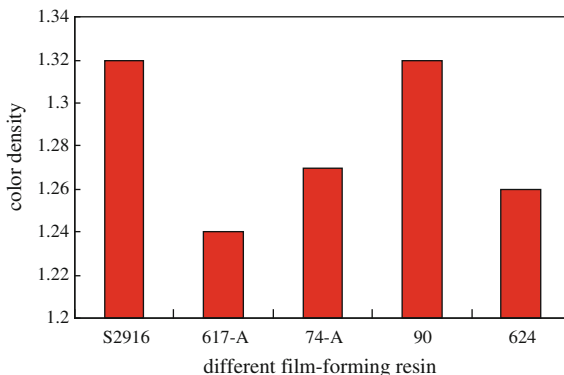
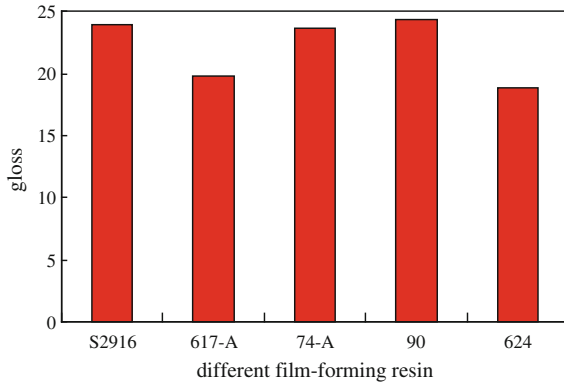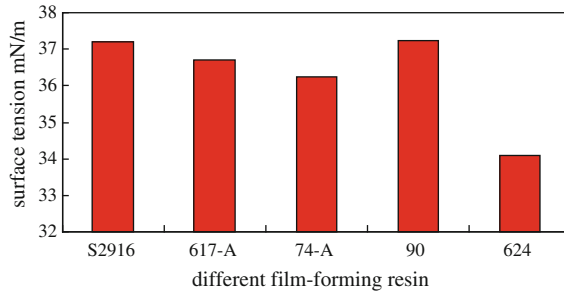Fig. 110.9 Effect of different film-forming resin on the gloss

Fig. 110.10 Effect of different film-forming resin on the surface tension

As shown in Fig. 110.10, in addition to lower the surface tension of the film-forming resin of the value of 624, the surface tension of the other types of film-forming resins are high, and it is not conducive to transfer ink onto the PP plastic film.

As shown in Table 110.3, after 74-A interacted with based ink, its leveling property is better than others. Because the components of the ink have a great effect for leveling property, a reasonable choice of film-forming resin is a key for the ink to have a good-leveling property.

110.5.2 Film-Forming Resin Formulation Experiments

Different types of film-forming resins have different effects on the performance of ink. According to the effect of the single film-forming resin on the performance of ink, the effects of composite resins on ink performance are studied. Three single film-forming resins such as S2916, 74-A, and 624 are selected as materials for composite resins and a simple center of gravity method is used. The test results are shown in Table 110.3.

Table 110.3 Formulation test results

NO	S2916	74-A	624	Color	Gloss	Surface	Leveling
1	1	0	0	1.32	24	37.19	4
2	0	1	0	1.27	23.7	36.25	5
3	0	0	1	1.26	18.9	34.09	3
4	1/2	1/2	0	1.25	15.6	37.44	3
5	1/2	0	1/2	1.30	14.7	37.38	3
6	0	1/2	1/2	1.29	15.2	37.12	3
7	1/3	1/3	1/3	1.27	13.9	37.14	3

Fig. 110.11 Sample of optimal formulation

Set the weight of color density, gloss, surface tension, and leveling as 0.3, 0.2, 0.3, and 0.2, respectively. The regression equation for the ink experiment can be calculated by the simplex centroid design principles:

$$y = 0.617x_1 + 0.475x_2 + 0.302x_3 - 1.116x_1x_2 - 0.67x_1x_3 - 0.934x_2x_3 \\ - 1.848x_1x_2x_3$$

Solver can be drawn, when $x_1:x_2:x_3 = 1:0:0$; the regression equation gets the maximum extreme value 0.617. It can be drawn only using film-forming resin S2916; the best print quality can be obtained.

As shown in Fig. 110.11, the final printing proofs with optimum ink formulations is shown above; from the value of the color density, gloss, and surface tension, the good print quality has been obtained.

110.6 Conclusions

Through the study of the properties of yellow water-based flexographic ink through formulation design optimization experiments, the final conclusions are as follows:

- Among benzidine yellow pigment, permanent yellow pigment and yellow sand pigment. The based ink with benzidine yellow dispersed best.

- In the choice of two grinding resin which are HPD96 and AZR, HPD96 has a better match with pigments, the dispersion of based ink with HPD96 is better, and ink with pigment/resin ratio 2:1 has a best dispersion.
- In the selection of two dispersants which are 750 and 760, the dispersion of based ink after adding 750 is better.
- S2916 is selected as film-forming resin; the best value of the color density, gloss, and the surface tension of the ink can be obtained.

References

1. Huang, W. (2013). *Study on the water-based ink for flexographic printing and synthesis of acrylic resin* (p. 42). Guangzhou: South China University of Technology.
2. Xin, X. (2011). Research progress of water-based ink. *China Printing And Packaging Study*, *03* (3), 1–3
3. Zhou, Z., Yang, L. (2006). The development direction of the printing ink. *Printing Quality &Standardization*, 16–18
4. Sun, B. (2014). *Development of low scratch resistance, high wear resistance of water-based flexo ink color* (pp. 23–28). Qufu: Qufu Normal University.

Chapter 111
Stearic Acid-Modified γ-Al$_2$O$_3$ Particles for Dispersion Properties

Zhengbo Li, Meijuan Cao, Limei Chen and Luhai Li

Abstract It is difficult for γ-Al$_2$O$_3$ particles to disperse due to a mismatch in the density of dispersion medium, which leads to agglomeration and sedimentation of the γ-Al$_2$O$_3$ particles. In the study, we use the orthogonal experiments of three factors and three levels to analyze the influence of related factors on modification effect and seek the most suitable modification conditions. In the experiment, the stearic acid (SA) was used to modify the surface of the γ-Al$_2$O$_3$ particles. γ-Al$_2$O$_3$ particles before and after surface modification were characterized by Fourier transform infrared spectroscopy (FTIR), scanning electron microscopy (SEM) and thermal gravity analysis (TG) and dynamic light scattering (DLS). The FTIR spectra showed that SA had been successfully grafted onto the surface of the γ-Al$_2$O$_3$ particles. Thermal gravity analysis showed that the coated amount of SA is 4.41 %. SEM shows that the agglomeration of Al$_2$O$_3$ particles after modification was reduced. DLS shows Al$_2$O$_2$ particles after modification have smaller particle size and more narrow distribution and better dispersion property. Determination of Oil-Wet Coefficient show Al$_2$O$_3$ particles after modification hydrophilic strengthen. Therefore, the SA-modified Al$_2$O$_3$ particles demonstrated better dispersion properties. Sedimentation test showed that the modified γ-Al$_2$O$_3$ particles had better suspension stability than the non-modified γ-Al$_2$O$_3$ particles.

Keywords Modification · Dispersion · Lipophilic property

Z. Li · M. Cao (✉) · L. Chen · L. Li (✉)
Beijing Engineering Research Center of Printed Electronics, Beijing Institute of Graphic Communication, Beijing, China
e-mail: caomeijuan@bigc.edu.cn

L. Li
e-mail: liluhai@bigc.edu.cn

111.1 Introduction

Nano γ-A1$_2$O$_3$ has high strength, rigidity, and heat and corrosion resistances [1–3] as well as other excellent physical and chemical performances that ordinary alumina own. In addition, γ-A1$_2$O$_3$ also has a series of bizarre features, given by the nanoparticles such as surface effect, small size effect, quantum tunnel effect etc. These features make it to have the general characteristics that the alumina materials do not have in the fields of catalysis, magnetic, optical, and electric. It was used as adsorbent, catalyst, and catalyst carrier in many chemical reactions, such as oil hydrogenation cracking and hydrogenation desulfurization and dehydrogenation catalyst carrier, and other fields also have a wider range of applications. The acidification of γ-Al$_2$O$_3$ with titania resulted in enhanced dispersion of copper [4]. Alumina was modified with 10 wt% MOx (MOx) TiO$_2$, ZrO$_2$, La$_2$O$_3$, or MgO prior to its impregnation with 12 wt% vanadia [5]. Alumina is an appropriate support for metallic as well as organometallic and oxide catalyst [6]. The removal or modification of surface hydroxyl groups can result in an increase in the hydrophobic nature of the catalyst, especially its capability to resist adsorption of water vapor [7, 8].

The γ-Al$_2$O$_3$ particle surface showed good hydrophilicity only in the polar system, but the hydrophilicity was poor in the nonpolar system. The γ-Al$_2$O$_3$ nanoparticles were difficult to spread out in the nonpolar system, and the function of nanoparticles was also limited. Therefore, the surface modification is necessary for γ-Al$_2$O$_3$ nanoparticles.

111.2 Experimental

111.2.1 Al$_2$O$_3$ Particles Modified by Stearic Acid

γ-Al$_2$O$_3$ particles (1.0 g) were placed in a three-necked flask that contained ethanol (40 ml) and stirred for 30 min at 50 °C. Then, 0.1 g SA was added. The reaction was allowed to proceed at 50 °C for 120 min. The particles were washed two times with ethanol. They were then separated by centrifugation and dried at 80 °C for 24 h to afford SA-modified Al$_2$O$_3$ particles.

111.2.2 Research on the Best Modification Conditions of γ-Al$_2$O$_3$

We use orthogonal test to determine the best modification conditions of γ-Al$_2$O$_3$ and take polydispersity index (PDI) to evaluate the modification effect.

Polydispersity index is a measurement of the diameter distribution width of the particle. If the value of PDI is less than 0.5, it suggests that dispersion is good.

111.2.3   Characterization of Al$_2$O$_3$ Particles

The morphology and shape of Al$_2$O$_3$ particles were observed using a scanning electron microscope (SEM; Hitachi SU8000 type, Japan). Chemical component of Al$_2$O$_3$ particles before and after SA modification was identified via infrared spectroscopy (NEXUS670 type, Thermo Nicolet Corp, USA). The amount of SA coupling is analyzed by the thermogravimetric curve of thermogravimetric analyzer (TG). FTIR spectra of Al$_2$O$_3$ and AS-Al$_2$O$_3$ were recorded on a Nicolet 6700 FTIR spectrometer (Thermo Scientific Instrument). The polydispersity index and size of Al$_2$O$_3$ particles were obtained by dynamic light scattering (DLS, Malvern Zetasizer Nano ZS).

111.2.4   Characterization of Al$_2$O$_3$ Particle Size

We prepared 0.08 g Al$_2$O$_3$ and 0.08 g SA-Al$_2$O$_3$ in a 10 ml sample bottle and then 10 ml of ethylene glycol was added. The solution is treated with ultrasound for 25 min, and a good dispersion is made. Now, the sample is prepared for size test.

111.3   Results and Discussion

111.3.1   Orthogonal Test

The main factors that influence modification effects are SA amount, modification time, and modification temperature. Therefore, we use the orthogonal experiments of three factors and three levels to analyze the influence of related factors on modification effect. Take PDI as target parameter and investigate the influence of each factor by range analysis of orthogonal test result as shown in Tables 111.1 and 111.2. It is shown in Table 111.2 that the best scheme was $A_2B_3C_1$, that is to say under the conditions that the SA amount 1.5 %, the modification time 120 min, and the modification temperature 40 °C, the PDI was the smallest and the dispersion was best.

Table 111.1 Levels of experimental factor (γ-Al_2O_3)

Quadrature level pilot factor	A stearic acid amount (%)	B modification time (min)	C modification temperature (°C)
1	1	40	40
2	1.5	80	60
3	2	120	80

Table 111.2 Orthogonal test result of extreme different analysis (γ-Al_2O_3)

Project	PDI		
	A	B	C
K1	1.357	1.265	1.133
K2	1.016	1.264	1.217
K3	1.242	1.086	1.265
k1	0.452	0.422	0.378
k2	0.338	0.421	0.406
k3	0.414	0.362	0.422
Range (R)	0.114	0.06	0.044
Primary and secondary factors	ABC		
The best scheme	$A_2B_3C_1$		

111.3.2 FTIR Analysis

Figure 111.1a shows the infrared spectra of Al_2O_3 particles before and after modification. The absorption peak at 801 cm^{-1} of Al_2O_3 before modification is attributed to Al–O skeleton stretching. The absorption peak at 1635 cm^{-1} is due to the vibration of absorbed water in Al_2O_3 particles. The absorption peak at 3469 cm^{-1} is attributed to the vibration of hydroxyl on the surface of Al_2O_3. In the infrared spectrum of SA-modified Al_2O_3, the absorption peak at 801 cm^{-1} is also attributed to Al-O skeleton stretching. The absorption peak at 2850 cm^{-1} and 2851 cm^{-1} is attributed to the vibration of CH_3 and CH_2 in SA molecule. And the peaks at 1407 cm^{-1} are attributed to –CH_2 and –CH_3 deformed vibration peak in SA molecule. The peaks at 1469 cm^{-1} are attributed to –COOH in SA molecule. Thus, the SA modifier has successfully grafted onto the surface of the γ-Al_2O_3 particles. Notably, the non-modified γ-Al_2O_3 particles have a significant peak at 3469 cm^{-1}, which is due to the vibration of hydroxyl on the surface of Al_2O_3 particles. This absorption peak is significantly weakened in the infrared spectrum of SA-modified Al_2O_3 particles, because the grafting reaction of SA with Al_2O_3 particles is an etherification reaction, in which the hydroxyl from SA is removed. The dehydrated etherification reaction is caused by the removal of hydrogen from hydroxyl on the surface of γ-Al_2O_3 particles. The decline in absorption peak at 3469 cm^{-1} also verifies that SA has been grafted onto the surface of γ-Al_2O_3 particles. This result also indicates that the reaction site of this reaction is located at the hydroxyls on the surface of γ-Al_2O_3 particles.

Fig. 111.1 **a** FTIR spectra of Al$_2$O$_3$ before and after SA modification,
b thermogravimetric of Al$_2$O$_3$ before and after SA modification, and **c** the size dispersion of non-modified Al$_2$O$_3$ and SA-modified Al$_2$O$_3$ particles
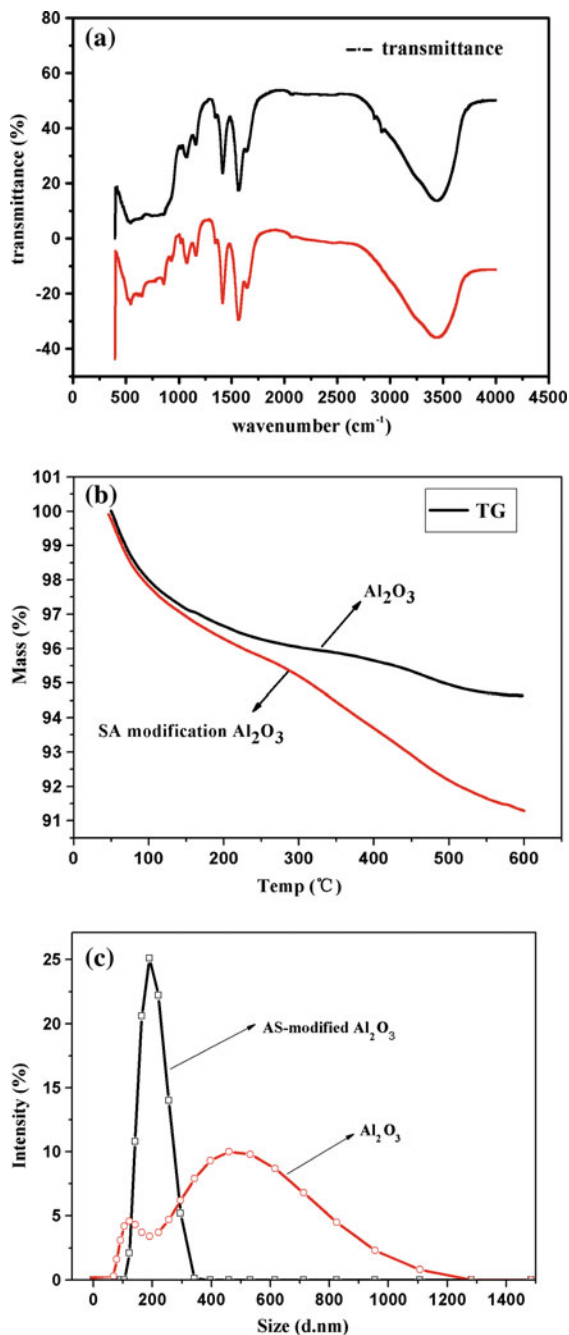
111.3.3 TG Analysis

From Fig. 111.1b, the weightlessness rate of Al_2O_3 is about 5.37 % and the Al_2O_3 modified with SA is 8.71 %. It is attributed to adsorption of water on the surface of the nanoparticles. Above 250 °C, for the Al_2O_3 with SA modification, the trend of curve glides is increasing stage by stage, and it is attributed to the decomposition of stearic acids. It shows that the amount of SA coupling is 4.41 %.

111.3.4 Size Test

Figure 111.1c shows that the majority of the Al_2O_3 was distributed in 270 nm, and the majority of AS-modified Al_2O_3 was distributed at 190 nm. It indicated that the dispersion has improved for SA-modified Al_2O_3 in the organic solvent.

111.3.5 SEM

Figure 111.2 shows the SEM images of the before and after SA-modified Al_2O_3 particles. Figure a and b show the agglomeration for the Al_2O_3 particles after modification was markedly reduced. However, the particle in Fig. 111.2a shows great agglomeration. The size of SA-modified Al_2O_3 particles becomes smaller, which is attributed to the steric hinderance effect. Because SA is chosen as 18 alkyl acid with a long carbon chain and the AS-Al_2O_3 steric hinderance effect is obvious and it is the dominate factor. In addition, the zeta potential has an effect on the dispersion of Al_2O_3, but it is secondary factor.
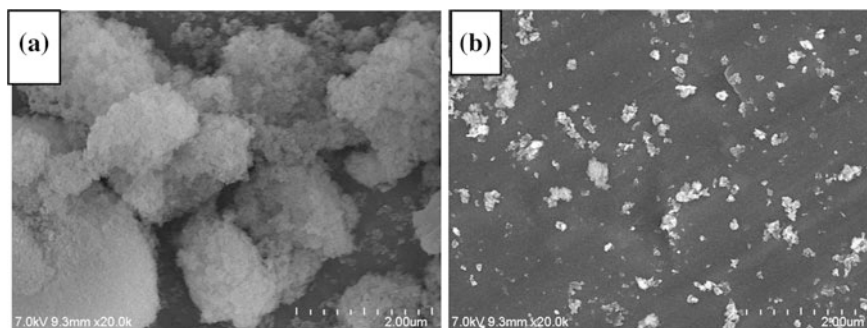
Fig. 111.2 SEM images of Al_2O_3 particles: **a** non-modified Al_2O_3 particles and **b** SA-modified Al_2O_3 particles

111.4   Conclusions

The method to modify the surface of alumina was presented, and the experimental condition for the surface modification of Al$_2$O$_3$ was optimized by orthogonal test. Under the condition of 1.5 %, 40°C, 80 min, SA-Al$_2$O$_3$ with small PDI was obtained. In addition, the infrared absorption band of SA has been observed by infrared spectrometer at the peak of 3000 and 2980 cm^{-1}. It is demonstrated that the SA and Al$_2$O$_3$ have a good coupling. We also obtained the amount of modifying agent by thermogravimetric analysis. TG curve demonstrated that the amount of modification agent coupling is 4.41 %. We tested the lipophilic property and found that the hydrophilicity of SA-Al$_2$O$_3$ gets weaker and the lipophilic property gets stronger compared with Al$_2$O$_3$. The SEM images showed the smaller size of SA-Al$_2$O$_3$ compared with Al$_2$O$_3$, and the size of AS-Al$_2$O$_3$ is observed attributed at 190 nm.

References

1. Zimmermann, K., Schneider, G. A., Bhattacharya, A. K., & Hintze, W. (2007). Surface modification of Al$_2$O$_3$/TiC cutting ceramics. *Journal of the American Ceramic Society, 90*(12), 3773–3778.
2. Adachi, S., Wada, T., Mihara, T., Miyamoto, Y., & Koizumi, M. (1990). High-Pressure Self-Combustion Sintering of Alumina-Titanium Carbide Ceramic Composite. *Journal of the American Ceramic Society, 73*(5), 1451–1452.
3. Kujawa, J., Kujawski, W., Koter, S., Rozicka, A., Cerneaux, S., Persin, M., & Larbot, A. (2013). Efficiency of grafting of Al$_2$O$_3$, TiO$_2$ and ZrO$_2$ powders by perfluoroalkylsilanes. *Colloids and Surfaces A: Physicochemical and Engineering Aspects, 420*, 64–73.
4. Lakshmi, L. J., Alyea, E. C., Srinivas, S. T., & Rao, P. K. (1997). Influence of metal oxide modification of alumina on the dispersion and activity of vanadia catalysts. *Journal of Physical Chemistry B, 101*(17), 3324–3328.
5. Akpati, H., Nordlander, P., Ohman, L. O., & Persson, P., (1996). In Presented at the 11th International Congress on Catalysis, Baltimore, MD, June, Po-137
6. Slavov, S. V., Chuang, K. T., & Sanger, A. R. (1995). Modification of. gamma.-Alumina with Chlorotrimethylsilane. *Journal of Physical Chemistry, 99*(46), 17019–17027.
7. Yates, D. J., Dembinski, G. W., Kroll, W. R., & Elliott, J. J. (1969). Infrared studies of the reactions between silica and trimethylaluminum. *Journal of Physical Chemistry, 73*(4), 911–921.
8. Angst, D. L., & Simmons, G. W. (1991). Moisture absorption characteristics of organosiloxane self-assembled monolayers. *Langmuir, 7*(10), 2236–2242.

Chapter 112
Research on Particle Size Influence Factors of Organic Pigment Microencapsulation

Zhengrong Yan, Qiong Xue, Chunyan Du and Jingjing Du

Abstract Microencapsulation of organic pigments can effectively improve the pigments' wettability and its dispersion. And controlling the particle size and its uniformity can significantly enhance its performance. The benzidine yellow microcapsules were prepared by single coacervation. The microcapsules had the core of benzidine yellow and the wall of the chitosan. The influences of the core/wall ratio, the emulsifier's dosage, pH value, and curing agent's dosage on the particle size of the microcapsules were investigated. The experimental results show that the core/wall ratio, the emulsifier's dosage, and pH change had the great influence on particle size. However, curing agent's dosage had less impact on particle size but more on its encystation effect. Controlling the parameters can effectively regulate the effect of microcapsules' encystment and provide uniform particle size distribution.

Keywords Chitosan · Size control · Coacervation · Organic pigment

112.1 Introduction

Printing ink is a uniform mixture composed of pigment, ink vehicle, fillers, and additives [1]. Along with the continuous renewal of printing process and its development, especially the emergence of high-speed printing, higher requirements on the application properties of the organic pigment such as transparency, tinting strength, and gloss are put forward. Pigment is evenly dispersed in aqueous oily ink medium. In order to make it disperse good and wettability, pigment must be carried on surface modification. The microencapsulation of organic pigment is one of the good ways to improve [2].

Z. Yan · Q. Xue (✉) · C. Du · J. Du
College of Packaging and Materials Engineering, Hunan University of Technology, Zhuzhou, Hunan, China
e-mail: 43653378@qq.com

Microencapsulation is an embedding technology that makes tiny core materials such as solid, liquid, and gas embed inside wall material consisting of natural or synthetic polymer compounds [3, 4]. Microcapsule technology began in the late 1940s and since then has developed for 70 years. Along with the development of science, microencapsulation is becoming more and more mature and has been widely applied in the areas of medicine, food, cosmetics, ink, pesticide, etc. [5–9]. The preparation of organic pigment microencapsulation can improve wettability and dispersion of pigment particles in the ink medium, which can significantly increase their application performance [10, 11].

Microencapsulation of organic pigment had been successfully made by single coacervation with benzidine yellow as core material and natural polymer chitosan as wall material. The influences of the core/wall ratio, the emulsifier's dosage, pH value, flocculant, and curing agent's dosage on the particle size of the microcapsules were mainly studied.

112.2　Materials and Methods

112.2.1　Experimental Reagents

Benzidine yellow from Shandong Yuhong New Pigment Co. was used as the core material. Chitosan (Biochemical Reagent) from Sinopharm Chemical Reagent Co. and acetic acid (Analytical Reagent) from Hunan Huihong Reagent Co. were used to prepare the shell. Tween 80(Analytical Reagent) from Hunan Huihong Reagent Co. was used as an emulsifier. NaOH (Analytical Reagent) from Sinopharm Chemical Reagent Co. was used to adjust pH value. 25 % Glutaraldehyde from Sinopharm Chemical Reagent Co. was used as a curing agent.

112.2.2　Experimental Apparatus

HJ3-Constant Temperature Magnetic Stirrer from Changzhou Guohua Electrical Appliance Co. and ER2000-Homogenizer from IKN Equipment Shanghai Co. were used to prepare microcapsules. ST130-Scanning Electron Microscope from Hitachi High-technology Co. and ZS-90 nanoparticle size analyzer from Malvern Instruments were used to characterize the microcapsules' morphology.

112.2.3 Microencapsulation of Organic Pigment by Single Coacervation

Put a certain amount of chitosan in 1 % dilute acetic acid solution, heating and stirring it. After chitosan fully dissolved, add some organic pigment benzidine yellow and emulsifying agent in the above chitosan solution. After that use high-speed homogenizer process solution for about 10 min and get organic pigment emulsion. When it reached to room temperature, use NaOH to adjust its pH value. Then, slowly add some flocculant $NaSO_4$ and dilute it with distilled water. Make the above emulsion quickly down below 10 °C through putting it into ice water bath. Stir the emulsion at the same time slowly adding the curing agent to it. Then by heating the prepared emulsion microcapsules of organic pigment could be obtained.

112.3   Results and Discussion

112.3.1 Core–Wall Ratio on the Particle Size of the Microcapsules

Chitosan and the dosage of the organic pigment and its proportion mainly have influence on the particle size, at the meantime affected encystment [12, 13]. Different core–wall ratios (12:1, 6:1, 3:1, 2:1, 1:1) on the shape and particle size of microcapsules were studied as shown in Fig. 112.1.

In a certain range, the mass ratio of wall materials to core material is higher; the more core content is embedded in the wall materials, and the larger is the particle size. When the core–wall ratio was greater than 6:1, the particle size was larger and the wall material's dosage was small leading to a thin wall which was easy to rupture, and the particle size distribution was wide; meanwhile, the ball was not

Fig. 112.1 The effect of different core–wall ratio on average particle size
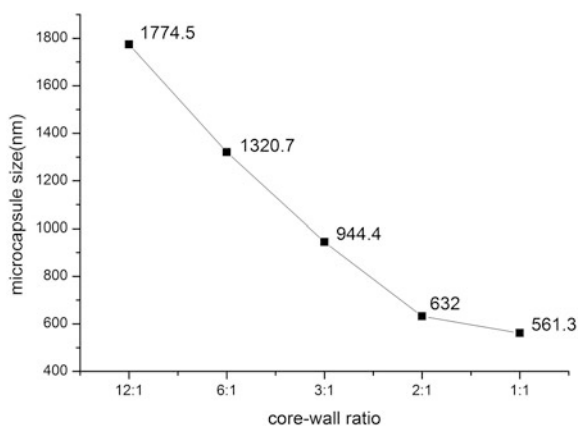
uniform. When the core–wall ratio was around 1:1, the average particle size was smaller; but because of the smaller core material, the core material coating rate was lower and the wall material waste was large. When the core–wall ratio ranged from 3:1 to 2:1, the capsules' size was small and its size distribution dispersed evenly.

112.3.2 The Effect of Emulsifier's Dosage on Particle Size

Emulsifier as a main substance in the process of pigment microencapsulation mainly influences the size of the dispersed organic pigment and maintains the stability of the emulsion performance [14]. The dosage of emulsifier has great influence on the particle's size and distribution [15]. When emulsifier's dosage accounted for 0.25, 0.5, 0.75, and 1 % (quality percentage), capsule size distribution and its shape were investigated; results are shown in the Table 112.1.

From Table 112.1, with the increase of the amount of emulsifier, the particle size decreased from 0.25 % 1211 nm to 1.5 % 501 nm. When 0.25 % of the emulsifier was added, due to the little amount of emulsifier was used, the stability and dispersion properties of the emulsion were poor, and the particle size of the capsules were larger and the distribution was not uniform. And when the quality of emulsifier was between 0.5 and 0.75 %, the emulsification effect was very well that prepared small size and uniform size distribution. However, the amount of emulsifier reached 1 %, and little size capsules were prepared successfully, but emulsifier elution was difficult due to large amount usage of it.

112.3.3 The Effect of Different PH Value on Particle Size

Slowly increasing chitosan solution's pH value could reduce chitosan solubility, which made chitosan deposit around pigment and finally formed capsules. From the above, it is obvious that adjusting solution's pH value played a much key step in the formulation of microcapsule. According to the experimental study, when pH value was about 7.0, the emulsion began to agglomerate obviously. And when continuing to increase pH value, it was impossible to form single ball because microcapsules' agglomeration became more severe. In this article, pigment microcapsules' size and its morphology's change with the pH value's change from 4.00 to 7.50 were observed by high electron microscopy, as shown in Fig. 112.2.

From Fig. 112.2, it was clearly showed that particle size of the microcapsules into sac and quantity first increased slow and at last increased rapidly. When the pH

Table 112.1 The effect of different emulsifier's dosage on average particle size

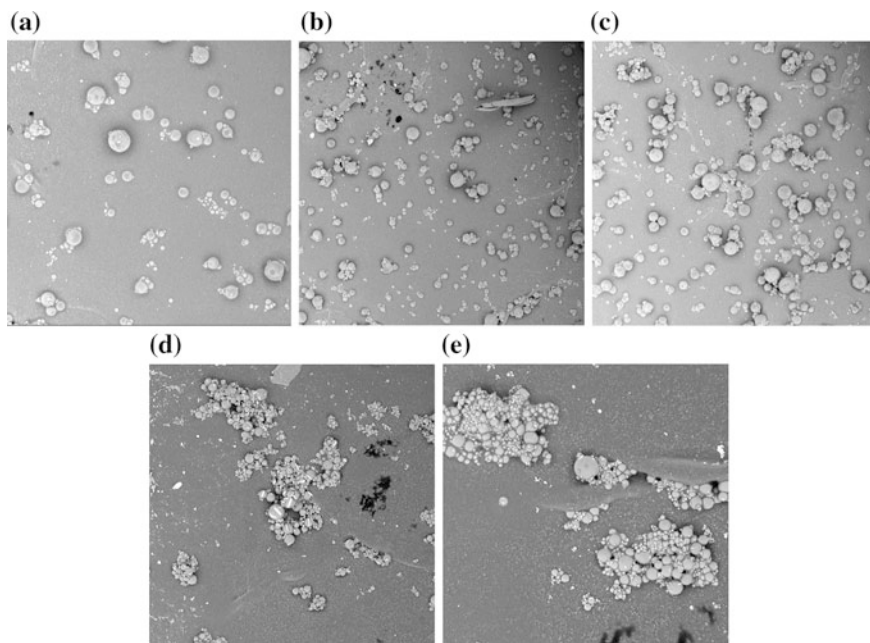| Emulsifier dosage (mass ratio)	0.25 %	0.50 %	0.75 %	1 %
Capsule average size (nm)	1211	755	670	501

Fig. 112.2 The effect of different pH value on average particle size and its shape. **a** pH = 4.01, **b** pH = 5.00, **c** pH = 6.00, **d** pH = 7.01, **e** pH = 7.50

value was just 4.01 (Fig. 112.2a), microcapsules were basically formed. Then, the value rose between 5.0–6.0 (Fig. 112.2b, c), and sac effect was very well. PH value rose to about 7.01 (Fig. 112.2d), and microcapsules started to reunite. Moreover, when the emulsion's pH value reached far above 7.0, the microcapsules gathered too severely and microcapsules' agglomeration was visible to the naked eye. So the value between 5.0 and 6.0, microcapsules of good shape, small size, and well dispersed could be prepared.

112.3.4   The Effect of Different Curing Agent's Dosage on Particle Size and Distribution

In the process of preparation, the curing agent was added to the emulsion to make the high polymer material crosslink to each other and deposit on the surface of the core material and form the wall to entrap core material completely, and finally the capsules with better stability were obtained. The cross-link reaction could change linear polymer into the reticular structure that could promote the stability of the high polymer. In order to make the chitosan deposit around the core materials no longer dissolved, it should be cured by cross-link reaction. In this experiment, different

Table 112.2 The effect of different curing agent's dosage on average particle size

Curing agent (%)	Average size (nm)
0.05	Curing incomplete
0.1	777
0.13	849
0.15	895
0.25	917
0.5	Agglomeratio

Fig. 112.3 The effect of different curing agent's dosage on average particle size
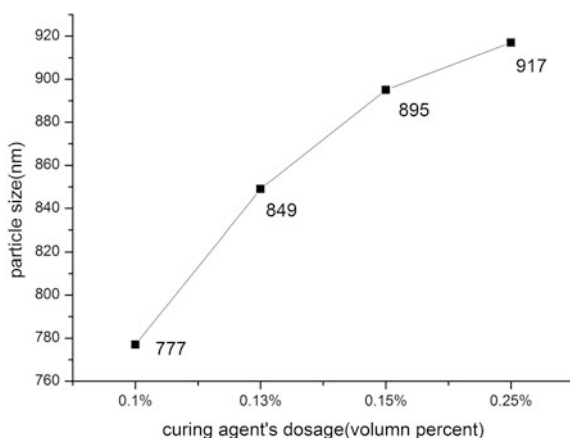
volume percent of glutaraldehyde effect on the microcapsules size and distribution was studied, as shown in Table 112.2 and Fig. 112.3.

From Table 112.2 and Fig. 112.3, it could be seen that the dosage of curing agent had little impact on particle size and its distribution. Only when curing agent's amount was less than 0.05 %, the curing process proceed incomplete leading to poor shape in the wall materials. But when the amount of the curing agent was more than 0.5 %, it could be observed that the solution quickly solidified into jelly due to the excessive amount of curing agent and the cross-linking reaction went into overdrive thus leading to rapid reunion of the microcapsules. Even when the dosage of the curing agent was 0.25 %, the amount of it was still more and the size and uniformity of the microcapsule were bigger and poor. However, when the amount of the curing agent ranged from 0.1 to 0.15 %, the average particle size was small and its distribution was relatively narrow and it showed good encystations property.

112.4 Conclusion

In this paper, microcapsule of organic pigment was successfully prepared by single coacervation method. The experiment used chitosan as shell material and organic pigment benzidine yellow as core material. The influence factor on the particle size

together with its distribution and its morphology in the preparation process such as core–wall material ratio, the dosage of emulsion, the dosage of curing agent, and pH value was carefully researched. The optimum preparing condition had been obtained: Core–wall ratio was 2:1, the amount of emulsion agent accounted for 0.5 % of the total system, pH value was from 5.0 to 6.0, and the dosage of curing agent was between 0.1 and 0.15 %. The next step for pigment microcapsules in the future is to research its wettability, coloring, and covering power in the ink. The pigment microcapsules prepared in this article were suitable for the preparation of water-based printing inks.

References

1. Zhang, L., Zhang, M. (2009). Research on ink pigment particle in gravure printing and flexo printing. *Packaging Engineering*, *30*(11), 81–82.
2. Zhang, C., Li, X., & Zhang, F., et al. (2013). Application progress of microcapsule technology in packaging and printing. *Packaging Engineering, 34*(21), 130–138.
3. Jiao, L. (2008). Application of microencapsulation technology in the printing inks. *Packaging Engineering, 29*(9), 21–23.
4. Deng, J., Tan, X., & Xue, Q. (2010). Optimization of microcapsule preparation technology condition of clove Oi-lB-Cy-clodextrin. *Packaging Engineering, 31*(10), 19–23.
5. Dubey, R., Shami, T. C., & Bhasker, R. K. U. (2009). Microencapsulation technology and application. *Defence Science of Journal*, 82–95.
6. Sunder, L. T., Achhrish, G., Keshari, J., et al. (2010). Microencapsulation techniques and its application: A review. *The Pharma Research, 3*(1), 112–116.
7. Martins, I. M., Barreiro, M. F., Coelho, M., et al. (2014). Microencapsulation of essential oils with biodegradable polymeric carriers for cosmetic applications. *Chemical Engineering Journal, 245*, 191–200.
8. Filomena, N., Pierangelo, O., & Florinda, F. (2012). Microencapsulation in food science and biotechnology. *Current Opinion in Biotechnology, 23*, 182–186.
9. Gordon, N. (2002). Application of microencapsulation in textiles. *International Journal of Pharmaceutics, 242/23*, 55–62/182–186.
10. Qi, D., Chen, Z., & Zhao, X., et al. (2013). Particle size control of organic pigment microcapsules prepared via micro-suspension polymerization. *CIESC, 64*(3), 1118–1123.
11. Mao, H., Wang, C., Fang, G., et al. (2011). Preparation and particle size analysis of phthalocyanine green pigment microcapsules coated by polyamide. *New Chemical Materials, 39*(10), 70–72.
12. Yang, W., Wang, T., & He, N. (2009). Preparation and property of chitosan/sodium tripolyphosphate microcapsules as drug carrier. *Chemical Journal of Chinese Universities, 30*(3), 625–628.
13. Jiao, L., Wang, X., & Bai, Y. (2010). Study on preparation and influence factors of limonene microcapsule. *Packaging Engineering, 31*(7), 1–3.

14. Xue, C., Zhu, Y., An, X., et al. (2009). Nanocapsules preparation by complex coacervation in microemulsion with chitosan-gelatin. *Journal of Nanjing Normal University: Natural Science Edition, 32*(2), 69–72.
15. Xiao, X., Guan, Y., & Wang, Z., et al. (2013). Preparation of chitosan/tripolyphosphate microcapsules by the method of water-in-water. *Journal of South-Central University for Nationalities: National Science Edition, 32*(1), 42–46.

Chapter 113
Study on the Stability and Color Property of Fluorescent Ink-jet Ink

Wan Zhang, Xing Feng, Yuanyuan Zhu and Xianfu Wei

Abstract Fluorescent ink is mainly applied in traditional printing methods which can affect fluorescent emission of ink seriously. However, ink-jet printing–applied fluorescent ink extensively cannot prevent fluorescent emission of ink due to dot paralleling. Therefore, in this paper, the properties of fluorescent ink-jet ink were studied. The fluorescent stability is one of the important properties for fluorescent ink-jet ink, which can limit the storage of fluorescent ink. The additive can adjust the certain property of ink but can also influence ink's stability among the components of ink. The effect of triethanolamine and UV absorbent on ink's stability was studied in this paper. Presently, there is no perfect means to control the color of fluorescent ink, the white balance were processed by using fluorescent ink-jet ink with three primary colors red, green, and blue and printing device ESPON7600 with dot paralleling. The results showed that the optimal quantity of triethanolamine was 0.6 %, the UV absorbent UV-7282 had the less effect on ink's stability and white balance curve with high accuracy and almost unbiased color was determined.

Keywords Fluorescent ink-jet ink · Additive · Stability · White balance

113.1 Introduction

Fluorescent ink is a functional ink, which is colorless under daylight and can emit visible light under UV light. Thus, it can print anti-fake information on prints. In addition, in order to present a special artistic effect, it can be used on art field by utilizing the property of emitting color light, such as wallpaper, stage background, and outdoor advertising [1]. Presently, fluorescent ink is mainly applied in traditional printing methods, for example screen printing [2] and offset printing [3]. However, the traditional printing methods affect the fluorescent property of ink significantly and prevent the fluorescent emission of ink possibly. The ink-jet

W. Zhang (✉) · X. Feng · Y. Zhu · X. Wei
Beijing Institute of Graphic Communication, Beijing, China
e-mail: zhangwan@bigc.edu.cn

919

printing which is one of the digital printing almost cannot impulses the fluorescent emission of ink due to dot paralleling [4]. Therefore, the fluorescent ink-jet ink was prepared so as to study the properties of ink well.

The stability of fluorescent property is important for fluorescent ink, because ink must have certain storage period. Fluorescent ink-jet ink is made up of fluorescent material, such as solvent, resin, and additive, and each component can affect its property. On the basis of the previous study, the fluorescent ink-jet ink was prepared and the effect of additive on ink's stability was studied by changing the type and quantity of additive. White balance is a common practice in photograph or image processing to compensate for the ambient light, which performs adjustment of the intensities of the primary colors, red, green, and blue, for a given image [5, 6]. At present, there is no perfect means to control the color of fluorescent ink. In this paper, the white balance were processed by using fluorescent ink-jet ink with three primary colors, red, green, and blue and printing device ESPON7600 with dot paralleling. Through testing color bar, the color reproduction of fluorescent ink-jet ink was studied, white balance curve was determined.

113.2 Experiment

113.2.1 Raw Materials

Solvent: acetone, ethyl acetate, propylene glycol monomethyl ether, butyl acetate, *N*,*N*-dimethylformamide; resin: acrylic 5391; pH modifier: triethanolamine; fluorescent material: red, green, and blue; and light offset paper.

113.2.2 Apparatuses

RF-5301PC fluorescence spectrophotometer; UV-2501PC UV–visible spectrophotometer; HJ-6A magnetic stirring apparatus; JJ-1 motor stirrer; KRUSS-K100 surface tension meter; pH meter, and ESPON7600.

113.3 Result and Discussion

113.3.1 Study of the Stability of Fluorescent Ink-jet Ink

113.3.1.1 Effect of Triethanolamine on the Stability of Fluorescent Ink-jet Ink

pH value is an important property for ink-jet ink, because if the pH value is too low, the ink will corrode ink box and if the pH value is too high, the ink will produce extra salt, reduce the lifetime of ink box, and improve the electrical conductivity of

Fig. 113.1 pH value of the inks prepared by changing the quantity of triethanolamine
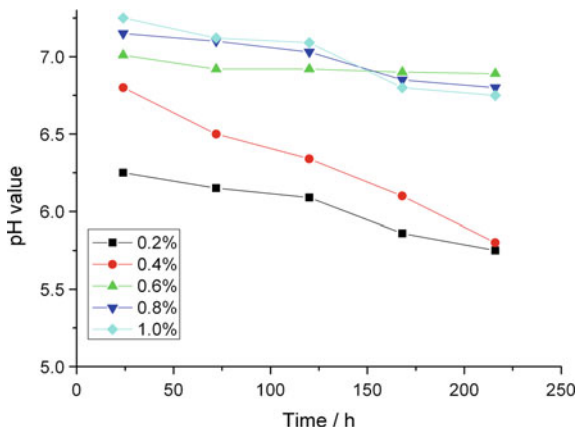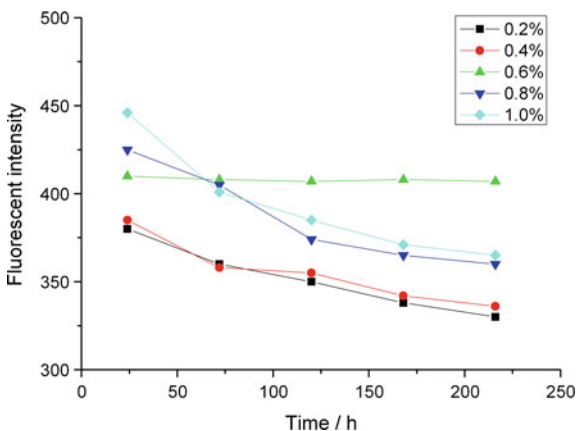

Fig. 113.2 Fluorescent intensity of the inks prepared by changing the quantity of triethanolamine

ink, which can limit its application in piezoelectric ink-jet printer [7]. Triethanolamine is one of the regulators for adjusting the pH value of ink. However, triethanolamine also affects the stability of fluorescent ink-jet ink. Thus, it is essential to determine the quantity of triethanolamine by comparing these two properties. The ink samples were prepared by changing the quantity of triethanolamine, and the pH value and fluorescent intensity of inks were measured at different times, as shown in Figs. 113.1 and 113.2.

Figures 113.1 and 113.2 shows that with the increase in the quantity of triethanolamine, the alkalinity of inks was raised and the fluorescent intensity of inks was obvious to reduce. The reason is the molecule structure of triethanolamine has –CN group with electronic absorption, which can weaken or prevent the generation of fluorescent light. The stabilities of the pH value and fluorescent intensity also had a little of change except the ink prepared by the quantity 0.6 % of triethanolamine. The main reason is related to the acid–base property of ink system; when the

acid–base property of the ink system changes to acidity or alkalinity, the activity of the fluorescent group in fluorescent material decreases and the fluorescent intensity of the inks also reduces. However, the fluorescent group has better stability property in neutral environment. Therefore, the optimal quantity of triethanolamine is 0.6 %.

113.3.1.2 Effect of UV Absorbent on the Stability of Fluorescent Ink-jet Ink

The UV absorbent can be added to fluorescent ink-jet ink so as to improve the stability of ink. The most UV absorbent can absorb UV light and convert it into chemical energy, thermal energy, or other energy due to the chromophore, for example –N=N–, –C=N–, –C=O, and –N=O [8]. The ink samples were prepared by choosing three kinds of UV absorbents and fluorescent intensity of inks were measured at different times, as shown in Fig. 113.3.

From Fig. 113.3, it is obvious that the fluorescent intensity of ink without UV absorbent decreased fast with the time increased and the stabilities of inks prepared by UV absorbents were better. Especially, the fluorescent intensity of ink prepared by UV-7282 almost had no change with the time increase. The molecule structure of benzophenone UV absorbent (UV-531) and benzotriazole UV absorbent (UV-328) has the chelate ring of hydrogen bond which can turn light energy into heat energy and reduce the fluorescence decay rate. Moreover, UV absorbent (UV-7282) belong to amine can not only absorb 300–320 nm UV light and reduce the excitation light power, but also have regeneration function in the process of light stabilization. Therefore, the optimal UV absorbent is UV-7282.

Fig. 113.3 Fluorescent intensity of the inks prepared by choosing three kinds of UV absorbents
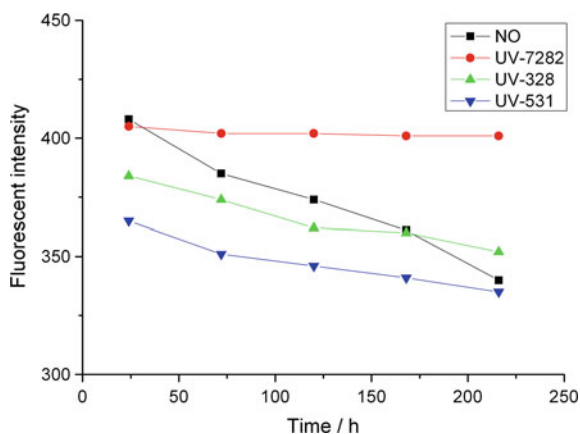
113.3.2 Study of White Balance of Fluorescent Ink-jet Ink

For color image printed by fluorescent ink-jet inks, white balance influences printing quality greatly. In this paper, the proofs were printed by using ESPON7600 and fluorescent ink-jet inks on light offset paper, and the color bars were measured by spectroradiometer (PR-655, Photo Research Inc., USA). The color values Δa^* and Δb^* between color bars and standard light D65 were calculated to confirm the 20 levels of neutral gray, because when the coordinates of color bars are close to the white point, the color can be named neutral gray. Then, these 20 levels of neutral gray were adjusted by changing output values R, G, and B. The last data of neutral gray are shown in Table 113.1 and Fig. 113.4.

Figure 113.4 reveals that the equivalent neutral gray was not mixed by the same amount of R, G, and B fluorescent ink-jet inks, because the fluorescent intensity of R fluorescent ink-jet ink was weaker than G and B. Therefore, more R fluorescent ink-jet ink was required to print proof so as to obtain the neutral gray and B fluorescent ink-jet ink was less. Table 113.1 shows that all color bars satisfy $|\Delta a*| \leq 7$, $|\Delta b*| \leq 7$, which illustrated that these color bars can represent the 20 levels of neutral gray. In addition, from Fig. 113.5, it is obvious that the color of adjusted proof was more accurate and unbiased.

Table 113.1 Data of white balance

Level	R^a	G^a	B^a	X^b	Y^b	Z^b	L^{*c}	Δa^{*c}	Δb^{*c}
1	75	60	0	2.444	2.429	3.383	17.59	2.77	−4.95
2	95	79	1	2.58	2.662	3.528	18.64	0.97	−4.04
3	109	90	2	2.74	2.839	3.532	19.39	0.78	−2.77
4	120	94	5	2.815	2.879	3.572	19.55	1.45	−2.72
5	145	106	8	3.13	3.137	3.708	20.58	2.57	−1.75
6	148	108	10	3.15	3.151	3.684	20.64	2.68	−1.51
7	159	110	11	3.176	3.169	3.818	20.71	2.82	−2.17
8	166	112	13	3.268	3.241	4.825	20.98	3.17	−7.00
9	182	116	16	3.407	3.447	4.952	21.75	2.13	−6.30
10	188	119	18	3.454	3.453	4.983	21.77	2.79	−6.41
11	199	125	20	3.654	3.695	5.113	22.64	2.21	−5.54
12	207	130	28	3.875	3.927	5.537	23.43	2.13	−6.11
13	214	140	31	4.041	4.135	5.671	24.11	1.61	−5.53
14	221	144	35	4.094	4.204	5.794	24.33	1.41	−5.68
15	228	150	42	4.264	4.392	6.015	24.93	1.25	−5.60
16	234	151	45	4.296	4.394	6.206	24.93	1.67	−6.39
17	238	154	49	4.314	4.397	6.297	24.94	1.88	−6.75
18	242	159	55	4.471	4.594	6.618	25.55	1.42	−7.00
19	251	162	63	4.514	4.618	6.633	25.62	1.68	−6.94
20	255	167	69	4.662	4.787	6.787	26.12	1.48	−6.68

[a]Output data; [b]measured by spectroradiometer (PR-655, Photo Research Inc., USA); [c]calculated by the formulation between XYZ and $L^*a^*b^*$
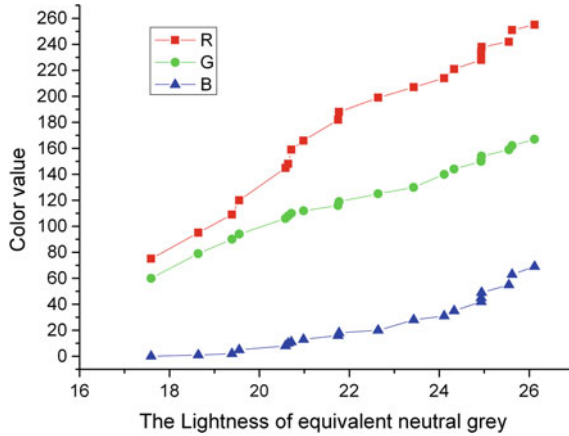
Fig. 113.4 Relationship between *color* value and the lightness of equivalent neutral *gray*

Fig. 113.5 20 levels of neutral *gray* before and after correction

113.4 Conclusion

The fluorescent ink-jet ink was prepared to study the stability and color property of ink. The results revealed that, the different quantities of triethanolamine and UV absorbents had certain effect on stability of ink and the optimal quantity of triethanolamine was 0.6 %, the UV absorbent UV-7282 had the less effect on ink's stability. At last, white balance curve with high accuracy and almost unbiased color was determined.

References

1. Wei, X., Gao, S., Huang, B., & Zhang, W. (2013). Research on the imaging mechanism of additive color of fluorescent. *Applied Mechanics and Materials, 262*, 22–26.
2. Coudray, M. A. (2004). Boosting process-color ink gamut with fluorescents. *Screen Printing, 94*(6), 28–32.
3. Feng, Y., Zhou, Q. H. (2012). *The method of printing anti-fake color image with colorless fluorescent ink*. Patent Number: CN102514408A, June 27.
4. Coyle, W. J. (Lebanon, O. H.), Smith, J. C. (Fletcher, N. C.). (2004). *Methods and ink compositions for invisibly printed security images having multiple authentication features*. Patent Number: USA33159785, April 5.
5. Kim, Y., Lee, J.-S., Morales, A. W., & Ko, S.-J. (2002). A video camera system with enhanced zoom tracking and auto white balance. *IEEE Transactions on Consumer Electronics, 48*, 428–434.
6. Chen, C.-L., & Lin, S.-H. (2011). Formulating and solving a class of optimization problems for high-performance gray world automatic white balance. *Applied Soft Computing, V11*, 523–533.
7. Zhou, Y. (2006). *Digital printing*. Wuhan: Wu Han university press.
8. Li, Q., Huang, F., & Feng, X. (2012). The organic ultraviolet absorption agent in textile. In *The 4th Annual Conference of China Textile Auxiliary Industrial Association*, pp. 123–131.

Chapter 114
Fabrication and Performance of Water-Based Near-Infrared Absorption Ink-Jet Ink

Lijuan Liang, Zhenzhen Chen, Hui Hao, Keyang Hu and Xianfu Wei

Abstract This thesis mainly studied the preparation of water-based near-infrared absorption ink-jet ink and analyzed anti-false property. Near-infrared absorption ink-jet ink is composed of infrared dyes, solvents, resins, additives, and so on. The dye was an important component which decided the security effect of ink, and the dyes had a great impact on the properties of infrared absorption intensity and the physical properties. The water-based near-infrared ink-jet ink sample with good comprehensive performance has been prepared, and the properties of the ink were adjusted according to the ink-jet printer which was used in this experiment. FDD-500 (Fang yuan anti-counterfeiting technology Co. Ltd.) was used to test the effect of anti-false. Experiments' results showed that solvent has a great effect on the solubility and surface tension of near-infrared-absorbing ink-jet ink, resin was a key factor determining the viscosity of the system, and the content of infrared dyes directly affected the infrared absorption intensity. The prepared water-based near-infrared absorption ink-jet ink sample has the good performance and anti-false effect.

Keywords Water-based · Infrared absorption · Ink-jet ink · Formulation design

L. Liang (✉) · Z. Chen · H. Hao · K. Hu · X. Wei
Beijing Institute of Graphic Communication, Beijing, China
e-mail: lianglijuan@bigc.edu.cn

Z. Chen
e-mail: 1339721514@qq.com

H. Hao
e-mail: 839331151@qq.com

K. Hu
e-mail: 371109684@qq.com

X. Wei
e-mail: weixianfu@bigc.edu.cn

927

114.1 Introduction

In recent years, with the rapid development of economy, enormous changes occurred in people's living standards. But the attendant is that counterfeiting of goods became increasingly rampant, the economic interests of the majority of manufacturers suffered huge losses, its credibility is subjected to an unprecedented test, so a means of security and combating counterfeit products were studied [1, 2]. With the rise of digital printing era, digital printing anti-counterfeiting technology also has been developed continuously [3]. The water-based near-infrared ink-jet ink can be used for printing various documents and labels. And infrared security ink has features such as strong security, technical difficulty, easy to use, providing virtually unlimited printing conditions, so it can print any security patterns, one-dimensional bar codes, and 2-dimensional bar codes; therefore, it has great potential applications in security printing [4]. The main purpose of this research is to use the near-infrared dye which having infrared absorption characteristics, to prepare ink-jet ink sample which could be excited by the infrared light. Through adding this special directly, after printing on substrates, a pattern printed on the substrates could not be seen with the naked eyes, but in the infrared excitation light, a clearly black symbol or picture can be observed, so as to achieve the purpose of security.

114.2 Experiment

114.2.1 Materials

Dye: infrared dye; solvent: deionized water, ethanol, methanol, propylene glycol, ethyl ether, acetone, butyl acetate, ammonia, ethylene glycol, propylene glycol methyl ether, isopropanol, etc; surfactant: 500, 805, 505; resin: polyethylene glycol 400; pH regulator: ammonia; and other additives: sodium chloride and sodium acetate.

114.2.2 Apparatus

HJ-6A-type digital thermostat long magnetic stirrer (Jintan Ronghua Instrument Manufacturing Co., Ltd.), K100 type static surface tension meter (Germany Kruss Company), U-4100 spectrophotometer, PH meter (Shanghai Zhi Guang Instrument Co. company), conductivity meter (Shanghai Zhi Guang instrument Co.), Portable Viscometer Viscolite 700 handheld viscometer (import), Epson K100 desktop printer (Epson), FDD-500 near-infrared light source (Beijing awarded a radius of security technology Co., Ltd.)

114.2.3 *Preparation of Infrared Absorption Ink-Jet Ink*

First, adhesives were predispersed in deionized water and dissolved by stirring at room temperature completely, and the infrared-absorbing dye was added to the carrier until it is completely dissolved and then got the fluorescent ink-jet ink after filtered.

114.3 Results and Discussion

114.3.1 *Absorption of Near-Infrared Dye*

Infrared-absorbing material is one the most important component of ink-jet ink system, which is a key factor of emerging anti-counterfeiting technology. In order to conform the absorption wavelength of the near-infrared dye and find the optimum excited wavelength, the absorption spectral has been studied, and the testing result has been shown as Fig. 114.1.

The same content of infrared-absorbing dye has different absorbent in different wavelengths of light. In this experiment, the absorption spectrum of infrared dye in the visible and near-infrared has been studied, as shown in Fig. 114.1, from the figure, the maximum absorption wavelength of the infrared-absorbing dye used in the experiment is 948 nm.

Fig. 114.1 The absorption spectral of infrared-absorbing dye
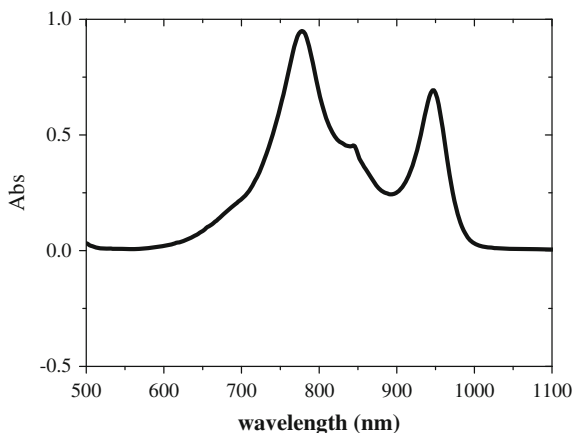
114.3.2 Effect of Solvent on the Properties of Infrared Absorption Ink-Jet Ink

In order to get water-based infrared absorption ink-jet ink with the best comprehensive performance, the method of simple gravity design which adopt three simple gravity design ($m = 3$) experiments has been applied [5]. Maintaining the same proportion of water and dye in the sample, assuming that X_1, X_2, and X_3 were the content proportions of propylene glycol, ethylene glycol, ethanol, respectively, in the ink, 7 kinds of formulas have been designed, and water-based near-infrared absorption ink have been prepared and the performance has been studied, as shown in Table 114.1.

According to the surface tension, conductivity, viscosity, pH value, and the drying time on the contribution to the comprehensive performance of infrared absorption ink-jet printing ink, the weights were set as follows: 0.2, 0.1, 0.2, 0.2, and 0.3, respectively. And the regression equation of the comprehensive performance of the infrared absorption ink-jet ink is obtained by the data processing:

$$Y = 45.952X_1 + 44.899X_2 + 20.046X_3 - 18.418X_1X_2 + 25.690X_2X_3 \\ - 37.844X_1X_3 \tag{114.1}$$

Through calculating, the best comprehensive performance of the water—absorbing ink-jet ink can be observed when $X_1: X_2: X_3 = 0.17:0:0.83$.

114.3.3 Resin on the Effect of the Performance of Water-Based Infrared Absorption Ink-Jet Inks

The resin is also an important component of the ink-jet ink sample, and the content of the resin has a great effect on the viscosity and film performance of the ink. In order to get the ink with good property and film making, the different content of the

Table 114.1 The effect of solvent on the performance of ink sample

No.	X_1	X_2	X_3	Surface tension (dyn/cm)	pH	C (μs/cm)	V (/s)	Drying time (/s)
1	1	0	0	52.5	8.32	50.6	31	61
2	0	1	0	54.5	8.39	61.3	34	47
3	0	0	1	43.4	9.26	24.2	16	8
4	1/2	1/2	0	47.8	8.41	34.6	32	57
5	1/2	0	1/2	45.5	8.68	22.8	18	18
6	0	1/2	1/2	52.3	8.95	91.2	18	19
7	1/3	1/3	1/3	48.2	8.78	22.5	24	35

Note: X_1 Propylene glycerin, X_2 glycol; X_3 ethyl alcohol; C Conductivity, V Viscosity

Table 114.2 The content of resin on the effect of performance of ink sample

Mass fraction	Viscosity	Surface tension	Conductivity	pH
(%)	(mPa·s)	(dyn/cm)	(μs/cm)	
0.0	2.7	30.7	45.6	8.49
0.5	3.0	30.1	31.5	8.54
1.0	3.4	29.2	35.1	8.28
2.0	4.2	29.6	46.7	8.47
3.0	4.8	30.9	65.2	8.26
4.0	6.1	29.6	49.4	8.28

Table 114.3 The comparison of the Epson ink and self-making ink

	Viscosity	Surface tension	Conductivity	pH value
	(mPa·s)	(dyn/cm)	(μs/cm)	
Epson ink	3.9	31.0	3460	8.25
Ink sample	4.8	29.6	49.4	8.28

polyvinyl pyrrolidone was studied, and the performance of the ink sample was tested, as shown in Table 114.2.

As shown in Table 114.2, the conductivity, pH value, and surface tension of the ink sample almost have no variations when the content of the polyvinyl pyrrolidone was increased, but the viscosity of the sample increased with the increasing of the content of resin. At the same time, because the viscosity of the original ink of Epson printer is about 3–5 mPa·s, so the mass fraction of the polyvinyl pyrrolidone was decided as 3 % (Table 114.3).

114.3.4 Effect of Surfactant on the Performance of Water-Based Infrared Absorption Ink-Jet Inks

The surface tension is an important performance of the ink-jet ink. As usual, the surface tension of the ink sample used in Epson printer is about 25–50 dyn/cm (20 ° C), However, the surface tension of the water is too high to print through using the digital printer. Therefore, the different surfactants were applied in this experiment to decrease the surface tension, and the testing results were shown as Fig. 114.2.

From Fig. 114.2, the surfactant such as 805, 505, 500 has great effect to decrease the surface tension of the ink-jet ink sample. And the surface tension was decreased below 32 dyn/cm when the mass fraction of 505 and 500 was 1 %, and surface tension was decreased obviously when the content of the 805 was 0.5 %, so in this experiment, the 805 was used as the surfactant.
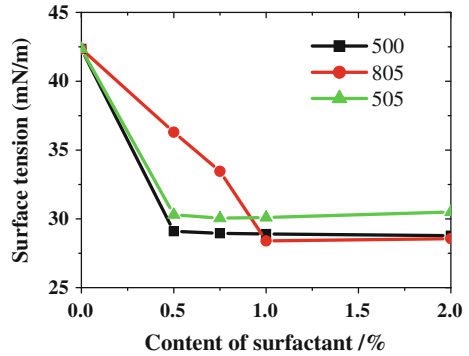
114.3.5 Anti-counterfeit Effect of the Printed Water-Based Infrared Absorption Ink-Jet Inks

According to the composition of the water-based infrared absorption ink-jet ink, the ink sample was prepared, and the performance of the ink-jet ink sample was compared with the Epson original ink, as shown in Table 114.3, and the anti-counterfeit effect was shown in Figs. 114.3 and 114.4, respectively.

As shown in the Table 114.3, the performance of the near-infrared absorption ink-jet ink which was prepared in this experiment has almost the same properties as the Epson original ink, which means that the self-making ink sample could printed through using the Epson printer. And from Figs. 114.3 and 114.4, the near-infrared absorption ink samples showed the good anti-counterfeit effect: under the ordinary light, almost nothing could be observed, but a clear pattern could be observed under the infrared light.
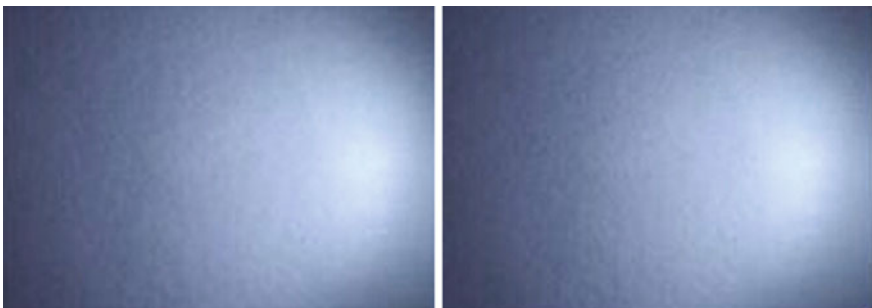
Fig. 114.3 Picture under the ordinary light
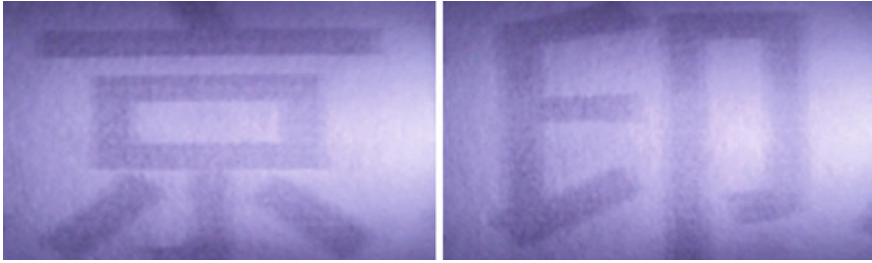
Fig. 114.4 Picture under infrared light with absorption length as 850 nm

114.4 Conclusions

1. The viscosity, surface tension, pH value, conductivity, and the infrared absorption intensity can meet the performance of the water-based infrared absorption ink-jet inks when the propylene glycol and ethanol were used as the solvent, and the comprehensive performance was get when the ratio of propylene glycol and ethanol is 0.17:0.83.
2. With the increasing of the content of infrared dye, the infrared absorption intensity also increased. The dye itself has a great effect on the viscosity of the ink-jet ink sample, so the mass fraction of the infrared dye was decided as 0.05 %.
3. The resin has a great effect on the viscosity of the ink-jet ink, and with the increasing of the content of the resin, the film performance also increased. In this experiment, the mass fraction was decided as 3 %.
4. The surfactant used in this experiment such as 805, 505, and 500 was very effective, and the surface tension of the ink sample could meet the requirements of the Epson printer applied in this experiment successfully.

References

1. Xin, X. (2005). *Water-based ink*. Beijing: Chemical Industry Press.
2. Zhu, C., Liu, X., & Chen, H. (2002). The configuration and application of the invisible infrared printing ink. *Chemical Progress, 21*(8), 851–854.
3. Wang, J., & Chen, D. (2005). Near infrared absorption ink and near infrared absorption material. *China Anti-Counterfeiting, 6*(8), 1944–1946.
4. Liu, C., & Liu, H. (2007). The performance and component of ink-jet ink. *Ink-Jet Printing, 12*, 22–25.
5. Liang, L., Huang, B., & Wei, X. (2010). Formulation design of fluorescent ink-jet ink. *China Printing and Packaging, 2*, 379–384.

Chapter 115
Study on the Preparation of Waterborne UV-Curable Polyurethane Acrylate

Yanling Guo, Chunbing Chen and Fuqiang Chu

Abstract The preparation of waterborne UV-curable urethane acrylate was studied in this paper. The synthetic urethane acrylate could be used in water-based UV-curable inkjet printing as an ink binder. The waterborne UV-curable anionic polyurethane acrylate was prepared by self-emulsifying process. Isophorone diisocyanate (IPDI), polyethylene glycol, dimethylol propionic acid (DMPA), and pentaerythritol triacrylate (PETA) were selected as main raw materials in the experiment. Some influence factors on the properties of the waterborne polyurethane acrylate emulsion were studied, such as the mole ratio of –NCO/–OH, the mass fractions of DMPA, and the degree of neutralization. The results indicated that when the mole ratio of –NCO/–OH was 2.8:1, the mass fraction of DMPA was 3.5 %, the degree of neutralization was 100 %, and the solids of waterborne polyurethane acrylate emulsion could be obtained up to 45 %. The viscosity was 30 mPa·s, and the average size of the particle was 50 nm.

Keywords Waterborne UV-curable urethane acrylate · UV curing · Urethane acrylate · Low viscosity

115.1 Introduction

The water-based resin was based on water as solvents instead of organic solvent, but the problem was that the drying speed was so slow [1]. Although the traditional UV-curable resin could be cured fast, but the use of reactive diluents was harmful to environmental protection [2]. The waterborne UV-curable resin as a new type of

Y. Guo · F. Chu (✉)
College of Printing and Packaging Engineering, Qilu University of Technology,
Jinan, Shandong, China
e-mail: fqchu@126.com

C. Chen
CJ (Liao Cheng) Biotech Co., Ltd, Liaocheng, Shandong, China

935

environmentally friendly resin was focused in the research, which was combined with the advantages of waterborne resin and UV-curable resin. The waterborne polyurethane acrylate (WUPUA) could be designed by hard and soft segments in order to achieve the required performance. It had many advantages such as low system viscosity, not easy to burn, and blended with other emulsions easily [3–5].

The process and control should be chosen properly in order to get superior prepolymer [6]. The superior emulsion had been prepared by exploring the mole ratio of –NCO/–OH, the mass fraction of DMPA, and the degrees of neutralization in this experiment, which had a good hydrophilicity, high solid content, and low viscosity. The emulsion could be used for the low viscosity of water-based ink as binding material.

115.2 Experimental Setup

115.2.1 Materials and Equipment

Polyester glycol (Mn = 2000, Tianjin Cinfeng Chemical Co.); isophorone diisocyanate (IPDI, Bayer Chemical Co.) was vacuum-distilled before use; dimethylol propionic acid (DMPA, Aladdin Chemical Co.) was dried for 8 h at 105 °C before use; pentaerythritol triacrylate (PETA, Liyang Hengyang Chemical Co.); triethylamine (TEA, Tianjin Ruijinte Chemical Co.); N-methyl pyrrolidone (NMP); dibutyltin dilaurate (DBTDL, Shanghai Shangpu Chemical Co.); acetone (Laiyang Chemical Co.); deionized water.

Thermostat water bath was purchased from Shanghai Shuli Instrument Co., the type of NEN-3690 nanoparticle was used to measure the size of the emulsion, electronic balance was purchased from Mettler-Toledo instrument (Shanghai) co., and LTD NDJ-8S viscosity meter was purchased from Shanghai Precision Scientific Instrument Co., Ltd.

115.2.2 Synthesis of Waterborne UV-Curable Polyurethane Acrylate

First of all, measured polyester glycol and IPDI were added into the four-necked flask equipped with a stirrer, a condenser, and a thermometer under 50 °C and then reacted at 80 °C for 1 h. When the content of –NCO reached the reserved value, the reaction temperature was reduced to 50 °C and the measured DMPA and DBTDL were added into the flask and then reacted at 80 °C for 2 h. Second, the temperature was reduced to 50 °C when the value of –NCO content reached the theoretical value. Then the measured PETA was added and reacted at 80 °C for another 3 h and the urethane acrylate prepolymer was obtained.

At last, the measured TEA was added and reacted at 50°C for 0.5 h when the content of –NCO reached to 0. Finally, measured deionized water was added to emulsify the WUPUA resin under high-speed agitation for 0.5 h, and the WUPUA emulsion was obtained. The actual content of –NCO was measured by the method of 2 measured n-butyl amine titration in the system [7].

115.2.3   Analysis and Test

The determination of emulsion solid content was tested according to the National Standard GB1725-79 (89). Tests of emulsion stability were measured by precipitation which was centrifuged by TGL-16c high-speed centrifuge at 3000 r/min. Tests of emulsion average particle size were measured by the type of NEN-3690 nanoparticle and zeta potentiometer. Tests of emulsion viscosity were measured by the type of NDJ-1 rotary viscometer at 23 °C.

115.3   Results and Discussion

115.3.1   Influence of N(–NCO)/N(–OH) on the Properties of Emulsion

This study was to investigate the influence of n (–NCO)/n (–OH) on the size and viscosity of the emulsion when the DMPA mass fraction was 3.5 %, solid content was 45 %, and the ratios of n(–NCO)/n(–OH) were 2.4, 2.6, 2.8, 3.0, 3.2, and 3.4, respectively.

Figure 115.1 shows that the size of the emulsion particle increased with the increasing of n(–NCO)/n(–OH) from 2.4 to 3.4. The main reason was that the residual –NCO in the emulsion was reacted with water to generate instead of urea which had strong polarity with the increasing of n (–NCO)/n (–OH). The size of emulsion particle was not easy to be sheared for the increasing of dispersed particle viscosity in the process and the size of emulsion particle increased.

As is shown in Fig. 115.2, the viscosity of emulsion declined with the increasing of n (NCO)/n (OH) when n (NCO)/n (OH) was below 2.8, the reason because that the hard segment twined less with the increasing of n (NCO)/n (OH). However, the viscosity of emulsion rose with the increasing of n (NCO)/n (OH) when n (NCO)/n (OH) was above 2.8, the reason because that redundant –NCO could react with water to produce high-viscosity urea.

In comprehensive consideration, the size of the emulsion particle and the viscosity of emulsion met the requirements when n (NCO)/n (OH) was 2.8.
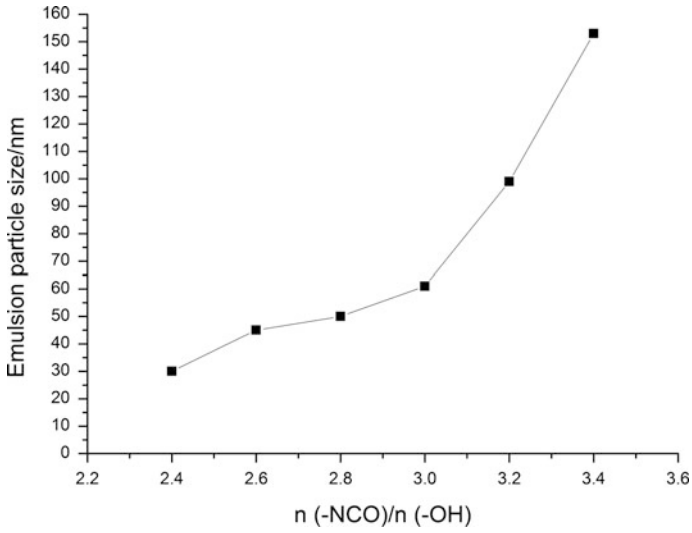
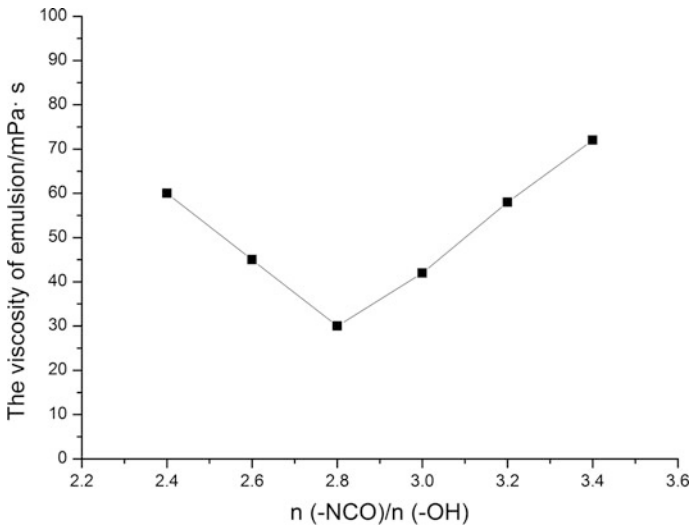**Fig. 115.1** Influence of n (–NCO)/n (–OH) on emulsion particle size

Fig. 115.2 The influence of n (–NCO)/n (–OH) on the viscosity of emulsion

Table 115.1 Effect of hydrophilic group content on the system

w (–COOH) (%)	Average particle size of the emulsion/nm	Emulsion appearance	Stability of the emulsion
4.5	34.8	Blue-ray nearly translucent	Stable
3.5	49.5	Blue-ray translucent	Stable
2.5	63.7	Blue-ray subtranslucent	Stable
1.5	82.1	White opaque	Stable
0.5	150.6	White not emulsifying	Unstable

115.3.2   Influence of the DMPA Mass Fraction on the Properties of Emulsion

The study was to investigate the influence of the DMPA mass fraction on average particle size of the emulsion, emulsion appearance, and stability of the emulsion when n (NCO)/n (OH) was 2.8, solid content was 45 %, and the DMPA mass fractions were 0.5, 1.5, 2.5, 3.5, and 4.5, respectively.

Table 115.1 shows that when w(–COOH) = 0.5 %, the resin could not be completely emulsified and the emulsion was unstable, because the hydrophilic group content in WUPUA resin was too low and resulted in part of the resin condensing into blocks. The hydrophilicity of the resin increased, the mean particle size of the emulsion reduced and the resin could be emulsified in the water by itself with the increasing of –COOH group content. The emulsion appearance turned from milky white to a blue-ray translucent and the stability of the emulsion was also increased.

115.3.3   Influence of the Degree of Neutralization on the Properties of Emulsion

The study was to investigate the influence of the neutralization on the emulsion appearance, such as the average particle size of the emulsion, viscosity and stability of the emulsion when n (–NCO)/n (–OH) was 2.8, solid content was 45 %, and the degrees of neutralization were 70, 80, 90, 100, and 110 %, respectively.

Table 115.2 shows that the emulsion appearance became transparent with the increasing degree of neutralization, but turned to opaque when the degree of neutralization was 110 %. The average particle size of the emulsion was reduced by increasing the degree of neutralization. The viscosity of the emulsion was decreased by increasing the degree of neutralization. The emulsion became stable with the increasing degree of neutralization, but turned to unstable when the degree of neutralization was 110 %.

Table 115.2 Effect of different neutralization on the hydrophilic properties of the resin

Neutralization (%)	Emulsion appearance	Average particle size of the emulsion (nm)	Viscosity (mPa s)	Stability of the emulsion
70	White, opaque	98.4	30	Sediment
80	Milky white, opaque	60.5	48	Little sediment
90	Light white, translucent	55.3	70	Less sediment
100	Light yellow, translucent	50.4	30	No sediment
110	Deep yellow, opaque	46.4	88	Less sediment

115.4 Conclusions

In comprehensive consideration, the suitable synthetic condition of waterborne UV-curable polyurethane acrylate was as follows: The ratio of n (–NCO)/n (–OH) was 2.8, the DMPA mass fraction was 3.5 %, and the degree of neutralization was 100 %. The emulsion size of the particle could be lower than 50 nm, the viscosity was not higher than 30 mPa·s, the appearance was transparent, and the stability was good.

References

1. Lili, L. (2013). Research status of water-based ink. *Chemical new materials, 41*(1), 9–12.
2. Rui, M., & Yongmei, M. (2014). Research progress of water based UV curable resin. *Adhesive of China, 23*(1), 46–49.
3. Xin, Y., & Ruixia, Z. (2014). UV-curable waterborne polyurethane acrylate resin synthesis and performance research. *The Key Reports, 17*(6), 5–9.
4. Tisheng, L. (2006). New progress in overseas inkjet printing ink technology innovation. *Imaging Techniques, 1*(1), 39–41.
5. Jiang, S. (2014). Environmentally friendly water-based UV synthesis of polyurethane acrylate resin. *Coating Industry, 44*(6), 49–53.
6. Huilu, L., & Kangchen, S. (2014). UV curing coating the synthesis and properties of polyurethane acrylates. *Insulation Materials, 47*(4), 21–25.
7. He, S. (1946). A method for the determination of isocyanates. *Analyst, 71*(849), 557–559.

Chapter 116
Study on the Synthesis and Property of Water-Based UV-Curable Epoxy Acrylate with Low Viscosity

Zhenzhen Zhang, Jilei Chao and Fuqiang Chu

Abstract The preparation method of water-based UV-curable epoxy acrylate with low viscosity was discussed in this paper. The epoxy acrylate was synthesized by epoxy resin, polyethylene glycol diglycidyl ether (PEGDE), polypropylene glycol diglycidyl ether (PPGDGE), acrylic acid, maleic anhydride, and trimethylamine through a method of "ring opening reaction—esterification reaction—neutralization reaction." The viscosity of synthetic material was low and could be used as the binder to prepare ink-jet ink. The results showed that the comprehensive performance of the prepared water-based UV-curable binder was optimal under the following synthetic conditions: The mole ratio of epoxy group and acrylic acid was 1.05:1, the reaction temperatures was 93 °C, the mole ratio of epoxy group and maleic anhydride was 1:0.9, the reaction temperatures was 90 °C and neutralization was 100 %. The characterization of the product was as follows: the viscosity was 24 mPa·s, UV curing time was 5 s, adhesion index was 1 class, and gloss was 95 Gs. In short, the synthesized epoxy acrylate can be used as binder of ink-jet ink.

Keywords UV curable · Water-based resin · Water-based UV-curable epoxy acrylate · Low viscosity

116.1   Introduction

In recent years, with the green environmental protection awareness continuously improving and increasingly attention to health, green environmental printing ink, for instance, water-based ink, UV ink, and water-based UV-curable ink came

Z. Zhang · J. Chao · F. Chu (✉)
College of Printing and Packaging Engineering, Qilu University of Technology, Shandong, China
e-mail: fqchu@126.com

into being and had caught the attention of the ink enterprise [1, 2]. Water-based UV-curable ink with water and ethanol as solvent and low VOCs content was a new type of green printing material in the twenty-first century.

Water-based resin which was used as the binder of water-based UV-curable ink plays a vital role in the performance of the ink. So far, the study of binders at home and abroad focuses on mainly the following several aspects, such as acrylic ester, unsaturated polyester, urethane acrylate, and epoxy acrylate [3]. Epoxy resin had a lot of advantages, for example, good chemical resistance, good adhesion with substrates, and high-temperature resistance [4, 5]. However, epoxy acrylate with the excellent characteristics of epoxy resin and acrylic resin [6] had been intensively applied because of its excellent performance, for example, low price, good adhesion, high gloss, and good chemical resistance. Generally, the viscosity of ink-jet ink was low and the epoxy acrylic resin prepared by traditional method was difficult to meet the requirements of low viscosity, so it needed to be modified to apply to the preparation of ink-jet ink.

In this paper, the water-based UV-curable epoxy acrylate with low viscosity was synthesized and the synthetic process of resin had been characterized by testing the epoxy value, acid value, and iodine value. By means of measuring the performance such as viscosity, adhesion, gloss, and UV curing time, it is concluded that the synthesized epoxy acrylate was suitable for the preparation of ink-jet ink.

116.2 Experimental

116.2.1 Materials and Equipment

Bisphenol-A epoxy resin (E-51) was supplied by Nantong Xingchen Synthetic Material Co., Ltd. Polyethylene glycol diglycidyl ether (PEGDE) and polypropylene glycol diglycidyl ether (PPGDGE), AR, were supplied by Shanghai Rufa Chemical Process Technology Co., Ltd. Acrylic acid, triethanolamine, and triethylamine, AR, were obtained from Tianjin Damao Chemical Reagent Factory. Maleic anhydride and hydroquinone, AR, were provided by Tianjin Kemiou Chemical Reagent Co., Ltd. N, N-dimethylbenzylamine, AR, was provided by Shanghai Reagent Factory.

Thermostat water bath was purchased from Shanghai Shuli Instrument Co., Ltd. UV LED curing machine was used for metering cure time. NDJ-8S viscosity meter was purchased from Shanghai Precision Scientific Instrument Co., Ltd. Film adhesion tester QFZ was used to measure adhesion. Mirror glossiness meter was purchased from Tianjin Qili Technology Co., Ltd.

116.2.2   Synthesis of the Water-Based UV-Curable Epoxy Acrylate

First of all, a certain quantity of epoxy resin, PEGDE, and PPGDGE were added into a four-necked flask placed in a thermostat water bath and equipped with a thermometer, condenser, mechanical stirrer and constant-voltage funnels. Then, the flask was heated to a proper temperature.

Secondly, the polymerization inhibitor was added and the mixture of the acrylic acid and catalyst was added dropwise into the four necked flask with constant pressure funnel in 30 min when the mixture was heated to a proper temperature, and then the acid value was tested every half an hour when the temperature rose to 93 °C. The reaction would not be stopped until the acid value was less than 5 mgKOH/g.

Thirdly, a certain quantity of maleic anhydride, catalyst, and polymerization inhibitor were fed into the reaction system when the temperature dropped to 50 °C, and then heating it to a certain temperature. The reaction would not be stopped until the acid value achieved the theoretical value.

Finally, a certain quality of neutralizer and deionized water were added into the reaction system in order when the temperature of the system dropped to 50 °C. Then, the reaction was ended after half an hour.

116.2.3   Characterization and Testing

Acid value was tested according to the national standard GB2897-82. Epoxy value was tested according to the national standard GB/T1677-8. Iodine value was tested according to the national standard GB/T1676-81. Viscosity was tested with the NDJ-8S viscosity meter. Adhesion was tested according to the national standard GB/1720-79. Gloss was tested with the mirror glossiness meter. The test method of UV curing time as follow: the resin was coated on the glass evenly and then exposed in the UV LED curing machine. The exposure time was recorded, and the cured film was pressed gently with the fingers. If no trace, the surface shall be deemed to have cured.

116.3   Results and Discussion

116.3.1   Influence of Reaction Temperature

The reaction of epoxy resin and acrylic acid belongs to exothermic reaction. If the temperature was too high in the reaction process, it was easy for unsaturated bond to polymerize because of the too fast reaction speed and the lots of heat in the reaction system [7].

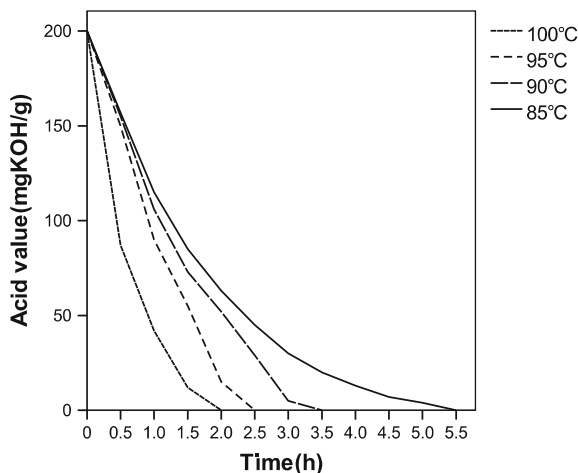**Fig. 116.1** Relationship between the temperature and the reaction speed of acrylic acid

Table 116.1 Iodine value of complete reaction system under different temperature

Temperature [°C]	Reaction time [h]	Iodine value [gI$_2$/100 g]
90	3.5	38.37
93	3	37.26
95	2.5	36.45
100	2	10.25

The effect of the temperature on the synthesis of epoxy acrylate was reflected by the change of the acid value.

Figure 116.1 illustrated the higher reaction temperature, the faster descent speed of the acid value. It took about 2 h for the acid value of the reaction system dropped to 5 mgKOH/g under the reaction temperature was 100 °C. As the above, it was about 3 and 3.5 h, respectively, when the temperature was 95 and 90 °C.

The iodine value of synthetic resin was tested under different temperature conditions after the completion of the reaction.

Iodine value was used to characterize the loss rate of the double bond. The low iodine value illustrated that the loss rate of the double bond was high and UV-curable properties of the resin was bad. The Table 116.1 showed that the iodine value was reducing with the increase of temperature. Therefore, taking the iodine value into consideration, 93 °C was selected as the best reaction temperature in this experiment.

116.3.2 Influence of the Amount of Maleic Anhydride

The amount of the maleic anhydride had an important influence on the water solubility of the prepolymer because the carboxyl got by the reaction between

Table 116.2 Influence of the amount of maleic anhydride on the water soluble of the resin

Mole ratio	1:1	1:0.9	1:0.8	1:0.7
Water soluble	Best	Better	Worse	Worst

maleic anhydride and the hydroxyl on the epoxy acrylate makes the prepolymer has hydrophilic. A small amount of samples were dissolved in the water and its dissolving property was observed. The Table 116.2 showed that the water soluble of the resin was best when the mole ratio of hydroxyl and maleic anhydride was 1:1. What is more, the water solubility of the resin became worse with the increase of the mole ratio. Taking cost into consideration, the best mole ratio of hydroxyl and maleic anhydride was 1:0.9.

116.3.3 Influence of the Kinds of Neutralizers

Though epoxy acrylate contained hydrophilic carboxyl, the content was less. The carboxyl was neutralized into carboxylate to improve its solubility in water. The ammonium hydroxide, triethanolamine, and triethylamine were selected as neutralizer and its influence on the water dispersion property of the resin with different solid content was discussed in the experiment.

Table 116.3 showed that the water solubility of the resin was better when the triethylamine and triethanolamine were used as neutralizer. By comparison, when the triethylamine was used as neutralizer, the curing speed of the resin was faster and the resin was not easy to turn yellow. Therefore, the triethylamine was selected as the neutralizer in this experiment.

116.3.4 Influence of Neutralization on the Viscosity of the Prepolymer System

Neutralization degree referred to that the mole percentage of the amount of the neutralizer added and used for neutralizing carboxyl completely [8]. In this experiment, with triethylamine as the neutralizer the viscosity of the system was tested under different neutralization because the size of the neutralization had an effect on the viscosity of the prepolymer system (Table 116.4).

Table 116.3 Influence of neutralizers on the water dispersion of the prepolymer

	20 %	40 %	60 %
Ammonium hydroxide	–	Milky white	Transparency
Triethanolamine	Milky white	Translucence	Transparency
Triethylamine	Transparency	Transparency	Transparency

Table 116.4 Relationship between neutralization and the viscosity of prepolymer system

Neutralization [%]	80	90	100	110
Viscosity [mPa·s]	43.2	30.6	24.0	23.5

It can be seen from the results that the viscosity of the prepolymer system was reducing with the increase of the neutralization. The viscosity of the prepolymer system was minimal when the neutralization was 110 %. Taking into account the cost, the viscosity of the prepolymer system had been basically stable and small when the neutralization was 100 %. Therefore, the 100 % neutralization was selected in this experiment.

116.3.5 Performance of the Prepolymer System After Film Formation

According to the optimum technological condition, a solid content of prepolymer was prepared with the photoinitiator was added. Then, the resin was coated into a thickness of the film about 50 μm on the glass and its performance was tested. The test results were as follows: the viscosity was 24 mPa·s, UV curing time was 5 s, adhesion index was 1 class, and gloss was 95 Gs.

116.4 Conclusions

The water-based UV-curable epoxy acrylate synthesized by epoxy resin, PEGDE, PPGDGE, acrylic acid, maleic anhydride, and triethylamine had a low viscosity, and it can satisfy the requirement of ink-jet ink. The optimal experimental scheme was showed as follows: the mole ratio of epoxy group between acrylic acid and the mole ratio of epoxy group between maleic anhydride was 1.05:1 and 1:0.9, the reaction temperatures were 93 and 90 °C, respectively, and neutralization was 100 %.

References

1. Xie, D., & Liu, X. (2008). Synthesis of epoxy-acrylate hybrid emulsion for water-borne ink. *Packaging Engineering, 29*(9), 28–31.
2. Zhang, K., Li, T., Zhang, T., et al. (2013). Adhesion improvement of UV-curable ink using silane coupling agent onto glass substrate. *Journal of Adhesion Science and Technology, 27*(13), 1499–1510.

3. Wang, F. (2008). *Synthesis of UV curable resins and studies on their films*. South China University of Technology, Guangzhou.
4. Gong, G., & Pyo, J. (2011). Tensile behavior, morphology and viscoelastic analysis of cellulose nanofiber-reinforced (CNF) polyvinyl acetate (PVAc). *Composites: Part A, 42*(9), 1275–1282.
5. Frone, A. N., Panaitescu, D. M. (2011). PVA based composite films with cellulose fibers prepared by acid hydrolysis. *Materiale Plastice*, *48*(2) 138–143.
6. Bajpai, M., Shukla, V., & Kumar, A. (2002). Film performance and UV curing of epoxy acrylate resins. *Progress in Organic Coatings, 44*(13), 271–278.
7. Zuren, P. (2003). *Polymer Chemistry*. Chemical Industry Press, Beijing.
8. Lin, X. (2004). *Synthesis of polyurethane-modified epoxy emulsion and study of its curing*. Hunan University, Hunan.

Chapter 117
Study on the Preparation of a Disperse Blue Ink-jet Ink for Textile Printing

Min Ji, Lijing Zhang and Fuqiang Chu

Abstract A preparation method of disperse blue ink for textile ink-jet printing was discussed in this paper. The disperse blue paste was prepared by wet grinding process, and then, the moderate paste was used with different additives to manufacture the ink-jet printing ink. By testing the particle size, zeta potential, moisture retentivity of the ink, the effects of different types and dosage of the disperse dye, dispersant, and humectant on the properties of the ink-jet printing ink were analyzed. The results showed that the dispersant B had better dispersion for dye particle than the dispersant NNO; and when the content of the disperse dye was 7 %, and the content of the dispersant B was 14 % in the paste, the minimum average particle size was 197.2 nm and zeta potential was −42 mV. The optimal formula of the disperse blue ink for textile ink-jet printing was adding 25 % of homemade paste, 25 % of glycerol, 0.3 % antiseptic, and adding deionized water to 100 %. The particle size and zeta potential could meet the requirements of the ink-jet printing ink.

Keywords Ink-jet printing · Disperse blue dye · Ink-jet disperse blue ink · Dispersant

117.1 Introduction

Digital ink-jet printing technology is a new type of technology for textile printing. Compared with the traditional printing technology for textile, this kind of technology has advantages such as no plate-making, rich patterns [1].

Ink-jet ink for textile printing holds pivotal status, because it is an important material consumption in ink-jet textile printing industry [2]. Ink-jet ink for textile

M. Ji · F. Chu (✉)
College of Printing and Packaging Engineering, Qilu University of Technology, Jinan, China
e-mail: fqchu@126.com

L. Zhang
Jinan Apollo Ink Corporation, Jinan, China

mainly includes dye-based ink and pigment-based ink. Disperse dye-based ink plays a major role in dye-based ink for textile printing. The reason is that disperse-based dye ink is applicable to all kinds of synthetic fiber products, such as polyester, acrylic, and nylon [3]. Disperse dye is a kind of nonionic dye with low solubility and strong hydrophobicity. Disperse-based dye ink is mainly composed of disperse dye, dispersing agent, deionized water, and various additives. Various additives have important effect on the dispersity, moisture retention, and stability of the ink-jet ink. At present, a large variety of the disperse dye ink appear in the market, but the common problems are large particle size, wide size distribution, and nozzle jamming [4, 5]. These problems are restricting its development in advertisement printing industry.

117.2 Experiment

117.2.1 Main Experimental Materials and Instruments

Materials included disperse blue dye (366), dispersant NNO, dispersant B, glycerol (analysis of pure), diglycol (analysis of pure), ethanediol (analysis of pure), antifoaming agent, (industrial product), and antiseptic (industrial product).

Instruments: mixing grinding installation (SF0.4KW), Long Tuo Equipment Company, Shanghai; rotational viscometer (NDJ-1), Santoku Instrument Equipment Company, Shanghai; laser particle size and zeta potential analyzer, Malvern Company, China; electrothermal blowing dry box, Ty Instrument company, Tianjin; electronic balance, Mettler Toledo Instrument Company, Shanghai.

117.2.2 Experimental Method

117.2.2.1 Preparation of the Disperse Blue Dye Ink

A certain amount of disperse blue dye, dispersing agent, and deionized water were mixed and added to the grinding machine with the speed of 2000 r/min, for 6 h. The disperse paste was got after filtered with filter paper in a size of 1 um aperture.

Preliminary formula of the ink was made up of 20 % of disperse-based paste, suitable amount of moisturizer, preservatives and deionized water.

117.2.2.2 Performance Test

The particle size: a suitable amount of disperse dye paste was diluted 1000 times with deionized water and then measured the particle size of the dye with nanometer particle size distribution apparatus under the condition of 25 °C.

The zeta potential: a suitable amount of disperse dye paste was diluted 1000 times with deionized water and then measured zeta potential with zeta potential analyzer under the condition of 25 °C.

The moisture retentivity test: Different humectants were added, and a certain quality of disperse-based dye ink was poured into the weighing bottle. The ink quality was recorded as A, when the weight is no longer changed at room temperature. Then, the disperse blue ink was placed into electrothermal blowing dry box at 70 °C and the weight was recorded as B when the weight of ink kept constant [6]. Calculate moisture rate which was denoted as C according to the following formula.

$$C = \frac{A - B}{A} \times 100 \ \% \qquad (117.1)$$

117.3   Results and Discussion

117.3.1   Effect of the Disperse Dye Content on the Particle Size and Zeta Potential of Paste

Figure 117.1 shows that with the increase of the disperse dye content in the disperse paste, the disperse particle size decreased first until the content was 7 % and then increased gradually. When the disperse paste dye content was 7 %, the average particle size of disperse paste was 197.3 nm. The reason may be that when the dye content was less than 7 %, the suspended dye particle in decentralized system was less. Therefore, the friction and collision probability and intensity between the dye particle and the grinding media was weak. With the increase of the disperse dye content, the friction and collision probability and intensity between dye particle and grinding media became strong. But when the dye content increased to 9 %, the dye

Fig. 117.1 Effect of disperse dye content on particle size
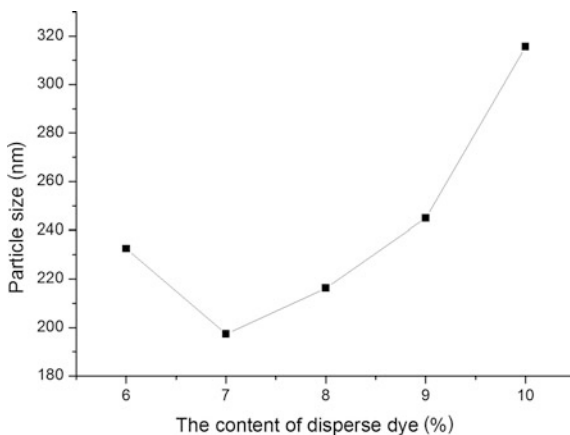
Fig. 117.2 Effect of disperse dye content on zeta potential
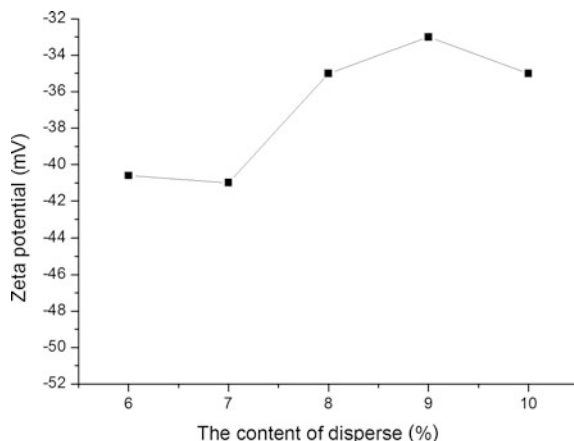
particle had more chance to contact. For the above reason, grinding effect was reduced and particle size increased obviously.

Figure 117.2 shows that with the increase of the disperse dye content in the disperse paste, the absolute value of zeta potential decreased. Zeta potential was one of the important indicator characterizations of dispersed system, and the paste stability was generally better when the absolute value of the zeta potential is between 40 and 60. Therefore, the dye content in the paste was 7 %, the zeta potential could represent better dispersion of the ink system.

117.3.2 Effect of Different Dispersants on the Ink Dispersity

The paste was prepared by adding 7 % of disperse dye, 0.25 % of antifoaming agent, 0.3 % of antiseptic, and different amount of dispersants. The dispersant with better dispersity was confirmed through the particle size test of the disperse paste.

Figure 117.3 shows that the particle size of the disperse paste decreased with the increase of the content of the dispersant. But at the same time, it could be found that when the content of dispersing agent NNO is 1.5 times of the disperse dye, and the minimum size was 243.7 nm. When the content of dispersant B was 2 times of the dye, the minimum size was 187.2 nm. Reason may be that the dispersant B as a water-based dispersion resin contained more water-based group which was advantageous to form the electrostatic repulsion inter-particle and smaller particle size.

117.3.3 Effect of Moisturizing Agent Type and Dosage

The disperse blue ink for textile ink-jet printing was prepared by adding 25 % of homemade paste, aseptic, deionized water and humectant which included different

Fig. 117.3 Effect of dispersing agent content on particle size
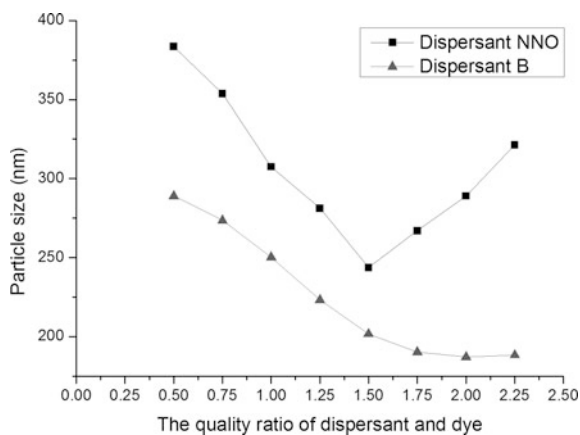
amount of glycerol, diglycol, and ethanediol. The best addition amount of moisturizer was ascertained with the test of ink moisturizing function.

Figure 117.4 shows that with the increase of the dosage of the polyhydric alcohols, the moisturizing function of the ink improve continually. The moisturizing function of polyhydric alcohols mainly lied in the structure of the hydroxy group, and the hydroxy group could combine with water molecules by hydrogen bonding. The water molecules evaporated after breaking hydrogen bonds. Therefore, with the more hydrogen bonding, the water molecules evaporated more hardly. The moisturizing function of glycerol was the best of three kinds of polyhydric alcohols, because glycerol contains most hydroxy groups in the same quality.

Fig. 117.4 The effect of humectant content on moisture rate of ink
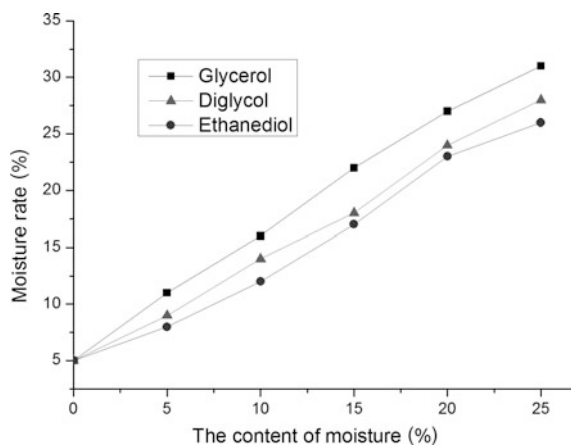
117.4 Conclusions

The experimental results showed that the optimal formula of the disperse blue paste was as follows: 7 % of the disperse dye, 14 % of the dispersant B, 0.25 % of the antifoaming agent, and deionized water with adding to 100 %. The average particle size of the disperse paste was 197.3 nm, and the zeta potential was −42 mV. According to these indicators, the dispersity and stability of disperse blue paste was good. Then, the disperse blue ink for textile ink-jet printing was prepared by adding 25 % of homemade paste, 25 % of glycerol, 0.3 % antiseptic, and adding deionized water to 100 %. The particle size and zeta potential could meet the requirements of the ink-jet printing ink.

References

1. Ding, L., Fu, S., & Gao, Z. (2009). Effects of additives on properties of disperse blue ink. *Dyeing and Finishing, 14*, 9–11.
2. Malik, S. K., Kadian, S., & Kumar, S. (2005). Advances in ink-jet printing technology of textile. *Indian Journal of Fiber and Textile Research, 30*(1), 99–113.
3. Yongqing, L. (2014). Development of sublimation transfer printing on natural fabrics. *Textile Dyeing and Finishing Journal, 36*(8), 10–13.
4. Kuanjun, F. (2006). Digital ink-jet printing technology. *Dyeing and Finishing, 32*(20), 40–43.
5. Gongpei, W. D. Z. (2012). Research on preparation and properties of a disperse red ink for ink-jet printing. *Dyestuffs and Coloration, 49*(2), 1–4.
6. Na, S., & Zhang, Q. (2008). Jetting fluency of acid-dye-based inkjet inks. *Dyeing and Finishing, 34*(23), 5–8.

Chapter 118
Study of Effectors on the Dispersing Property of Water-Based Silver Ink

Tengfei Zhou, Beiqing Huang and Xianfu Wei

Abstract In recent years, with the continuous improvement of environmental requirements, research and development of water-based ink has become a trend. And silver ink has got much attention among people because of its attractive packaging effect. So the development of water-based silver ink is necessary. The dispersion property of ink has a close contact with covering property and stability of ink. It is one of the important indices of measuring ink. In order to research the dispersion property of water-based silver ink, we test the coating layer of aluminum powder with FT-IR, and different inks were prepared by changing the different pigment/binder ratios, different dispersing process including varied speed and time, type of dispersant. The particle size and distribution of aluminum pigment are texted. Studies have shown that the best pigment/binder ratio is 1:3, the effect of dispersing agent 750 is best, and it can maintain good stability of dispersion, and the best dispersing process is stirring for 100 min at the speed of 300 r/min.

Keywords Water-based silver ink · Dispersion property · Particle size

118.1 Introduction

Aluminum powder ink is one of the most widely used and the most various metal inks. It has good metal property [1], exquisite packaging effect. It is much favored by people, hence the big demand for it. Water-based ink has the characteristic of no VOC emissions, nonflammable, and other characteristics, and it is a very promising

T. Zhou (✉) · B. Huang · X. Wei
Beijing Institute of Graphic Communication, Beijing, China
e-mail: 937328516@qq.com

B. Huang
e-mail: huangpeiqing@bigc.edu.cn

X. Wei
e-mail: weixianfu@bigc.edu.cn

environment-friendly printing ink. It is a new green supplies, which can be widely used in the green printing and packaging industry, and it has broad market prospects [2], and therefore, the development of water-based silver ink has become a necessity.

Dispersion is one of the important properties of the ink, and it not only affects the optical properties of the ink, such as color strength and transparency (opacity), but also has an impact on the viscosity of ink and the transfer of the gravure ink [3–6]. When the components of the ink are determined, preparation process of ink plays a decisive role for ink dispersion property. During the preparation process of gravure ink, the ink needs effective shearing actions in order to getting a good dispersion property. This has a great relationship with the ratio of pigment and resin (pigment to binder ratio); dispersion process and assistant selection also have some impact on the dispersion of the ink.

118.2   Experiments

118.2.1   Experimental Materials

Aluminum pigment YYH-15 (JINJIANG YAKUN PIGMENT CO.); aqueous acrylic resin (TianJin ATOZ Fine Chemicals Co.); Defoamer810; Dispersant750; Dispersant760; DispersantJL115A; DispersantJL254Y; deionized water.

118.2.2   Experimental Apparatus

Microtrac S3500 Laser particle size analyzer (AMERICA); D2004 W electric mixer (Shanghai Division Music Instrument Co.); Electronic balance UX2200H (Shimadzu); 400-ml beaker; glass rod; Ncolet is 50 Infrared spectrometer.

118.2.3   Method of Ink Preparation

Aluminum powder, grinding resin, foaming agent, and deionized water are added to the beaker, stirring with a glass rod until the predispersing uniformly. And then they are placed in a high-speed mixer with 400 n/min stirring rate for 2 h, and the silver water ink is finally obtained.

118.2.4   Test Methods

- Test the ink's dispersion by the laser particle size analyzer to obtain aluminum pigment particle size distribution, and the particle size at 95 % works as the final particle size of ink.

- FT-IR Test: Room temperature, KBr compression method. Take a small amount of samples to grind uniform with KBr. Tablet under compression machine, and then test it (32 times the number of scans, scanning range of 400–4000 cm^{-1}).

118.3   Results and Discussion

118.3.1   Infrared Testing of Coated Aluminum Particles

In this experiment, the aluminum powder particles are coated with fatty acids. Do infrared testing to verify the presence of aluminum-coated layer. As shown in Fig. 118.1, the absorption peak of 2800–3000 cm^{-1} shows a sp3 hybridized C–H stretching vibration. The absorption peak of 1400 cm^{-1} indicates the bending vibration of C–H. The peak near 1700 cm^{-1} indicates the presence of a carbonyl group. This is entirely different from the ordinary aluminum particles (only with the O–H stretching vibration's infrared absorption peak at 3300–3500 cm^{-1}). Therefore, this is verified in Fig. 118.1 that the aluminum powder used in this experiment is coated with a fatty acid.

118.3.2   Influence of Pigment/Binder Ratios on the Dispersing Properties

Pigment to binder ratio has a great impact on the dispersion of ink. This is because the dispersion process is actually a flow process; only to achieve the best flow point, ink can get effective shear effect and the dispersion can reach the best state. The shear action is different due to the different pigment/binder ratio. In order to make the ink as the best dispersing state, we should first determine the best

Fig. 118.1 Infrared spectrum of coated aluminum particles
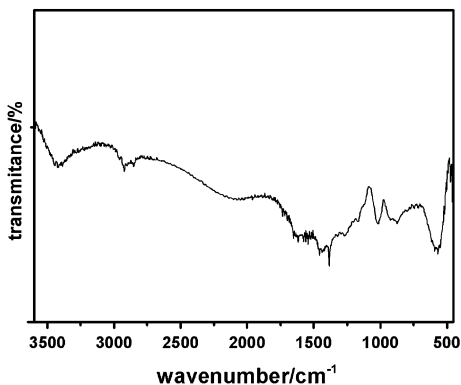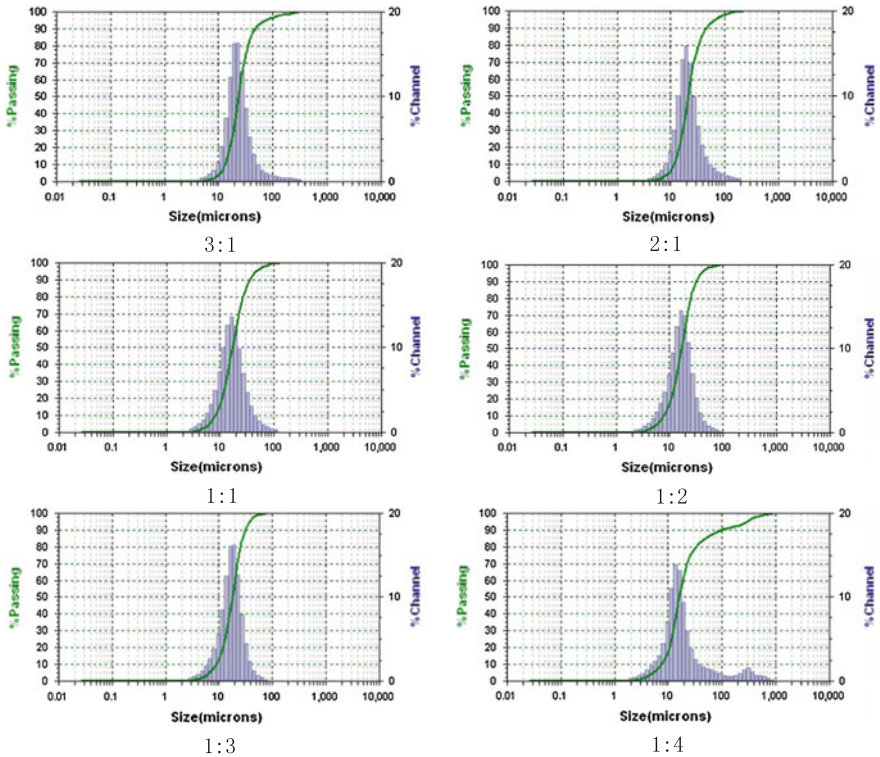
Fig. 118.2 Particle size distribution map of different pigment/binder ratio

pigment/binder ratio, and then use the best ratio to prepare the ink. Figure 118.2 shows the particle size distribution of aluminum powder ink which is measured by laser particle size analyzer.

As shown in Fig. 118.2, when the pigment/binder ratio is too small or too large, the particle size distribution of the ink is discrete and the large particle size is possible to exit. Only using the appropriate ratio, the ink with concentrated particle size distribution can be prepared.

When the laser particle size analyzer is used to test the particle size of the aluminum powder, the particle size at 95 % is more accurate. Figure 118.3 shows the column chart of the aqueous silver ink particle size at different pigment/binder ratios.

As shown in Fig. 118.3, with the increase in resin proportion in ink system, the overall presentation of the ink particle size tends to first increase and then decrease. In particular in the pigment to binder ratio of 1: 3, the performance of aluminum powder ink particle size is the minimum. This figure explains that the best pigment/binder ratio of water-based silver ink is 1: 3 under the experimental conditions.

Fig. 118.3 Effect of pigment/binder ratio on the particle size
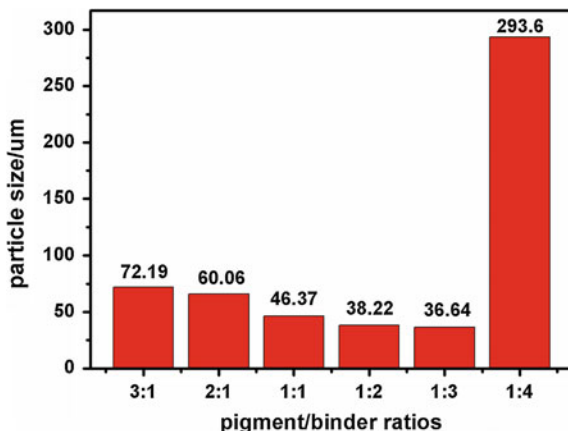
118.3.3   Influence of the Dispersant' on the Dispersion Properties

Dispersing agent has a certain effect on the dispersion of pigment particles in ink. In order to study the effect of dispersing agent on the dispersion properties of ink, four kinds of dispersing agents are selected (dispersing agents 750, 760, JL115A, JL254Y). They are added to the raw materials to prepare the corresponding ink. As shown in Fig. 118.4, the A represents the particle size measured on the day that the ink is preparing, and the B represents the particle size measured after a week.

As shown in Fig. 118.4, among the four kinds of inks with different dispersing agents, the ink with dispersing agent 750 has the best dispersion property. And then the dispersing agent 760, JL254Y, JL115A are following in order. After standing for a week, the four kinds of inks were tested by the laser particle size analyzer

Fig. 118.4 Effect of dispersants on the particle size
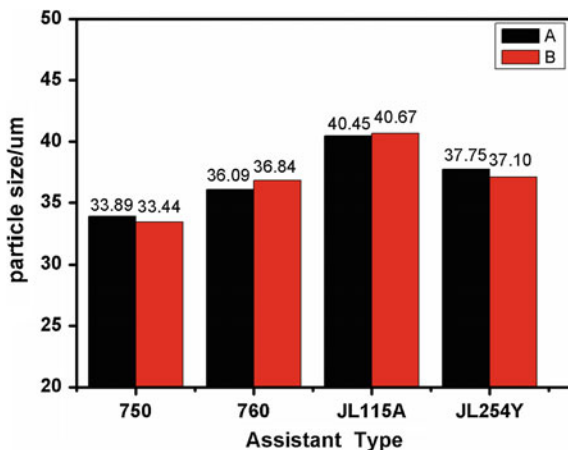
again. By comparing the numerical values of A and B, the particle size did not change too much after one week, which shows that the dispersion stability of ink has a good performance.

118.3.4 Influence of the Dispersed Process on the Dispersing Properties

118.3.4.1 Comparison Between Stirring and Grinding Dispersing Process

In the process of preparing ink, two kinds of dispersing technology are usually used. And different dispersion processes have different effects on the dispersion of ink. Therefore, we use the stirring and grinding process to prepare two sets of inks and contrast the two sets of inks' particle size as shown in Fig. 118.5 (A grinding, B stirring).

From Fig. 118.5, it can be seen that there is no difference in the effect of stirring and grinding process on ink dispersion. But the ink that is obtained by grinding process is easy to be black because of the oxidation of aluminum powder. YH15 is a kind of aluminum powder with coating layer, and grinding will destroy the coating structure, so that the aluminum powder is easy to react with water and oxygen. Therefore, we use the stirring process in this experiment.

118.3.4.2 Influences of Stirring Speed and Time on the Dispersing Properties

In the process of preparing ink, the speed and time of stirring will also have a certain effect on the dispersion of aluminum powder ink. If the stirring speed is too slow and the stirring time is too short, aluminum pigment cannot get sufficient

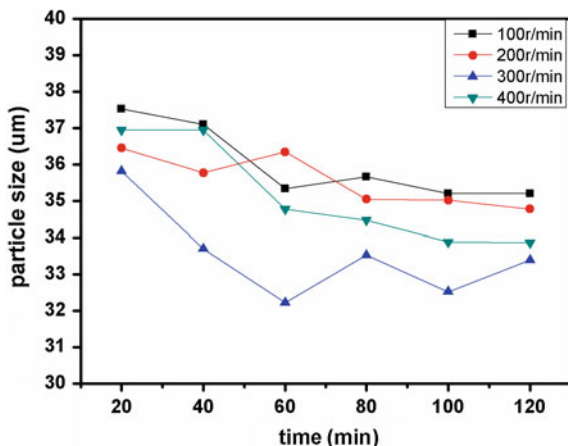**Fig. 118.5** Effect of dispersion process on particle size
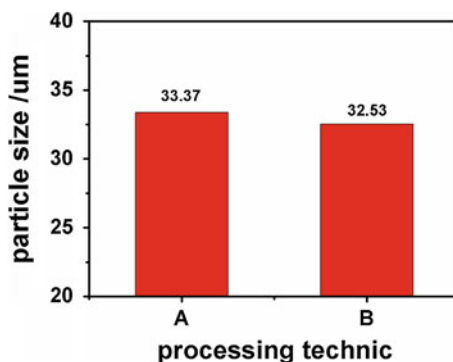
Fig. 118.6 Effect of stirring speed and time on particle size

shearing action. Excessive stirring speed makes the heavy and large aluminum powder group do eccentric exercise, and it cannot get effective collision by the stirring paddle, so that it also cannot get sufficient shearing action. We have prepared four sets of inks by the best pigment/binder ratio at the speeds of 100, 200, 300, and 400 r/min, which are stirring for 2 h and each 20 min to sampling to measure its particle size. Figure 118.6 shows the influence of stirring speed and stirring time on particle size of aluminum powder ink.

The results are shown in Fig. 118.6, when the stirring speeds are 100, 200, 400 r/min and the dispersed effect is not very good. However, when the stirring speed is 300 r/min, the particle size of the aluminum powder inks shows a minimum. For stirring time, under the four stirring speeds, the changing trend of particle size is gradually decreasing and then to a level. When the length of time is 100 min, the particle sizes have no significant changes. Therefore, the optimal dispersed process for the water-based silver ink is stirring for 100 min at the speed of 300 r/min.

118.4 Conclusions

Through the study of effectors on the dispersion property of water-based silver ink, the final conclusions are given as follows:

- Pigment/binder ratio has a greater impact on the ink dispersion. In order to get good dispersion properties of the ink, it is necessary to use the best pigment/binder ratio. Under the experimental conditions, the best pigment/binder ratio of water-based ink is 1: 3.
- Under the experimental conditions, the effect of dispersing agent 750 is best, and its ink can maintain good stability of dispersion.
- Under the experimental conditions, the best dispersing process of water-based silver ink is stirring for 100 min at the speed of 300 r/min.

References

1. Wang, N. (2012). *Research of silver inks' formulated process and tinting*. Xi'an: Xi'an University of Technology.
2. Zhang, F., Huang, P., Wei, X., & Xin, L. (2014). Influence factors of water-based gravure inks' gloss. *Journal of Beijing Institute of Graphic Communication, 22*(2), 17–19.
3. Huang, P., Gaojie, X., & Chen, Y. (2007). Study of dispersion property of water-based gravure ink. *Packaging Engineering, 28*(11), 65–67.
4. Yang, X., & Wang, J. (2000). *Printing materials and suitable* (pp. 65–67). Beijing: Printing Industry Press.
5. Bei, J. (2002). *Gravure printing* (pp. 21–27). Beijing: Chemical Industry Press.
6. Qian, J. (2003). *Printing ink application technology* (pp. 42–45). Beijing: Chemical Industry Press.

Chapter 119
Preparation and Research
of UV Gravure Ink

**Peiqing Huang, Yiran Li, Liping Yang, Xianfu Wei, Ran Zhang,
Dawei Cao and Huangbin Wu**

Abstract In order to gain UV gravure ink that has good performance and print quality, the study determined the prepolymer and the ratio of pigment and binder applied in the primary ink according to the study of ink dispersibility. In the ink preparation process, the effect of monomer and prepolymer on curing speed, adhesive force, and transfer performance of ink was studied; meanwhile, the effect of different kinds of photoinitiator on curing speed of ink was studied, and finally, we used formulation design principles to optimize the ink formulation. Study shows that the gravure ink has great dispersibility, relatively high curing speed, and good adhesion performance on plastic substrate, good ink transfer ability, and relatively high printing density.

Keywords UV gravure ink · Performance · Preparation

119.1 Introduction

As one of the important package printing methods, gravure printing has huge market, but at present, most domestic gravure inks are solvent ink and water-based ink that contain a certain amount of alcohols; they all have large amount of VOC and pollute the environment badly, in a state of being governed [1]. Due to its environmentally friendly, energy saving, high efficiency, high quality, better adaptability, and so on, UV ink becomes one of the noteworthy environmental printing inks [2]. As one of the alternatives of gravure solvent printing ink, UV gravure printing ink can be widely used in cigarette package, wine package, cosmetics package, and other high-grade packaging and printing field, so it has a great prospect for development.

P. Huang (✉) · Y. Li · L. Yang · X. Wei · R. Zhang · D. Cao · H. Wu
Beijing Institute of Graphic Communication, Beijing, China
e-mail: huangpeiqing@bigc.edu.cn

119.2   Experiments

119.2.1   Experimental Materials

Pigment: Benzedrine yellow, pigment lithol rubine, phthalocyanine blue; Prepolymer: V100, 6362-100, 6215-100, EB270, EB811; Monomer: EOEOEA, DPGDA, TPGDA, NPGDA, HDDA, TMPTA; Photoinitiator: 184, 907, 1173; Auxiliaries: dispersing agents, EHA, etc.

119.2.2   Equipment

Isothermal magnetic agitator (Jiangsu Ronghua instrument Co.); JJ-I-type mechanical agitator (Changzhou guohua electric appliance Co., Ltd); GJ-2S type high-speed grinding machine (Qingdao haitong dedicated instrument Co., Ltd); Microtrac S3500 Laser Particle Sizer (US Microtrac Co.); portable viscometer (Hydramotion Ltd.); Light Hammer 6 type UV-curing-type machine (America fusion uv co., Ltd); X-Rite530 densitometer (America X-Rite co., Ltd); and photogravure proofing machine (British RK Corporation).

119.2.3   Preparation of Printing Ink

UV gravure ink preparation process includes two parts: based ink preparation and the adjustment of the ink [3]. We add the prepolymer, monomer, and dispersant separately to the beaker, put the beaker onto the magnetic mixer and move it until the liquor is uniform, and then put pigment added liquor under the JJ-I-type mechanical agitator to predisperse for about 30 min. Then, the pre-dispersed paste should be poured into a grinder and added in the appropriate weight of zirconium beads (diameter 1.6–1.8 mm), and we let the high-speed grinder mill for 120 min, so that the pigment can disperse in connection with compound well.

The adjustment of the ink is the process that adds prepolymer, photoinitiator, monomer, and additives to the based ink, and we put the mixer under the JJ-I-type mechanical agitator for about 30 min. By adjusting the ratio of prepolymer to monomer in the formulation, the viscosity of the ink prepared was controlled to 200 mPa·s, which ensures the ink has a good transfer performance. Use the portable viscosimeter to test the viscosity of each ink sample.

119.2.4   Ink Proofing Methods

In the study, we use photogravure proofing machine to print the ink prepared onto the BOPP film; in the proof process, the printing speed is 32 m/min, the print plate is dual 8-cell-level version style plate whose screen rulings are 150 lines/inch and depths are 40, 38, 36, 34, 32, 30, 28, and 24 μm, respectively.

119.2.5   Test Methods of Ink Performance and Printing Quality

119.2.5.1   Test Method of Ink's Dispersibility

The dispersibility of ink can be tested by the laser particle sizer; the particle size and distribution of ink can be obtained from the particle size distribution graphs of the ink. In this paper, the particle size of ink was expressed by 95 % of the maximum particle size distribution of ink.

119.2.5.2   Test Method of Ink's Curing Speed

Put the UV-curable ink proofing sample on the UV-curing machine for curing; there are two kinds of test methods: (1) Direct method controls the light source power to be 200 w/cm, changes the UV-curing machine's conveyor speed, and marks the maximum speed that needed for drying a color piece at 40 μm depth part as ink's curing speed. (2) Indirect method controls the UV-curing machine's conveyor speed to be 75 m/min, changes the light source power, and marks the minimum power that needed for drying a color piece at 40-μm-depth part as the ink's critical curing power; the smaller the value, the faster the ink curing speed. We use finger-touch method to characterize the maximum curing speed of ink; this method is using finger to touch the color piece at 40-μm-depth part, if the ink is not sticky and the finger can stick nothing, which means the ink is totally dry [4].

119.2.5.3   Test Method of Ink's Adhesive Force

After curing process, we use 3-M adhesive tape to cling to the color piece at 40-μm-depth part solidly and quickly to remove it and observe the area ratio of ink film clinging to the 3-M tape after its removement. When the area ratio is 0 %, mark it as level-5; when the area ratio is lesser than or equal to 5 %, mark it as level-4; when the area ratio is greater than 5 % and lesser than or equal to 15 %, mark it as level-3; when the area ratio is greater than 15 % and lesser than or equal to 35 %, mark it as

level-2; when the area ratio is greater than 35 % and lesser than or equal to 65 %, mark it as level-1 and; when the area ratio is greater than 65 %,mark it as level-0.

119.2.5.4 Test Method of Ink's Color Density

Use densitometer to test color density of the cured color piece at 40 μm depth.

119.3 Experiment Results and Analysis

119.3.1 Reaserch of Ink's Dispersibility

The dispersibility is one of the important physical properties for ink, not only does it affects the optical properties of the ink, such as tinting strength and transparency (opacity), but also it has a certain impact on the viscosity and transfer of the ink [5]. Dispersibility of the ink refers to the degree of pigment dispersion in the ink vehicle. In order to make pigment to have better dispersibility, first, we should guarantee the ink vehicle can wet the pigment well [6] and second, it should have a great relationship with the flow state of system when grinding; the system should reach the laminar flow state that means to break pigment aggregates under the action of viscous shear force. Therefore, the choice of prepolymer and the proportion of pigment and prepolymer (the ratio of pigment and binder) of the based ink have relatively large influence on the dispersibility of ink. Fixing species of pigment and monomers, and the content of pigments, we use different kinds of prepolymer and the ratio of pigment and binder to make cyan and magenta UV gravure based ink and test their dispersibility, and the results are shown in Fig. 119.1.
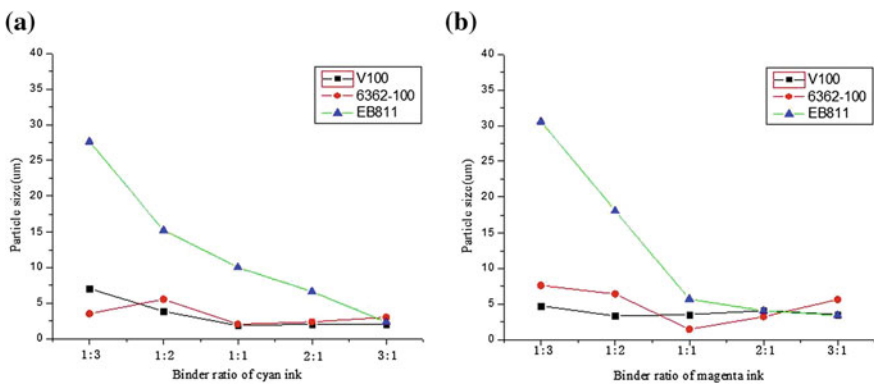
Fig. 119.1 **a** Influence of prepolymer on dispersibility of the cyan ink. **b** Influence of prepolymer on dispersibility of the magenta ink

As shown in Fig. 119.1, for prepolymer V100 and 6362-100, with the reduction of the ratio of pigment and binder, the particle size of prepared based ink decreases; when the ratio of pigment and bindero reaches a certain value, with the reduction of the ratio of pigment and binder, the particle size of prepared based ink increases on the contrary. In the case of prepolymer EB811, under the experimental design of this study, with the reduction of the ratio of pigment and binder, the particle size of prepared based ink decreases. This is due to that the substance of the preparation of the based ink is making pigment disperse in the ink vehicle by grinding way, and the process of dispersion is also the process of flow, only achieving the best flow point, the ink can get the most effective grinding and shearing action, thus the dispersion is the best. The reduction of the ratio of pigment and binder means the reduction of prepolymer, so the viscosity of the ink system reduced; when grinding, the difference of the ratio of pigment and binder causes the difference of ink's viscosity and the difference of shearing action too [6]. Therefore, in order to make the ink prepared has best dispersibility, firstly we should test the best ratio of pigment and binder, and then use the best ratio of pigment and binder to prepare the based ink. Different prepolymers have different viscosities; the difference of fluidity of oil absorption of different pigments causes the difference of the best ratio of pigment and binder. As shown in Fig. 119.1, when preparing the cyan and magenta based ink, the ratio of pigment and binder of EB811 is 3:1, the ratio of pigment and binder of 6362-100 is 1:1, the ratio of pigment and binder of V100 is 1:1 and 1:2, and the prepared ink has the lowest particle size. Because the viscosity of prepolymer EB811 is large, its best ratio of pigment and binder is less than other two kinds of prepolymer.

To sum up, and known from Fig. 119.1, under this experimental condition, when the ratio of pigment and binder is 1:1, using prepolymer V100 and 6362-100 to prepare cyan and magenta UV gravure ink, respectively, the dispersibility of them is the best, and the dispersibility of prepared based ink is shown in Fig. 119.2; we can see that the ink have relatively small particle size and narrow distribution.

As shown in Fig. 119.1, we can also know that the based ink prepared by different types of prepolymer has different dispersibility, the based cyan and magenta inks prepared by V100 and 6362-100, respectively, have the smallest particle size. This is due to that the pigment's dispersibility closely relates to prepolymer's wetting ability for pigment, the difference of prepolymer's structure causes the difference of its wetting ability for pigment, and the better the wet ability, the better the dispersion of
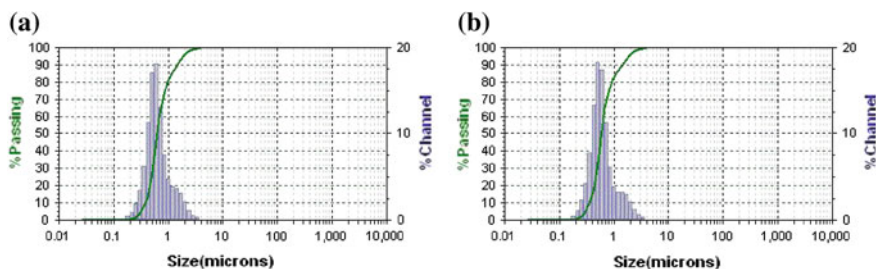

Fig. 119.2 Particle size distribution of prepared based ink. **a** cyan **b** magenta

pigment. Similarly, the different pigments corresponds to different prepolymers that can well wet it; thus, in order to make the ink have great dispersibility, different pigments need to be dispersed by different prepolymers.

119.3.2 Research of the Components in Ink's Adjustment

After the based ink was prepared, we need to adjust the ink performance to make sure that the ink has great printability. The components needed to be adjusted are prepolymer, monomer, photoinitiator, and so on.

119.3.2.1 Prepolymer

Prepolymer is an important component in UV ink's vehicle; it has an important impact on the transfer and film-forming ability. We fixed the other components of the ink, ensuring the viscosity of the ink prepared is consistent and can meet the requirements of gravure printing, used different prepolymer to prepare the yellow UV gravure ink, tested the curing speed, adhesive force and color density of the ink, the results are shown in Figs. 119.3, 119.4, and 119.5.

As shown in Fig. 119.3, the ink prepared by different types of prepolymer has different critical curing speed; the critical curing speed of EB811-prepared ink is minimum, which means it has the highest curing speed. This is associated with the structure of prepolymer, the functionality of EB811 is 4, but the functionality of the other two prepolymer are both 2, the more functionality, the faster the reaction, and the viscosity of EB811 is the lowest, so that the monomer can be less used when prepare the ink that have same viscosity, this is also the reason why EB811-prepared ink has high curing speed.

Fig. 119.3 Influence of prepolymer on critical curing power of the ink
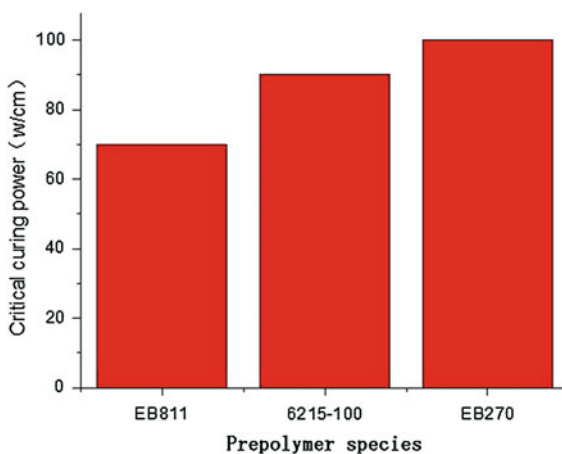
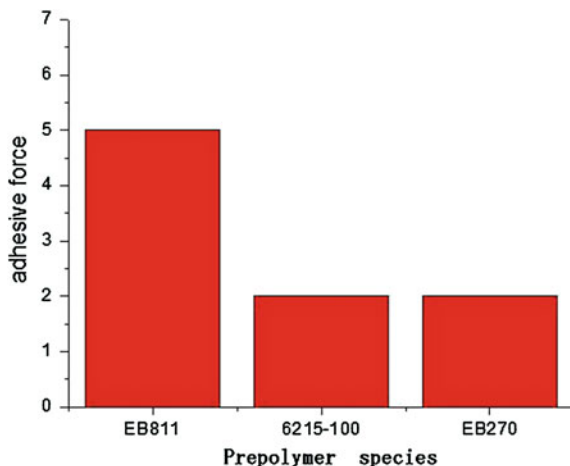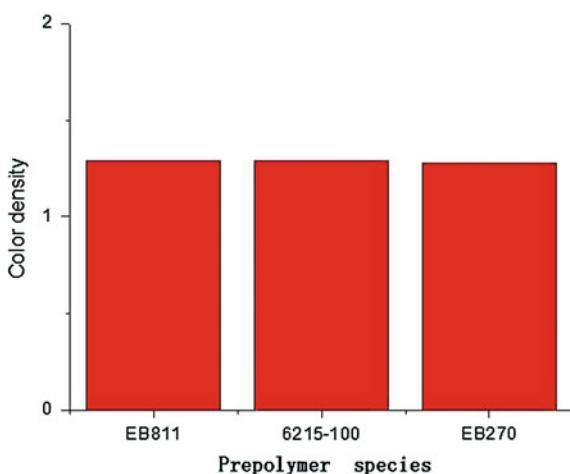**Fig. 119.4** Influence of prepolymer on adhesive force of the ink

Fig. 119.5 Influence of prepolymer on color density of the ink

As shown in Fig. 119.4, the ink prepared by different types of prepolymer has different adhesive force; the adhesive force of EB811-prepared ink on plastic substrate is the best. This is associated with the structure of prepolymer, prepolymer EB811 is polyester acrylate, and it has great adhesive force. Prepolymer 6215-100 is epoxy acrylate, it has worse adhesive force, and prepolymer EB270 is aliphatic polyurethane acrylate, its poor adhesion related to its structure.

As shown in Fig. 119.5, the proof printed by the ink prepared by different types of prepolymer has basically same color density. Color density is closely related to the transfer ability of the ink; if the transfer performance of the ink is great, the volume of ink that transferred to the substrate is large, and thus, the color density is high [7]. The transfer performance of the ink is mainly influenced by ink's rheological property; since the viscosity of the ink prepared by different types of

prepolymer is controlled to be same; same color density means the ink prepared by different types of prepolymer has the same rheology ability.

119.3.2.2 Monomer

As the active diluent, monomer is also an important component in UV ink's vehicle, and it has an important impact on the transfer and film-forming ability. We fix the other components of the ink, ensure the viscosity of the ink prepared is consistent and can meet the requirements of gravure printing, use different monomer to prepare the yellow UV gravure ink, and test the curing speed, adhesive force, and color density of the ink, the results are shown in Figs. 119.6, 119.7, and 119.8.

As shown in Fig. 119.6, the ink prepared by different types of monomer has different critical curing speed; the critical curing power of HDDA-prepared ink is minimum, that means it has the highest curing speed. Although the impact of the monomer's functionality on UV ink's curing speed is large, the impact of ratio of prepolymer and monomer on UV ink's curing speed is not small; although HDDA is a kind of double functional monomer and its viscosity is small, its dilution effect is obvious; thus, the monomer can be less used when preparing the ink that has same viscosity, so that the prepared ink contains more prepolymer, this is the reason why the prepared ink has high curing speed. Similarly, as shown in Fig. 119.6, the critical curing speed of the ink prepared by three faculties' monomer TMPTA is not the fastest, it is because of its large viscosity and worse dilution effect, so that the monomer can be largely used and prepolymer can be lessly used when prepared ink has same viscosity.

As shown in Fig. 119.7, the ink prepared by different types of monomer has different adhesive force; the adhesive force of TPGDA-prepared ink and HDDA-prepared ink on plastic substrate is great; however, the adhesive force of EOEOEA-prepared is worst. This is related to the monomer's structure; the

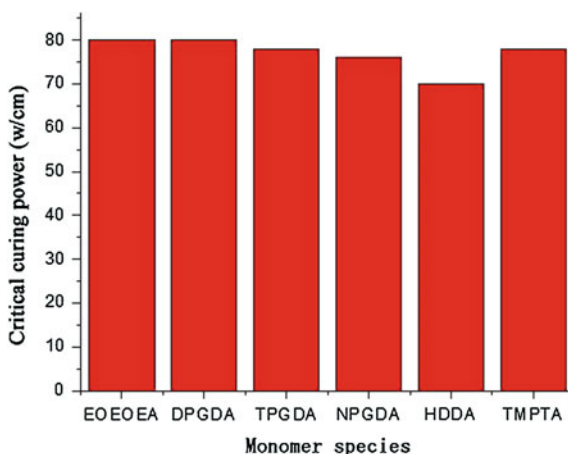**Fig. 119.6** Influence of monomer on the critical curing power of the ink

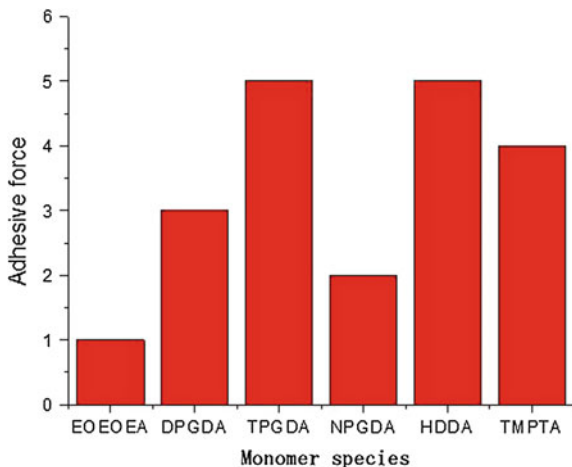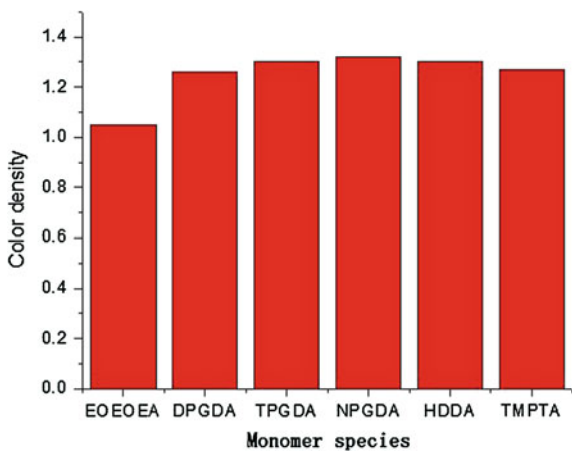**Fig. 119.7** Influence of monomer on the adhesive force of the ink

Fig. 119.8 Influence of monomer on the color density of the ink

structures of monomer used in the study are shown Fig. 119.9. Monomer TPGDA is tripropylene glycol diacrylate, and monomer HDDA is 1,6-Hexanediol diacrylate, and their molecular chain are quite long and branched-chain are less, all of this help to improve the ink's adhesion on plastic.

As shown in Fig. 119.8, the ink prepared by different types of monomer has different color density, the color density of EOEOEA-prepared ink is minimum, the color density of ink prepared by other monomers has little difference, and the color density of NPGDA-prepared ink is maximum. Ink's viscosity is not the only factors deciding the ink's rheological properties, so the ink having same viscosity is not necessarily to have same rheological properties. Although the viscosity of different monomers' prepared ink may be same, their rheological properties have difference, so the ink transfer amount has difference and the color density of the ink has difference.

Fig. 119.9 Structures of
monomer

EOEOEA   NPGDA   DPGDA

HDDA   TMPTA   TPGDA
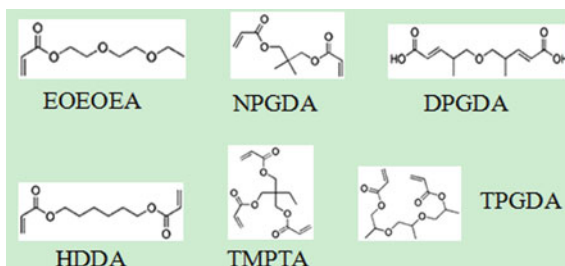
119.3.2.3 Photoinitiator

In the UV-curing system, photoinitiator firstly absorbs ultraviolet light and then triggers the polymerization reaction in the system, so it is an important component in UV ink; it has an important impact on the curing speed of the ink. We fix the other components of the ink, use different photoinitiator to prepare the cyan and magenta UV gravure ink, and test the curing speed of the ink; the results are shown in Fig. 119.10. And the adsorption spectrum curves of cyan and magenta pigment were also tested, and the results are shown in Figs. 119.11 and 119.12.

As shown in Fig. 119.10, the ink prepared by different types of photoinitiator has different critical curing speeds; the critical curing speed of 1173-prepared cyan ink and 907-prepared magenta ink are the fastest. In the UV-curing system, photoinitiator needs to firstly absorb the ultraviolet radiation to produce reactive intermediate and then triggers the polymerization reaction in the system; therefore, the light absorption efficiency of photoinitiator and its initiator efficiency can directly influence the curing speed of the ink [8]. For UV ink, if you want to improve the light absorption efficiency of photoinitiator, the adsorption spectrum curves of photoinitiator should not only match with the emission spectrum of light source but also match with the spectrum window of the pigment where the pigment absorption in the UV region is relatively weak [9]. As shown in Fig. 119.11, the spectrum

Fig. 119.10 Influence of
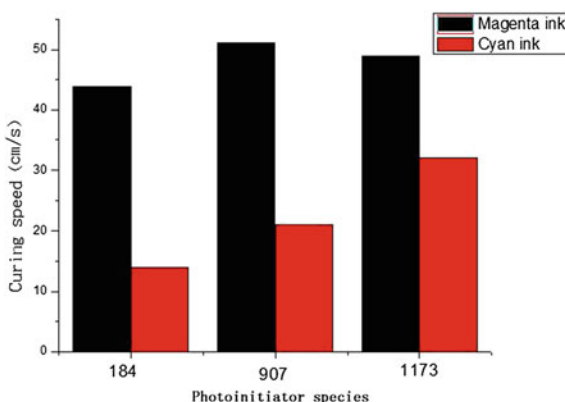photoinitiator on curing speed
of the ink

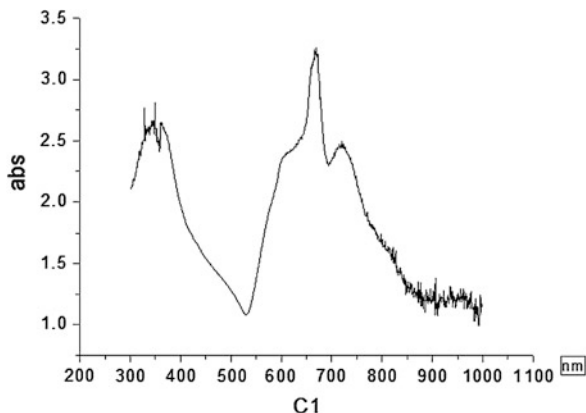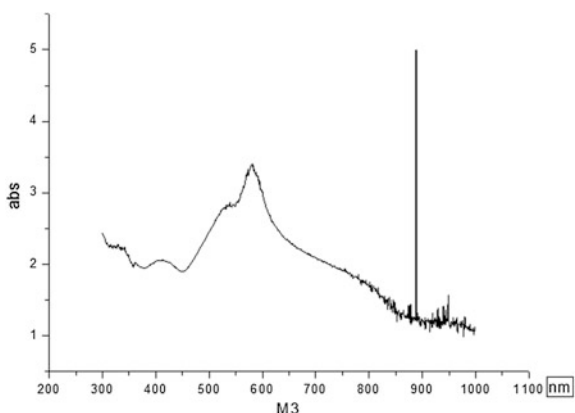**Fig. 119.11** Adsorption
spectrum curve of cyan
pigment

Fig. 119.12 Adsorption
spectrum curve of magenta
pigment

window of cyan pigment is nearly 355 and 335 nm, and photoinitiator 1173 pho-toinitiator 184 have adsorption spectrum curves at 320–335 nm, which means they can match with the spectrum window of the pigment, but due to that photoinitiator 1173 has larger molar extinction coefficient than photoinitiator 1173 at other high-pressure mercury lamp emission wavelengths except 365 nm [10], so the critical curing speed of 1173-prepared cyan ink is faster. The UV absorption peak of photoinitiator 907 is at 320–325 nm, although the match of 907 and the spectrum window of cyan pigment are not good; its photoinitiation efficiency is high, so the prepared cyan ink has high curing speed. Similarly, as shown in Fig. 119.12, the spectrum window of magenta pigment is around 360 and 380 nm, the match of magenta pigment and other photoinitiator are all not good, but because of the high photoinitiation efficiency of 907, the prepared cyan ink has high curing speed.

As shown in Fig. 119.11, magenta ink's curing speed is higher than cyan ink's curing speed; this is associated with the absorption of pigment to light [10]; cyan pigment's absorption of light is greater than the magenta pigment, so the curing speed of cyan ink is low.

Table 119.1 Performance and printing quality of UV gravure ink prepared

Particle size (μm)	Viscosity (mPa·s)	Curing speed (m/min)	Adhesive force (grade)	color density
1–5	190–210	40–70	4–5	Y: 1.2–1.3; M: 1.8–1.9; C: 2.0–2.1; BK: 2.3–2.4

119.3.3 Performance and Printing Quality of UV Gravure Ink Prepared

Based on the above research results, and by using the formula design experiment to optimize the ink formula and adding the appropriate additives, we prepared the four-color UV gravure printing ink, and their performance and printing quality are shown in Table 119.1.

As shown in Table 119.1, the prepared UV gravure printing ink has great dispersibility, relatively high curing speed, good adhesion ability on plastic, and great transfer ability; the prints have relatively high printing density, so the prepared UV gravure printing ink has good performance and printing quality.

119.4 Conclusions

Through the research above, we get the following conclusions under this experimental condition:

1. Prepolymer's species and its ratio of pigment and binder have a great influence on the dispersibility of the UV gravure ink, the ink prepared by the prepolymer that can wet the pigment well according to the best ratio of pigment and binder can get great dispersibility. When the ratio of pigment and binder is 1:1, use prepolymer V100 and 6362-100 to prepare cyan and magenta UV gravure ink, respectively; the dispersibility of them are the best.
2. Prepolymer and monomer have an influence on the curing speed and adhesive force of the UV gravure ink. The ink prepared by prepolymer EB811 and monomer HDDA has high curing speed; the ink prepared by prepolymer EB811 and monomer TPGDA and HDDA has good adhesion ability on plastic. When the prepared ink has the same viscosity, the species of prepolymer have little influence on ink's transfer ability, but the species of monomer have influence on ink's transfer ability.
3. Photoinitiator have a great influence on the curing speed of the UV gravure ink, the adsorption spectrum curves of photoinitiator should match with the spectrum window of the pigment, and the photoinitiator should have high initiator

efficiency. The cyan and magenta UV gravure ink prepared by photoinitiator 1173 and 907 respectively have high curing speed.

4. The four-color UV gravure printing ink prepared has good performance and printing quality.

References

1. Wei, X. (2009). Printing ink technology and development trend. *Printing Technique*.
2. Jin, Y. (2008). The progress of the market radiation curing technology. In *The silver halide imaging conference on development and application of technology and materials*.
3. Lin, Y., & Xue, L. (2009). *Ink technical manuals*. Beijing: Printing Industry Press.
4. Wei, J., & Jin, Y. (2013). *Photocureable coating*. Beijing: Chemical Industry Press.
5. Qi, X., Zhou, W., & Yang, Y. (2008). *Printing materials and eligibility*. Beijing: Printing Industry Press.
6. Li, X. (1986). *Printing ink*. Beijing: Printing Industry Press.
7. Wei, X., Huang, B., & Deng, P. (2014). *The printing principle and process*. Beijing: China Light Industry Press.
8. Yang, J., Zeng, Z., & Cheng, Y. (2006). *Uv-curable coatings and application*. Beijing: Chemical Industry Press.
9. Wang, D., Jiang, L., & Cheng, Y. (2003). *UV-curable materials—theory and applications*. Beijing: Science Press.
10. Jin, Y. (2010). *Light curing material performance and application manual[M]*. Beijing: Chemical Industry Press.

Chapter 120
Preparation and Performance of Edible Screen-Printing Ink with Chitosan

Yanfen Zhang, Xiaodong Li, Xiaozhu Mou and Na Li

Abstract Chitosan was used as a binder of edible screen-printing ink by analysis and exclusion methods in this paper. By the research of the dissolubility of chitosan, viscosity of solution, concentration and pH of acetic acid, amount of alcohol, and amount of pigment had been determined. Results showed that chitosan solution was used as binder of edible screen-printing ink was feasible. This edible screen-printing ink prepared with the method has excellent properties such as fineness, viscosity, initial dryness, tinting strength, and adhesion to substrate. So it can be used safely in food package printing industry. And it should decrease food pollution bringed by printing ink. The study on edible ink meets with the requirement of green printing.

Keywords Chitosan · Edible screen-printing ink · Acetic acid

120.1 Introduction

In particular, when ink was used in food and drug package printing, the harmful substances in the dry ink film would penetrate into food and drugs [1, 2]. As these problems were worrisome, many developed countries offered the concepts of edible

Y. Zhang (✉) · X. Li
Media Communication System, Dongguan Polytechnic, Guangdong, China
e-mail: whzhangyanfen@163.com

X. Mou
Department of Printing and Packaging Engineering, Shanghai Publishing and Printing College, Shanghai, China

N. Li
Patent Examination Cooperation Jiangsu Center of the Patent Office, Jiangsu, China

ink. Del Monte Pet Corporation in the USA launched a new kind of dog food with edible ink printed on the edge of dog food [3, 4]. A kind of P&G potato chip with edible ink printed on it was popular in Europe [5, 6]. The food industry association in Germany reported a new kind of edible ink with glue of animal protein, vegetable oil, bee sugar, butter, and alcohol. And this edible ink had received the widespread attention. Many literatures showed that the products with edible ink were quite commonly used abroad, and unexpected successes had been achieved. But in China, the edible ink was still under development.

Edible ink should not only have the printing properties like tradition ink, but also should be eatable. Chitosan, as a kind of promising natural biomaterial, had advantages of antibacterial activity, non-poisonous and biodegradable. And the chitosan solution was ideal binder to prepare edible screen-printing ink. Therefore, developing edible ink with chitosan solution had important practical significance and practical value [7–9].

120.2 Experiment

120.2.1 Materials

Food-grade acetic acid (concentration: 99 %) was produced by Xinwang Chemical Co., Ltd., Jinan, China. Chitosan (molecular weight: 220000, deacetylation degree: 85 %) was purchased from Yuhuan Dayang Bio-chemical Co., Ltd., Zhejiang, China. Distilled water was made in Wuhan University of chemistry, Hubei, China. Food-grade ethyl alcohol (concentration: 95 %) was produced by Xilong Chemical Co., Ltd., Guangdong, China. Natural pigment was produced by Oriental kyle Trade Co., Ltd., Beijing, China. Soybean oil was produced by COFCO Co., Shanghai, China. Tween −80 was produced by Yuanye Technology Co., Ltd., Shanghai, China. Glycerin was produced by chuzhou district chang tai glycerin factory Huai'an, China.

120.2.2 Preparation of the Edible Screen-Printing Ink

Chitosan, acetic acid, and alcohol were firstly mixed to get the binder of edible screen-printing ink. And then, nature pigment and proper additives were added into the binder. All materials above should be mixed completely to ensure that the ink was easy to print and possess excellent properties (Table 120.1).

Table 120.1 A formula of black screen-printing ink

Element	Ingredient	The proportion of ingredients (%)
Binder	Chitosan	4
	3 % acetic acid solution	27
	Alcohol	31
Pigment	Edible carbon black	30
Defoamer	Soybean oil	0.5
Dispersant	Tween −80	2
Plasticizer	Glycerin	5
Antifriction	Beeswax	0.5

Table 120.2 Properties of black screen-printing ink

Test item	Technical indicator
Fineness (μm)	15
Viscosity (mPa s)	4000
Initial dryness (mm/30 s)	25
Tinting strength (%)	90
Adhesion	Grade 8
Density	1.9
Stability	good

120.2.3   Test Methods for Ink Properties

According to China standard testing methods, the paper focused on testing edible screen-printing ink properties such as fineness, viscosity, initial dryness, tinting strength, and adhesion to substrate. China standard testing methods were as follows: [10–12] GB/T 6753.1-2007/ISO 1524:2000 *Paints, Varnishes, and Printing Inks—Determination of Fineness of Grind*, GB/T13217.4-2008 *Test Method for Viscosity of Liquid Ink,* GB/T13217.5-2008 *Test Method for Initial Dryness of Liquid Ink*, GB/T13217.6-2008 *Test Method for Relative Tinting Strength of Liquid Ink,* and GB/T13217.7-1991 *Test Method for Adhesion To Substrate of Liquid Ink.* And the results of tests were showed in Table 120.2.

120.3   Result and Discussion

120.3.1   Effect of Adding Sequence on Dissolution and Viscosity

Through changing sequence of adding chitosan or alcohol to 3 % acetic acid solution, the different results are shown in Table 120.3.

Table 120.3 Different results of different adding sequences

Test method	Phenomenon	Viscosity (mPa s)
Adding order: alcohol first, chitosan second	Completely dissolve, less foam	2500
Adding order: chitosan first, alcohol second	Completely dissolve, much foam	1500

It is shown in Table 120.3 that phenomenon and viscosity of binder mixed by chitosan and alcohol as methods in Table 120.3 were different. If alcohol was added to 3 % acetic acid solution before chitosan, the solution could be mixed with less foam and high viscosity. It was better to be part of printing ink. And the reason why this happened was that alcohol not only diluted acid solution, but also could restrict the degradation of chitosan in 3 % acetic acid solution.

120.3.2 Effect of the Concentration and PH of Acetic Acid on Viscosity of Chitosan Solution

To examine the effect of concentration and pH of acetic acid on viscosity of chitosan solution, a given quality of chitosan was added into sample solution with the concentration of 1, 3, 5, 7, and 9 % of acetic acid. And sample mixtures were labeled 1, 2, 3, 4, and 5. The effects of concentration and pH of acetic acid on viscosity were analyzed under different sample solutions, respectively (see Figs. 120.1 and 120.2).

It is shown in Fig. 120.1 that 3 % concentration of the acetic acid solution maximizes the viscosity of chitosan solution. No matter the concentration of acetic acid gets higher or lower, the viscosity of chitosan solution gets lower. From Fig. 120.2, it can be seen that the viscosity of chitosan solution peaks when pH is 4.74 and pH higher or than that also lowers the viscosity of chitosan solution.
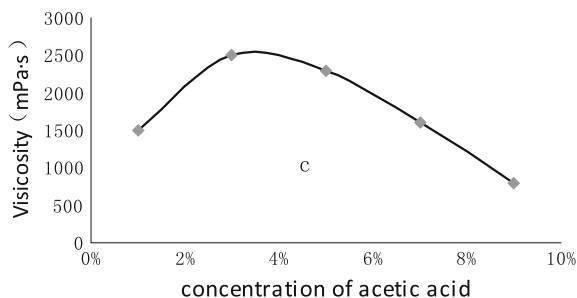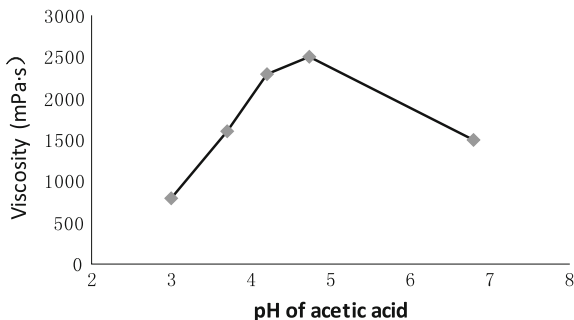

Fig. 120.1 Effect of concentration of acetic acid on viscosity of chitosan solution

**Fig. 120.2** Effect of pH of acetic acid on viscosity of chitosan solution

It can be concluded from the results that when the concentration of the acetic acid solution is around 3 % or 5 %, chitosan completely dissolves. When the pH of the solution is around 4.74, the viscosity of the chitosan solution reached maximal [13]. This proves that the dissolution is adequate and the degradation of chitosan is the slightest when the pH of the chitosan solution is around 4.74. However, when the concentration of the acetic acid solution is low, the viscosity is also low because the H^+ in the acetic acid solution is insufficient to combine with chitosan so that the chitosan cannot dissolve completely. When the concentration of acetic acid solution was low, the chitosan solution is almost neutral with pH around 6.80, proving that the chitosan almost consumes all the free H^+. On the contrary, when the concentration of the acetic acid solution is too high, the free H^+ is much more than the consumption of the chitosan. The remnant H^+ lowers pH and intensifies the degradation of chitosan and thus results in a low viscosity [14].

120.3.3   Effect of the Amount of Alcohol on Viscosity of Chitosan Solution

The amount of 15.7, 31, 47.4, 63, and 79 % of alcohol was mixed with 3 % chitosan and acetic acid solution completely. The effect of the amount of alcohol on viscosity of chitosan and acetic acid was shown in Fig. 120.3.

**Fig. 120.3** Effect of amount of alcohol on viscosity of chitosan and acetic acid solution
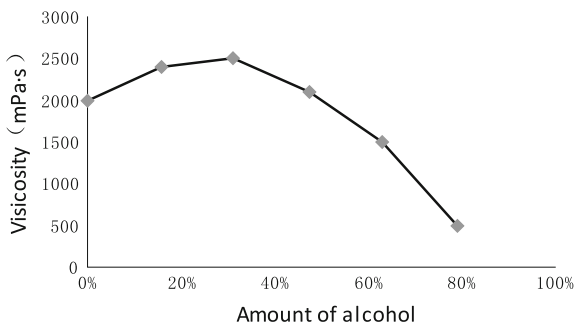
As shown in Fig. 120.3, with the amount of alcohol increasing, the viscosity of chitosan and acetic acid solution increases gradually. When amount of alcohol is 31 %, the viscosity of chitosan and acetic acid solution gets the highest value of 2500. But then, the viscosity of chitosan and acetic acid solution decreased quickly with the amount of alcohol increasing more. The result suggests that alcohol, when less than 31 %, could restrict the degradation of chitosan. But once, more than 31 % of alcohol was added into 3 % chitosan and acetic acid solution, alcohol promotes a negative role in diluting the chitosan solution.

120.3.4 Effect of the Amount of Pigment on Tinting Strength and Density

The amount of 31, 34.5, 38, 41, and 45 % of pigment was firstly added into chitosan solution and stirred for 30 min. The mixture which was mixed by materials above was tested by china standard testing methods like traditional screen-printing ink. The results of tests were analyzed, respectively (see Fig. 120.3).

As shown in Fig. 120.4, the tinting strength and density of edible ink increase with the increased amount of pigment. When the amount of pigment reached 41 %, the density of edible ink would not increase higher. And if pigment is added more into chitosan solution, the pigment will not dissolve in chitosan solution completely [15].

Fig. 120.4 Effect of amount of pigment on tinting strength and density of edible ink
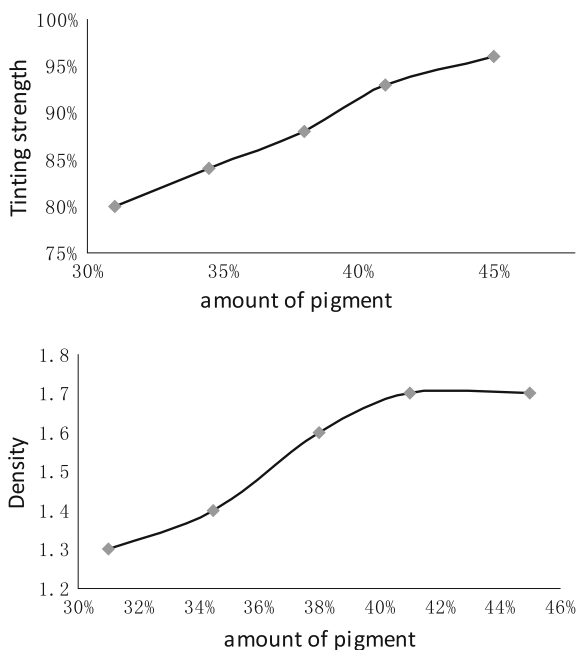
120.4   Conclusion

The edible screen-printing ink with chitosan solution has been described in this paper. It not only has excellent properties of traditional ink such as fineness, viscosity, initial dryness, tinting strength, and adhesion to substrate, but also can be eaten safely. So it is usable in the food package printing industry.

References

1. Davison, R. W. (1974). Electrokinetic effects in papermaking processes. *Tappi Journa, 56*, 85–89.
2. Qin, C. Q., Du, Y. M., & Xiao. L. (2002). Effect of hydrogen peroxide treatment on the molecular weight and structure of chitosan. *Polymer Degradation and Stability, 76*, 211–218.
3. Nixon, K. (1999). Modern trends in ink jet ink. *Professional Printer, 43*, 18–20.
4. Yandell, P., & Nixon, K. (1998). Wide format Inkjet. *Printer.*
5. Wolfgang, R. W. (1998). Ink-jet printing: the present state of the art. *VLSI and Computer Peripheral*, 46–52.
6. Allen, R. R. (1995). Black and color resolution enhancement technology used in the Hewlett-Packard Desk Jet 850°C printer. In *Proceeding of IS&T'S 11th International Congress Advances in Non-Impact Printing Technologies.*
7. Lu, F. (2006). Ink jetting inks for food application. *US Patent 20060038866,*
8. Hiroaki, K. (1995). Image processing and printing methods. In *Proceeding of IS&T'S 11th International Congress Advances in Non-Impact Printing Technologies,*
9. Churnick, L. (2006). Method of adorning foodstuff. *US Patent 20060210681.*
10. Ahn, S. A. (1998). Method for imprinting confectionery products with edible ink. *US Patent 5834047.*
11. Marcos, A. (1998). System and method for optically tracking objects using a spectral fingerprint of fluorescent compounds. *US Patent 20060222702.*
12. Laleg, M., Pikulik I. I. (1991). Wet-web strength increase by chitosan. *Nordic Pulp and Paper Research Journal.*
13. Yui, T.,Imada K., Okuyama K., Obata Y., Suzuki, K., & Ogawa K. (1994). Molecular and crystal structure of anhydrous for of chitosan. *Macromolecules*, 7601–7605.
14. Morita, Y., Sugahara, Y., Ibonai, M.,& Takahashi, A. (1999). Synthesis of deoxy (thiosulfato) chitin as the precursor for noncatalytic photoinduced graft copolymerization. *Journal of Applied Polymer Science, 71,* 189.
15. Allen, L., Polverari, M., Levesque, B., & Francis, W. (1999). Effect of system closure on retention- and drainage- aid performance in TMP newsprint manufacture. *Tappi Journal, 82*, 188–195.

Chapter 121
Impact of Leveling Agents on the Film-Forming Performance of Water-Based Inks

Jingyang Li, Xiaofang Wang, Yun Ouyang and Haiqiao Wang

Abstract In this contribution, the three leveling agents with different chemical structures were applied in a water-based polyacrylic ink to investigate the effect of leveling agents on the film-forming performance of the ink. The results showed that polyether-modified dimethylpolysiloxane leveling agent has advantages in reducing the surface tension of the ink and increasing the smoothness of the ink film. The polydimethylsiloxane-based leveling agent with high molecular weight is more suitable for defoaming the ink and increasing the smoothness of the ink film, while polyacrylate-based leveling agent has more distinct advantages in improving the flow property and wetting effect of the ink on substrate than the other two leveling agents.

Keywords Leveling agent · Water-based ink · Polyacrylic acid · Film-forming performance

121.1　Introduction

Water-based inks have attracted significant attention as a promising alternative to organic solvent-based inks due to their low or zero volatile organic content (VOC) and environment-friendly. However, compared with solvent-based ink, water-based inks often possess low liquidity which can cause imprinting, shrinkage,

J. Li · H. Wang (✉)
Beijing Engineering Research Center for the Synthesis and Applications of Waterborne Polymers, Beijing University of Chemical Technology, Beijing, China
e-mail: wanghaiqiao@mail.buct.edu.cn

J. Li · X. Wang · Y. Ouyang
Beijing Key Laboratory of Packaging and Printing New Technology, China Academy of Printing Technology, Beijing, China

pinhole, sagging, and other ink layer defects in the printing process. Adding leveling agents is an effective method to improve the liquidity of water-based inks.

Leveling agent is a kind of coating agent, which can cause the coating to form a smooth, glossy, and uniform film in the process of drying [1]. In general, leveling agents should possess the following three functions: (1) reducing the difference in surface tension between the coating and the substrate, making the coating and the substrate have the best wettability, namely, reducing the tension gradient caused by solvent evaporation. The typical examples are long-chain resins with limited compatibility; (2) regulating the solvent evaporation, reducing the viscosity, and increasing the fluidity of the ink, such as high boiling point solvent mixtures; and (3) forming a single molecular layer on the surface of the film to provide uniform surface tension, such as long-chain silicone greases with limited compatibility [2]. Thus, it can be seen that the different leveling agents have complicated effect on the performance of water-based inks.

In search of effective leveling agents for improving the printing quality of water-based inks, in this paper, we chose three different leveling agents commercially available to study the effect on the film-forming performance of water-based polyacrylate flexo-printing inks. We hope that we provided an important guideline for the majority of peers through this study.

121.2 Experiments

121.2.1 Materials

Acrylic resin emulsion was prepared by our group. Polymer water-based color paste W5022 was purchased from Beijing Innoan Polymer Powder Co. Ltd. Leveling agent A (polyether-modified dimethylpolysiloxane-based leveling agent) and leveling agent B (emulsion of a high molecular weight polydimethylsiloxane-based leveling agent) were purchased from Tego. Leveling agent C (polyacrylate-type leveling agent) was purchased from BYK Chemical Inc.

121.2.2 Printing Ink Sample Preparation

In accordance with the ink formulation, the printing ink samples were prepared by a high-speed dispersion machine. A certain amount of emulsion, defoamer, color paste, and leveling agent were added in turn and then dispersed and mixed for 60 min. Finally, it was cooled to room temperature and filtered through a 200-mesh filter cloth.

121.2.3 Printing Sample Preparation

Printing ink samples were printed using IGT F1 Basic to simulate printing process. A certain amount of inks were added between the blade and the anilox roller. When anilox roll rotated two laps, the plate cylinder completed a lap of rotation. After each turn of the plate cylinder rotated, the ink will be transferred completely from the anilox roll to a photosensitive resin plate, and then transferred to the substrate version.

121.2.4 Characteristic

1. Surface tension: The surface tension of ink was measured by surface tension meter BZY-1. Each sample was measured three times, and then, the average was calculated. The mean value is defined as the surface tension.
2. Rubbing fastness: The rubbing fastness of printing sample was measured by rubbing fastness tester 2000TM. Dry rub measurement was conducted using 4 pounds weights with 42 times/min testing speed.
3. Glossiness: The glossiness was measured by digital glossiness meter YT-GM. Selecting 5 different points in the sample to measure the gloss, and then, the average value was calculated. The mean value is defined as the glossiness.
4. Surface roughness: The surface roughness of printing sample was measured by surface roughness meter M590-PPS. Five different points in the sample to measure the surface roughness were selected, and then, the average value was calculated. The mean value is defined as the surface roughness.

121.3 Results and Discussion

In the process of ink film formation, most of the leveling agent molecules tend to move to the top layer of the ink film due to their lower surface energy (see Fig. 121.1), leading to the formation of a smooth and flat film. Thus, the leveling agents have significant influence on the film-forming performance of ink films, including surface tension, glossiness, rub resistance, and surface roughness.
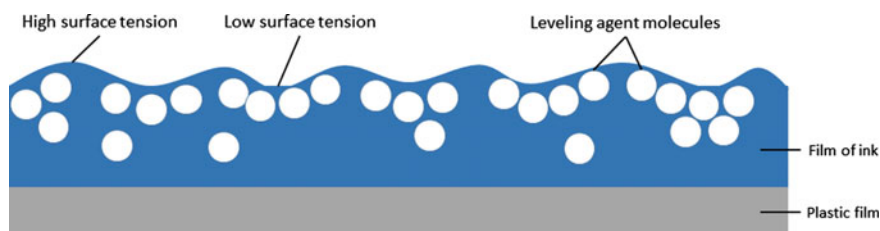

Fig. 121.1 Schematic diagram of distribution of leveling agent molecules in the layer of ink films

Surface tension can drive the droplet to form a ball and also can make the large area of the liquid to form a smooth layer [3]. Because the water-based inks have very high surface tension due to high surface energy nature of water, the fluidity of the inks on the surface of the substrates, such as PP and PE, is often not good. Thus, it is usually needed to add some leveling agents to reduce the surface tension. The ability to reduce the surface tension is an important indicator of the quality of a leveling agent.

We chose three commercially available leveling agents with different chemical structures added to the polyacrylate emulsion to prepare water-based inks and studied the effects on surface tension. From Fig. 121.2, one can observe that the three leveling agents all show the same function of reducing the surface tension, but the effect is not the same. Among them, leveling agent A is the most effective and also the leveling agent C, while leveling agent B has the least influence on the surface tension, which means that the chemical structures of the leveling agents must be taken into account in the practical application.

The most important role of the leveling agents is to improve the flatness of the ink films. Figure 121.3 shows the effect of the three leveling agents on the surface roughness of the ink film. Surprisingly, leveling agent B reduces the surface roughness most effectively, although it has the worst ability in lowering the surface tension. In fact, the surface roughness of the ink film has a close relationship

Fig. 121.2 Effect of the leveling agents on the surface tension of the ink film
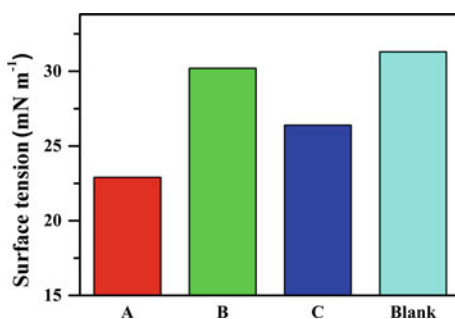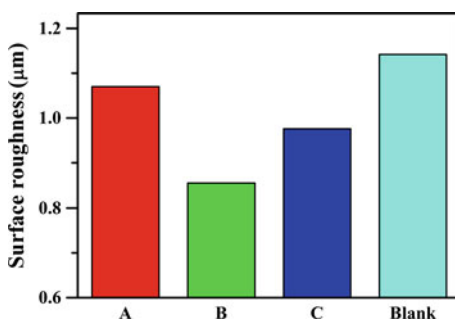

Fig. 121.3 Effect of the leveling agents on the surface roughness of the ink film

with the shrinkage cavity and wrinkle in the surface [4]. Observing the film morphology under the electron microscope, it is not difficult to find more or less shrinkage cavities and wrinkles existing on the surface of the ink film, which partially determined the surface roughness. Emergence of them, on the one hand, may been partially ascribed to some spiral structures caused by some of the particles not wetted enough, or by some resins incompatible with surrounding macromolecules; on the other hand, in the flow process of the ink, it usually forms a surface tension gradient in local areas. Because the materials with low surface tension always show expansion trend, this would make them spread from the center to the periphery; therefore, the periphery with high surface tension often tends to shrinkage [5], which results in the formation of shrinkage cavities or wrinkles. This implies that the rheological property of the leveling agents is the most important factor on determining the surface roughness of the ink films.

Based on the above analysis, it is not difficult to understand the reason why the high molecular weight polydimethylsiloxane-based leveling agent has stronger resistance to shrink cavities than the polyether-modified silicone, because it has better compatibility with ink. Polyether-modified silicone leveling agent is easier to form surface tension gradient, so its ability to resist shrinkage is weaker [6]. But for polyacrylate-based leveling agent, because it generally has function on stabilizing foam, it would introduce a lot of bubbles into the ink layer, resulting in many shrinkage cavities in the ink films.

As for glossiness, it can be apparent from Fig. 121.4 that leveling agent A has little effect on the glossiness, while leveling agent C can notably improve the glossiness. As is well known, influence factors on glossiness are very complicated. Thus, to improve the glossiness of the ink film, the leveling agents must be selected carefully for different water-based ink systems.

Figure 121.5 shows the effect of the three leveling agents on the rub resistance of the ink films. It is obvious that all the three leveling agents can effectively improve the rub resistance. Among them, the effect of leveling agent C is best, followed by leveling agent B, whereas leveling agent A shows the worst effect.

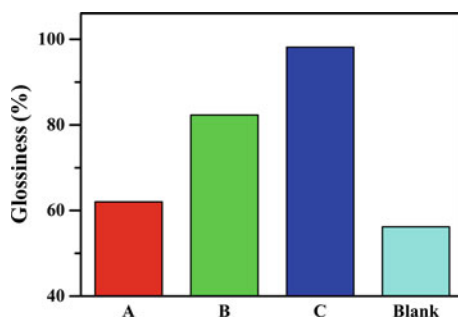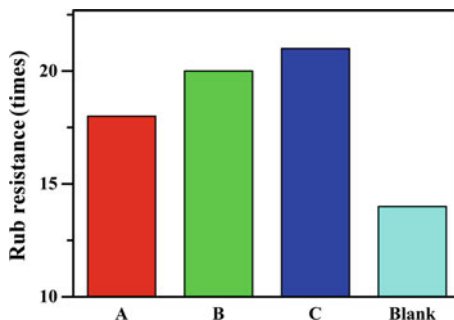Fig. 121.4 Effect of the leveling agents on the glossiness of the ink film

Fig. 121.5 Effect of the
leving agents on the rub
resistance of the ink film

121.4   Conclusions

The three leveling agents with different chemical structures were applied in a
water-based polyacrylic ink to investigate the effect on film-forming performance of
the ink film. The results showed that the leveling agents all have positive effect on
reducing the surface tension, increasing the flatness, and improving the smoothness
and rub resistance of the ink film. However, influence on each kind of performance
is not the same, depending on the chemical structures of leveling agents. Among the
three leveling agents, polyether-modified dimethylpolysiloxane is more beneficial
for reducing the surface tension and increasing the smoothness of the ink film, and
the polydimethylsiloxane emulsion with high molecular weight is more suitable for
improving the resistance of shrinkage holes and increasing the smoothness, while
polyacrylate-based addictive has more distinct advantages in improving the flow
property. Thus, in the practical application, to acquire polyacrylic inks with
excellent film-forming performance, several leveling agents with different functions
should be used in combination.

References

1. Zhijun, W. (2009). Leveling agent (part 1). *Coatings Technology & Abstracts, 2009*(7), 2–9.
2. Boke, L., Libin, C., & Yingde, C. (2002). Research progress of paint leveling agent application. *Guangzhou Chemical Industry, 30*(4), 18–20.
3. Youxue, Q. (2013). Rheological agent in surface active agent of ink. *Silk-Screen Printing, 2*, 29–34.
4. Youxue, Q. (2012). Ink surface tension and leveling. *Silk-Screen Printing, 12*, 25–32.
5. Hobisch, G., Kriess-mann, I., Staritzbichler, W., et al. (2002). Leveling agents for waterborne coatings. *Coatings Industry, 32*(6), 34–36.
6. Zhijun, Wang. (2009). Leveling agent (part 2). *Coatings Technology & Abstracts, 2009*(7), 18–34.

Chapter 122
Effect of Prepolymer on the Performance of UV-LED Ink-jet Ink

Yiran Li, Xianfu Wei, Peiqing Huang and Hao Zhang

Abstract Prepolymer is a kind of film-forming material of the ink system; constituting the basic skeleton of the ink, its performance plays a very important role on the quality of ink film. In order to investigate the performance of UV-LED ink-jet ink prepared by four kinds of prepolymers (Viajet100, Viajet400, 6215-100, and 6361-100), we tested the viscosity, surface tension, curing speed, and particle size of pigment in the paste and the adhesion of ink film, these data were used to analyze the effect of prepolymer on the performance of UV-LED ink-jet ink, in addition, simplex centroid design experiment was done on the three kinds of prepolymers to study the best prepolymer mass ratio of the UV-LED ink-jet ink. In research, we find that there are differences in performance between ink-jet ink prepared by different prepolymers, and when the mass ratio of composite prepolymer is Viajet100:Viajet400:6215-100 = 0:1:1, the UV-LED ink-jet ink can get the best comprehensive quality.

Keywords Prepolymer · UV-LED · Ink-jet ink · Comprehensive quality

122.1 Introduction

UV-LED curing system was born for the demand of adapting the diversity of substrates, short delivery time, producing high value-added products, saving printing field space, and so on. Compared to the traditional UV lamps, UV-LED system is not only mercury free, but also have many advantages such as (1) higher energy efficiency, (2) ozone free, (3) low ink off-flavor, (4) longer lifetime,

Y. Li (✉) · X. Wei · P. Huang · H. Zhang
Beijing Institute of Graphic Communication, Beijing, China
e-mail: 547673002@qq.com

(5) environment-friendly quality, (6) more constant light intensity, and (7) easily controlled temperature and heat [1]. For all these reasons, UV-LED is expected to be more widely used in the future, and the study chose four kinds of prepolymers to prepare ink samples and test several performance parameters to study the effect of prepolymer on the performance of UV-LED ink-jet ink. UV-LED light curing technology first appeared in the 2008 Drupa printing exhibition, its further maturation application was shown in the 2012 Drupa printing exhibition. This technology is used for curing the digital ink-jet ink, and it can also be used in other printing processes such as curing flexo [2]. The UV-LED lamps manufactured by US Phose on company have been applied to the label industry, American Sun Chemical also manufactures UV-LED ink, but did not produce much benefit; in general, the researches of UV-LED ink are basically in the most preliminary stage, and we should do more studies in this area.

122.2 Experiment

122.2.1 Materials

Prepolymers: Viajet100 and Viajet400 (Allnex Ltd.), 6215-100 (Eternal Chemical Co., Ltd); monomers: EOEOEA, HDDA, DPGDA, TPGDA, and TMPTA (Tianjin tianjiao Co.); photoinitiators: 184, ITX (Beijing YINGLI technology development Co., Ltd); active amines: EHA (Beijing YINGLI technology development Co., Ltd); wetting and dispersing agents: 9077 (BYK Chemie); flatting agents: 432; pigment: carbon black R250 (Cabot Corporation).

122.2.2 Equipment

Isothermal magnetic agitator (Jiangsu Ronghua instrument Co.), JJ-I-type mechanical agitator (Changzhou Guohua Electric Appliance Co., Ltd), GJ-2S-type high-speed grinding machine (Qingdao Haitong dedicated instrument Co., Ltd), UV-2501PC ultraviolet and visible spectrophotometer (Shimadzu Corporation), photogravure proofing machine (British RK Corporation), 3-M adhesive tape (Minnesota Mining and Manufacturing), Microtrac S3500 Laser Particle Sizer (US Microtrac Co.), K100-type surface tensiometer (Germany KRUSS Ltd.), portable viscometer (Hydramotion Ltd.), and UV-LED curing illuminator (Uvata (Shanghai) precision photoelectric Co., Ltd).

122.2.3 Experimental Method

122.2.3.1 Preparation of Printing Ink

In this experiment, the UV-LED printing ink was produced by grinding dispersion method; dispersion in a broad sense refers to the dispersion of solid powdery substance in gas, liquid, or another solid powdery substance. In the area of ink production, it refers to the process that solid powdered pigment (fill) material distributes in liquid binder and forms a stable colloidal dispersion.

1. The preparation of color paste

We add the prepolymer, monomer, and dispersant separately to the beaker, put the beaker onto the magnetic mixer, and move it until the liquor is uniform, and then put pigment-added liquor under the JJ-I-type mechanical agitator to predisperse for about 30 min. Then, the predispersed paste should be poured into a grinder, and we add in the appropriate weight of zirconium beads, let us use the high-speed grinder mill for 60–120 min, so that the pigment can be well dispersed in the connection compound, and thus, we can get the ink paste. All ink produced in this study were used the same formulation of paste.

2. The preparation of printing ink

Blend the three kinds of prepolymers (Viajet100, Viajet400, and 6215-100) with photoinitiator, monomer, additives, respectively, according to the formulation to prepare the diluents, and mix it with color paste, put the mixer under the JJ-I-type mechanical agitator for about 30 min, and filter the liquor after it is well dispersed; thus, we can get three kinds of UV-LED printing ink, mark them as sample 1, sample 2, and sample 3, respectively.

122.2.3.2 Performance Test

1. Viscosity testing: Use the portable viscosimeter to test the viscosity of each sample.
2. Surface tension test: Use K100-type surface tensiometer to test the surface tension of each sample.
3. Curing speed test: The main methods for the characterization of the maximum curing speed are as follows: finger-touch method, infrared method, and the gel content measurement method. In this study, we used the photogravure proofing machine to print the ink onto the PET film and then set the power of UV-LED curing system to be a constant value and change the speed of conveyor to make the ink film to be cured. We use the finger-touch method to characterize the maximum curing speed of each sample.
4. Dispersibility test: Use Microtrac S3500 laser particle sizer to test the dispersibility of each sample.

5. Adhesion test: Use crosshatch method to test the adhesion of proof sample printed on the PET film by photogravure proofing machine and then cure by using UV-LED curing system. The exact approach is that scratch out 10×10 squares equally spaced in the upper area of the 1 cm × 1 cm spacing sample, and then use 3-M adhesive tape to cling to the ink film and remove it. We calculate the area ratio of ink film stuck out after the removement of 3-M tape. By this method, the adhesion of ink film on the substrate can be characterized, and according to GB/T9286-88 standard to assess its level which was divided into six (0–5), the level 0 is the best and the level 5 is the worst.

122.3   Results and Analysis

122.3.1   Influence of Prepolymer on Ink Performance

122.3.1.1   Viscosity

Viscosity is a measure of inter-obstruction due to the interaction between the fluid molecules produced by their molecular size and relative motion capability. It is an important performance parameter of UV-LED ink-jet ink, when the viscosity of ink-jet printing ink is greater, the cohesion of droplet formatted is larger, and it is more difficult to eject ink droplets. In addition, the ink drop will have a drawing-shaped tail affecting the printing quality [3]. In the study, ink samples were prepared by three kinds of prepolymers, respectively, we tested their viscosity, and the results are shown in Fig. 122.1.

As shown in Fig. 122.1, the viscosity of sample 2 is minimum (90.2 MPa s), the viscosity of sample 3 is maximum (456 MPa s), and the viscosity of sample 1 is in

Fig. 122.1 Viscosity of ink sample and prepolymer
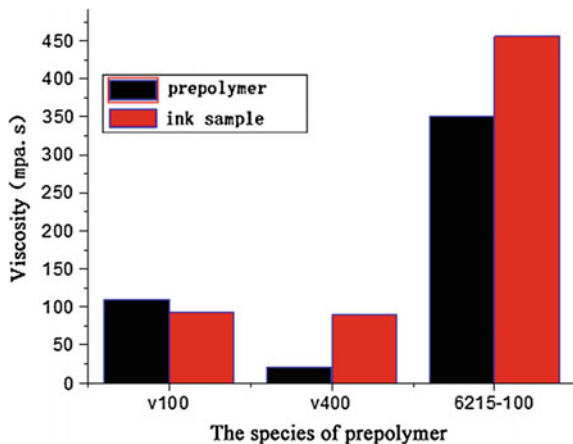
the middle (93.5 MPa s). Usually, the viscosity of ink influenced largely by the viscosity of prepolymer itself and the functionality of prepolymer. The viscosities of three kinds of prepolymers are as follows: 110 MPa s (Viajet100), 20 MPa s (Viajet400), 350 MPa s (6215-100); from this, we can know that the viscosity of ink increases with the increasing of the prepolymer's viscosity. In addition, Viajet100 and Viajet400 are both hyperbranched polymers and the 6215-100 is the linear prepolymer. Compared to the traditional linear prepolymer, the hyperbranched polymer has many unique characters, such as spherical configuration, a large number of end groups, and no entanglement intramolecularly [4]. These characters can provide lower viscosity for the ink.

122.3.1.2 Surface Tension

Surface tension is an important parameter of the ink-jet ink, which directly determines the ejection speed, size, roundness, and tail length of the droplet. It refers to a liquid surface traction in unit length of the two portions adjacent to the other [5]. In this experiment, we changed the type of the prepolymer to prepare different inks and test their surface tension, and the results are shown in Fig. 122.2.

As shown in Fig. 122.2, the surface tension's difference between ink samples is small: The surface tension of ink prepared by 6215-100 is maximum and the surface tension of ink prepared by Viajet400 is minimum. This is due the little difference of ink surface molecular attraction caused by the difference of prepolymer's structure.

122.3.1.3 Curing Speed

Curing speed characterizes the ink layer's curing velocity printed on the substrate, it is an important property for UV-LED ink. UV-LED ink should be able to cure
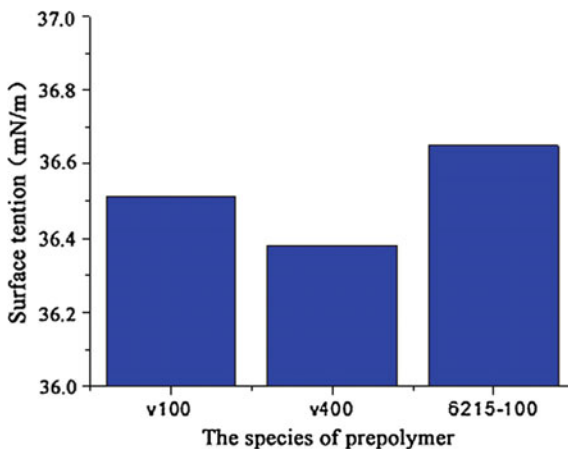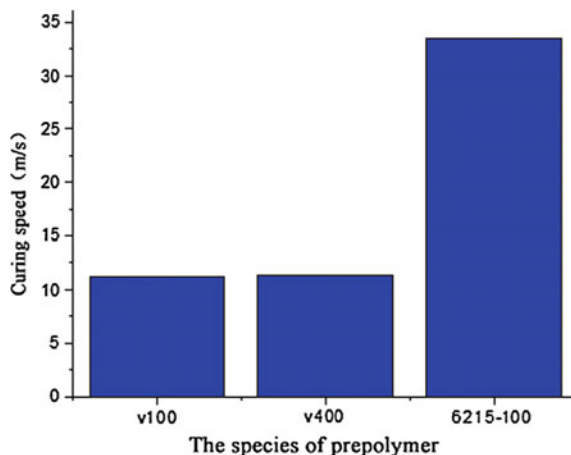

Fig. 122.2 Surface tension of ink sample

Fig. 122.3 Curing speed of ink sample

rapidly under UV-LED curing system which has relatively low power, and its products should have high gloss and hypercolor. The results are shown in Fig. 122.3.

As shown in Fig. 122.3, the curing speed of Viajet100-prepared ink and Viajet400-prepared ink is much slower than 6215-100-prepared ink. The functionality of Viajet100, Viajet400, and 6215-100 are all two. Viajet100 and Viajet400 are both hyperbranched polymers and 6215-100 is the linear polymer. The structures of three kinds of prepolymers are different and this suggests that the structure of prepolymer influences the curing speed of UV-LED ink-jet ink.

122.3.1.4 Dispersibility

The dispersibility is one of important physical properties of ink-jet ink. It has a vital role on determining whether the ink can be sprayed out smoothly or block the nozzle. It is related directly to the stability of the ink system and the uniformity of pigment particle size. The matching between pigment and prepolymer and the determining of binder ratio are both the key factors affecting the dispersibility of ink-jet ink. Generally speaking, the better wetting state the pigment particles has, the better the dispersibility of the ink owns. In this study, we kept the content of pigment, species, and mixing ratio of monomer to be fixed; change the species and pigment binder ratio of the prepolymer to prepare UV-LED black ink paste; and test the sample's particle dispersibility. The results are shown in Fig. 122.4.

As shown in Fig. 122.4, with the increase of binder ratio, the particle size in the color paste decreases first and then increases. When the binder ratio is 1:3, all the color pastes prepared by different prepolymers achieve their best dispersion. The color paste prepared by Viajet100 has the best dispersibility. This is due to the process that Viajet100 is hyperbranched polyester acrylic resin, and 6215-100 is the linear prepolymer. Compared with 6215-100, Viajet100 has better rheology and

Fig. 122.4 Particle size of ink sample
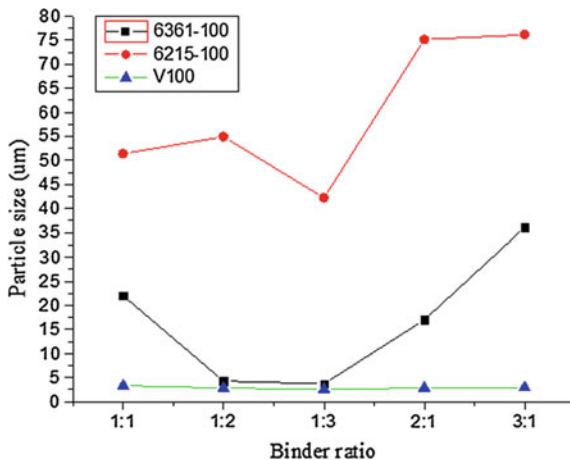
solubility. It can get the pigment to be well wetted. The process of dispersion is also the process of flow. Only achieving the best flow point, the ink can get the most effective grinding and shearing action; thus, the dispersion is best. In order to make the ink with best dispersibility, first we should test the best binder ratio, under the following experimental conditions: the prepolymer is Viajet100 and the binder ratio is 1:3

122.3.1.5   Adhesion Ability

Adhesion ability characterizes the bond capacity between ink film and substrate bonding under the effect of chemistry and physics. It is an important indicator of the performance of the ink film. Generally considered that the polar groups in monomer and prepolymer, such as –COOH and –OH integrating with the polar groups in substrate, have important effect on the adhesion ability of ink film [6]. Usually, the monomer and prepolymer should have a certain degree of mobility, so that the integration between polar groups and the wettability of substrate can be better. It is because of the proximity of polar groups between polymer and substrate surface that the polar groups can produce adhesion balance owing to the function of hydrogen bond and Van der Waals force when the distance between two kinds of molecules gets closer [7]The results are shown in Fig. 122.5.

As shown in Fig. 122.5, the adhesion of ink prepared by Viajet400 is worst, and the adhesion of ink prepared by 6215-100 is best. This is because 6215-100 is modified epoxy acrylate resin, whereas Viajet400 and Viajet100 are polyester acrylate resin. Compared to polyester acrylate resin, epoxy acrylate resin has better performance on adhesion ability; modified epoxy acrylate resin is the semi-IPN-structured prepolymer which is chemical compounded by epoxy resin and polyester acrylate resin. Epoxy resin is a good adhesive itself, and it can be well attached to the surface of the PET substrate.

Fig. 122.5 Adhesion of ink sample
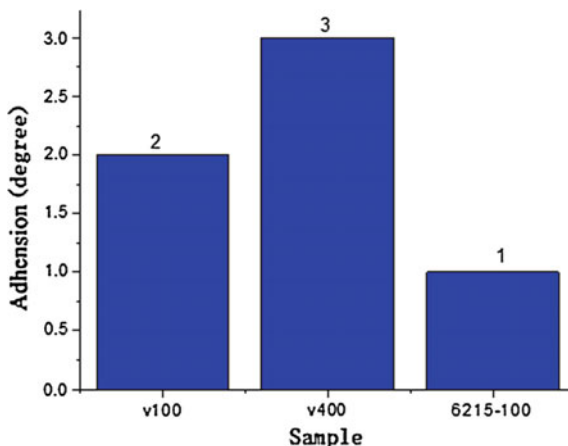
122.3.2 Formulation Design of Mixed Prepolymer and Performance Analysis

122.3.2.1 Comprehensive Evaluation Method

Comprehensive evaluation method is a means that analyzes the experimental result according to the importance of the various indicators impacting the experimental results. We first need to provide grades for every indicator according to a certain rating criteria, if the importance of each of the indicators is different, first we need to determine the weight of every indicator according to their importance and then calculate the weighted summation. Finally, we get every sample's gross score. Membership grade can be used to express the score; it can be calculated in this way:

membership grade = (indicator value—the minimum indicator value)/(the maximum indicator value—the minimum indicator value)

In the upper equation, the minimum indicator value is 0, and the maximum indicator value is 1.

122.3.2.2 Formulation Design of Prepolymer of UV-LED Ink-jet Ink

By investigating ink sample prepared by single prepolymer, we know that Viajet100 and Viajet400 can reduce the system's viscosity and 6215-100 can improve the curing speed, so we choose these three kinds of prepolymers to design the formulation experiment. The study took three factors and three-order simplex centroid design experiment. We set X_1, X_2, and X_3 represent the percentage of Viajet100, Viajet400, and 6215-100, respectively, in the diluents and produce black ink samples. Various data of them were tested. The experimental results are shown in Table 122.1.

Table 122.1 Data of formulation experiment

Group	X_1	X_2	X_3	Surface tension (mN/m)	Viscosity (mPa s)	Adhesion (degree)	Curing speed (Cm/s)	Comprehensive score
1	1	0	0	36.51	93.5	2	11.2	0.323
2	0	1	0	36.38	90.2	3	11.4	0.396
3	0	0	1	36.65	456	1	33.5	0.48
4	1/2	1/2	0	36.19	92.4	2	16.8	0.423
5	1/2	0	1/2	36.64	205	5	22.4	0.696
6	0	1/2	1/2	36.34	168	4.5	28.1	0.768
7	1/3	1/3	1/3	36.39	123.7	4.5	28.3	0.615

According to experiment conditions and different importance each indicator impacts on the ink, we valued the weight of surface tension, viscosity, adhesion, and curing speed as 0.1, 0.2, 0.3, and 0.4 respectively. By calculation, we got the regression equation of comprehensive score and variate, as shown in the Formula (122.1)

$$Y = 0.323X_1 + 0.396X_2 + 0.48X_3 + 0.254X_1X_2 + 1.178X_1X_3 + 1.32X_2X_3 \quad (122.1)$$

The bigger the value of the regression equation is, the better comprehensive quality the ink has, according to the experimental data analysis under the experimental condition, the best mass ratio of composite prepolymer is, Viajet100: Viajet400: 6215-100 = 0:1:1.

122.4   Conclusions

Using three kinds of prepolymers according to the same formula to prepare different kinds of UV-LED ink-jet ink, and testing each property, such as viscosity, surface tension, curing speed, dispersibility and adhesion, we can draw the following conclusions:

1. There are differences in performance between ink-jet ink prepared by different prepolymers. The ink-jet ink prepared by Viajet400 and Viajet100 has lower viscosity and surface tension, but at the same time their curing speed is lower too, whereas the ink-jet ink prepared by 6215-100 has the highest curing speed.
2. A variety of prepolymers can be formulated to reach better performance. Under the following experiment condition, when mass ratio of composite prepolymer is, Viajet100: Viajet400: 6215-100 = 0:1:1, the UV-LED ink-jet ink can get the best comprehensive quality.

References

1. Ji, D. (2010). The application and development of LED on the area of UV printing[J]. *Printing Field, 05*, 56–58.
2. Gao, J. (2012). UV LED curing technology. *Printing Field, 02*, 54–56.
3. Yi, Q., & Wang, Q. (2014). Effect of monomer on the performance of UV-LED inkjet ink. *Packaging Engineering, 7*(35), 127–132.
4. Zhang, X., & Zhang, Y. (2011). Recent research of hyperbranched polymer. *Chinese Science Bulletin, 21*(56), 1683–1695.
5. Jiang, H., & Huang, P. (2009). Effect of prepolymer and monomer on the performance of UV flexography ink. *Journal of Beijing Institute of Graphic Communication, 17*(6), 26–29.
6. Wei, X., & Huang, P. (2007). Corona treated plastic's surface properties and printability. *Journal of Beijing Institute of Graphic Communication, 15*(4), 1–4.
7. Zhang, W., Wei, X., Huang, P. (2008). Study on UV-curable inkjet ink. *Beijing Institute of Graphic Communication*, P17–34.

Chapter 123
Preparation and Performance Study of Paper-Based Resin Nano-silver Inkjet Conductive Ink

Yanyan Chen, Guangxue Chen, Yanyan Cui and Yu Yang

Abstract Development and innovation researches of conductive ink have practical significance because conductive ink is a key material for printed electronic technology. To solve the poor adhesion problem of pure nano-silver ink on a paper substrate, paper-based resin nano-silver conductive ink for inkjet printing was produced by adding acrylic resin and photo-initiator into silver nano-colloids. The electrical conductivity and mechanical properties of the conductive ink layer were analyzed and discussed. Firstly, a certain proportion of the nano-silver and photo-curable acrylic resin were dispersed in an organic solvent, and a small amount of additives were added to obtain conductive ink suitable for inkjet printing. Then, different sintering conditions of pure nano-silver ink were analyzed to discuss the effects of sintering temperature on the nano-silver resistivity, and conductive property of resin nano-silver ink was discussed. Finally, the mechanical stability of pure nano-silver ink and resin nano-silver ink was compared. The results showed that the conductive ink containing 20 % of the nano-silver obtained the conductivity of 2.72×10^5 S/m when sintered at 170 °C for 2 min, while the conductive ink containing resin obtained the conductivity of 3.3×10^4 S/m. The addition of acrylic resin has a positive effect on improving the mechanical stability, especially in the vertical direction of the resistance force.

Keywords Nano-silver · Paper-based · Acrylic resin · Conductive ink · Inkjet

Y. Chen · G. Chen (✉) · Y. Yang
State Key Laboratory of Pulp and Paper Engineering, South China University of Technology, Guangdong, China
e-mail: chengx@scut.edu.cn

Y. Chen
Shenzhen Engineering Laboratory of 3D Printing Technology, Shenzhen, China

Y. Cui
School of Materials and Energy, Guangdong University of Technology, Guangzhou, China

123.1   Introduction

With the rapid development of electronic technology, printed electronic technology provides a solution to miniature electronics, flexible electronics, and environmentally friendly electronics. Printed electronic technology uses a convenient, high-speed digital inkjet printing to efficiently prepare continuously conductive patterns on a substrate, or even directly generate the entire printed circuit board, making electronic products become increasingly thin, delicate, cost-saving, and versatile. Nano-silver conductive ink preparation process has been extensively studied [1, 2]. It provides an easy way to get high-conductivity products. Paper-based printed electronic applications gradually got people's attention. Unlike fiberglass, ceramic, or polyimide printed circuit boards, paper can be repeatedly folded and of three-dimensional configuration and can be scrapped after incineration. Thin paper-based electronic circuit has greater applications in the consumer electronics, packaging, disposable military defense systems, sensors, low-cost portable medical diagnostic systems, and other areas [3]. Therefore, paper was chosen as a substrate for nano-silver conductive ink.

Improving the adhesion performance between conductive ink and paper has been a common issue because poor adhesion performance may lead to the poor stability and durability of electronic products, so this paper is focused on the development of excellent adhesion of conductive inks. In the preparation of the ink, UV-curable acrylic resin was introduced. The loading of resin was expected to improve the ink adhesion. The properties such as electrical conductivity and mechanical stability of the conductive nano-silver inks with and without resin have been studied and discussed.

123.2   Experimental Section

123.2.1   Chemicals and Materials

Chemicals. Polyethylene glycol thioglycolate capping nano-silver particles (provided by Yu [4]), anhydrous ethanol (Sinopharm Chemical Reagent Co., AR grade), ethylene glycol (EG, Jiang Su Chinasun Specialty Products Co., Ltd., AR grade), polyethylene glycol (PEG, Guangdong Guanghua Science and Technology Co., Ltd.), acrylic resin, and photo-initiator 1173 were used.

Materials. RTS-4-type four-point probe, UT136B multimeter, MJ-LD1816 rubbing fastness tester, UV-curing machine, RE rotary evaporator, BDG 206/1 coating device, DHG-9140A hot air oven, and Canon IP1188 desktop printer were used.

123.2.2 Experimental Procedure

123.2.2.1 Ink Formulations

In this paper, two ink samples, A and B, were prepared.

A: nano-silver particles was mixed completely with ethylene glycol. The nano-silver solid content was 20 wt%.
B: nano-silver particles, ethylene glycol, acrylic resin, photo-initiator 1173, and a small amount of additives were used to prepare resin nano-silver conductive ink. The nano-silver solid content of the ink was the same as sample A. Table 123.1 shows the formulation of B sample.

Sample A was used to discuss the impact of sintering temperature on the conductive properties of the nano-silver ink. And it served as a comparative experiment to discuss the impact of acrylic resin on electrical conductivity and mechanical stability performance of resin nano-silver conductive ink.

123.2.2.2 Electrical Conductivity Characterization of Conductive Ink

Prepare ink samples (A and B) on the paper surface, and the film layer thickness of sample A was controlled using coating device. But the film layer thickness of ink sample B on paper cannot be controlled accurately due to the presence of solvents and resin in the ink. The coating thickness should be further determined by SEM after drying. RTS-4-type four-point probe was used to calculate the ink conductivity. Electrical resistivity of the conductive ink was calculated using the formula 123.1, and the electrical conductivity σ was further obtained by the formula 123.2.

$$\rho_F = \frac{\pi}{\ln 2} \cdot \frac{V}{I} \cdot d \qquad (123.1)$$

$$\sigma = \frac{1}{\rho_F} \qquad (123.2)$$

Table 123.1 Ink formulations for B sample

Ingredients	Weight percentage (%)	Roles
Nano-silver	20	Conductive element
EG	66	Solvent
Anhydrous ethanol	5	Drying rate adjustment
Acrylic resin	8.5	Binder
PEG	Trace	Stable dispersion
Photo-initiator 1173	Trace	Photo-initiator

where ρ_F is the resistivity of the conductive films; I is provided by a constant current source which flows through the conductive films; V is the voltage generated when current I flows through the conductive film; and d is the thickness of the electroconductive film.

123.2.2.3 Characterization of the Mechanical Properties of the Ink

Ink samples A and B coated on the paper surface were torn with 3-M tapes, respectively, to test their resistance to tearing performance, rubbing fastness tester was used to test the abrasion performance, and a self-made bending test apparatus was used to test ink film resistant to bending.

123.3 Results and Discussion

123.3.1 Thermodynamic Characterization of Nano-silver Ink

Figure 123.1 shows the SEM images of non-resin-contained nano-silver ink sintered for two minutes at different temperatures. As shown in Fig. 123.1a, only the physical contact existed between the nano-silver particles, and close connections failed, so it cannot provide good mechanical properties. When the sintering temperature was 150 °C, the morphology of the silver particles (in Fig. 123.1c) had no major differences from that shown in Fig. 123.1a, b. However, tests showed that the conductivity of the ink layer was significantly different. This suggested that the protective agent capping the nano-silver particles has been desorbed during sintering. When the temperature was 170 °C, the silver particles fused together (in Fig. 123.1d), building conductive ink capacity. As is clearly shown in Fig. 123.1d), after the high-temperature sintering, nano-particles had a greater contraction, leading to a large number of voids, which thereby reduced the ink film's strength and adhesion.

123.3.2 Characterization of Resin Nano-silver Conductive Ink Film

Ink sample B was printed on the paper surface by an inkjet printing. Then, the ink film was prebaked at 80 °C for 60 min. In this process, the organic solvent was freed from the resin and volatilized into the air at a high temperature. When the solvents were removed from the resin, the resins produced physical cross-links and gradually shifted from sol state to gel state. The samples were then placed in the
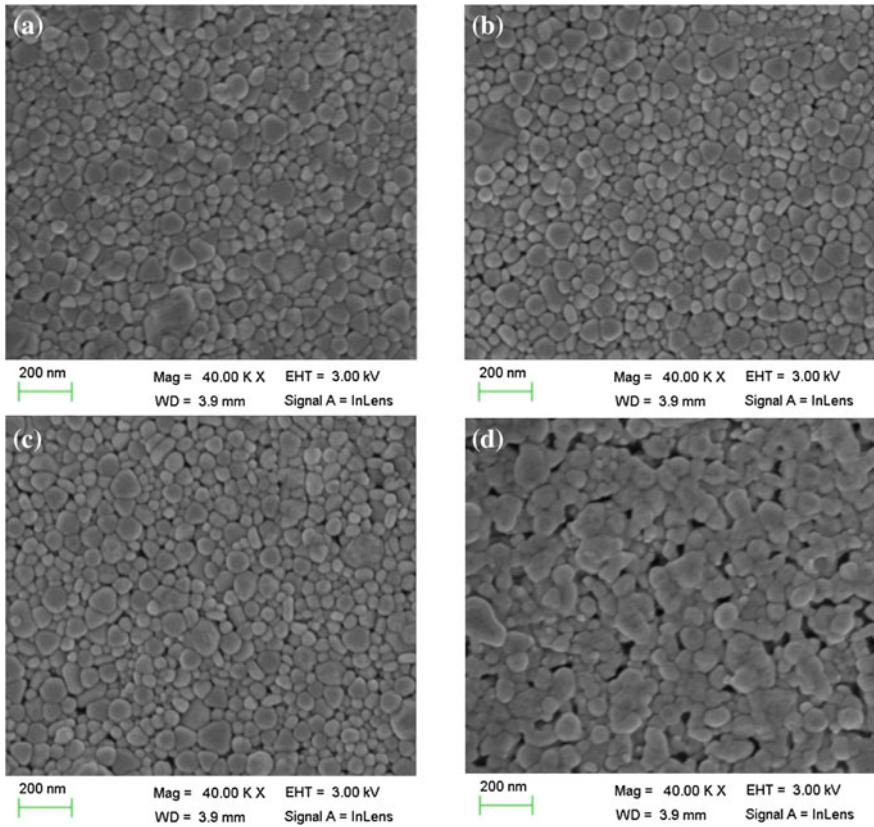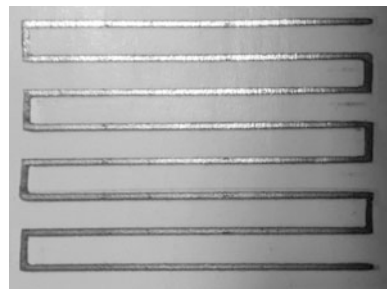
Fig. 123.1 SEM images of the surface of nano-silver films sintered at 110 °C (**a**), 130 °C (**b**), 150 °C (**c**), and 170 °C (**d**) for 2 min

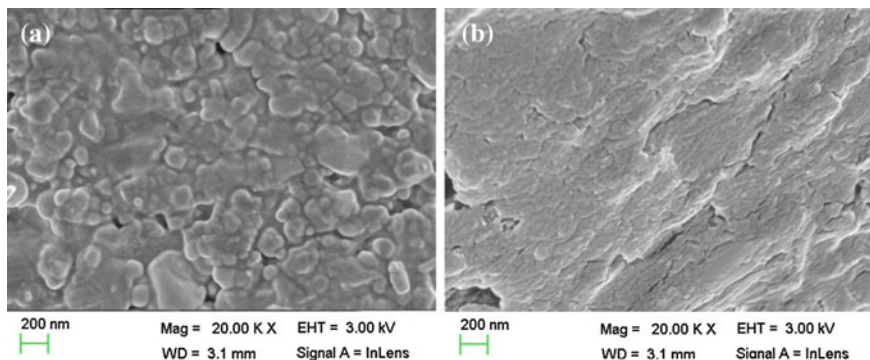**Fig. 123.2** Inkjet printed circuit pattern of resin nano-silver ink

Fig. 123.3 SEM images of surface (**a**) and cross section (**b**) of paper-based resin nano-silver film sintered at 170 °C for 2 min

UV-curing machine and cured for 30 s. Finally, these samples were placed in an oven at 170 °C for 2 min. Figure 123.2 shows a macroscopic state of inkjet printing lines. Limited to inkjet printers, concentration of nano-silver solid content in inks cannot be too high. So a single inkjet of nano-silver ink could not form a continuous conductive line, which required multiple trapping to increase the silver content on the paper surface.

Figure 123.3 shows the SEM images of the sintered conductive ink. It showed that due to the addition of the resin, most of the voids in Fig. 123.1d have been filled with the resin, so that the adherence of overall film became tighter. It is also shown in Fig. 123.3b that the presence of the resin in the longitudinal direction of nano-silver also had a good bonding effect.

Percolation theory [5] stated that nano-silver conductive ink formed a continuous conductive path by mutual contact between the nano-silver particles, which made the ink conductive. After the conductive ink was printed on the substrate, the solvents were not dried and the resin was uncured at the initial step, so the nano-silver particles dispersed in a relatively independent state and contacts between the particles failed, which cannot form a conductive path. In the ink drying process, the solvent evaporation and resin curing resulted in the ink volume contraction, and the conductive particles formed a network structure in close contact, so the ink imparted conductivity. Due to the capillary force of the paper, the oily medium, which was separated from the ink, gradually penetrated into the pores beneath the paper surface until the ink film was completely dried up [6]. So nano-silver particles get precipitated, and the conductive layers on the paper surface were formed.

123.3.3   Characterization of the Mechanical Properties of the Ink Layer

123.3.3.1   Ink Film Tearing Resistance Performance

Ink film layers on the paper surface were torn with 3-M tape, and the relation between tearing times and the sample's surface ink resistivity is shown in Fig. 123.4. It can be seen that there was a high conductivity in the beginning for ink sample A, but the conductivity decreased rapidly with the increase in the tearing times. Decreasing conductivity can be divided into two distinct phases. The first phase of decreasing conductivity can be attributed to the weak connections between ink films sintered from silver nano-particles. When exerted an external force by tape stripping, silver pieces were torn apart from each other, which caused decreasing conductivity. The second stage can be explained that the silver layers were peeled off from the surface of the paper by tape due to a weak binding between silver piece and paper surface. In contrast, the conductivity of the ink sample B has stabilized at the level of 10^5 S/m. In the beginning of tearing, the conductivity increased. This can be attributed to the removal of protection agents desorbed from the surface of the sintered ink. The presence of capping agents increased the ink surface resistance due to their non-conductive properties, but they can be easily removed by the tape. This suggests that adding the right amount of acrylic resin can not only greatly enhance ink adhesion, but also increase the conductivity of the conductive ink during the ink tear ability test. However, when torn 10 times, ink sample A on paper was substantially stripped from the paper, losing the electrical conductivity.

Fig. 123.4 Conductivity varied with peeling times. A—resin-free nano-silver ink. B—resin nano-silver ink
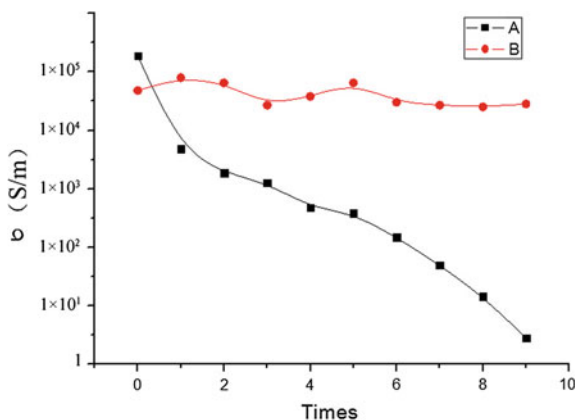
123.3.3.2 Ink Film Abrasion Performance

Ink film abrasion performance was tested by rubbing fastness tester. The results are shown in Fig. 123.5. In general, both inks had good ability to resist lateral friction. Conductive ink sample A had a slight increase in conductivity during the initial friction and then stabilized, while group B remained nearly unchanged during the friction. Although the conductivity of ink sample A increased, deinking phenomenon was more frequently observed. In comparison, there was basically non-existence of deinking phenomenon in sample B ink film layer. The reason for deinking of sample A can also be attributed to some poor bindings between the nano-silver melted films which were removed during friction, and interlayer bindings of ink films strengthened simultaneously, so the conductivity is finally increased.

123.3.3.3 Ink Film Bending Resistance Performance

Conductive ink is mainly used in flexible printed circuits, so conductive ink should have good resistance to bending, maintaining a stable conductivity during repeated bending. To test the changes in ink conductivity under bending, we made a simple test apparatus, as shown in Fig. 123.6.

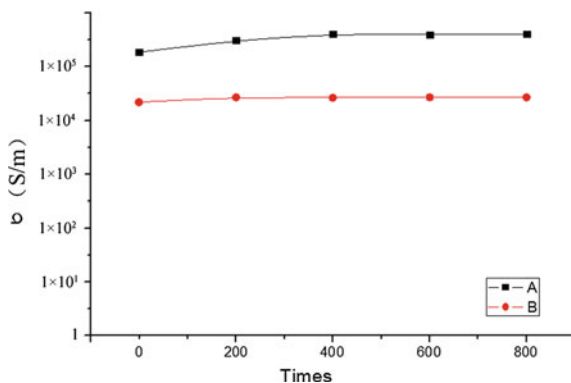**Fig. 123.5** Conductivity varied with friction times. A —resin-free nano-silver ink. B—resin nano-silver ink
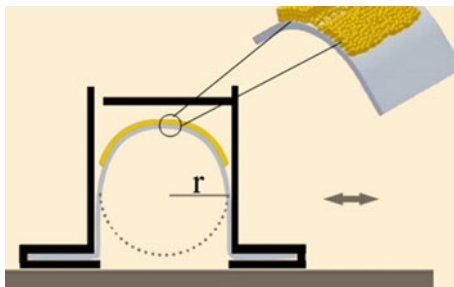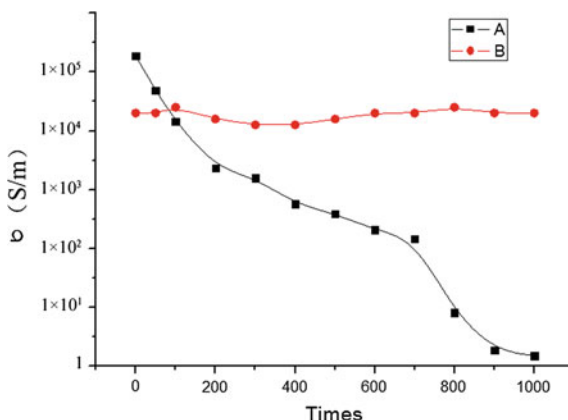

Fig. 123.6 Equipment for bending test

Table 123.2 Resistance of A and B with varied bending times

Bending times	0	100	200	300	400	500	600	700	800	900	1000
A (Ω)	0.3	12	50	220	410	1060	1370	2556	5432	9817	36312
B (Ω)	1.2	1.2	1.1	1.3	1.4	1.4	1.2	1.1	1.1	1.2	1.2

Fig. 123.7 Conductivity varied with bending times. A —resin-free nano-silver ink. B—resin nano-silver ink

The left side of the sample was fixed by one clip and the right side by another clip. One of the clips remained unmovable, while the other clip moved back and forth along the horizontal direction with a certain radius value of the bend. The bending degree can be controlled by the bend radius r. While testing, the bend radius used in this paper was 5 mm. Under repeated bending, ink samples A and B reflected distinct change in resistance with different bending frequencies, as shown in Table 123.2.

Figure 123.7 shows the conductivity changed with bending times. It can be seen clearly that although the initial resin-free conductive inks had high conductivity, its conductivity decreased rapidly with the increase in bending times. The resin nano-silver conductive ink was basically not affected by the bending, showing a stable conductivity. The reason was that the resin-free nano-silver layer can be easily separated from each other by an external force, while the ink containing the resin remained relatively stable during repeated bending due to the presence of the resin.

123.4 Conclusion

In this paper, acrylic resin nano-silver conductive ink containing 20 wt% nano-silver was prepared for inkjet printing. Paper-based materials were used as substrate to discuss the electrical and mechanical properties of resin-free nano-silver

ink and resin nano-silver ink. Experiments showed that resin-free nano-silver obtained the conductivity of 2.72×10^5 S/m when sintered at 170 °C for two minutes, while the conductivity of the resin nano-silver ink obtained the conductivity of 3.3×10^4 S/m. After adding the resin, conductivity declined, but ink film coated on the paper showed excellent mechanical properties such as resistance to tearing, abrasion, and bending.

References

1. Kim, D., & Moon, J. (2005). Highly conductive ink jet printed films of nanosilver particles for printable electronics. *Electrochemical and Solid-State Letters, 2005*(8), J30–J33.
2. Kim, D., Jeong, S., Park, B. K., & Moon, J. (2006). Direct writing of silver conductive patterns: improvement of film morphology and conductance by controlling solvent compositions. *Applied Physics Letters, 2006*(89), 264101.
3. Siegel, A. C., Phillips, S. T., Dickey, M. D., Lu, N., Suo, Z., & Whitesides, G. M. (2010). Foldable printed circuit boards on paper substrates. *Advanced Functional Materials, 20*, 28–35.
4. Yu, Y., Cui, Y., Chen, G., He, M. (2015). Preparation and study of ink-jet printing of Ag based conductive ink on paper. *Applied Mechanics and Materials*, *731*, 524–527, doi:10.4028/www.scientific.net/AMM.731.524
5. He, W., Yang, Y., Wang, S., He, B., & Hu, K. (2009). Preparation technology and application progress of conductive inks. *Materials Review, 21*, 30–33.
6. Xiang, Y., Lu, Q., & Wang, Z. (1997). Study on the ink penetration of offset newsprint. *China Pulp & Paper, 01*, 28–32.

Chapter 124
Study on Influence of Epoxy Resin for UV Curing System

Changlong Guo, Peiqing Huang and Xianfu Wei

Abstract This paper chooses the radical cationic hybrid UV curing systems and oxetane cationic UV curing system as rapid prototyping, studies the performance of the system as the change of the kinds and the amount of pre-polymer, and the impact of the ratio of the pre-polymers to the system volume shrinkage. Studies show that the type and content of the pre-polymer have a great impact on the system volume shrinkage, and analyze the result from the perspective of the theory. The results shows that the epoxy resin can reduce the volume shrinkage hybrid UV curing system and can also improve the flexibility of the material cured film.

Keywords Hybrid photo-curable · Epoxy resin · Curing speed · Curing shrinkage · Flexibility

124.1 Introduction

Ultraviolet (UV) curing technology uses the UV light as energy, which can make the pre-polymer becoming a photoactive polymerization in a short time [1]. Currently, light curing technology is a new technology regarded as a "green industry in the twenty-first century" in China and has been widely used in many sectors of the national economy [2]. The volume shrinkage has been an important factor not only for shaping the accuracy of the photo-curable material, but also for restricting the application and development of the light curing technology [3].

C. Guo (✉) · P. Huang · X. Wei
Beijing Institute of Graphic Communication, Beijing, China
e-mail: bygcl1989@126.com

P. Huang
e-mail: huangpeiqing@bigc.edu.cn

X. Wei
e-mail: weixianfu@bigc.edu.cn

The emergence of UV curing is regarded as a new green technology in the 1960s [4]. Ultraviolet (UV) curing technology use the ultraviolet light as the energy, which can make the pre-polymer becoming a photoactive polymerization in a short time. At present, light-cured mainly products such as UV coatings, UV inks, UV adhesives, photosensitive printing plates, photo-resists, light rapid prototyping materials appear [5]. However, due to the curing light, van der Waals forces between molecules when cured material becomes a covalent bond would produce certain volume shrinkage. Besides, since the cross-linking polymerization reaction of the polymerization, the material becomes hard, brittle, and lacking of flexibility after curing [6]. This will severely restrict the applications and application range of the light curable materials. What is more, the volume shrinkage can also be effectively reduced in epoxy system. From this, based on the basic components of hybrid UV curable materials, this paper investigates the effect of volume shrinkage performance and flexibility by different epoxy resin to explore the ways to improve the performance of hybrid UV curable material.

124.2 Experiment

124.2.1 Experiment Material

Pre-polymer: bisphenol A epoxy resin (E44, Shandong Tianmao Chemical), hyper-branched polyester acrylate pre-polymer (V400, Cytec Industries), monofunctional oxetane MOX; bifunctional oxetane butane DOX; monomer: ethoxyethoxy ethoxyacrylate (EOEOEA, Taiwan Changxing Chemical), 1,6-hexane dioldiacrylate (HDDA, Taiwan Changxing Chemical), 3,4 epoxy ring hexyl methyl-3,4-epoxycyclohexyl carboxylate (TTA21 Jiangsu Tai Teer chemical); initiator: 1-hydroxy—cyclohexyl benzophenone (184, long day Tianjin chemical), mixed tri-aryl sulfonium six fluorophosphate (PAG202, Changzhou strong electronics); auxiliaries: leveling agent 432. Main material in the formula is shown in Fig. 124.1.

124.2.2 Instrument

Instruments used in the experiment are 81-2 type constant temperature magnetic stirrer, German KRUSS K100 automatic surface tensiometer, AR2000ex rheometer, the FUSION UV curing machine, Fourier infrared spectrometer IS50FT—IR, and QTY-32 toughness-type film tester.
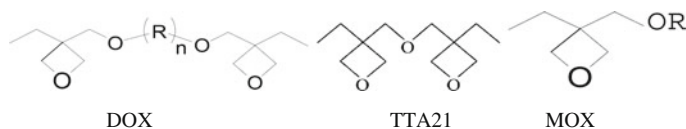

Fig. 124.1 Main material of the formula

124.2.3   Sample Preparation

According to the formula with the same quality of reactive diluent and light initiator mixed, take the defined quality of pre-polymer, and then add a small amount of antifoaming agent. In order to make the mix of components, scatter the pre-polymer on the magnetic stirrer for 30 min. Finally, the samples of flexible version of UV curing materials are obtained.

124.2.4   Test Method

124.2.4.1   Ink Viscosity Test

Using AR2000 rheometer, set the temperature as 25 °C and rotor by 60 mm aluminum plate to test the viscosity value when shear rate is 1 s^{-1}, the Pa s as the units.

124.2.4.2   Flexibility Test

The QTY-32 toughness-type film tester (fruits of letter test factory) coated on PET substrate is made up of 3d printing flexible version of UV-LED curing materials test, and under the condition of the specified standards, the flexibility of the ink film is in 1–3 s to test plate around the shaft rod bent 180° (do not cause the minimum mandrel diameter said film cracking).

124.2.4.3   Cure Speed Test

After the samples were coated on PET substrate, use the UV light curing machine to test the cure speed, light source power of 4 w/cm^2, dominant wavelength of 365 nm, measured by touch method flexible version of the 3d printing to make maximum light curing speed of UV curing materials.

124.2.4.4   Cure Shrinkage Rate Test

According to ISO 3521:3521, liquid resin curing shrinkage rate (shrinkage ratio, SR) is calculated by the formula (124.1). Type of $\rho1$ is the density of the liquid resin, and its value is measured by pycnometer QBB type; $\rho2$ is for the density of cured rho, and its value is measured by precision density balance.

$$SR = \frac{\rho_2 - \rho_1}{\rho_2} \times 100\,\% \qquad (124.1)$$

124.3 Results and Discussion

124.3.1 Kind of Pre-polymer Affect the Viscosity of the System

The pre-polymer is an important part of UV curable material. It is the basic skeleton of light-cured material which determines the basic performance of the cured material. In order to study the effect of different kinds of pre-polymer to the viscosity, the same quality of pre-polymer V400, E44, MOX, and DOX, the same proportion of reactive monomer, and the same photo-initiator are used to prepare the hybrid UV light curable material samples. The viscosity is tested with the AR2000 rheometer at 25 °C. The results are shown in Fig. 124.2.

Figure 124.2 shows the viscosity of V400 is as relatively lower, TTA21 system has the low viscosity too but both the oxetane (MOX, DOX), and E44 have the high viscosity. That is because the epoxy resin contains epoxy group, and that epoxy resin has large molecular weight than the other pre-polymer.

Fig. 124.2 Kind of pre-polymer affects the viscosity of the system
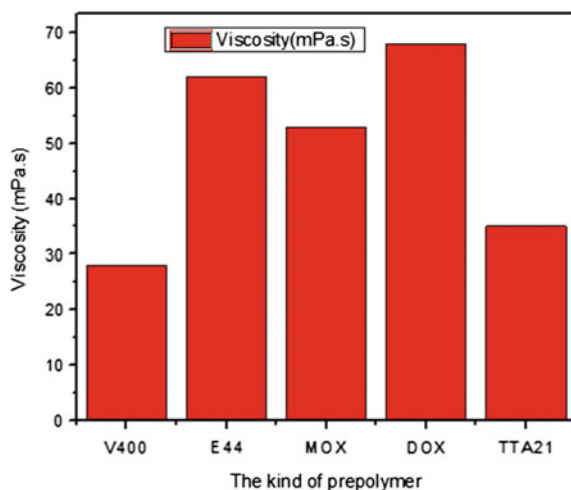
124.3.2   Kind of Pre-polymer Affect Curing Speed of the System

Do as 2.1 to prepare hybrid UV light curable material sample. The curing speed of each sample is tested using the UV-LED laser machine. The results are shown in Fig. 124.3.

From Fig. 124.3, the sort order of curing speed is V400 > DOX > MOX > TTA21 > E44. It follows that the oxetane has the high curing speed, and the price is relatively cheap; the TTA21 curing properties are similar to curing properties of the oxetane, both have the preferable curing performance. However, compared with the v400, the curing speed is lower; because the V400 is hyper-branched polyester acrylate pre-polymer, it contains more double bond and can react in more than one branch.

124.3.3   Kind of Pre-polymer Affect the Flexibility of the System

Do as 2.1 to prepare hybrid UV light curable material sample. The flexibility of each sample is tested using the QTY-32 toughness-type film tester. The results are shown in Fig. 124.4.

Figure 124.4 reflects that the bisphenol A epoxy resin E44 has better flexibility than hyper-branched polyester acrylates, and oxetane resin (DOX and MOX) also has good flexibility. This is due to the E44 bisphenol A epoxy resin having a long molecular chain, and the degree of cross-link is less than the cured hyper-branched acrylate V400, so the cured film also has good flexibility, while having a single

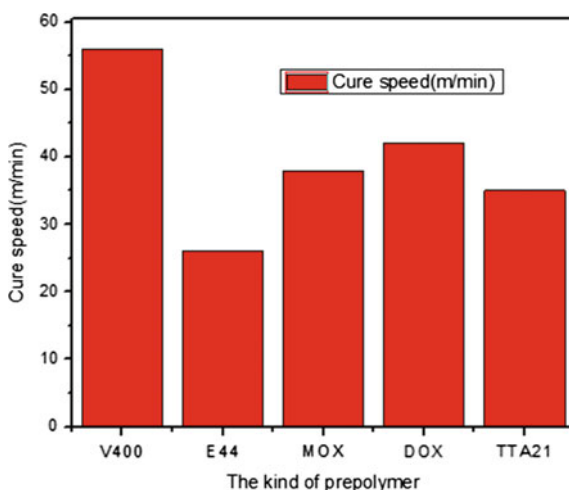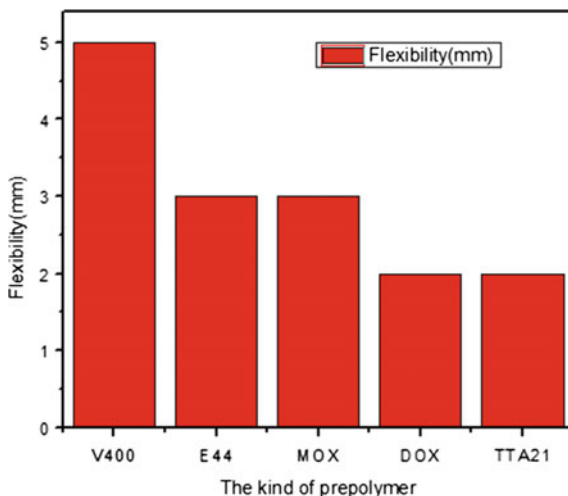**Fig. 124.3** Kind of pre-polymer affects curing speed of the system

Fig. 124.4 Kind of
pre-polymer affects the
flexibility of the system

oxetane polymerization direction; the polymerization product is a single-chain
polymer, so the flexibility is better.

124.3.4 Kind of Pre-polymer Affect the Volume Shrinkage of the System

To study the influence of UV curable epoxy resin system on volume shrinkage, test
the volume shrinkage of each sample. The results are shown in Fig. 124.5.

Fig. 124.5 Kind of
pre-polymer affects the
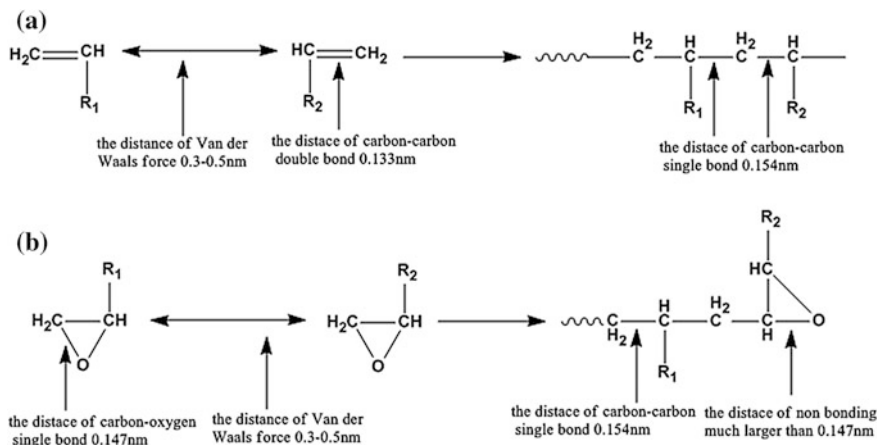volume shrinkage of the
system
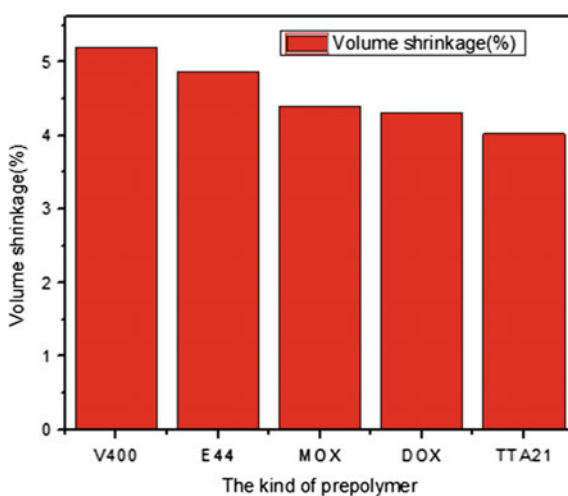
Fig. 124.6 Volume change with the mixed resin polymerization

Figure 124.5 shows that the hyper-branched polyester acrylate pre-polymer (V400), bisphenol A epoxy resin E44, mono-functional oxetane MOX, bi-functional oxetane, and 3, 4 epoxy ring DOX cyclohexylmethyl 3, 4-epoxycyclohexyl carboxylate TTA21 in hybrid photo-curable material system volume shrinkage decreases, V400 acrylic resin system, the volume shrinkage ratio is about 5.87 %, while the bifunctional oxetane DOX is about 4.02 %, TTA21 is about 4.08 %. This is due to the hybrid material that occurs in the photocurable polymerization, the intermolecular van der Waals force distance become into covalently bond, producing the bigger volume shrinkage [7]. Figure 124.6a, the acrylic resin polymerization, monomers or pre-polymers spacing effect by van der Waals forces into a covalent bond from operating range, a large volume contraction [8]; and the ring-opening epoxy compound. On one other hand, when the epoxy polymerizable monomer; polymerization, Fig. 124.6b, on the other hand, the distance between the epoxy monomer by van der Waals forces into a covalent bond from operating range, resulting in volume contraction; as shown the molecular ring structure is open and the cell size is larger than the monomer molecules are formed, partially offset by volume contraction, expressed as the total volume shrinkage is small [9, 10].

124.4   Conclusions

Compared to hyper-branched, polyester epoxy acrylate has low viscosity, senior curing speed; the epoxy resin, which can be used as a pre-polymer to change the properties of the system apply to the UV light curable material; an epoxy resin and an oxetane resin as pre-polymer may improve the flexibility of the cured material; at

the same time, the epoxy resin can also reduce the volume shrinkage of the system, and the system was reduced to a volume shrinkage of 4.02 % to improve UV curable material molding accuracy.

References

1. Crivello, J. V. (2013). Redox intitiated cationic polymerization. In *Macromolecular Symposia* (Vol. 323, no. 1, pp. 75–85). Weinheim: WILEY-VCH Verlag.
2. Zhang, H. (2013). *The application research for the cation and hybrid light-cured resin system.* Guangzhou: South China University of Technology.
3. Sangermano, M., Razza, N., Crivello, J. V. (2014). Cationic UV-curing: Technology and applications. *Macromolecular Materials and Engineering.*
4. Crivello, J. V. (1995). Photocurable silicone oxetanes, *US 5463084 A.*
5. Crivello, J. V., & Reichmanis, E. (2013). Photopolymer materials and processes for advanced technologies. *Chemistry of Materials, 26*(1), 533–548.
6. Liu, H. (2009). *Light curing material research and application of three dimensional printing.* Wuhan: Huazhong University of Science and Technology.
7. Kong, S. (2011). Composition of cationic initiator and oxetane compound. *U.S. Patent 7,902,305.*
8. Corcione, C. E., Striani, R., & Frigione, M. (2014). UV-cured methacrylic-silica hybrids: Effect of oxygen inhibition on photo-curing kinetics. *Thermochimica Acta, 576,* 47–55.
9. Duan, Y., Wang, S., Lu, B. (2000). Used for three-dimensional modelling method of light curing of the resin shrinkage study. *Journal of Xi'an Jiaotong University, 3,* 48+45–59.
10. He, X., Wang, D., Ma, G. (2009). Epoxy acrylates structure and performance of hybrid uv curing materials. *Journal of chemical engineering, 3,* 769.

Chapter 125
Study on the Performance of Adherence of Plastic Water-Based Flexographic Ink

Xiaofang Wang, Jingyang Li, Yanchao Yu, Haiqiao Wang and Xue Gao

Abstract The formula of water-based ink is designed to study the performance of adherence of water-based flexographic ink on plastic. Three kinds of film-forming resins are selected, and the proper additives are added to improve the ink printing capacity. The flexographic printing test machine is used to print ink proof. And the influence of film-forming resin and leveling agent on the properties of water-based ink adhesion is discussed. The results show that the water-based ink by film-forming resin Y2 has good adhesion on the BOPP film and that by film-forming resin Y3 has bad adhesion on the BOPP film The leveling agent can effectively improve the adhesion. The inks prepared by resin Y1 have good adherence to the BOPP film when the leveling agent L1 of 0.5 % is used. The inks have good adherence to the BOPP film when the film-forming resin Y3 and the leveling agent L3 of 1 % are used.

Keywords Plastic water-based · Flexographic ink · Adherence · Wet

X. Wang (✉) · J. Li · X. Gao
Beijing Key Laboratory of Packaging and Printing New Technology,
China Academy of Printing Technology, Beijing, China
e-mail: wangxiaofang@keyin.cn

J. Li
Beijing University of Chemical Technology, Beijing, China

Y. Yu
Food Science and Engineering College, Beijing University of Agriculture,
Beijing, China

H. Wang
Beijing Engineering Research Center for the Synthesis and Applications of Waterborne
Polymers, Beijing University of Chemical Technology, Beijing, China

125.1   Introduction

In recent years, the "green printing" has been the great attention of government and society, and water-based ink usage has reached 35 % in terms of flexible packaging, in the first row of other inks. Some products of flexible packaging such as cigarette packets, wine packet bag, kits, cosmetics packaging, and children's toys have been prepared using water-based flexographic printing ink, and the proportion will gradually increase. Therefore, the development and production of high-grade water-based flexographic ink for flexible packaging is urgently needed, and there is a very broad market prospect [1]. By using water as the main solvent, without other solvents, environmental protection as well as making the water-based ink film on the packaging material is restricted to further use, especially in the drying speed and adhesion performance, the two main performance of water-based ink has yet to be further improved in order to improve the printing quality of their products.

The adhesion performance of water-based ink on the plastic substrate which is smooth and non absorbent is very important. In this paper, the flexographic water-based ink formula of suitable for plastic film printing is designed, using different aqueous film-forming resin preparation of water-based ink, and add the appropriate flow ping agent, and then ink proof are prepared by flexographic printing test machine, discussing the adhesion between the film-forming resin and leveling agent for water-based ink on thin film.

125.2   Experiments

125.2.1   Raw Materials

Pigment: Phthalo blue BGS.
Resin: AZR acrylic dispersion resin, acrylic film-forming resin Y1, polyurethane film-forming resin Y2, acrylic film-forming resin Y3.
Additives: Antifoaming agent 810, dispersing agents 750 and 760, and leveling agents 410, 450, and 381.
Printing substrate: BOPP film.

125.2.2   Apparatuses

D2004 electric mixer (Shanghai Sile Instrument Corporation); SWFS-400 Lab dispersion machine (Shanghai Sower Mechanical and Electrical Equipment Co., Ltd.); KY-RY105 flexographic printing machine, 3-M tape; KRUSS surface tension meter K100.

125.2.3 Preparation of the Samples

125.2.3.1 Ink Preparation

According to the paste formula, the required paint, grinding resin, additives, and deionized water in accordance with the quality fraction are mixed in a beaker and stirred 30 min. Then, the predispersed paste is dispersed into the sand mill grinding for 2.5 h and the paste is filtered. Then, according to the cyan ink formula, the film-forming resin, the paste, and other additives are mixed and stirred 30 min at 3000 r/min, and in the last step, the water-based ink is filtered.

125.2.4 Performance Test

1. Proof: Testing proof is printed with KY-RY105 flexographic printing machine.
2. Surface tension: Surface tension is tested with KRUSS surface tension meter K100.
3. Adherence test: Mark out crossbars with QFH, use 3-M tape to stick the grids, and then observe to evaluate the adherence of the ink to the remaining grids.
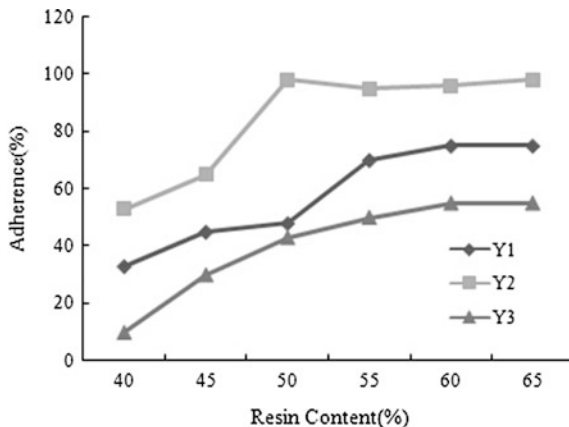
125.3 Results and Discussion

125.3.1 Effect on the Adherence of the Water-Based Ink Prepared by Different Types of Film-Forming Resins

To study the effect on the adherence of the water-based ink, the other composition and the content of water-based ink are fixed, water-based ink samples are separately prepared by different kinds of resins Y1, Y2, and Y3, and tested. The adherence is tested at the normal condition (temperature 25 °C, humidity 24 ± 2 %). The results are shown in Fig. 125.1.

From Fig. 125.1, film-forming resin types have a greater influence on the adherence of ink on the film. The adherence of water-based ink prepared by film-forming resin Y2 on the BOPP film is the best which one prepared by film-forming resin Y3 is the worst. Because the film-forming resin is the key factor affecting ink printing performance, its own performance directly affects the ink film-forming properties. And the film-forming resin performance quality mainly depends on its structure and characteristic. Part of Film-forming resin Y2 is the waterborne polyurethane resin, on the one hand, non-absorbent substrates such as plastic have good affinity, on the other hand has a lower Tg value, the more excellent film-forming properties, so the preparation of water-based ink has good adhesion [2].

Fig. 125.1 Adherence of the water-based ink prepared by different types of film-forming resins

125.3.2 Effect on the Adherence of the Water-Based Ink Prepared by Different Types of Leveling Agents

Leveling agents can improve wetting and leveling before the ink curing system in order to reduce or eliminate defects in the ink film surface. Adding a certain amount of leveling agent can make the surface tension of the ink to be in a more uniform state, cause no change in the process of evaporation of the solvent, maintain the best flow property, and help to improve the film-forming properties of the ink.

The other composition and the content of water-based ink are fixed, plastic water-based flexographic ink samples are separately prepared by different kinds of leveling agents L1, L2, and L3, and the film-forming resins are Y1 and Y3. Ink proof is prepared by flexographic printing test machine, and the adherence is tested after drying. The results are shown in Fig. 125.2.
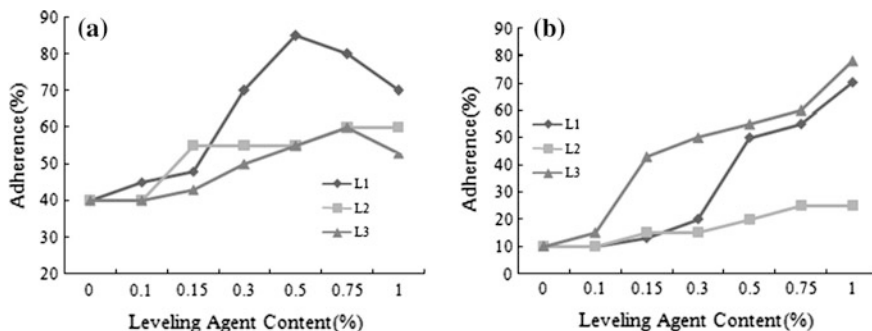

Fig. 125.2 Adherence of the water-based ink prepared by different types of leveling agents, and the film-forming resins are Y1 (**a**) and Y3 (**b**)

From Fig. 125.2, the adherence of the water-based ink on the BOPP film has been improved by adding three types of leveling agents. The adherence of the water-based ink prepared adding leveling agent L1, the adherence of ink with other two leveling agents L2 and L3 is the lower, but they can also improve adhesion. Because the plastic film surface is smooth with less absorbing capacity, the adhesion of ink depends mainly on the two aspects: One is the wetting of the ink on the substrate, that is, the liquid to the solid surface affinity state and the other is the binding force between ink and plastic substrates [3, 4].

The wetting and leveling of the water-based ink on the film depend on its surface tension. There are two effects of surface tension: one is driven by liquid surface area of the contraction to as small as possible, and second surface tension or surface tension gradient difference having a low surface tension of the liquid tends to cover the high surface tension of phase [5].

On the other hand, when there is strong opposite polarity between ink and plastic substrate, the traction is induced, which is called secondary binding force [6, 7]. Usually, secondary binding force between ink and plastic substrates is greater, thus the better ink adhesion [8]. Secondary binding force increases rapidly with decrease in the distance between molecules. Test the surface tension of the ink leveling agent added before and after, and the results are shown in Table 125.1.

As shown in Table 125.1, the two leveling agents effectively reduce the surface tension of the water-based ink. When leveling agent L1 is added, the surface tension of the water-based ink (the film-forming resin is Y1) drops from 35.3 to 22.9 mN/m. When leveling agent L3 is added, the surface tension of the water-based ink (the film-forming resin is Y3) drops from 34.2 to 23.7 mN/m. The wettability of ink on the BOPP film has improved greatly. Chemical bonding force between the ink and the film are enhanced, and adhesion is increasing.

In addition, as a result of high-speed printing, ink and film molecular sharply reduce, the distance between the secondary bonding force increased significantly, also helps to improve the adhesion of ink on the film.

Table 125.1 Surface tension of the ink by different leveling agents

Sample	Surface tension (mN/m)	
	Before	After
Y1/L1	35.3	22.9
Y1/L3		26.4
Y3/L1	34.2	26.5
Y3/L3		23.7

125.4 Conclusions

1. Film-forming resin type has a great influence on the performance of water-based ink, and the film-forming resin Y2 flexographic water-based ink on the BOPP film that is prepared has good adhesion.
2. Leveling agent for ink adhesion on the BOPP film has some improvement. When using different film-forming resins, the selection of appropriate leveling agent is done according to the actual need. The inks have good adherence to the BOPP film when the film-forming resin Y1 and the leveling agent L1 of 0.5 % are used. The inks have good adherence to the BOPP film when the film-forming resin Y3 and the leveling agent L3 of 1 % are used.

References

1. Xin, X. (2012). *Water-based Ink*, pp. 4–5.
2. Zhou, Z. (2006). The development direction of the printing ink. *Printing Quality & Standardization, 8*, 15–20.
3. Wang, N. (2005). Ink film adhesion testing. *Screen Printing, 1*, 24–25.
4. Liu, P. (2009). *Bond Paper Printing Performance Research*
5. Wang, X., Wei, X., & Huang, B. (2009). Influence of promoter on the characters of water-base UV varnish. *Packaging Engineering, 11*, 86–89.
6. Wang, N. (2005). The detection and analysis of packaging film adhesion. *China Packing Industry, 4*, 54–55.
7. Dongyu, C., Shanglin, X., & Chen, X. (2009). Preparation of aqueous intaglio printing ink based on polyurethane-acrylate hybrid emulsions. *Packaging Engineering, 3*, 26–29.
8. Rentzhog, M., & Fogden, A. (2006). Print quality and resistance for water-based flexography on polymer-coated boards: Dependence on ink formulation and substrate pretreatment. *Progress in Organic Coating.*

Chapter 126
Synthesis and Mesomorphism of a Novel Triphenylene-Based Discotic Liquid Crystal with Unsaturated Side Chain

Xingtian Hao, Jianchuang Wang, Feng Hong, Shuaifeng Zhang, Chunxiu Zhang and Jialing Pu

Abstract A novel triphenylene-based discotic liquid crystal 2-allylcarboxyl-3,6,7,10,11-pentapentyloxytriphenylene was synthesized. The chemical structure was determined by ^{1}H-NMR and FT-IR spectrum, and its mesomorphism was investigated by differential scanning calorimeter (DSC) and polarizing optical microscopy (POM) method. The compound showed classical texture of columnar phase in a wide mesophase temperature from the room temperature to 175 °C during cooling. It also sets the foundation of designing and preparing liquid crystal polymer due to its double bond of the side chain.

Keywords Liquid crystal · Columnar phase · Triphenylene

126.1 Introduction

Since the discovery of discotic liquid crystals by Chanderasekhar in 1977, there has been an ever-increasing interest in the study of its synthesis and optoelectronic property. Discotic liquid crystals can be characterized as having a rigid and usually planar aromatic core provided with flexible chains at the periphery and typically rotational symmetry. The radical anisotropy within the molecules generally induces an assembly of the molecules into columns. The molecules within these columns can stack in a variety of orientations, and the columns themselves can further

X. Hao · J. Wang · F. Hong · S. Zhang · C. Zhang (✉) · J. Pu
Beijing Institute of Graphic Communication, Beijing, China
e-mail: zhangchunxiu@bigc.edu.cn

X. Hao
e-mail: haoxingtian123@163.com

self-assemble in a variety of ways [1]. Therefore, columnar phases are characteristic for rapid one-dimensional transport of charge carriers and energy. All these properties make discotic liquid crystal as a potential material in the areas of OLEDs, photoconductors, information storage, photovoltaic solar cells, etc. [2–4].

Triphenylene derivatives are easily to synthesis and purify, various in structure, having lower melting point and good thermal stability, all of which make them one of the excellent materials that have been long studied in the families of discotic liquid crystals [5, 6]. In this work, a novel triphenylene-based discotic liquid crystal 2-allylcarboxyl-3,6,7,10,11-pentapentyloxytriphenylene was synthesized to make use the advantages of triphenylene derivatives. Its chemical structure was determined by ^{1}HNMR and FT-IR spectrum, and mesomorphism was classified by DSC and POM methods.

126.2 Experimental

Chemicals used in the synthesis if not specified were all analytic reagents (Beijing Chemical Reagents Co). The chemical structure was characterized by measuring on a Brucker DMX-300 300 MHz NMR spectrometer and FTIR-8400.

126.2.1 Synthesis of 2-allylcarboxyl-3,6,7,10,11-pentapentyloxytriphenylene

The target compound 4 was synthesized by the route which was shown in Fig. 126.1.

The compound 1 was prepared on the basics of the Williamson reaction. Then, 2,3,6,7,10,11-hexapentyloxytriphenylene was prepared by the trimerization reaction of veratrol in the presence of iron (III) chloride [7]. The process of preparing 2-hydroxyl-3,6,7,10,11-pentapentyloxytriphenylene (compound 3) was carried by selective ether cleavages with B-bromocate-cholborane [8]. 2-hydroxyl-3,6,7,10,11-pentapentyloxy-triphenylene (300 mg, 0.44 mmol), acrylic acid (38 mg, 0.53 mmol) and 4-N,N-dimethylamino pyridine (DMAP, 8 mg) were dissolved in anhydrous dichloromethane and stirred for 10–15 min. Then, dicyclohexylcarbodiimide (DCC, 128 mg, 0.66 mmol) was added and refluxed for 12 h with the protection of nitrogen on an oil bat at a sufficiently high temperature. The product was purified by chromatography with the eluent of dichloromethane–petroleum ether (3:1 v/v) and was recrystallized from ethanol, which yields 32.6 %. FT-IR (KBr): V_{max} (cm^{-1}): 3109 (–CH=C–), 2965, 2865 (–CH$_3$/–CH$_2$), 1742 (–COO), 1605, 1521, 1437 (–C=C–),
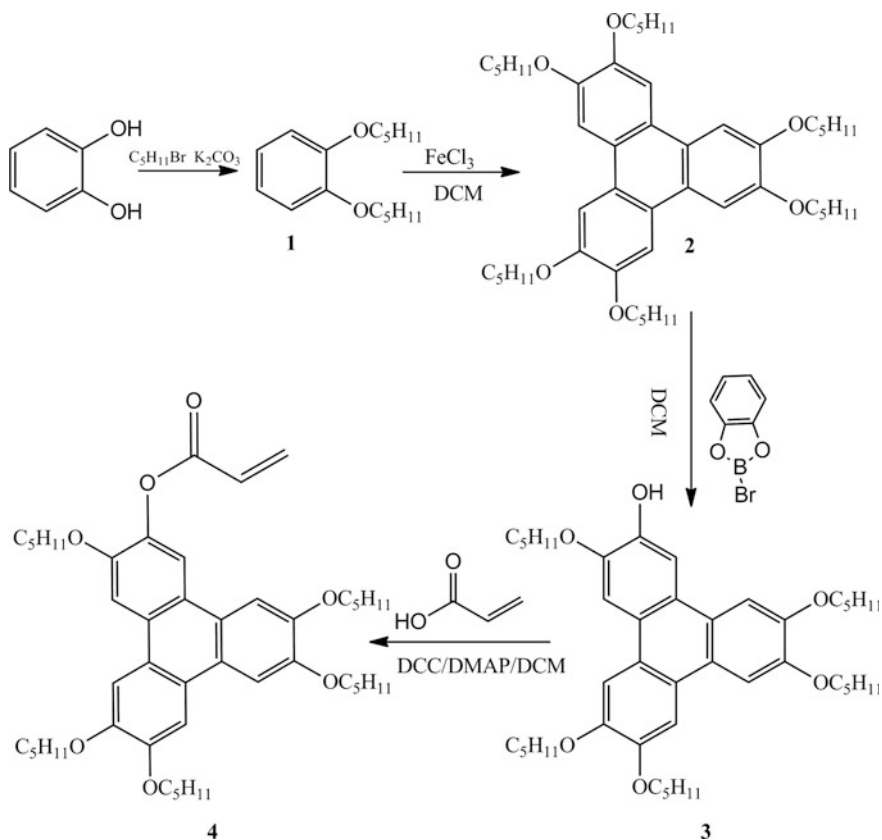
Fig. 126.1 Synthetic route of compound 4

1262 (–C–O–C).^{1}H-NMR:δH (300 MHz, CDCl$_3$):8.13 (s, 1H), 7.79–7.89 (m, 5H), 6.68–6.74 (d, 1H), 6.41–6.50 (m, 1H), 6.07–6.10 (d, 1H), 4.21–4.25 (q, 10H), 1.84–1.97 m, 10H), 1.12–1.49 (m, 20H), 0.88–1.10 (m, 15H).

126.2.2   *Characterization*

Thermal and optical properties of the synthesized material were observed by using a Leica polarizing optical microscope equipped with a Linkam LC600 hot stage and a Netzsch differential scanning calorimeter DSC (Thermal Analysis DSC 2010). The phase transition temperatures and the associated enthalpy were determined by DSC in the temperature range of 40–230 °C at a scanning rate of 10 °C min^{-1}, and the optical textures were studied by using the polarizing microscope at the same rate.

126.3   Results and Discussion

126.3.1   DSC

In the DSC thermograms (Fig. 126.2), the compound 4 undergoes a endothermic transition(18.68 J/g) located at 174.8 °C which is the clearing point during the second heating run, corresponding to a transition of mesophase to isotropic phase, and no other phase transition was detected. On cooling, the sample undergoes an exothermic transition (−18.29 J/g) located at 171.6 °C. The absence of other transitions and the similarity of the enthalpies associated with transitions from columnar discotic mesophase to isotropic liquid [9] supports the hypothesis that compound 4 is liquid crystalline from room temperature to its clearing point.

126.3.2   POM

Compound 4 is a yellow viscous liquid crystal that is birefringent at room temperature, and no crystalline phase was seen. As it is heated, it becomes a mobile liquid, which becomes isotropic at 175 °C. The texture displayed in Fig. 126.3 forms when a liquid crystalline sample is cooled from 175 °C to the room temperature. The POM revealed that it has the classical columnar phase textures.

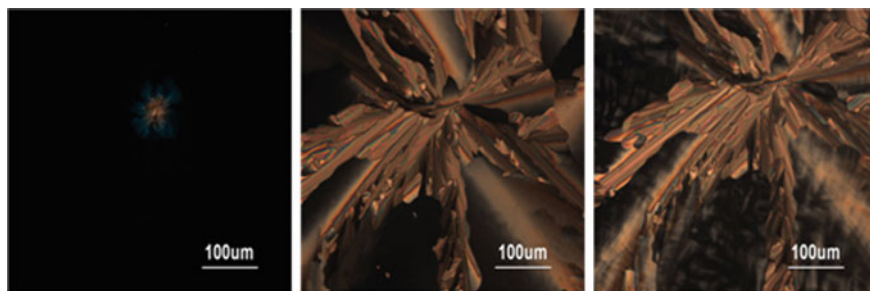**Fig. 126.2** DSC curves of the compound with rate of 10 °C min^{-1}
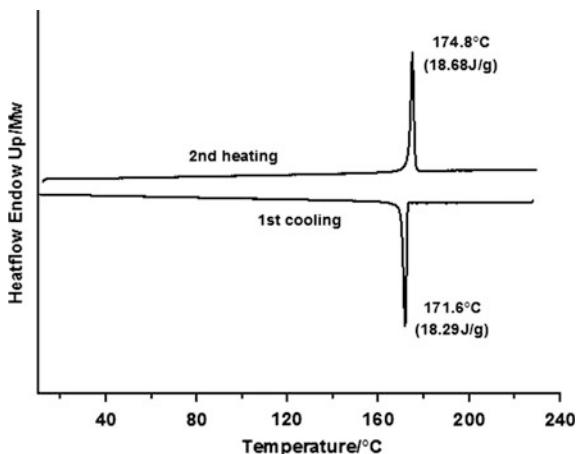
Fig. 126.3 Textures observed at 175 °C (*left*), 173 °C (*middle*) and room temperature (*right*) during cooling process (magnification 100×)

126.4 Conclusions

A novel triphenylene-based discotic liquid crystal compound has been prepared and fully characterized. Its structure was confirmed by the 1HNMR and FT-IR spectrum, and its liquid crystal property was characterized by the POM and DSC. It showed a columnar discotic mesophase between the room temperature and 175 °C and has a wide temperature range of mesophase. It is a planar discotic mesogen with double bond in the side chains which can be the precursor of liquid crystal polymer.

References

1. Chandrasekhar, S., Sadashiva, B. K., & Suresh, K. A. (1977). Liquid crystals of disc-like molecules. *Pramana, 9*, 471–480.
2. Boden, N., Bushby, R. J., Clements, J., & Movaghar, B. (1999). Device applications of charge transportant in discotic liquid crystals. *Journal of Materials Chemistry, 9*, 2081–2086.
3. Pecchia, A., Lozman, O. R., Movaghar, B., et al. (2002). Photoconductive transients and one-dimensional charge-carrier dynamics in discotic liquid crystal. *Physical Review B*, 65, Art. No. 104204
4. Schmidt-Mende, L., Fechtenkotter, A., Mullen, K., Moons, E., Friend, R. H., & Mackenzie, J. D. (2001). Self-organized discotic liquid crystals for high-efficiency organic photovoltaics. *Science, 293*, 1119–1122.
5. Bushby, R. J., & Lozman, O. R. (2002). Discotic liquid crystals 25 yesrs on. *Current Opinion in Colloid & Interface Science, 7*, 342–354.
6. Kumar, S. (2004). Recent developments in the chemistry of triphenylene-based discotic liquid crystals. *Liquid Crystals, 31*(8), 1037–1059.

7. Boden, N., Borner, R. C., Bushby, R. J., Cammidge, A. N., & Jesudason, M. V. (1993). The synthesis of triphentlene-based discotic mesogens new and improved routes. *Liquid Crystals, 15* (6), 851–858.
8. Kumar, S., & Manickam, M. (1998). Synthesis of functionalized triphenylenes by selective ether cleavage with B-bromocateholboane. *Synthesis, 8*, 1119–1122.
9. Nuckolls, C., & Katz, T. J. (1998). Synthesis, structure, and properties of a helical columnar liquid crystal. *Journal of the American Chemical Society, 120*, 9541–9544.

Chapter 127
Synthesis and Characterization of Polyaniline Coating Modification Micro Copper Powder

Wensheng Wang, Chao Li, Xiaojuan Shi, Huanxiu Liu and Liyu Sun

Abstract The coating effect of fine copper powder in situ polymerization is discussed in this paper. A certain amount of aniline hydrochloride is taken and dissolved in 20 ml deionized water. Appropriate amount of copper is added to it and stirred with ultrasounds for 10 min to form suspension; then adding ammonium persulfate and hydrogen peroxide through constant-pressure titration funnel to the mixed solution of copper/aniline hydrochloride suspension reaction under the condition of the ice bath for 4 h and after centrifugal, filtration, washing, collect the resulting product and dry it under the temperature of 80 °C for 2 h. Transform infrared spectroscopy analyzer is used for analyzing, and field emission scanning electron microscopy is employed for product observation. The result shows that when 0.45 ml hydrogen peroxide and 0.35 g aniline hydrochloride are added, copper surface coating material gives the best performance in terms of both density and uniformity.

Keywords Ultrafine copper powder · Aniline hydrochloride · Polyaniline · Surface coating

127.1 Introduction

Copper powder has good metallic luster, low production cost, and superior conductive performance [1]. Compared with gold, silver, aluminum, iron, and zinc, copper is an ideal conductive filler material. Therefore, with copper powder as conductive filler electronic pastes material has the broad development prospects. But there is also the restrictive in widely used. The most significant problem is that copper powder is micron particles, has large specific surface area and high specific

W. Wang (✉) · C. Li · X. Shi · H. Liu · L. Sun
Dalian Polytechnic University, Dalian, Liaoning, China
e-mail: wangws@dlpu.edu.cn

surface energy, belong to the unstable system of thermodynamics. Moreover, copper powder can be easily oxidized in the heat-curing resin adhesive, reducing its ability to conduct electrons. How to avoid the oxidation of copper is the key problem to ensure the stability of the electric conductivity and is also the hot spot of the research of the copper slurry at present.

In order to solve the above problems, we must modify the micro copper powder. To modify the surface of ultrafine copper powder, there are two kinds of methods: One is surface conversion. The structure of the material itself is changed, so as to achieve the change in performance. Phosphating, passivation, radiation treatment, ultrasonic processing, and heat treatment are common methods [2–4]. Two is the surface coating method; it is coated with a suitable material. It enhances the physical and chemical properties of the coated material. In order to keep the copper excellent conductive performance, now existing coating materials of metal, coupling agent, corrosion inhibitor and conductive polymer [5–11].

The commonly used conducting polymers are polyaniline, polypyrrole, and thiophene. The commonly used coating technologies are dissolved coating, precipitation, in situ polymerization, and others [12]. Pyrrole was polymerized through electrochemical method. Research shows that compared with the untreated copper, the coated ones have better antioxidant capacity [13]. The oxidation resistance and corrosion resistance of the composite particles were improved by the conductive polymer coating. The affinity with the organic material is strong; the surface energy is smaller and not easy to reunite; because of the electrical conductivity of the conductive polymer, the conductivity of the composite particles is not much lost. Based on the excellent properties of conducting polymer, the preparation of Polyaniline/Cu Composites by catalytic oxidation was used in this experiment.

127.2 Experiments

127.2.1 Experimental Reagents and Equipment

The copper powder (1000 mesh), Aniline (C_6H_7N), Chloroform (CCl_4), the recovery of Tianjin Science and Technology Development Co Ltd, CP; Hydrochloric acid (36 %), the recovery of Tianjin Science and Technology Development Co Ltd; H_2O_2, ammonium persulfate ((NH_4)$_2S_2O_8$), Tianjin Da Mao chemical reagent plant, CP.

Collector magnetic agitator (DF-10S), ultrasonic cleaner (JP-009D), circulating water vacuum pump (SHZ-D), Buchner funnel, electro thermal constant temperature air blast dryer (ZBY149-83), field emission scanning electron microscopy (SEM), X ray spectrometer, Japan Electronics Corporation, JEOL JSM-6460LV; Fourier transform infrared spectroscopy (FTIR) U.S. platinum Elmer company, Spectrum One-B.

127.2.2   Experimental Method

127.2.2.1   Aniline Hydrochloride Preparation

The appropriate amount of aniline was distilled by water vapor method using vacuum distillation for two times. The collected fractions were placed in dark and cold storage environment for use. The amount of aniline was dissolved in the amount of chloroform, and hydrochloric acid (36 %) was added. Take the white solid floating on the liquid surface (aniline hydrochloride), vacuum drying sealed.

127.2.2.2   Polyaniline-Coated Copper Powder

Take proper amount of aniline hydrochloride dissolved in 20 ml deionized water, add 1 g copper powder, and perform ultrasonic stirring for 10 min. Move the aniline hydrochloride/copper powder suspension in three-mouthed flask containing ice bath and regulate the stirring speed of the rotor suspension to maintain a steady state. Then, move the 15 ml preparation of ammonium sulfate/H_2O_2 water solution into constant-pressure titration funnel, slowly add the aniline hydrochloride/copper powder suspension, and then continue the reaction for 4 h. Separate centrifugally (4000 r/min) the suspension, collect the precipitation part, and wash it with deionized water. Filter with Buchner funnel and dry at 80 °C for 2 h. The samples were analyzed by EDS, FTIR, and SEM.

127.3   Results, Discussion, and Analysis

127.3.1   Effect of the Dosage of Aniline Hydrochloride on the Morphology of the Product

Figure 127.1a shows the surface of copper before treatment. The particle size distribution of copper powder is flaky, and the surface is smooth. Figure 127.1 shows the micrographs of the composite products prepared with different aniline dosage. The obvious changes in the particle surface after modification can be seen in the graph. However, the coating with different aniline dosage is different.

Figure 127.1b is a small amount of aniline hydrochloride (0.15 ml) product images. It can be seen from the figure product coating layer was thin, and we can faintly see the smooth surface at the bottom. There are many fine particles between a piece of which may be a composite of a not wrapped polyaniline. After increasing the dosage (0.25 ml), the product of Fig. 127.1c was obtained. By the graph, the thickness of the surface coating layer of the composite can be obviously improved, regardless of the particle size. To further increase the amount of aniline hydrochloride (0.35 ml) to obtain the product morphology as shown in Fig. 127.1d.
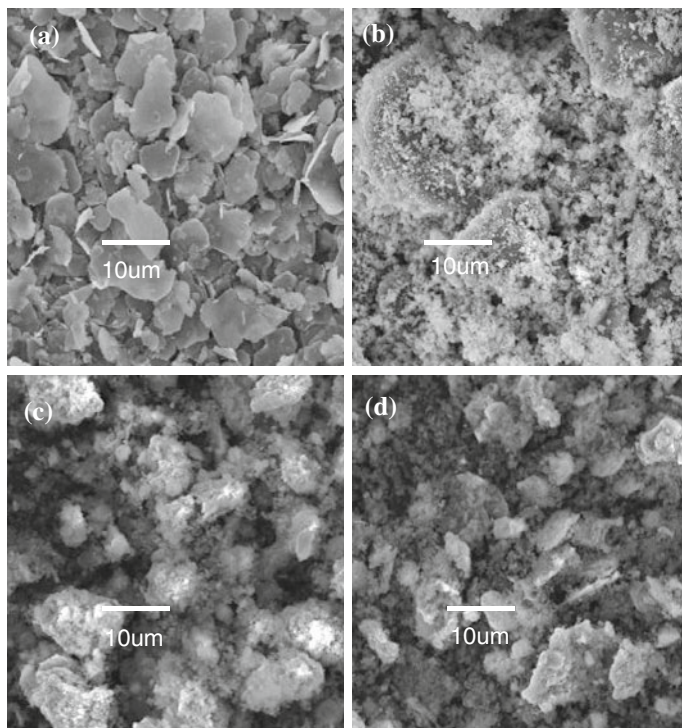
Fig. 127.1 SEMs of the composite products were prepared with different aniline dosage (**a** unmodified copper powder; **b** 0.15 ml; **c** 0.25 ml; **d** 0.35 ml) (1 g, 0.45 ml, APS 0.2 g hydrogen peroxide)

From he figure we can see the densely coated copper particles and coating complexes between the fragments of a large number of tiny fragments. The chronologies of these fragments appear to have a lot of polyaniline not coated on the surface of the flaky copper powder. From the above analysis, it is clear that only the amount of aniline in a certain range can lead to well coating. If the amount of aniline hydrochloride is too small, the coating layer will be thin. But the excessive amount of aniline hydrochloride may cause monomer in solution polymerization of polyaniline produces a large amount of debris.

127.3.2   Effect of H_2O_2 Dosage on the Morphology of the Product

Hydrogen peroxide is the oxidant of aniline polymerization, and its dosage is another major factor affecting the morphology of the product. The other factors are constant, and the amount of hydrogen peroxide is changed between 0.35 and
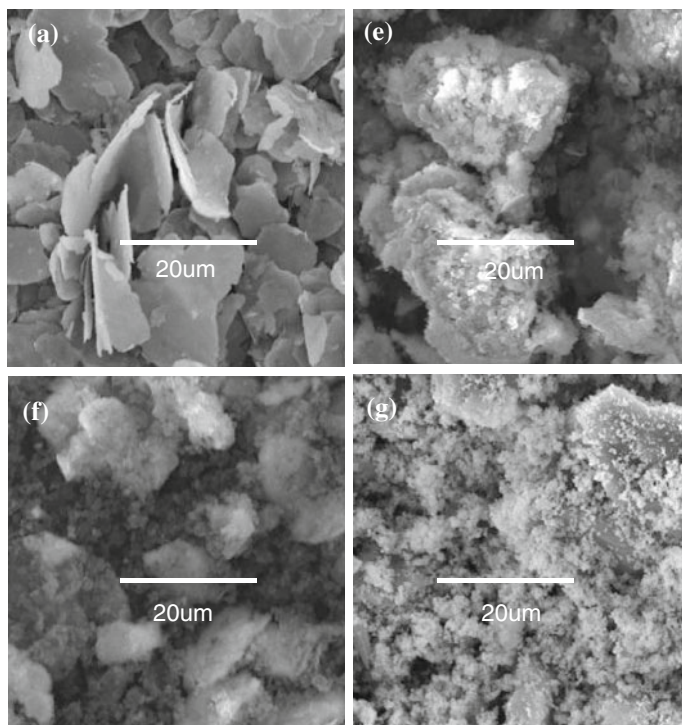
Fig. 127.2 SEMs of the composite products were prepared with different aniline dosage (**a** unmodified copper powder; **e** 0.35 ml; **f** 0.45 ml; **g** 0.55 ml) (1 g, 0.25 ml, APS 0.2 g aniline)

0.55 ml; the surface of the products was changed. As shown in Fig. 127.2g, when the amount of H_2O_2 was high (0.55 ml), the catalytic oxidation of H_2O_2 was stronger, so the coating layer of polyaniline forms rapidly. The surface of the composites was rough, and the size of the particles increased significantly. The amount of H_2O_2 in 2f was 0.45 ml, the surface of the coating is uniform and smooth, and the debris of polyaniline was less.

The amount of H_2O_2 in 2e was reduced to 0.35 ml. This made the composite surface coating coarse and started to appear in the bulk fragments. This is because less H_2O_2 made the formation of polyaniline slow, the initiator of ammonium sulfate oxidation. The initiator of ammonium sulfate has the oxidation, corroded a part of the copper sheet. The corroded copper was into the solution in the form of Cu^{2+}. Aniline HCl in solution was rapidly polymerized under the catalysis of copper ions, and a lot of polyaniline fragments were generated. By the analysis, only the amount of the appropriate range of H_2O_2 leads to the formation of smooth and dense coating.

Fig. 127.3 EDS spectrum of
the product
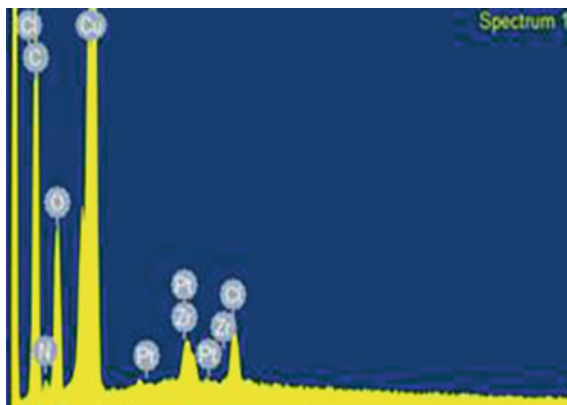
127.3.3 Product's EDS Analysis and Identification

The product (copper 1 g, hydrogen peroxide 0.45 ml, aniline hydrochloride 0.35 g, APS 0.2 g) EDS spectrum, as shown in Fig. 127.3.

127.3.4 Product's FTIR Analysis and Identification

The product (copper 1 g, hydrogen peroxide 0.45 ml, aniline hydrochloride 0.35 g, APS 0.2 g) FTIR spectrum, as shown in Fig. 127.4.

Standard spectrum of polyaniline: absorption peak of quinone ring (1582 cm^{-1}, 1120 cm^{-1}) and absorption peak of benzene ring (1492 cm^{-1}, 801 cm^{-1}). From Fig. 127.4, we could see that absorption peak of quinone ring corresponds to (1610 cm^{-1}, 1130 cm^{-1}) and that of benzene ring corresponds to (1469 cm^{-1},

Fig. 127.4 FTIR spectrum of
the product
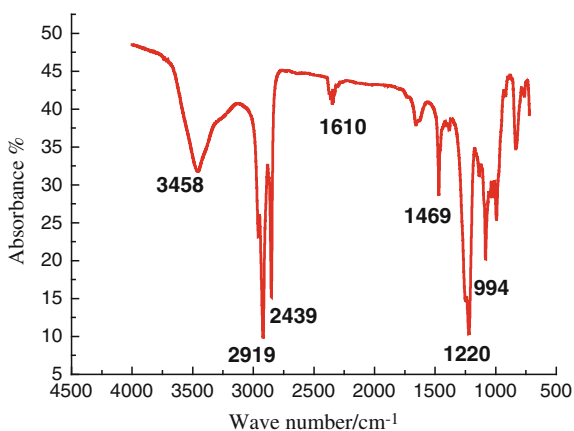
810 cm^{-1}). The obtained polyaniline was doped polyaniline, as a result, peak has a redshift tends to conform to the actual situation; it is possible to show that aniline hydrochloride polymerization reaction of the doped polyaniline.

127.4 Conclusions

Polyaniline conductive polymer of micro flake powder were surface modified, polyaniline well coated on the copper surface, forming a dense and smooth coating. The amount of H_2O_2 and aniline hydrochloride both play important role in the formation of coating layer; too much or too little dosage creates a comprehensive effect on the coating layer. When the dosage of aniline hydrochloride was 0.35 g, H_2O_2—0.45 ml, APS—0.2 g, and copper powder—1 g, the good comprehensive effect of polyaniline coating layer could be formed.

References

1. Lu, W., Zhang, L., Zhang, Q., et al. (2013). Effect of nitric acid on the dispersion characteristics of erosion of nano Cu powder in lubricating oil. *Journal of Lanzhou University of Technology, 39*(3), 5–8.
2. Chang, S., & Guo, Z. (2007). Progress in technology of anti-oxidation copper powder. *Powder Metallurgy Industry, 17*(1), 49–53.
3. Cao, W. (2008). *Study on anode materials for electroplating copper nickel alloy*. Nanjing: Nanjing University of Science and Technology.
4. He, Tian. (2012). *Ultrasonic emulsion prepared by electrolysis of Cu and MBT, HQ inhibition treatment*. Changsha: Central South University.
5. Li, C. (2013). Status quo and prospect of research on surface modification of ultrafine copper powder. *Global Market Information, 19*(12), 146–147.
6. Anonymous, (2009). The performance of modified ultrafine copper imidazole. *Material Protection, 42*(11), 33–35.
7. Tan, N., Guo, Z., Chen, B., et al. (2010). Preparation of ultrafine copper powder by technology and surface modification in liquid phase reduction. *Powder Metallurgy Industry, 20*(3), 47–51.
8. Zhou, Q., Jiang, P., Zhu, W., et al. (2004). Preparation and characterization of nano copper powder oxidation. *Rare Metal Materials and Engineering, 33*(2), 179–182.
9. Ren, Z. (2012). *Study on preparation of ultrafine nickel coated copper powders by electroless plating*. Harbin: Harbin Institute of Technology.
10. Zhao, Y., Zhao, Q., Du, S., et al. (2004). Research progress in the technology of surface anti oxidation of copper powder. *Surface Technology, 33*(6), 4–6.
11. Hao, L., Yu, J., Li, R., et al. (2007). Electroless Ni-P coating and its corrosion behavior of tungsten copper powder alloy. In *Proceedings of the Yuxiang Cup Cum of Commenting on the Tenth Session of the National Youth Corrosion and Protection Technology of the Eighth China Youth Corrosion and Protection Conference* (pp. 112–115), Shenyang.
12. Chen, Y. (2009). Preparation of new type of conductive ink. *Guangdong Printing, 1*(3), 51–52.
13. Qin, Y., Qi, S., Yang, Y., et al. (2011). Research progress of improving the properties of conductive adhesive. *Chinese Adhesive, 20*(9), 53–58.

Chapter 128
Synthesis and Mesophases of 2-Allyloxy-3,6,7,10,11-Penta-Pentyloxytriphenylene

Feng Hong, Shuaifeng Zhang, Xingtian Hao, Jianchuang Wang, Chunxiu Zhang and Jialing Pu

Abstract A novel triphenylene-based discotic liquid crystal 2-allyloxy-3,6,7,10,11-penta-pentyloxytriphenylene was firstly synthesized. The chemical structure was determined by ^{1}H-NMR and Fourier transform infrared spectrometer (FT-IR), and its mesophase was investigated by differential scanning calorimeter (DSC) and polarizing optical microscopy (POM) methods. It has a large range of mesophase from 111 °C to room temperature. During the cooling process, liquid crystal textures with typical conical fan shape were observed.

Keywords Discotic liquid crystal · Triphenylene · Columnar phase · Allyloxy

128.1 Introduction

Organic electronics using conjugated molecules as active components in electronic devices is a field of intense scientific activity [1]. In recent years, discotic liquid crystals especially triphenylene derivative with variable structures, good process-ability and high charge carrier mobilities, have been instructing a large extent interests for the workers in the field of organic semicondutor materials [2, 3]. Based on triphenylene-based discotic liquid crystals, materials of the electronic devices such as light-emitting diodes (LEDs), photovoltaic diodes (PVDs), field effect transistors (FETs), memory elements, and sensors are now commonly used in the chemical literature [3].

Triphenylene-based discotic liquid crystals comprising the rigid core and the flexible peripheral chains make it available for the disk-like molecules to form the columnar mesophase through self-assembly [4–9]. In this work, the target com-

F. Hong · S. Zhang · X. Hao · J. Wang · C. Zhang (✉) · J. Pu
Beijing Institute of Graphic Communication, Beijing, China
e-mail: zhangchunxiu@bigc.edu.cn

pound 2-allyloxy-3,6,7,10,11-penta-pentyloxytriphenylene was synthesized, and its structure was determined by ^{1}H-NMR spectrum and FT-IR. Its characteristics were studied by DSC and POM methods.

128.2 Experimental

Chemicals used in the synthesis if not specified were all analytic reagents (Beijing Chemical Reagents Co). The chemical structures were characterized by measuring on a Brucker DMX-300 300 MHz NMR spectrometer and FTIR-8400. Thermal and optical properties of the synthesized materials were observed by using a Leica polarizing optical microscope equipped with a Linkam LC600 hot stage and a Netzsch differential scanning calorimeter DSC (Thermal Analysis DSC 2010).

128.2.1 Synthesis of 2-Allyloxy-3,6,7,10,11-Penta-Pentyloxytriphenylene

The crude product of 2-hydroxy-3,6,7,10,11-penta-pentyloxytriphenylene was synthesized as described in the literature [2, 6]. The synthesis route of the target molecule 2-allyloxy-3,6,7,10,11-penta-pentyloxytriphenylene was shown in Fig. 128.1. 0.5 g (0.74 mmol) of 2-hydroxy-3,6,7,10,11-penta-pentyloxytriphenylene, 0.3 g (2.22 mmol) of K_2CO_3 and 0.107 g (0.89 mmol) of 3-bromopropene in 50 ml of acetoriphne were refluxed for 12 hours under a nitrogen atmosphere. Once the reaction was complete, pour the water into it and then use dichloromethane to extract. The organic layer was dried and passed through a silica column to get the crude product. After that, the ethanol was used to recrystallize to get the white ponder solid (0.51 g) (yield 96.4 %); FT-IR (KBr): vmax/cm 1259 (C–O–C); δH (300 MHz, CDCl$_3$), 7.8–7.89 (t, 6H), 6.18–6.27 (m, 1H), 5.52–5.58 (d, 1H), 5.35–5.38 (d, 1H), 4.82–4.84 (d, 2H), 4.21–4.26 (t, 10H), 1.91–1.98 (m, 10H), 0.87–1.65 (m, 35H).
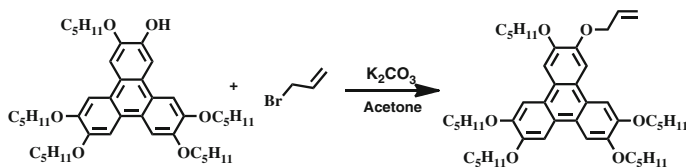

Fig. 128.1 The synthesis route of target compound

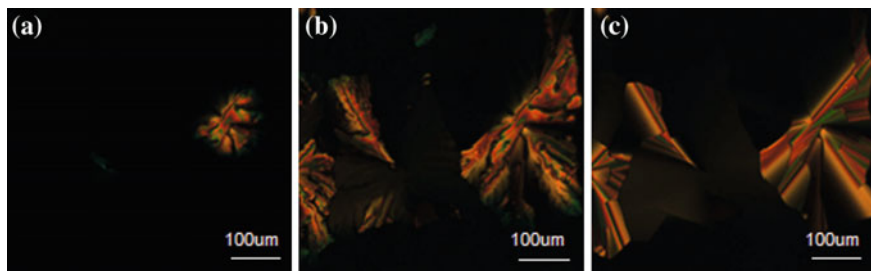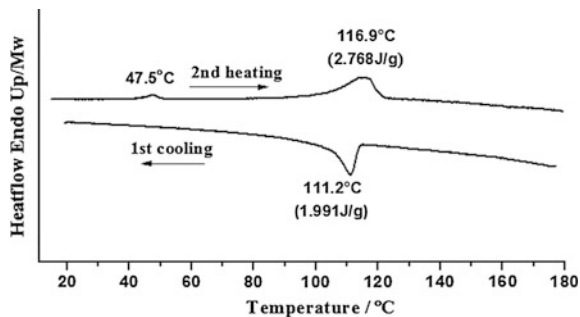**Fig. 128.2** DSC curves of the compound with rate of 10 °C/min

Fig. 128.3 Textures observed at 132.7 °C (**a**), 132.4 °C (**b**), 125.4 °C (**c**) during cooling process (magnification 100×)

128.2.2   Characterization

The phase transition temperatures and the associated enthalpy were determined by DSC with the temperature rising from 30 to 180 °C at 30 °C/min at first. Subsequently, the sample was cooled at 20 °C and then heated at 180 °C at 10 ° C/min as DSC curve shown in Fig. 128.2. The optical textures were studied by a polarizing microscope (POM) with a hot stage. The sample was heated (10 °C/min) at 135 °C (isotropic phase) and then cooled (10 °C/min) at room temperature, and the typical focal-conic liquid crystal texture was observed only during the cooling process (Fig. 128.3). During the heating, in order to get the oriented samples, a small amount of the solid was sheared (spread with a spatula) on a glass slide lying on the stage at a temperature corresponding to the liquid crystalline domain. Shearing was repeated up to several times along the same direction until a thin film was formed.

128.3   Result and Discussion

In the DSC thermograms of the compound, two endothermic peaks located at 47.5 and 116.9 °C were observed during the second heating run identifying two phase transitions (Fig. 128.2). The DSC curve of the first cooling run exhibited only one

exothermic peak at 112.2 °C. During the cooling process, the typical focal-conic liquid crystal textures were observed and could be retained in room temperature under POM.

Figure 128.3 shows the process of phase transitions under polar microscope (POM), and the liquid crystal domain was increasing continuously with the birefringence phenomenon in a short time during the first cooling process. The evolution of the characteristic textures were displayed in Fig. 128.3, identifying that the discotic molecules self-organized to form the order columnar phase overcoming the defects of the molecular itself.

128.4 Conclusion

The novel 2-allyloxy-3,6,7,10,11-penta-pentyloxytriphenylene was firstly synthesized, and the structure was confirmed by the ^{1}H-NMR and FT-IR methods. The phase analysis was conducted by DSC, combining with POM. During the cooling process, the characteristic columnar mesophase with focal-conic texture were observed under POM, indicating that the order of molecular packing was proceeding in the domain areas by molecular self-assembly. In general, discotic liquid crystals consist of rigid core and flexible peripheral chains; however, the liquid crystal molecules with rigid lateral chains possessing order columnar mesophase were few reported. Meanwhile, the double bond in the bulk molecule proves function monomer available for the triphenylene-based discotic liquid crystals polymers prepared by the solution or photo-polymerization. In addition, the molecule with rigid and short lateral chain makes a difference in the contrastive study with that which has flexible and long lateral chain. It has a great potential for application such as organic solar cells, OLED electronic devices.

References

1. Sergeyev, S., Pisula, W., et al. (2007). Discotic liquid crystals: A new generation of organic semiconductors. *Chemical Society Reviews,*. doi:10.1039/b417320c.
2. Boden, N., Borner, R. C., et al. (1993). The synthesis of triphenylene-based discotic mesogens new and improved routes. *Liquid Crystals,*. doi:10.1080/02678299308036504.
3. Bushby, R. J., & Lozman, O. R. (2002). Photoconducting liquid crystals. *Current Opinion in Solid State and Materials Science,*. doi:10.1016/S1359-0286(03)00007-X.
4. Chandrasekhar, S., Sadashiva, B. K., & Suresh, K. A. (1977). Liquid crystals of dis-like molecules. *Pramana,*. doi:10.1007/BF02846252.
5. Kumar, S. (2005). Triphenylene-based discotic liquid crystal dimers, oligomers and polymers. *Liquid Crystals,*. doi:10.1080/02678290500117415.

6. Kumar, S., et al. (1998). Synthesis of functionalized triphenylenes by selective ether cleavage with B-bromocatecholborane. *Synthesis,*. doi:10.1055/s-1998-2133.
7. Hoeben, F. J. M., et al. (2005). About superamolecular assemblies of π-conjugated systems. *Chemical Reviews,*. doi:10.1021/cro30070z.
8. An, Z., et al. (2005). High electron mobility in room-temperature discotic liquid-crystalline perylene diimides. *Advanced Materials,*. doi:10.1002/adma.200500027.
9. Wu, J., Pisula, W., et al. (2007). Graphenes as potential material for electronics. *Chemical Reviews,*. doi:10.1021/cr068010r.

Chapter 129
Synthesis and Photoreaction of Poly[4-(6-Methacryloxyhexyloxy) Biphenyl-7-(6-Hexyloxy)Coumarin]

Yuanli Sun, Weimin Zhang, Jin Cao and Jialing Pu

Abstract 4-(6-Methacryloxyhexyloxy)biphenyl-7-(6-hexyloxy)coumarin (M) and its polymer poly[4-(6-Methacryloxyhexyloxy)biphenyl-7-(6-hexyloxy)coumarin] (P) were synthesized. The structure of the monomer was confirmed by ^{1}H NMR and IR. The liquid crystal property was studied by DSC and polarizing optical microscope. Irradiating the polymer film with LPUV light can generate an axis-selective photoreaction. By changing exposure temperature, when the film was irradiated over clearing point temperature, the photoreaction rate was faster than at the room temperature. In addition, when exposure energy was 3180 mJ/cm^2, the photochemical reaction was carried out at room temperature, while when exposure energy was 2544 mJ/cm^2, the photochemical reaction reached saturation over clearing point temperature. Finally, annealing the exposed film was conducted to investigate the change of the optical anisotropy. The results show the photoinduced optical anisotropy ΔA has mostly not changed after annealing.

Keywords Liquid crystal · Coumarin · Photoinduced optical anisotropy · Photoalignment

129.1 Introduction

Liquid crystal is a transition state between solid and liquid. At the same time, it has the property of phase-ordering like amorphous material, as well as fluidity like liquid material. Liquid crystal molecules can rearrange under the condition of

Y. Sun (✉) · W. Zhang (✉) · J. Cao · J. Pu
Lab. Printing and Packaging Material and Technology,
Beijing Institute of Graphic Communication, Beijing, China
e-mail: syl01007@sina.com

W. Zhang
e-mail: zhangweimin@bigc.edu.cn

electric field, magnetic field, temperature, stress, and so on. There are many ways to induce liquid crystal alignment, such as friction method, inclined evaporation method, and LB technique. [1–3]. Since the twentieth century, photoalignment technique has attracted more and more attention. It is a non-contact method. To perform photoalignment, a substrate must be coated with a layer of photosensitive material whose molecules can orientate in an ordered manner under irradiation by light. The photoalignment materials and the development of photoalignment technology have become an important topic nowadays. Three classes of photochemistry materials have been investigated, in which the first involves the photochromic reaction of azobenzenes and stilbenes. The second class displays [2 + 2] photodimerization of cinnamates, chalcones, and coumarins. The last is the photolysis of imide groups of polyimides [4–6].

The polymer containing coumarin photosensitive group has the properties of thermal stability and photochemical stability, and the photochemical reaction is not occur photoisomerization. Therefore, in this paper, we synthesis the polymer containing coumarin group and use it into optical orientation. When the photoreactive polymeric film is exposed to linearly polarized (LP) light, a small optical anisotropy is created based on a polarization-axis-selective photoreaction; the axis-selective photoreactive groups act as a photo-crosslinked anchor, when liquid crystal molecules are annealed at liquid crystal temperature, liquid crystal molecules will orient in accordance with the direction of anchoring force as to the characters of the self-assembly. However, in the non-exposure areas, liquid crystal molecules do not generate photochemical reactions and no anchoring force, and the arrangement of molecules is disordered. Therefore, it produces the different orientation in exposure and non-exposure areas and forms the visual difference. It can be used in liquid crystal displays.

129.2 Experimental Section

129.2.1 Materials and Instruments

2,2′-Dihydroxybiphenyl, 98 %. 1,6-Dibromohexane, 98 %. 7-Hydroxycoumarin, 98 %. 2,2′-Azoisobutyronitrile (AIBN), 99 %. Other organic reagents were purified and dehydrated before used.

^{1}H NMR spectra were obtained on an ANMR-ARX400 spectrometer, and FTIR spectra were recorded on a SHIMADZU FTIR-8400 spectrometer. The liquid crystal properties were examined using a polarizing optical microscope (POM-LEICA DM4500P) and differential scanning calorimetry (DSC-NETZSCH DSC 200PC) analysis at a heating and cooling rate of 10 °C/min. LPUV light, which had an intensity of 0.53 mW/cm^2 by using HXUV300 Xenon Light Source, was used in the photoreaction. Color filter with centre wavelength is 320 nm, and the half wave width is 15 nm. A ultraviolet polarizer is 240–320 nm.
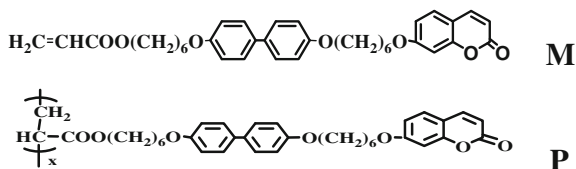
Fig. 129.1 Chemical structure of monomer and polymer

129.2.2   Molecules Synthesis

A monomer 4-(6-Methacryloxyhexyloxy)biphenyl-7-(6-hexyloxy)coumarin was synthesized according to the literatures [7]. The poly[4-(6-Methacryloxyhexyloxy) biphenyl-7-(6-hexyloxy)coumarin] was synthesized from corresponding monomer by a free-radical solution polymerization in dehydrated DMF with AIBN as initiator. Chemical structure is shown in Fig. 129.1. The structure of the monomer was confirmed by ^{1}HNMR and IR.^{1}HNMR (CDCl$_3$): δ (ppm) 1.46 ~ 1.73 (m, 8H, CH$_2$), 1.75 ~ 2.22 (m, 8H, CH$_2$), 3.91 ~ 4.06 (t, 6H, OCH$_2$), 4.16 ~ 4.2 (t, 2H, COOCH$_2$), 5.8 ~ 6.26 (t, 3H, CH$_2$ = CH), and 6.23 ~ 7.65 (d, 13H, Ar–H). FTIR (KBr, cm^{-1}): 3064 cm^{-1} (C = C); 2933, 2858 cm^{-1} (CH$_2$); 1722 cm^{-1} (C = O); 1616, 1498 cm^{-1} (C = C in Ar); and 1201 cm^{-1} (C–O–C).

129.2.3   The Preparation of Polymer Film

Thin polymer films were prepared by spin coating a chloroform solution of polymers (2 % w/w) onto the deoiled quartz. The speed of the spin coating was 2000 rpm, and time was 20 s. The film thickness was approximately 0.15 μm. The sample was dried in an open-air oven at 100 °C for 10 min.

129.3   Results and Discussion

129.3.1   Liquid Crystal Property of Molecules

The property of liquid crystal was studied by DSC and polarizing optical microscope. The liquid crystal temperature range of the monomer is 85–131.1 °C. In the liquid crystal temperature range, a SmA liquid crystal texture was observed in the POM. Liquid crystal property of polymer was investigated as well, and the DSC shows two exothermic peaks, corresponding to the temperature for 86.5 and 108 ° C, respectively. But we did not observe the liquid crystal texture in polarizing optical microscope. It is possible that the texture of the polymer is not easy to grow, so the liquid crystal property of the polymer is to be investigated.

129.3.2 Photoreaction of Polymer Film

The UV–vis absorption peaks of the polymer film on quartz substrates at around 285 and 325 nm, correspond to the wavelength of the biphenyl group and coumarin unit, respectively. Photoreaction of polymer is known to undergo a [2 + 2] cycloaddition reaction of coumarin group [8]. The degree of photoreaction (DP) is estimated by monitoring the decrease in absorbance at 325 nm using UV spectroscopy, and DP is expressed as

$$DP = \left[(ABS)_t - (ABS)_{t0}\right] / \left[(ABS)_T - (ABS)_{t0}\right]$$

where $(ABS)_{t0}$ is the ultraviolet absorption value before exposure, $(ABS)_t$ is the ultraviolet absorption value of any exposure time, and $(ABS)_T$ is the maximum value of ultraviolet absorption.

Figure 129.2 shows the absorbance of the polymer film in the parallel and perpendicular polarization optical vector direction at 325 nm, where $A_{\parallel}$ and $A_{\perp}$ are the absorbances parallel and perpendicular to E, respectively. With the increase of exposure, the absorbance of both parallel direction and perpendicular direction decreased, this is due to the photoreaction of the coumarin group. While the photoreaction rate in the parallel direction is faster than in the perpendicular direction, it shows that irradiating with the linearly polarized UV light causes an axis-selective photoreaction in polymeric films.

Figure 129.3 shows the degree of the photoreaction as a function of exposure energy under different irradiation conditions. It shows that the photoreaction was much faster at 110 °C than at 30 °C. Irradiated at higher temperature, the exposure energy was 2544 mJ/cm^2, the photochemical reaction reached saturation, while at room temperature, the exposure energy was 3180 mJ/cm^2, and the photochemical

Fig. 129.2 The absorbance of the polymer film in the parallel and perpendicular direction
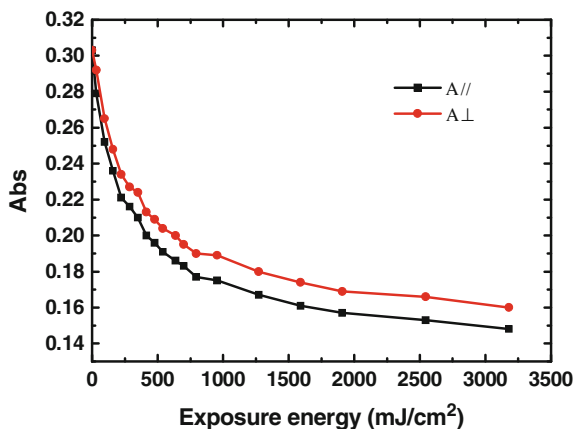
Fig. 129.3 The photoreaction degree of polymer
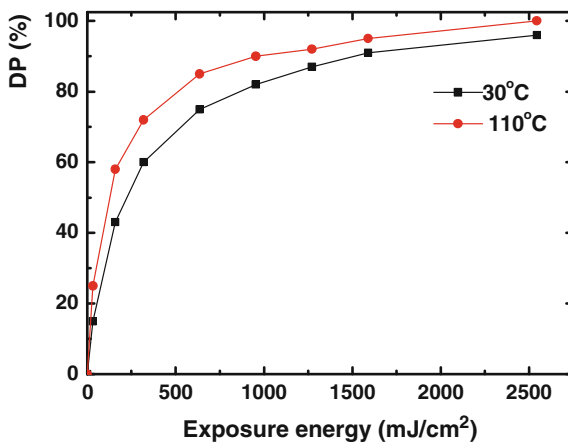
reaction was finished. The fast photoreaction in high temperature arises from the high mobility of the chromophore and the preferable arrangement of the coumarin group for the photoreaction.

129.3.3 Photochemical Orientation of Polymer

Irradiating the polymer film at room temperature, the exposure energy was 318 mJ/cm^2. The exposed film was annealed in the temperature between 86 and 108 °C. Orientation effect was investigated after annealing. Figure 129.4 shows the changes of optical anisotropy after annealed for 20 min. Photoinduced optical

Fig. 129.4 Optical anisotropy of polymer film as a function of annealing temperature
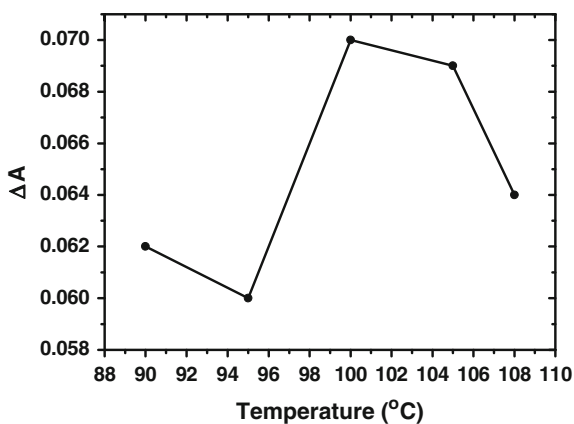
anisotropy ΔA is expressed as $\Delta A = A_\perp - A_{//}$, and the orientation direction is perpendicular to E of the linearly polarized ultraviolet light for $\Delta A > 0$ and parallel for $\Delta A < 0$. The maximum optical anisotropy ΔA value (0.07) was obtained when the film was annealed at 100 °C. Annealing the exposed polymer film, the obvious amplification should be obtained [9], but for the polymer film, the amplification of optical anisotropy is essentially unchanged. So we can draw a conclusion that the photocross-linkable polymer did not induce molecular reorientation after annealing the exposed film.

129.4   Conclusion

The monomer and polymer containing coumarin group were synthesized, the monomer had liquid crystal property, and the liquid crystal property of the polymer is to be investigated further. The polymer film was exposed with the linearly polarized ultraviolet light, and the photochemical reaction and orientation were investigated. Results show that irradiating the film with LPUV light can generate the axis-selective photoreaction. When the film was irradiated at high temperature, the photoreaction rate was faster than irradiated at the room temperature. Annealing the exposed polymer film between 86 and 108 °C, the amplification of optical anisotropy is essentially unchanged. So the photocross-linkable polymer did not induce molecular reorientation after annealing the exposed film.

References

1. Toney, M. F., Russell, T. P., Logan, J. A., Kikuchi, H., Sands, J. M., & Kumar, S. K. (1995). Near-surface alignment of polymers in rubbed films. *Nature, 374*, 709–711. (London).
2. Seki, T., Fukuda, R., Tamaki, T., & Ichimura, K. (1994). Alignment photoregulation of liquid crystals on precisely area controlled azobenzene Langmuir-Blodgett monolayers. *Thin Solid Films, 243*, 675–678.
3. Bechtold, I. H., De Santo, M. P., Bonvent, J. J., Oliveira, E. A., Barberi, R., & Rasing, T. (2003). Rubbing-induced charge domains observed by electrostatic force microscopy: Effect on liquid crystal alignment. *Liquid Crystals, 30*, 591–598.
4. Ichimura, K., Akiyama, H., Ishizuki, N., & Kawanishi, Y. (1993). Command surfaces, 6 Azimuthal orientation of liquid crystals photo-controlled by an azobenzene pendent polymer. *Rapid Communications, 14*, 813–817.
5. Schadt, M., Seiberle, H., & Schuster, A. (1996). Optical patterning of multidomain liquid-crystal displays with wide viewing angles. *Nature, 381*, 212–215.
6. Hasegawa, M., & Taira, Y. (1995). Nematic homogeneous photo alignment by polyimide exposure to linearly polarized UV. *Journal of Photopolymer Science and Technology, 8*, 241–248.
7. Kawatsuki, N., Takatani, K., Yamamoto, T., & Sangen, O. (1997). Synthesis, characterization and photoreaction of side-chain liquid-crystalline polymers and copolymers comprising alkenyloxy-biphenyl mesogen. *Macromolecular Chemistry and Physics, 198*, 2853–2866.

8. Kim, C., Trajkovska, A., Wallace, Jason U., & Chen, Shaw H. (2006). New insight into photoalignment of liquid crystals on coumarin-containing polymer films. *Macromolecules, 39*, 3817–3823.
9. Kawatsuki, N., Tsumi, R., Hiraiwa, A., Takatsuka, H., & Sakai, T. (2008). Thermally enhanced photoinduced in-plane reorientation in photo-cross-linkable polymer liquid crystalline films and its application to linear polarizer. *Journal of Polymer Science Part A: Polymer Chemistry, 46*, 4712–4718.

Chapter 130
Optimized Surfactants Suitable for Alcohol-Free Fountain Solution

Lianfang Li, Weimin Wang, Yiyi Zhou and Chengyuan He

Abstract Green printing is generally defined as using a product that has a lesser or reduced negative effect or increased positive effect on human health and the environment. However, the contemporary fountain solution mostly utilized in printing production contains alcohol, which is not so environmentally friendly and not beneficial to the realization of green printing. Therefore, it is highly necessary to develop an environment-friendly alcohol-free fountain solution. In this paper, one alcohol-free fountain solution, with high wetting effect, stable performance, and economical benefit, was accomplished by means of selecting the surfactants and optimizing the fountain solution system. The results indicate that prepared alcohol-free fountain solution can not only meet printing requirements but also be environmentally sustainable.

Keywords Alcohol-free · Fountain solution · Surfactant · Optimized formula

130.1 Introduction

Green printing strongly requests to use a product that has a lesser or reduced negative effect or increased positive effect on human health and the environment. The defect of offset printing fountain solution with alcohol from market is volatile and expensive [1]. It is well known that alcohol is not healthy for workers and causes pollution to the environment. Therefore, it is of great importance to study on alcohol-free fountain solution.

L. Li · W. Wang (✉) · Y. Zhou · C. He
School of Printing and Packaging, Beijing Institute of Graphic Communication,
Beijing, China
e-mail: wangweimin@bigc.edu.cn

L. Li
e-mail: lilianfang@bigc.edu.cn

1053

130.2   Results and Discussion

The whole research includes 5 steps to optimize the formula of alcohol-free fountain solution: (1) determination of basic formula, (2) determination of ideal value for the surfactant, (3) selection of ideal surfactant by means of experiment, (4) the preparation of alcohol-free fountain solution and selection of ideal formula, and (5) verification of results of selected surfactant by printing.

130.2.1   The Selection of Surfactant

Because the fountain solution must form a uniform water-phase membrane in the blank part of the printing plate, the surfactant should preferably reduce the surface tension of water and have good wetting property. The speed of printing is so fast that the surfactant should have relatively good spreading ability. Many impurities come into printing system on the printing plate and other places during the printing process. Excessive accumulation of these impurities will affect the normal printing, thus the surfactant should have cleaning effect enough to maintain a high printing resistance. When the surfactant is added into fountain solution, the less foam is better, because too much foam will affect printing process. Thus, we think that the ideal surfactant should satisfy these conditions mentioned above.

With recommending from surfactant manufacturers and combining with parameters of fountain solution, we chose 7 surfactants below: heterogeneous 10-carbon alcohol polyoxyethylene alcohol (represented as A), long-chain carboxylic acid ester polyoxyethylene sulfonate (LMES, as B), polyethylene glycol 400 (as C), fatty acid methyl ester ethoxylates (FMEE, as D), 10-carbon alcohol polyoxyethylene ether isomers (as E), and polyglycol lauryl ether (AEO-7, as F).

130.2.2   Determining the Ideal Parameters for Alcohol-Free Fountain Solution

By the performance analysis of the alcohol-free fountain solution from the market, the parameters of ideal alcohol-free fountain solution expected in this experiment were determined, as shown in Table 130.1 [2–4].

According to Table 130.1, the average values of pH, surface tension, and conductivity after diluting by 20 times as the standard of alcohol-free fountain solution should be about 4.7, 33.00 mN/m, and 916.7 μs/cm, respectively.

Table 130.1 The performance of alcohol-free fountain solution from native market

Brands from market		Xinsujie	Some brand 1	Some brand 2	Average value
Original liquid	Surface tension value (mN/m)	29.31	26.98	26.10	27.46
	pH	3.54	2.86	3.52	3.31
	Conductivity (μs/cm)	–	–	–	–
Diluted solution	Surface tension value (mN/m)	32.95	37.20	28.87	33.00
	pH	4.68	4.48	4.94	4.70
	Conductivity (μs/cm)	810	880	1060	916.7

Note Dilution solution formed from the stock solution added with 20-fold of water (v/v)

130.2.3   Optimizing Formula for Alcohol-Free Fountain Solution by Choosing Surfactants [5, 6]

We think that the key performance indicators of alcohol-free fountain solution are surface tension, pH value, and conductivity values in offset printing. The first, most parameter, is the surface tension value, which determines the performance of fountain solution. The main performance is the affinity capacity of fountain solution in the blank part of the plate. It plays an important role in printing completion and printing quality. The second is the pH value. It impacts the resistance rate of printing plates; at the same time, it affects the drying properties of the ink. Finally, the conductivity value has an extent influence on the comprehensive indicators of fountain solution, but its tolerance is relatively large. Therefore, the study that determines the surface tension of the fountain solution plays an important role in the pros and cons of the fountain solution. Of course, the pH value and conductivity are used as unchanging factors in this experiment.

In order to find the ideal alcohol-free fountain solution, this experiment only changed the surfactants with the same basic formula of fountain solution (found in experimental part). Comparative experiments were conducted by using different surfactants and by measuring the surface tension value of fountain solution. The surface tensions of both original liquid and dilution liquid are shown in Table 130.2.

As shown in Table 130.2, surface tensions of the pre-dilution and post-dilution containing surfactant D and F are ideal. The surface tension is closer to the ideal value when the added quantity of surfactant D and F is 0.8 ml per 100 ml. The results of A, B, C, and E were far away from the ideal model. Thus, we gave a conclusion that both surfactants D and F are ideal surfactants.

Table 130.2 The surface tension of pre-dilution (M) and post-dilution (N) (mN/m)

Groups	1		2		3		4		5		Effect judgment
	M	N	M	N	M	N	M	N	M	N	
A	28.10	29.68	23.50	27.85	6.89	28.88	6.62	26.31	28.55	16.79	More foam
B	37.84	69.70	33.43	66.68	32.19	62.13	30.89	60.77	29.84	58.90	Surface tension is not ideal
C	43.64	69.53	41.83	65.74	40.36	66.32	38.33	61.56	37.78	60.54	Surface tension is not ideal
D	31.55	44.37	27.43	40.31	25.66	36.19	23.58	33.43	22.87	30.99	Ideal
E	44.76	71.34	40.68	65.38	36.94	60.65	32.14	55.17	31.54	53.77	Not soluble, volatile
F	29.43	40.56	27.51	36.44	25.64	33.87	24.46	33.31	23.99	31.98	Ideal

Table 130.3 Parameters of printing and amount of water (fountain solution containing D and F, respectively)

	Water temperature (°C)	Machine speed (sheets/hour)	Amount of water (%)	Number of printed sheets
D	9.6	4000	64	6000
F	8.6	8000	58	5000

Note The printing equipment is Heidelberg SM-52 with Bauhinia brand ink and 157 g/m^2 coated paper

130.2.4 Printing Test

In order to verify the performance of the above-mentioned ideal dampening solution, a printing test was conducted with only replaced fountain solution, while other conditions remain unchanged. If the printing process could work as usual with replaced fountain solution, it means that the fountain solution can be considered to meet printing requirements.

Without transferring paper, only the beginning twenty piece of paper appeared dirty. This situation is close to the fountain solutions from market which is used in the normal printing. As shown in Table 130.3, it is the parameters of printing and amount of water needed with fountain solution containing D and F, respectively. The amount of water needed is 64 and 58 % compared with the fountain solution from the present market, respectively. Under normal printing conditions remaining unchanged, the printing effect was very satisfactory. The blank part of the printed matter was very clean and the ink of the graphic part was thick. Following that, the surfactants D and F are suitable for alcohol-free fountain solution.

130.3 Experimental

130.3.1 Materials and Instruments

The reagents used include heterogeneous 10-carbon alcohol polyoxyethylene alcohol (represented as A, Guangdong Jun Xin Chemical), long-chain carboxylic acid ester polyoxyethylene sulfonate (LMES represented as B, Guangdong Jun Xin Chemical), Polyethylene glycol 400 (represented as C, Guangdong Jun Xin Chemical), fatty acid methyl ester ethoxylates (FMEE represented as D, Jiangsu Haian Chemical Factory), 10-carbon alcohol polyoxyethylene ether isomers (represented as E, Jiangsu Haian Chemical Factory), polyglycol lauryl ether (AEO-7 represented as F, Nantong Zhanyi Chemical Co., Ltd.). Acacia, magnesium nitrate, phosphate, disodium hydrogen phosphate, diethylene glycol diethyl ether, diethylene glycol monomethyl ether (Tianjin Guangfu Institute of Superfine Chemical Industry). The main experimental apparatuses include conductive meter (Shanghai Zhiguang Instrument Co. Ltd.), acidity tester (Shanghai Zhiguang Instrument Co. Ltd.), and surface tension meter [K100-type static surface tension meter (Germany Kruss Company)].

Table 130.4 The basic formula of the fountain solution

Materials	Feeding quantity	Materials	Feeding quantity
Arabia gum	3.0 g	Epoxy propane	0.50 ml
Magnesium nitrate	0.8 g	Formaldehyde solution	0.30 ml
Phosphate	1.0 ml	Anti foaming	0.10 ml
Sodium hydrogen phosphate	0.80 g	Agent (ST-TX) fountain solution	0.10 ml X
Diethylene glycol ether	1.5 ml	(ST-NTH) surfactant	100 ml
Diethylene glycol ethyl ether	1.5 ml	Deionized water	

Note In all experiments, except changing the type of surfactants, other conditions are the same

130.3.2 Basic Formula of the Fountain Solution [5, 6]

See Table 130.4.

130.3.3 Method of Determining Ideal Value for the Alcohol-Free Fountain Solution

Three stock solutions of alcohol-free fountain solution were purchased from native market. Then, they, including the pre-dilution and post-dilution, are tested by conductive meter, acidity tester, and surface tension meter. At last, their pH, surface tension, and conductivity are measured, and their average values are acquired after being calculated.

130.3.4 Measuring for the Alcohol-Free Fountain Solutions with Different Surfactants

In whole experimental processes, the formula of fountain solution is the same like basic formula except that only the surfactants are changed.

Specific methods and steps are as follows: First, we take surfactant A as an example to explain this method. The original liquid A-M was prepared according to the basic formula in Table 130.2. Surfactant A is measured as 0.2, 0.4, 0.6, 0.8, and 1.0 ml, respectively, and the surfactant is then added to 100 ml demonized water accompanying other materials shown in Table 130.4. The sequence number is shown as A-M-1, A-M-2, A-M-3, A-M-4, and A-M-5, respectively, and their surface tensions are measured and recorded in Table 130.2. Then, the above 5 solutions are diluted by 20-fold water according to the ratio of v/v; their surface

tensions are measured again and recorded as A-N-1, A-N-2, A-N-3, A-N-4, and A-N-5, respectively, as shown in Table 130.2. Other surfactants such as B, C, D, E, and F also are done repeatedly and the data are recorded in sequence in Table 130.2 as B-M-1, B-M-2, B-M-3, B-M-4, and B-M-5, B-N-1, B-N-2, B-N-3, B-N-4, and B-N-5; C-M-1, C-M-2, C-M-3, C-M-4, and C-M-5, C-N-1, C-N-2, C-N-3, C-N-4, and C-N-5; D-M-1, D-M-2, D-M-3, D-M-4, and D-M-5, D-N-1, D-N-2, D-N-3, D-N-4, and D-N-5; E-M-1, E-M-2, E-M-3, E-M-4, and E-M-5, E-N-1, E-N-2, E-N-3, E-N-4, and E-N-5; F-M-1, F-M-2, F-M-3, F-M-4, and F-M-5, F-N-1, F-N-2, F-N-3, F-N-4, and F-N-5.

130.3.5 Printing Test

The printing experiments were carried at the Educational Practice Center, Beijing Institute of Graphic Communication. The printing equipment came from Heidelberg SM-52 with Bauhinia brand ink and 157 g/m^2 coated paper. Only the fountain solution was replaced, other condition of the experiment remained unchanged in normal condition of printing. The parameters of printing and amount of water needed are shown in Table 130.3.

130.4 Conclusions

Based on the evaluations of the fountain solutions containing seven different surfactants mentioned above, it is found out that the fountain solution containing fatty acid methyl ester ethoxylate (FMEE) and polyglycol lauryl ether (AEO-7) is the ideal fountain solution. Such alcohol-free fountain solutions are environmentally sustainable and wonderfully meet the needs of printing.

References

1. Zhang, Y. (2006). The application of fountain solution in the printing technology and the influence factors. *Printing World, 1*, 62–64.
2. Li, Y.-L. (2007). Brief talking of function solution in offset printing. *Printing World, 6*, 4–6. (Xi'an University of Technology).
3. Li, M. (2006). The investigation and analysis of normal index of fountain solution. *Printing Technology, 28*, 43–45.
4. Fang, J. (2011). The performance of alcohol-free fountain solution. *Printing Technology, 1*, 60–61.
5. Pang, L.-J. (2000). The adhesion and cohesion in moist phenomenon. *Journal of Guizhou Normal University, 11*, 89–91.
6. Wang, S.-Q. (2007). Fountain solution used in offset printing. *Imaging Technology, 2*, 41–47.